

# 2020

# **Mg** Magnesium Technology

EDITED BY  
J. Brian Jordon  
Victoria Miller  
Vineet V. Joshi  
Neale R. Neelameggham

---

## **The Minerals, Metals & Materials Series**



---

J. Brian Jordon • Victoria Miller •  
Vineet V. Joshi • Neale R. Neelameggham  
Editors

# Magnesium Technology 2020

TMS

 Springer

*Editors*

J. Brian Jordon  
The University of Alabama  
Tuscaloosa, AL, USA

Victoria Miller  
University of Florida  
Gainesville, FL, USA

Vineet V. Joshi  
Pacific Northwest National Laboratory  
Richland, WA, USA

Neale R. Neelameggham  
IND LLC  
South Jordan, UT, USA

ISSN 2367-1181                      ISSN 2367-1696 (electronic)  
The Minerals, Metals & Materials Series  
ISBN 978-3-030-36646-9              ISBN 978-3-030-36647-6 (eBook)  
<https://doi.org/10.1007/978-3-030-36647-6>

© The Minerals, Metals & Materials Society 2020, corrected publication 2020

This work is subject to copyright. All rights are reserved by the Publisher, whether the whole or part of the material is concerned, specifically the rights of translation, reprinting, reuse of illustrations, recitation, broadcasting, reproduction on microfilms or in any other physical way, and transmission or information storage and retrieval, electronic adaptation, computer software, or by similar or dissimilar methodology now known or hereafter developed.

The use of general descriptive names, registered names, trademarks, service marks, etc. in this publication does not imply, even in the absence of a specific statement, that such names are exempt from the relevant protective laws and regulations and therefore free for general use.

The publisher, the authors and the editors are safe to assume that the advice and information in this book are believed to be true and accurate at the date of publication. Neither the publisher nor the authors or the editors give a warranty, expressed or implied, with respect to the material contained herein or for any errors or omissions that may have been made. The publisher remains neutral with regard to jurisdictional claims in published maps and institutional affiliations.

This Springer imprint is published by the registered company Springer Nature Switzerland AG  
The registered company address is: Gewerbestrasse 11, 6330 Cham, Switzerland

---

## Preface

Magnesium and its alloys are being investigated widely for applications that require extraordinarily high strength-to-weight ratio, vibration damping, electromagnetic shielding, reduction in carbon footprint, sustainability improvements, and low toxicity. In the past decade or so, this drive has led to increased adoption of magnesium and its alloys in everyday products and it is no longer regarded as an esoteric material. The overarching goal of its widespread adoption and replacement of conventional materials such as steel and aluminum alloys has been restricted because of the cost of the material, limited sources of primary material, alloying constraints, high chemical reactivity, and challenges associated with its plasticity. Researchers, scientists, engineers, and economists from industry, government agencies and laboratories, and academic institutions alike are actively developing roadmaps for next-generation products and addressing these challenges as quickly as possible through unique and innovative methods. The TMS Magnesium Committee has been actively involved in providing a platform to these entities for disseminating the latest information, developments, and cutting-edge research and development, and showcasing the latest research and development trends related to magnesium and its alloys through the Magnesium Technology Symposium, which takes place every year at the TMS Annual Meeting. This proceedings volume retains the essence of this longstanding tradition. The twenty-first volume in the series, *Magnesium Technology 2020*, is the proceedings of the Magnesium Technology Symposium held during the 149th TMS Annual Meeting & Exhibition in San Diego, CA, February 23–27, 2020. The volume captures commentaries and papers from 15 different countries. The papers have been categorized systematically based on topics pertaining to magnesium production, casting and solidification, thermomechanical processing, deformation mechanisms, modeling, corrosion, and applications.

The symposium began with keynote sessions that featured several distinguished invited speakers from government organizations and academia, who provided their perspectives on the state of the art, goals, and opportunities in magnesium alloy research and development. Dr. Carlos Tomé from Los Alamos National Laboratory, U.S. Department of Energy, discussed 3D characterization of mechanical twins across grain boundaries. This was followed by a talk on hierarchically structured ultrafine-grained magnesium alloys by Dr. Rajiv Mishra from the University of North Texas, USA, who presented an example of using friction stir additive manufacturing for implementing such microstructures at a component level. Dr. Mark Horstemeyer from Liberty University, USA, presented an overview of fatigue modeling to capture the corrosion-fatigue behavior of magnesium alloys. The final talk in this session was presented by Dr. Bin Jiang from Chongqing University, China, who presented a novel extrusion approach for achieving high-strength magnesium alloy plates.

Finally, the 2019–2020 Magnesium Committee is grateful to and expresses deep appreciation for all authors for contributing to the success of the symposium; our panel of distinguished keynote speakers for sharing their valuable thoughts on the future of magnesium

technology; the reviewers for their best efforts in reviewing the manuscripts; and the session chairs, judges, TMS staff members, and other volunteers for their excellent support, which allowed us to develop a successful, high-quality symposium and proceedings volume.

J. Brian Jordon  
Chair

Victoria Miller  
Vice Chair

Vineet V. Joshi  
Past Chair

Neale R. Neelameggham  
Advisor

---

# Contents

## Part I Keynote Session

<b>Twin Transmission Across Grain Boundaries in Mg</b> . . . . .	3
Carlos N. Tomé, Mariyappan Arul Kumar, John Graham, Khanh Dang, Yue Liu, Pengzhang Tang, Shujuan Wang, Rodney J. McCabe, and Laurent Capolungo	
<b>Hierarchically Structured Ultrafine Grained Magnesium Alloys</b> . . . . .	7
Rajiv S. Mishra	
<b>Multistage Fatigue (MSF) Modeling of Magnesium in a Corrosion Environment</b> . . . . .	13
Mark F. Horstemeyer	
<b>Novel Texture Controlling of Mg Alloys</b> . . . . .	15
Bin Jiang, Guangsheng Huang, Jiangfeng Song, Dingfei Zhang, and Fusheng Pan	

## Part II Alloy Development

<b>Design of Ductile Rare-Earth-Free Magnesium Alloys</b> . . . . .	19
W. A. Curtin, Rasool Ahmad, Binglun Yin, and Zhaoxuan Wu	
<b>Microstructure Evolution and Precipitation Strengthening in Ca-Containing Mg-Rare Earth Alloys</b> . . . . .	25
Qianying Shi, Bruce Williams, and John Allison	
<b>A Die-Cast Magnesium Alloy for Applications at Elevated Temperatures</b> . . . . .	31
Xixi Dong, Eric A. Nyberg, and Shouxun Ji	
<b>Effect of Gd and Nd Additions on the Thermo-Mechanical Response of a MgMn Alloy</b> . . . . .	37
D. Tolnai, S. Gavras, P. Barriobero-Vila, A. Stark, and N. Schell	
<b>Development of Ultra Lightweight, Corrosion Resistant Mg Alloys</b> . . . . .	43
T. W. Cain and J. P. Labukas	

## Part III Alloy Design and Solidification

<b>Insights on Solidification of Mg and Mg–Al Alloys by Large Scale Atomistic Simulations</b> . . . . .	51
Avik Mahata and Mohsen Asle Zaeem	
<b>Two-Stage Settling Approach to Purify Mg Alloy</b> . . . . .	55
Jiawei Liu, Tao Chen, Yuan Yuan, Jiajia Wu, Li Yang, Aitao Tang, Dajian Li, and Fusheng Pan	

<b>CALPHAD Modeling and Microstructure Investigation of Mg–Gd–Y–Zn Alloys</b> . . . . .	61
Janet Meier, Josh Caris, and Alan A. Luo	
<b>Intermetallic Phase Formation in Mg–Ag–Nd (QE) and Mg–Ag–Nd–Zn (QEZ) Alloys</b> . . . . .	71
Rainer Schmid-Fetzer, Jian-Feng Nie, Xiaojun Zhao, and Houwen Chen	
<b>Investigation on the Microstructure and Mechanical Properties of Mg–Gd–Nd Ternary Alloys</b> . . . . .	79
Yuling Xu, Lixiang Yang, Weili Liu, Jingli Sun, Lu Xiao, Xianquan Jiang, and Norbert Hort	
<b>Recrystallization Effects on the Forming Behaviour of Magnesium Alloy Sheets with Varied Calcium Concentration</b> . . . . .	87
Jan Bohlen, Huu Chanh Trinh, Klaus Rätzke, Sangbong Yi, and Dietmar Letzig	
<b>Towards the Development of High Ductility Mg–Al Based Alloys Through Second-Phase Refinement with Trace Yttrium Additions</b> . . . . .	95
Konstantinos Korgiopoulos and Mihriban Pekguleryuz	
<b>Design of Heat-Dissipating Mg–La–Zn Alloys Based on Thermodynamic Calculations</b> . . . . .	101
Hui Shi, Qun Luo, Qian Li, Jieyu Zhang, and Kuo-Chih Chou	
<b>Effects of Zn Additions on the Room Temperature Formability and Strength in Mg–1.2Al–0.5Ca–0.4Mn Alloy Sheets</b> . . . . .	105
Z. H. Li, T. T. Sasaki, M. Z. Bian, T. Nakata, Y. Yoshida, N. Kawabe, S. Kamado, and K. Hono	
<b>Part IV Fundamentals, Mechanical Behavior, Twinning, Plasticity, and Texture I</b>	
<b>An Investigation into the Role of Dislocation Climb During Intermediate Temperature Flow of Mg Alloys</b> . . . . .	115
Michael A. Ritzo, Jishnu J. Bhattacharyya, Ricardo A. Lebensohn, and Sean R. Agnew	
<b>Deviations from Theoretical Orientation Relationship Along Tensile Twin Boundaries in Magnesium</b> . . . . .	123
B. Leu, M. Arul Kumar, Y. Liu, and I. J. Beyerlein	
<b>The Role of Faceting in <math>\{10\bar{1}2\}</math> Twin Nucleation</b> . . . . .	129
Christopher D. Barrett	
<b>In Situ TEM Investigation of <math>\langle c + a \rangle</math> Dislocations in Magnesium</b> . . . . .	135
Bo-Yu Liu, Fei Liu, Bin Li, Jian-Feng Nie, and Zhi-Wei Shan	
<b>Full-Field Crystal Plasticity Modeling of <math>\{10\bar{1}2\}</math> Twin Nucleation</b> . . . . .	141
YubRaj Paudel, Christopher D. Barrett, and Haitham El Kadiri	
<b>The Incorporation of Discrete Deformation Twins in a Crystal Plasticity Finite Element Framework</b> . . . . .	147
Matthew Kasemer and Paul Dawson	

<b>On the Load Multiaxiality Effect on the Cyclic Behaviour of Magnesium Alloys</b> .....	151
A. Gryguć, S. M. H. Karparvarfard, A. Roostaei, D. Toscano, S. Shaha, B. Behraves, and H. Jahed	
<b>Part V Thermomechanical Processing</b>	
<b>Deformation Driven Precipitation in Binary Magnesium Alloys</b> .....	163
Suhas Eswarappa Prameela and Timothy P. Weihs	
<b>Effect of Second Phase Particle Size on the Recrystallized Microstructure of Mg–Al Alloys Following ECAE Processing</b> .....	167
Suhas Eswarappa Prameela, Peng Yi, Vance Liu, Beatriz Medeiros, Laszlo J. Kecskes, Michael L. Falk, and Timothy P. Weihs	
<b>Relating Texture and Thermomechanical Processing Variables in Mg–Zn–Ca Alloys</b> .....	175
Tracy D. Berman and John E. Allison	
<b>Variation of Extrusion Process Parameter for the Magnesium Alloy ME21</b> .....	181
G. Kurz, M. Nienaber, J. Bohlen, D. Letzig, and K. U. Kainer	
<b>Asymmetric Rolling of TZ73 Magnesium Alloy to Improve Its Ductility</b> .....	189
Krishna Kamlesh Verma, Satyam Suwas, and Subodh Kumar	
<b>Friction Stir Processing of Magnesium Alloy with Spiral Tool Path Strategy</b> .....	197
Abhishek Kumar, Aarush Sood, Nikhil Gotawala, Sushil Mishra, and Amber Shrivastava	
<b>Joining Dissimilar Materials via Rotational Hammer Riveting Technique</b> .....	207
Tianhao Wang, Scott Whalen, Piyush Upadhyay, and Keerti Kappagantula	
<b>Part VI Corrosion</b>	
<b>Anomalous Hydrogen Evolution on Magnesium</b> .....	215
Aline D. Gabbardo and G. S. Frankel	
<b>Numerical Investigation of Micro-Galvanic Corrosion in Mg Alloys: Role of the Cathodic Intermetallic Phase Size and Spatial Distributions</b> .....	217
V. K. Beura, P. Garg, V. V. Joshi, and K. N. Solanki	
<b>The Corrosion Behavior of High Purity Mg According to Process History</b> .....	225
Sang Kyu Woo, Byeong-Chan Suh, Nam Ryong Kim, Ha Sik Kim, and Chang Dong Yim	
<b>Design of the Magnesium Composite with High Corrosion Resistance and High Deformability</b> .....	231
Yue-Cun Wang, Bo-Yu Liu, and Zhi-Wei Shan	
<b>Advanced Immersion Testing of Model Mg-Alloys for Biomedical Applications</b> .....	235
Dmytro Orlov, Bastien Reinwalt, Ilyes Tayeb-Bey, Lars Wadsö, Jelena Horky, Andrea Ojdanic, Erhard Schafner, and Michael Zehetbauer	
<b>Effect of 2 wt% Ag Addition on Corrosion Properties of ZK40 for Biodegradable Applications</b> .....	243
M. AbdelGawad, B. Mansoor, M. W. Vaughan, and I. Karaman	

<b>Study of In Vitro Biodegradation Behavior of Mg–2.5Zn–xES Composite</b> . . . . .	253
Srinivasan Murugan, Paul C. Okonkwo, Ahmed Bahgat, Gururaj Parande, Aboubakr M. Abdullah, and Manoj Gupta	
<b>Corrosion Behavior of Squeeze Cast Mg Alloy AM60-Based Hybrid Nanocomposite</b> . . . . .	259
Xinyu Geng, Luyang Ren, Zixi Sun, Henry Hu, and Xueyuan Nie	
<b>Part VII Solidification and Production of Magnesium</b>	
<b>Thermodynamic Descriptions of the Quaternary Mg–Al–Zn–Sn System and Their Experimental Validation</b> . . . . .	269
Ting Cheng and Lijun Zhang	
<b>Investigation and Modelling of the Influence of Cooling Rates on the Microstructure of AZ91 Alloys</b> . . . . .	281
S. Gavras, M. U. Bilal, D. Tolnai, and N. Hort	
<b>The Independent Effects of Cooling Rate and Na Addition on Hydrogen Storage Properties in Hypo-eutectic Mg Alloys</b> . . . . .	289
Manjin Kim, Yahia Ali, Stuart D. McDonald, Trevor B. Abbott, and Kazuhiro Nogita	
<b>Producing High Purity Magnesium (99.99%) Directly by Pidgeon Process</b> . . . . .	299
Bo Yang, Fei Liu, Bo-Yu Liu, Zhi-Min Chang, Lu-Yao Mao, Jiao Li, and Zhi-Wei Shan	
<b>Research on Properties of Prefabricated Pellets of Silicothermic Process After Calcination in Flowing Argon Atmosphere</b> . . . . .	303
Junhua Guo, Ting'an Zhang, Daxue Fu, Jibiao Han, Zonghui Ji, and Zhi'he Dou	
<b>Producing Pure Magnesium Through Silicothermic Under the Atmospheric Pressure</b> . . . . .	309
Fei Liu, Bo Yang, Bo-Yu Liu, Jiao Li, Zhi-Min Chang, and Zhi-Wei Shan	
<b>Effect of Temperature on Magnesium Vapor Condensation in Inert Carrier Gas</b> . . . . .	313
Jibiao Han, Ting'an Zhang, Daxue Fu, Junhua Guo, Zonghui Ji, and Zhihe Dou	
<b>Part VIII Fundamentals, Mechanical Behavior, Twinning, Plasticity, and Texture II</b>	
<b>Mapping Anisotropy and Triaxiality Effects in Magnesium Alloys</b> . . . . .	321
Padmeya P. Indurkar, Shahmeer Baweja, Robert Perez, Amol Vuppuluri, and Shailendra P. Joshi	
<b>Cold Formability of Extruded Magnesium Bands</b> . . . . .	329
Maria Nienaber, Jan Bohlen, Jose Victoria-Hernández, Sangbong Yi, Karl Ulrich Kainer, and Dietmar Letzig	
<b>The Effect of Plastic Deformation on the Precipitation Hardening Behavior of Biodegradable Mg–Sr–Ca–Zn Based Alloys</b> . . . . .	335
Matteo Nicolosi, Baoqi Guo, Mihriban Pekguleryuz, and Mert Celikin	
<b>Experimental Investigation of Raster Tool Path Strategy for Friction Stir Processing of Magnesium Alloy</b> . . . . .	341
Abhishek Kumar, Nikhil Gotawala, Aarush Sood, Sushil Mishra, and Amber Shrivastava	



---

<b>Quantitative Relationship Analysis of Mechanical Properties with Microstructure and Texture Evolution in AZ Series Alloys</b> . . . . .	347
Joung Sik Suh, Byeong-Chan Suh, Jun Ho Bae, Sang Eun Lee, Byoung-Gi Moon, and Young Min Kim	
<b>On the Influence of Twinning and Detwinning on the Deformation of Mg at the Micron Scale</b> . . . . .	355
Mohammadhadi Maghsoudi, Gyuseok Kim, Markus Ziehmer, and Erica T. Lilleodden	
<b>An Investigation on the Microstructure and Mechanical Properties of the Hot-Dip-Aluminized-Q235/AZ91D Bimetallic Material Produced by Solid-Liquid Compound Casting</b> . . . . .	361
Jun Cheng, Jian-hua Zhao, Yao Tang, and Jing-jing Shang-guan	
<b>Part IX Poster Session</b>	
<b>Effect of Zinc on Solidification and Aging Behaviour of Magnesium Alloys Containing Rare Earths</b> . . . . .	371
A. Javaid and F. Czerwinski	
<b>Influence of Manganese on Deformation Behavior of Magnesium Under Dynamic Loading</b> . . . . .	381
Ryutaro Goeda, Masatake Yamaguchi, Tatsuya Nakatsuji, Naoko Ikeo, and Toshiji Mukai	
<b>Microstructure and Hardness of Porous Magnesium Processed by Powder Metallurgy Using Polystyrene as the Space Holder</b> . . . . .	387
Ning Zou and Qizhen Li	
<b>Correction to: Effects of Zn Additions on the Room Temperature Formability and Strength in Mg-1.2Al-0.5Ca-0.4Mn Alloy Sheets</b> . . . . .	C1
Z. H. Li, T. T. Sasaki, M. Z. Bian, T. Nakata, Y. Yoshida, N. Kawabe, S. Kamado, and K. Hono	
<b>Author Index</b> . . . . .	393
<b>Subject Index</b> . . . . .	397

---

## About the Editors

---

### Lead Editor



**J. Brian Jordon** is Associate Professor in the Department of Mechanical Engineering at The University of Alabama. He has extensive experience in fatigue and fracture of metals, and in particular he has studied fatigue in solid state processing for over a decade. His other interests include process–structure–property relationships of lightweight metals, process modeling of welding and joining, and fracture of cold spray depositions. Recently he has been leading efforts in additive friction stir deposition (AFSD), a solid-state additive manufacturing technique, for fabrication and repairs of structural components. In particular, he is helping develop the AFSD process for hard-to-weld metals such as magnesium alloys. He has published more than 90 refereed journal articles and conference proceedings papers, and recently coauthored the book *Fatigue in Friction Stir Welding* (Elsevier). His research has been supported by the Department of Energy, the Department of Defense, the State of Alabama, and various private industries. Professionally, he has chaired committees and organized symposia at various international conferences including The Minerals, Metals & Materials Society (TMS) meetings. He was a recipient of the 2014 TMS Young Leaders Professional Development Award and was a finalist for the 2017 University of Alabama President’s Faculty Research Award. He currently serves on the editorial board of *Materials and Manufacturing Processes* journal. Prior to coming to The University of Alabama, he was Interim Associate Director and Assistant Research Professor at the Center for Advanced Vehicular Systems at Mississippi State University. He holds a Ph.D., M.S., and B.S. in mechanical engineering from Mississippi State University. Presently, he serves as Chair of the TMS Magnesium Committee.

## Magnesium Technology 2020 Editors



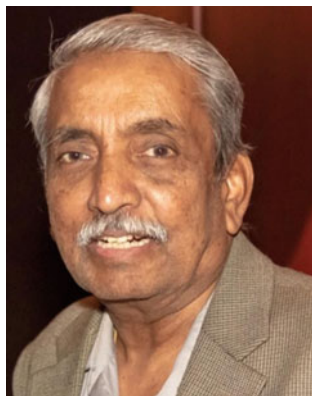
**Victoria Miller** has been Assistant Professor in the Department of Materials Science and Engineering at the University of Florida since September 2019. She was previously Assistant Professor at North Carolina State University from 2017 to 2019. Originally from Michigan, she received her B.S.E. in materials science and engineering from the University of Michigan in 2011 and completed her Ph.D. in materials at the University of California, Santa Barbara in 2016. After graduate school, she worked for a year at UES, Inc. onsite in the Materials and Manufacturing Directorate of the Air Force Research Laboratory in Dayton, Ohio. She also previously worked at Ford Motor Company, Toyota Engineering and Manufacturing, and Lockheed Martin Aeronautics. Her primary research interest is microstructural evolution during thermomechanical processing of metals and alloys, particularly for those with low-symmetry crystal structures.



**Vineet V. Joshi** is Materials Scientist in the Energy and Environment Directorate at the Pacific Northwest National Laboratory located in Richland, Washington, USA. He holds an M.S. degree in materials science and engineering from Alfred University in New York, which he earned in 2010. He is currently National Technical Lead for the fabrication of monolithic uranium fuels for the United States High-Performance Research Reactors. He is the past Chair of the Magnesium Committee of The Minerals, Metals & Materials Society (TMS).

He currently leads several projects at the laboratory related to development of lightweight structural materials and processing of metallic nuclear fuels. He has made numerous original and important contributions through his research related to lightweight structural materials and nuclear materials processing, has published over 50 articles and delivered as many talks at international meetings or conferences, and has two granted patents and five patent applications. His primary forte is correlating fundamental processing–microstructure–property–performance relationships in metallic and ceramic materials. Over the years, he helped develop a process to make high-strength titanium alloy, the results of which were published in *Nature Communications*. He and his team have made significant contributions in developing the Shear-Assisted Processing and Extrusion (ShAPE™) technique to form magnesium and other lightweight structures. Earlier, he was involved in the development of a new reactive air brazing technique, which enabled joining of mixed ionic and electronic conducting ceramics to metals in air.

He served as Guest Editor for the topic “Corrosion of Magnesium in Multimaterial Systems” in *JOM* and “Oxidation of Metals” for the journal *Metals*. He is the recipient of several awards at the laboratory. He has been Member of TMS since his undergraduate days in India.



**Neale R. Neelameggham** is “The Guru” at IND LLC, involved in international technology and management consulting in fields such as metals and associated chemicals, thiometallurgy, energy technologies, soil biochemical reactor design, lithium-ion battery design, and agricultural uses of coal.

He has over 38 years of expertise in magnesium production and was involved in process development of the startup company NL Magnesium through to the present US Magnesium LLC until 2011, during which time he was instrumental in process development from the solar ponds to magnesium metal foundry. His expertise includes competitive magnesium processes worldwide and related trade cases.

He and Brian Davis authored the ICE-JNME award-winning (2016) article “21st Century Global Anthropogenic Warming Convective Model.” He is presently developing Agricoal® for greening arid soils and has authored the e-book *The Return of Manmade CO<sub>2</sub> to Earth: Ecochemistry*, published by Smashwords in 2018.

He holds 16 patents and patent applications, and has published several technical papers. He has served on the TMS Magnesium Committee since its inception in 2000, chaired the committee in 2005, and since 2007 has been a permanent co-organizer for the Magnesium Technology Symposium. He has been Member of the Reactive Metals Committee, Recycling Committee, Titanium Committee, and Program Committee.

He was the inaugural Chair of the TMS Energy Committee and has been Co-organizer of the Energy Technology Symposium through the present. He received the Light Metals Division Distinguished Service Award in 2010. As Chair of Hydrometallurgy and Electrometallurgy Committee, he initiated the Rare Metal Technology Symposium in 2014 and was Co-organizer for it through 2019. He organized the 2018 TMS symposium Stored Renewable Energy in Coal.

---

## Session Chairs

### **Magnesium Technology**

#### **Keynote Session**

J. Brian Jordon, The University of Alabama

Victoria Miller, University of Florida

#### **Alloy Development**

Norbert Hort, Helmholtz-Zentrum Geesthacht

Neale Neelameggham, IND LLC

#### **Alloy Design and Solidification**

Mark Easton, RMIT University

Matthew Kasemer, The University of Alabama

#### **Fundamentals, Mechanical Behavior, Twinning, Plasticity, and Texture I**

Mohsen Asle Zaeem, Colorado School of Mines

Dmytro Orlov, Lund University

#### **Thermomechanical Processing**

Christopher Barrett, Mississippi State University

Vineet Joshi, Pacific Northwest National Laboratory

#### **Corrosion**

Bin Li, University of Nevada

Domonkos Tolnai, Helmholtz-Zentrum Geesthacht

#### **Solidification and Processing**

Neale Neelameggham, IND LLC

Yuan Yuan, Chongqing University

#### **Fundamentals, Mechanical Behavior, Twinning, Plasticity, and Texture II**

Tracy Berman, University of Michigan

Keerti Kappagantula, Pacific Northwest National Laboratory

---

## Reviewer Pool

Neale R. Neelameggham, IND LLC, USA  
Raymond Decker, Thixomat Inc., USA  
Vineet V. Joshi, Pacific Northwest National Laboratory, USA  
Rajib Kalsar, Pacific Northwest National Laboratory, USA  
Sina Shahrezaei, Pacific Northwest National Laboratory, USA  
Petra Maier, Stralsund University of Applied Sciences, Germany  
Benjamin Schuessler, Pacific Northwest National Laboratory, USA  
Yang Tian, Kunming University of Science and Technology, China  
Huimin Lu, Beihang University, China  
Benjamin Anthony, University of Florida, USA  
Victoria Miller, University of Florida, USA  
Kiran Solanki, Arizona State University, USA  
J. Brian Jordon, The University of Alabama, USA  
Harish Rao, The University of Alabama, USA  
Eric Nyberg, Tungsten Parts Wyoming, USA  
Norbert Hort, Helmholtz-Zentrum Geesthacht, Germany

---

**Part I**  
**Keynote Session**



# Twin Transmission Across Grain Boundaries in Mg

Carlos N. Tomé, Mariyappan Arul Kumar, John Graham, Khanh Dang, Yue Liu, Pengzhang Tang, Shujuan Wang, Rodney J. McCabe, and Laurent Capolungo

## Abstract

Transmission of  $\{10\bar{1}2\}\{\bar{1}011\}$  mechanical twins across grain boundaries in Mg is a mechanism that can facilitate shear accommodation but also provide a path for failure via intergranular crack propagation. Until recently the twin research has focused on a 2D characterization of intra-granular propagation and intergranular transmission along the forward propagation direction. Recent 3D studies of the twin domain interface reveal a faceted structure, anisotropic mobility, and a relative easiness of lateral twin propagation (as opposed to forward or normal propagation). Here we describe a study of the forward and the lateral twin transmission into neighbors applying a variety of experimental and computational characterization techniques, namely: (1) statistical EBSD analysis of twin

sections; (2) 3D Phase Field and Molecular Dynamic simulations of twins propagating and reacting with grain boundaries. This study improves our understanding of the transmission mechanisms in a 3D aggregate, and helps us to develop criteria for treating twin modeling in CP simulations.

## Keywords

Mg • 3D twin characterization • Twin propagation • Twin transmission

## Introduction

Transmission of  $\{10\bar{1}2\}\{\bar{1}011\}$  mechanical twins across grain boundaries in Mg is a mechanism that can facilitate intergranular crack propagation by providing a path to cracks along the twin interface. Clearly, understanding twin transmission requires us to understand twin growth. Traditionally, both mechanisms have been characterized as 2D processes, defined by the ‘forward’ twin shear direction  $\eta_1$ , and the direction  $k_1$  normal to the coherent twin boundary. Our recent 3D studies of twin domain interfaces reveal anisotropic mobility and a relative easiness of lateral twin propagation along  $\lambda = k_1 \times \eta_1$  and point to the need for regarding twins as 3D growing domains in order to fully understand their behavior. As a consequence, it is natural to wonder what is the role of both, the forward and the lateral motion of the twin, concerning transmission across grain boundaries.

In this talk, we review the most recent experimental and modeling information related to twin transmission across grain boundaries and discuss new results associated with the lateral motion. In brief, we examine experimental and computational results from: (1) statistical EBSD analysis of twin sections and (2) phase field and 3D molecular dynamic simulations of twins reacting with grain boundaries.

C. N. Tomé (✉) · M. A. Kumar · J. Graham · K. Dang · S. Wang · R. J. McCabe · L. Capolungo  
MST-8, Los Alamos National Laboratory, Los Alamos, NM 87544, USA  
e-mail: [tome@lanl.gov](mailto:tome@lanl.gov)

M. A. Kumar  
e-mail: [marulkr@lanl.gov](mailto:marulkr@lanl.gov)

J. Graham  
e-mail: [jtgraham@lanl.gov](mailto:jtgraham@lanl.gov)

K. Dang  
e-mail: [kqdang@lanl.gov](mailto:kqdang@lanl.gov)

S. Wang  
e-mail: [shujuan@lanl.gov](mailto:shujuan@lanl.gov)

R. J. McCabe  
e-mail: [rmccabe@lanl.gov](mailto:rmccabe@lanl.gov)

L. Capolungo  
e-mail: [laurent@lanl.gov](mailto:laurent@lanl.gov)

Y. Liu · P. Tang  
School of Materials Science and Engineering,  
Shanghai Jiao Tong University, Shanghai, 200240,  
People’s Republic of China  
e-mail: [yliu23@sjtu.edu.cn](mailto:yliu23@sjtu.edu.cn)

P. Tang  
e-mail: [pztang@sjtu.edu.cn](mailto:pztang@sjtu.edu.cn)



- 1. Statistical EBSD analysis of twin sections:** Statistical analysis involving thousands of twins in Mg reveals that forward propagation into the neighboring grains is favored by low grain misorientations, which tend to align the shear planes and directions of the twins [1] (Fig. 1b). The twin transmission is accompanied by a relaxation of the back stress in the impinging twin and its surroundings, and by an increase in thickness at the intersection point (Fig. 1c).
- 2. Phase Field and 3D Molecular Dynamic simulations:** The results of Fig. 1 correspond to twins propagating forward, along the shear direction  $\eta_1$ . Recent statistical EBSD analysis reveals that lenticular twins exhibit a systematically larger  $\lambda$  axis than  $\eta_1$  axis, indicating that twins propagate faster in the lateral direction  $\lambda$  than along the shear direction  $\eta_1$  [3]. Molecular dynamics and phase

field simulations support such conclusion. In addition, EBSD shows that the twin expansion viewed from the direction normal to the twin plane adopts an irregular shape, and that the lateral side is as likely as the forward side to start propagation from the GB (Fig. 2a, b). Statistical analysis is in progress to determine the frequency and characteristics of transmission along those two directions.

Both phase field and molecular dynamics show that a twin nucleus propagates faster along the lateral direction (Figs. 2c and 3) and that the twin-driving-shear TRSS at the lateral side is larger than at the forward side [2]. As a consequence, it is to be expected that lateral transmission will be induced in properly oriented neighbors, an example of which is given in Fig. 2b. A possible

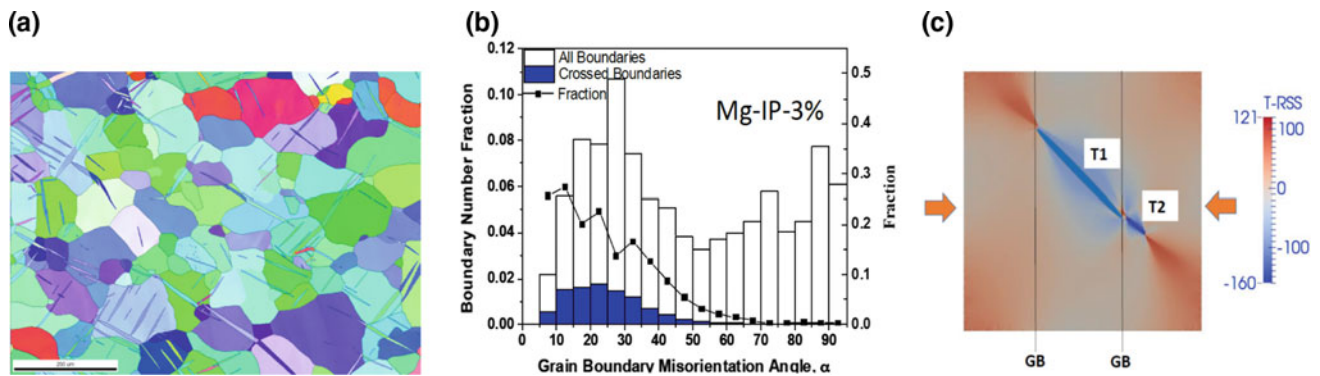


**Fig. 1** a EBSD of Mg compressed 1% along RD (viewed along the  $\lambda$  direction) showing several instances of twin transmission; b fraction of GB's exhibiting twin propagation as a function of GB misorientation;

and c CP-FFT simulation map of RSS on twin plane (TRSS), showing relaxation of back stress associated with twin transmission

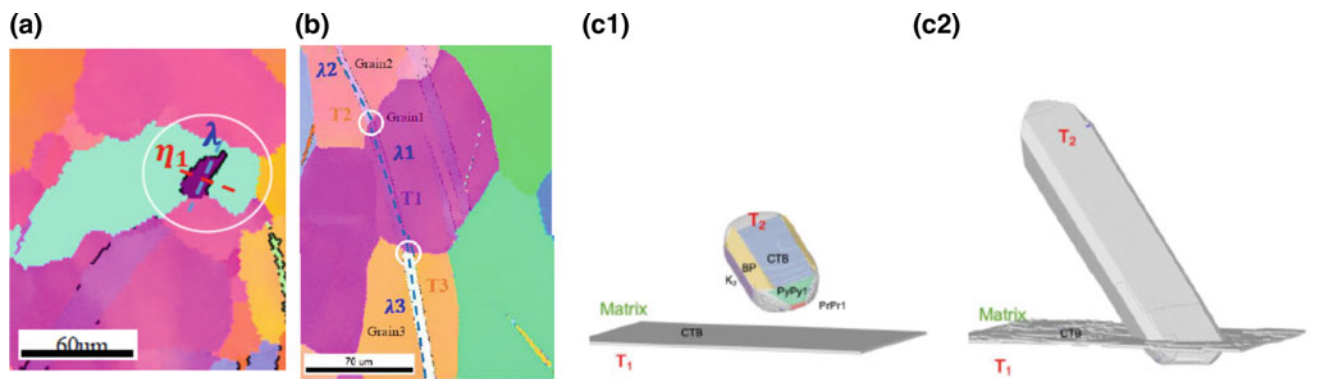
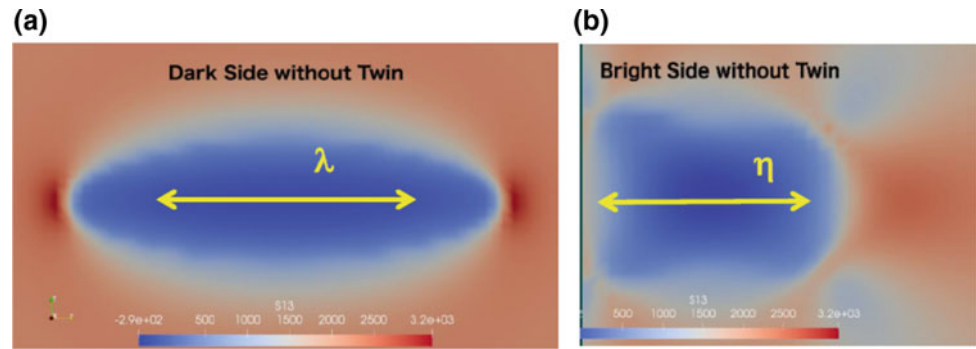


**Fig. 2** a EBSD of an incipient twin viewed along the  $k_1$  direction, showing 'lateral-side' growth from the GB; b twins viewed along the shear direction  $\eta_1$  showing lateral transmission across three grains; and c MD simulation of lateral propagation: noncozone  $\{10\bar{1}2\}$  twin-twin

interaction under 2 GPa uniaxial tension along the c-axis at 10 K; c1 initial settings with T2 twin nucleus and the CTB of T1; c2 final state showing incipient lateral transmission

**Fig. 3** 3D phase field simulation of twin expansion. Maps of the shear stress on the twin plane along the twin direction  $\eta_1$ .  
**a** Section perpendicular to  $\eta_1$ ;  
**b** section perpendicular to  $\lambda$



conclusion of this study is that intergranular twin propagation has the possibility of choosing a tortuous path inside the polycrystal.

## Summary

A complete understanding of twinning in HCP and of its role as a deformation mechanism requires to regard it as a full 3D mechanism. Twin transmission across GBs is a fairly frequent occurrence in Mg alloys and has to be assessed as both a shear accommodation and a crack-enhancing propagation mechanism.

## References

1. M. Arul Kumar, I.J. Beyerlein, R.J. McCabe, C.N. Tomé, “Grain neighbor effects on twin transmission in hexagonal close packed materials”, *Nature Communications* 7:13826 (2016)
2. M.Y. Gong, G. Liu, J. Wang, L. Capolungo, C.N. Tomé, “Atomistic simulations of basal  $\langle a \rangle$  dislocations and a 3-dimensional twin interactions in Mg”, *Acta Materialia* 155 (2018) 187–198
3. Y. Liu, P.Z. Tang, M.Y. Gong, R.J. McCabe, J. Wang, C.N. Tomé, “Three dimensional character of the deformation twin in Mg”, *Nature Communications* (2019) 10:3308

# Hierarchically Structured Ultrafine Grained Magnesium Alloys

Rajiv S. Mishra

## Abstract

The intrinsic low density of magnesium drives research towards high-performance magnesium alloys. Hierarchically structured ultrafine grained magnesium alloys possess exceptional strength-ductility combination and eliminate many of the traditional drawbacks like low strength, high yield strength asymmetry, poor formability, and limited superplasticity. In this overview presentation, friction stir processed microstructures are used as examples to discuss the microstructural paradigms that can exhibit excellent balance of mechanical properties. These show the possibilities of exceeding 500 MPa strength with good work hardening and >10% ductility. Use of micron-sized boron carbide ( $B_4C$ ) and nano-sized yttria ( $Y_2O_3$ ) powder can simultaneously enhance modulus-strength-ductility combination. High-strength ultrafine grained magnesium alloys also show high strain rate superplasticity which can provide pathways for overcoming poor formability. An example of friction stir additive manufacturing will be used to discuss possibilities of implementing such microstructures at component level with emerging solid-state additive manufacturing techniques.

## Keywords

Strength-ductility combination • Microstructural efficiency • Alloying efficiency • High performance

## Introduction

Three lightweight elements vie for structural space that steels occupy. These are magnesium, aluminium, and titanium, and the density of these elements scales in the same order they are mentioned here. Ashby [1] has developed a materials selection for mechanical design framework that is a very good way to consider materials for structural applications. The five design approaches under this framework are

1. Stiffness-limiting design,
2. Strength-limiting design,
3. Toughness-limiting design,
4. Fatigue-limiting design, and
5. Creep-limiting design.

An interesting correlation is that the specific stiffness (Young's modulus normalized by density) of steel is similar to magnesium, aluminium, and titanium. The implication is that substitution of one alloy with other for stiffness-limiting application is performance neutral, and therefore, other considerations including non-structural properties/attributes such as corrosion resistance and cost become important factors in final selection of the alloy. Whenever we are looking for opportunities to replace legacy alloys, the implementation barriers include technical and non-technical considerations. Sankaran and Mishra [2] have recently reviewed the development of magnesium alloys in the context of aerospace alloys using Ashby's framework. Apart from highlighting the physical metallurgy and a summary of mechanical properties, the book introduced the concepts of "*microstructural efficiency*" and "*alloying efficiency*" [2]. These two terms are very important for magnesium alloys. This overview presentation is primarily focussed on key microstructural features and how some of these can be altered by friction stir processing. The ultrafine grained region is defined as a range with grain size in the range of 100–1000 nm, and this is particularly highlighted. While the

R. S. Mishra (✉)  
Advanced Materials and Manufacturing Processes Institute,  
Department of Materials Science and Engineering,  
University of North Texas, Denton, TX 76203, USA  
e-mail: [Rajiv.Mishra@unt.edu](mailto:Rajiv.Mishra@unt.edu)

attempt is only to cover a few illustrative examples, the papers by Mishra and co-workers on various aspects of magnesium alloys are listed to help the readers [3–37].

## Microstructural Efficiency and Alloying Efficiency

The concept of microstructural efficiency can be appreciated in the context of a review by Nie [38] on precipitation hardening in magnesium alloys. The primary strengthening mechanisms in various magnesium alloys are (a) solid-state strengthening, (b) grain boundary strengthening, (c) precipitation/dispersion strengthening, and (d) texture strengthening. Nie [38] has highlighted the importance of precipitation strengthening and compared with development of precipitation-strengthened aluminium alloys over a century. Because of the hexagonal closed packed (h.c.p.) crystal structure, slip in magnesium alloys occurs through basal, pyramidal, and prismatic dislocations. In addition, twinning is an important deformation mechanism. Non-basal slip systems can be activated by refining the grain size, and at the same time, below a critical grain size, the twinning can be suppressed or eliminated. In this context, shape and orientation of precipitates become very important. If the precipitates are elongated and oriented along basal plane, they are less effective in blocking the basal slip. On the other hand, precipitates that are oriented along prismatic planes can be highly effective in blocking basal and pyramidal slip planes. This is the basis for discussion of microstructural efficiency. Figure 1 shows a conceptual map where microstructural efficiency would be high. The microstructural efficiency for strength,  $\eta_{\text{micro}}$ , can be calculated as,

$$\eta_{\text{micro}} = \frac{\sigma_{\text{expt.}}}{\sum \sigma_{\text{theo.}}} \quad (1)$$

where  $\sigma_{\text{expt.}}$  is the experimental measured strength and  $\sum \sigma_{\text{theo.}}$  is summation of all strengthening mechanism for theoretically ideal microstructure. For example, the maximum in precipitation strengthening is obtained at the intersection of particle cutting and Orowan looping. So, this value should be inserted as the maximum potential of the precipitation-strengthened microstructure. Additional ideal microstructures can be generated to calculate maximum strength possible for a given volume fraction of second phase particles. On the other hand, for strengthening mechanisms like solid solution strengthening and grain size strengthening, calculation would be simply based on the level of solute and average grain size. The lower values of  $\eta_{\text{micro}}$  indicates lower efficacy of that particular alloy system.

In a similar way, the alloying efficiency for strength,  $\eta_{\text{alloy}}$ , can be defined as,

$$\eta_{\text{alloy}} = \frac{\sigma_{\text{expt.}}}{\sum \sigma_{\text{theo.}}} \quad (2)$$

where  $\sigma_{\text{expt.}}$  is the experimental measured strength and  $\sum \sigma_{\text{theo.}}$  is summation of all strengthening mechanism for theoretically ideal microstructure. The way the theoretically ideal microstructure is calculated for  $\eta_{\text{alloy}}$  is different when applied to alloy design as compared to calculation for a given alloy. Sankaran and Mishra [2] have highlighted the implication of alloying efficiency for alloy design. This approach involves consideration of the type of second phase particles that forms. If the alloying element X results in a phase  $\text{Mg}_3\text{X}$  and the alloying element Y results in  $\text{Mg}_2\text{Y}$ , then X has a higher alloying efficiency, as it results in higher volume fraction of precipitate per atom% of addition. Additionally, the location of where alloying elements are present needs to match with the intended target. For example, if an element is added to enhance strength through intragranular precipitate formation, loss of these precipitate to grain boundaries lowers the alloying efficiency. Similarly, if thermomechanical processing leads to undesirably coarse phases of the critical alloying element, then the alloying efficiency goes down. Constituent particles are another source of loss of alloying efficiency as they are undesirable microstructural features.

The desired microstructural features for high-strength magnesium alloys are summarized below along with typical microstructural features observed in conventionally processed magnesium alloys.

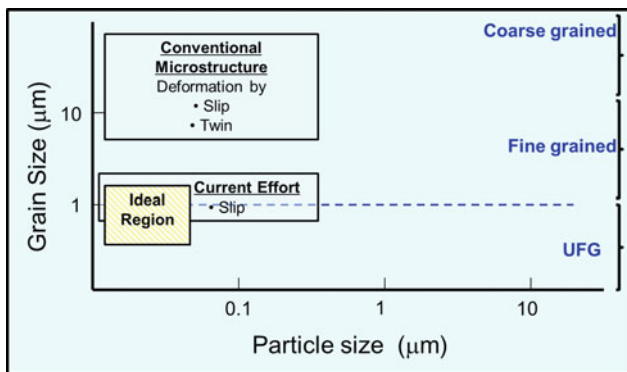
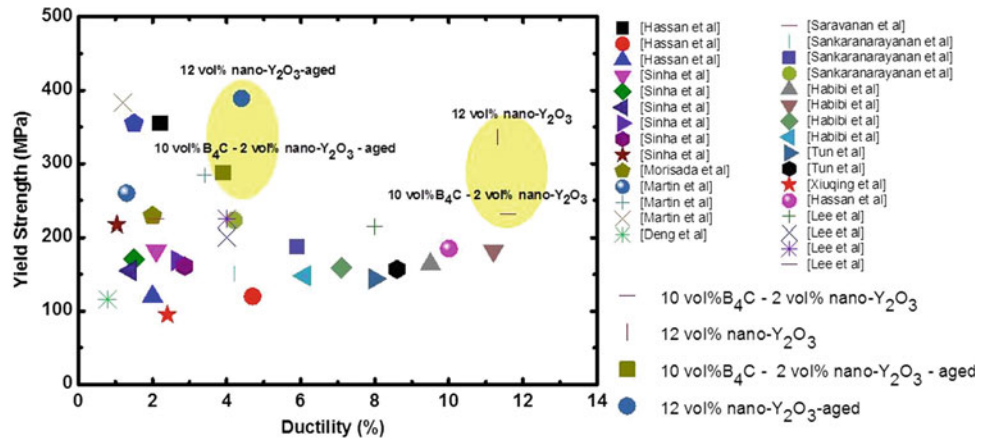


**Fig. 1** A microstructural map with depiction of deformation mechanism as a function of grain size and second phase particle size

**Fig. 2** An overview of particulate reinforced magnesium composites. Hierarchical composites can provide synergy in strengthening mechanisms and ductility (Das and Mishra [40])



Desired microstructure	Usually obtained in practice	Reason
Effective precipitate size, morphology, and distribution	Highly elongated with low density	Low nucleation density and anisotropic growth along preferred growth direction
Fine grain size	Coarse or mixed distribution	Grain boundaries are nucleation sites for grains during recrystallization
Random texture	Highly textured	Dominance of certain slip systems during deformation

### Friction Stir Processing as a Microstructural Engineering Tool

The friction stir processing (FSP) is a high temperature severe plastic deformation (HT-SPD) process. Its attributes include high strain rate, high process strain, and elevated temperatures. These attributes separate FSP from other SPD techniques like equal channel angular extrusion/pressing, torsional straining, accumulative roll bonding, etc. The way UFG microstructure forms in FSP is quite different from other SPD techniques. In FSP, UFG microstructure is obtained by restricting the growth of recrystallized grains at elevated temperatures and this results in predominantly high-angle grain boundaries and random texture. This aspect is particularly important for magnesium alloys, which are very difficult to process by other SPD techniques. Mishra et al. [39] and Sankaran and Mishra [2] have reviewed specific aspects of FSP magnesium alloys. Readers are encouraged to see references [3–37] for details of various aspects covered through the years. This set of papers cover strength-ductility combination, texture evolution, strengthening mechanisms, friction

stir additive manufacturing, superplasticity, and additive manufacturing. Many of these are focussed on ultrafine grained microstructure. Panigrahi et al. [24] have discussed the critical grain size below which dislocation storage in the grain is limited and this impacts the work hardening. So, this defines a limiting grain size for engineering applications. Kumar et al. [10] have discussed some unique precipitate morphologies, including use of dislocation core and network for precipitation in Mg–Nd–Y alloy. Palanivel et al. [7] have established a framework for enhanced dissolution during FSP as well as showed example of Mg<sub>2</sub>Y in WE43 alloy, which decreases the alloying efficiency.

An emerging opportunity is to use FSP to create magnesium composite with hierarchical microstructure. Figure 2 shows an overview of composite with nano- and micro- scale reinforcements. An important observation is the combined improvement of stiffness-strength-ductility. The combined effect of load transfer to coarser particulates and activation of non-basal slip activities due to nano-particles leads to synergy in strengthening mechanisms. This approach is also impactful for grain size control and texture control, both of which are important for magnesium alloys and composites. At this stage, very limited work is available on combining synergistic mechanisms and its theoretical foundation.

### Remarks for Future Research

To take full advantage of lower density, the research needs to strive to obtain mechanical properties equivalent to aluminium alloys without the need for density-based normalization. New alloys should be designed to enhance the microstructural efficiency and alloying efficiency. Significant scientific understanding exists to exploit the mechanisms to create a high-strength low-alloy framework for magnesium alloys. Key is to overcome historical negative perceptions as well as grand challenges related to corrosion and toughness.



**Acknowledgements** The author gratefully acknowledges support from ARL, NSF, and members of NSF IUCRC (CFSP) over the years. Heartfelt thanks to all the students, post-docs, and collaborators who are authors and co-authors of references [3–37, 40]; these interactions have shaped the thoughts expressed in this overview presentation.

## References

1. M. Ashby, *Materials Selection in Mechanical Design*, 2016, Butterworth-Heinemann, 5th Edition, ISBN: 9780081005996.
2. K.K. Sankaran, R.S. Mishra, *Metallurgy and Design of Alloys with Hierarchical Microstructures*, 2017, Elsevier, ISBN: 978-0-128-12068-2, 345-84.
3. S. Gangireddy, B. Gwalani, K. Liu, E.J. Faierson, R.S. Mishra, Microstructure and mechanical behavior of an additive manufactured (AM) WE43-Mg alloy, 2019, *Additive Manufacturing*, 26, 53–64.
4. G.R. Argade, S. Sanders, G. Mohandass, A. Alsaleh, F. D'Souza, T.D. Golden, R.S. Mishra, Corrosion Inhibition Study of Mg-Nd-Y High Strength Magnesium Alloy Using Organic Inhibitor, 2019, *Journal of Materials Engineering and Performance*, 28, 852–862.
5. S.S. Nene, S. Zellner, B. Mondal, M. Komarasamy, R.S. Mishra, R.E. Brennan, K.C. Cho, Friction stir processing of newly-designed Mg-5Al-3.5Ca-1Mn (AXM541) alloy: Microstructure evolution and mechanical properties, 2018, *Materials Science and Engineering A*, 729, 294–299.
6. S. Palanivel, R.S. Mishra, R.E. Brennan, K.C. Cho, Accelerated age hardening response by in-situ ultrasonic aging of a WE43 alloy, 2018, *Materials and Manufacturing Processes* 33 (1), 104–108.
7. S. Palanivel, A. Arora, K.J. Doherty, R.S. Mishra, A framework for shear driven dissolution of thermally stable particles during friction stir welding and processing, 2016, *Materials Science and Engineering A*, 678, pp. 308–314.
8. N. Kumar, R.S. Mishra, N.B. Dahotre, R.E. Brennan, K. J. Doherty, K.C. Cho, Effect of friction stir processing on microstructure and mechanical properties of laser-processed Mg-4Y-3Nd alloy, 2016, *Materials and Design*, 110, 663–675.
9. C.A. Lipscomb, A. Fortier, F. Kong, S. Das, N. Kumar, R.S. Mishra, Evaluation of plastic zone development in WE43 magnesium alloy upon friction stir processing using finite element modeling, 2016, *Materials Science and Engineering A*, 673, pp 178–184.
10. N. Kumar, D. Choudhuri, R. Banerjee, R.S. Mishra, Strength and ductility optimization of Mg-Y-Nd-Zr alloy by microstructural design, 2015, *International Journal of Plasticity* 68, 77–97.
11. S. Palanivel, P. Nelaturu, B. Glass, R.S. Mishra, Friction stir additive manufacturing for high structural performance through microstructural control in an Mg based WE43 alloy, 2015, *Materials & Design* 65, 934–952.
12. N. Kumar, N. Dendge, R. Banerjee, R.S. Mishra, Effect of microstructure on the uniaxial tensile deformation behavior of Mg-4Y-3RE alloy, 2014, *Materials Science and Engineering: A* 590, 116–131.
13. S. Santhanakrishnan, N. Kumar, N. Dendge, D. Choudhuri, S. Katakam, S. Palanivel, H.D. Vora, R. Banerjee, R.S. Mishra, N.B. Dahotre, Macro- and microstructural studies of laser-processed WE43 (Mg-Y-Nd) magnesium alloy, 2013, *Metallurgical and Materials Transactions B: Process Metallurgy and Materials Processing Science* 44 (5), pp. 1190–1200.
14. W. Yuan, S.K. Panigrahi, R.S. Mishra, Achieving high strength and high ductility in friction stir-processed cast magnesium alloy, 2013, *Metallurgical and Materials Transactions A: Physical Metallurgy and Materials Science* 44 (8), pp. 3675–3684.
15. A. Mohan, S.K. Panigrahi, R.S. Mishra, R. Verma, Influence of strain and strain rate on microstructural evolution during superplasticity of Mg-Al-Zn sheet, 2013, *Journal of Materials Science* 48 (16), pp. 5633–5644.
16. V. Jain, R.S. Mishra, R. Verma, E. Essadiqi, Superplasticity and microstructural stability in a Mg alloy processed by hot rolling and friction stir processing, (2013) *Scripta Materialia*, 68 (7), pp. 447–450.
17. A. Mohan, W. Yuan, R.S. Mishra, High strain rate superplasticity in friction stir processed ultrafine grained Mg-Al-Zn alloys, (2013) *Materials Science and Engineering A*, 562, pp. 69–76.
18. J. Kang, D.S. Wilkinson, R.K. Mishra, W. Yuan, R.S. Mishra, Effect of inhomogeneous deformation on anisotropy of AZ31 magnesium sheet, 2013, *Materials Science and Engineering A*, 567, 101–109.
19. V. Jain, R.S. Mishra, A.K. Gupta, Gouthama, Study of  $\beta$ -precipitates and their effect on the directional yield asymmetry of friction stir processed and aged AZ91C alloy, 2013, *Materials Science and Engineering A*, 560, pp. 500–509.
20. S. Das, R.S. Mishra, K.J. Doherty, K.C. Cho, B. Davis, R. DeLorme, Magnesium based composite via friction stir processing, 2013, *TMS Annual Meeting*, pp. 245–252.
21. S. Palanivel, R.S. Mishra, B. Davis, R. DeLorme, K.J. Doherty, K. C. Cho, Effect of initial microstructure on the microstructural evolution and joint efficiency of a WE43 alloy during friction stir welding, 2013, *TMS Annual Meeting*, pp. 253–261.
22. W. Yuan, R.S. Mishra, Grain size and texture effects on deformation behavior of AZ31 magnesium alloy, 2012, *Materials Science and Engineering A*, 558, pp. 716–724.
23. G.R. Argade, W. Yuan, K. Kandasamy, R.S. Mishra, Stress corrosion cracking susceptibility of ultrafine grained AZ31, 2012, *Journal of Materials Science* 47 (19), pp. 6812–6822.
24. S.K. Panigrahi, K. Kumar, N. Kumar, W. Yuan, R.S. Mishra, R. DeLorme, B. Davis, R.A. Howell, K. Cho, Transition of deformation behavior in an ultrafine grained magnesium alloy, 2012, *Materials Science and Engineering A549*, pp. 123–127.
25. G.R. Argade, K. Kandasamy, S.K. Panigrahi, R.S. Mishra, Corrosion behavior of a friction stir processed rare-earth added magnesium alloy, 2012, *Corrosion Science*, 58, pp. 321–326.
26. W. Yuan, R.S. Mishra, B. Carlson, R. Verma, R.K. Mishra, Material flow and microstructural evolution during friction stir spot welding of AZ31 magnesium alloy, 2012, *Materials Science and Engineering A543*, pp. 200–209.
27. G.R. Argade, S.K. Panigrahi, R.S. Mishra, Effects of grain size on the corrosion resistance of wrought magnesium alloys containing neodymium, 2012, *Corrosion Science*, 58, pp. 145–151.
28. V. Jain, W. Yuan, R.S. Mishra, Gouthama, A.K. Gupta, Directional anisotropy in the mechanical behavior of friction stir processed and aged AZ91 alloy, 2012, *Materials Science Forum* 702–703, pp. 64–67.
29. W. Yuan, R.S. Mishra, Effect of heat index on microstructure and mechanical behavior of friction stir processed AZ31, 2011, *Magnesium Technology*, pp. 205–209.
30. V. Jain, J.Q. Su, R.S. Mishra, R. Verma, A. Javaid, M. Aljarrah, E. Essadiqi, Microstructure and mechanical properties of Mg-1.7 Y-1.2 Zn sheet processed by hot rolling and friction stir processing, 2011, *Magnesium Technology*, pp. 565–570.
31. W. Yuan, R.S. Mishra, B. Carlson, R. Verma, R. Szymanski, Effect of coating on mechanical properties of magnesium alloy friction stir spot welds, 2011, *TMS Annual Meeting*, pp. 401–407.
32. S.K. Panigrahi, W. Yuan, R.S. Mishra, R. DeLorme, B. Davis, R. A. Howell, K. Cho, A study on the combined effect of forging and aging in Mg-Y-RE alloy, (2011) *Materials Science and Engineering A* 530 (1), pp. 28–35.

33. W. Yuan, S.K. Panigrahi, J.-Q. Su, R.S. Mishra, Influence of grain size and texture on Hall-Petch relationship for a magnesium alloy, (2011) *Scripta Materialia* 65 (11), pp. 994–997.
34. W. Yuan, R.S. Mishra, B. Carlson, R.K. Mishra, R. Verma, R. Kubic, Effect of texture on the mechanical behavior of ultrafine grained magnesium alloy, (2011) *Scripta Materialia* 64 (6), pp. 580–583.
35. G. Bhargava, W. Yuan, S.S. Webb, R.S. Mishra, Influence of texture on mechanical behavior of friction-stir-processed magnesium alloy, (2010) *Metallurgical and Materials Transactions A* 41 (1), pp. 13–17.
36. T.A. Freeney, R.S. Mishra, Effect of Friction Stir Processing on Microstructure and Mechanical Properties of a Cast-Magnesium-Rare Earth Alloy, (2010) *Metallurgical and Materials Transactions A* 41 (1) pp. 73–84.
37. T. Freeney, R. S. Mishra, G. Grant, and R. Verma, “Friction Stir Processing of a Cast WE43 Magnesium Alloy,” *Friction Stir Welding and Processing IV*, 2007 TMS Annual Meeting; Orlando, FL, 2007, 429–438.
38. J.F. Nie, Precipitation and Hardening in Magnesium Alloys, *Metallurgical and Materials Transactions A*, 43 (2012) pp. 3891–3939.
39. R.S. Mishra. P.S. De and N. Kumar, *Friction Stir Welding and Processing: Science and Engineering*, Springer, 2014, ISBN-13: 978-3-319-07043-8.
40. S. Das, R.S. Mishra, unpublished research, 2017.

# Multistage Fatigue (MSF) Modeling of Magnesium in a Corrosion Environment

Mark F. Horstemeyer

---

## Extended Abstract

This work presents an overview of using the multistage fatigue model with a corrosion model to capture the behavior of magnesium alloys. One can argue that magnesium alloys used for structural components are always in a corrosive environment as no real practical structural component operates in a vacuum. As such, different magnesium alloys are analyzed in the context of their fatigue incubation, microstructurally small crack (MSC), and long crack regimes under a vacuum, air, and saltwater environments. The different magnesium alloys analyzed, including AE44, AM30, AM50, AM60, AZ31, AZ61, AZ91 alloys. These alloys were fabricated under different methods and each had different heat treatments. The levels of corrosion pitting, general corrosion, and filiform corrosion were quite different for each alloy, meaning that the interdependence of the

different corrosion mechanisms interacted differently with each alloy's incubation, MSC, and LC fatigue lives.

General corrosion, illustrated in Fig. 1 for pure magnesium and magnesium–aluminum alloys, occurs along with pitting, and filiform corrosion occurs for magnesium and its alloys. There is an associated hydrogen release from the chemical reaction that can be quantitatively measured as per Fig. 2 so the association cause–effect relation of the microstructure–property relationship can be known. When you apply the fatigue environment with the corrosion environment, different strain–life curves arise as per Fig. 3. It is these differences that the multistage fatigue (MSF) model combined with the internal state variable (ISV) corrosion model can be used to address the behavior of the material.

---

M. F. Horstemeyer (✉)  
School of Engineering, Liberty University, Lynchburg, VA  
24515, USA  
e-mail: [mfhorstemeyer@liberty.edu](mailto:mfhorstemeyer@liberty.edu)



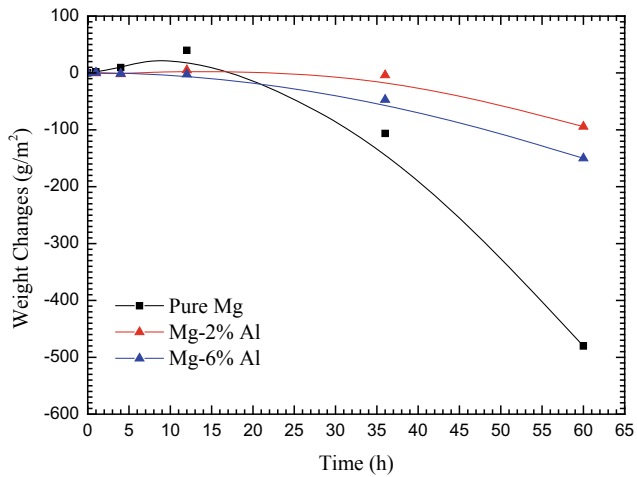


**Fig. 1** Weight change of magnesium versus time illustrating general corrosion for differing amounts of aluminum in solution of magnesium

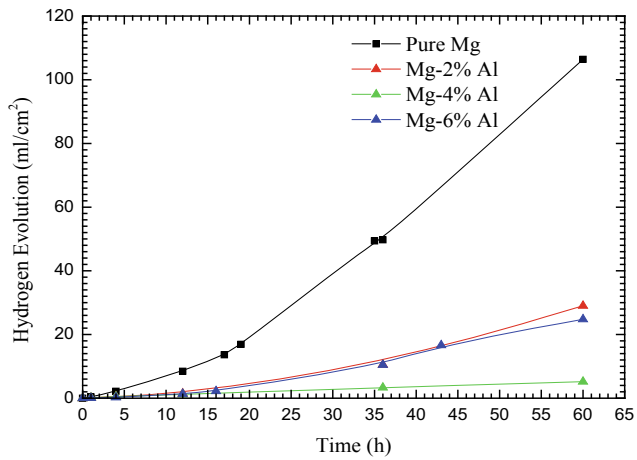


**Fig. 2** Hydrogen release versus time under immersion corrosion environments associated with the general corrosion of Fig. 1

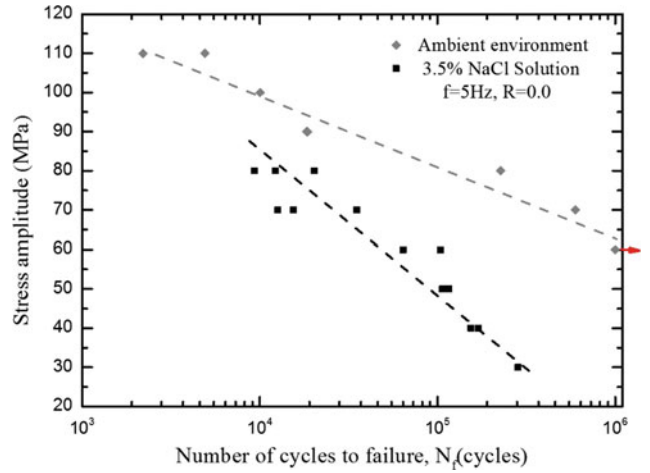


**Fig. 3** S-N curves for an extruded AM30 magnesium alloy tested in laboratory ambient environment (30–45% RH) and 3.5 wt% NaCl solution environment. Fatigue specimens for both environments were tested with a frequency of 5 Hz and a stress ratio of 0.0. Large variation in corrosion fatigue life was present at stress amplitudes higher than 60 MPa. The fatigue run out stress level was 60 MPa in the air environment and was not found in the 3.5 wt% NaCl solution environment

# Novel Texture Controlling of Mg Alloys

Bin Jiang, Guangsheng Huang, Jiangfeng Song, Dingfei Zhang,  
and Fusheng Pan

## Extended Abstract

Magnesium (Mg) alloys have attracted considerable attention for a promising application in the automotive and electronics owing to their high specific strength and high electromagnetic shielding. However, the application of wrought Mg alloys has been limited by poor room temperature ductility. It was ascribed to the large difference in critical resolved shear stresses (CRSS) between basal and prismatic slip in hexagonal close-packed (hcp) crystal structure in Mg alloy. This results in a lack of the active slip systems and can hardly offer an arbitrary shape change at the grain level.

Conventionally extruded Mg alloy sheets possess poor mechanical properties due to the strong basal texture where *c*-axes of the grains are predominantly aligned parallel to the sheet normal. This brings about a poor deformation capability of sheet thinning and a stronger anisotropy and consequently results in a limited number of available plastic deformation modes. In this work, a novel extrusion approach

to get high strength magnesium alloy plates will be introduced through differential speed processing. A suitable constitutive model of differential speed extrusion is established to ameliorate the texture-dependent mechanical properties. The velocity evolutions of the extruded sheets at near-surface and mid-layer regions are different due to the extra asymmetric shear deformation. This simple shear enforces the near-surface microstructure to exhibit more dynamically recrystallized grains having the *c*-axis tilted toward the extrusion direction. The yield stress of AZ31 alloy sheet has been increased from 161.2 to 179.9 MPa, and the elongation has been improved from 15.4 to 20.1%. Moreover, as for the high strength AZ61 alloy sheets, the ultimate tensile strength was increased from 387.9 to 427.1 MPa and the yield stress was improved from 147.7 to 195.9 MPa. Grain refinement and tilted weak basal texture obtained by differential speed extrusion process. This approach is an efficient substitute to increase the texture-induced softening and ductility and thus favorable for the thin sheet fabrication.

---

B. Jiang (✉) · G. Huang · J. Song · D. Zhang · F. Pan  
National Engineering Research Center for Magnesium Alloys,  
Chongqing University, Chongqing, China  
e-mail: [jiangbinrong@cqu.edu.cn](mailto:jiangbinrong@cqu.edu.cn)

---

**Part II**  
**Alloy Development**

# Design of Ductile Rare-Earth-Free Magnesium Alloys

W. A. Curtin, Rasool Ahmad, Binglun Yin, and Zhaoxuan Wu

## Abstract

Pure Mg has low ductility due to a transition of  $\langle c+a \rangle$  pyramidal dislocations to a sessile basal-oriented structure. Dilute alloying generally improves ductility. Enhancement of pyramidal cross-slip from the lower-energy pyramidal II plane to the higher-energy pyramidal I plane has been proposed as the mechanism. Here, the theory is applied to ternary and quaternary alloys of Zn, Al, Li, Ca, Mn, Sn, K, Zr, and Sr at dilute concentrations, and a wide range of compositions are predicted to have good ductility. Interestingly, while Zn alone is insufficient for achieving ductility, its inclusion in multicomponent alloys at 0.5 at.% enables ductility at the lowest concentrations of other alloying elements. Further implications of the theory are discussed.

## Keywords

Magnesium alloys • Theory • Ductility

## Introduction

Magnesium (Mg) is the lightest structural metal but has a hexagonal close packed (HCP) crystal structure. The HCP structure has crystallographically different slip systems with distinct slip planes (basal, prism, and pyramidal), slip steps

( $\langle a \rangle$  and  $\langle c+a \rangle$  Burgers vectors) and slip resistance ( $\gamma$ -surface). Generally, plastic slip with  $\langle a \rangle$  dislocations on basal and prism planes is intrinsically easier than that of  $\langle c+a \rangle$  dislocations on pyramidal planes, as dictated by crystallography and the electronic structure of Mg in the HCP lattice [1]. Furthermore,  $\langle c+a \rangle$  dislocations dissociated on pyramidal glide planes are thermodynamically unstable and can transform into lower energy, sessile structures along basal planes through pyramidal-to-basal (PB) transition [2]. The energy barriers of the  $\langle c+a \rangle$  PB transitions are low ( $\sim 0.5$  eV for pyramidal II plane [2] and  $\sim 0.3$  eV for pyramidal I plane [3]) and comparable to other plasticity mechanisms at room temperature. Plastic slip with  $\langle c+a \rangle$  dislocations can thus only provide very limited  $\langle c \rangle$  axis strain capability initially upon their activation; the PB transition will quickly increase the critical resolved shear stress (CRSS) for  $\langle c+a \rangle$  slip systems and effectively eliminate the critical  $\langle c+a \rangle$  dislocation slip systems [2]. The PB transition thus further increases plastic anisotropy, with  $\langle c+a \rangle$  CRSS measured at  $\sim 100$  times that of basal  $\langle a \rangle$  [4]. The difficulty in  $\langle c+a \rangle$  dislocation slip also contributes to strong textures developed in wrought Mg products, such as strong basal textures with  $c$ -axis in the normal direction of rolled sheets and strong fiber textures with  $c$ -axis in radial direction in extruded products. Strong plastic anisotropy and texture cause HCP Mg exhibit low ductility [2] and intrinsic brittleness [5], which are detrimental in load-carrying or energy-absorption structure applications.

Achieving high ductility and high fracture toughness in Mg is thus a long-standing barrier for its wide range, large-scale structure applications across various industries, such as the automotive and aerospace industries [6, 7]. Increasing ductility is, however, particularly challenging in HCP Mg, since its plastic anisotropy arises from the intrinsic properties of the slip systems and changing intrinsic properties is difficult. Increasing ductility is also generally less straightforward as compared to increasing strength, since the former depends on the plastic evolution of the underlying microstructure. Various metallurgical strategies, such as

W. A. Curtin (✉) · R. Ahmad · B. Yin

Laboratory for Multiscale Mechanics Modeling, Institute of Mechanical Engineering, EPFL, 1015 Lausanne, Switzerland  
e-mail: [william.curtin@epfl.ch](mailto:william.curtin@epfl.ch)

R. Ahmad  
e-mail: [rasool.ahmad@epfl.ch](mailto:rasool.ahmad@epfl.ch)

B. Yin  
e-mail: [binglun.yin@epfl.ch](mailto:binglun.yin@epfl.ch)

Z. Wu  
Department of Materials Science and Engineering, City University of Hong Kong, Tat Chee Avenue, Kowloon, Hong Kong, China  
e-mail: [zhaoxuwu@cityu.edu.hk](mailto:zhaoxuwu@cityu.edu.hk)

changing alloy composition, grain size, and texture, have been attempted to increase ductility and fracture toughness. Improved ductility has been demonstrated in some Mg alloys and under certain thermomechanical processing conditions. In particular, a wide range of experimental studies suggest that Mg alloyed with rare-earth elements in solid solution state [8–13], grain refinement [14] and texture randomization [15, 16] are effective methods to increase ductility. While these experimental successes are consistent with metallurgical wisdom, current understanding of ductility improvement in Mg is generally empirical, not mechanistic, qualitative, and thus of less predictive power in guiding new alloy designs.

We recently proposed a new quantitative mechanism [14] to capture the effects of solutes in enhancing ductility in Mg alloys. This mechanism is based on the acceleration of cross-slip of the pyramidal II  $\langle c+a \rangle$  screw dislocations due to a solute-driven decrease in the cross-slip energy barrier. If the acceleration is significant enough, cross-slip will enable fast  $\langle c+a \rangle$  dislocation multiplication that can generate plastic strain in spite of the on-going deleterious PB transitions (Fig. 1). The predictions based on the new mechanistic model were shown to be in broad agreement with experimental results on existing Mg alloys. Moreover, application of the mechanistic model to study a much wider range of

possible alloys, especially those without RE additions, holds the promise of accelerating the design of new ductile Mg.

In this work, we briefly present key features of the model for solute-enhanced cross-slip and then focus on the predictions of the model for a range of non-RE multicomponent alloys. This work summarizes a much more complete study that was recently published by the same authors [17], and many details can be found there.

## Ductility Enhancement via Accelerated Cross-Slip: Theory

Plastic slip via  $\langle c+a \rangle$  dislocations are critical to achieving high ductility in HCP Mg. During plastic straining,  $\langle c+a \rangle$  dislocation loops, either preexisting inside grains or nucleated from grain boundaries, will expand and carry the plastic strain. The edge segments of the dislocation loop are prone to undergo the PB transition and become sessile, locking the dislocation segments and further blocking subsequent  $\langle c+a \rangle$  dislocations on the same or nearby parallel pyramidal planes. Plastic slip in the  $\langle c+a \rangle$  dislocation Burgers vector direction thus becomes difficult, requiring a much higher CRSS to continue [2]. While the edge segments become sessile, the screw segments can continue to glide, expand,

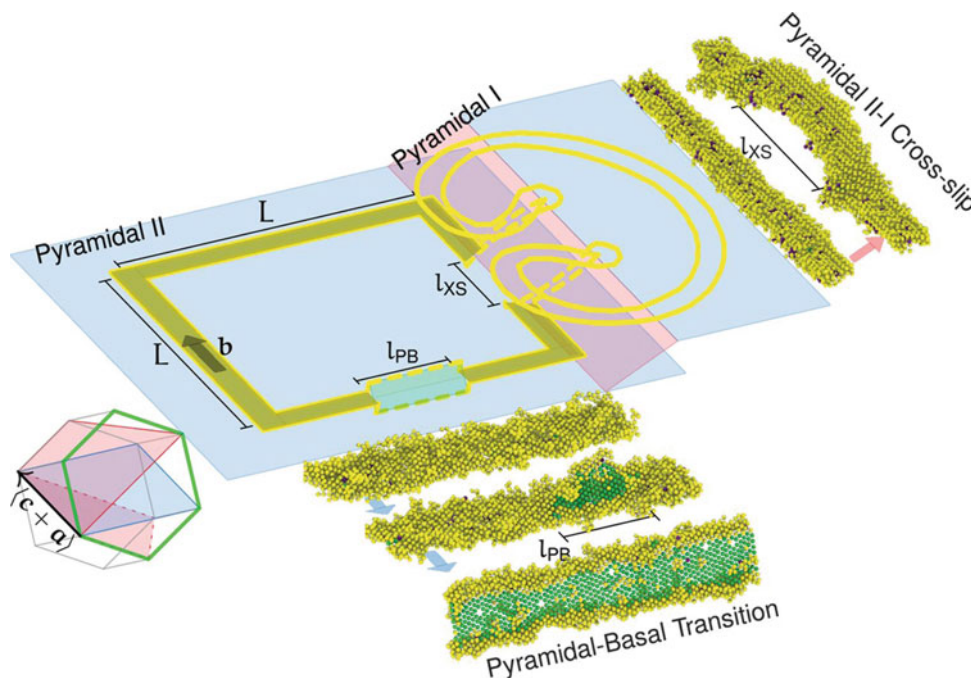


**Fig. 1** Schematic of the competing thermally activated dislocation phenomena in magnesium. Mobile edge dislocation segments of a pyramidal II  $\langle c+a \rangle$  dislocation undergo a thermally activated transformation to a sessile structure with a barrier of  $\Delta G_{PB} = 0.5\text{eV}$ . Mobile screw dislocation segments of the same dislocation can undergo thermally activated cross-slip and double cross-slip, leading to

dislocation multiplication, with a barrier of  $\Delta G_{XS}$ . If the rate of screw cross-slip sufficiently exceeds the rate of edge immobilization, then plastic straining can be sustained and high ductility can be achieved. Solute additions can change the cross-slip barrier  $\Delta G_{XS}$  which, if reduced sufficiently by solutes, can provide the conditions for ductility. From Ref. [14], and reprinted with permission from AAAS

and potentially undergo a cross-slip and double cross-slip process. Dislocation cross-slip and double cross-slip effectively create a new dislocation loop on a new slip plane, which can overcome the locking of the original edge segment, and glide further to accommodate the imposed plastic strain. The newly formed dislocation loop can also serve as a  $\langle \mathbf{c} + \mathbf{a} \rangle$  dislocation Frank–Read source, potentially supplying many new  $\langle \mathbf{c} + \mathbf{a} \rangle$  dislocations. To sustain plastic slip along the  $\langle \mathbf{c} + \mathbf{a} \rangle$  direction and thus satisfying strain compatibility requirement for continued plastic deformation, the rate of cross-slip of the screw segments and thus generation of new dislocation loops must be much faster than the rate of the deleterious PB transition occurring at the edge segments. The two crucial processes at the screw and edge segments are both thermally activated and their competition governs the  $\langle \mathbf{c} + \mathbf{a} \rangle$  strain capability and ductility. To achieve high ductility, the following condition on their respective rates  $R_{XS}$  and  $R_{PB}$  along the dislocation loop of size  $L$  occurring at segments of size  $l_{XS}$  and  $l_{PB}$  (see Fig. 1) at temperature  $T$  must be satisfied,

$$R_{XS} = v_0 \frac{L}{l_{XS}} \exp\left(-\frac{\Delta G_{XS}}{kT}\right) \gg R_{PB} = v_0 \frac{L}{l_{PB}} \exp\left(-\frac{\Delta G_{PB}}{kT}\right) \quad (1)$$

where  $G_{XS}$  and  $G_{PB}$  are the activation energy barriers,  $v_0$  is an attempt frequency and  $k$  is Boltzmann constant. We introduce a ductility index  $\chi$  where the rate of cross-slip is 10% of the rate of PB transition, i.e.,  $R_{XS} = 10\% R_{PB}$ . We consider  $\chi > 1$ , i.e.,  $R_{XS} > 10R_{PB}$ , as a necessary condition for high ductility. For alloys satisfying the above condition, deformation will follow normal plastic flow and hardening, and failure may be governed by other criteria such as the Considere criterion for the onset of necking in elastic-plastic materials. When  $\chi < 0$ , poor ductility is predicted since  $\langle \mathbf{c} + \mathbf{a} \rangle$  cross-slip is too slow relative to the PB transition and cannot create enough  $\langle \mathbf{c} + \mathbf{a} \rangle$  dislocation and plastic strain to overcome the immobilization caused by the PB transition. Our strategy to enhance ductility relies mainly on reducing the cross-slip barrier  $\Delta G_{XS}$  through solid solution alloying, since all other parameters are insensitive to changes of alloy compositions. Solute interact with dislocation core, stacking fault and its elastic field. Solute can thus have subtle effects on dislocation cross-slip energy barriers and rates [18]. The central part of the theory and alloy design thus essentially reduce to the determination of the effects of solutes on the cross-slip barrier  $\Delta G_{XS}$  as a function of solute composition and concentration.

In HCP structures, pyramidal II planes do not intersect with each other and  $\langle \mathbf{c} + \mathbf{a} \rangle$  dislocations on pyramidal II planes must first cross-slip to an intersecting pyramidal I plane sharing the same Burgers vector. In HCP Mg, screw  $\langle \mathbf{c} + \mathbf{a} \rangle$  dislocations have lower energy on pyramidal II

planes than on pyramidal I planes. The energy barrier for cross-slip thus has contributions from the dislocation energy difference  $\Delta E^{I-II}$  between the two pyramidal planes, in addition to the usual energies associated with dislocation jog/junctions formations and line tensions. Using the dislocation line tension model, the cross-slip energy barrier can be written as

$$\Delta G_{XS} = \Delta G_{XS,i} + \Delta E^{I-II} l_{XS} + \Gamma \Delta s(l_{CXS}) - \Delta \tau b A(l_{CXS}) \quad (2)$$

where  $\Delta G_{XS,i} = 0.23$  eV [19] is the intrinsic barrier associated with jog/junctions formation during cross-slip;  $l_{XS}$  is the length of the cross-slip nucleus at the transition state,  $l_{CXS}$  the nucleation length that includes the length of the pyramidal I/II junction,  $\Gamma$  is the screw dislocation line tension on pyramidal I planes,  $b$  the Burgers vector,  $\Delta s$  the additional length of the cross-slipped bow-out segment on the pyramidal I plane,  $A$  the bow-out area, and  $\Delta \tau$  the resolved shear stress on the pyramidal I  $\langle \mathbf{c} + \mathbf{a} \rangle$  dislocation in excess of the corresponding CRSS that performs work by bowing out the cross-slipping nucleus.

A solute at site  $i$  can interact with the dislocation on the pyramidal II plane before cross-slip and with the dislocation on the pyramidal I plane after cross-slip. The change in interaction energy of a solute of type  $m$  at site  $i$  is denoted as  $\Delta U_i^{I-II,m}$ . The average change in energy per unit dislocation length upon cross-slip can then be written as

$$\langle \Delta E^{I-II} \rangle = \Delta E_{Mg}^{I-II} + \frac{1}{b} \sum_m c_m \sum_{i \in N_T} \Delta U_i^{I-II,m} \quad (3)$$

where  $\Delta E_{Mg}^{I-II}$  is the energy difference in pure Mg,  $c_m$  is the solute concentration of solute type  $m$ , and the sum is over all unique sites  $i$  around the dislocation within one Burgers vector length where the energy difference is nonzero. These energies cannot be computed fully with ease, and hence, it was postulated that the dominant interaction energy arises from the solute interactions with the dislocation stacking faults, as both pyramidal I and II dislocations are dissociated into partial dislocations separated by a stacking fault. The average energy difference can then expressed as

$$\langle \Delta E^{I-II} \rangle = \Delta E_{Mg}^{I-II} + \sum_m \Delta E_{avg,SF}^{I-II,m} c_m \quad (4)$$

where  $\Delta E_{avg,SF}^{I-II,m}$  is the contribution of type  $m$  solute/stacking fault interaction energies in the average dislocation energy difference.  $\Delta E_{avg,SF}^{I-II,m}$  is computed from first-principles density functional theory calculations [1, 17]. In a random solid solution alloy, there are local fluctuations in the concentration of the alloying elements. Thus, there are fluctuations in the local pyramidal I and II screw dislocation energies over



the scale of the nucleation length  $l_{XS}$ . The standard deviation in pyramidal I/II energy difference, due to these fluctuations, over the length of  $l_{XS}$  can be computed as

$$\sigma[l_{XS}] = \sqrt{\frac{l_{XS}}{b} \sum_m c_m \sum_{i \in N_T} (\Delta U_i^{I-II,m})^2} = \sqrt{\frac{l_{XS}}{b} \sum_m c_m (\Delta E_{\text{fluc,SF}}^{I-II,m})^2} \quad (5)$$

where the second term considers only the energy contributions due to the solute/stacking fault interactions. Some fluctuations raise the energy and others lower it; only those that reduce the local barrier are relevant, and so the magnitude of the fluctuation contribution is always subtracted from the average barrier to obtain the operative barrier. Assembling all the factors that determine the activation barrier and critical cross-slip nucleation length, the ductility index  $\chi$  can be expressed as

$$\chi = \frac{1}{\ln 10} \left[ \ln \left( \frac{l_{PB}}{l_{XS}} \right) + \frac{\Delta G_{PB} - (\langle \Delta G_{XS} \rangle - \sigma[l_{XS}])}{kT} \right]. \quad (6)$$

The DFT calculations on a wide range of solutes led to the determination of the average and fluctuation contributions to the energy barrier as shown in Fig. 2. Figure 2 immediately shows that the rare-earth elements and Zr are highly effective in reducing the cross-slip barrier, both on average and due to fluctuations. The solutes Ca and Sr are also effective on average, being negative, with significant fluctuations as well, while Mn is effective on average but with smaller fluctuation contributions. The solutes Sn, Li, and K have almost no effect on average, but some fluctuation contribution, especially K. The solutes Zn, Al, and Ag are all, on average, deleterious for ductility, but the fluctuation contributions, being always negative, can cancel or exceed the average contributions at some concentrations, leading to some reduction of the ductility index  $\chi$ .

More detailed predictions of  $\chi$  require the full theory. Two quantities that are not directly computable in the theory, but fall in a narrow range and can be estimated, are  $\Delta E_{\text{Mg}}^{I-II}$  and  $\Delta \tau$ . Examination of theory predictions versus experiments for the well-established solute elements of Al, Zn, and Y led to the deduction of  $\Delta E_{\text{Mg}}^{I-II} = 25 \text{ meV/nm}$  and  $\Delta \tau = 20 \text{ MPa}$ . Finally, for very low solute concentrations, where single solutes may have some effect and random statistics does not apply, additional analysis is required (see Ref. [17]).

## Representative Results

We now present a subset of results on ternary and quaternary alloys. The theory is used to compute  $\chi$  as a function of alloy composition, and ductility is indicated if  $\chi > 1$ . Since Zn is a

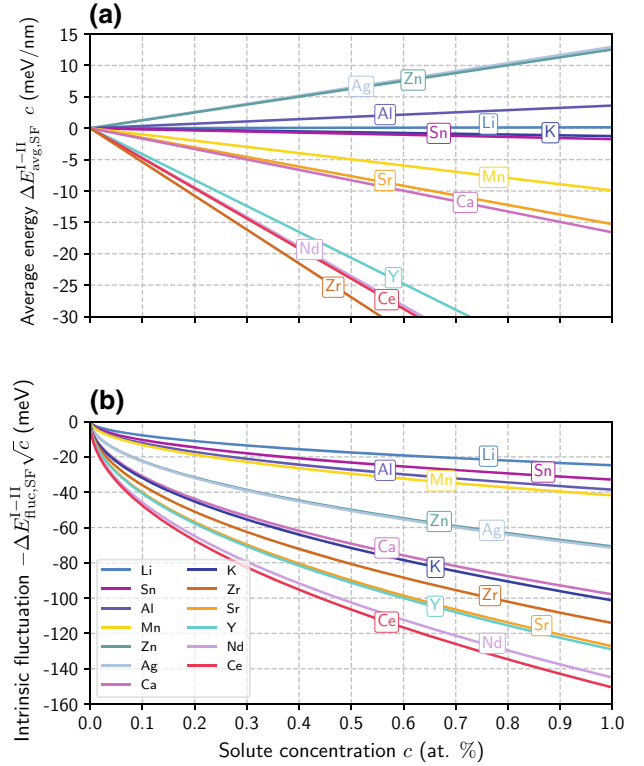


**Fig. 2** Variation of (a) average effect and (b) intrinsic fluctuation of various solutes on pyramidal I/II  $\langle c + a \rangle$  dislocation energy difference as a function of corresponding solute concentrations  $c$ . From Ref. [17], and reprinted with permission from Elsevier

common alloying element for various reasons, we first consider Zn ternary alloys. Zn alone is not predicted to enable ductility—the negative fluctuation contribution is never large enough compared to the positive average contribution to reduce  $\chi$  below 0. However, since Zn does lower  $\chi$  relative to pure Mg, it has a beneficial effect when combined with other more favorable solutes. Figure 3a shows the predictions for  $\chi$  as a function of the Zn concentration and the concentration of a third alloy element X (X=K, Mn, Zr, Sr, Ca). In all cases, Mg can be made ductile by the addition of a small concentration of X as long as the concentration of Zn is less than about 1.5 at.%. For all cases, the addition of 0.5 at.% Zn enables ductility at the lowest concentration of the second element X. The effect is especially strong for Mn, where  $\chi = 1$  is reduced from  $\sim 0.4$  at.% Mn at 0 at.% Zn to  $\sim 0.2$  at.% Mn at 0.5 at.% Zn. The theory thus predicts that the addition of Zn at 0.5 at.% is broadly useful for enhancing the ductility across a range of alloys. Zn is not necessary for ductility, but its addition may be beneficial for other reasons such as its effects on the  $\langle a \rangle$  dislocations.

Figure 3b shows predictions for the ductility limit  $\chi = 1$  for various Al–Li–X quaternary alloys, for X=Mn, K, Sr. The lines in the figure correspond to the boundary between

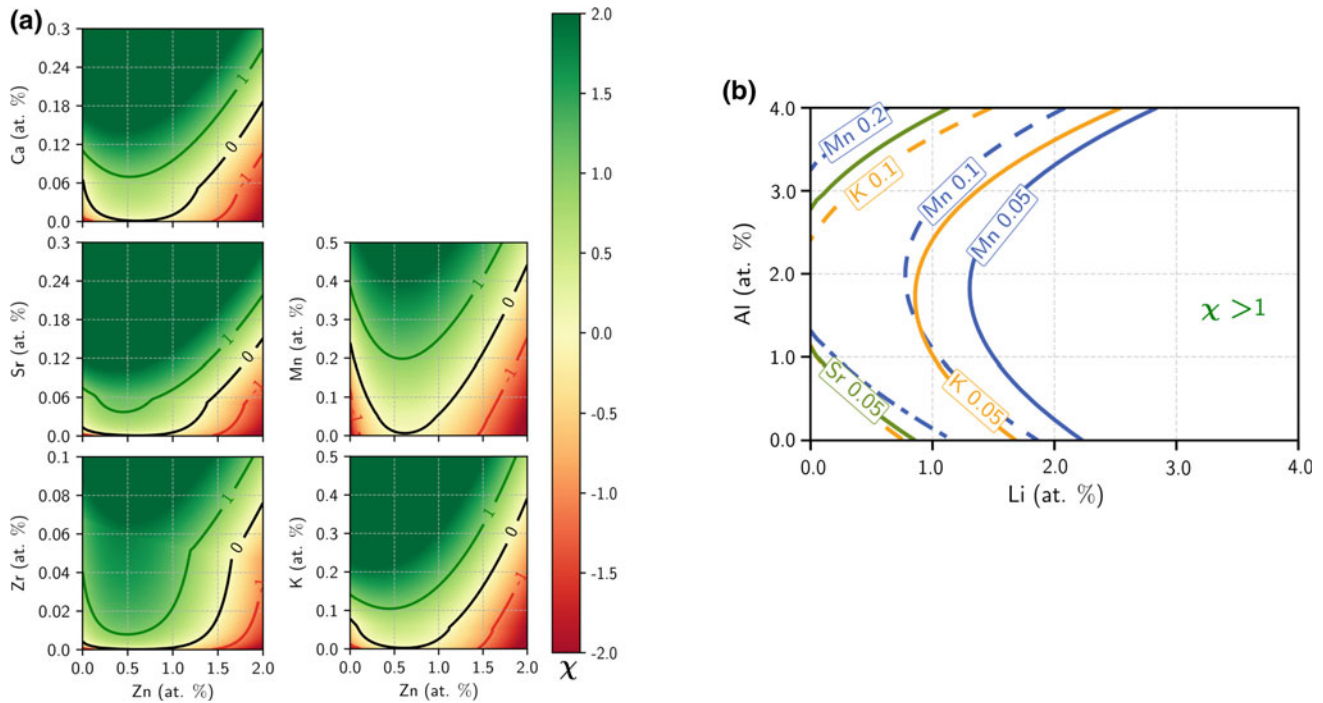


**Fig. 3** **a** Ductility index  $\chi$  for a range of Mg–Zn–X ternary alloys.  $\chi > 1$  corresponds to predictions of good ductility, while  $\chi < 0$  corresponds to predictions of poor ductility. A wide range of composition space, at very low alloying concentrations, is predicted to enable ductility in these ternary alloys. **b** Ductility index  $\chi$  for a range

of Mg–Al–Li quaternary alloys.  $\chi > 1$  corresponds to predictions of good ductility, while  $\chi < 0$  corresponds to predictions of poor ductility. A wide range of composition space, at very low alloying concentrations, is predicted to enable ductility in these quaternary alloys. Adapted from Ref. [17], and reprinted with permission from Elsevier

$\chi > 1$  (right) and  $\chi < 1$  (left), for each concentration of X indicated. For instance, in the Mg–Al–Li–Mn quaternary, ductility ( $\chi > 1$ ) can be achieved at 2.0 at.% Al, 1.0 at.% Li with the addition of 0.1 at.% Mn. Many other examples are provided in similar graphical form in the related publication [17].

## Discussion

The theory makes predictions for a wide range of alloying elements and compositions that can lead to high ductility. This wide space thus enables possible optimization of other important alloy properties (e.g. yield strength, toughness, corrosion resistance, and bio-compatibility) that are needed for using Mg alloys in various applications. Related to strengthening, we note that precipitation removes solutes from the matrix. If the residual total solute concentrations in the matrix are too low, the matrix composition may drop below the conditions predicted for ductility. The strengthening that accompanies precipitation may then lead to a significant reduction in ductility. The identification here of a wide range of ductilizing alloying elements at low concentrations opens, however, the possibility that alloys can be developed with elements that

form desirable precipitates and other elements that remain in solution such that the matrix remains ductile after precipitation, thus achieving both strength and ductility. Pursuing such concepts requires combining the present analysis of ductility with thermodynamic calculations of phase diagrams and solution limits of alloying elements in complex alloys.

**Acknowledgements** WAC and RA acknowledge financial support of this work through a grant from the Swiss National Science Foundation entitled “Control of Atomistic Mechanisms of Flow in Magnesium Alloys to Achieve High Ductility” (project #162350). The authors also acknowledge support from EPFL to the Laboratory for Multiscale Mechanics Modeling that enabled the required high-performance computing provided by Scientific IT and Application Support (SCITAS) at EPFL.

## References

1. B. Yin, Z. Wu, W. A. Curtin, Comprehensive first-principles study of stable stacking faults in hcp metals, *Acta Materialia* 123 (2017) 223–234.
2. Z. Wu, W. A. Curtin, The origins of high hardening and low ductility in magnesium, *Nature* 526 (2015) 62–67.
3. Z. Wu, W. A. Curtin, Intrinsic structural transitions of the pyramidal I  $\langle c+a \rangle$  dislocation in magnesium, *Scripta Materialia* 116 (2016) 104–107.



4. H. Tonda, S. Ando, Effect of temperature and shear direction on yield stress by  $\{11\bar{2}2\}\langle\bar{1}123\rangle$  slip in HCP metals, *Metallurgical and Materials Transactions A* 33 (2002) 831–836.
5. Z. Wu, W. A. Curtin, Brittle and ductile crack-tip behavior in magnesium, *Acta Materialia* 88 (2015) 1–12.
6. H. Friedrich, S. Schumann, Research for a “new age of magnesium” in the automotive industry, *Journal of Materials Processing Technology* 117 (2001) 276–281.
7. M. K. Kulekci, Magnesium and its alloys applications in automotive industry, *International Journal of Advanced Manufacturing Technology* 39 (2008) 851–865.
8. S. R. Agnew, J. W. Senn, J. A. Horton, Mg sheet metal forming: Lessons learned from deep drawing Li and Y solid-solution alloys, *JOM* 58 (2006) 62–69.
9. S. Sandlöbes, S. Zaefferer, I. Schestakow, S. Yi, R. Gonzalez-Martinez, On the role of non-basal deformation mechanisms for the ductility of Mg and Mg–Y alloys, *Acta Materialia* 59 (2011) 429–439.
10. S. Sandlöbes, M. Friák, J. Neugebauer, D. Raabe, Basal and non-basal dislocation slip in Mg–Y, *Materials Science and Engineering: A* 576 (2013) 61–68.
11. S. Sandlöbes, Z. Pei, M. Friák, L. F. Zhu, F. Wang, S. Zaefferer, D. Raabe, J. Neugebauer, Ductility improvement of Mg alloys by solid solution: Ab initio modeling, synthesis and mechanical properties, *Acta Materialia* 70 (2014) 92–104.
12. Y. Huang, W. Gan, K. U. Kainer, N. Hort, Role of multi-microalloying by rare earth elements in ductilization of magnesium alloys, *Journal of Magnesium and Alloys* 2 (2014) 1–7.
13. H. Rikihisa, T. Mori, M. Tsushida, H. Kitahara, S. Ando, Influence of yttrium addition on plastic deformation of magnesium, *Materials Transactions* 58 (2017) 1656–1663.
14. Z. Wu, R. Ahmad, B. Yin, S. Sandlöbes, W. A. Curtin, Mechanistic origin and prediction of enhanced ductility in magnesium alloys, *Science* 359 (2018) 447–452.
15. R. K. Mishra, A. K. Gupta, P. R. Rao, A. K. Sachdev, A. M. Kumar, A. A. Luo, Influence of cerium on the texture and ductility of magnesium extrusions, *Scripta Materialia* 59 (2008) 562–565.
16. R. K. Sabat, A. P. Brahme, R. K. Mishra, K. Inal, S. Suwas, Ductility enhancement in Mg-0.2% Ce alloys, *Acta Materialia* 161 (2018) 246–257.
17. R. Ahmad, B. Yin, Z. Wu, W. Curtin, Designing high ductility in magnesium alloys, *Acta Materialia* 172 (2019) 161–184.
18. W. G. Nöhring, W. A. Curtin, Dislocation cross-slip in fcc solid solution alloys, *Acta Materialia* 128 (2017) 135–148.
19. Z. Wu, W. A. Curtin, Mechanism and energetics of  $\langle c+a \rangle$  dislocation cross-slip in hcp metals, *Proceedings of the National Academy of Sciences* 113 (2016) 11137–11142.

# Microstructure Evolution and Precipitation Strengthening in Ca-Containing Mg-Rare Earth Alloys

Qianying Shi, Bruce Williams, and John Allison

## Abstract

The significant precipitation strengthening during aging provides Mg-rare earth (RE) alloys with exceptional strength. The low density and reasonable cost of Ca could favor Mg alloys for commercial use with improved properties. In order to investigate the potential interaction effect of Ca for improving the aging response and strength of Mg-RE alloys, this study was performed. 0.5 wt% and 1.0 wt% Ca were added to the ternary alloy Mg-2 wt% Nd-4 wt% Y. The microstructures of different processing conditions were examined by a series of experimental characterization techniques. The microstructure evolution and phase transformations were also calculated by commercial CALPHAD software. Vickers hardness tests were performed to characterize the aging response of the quaternary Mg-2 wt% Nd-4 wt% Y-0.5 wt% Ca alloy. Current results showed that 0.5 wt% Ca addition accelerated the peak aging, as compared to the previously studied ternary Mg-Nd-Y alloy. The initial APT analysis on the aged samples indicated that Ca segregated with Nd and Y in the precipitates in Mg-RE alloys.

## Keywords

Magnesium alloys • Rare earth • Calcium • Precipitation • Microstructure

## Introduction

Because of its inherent soft nature, pure Mg needs to be strengthened for use as a structural material. Precipitation hardening, as one common method to strengthen alloys, is an especially effective strengthening method for Mg alloys containing rare earth (RE) elements [1]. RE elements have relatively high solubility in Mg-matrix at high temperatures, allowing the formation of fine precipitates during aging at lower temperatures. The unique crystallographic orientation relationship between these precipitates and Mg-matrix (the habit planes of precipitates are parallel to the prismatic planes of Mg-matrix) in Mg-RE alloy provides a significant effect on impeding dislocation motion [2]. However, RE elements are expensive for commercial applications. Therefore, it is necessary to optimize the level of RE elements in Mg alloys and explore alternative alloying elements to achieve the comparable strengthening effect.

Previous studies showed that Ca is a strong candidate element to be considered to add into Mg-RE alloys, since Ca benefits Mg alloys in many different ways, such as the low density, reduced cost, as well as the positive effect on the refinement of grains, texture and formability, and oxidation resistance [3-7]. However, the Ca effect on the precipitation strengthening in Mg alloys have primarily been investigated in Mg-Al/Zn based alloys [8-11]. There is a very limited study of Ca effect on the metastable precipitates in Mg-RE alloys [12]. The potential interaction of Ca with RE elements such as Nd and Y is interesting for the possibility that Ca may play a role in increasing the precipitation strengthening and allow reduction in RE elements. Here, an initial investigation on the microstructural evolution and precipitation for Ca-containing Mg-Nd-Y alloys is presented. Microstructures at different processing conditions were analyzed and discussed. The aging response and precipitation strengthening were also examined and compared between alloys with and without Ca addition.

Q. Shi (✉) · J. Allison  
Department of Materials Science and Engineering, University of Michigan, 2300 Hayward Street, Ann Arbor, MI 48109, USA  
e-mail: [shiqiany@umich.edu](mailto:shiqiany@umich.edu)

B. Williams  
CanmetMATERIALS, Natural Resources Canada, 183 Longwood Road South, Hamilton, ON L8P 0A5, Canada

## Experimental Procedures

The alloys used in this study were provided by CanmetMATERIALS, Canada. As listed in Table 1, five casting Mg–2 wt%Nd–4 wt%Y-based alloys with different Ca additions were examined. Three alloys with 0 Ca, 0.5 wt% Ca, and 1 wt% Ca were cast as small bars with 25 mm diameter, which are named as alloy SC0, alloy SC0.5, and alloy SC1, respectively. The other two alloys named alloy LC0.5 and alloy LC1 were cast as large cylindrical billets with 85 mm diameter. These five alloys were solution treated for 24 h at a temperature determined by differential scanning calorimetry (DSC) measurements and several solution heat treatment trials. One large cast billet of alloy LC0.5 was extruded into 15 mm bar at CanmetMATERIALS. The as-received alloy LC0.5 extruded bar was then solution heat treated and aged at 200 and 250 °C for different time periods to obtain aging curves. Aging response was characterized by hardness measurements, which were performed using a Vickers microhardness indenter with a load of 100 g and dwell time of 15 s. Each heat treatment step was followed by water quenching.

The microstructures of these alloys after different processing procedures were examined by a series of microstructural characterization tools including optical microscope (OM), scanning electron microscope (SEM), energy dispersive spectroscopy (EDS), and electron backscatter diffraction (EBSD). Needle-like atom probe tomography (APT) specimens were prepared using focused ion beam (FIB) lift-out technique on a FEI Helios 650 dual-beam system. APT data was collected on a Cameca LEAP 5000XR instrument operated in the laser-pulsing mode with a pulse energy of 50pJ and a specimen temperature of 30 K. Post-analysis data visualization and evaluation were carried out using the Integrated Visualization and Analysis Software (IVAS) package. For the comparison with the experimental results,

**Table 1** Nominal compositions of investigated Mg–Nd–Y–(Ca) alloys (wt%)

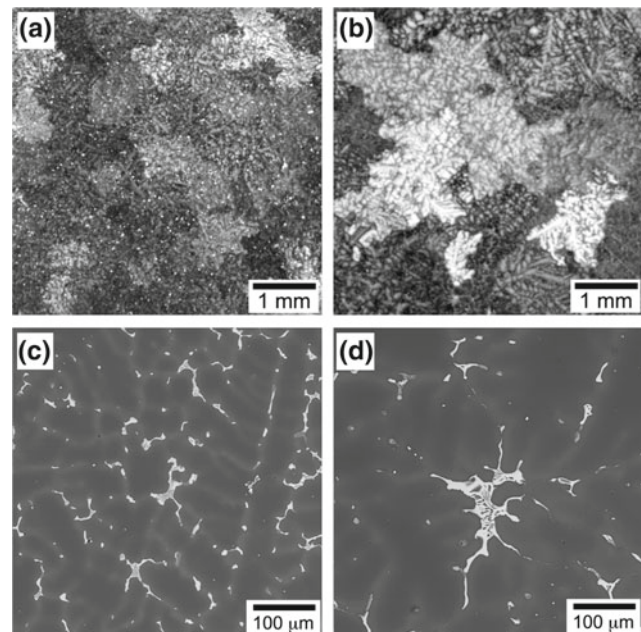
Alloy	Mg	Nd	Y	Ca	Casting geometry
SC0	Bal.	2.0	4.0	0	Small casting bar with 25 mm diameter
SC0.5	Bal.	2.0	4.0	0.5	Small casting bar with 25 mm diameter
SC1	Bal.	2.0	4.0	1.0	Small casting bar with 25 mm diameter
LC0.5	Bal.	2.0	4.0	0.5	Large casting cylinder with 85 mm diameter
LC1	Bal.	2.0	4.0	1.0	Large casting cylinder with 85 mm diameter

thermodynamic calculations on the microstructural evolution and phase transformation were performed using commercial CALPHAD software ThermoCalc.

## Results and Discussion

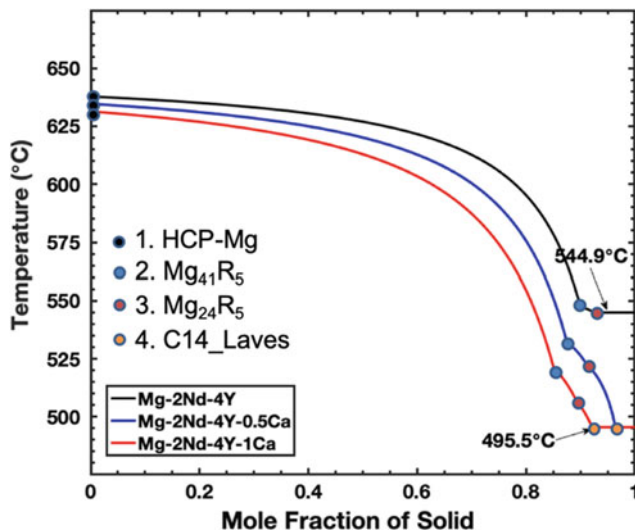
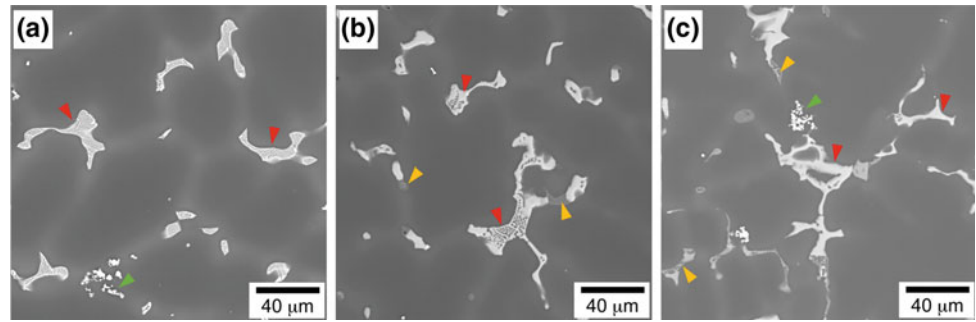
### As-Cast Microstructure

Figure 1 shows the typical as-cast microstructures of these alloys, taking the alloys SC0.5 and LC0.5 as an example to compare the effect of different casting geometry. It is clearly shown that the grain size and secondary dendrite arm spacing in large casting cylinders are much larger (Fig. 1b, d) than that in small casting bars (Fig. 1a, c), while the consistency of phase constitution for same alloy composition with two different casting conditions is observed (Fig. 1c, d). Different types and amounts of primary intermetallic phases in as-cast microstructures of alloys with different Ca additions were found, as shown in Fig. 2. For the baseline alloy without Ca addition, the microstructure consists of the Mg-matrix and primary  $\beta$  phase (marked by red arrows in Fig. 2a), which is concentrated with Nd and Y as measured by EDS. With the Ca addition,  $Mg_2Ca$ -Laves phase appears (marked by yellow arrows in Fig. 2b, c). Ca addition increases the amount of  $\beta$  phase and changes the morphology of  $\beta$  phase from the nearly lamellar shape to nearly blocky shape. EDS measurement showed that Ca also enriches in  $\beta$  phase. It should be mentioned that those dispersed particles with a relatively



**Fig. 1** Typical as-cast microstructures in alloys SC0.5 and LC0.5. **a** alloy SC0.5, OM; **b** alloy LC0.5, OM; **c** alloy SC0.5, SEM; **d** alloy LC0.5, SEM

**Fig. 2** Primary intermetallic phases in as-cast microstructures of alloys with different Ca additions. **a** alloy SC0; **b** alloy SC0.5; **c** alloy SC1



**Fig. 3** Scheil solidification prediction using commercial CALPHAD software ThermoCalc

low fraction observed in the as-cast microstructure (marked by green arrows in Fig. 2a, c) are strongly concentrated with Y, which are identified as  $Mg_2Y$  phase.

Scheil solidification predictions were performed using ThermoCalc software with database TCMG5 for each alloy composition. As presented in Fig. 3 and Table 2, the Scheil calculation is consistent with the above experimental observation, including the appearance of  $Mg_2Ca$ -Laves phase and the amount change of  $\beta$  phase. Two types of  $\beta$  phase,  $Mg_{41}R_5$  and  $Mg_{24}R_5$ , were predicted in the Scheil calculation. In the thermodynamic database of ThermoCalc software,  $Mg_{41}R_5$  is the equilibrium  $\beta$  phase in Mg–Nd binary system, and

$Mg_{24}R_5$  is the equilibrium  $\beta$  phase in Mg–Y binary system. As listed in Table 2, with increasing Ca addition, the mole fraction of  $Mg_2Ca$ -Laves and  $\beta$  phase increases accordingly. In addition, the Scheil calculation also indicates that Ca addition decreases the formation temperature of Mg-matrix and  $\beta$  phase. This can be confirmed by DSC experimental measurements. Figure 4 is the DSC heating curves of five as-cast alloys measured with a heating rate of 10 K/min. Those peaks appearing in the DSC measurement represent different phase transformations. Peak A indicates the dissolution of  $Mg_2Ca$ , peak B indicates the dissolution of  $\beta$  phase, peak C indicates the formation of liquid, and the location C' is the starting point of peak C transformation. It can be seen that the phase transformation peaks B and C shift to the left towards the lower temperature with increasing Ca addition. No significant difference between alloys with different casting geometry was observed. The Scheil calculation and DSC experimental measurement provide a guideline to determine the appropriate solution heat treatment, such that the solution heat treatment temperature has to be lower than C' temperature, in order to acquire a homogenous solid solution without any transformation from the solid phases into liquid.

### Solution Heat Treated Microstructure

Based on the above results, the appropriate solution heat treatment temperature for each alloy was determined, which is 560 °C for alloy without Ca addition, 520 °C for alloy with 0.5 wt% Ca, and 510 °C for alloy with 1 wt% Ca. Figure 5 shows the microstructure after the solution heat treatment at the determined temperature for 24 h for each

**Table 2** Mole fraction of phases predicted by the Scheil solidification model for investigated Mg–Nd–Y–(Ca) alloys

Phases	Mg–2 wt%Nd–4 wt%Y (%)	Mg–2 wt%Nd–4 wt%Y–0.5 wt%Ca (%)	Mg–2 wt%Nd–4 wt%Y–1 wt%Ca (%)
$Mg_{41}R_5$ (Nd– $\beta_c$ phase)	4.5	4.6	4.6
$Mg_{24}R_5$ (Y– $\beta_c$ phase)	1.9	2.4	2.5
$Mg_2Ca$ -Laves	–	0.7	1.6

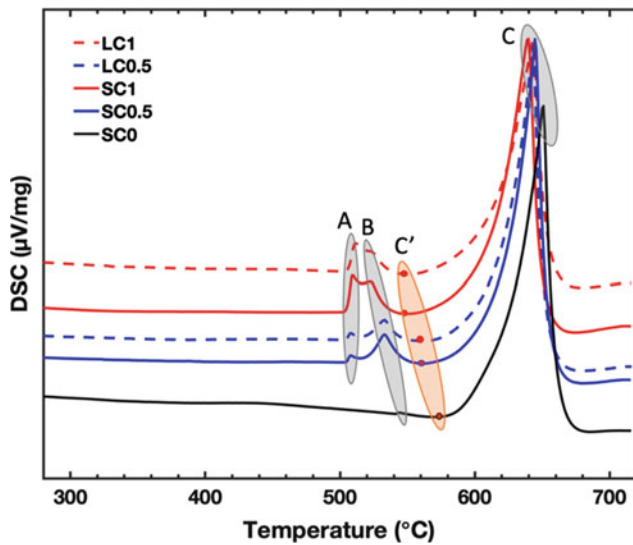


**Fig. 4** DSC heating curves of five as-cast Mg–Nd–Y–(Ca) alloys

alloy. It should be noticed that the solution heat treatment could not completely dissolve  $\beta$  phase in Ca-containing alloys (Fig. 5b–e), even though the solution heat treatments with higher temperature and multi-steps were investigated. The amount of remaining  $\beta$  phase is higher in alloys SC1 (Fig. 5c) and LC1 (Fig. 5e), compared to alloys SC0.5 (Fig. 5b) and LC0.5 (Fig. 5d), respectively. The incipient melting, instead of the elimination of  $\beta$  phase, occurred at the higher temperature, for instance, 540 °C for alloy SC0.5, as shown in Fig. 5f. Because of the remaining  $\beta$  phase in the solution heat treated microstructure of Ca-containing alloys, the Mg-matrix composition would be different from the overall alloy composition which affects the precipitation

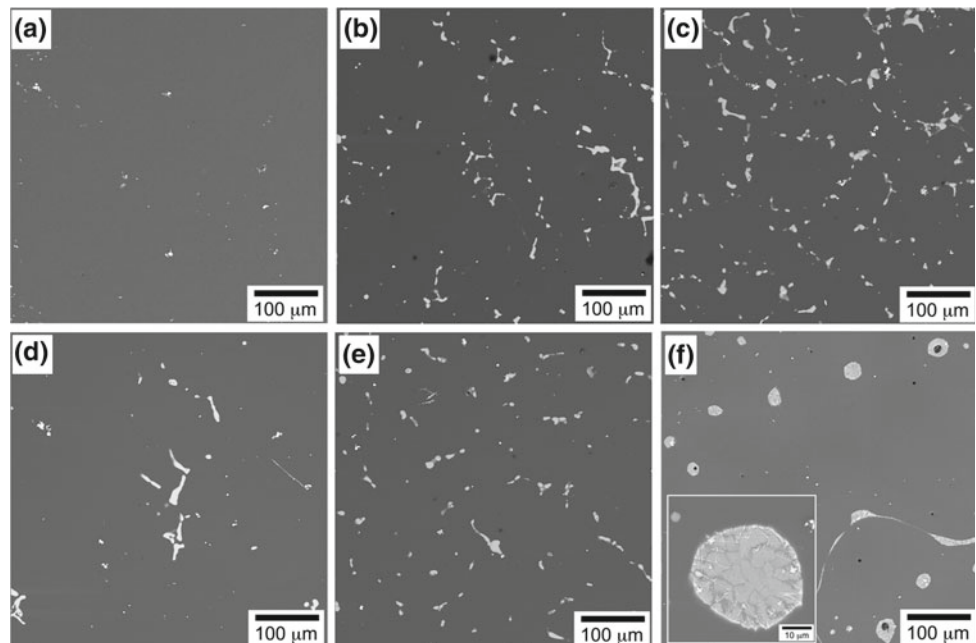
prediction since the precipitate phases form from the matrix. The actual matrix composition (instead of the alloy composition) should be used to predict the precipitation behavior in the future studies. Additionally, considering the undissolved large  $\beta$  phase in Ca-containing Mg–RE alloys, higher amounts of Ca could be detrimental.

Figure 6 shows the microstructure and texture of the extruded alloy LC0.5 after solution heat treatment at 520 °C for 24 h. Compared to the as-extruded condition (Fig. 6a), the amount of primary intermetallic phases (mainly  $\beta$  phase) was reduced, although  $\beta$  phase was still not completely dissolved, as expected (Fig. 6b). In addition, the grain growth and texture were also observed at the solution heat treated condition (Fig. 6b–d). A large grain size ( $\sim 100$  to 200  $\mu\text{m}$ ) was found in this alloy after heat treated at 520 °C for 24 h, as shown in the EBSD map in Fig. 6c. The fiber texture which was usually observed in extruded Mg alloys was weakened in the currently studied Ca-containing Mg–RE alloy. This is consistent with the previous studies that indicated RE elements and Ca can promote the texture weakening of Mg alloy [6, 7, 13, 14].

### Aging Response and Precipitation

The aging curves for the extruded alloy LC0.5 at 200 and 250 °C are shown in Fig. 7. For 200 °C, the hardness gradually increases until the peak aging appears at 96 h, which is then followed by a gradual decrease. Compared to the aging response of a ternary Mg–Nd–Y alloy (Mg–1.64 wt%Nd–3.72 wt%Y) at 200 °C [15], the hardness increases, and an earlier peak aging time is observed. This

**Fig. 5** Microstructure after the solution heat treatment for each alloy. **a** alloy SC0 at 560 °C for 24 h; **b** alloy SC0.5 at 520 °C for 24 h; **c** alloy SC1 at 510 °C for 24 h; **d** alloy LC0.5 at 520 °C for 24 h; **e** alloy LC1 at 510 °C for 24 h; **f** alloy SC0.5 at 540 °C for 2 h





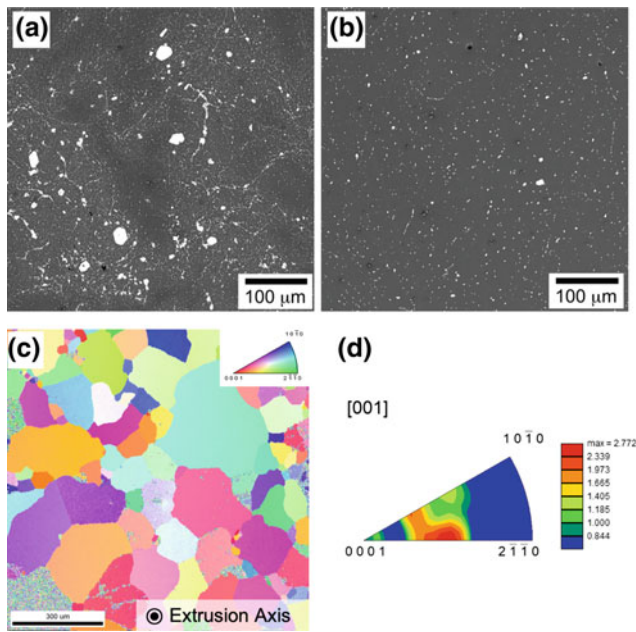


**Fig. 6** Microstructure and texture of extruded alloy LC0.5 at as-extruded condition (a) and after solution heat treatment at 520 °C for 24 h (b, c, d). The inverse pole figure in (d) is viewed from extrusion axis

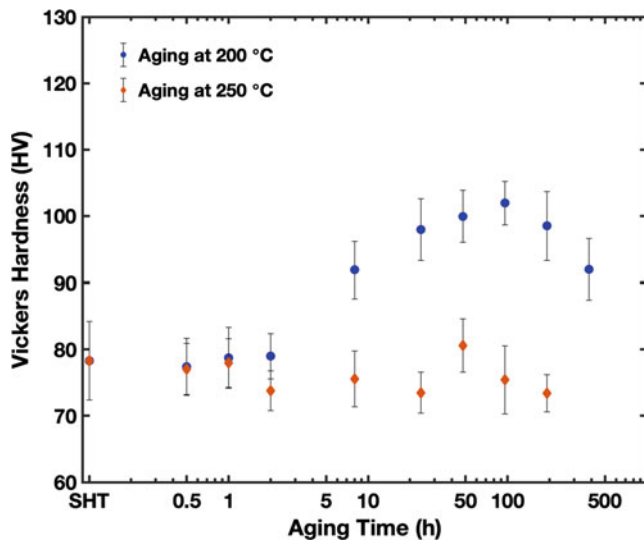


**Fig. 7** Aging response curves of extruded alloy LC0.5 at 200 and 250 °C

could be partially attributed to the effect of 0.5 wt% Ca addition. However, it is difficult to locate the peak aging time at 250 °C for this currently investigated alloy, although the average hardness reached the maximum after aging for 48 h at 250 °C.

Samples from different aging stages (0.5 h, 2 h, 8 h, and 96 h at 200 °C and 48 h at 250 °C) were picked to investigate the precipitation behavior. In order to figure out the distribution of those solute elements (Nd, Y, and Ca),

especially with the question whether Ca would stay in the Mg-matrix or it would segregate in the precipitates, APT analysis was performed. With extended aging time at 200 °C, the concentrated regions for Nd, Y, and Ca appear to be more evident, indicating the precipitate evolution process from GP zones to precipitate phases ( $\beta'''$  and  $\beta'$ ). The precipitation sequences in ternary Mg–Nd–Y alloy with the similar composition as the 0Ca baseline alloy in this study were systematically investigated in previous studies [15, 16]. Precipitate phases form in the order of GP zones,  $\beta'''$ ,  $\beta'$ , and  $\beta_1$  with aging. Figure 8 demonstrates the APT reconstruction results with the distribution of elements Nd, Y, and Ca in extruded alloy LC0.5 at peak aging condition (200 °C/96 h).  $\beta'''$  and  $\beta'$  phases are expected to form at this condition, according to the previous studies [15, 16]. As shown in Fig. 8b, c, regions concentrated by Nd and Y could be easily identified as the precipitation phase. It is interesting to note that Ca appears to combine with Nd and Y in the precipitates (Fig. 8d). APT analysis on the sample aged at 250 °C/48 h also showed that Ca appears to combine with Nd and Y in the precipitates, which are expected to be  $\beta_1$  phase. This finding supports our initial hypothesis that Ca has a potential positive effect to promote the formation of  $\beta$ -family precipitates in Mg–RE alloys, which makes the thought of using Ca to increase the precipitation strengthening and replace a part of RE elements promising. In order to quantitatively characterize the segregation degree of Ca in different precipitate phases, additional TEM and APT investigations are ongoing.

## Conclusions

This study characterized the microstructures of investigated Mg–RE alloys with various Ca additions at different processing conditions through the experimental examinations and thermodynamic calculations. It has been demonstrated that Ca addition increases the amount of primary  $\beta$  phase that forms in the as-cast microstructure and also changes the  $\beta$  phase morphology. Guided by DSC measurements and CALPHAD (ThermoCalc) calculations, the appropriate solution heat treatment temperature was determined for each studied alloy. By avoiding incipient melting, the solution heat treatment for Ca-containing Mg–RE alloys would not completely dissolve the primary  $\beta$  phase, and the amount of remaining  $\beta$  phase is higher in alloys with high level of Ca addition. The aging response of the quaternary Mg–Nd–Y–Ca alloy shows an acceleration of peak aging at 200 °C, compared to the Mg–Nd–Y ternary alloy. APT characterization showed the Ca segregation in the strengthening precipitates, indicating the positive effect of Ca to promote the precipitation in Mg–RE alloys and thus increase the precipitation strengthening. The results from this study lay the

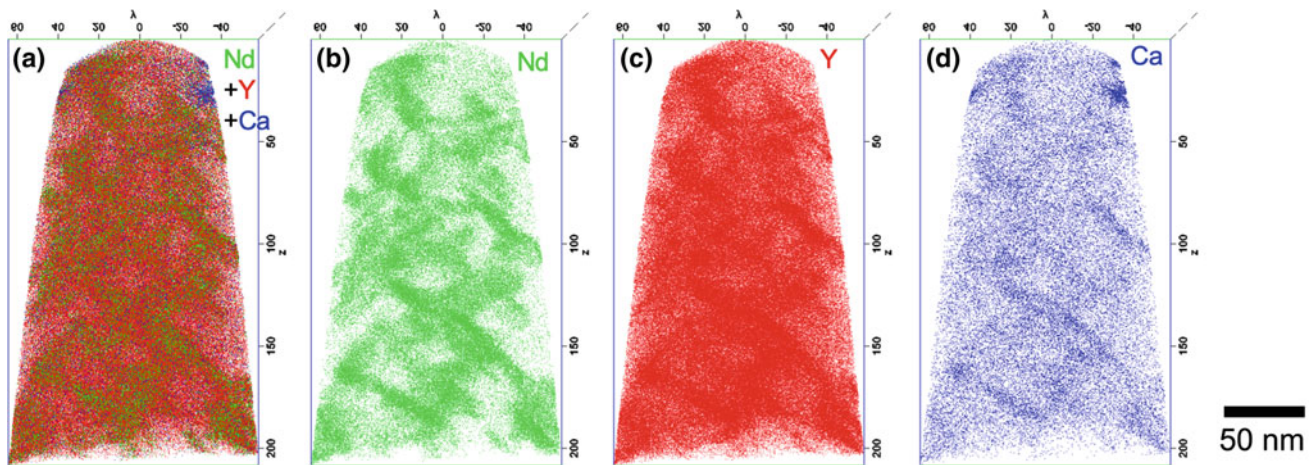


**Fig. 8** APT reconstruction with the distribution of alloying elements in extruded alloy LC0.5 after aging at 200 °C for 96 h. **a** Nd, Y, and Ca atoms; **b** Nd atoms only; **c** Y atoms only; **d** Ca atoms only

groundwork for the strength prediction in a quaternary Mg-alloy system using a multi-scale optimization framework which is currently under development within the PRISMS Center at University of Michigan.

**Acknowledgements** This work was supported by the U.S. Department of Energy, Office of Basic Energy Science, Division of Materials Science and Engineering (Grant award number DE-SC0008637). Authors acknowledge the access to and the support from Michigan Center for Materials Characterization (MC2) at University of Michigan.

## References

- Nie JF (2012) Precipitation and hardening in magnesium alloys. *Metall Mater Trans A Phys Metall Mater Sci* 43:3891–3939. <https://doi.org/10.1007/s11661-012-1217-2>
- Nie JF (2003) Effects of precipitate shape and orientation on dispersion strengthening in magnesium alloys. *Scr Mater* 48:1009–1015. [https://doi.org/10.1016/S1359-6462\(02\)00497-9](https://doi.org/10.1016/S1359-6462(02)00497-9)
- Nie JF, Muddle BC (1997) Precipitation hardening of Mg–Ca(–Zn) alloys. *Scr Mater* 37:1475–1481. [https://doi.org/10.1016/S1359-6462\(97\)00294-7](https://doi.org/10.1016/S1359-6462(97)00294-7)
- Mendis CL, Oh-Ishi K, Hono K (2012) Microalloying effect on the precipitation processes of Mg–Ca alloys. *Metall Mater Trans A Phys Metall Mater Sci* 43:3978–3987. <https://doi.org/10.1007/s11661-011-1049-5>
- Rad HRB, Idris MH, Kadir MRA, Farahany S (2012) Microstructure analysis and corrosion behavior of biodegradable Mg–Ca implant alloys. *Mater Des* 33:88–97. <https://doi.org/10.1016/j.matdes.2011.06.057>
- Zhang B, Wang Y, Geng L, Lu C (2012) Effects of calcium on texture and mechanical properties of hot-extruded Mg–Zn–Ca alloys. *Mater Sci Eng A* 539:56–60. <https://doi.org/10.1016/j.msea.2012.01.030>
- Stanford N (2010) The effect of calcium on the texture, microstructure and mechanical properties of extruded Mg–Mn–Ca alloys. *Mater Sci Eng A* 528:314–322. <https://doi.org/10.1016/j.msea.2010.08.097>
- Mendis CL, Oh-ishi K, Kawamura Y, et al (2009) Precipitation-hardenable Mg–2.4Zn–0.1Ag–0.1Ca–0.16Zr (at.%) wrought magnesium alloy. *Acta Mater* 57:749–760. <https://doi.org/10.1016/j.actamat.2008.10.033>
- Bettles CJ, Gibson MA, Venkatesan K (2004) Enhanced age-hardening behaviour in Mg–4 wt% Zn micro-alloyed with Ca. *Scr Mater* 51:193–197. <https://doi.org/10.1016/j.scriptamat.2004.04.020>
- Du W, Sun Y, Min X, et al (2003) Microstructure and mechanical properties of Mg–Al based alloy with calcium and rare earth additions. *Mater Sci Eng A* 356:1–7. [https://doi.org/10.1016/S0921-5093\(02\)00551-8](https://doi.org/10.1016/S0921-5093(02)00551-8)
- Luo AA, Powell BR, Balogh MP (2002) Creep and microstructure of magnesium-aluminum-calcium based alloys. *Metall Mater Trans A Phys Metall Mater Sci* 33:567–574. <https://doi.org/10.1007/s11661-002-0118-1>
- Zheng J, Li Z, Luo Z, et al (2017) Precipitation in Mg–Nd–Y–Zr–Ca alloy during isothermal aging: A comprehensive atomic-scaled study by means of HAADF-STEM. *Adv Eng Mater* 19:1–9. <https://doi.org/10.1002/adem.201600244>
- Jung IH, Sanjari M, Kim J, Yue S (2015) Role of RE in the deformation and recrystallization of Mg alloy and a new alloy design concept for Mg–RE alloys. *Scr Mater* 102:1–6. <https://doi.org/10.1016/j.scriptamat.2014.12.010>
- Imandoust A, Barrett CD, Al-Samman T, et al (2017) A review on the effect of rare-earth elements on texture evolution during processing of magnesium alloys. *J Mater Sci* 52:1–29. <https://doi.org/10.1007/s10853-016-0371-0>
- Solomon ELS, Chan T, Chen A, et al (2017) Aging behavior of Mg alloys containing Nd and Y. *Magnes Technol* 2017 349–352. [https://doi.org/10.1007/978-3-319-52392-7\\_50](https://doi.org/10.1007/978-3-319-52392-7_50)
- Solomon ELS (2017) Precipitation behavior of magnesium alloys containing neodymium and yttrium [D]. University of Michigan

# A Die-Cast Magnesium Alloy for Applications at Elevated Temperatures

Xixi Dong, Eric A. Nyberg, and Shouxun Ji

## Abstract

The application of magnesium alloys in internal combustion engines has advantages of lightweight, better damping and noise reduction and less vibration during operation. However, the applications of magnesium pistons in internal combustion engines are still difficult due to the demanding work environment and the rigorous requirements of the increased mechanical performance, thermal conductivity, and corrosion resistance at elevated temperatures. The development of high temperature die-cast magnesium alloys for piston applications is therefore challenging, as the high temperature mechanical performance, the die casting capability, and the thermal conductivity usually conflict with each other. Here we report a die-cast magnesium alloy for the piston applications at elevated temperatures, and the alloy development and the piston manufacturing process are introduced.

## Keywords

Magnesium alloy • High pressure die casting • High temperature application

## Introduction

Magnesium alloys have a great potential for structural applications in industries due to their significant weight savings, thus improving fuel economy and lessening environmental impact. The most significant magnesium applications are in castings, such as instrument panel, transfer cases, valve covers, various housings and brackets, and

steering components in automobiles [1]. High pressure die casting is a high efficiency process for the massive casting of the magnesium alloys [2]. Commercial die-cast magnesium alloys of AZ91, AM50, and AM60 are widely used in industry, and these alloys offer excellent combination of cast-ability, corrosion resistance and room temperature mechanical properties [3, 4]. However, it is hard for these widely applied die-cast magnesium alloys to use at elevated temperatures.

The limitation of the industrially widely used die-cast AZ91, AM50 and AM60 magnesium alloys in high temperature applications is due to the poor creep resistance of these Mg–Al based alloys at the elevated temperatures, as the low melting point  $\beta$ -Mg<sub>17</sub>Al<sub>12</sub> phase is not stable when the temperature increases to the level of  $\sim 175$  °C [5]. Improvements of creep resistance at elevated temperatures have been made by the introduction of alloying elements such as Si, Ca, Sr, and rare earth (RE) elements to the magnesium alloys [6–9], and RE elements is well accepted helpful for the improvement of mechanical performance at elevated temperatures [10, 11]. There have been a number of successful Mg–RE based alloys developed for semi-solid processing [12], sand-casting and permanent-mould casting, including WE54/43 [13] and AM-SC1 [14], but it has proven very challenging to make these alloys cast-able in high pressure die casting, as high pressure die casting is demanding for the low solid-liquid solidification temperature range, hot-tearing resistance, die soldering resistance, and excellent fluidity of the alloy, while the heavy addition of the RE in these Mg–RE based alloys deteriorate the features that required for high pressure die casting.

For die-cast magnesium alloys focusing on applications at elevated temperatures, in the earlier time, modifications and improvements have been focused on the Mg–Al based alloy system by the addition of the alkaline earth and RE elements [6–11]. Nissan patent [15] on a Mg–Al–Ca–RE alloy and later a Honda alloy ACM522 (Mg–5Al–2Ca–2RE) [16]. Two separate alloy systems with combined additions of Sr and Ca but no rare-earths have been developed by Noranda

X. Dong · S. Ji (✉)  
Brunel Centre for Advanced Solidification Technology (BCAST),  
Institute of Materials and Manufacturing, Brunel University  
London, Uxbridge, Middlesex UB8 3PH, UK  
e-mail: [shouxun.ji@brunel.ac.uk](mailto:shouxun.ji@brunel.ac.uk)

E. A. Nyberg  
Tungsten Parts Wyoming, Laramie, WY 82072, USA



[17] and General Motors [18]. The Noranda alloy is a Mg–Al–Sr–Ca alloy with small amounts of Sr and Ca (AJX Alloy). The GM version is a Mg–Al–Ca–Sr alloy with substantial Ca and a small amount of Sr (AXJ Alloy) [19]. A major development was the AE42 alloy including 4 wt% Al and 2 wt% RE, and the addition of the RE can suppress the formation of the  $\beta$ -Mg<sub>17</sub>Al<sub>12</sub> through the priority formation of the more thermal stable Al–RE containing intermetallics [20]. The AE42 alloy was further improved to the AE44 alloy with the increased addition of the RE of up to 4 wt% [5, 21]. Recently, a new Mg–RE based high temperature die-cast magnesium alloy HP<sub>2</sub><sup>+</sup> has been developed, which demonstrates better mechanical performance especially creep resistance at elevated temperatures than the previous reported high temperature die-cast magnesium alloys [22]. The HP<sub>2</sub><sup>+</sup> alloy includes (in wt%) 2.0–2.8La/Ce, 1.0Nd, 0.3Mn, up to 0.5Zn, less than 0.2Al and minor addition of Y or Be, and RE elements La/Ce acts as the cast base in the alloy rather than Al.

The application of magnesium alloys in internal combustion engines has advantages of lightweight, better damping and noise reduction and less vibration during operation. However, the applications of magnesium pistons in internal combustion engines are still difficult due to the demanding work environment and the rigorous requirements of the increased mechanical performance, thermal conductivity and corrosion resistance at the elevated temperature of at least 250 °C. The AE44 and HP<sub>2</sub><sup>+</sup> alloys might be the two promising high temperature die-cast magnesium alloys for applications at the elevated temperatures of ~200–250 °C, and it is hard for these alloys to be pistons alloys working at the elevated temperatures of at least 250 °C in engines. The development of high temperature die-cast magnesium alloys for piston applications is necessary but challenging [23], as the high temperature mechanical performance, the die cast-ability and the thermal conductivity usually conflict with each other.

In this work, the Mg–RE based Mg<sub>2</sub>.0La<sub>1</sub>.0Ce alloy was focused, and the effects of the RE element Y on the die-cast-ability and high temperature mechanical performance of the alloy were investigated. The optimized alloy with appropriate Y content was selected for the high pressure die casting trial of the magnesium piston.

## Experimental

### Material Preparation

The designed die-cast magnesium alloys, with the actual compositions (in wt%) of Mg<sub>2</sub>.0La<sub>1</sub>.0Ce<sub>0.3</sub>Mn<sub>0.3</sub>Zn<sub>x</sub>Y ( $x = 0.5, 1.0, 2.0$ ), were melted in the steel crucible using the

electric resistance furnace. The covering gas of N<sub>2</sub> and SF<sub>6</sub> with a volume ratio of 240:1 was used for the protection of the melts. The commercial purity ingot of pure Mg was first melted in the crucible, then the pure ingot of Zn and the master alloys of Al–30 wt% La, Al–30 wt% Ce, and Al–5 wt% Mn were added into the molten Mg to make the desired composition. During melting, the temperature of the furnace was controlled at 710 °C, and the melts were stirred at least three times for homogenisation. Afterwards, the melts were held for 30 min, and then the melts were ready for high pressure die casting.

### High Pressure Die Casting

The high pressure die casting was conducted on a 4500 kN cold chamber high pressure die casting machine. Two kinds of dies were applied for the high pressure die casting. The die shown in Fig. 1a was used for the high pressure die casting of the ASTM B557 standard round tensile test bars with the gauge dimension of  $\phi 6.35$  mm  $\times$  50 mm, for the tests of the room temperature and high temperature tensile properties of the developed die-cast magnesium alloys. The die shown in Fig. 1b was applied for the high pressure die casting of the magnesium piston using the developed die-cast magnesium alloy. The casting dies were heated by the circulation of the mineral oil, and the shot sleeve was heated by the circulation of the compressed hot water. The prepared magnesium alloy melts were loaded into the shot sleeve for high pressure die casting, and the pouring temperature of the melts was controlled at 690 °C by the K-type thermocouple.

### Tensile Tests at Room and Elevated Temperatures

The tensile tests of the die-cast ASTM B557 standard round tensile test bars were performed on an Instron 5500 Universal Electromechanical Testing Systems equipped with Bluehill software and a 50 kN load cell, at room temperature and the elevated temperature of 250 °C. Room temperature tensile test was conducted according to ASTM E8/E8 M [24]. During room temperature tensile test, the extensometer with a gauge length of 50 mm was applied for the monitoring of the strain, and the ramp rate for extension was set as 1 mm/min. High temperature tensile test was carried out according to the ASTM E21 [25] in which specimens were exposed to 250 °C for at least 40 min in an electrically heated air-circulating chamber before performing the tensile test. During high temperature tensile test, the straining rate for extension was set as 0.0002/s.

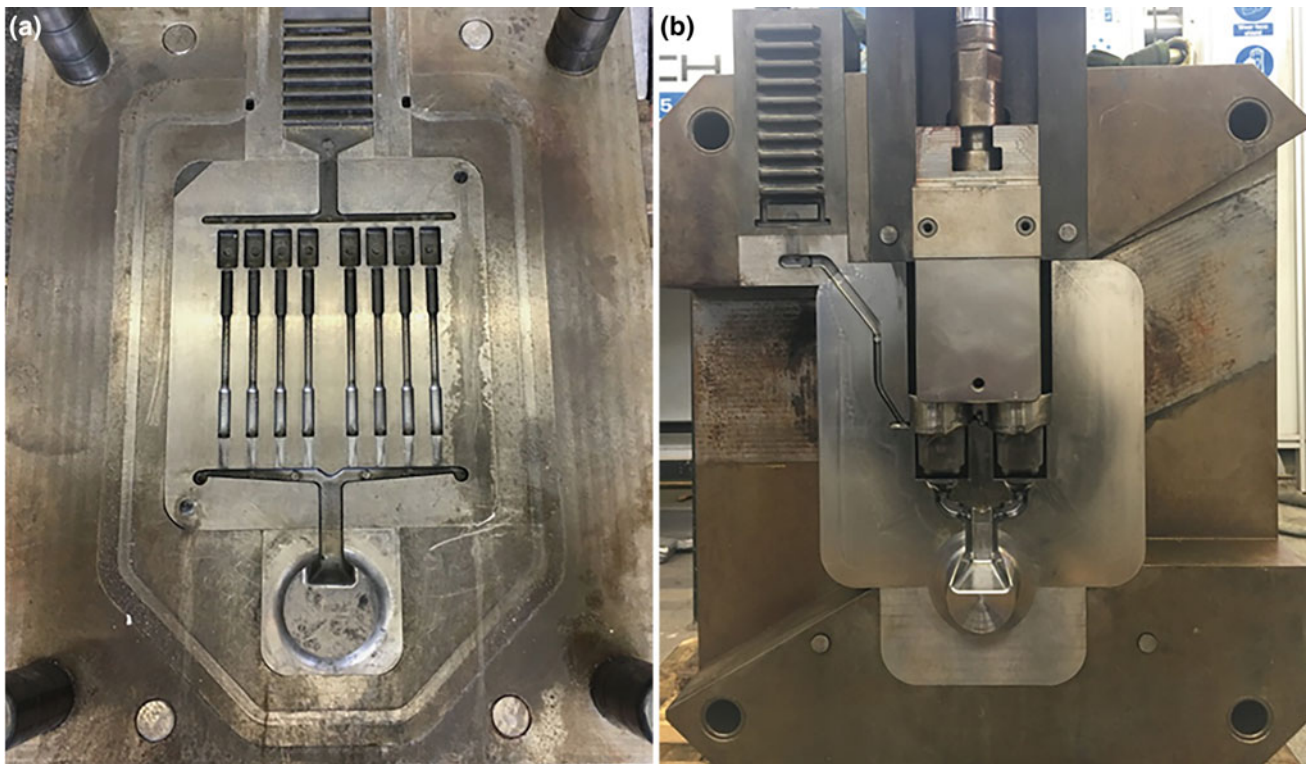


**Fig. 1** **a** Die-set for the high pressure die casting of the ASTM B557 standard round magnesium tensile test bars, **b** die-set for the high pressure die casting of the magnesium piston

## Results and Discussion

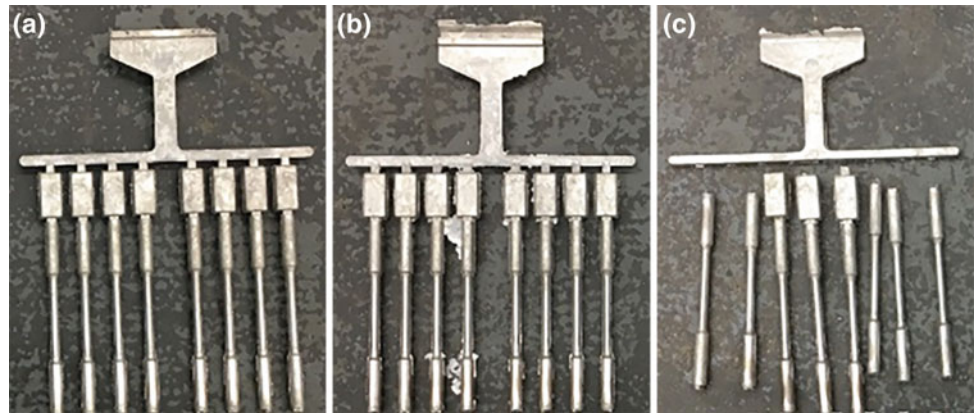
### Die-Cast-Ability

Figure 2a, b, and c present the ASTM B557 standard castings made under high pressure die casting using the 0.5 wt% Y, 1.0 wt% Y, and 2.0 wt% Y die-cast magnesium alloys, respectively. Complete castings were obtained under the conditions of the 0.5 wt% Y and 1.0 wt% Y die-cast magnesium alloys, as shown in Fig. 2a and b, also no hot-tearing was observed in the castings, indicating the good die-cast capability of the 0.5 wt% Y and 1.0 wt% Y die-cast magnesium alloys. Incomplete casting was obtained under the condition of the 2.0 wt% Y die-cast magnesium alloy, as shown in Fig. 2c, indicating that the die-cast capability of the 2.0 wt% Y die-cast magnesium alloy was not good. Therefore, the die-cast capability of the designed die-cast magnesium alloy is acceptable within the Y content of 1.0 wt%, and the designed die-cast magnesium alloy became hard for die casting with the increase of the Y content of up to 2.0 wt%.

### Tensile Properties at Elevated Temperatures

Figure 3 presents the tensile properties of the die-cast magnesium alloys at the elevated temperature of 250 °C, basing on the ASTM B557 standard round tensile test bars with the gauge dimension of  $\phi 6.35 \text{ mm} \times 50 \text{ mm}$  that were cast under cold chamber high pressure die casting. Figure 3a shows the typical tensile stress-strain curves of the die-cast magnesium alloys in as-cast state with different Y contents. With the increase of the Y content, the strength of the die-cast magnesium alloys at 250 °C increased, while the ductility of the die-cast magnesium alloys at 250 °C first increased and then decreased. Figure 3b presents the average tensile properties of the as-cast die-cast magnesium alloys at 250 °C with different Y contents. The yield strength, UTS, and elongation of the 0.5 wt% Y die-cast magnesium alloy at 250 °C were  $105 \pm 2 \text{ MPa}$ ,  $119 \pm 2 \text{ MPa}$ , and  $10.7 \pm 0.9\%$ , respectively. The 1.0 wt% Y die-cast magnesium alloy provided the yield strength of  $121 \pm 3 \text{ MPa}$  and UTS of  $134 \pm 3 \text{ MPa}$  in conjunction with the ductility of  $12.3 \pm 1.0\%$  at 250 °C, while the 2.0 wt% Y die-cast magnesium alloy delivered the yield strength of

**Fig. 2** ASTM B557 standard castings made under high pressure die casting. **a** 0.5 wt% Y magnesium alloy, **b** 1.0 wt% Y magnesium alloy, **c** 2.0 wt% Y magnesium alloy



136 ± 3 MPa and UTS of 155 ± 3 MPa in association with the ductility of 8.6 ± 0.7% at 250 °C. It should be mentioned that the mechanical properties of the high pressure die castings depend on the wall thickness of the castings, and the mechanical properties of the die castings usually decrease with the increase of wall thickness. For high pressure die castings, the wall thickness ranges generally between 2 and 7 mm. Here the wall thickness of the ASTM B557 standard round tensile test bars was in the high level of 6.35 mm, which was significantly higher than the 2–3 mm wall thickness applied in some reports, and the difference of the wall thickness should be considered when compare the mechanical properties between different reports.

### Die-Cast Magnesium Piston

According to Sect. “Die-Cast-Ability”, the 1.0 wt% Y die-cast magnesium alloy has good die-cast capability, while the die-cast capability of the 2.0 wt% Y die-cast magnesium

alloy was insufficient. According to Sect. “Tensile Properties at Elevated Temperatures”, the high temperature strength of the investigated die-cast magnesium alloys increases with increasing content of Y, and the 1.0 wt% Y die-cast magnesium alloy has good strength and ductility at the elevated temperature of 250 °C. Therefore, the 1.0 wt% Y die-cast magnesium alloy was chosen for the high pressure die casting trial of the magnesium piston using the piston die shown in Fig. 1b. Figure 4 shows the magnesium piston made under high pressure die casting using the 1.0 wt% Y die-cast magnesium alloy. Complete casting of the magnesium piston was well obtained, as shown in Fig. 4a. Figure 4b presents the top view showing the inner side of the cast piston, and the piston had good surface quality. Also no hot-tearing was found in the die-cast piston. Thus, the designed 1.0 wt% Y die-cast magnesium alloy demonstrated good die-cast capability for the manufacturing of the magnesium piston through the high efficiency high pressure die casting process.

**Fig. 3** Tensile properties of the die-cast magnesium alloys at the elevated temperature of 250 °C. **a** Typical tensile stress-strain curves, **b** average tensile properties

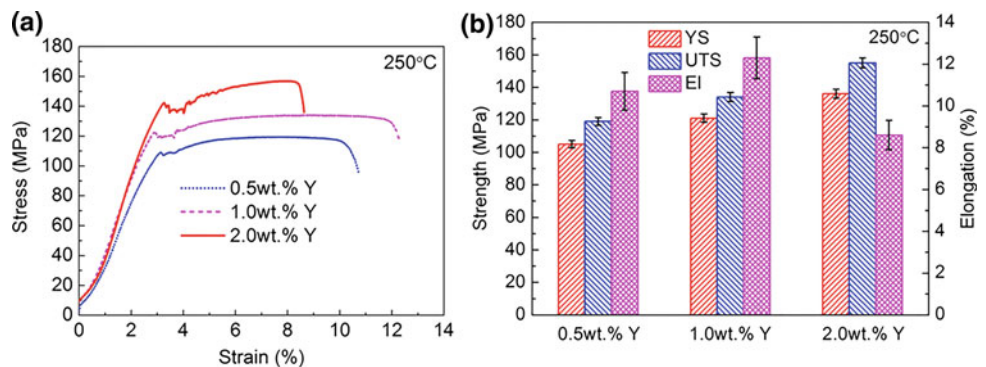
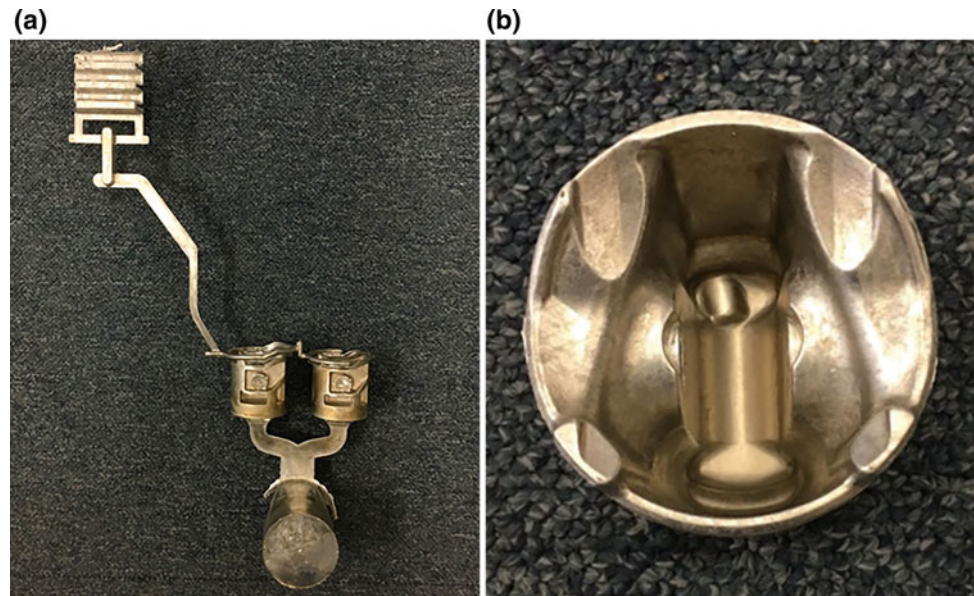




**Fig. 4** Magnesium piston made under high pressure die casting using the 1.0 wt% Y die-cast magnesium alloy. **a** Complete casting of the magnesium piston, **b** top view of the magnesium piston



## Conclusions

- (1) The addition of the rare earth element Y decreases the die-cast capability of the Mg<sub>2.0</sub>La<sub>1.0</sub>Ce<sub>0.3</sub>Mn<sub>0.3</sub>Zn<sub>x</sub>Y (in wt%) alloy, and the die-cast capability of the alloy is good within the addition of 1 wt% Y, while the die-cast capability of the alloy is not acceptable with the addition of the Y of up to 2 wt% Y.
- (2) The high temperature strength of the Mg<sub>2.0</sub>La<sub>1.0</sub>Ce<sub>0.3</sub>Mn<sub>0.3</sub>Zn<sub>x</sub>Y alloy increases with the increase of Y content. The yield strength, UTS, and elongation of the 0.5 wt% Y alloy at 250 °C are 105 ± 2 MPa, 119 ± 2 MPa, and 10.7 ± 0.9%, respectively. The 1.0 wt% Y alloy provides the yield strength of 121 ± 3 MPa and UTS of 134 ± 3 MPa in association with the ductility of 12.3 ± 1.0%, while the 2.0 wt% Y alloy delivers the yield strength of 136 ± 3 MPa and UTS of 155 ± 3 MPa in conjunction with the ductility of 8.6 ± 0.7%, at 250 °C.
- (3) The Mg<sub>2.0</sub>La<sub>1.0</sub>Ce<sub>0.3</sub>Mn<sub>0.3</sub>Zn<sub>1.0</sub>Y die-cast magnesium alloy demonstrates good die-cast capability for the manufacturing of the magnesium piston through the high efficiency high pressure die casting process.

**Acknowledgements** Husqvarna Group is greatly appreciated for the financial and technical support of the work. Jon Gadd from BCAST laboratory is acknowledged for the technical support of the high pressure die casting experiments.

## References

1. Okamoto K, et al. (2011) Applicability of Mg-Zn-(Y, Gd) alloys for engine pistons. In: Sillescu, WH (ed) Magnesium technology 2011. The Minerals, Metals & Materials Society, pp 73–78.
2. Javidani M, Larouche D (2014) Application of cast Al-Si alloys in internal combustion engine components. *Int. Mater. Rev.* 59:132–158.
3. Aune TK, Westengen H, Ruden T (1993) Mechanical properties of energy absorbing magnesium alloys. SAE Technical Paper 930418.
4. Nyberg EA, Luo AA, Sadayappan K, Shi WF (2008) Magnesium for future autos. *Adv. Mater. Process.* 166:35–37.
5. Zhu SM, Nie JF, Gibson MA, Easton MA, Bakke P (2012) Microstructure and creep behavior of high-pressure die-cast magnesium alloy AE44. *Metall. Mater. Trans. A* 43A:4137–4144.
6. Foerster GS (1972) Designing diecasting alloys. *Light Metal Age* 30:11–13.
7. Ninomiya R, Ojio T, Kubota K (1995) Improved heat resistance of Mg-Al alloys by the Ca addition. *Acta Metall.* 43:669–674.
8. Pegguleryuz MO, Baril E (2001) Development of creep resistant Mg-Al-Sr alloys. In: Hryn, JN (ed) Magnesium technology 2001. The Minerals, Metals & Materials Society, pp 119–125.
9. Baril E, Labelle P, Pegguleryuz M (2003) Elevated temperature Mg-Al-Sr: Creep resistance, mechanical properties, and microstructure. *JOM* 55:34–39.
10. Zhu SM, Gibson MA, Easton MA, Nie JF (2010) The relationship between microstructure and creep resistance in die-cast magnesium-rare earth alloys. *Scr. Mater.* 63:698–703.
11. Gavras S, Easton MA, Gibson MA, Zhu SM, Nie JF (2014) Microstructure and property evaluation of high-pressure die-cast Mg-La-rare earth (Nd, Y or Gd) alloys. *J. Alloys Compd.* 597:21–29.
12. Carnahan RD, Decker RF, Nyberg EA, Jones RH, Pitman SG (2000) Development of semi-solid molded magnesium components from alloys with improved high temperature creep properties. In: Kaplan, HL (ed) Magnesium technology 2000. The Minerals, Metals & Materials Society, pp 403–409.

13. Ahmed M, Lorimer GW, Lyon P, Pilkington R (1992). The effect of heat treatment and composition on the microstructure and properties of cast Mg–Y–RE alloys. In: Mordike, BL (ed) Magnesium alloys and their applications. DGM, Garmisch Partenkirchen; DGM Metallurgy Information, New York, pp 301–308.
14. Gibson MA, Bettles CJ, Zhu SM, Easton MA, Nie JF (2009) Microstructure and mechanical properties of a Mg-rare earth based alloy AM-SC1. In: Nyberg, EA (ed) Magnesium technology 2009. The Minerals, Metals & Materials Society, pp 243–245.
15. Samato K, Yamamoto Y, Sakate N, Hirabara S (1997) Heat-Resistant Magnesium Alloy Member. EP 0 799 901 A1. 10 Aug 1997.
16. Koike S, Wasizu K, Tanaka S, Baba T, Kikawa K (2000) SAE Technical Paper 2000-01-1117.
17. Lefebvre M, Pekguleryuz M, Labelle P (2002) Magnesium-based casting alloys having improved elevated temperature performance. US. Patent 6,342,180. 29 Jan 2002.
18. Powell BR, Rezhets V, Luo AA, Bommarito JJ, Tiwari BL (2001) Creep resistant magnesium alloy die casting. US. Patent 6,264,763, 24 July 2001.
19. Luo A, Balough M, Powell BR (2001) Development of creep-resistant magnesium alloys for powertrain applications: part 1 of 2. SAE Technical Paper 2001-01-0422.
20. Aune T, Westengen H (1995) Property update on magnesium die casting alloys. SAE Technical Paper 950424.
21. Xiao WL, Easton MA, Dargusch MS, Zhu SM, Gibson MA (2012) The influence of Zn additions on the microstructure and creep resistance of high pressure die cast magnesium alloy AE44. Mater Sci Eng A 539:177–184.
22. Easton M et al. (2018) Development of magnesium-rare earth die-casting alloys. In: Orlov, D (ed) Magnesium technology 2018. The Minerals, Metals & Materials Society, pp 329–336.
23. Hort N, Dieringa H, Kainer KU. (2018) Magnesium Pistons in Engines: Fiction or Fact? In: Orlov, D (ed) Magnesium technology 2018. The Minerals, Metals & Materials Society, pp 349–353.
24. ASTM committee, Standard Test Methods for Tension Testing of Metallic Materials, 2003.
25. ASTM committee, Standard Test Methods for Elevated Temperature Tension Tests of Metallic Materials, 2003.

# Effect of Gd and Nd Additions on the Thermo-Mechanical Response of a MgMn Alloy

D. Tolnai, S. Gavras, P. Barriobero-Vila, A. Stark, and N. Schell

## Abstract

Alloying Mg with Mn improves the strength and corrosion resistance. The addition of rare-earth elements weakens the texture and improves the age hardening response. Nd and Gd are ideal elements to investigate the effect of low and high solid soluble rare-earth elements in Mg on the thermo-mechanical behavior of MgMn alloy. For this purpose, a Mg alloy with 1 wt% Mn and 1 wt% Nd was produced and then modified with the addition of 1 wt% Gd. In situ high-energy synchrotron X-ray diffraction was performed during compression to analyse the deformation behavior of the material. The compression experiments have been performed at room temperature and 350 °C up to a deformation of 0.3 with a deformation rate of  $10^{-3} \text{ s}^{-1}$ . The compressed samples were subsequently subjected to electron-backscattered diffraction to investigate the post-mortem microstructure.

## Keywords

In situ • Deformation • ME alloys • Mg–Mn–Nd–Gd • Synchrotron radiation • Diffraction

## Introduction

The growing concern about environmentally friendly solutions calls for lightweight design in the transportation industries [1]. The use of Mg as a material with high specific

strength and stiffness is an ideal solution to substitute heavier parts [2]. Although Mg alloys have moderate strength and poor corrosion resistance and ambient temperature formability [3], a large body of work has been conducted to overcome these issues and to enable the wide use of Mg alloys. One relatively new application is the production of medical implants out of Mg alloys, where controlled corrosion is a necessity [4].

Alloying additions of Mn improve the formability and the corrosion resistance of Mg [2]. To further improve the workability by decreasing the texture, rare-earth elements (RE) can be added. The Mg–Mn–RE alloy system is therefore a topic of several investigations striving to design an alloy for wrought applications [5]. Neodymium, due to its low solid solubility in Mg (3.6 wt% at 549 °C [6]), is an ideal element, since relatively low concentrations are necessary to introduce secondary phase particles to further improve strength at elevated temperatures [7, 8]. The addition of Gd with a high solid solubility in Mg gives room to tailor the mechanical property profile in a broad range. Both RE elements are considered bio-compatible and therefore are prospective elements for bio-absorbable implants [9].

The high flux at the large-scale sources makes synchrotron radiation- and neutron-diffraction unique methods to observe dynamic microstructural changes in situ [10]. The transmission geometry of these measurements enables the investigations in the bulk undergoing thermo-mechanical loads. The diffraction patterns and their evolution allow to characterize the changes [11] in the grain structure, e.g. texture evolution, strain build-up, twinning, recrystallization, and recovery [12, 13]. The beam cross section at synchrotron sources can examine samples with a geometry of limited size; however, the time resolution is superior to that achieved by neutron diffraction. The aim of this study is to investigate the effect of 1 wt% Gd addition in Mg1Mn1Nd on the behaviour under thermo-mechanical compression load using in situ high-energy synchrotron X-ray diffraction.

D. Tolnai (✉) · S. Gavras · A. Stark · N. Schell  
Institute of Materials Science, Helmholtz-Zentrum Geesthacht,  
Max-Planck Str. 1, D21502 Geesthacht, Germany  
e-mail: [domonkos.tolnai@hzg.de](mailto:domonkos.tolnai@hzg.de)

P. Barriobero-Vila  
Institute of Materials Research, German Aerospace Center, Linder  
Höhe, 51147 Cologne, Germany

## Materials and Methods

Permanent-mould indirect-chill casting was used to prepare the alloys, described in [14]. First, pure Mg was melted in an electric resistance furnace under protective atmosphere of 2 vol% SF<sub>6</sub> and Ar. The alloying elements were added as pure materials. After mixing, the melt was held at 720 °C for 10 min and then was poured into a steel mould preheated to 660 °C. After 5 min of isothermal holding, the mould was quenched into water at a rate of 10 mm s<sup>-1</sup> until the top of the melt was in line with the cooling water level. Two alloys were cast with the compositions of Mg1Mn1Nd and Mg1Mn1Nd1Gd, respectively. The composition of the ingots was measured with spark optical emission spectroscopy and X-ray fluorescence spectroscopy.

For scanning electron microscopy (SEM), the alloys were grounded and polished using standard metallographic techniques. The final stage of polishing used a combination of oxide polishing suspension (OPS) water-free solution and 0.25- $\mu$ m-diamond suspension solution. The microstructure of the alloys was investigated using a TESCAN Vega II SEM in backscattered electron mode. A more detailed investigation of the intermetallics was conducted using a Philips CM200 transmission electron microscope (TEM) equipped with an Oxford EDS detector. The TEM samples were cut using a slow-speed saw and then cut into 3-mm-diameter discs. The discs were then grounded to a thickness of approximately 100  $\mu$ m. The samples were then electropolished using a 1.5% perchloric acid in ethanol solution at -45 °C.

For the in situ compression experiments, cylindrical specimens were machined from cast ingots with a diameter of 5 mm and length of 10 mm. The in situ synchrotron radiation diffraction was performed at the P07 beamline of PETRA III, DESY (Deutsches Elektronen-Synchrotron). A monochromatic beam with the energy of 100 keV ( $\lambda = 0.0124$  nm) and with a cross section of  $1 \times 1$  mm<sup>2</sup> was used. Diffraction patterns were recorded with a PerkinElmer 1621 flat-panel detector with a pixel size of (200  $\mu$ m)<sup>2</sup> which was placed at a sample-to-detector distance of 1820 mm from the specimen (calibrated with a LaB<sub>6</sub> standard powder sample). The acquisition time for each image was 0.1 s. The specimens were placed in the chamber of a dilatometer DIL 805A/D (TA Instruments), combined with a modified heating induction coil in order for the beam to pass only through the sample [15]. The specimens were compressed at room temperature and at 350 °C. For the tests, the specimens were

heated to the test temperature at a rate of 30 Ks<sup>-1</sup> and held for 3 min before the compression started to ensure temperature homogeneity. The specimens were compressed with an initial strain rate of 10<sup>-3</sup> s<sup>-1</sup>. The tests were terminated at a strain of 0.3 or at fracture. The Debye–Scherrer rings were analysed using the Fit2D<sup>®</sup> software and converted into azimuthal-angle time (AT) plots by using the ImageJ<sup>®</sup> software package.

## Results and Discussion

The studied alloy compositions measured with spark optical emission spectroscopy and X-ray fluorescence spectroscopy ( $\mu$ XRF) are listed in Table 1.

The alloy compositions are close to the intended, with an acceptable difference for such a small batch of castings. The as-cast microstructure of the alloys is shown in Fig. 1.

The Mg1Mn1Nd alloy has a larger grain size than the alloy modified with the Gd. This unmodified alloy consists of Mg grains and precipitates within these grains. The EDX measurements suggest that the precipitates contain only Mg and Nd. Based on that information, they are most likely to be Mg<sub>3</sub>Nd or Mg<sub>12</sub>Nd secondary phases. The Mn content seems to be completely in solution. In the case of the Gd-containing alloy, the grain size is smaller, and with exception to some precipitates, some intermetallic particles also can be seen. Based on EDX mapping, the precipitates contain Mg, RE, and Mn, while the structured intermetallic particles in the segregated areas are lowly concentrated in Mn. In order to have more detailed information about the secondary phase particles, TEM investigations were performed. The TEM results are presented in Fig. 2.

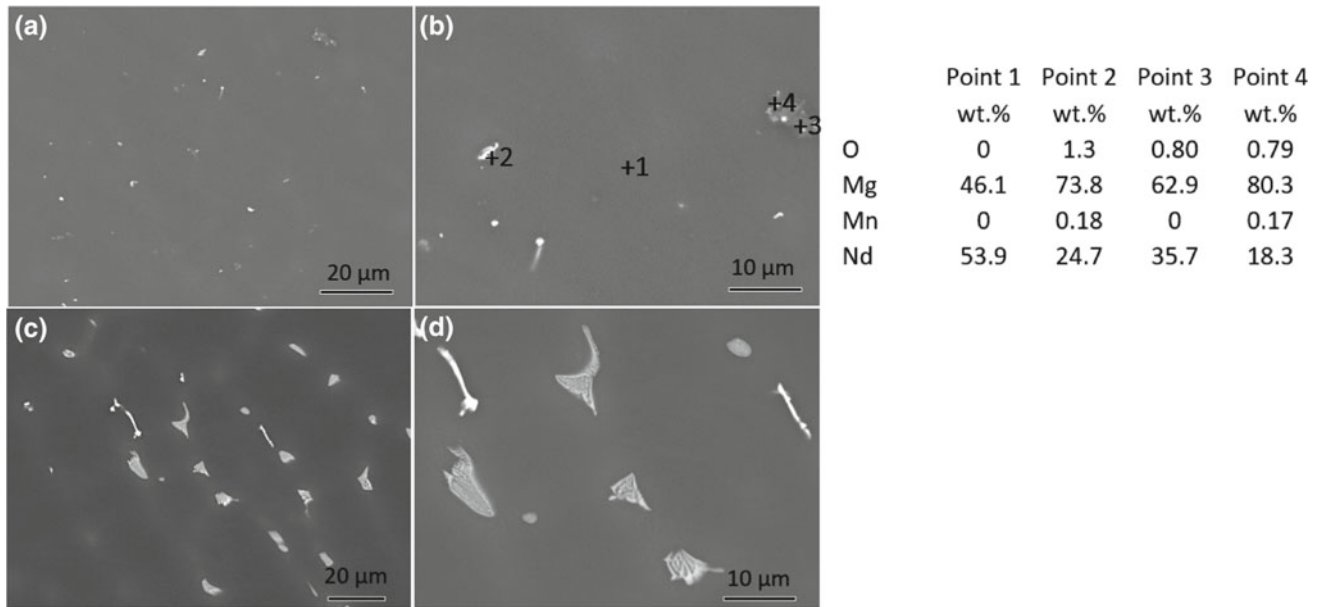
The results of the TEM EDS analysis are shown in Table 2. The results suggest that the precipitates on the prismatic plane in Fig. 2a  $\times 1$  and  $\times 2$  indeed do not contain Mn. Their stoichiometric ratio is close to that of Mg<sub>12</sub>Nd ( $\times 1$ ) and M<sub>3</sub>Nd ( $\times 2$ ), respectively. The precipitates in the  $\times 3$  region show some Mn content, but it is very low. It can originate from the surrounding matrix. In the Gd-containing alloy Fig. 2 b–d, the secondary phases (intermetallics and precipitates on the prismatic plane) all contain Nd and Gd as well, but no or very little amount of Mn. Contradictory to the SEM results, the TEM suggests a ternary intermetallic phase.

The results of the in situ compression test are shown in Fig. 3.

**Table 1** Chemical composition of the alloys

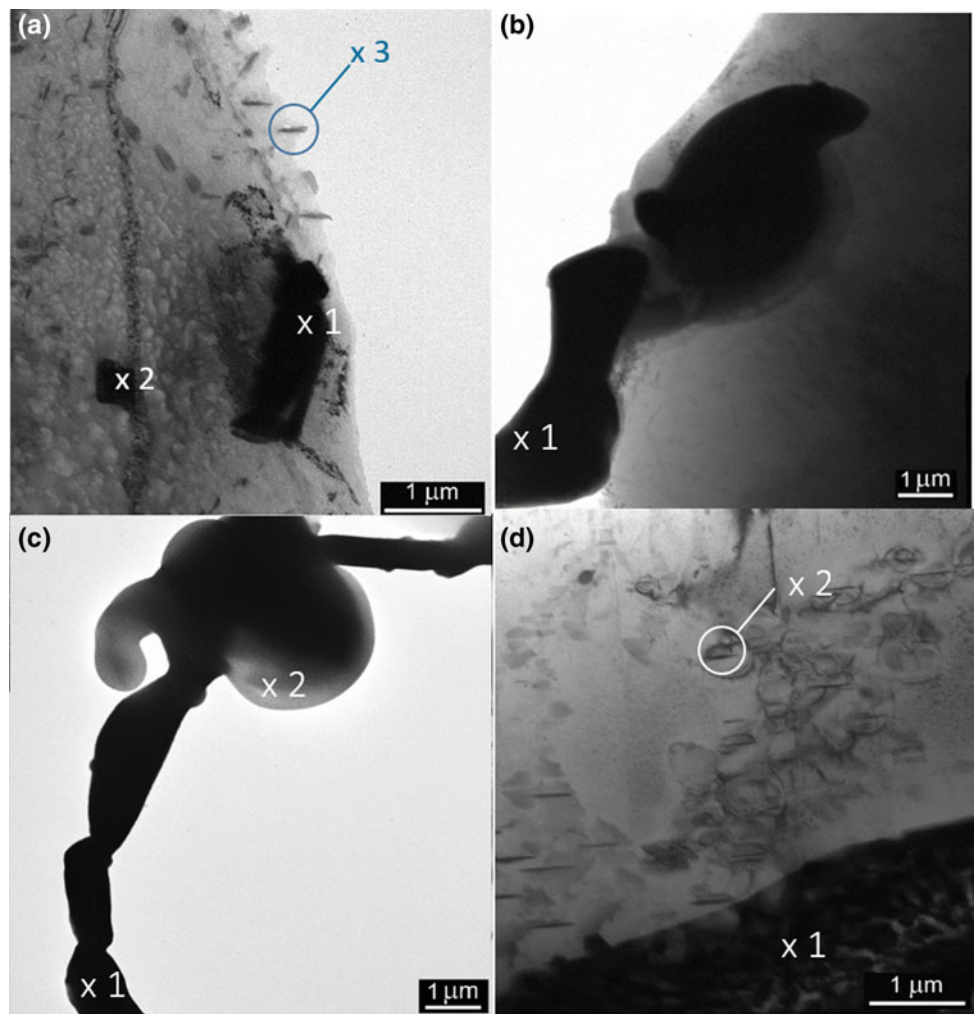
Alloy	Mn (wt%)	Nd (wt%)	Gd (wt%) ( $\mu$ XRF)
Mg1Mn1Nd	0.9	1.34	–
Mg1Mn1Nd1Gd	0.95	1.09	0.79





**Fig. 1** Secondary electron images of **a–b** Mg1Mn1Nd and **c–d** Mg1Mn1Nd1Gd with EDX point measurements presented in 1b

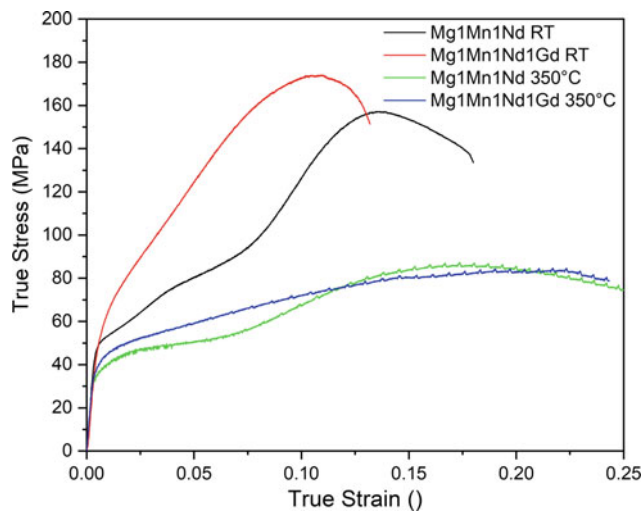
**Fig. 2** TEM bright-field images of the secondary phases in **a** Mg1Mn1Nd and **b–d** Mg1Mn1Nd1Gd





**Table 2** Results of the TEM EDX analysis

Figure 2a ×1		Figure 2b ×1		Figure 2c ×1		Figure 2d ×1	
Element	at. %	Element	at. %	Element	at. %	Element	at. %
O	6.73	C	6.12	O	2.48	O	1.95
Mg	83.03	O	10.1	Mg	11.31	Mg	77.5
Cu	3.16	Na	2.32	Al	2.08	Cu	7.25
Nd	6.71	Mg	11	Si	0.42	Nd	10.76
Figure 2a ×2		Cu	15.62	Ni	0.77	Gd	2.54
Element	at. %	Nd	39.15	Cu	27.2	Figure 2d ×2	
C	3.82	Gd	15.69	Nd	55.74	Element	at. %
O	17.39			Figure 2c ×2		O	7.5
Mg	47.37			Element	at. %	Mg	88.7
Cu	7.49			C	17.28	Cu	1.73
Nd	22.58			O	50.82	Nd	1.68
Figure 2a ×3				Mg	24.64	Gd	0.40
Element	at. %			Si	1.91		
C	6.13			Mn	0.77		
O	48.39			Fe	1.59		
Mg	38.68			Cu	1.46		
Mn	1.00			Zn	0.11		
Cu	1.65			Nd	0.45		
Nd	4.15			Gd	0.98		

**Fig. 3** True stress–true strain curves obtained from the in situ compression testing of the samples

At room temperature, the addition of 1 wt% of Gd increased the yield strength and the ultimate compression strength (UCS) of the base alloy. The UCS shows an increase of 8% from 157 to 170 MPa. At the same time, the ductility shows a decrease possibly due to the presence of the rigid intermetallic phases and the smaller grain size. At 350 °C, the effect of Gd is not pronounced. The ductility

shows a marginal decrease as well, and the yield strength is also increased. However, the UCS is only increased by less than 3% from 83 to 86 MPa. At both temperatures, the base alloy shows inflection points which are affiliated with twinning activity. This is not so remarkable in the case of the modified alloy; however, on the RT curve, an inflection point is visible. The azimuthal angle–time plots derived from the Debye–Scherrer patterns obtained during compression with the in situ synchrotron radiation diffraction are shown in Fig. 4.

The diffraction results show more spotty patterns for the initial condition of the unmodified alloy associated with a larger grain size compared to the one with the Gd addition. Only a few crystalline regions (coherent domains) fulfil the Bragg equation. Twinning activity can be observed during room temperature compression of the unmodified alloy, what that can also be inferred from the observed deformation curves. The emerging timelines on the 1000 and the 0002 plots at the same azimuthal angle show the parent–twinned region of the crystalline region and can be associated with tensile twinning. This twinning mode causes a reorientation of 86° which is very close to the difference between the two investigated planes. The broadening of the lines at the end of the deformation is signs of increasing dislocation density and building up low-angle grain boundaries within the grain, and thus, the formally uniform orientation broadens. The

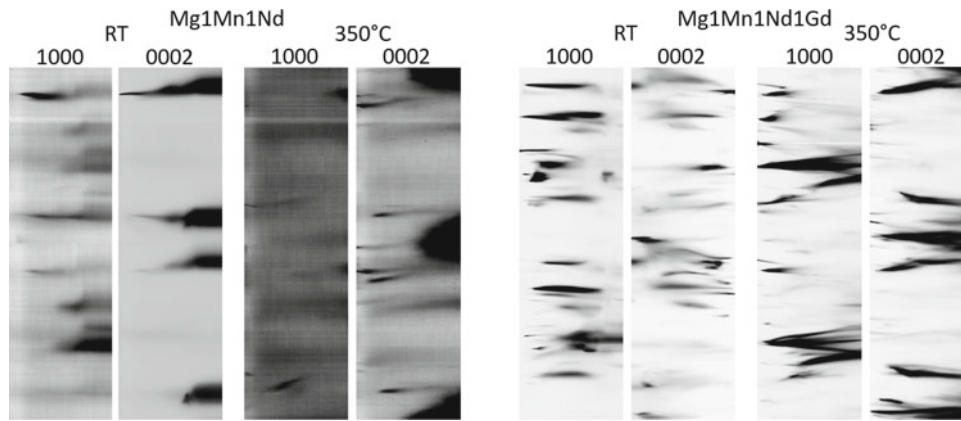


**Fig. 4** Azimuthal angle–time plots derived from the Debye–Scherrer patterns obtained during compression with in situ synchrotron radiation diffraction

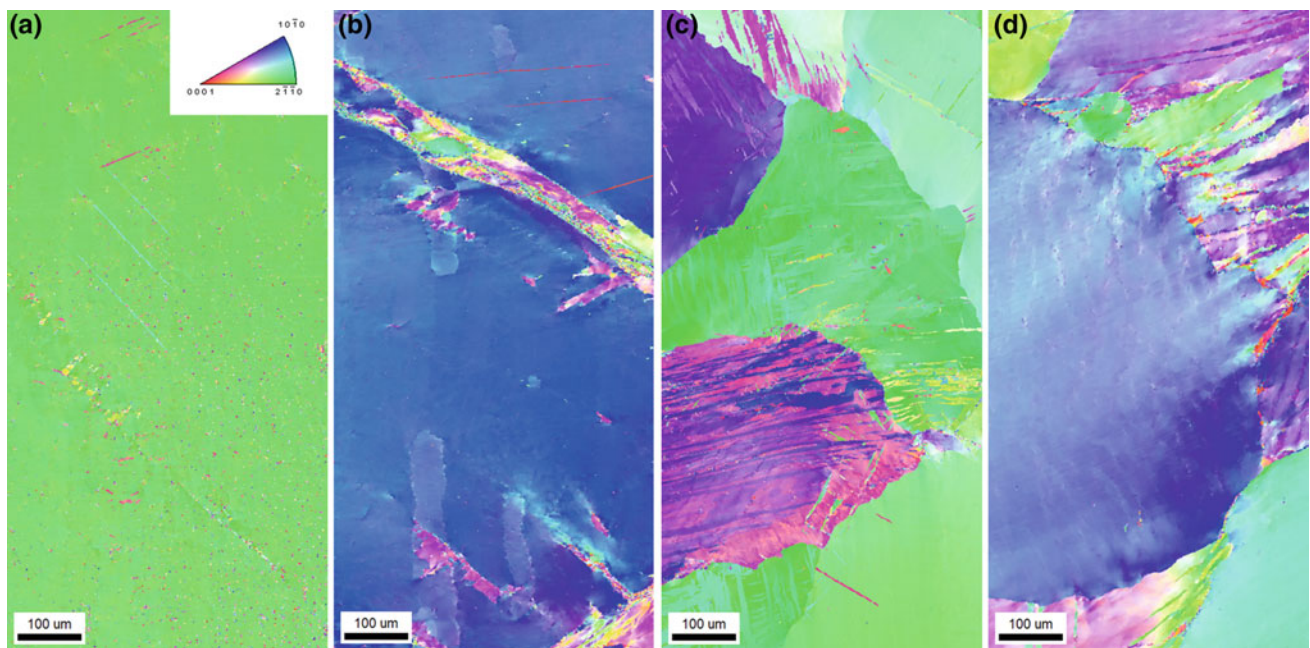


**Fig. 5** Post-mortem EBSD maps of **a** Mg1Mn1Nd deformed at RT, **b** Mg1Mn1Nd deformed at 350 °C, **c** Mg1Mn1Nd1Gd deformed at RT, and **d** Mg1Mn1Nd1Gd deformed at 350 °C

twinning is not so pronounced at 350 °C, but the broadening of the timelines also suggests the formation of sub-grains. In the case of the modified alloy with the Gd addition, twinning can be also seen, but there is no strong sub-grain formation in the microstructure. At 350 °C apart from the twinning and the broadening effects, grain rotation associated with the deviation of reflections from the horizontal can be observed. As the deformation proceeds, grain rotation and sub-grain formation can be seen. The results of the post-mortem EBSD analysis are shown in Fig. 5.

The post-mortem EBSD analysis of the unmodified RT-deformed alloy (Fig. 5a) reflects a very large grain size of the deformed sample. Some twinning can be perceived, but in general, the results are not for quantitative analysis. The misorientation angle distribution is shown in Fig. 6.

In the case of the 350 °C (Fig. 5b) deformed sample, twins can be seen clearly and demonstrate the occurrence of sub-grain formation in the twinned volume. The misorientation angle distribution is homogeneous with a small peak at 86° which can be attributed to the twinning. For the

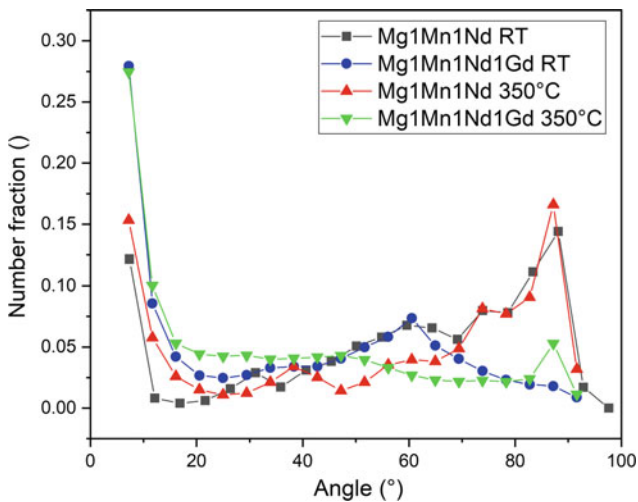


**Fig. 6** Misorientation angles obtained from the post-mortem EBSD results

Gd-containing alloy, the grain size allows a more detailed analysis. In the case of the RT-deformed sample (Fig. 5c), twinning can be observed, correlating with the diffraction results. The misorientation angle distribution has a large peak at  $86^\circ$  which shows that the crystalline regions undergo twinning. The  $350^\circ\text{C}$  deformed sample (Fig. 5d) shows signs of recrystallization at the grain boundaries as the sub-grain structure forms. The misorientation angle distribution lacks the typical peak associated with twinning, suggesting that dynamic recrystallization is the main deformation mechanism in this case.

## Conclusions

From the analysis of the experimental results, the following conclusions can be drawn:

- The precipitates and intermetallic particles are composed of Mg and RE elements, and the Mn content is in solid solution in the matrix.
- The addition of 1 wt% Gd to Mg1Mn1Nd increases the strength of the materials in compression at room temperature and marginally at  $350^\circ\text{C}$ . The ductility is decreased in both cases.
- There is strong twinning activity in the unmodified alloy during compression, which is complemented by the build-up of low-angle grain boundaries at the latter stage of deformation.

- In the case of the Gd-modified alloy at RT compression, twinning is the main deformation mechanism, while at  $350^\circ\text{C}$ , signs of grain rotation and sub-grain formation could be observed.

**Acknowledgements** The authors acknowledge the Deutsches Elektronen-Synchrotron for the provision of facilities within the framework of the proposal I-20180949.

## References

1. M. Pekguleryuz, K. Kainer, A. Kaya, Fundamentals of magnesium alloy metallurgy, first ed. Woodhead, Philadelphia, 2013.
2. M.M. Avedesian, H. Baker, Magnesium and magnesium alloys, ASM Speciality Handbook, ASM International, United States of America, 1999.
3. M.H. Yoo et al: "Nonbasal deformation modes of metals and alloys: Role of dislocation source and mobility" *Metall. Mater. Trans. A* 41 (2002) 813–822.
4. H. Hermawan, D. Dubé, D. Mantovani, "Developments in metallic biodegradable stents" *Acta Biomaterialia* 6 (2010) 1693–1697.
5. P. Hidalgo-Manrique et al: "Effect of Nd Additions on Extrusion Texture Development and on Slip Activity in a Mg–Mn Alloy" *Met. Trans. A*. 44 (2013) 4819–4829.
6. L.L. Rokhlin, Magnesium Alloys Containing Rare Earth Metals Taylor & Francis: London, UK, 2003.
7. P.H. Fu et al: "Effects of heat treatments on the microstructures and mechanical properties of Mg–3Nd–0.2Zn–0.4Zr (wt%) alloy" *Mat. Sci. Eng. A* 486. (2008) 183–192.
8. D. Wu, R.S. Chen, W. Ke: "Microstructure and mechanical properties of a sand-cast Mg–Nd–Zn alloy". *Mater. Des.* 58. (2014) 324–331.
9. J. Zhang et al: "The degradation and transport mechanism of a Mg–Nd–Zn–Zr stent in rabbit common carotid artery: A 20-month study" *Acta Biomater.* 69 (2018) 372–384.
10. I. Lonardelli et al: "In situ observation of texture evolution during  $\alpha \rightarrow \beta$  and  $\beta \rightarrow \alpha$  phase transformations in titanium alloys investigated by neutron diffraction" *Acta Mater.* 55. (2007) 5718–5727.
11. K.-D. Liss and K. Yan: Thermo-mechanical processing in a synchrotron beam, *Mater. Sci. Eng. A*, 528, (2010) 11–27.
12. R.H. Buzolin et al.: In situ synchrotron radiation diffraction study of the role of Gd, Nd on the elevated temperature compression behavior of ZK40 *Mat. Sci. Eng. A*, 640, (2015) 129–136.
13. R.H. Buzolin et al.: In situ synchrotron radiation diffraction investigation of the compression behaviour at  $350^\circ\text{C}$  of ZK40 alloys with addition of CaO and Y *Mat. Sci. Eng. A*, 664, (2016) 2–9.
14. F.R. Elsayed et al., Magnesium permanent mold Castings optimization *Materials Science Forum* 690 (2011) 65–68.
15. D. Tolnai et al.: Study of the solidification of AS alloys combining in situ synchrotron diffraction and differential scanning calorimetry *Mater Sci Forum*, 765, (2013) 286–290.

# Development of Ultra Lightweight, Corrosion Resistant Mg Alloys

T. W. Cain and J. P. Labukas

## Abstract

The corrosion behavior of BCC Mg–11Li–*x*Ge (*x* = 0, 0.3, 0.5 wt%) alloys was evaluated in quiescent 3.5 wt% NaCl(aq) via potentiodynamic polarization, in situ optical imaging, and hydrogen volume capture in comparison with commercial Mg alloy AZ31B-H24. It is shown that Mg–11Li and Mg–11Li–0.3 Ge alloys possessed a lower corrosion rate after 24 h immersion at open circuit potential with respect to AZ31B-H24. Mg–11Li–0.3Ge alloy possessed the lowest corrosion rate due to simultaneous reduction of cathodic kinetics and an improved pseudo passive film. Increasing the Ge concentration to 0.5 wt% was found to be detrimental to cathodic kinetics and passive film stability due to micro-galvanic coupling.

## Keywords

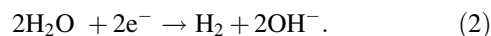
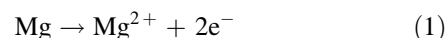
Magnesium • Lithium • Alloy • Corrosion • Passivity • Germanium

## Introduction

Magnesium and its alloys possess a nominally hexagonal close packed (HCP) structure whose deformation twin formation, strong basal texture, and limited number of available slip modes provide limited deformation capability within the context of wrought products [1, 2]. Furthermore, the corrosion resistance of Mg alloys is well known to be the worst among structural materials owing to their high reactivity and lack of a sufficient naturally forming passive film in aqueous environments [3]. Although the corrosion resistance of magnesium alloys has improved tremendously in recent years, further reduction in corrosion rate of Mg alloys is

crucial for materials applications where a high strength-to-weight ratio is necessary.

Magnesium corrosion proceeds by the following anodic (1) and cathodic (2) electrochemical reactions:



Several alloying elements have been shown to alter the corrosion rate by increasing or decreasing the anodic reaction kinetics, cathodic reaction kinetics, or both [4–6]. The most promising elements for the reduction of the cathodic corrosion kinetics have come from groups 13–15 of the periodic table [5–15]. Elements from these groups of so-called cathodic poisons such as As, Ge, and Sn slow the hydrogen evolution reaction (HER) by inhibiting hydrogen recombination on the alloy surface. Introduction of these elements as a means of reducing corrosion rate has been shown to be effective as Mg corrosion is controlled by HER [16]. Another approach to reduce the overall corrosion rate of Mg alloys is by passivating the surface with a dense oxide layer that slows or stops diffusion of water to the metal-oxide interface. Although the native oxide on Mg, MgO/Mg(OH)<sub>2</sub>, does not provide protection from corrosion, recent work has shown that MgCO<sub>3</sub> can offer some protection [17, 18]. In recent research, the addition of Li to Mg alloys at concentrations greater than 30 at. % (≈10.3 wt%) Li has been shown to form a strong pseudo-passive layered film on the surface comprising a mixture of magnesium oxide, hydroxide, and carbonate as well as lithium oxide and carbonate [18–20]. The establishment of such a film due to Li has decreased the corrosion resistance of Mg by more than an order of magnitude, and Li also provides the added benefit of decreased alloy density (<1.6 g/cm<sup>3</sup>) and a primary crystal structure that is body centered cubic (BCC). The prospects of a BCC structure are exciting in that it provides greater ductility by the increase number of slip systems when compared to HCP and thus improved formability [18, 19].

T. W. Cain (✉) · J. P. Labukas  
CCDC Army Research Laboratory, Aberdeen Proving Ground,  
6300 Rodman Rd, Aberdeen, MD 21005, USA  
e-mail: [taylor.w.cain2.civ@mail.mil](mailto:taylor.w.cain2.civ@mail.mil)



In the present work, the combined effect of alloying magnesium with lithium and germanium is investigated. In situ corrosion is observed and recorded to understand film growth and breakdown. Potentiodynamic polarization is used to characterize anodic and cathodic kinetics in 3.5 wt% NaCl (aq). Scanning electron microscopy (SEM) and energy dispersive X-ray spectroscopy (EDS) are used to observe the microstructure and map chemistry across the surface. X-ray diffraction (XRD) was used to verify the crystal structure of the alloys.

## Materials and Methods

### Materials Processing and Microstructural Characterization

Mg–12Li– $x$ Ge ( $x = 0, 0.3, 0.5$ ) were targeted in this investigation whose actual compositions determined by direct current plasma optical emission (DCPOES) are reported in Table 1. The alloys were produced via induction melting of 99.9% pure lithium rod (Alfa Aesar), 99.99% pure Mg (US Magnesium LLC), and 99.999% pure germanium (Alfa Aesar). Approximately 150 g total charge of the intended alloy was loaded into a boron nitride (BN) coated stainless steel beaker in an Ar filled glovebox ( $<0.1$  ppm  $O_2, H_2O$ ) and sealed in a quartz tube with a vacuum flange assembly. The sealed quartz tube was transported outside the glovebox to the induction furnace where gettered Ar (Oxy-Gon 120 gas purification furnace,  $<1$  ppb  $O_2$ ) was circulated through the quartz tube under a slight positive pressure to minimize oxidation during melting. The melt was held between approximately 650–700 °C for 15 min, periodically stirred via high current (1200 A) pulsing of the induction coil and allowed to furnace cool. The furnace cooled Mg–Li– $x$ Ge alloys were then homogenized at 380 °C for 18 h under argon, water quenched, and hot rolled to a 50% reduction. Hot rolling was performed by heating alloys at 400 °C for 15 min prior to rolling and by holding at this temperature for 5 min in between passes. Rollers were pre-heated to their maximum temperature of 200 °C to minimize heat loss. The AZ31B sheet used in this investigation was supplied by Magnesium Elektron in the H24 condition.

X-ray diffraction of hot rolled specimens was measured with a Panalytical X'Pert Pro X-ray diffractometer using Cu

$k_\alpha$  radiation in a Bragg-Brentano  $\theta$ – $2\theta$  geometry, a step size of 0.01°, dwell time of 10 s per step, and a flat bracket mount to determine the crystal structure. In addition, the grain size, phase morphology, and phase area fraction were analyzed using a combination of optical microscopy (Dino-Lite AM7915MZTL) and scanning electron microscopy (Phenom XL, and Hitachi S-4700). Samples for X-ray analysis were ground to a 1200 grit finish using SiC papers and ethanol as lubricant, while optical and SEM samples were additionally prepared by polishing with an oil-based polycrystalline 1  $\mu$ m diamond suspension (Buehler). Samples for grain size analysis were etched using a mixture of 98% methanol, 2% concentrated nitric acid by volume, while grain size measurement was performed using the lineal intercept method in accordance with ASTM E 112. The area fraction of Ge-rich phases was determined from the average of five backscattered electron (BSE) images using the Phenom XL with an area of 4.5 mm  $\times$  4.5 mm using ImageJ software package. Energy dispersive X-ray spectroscopy was performed at 15 kV. Additionally, the localized corrosion of Mg alloy surfaces was observed by in situ optical microscopy using a Dino-Lite microscope over a 24 h immersion period.

### Electrochemical Testing

All electrochemical testing was performed in 250 mL of unbuffered quiescent 3.5 wt% NaCl(aq) (pH  $\approx$  5.6) using a conventional three electrode cell with 1 cm<sup>2</sup> exposed surface area of Mg alloy as the working electrode, a platinum mesh counter electrode, and a saturated calomel (SCE) reference electrode using a Bio-Logic VSP-300 potentiostat. To assess the passivity of each alloy, anodic potentiodynamic polarization was performed after 1 h at the open circuit potential (OCP) by scanning in the positive direction from OCP<sub>SCE</sub> to +500 mV above OCP at a scan rate of 1 mV/s, while cathodic potentiodynamic polarization was scanned from OCP to  $-2.3$  V<sub>SCE</sub>. Ohmic resistance was compensated at 85% of the measured value during polarization scans by using a high frequency impedance measurement at 10<sup>6</sup> Hz prior to each scan. The corrosion resistance of Mg alloys were further evaluated by measuring the amount of hydrogen evolved after 24 h of immersion with an inverted funnel attached to a burette, centered over the sample.

**Table 1** Composition of Mg–Li– $x$ Ge alloys used in this study as determined by direct current plasma emission spectroscopy (Luvak Inc.)

Alloy	wt%			ppmw					
	Mg	Li	Ge	Al	Ca	Fe	Mn	Na	Ni
Mg–11Li	Bal.	10.5	–	102	29	150	59	25	10
Mg–11Li–0.3Ge	Bal.	10.8	0.27	55	12	57	57	16	67
Mg–11Li–0.5Ge	Bal.	11	0.42	48	22	44	56	29	23

## Results

The representative microstructure of solidified, hot rolled alloys can be elucidated by the powder XRD data and BSE EDS maps shown in Figs. 1 and 2, respectively. The XRD patterns show that the crystal structure is primarily  $\beta$ -BCC with some residual  $\alpha$ -HCP and some unidentified peaks. There were no peaks indicative of the presence of  $Mg_2Ge$ . However, EDS mapping in Fig. 2 shows clearly that there is the presence of a Ge-rich lamellar phase in the Mg-11Li-0.5Ge alloy. This type of

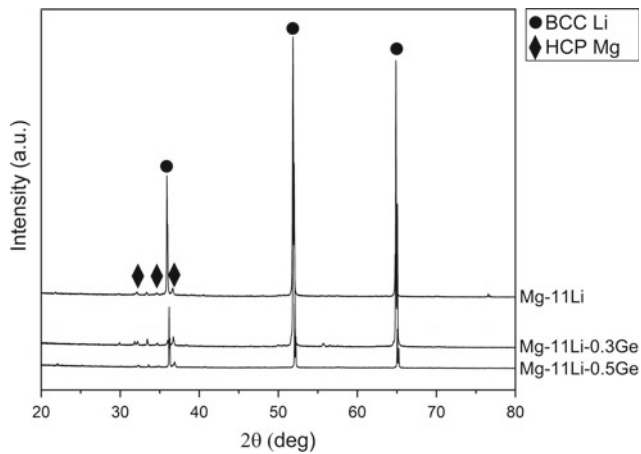
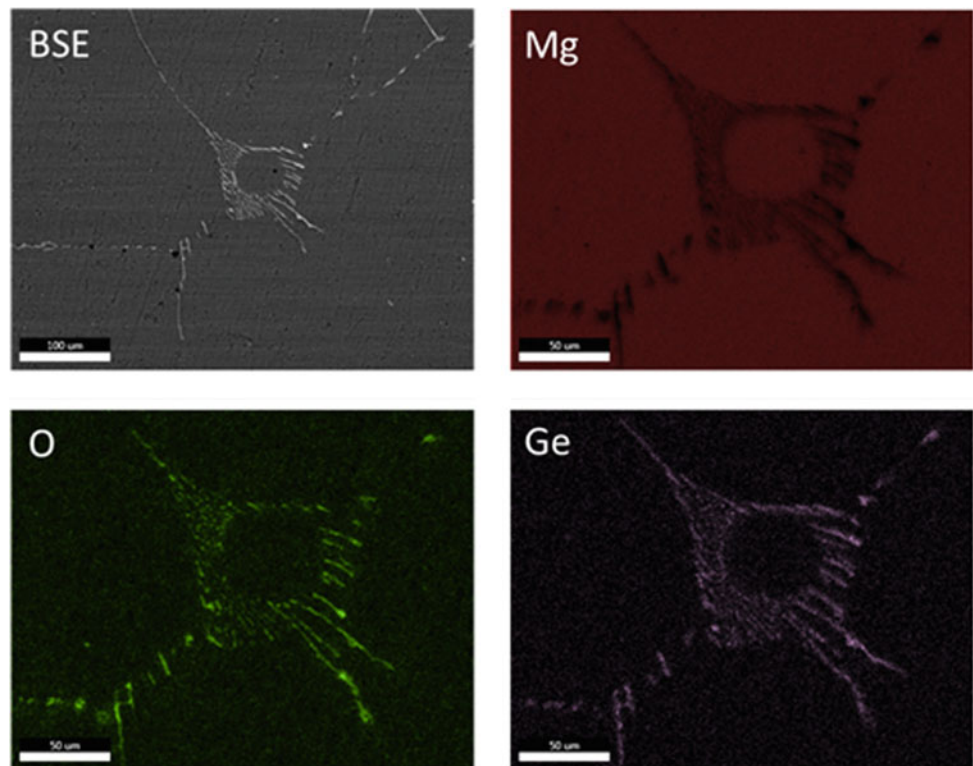


**Fig. 1** X-ray diffraction patterns for Mg-11Li, Mg-11Li-0.3Ge, Mg-11Li-0.5Ge alloys

**Fig. 2** BSE image and EDS maps of a Ge rich lamellar phase region of Mg-11Li-0.5Ge



lamellar phase along the grain boundaries is uniformly present in both Mg-11Li-0.3Ge and Mg-11Li-0.5Ge alloys. The lack of  $Mg_2Ge$  in XRD data is likely due to the large grain size (Mg-11Li =  $746 \pm 56 \mu m$ , Mg-11Li-0.3Ge =  $525 \pm 9 \mu m$ , Mg-11Li-0.5Ge =  $503 \pm 14 \mu m$ ) in combination with low area fraction of Ge-rich phase present (Mg-11Li-0.3Ge =  $0.58 \pm 0.09\%$ , Mg-11Li-0.5Ge =  $1.10 \pm 0.05\%$ ), Table 2. The grain size of Mg-Li alloys is much greater than that of commercial Mg alloys which is typically  $<50 \mu m$ .

The anodic and cathodic kinetic behavior of each alloy is shown by the potentiodynamic polarization curves in Fig. 3. This figure revealed that Mg-11Li-0.3Ge had the lowest cathodic kinetics of all alloys. Indeed, the cathodic kinetics are more than an order of magnitude less than that of AZ31B which indicates roughly an order of magnitude decrease in corrosion rate as the corrosion rate of Mg is controlled by HER. Furthermore, Mg-11Li-0.3Ge was the only alloy that had any type of pseudo passive behavior with a small pseudo passive region from roughly  $-1.68 V_{SCE}$  to  $-1.61 V_{SCE}$ . At potentials, more noble than  $-1.61 V_{SCE}$ , the native surface film breaks down and the anodic current increases rapidly. In comparison to AZ31B, the cathodic kinetics of both Mg-11Li and Mg-11Li-0.5Ge were roughly one order of magnitude less, but the cathodic kinetics of Mg-11Li-0.5Ge were faster than that of Mg-11Li.

Optical images after immersion in 3.5 wt% NaCl(aq) for 1 and 24 h are shown in Figs. 4 and 5, respectively. After 1 h immersion, AZ31B, Mg-11Li, and Mg-11Li-0.5Ge

**Table 2** Average grain size (ASTM E112) and area fraction of the Ge-rich lamellar phase for each alloy in this investigation

Alloy	Grain size ( $\mu\text{m}$ )	Area fraction Ge-rich phase in (%)
Mg-11Li	$746 \pm 56$	–
Mg-11Li-0.3Ge	$525 \pm 9$	$0.58 \pm 0.09$
Mg-11Li-0.5Ge	$503 \pm 14$	$1.10 \pm 0.05$

$\pm$  values are standard error of the mean

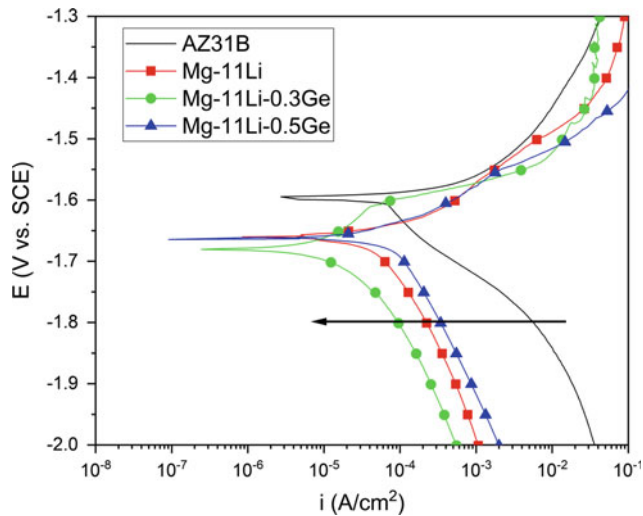


**Fig. 3** Potentiodynamic polarization scans measured after 1 h immersion in quiescent 3.5 wt% NaCl

have shown breakdown of the native surface film and the appearance of filiform corrosion morphology that is characteristic of Mg alloys in unbuffered chlorides [21–24]. AZ31B and Mg-11Li both experienced consistent surface breakdown within 10 min of immersion, while Mg-11Li-0.5Ge experienced breakdown after approximately  $50 \pm 8$  min. However, there is no evidence of breakdown of the surface film on Mg-11Li-0.3Ge, which is in agreement with the pseudo passive window shown in Fig. 3. Breakdown of the surface film on Mg-11Li-0.3Ge was observed only after approximately  $94 \pm 15$  min of immersion at which time filiform corrosion propagated on part of the surface. The appearance of alloy surfaces after 24 h varied greatly from one another. The surface of AZ31B displayed two areas of filiform corrosion; one noted by thin gray contrast and the second by a much darker contrast and deeper filaments which has been more thoroughly characterized by Melia et al. [23]. The Mg-11Li alloy, which showed significant coverage of filiform corrosion after 1 h, did not reveal any filiform corrosion after 24 h but rather an almost uniform corrosion product layer on the entire surface. The corrosion surface morphologies of Mg-11Li-0.3Ge and Mg-11Li-0.5Ge were similar in nature in that part of the exposed surface revealed a tarnish, while severe localized corrosion attack was observed on other parts; the extent of severe localized corrosion damage occupied a larger

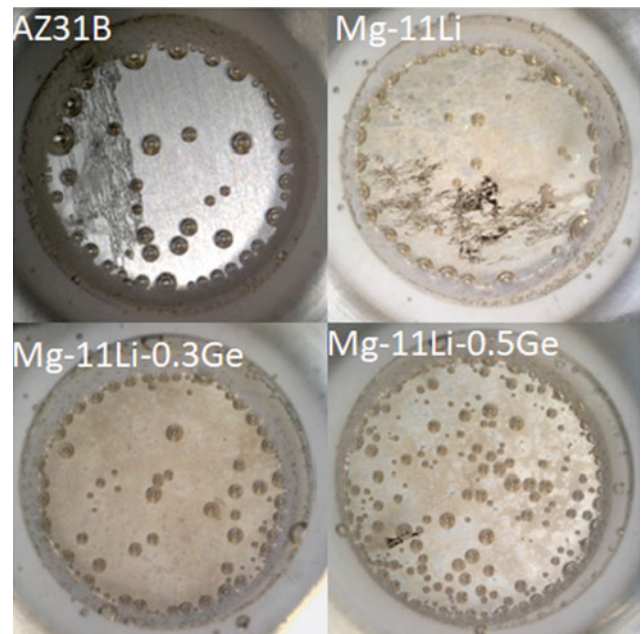


**Fig. 4** In situ optical images of the exposed alloy surface after 1 h immersion in quiescent 3.5 wt% NaCl. The sample area was  $1 \text{ cm}^2$

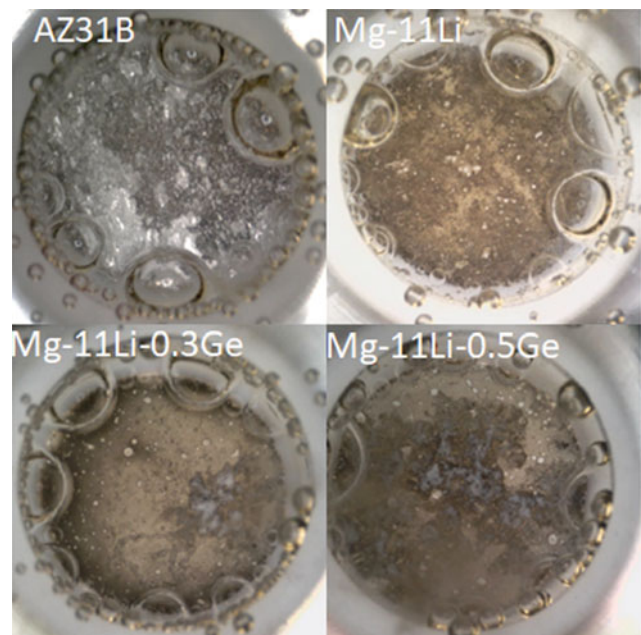


**Fig. 5** In situ optical images of the exposed alloy surface after 24 h immersion in quiescent 3.5 wt% NaCl. The sample area was  $1 \text{ cm}^2$



**Table 3** Volume of hydrogen captured after 24 immersion in quiescent 3.5 wt% NaCl(aq)

Alloy	Hydrogen capture (mL/cm <sup>2</sup> )
Mg-11Li	0.19 ± 0.01
Mg-11Li-0.3Ge	0.16 ± 0.08
Mg-11Li-0.5Ge	2.33 ± 0.12
AZ31B-H24	0.53 ± 0.12

percentage of the surface on Mg-11Li-0.5Ge than Mg-11Li-0.3Ge based upon visual inspection likely due to the increased area fraction of Mg<sub>2</sub>Ge present.

The corrosion rate for each alloy as measured by hydrogen capture after 24 h immersion in 3.5 wt% NaCl(aq) is shown in Table 3. The corrosion rate followed the order Mg-11Li-0.3Ge < Mg-11Li < AZ31B-H24 < Mg-11Li-0.5Ge from the lowest to the highest corrosion rate.

## Discussion

The results of this investigation show that Ge alloyed with BCC Mg-Li can be effective at reducing the corrosion rate by simultaneously decreasing HER and imparting pseudo passivity on exposed surfaces. It has been theorized and shown that Ge poisons hydrogen recombination on Mg alloy surfaces as indicated by decreased cathodic kinetics [10, 11, 16, 25, 26]. Thus, the presence of Mg<sub>2</sub>Ge at grain boundaries, as the primary cathode on the Mg surface, can explain the observed reduction in cathodic kinetics for Mg-11Li-0.3Ge versus Mg-11Li. This is even more striking considering that the impurity level of Ni in Mg-11Li-0.3Ge is 10× greater than the tolerance limit established by Hanawalt et al. (5 ppmw), whereby the corrosion rate of Mg increases rapidly with increasing Ni [27]. It is likely that the Ni originated from the stainless steel crucible that alloys were melted in; all other impurity levels were below their respective tolerance threshold. Despite the benefit of Ge observed for Mg-11Li-0.3Ge, there is an apparent limit upon which Ge is beneficial as observed with the increased cathodic kinetics and high corrosion rate observed with Mg-11Li-0.5Ge in comparison with Mg-11Li and Mg-11Li-0.3Ge. This limit to the protective nature of Ge is attributed to the increased area fraction of the Ge-rich phase present on the exposed alloy surface that may result in detrimental micro-galvanic coupling. Increasing cathode area and decreasing anode area result in increased couple current density based on mixed potential theory for a galvanic couple. Thus, the corrosion rate increases as the anode and cathode are on the same surface. In addition, harmful micro-galvanic coupling is likely exacerbated via anodically induced cathodic activation in corrosion damaged areas [3,

22]. It is unclear from this investigation how the corrosion behavior will differ with a change in the distribution of Ge-rich phase on the surface (i.e. varying grain size). We hypothesize that decreasing grain size and thus a finer distribution of Ge-rich phase for the same area fraction will result in increased corrosion rate based on the increased number density of cathodic sites on the surface which act as corrosion initiation sites via micro-galvanic coupling. Based on this hypothesis, beneficial addition of Ge to Mg-Li alloys may lie below 0.3 wt%, but this will depend on complex interactions with other alloying elements. Despite the increase in pseudo passive behavior shown by Mg-11Li-0.3Ge, there is still native film breakdown of the surface and significant corrosion damage on the areas of the surface. To this end, additional work is needed to improve the stability of the native film and thick film formed during immersion experiments in order to provide an improved passive layer. Such alloying additions will be likely to include Al [4] and Sn [8] which have been shown to improve the passive film layer in Mg alloys and also rare earth elements to provide precipitation hardenable alloys [2]. The design of such an alloy will need to find a synergy between the age hardening response and improved passive film formation. A further consideration for the development of BCC Mg-Li alloys is the minimum and maximum concentration of Li needed to sustain improved corrosion resistance imparted by Li. While Li alone helps decrease the corrosion rate as shown by this investigation and by others [20], it is expected that alloying at higher Li concentrations will lead to an unwanted increase in reactivity.

## Conclusions

- Ge and Li alloying additions to Mg work to synergistically decrease cathodic kinetics and increase passivity.
- Binary BCC Mg-11Li alloy and Mg-11Li-0.3Ge are more corrosion resistant than the widely used commercial Mg alloy AZ31B-H24. Ge when alloyed with BCC, Mg-Li improves the corrosion rate at concentrations <0.5 wt % compared to binary Mg-Li.
- A short lived partially protective film is formed on Mg-Li-Ge alloy surfaces immersed in 3.5 wt% NaCl(aq).



**Acknowledgements** The authors would like to thank Cadet Michael Sullivan who helped with sample preparation and the collection of electrochemical data.

## References

1. S. You, Y. Huang, K.U. Kainer, N. Hort, Recent research and developments on wrought magnesium alloys, *Journal of Magnesium and Alloys*, 5 (2017) 239–253.
2. I.J. Polmear, *Light Alloys*, 4th Edition ed., Butterworth-Heinemann, Oxford, 2005.
3. M. Esmaily, J.E. Svensson, S. Fajardo, N. Birbilis, G.S. Frankel, S. Virtanen, R. Arrabal, S. Thomas, L.G. Johansson, Fundamentals and advances in magnesium alloy corrosion, *Progress in Materials Science*, 89 (2017) 92–193.
4. K. Gusieva, C.H.J. Davies, J.R. Scully, N. Birbilis, Corrosion of magnesium alloys: the role of alloying, *International Materials Reviews*, 60 (2014) 169–194.
5. K.R. Limmer, K.S. Williams, J.P. Labukas, J.W. Andzelm, First Principles Modeling of Cathodic Reaction Thermodynamics in Dilute Magnesium Alloys, *Corrosion*, 73 (2017) 506–517.
6. J.A. Yuwono, N. Birbilis, R. Liu, Q. Ou, Q. Bao, N.V. Medhekar, Aqueous Electrochemical Activity of the Mg Surface: The Role of Group 14 and 15 Microalloying Elements, *Journal of The Electrochemical Society*, 164 (2017) C918–C929.
7. N. Birbilis, G. Williams, K. Gusieva, A. Samaniego, M.A. Gibson, H.N. McMurray, Poisoning the corrosion of magnesium, *Electrochemistry Communications*, 34 (2013) 295–298.
8. T.W. Cain, C.F. Glover, J.R. Scully, The corrosion of solid solution Mg-Sn binary alloys in NaCl solutions, *Electrochimica Acta*, 297 (2019) 564–575.
9. P. Jiang, C. Blawert, R. Hou, N. Scharnagl, J. Bohlen, M.L. Zheludkevich, Microstructural influence on corrosion behavior of MgZnGe alloy in NaCl solution, *Journal of Alloys and Compounds*, 783 (2019) 179–192.
10. R.L. Liu, M.F. Hurley, A. Kvryan, G. Williams, J.R. Scully, N. Birbilis, Controlling the corrosion and cathodic activation of magnesium via microalloying additions of Ge, *Sci Rep*, 6 (2016) 28747.
11. R.L. Liu, J.R. Scully, G. Williams, N. Birbilis, Reducing the corrosion rate of magnesium via microalloying additions of group 14 and 15 elements, *Electrochimica Acta*, 260 (2018) 184–195.
12. G. Williams, H.A.-L. Dafydd, H.N. McMurray, N. Birbilis, The influence of arsenic alloying on the localised corrosion behaviour of magnesium, *Electrochimica Acta*, 219 (2016) 401–411.
13. I.J. Polmear, Recent Developments in Light Alloys, *Materials Transaction JIM*, 37 (1996) 12–31.
14. X. Liu, M. Yin, S. Zhang, H. Wei, B. Liu, H. Du, L. Hou, Y. Wei, Corrosion Behavior of the As-Cast and As-Solid Solution Mg–Al–Ge Alloy, *Materials (Basel)*, 11 (2018).
15. B. Kim, K. Park, H. Kimura, Y. Park, I. Park, Influence of Addition of Ge on the Microstructure and Corrosion Properties of Magnesium, *MATERIALS TRANSACTIONS*, 53 (2012) 240–243.
16. R.L. Liu, Z.R. Zeng, J.R. Scully, G. Williams, N. Birbilis, Simultaneously improving the corrosion resistance and strength of magnesium via low levels of Zn and Ge additions, *Corrosion Science*, 140 (2018) 18–29.
17. Y. Wang, B. Liu, X.a. Zhao, X. Zhang, Y. Miao, N. Yang, B. Yang, L. Zhang, W. Kuang, J. Li, E. Ma, Z. Shan, Turning a native or corroded Mg alloy surface into an anti-corrosion coating in excited CO<sub>2</sub>, *Nature Communications*, 9 (2018) 4058.
18. W. Xu, N. Birbilis, G. Sha, Y. Wang, J.E. Daniels, Y. Xiao, M. Ferry, A high-specific-strength and corrosion-resistant magnesium alloy, *Nat Mater*, 14 (2015) 1229–1235.
19. Y.M. Yan, O. Gharbi, A. Maltseva, X.B. Chen, Z.R. Zeng, S.W. Xu, W.Q. Xu, P. Volovich, M. Ferry, N. Birbilis, Investigating the Structure of the Surface Film on a Corrosion Resistant Mg–Li(–Al–Y–Zr) Alloy, *CORROSION*, 75 (2018) 10.
20. C.Q. Li, D.K. Xu, X.B. Chen, B.J. Wang, R.Z. Wu, E.H. Han, N. Birbilis, Composition and microstructure dependent corrosion behaviour of Mg-Li alloys, *Electrochimica Acta*, 260 (2018) 55–64.
21. Z.P. Cano, J.R. McDermid, J.R. Kish, Cathodic Activity of Corrosion Filaments Formed on Mg Alloy AM30, *Journal of The Electrochemical Society*, 162 (2015) C732–C740.
22. G. Williams, K. Gusieva, N. Birbilis, Localized Corrosion of Binary Mg–Nd Alloys in Chloride-Containing Electrolyte Using a Scanning Vibrating Electrode Technique, *Corrosion*, 68 (2012) 489–498.
23. M.A. Melia, T.W. Cain, B.F. Briglia, J.R. Scully, J.M. Fitz-Gerald, Evolution of the Corrosion Morphology on AZ31B Tracked Electrochemically and by In Situ Microscopy in Chloride-Containing Media, *Jom*, 69 (2017) 2322–2327.
24. R.M. Asmussen, W.J. Binns, P. Jakupi, D. Shoesmith, The Influence of Microstructure on the Corrosion of Magnesium Alloy ZEK100, *Corrosion*, 71 (2015) 242–254.
25. R.L. Liu, S. Thomas, J.R. Scully, G. Williams, N. Birbilis, An Experimental Survey of the Cathodic Activation of Metals Including Mg, Sc, Gd, La, Al, Sn, Pb, and Ge in Dilute Chloride Solutions of Varying pH, *Corrosion*, 73 (2017) 494–505.
26. M. Zhang, L.G. Hector, Y. Guo, M. Liu, L. Qi, First-principles search for alloying elements that increase corrosion resistance of Mg with second-phase particles of transition metal impurities, *Computational Materials Science*, 165 (2019) 154–166.
27. J.D. Hanawalt, C.E. Nelson, J.A. Peloubet, Corrosion Studies of Magnesium and Its Alloys, *Trans. AIME*, 147 (1942) 273.

---

**Part III**

**Alloy Design and Solidification**

# Insights on Solidification of Mg and Mg–Al Alloys by Large Scale Atomistic Simulations

Avik Mahata and Mohsen Asle Zaeem

## Abstract

We investigate the evolution of solid–liquid interfaces in Mg and Mg–9 at % Al during directional solidification by molecular dynamics (MD) simulations. At the initial stages of solidification, several solidification defects such as twins, stacking faults, and grain boundaries form, and at the final stages of solidification no new defects or grain boundaries form. The directional solidification in Mg–Al contains a considerable amount of heterogeneity due to formation of several Mg<sub>17</sub>Al<sub>12</sub> precipitates.

## Keywords

Mg alloys • Directional solidification • Molecular dynamics simulations

The evolution of solid–liquid interface in Mg and Mg–9 at % Al is analyzed during directional solidification by molecular dynamics (MD) simulations utilizing the second nearest neighbor modified embedded atom method (2NN-MEAM) interatomic potential. The condition for directional solidification is produced by imposing dissimilar temperatures at the model boundaries along the solidification direction to create a temperature gradient. During solidification, the solid–liquid front travels through the Mg and Mg–Al liquid along solidification direction towards the high temperature end. At the initial stages of solidification, several solidification defects such as twins, stacking faults, and grain boundaries form. As directional solidification progresses, grains elongate along the solidification direction, and at the final stages of solidification, no new defects or grain boundaries form. The elongated grain boundaries form a few layers with lamellar like structures along the

solidification direction. Unlike the single crystal, Mg, the directional solidification in Mg–Al consists of considerable amount of heterogeneity as there are several Mg<sub>17</sub>Al<sub>12</sub> precipitate form.

The simulation box with size of 50 × 50 × 50 nm<sup>3</sup> (125 × 125 × 125 unit cells, with ~8 M atoms) was utilized for the directional solidification of both Mg and Mg–9% Al. Figure 1a shows the initial dimensions for the simulation box for Mg. The simulation box will be identical for all the Mg–Al simulations. 2NN-MEAM interatomic potential for Mg [1] was used, and a 2NN-MEAM interatomic potential for Mg–Al system is developed that predicts the melting point and solid–liquid coexistence properties of Mg–Al very accurately. To prepare the homogenous Mg melt, the simulation box of hcp crystalline Mg was equilibrated at 1500 K for 150 ps with a time step of 3 fs. The similar procedure was also applied to Mg–9%Al. However, the equilibrating temperature was 2000 K. The crystalline structure almost immediately becomes liquid at higher temperatures; however, to get a homogenous liquid structure, it is equilibrated 150 ps. Temperature and pressure were controlled by Nose–Hoover thermostat and Parrinello–Rahman barostat [2], respectively. Periodic boundary conditions were employed in all three directions during the melt preparation. All the MD simulations were performed in parallel LAMMPS [3] code. The OVITO visualization package was used to monitor the melting, solidification, and deformation processes [4]. Within OVITO, common neighbor analysis (CNA) was used [5] to identify the local crystalline structure of atoms. We also utilized orientation coloring to study the grain orientations. CNA was used to identify the primary fcc crystal structures. These fcc atoms are always aligned along the coordination axes (i.e., x', y', z'), but these coordination axes are not always aligned with the principle axes (i.e., x, y, z) of simulation box. The orientation coloring shows orientation of the grains from the principle axes, and for the coloring purposes, we only considered the orientation from the principle axis Z. The coloring scheme was applied in OVITO, and the details of the implementation can be found in Larsen et al. work [6].

A. Mahata · M. Asle Zaeem (✉)

Department of Materials Science and Engineering, Missouri University of Science and Technology, Rolla, MO 65409, USA  
e-mail: [zaeem@mines.edu](mailto:zaeem@mines.edu)

M. Asle Zaeem

Department of Mechanical Engineering, Colorado School of Mines, Golden, CO 40801, USA

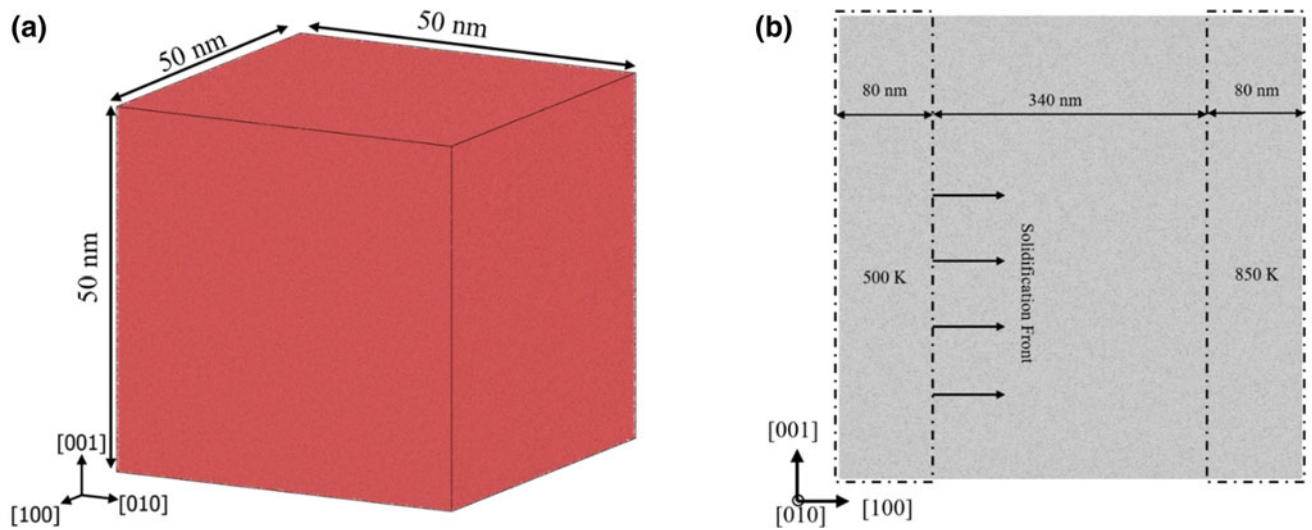


**Fig. 1** Simulation box at **a** initial melt with temperature of 1500 K. **b** The initial simulation set up for the directional solidification. The solid front travel in the solidification direction, [100], towards the hotter region (850 K in this case)

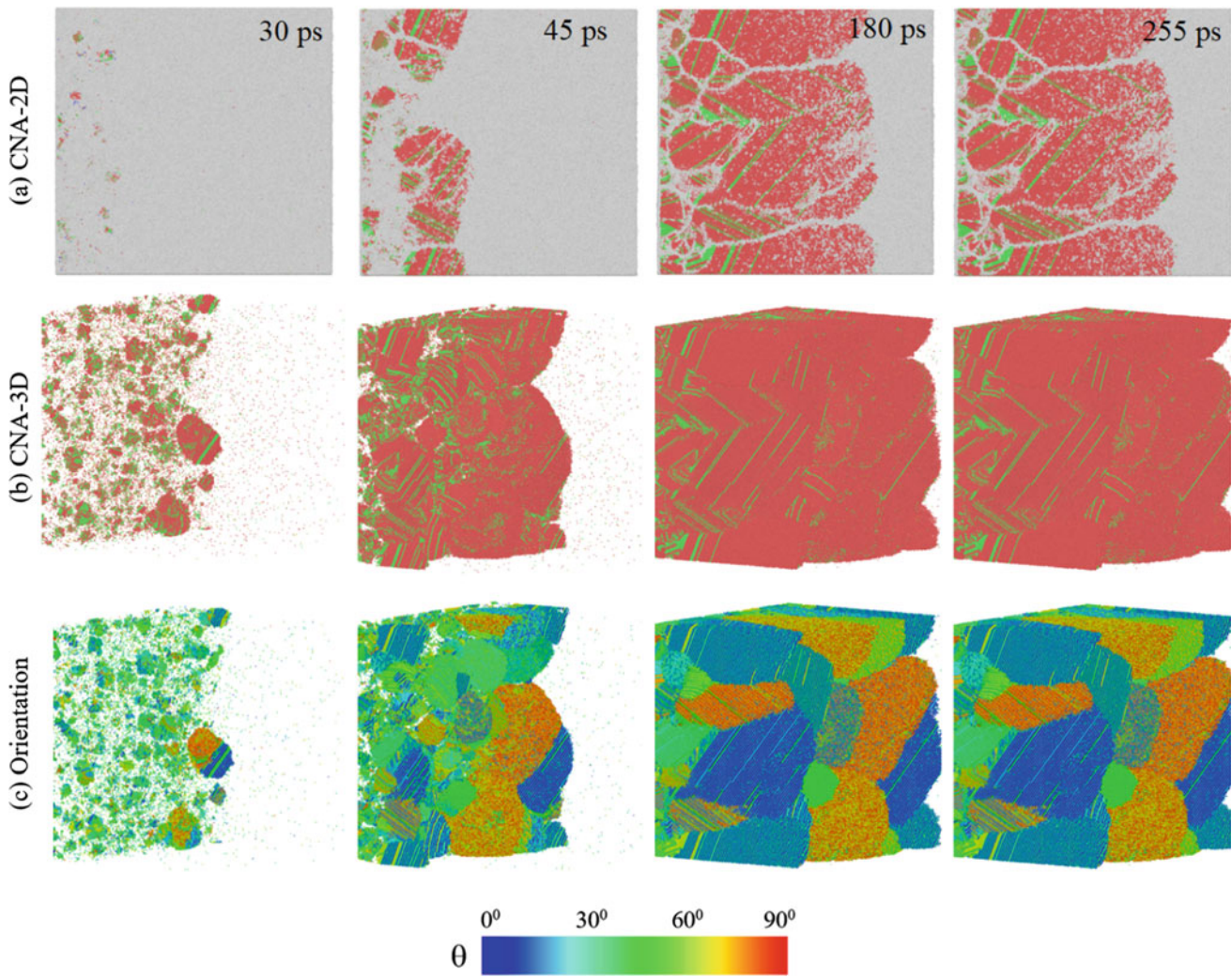


**Fig. 2** Snapshots of the directional solidification of liquid Mg. **a** 2D and **b** 3D views of solidification front travelling through the simulation box; atoms are colored by CNA coloring: green atoms are fcc, red atoms are hcp, and the white atoms represent the liquid and amorphous solids. **c** 3D views of grains forming during the solidification with different orientations

In rapid directional solidification process, several fcc twins form (red atoms in Fig. 2a, b) inside the hcp Mg grains (green atoms in Fig. 2a, b), especially in the beginning of the process when smaller grains are forming. At each spontaneous time, the solidified part of the Mg simulation box acts as solid seeds for rest of the liquid. The solidification front moves towards the liquid and gradually transforms it into solid crystalline. The new solid formation happens in a much slower pace than the initial solidification, and as a result, there is not much defects or twins observed after initial solidification stages. Three dimensional (3D) views are shown in Fig. 2b, c. The grains generally elongate along the temperature gradient. Figure 2c shows the grain boundaries (GBs) and grain orientations. Initially, several randomly orientated grains form; however, as the solidification front travelled towards the liquid region, many of them dissolved in the surviving grains. It can be also visualized from Fig. 2 that only few grains actually elongate.

## References

1. E. Asadi, M. Asle Zaeem, The anisotropy of hexagonal close-packed and liquid interface free energy using molecular dynamics simulations based on modified embedded-atom method, *Acta Materialia*, 107 (2016) 337–344.
2. M. Parrinello, A. Rahman, Polymorphic transitions in single crystals: A new molecular dynamics method, *Journal of Applied physics*, 52 (1981) 7182–7190.
3. S. Plimpton, Fast parallel algorithms for short-range molecular dynamics, *Journal of computational physics*, 117 (1995) 1–19.
4. A. Stukowski, Visualization and analysis of atomistic simulation data with OVITO—the Open Visualization Tool, *Modelling and Simulation in Materials Science and Engineering*, 18 (2009) 015012.
5. H. Tsuzuki, P.S. Branicio, J.P. Rino, Structural characterization of deformed crystals by analysis of common atomic neighborhood, *Computer physics communications*, 177 (2007) 518–523.
6. P.M. Larsen, S. Schmidt, J. Schiøtz, Robust structural identification via polyhedral template matching, *Modelling and Simulation in Materials Science and Engineering*, 24 (2016) 055007.



# Two-Stage Settling Approach to Purify Mg Alloy

Jiawei Liu, Tao Chen, Yuan Yuan, Jijia Wu, Li Yang, Aitao Tang, Dajian Li, and Fusheng Pan

## Abstract

Poor corrosion resistance, especially galvanic corrosion related to impurities, greatly limits the application of magnesium alloys. In the current work, iron content distribution in Mg melts and solidified alloys, as well as settling velocity of Fe-containing particles during settling process, was calculated. Based on the calculation, a new purification process, two-stage settling method, was designed to purify the Mg alloy by reducing content of Fe impurities. The two-stage settling method was carried out using AZ91 alloy as the sample material.

## Keywords

Magnesium alloys • Impurity • Iron • Purification

## Introduction

Magnesium alloys, as the lightest structure metallic materials, have attracted a broad attention [1–4]. However, the applications of Mg alloys in the automobile and aerospace industries are limited by its poor anti-corrosion property [5–7]. Many metallic elements have a very small solubility in primary Mg phase and tend to precipitate in the form of Mg–X compounds during solidification process. Because of Mg has the lowest standard electrochemical potential in room

temperature range, the formed precipitates can often cause severe galvanic corrosion as the impurity elements have higher corrosion potential compared to that of primary Mg phase and form micro-galvanic cells [7]. Especially, small quantity of impurities of Fe, Ni, and Cu in magnesium alloy will greatly deteriorate the corrosion resistance [5, 8–10]. Many literature works are devoted to decrease the quantity of these impurities, especially iron, which is commonly found in the commercial magnesium alloy [8, 9, 11–20].

The common synthesis process of Magnesium alloys can introduce a large amount of Fe impurities from (1) melting crucibles, which are usually made by iron alloys; (2) master alloys, which usually contain iron impurities. Regardless many approaches have been developed to get rid of Fe impurities, the purification process of the magnesium alloy is still insufficient. For example, the tolerance limit of iron in AZ series magnesium alloy is only in ppm magnitude, which is quite strict for the starting materials and the synthesis method. Additionally, cost is one of the most key-point for the industry field. The high production cost of Mg alloys retards its replacement of aluminum products for industrial applications. Hence, people continuously pursue high purity magnesium alloys with low production costs [21].

The general purification method is to let the melt impurities to form high-density precipitate and be settled to the bottom during a settling process. Some elements, like Zr, can enhance the formation of high-density compounds containing Fe impurities.

Generally, the solubility of element in another element primary phase including liquid phase decreases with descending temperature. However, the settling efficiency is also related to the property of formed particles. In the current work, after a thermodynamic calculation, we propose a new low-cost method, namely two-stage isothermal process, which can reduce the Fe content in Mg melts effectively.

J. Liu · T. Chen · Y. Yuan (✉) · J. Wu · L. Yang · A. Tang · F. Pan

College of Materials Science and Engineering, Chongqing University, Chongqing, 400000, People's Republic of China  
e-mail: [yuanyuan17@cqu.edu.cn](mailto:yuanyuan17@cqu.edu.cn)

D. Li  
Institute for Applied Materials—Applied Materials Physics (IAM-AWP), Karlsruhe Institute of Technology, Karlsruhe, 76344, Germany

Y. Yuan · A. Tang · F. Pan  
National Engineering Research Center for Magnesium Alloys, Chongqing, 400000, People's Republic of China

## Experimental Methods

### Determination of Iron Solubility in the AZ91 Melt

During cooling of Mg alloys, formation and growth of the precipitates are thermodynamically driven by chemical potential gradient, and meanwhile limited by the diffusion process. Therefore, considering the settling process, the solidification process of alloys was calculated using lever mode in this work, where the whole system is considered to be at thermodynamic equilibrium state. Pandat software (PanMg2013) was applied for the current thermodynamic calculation.

### Calculation of Settling Velocity of Precipitates with Density and Temperature Dependence

Efficiency of settling process can be qualitatively evaluated using the terminal settling velocities of precipitations following Stokes law [Eq. (1)]

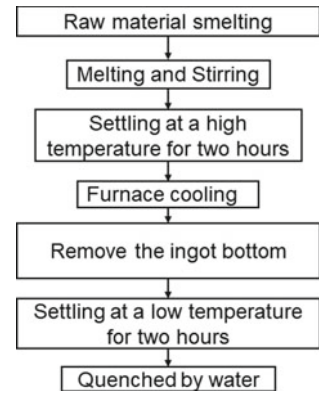
$$v = \frac{2gr_{\text{par}}^2(\rho_{\text{par}} - \rho_{\text{melt}})}{9\eta_{\text{melt}}\rho_{\text{melt}}} \quad (1)$$

where  $g$  is the gravitational acceleration and  $r$  is the mean radius of the settled particles;  $\rho_{\text{par}}$  denotes the density of the particles and  $\rho_{\text{melt}}$  is the density of melt,  $1.61 \text{ g/cm}^3$ ;  $\eta_{\text{melt}}$  is the viscosity of the current melt and  $\gamma$  denotes the kinematic viscosity.

### Two-Stage Isothermal Treat of AZ91 Alloy

AZ91 alloys (Mg–9Al1Zn, wt%) were synthesized using pure Mg, Al, Zn, and Mg–Mn master alloys according to the defined composition. Starting materials of present alloys are pure Mg (99.97 wt%, with 75 ppm Fe) blocks, aluminum (99.95 wt%) sheets, zinc (99.8 wt%) pieces, and Mg–3Mn (wt%) (Mg–2.684 wt% Mn measured by chemical analysis) master alloy. All alloys were melted in a resistance furnace under protection of mixed gas of 99.5 vol% CO<sub>2</sub> and 0.5 vol% SF<sub>6</sub> in a steel crucible. The melt was first kept at a defined temperature for two hours and then cooled with furnace to

**Fig. 1** Scheme of the synthesis process of AZ91 alloy in this work



room temperature. Bottom of the ingot was cut away and the remaining ingot was re-melted in a new steel crucible and kept at a second settling temperature for two hours and quenched in cold water. The whole synthesis process is shown in Fig. 1.

The samples getting from the ingots from different stages were analyzed using inductively coupled plasma optical emission spectrometry (ICP-OES, Optima 8000) analysis for its composition analysis. The composition of the obtained alloys is given in Table 1.

## Results and Discussion

### Two-Stage Settling Treatment in Synthesis and Purification of AZ91 Alloy

The calculated solidification path of AZ91 alloy with composition 90.2 Mg–9Al0.7Zn0.1Fe (wt%) following the lever mode is shown in Fig. 2.

Following Fig. 2, the precipitated phase is Bcc\_B2 above 760 °C during the cooling process. When the melt is cooled to 760 °C, Bcc\_B2 phase is disappeared, accompanied by the formation of Al<sub>2</sub>Fe. When the temperature is below 662 °C, the Al<sub>2</sub>Fe disappears and Al<sub>5</sub>Fe<sub>2</sub> appears. The calculated compositions of equilibrium phases at each stage are listed in Table 2.

As shown in Table 2, if the Mg melt is settled at 760 °C for a long time to allow Bcc\_B2 phase fully settled to the bottom, the iron content in the remaining liquid will be

**Table 1** Compositions and settling process of investigated alloys

No.	Composition (final alloy measured using ICP analysis)				Settling temperature T (°C)
	Al (wt%)	Zn (wt%)	Mn (wt%)	Mg (wt%)	
AZ91 (0Mn)	9.14	0.91	0	Bal.	730 + 660
AZ91 (0.1Mn)	8.50	0.85	0.10	Bal.	730 + 660
AZ91 (0Mn)	8.24	0.84	0	Bal.	660

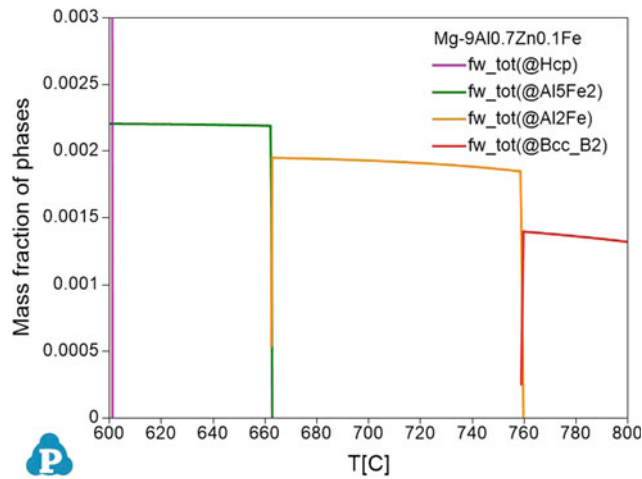


**Fig. 2** Solidification path of AZ91 without Mn using lever mode

**Table 2** Composition of equilibrium phases at each stage of AZ91 alloy

T (°C)	Phases	Composition (wt%)				Density (g/cm <sup>3</sup> )
		Al	Zn	Fe	Mg	
785	Liquid	8.96	0.70	0.0087	Bal.	1.58
	Bcc_B2	32.38	0	68.5788	Bal.	5.30
760	Liquid	8.96	0.7	0.0073	Bal.	1.58
	Bcc_B2	32.54	0	67.4250	Bal.	5.30
663	Liquid	8.91	0.7	0.0010	Bal.	1.58
	Al <sub>2</sub> Fe	49.14	0	50.8574	Bal.	4.43
601	Liquid	54.71	0.7	0.0002	Bal.	1.58
	Al <sub>5</sub> Fe <sub>2</sub>	71.42	0	28.5714	Bal.	4.18

**Table 3** Settling velocity of the different precipitates of AZ91 alloy at different temperatures

T (°C)	Viscosity of the melt (m <sup>2</sup> /s)	Precipitated particle	Density (g/cm <sup>3</sup> )	Terminal settling velocity (m/s)
760	7.3E-7	Bcc (Fe, Al)	5.61	6.6E-5
730	7.5E-7	Al <sub>2</sub> Fe	4.08	4.0E-5
700	7.8E-7	Al <sub>2</sub> Fe	4.08	3.8E-5
663	8.5E-7	Al <sub>2</sub> Fe	4.08	3.5E-5
640	9.1E-7	Al <sub>5</sub> Fe <sub>2</sub>	3.96	3.1E-5
601	1.1E-6	Al <sub>5</sub> Fe <sub>2</sub>	3.96	2.6E-5

73 ppm. After removing the bottom part of the melt with the precipitate particles, the remaining melt is settled again at 663 °C for a second settling stage, the content of iron in the remaining liquid will be only 10 ppm, which fulfills the purity requirement of the final alloy.

However, infinite settling time can never be achieved. Therefore, the efficiency, i.e., settlement velocity of precipitates must be taken into consideration. Currently, the industry often holds the melt at 700–730 °C for 0.5–1 h. In current commercial settling process, there will be still a lot of Al<sub>2</sub>Fe dispersed in the liquid, which will transform to Al<sub>5</sub>Fe

that have lower density and be more difficult to be settled to the bottom.

According to the Stokes law [Eq. (1)], the settling velocity is inversely proportional to the viscosity of the fluid and the density difference of the precipitates and the fluid. Table 3 shows the calculated settling velocity of the precipitates. The viscosity data were taken from the scheme plot in Ref. [22].

A two-stage settling purification method is proposed as following. The first settlement is performed at 760 °C where most of the iron forms as high-density Bcc\_B2 precipitates



and be taken away. Then, a second settlement process is performed at 660 °C to let the final alloy achieve higher purity.

According to the calculation results, it is seen the settling velocity of precipitates at 760 °C is almost twice of that one at 600 °C. At the second isothermal stage, the remaining iron which has not deposited completely can still form Al<sub>2</sub>Fe and deposited to the bottom. Therefore, it is expected that the remaining liquid phase will achieve high purity after a two-stage settling process.

Clearly, temperature selection is critical for the two-stage settling process if we are thinking about industrial applications. The energy consumption is very important for the cost control for massive production. Therefore, the settling temperatures are ideally chosen just above the phase transformation temperatures. However, this will require high precision database as well as temperature control. In the current case, if we look 760 and 660 °C on Fig. 1, several degrees lower than the designed temperatures will lead to full transformation of the precipitates into other phases which are less efficient for the settlement. Because no experimental information or theoretical information is available for the applied end-part phase diagram with ppm magnitude, the calculated phase transformation temperatures might have some deviation from the reality. Therefore, it is suggested to choose a temperature slightly higher than the calculated temperatures to ensure the formation of expected phases.

On the other hand, the temperature of the first settlement process at 760 °C for AZ91 is too high for the normal melting process of the magnesium alloy. A little Mn is added to the AZ91 to show its effect on the phase transformation during the solidification process. Figure 3 shows the solidification path of alloy AZ91 (wt%).

It is shown, with Mn addition, the high density of the precipitates (Bcc\_B2) can be kept to a lower temperature. It is seen the settling velocity is with strong relation with the

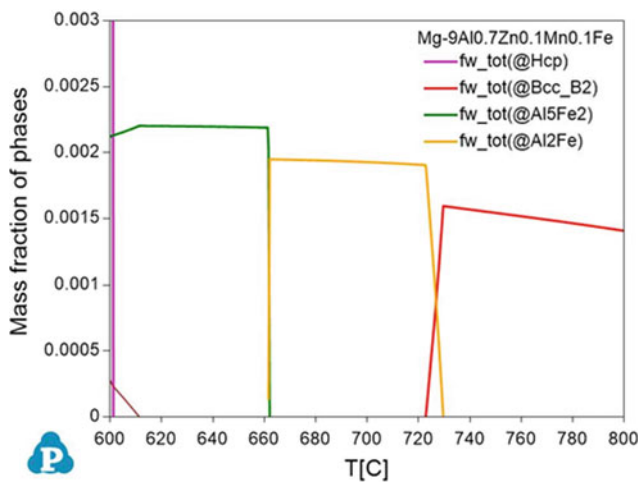


**Fig. 3** Solidification path of AZ91 with 0.1 wt% Mn using lever mode

density of the precipitates. Hence, the type of the precipitates is quite important for the effect of the settling process.

## The Application of a Two-Stage Settling Treatment in Synthesis and Purification of AZ91 Alloy

Figure 4 shows the purification effect of AZ91 in a two-stage settling process. The synthesized AZ91 in the current work contains around 200 ppm Fe getting from starting materials and contaminations. The second stage of low temperature settling can further reduce the iron content of AZ91 compared to a one-stage settling process. The Fe content of the AZ91 alloy melts after settling at 730 °C for 2 h are ~120 ppm. In the second stage, after settling at 660 °C for two hours, the iron content in AZ91(0.1Mn) was reduced to ~70 ppm.

In addition, the remaining Fe content in the reference group, AZ91 (0.1 Mn) which was settled at 660 °C for four hours, is ~100 ppm, higher than that alloy with a two-stage settling treatment.

The compositions of the parts from the bottom of the ingots which were also examined by ICP are 1046 ppm and 235 ppm after the first and second settlement, respectively.

## Conclusion

A new approach for melt purification of magnesium alloys, two-stage settling treatment, has been proposed. During the process of static purification of magnesium alloy, the iron-containing phase will aggregate to the bottom of the melt

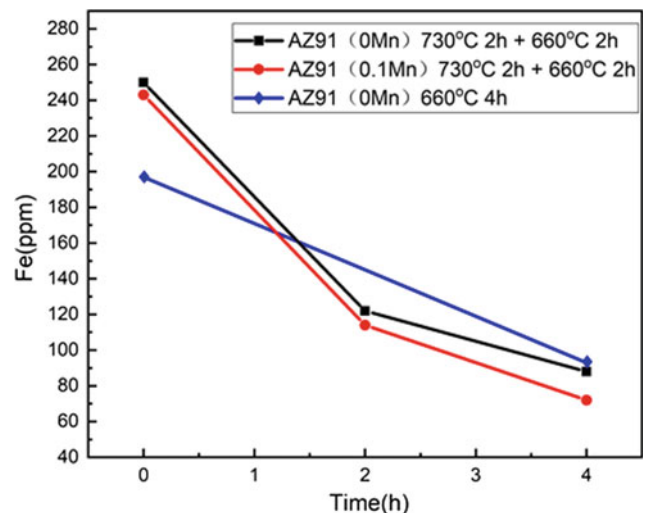


**Fig. 4** Fe contents in the melt after the melt treatment for AZ91 (0Mn), AZ91 (0.1Mn) using different settling treatments

under the action of gravity. If the iron-containing phase at the bottom is removed and a second settling process is carried out, the iron of the melt can be more effectively reduced.

**Acknowledgements** The authors thank the fund supported by National Natural Science Foundation of China with Grant No. 51971044, the fund supported by National Key Research and Development Program of China with Project No. 2016YFB0301100 and the fund supported by the Fundamental Research Funds for the Central Universities with Project No. 2019CDJGFCL005.

## References

- Abbott T B (2015) Magnesium: Industrial and Research Developments Over the Last 15 Years. *Corrosion-Us* 71:120–127. <https://doi.org/10.5006/1474>
- Mordike B L, Ebert T (2001) Magnesium - Properties - applications - potential. *Mat Sci Eng a-Struct* 302:37–45. [https://doi.org/10.1016/s0921-5093\(00\)01351-4](https://doi.org/10.1016/s0921-5093(00)01351-4)
- Wang X J, Xu D K, Wu R Z, Chen X B, Peng Q M, Jin L, Xin Y C, Zhang Z Q, Liu Y, Chen X H, Chen G, Deng K K, Wang H Y (2018) What is going on in magnesium alloys? *J Mater Sci Technol* 34:245–247. <https://doi.org/10.1016/j.jmst.2017.07.019>
- Joost W J, Krajewski P E (2017) Towards magnesium alloys for high-volume automotive applications. *Scrip Mater* 128:107–112. <https://doi.org/10.1016/j.scriptamat.2016.07.035>
- Esmaily M, Svensson J E, Fajardo S, Birbilis N, Frankel G S, Virtanen S, Arrabal R, Thomas S, Johansson L G (2017) Fundamentals and advances in magnesium alloy corrosion. *Prog Mater Sci* 89:92–193. <https://doi.org/10.1016/j.pmatsci.2017.04.011>
- Atrens A, Song G L, Liu M, Shi Z M, Cao F Y, Dargusch M S (2015) Review of Recent Developments in the Field of Magnesium Corrosion. *Adv Eng Mater* 17:400–453. <https://doi.org/10.1002/adem.201400434>
- Song G L, Atrens A (2003) Understanding magnesium corrosion - A framework for improved alloy performance. *Adv Eng Mater* 5:837–858. <https://doi.org/10.1002/adem.200310405>
- Liu M, Uggowitzer P, Schmutz P, Atrens A (2008) Calculated phase diagrams, iron tolerance limits, and corrosion of Mg-Al alloys. *Jom-Us* 60:39–44. <https://doi.org/10.1007/s11837-008-0164-2>
- Liu M, Song G L (2013) Impurity control and corrosion resistance of magnesium-aluminum alloy. *Corro Sci* 77:143–150. <https://doi.org/10.1016/j.corsci.2013.07.037>
- Gusieva K, Davies C H J, Scully J R, Birbilis N (2015) Corrosion of magnesium alloys: the role of alloying. *Int Mater Rev* 60:169–194. <https://doi.org/10.1179/1743280414y.0000000046>
- Gao H T, Wu G H, Ding W J, Liu L F, Zeng X Q, Zhu Y P (2004) Study on Fe reduction in AZ91 melt by B<sub>2</sub>O<sub>3</sub>. *Mat Sci Eng a-Struct* 368:311–317. <https://doi.org/10.1016/j.msea.2003.11.017>
- Qiao Z X, Shi Z M, Hort N, Abidin N I Z, Atrens A (2012) Corrosion behaviour of a nominally high purity Mg ingot produced by permanent mould direct chill casting. *Corro Sci* 61:185–207. <https://doi.org/10.1016/j.corsci.2012.04.030>
- Prasad A, Uggowitzer P J, Shi Z M, Atrens A (2012) Production of High Purity Magnesium Alloys by Melt Purification with Zr. *Adv Eng Mater* 14:477–490. <https://doi.org/10.1002/adem.201200054>
- Parthiban G T, Palaniswamy N, Sivan V (2009) Effect of manganese addition on anode characteristics of electrolytic magnesium. *Anti-Corro Methods and Mater* 56:79–83. <https://doi.org/10.1108/00035590910940069>
- Matsubara H, Lchige Y, Fujita K, Nishiyama H, Hodouchi K (2013) Effect of impurity Fe on corrosion behavior of AM50 and AM60 magnesium alloys. *Corro Sci* 66:203–210. <https://doi.org/10.1016/j.corsci.2012.09.021>
- Birbilis N, Williams G, Gusieva K, Samaniego A, Gibson M A, McMurray H N (2013) Poisoning the corrosion of magnesium. *Electrochem Commun* 34:295–298. <https://doi.org/10.1016/j.elecom.2013.07.021>
- Pan F S, Chen X H, Yan T, Liu T T, Mao J J, Luo W, Wang Q, Peng J, Tang A T, Jiang B (2016) A novel approach to melt purification of magnesium alloys. *Journal of Magnesium and Alloys* 4:8–14. <https://doi.org/10.1016/j.jma.2016.02.003>
- Wu G H, Gao H T, Ding W J, Zhu Y P (2005) Study on mechanism of iron reduction in magnesium alloy melt. *J Mater Sci* 40:6175–6180. <https://doi.org/10.1007/s10853-005-3161-7>
- Gao J W, Shu D, Wang J, Sun B D (2009) Study on iron purification from aluminium melt by Na<sub>2</sub>B<sub>4</sub>O<sub>7</sub> flux. *Materials Science and Technology* 25:619–624. <https://doi.org/10.1179/174328408x339288>
- Chen T, Yuan Y, Wu J, Liu T, Chen X, Tang A, Pan F (2019) Alloy Design Strategies of the Native Anti-corrosion Magnesium Alloy. Paper presented at the TMS 2019 Annual Meeting, San Antonio, Texas, 10–14 March 2019
- Gandel D S, Easton M A, Gibson M A, Abbott T, Birbilis N (2014) The influence of zirconium additions on the corrosion of magnesium. *Corrosion Science* 81:27–35. <https://doi.org/10.1016/j.corsci.2013.11.051>
- Abaturov I S, Popel P S, Brodova I G, Astafiev V V, Peijie L (2008) Exploration of the viscosity temperature dependences and microstructure of magnesium-based commercial alloy AZ91D with small additions of calcium. 98:6–10. <https://doi.org/10.1088/1742-6596/98/6/062023>

# CALPHAD Modeling and Microstructure Investigation of Mg–Gd–Y–Zn Alloys

Janet Meier, Josh Caris, and Alan A. Luo

## Abstract

In this study, CALPHAD (CALCulation of PHase Diagrams) modeling was used to design and optimize Mg–Gd–Y–Zn alloys containing long period stacking order (LPSO) phases. The selected compositions were evaluated using scanning electron microscopy, energy dispersive spectroscopy, and X-ray diffraction to identify major phases and determine their area fractions. It was seen in as-cast samples that a blocky LPSO 14H phase formed at the grain boundaries while a filament-type LPSO 14H formed in the Mg grains. As the rare earth (RE) and Zn concentrations increased, eutectic Zn-rich intermetallics and more of the RE-rich blocky LPSO formed along grain boundaries. After annealing, an increase in the Zn-rich intermetallic area fraction, decrease in bulky LPSO area fraction, and increase in filament-type LPSO were observed. In higher alloyed samples, a Zn- and Y-rich phase was observed that was not consistent with the predicted or reported phase. These results indicate the present CALPHAD databases well represent the LPSO 14H formation in the Mg–Gd–Y–Zn system studied and can be used to tailor the microstructure to potentially improve the strength and ductility in these alloys. Further investigation is needed to determine if the existing reliably databases model the other secondary phases.

## Keywords

Long period stacking order (LPSO) • Microstructure • Magnesium alloys • CALPHAD • Alloy development

## Introduction

As magnesium alloys become more widely used in structural applications, there is a growing need for improvements in strength and ductility for these alloys. In recent years, such improvements in properties have been found in alloys containing long period stacking ordered (LPSO) phases [1–4]. LPSO phases can form in Mg alloys that contain a smaller atomic radius transition metal, such as Zn, and larger rare earth elements (RE), such as Y and Gd, due to the reduction in stacking fault energy caused by these alloying elements [5–8]. The RE and Zn atoms cluster along the basal plane to form enriched layers [9]. These layers form building blocks with a local face centered cubic structure that is bounded by Shockley partial dislocations [9]. The spacing and combination of these building blocks with the Mg lattice produce several different LPSO structures, where the most frequently observed are 14H and 18R. The difference between the two phases is the number of Mg layers between the building blocks: LPSO 14H has three layers and 18R has two [9, 10].

The LPSO phase in Mg alloys forms in two major morphologies, depending on composition and thermomechanical processing [8, 11–17]. The first morphology is a blocky phase found at the grain boundaries. As the volume fraction of LPSO increases, the blocky phase forms a network around the  $\alpha$ -Mg grains. The second morphology is a fine lamellar phase located in the  $\alpha$ -Mg grains. Improved strength and ductility in LPSO-containing alloys come from the impedence of dislocation motion and twin formation by the relatively thick LPSO phases [8, 10, 13, 16, 18]. The LPSO structure increases the critical resolve shear stress for basal and prismatic slip, which provides strengthening and activates slip in other grains to improve ductility [11, 19]. As a result, maximizing the phase fraction of LPSO could greatly improve the mechanical properties of Mg alloys.

Previous researchers have developed criteria for the critical ratio of RE to Zn to produce LPSO phases, but as the alloy systems become more complex it is more difficult to

J. Meier · A. A. Luo (✉)  
The Ohio State University, Columbus, OH, USA  
e-mail: [luo.445@osu.edu](mailto:luo.445@osu.edu)

J. Caris  
Terves LLC, Euclid, OH, USA

predict the resulting microstructures. A CALPHAD (CALculation of PHase Diagrams)-based approach [20] provides an opportunity to quantitatively predict the phase composition of these more complex alloys. In this work, the available databases for two CALPHAD software packages, Thermo-Calc and PANDAT, were evaluated to predict the phases of three Mg–Gd–Y–Zn alloys, followed by experimental validation.

## Modeling and Experimental Methods

Equilibrium and Scheil calculations were conducted using Thermo-Calc and PANDAT for several compositions in the Mg–Gd–Y–Zn system to assess the predicted phase fractions of LPSO and intermetallic phases. Three compositions, shown in Table 1, were selected and cast for microstructural analysis.

The alloys were prepared and cast by Terves LLC. The raw materials (commercially pure Mg, Zn, Gd, and Y) were melted in a 75 lb gas fired furnace with a pneumatic shear mixer. A CO<sub>2</sub> and SF<sub>6</sub> gas mixture was used as a cover gas in the furnace and applied to the mold riser to prevent oxidation of the melt. The samples were cast into a 7" × 7" × 4" steel permanent mold. The castings were then sectioned, annealed at 500° for 9 h and water quenched, and mounted in Bakelite for scanning electron microscope (SEM) analysis. Final alloy compositions (Table 1) were determined using a combination of inductively coupled plasma mass spectroscopy (ICP) and spark optical emission spectroscopy (OES).

Samples were ground and polished to 0.05 μm colloidal silica, and SEM analysis was performed using a FEI Apreo FEG microscope with EDAX Octane Elect energy dispersive spectroscopy (EDS) capabilities. EDS spot and mapping analysis was performed using a TEAM software.

**Table 1** Compositions of the three samples used in this study (determined using ICP and OES)

Sample	Mg (wt%)	Gd (wt%)	Y (wt%)	Zn (wt%)
MC07	82.98	10.4	3.62	3.00
MC14	81.73	10.57	5.25	2.45
MC21	79.95	10.2	4.74	5.1

**Table 2** Existing ternary systems and LPSO phases present in the Thermo-Calc TCMG5 and PANDAT PanMg2018\_TH + MB databases

	Thermo-calc	PANDAT
Ternary systems	Mg–Gd–Y Mg–Gd–Zn Mg–Y–Zn	Mg–Gd–Y Mg–Gd–Zn Mg–Y–Zn
LPSO phases	LPSO_14H LPSO_18R	LPSO_14H LPSO_18R LPSO_10H

The area fraction of each phase was determined from ten images from each sample using ImageJ. The samples were then removed from the Bakelite mounts and polished to 1200 grit for X-ray diffraction (XRD) analysis. A Rigaku MiniFlex 600 system with a Cu source and Ni filter set to 40 kV and 15 mA was used for phase identifications. The Rigaku PDXL 2 software and literature data were used to identify the XRD peaks.

## Results and Discussion

### CALPHAD Modeling

In order to appropriately model a multicomponent alloy system with CALPHAD, there must be a reliable database that represents all related binary and ternary systems. The ternary systems included in the Thermo-Calc and PANDAT databases are listed in Table 2. Both systems contain data for the three ternary systems for the Mg rich corner, but PANDAT also has the LPSO 10H phase defined in their database. It should be noted that although both programs contain data for the same ternary systems, they may be using different datasets or computational methods. As a result, there will likely be variations in the predicted results.

For each alloy, both equilibrium and Scheil calculations were performed to represent the two extremes seen in cast alloys. The Scheil calculation represents rapid cooling during solidification, where diffusion can occur in the liquid but not the solid. On the other hand, the equilibrium calculation better represents alloys with very slow cooling during solidification or after annealing heat treatment. The predicted phases for the three alloys studied in this work can be seen in Fig. 1.

For the compositional range, there were a total of seven predicted phases between the two programs. The primary

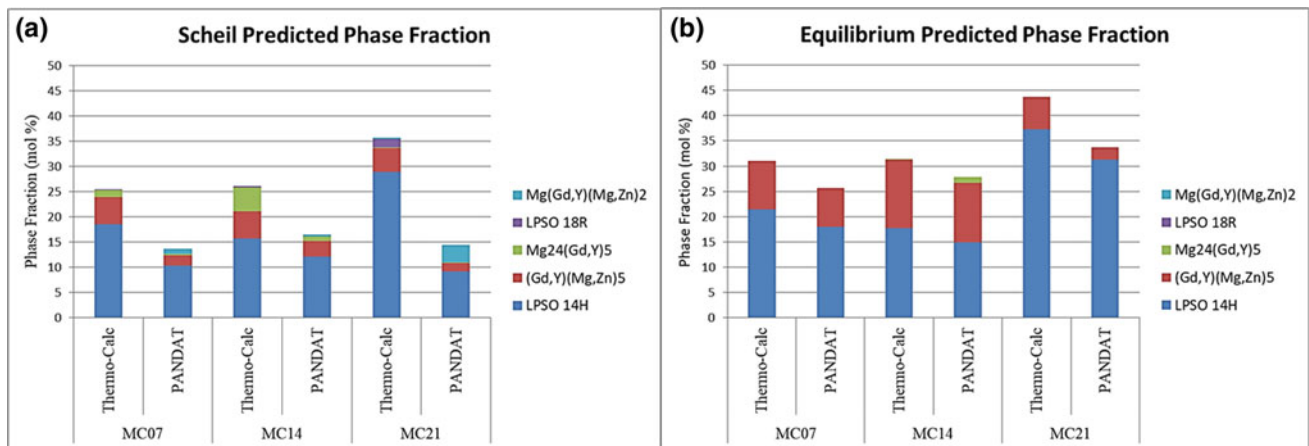


**Fig. 1** Predicted phases and mole fractions of each phase in the (a) Scheil and (b) equilibrium conditions

phase predicted for all compositions was the hexagonal close packed (hcp) Mg matrix, as expected. In the case of the LPSO phases, both programs predicted the presence of the LPSO 14H phase. The LPSO 14H phase has been reported as a very stable phase that can form both at the grain boundaries and in the primary Mg grains [8, 11–17]. Also, the LPSO 14H phase has been reported to transform from other phases, and intragranular growth is driven by the diffusion of Zn and the RE [8–12, 15, 16]. The increase in the mole fraction of LPSO 14H between the Scheil and equilibrium conditions predicted by both programs is consistent with these previous findings.

Thermo-Calc also predicted 0.34 and 1.7 mol% of the LPSO 18R for MC14 and MC21 samples, respectively, in the Scheil condition (Fig. 1). In the equilibrium condition, no LPSO 18R is predicted. Previous studies have found that LPSO 18R forms at the grain boundaries during solidification in Mg–Y–Zn and Mg–Gd–Y–Zn alloys [8, 21–23]. The LPSO 18R transforms into 14H during annealing, and both phases can exist simultaneously in the same grain [19]. Due to the low predicted fractions and the deviations from the Scheil condition seen in the as-cast samples, the LPSO 18R phase may not be observable in this study.

PANDAT predicts a phase called RM3\_W in the Scheil condition for all three alloys that is defined as  $Mg_{0.25}(Gd, Y)_{0.25}(Mg, Zn)_{0.5}$ . Thermo-Calc also predicts a similar phase called L12\_RMGN2, defined as  $Mg_1(Gd, Y)_1(Mg, Zn)_2$ , for the MC21 alloy in the Scheil condition. For similar compositions, there has been a reported  $Mg_3(Gd, Y)$  phase [12, 17, 24–26] and a reported  $W-Mg_3Y_2Zn_3$  phase [8, 15, 17, 27, 28]. In their 2018 paper, Luo et al. discussed that the  $W-Mg_3Y_2Zn_3$  phase had been misidentified as  $Mg_3(Gd, Y)$  in past studies [16]. Neither Thermo-Calc or PANDAT has the  $W-Mg_3Y_2Zn_3$  phase in their databases, so it is possible that these phases were not separately identified in either program. For this study, the predicted mole fractions of the RM3\_W

and L12\_RMGN2 phases are predicted in low amounts in the Scheil condition and are not predicted in the equilibrium condition (Fig. 1). As a result, they may not be observable in this study. Future work will be needed to evaluate these two phases in the databases.

In the Scheil and equilibrium conditions, both programs predict the presence of a  $(Mg, Zn)_5(Gd, Y)$  phase. This phase is generally reported as the  $\beta$  phase and has been observed in a wide range of LPSO-forming alloys [10, 11, 16, 24, 25, 29]. The mole fraction of  $(Mg, Zn)_5(Gd, Y)$  is predicted to increase between the Scheil and equilibrium conditions, which is consistent with proposed precipitation sequences that have  $(Mg, Zn)_5(Gd, Y)$  as an equilibrium phase [26]. The final predicted phase is  $Mg_{24}(Gd, Y)_5$ . Both programs predict small mole fractions of this phase in the Scheil condition and in the equilibrium condition for MC14.  $Mg_{24}(Gd, Y)_5$  has also been reported as the  $\beta$  phase in some studies [8, 12, 25], as a result the two phases will be referred to by their compositions in this work. The  $Mg_{24}(Gd, Y)_5$  phase has been observed in Mg–Gd–Zn–Zr and Mg–Y–Zn–Zr alloys, but is predicted at relatively low mole fractions in the present alloys.

The predicted mole fractions for each phase at the end of solidification for the Scheil model and at room temperature for equilibrium model were calculated in both programs (Fig. 1). For the LPSO 14H phase, Thermo-Calc consistently predicts a higher mole fraction. This is also true for the  $(Mg, Zn)_5(Gd, Y)$  phase. For the Scheil model, which more closely represents the as-cast state, Thermo-Calc also predicts a higher mole fraction of the  $Mg_{24}(Gd, Y)_5$  phase for the three compositions. In the equilibrium calculation, which more closely represents the annealed state, only MC14 is predicted to have the  $Mg_{24}(Gd, Y)_5$  phase, and PANDAT predicts a larger mole fraction. The mole fraction of LPSO is predicted by both programs to increase with annealing. This prediction is consistent with the expected diffusion of RE and Zn during annealing reported in literature [9, 16].



There is also a predicted increase in the mole fraction of the  $(\text{Mg,Zn})_5(\text{Gd,Y})$  phase with annealing as well.

### Microstructural Analysis

The microstructure from SEM of the as-cast and annealed samples can be seen in Fig. 2. The T1 detector used acts similar to a backscatter detector and collects the high-energy,

low-angle electrons. As a result, Z-contrast can be used to help identify phases. The dark, background phase was identified as the primary Mg grains using EDS spot and mapping analysis. Dark spots seen in the Mg grains, particularly in the as-cast samples, are believed to be corrosion pits formed during sample preparation. In all the samples, there is a small amount of a small, bright rectangular phase. Upon EDS analysis, there were high Y and O signals, which are most likely yttrium oxide formed during the casting process.

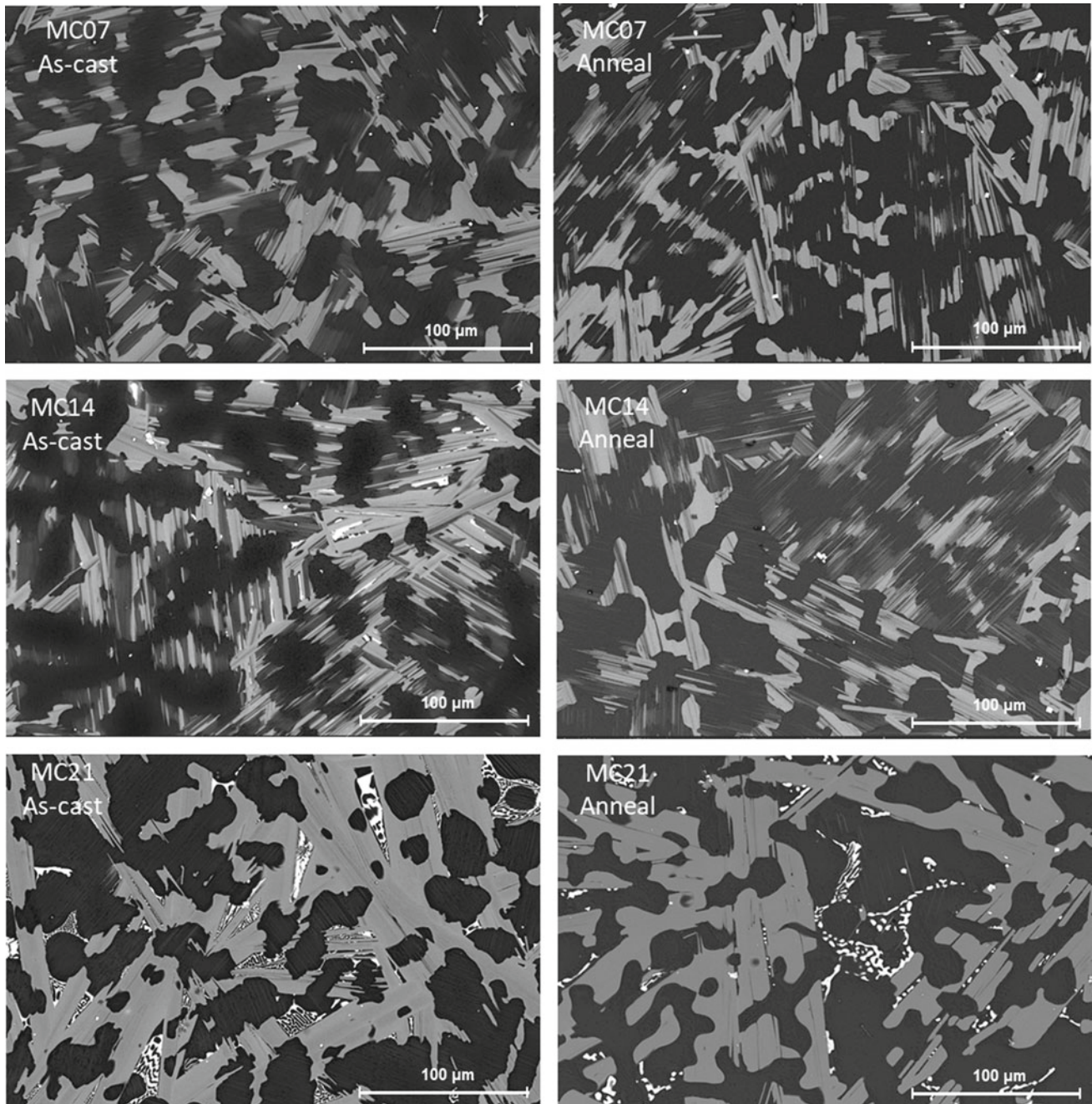


**Fig. 2** SEM images using a T1 (backscatter-like) detector for the as-cast and annealed conditions



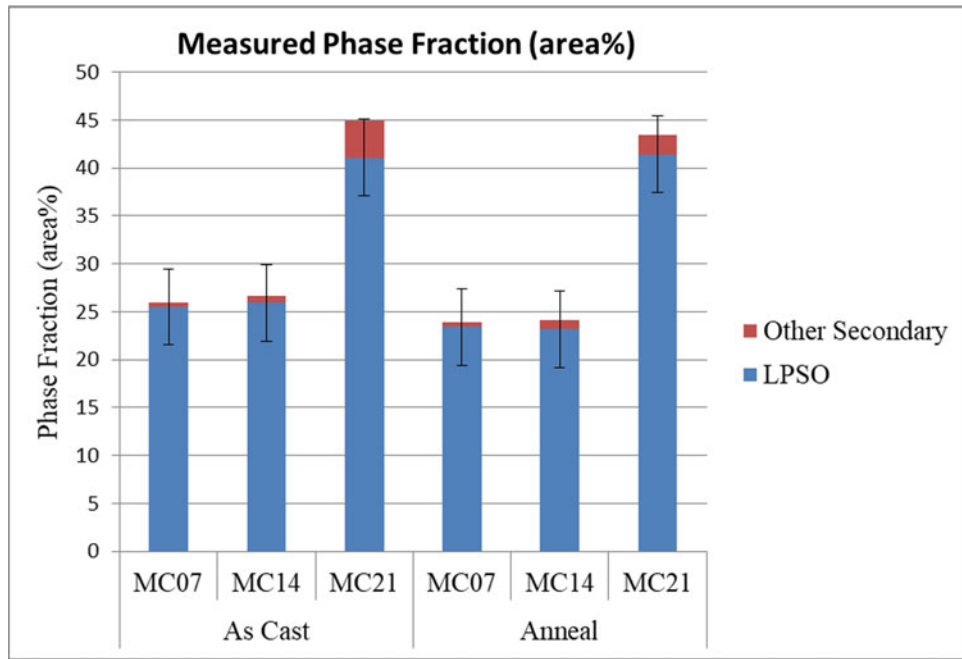


Fig. 3 Measured area fractions of the LPSO 14H and other secondary phases in the as-cast and annealed conditions

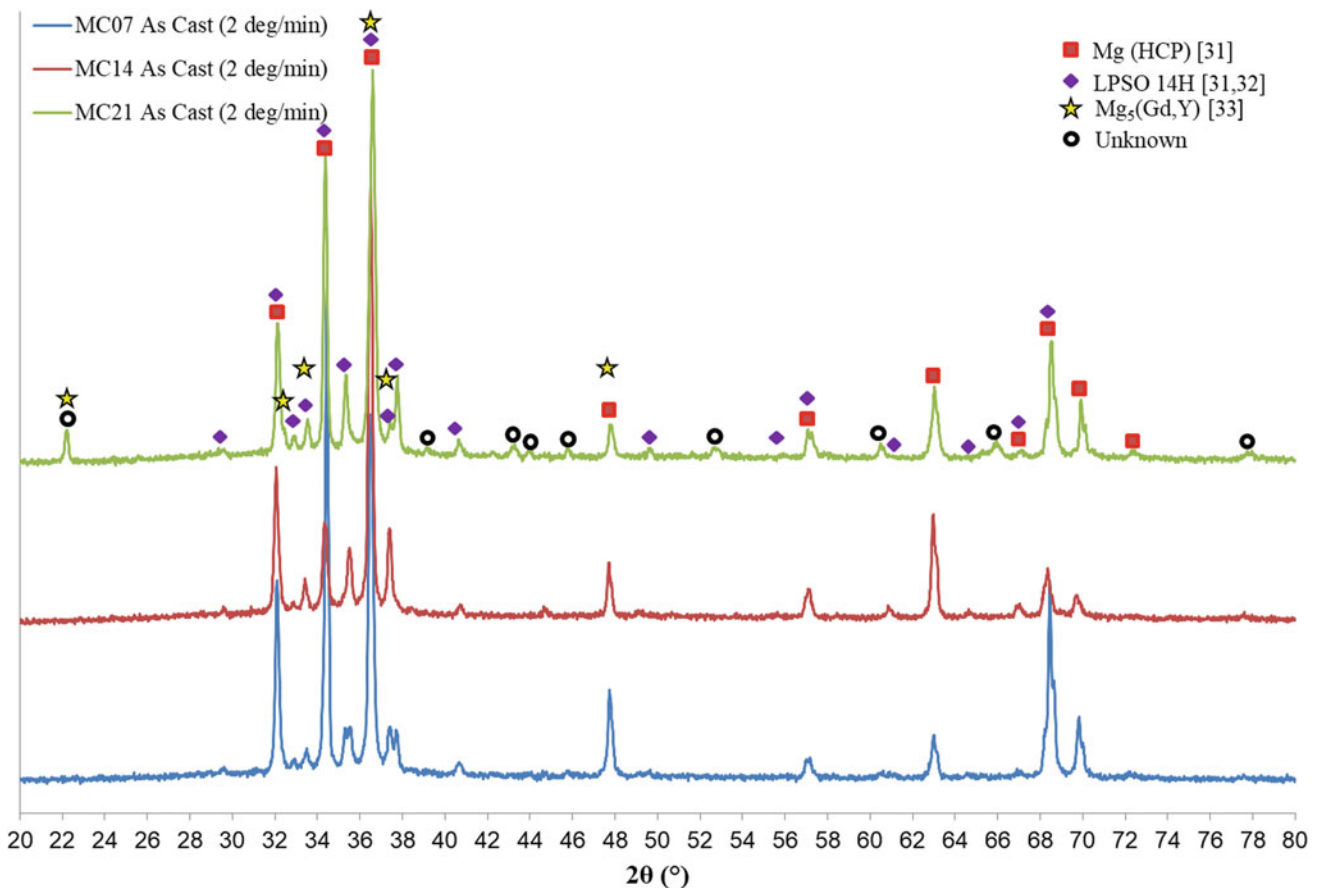


Fig. 4 XRD analysis of the as-cast samples

The high area fraction medium grey phase seen in all of the samples has a blocky morphology that becomes more lamellar with annealing. EDS mapping of this phase indicates it has a higher Y and Zn signal than the Mg matrix. As the Gd concentration increases, EDS mapping shows that the relative Gd concentration in the medium grey phase also increases. This is due to the lower solubility of Y and Zn in Mg and the higher solubility of Gd in Mg [30]. The area fraction of the phase also increases with increased alloying, with MC21 showing the largest area fraction of this phase (Fig. 3). Based on the CALPHAD predictions, this phase is most likely the LPSO 14H phase. This is supported by XRD analysis (Figs. 4 and 5), which has Mg and the LPSO 14H as the dominant phases.

After annealing, there is a small reduction in the measured  $\omega$ LPSO 14H area fraction (Fig. 3). One explanation for this could be the formation of lamellar LPSO 14H in the Mg grains that is not easily observable at the magnification used for volume fraction measurements. At higher magnification, small bright lamellar features can be seen extending from the grain boundaries into the Mg matrix (Fig. 6). This phase is in one orientation in each grain. The presence of this

lamellar phase increases with increased alloying and with annealing, with the possible exception of the MC21 sample. This phase is most likely LPSO 14H, and the increase in its formation after annealing is consistent with the diffusion of RE and Zn from the grain boundaries into the grains, as reported in literature [8, 12–17, 27, 31]. As a result, there is a decrease in the area fraction of bulky LPSO 14H at the grain boundaries.

In the as-cast MC14 and MC21 samples, there is a bright phase along the grain boundaries (Figs. 2 and 6). In the MC21 sample, this phase has a eutectic morphology and increases in area fraction in comparison with the lower alloy MC14 sample. With annealing, the area fraction of the bright phase is reduced in MC21 and is no longer observable in MC14. Based on the CALPHAD analysis, this bright phase is most likely  $(\text{Mg,Zn})_5(\text{Gd,Y})$  or  $\text{Mg}_{24}(\text{Gd,Y})_5$  due to predicted mole fraction. EDS mapping of this phase indicates there are relatively high Zn and Y concentrations and no presence of Mg and Gd. In the as-cast MC14 sample, there was some Gd signal in the EDS map for the bright phase. Based on the high Zn content, this phase is unlikely to be  $\text{Mg}_{24}(\text{Gd,Y})_5$ . XRD analysis (Figs. 4 and 5) indicates that

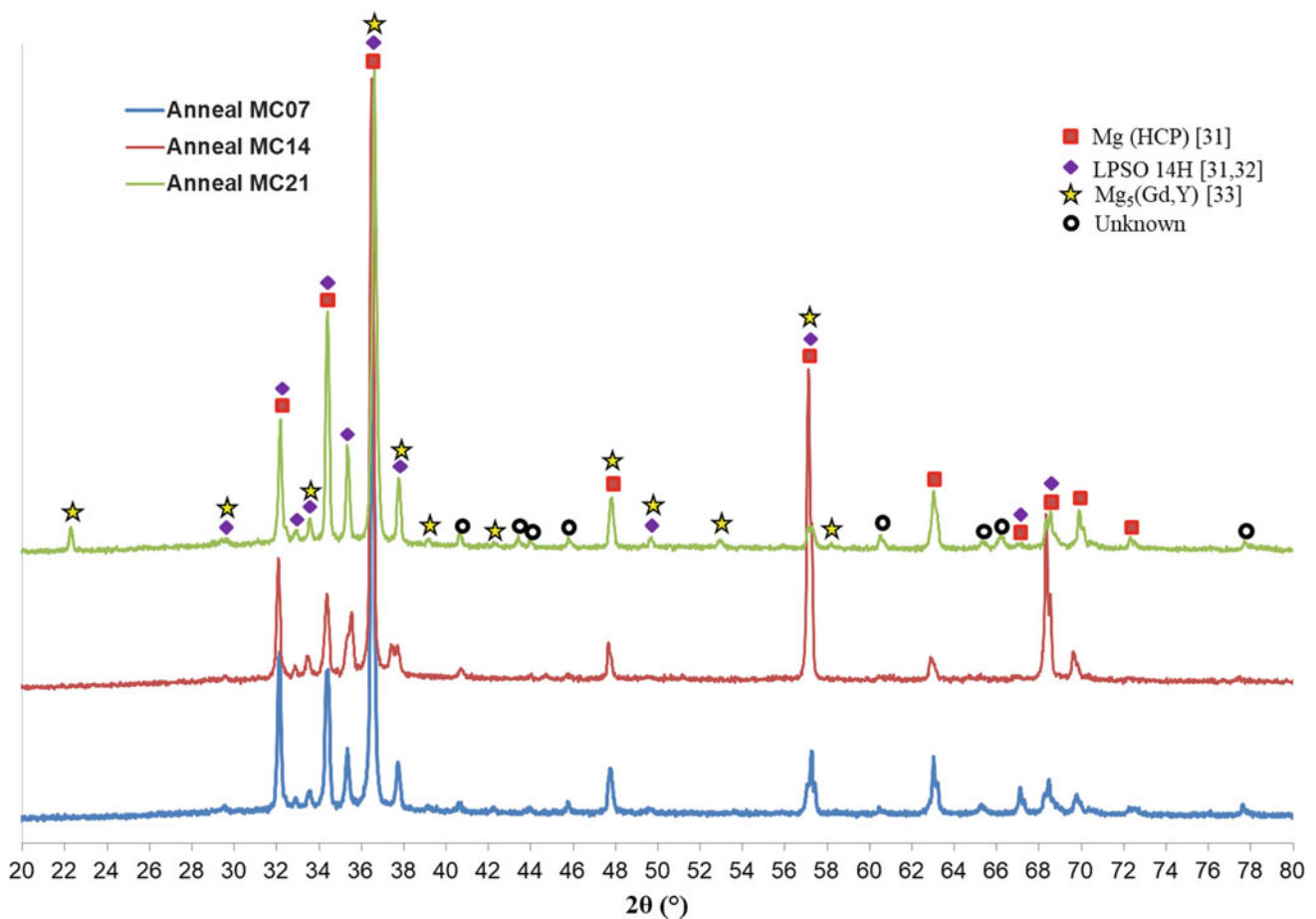


**Fig. 5** XRD analysis of the annealed samples

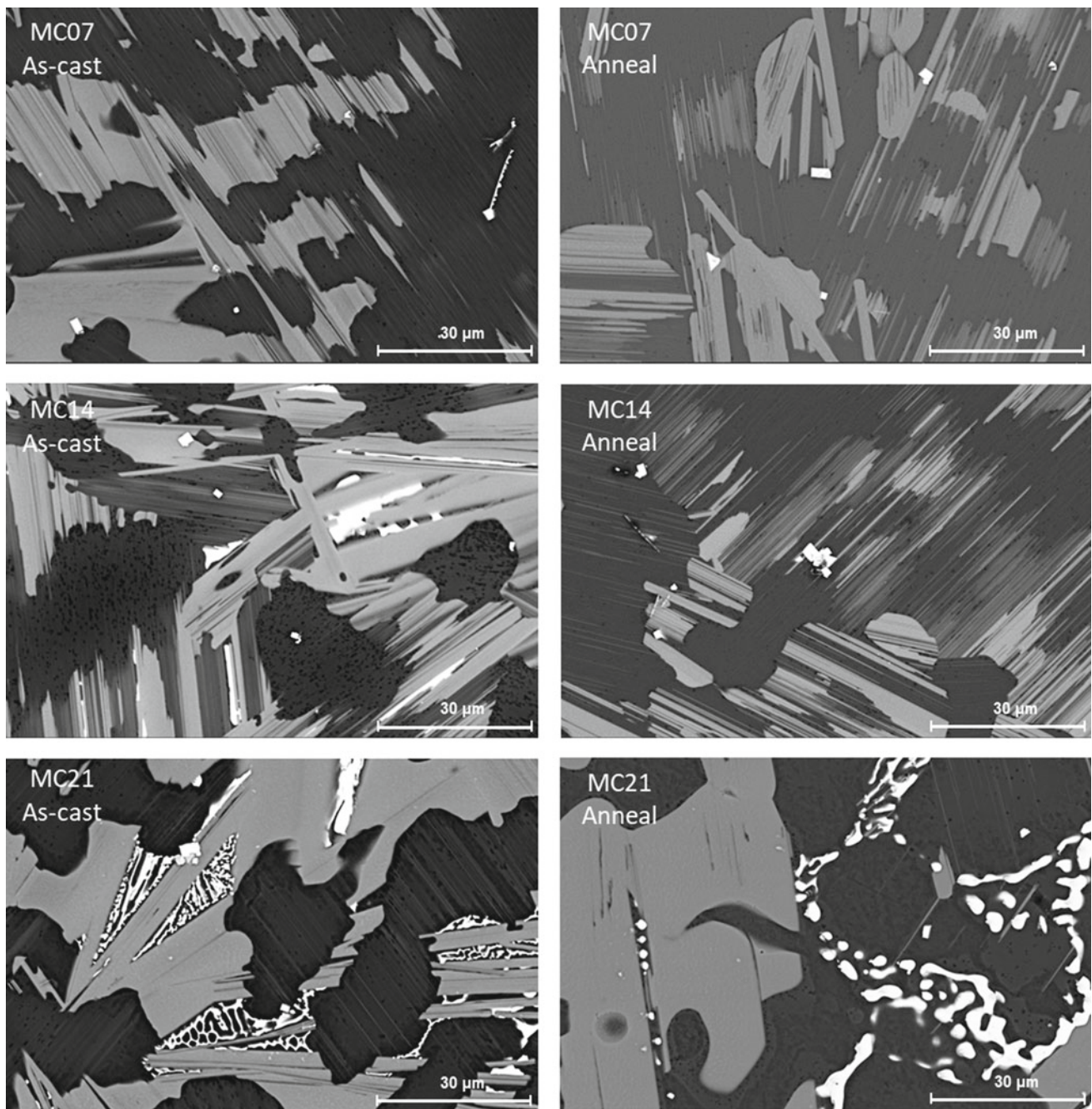


**Fig. 6** SEM images using a T1 (backscatter-like) detector for the as-cast and annealed conditions

$Mg_{24}(Gd,Y)_5$  and  $W-Mg_3Y_2Zn_3$  were either not present in the alloys or not in large enough quantities to be observed. Looking more closely at the CALPHAD predictions, the  $(Mg,Zn)_5(Gd,Y)$  phase has a composition consistent with  $Mg_5Gd$ , so it is unlikely to be the bright phase in the SEM images. At this point, literature has not reported a Zn–Y binary phase, and further analysis is needed for phase identification.

For the LPSO 14H phase, the existing CALPHAD databases evaluated in this study predict a high phase fraction that is reasonable. The predicted increase of the LPSO 14H phase with increased alloying and annealing was consistent with both literature and microstructural analysis. In terms of the other intermetallic phases, the predictive capabilities of the model were less reliable. Part of this is due to the lower predicted phase fraction of the intermetallics and partly due



to the phase definitions in the database. The biggest discrepancy is the prediction of the Mg<sub>5</sub>Gd phase and the presence of a Zn- and Y-rich intermetallic phase in the MC14 and MC21 samples. As a result, it was determined that the existing CALPHAD databases evaluated in this study can represent the LPSO 14H phase, but more evaluation is needed for the other secondary intermetallic phases.

## Conclusions

The existing databases for two CALPHAD programs, PANDAT and Thermo-Calc, were evaluated for their predictive capabilities for LPSO-forming alloys in the Mg–Gd–Y–Zn system. Three compositions were examined in the as-cast and annealed conditions using SEM, EDS, and XRD analysis. It was shown that the CALPHAD programs reasonably predicted the presence of the LPSO 14H phase in these alloys. The other phases predicted by the programs were consistent with phases previously observed in the literature. The phases predicted by both programs were generally consistent with each other, although the mole fractions of these phases were different. Unlike the LPSO 14H phase, the other predicted phases were not observed during SEM analysis. This is possibly due to low phase fractions for these phases. Query ID="Q4" Text="Please check whether the edits made in the sentence ‘...with either the predicted phases or reported phases’ convey the intended meaning.’ In the higher alloy samples, there was a Zn- and Y-rich phase that was not consistent with either the predicted phases or reported phases. Based on these findings, it is concluded that the existing CALPHAD databases are reliable for LPSO 14H prediction for the Mg–Gd–Y–Zn system, but more work is needed to improve the reliability of the other predicted phases.

**Acknowledgements** This work was funded by the Army Research Laboratory (ARL) and Terves LLC. The authors would like to acknowledge Dr. Vincent Hammond with ARL, Dr. William Meier of Oak Ridge National Laboratory, and the Light Metals and Manufacturing Laboratory members at The Ohio State University for their insightful discussions. This material is based upon the work supported by the Army Contracting Command—Adelphi, MD under Contract No W911QX-18-P-0038. Any opinions, findings, and conclusions or recommendations expressed in this material are those of the author(s) and do not necessarily reflect the views of ARL.

## References

1. Abe E, Kawamura Y, Hayashi K, Inoue A (2002) Long-period ordered structure in a high-strength nanocrystalline Mg-1 at% Zn-2 at% Y alloy studied by atomic-resolution Z-contrast STEM. *Acta Mater* 50(15):3845–3857
2. Kawamura Y, Kasahara T, Izumi S, Yamasaki M (2006) Elevated temperature Mg<sub>97</sub>Y<sub>2</sub>Cu<sub>1</sub> alloy with long period ordered structure. *Scripta Mater* 55(5):453–456
3. Du XH, Duan GS, Hong M, Wang DP, Wu BL, Zhang YD, Esling C (2014) Effect of V on the microstructure and mechanical properties of Mg–10Er–2Cu alloy with a long period stacking ordered structure. *Mater Lett* 122:312–314
4. Bi GL, Li YD, Huang XF, Chen TJ, Lian JS, Jiang ZH, Ma Y, Hao Y (2015) Deformation behavior of an extruded Mg–Dy–Zn alloy with long period stacking ordered phase. *Mat Sci Eng A—Struct*, 622:52–60
5. Kawamura Y, Yamasaki M (2007) Formation and Mechanical Properties of Mg<sub>97</sub>Zn<sub>1</sub>RE<sub>2</sub> Alloys with Long-Period Stacking Ordered Structure. *Mater Trans* 48(11): 2986–2992
6. Datta A, Waghmare UV, Ramamurty U (2008) Structure and stacking faults in layered Mg–Zn–Y alloys: A first-principles study. *Acta Mater* 56(11): 2531–2539
7. Suzuki M, Kimura T, Koike J, Maruyama K (2003) Strengthening effect of Zn in heat resistant Mg–Y–Zn solid solution alloys. *Scripta Mater* 48(8):997–1002
8. Lu FM, Ma AB, Jiang JH, Yang DH, Zhou Q (2012) Review on long-period stacking-ordered structures in Mg–Zn–RE alloys. *Rare Metals* 31(3): 303–310
9. Kim JK, Jin L, Sandlöbes S, Raabe Dierk (2017) Diffusional-displacive transformation enables formation of long-period stacking order in magnesium. *Sci Rep-UK* <https://doi.org/10.1038/s41598-017-04343-y>
10. Xu D, Han EH, Xu YB (2016) Effect of long-period stacking ordered phase on microstructure, mechanical property and corrosion resistance of Mg alloys: A review. *Prog Nat Sci Mater* 26(2): 117–128
11. Wang K, Wang JF, Huang S, Gao SQ, Guo SF, Liu SJ, Chen XH, Pan FS (2018) Enhanced mechanical properties of Mg–Gd–Y–Zn–Mn alloy by tailoring the morphology of long period stacking ordered phase. *Mat Sci Eng A Struct* 733: 267–275
12. Zhang S, Yuan GY, Lu C, Ding WJ (2011) The relationship between (Mg,Zn)3RE phase and 14H-LPSO phase in Mg–Gd–Y–Zn–Zr alloys solidified at different cooling rates. *J Alloy Compd* 509(8): 3515–3521
13. Honma T, Ohkubo T, Kamado S, Hono K (2007) Effect of Zn additions on the age-hardening of Mg–2.0Gd–1.2Y–0.2Zr alloys. *Acta Mater* 55(12): 4137–4150
14. Yamada K, Okubo Y, Shiono M, Watanabe H, Kamado S, Kojima Y (2006) Alloy Development of High Toughness Mg–Gd–Y–Zn–Zr Alloys. *Mater Trans* 47(4):1066–1070
15. Shi F, Wang CQ, Guo XF (2015) Microstructures and Properties of As-Cast Mg<sub>92</sub>Zn<sub>4</sub>Y<sub>4</sub> and Mg<sub>92</sub>Zn<sub>4</sub>Y<sub>3</sub>Gd<sub>1</sub> Alloys with LPSO Phase. *Rare Metal Mat Eng* 44(7): 1617–1622
16. Luo L, Liu Y, Duan M (2018) Phase Formation of Mg–Zn–Gd Alloys on the Mg-rich Corner. *Materials* 11(8): <https://doi.org/10.3390/ma11081351>
17. Hu YB, Zhang C, Zheng TX, Pan FS, Tang AT (2018) Strengthening Effects of Zn Addition on an Ultrahigh Ductility Mg–Gd–Zr Magnesium Alloy. *Materials* 11(10): <https://doi.org/10.3390/ma11101942>
18. Wen K, Liu K, Wang ZH, Li SB, Du WB (2016) Effect of pre-solution treatment on mechanical properties of as-extruded Mg<sub>96.9</sub>Zn<sub>0.43</sub>Gd<sub>2.48</sub>Zr<sub>0.15</sub> alloy. *Mat Sci Eng A Struct* 674: 33–39
19. Matsuda M, Ando A, Nishida M (2005) Dislocation Structure in Rapidly Solidified Mg<sub>97</sub>Zn<sub>1</sub>Y<sub>2</sub> Alloy with Long Period Stacking Order Phase. *Mater Trans* 46(2): 361–364
20. Luo AA (2015), Material Design and Development: from Classical Thermodynamics to CALPHAD and ICME Approaches. *CALPHAD*, 50: 6–22

21. Li YX, Yang CL, Zeng XQ, Jin PP, Qiu D, Ding WJ (2018) Microstructure evolution and mechanical properties of magnesium alloys containing long period stacking ordered phase. *Mater Charact* 141: 286–295
22. Itoi T, Seimiya T, Kawamura Y, Hirohashi M (2004) Long period stacking structures observed in Mg<sub>97</sub>Zn<sub>1</sub>Y<sub>2</sub> alloy. *Scripta Mater* 51 (2): 107–111
23. Zhu YM, Morton A, Nie JF (2012) Growth and transformation mechanisms of 18R and 14H in Mg–Y–Zn alloys. *Acta Mater* 60 (19): 6562–6572
24. Yamasaki M, Sasaki M, Nishijima M, Hiraga K, Kawamura Y (2007) Formation of 14H long period stacking ordered structure and profuse stacking faults in Mg–Zn–Gd alloys during isothermal aging at high temperature. *Acta Mater* 55(20): 6798–6805
25. Li B, Teng BG, Luo DG (2018) Effects of Passes on Microstructure Evolution and Mechanical Properties of Mg–Gd–Y–Zn–Zr Alloy During Multidirectional Forging. *Acta Metall Sin-Engl* 31 (10): 1009–1018
26. Yamasaki M, Anan T, Yoshimoto S, Kawamura Y (2005) Mechanical properties of warm-extruded Mg–Zn–Gd alloy with coherent 14H long periodic stacking ordered structure precipitate. *Scripta Mater* 53(7): 799–803
27. Wu J, Chiu YL, Jones IP (2014) Microstructure of as-cast Mg–4.2Zn–0.8Y (at.%) alloys containing Gd. *J Phys Conf Ser* 522: 8–12
28. Kishida K, Nagai K, Matsumoto A, Yasuhara A, Inui H (2015) Crystal structures of highly-ordered long-period stacking-ordered phases with 18R, 14H and 10H-type stacking sequences in the Mg–Zn–Y system. *Acta Mater* 99: 228–239
29. Garces G, Pérez P, Barea R, Medina J, Stark A, Schell N, Adeva P (2019) Increase in the Mechanical Strength of Mg–8Gd–3Y–1Zn Alloy Containing Long-Period Stacking Ordered Phases Using Equal Channel Angular Pressing Processing. *Metals* 9(2): <https://doi.org/10.3390/met9020221>
30. Zhang JY, Xu M, Teng XY, Zuo M (2016) Effect of Gd addition on microstructure and corrosion behaviors of Mg–Zn–Y alloy. *J Magnesium and Alloys* 4: 319–325
31. Wang K, W JF, Huang S, Gao SQ, Guo SF, Liu SJ, Chen XH, Pan FS (2018) Enhanced mechanical properties of Mg–Gd–Y–Zn–Mn alloy by tailoring the morphology of long period stacking ordered phase. *Mat Sci Eng A Struct* 33: 267–275

# Intermetallic Phase Formation in Mg–Ag–Nd (QE) and Mg–Ag–Nd–Zn (QEZ) Alloys

Rainer Schmid-Fetzer, Jian-Feng Nie, Xiaojun Zhao, and Houwen Chen

## Abstract

The intermetallic phase (designated  $\delta$  phase) in the solution-treated microstructure of commercial magnesium alloy QE22 (Mg–2.5Ag–2.0Nd–0.7Zr, wt%) has been investigated using scanning electron microscopy, electron diffraction, atomic-resolution scanning transmission electron microscopy (STEM), and thermodynamic modeling. In contrast to the previous reports, an orthorhombic structure (space group Cmc<sub>m</sub>) and a composition of NdAgMg<sub>11</sub> are determined. The present experimental data are used to construct a thermodynamic description of the Mg–Ag–Nd system which is embedded in a multicomponent Mg alloy database. Implications on the formation of temperature range and thermal stability of this phase and alloy solidification are discussed based on the calculated Mg–Nd–Ag phase diagram and Scheil solidification paths of alloys. The impact of Ag-replacement in such QE alloys by Zn-addition in the Mg–Ag–Nd–Zn (QEZ) alloy system is elaborated using appropriate thermodynamic

simulations to reveal the competition with other intermetallics. These data are suggested to contribute to ICME of magnesium alloys.

## Keywords

Crystal structure • Thermodynamics • ICME • Secondary phases

## Introduction

Addition of Ag in many rare-earth (RE) containing Mg alloys can remarkably improve the age hardening response of these alloys such as Mg–Nd, Mg–Gd, Mg–Gd–Zn, and Mg–Y–Zn alloys [1–3]. This phenomenon was originally observed by Payne and Bailey in Mg–Nd alloys early in 1960s [1], which led to the development of a commercial Mg alloy QE22 (Mg–2.5Ag–2Nd–0.7Zr, wt%). However, the phase transformation of QE22 alloy has not been unambiguously established. One important reason is the lack of Mg–Nd–Ag ternary phase diagram. For the equilibrium of intermetallic phase in QE22 alloy, there have been controversial views on whether it is Mg<sub>12</sub>Nd<sub>2</sub>Ag with a complex hexagonal structure [4] or (Mg, Ag)<sub>12</sub>Nd with a tetragonal structure (I4/m<sub>m</sub>,  $a = 1.031$  nm;  $c = 0.593$  nm) [5]. Both structures are not supported by convincing experimental evidence. Thus, it is necessary to use modern techniques such as atomic-resolution high-angle annular dark-field scanning transmission electron microscopy (HAADF-STEM) and atomic-scale energy-dispersive X-ray spectroscopy (EDS-STEM) and to conduct thermodynamic assessments of the Mg–Ag–Nd alloy system. Together with Ag, Zn is another effective alloying addition in Mg–Gd–Ag–Zn and Mg–Y–Ag–Zn alloys [2, 3]. It is for this reason that the intermetallic phase formation in the Mg–Ag–Nd–Zn alloy system is also elaborated using appropriate thermodynamic simulations to reveal the competition within the related intermetallic phases.

R. Schmid-Fetzer (✉)  
Institute of Metallurgy, Clausthal University of Technology,  
Robert-Koch-Str. 42, 38678 Clausthal-Zellerfeld, Germany  
e-mail: [schmid-fetzer@tu-clausthal.de](mailto:schmid-fetzer@tu-clausthal.de)

J.-F. Nie  
Department of Materials Science and Engineering,  
Monash University, Victoria, 3800, Australia  
e-mail: [jianfeng.nie@monash.edu](mailto:jianfeng.nie@monash.edu)

X. Zhao · H. Chen  
International Joint Laboratory for Light Alloys (Ministry  
of Education), College of Materials Science and Engineering,  
Chongqing University, 400044 Chongqing,  
People's Republic of China  
e-mail: [xiaojunzhao@cqu.edu.cn](mailto:xiaojunzhao@cqu.edu.cn)

H. Chen  
e-mail: [hwchen@cqu.edu.cn](mailto:hwchen@cqu.edu.cn)



## Experimental Procedures and Results

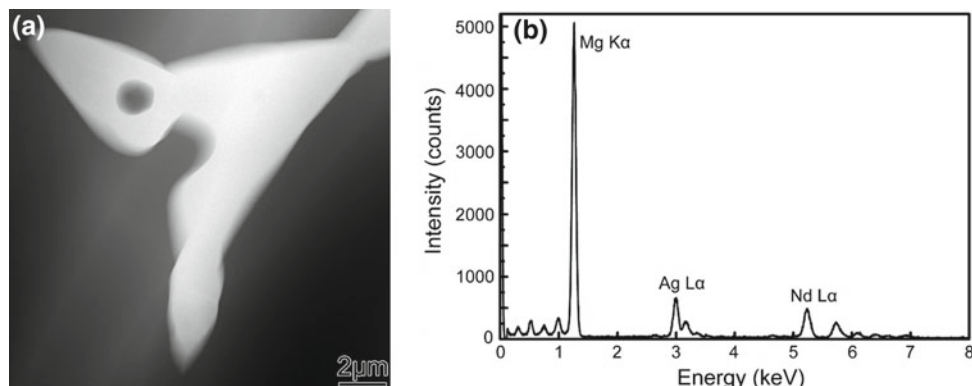
### Experimental Procedures

Samples used in the present investigation were cut from a cast bar of commercial alloy QE22 (Mg–2.5Ag–2.0Nd–0.7Zr, wt%). The actual alloy composition was measured by inductively coupled plasma atomic emission spectroscopy to be Mg–3.01Ag–2.10Nd–0.34Zr (wt%). Bulk samples were solution-treated at 520 °C for 6 h and then water-quenched. Samples for transmission electron microscopy (TEM) were cut into 500- $\mu\text{m}$ -thick slices, grounded to 50–70  $\mu\text{m}$  thickness, punched to discs of 3 mm in diameter, and then ion-milled using Gatan PIPS 695. HAADF-STEM images and atomic-scale EDS-STEM maps were acquired from a FEI Titan G<sup>2</sup> 60–300 ChemiSTEM operating at 300 kV and equipped with a Cs probe corrector and a Super-X EDS with four windowless silicon drift detectors. A convergence semi-angle of 15 mrad and collection semi-angle of 45–262 mrad were used. To test the validity of the assessments, an additional alloy with a measured composition of Mg–1.63Ag–1.85Nd (wt%) was made. The as-cast microstructure of this alloy was characterized using SEM, TEM, and STEM. Some samples of QE22 alloy, solution-treated at 520 °C for 6 h and water-quenched, were also aged at 300 °C for 4 h.

### Results

The retained  $\delta$  intermetallic phase in solution-treated QE22 alloy appeared in grain boundaries with coarse irregular shape, Fig. 1a. A representative EDS spectrum obtained from such  $\delta$  particles is shown in Fig. 1b. The presence of characteristic peaks of Mg, Ag, and Nd indicated that  $\delta$  is a Mg–Ag–Nd ternary phase. An average composition of Mg–7.7  $\pm$  1.0 Nd–8.6  $\pm$  1.0 Ag (at.%) was obtained for  $\delta$  phase by the standardless semi-quantitative analysis of ten particles.

**Fig. 1** **a** Low-magnification HAADF-STEM image showing morphology of  $\delta$  intermetallic phase in a solution-treated sample. **b** EDS spectrum recorded from a  $\delta$  particle



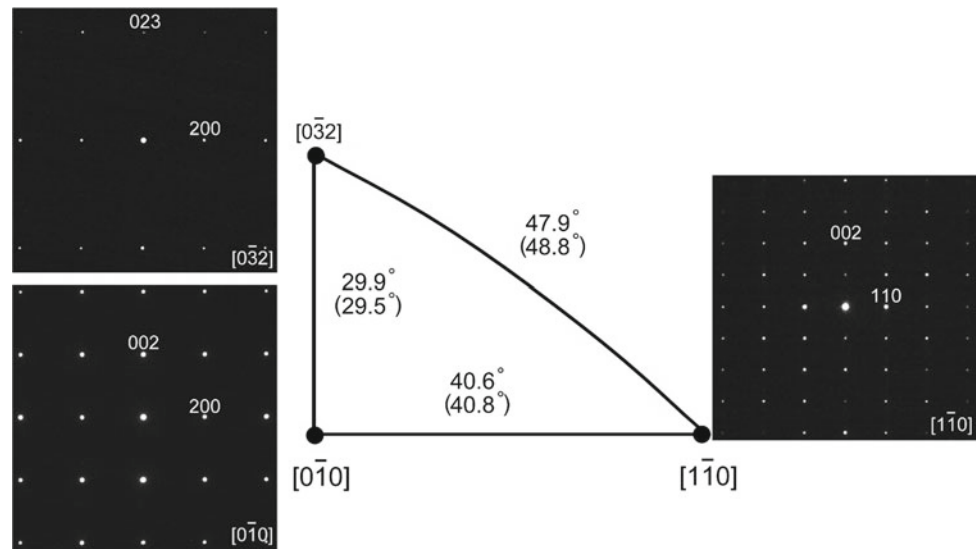
A set of selected area electron diffraction (SAED) patterns, which were acquired by large-angle tilting of a single  $\delta$  particle, is shown in Fig. 2. These SAED patterns could be indexed consistently based on an orthorhombic structure with lattice parameters of  $a = 1.02$  nm,  $b = 1.18$  nm, and  $c = 1.00$  nm ( $\pm 0.01$  nm), which was entirely different from the previous hexagonal or tetragonal structure for the equilibrium intermetallic phase in QE22 alloy [4, 5]. A schematic diagram showing the measured and calculated (with brackets) tilting angles between any two of the three axes is provided in Fig. 2. The good agreement of the measured and calculated tilting angles indicated the validity of the proposed orthorhombic structure. Based on atomic-resolution HAADF-STEM images and EDS maps obtained, the structure of  $\delta$  was determined to have Cmc<sub>2</sub>m space group and composition of NdAgMg<sub>11</sub>.

## Thermodynamic Modeling and Calculations

### Thermodynamic Modeling

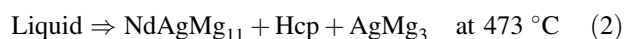
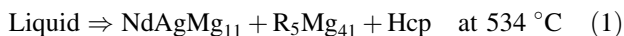
No published thermodynamic assessment of the ternary Mg–Ag–Nd phase diagram is available. The phase equilibria in the Mg-rich region were elaborated, and the existence of the ternary compound NdAgMg<sub>11</sub> in equilibrium with the (Mg) matrix phase, Hcp, was unambiguously determined in the alloy QE22. The present thermodynamic assessment was started by combination of the three binary edge systems, and the Mg–Zr system is taken from the thermodynamic database PanMg [6]. All calculations were performed with the Pandat software [7]. These initial calculations, without considering any ternary intermetallic phase, predict that the QE22 alloy composition (measured at Mg–2.1Nd–3.01Ag–0.34Zr wt%) should be located in the single-phase region of Hcp (Mg) at 520 °C, opposing the experimental observation. It was also found in the calculations that all zirconium is dissolved in the liquid and (Mg) Hcp phases, and no Zr-rich phase appears. That also agrees with the experimental

**Fig. 2** A set of SAED patterns recorded by tilting a single  $\delta$  particle and schematic solutions to the diffraction patterns. Angles with and without brackets represent those of calculated and measured values, respectively



observation and enabled the thermodynamic assessment of the newly detected stoichiometric compound  $\text{NdAgMg}_{11}$  as ternary phase. This is demonstrated in Fig. 3a, showing the calculated Mg-rich part of the isothermal Mg–Ag–Nd phase diagram section at 520 °C without consideration of any ternary intermetallic phase, i.e. a simple extrapolation from the binary edge systems. It is evident that both the alloy and matrix composition (measured at Mg–1.2Nd–2.9Ag–0.4Zr) are located in the single-phase (Mg) Hcp region. The correct phase diagram including the assessed compound  $\text{NdAgMg}_{11}$  is shown in Fig. 3b, where the alloy composition is in the two-phase Hcp +  $\text{NdAgMg}_{11}$  region and the Hcp matrix composition perfectly matches the calculated solubility limit.

Evaluation of the present experimental findings at other temperatures also enabled a realistic assessment of the entropy of formation of  $\text{NdAgMg}_{11}$  and calculations at varying temperature. As a result, a similar comparison as given in Fig. 3 is also made for the calculated liquidus projection to emphasize the impact of proper consideration of the intermetallic phase  $\text{NdAgMg}_{11}$ . Figure 4a shows the calculated Mg-rich part of the Mg–Ag–Nd liquidus without consideration of any ternary intermetallic phase, again a simple extrapolation from the binary edge systems. It displays only one eutectic with (Mg) Hcp at 11 wt% Nd, 33 wt% Ag and 462 °C. By contrast, the correct liquidus in Fig. 4b includes the  $\text{NdAgMg}_{11}$  phase and two eutectic reactions involving (Mg)-Hcp:



The thermodynamic simulations of solidification and phase diagram in the Mg–Ag–Nd system of this completed

database agree with all of the experimental findings. More details can be found in a recently submitted work [8].

### Thermodynamic Simulation of QEZ Alloys in the Mg–Ag–Nd–Zn System

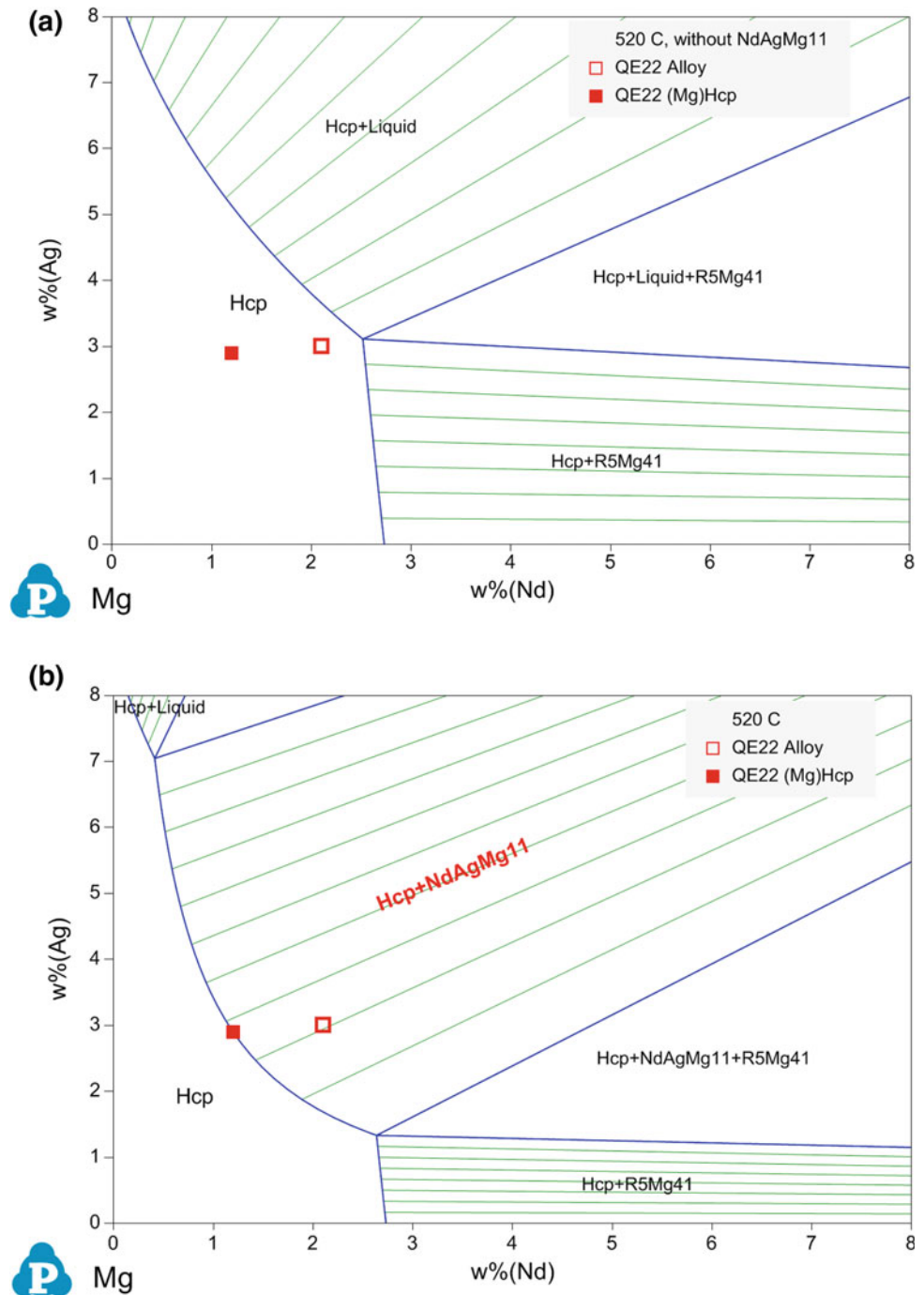
The present thermodynamic assessment is also merged with the complete PanMg database [6], allowing extended calculations of multicomponent Mg alloys based on the QE Mg–Ag–Nd system with additions of other components, such as Zn, Zr, and so on. Zinc is a useful alloying element in Mg alloys for many reasons. Mg–Zn alloys combined with rare earths (RE) in ternary Mg–RE–Zn systems typically show complex intermetallic phase formation offering a wide range of alloy design. The Mg–Nd–Zn system studied by Zhang et al. [9] and Wilson et al. [10] is a good example. Since this ternary is also fully modelled in PanMg, the simulations in the quaternary Mg–Ag–Nd–Zn system, QEZ, are considered to be reliable.

### Equilibrium Phase Formation in Heat Treatment Simulation

The most attractive question would be what happens if Ag is substituted by Zn in a QE22 alloy. Specifically, we will start with QE22 of nominal composition of Mg–2.5Ag–2.5Nd and replace up to 1 wt% of Ag by up to 1 wt% Zn, ending at EQZ211 alloy of Mg–2.5Nd–1.5Ag–1Zn. As an overview, the corresponding phase diagram section is shown in Fig. 5.

Figure 5 demonstrates that the primary solidification of Hcp persists for all alloys. The equilibrium freezing range is almost unchanged by the Ag/Zn substitution, and the solidus is around 537–515 °C.

**Fig. 3** Calculated Mg-rich part of the Mg–Ag–Nd phase diagram at 520 °C: **a** without consideration of any ternary intermetallic phase, **b** including the assessed compound  $\text{NdAgMg}_{11}$  which is the correct phase diagram



On the Zn-poor side, the secondary phase is  $\text{NdAgMg}_{11}$  and above 0.47 wt% Zn it is  $\text{RMg}_3$ . Here, the phase name  $\text{RMg}_3$  stands for  $\text{Nd}(\text{Mg},\text{Zn})_3$  which is stable as binary  $\text{NdMg}_3$  (and other  $\text{RMg}_3$  binary phases) but also dissolves Zn by substitution of Mg. Typical constitution of  $\text{RMg}_3$  in Fig. 5 is  $\text{Nd}(\text{Mg}_{0.8}\text{Zn}_{0.2})_3$ . All other intermetallics are formed in solid-state reaction below about 355 °C. The first appearance of intermetallic phase  $\text{Nd}_8\text{Mg}_{50}\text{Zn}_{42}$ , highlighted by red font in Fig. 5, is above 0.35 wt% Zn at 338 °C.  $\text{Nd}_8\text{Mg}_{50}\text{Zn}_{42}$  is

again a complex phase with limited solubility range in the ternary Mg–Nd–Zn system. It is also noted that  $\text{NdAgMg}_{11}$  is predicted to be not stable below 172 °C, transforming to  $\text{R}_5\text{Mg}_{41}$  in the invariant reaction

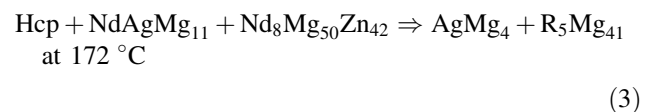
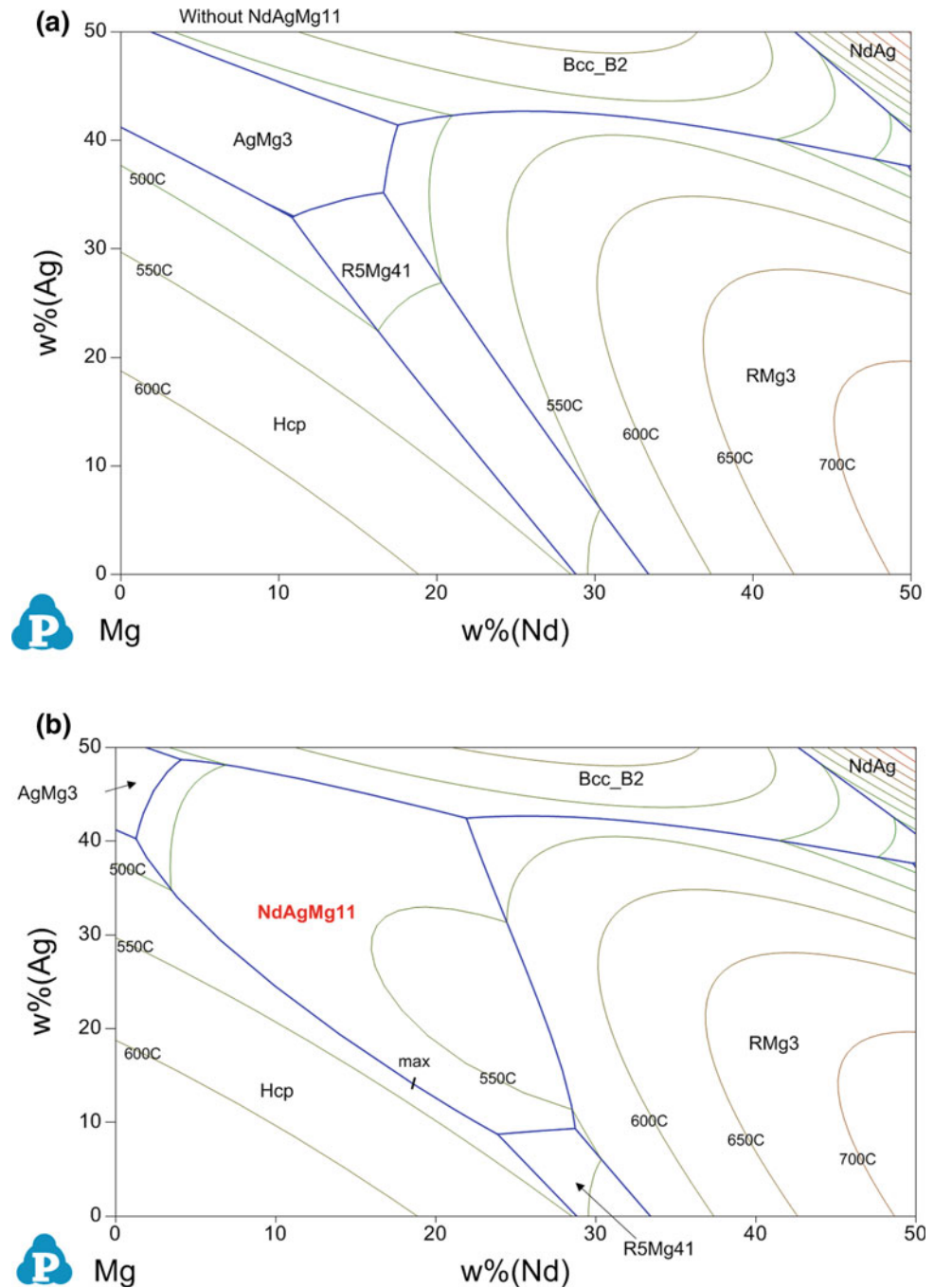


**Fig. 4** Calculated Mg-rich part of the Mg–Ag–Nd liquidus projection: **a** without consideration of any ternary intermetallic phase, **b** including the assessed compound  $\text{NdAgMg}_{11}$  which is the correct phase diagram



The phase amounts cannot be read from the section of Fig. 5. For a better understanding of achievable fractions of intermetallic phases by isothermal heat treatment in a temperature range of 360–270 °C, these calculated equilibrium fractions at four selected temperatures (360, 330, 300, and 270 °C) along the section of Fig. 5 are shown in Fig. 6a–d.

The key messages of these secondary phase heat treatment simulations may be summarized as follows:

- $\text{NdAgMg}_{11}$  is major secondary phase in entire range of 360–270 °C and 0–1 wt% Zn.
- $\text{RMg}_3$  comes next in phase fraction at 360 °C, with shrinking fraction to lower  $T$ .
- $\text{RMg}_3$  is essentially replaced by  $\text{Nd}_8\text{Mg}_{50}\text{Zn}_{42}$  at lower  $T$ .
- $\text{AgMg}_4$  occurs only at low wt%Zn and low  $T \approx 300$ –270 °C.

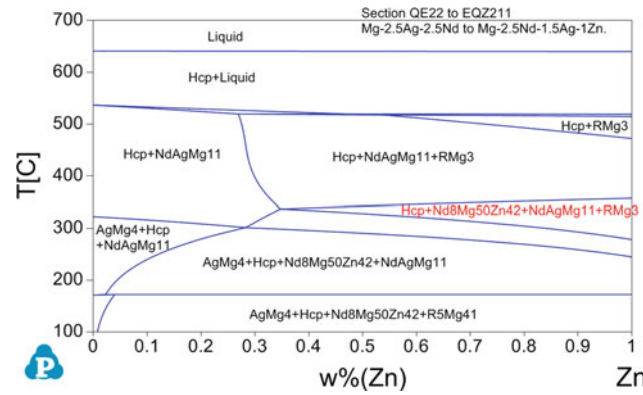


**Fig. 5** Calculated phase diagram section of QE22 to EQZ211 in the Mg–Ag–Nd–Zn system, (Mg–2.5Ag–2.5Nd) to (Mg–2.5Nd–1.5Ag–1Zn), wt%

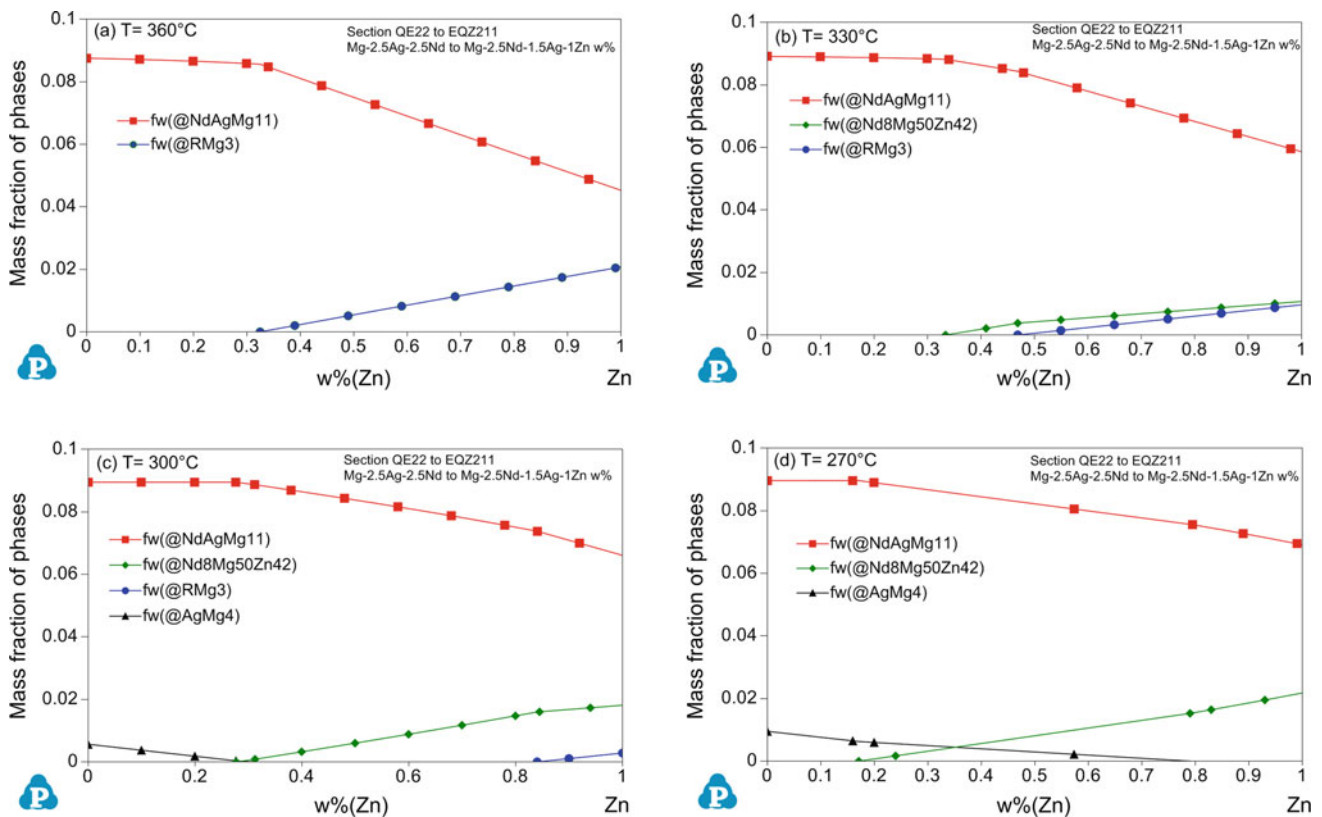


**Fig. 6** Calculated mass fraction of intermetallic phases (balance to 1 is (Mg)-Hcp phase) along the section QE22 to EQZ211 of Fig. 5 at fixed temperatures: **a** 360 °C, **b** 330 °C, **c** 300 °C, and **d** 270 °C

### Scheil Solidification Simulation of As-Cast State

For the two limiting alloys of the Ag/Zn substitution discussed in Fig. 5, QE22 and EQZ211, the phase formation during casting is simulated under Scheil conditions, i.e. no diffusion in the solid state, complete mixing in the liquid, and local equilibrium at the liquid/solid interface. The results are shown in Fig. 7.

For the Zn-free alloy QE22 in Fig. 7a, secondary NdAgMg<sub>11</sub> precipitates from 537 to 473 °C where solidification terminates in the eutectic of Eq. (2) with a small fraction (0.002) of additional AgMg<sub>3</sub> phase. That may be compared to solidification under equilibrium conditions terminating with the reaction Liquid  $\Rightarrow$  NdAgMg<sub>11</sub> + Hcp at almost constant 537 °C as seen at the left edge of Fig. 5.



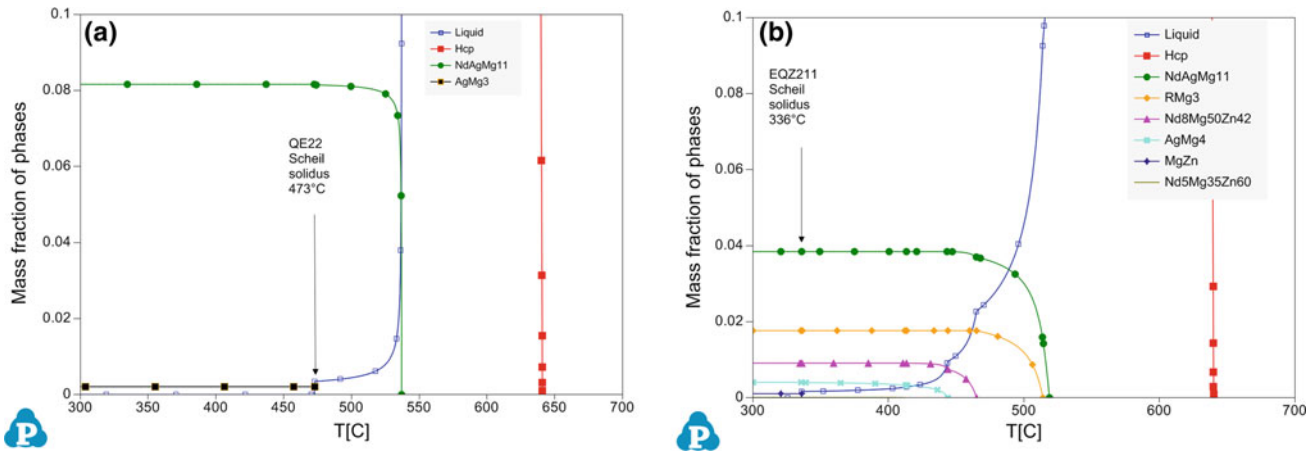
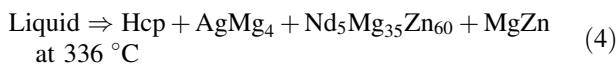


**Fig. 7** Scheil solidification simulation of alloys: **a** QE22 (Mg–2.5Ag–2.5Nd–0Zn) and **b** EQZ211 (Mg–2.5Nd–1.5Ag–1Zn)

The Ag/Nd ratio of the ternary QE alloy decides on the path of the residual liquid and determines which one of the two ternary eutectics, Eqs. (1) or (2), will be approached for termination of Scheil solidification. Coincidentally, 537 °C is also the maximum temperature in the monovariant eutectic line Liquid  $\Rightarrow$  Hcp + NdAgMg<sub>11</sub> with liquid composition of Mg–18.6Nd–14.1Ag marked in Fig. 4. While the eutectic (2) with AgMg<sub>3</sub> is approached for Ag/Nd = 1.0 in QE22, a shift to Ag/Nd = 0.85 in alloy Mg–2.3Ag–2.7Nd results in termination at eutectic (1) with R5Mg<sub>41</sub> at 534 °C. The critical limit is Ag/Nd = 0.92 in alloy Mg–2.4Ag–2.6Nd, and this alloy solidifies isothermally at 537 °C, the invariant maximum reaction Liquid  $\Rightarrow$  Hcp + NdAgMg<sub>11</sub>, even under Scheil conditions.

Figure 7b shows that for alloy EQZ211 with 1 wt% Ag substituted by 1 wt% Zn six different secondary phases precipitate from 519 to 336 °C. Secondary NdAgMg<sub>11</sub> starts at 519 °C, followed sequentially by RMg<sub>3</sub>, Nd<sub>8</sub>Mg<sub>50</sub>Zn<sub>42</sub>, AgMg<sub>4</sub>, and traces of Nd<sub>5</sub>Mg<sub>35</sub>Zn<sub>60</sub>. Finally, a small fraction (0.001) of MgZn precipitates in the quaternary eutectic



This is marked by the Scheil solidus in Fig. 7b.

## Conclusion

- The ternary intermetallic phase occurring in Mg-rich Mg–Ag–Nd alloys is determined as ternary compound of NdAgMg<sub>11</sub> and the orthorhombic structure (space group Cmcm,  $a = 1.02$  nm,  $b = 1.18$  nm, and  $c = 1.00$  nm).

- A thermodynamic description of the Mg–Ag–Nd system is developed based on these experimental data. Phase diagram calculations of this ternary system are presented revealing the dominating impact of NdAgMg<sub>11</sub> on such Mg alloys.
- The thermodynamic description is embedded in a multicomponent Mg alloy database, and the quaternary Mg–Ag–Nd–Zn (QEZ) alloy system is studied as an example. Thermodynamic simulations reveal the competition of NdAgMg<sub>11</sub> with other intermetallics when Ag is substituted by Zn in these alloys.
- Equilibrium phase formation in heat treatment is simulated, revealing that NdAgMg<sub>11</sub> is major secondary phase in alloys ranging from QE22 to EQZ211; the content of NdAgMg<sub>11</sub> and other secondary phases such as RMg<sub>3</sub>, Nd<sub>8</sub>Mg<sub>50</sub>Zn<sub>42</sub>, and AgMg<sub>4</sub> can be controlled by selecting the appropriate heat treatment and alloy content.
- Scheil solidification simulation of as-cast state demonstrates that QE22 is predicted with only two secondary phases, NdAgMg<sub>11</sub> and AgMg<sub>3</sub>. By contrast, the EQZ211 alloy comprises six different secondary phases: NdAgMg<sub>11</sub>, RMg<sub>3</sub>, Nd<sub>8</sub>Mg<sub>50</sub>Zn<sub>42</sub>, AgMg<sub>4</sub>, Nd<sub>5</sub>Mg<sub>35</sub>Zn<sub>60</sub>, and MgZn in the as-cast state.
- This knowledge is suggested to be helpful in the tailoring of secondary phase constitution in as-cast and heat-treated Mg–Ag–Nd–Zn (QEZ) alloys.

**Acknowledgements** This study is supported by the Australian Research Council and National Natural Science Foundation of China (51771036, 51131009, and 51421001), National Key Research and Development Program of China (2016YFB0700402), Fundamental Research Funds for the Central Universities (2018CDJDCL0019), and Graduate Student Research Innovation Project of Chongqing University.



## References

1. Payne RJM, Bailey N (1960) Improvement of the age-hardening properties of magnesium-rare-earth alloys by addition of silver. *J. Inst. Met.* 88: 417–427.
2. Gao X, Nie JF (2008) Enhanced precipitation-hardening in Mg–Gd alloys containing Ag and Zn. *Scr. Mater.* 58: 619–622.
3. Zhu YM, Morton AJ, Nie JF (2008) Improvement in the age-hardening response of Mg–Y–Zn alloys by Ag additions. *Scr. Mater.* 58: 525–528.
4. Gradwell KJ (1972) Ph.D. thesis, University of Manchester.
5. Barucca G, Ferragut R, Lussana D, Mengucci P, Moia F, Riontino G (2009) Phase transformations in QE22 Mg alloy. *Acta Mater.* 57: 4416–4425.
6. Schmid-Fetzer R, Zhang F (2018) The light alloy Calphad databases PanAl and PanMg. *Calphad.* 61:246–63.
7. Cao W, Chen SL, Zhang F, Wu K, Yang Y, Chang YA, et al (2009) PANDAT software with PanEngine, PanOptimizer and PanPrecipitation for multi-component phase diagram calculation and materials property simulation. *Calphad.* 33(2):328–42.
8. Zhao Xiaojun, Li Zhiqiao, Chen Houwen, Schmid-Fetzer Rainer, Nie Jian-Feng (2019) On the equilibrium intermetallic phase in Mg–Nd–Ag alloys. *Metall. Mater. Trans. A.* in press.
9. Zhang C, Luo AA, Peng L, Stone DS, Chang YA (2011) Thermodynamic modeling and experimental investigation of the magnesium–neodymium–zinc alloys. *Intermetallics.* 19(11): 1720–6.
10. Wilson R, Bettles CJ, Muddle BC, Nie JF (2003) Precipitation and hardening in Mg–3 wt%Nd(–Zn) casting alloys. *Mater. Sci. Forum,* 419–422:267–72.

# Investigation on the Microstructure and Mechanical Properties of Mg–Gd–Nd Ternary Alloys

Yuling Xu, Lixiang Yang, Weili Liu, Jingli Sun, Lu Xiao, Xianquan Jiang, and Norbert Hort

## Abstract

The present work deals with microstructure and mechanical properties of Mg– $x$ Gd– $y$ Nd ( $x = 10, 15$ ;  $y = 2, 5$ ) ternary alloys. Hardness, tensile, and compressive properties are measured on the as-cast alloys and the alloys after solid solution treatment (T4 state). The hardness, tensile yield stress (TYS), and ultimate tensile stress (UTS) are increased with increasing amount of alloying elements for both as-cast and T4 state. The elongation (EI) of alloys is lower with higher Nd content. The compressive properties of all studied alloys are increased by T4 treatment. With increasing of alloy concentration, both compressive yield stress (CYS) and ultimate compressive stress (UCS) of alloys are enhanced, but the compressibility is decreased. Intermetallic compounds which appear along the grain boundary are reduced after T4 treatment for alloys with 2% Nd. However, large amount of intermetallic compounds with high Nd concentrations remains on the grain boundary of Mg– $x$ Gd–5Nd alloys.

## Keywords

Mg–RE alloy • Mechanical properties • Microstructure

Y. Xu (✉) · X. Jiang  
Chongqing Academy of Science & Technology,  
401123 Chongqing, China  
e-mail: [sharlin\\_xu@hotmail.com](mailto:sharlin_xu@hotmail.com)

L. Yang · W. Liu · J. Sun · L. Xiao  
Shanghai Spaceflight Precision Machinery Institute,  
201600 Shanghai, China

Y. Xu · N. Hort (✉)  
MagIC-Magnesium Innovation Center, Helmholtz-Zentrum  
Geesthacht, 21502 Geesthacht, Germany  
e-mail: [norbert.hort@hzg.de](mailto:norbert.hort@hzg.de)

## Introduction

Magnesium and its alloys as one of lightest weight structure materials have good casting and recycling properties with low cost [1–3]. On the other hand, the applications of Mg and its alloys still limited, due to their defects or performance deficiency [4]. The improvement of mechanical properties of Mg alloys is becoming of key importance and challenge.

The mechanical properties of Mg alloys can be greatly improved by adding rare earth elements (RE) [5, 6], such as Gd and Nd, which meet the higher demands for certain applications. Gd and Nd have different solid solubility in Mg alloy, which are 4.41 and 0.63 at.% at eutectic temperature, respectively [7, 8]. Wang et al. reported that the addition of Gd to Mg–5Y–3Nd–Zr– $x$ Gd alloys caused a great improvement in mechanical properties at both room and elevated temperature. The UTS of alloy with 4 wt% Gd reached 200 MPa at 225 °C [9]. The research on the extruded Mg–6Gd–2.5Y– $x$ Nd–0.6Zr alloys by Guan et al. has shown that Nd enhanced the mechanical properties of Mg alloys, and the UTS of Mg–6Gd–2.5Y–1Nd–0.6Zr alloy after ageing improved 70–350 MPa [10].

The influence of alloy element content of Mg–Gd and Mg–Nd binary alloys on mechanical properties has been systematically reported in the previous studies [11, 12]. The present work deals with mechanical behaviors of Mg–Gd–Nd ternary alloys. Mg– $x$ Gd– $y$ Nd ( $x = 10, 15$ ;  $y = 2, 5$ ) ternary alloys were prepared by permanent mould direct chill casting method. The microstructure and the mechanical properties of those alloys at room temperature were analysed in as-cast and after solution treatment (T4).

## Experimental Procedures

### Materials

Mg– $x$ Gd– $y$ Nd ( $x = 10, 15$ ;  $y = 2, 5$ ) ternary alloys were investigated in this study. The cast processing was reported

in the previous publication [11]. The chemical compositions of all alloys were analyzed by A PerkinElmer, 7300 DV inductively coupled plasma atomic emission spectrometer (Table 1). All alloys were heat-treated at 530 °C for 8 h (T4 state). The billets were quenched in water (18 °C) immediately after the heat treatment.

## Experimental Techniques

The metallographic specimens for microstructural observations were etched in a solution of 8 g picric acid, 5 mL acetic acid, 10 mL distilled water, and 100 mL ethanol after mechanical polishing. A FEI Quanta 450 (FEI Company, Hillsboro, USA) scanning electron microscope (SEM) equipped with energy-dispersive X-ray (EDS) analyzer was further used to observe the microstructure at an accelerative voltage of 20 kV. EDS was used to analyze the compositions of different phases with a minimum live time of 50 s. The X-ray diffraction (XRD) measurements were performed using a 18-kW D/max-2550 diffractometer (40 kV, 450 mA) with Cu K $\alpha$ 1 radiation ( $\lambda = 0.15406$  nm), at a step size of 0.02° and a step time of 0.2 s, the Pearsons crystal database was used for XRD results analyzing.

Vickers hardness, tension and compression tests were measured on the as-cast and T4 state alloys. The specimens for hardness tests were prepared by grinding with silicon carbide emery paper up to 2500 grid. The hardness measurement was carried out using a Vickers hardness testing machine (Karl Frank GmbH) with a load of 5 kg and a dwell time of 10 s [13]. An average of ten measurements was made for each specimen to ensure the reproducibility of results. Tension and compression tests were performed at room temperature using a Zwick 050 testing machine (Zwick GmbH & Co., KG, Ulm, Germany) according to DIN EN ISO 6892-1 [14] and DIN 50106 [15], respectively. Tensile specimens had a 30 mm gauge length, 6 mm diameter, and threaded heads. The compressive specimens were cylinders of height of 16.5 mm and diameter of 11 mm. Both tension and compression tests were done under a strain rate of  $1 \times 10^{-3} \text{ s}^{-1}$ . Three parallel specimens were taken for each group.

## Results and Discussion

The SEM images of as-cast and T4 state Mg–Gd–Nd ternary alloys are shown in Fig. 1. A large amount of continuous equiaxed dendrites is present in the Mg matrix because of Gd and Nd segregation during the non-equilibrium solidification process for as-cast alloys. The amount of intermetallic phase is increased with increasing of alloys concentration. After T4 treatment, only few intermetallic phases remain in the alloy with 10 wt% Gd (Fig. 1a, c). It is obviously that less intermetallic phase is observed in Mg–15Gd–2Nd (Fig. 1b) and Mg–15Gd–5Nd alloys (Fig. 1d); the part of the intermetallic phases is dissolved in the Mg matrix. The intermetallic phases in Mg–15Gd–5Nd alloys remain continuous distribution.

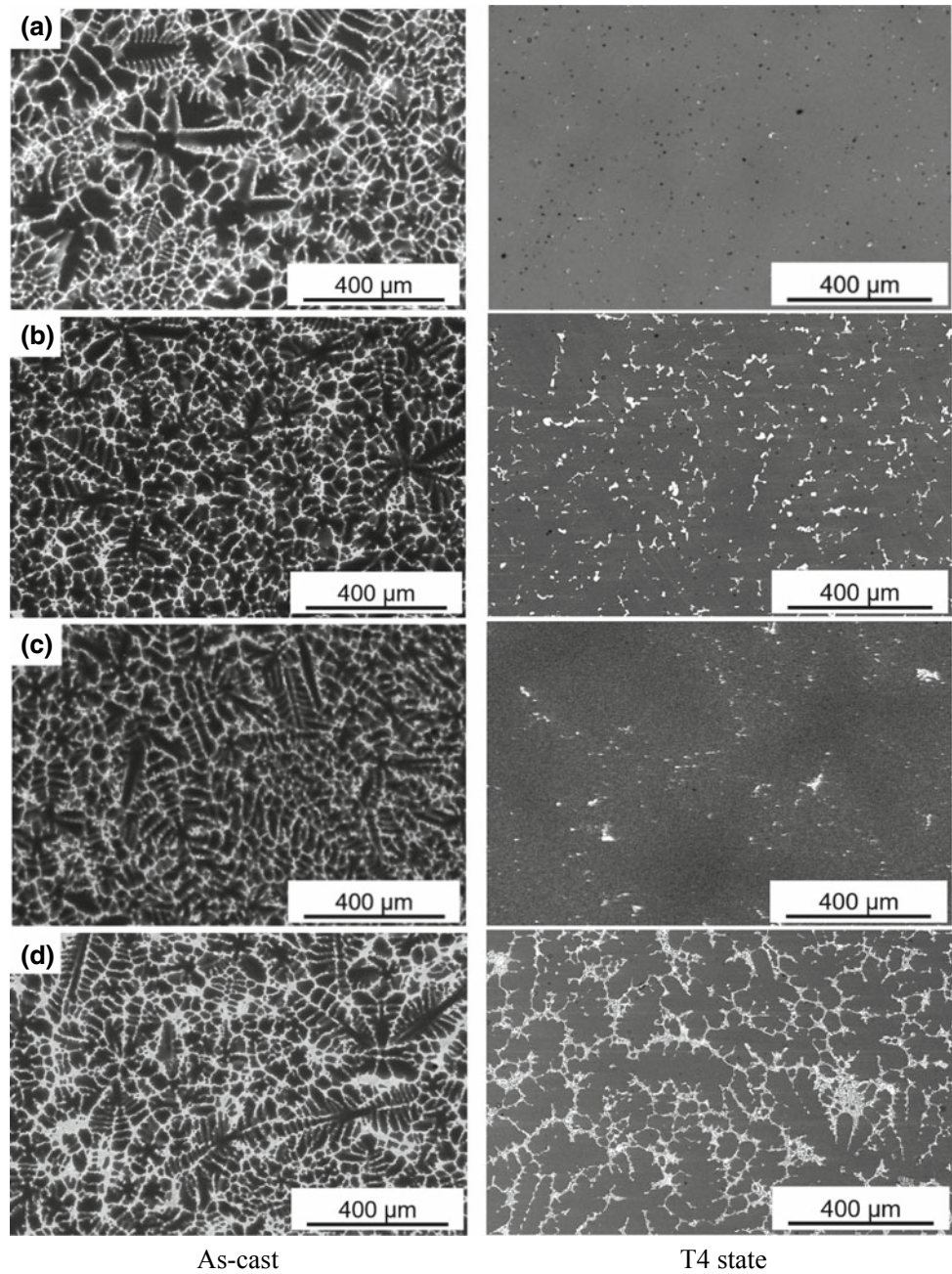
Figure 2 shows the typical SEM graphs of the microstructure and EDS analysis for Mg–xGd–5Nd alloys. The distributions of Gd and Nd differ in different zones. Some of white particles are observed in Fig. 2a, c, d (Point 3), a very regular blocky shape, chosen as examples that are extremely rich in Gd (around 20–40 at.%). For as-cast alloys (Fig. 2a, c), little Gd and Nd (around 1 at.%) are observed in the Mg matrix (Point 1), but high Gd and Nd content (around 8 at.%) are observed at intermetallic zone with network shape (Point 2). After T4 treatment (Fig. 2b, d), the alloy element contents both in matrix and precipitates are increased to above 2 and 10 at.%, respectively. The element distributions are easier observed from the EDS mapping images corresponding to the SEM images. The Gd concentration in blocky-shape phase is extremely high, which was proved to be GdH<sub>2</sub> precipitate [16].

The XRD phase analysis of the as-cast and T4 state alloys is shown in Fig. 3a, b, respectively. The result shows that the intermetallic phases in Mg–Gd–Nd ternary alloys are Mg<sub>5</sub>Gd and Mg<sub>41</sub>Nd<sub>5</sub>. The amount of Mg<sub>5</sub>Gd phase decreases after T4 treatment, especially for alloys with 10 wt %Gd–Nd. This result also agrees with EDS mapping analysis, which is shown in Fig. 2b. The Gd randomly distributes in both matrix and intermetallic phase areas compared with as-cast alloy (Fig. 2a). On the other hand, the Mg<sub>5</sub>Gd phase remains in Mg alloys with 15 wt% Gd after solid solution treatment. Due to the low solid solubility of Nd in Mg, the diffraction peaks of Mg<sub>41</sub>Nd<sub>5</sub> phase in both as-cast and T4 state alloys are high.

**Table 1** Chemical composition of studied alloys

Alloys	Elements content (at.%)		
	Gd	Nd	Mg
Mg–10Gd–2Nd	1.62	0.34	98.04
Mg–10Gd–5Nd	1.61	0.92	97.47
Mg–15Gd–2Nd	2.60	0.45	96.95
Mg–15Gd–5Nd	2.59	1.04	96.37

**Fig. 1** SEM images of as-cast and T4 state Mg–Gd–Nd ternary alloys: **a** Mg–10Gd–2Nd, **b** Mg–10Gd–5Nd, **c** Mg–15Gd–2Nd, and **d** Mg–15Gd–5Nd



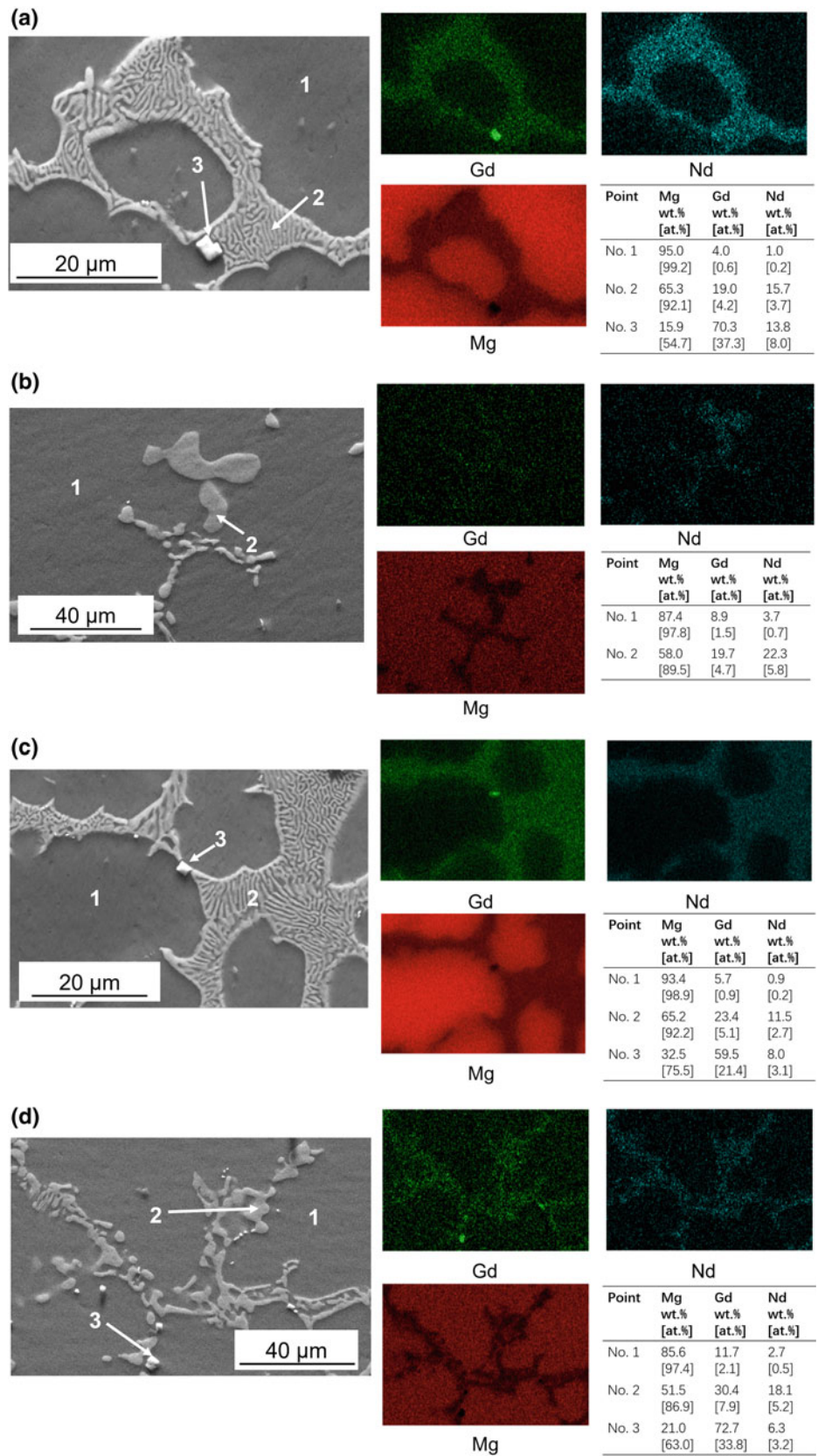
The hardness test results of as-cast and T4 state alloys are presented in Fig. 4. The hardness values increase from 70 to 95 kg mm<sup>-2</sup> with increasing of alloy elements. The solid solution treatment has little effect on the hardness of Mg–Gd–Nd ternary alloys, especially for alloys with 10 wt% Gd.

Figure 5a, b presents the tensile and compression properties of Mg at room temperature, respectively. The yield strength increases 80 and 45 MPa with increasing alloying element content for as-cast and T4 state alloys, respectively.

The tensile and compressive yield strength (TYS and CYS) of Mg–10Gd–2Nd alloy are increased after T4 treatment. However, the TYS and CYS are decreased by T4 treatment for other three studied alloys with higher alloy concentration. For as-cast alloys, the ultimate tensile strength (UTS) increases from 182 to 249 MPa and the ultimate compressive strength (UCS) increases from 280 to 387 MPa with increasing alloying element concentration. Here, the ultimate strength is the maximal strength during the whole



**Fig. 2** SEM images of Mg–Gd–Nd ternary alloys and EDS analysis result: **a** as-cast Mg–10Gd–5Nd, **b** T4 state Mg–10Gd–5Nd, **c** as-cast Mg–15Gd–5Nd, and **d** T4 state Mg–15Gd–5Nd alloys



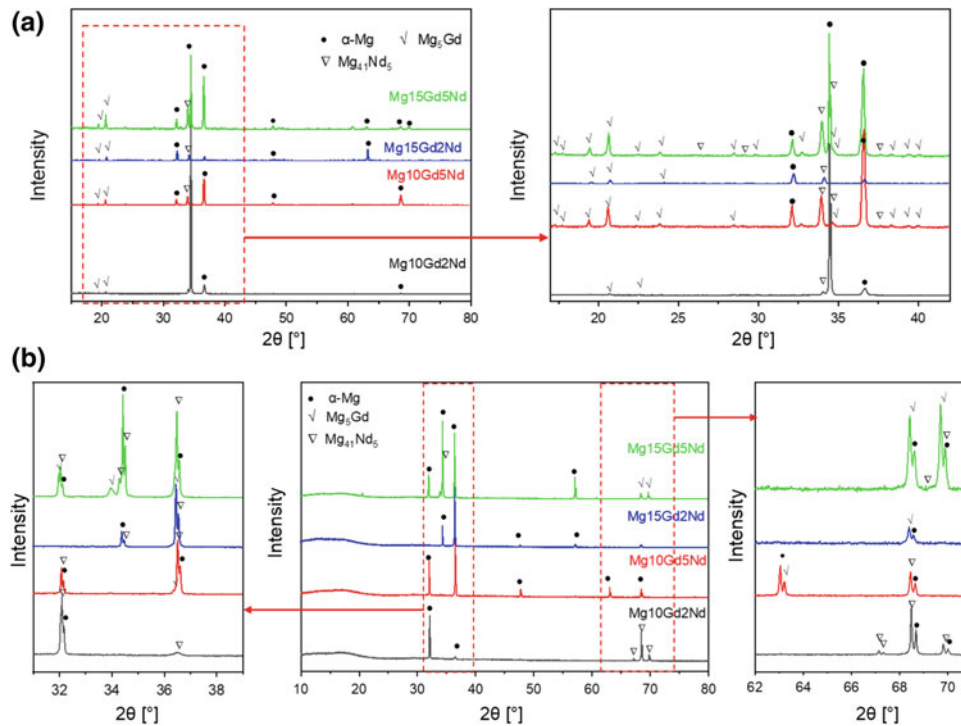


**Fig. 3** XRD patterns of **a** as-cast and **b** T4 state Mg–Gd–Nd ternary alloys

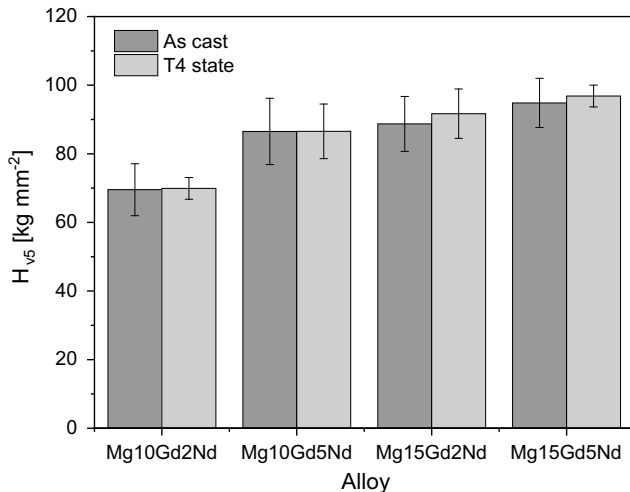


**Fig. 4** Hardness test result of as-cast and T4 state Mg–Gd–Nd ternary alloys

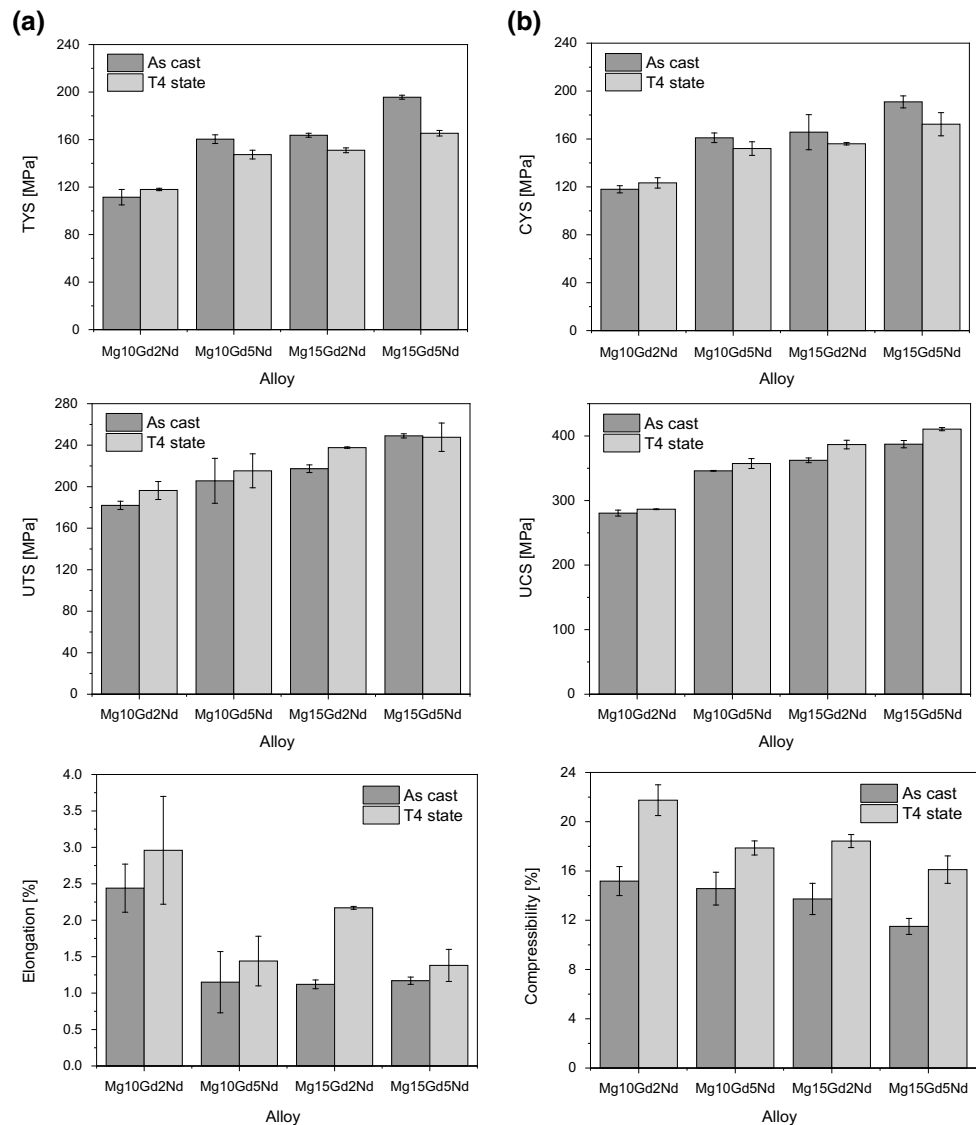
strain range. After T4 treatment, both UTS and UCS are slightly increased. The maximum tensile elongation to failure for those alloys is observed for Mg–10Gd–2Nd after T4 treatment, and the average value is 3%. The alloys with 5%

Nd have lower tensile elongation. The alloying elements have limited effect on compressibility of Mg alloys, and the compression rates decrease about 3% with rising of alloying element concentration. T4 treatment greatly improves the compressibility of Mg–Gd–Nd ternary alloys. The maximum compression rate raises to 22% for Mg–10Gd–2Nd alloy.

The additions of Gd and Nd have positive effects on the mechanical properties, such as hardness, yield strength, and ultimate strength. The previous investigations have shown that the solid solutes and intermetallic phases enhance the mechanical properties of metallic materials. The atomic radius follows the sequence of Mg (160 pm) < Gd (180 pm)  $\approx$  Nd (182 pm) [17]. The difference in the atomic radius can cause lattice distortion and results in strengthening the alloys due to the solid solution strengthening. Additionally, hard intermetallic phases act as obstacles to dislocation motion. Moreover, dislocation can shear or cut softer intermetallic phases which increasing the dislocation density and the strength of materials. In this case, the yield strength is decreased by T4 treatment which reduces the concentration of intermetallic phases. However, the fracture earlier occurred on the interface between the matrix and the intermetallic phases, so that the ultimate strength and ductility of T4 state materials are higher than that of as-cast alloys.



**Fig. 5** Tensile (a) and compressive (b) properties of as-cast and T4 state Mg–Gd–Nd ternary alloys



## Summary

The microstructure and mechanical properties at room temperature of as-cast and T4 state Mg–Gd–Nd ternary alloys are studied. Large amount of continuous dendrites distributes on the grain boundary in all as-cast alloys. The majority of intermetallic phases in Mg– $x$ Gd–2Nd alloys is dissolved in Mg matrix, and the content of intermetallic phases is decreased in Mg– $x$ Gd–5Nd alloys after T4 treatment. Both Gd and Nd enhance the hardness, yield strength, and ultimate strength of Mg alloys. The T4 treatment decreases the yield strength and increases the ultimate strength and ductility of alloys due to the reducing of intermetallic phases.

**Acknowledgements** The authors would like to acknowledge the help of Mr. Günther Meister (HZG, Germany) during casting and heat treatment.

## References

1. Gupta M, Ling SNM (2011) Magnesium, magnesium alloys, and magnesium composites. Wiley, New Jersey, USA
2. Kainer KU (2003) Magnesium alloys and technology. Wiley, Weinheim, Germany
3. Polmear I, John D, Nie J-F, Qian M (2017) Light alloys: metallurgy of the light metals. Butterworth-Heinemann, Oxford, UK
4. Ali Y, Qiu D, Jiang B, Pan F, Zhang M-X (2015) Current research progress in grain refinement of cast magnesium alloys: A review article. Journal of Alloys and Compounds 619: 639–651

5. Jung IH, Sanjari M, Kim J, Yue S (2015) Role of RE in the deformation and recrystallization of Mg alloy and a new alloy design concept for Mg-RE alloys. *Scripta Materialia* 102:1-6
6. You S, Huang Y, Kainer KU, Hort N (2017) Recent research and developments on wrought magnesium alloys. *Journal of Magnesium and Alloys* 5(3):239-253
7. Rokhlin LL (2003) *Magnesium alloys containing rare earth metals: structure and properties*. Crc Press, London
8. Gorsse S, Hutchinson CR, Chevalier B, Nie JF (2005) A thermodynamic assessment of the Mg-Nd binary system using random solution and associate models for the liquid phase. *Journal of Alloys and Compounds* 392(1-2):253-262
9. Wang L, Xing C, Hou X, Wu Y, Sun J, Wang L (2010) Microstructures and mechanical properties of as-cast Mg-5Y-3Nd-Zr-xGd ( $x = 0, 2$  and 4wt.%) alloys. *Materials Science and Engineering: A* 527(7-8):1891-1895
10. Guan L, Deng Y, Shi H, Yang L, Chen M (2017) Effects of Nd Addition on the Microstructure and Mechanical Properties of Extruded Mg-6Gd-2.5Y-0.5Zr Alloy. *Journal of Materials Engineering and Performance* 27(1):243-252
11. Xu YL, Wang L, Huang M, Gensch F, Kainer KU, Hort N, (2018) The Effect of Solid Solute and Precipitate Phase on Young's Modulus of Binary Mg-RE Alloys. *Advanced Engineering Materials*, 1800271
12. Xu YL, Gensch F, Ren Z, Kainer KU, Hort N, (2018) Effects of Gd solutes on hardness and yield strength of Mg alloys. *Progress in Natural Science: Materials International* 28:724-730
13. 13.STM E18-17e1 (2017) *Standard Test Methods for Rockwell Hardness of Metallic Materials*, ASTM International, USA.
14. DIN EN ISO 6892-1 (2017) *Metallic materials—Tensile testing—Part 1: Method of testing at ambient temperature*, DIN, Germany
15. DIN 50106:2016-11 (2016) *Testing of metallic materials—Compression test at room temperature*, DIN, Germany
16. Vlček M, Čížek J, Lukáč F, Hruška P, Smola B, Stulíková I, et al. (2017) Hydrogen absorption in Mg-Gd alloy. *International Journal of Hydrogen Energy* 42(35):22598-22604
17. Pauling L (1947) Atomic radii and interatomic distances in metals. *Journal of the American Chemical Society* 69(3):542-553

# Recrystallization Effects on the Forming Behaviour of Magnesium Alloy Sheets with Varied Calcium Concentration

Jan Bohlen, Huu Chanh Trinh, Klaus Rätzke, Sangbong Yi, and Dietmar Letzig

## Abstract

The formation of strong textures with a preferential alignment of the basal planes in the sheet plane was an important disadvantage for the formability of magnesium alloy sheets. Rare earth or calcium-alloying concepts allow significant texture changes during rolling, resulting in weaker textures, and thus improved the formability. Such a texture development has also been associated with retarded recrystallization. However, this retardation affects the formability during sheet forming operations at elevated temperature. The wrought alloy AZ31 and its Ca-modified counterpart AZX310 are used for Nakajima forming tests at different temperatures. The influence of recrystallization on the sheet formability is demonstrated along different strain paths including local microstructure analysis. The weaker texture due to the addition of Ca allows maintaining the improved formability, which is counteracted by retarded recrystallization.

## Keywords

Magnesium sheet • Formability • Calcium • Recrystallization • Microstructure • Texture

## Introduction

For a broader use of lightweight magnesium alloys, the production of large-area, thin components from magnesium sheets is envisioned. Generally, sheets are a basic form for a metal or alloy as a semi-finished product to feed-forming

processes. While the feasibility of forming parts from magnesium sheets has been demonstrated, e.g. for automotive applications [1, 2], the forming performance using stretching and deep-drawing processes remains a challenge. Such drawbacks have been associated with the hexagonal lattice structure of magnesium and all technically relevant magnesium alloys and a resulting limitation in the activation of deformation mechanism. A dominance of basal slip as the main slip mode and tensile twinning in magnesium alloys is also seen as the reason for the development of strong textures with a preferential alignment of basal planes parallel to the sheet plane [3–5], geometrically resulting in a limitation of the forming ability [6, 7].

An important milestone for enhancing the formability of magnesium sheets has been the ability to weaken the sheet textures by alloy development. In such approaches, rare-earth additions as well as alloying with Ca [8–10] came into the spotlight as elements that would change the texture development during rolling of sheets. This change is based on variations in the activation of the ensemble of deformation mechanisms [e.g. 11] as well as in changes in the recrystallization behaviour of these alloys during thermomechanical treatment [9, 12]. Thus, a texture-based increase of the ductility and the formability of sheets has been demonstrated [6, 8]. Furthermore, it has been shown that Ca also enables such a texture weakening in common Mg–Al–Zn alloy sheets such as of alloy AZ31, especially when the feedstock for rolling is twin-roll cast strip [13].

Due to the limited formability at room temperature, forming processes of components have to be carried out at elevated temperatures, therefore enhancing the activation of slip systems. This also results in thermally activated recrystallization, which leads to a change in the initial microstructure during forming. As a softening mechanism, recrystallization will also have an impact on the forming ability itself which has not been specifically addressed yet. However, alloying, especially with RE or Ca [14], itself has also an influence on the temperature-related activity of deformation and recrystallization mechanisms.

J. Bohlen (✉) · H. C. Trinh · S. Yi · D. Letzig  
Magnesium Innovation Centre (MagIC), Helmholtz-Zentrum  
Geesthacht, Max-Planck Str. 1, D 21502 Geesthacht, Germany  
e-mail: [jan.bohlen@hzg.de](mailto:jan.bohlen@hzg.de)

H. C. Trinh · K. Rätzke  
Faculty of Engineering at Christian-Albrechts-University, Chair  
for Multicomponent Materials, Institute for Materials Science,  
Kaiserstr. 2, 24143 Kiel, Germany

In this work, recrystallization effects during the forming of two industrially manufactured semi-finished sheets from the classical wrought alloy AZ31 and its Ca-modified counterpart AZX310 are used to investigate the formability at varied temperatures and the effect on the microstructure development. Nakajima forming tests were used to reveal the formability of both alloys and to determine forming limits along different strain paths.

## Experiments

Two commercial Mg sheets of alloys such as AZ31 with an initial thickness of 1.5 mm (former Salzgitter Magnesium Technology GmbH, SZMT) and AZX310 (POSCO) with an initial thickness of 1.2 mm in a tempered (i.e. fully recrystallized) condition have been used for the study. Initially, it is believed that this difference in the sheet thickness, which is likely to influence the forming behaviour [15, 16], does not have an impact on the considerations about the microstructure in this work. The chemical composition of the sheets is shown in Table 1, revealing that the addition of Ca into AZX310 is the sole difference between the alloy compositions.

Microstructure analysis was carried out by applying typical metallographic procedures on longitudinal sections of the two sheets. Grinding and polishing are followed by etching with a picric acid-based solution to reveal the grains [17], and a linear intercept method has been applied to determine the grain sizes. The same grinding and polishing procedures have been applied on samples on the sheet surface to mid-plane for texture measurements. Pole figures of the first six reflections were measured up to a tilt angle of 70°. An open-source code MTEX [18] designed for a MATLAB computing environment has been applied to recalculate the orientation distribution function and enables the presentation of full pole figures. The (0002) pole figures of the basal planes and the (10-10) pole figures of the prismatic planes are used to characterize the textures in this study.

Flat dogbone-shaped samples in rolling direction (RD) and transverse direction (TD) of the sheets have been prepared for tensile tests at ambient temperature using a universal testing device ZWICK Z050 and constant initial strain rates of  $10^{-3} \text{ s}^{-1}$ .

Formability tests were carried out by using Nakajima forming tests with sample geometries according to Hasek [19]

in a temperature interval of room temperature and 250 °C. Similar to an approach in earlier works [20, 21], the samples were scaled down from the original size to round discs with a diameter of 100 mm. Two variations of this geometry have been realized by semi-circular recesses from the TD, with 28.75 mm radius and 40 mm radius, respectively. Figure 3 includes a sketch of the sample shapes along with the forming curves. With these recesses and the concurrent change in the material deformation during the forming test, different strain paths can be realized. This includes a biaxial “stretch forming” condition which is characterized by maximum thinning of the sheet samples, referred to as the strain path with the “highest minor strain”. Furthermore, a plane strain condition is considered with vanishing minor strain. Finally, a third sample will be deformed along a strain path with basically no thinning of the sheet samples, referred to as the strain path with the “lowest minor strain”. The samples were clamped with 200 kN and deformed with a hemispherical punch with a diameter of 50 mm in a universal forming machine, Erichsen 145-60 (Erichsen, Germany). PTFE foil with a thickness of 500 µm and oiled with OKS 352 has been used as a lubrication system. In situ local strain measurements on the sample surfaces were carried out by applying a fast optical deformation measuring system, ARAMIS™ (GOM, Germany) with pictures taken by two high-resolution cameras at a sampling rate of  $12 \text{ s}^{-1}$ . For this purpose, the sample surfaces were sprayed with a statistical pattern based on graphite spray. A corresponding software has been applied to recalculate local true strain levels in the region of sample fracture during the test based on the displacement of the sprayed pattern. The resulting strain levels along the major and minor strain directions were used to calculate forming limits for the different sample geometries and plot a simple forming limit curve (FLC) with the three geometries used.

Electron backscatter diffraction measurements (EBSD) have been carried out on longitudinal sections of the sheet samples for a more detailed local analysis of the microstructures. A field emission gun scanning electron microscope (Zeiss Ultra 55, EDAX/TSL EBSD system and Hikari detector) has been used, and an accelerating voltage of 15 kV has been applied to reveal local orientations. A software “TSL orientation imaging microscopy analysis” of EDAX© was used to analyze the measurements.

**Table 1** Chemical composition of the sheets of this study in wt% (max.  $\pm 0.05$  wt%) as determined by spark emission spectroscopy

Alloy	Mg	Al	Zn	Mn	Ca
AZ31	95.7	3.0	0.9	0.4	0.0
AZX310	95.8	2.9	0.8	0.3	0.2

## Results

Figure 1 shows the original microstructures and textures of the two sheets of this study. Fully recrystallized microstructures are shown with distributed precipitates throughout the grains. The addition of Ca to AZ31 promotes the formation of such precipitates. While in the framework of this study, the nature of these particles is not investigated again, and it is hypothesized that this finding is consistent with earlier work [22] revealing stable precipitates such as  $Al_8Mn_5$  in AZ31 and  $Al_2Ca$  in a Ca-modified version of this alloy. A discussion of separating solute or particle effect will therefore be beyond the scope of this study.

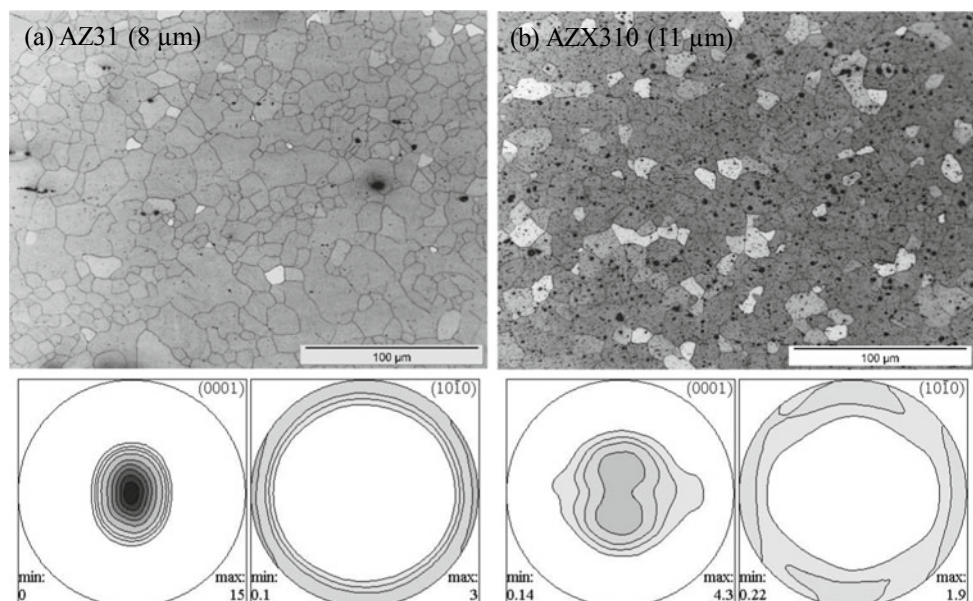
The addition of Ca clearly changes the texture of the resulting sheets. In the case of AZ31, a typical texture with a strong alignment of basal planes parallel to the sheet surface is found which is often referred to as a “basal texture”. In this texture, the angular tilt is broader towards RD rather than towards TD. A similar tendency is found for the AZX310 sheet which reveals a much lower significance in this alignment, resulting in a weaker texture. An additional angular spread towards TD with lower intensities hints towards texture components which are often found in rare-earth or Ca-containing magnesium alloy sheets [9, 23, 24].

Figure 2 shows stress–strain diagrams from tensile tests at room temperature for two directions, RD and TD, of the two alloys. Typical strain hardening after a continuous elasto-plastic transition is observed in all cases. Stress-related anisotropic behaviour is directly visible for AZ31 but not for AZX310. However, the fracture strain for AZX310 in TD is rather low. These findings are also visible in the mechanical properties in Table 2. The yield stress (TYS) for AZ31 is higher along TD than along RD, but the reached ultimate tensile stress (UTS) is comparable. This UTS is

slightly lower for AZX310 as well as the TYS which, however, are not very dependent on the direction of testing. If earlier works are considered [23, 25, 26], the anisotropy and the yield stress will be preferentially a result of enhanced basal slip also allowing higher strain hardening and therefore higher uniform elongation. This is more pronounced in AZ31 along RD (lower TYS and higher uniform strain) than TD. In comparison, AZX310 allows earlier slip as a result of a weaker texture, leaving lower yield stress levels and higher uniform elongation, at least along RD. The low uniform elongation along TD and the fact that the fracture strain is quite similar to the uniform strain allow assuming that brittle fracture is the more likely reason for this direction. Although this may be counterintuitive from the weak textures point of view, the higher amount of particles and their preferential alignment along the RD would be consistent with this finding. Another parameter in Table 2, the *r*-value is calculated as the ratio between compressive strains along the width and the thickness of the sample (as true strains). Thus, a higher value of *r* is consistent with higher strain along the width direction as well as lower strain along the thickness direction; i.e. thinning is restricted. Higher values and a restriction of thinning, respectively, are preferentially found in AZ31 and are revealed to be direction dependent. This is not the case in AZX310 at values rather close to 1.

In Fig. 3 the forming limit diagrams (FLD) are shown for the two alloys with test results from the Nakajima forming tests in three different geometries. The respective data therefore do not reveal full forming limit curves (FLC) but only three particular values including those with highest (biaxial forming) and lowest (no sample thinning) minor strain as well as the plain-strain test (minor strain vanishes). Very low values for the room temperature tests are revealed for both alloys with two specific observations: One is that

**Fig. 1** Microstructure from longitudinal sections of the sheets and average grain sizes (RD horizontal) and pole figures (RD vertical, TD horizontal; contour lines: 1.0, 1.5, 2.0, 3.0, 5.0, ... multiples of random distribution); **a** AZ31, **b** AZX310





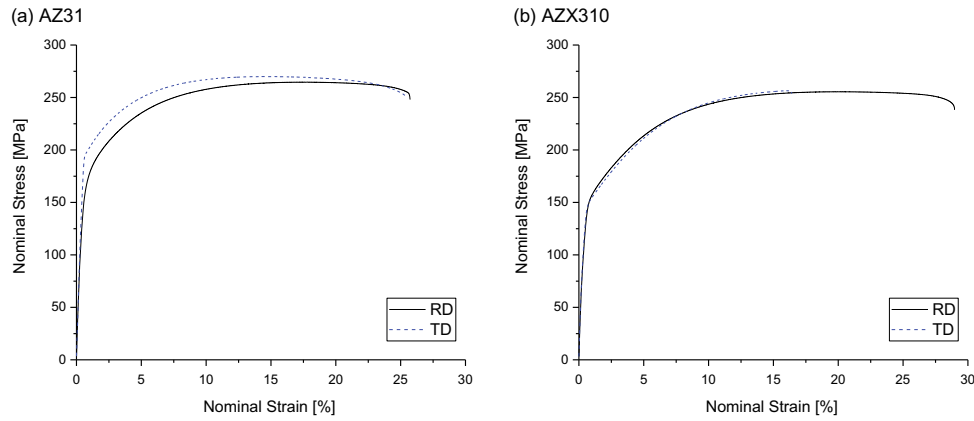


**Fig. 2** Nominal stress–strain diagrams from tensile tests at room temperature; **a** AZ31, **b** AZX310

**Table 2** Mechanical properties from tensile tests along RD and TD; standard deviation in brackets—tensile yield stress (TYS), ultimate tensile stress (UTS), plastic strain at maximum stress (uniform elongation), and plastic strain at fracture (fracture strain) as well as the planar anisotropy at 10% nominal strain ( $r$ -value)

Alloy	Direction	TYS (MPa)	UTS (MPa)	Uniform strain (%)	Fracture strain (%)	$r$ -value
AZ31	RD	154 (1)	264 (2)	16.4 (0.2)	24.6 (1.7)	1.8 (0.1)
	TD	196 (1)	269 (1)	13.8 (0.6)	24.9 (0.2)	4.0 (0.2)
AZX310	RD	133 (1)	255 (1)	19.3 (0.3)	27.7 (0.6)	1.1 (0.2)
	TD	139 (1)	254 (1)	13.8 (2.1)	14.2 (2.2)	1.4 (0.1)

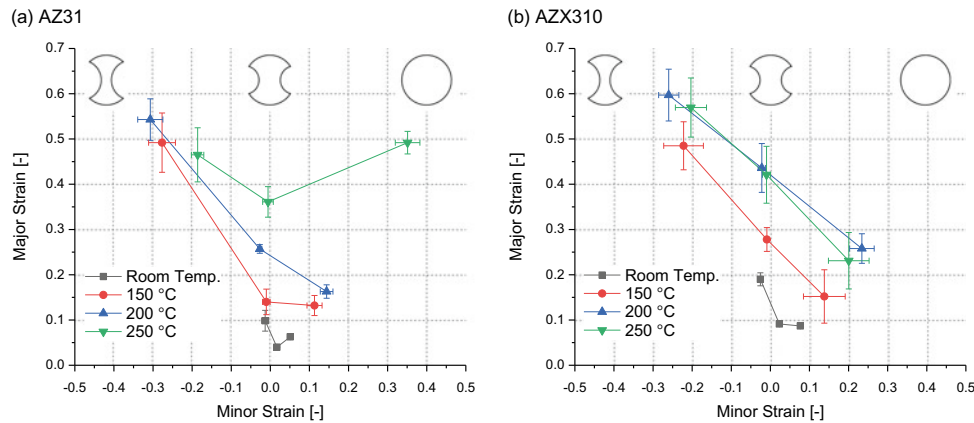


**Fig. 3** Forming limit diagrams with edge points of the forming limit curves from uniform elongations along the strain path at various temperatures; **a** AZ31, **b** AZX310

the strain path with lowest minor strain in both cases allows achieving higher strains compared to the strain path with highest minor strain. Second, all strain levels of AZX310 exceed the corresponding values for AZ31. With increasing temperature to 150 or 200 °C, respectively, an increase in the strain levels is observed which is more pronounced on the left-hand side of the FLD (negative minor strain) rather than on the right-hand side (positive minor strain). In result, this is visible in the form of a continuous decrease of the strain level with increasing minor strain for both alloys.

Furthermore, although the strain is higher along all strain paths for AZX310 than for AZ31, the benefit is not very significant any more at 200 °C. A further temperature increase to 250 °C results in comparable or even slightly lower strain levels for AZX310, whereas the situation is more complex for AZ31. For the left-hand side of the FLD, a decrease of the forming limit strain is found, whereas the plain strain path and the right-hand side of the FLC show a distinct increase in the strain. This is the only condition in this study where a V-shaped FLC and a comparably high-strain level on both sides of the FLD are found. In

summary, there is a distinct change in the forming behaviour of AZ31 at 250 °C, whereas, at all other temperatures of AZ31 and for all conditions of AZX310, a continuous increase of the formability with the temperature is found which is more pronounced on the left-hand side rather than on the right-hand side of the FLD.

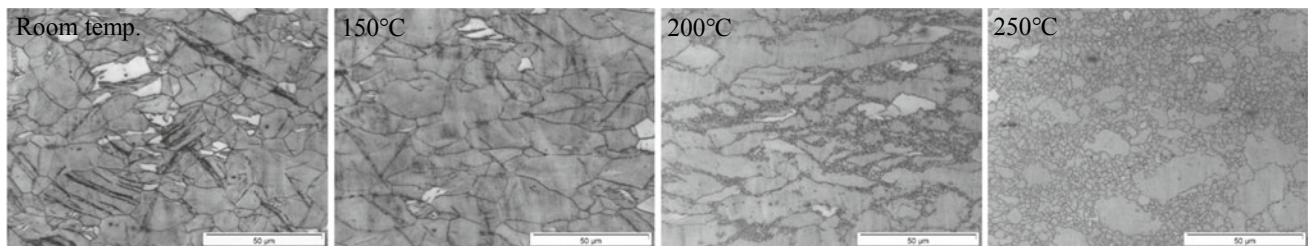
Figure 4 shows micrographs taken from longitudinal sections of the formed samples after testing and close to the cracking position. As the formed samples have been water-quenched in order to stop static microstructure changes (such as static recrystallization or grain growth), it is hypothesized that this figure collects the microstructure development up to the forming limits at the various temperatures for both alloys. Note, that for both sample

geometries shown, lowest and highest minor strain testing, the results are qualitatively comparable.

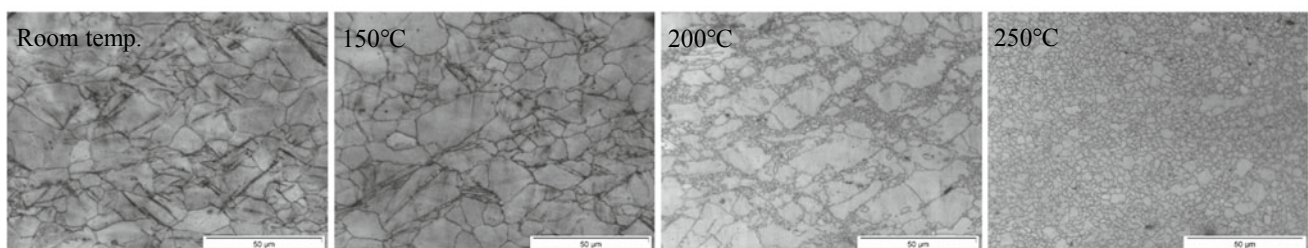
For both alloys tested at room temperature and 150 °C, a deformed microstructure with deformation bands and twins is revealed. No clear new grain formation due to recrystallization becomes visible anyhow. At 200 °C, an onset of recrystallization is easily seen for AZ31 in the form of a band-like and necklace sub-structure of new small grains. This is less pronounced for AZX310. After testing at 250 °C, fairly recrystallized microstructures are found for both samples of AZ31 but not so much for AZX310 where recrystallization appears to be retarded.

A more detailed analysis of the degree of the recrystallized microstructure is carried out using EBSD orientation

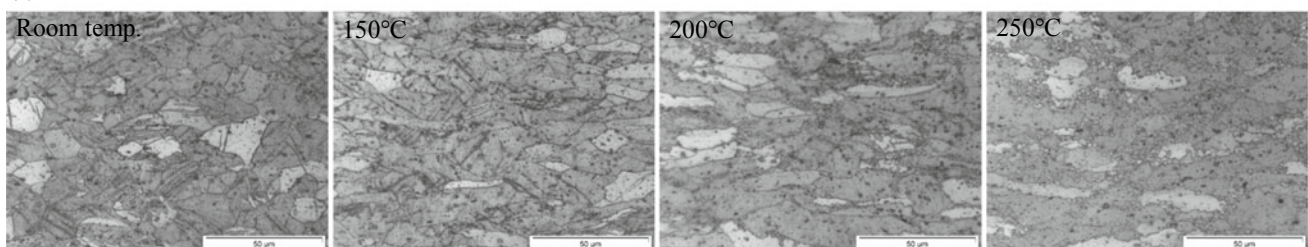
(a) AZ31 – lowest minor strain



(b) AZ31 – highest minor strain



(c) AZX310 – lowest minor strain



(d) AZX310 – highest minor strain

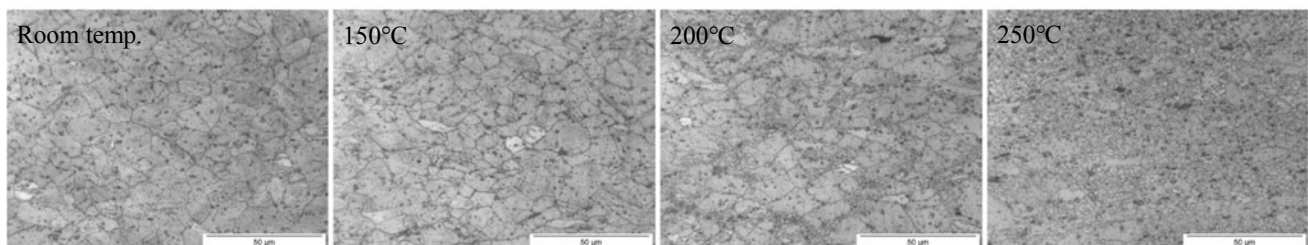


**Fig. 4** Microstructure analysis in the vicinity of the sample crack after the forming test from longitudinal sections



**Fig. 5** Sample orientation maps from longitudinal sections (RD horizontal, ND vertical) after testing samples with highest recess (lowest minor strain) at 200 °C; **a** AZ31 sample with grain boundaries, **b** AZ31 recrystallized grain fraction, **c** AZX310 sample with grain boundaries, **d** AZX310 recrystallized grain fraction

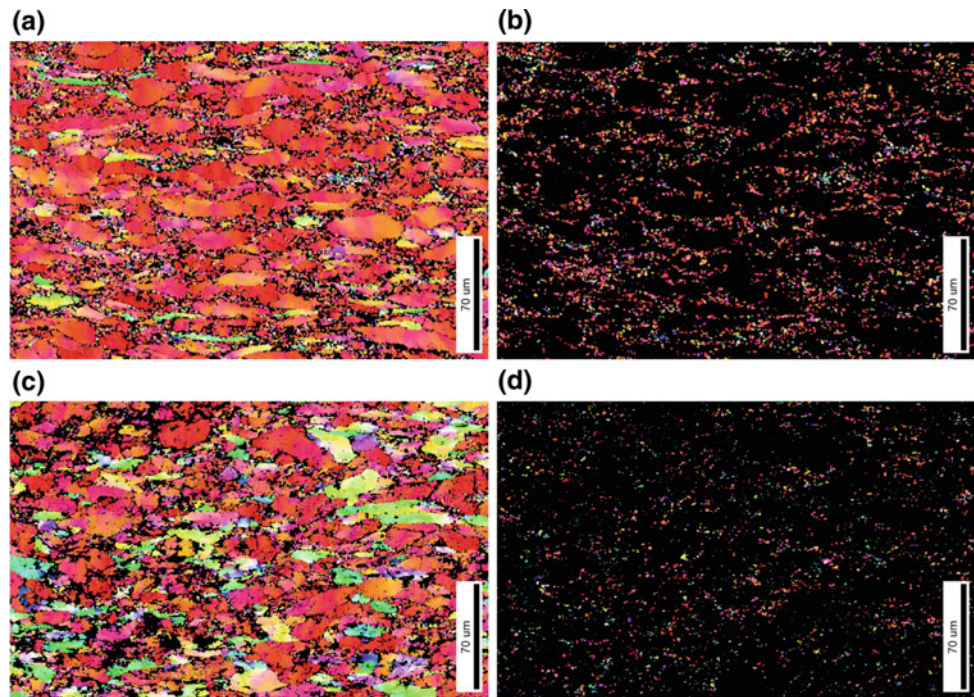


**Table 3** Fraction of recrystallized microstructure after testing as determined from the fraction of grains with GOS < 1° in the corresponding EBSD orientation maps

Strain path	Alloy	Fraction of recrystallized microstructure after testing at	
		200 °C	250 °C
Lowest minor strain	AZ31	16.0	49.0
Lowest minor strain	AZX310	6.6	34.1
Highest minor strain	AZ31	23.8	39.7
Highest minor strain	AZX310	11.1	29.7

maps, exemplarily shown in Fig. 5. While the full micrographs allow revealing grains and grain boundaries, assumptions can be made over the nature of newly recrystallized grains [27]. In earlier works, a constraint of the grain orientation spread (GOS), the variation of the orientation within one grain, has been suggested for such a purpose. Grains that did not undergo recrystallization but experienced active slip modes during deformation in tendency will have a higher spread of the orientation rather than those which underwent a nucleation and growth process in their latest development of history. Thus, grains with low GOS (in this study smaller than 1°) are hypothesized to be recrystallized grains which did not experience active slip modes. For the samples tested at 200 and 250 °C, this respective fraction of the microstructure is collected as the fraction of recrystallized microstructure in Table 3.

After testing at 200 °C, the degrees of the recrystallized microstructure remain low, however, clearly lower for AZX310 than for AZ31. Considerable degrees of recrystallization are found at 250 °C, highest for AZ31. It can be

assumed that the forming behaviour of AZ31 at 250 °C receives an influence from recrystallization, whereas this may not be pronounced for AZX310.

## Discussion

Using the different geometries for forming tests enables to show the significant differences that occur if the strain path during forming is changed. Both alloys of this study are favourably formable along a strain path with negative minor strain, and thus, material flows from the width rather than from the thickness of the sample. In other words, thinning of the sample is not favoured along this strain path. This formability is enhanced at higher temperatures. The material flow along this strain path is somewhat comparable to the one in a tension test along the RD. It becomes visible in Fig. 2 and Table 2 that AZX310 has an advantage here over AZ31. Earlier works [23, 25, 26] confirm that the weaker texture like in the case of AZX310 favours basal slip which

is consistent with the lower yield stress and higher uniform strain of this alloy compared to AZ31. However, an increase of the temperature up to 150 °C or 200 °C changes the resulting strain if the minor strain is negative in the forming tests in Fig. 3. A typical athermal behaviour of basal slip (i.e. a low change of the critical stress of activation [28]) does not help to understand this behaviour but the ability to easier activation on non-basal slip modes as well as potential dynamic recovery can be reasons for this behaviour [29]. They are also consistent with earlier findings from elevated temperature testing of magnesium sheets. In the case of positive minor strain, the weaker texture of AZX310 also promotes the impact of basal slip which does not lead to the same enhancement of strain if the temperature is increased. Then, a weak texture will be beneficial for room temperature forming, but hypothetically loses its impact with increasing temperature if compared to a material with a stronger texture. Furthermore, if dynamic recrystallization is active at higher temperature (higher than 200 °C in this study), the strain increase may even be reversed which is consistent with a decrease of uniform strain in such cases [29]. In the case of the plane strain condition and the biaxial forming case at high minor strain, the strain levels typically remain lower compared to the above-discussed forming case at low minor strain. In these sample geometries, material deformation is realized by thinning, especially in the stretch forming case where thinning needs to additionally contribute to the positive in-plane strain achieved in all directions. If this is compared with the indications about the directionality of material flow from the r-value in Table 2 (at room temperature), AZX310 allows easier thinning of the sample compared to AZ31 with the higher r-value. Anyway, in both cases, the stretch formability remains low with a slight advantage for AZX310, now explained with the weaker texture of this material. This advantage remains visible and is more distinct at higher temperatures up to 200 °C. Again, the additional activation of non-basal slip can help to motivate this behaviour as well as dynamic recovery. However, unlike for AZ31, there is no further improvement if the temperature is increased to 250 °C, but the performance remains to the one at 200 °C. The one difference for AZ31 at this temperature, however, again is the enhanced recrystallization observed [30, 31]. Interestingly, the effect is opposite to the one after testing with the sample geometry for negative minor strain.

If thinning is promoted by any mechanism, e.g. by recrystallization in this case, it will be visible by a shift of the minor strain levels to higher values (i.e. to the right in the FLD, Fig. 3). This is exactly observed for AZ31 tested at 250 °C. In cases where thinning of the sample needs to be enhanced, a resulting increase of the strain is then achieved. In this consideration, the enhanced formability of AZ31 at

250 °C is mainly carried by enhanced dynamic recrystallization which is retarded in the case of AZX310, see Fig. 4 and Table 3.

## Conclusions

Sheet metal forming of magnesium alloy AZ31 leads to microstructure changes by recrystallization if the forming temperatures are higher than 200 °C. For low temperatures, enhanced activity of non-basal slip modes leads to increased formability preferentially in cases with low or negative minor strain. Recrystallization appears to promote the ability to material thinning. The calcium addition (and corresponding microstructure) reduces the tendency to recrystallization. Although enhanced formability is found in AZX310 due to the weak texture of the material especially in geometries that require sheet thinning, the increase of formability with increasing temperature is somewhat limited. Then, the texture-related benefit of enhanced formability at room temperature is not increased with increasing temperature.

## References

1. Klaumünzer D., Victoria Hernandez J., Yi S., Letzig D., Kim S.H., Kim J.J., Seo M.H., Ahn K. (2019) Magnesium Process and Alloy Development for Applications in the Automotive Industry. *Magnesium Technology 2019* (TMS – The Minerals, Metals and Materials Society): 15–20.
2. Friedrich H., Schumann S. (2001) Research for a “new age of magnesium” in the automotive industry. *J. Mater. Process. Technol.* 117:276–281.
3. Styczynski A., Hartig C., Bohlen J., Letzig D. (2004) Cold rolling textures in AZ31 wrought magnesium alloy. *Scripta Materialia* 50:943–947.
4. Jia W.P., Hu X.D., Zhao H.Y., Ju D.Y., Chen D.L. (2015) Texture evolution of AZ31 magnesium alloy sheets during warm rolling. *Journal of Alloys and Compounds* 645:70–77.
5. Emley E.F. (1966) *Principles of Magnesium Technology*. Pergamon Press London.
6. Stutz L., Bohlen J., Kurz G., Letzig D., Kainer K.U. (2011) Influence of the processing of magnesium alloys AZ31 and ZE10 on the sheet formability at elevated temperature. *Key Eng. Mater.* 473:335–342.
7. He J., Mao Y., Fu Y., Jiang B., Xiong K., Zhang S., Pan F. (2019) Improving the room-temperature formability of Mg<sub>3</sub>Al<sub>1</sub>Zn alloy sheet by introducing an orthogonal four-peak texture. *Journal of Alloys and Compounds* 797:443–455.
8. Chino Y., Ueda T., Otomatsu Y., Sassa K., Huang X., Suzuki K., Mabuchi M. (2011) Effects of Ca on Tensile Properties and Stretch Formability at Room Temperature in Mg–Zn and Mg–Al Alloys. *Materials Transactions* 52(7):1477–1482.
9. Bohlen J., Wendt J., Nienaber M., Kainer K.U., Stutz L., Letzig D. (2015) Calcium and zirconium as texture modifiers during rolling and annealing of magnesium–zinc alloys. *Materials Characterization* 101:144–152.

10. Victoria-Hernández J., Yi S., Klaumünzer D., Letzig D. (2019) Recrystallization behavior and its relationship with deformation mechanisms of a hot rolled Mg-Zn-Ca-Zr alloy. *Materials Science and Engineering A* 761 in press.
11. Ha C., Bohlen J., Yi S., Zhou X., Brokmeier H.G., Schell N., Letzig D., Kainer K.U. (2019) Influence of Nd or Ca addition on the dislocation activity and texture changes of Mg-Zn alloy sheets under uniaxial tensile loading. *Materials Science and Engineering A* 761 in press.
12. Guo F., Jiang L., Yang M., Ma Y., Deng Y., Zhang D., Pan F. (2019) Tailoring the rolling texture of AZ31 Mg Alloy with Calcium and Tin Addition. *Advanced Engineering Materials* 21:1800920.
13. Yi S., Park J.H., Letzig D., Kwon O.D., Kainer K.U., Kim J. J. (2016) Microstructure and mechanical properties of Ca containing AZX310 alloy sheets produced via twin roll casting technology. *Magnesium Technology 2016 (TMS – The Minerals, Metals and Materials Society)*: 383–387.
14. Chaudry U.M., Kim T.H., Park S.D., Kim Y.S., Hamad K., Kim J. G. (2019) Effects of calcium on the activity of slip systems in AZ31 magnesium alloy. *Materials Science and Engineering A* 739:289–294.
15. Dilmeç M., Halkacı H.S., Oztürk F., Livatyali H., Yigit, O. (2013) Effects of sheet thickness and anisotropy on forming limit curves of AA2024-T4. *Int. J. Adv. Manuf. Technol.* 67:2689–2700.
16. Ricci, P.; El Mehtedi, M.; Barone, L.; Spigarelli, S. (2009) Effects of temperature and sheet thickness on formability of AZ31 magnesium alloy. *Mater. Sci. Forum* 604–605:147–152.
17. Kree V., Bohlen J., Letzig D., Kainer K.U. (2004) The metallographical examination of magnesium alloys. *Praktische Metallographie/Practical Metallography* 41:233–246.
18. Bachmann F., Hielscher R., Schaeben H. (2010) Texture Analysis with MTEX – Free and Open Source Software Toolbox. *Solid State Phenomena* 160:63–68.
19. Hasek V. (1978) Untersuchung und theoretische Beschreibung wichtiger Einflußgrößen auf das Grenzformänderungsschaubild. *Blech Rohre Profile* 25(10):213–220, 285–292, 493–499, 613–627.
20. Bohlen J., Cano G., Drozdenko D., Dobron P., Kainer K., Gall S., Müller S., Letzig D. (2018) Processing Effects on the Formability of Magnesium Alloy Sheets. *Metals* 8(2):147.
21. Bohlen J., Schlung O., Gall S., Müller S., Letzig D. (2016) Formability of extruded magnesium alloy sheets with different textures. *Magnesium Technology 2016 (TMS – The Minerals, Metals and Materials Society)* 251–256.
22. Shang L., Jung I.H., Yue S., Verma R., Essadiqi E. (2010) An investigation of formation of second phases in microalloyed AZ31 Mg alloys with Ca, Sr and Ce. *Journal of Alloys and Compounds* 492:173–183.
23. Bohlen J., Nürnberg M.R., Senn J.W., Letzig D., Agnew S.R. (2007) The texture and anisotropy of magnesium-zinc-rare earth alloy sheets. *Acta Materialia* 55(6):2101–2112.
24. Al-Samman T., Li X. (2011) Sheet texture modification in magnesium-based alloys by selective rare earth alloying. *Materials Science and Engineering A* 528:3809–3822.
25. Agnew S.R. (2002) Plastic anisotropy of magnesium alloy AZ31B sheet. *Magnesium Technology 2002 (TMS—The Minerals, Metals and Materials Society)*: 169–173.
26. Agnew S.R., Yoo M.H., Tome C.N. (2001) Application of texture simulation to understanding mechanical behaviour of Mg and solid solution alloys containing Li or Y. *Acta Materialia* 49:4277–4289.
27. Bohlen J., Yi S., Letzig D., Kainer K.U. (2010) Effect of rare earth elements on the microstructure and texture development in magnesium-manganese alloys during extrusion. *Mater. Sci. Eng.* A527:7092–7098.
28. Cepeda-Jiménez C.M., Molina-Aldareguia J.M., Carreño F., Pérez-Prado M.T. (2015) Prominent role of basal slip during high-temperature deformation of pure Mg polycrystals. *Acta Materialia* 85:1–13.
29. Jäger A., Lukáč P., Gärtnerová V., Bohlen J., Kainer K.U. (2004) Tensile properties of hot rolled AZ31 Mg alloy sheets at elevated temperatures. *Journal of Alloys and Compounds* 378:184–187.
30. Zeng Z.R., Zhu Y.M., Nie J.F., Xu S.W., Davies C.H.J., Birbilis N. (2019) Effects of calcium on Strength and Microstructural Evolution of Extruded Alloys Based on Mg-3Al-1Zn-0.3Mn. *Metallurgical and Materials Transactions A* 50:4344–4363.
31. Chaudry U.M., Kim T.H., Kim Y.S., Hamad K., Ko Y.G., Kim J. G. (2019) Dynamic recrystallization behaviour of AZ31–0.5Ca magnesium alloy during warm rolling. *Materials Science and Engineering A* 762: in press.



# Towards the Development of High Ductility Mg–Al Based Alloys Through Second-Phase Refinement with Trace Yttrium Additions

Konstantinos Korgiopoulos and Mihriban Pekguleryuz

## Abstract

Magnesium alloys are attractive lightweight materials for transportation industry as they offer a viable approach for reduced CO<sub>2</sub> emissions and fuel economy. The most widely used alloys for automotive applications are based on the Mg–Al system where the principal second-phase  $\beta$ -Mg<sub>17</sub>Al<sub>12</sub> provides strengthening but reduces ductility. A key factor in widening the use of magnesium in crashworthy components such as vehicle body applications is the availability of cost-effective Mg casting alloys with improved ductility. Modification of the Mg<sub>17</sub>Al<sub>12</sub> in Mg–Al alloys via trace additions is a promising approach to enhance the ductility while maintaining the strength. Our research has found that only trace levels of yttrium (Y) can modify the Mg<sub>17</sub>Al<sub>12</sub> and improve the ductility of Mg–6Al alloy by 63%. To elucidate the mechanism of this refinement, different methods are used including thermodynamic calculations, image analysis, scanning and transmission electron microscopy.

## Keywords

Magnesium • Mg<sub>17</sub>Al<sub>12</sub>-refinement • Rare-Earth • Thermodynamic calculations

## Introduction

Mg–Al based cast alloys are attractive lightweight materials for automotive parts due to their low density, high ductility and fracture toughness. Al addition widens the freezing range making the alloys more castable and it improves the

strength and hardness by the precipitation of  $\beta$ -Mg<sub>17</sub>Al<sub>12</sub> intermetallic. Furthermore, the optimum combination of ductility and strength occurs for 6 wt% Al [1, 2]. Improving the ductility of these alloys is a key factor in widening the use of cast Mg–Al alloys in crashworthy interior automotive components.

Mg-6 wt% Al cast alloy microstructure consists of  $\beta$ -Mg solid solution ( $\sim 2$  wt% Al) and the Mg<sub>17</sub>Al<sub>12</sub> intermetallic phase in the interdendritic regions. The Mg<sub>17</sub>Al<sub>12</sub> precipitates present different morphologies such as lamellar, fibrous, granular, divorced, or partially divorced and it depends on the amount of Al and the cooling rate. As aluminum increases, the  $\beta$ -phase becomes less divorced [3]. The strength and ductility of cast Mg–Al alloys are governed by the amount of  $\beta$ -Mg<sub>17</sub>Al<sub>12</sub> phase and its morphology. Increasing amount of the phase increases strength but reduces ductility. Certain combinations of strength and ductility can be obtained by controlling the amount of  $\beta$ -Mg<sub>17</sub>Al<sub>12</sub> in the alloy. Hence, higher ductility is possible by lowering the Al level in the alloy which reduces the wt% Mg<sub>17</sub>Al<sub>12</sub>, but at the expense of strength [2, 4].

The morphology, distribution, and nature (stoichiometry, bonding, hardness, ductility) of the second phases are also factors that influence ductility. Continuous network of Mg<sub>17</sub>Al<sub>12</sub> can be detrimental to ductility [5]. The sharp corners of the eutectics can act as stress concentrators and bulky intermetallics facilitate crack propagation.

Trace element additions have been reported to refine the Mg alloys microstructure. Koubichek [6] identified the refining effect of trace additions of Sr and Ca on the grain size and the Mg<sub>17</sub>Al<sub>12</sub> phase in Mg–Al alloys. In recent years, more work has been carried out on the grain refining of Mg alloys via Sr. Wang et al. [7] examined the effect of yttrium addition to a Mg–Al–Zn (AZ91) alloy. With Y addition, the volume fraction of  $\beta$ -Mg<sub>17</sub>Al<sub>12</sub> reduced and the phase became more dispersed with the presence of Al<sub>2</sub>Y. Turen Y. [8] examined the effect of Sn in Mg–Al–Zn alloy where the  $\beta$ -phase morphology changed from lamellar into fully divorced leading to enhanced tensile elongation with an

K. Korgiopoulos (✉) · M. Pekguleryuz  
Department of Mining and Materials Engineering, McGill  
University, 3610 University Street Montreal, Quebec, H3A 0C5,  
Canada  
e-mail: [konstantinos.korgiopoulos@mail.mcgill.ca](mailto:konstantinos.korgiopoulos@mail.mcgill.ca)

M. Pekguleryuz  
e-mail: [mihriban.pekguleryuz@mcgill.ca](mailto:mihriban.pekguleryuz@mcgill.ca)

optimum at 0.5% Sn. Nd addition shows similar effect as Y and improves ductility as it suppresses the formation of  $Mg_{17}Al_{12}$  due to the higher affinity of Al to create  $Al_2Nd$  intermetallics instead of  $\beta$ -phase [9]. In other studies, the Mg–4Al based casting alloy has been modified with Ce additions where the ductility increased due to the refinement of the microstructure and the suppression of  $\beta$ -phase. Er seems to be an effective alloying addition for the improvement of the mechanical properties as it increased the ductility in the Mg–Al binary system [10, 11]. However, not all these changes led to an improvement in ductility. High amounts of Ce (6 wt%) lead to ductility decrease because of the formation of the coarse and brittle  $Al_2Ce$  intermetallics [12, 13]. Candan et al. results show that the addition of Ti in AZ91 alloy suppresses the partially divorced  $\beta$ -phase but without any essential change of ductility [14].

This work investigates the  $\beta$ -phase modification with trace Y and its effect on the tensile properties of Mg–Al based alloys. Thermodynamic calculations are also employed to better understand the effect of trace additions on the modification of  $Mg_{17}Al_{12}$  precipitate.

## Experimental Procedure

Mg–Al alloys with different levels of Y were prepared using a Norax induction furnace. The raw materials used to synthesize the alloys were Mg ingot of 99.9% purity (Magnesium Electron), 99.9% pure Al granules (Alfa Aesar), and 99.9% pure Y rods (Hefa Rare Earth Canada). Pure Mg was heated to 700 °C inside a graphite crucible under protective atmosphere of  $CO_2/SF_6$  gas. Consecutive additions of Al and Y were done at 720 °C and the melt was held at temperature for 20 min. After skimming and stirring, the alloys were poured under protective atmosphere into a boron-nitride coated steel mold which was preheated at 400 °C. The actual compositions were determined by inductively coupled plasma (ICP) analysis (Table 1). Alloy 1 was also analyzed with laser-ablation/inductively coupled plasma mass-spectrometry (LA/ICP-MS) because the Y level was very low.

Tensile test samples were machined according to the ASTM E8 standard. The elongation was measured with an

extensometer (25 mm gauge length) at  $0.001s^{-1}$  strain rate. Scanning electron microscopy investigation (SEM, Hitachi SU3500 with an energy dispersive X-ray spectroscopy [EDS] detector) was conducted on the as-cast and tensile deformed samples after grinding and polishing up to 1200 grid SiC and 0.05  $\mu m$  colloidal silica, respectively. The TEM sample was prepared by focused ion beam (FEI Helios Nanolab 660 DualBeam) and it was analyzed by a FEI Tecnai G2 F20 Cryo-STEM microscope operating at 200 kV.

## Results and Discussion

The as-cast microstructures of the four alloys (Fig. 1) as per EDS analysis consist of Al supersaturated  $\alpha$ -Mg matrix,  $\beta$ - $Mg_{17}Al_{12}$ , and Mg–Al–Mn–Fe precipitates in the interdendritic regions and in the grain boundaries. In the case of Alloys 2 and 3 (Fig. 1c, d), the Mg–Al–Mn–Fe phase is enriched in Y and Mg–Al–Y precipitates also exist; no Y signal is detected in the matrix. No Y was detected in Alloy 1 (Fig. 1b) neither in matrix nor in precipitates. There is also association of Mg–Al–Mn–Fe and Mg–Al–Y precipitates with the  $Mg_{17}Al_{12}$  phase. This association could lead to the assumption that these particles (coarse or fine) may have a role in the nucleation of  $\beta$ - $Mg_{17}Al_{12}$ . It is suggested that only the fine precipitates can act as effective refiners for the  $\beta$  phase.

The microstructures were analyzed using the ImageJ software to investigate the effect of Y addition on the refinement of the  $Mg_{17}Al_{12}$  precipitate. For each alloy, an average of 20 SEM images and 1000 precipitates were measured. Figure 2 presents the histogram of the size of  $\beta$  phase using the average precipitate size from each image. According to these results, most of the  $Mg_{17}Al_{12}$  precipitates are in the range of 26–35  $\mu m^2$  in the binary Mg–Al alloy. When ppm levels of Y are added (Alloy 1), the  $\beta$  phase becomes finer being mostly at the range of 10–15  $\mu m^2$ . For higher Y additions,  $Mg_{17}Al_{12}$  becomes coarser having mostly a size of 16–25  $\mu m^2$ . Furthermore, the area fraction (Fig. 3) of  $\beta$  phase increases in Alloy 1 and then decreases for higher Y additions (Alloys 2 and 3). These results show

**Table 1** Chemical composition of the alloys

Target alloy <sup>a</sup> (wt%)	Designation	Al (wt%)	Y (ppm)	Fe (wt%) <sup>c</sup>	Mn (wt%) <sup>c</sup>
Mg–6Al	Mg–6Al	6.23	–	0.027	0.015
Mg–6Al–0.01Y	Alloy 1	6.28	0.2–1.5 <sup>b</sup>	0.023	0.015
Mg–6Al–0.03Y	Alloy 2	6.18	130	0.009	0.004
Mg–6Al–0.06Y	Alloy 3	6.16	280	0.010	0.014

<sup>a</sup>Mg: balance

<sup>b</sup>Average from LA & AES ICP

<sup>c</sup>Impurities from raw materials

**Fig. 1** As cast microstructures of Mg–Al based alloys with different levels of Y. **a** Mg–6Al. **b** Alloy 1. **c** Alloy 2. **d** Alloy 3

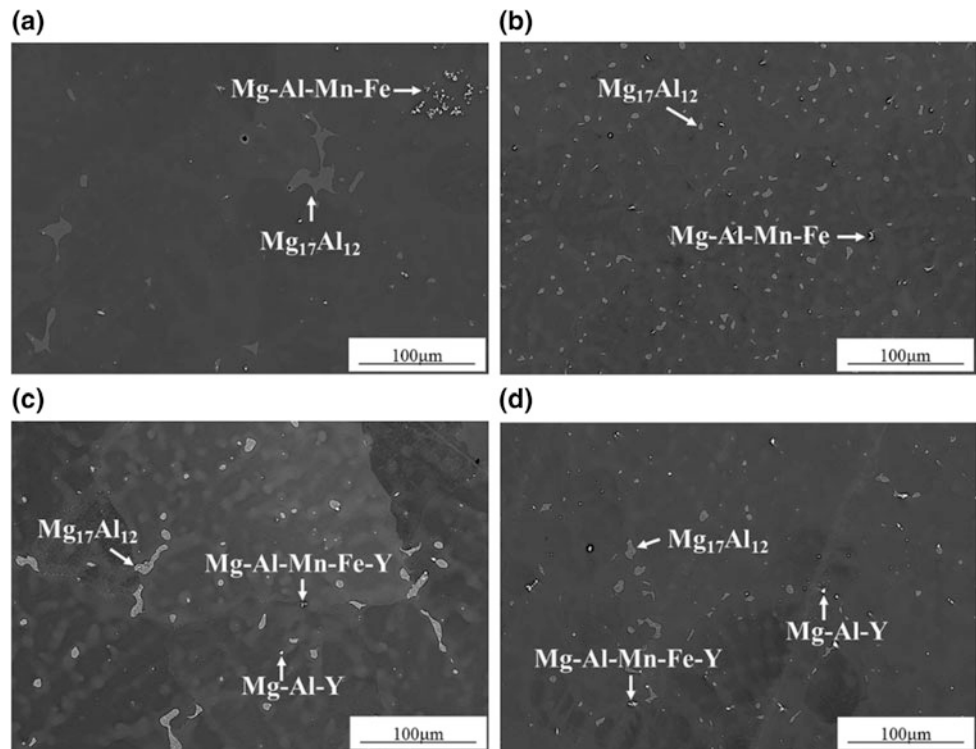
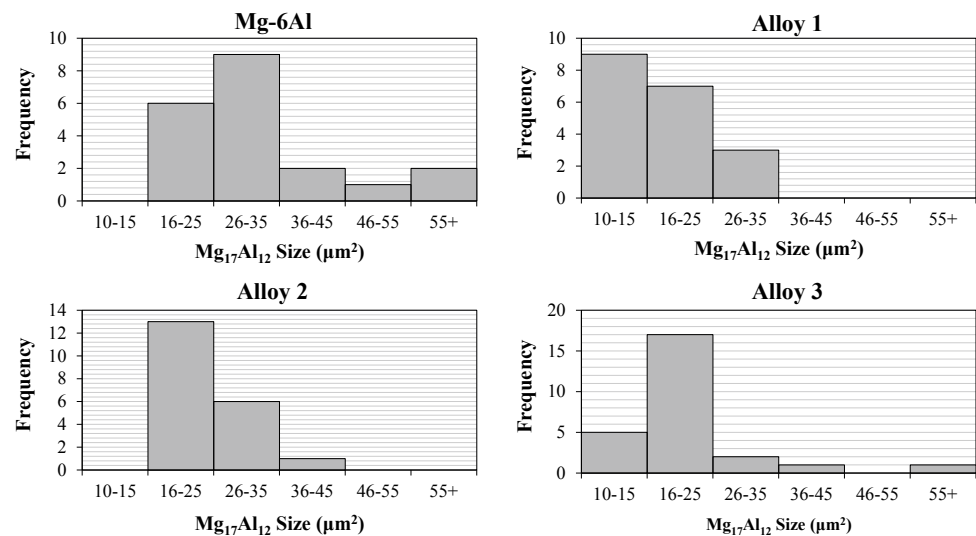


**Fig. 2** Histogram showing the average size of  $Mg_{17}Al_{12}$  in the 4 as cast alloys



that there is a refining effect of  $Mg_{17}Al_{12}$  at ppm Y levels which is lost at higher Y additions.

Tensile tests were conducted at room temperature (Fig. 4) to determine the effect of Y on the mechanical properties of the as cast alloys. Alloy 1 presents ~63% increase in ductility and it has the highest ultimate tensile strength (UTS) but the yield strength (YS) is similar to the other alloys. When Y increases, the UTS and elongation slightly

decrease in Alloy 2. In Alloy 3, the elongation slightly increases compared to the binary Mg–6Al, but the UTS remains similar.

For each alloy, a tensile specimen (cross section of gauge length) was examined via SEM/EDS (Fig. 5a–d). Partially divorced (PD) and lamellar  $Mg_{17}Al_{12}$  appear in the Mg matrix. Cracks appear mostly on the coarse partially divorced  $\beta$ - $Mg_{17}Al_{12}$ . It is interesting to mention that for the

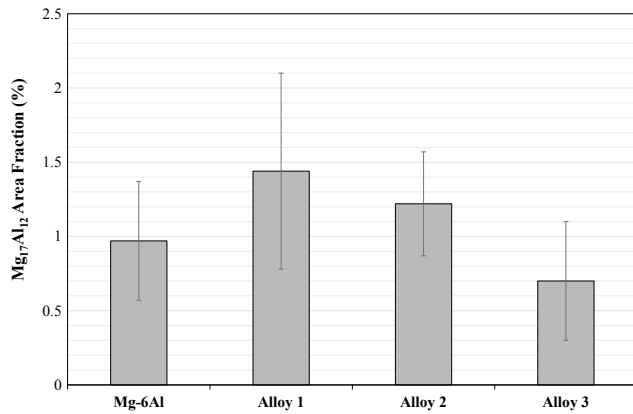


**Fig. 3** Area fraction of Mg<sub>17</sub>Al<sub>12</sub> for the different alloys

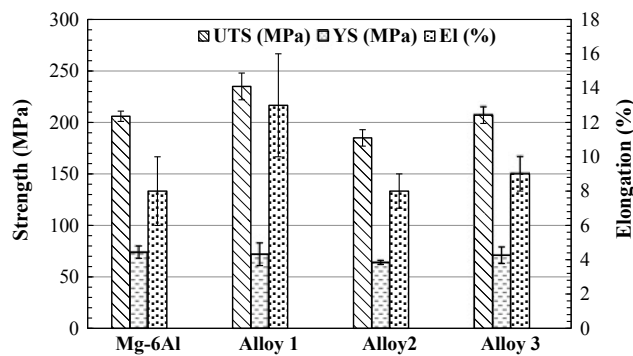
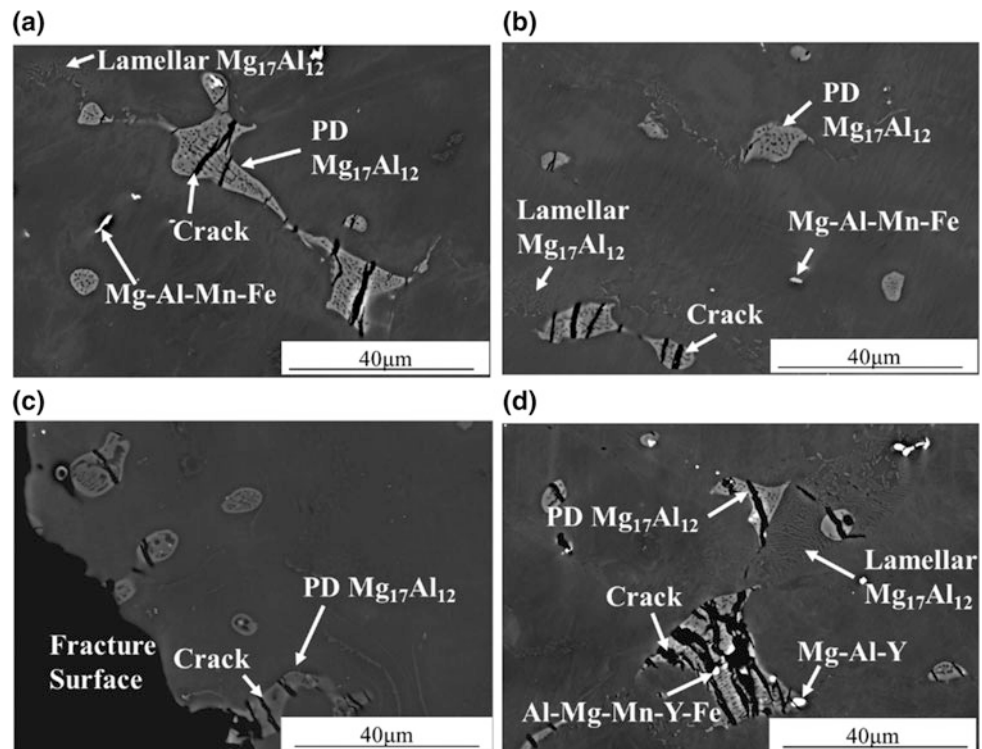


**Fig. 4** Tensile properties of the four alloys at room temperature in as cast condition

**Fig. 5** SEM microstructure of tensile samples **a** Mg-6Al. **b** Alloy 1. **c** Alloy 2. **d** Alloy 3



Alloy 2 (Fig. 5c), the cracked coarse precipitates are on the surface fracture of the tensile sample which shows why the refinement of Mg<sub>17</sub>Al<sub>12</sub> is essential for the ductility improvement. A question that could arise at this point would be if Y diffuses into β phase without creating Al–Y enriched precipitates when it is added at low levels. This could possibly change the intrinsic properties of the precipitate making it more ductile. Future studies could elucidate the effect of Y in the crystal structure of Mg<sub>17</sub>Al<sub>12</sub>.

As previously mentioned, the Mg–Al–Y precipitates are in close association with Mg<sub>17</sub>Al<sub>12</sub> (Fig. 6a). Preliminary TEM bright field characterization of these precipitates in Alloy 3 (Fig. 6b) shows this association. Mg–Al–Y size is 0.327 μm<sup>2</sup> which seems to be too coarse to refine the Mg<sub>17</sub>Al<sub>12</sub> during solidification. TEM/EDS characterization on Alloy 1 did not show any signal of Y so it is at this time difficult to elucidate the mechanism of β-phase refinement in this alloy. Future TEM investigation will focus on the characterization of the Mg<sub>17</sub>Al<sub>12</sub>/Mg–Al–Y interface as well as any existing orientation relationship.

Currently, non-equilibrium thermodynamic calculations (FactSage/FTlite database-Scheil cooling) were utilized to shed light onto the mechanism behind the refinement of Alloy 1. According to the results (Fig. 7), Al<sub>4</sub>MgY precipitate forms when low levels of Y are added in the Mg-6Al alloy. It is interesting that the forming temperature of Al<sub>4</sub>MgY precipitate coincides with the forming temperature of Mg<sub>17</sub>Al<sub>12</sub> when Y is at low levels. For Y additions more



**Fig. 6** **a** SEM image showing the correlation of Mg–Al–Y precipitate with  $Mg_{17}Al_{12}$ . **b** TEM bright field image of the same precipitate as (a)

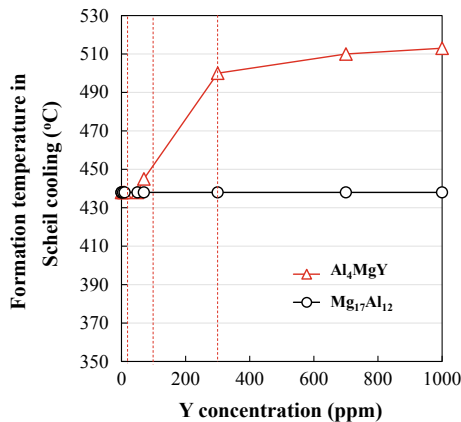
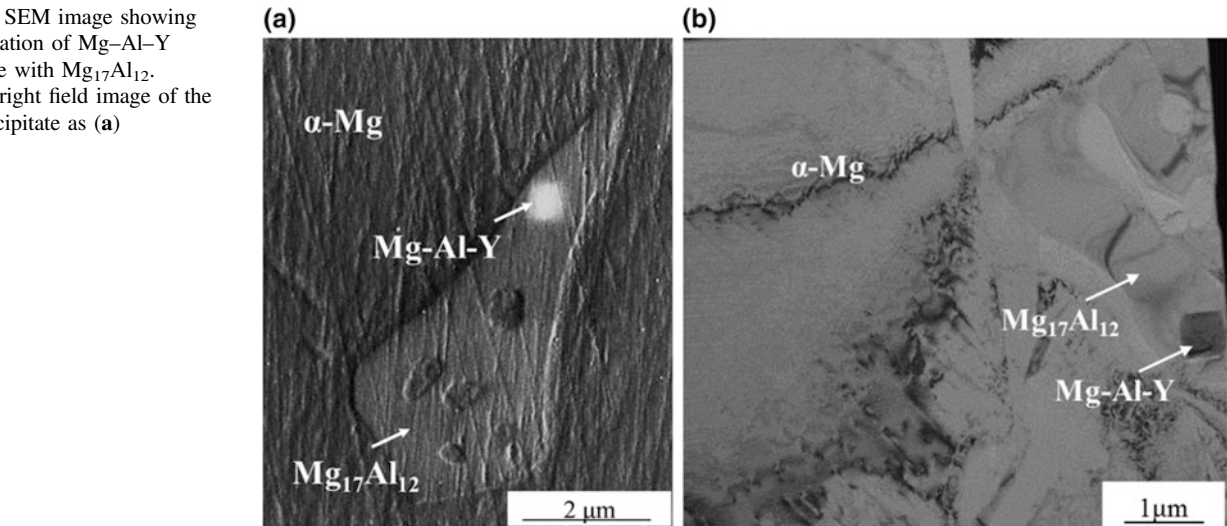


**Fig. 7** Scheil cooling calculation of  $Mg_{17}Al_{12}$  and  $Al_4MgY$  at different levels of Y. The three vertical square dot lines show the composition of Alloy 1, Alloy 2, and Alloy 3

than 50 ppm, the forming temperature of  $Al_4MgY$  is higher at the earlier stage of the solidification path. It is possible that  $Al_4MgY$  is a proper refiner for  $Mg_{17}Al_{12}$  when the two phases co-precipitate. This refinement effect is lost when  $Al_4MgY$  precipitates earlier as it becomes coarser.

## Conclusions

Trace addition of Y in Mg–6Al alloy can refine the  $Mg_{17}Al_{12}$  precipitates leading to the increase of ductility and ultimate tensile strength at room temperature. This refinement effect is lost when Y level increases due to the formation of Mg–Al–Y and the dissolution of Y in Mg–Al–Fe–Mn–Y precipitates. The SEM investigation of the tensile samples reveals that the cracks propagate through the  $Mg_{17}Al_{12}$  causing ductility loss. Preliminary TEM

characterization shows the correlation of  $\beta$ - $Mg_{17}Al_{12}$  with Mg–Al–Y which is too coarse to refine the  $\beta$  phase. Scheil cooling calculations show that Y additions in Mg–6Al lead to the formation of the  $Al_4MgY$  precipitate which co-precipitates with  $Mg_{17}Al_{12}$  for trace additions but it forms at higher temperatures when more Y is added. This could possibly explain why the refinement of  $Mg_{17}Al_{12}$  is lost for higher Y levels.

**Acknowledgements** This project has been supported through a Discovery Grant from the Natural Sciences and Engineering Research Council of Canada (NSERC). The authors thank Pierre Vermette and Dr. Amir Farkoosh from McGill University for their assistance in alloy making and casting as well as the Centre de métallurgie du Québec-CMQ. Konstantinos Korgiopoulos gratefully acknowledges the financial support of Hellenic Scholarship Foundation for his scholarship and McGill Engineering Doctoral Award program (MEDA). We are also grateful for the help and assistance of, Weawkamol Leelapornpisit (FIB), Xue-Dong Liu (TEM), and Longbo Yang (LA ICP).

## References

1. F. Kaiser, K.U. Kainer, Magnesium alloys and technology, John Wiley & Sons, 2003.
2. M. Avedesian, H. Baker, Magnesium and magnesium alloys, 1998.
3. M.D. Nave, A.K. Dahle, D.H. St. John, Eutectic growth morphologies in magnesium-aluminium alloys, in: TMS Annu. Meet., 2000. <https://doi.org/10.1002/9781118808962.ch33>.
4. H.E. Friedrich, B.L. Mordike, Magnesium technology, Springer, 2006.
5. S. Kleiner, O. Beffort, A. Wahlen, P.J. Uggowitzer, Microstructure and mechanical properties of squeeze cast and semi-solid cast Mg–Al alloys, J. Light Met. (2002). [https://doi.org/10.1016/s1471-5317\(03\)00012-9](https://doi.org/10.1016/s1471-5317(03)00012-9).
6. L. Koubichek, Effect of small additions of elements on grain size and the refinement of the  $Mg_4Al_3$  [ $Mg_{17}Al_{12}$ ] phase in ml5 alloy. Izv. Vyschikh. Outchebnykh Za Vedeny, Metall. Non-Ferrous Met. 6 (1959).



7. S.-R. Wang, P.-Q. Guo, L.-Y. Yang, Y. Wang, Microstructure and mechanical properties of AZ91 alloys by addition of yttrium, *J. Mater. Eng. Perform.* 18 (2009) 137–144. <https://doi.org/10.1007/s11665-008-9255-z>.
8. Y. Turen, Effect of Sn addition on microstructure, mechanical and casting properties of AZ91 alloy, *Mater. Des.* (2013). <https://doi.org/10.1016/j.matdes.2013.02.037>.
9. J. Zhang, J. Wang, X. Qiu, D. Zhang, Z. Tian, X. Niu, D. Tang, J. Meng, Effect of Nd on the microstructure, mechanical properties and corrosion behavior of die-cast Mg–4Al-based alloy, *J. Alloys Compd.* (2008). <https://doi.org/10.1016/j.jallcom.2007.10.056>.
10. S. Seetharaman, C. Blawert, B.M. Ng, W.L.E. Wong, C.S. Goh, N. Hort, M. Gupta, Effect of erbium modification on the microstructure, mechanical and corrosion characteristics of binary Mg–Al alloys, *J. Alloys Compd.* (2015). <https://doi.org/10.1016/j.jallcom.2015.05.284>.
11. S. Sankaranarayanan, B.M. Ng, S. Jayalakshmi, M.G. Kumar, Q. B. Nguyen, M. Gupta, Microstructure and Mechanical Properties of a Magnesium-Aluminium-Erbium Alloy, in: *Magnes. Technol.* 2015, Springer, 2015: pp. 445–449.
12. J. Zhang, Z. Leng, M. Zhang, J. Meng, R. Wu, Effect of Ce on microstructure, mechanical properties and corrosion behavior of high-pressure die-cast Mg–4Al-based alloy, *J. Alloys Compd.* (2011). <https://doi.org/10.1016/j.jallcom.2010.09.185>.
13. A.K. Chaubey, S. Scudino, K.G. Prashanth, J. Eckert, Microstructure and mechanical properties of Mg–Al-based alloy modified with cerium, *Mater. Sci. Eng. A.* (2015). <https://doi.org/10.1016/j.msea.2014.11.081>.
14. S. Candan, M. Unal, E. Koc, Y. Turen, E. Candan, Effects of titanium addition on mechanical and corrosion behaviours of AZ91 magnesium alloy, *J. Alloys Compd.* (2011). <https://doi.org/10.1016/j.jallcom.2010.10.100>.

# Design of Heat-Dissipating Mg–La–Zn Alloys Based on Thermodynamic Calculations

Hui Shi, Qun Luo, Qian Li, Jieyu Zhang, and Kuo-Chih Chou

## Abstract

How to design alloys with good heat-dissipating capacity and predict the thermal conductivities of Mg–La–Zn alloys is an interesting and important topic. In this study, nine alloys were designed by thermodynamic phase diagram calculations in Mg–La–Zn system. Their compositions were determined by controlling phase components and the solid solubility of Zn in  $\alpha$ -Mg. The temperature dependence of thermal conductivities of as-cast Mg– $x$ La– $y$ Zn ( $x = 0.18$ – $0.37$  at.%,  $y = 0$ – $2.55$  at.%) alloys were investigated using flash method. Phase compositions and microstructure of heat-dissipating Mg–La–Zn alloys were also analyzed using X-ray diffraction and scanning electron microscopy. Considering the thermal conductivity of single-phase LaMg<sub>12</sub> alloy measured in the present work, the thermal conductivities of Mg–La–Zn alloys in the two-phase regions ( $\alpha$ -Mg + LaMg<sub>12</sub>) were also evaluated using the CALPHAD method. Results indicated that the Mg–La–Zn alloys with secondary phase (LaMg<sub>12</sub>) exhibited higher thermal conductivity than those with  $\tau_1$ , and the high solid solubility of Zn in  $\alpha$ -Mg was detrimental to the heat dissipation of Mg alloys. Meanwhile, the calculated thermal conductivities show good agreements with the corresponding experimental values.

## Keywords

Mg–La–Zn alloys • Thermal conductivity • CALPHAD • Microstructure

## Introduction

The Mg alloys are widely used in automotive, aircraft, aerospace, and 3C products as the lightweight metallic materials [1–4]. But the majority of commercial Mg alloys exhibit low thermal conductivity ( $\leq 100$  W/m K) [5–7]. So it is essential to develop new Mg-based alloys with excellent heat dissipation. In the past decade, Mg–RE-based alloys containing Zn elements have also aroused great interests among researches for their good heat dissipation [8]. The thermal conductivities of Mg–La–Zn alloys are investigated in our work because the solid solubility of La in  $\alpha$ -Mg is very low [9] and the element Zn has the minimal impact on the thermal conductivity of Mg alloys compared with other metallic elements [10]. However, most researches obtain alloys with good performance through trial-and-error, while CALPHAD is a powerful method for the determination of phase equilibria and can also be used in alloy design [11]. In our previous unpublished work, we have already optimized the thermodynamic database of Mg–La–Zn system, which offers a way for designing heat-dissipating alloys.

For heat-dissipating Mg alloys, phase composition and the solid solubility of Zn in  $\alpha$ -Mg are the main parameters which will have effects on the heat dissipation performance of Mg–La–Zn alloys [12]. Therefore, the Mg–La–Zn alloys with different secondary phase were designed based on the phase diagram. And the thermal conductivity of these alloys was experimentally measured. In addition, the thermal conductivities of alloys placed in the  $\alpha$ -Mg + LaMg<sub>12</sub> region were calculated using the CALPHAD method, which can predict that of other alloys in the same two-phase region.

## Experimental Details

Pure Mg (99.99 wt%), La (99.99 wt%), and Zn (99.99 wt%) were used as raw materials to synthesize the heat-dissipating Mg–La–Zn alloys #1–#4. The alloys were melted in vacuum

H. Shi · Q. Luo (✉) · Q. Li · J. Zhang · K.-C. Chou  
State Key Laboratory of Advanced Special Steel & Shanghai Key  
Laboratory of Advanced Ferrometallurgy & School of Materials  
Science and Engineering, Shanghai University & Shanghai  
Institute of Materials Genome & Materials Genome Institute,  
Shanghai University, 333 Nanchen Road, Shanghai, 200444,  
China  
e-mail: [qunluo@shu.edu.cn](mailto:qunluo@shu.edu.cn)

induction melting furnace under the protection of high purity Ar gas. The actual compositions of Mg–La–Zn alloys were measured by inductively coupled plasma atomic emission spectrometry (ICP-AES). The cast alloys were then analyzed by scanning electron microscopy (SEM) for the microstructure observation.

The samples were cut from cast ingots in the form of disks with a size of  $\varphi 10 \times 4$  mm. The thermal diffusivity measurements were performed by the laser-flash method ranging from 30 to 300 °C. The density of samples was determined using the method of Archimedes, and the specific heat capacity of alloys was measured by NETZSCH 204HP DSC from room temperature to 400 °C. The thermal conductivity  $\lambda$  [W/(m K)] was calculated as follows:

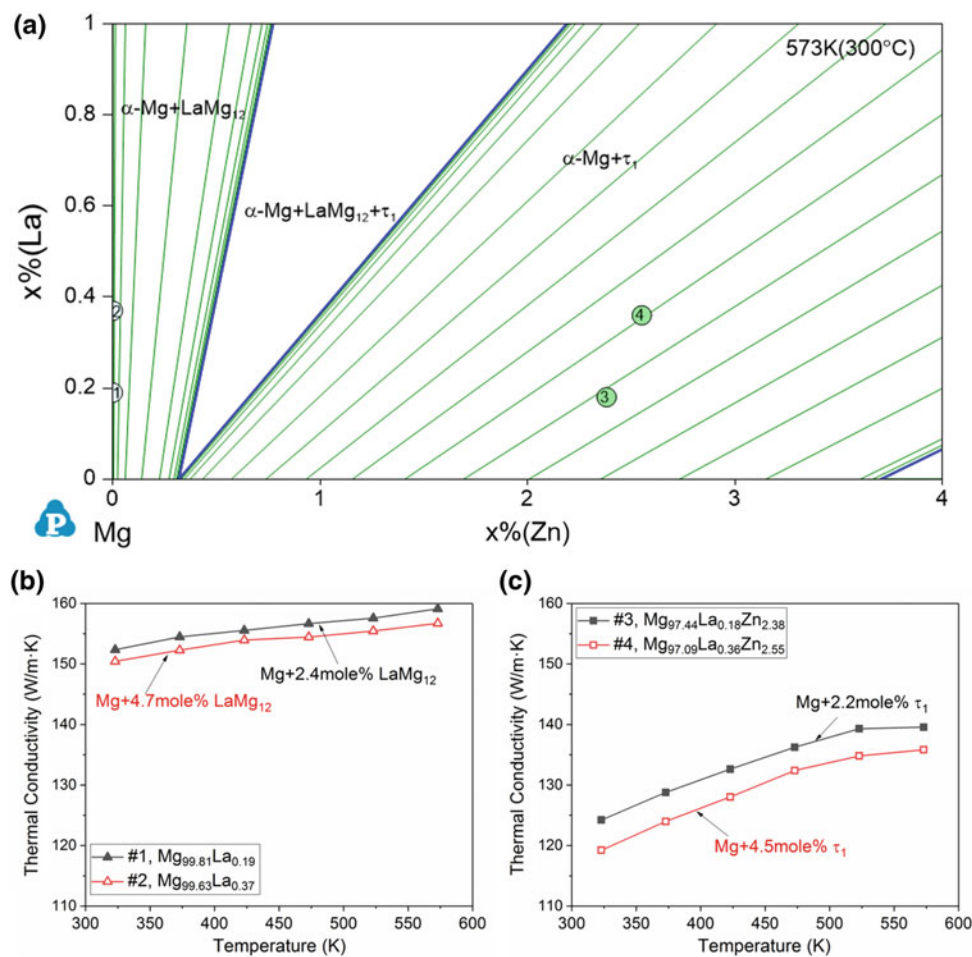
$$\lambda = \alpha \cdot \rho \cdot C_p \quad (1)$$

where  $\alpha$  is the thermal diffusivity ( $\text{mm}^2/\text{s}$ ),  $\rho$  is the density ( $\text{g}/\text{cm}^3$ ), and  $C_p$  is the specific heat capacity ( $\text{J}/\text{g K}$ )

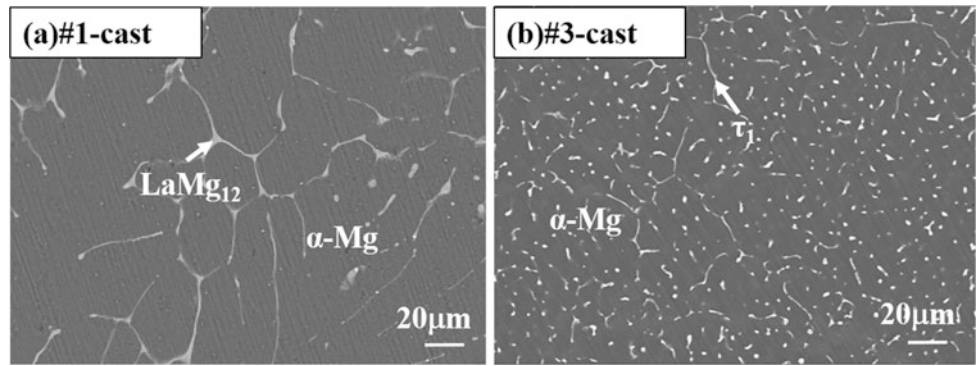
## Results and Discussion

### Thermal Conductivity of Mg–Zn–La Cast Alloys

The calculated isothermal section of the Mg–La–Zn system at 300 °C in the Mg-rich corner is shown in Fig. 1a, which indicates that several two-phase regions exist. Based on the aforementioned results, the intermetallic compounds,  $\text{LaMg}_{12}$  and  $\tau_1$ , equilibrate with the phase  $\alpha\text{-Mg}$ . However, the effect of the compounds on the thermal conductivity of Mg–La–Zn alloys remains unclear. Therefore, four alloys were designed in this work in order to investigate the influence of the types and amounts of intermetallic compounds on the heat dissipation. As we can see in Fig. 1a, among these four alloys, two alloys (#1-Mg<sub>99.81</sub>La<sub>0.19</sub> and #2-Mg<sub>99.63</sub>Mg<sub>0.37</sub>) were located in the  $\text{LaMg}_{12} + \alpha\text{-Mg}$  region and another two alloys (#3-Mg<sub>97.44</sub>La<sub>0.18</sub>Zn<sub>2.38</sub> and #4-Mg<sub>97.09</sub>La<sub>0.36</sub>Zn<sub>2.55</sub>) had the same precipitation phase  $\tau_1$ . The temperature dependence of the thermal conductivity of



**Fig. 1** a Calculated isothermal section of the Mg–La–Zn system at 300 °C in the Mg-rich corner, the temperature dependence of thermal conductivity of as-cast alloys, b #1 and #2, c #3 and #4

**Fig. 2** BSE images of cast alloys, a #1 and b #3**Table 1** Temperature dependence of thermal conductivity of single-phase LaMg<sub>12</sub>

Temperature (K)	323	373	423	473	523	573
Thermal conductivity $\lambda$ (W/m K)	27.95	29.96	32.10	33.39	35.46	36.68

the Mg–La–Zn alloys is shown in Fig. 1b, c. The thermal conductivity of the Mg–La–Zn cast alloys increased with increasing temperature and decreased with increasing La and Zn content.

### Microstructures of As-Cast Mg–La–Zn Alloys

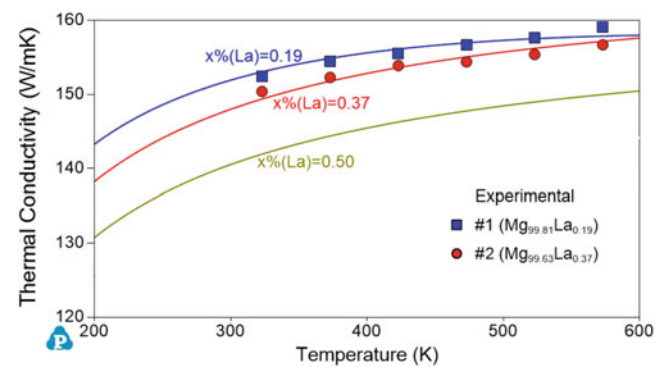
Figure 2 shows the BSE images of #1 (Mg<sub>99.81</sub>La<sub>0.19</sub>) and #3 (Mg<sub>97.44</sub>La<sub>0.18</sub>Zn<sub>2.38</sub>). The coexistence of LaMg<sub>12</sub> phase in white and  $\alpha$ -Mg in dark gray can be seen in sample #1, and the two-phase equilibrium of  $\tau_1 + \alpha$ -Mg is confirmed in sample #3. Compared with #1, the thermal conductivity of #3 decreased remarkably, which can be attributed to the  $\tau_1$  phase in the sample #3. The volume fraction of LaMg<sub>12</sub> in sample #1 is about 2.4 mol%, similar with that of  $\tau_1$  in sample #3. Therefore, both the phase  $\tau_1$  and LaMg<sub>12</sub> are detrimental to the heat dissipation performance of Mg–La–Zn alloys. But the inhibition effect of  $\tau_1$  on heat transfer is larger than that of LaMg<sub>12</sub>.

### Calculated Thermal Conductivity of Mg–La–Zn Alloys in $\alpha$ -Mg + LaMg<sub>12</sub> Region

The thermal conductivity of single-phase alloy LaMg<sub>12</sub> is shown in Table 1. The presence of the secondary phase LaMg<sub>12</sub> introduces new interfaces, and the  $^jM_{\alpha+\beta}$  ( $j$ th interface scattering parameter) was used to describe the influence of the second phase on the thermal conductivity. The thermal conductivity of the alloys in  $\alpha$ -Mg + LaMg<sub>12</sub> region is described by the following equation:

$$\lambda_{\alpha+\beta} = n_{\alpha} \cdot \lambda_{\alpha} + n_{\beta} \cdot \lambda_{\beta} - n_{\alpha} \cdot n_{\beta} \sum_{j=0}^j M_{\alpha+\beta} \cdot (n_{\alpha} - n_{\beta})^j \quad (2)$$

where  $\lambda_{\alpha+\beta}$  is the thermal conductivity of the alloys in two-phase region, and  $n_{\alpha}$ ,  $n_{\beta}$ ,  $\lambda_{\alpha}$ , and  $\lambda_{\beta}$  are the mole fraction and thermal conductivity of the phase  $\alpha$  and  $\beta$ . The parameter  $^jM_{\alpha+\beta}$  can be evaluated through the experimental data. Figure 3 shows the calculated thermal conductivities of #1 (Mg<sub>99.81</sub>La<sub>0.19</sub>) and #2 (Mg<sub>99.63</sub>La<sub>0.37</sub>) alloys in  $\alpha$ -Mg + LaMg<sub>12</sub> region, in good agreement with the experimental data in this work. Based on the database of thermal conductivity in Mg–La–Zn system, the predicted thermal conductivity of Mg<sub>99.5</sub>La<sub>0.5</sub> is also shown in Fig. 3.

**Fig. 3** Calculated thermal conductivities of #1 (Mg<sub>99.81</sub>La<sub>0.19</sub>) and #2 (Mg<sub>99.63</sub>La<sub>0.37</sub>) alloys in  $\alpha$ -Mg + LaMg<sub>12</sub> region, compared with the experimental data in this work and the predicted thermal conductivity of Mg<sub>99.5</sub>La<sub>0.5</sub>

## Conclusions

The thermal conductivity of as-cast Mg- $x$ La- $y$ Zn ( $x = 0.18$ – $0.37$  at.%,  $y = 0$ – $2.55$  at.%) alloys were measured from 30 to 300 °C. The results are summarized as follows:

- (1) The calculated isothermal section of Mg–La–Zn system in the Mg-rich corner can predict the phase composition and phase content of as-cast Mg–La–Zn alloys, which offers a flexible way for heat-dissipating Mg–La–Zn alloys design.
- (2) The thermal conductivities of as-cast Mg- $x$ La- $y$ Zn ( $x = 0.18$ – $0.37$  at.%,  $y = 0$ – $2.55$  at.%) alloys are greater than 120 W/(m K). The thermal conductivity of Mg–La–Zn alloys is closely related to the temperature, the solid solubility of Zn in  $\alpha$ -Mg, and the composition of secondary phase. The alloys containing the LaMg<sub>12</sub> phase exhibit higher thermal conductivity than  $\tau_1$  phase.
- (3) Based on the thermal conductivity of single-phase alloy LaMg<sub>12</sub>, the calculated thermal conductivities of alloys in the  $\alpha$ -Mg + LaMg<sub>12</sub> region show good agreements with the experimental results.

**Acknowledgements** This work was financially supported by the National Natural Science Foundation of China (51871143 and 51671118), Young Elite Scientists Sponsorship Program by CAST (2017QNRC001), Science and Technology Committee of Shanghai (16520721800), the “Chenguang” project supported by Shanghai Municipal Education Commission and Shanghai Education Development Foundation (17CG42), and the “111” projects (Grant No. D16002 and D17002).

## References

1. T.T. Zhang, H.W. Cui, X.L. Cui, E. Zhao, Y.K. Pan, R. Feng, Q.R. Jia, J. Zhao, Ductility enhancement in an as-extruded Mg-5.5Zn-0.8Zr alloy by Sm alloying, *J. Alloys Compd.*, 784 (2019) 1130–1138.
2. X.J. Wang, D.K. Xu, R.Z. Wu, X.B. Chen, Q.M. Peng, L. Jin, Y. C. Xin, Z.Q. Zhang, Y. Liu, X.H. Chen, G. Chen, K.K. Deng, H.Y. Wang, What is going on in magnesium alloys? *J. Mater. Sci. Technol.*, 34 (2018) 245–247.
3. M.Q. Zhang, Y. Feng, J.H. Zhang, S.J. Liu, Q. Yang, Z. Liu, R.G. Li, J. Meng, R.Z. Wu, Development of extruded Mg-6Er-3Y-1.5Zn-0.4Mn (wt.%) alloy with high strength at elevated temperature, *J. Mater. Sci. Technol.*, 35 (2019) 2365–2374.
4. C.C. Kammerer, S. Behdad, L. Zhou, et al., Diffusion kinetics, mechanical properties, and crystallographic characterization of intermetallic compounds in the Mg-Zn binary system, *Intermetallics*, 67 (2015) 145–155.
5. J.W. Yuan, K. Zhang, X.H. Zhang, X.G. Li, T. Li, Y.J. Li, M.L. Ma, G.L. Shi, Thermal characteristics of Mg–Zn–Mn alloys with high specific strength and high thermal conductivity, *J. Alloys Compd.*, 578 (2013) 32–36.
6. A. Rudajevová, P. Lukáč, Comparison of the thermal properties of AM20 and AS21 magnesium alloys, *Mater. Sci. Eng., A*, 397(2005) 16–21.
7. M. Yamasaki, Y. Kawamura, Thermal diffusivity and thermal conductivity of Mg–Zn–rare earth element alloys with long-period stacking ordered phase, *Scripta Mater*, 60(2009) 264–267.
8. A. Zafari, H.M. Ghasemi, R. Mahmudi, An investigation on the tribological behavior of AZ91 and AZ91 + 3 wt% RE magnesium alloys at elevated temperatures, *Mater Design*, 54(2014) 544–552.
9. L.L. Rokhlin, Structure and properties of alloys of the Mg-REM system, *Met Sci Heat Treat*, 48(2006) 487–490.
10. H.C. Pan, F.S. Pan, R.M. Yang, J. Peng, C.Y. Zhao, J. She, Z.Y. Gao, A.T. Tang, Thermal and electrical conductivity of binary magnesium alloys, *J. Mater Sci*, 49(2014) 3107–3124.
11. A.E. Gheribi, P. Chartrand, Application of the CALPHAD method to predict the thermal conductivity in dielectric and semiconductor crystals, *CALPHAD*, 39 (2012) 70–79.
12. T. Ying, M.Y. Zheng, Z.T. Li, X.G. Qiao, S.W. Xu, Thermal conductivity of as-cast and as-extruded binary Mg–Zn alloys, *J. Alloys Compd.*, 621(2015) 250–255.



# Effects of Zn Additions on the Room Temperature Formability and Strength in Mg–1.2Al–0.5Ca–0.4Mn Alloy Sheets

Z. H. Li, T. T. Sasaki, M. Z. Bian, T. Nakata, Y. Yoshida, N. Kawabe, S. Kamado, and K. Hono

## Abstract

We investigated the effects of Zn additions on the mechanical properties and microstructure of Mg–1.2Al–0.5Ca–0.4Mn and Mg–1.2Al–0.5Ca–0.4Mn–1.6Zn (wt %) alloy sheets fabricated by twin-roll casting and conventional hot rolling. The room temperature stretch formability of the solution-treated alloy sheet is improved by the addition of Zn. The Mg–1.2Al–0.5Ca–0.4Mn–1.6Zn alloy shows an excellent stretch formability with the larger Index Erichsen value of 8.2 mm due to a weak transverse direction split texture. The development of the weak texture is attributed to the uniform grain growth by the solute segregation to the recrystallized grain boundaries. Subsequent bake-hardening treatment, 2% pre-strain at 170 °C for 20 min leads to substantial increase in strength without the loss of ductility. The bake-hardened Mg–1.2Al–0.5Ca–0.4Mn–1.6Zn alloy exhibits a high tensile yield strength of 235 MPa with an elongation to failure of 27.1%.

## Keywords

Magnesium alloy • Formability • Bake hardening • Texture weakening • Recrystallization

## Introduction

Interstitial free steels and 6000 series aluminum alloys have been the materials of choice for automotive outer body panels for over decades as they offer a premium formability during the press-forming process and subsequently a prominent strengthening by the paint baking cycle, i.e. bake hardenability (BH) [1, 2]. Lightweight magnesium (Mg) alloys, especially wrought sheets, have recently drawn considerable attention due to the ever-growing demands for weight savings in the automotive industry [3, 4]. However, the actual usage of commercially available Mg sheets, such as Mg–3Al–1Zn–0.3Mn (wt%, AZ31) and Mg–1.5Zn–0.2Ce (wt%, ZE10), is quite limited because of their inferior mechanical properties in the room temperature (RT) formability or strength [5, 6]. The AZ31 alloy sheet shows a yield strength of 200 MPa, but a poor RT formability with the Index Erichsen (I.E.) value of less than 4 mm due to the strong basal texture; a distinct alignment of (0002) planes parallel to the sheet plane developed during the hot rolling [5]. The ZE10 alloy sheet, in contrast, exhibits a weak basal texture, and thus a much higher I.E. value of over 9 mm, while the low yield strength of below 150 MPa falls far behind the value required for the body panels [6]. To broaden the applications of Mg alloy sheets in the automotive industries, it is essential to develop the Mg alloy sheets with a good combination of the high-RT formability and high strength.

Mg–Al–Zn–Mn–Ca system is promising to overcome the strength-formability trade-off as evidenced in recent studies [7–9]. A Mg–3Al–1Zn–1Mn–0.5Ca (wt%, AZMX3110) alloy sheet produced by twin-roll casting (TRC) shows a good RT formability, I.E. value of 8 mm, and yield strength of 219 MPa in the solution-treated (T4) condition [7]. Following

The original version of this chapter was revised: Author provided figure corrections have been incorporated. The correction to this chapter is available at [https://doi.org/10.1007/978-3-030-36647-6\\_58](https://doi.org/10.1007/978-3-030-36647-6_58)

Z. H. Li (✉) · K. Hono  
Graduate School of Pure and Applied Science, University of Tsukuba, Tsukuba, 305-8577, Japan  
e-mail: [LI.Zehao@nims.go.jp](mailto:LI.Zehao@nims.go.jp)

Z. H. Li · T. T. Sasaki (✉) · M. Z. Bian · K. Hono  
National Institute for Materials Science, 1-2-1 Sengen, Tsukuba, 305-0047, Japan  
e-mail: [SASAKI.Taisuke@nims.go.jp](mailto:SASAKI.Taisuke@nims.go.jp)

T. Nakata · S. Kamado  
Nagaoka University of Technology, 1603-1, Kamitomioka, Nagaoka, 940-2188, Japan

Y. Yoshida · N. Kawabe  
Sumitomo Electric Industries, Ltd, 1-1-1 Koyakita, Itami, 664-0016, Japan

the IF steels and 6xxx series Al alloys, a bake-hardenable Mg–1.3Al–0.8Zn–0.7Mn–0.5Ca (wt%, AZMX1110) alloy was developed by TRC and exhibits a large I.E. value of 7.8 mm in the T4-treated condition at RT due to the weak basal texture; thereafter, this alloy can be substantially strengthened from 177 to 238 MPa by a bake-hardening treatment, 2% pre-strain and aging for only 20 min at 170 °C [9]. Since the development of weak basal texture in the AZMX alloy is mainly due to the addition of Zn, and the segregation of Zn with Ca and Al to the dislocations as well as the co-clustering is contributed to the strengthening by the bake-hardening treatment [8, 9], the Zn addition critically affects the microstructure and mechanical properties in the AXMZ dilute alloys. The aim of this work is to clarify the role of the Zn addition on the texture evolution and the mechanical properties such as the stretch formability and bake hardenability in a Mg–1.2Al–0.5Ca–0.4Mn alloy based on the detailed microstructure characterization.

## Experimental Procedure

Alloy sheets with nominal compositions of Mg–1.2Al–0.5Ca–0.4Mn and Mg–1.2Al–0.5Ca–0.4Mn–1.6Zn in wt% or Mg–1.1Al–0.3Ca–0.2Mn and Mg–1.1Al–0.3Ca–0.2Mn–0.6Zn in at.%, 260 mm wide × 4 mm thick were prepared by TRC process. The TRC sheets were homogenized at 450 °C for 2 h in a muffle furnace and followed by water quenching. The homogenized samples were subsequently rolled to a thickness of around 1 mm over four passes at 100 °C, with ~30% thickness reduction per pass. After each rolling pass, the sheets were reheated at 450 °C for 5 min prior to subsequent rolling. The as-rolled samples were subjected to a solution treatment at 450 °C for 1 h in a muffle furnace and artificially aged at 170 °C in an oil bath.

To evaluate the stretch formability of the solution-treated sheets, Erichsen cupping tests were performed on 55-mm<sup>2</sup> samples using an Erichsen 111 sheet metal testing machine with a 20-mm hemispherical punch at RT. The punch speed and blank-holder force were around 6 mm/min and 10 kN, respectively. Tensile tests were conducted at RT using a screw-driven Instron 5567 tensile test machine at an initial strain rate of 10<sup>-3</sup> s<sup>-1</sup>. Tensile specimens with a gage length of 12.5 mm and a width of 5 mm were machined from the solution-treated samples along the rolling direction, RD. To measure the bake-hardening behavior, the solution-treated tensile specimens are initially stressed to a nominal strain of 2%, then unloaded and aged at 170 °C for 20 min, and finally reload at RT. The difference between the flow stress at 2% strain and the 0.2% proof strength after aging is defined as the amount of bake hardening [10]. At least five samples were tested to ensure reproducibility of the tensile and Erichsen cupping test results.

Macrotextures were measured by X-ray diffraction (XRD) in Rigaku Smartlab 4-axis diffractometer using Cu–K $\alpha$  radiation at 40 kV with 200 mA. Pole figure data were analyzed using ResMat Textool 3.3 software. Microstructure and microtexture were characterized by a field emission scanning electron microscope (SEM), Carl Zeiss Cross Beam 1540EsB, equipped with an Oxford Instruments HKL Channel 5 electron backscatter diffraction (EBSD) system. The samples for the EBSD analysis were prepared by mechanical polishing and subsequent ion milling in Hitachi IM4000 system. For the quasi-in situ EBSD analysis, the samples were sealed in an Al foil and annealed at 450 °C in a salt bath. After annealing, the samples were water-quenched and slightly polished using OPS. EBSD data were analyzed using the TSL OIM 7.0 software. Transmission Kikuchi diffraction (TKD) was used to characterize the local microstructure of as-rolled samples. The TKD was conducted in a FEI Helios Nanolab 650 SEM equipped with a Bruker on-axis OPTIMUS<sup>TM</sup> TKD detector. High-angle annular dark-field scanning transmission electron microscopy (HAADF-STEM) and energy-dispersive X-ray (EDX) spectroscopy analysis were carried out using FEI Titan G<sup>2</sup> 80–200 TEM operated at 200 kV. Thin foils for the TEM observation were prepared by punching 3 mm-diameter and twin-jet electro-polishing in a solution of 5.3 g LiCl, 11.2 g Mg (ClO<sub>4</sub>)<sub>2</sub>, 500 ml methanol, and 100 ml 2-butoxy-ethanol at about –45 °C with a voltage of 90 V. Afterwards, the foils were cleaned using ion milling (Gatan PIPS) at 2 kV for 20 min.

## Results and Discussion

Figure 1 shows nominal tensile stress–strain curves of the solution-treated and bake-hardened (BH) AXM100 and AXMZ1002 alloys stretched along the RD. Table 1 summarizes the tensile yield strength,  $\sigma_{\text{TYS}}$ , ultimate tensile strength,  $\sigma_{\text{UTS}}$ , elongation to failure,  $\epsilon_T$ , and bake-hardening amount,  $\Delta\sigma_{\text{BH}}$ , obtained from the stress–strain curves. The solution-treated AXM100 alloy shows the  $\sigma_{\text{TYS}}$  and  $\sigma_{\text{UTS}}$  of 149 and 234 MPa with a  $\epsilon_T$  of 27.2%. The bake-hardened (BH) treatment resulted in remarkable increase in the  $\sigma_{\text{TYS}}$  and  $\sigma_{\text{UTS}}$  to 202 and 251 MPa at a slight expense of  $\epsilon_T$  to 25.3%. The  $\Delta\sigma_{\text{BH}}$  of the AXM100 alloy is about 29 MPa after the bake-hardening process, Fig. 1a. The solution-treated AXMZ1002 alloy exhibits higher  $\sigma_{\text{TYS}}$  and  $\sigma_{\text{UTS}}$  of 170 and 268 MPa but slightly lower  $\epsilon_T$  of 26.5% compared to the solution-treated AXM100 alloy. The BH treatment resulted in substantial increase in the  $\sigma_{\text{TYS}}$  and  $\sigma_{\text{UTS}}$  to 235 and 278 MPa without loss of the  $\epsilon_T$  to 27.1%. The addition of 1.6 wt% Zn led to an increase in the  $\Delta\sigma_{\text{BH}}$  to 37 MPa, which is larger than that of the AXM100 alloy, Fig. 1b. The stretch formability of solution-treated AXM100 and AXMZ1002 alloy sheets are evaluated by Erichsen cupping test at RT, and the snapshots of fractured samples after the test are shown elsewhere [11].

**Fig. 1** Nominal stress-strain curves of T4-treated and bake-hardened (BH) **a** AXM100 and **b** AXMZ1002 alloys

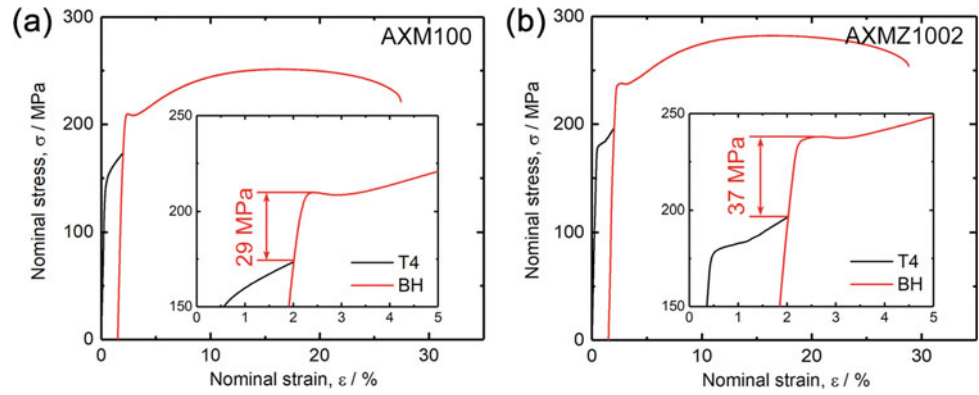


**Table 1** RT tensile properties of solute-treated (T4) and bake-hardened (BH) AXM100 and AXMZ1002 alloys stretched along the RD

Alloy	Condition	$\sigma_{TYS}$ , MPa	$\sigma_{UTS}$ , MPa	$\epsilon_T$ , %	$\Delta\sigma_{BH}$ , MPa	I.E., mm
AXM100	T4	$149 \pm 1$	$234 \pm 3$	$27.2 \pm 1.9$	29	$6.3 \pm 0.1$
	BH	$202 \pm 2$	$251 \pm 1$	$25.3 \pm 0.5$		–
AXMZ1002	T4	$170 \pm 1$	$268 \pm 2$	$26.5 \pm 1.1$	37	$8.2 \pm 0.1$
	BH	$235 \pm 2$	$278 \pm 2$	$27.1 \pm 1.3$		–

The solution-treated AXMZ1002 alloy sheet shows a large I.E. value of 8.2 mm, which is substantially higher than that of the AXM100 alloy sheet; 6.3 mm.

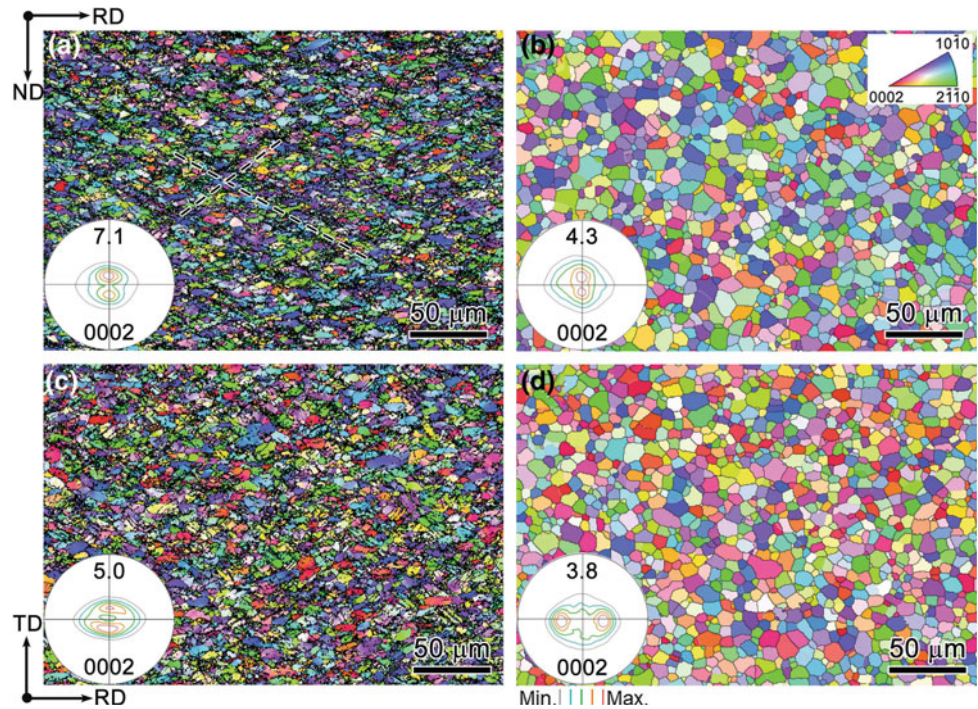
Figure 2 shows inverse pole figure (IPF) maps and (0002) pole figures of the as-rolled and solution-treated AXM100 and AXMZ1002 alloys. Note that the IPF maps were obtained by EBSD and taken from the planes normal to the TD, and the (0002) pole figures analyzed by the XRD were measured from the sheet normal direction (ND). The as-rolled AXM100 alloy shows a fraction of dark-colored areas with a band-like shape as indicated by dashed lines, which are regarded as shear bands, Fig. 2a. The as-rolled AXMZ1002 alloy, in contrast, shows no obvious shear bands but containing a large number of deformation twins within the deformed grains, Fig. 2c. The solution-treated samples consist of fine recrystallized grains with equiaxed shape, and the mean grain size is 8.9 and 8.4  $\mu\text{m}$  for the AXM100 and AXMZ1002 alloys, respectively, Fig. 2b, d. The (0002) pole figures show that the as-rolled AXM100 alloy exhibits an RD-split texture; the (0002) poles are tilted by  $\sim 15^\circ$  toward the RD as well as the solution-treated sample, Fig. 2a, b, but has a higher texture intensity. The 1.6 wt% Zn addition does not influence the texture distribution of the as-rolled sample, which also shows a strong RD-split texture, Fig. 2c, but significantly modifies the solution-treated texture from the RD-split texture to the TD-split texture; the (0002) poles are tilted by  $\sim 40^\circ$  towards the TD,

Fig. 2d. These results indicate that the Zn addition leads to the development of the TD-split texture during the solution treatment.

To reveal the texture evolution by the Zn addition, the static recrystallization behaviors of the AXM100 and AXMZ1002 alloys subjected to 450  $^\circ\text{C}$  annealing were tracked by a quasi-in situ EBSD method [12]. Figure 3 shows the IPF maps and (0002) pole figures of the AXM100 and AXMZ1002 alloys at various annealing intervals; taken from 0 s, the as-rolled condition, to 10 s, nearly the full recrystallization of same sampling areas, and the corresponding recrystallized grains are extracted by defining a maximum grain orientation spread of  $1^\circ$ . The microstructure and texture of the AXM100 and AXMZ1002 alloys evolve with the increasing annealing time. The as-rolled AXM100 sample shows a number of shear bands and few recrystallized grains,  $\sim 1.3\%$  of the area surveyed. The area fraction of shear bands shows little change after 2 s of annealing, and the fraction of recrystallized grains slightly increases to  $\sim 3.1\%$ . However, few shear bands are observed after annealing for 5 s, and the recrystallized area fraction significantly increases and occupies about 27.8% of the sampling area. The sample is almost fully recrystallized after 10 s of annealing with a recrystallized area fraction of  $\sim 90.1\%$ . From the (0002) pole figures, the RD-split texture is observed in both as-rolled AXM100 sample and the corresponding recrystallized grains, and it remains with



**Fig. 2** EBSD IPF maps and (0002) pole figures of the as-rolled and solution-treated **a**, **c** AXM100 and **b**, **d** AXMZ1002 alloys



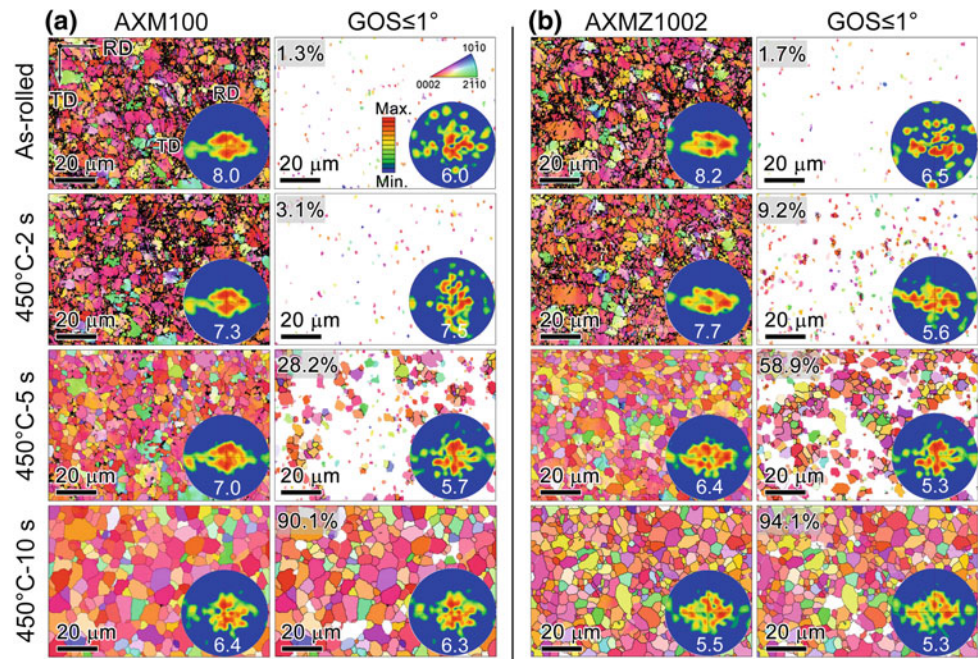
increasing annealing time, which is consistent with the above XRD results. The maximum intensity of basal poles gradually decreases from 8.0 m.r.d in the as-rolled state to 6.4 m.r.d in the fully recrystallized state, Fig. 3a. The recrystallization kinetics of the AXMZ1002 alloy is much faster compared to the AXM100 alloy; the recrystallized area fraction of about 58.9% after 5 s of annealing is about twice larger than that of the AXM100 alloy. The (0002) pole figures of the as-rolled AXMZ1002 sample shows a quadruple-split texture; the basal poles are tilted by  $\sim 15^\circ$  towards the RD and  $\sim 40^\circ$  towards the TD as well as the corresponding recrystallized grains, which are different from the aforementioned RD-split texture. The quadruple-split texture subsequently evolves to the TD-split texture with increasing annealing time, and suggesting the TD-split texture is produced during annealing in the AXMZ1002 alloy, Fig. 3b.

To explore the growth behavior of recrystallized grains with specific orientations during the annealing, the two groups of recrystallized grains: RD-tilted texture components (RTC) with the basal poles tilted by  $10\text{--}20^\circ$  towards the RD and TD-tilted texture components (TTC) with the basal poles tilted by  $35\text{--}45^\circ$  towards the TD are tracked. Figure 4a shows the average grain size of recrystallized grains with RD- and TD-tilted texture components in the AXM100 and AXMZ1002 alloys as a function of annealing time at  $450^\circ\text{C}$ . The average grain size of both alloys slightly increases from 0 to 2 s annealing, and substantial grows afterwards. The average grain size of the RTC in the AXM100 alloy increases to  $\sim 8.2\ \mu\text{m}$  after annealing for 10 s, which is larger than that of the TTC,  $\sim 6.1\ \mu\text{m}$ . The AXMZ1002 alloy, in contrast,

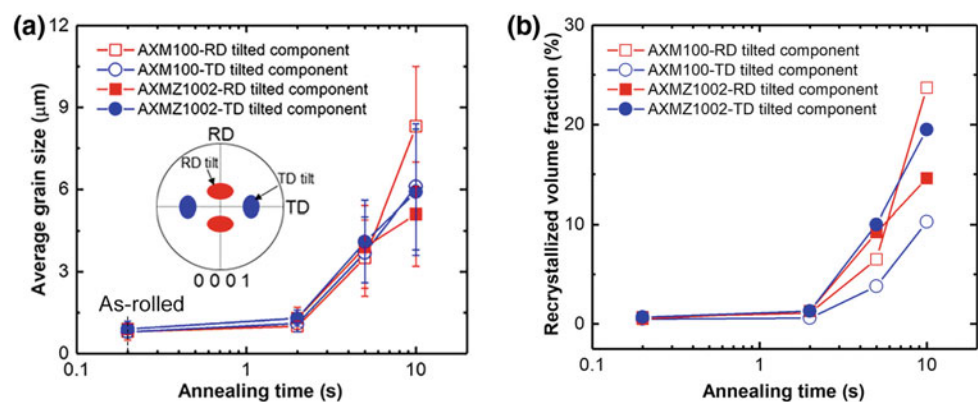
exhibits a uniform grain growth for the RTC and the TTC, about 5.1 and  $5.9\ \mu\text{m}$  after 10 s of annealing, which is smaller than those of the AXM100 alloy. Figure 4b exhibits the recrystallized area fraction of the RD- and TD-tilted texture components in the AXM100 and AXMZ1002 alloys as a function of annealing time. The area fraction of each component in both alloys shows a similar tendency as the average grain size with increasing annealing time. The area fraction of the RTC in the AXM100 alloy is much larger than that of TTC after annealing for 10 s; the area fraction of RTC increases from 1.1 to 23.7% with increasing the annealing time from 2 to 10 s while the TTC increases from 0.6 to 10.3%. 1.6 wt% Zn additions lead to a decrease in the area fraction of the RTC,  $\sim 14.6\%$  after 10 s annealing, which is smaller than that of the AXM100 alloy, while the area fraction of 19.5% in the TTC is larger than that of the RTC as well as the AXM100 alloy.

Figure 5a shows the HADDF-STEM image and EDX elemental maps of the solution-treated AXMZ1002 alloy. A large number of nano-scale particles are observed within the grains and along the grain boundaries. The EDS elemental maps indicate that most of particles are enriched in Al and Ca or Al and Mn, which are identified as  $\text{Al}_2\text{Ca}$  and  $\text{Al}_8\text{Mn}_5$  phases [7]. Beside, a few undissolved Ca par Fig. 5b exhibits the atomic resolution HAADF-STEM image of the grain boundary indicated by an arrow in Fig. 5a and the corresponding EDX elemental maps, suggesting that Al, Ca, and Zn co-segregated along the grain boundary. The EDX line scan across the grain boundary shows that the concentration of Zn solute in the grain boundary is higher

**Fig. 3** Quasi-in situ EBSD IPF maps and (0002) pole figures of the as-rolled samples recrystallized at the various annealing intervals and the corresponding recrystallized grains extracted by defining a maximum GOS of  $1^\circ$ . **a** AXM100 and **b** AXMZ1002 alloys



**Fig. 4** **a** Average grain size and **b** recrystallized volume fraction of RD-tilted and TD-tilted recrystallized texture components as a function of annealing time in the AXM100 and AXMZ1002 alloys



than those of Ca and Al, while the Mn shows no segregation along the grain boundary. Table 2 summarizes the solute content in the matrix of solution-treated AXM100 and AXMZ1002 alloys. The concentration of Al, Ca, and Mn solutes in the matrix of the AXM100 alloy is about 0.45, 0.18, and 0.07 at.%, respectively. The AXMZ1002 alloy not only shows a similar content of Al, Ca, and Mn solutes as in the AXM100 alloy but also contains  $\sim 0.36$  at.% Zn in the matrix.

In this work, we have investigated the effect of Zn additions on the mechanical properties and microstructure of the AXM100 and AXMZ1002 alloys. The AXMZ1002 alloy exhibits a large I.E. value of 8.2 mm in the solution-treated condition at RT and a high yield strength of 235 MPa in the bake-hardened condition with a bake hardenability of 37 MPa, which are comparable to those of 6xxx series Al alloys [2, 13].

The Zn addition improves the RT stretch formability of the solution-treated sample with the I.E. value substantially increased from 6.3 to 8.2 mm by the addition of 1.6 wt% Zn, Fig. 1. The improved RT formability is mainly attributed to the formation of the weak TD-split (0002) texture, Fig. 2; therefore, a greater number of grains in the AXMZ1002 alloy are favorably oriented for basal  $\langle a \rangle$  slip to activate during the stretch forming at RT compared to the AXM100 alloy. Besides, a first-principle calculation by Yuasa et al. suggested that prismatic  $\langle a \rangle$  slip could occur more easily by the addition of Zn in the Mg–Ca alloy [14], and the recent experiment by the EBSD-assisted slip trace analysis also identified that the AXMZ1002 alloy shows the enhanced activity of prismatic  $\langle a \rangle$  slip during the stretch forming compared to the AXM100 alloy [11]. Thus, we can conclude that the improved stretch formability by the Zn addition is attributed to the development of the TD-split texture as well



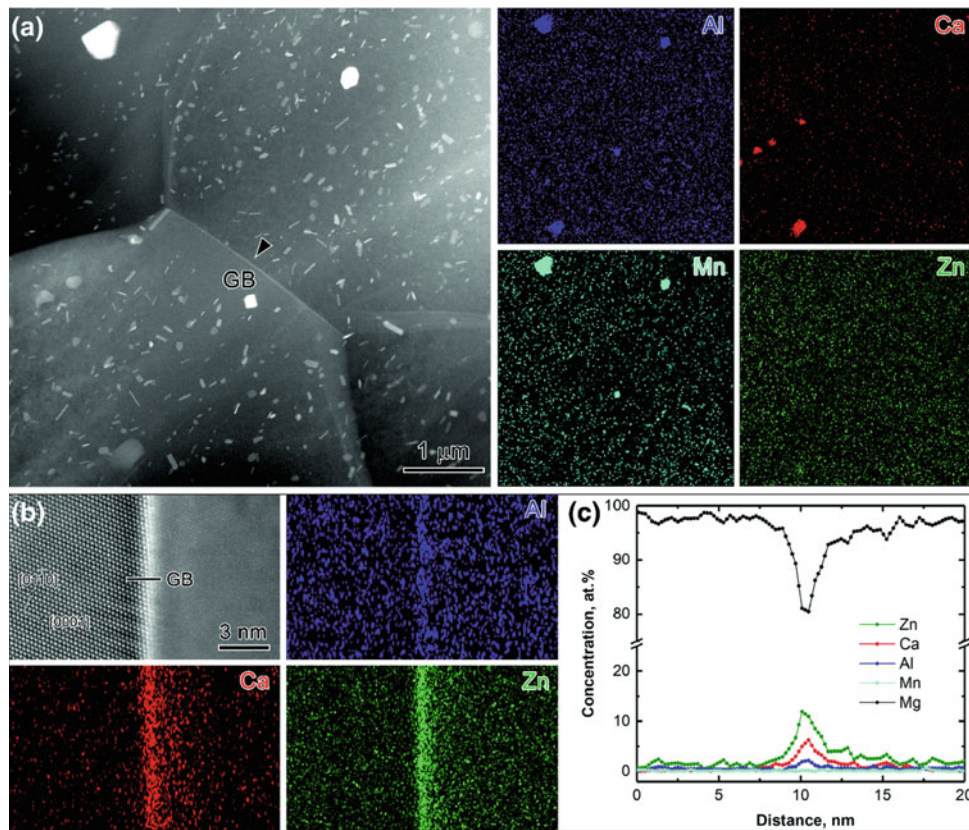


**Fig. 5** **a** Low magnification HAADF-STEM image and corresponding STEM-EDX elemental maps of Al, Ca, Mn, and Zn in the T4-treated AXMZ1002 sample, **b** atomic resolution HAADF-STEM image of the grain boundary indicated by an arrow in **(a)** and

corresponding STEM-EDX elemental maps of Al, Ca, and Zn, and **c** the compositional profile across the grain boundary indicated by a solid line in **(b)**

**Table 2** STEM-EDS results obtained from the matrix of T4-treated AXM100 and AXMZ1002 alloys

Alloy (at.%)	Al	Ca	Mn	Zn	Mg
AXM100	0.45 ± 0.01	0.18 ± 0.01	0.07 ± 0.02	–	Bal.
AXMZ1002	0.51 ± 0.02	0.19 ± 0.01	0.08 ± 0.01	0.36 ± 0.02	Bal.

as the activation of the non-basal slip as mechanisms to accommodate the deformation along the thickness direction.

The formation of the TD-split texture by the Zn addition is tightly bound up with the recrystallization during the solution treatment since both AXM100 and AXMZ1002 alloys show a similar RD-split texture in the as-rolled condition, Fig. 2. Quasi-in situ EBSD analysis shows that the AXM100 alloy maintains the RD-split texture throughout the recrystallization process, while the TD-tilted texture components are developed even in the as-rolled AXMZ1002 alloy and becomes stronger with the progress of recrystallization, Fig. 3. Since the deformation texture is determined by the different deformation mechanism operating during hot rolling, detailed studies by Kim et al. indicate that the compression or double twins formed in deformation bands can induce the splitting of

basal poles toward the RD [14]. The recent work shows that the double twins are prominent in both as-rolled AXM100 alloy and AXMZ1002 alloy, leading to the formation of the RD-split texture [11], while the enhanced activation of prismatic  $\langle a \rangle$  slip in the AXMZ1002 alloy might be responsible for the development of the TD-tilted component as mentioned above. The increased double twins and prismatic  $\langle a \rangle$  slip may also improve the stored energy of hot rolling, giving rise to the faster recrystallization kinetics in the AXMZ1002 alloy. As the recrystallized grains with the RD-tilted texture in the AXM100 alloy shows a faster growth than the TD-tilted components, Fig. 4, the preferential growth of these recrystallized grains would largely preserve the deformation texture; the RD-split texture as evidenced in other conventional Mg alloys, e.g. AZ31 alloy [15]. The AXMZ1002 alloy, in

contrast, exhibits a more uniform growth of recrystallized grains, leading to the TD-split texture evolved during the static recrystallization. Since the preferential growth of RD-tilted recrystallized grains is normally due to the high-energy grain boundaries; resulting in high boundary mobility [16], the strong co-segregation of Zn with Ca and Al atoms to the grain boundaries in the AXMZ1002 alloy may reduce the boundary energy and restricts the fast growth of recrystallized grains along the grain boundaries, Fig. 5. Therefore, the Zn addition plays an important role in promoting the uniform grain growth, leading to the formation of the TD-split texture. The similar viewpoint has also been reported in the recent studies [12, 17]. However, a clear correlation between the orientation of the TD-tilted component; c-axis tilted 30–45 away from ND to the TD, and the nucleation sites of recrystallized grains remain to be clarified in the future work.

The addition of Zn leads to the increase in the bake hardenability; the  $\Delta\sigma_{BH}$  of 37 MPa by 2% pre-strain and aging at 170 °C for 20 min in the AXMZ1002 alloy is larger than that of the AXM100 alloy, 29 MPa, and even comparable to the reported 6016 Al alloy sheet, 35 MPa [2]. This is owing to the dissolution of 0.36 at.% Zn atoms in the matrix of the AXMZ1002, Table 2, which contributed to the solute segregation along the dislocations and the formation of nano-clusters with the Ca and Al [9]. Considering other factors that affect the bake hardenability, e.g. dislocation density, grain size, etc. [18], although the Zn addition does not change the average grain size, about 8.9 and 8.4  $\mu\text{m}$  for the AXM100 and AXMZ1002 alloys, respectively, the texture modification by the addition of Zn would affect the activation of dislocations during the pre-strain along the RD and thus may influence the dislocation density before baking. Future work needs to shed light on the effect of texture distribution on the dislocation density during the pre-strain.

## Summary

In this work, the effect of Zn additions on the microstructure and mechanical properties was thoroughly investigated. A large I.E. value of 8.2 mm with a high tensile yield strength of 235 MPa is achieved in the developed Mg–1.2Al–0.5Ca–0.4Mn–1.6Zn (AXMZ1002) alloy. The addition of 1.6 wt% Zn to the Mg–1.2Al–0.5Ca–0.4Mn (AXM100) alloy results in a significant RT formability improvement; I.E. value increases from 6.3 to 8.2 mm in the solution-treated samples due to the texture weakening and enhanced activity of prismatic  $\langle a \rangle$  slip during the stretch-forming process. The development of TD-split texture is the uniform grain growth by the strong solute segregation along the grain boundaries.

**Acknowledgements** This work was supported by Advanced Low Carbon Technology Research and Development Program (ALCA), 12102886, JSPS KAKENHI Grant Number JP18H01756, and Iketani Science and Technology Foundation.

## References

1. L.J. Baker, S.R. Daniel, J.D. Parker, *Mater. Sci. Technol.* 18 (2002) 355–368.
2. Y. Birol, Pre-aging to improve bake hardening in a twin-roll cast Al–Mg–Si alloy, *Mater. Sci. Eng. A* 391 (2005) 175–180.
3. W.J. Joost, P.E. Krajewski, Towards magnesium alloys for high-volume automotive applications, *Scr. Mater.* 128 (2017) 107–112.
4. D. Letzig, J. Bohlen, Gerrit Kurz, J. Victoria-Hernandez, R. Hoppe, S. Yi, Development of magnesium sheets, *Magnesium Technology 2018*, TMS, 2018, pp. 355–360.
5. A. Styczynski, Ch. Hartig, J. Bohlen, D. Letzig, Cold rolling textures in AZ31 wrought magnesium alloy, *Scr. Mater.* 50 (2004) 943–947.
6. S. Yi, J. Bohlen, F. Heinemann, D. Letzig, Mechanical anisotropy and deep drawing behaviour of AZ31 and ZE10 magnesium alloy sheets, *Acta Mater.* 58 (2010) 592–605.
7. T.T.T. Trang, J.H. Zhang, J.H. Kim, A. Zargar, J.H. Hwang, B.-C. Suh, N.J. Kim, Designing a magnesium alloy with high strength and high formability, *Nat. Commun.* 9 (2018) 2522.
8. M.Z. Bian, T.T. Sasaki, B.C. Suh, T. Nakata, S. Kamado, K. Hono, A heat-treatable Mg–Al–Ca–Mn–Zn sheet alloy with good room temperature formability, *Scr. Mater.* 138 (2017) 151–155.
9. M.Z. Bian, T.T. Sasaki, T. Nakata, Y. Yoshida, N. Kawabe, S. Kamado, K. Hono, Bake-hardenable Mg–Al–Zn–Mn–Ca sheet alloy processed by twin-roll casting, *Acta Mater.* 158 (2018) 278–288.
10. S. Hanai, N. Nahayasu, Y. Tokunaga, Y. Mizuyama, Effect of grain size and solid solution the bake hardenability of low carbon strengthening elements aluminum-killed steel, *Trans. Iron Steel Inst. Jpn* 24 (1984) 17–23.
11. Z.H. Li, T.T. Sasaki, M.Z. Bian, T. Nakata, Y. Yoshida, N. Kawabe, S. Kamado, K. Hono, Effects of Zn additions on the room temperature formability and strength in Mg–1.2Al–0.5Ca–0.4Mn alloy sheets, Under Review.
12. Z.R. Zeng, Y.M. Zhu, S.W. Xu, M.Z. Bian, C.H.J. Davies, N. Biribilis, J.F. Nie, Texture evolution during static recrystallization of cold-rolled magnesium alloys, *Acta Mater.* 105 (2016) 479–494.
13. M. Sugamata, J. Kaneko, M. Numa, Evaluation of formability of light metal sheets at high temperatures by conical cup and erichsen tests, *J. Jpn. Soc. Technol. Plast.* 41 (2000) 233–238.
14. M. Yuasa, N. Miyazawa, M. Hayashi, M. Mabuchi, Y. Chino, Effects of group II elements on the cold stretch formability of Mg–Zn alloys, *Acta Mater.* 83 (2015) 294–303.
15. D.W. Kim, B.C. Suh, M.S. Shim, J.H. Bae, D.H. Kim, N.J. Kim, *Metall. Mater. Trans. A* 44 (2013) 2950–2961.
16. J.Y. Lee, Y.S. Yun, B.C. Suh, N.J. Kim, W.T. Kim, D.H. Kim, Comparison of static recrystallization behavior in hot rolled Mg–3Al–1Zn and Mg–3Zn–0.5Ca sheets, *J. Alloys Compd.* 589 (2014) 240–246.
17. J.W. Cahn, The impurity-drag effect in grain boundary motion, *Acta Metall.* 10 (1962) 789–798.
18. S. Das, S.B. Singh, and O.M. Mohanty, *Encyclopedia of Iron, Steel, and Their Alloys*, CRC Press, 2016, pp. 306–319.
19. D. Guan, X. Liu, J. Gao, L. Ma, B.P. Wynne, W.M. Rainforth, exploring the mechanism of “Rare earth” texture evolution in a lean Mg–Zn–Ca alloy, *Sci. Rep.* 9 (2019) 7152.

---

**Part IV**

**Fundamentals, Mechanical Behavior, Twinning,  
Plasticity, and Texture I**

# An Investigation into the Role of Dislocation Climb During Intermediate Temperature Flow of Mg Alloys

Michael A. Ritzo, Jishnu J. Bhattacharyya, Ricardo A. Lebensohn, and Sean R. Agnew

## Abstract

Textured Mg alloy sheet samples were tensile tested parallel to the transverse direction, at Zener–Hollomon parameter values ranging from  $Z \sim 50$  at room temperature and  $10^{-3} \text{ s}^{-1}$  down to  $Z \sim 18$  at  $350 \text{ }^\circ\text{C}$  and  $10^{-5} \text{ s}^{-1}$ . At high  $Z$ , the samples exhibit strong texture evolution indicative of significant prismatic slip of dislocations with  $\langle a \rangle$  Burgers vectors. Correspondingly, the plastic anisotropy is high,  $r \sim 4$ . At low  $Z$ , the texture evolution is minimal and the response is nearly isotropic,  $r \sim 1$ . Previously, it has been asserted that the high ductility and low plastic anisotropy observed at low  $Z$  conditions is due to enhanced activity of non-basal slip modes, including prismatic slip of  $\langle a \rangle$  dislocations and pyramidal slip of  $\langle c+a \rangle$  and  $\langle c+a \rangle$  dislocations. The present results call this understanding into question and suggest that the enhanced ductility is more closely associated with the climb of  $\langle a \rangle$  dislocations.

## Keywords

Texture • Anisotropy • Dislocation • Climb • Glide

## Introduction

The use of polycrystal plasticity modeling has radically changed our understanding of the deformation of hexagonal close-packed (hcp) Mg alloys. Historically, it was believed that non-basal slip was not a significant contributor to the deformation of polycrystalline Mg alloys, unless the temperature was in excess of  $200 \text{ }^\circ\text{C}$  [e.g., 1]. Since that time, it has been repeatedly shown that non-basal slip of  $\langle a \rangle$  dislocations is surprisingly active in textured Mg alloy polycrystals, even at room temperature [e.g., 2]. Evidence in support of this fact are the observed high  $r$ -values of tensile tested Mg alloy sheets with strong basal textures, as well as the evolution of that texture toward one which exhibits near sixfold symmetry in the prismatic pole figure. Along with this new understanding of the low temperature deformation came another surprising revelation. The relative activity of non-basal  $\langle a \rangle$  slip could not continue increasing at elevated temperatures because the  $r$ -values were shown to decrease with temperature, not increase. Furthermore, the characteristic sixfold feature in the prismatic pole figures becomes weaker, not stronger.

A possible solution to the problem was offered in terms of pyramidal  $\langle c+a \rangle$  slip, which provides the hcp crystals with a way to accommodate compression along their  $c$ -axes [e.g., 3]. It was shown that increasing the activity of  $\langle c+a \rangle$  slip would lead to a reduction in  $r$ -value (and even a reduction in the intensity of the sixfold symmetric texture), in agreement with what is observed during higher temperature deformation. It was reasonably concluded that increased temperature must lead to increased activity of this thermally activated deformation mechanism. This hypothesis has become widely accepted, leading to a worldwide focus on better understanding the behavior of these unusual  $\langle c+a \rangle$  dislocations, which have a Burgers vector which is nearly twice as large as that of the common  $\langle a \rangle$ -type dislocation [e.g., 4–6]. Researchers have furthermore come to accept the notion that increasing  $\langle c+a \rangle$  slip activity may hold the key to

M. A. Ritzo · J. J. Bhattacharyya · S. R. Agnew (✉)  
 Department of Materials Science and Engineering, University of Virginia, Charlottesville, VA 22904, USA  
 e-mail: [agnew@virginia.edu](mailto:agnew@virginia.edu)

M. A. Ritzo  
 e-mail: [mar3dm@virginia.edu](mailto:mar3dm@virginia.edu)

J. J. Bhattacharyya  
 e-mail: [jjb4cp@virginia.edu](mailto:jjb4cp@virginia.edu)

R. A. Lebensohn (✉)  
 Materials Science and Technology Division, Los Alamos National Laboratory, MS G755, Los Alamos, NM 87545, USA  
 e-mail: [lebenso@lanl.gov](mailto:lebenso@lanl.gov)



unlocking potential ductility of Mg alloys [7–9]. The notion that  $\langle c+a \rangle$  slip occurs is not in question, because both texture data and TEM investigation have repeatedly shown evidence for this slip mode. However, the idea that increased temperature leads to greatly increased  $\langle c+a \rangle$  slip activity is not strongly supported by the data.

In this paper, we propose an alternative explanation for the changes in  $r$ -value and texture evolution, which are observed at elevated temperatures. *It is hypothesized that the climb of  $\langle a \rangle$  dislocations (rather than slip of non-basal dislocations) is responsible for the reduced  $r$ -values, altered texture evolution, and even improved ductility of textured Mg alloys which is observed at elevated temperatures.* The notion that dislocation climb becomes more important at elevated temperatures is not at all revolutionary. However, it has only recently become possible to explore the effect that dislocation climb will have on the anisotropy and texture evolution of textured polycrystals. Along with collaborators, one of the co-authors developed a viscoplastic self-consistent (VPSC) polycrystal modeling code, which accounts for the non-conservative (climb) motion of dislocations [10, 11].

We begin by providing a brief introduction to the model, followed by a description of experimental methods and results which highlight the effects we are hoping to explain, and then enumerate simulation results which illustrate that a model which accounts for dislocation climb mediated flow can provide a satisfactory explanation for observed transitions in both anisotropy and texture evolution. Only tensile deformation of a well-studied case, basal textured Mg alloy AZ31B sheets is considered in this preliminary study. This avoids the complexity of simultaneous consideration of dislocation motion and deformation twinning-mediated plasticity. Only tensile deformation parallel to the sheet transverse direction is considered because previous studies have revealed this direction exhibits the most contrast with respect to the temperature-dependent phenomena of interest.

## Modeling Background

Crystal plasticity models generally consider dislocation glide and twinning [12, 13] as the only dissipative processes. In addition, both slip and twinning are assumed to be governed the generalized Schmid law, which computes the resolved shear stress on a slip system as follows:

$$\boldsymbol{\tau} = \mathbf{m} : \boldsymbol{\sigma} \quad (1)$$

where  $\mathbf{m} = \text{sym}(\hat{\mathbf{b}} \otimes \hat{\mathbf{n}})$  is the Schmid tensor, which resolves the grain-level stress  $\boldsymbol{\sigma}$  onto the slip plane and in the slip direction [e.g., 14]. The role of cross-slip is usually loosely connected to the process of dynamic recovery [15],

and dislocation climb is for the most part disregarded. Lebensohn et al. [10] generalized the connection between stress and dislocation motion, beyond the Schmid law of Eq. 1, by appealing to the full Peach–Koehler relationship,

$$\mathbf{f} = (\boldsymbol{\sigma} \cdot \mathbf{b}) \times \hat{\mathbf{t}} \quad (2)$$

where  $\mathbf{b}$  is the Burgers vector and  $\hat{\mathbf{t}}$  is the dislocation line direction. The forces which drive dislocation glide can then be parsed from those which drive climb. The force which drives glide is nothing other than the Schmid stress times the magnitude of the Burgers vector.

$$\mathbf{f}_g = \{(\boldsymbol{\sigma} \cdot \mathbf{b}) \times \hat{\mathbf{t}}\} \cdot \hat{\boldsymbol{\chi}} = \{\boldsymbol{\sigma} : (\hat{\mathbf{b}} \otimes \hat{\mathbf{n}})\} |\mathbf{b}| \quad (3)$$

where  $\hat{\boldsymbol{\chi}}$  is the direction of dislocation glide (orthogonal to the line direction). On the other hand, the climb force is resolved along the glide plane normal direction.

$$\mathbf{f}_c = \{(\boldsymbol{\sigma} \cdot \mathbf{b}) \times \hat{\mathbf{t}}\} \cdot \hat{\mathbf{n}} = -\{\boldsymbol{\sigma} : (\hat{\mathbf{b}} \otimes \hat{\boldsymbol{\chi}})\} |\mathbf{b}| \quad (4)$$

Notably, the glide force only depends upon the deviatoric stress (the addition of pressure has no effect), whereas the climb force depends on the full stress tensor. For dislocation glide, the dyadic cross product  $\hat{\mathbf{b}} \otimes \hat{\mathbf{n}}$  can be decomposed into symmetric (strain,  $\mathbf{m}$ ) and antisymmetric (rotation,  $\mathbf{q}$ ) components. Indeed, this slip-induced rotation is the basis of texture evolution during glide. For climb, the analogous tensor,  $\hat{\mathbf{b}} \otimes \hat{\boldsymbol{\chi}}$ , can be decomposed into symmetric strain ( $\mathbf{k}$ ) and rotation ( $\mathbf{r}$ ) components. The distinct types of strain and rotation associated with climb and glide provide a means by which their contributions to the deformation may be parsed. For example, the strain rate within a crystal undergoing glide and climb may be expressed as a function the applied stress as follows.

$$\dot{\boldsymbol{\epsilon}} = \sum_s \mathbf{m}^s \left( \frac{f^s}{\tau_c^s b^s} \right)^{n_g} \text{sign}(\mathbf{m} : \boldsymbol{\sigma}) + \sum_s \mathbf{k}^s \left( \frac{f^c}{\sigma^c b^s} \right)^{n_c} \text{sign}(\mathbf{k} : \boldsymbol{\sigma}) \quad (5)$$

Although it is not a focus of the present work, it is mentioned that the code incorporates an adaptation in which Lebensohn et al. [11] expanded the model to account for the “chemical” (or osmotic) force due to the non-equilibrium vacancy concentration that will develop in the vicinity of the climbing dislocations which was expressed as follows:

$$\mathbf{f}_{\text{chem}} = \left\{ \frac{kT}{\Omega} \ln \left( \frac{c}{c_{0,P,T}} \right) \mathbf{I} : (\hat{\mathbf{b}} \otimes \hat{\boldsymbol{\chi}}) \right\} |\mathbf{b}| \quad (6)$$

where  $k$  is Boltzman’s constant,  $\Omega$  is the atomic volume,  $c$  is the vacancy concentration near the dislocation,  $c_{0,P,T}$  is the equilibrium vacancy concentration at the given pressure and



temperature, and  $\mathbf{I}$  is the identity matrix. The relationship is further complicated by the fact that one must track the character of dislocations in order to implement the climb model. Indeed, the “climb strain tensor,”  $\mathbf{k} = \text{sym}(\hat{\mathbf{b}} \otimes \hat{\chi})$ , can be expressed in terms of the angle between the Burgers vector and line direction.

In this study, the experimentally measured texture is used as an input and boundary conditions appropriate for uniaxial tension parallel to the sheet transverse direction (TD) are imposed. The parameters which were explored include the relative critical resolved shear strengths ( $\tau$ ) of the basal  $\langle a \rangle$ , prismatic  $\langle a \rangle$ , and pyramidal  $\langle c+a \rangle$  for a number of glide-only cases. Upon determining which cases were most relevant, we then explored the effect of incorporating climb of  $\langle a \rangle$  dislocations. The outputs presently under consideration are the  $r$ -value and the evolved texture after TD tension. The power-law exponents employed in this study were fixed at  $n_g = 20$  and  $n_c = 3$ , though further exploration of the effects of these parameters on the constitutive response and texture evolution is merited.

## Experimental Methods

Mg alloy AZ31B sheet with 1 mm thickness was provided by the former Magnesium Elektron North America, part of the Luxfer group. The samples were examined in the O temper, which involves warm rolling followed by annealing at 340 °C for 1 h. The microstructure of the samples had been examined in previous study and found to be comprised of equiaxed grains with a lineal intercept grain size of  $\sim 8.3 \pm 0.1 \mu\text{m}$  with only occasional twins from the prior deformation [16]. The texture is measured using X-ray diffraction from the sheet midplane, both before and after deformation, using a Panalytical X’pert Pro MPD diffractometer, as described previously [16]. The texture analysis and graphing were performed using the MTEX toolbox for MATLAB.

Tensile samples with a test geometry developed for examining the superplastic behavior of sheet metals [17] were cut from the sheets using electrodischarge machining. The effective gage section of the samples is approximately 38 mm long by 6 mm wide. The  $r$ -values were measured as the ratio of the logarithmic true plastic strains along the width and thickness directions, after deforming the samples to a plastic strain of 0.08–0.12 along the TD. One test of the accuracy of the strain measurements was to examine volumetric strain implied, and since plasticity is known to be volume constant, only those measurements with implied absolute dilatation of less than  $\sim 0.005$  were retained in the final analysis.

Tensile tests were performed at temperatures ranging from room temperature up to 350 °C, at strain rates ranging

from  $1\text{E-}5 \text{ s}^{-1}$  up to  $1\text{E-}3 \text{ s}^{-1}$ . The tensile test data were analyzed in terms of the flow stress measured at a plastic strain of 0.10. The test conditions were chosen in order to obtain a wide range of Zener–Hollomon parameter,  $Z$ , also known as the temperature compensated strain rate:

$$Z = \dot{\epsilon} \exp\left(\frac{Q}{RT}\right) \quad (7)$$

where  $Q$  is the activation energy and  $R$  is the universal gas constant. Sellars and Tegart [18] suggested a hyperbolic sine function would describe the relationship between rate and flow stress over a wide range of hot working and creep conditions.

$$Z = A \{\sinh(\alpha\sigma)\}^n \quad (8)$$

At low stress (or  $Z$ ) conditions, this relationship is asymptotic to a simple power-law indicative of high temperature creep, whereas it is asymptotic to an exponential function of stress at high stresses, which is typical of thermally activated slip. That is, it does a reasonably good job of describing both the power-law and power-law breakdown regimes. The empirical parameters  $A$ ,  $\alpha$ ,  $n$ , and  $Q$  were obtained by least squares nonlinear regression.

## Experimental Results

Figure 1 presents the flow stress during uniaxial straining parallel to the TD, at a tensile plastic strain of 0.10, plotted as a function of the Zener–Hollomon parameter,  $Z$ . Superimposed on the experimental data is a best-fit Sellars–Tegart

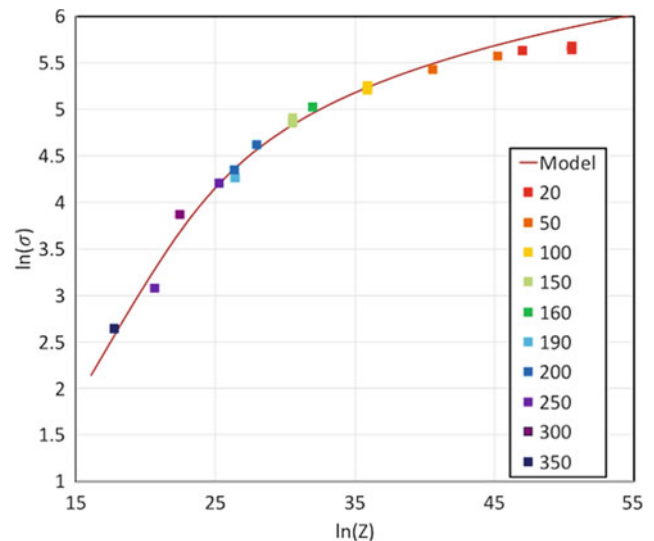


**Fig. 1** Plot of log-stress versus log- $Z$  (where  $Z$  is the temperature-compensated strain rate or Zener–Hollomon parameter, with a best-fit activation energy of  $\sim 140 \text{ kJ/mol}$ )

function (Eq. 8), where the stress exponent  $n = 3.8$ . Such a value suggests that the rate-controlling deformation mechanism is dislocation climb at conditions of  $Z \sim 24$  or less. The transition to rate-insensitive plasticity (or power-law breakdown) occurs over the range of  $24 \leq Z \leq 40$ . At higher  $Z$  levels, the plasticity is clearly rate-insensitive, and even the Sellars–Tegart function fails to describe the flow stress well. As such, the focus of this study is placed upon examining the texture evolution and strain anisotropy over these three  $Z$ -value regimes (low, intermediate, and high).

Figure 2 presents the  $r$ -value measured at a plastic tensile strain of 0.08–0.12 and plotted as a function of applied  $Z$ . As was observed above, there are three regimes, a low  $Z$  regime in which the  $r$ -value is close to 1 (near plastic isotropy), an intermediate regime, and a high  $Z$  regime in which the  $r$ -value is  $\sim 3.5$ . It is notable to the present authors that the transitions in  $r$ -value occur at nearly the same points that the constitutive relationship between flow stress and applied  $Z$  exhibits transitions. Specifically, under conditions where the constitutive modeling suggests the onset of significant strain accommodation by dislocation climb, the  $r$ -value begins to decrease.

Finally, the crystallographic texture and its evolution after tensile deformation within each of the aforementioned  $Z$ -regimes are presented in Fig. 3. Note that a near sixfold symmetry develops in the prismatic  $(10\bar{1}0)$  pole figures, within the high  $Z$  regime, which is indicative of significant activity of the prismatic slip of  $\langle a \rangle$  dislocations. This

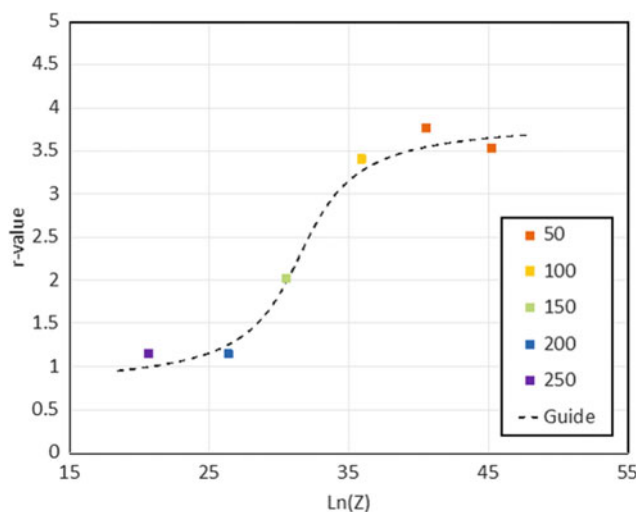


**Fig. 2**  $r$ -value (ratio of the width strain to the thickness strain) for samples of textured Mg alloy, AZ31B, sheet material tested parallel to the sheet transverse direction (TD) at the aforementioned temperatures and strain rates (see Fig. 1). The dotted curve is merely to guide the eye, but suggests three mechanistic regimes at low, intermediate, and high  $Z$  values

significant non-basal slip of  $\langle a \rangle$  dislocations has been used to explain the observed high  $r$ -values of this basal textured sheet material [2]. As the temperature is increased (and  $Z$ -value is correspondingly decreased), the texture evolution undergoes a transition, whereby this characteristic sixfold symmetry fades and then disappears. In the low  $Z$  regime, where the  $r$ -value approaches 1, the prismatic  $(10\bar{1}0)$  pole figure exhibits radial symmetry.

## Modeling Results

Numerous authors have explored the effects of varying the critical resolved shear stress (CRSS) ratios of basal, prismatic  $\langle a \rangle$ , and pyramidal  $\langle c+a \rangle$  slip can have on the  $r$ -values and texture evolutions [e.g., 19]. Here, we present a succinct review of those effects and add to it the effect of climb of basal  $\langle a \rangle$ -type dislocations. For the present basal texture, the predicted  $r$ -values after simulations up to a plastic strain of 0.20 are presented in Fig. 4. The region colored aqua includes  $r$ -values typical of the present study at high  $Z$  (low temperature). The regime where the ratio between strength of  $\langle c+a \rangle$  and prismatic slip  $\sim 1$  is where the  $r$ -values approach 1. The portion of the figure where  $\langle c+a \rangle$  is much softer than prismatic slip is viewed as unfeasible (and colored black).

The simulated textures after a TD tensile strain of 0.20 are presented in Fig. 5. (Note, the reader should exercise caution in comparing the absolute intensities of the simulated and experimental pole figures, because the discretized texture employed in the simulations only contains 2000 orientations and a kernel half-width of  $9^\circ$  was used within MTEX for recalculating the ODF.) The first texture is typical of the high  $Z$  regime, where prismatic slip is quite active and the  $r$ -value is high. The second texture is typical of what happens if the CRSS for  $\langle c+a \rangle$  slip is reduced sufficiently to induce an  $r$ -value near 1. Notably, the sixfold symmetry in the prismatic pole figure remains, and in some cases (only slight in the present case), the basal pole figure exhibits splitting toward the TD. Finally, a case is shown in which the predicted  $r = 1.2$  and the predicted prismatic pole figure exhibit radial symmetry, both of which are features that match what is observed experimentally (see Figs. 2 and 3). Surprisingly, despite having a higher critical (normal) stress for climb, as compared to the CRSS values for glide on any slip system, climb was shown to accommodate 80% of the strain in this example where the  $r$ -value and texture evolution match that observed experimentally. Only when the activity of prismatic  $\langle a \rangle$  slip is reduced to a low level (nil) is the appearance of the sixfold symmetry in the  $(10\bar{1}0)$  pole figures eliminated.

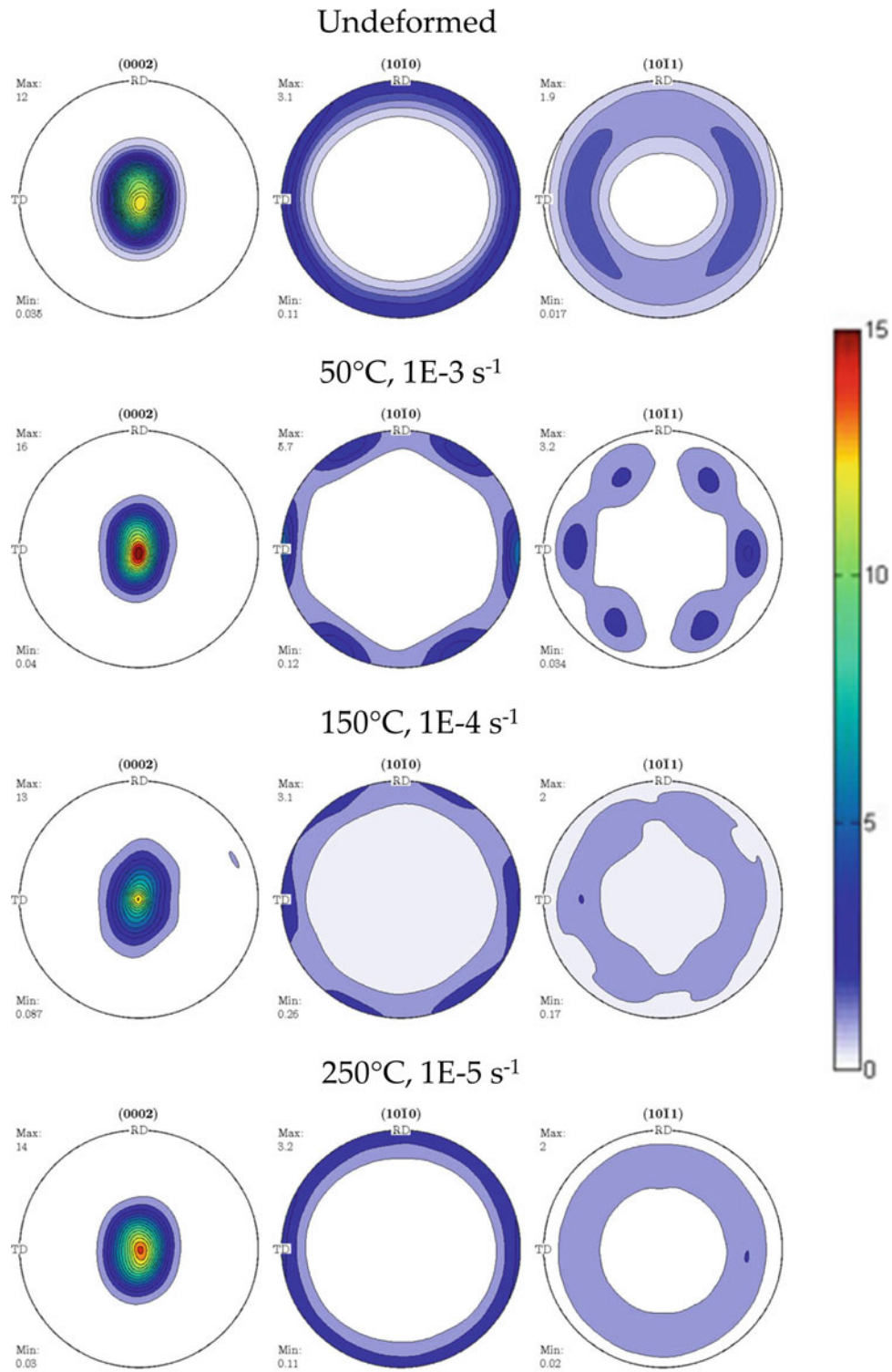


**Fig. 3** Crystallographic textures of samples of textured, commercial Mg alloy AZ31B sheet material tensile tested parallel to the sheet transverse direction (TD) at the conditions listed in the figure

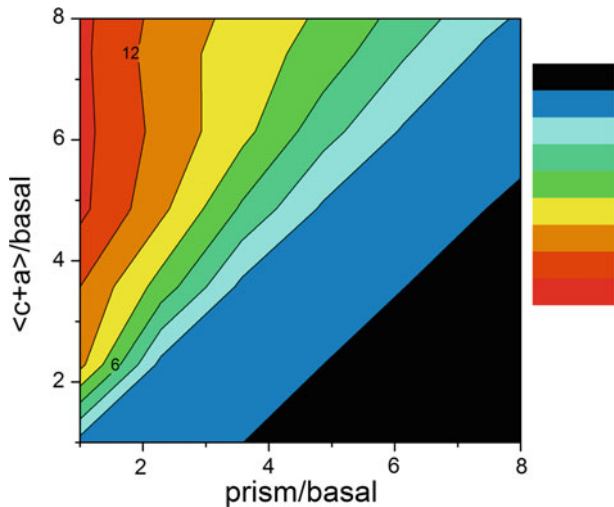


**Fig. 4**  $r$ -values plotted as a function of CRSS ratios ranging from 1 to 8 for slip of  $\langle c+a \rangle$  and prismatic  $\langle a \rangle$  dislocations

## Discussion

Dislocation climb and cross-glide are obviously relevant to applications involving creep, load relaxation (such as bolt-load retention), and hot/warm forming operations. However, there are vast fundamental unknowns, since much of the current thinking about the warm deformation of Mg is dominated by considerations of which dislocation glide mechanisms are operative, deformation twinning, and grain boundary sliding [20, 21], despite the fact that the measured constitutive response of Mg and its alloys frequently exhibits power-law type constitutive behavior [e.g., 22]. Rarely have crystal plasticity modelers considered these aspects, though the work of Staroselsky and Anand [23], notably considered the possible role of grain boundary sliding. Here, it has been hypothesized that the behavior of Mg alloys (flow strength, ductility, formability, etc.) could be as much controlled by thermally activated motion of dislocations out of their glide planes as it is by glide motion.

It is further noted that the interplay between cross-slip and climb is subject to controversy. Historically, there has been significant opposition to the notion of cross-slip controlled creep [24]. In fact, a recent monograph on creep suggests that though the issue has not reached consensus, “it is widely accepted that the activation energy for [power law] creep closely corresponds to that of lattice self-diffusion” [25]. However, Poirier [26] advances the very reasonable notion that cross-slip of screw dislocations and climb of edge (and mixed) dislocations are mechanisms that must occur in parallel. There have been strong arguments, based upon experimental evidence, that Mg [27], Mg-Al [28], and very recently a Zr alloy [29] undergo cross-slip controlled

creep. On the other hand, while it is accepted that cross-slip of  $\langle a \rangle$  dislocations from the basal plane onto the prismatic plane may be the rate-controlling mechanism at some temperatures, Couret and Caillard [30] assert that cross-glide cannot be controlling at the highest temperatures, as previously claimed [e.g., 27,28], because their in situ TEM results show cross-glide to be very easy at those temperatures. Instead, they hypothesize cross-slip control at intermediate temperatures and  $[c]$  dislocation climb control at the highest temperatures.

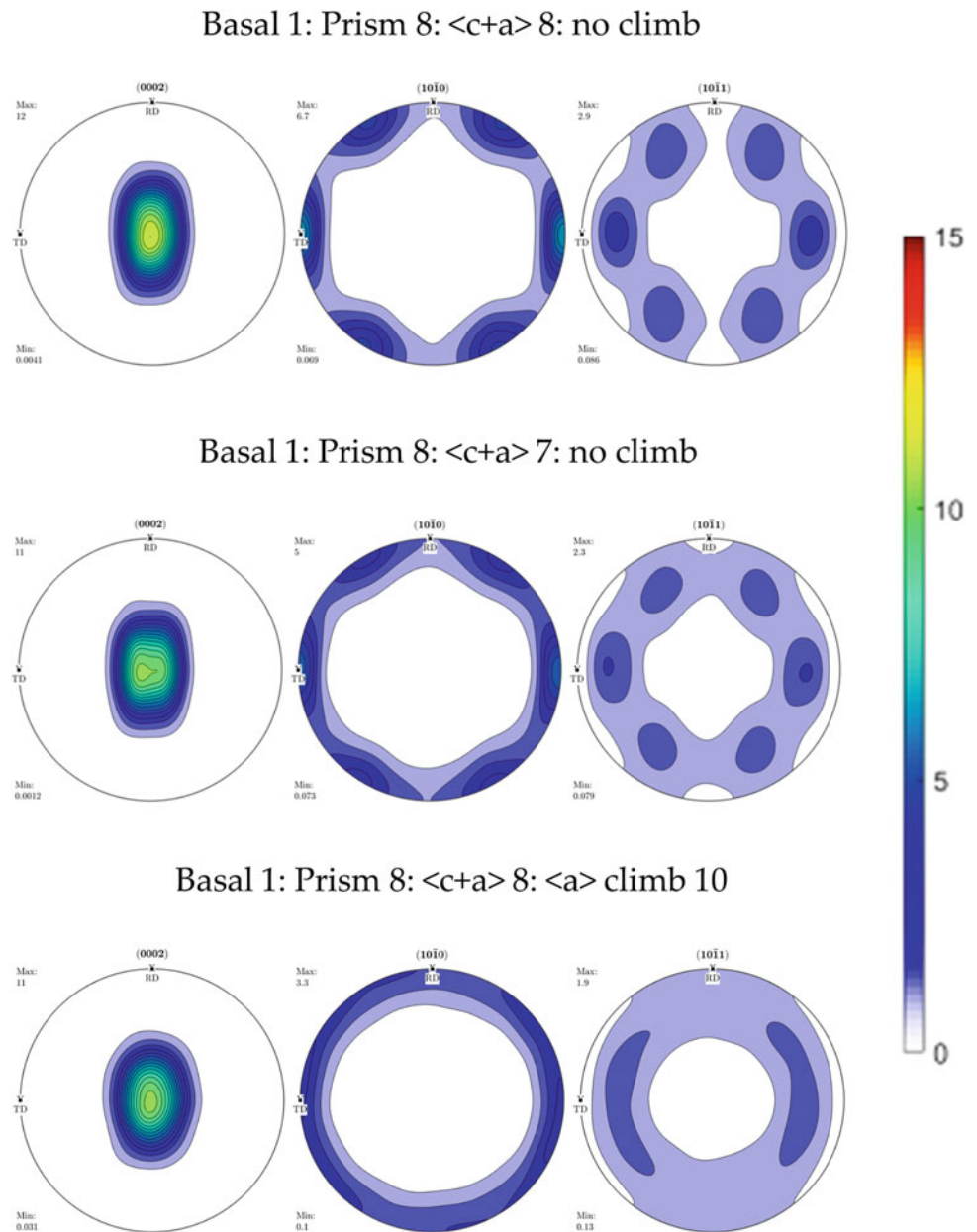
Indeed, there are a large number of thermally activated deformation mechanisms which can be rate controlling, in the case of hexagonal close-packed Mg and its alloys, depending upon (at least): temperature, applied stress level (or strain rate), and the state of stress. These mechanisms include: climb of basal  $\langle a \rangle$  and non-basal  $[c]$  dislocations; glide of the harder, non-basal dislocations (e.g., pyramidal glide of  $\langle c+a \rangle$  dislocations); grain boundary sliding; and diffusional flow. The higher stress conditions presently of interest ensure that diffusional flow will not be controlling. However, the other mechanisms are real candidates. Curiously, dislocations with  $[c]$  Burgers vectors have been discussed far less in the recent literature. One reason is the fact that there is no loading condition that will favor the glide of these large Burgers vector dislocations over  $\langle a \rangle$  type dislocations. However, past investigations of Edelin and Poirier [31] found climb of basal dislocation loops with  $[c]$  Burgers vectors to be the controlling mechanism, during  $c$ -axis compression of single crystals, rather than glide of  $\langle c+a \rangle$  dislocations. These ideas undergird the present hypothesis that *climb may sometimes obviate the need for hard dislocation slip*.

## Conclusions

Measurements of the flow stress,  $r$ -values, and texture evolution during TD tension of basal textured Mg alloy AZ31B sheets have revealed three behavioral regimes corresponding to low ( $Z < 24$ ), intermediate ( $24 \leq Z \leq 40$ ), and high ( $Z > 40$ ) rate regimes. Simple constitutive modeling reveals the behavior within each of these regimes to be characteristic of power-law creep, power-law breakdown, and thermally activated plasticity, respectively. Within the high  $Z$ , thermally activated plasticity regime, non-basal slip of  $\langle a \rangle$  dislocations is shown to prevail and explains the widely observed high  $r$ -values and the sixfold symmetry which develops within the  $(10\bar{1}0)$  pole figures. A new crystal plasticity model, which incorporates the strain and reorientation characteristic of dislocation climb, is used to show that the transitions in both the  $r$ -value and texture evolution can be described if one accounts for dislocation climb of



**Fig. 5** Predicted textures which evolve for model cases in which the  $r$ -values match the high  $Z$  (low temperature) regime and those which match the low  $Z$  regime by increasing the activity of  $\langle c+a \rangle$  slip or basal  $\langle a \rangle$  dislocation climb. The numbers in the figure headings indicated the relative CRSS and critical climb stress values employed in the simulations. Intermediate cases (in terms of  $r$ -value and texture) are obtained by incorporating an intermediate level of dislocation climb



basal  $\langle a \rangle$  dislocations. The present report only scratches the surface, and numerous areas remain to be explored, such as the possible roles of other climb modes and the possible effects distinct rate sensitivities of the various climb and glide modes.

**Acknowledgements** The authors would like to thank the United States National Science Foundation, Division of Materials Research, Metals and Metallic Nanostructures (NSF-DMR-MMN) program, Grant No. 1810197, overseen by program manager Dr. Lynnette Madsen, for financial support of this research.

## References

1. C.S. Roberts, "The Deformation of Magnesium", in *Magnesium and Its Alloys*, (New York: John Wiley, 1960), p. 81–107.
2. Agnew, S. R. (2002). Plastic anisotropy of magnesium alloy AZ 31 B sheet. In *Magnesium Technology 2002* (pp. 169-174).
3. Agnew, S. R., & Duygulu, Ö. (2005). Plastic anisotropy and the role of non-basal slip in magnesium alloy AZ31B. *International Journal of Plasticity*, 21(6), 1161-1193.
4. Sandlöbes, S., Zaeferrer, S., Schestakow, I., Yi, S., & Gonzalez-Martinez, R. (2011). On the role of non-basal



- deformation mechanisms for the ductility of Mg and Mg–Y alloys. *Acta Materialia*, 59(2), 429-439.
5. Sandlöbes, S., Pei, Z., Friák, M., Zhu, L. F., Wang, F., Zaefferer, S.,... & Neugebauer, J. (2014). Ductility improvement of Mg alloys by solid solution: Ab initio modeling, synthesis and mechanical properties. *Acta Materialia*, 70, 92-104.
  6. Fan, H., & El-Awady, J. A. (2015). Towards resolving the anonymity of pyramidal slip in magnesium. *Materials Science and Engineering: A*, 644, 318-324.
  7. Wu, Z., & Curtin, W. A. (2015). The origins of high hardening and low ductility in magnesium. *Nature*, 526(7571), 62.
  8. Wu, Z., & Curtin, W. A. (2016). Mechanism and energetics of  $\langle c + a \rangle$  dislocation cross-slip in hcp metals. *Proceedings of the National Academy of Sciences*, 113(40), 11137-11142.
  9. Wu, Z., Ahmad, R., Yin, B., Sandlöbes, S., & Curtin, W. A. (2018). Mechanistic origin and prediction of enhanced ductility in magnesium alloys. *Science*, 359(6374), 447-452.
  10. Lebensohn, R. A., Hartley, C. S., Tomé, C. N., & Castelnau, O. (2010). Modeling the mechanical response of polycrystals deforming by climb and glide. *Philosophical Magazine*, 90(5), 567-583.
  11. Lebensohn, R. A., Holt, R. A., Caro, A., Alankar, A., & Tomé, C. N. (2012). Improved constitutive description of single crystal viscoplastic deformation by dislocation climb. *Comptes Rendus Mecanique*, 340(4), 289-295.
  12. Izadbakhsh, A., Inal, K., Mishra, R. K., & Niewczas, M. (2011). New crystal plasticity constitutive model for large strain deformation in single crystals of magnesium. *Computational materials science*, 50(7), 2185-2202.
  13. Proust, G., Tomé, C. N., Jain, A., & Agnew, S. R. (2009). Modeling the effect of twinning and detwinning during strain-path changes of magnesium alloy AZ31. *International Journal of Plasticity*, 25(5), 861-880.
  14. Kocks, U. F., Tomé, C. N., & Wenk, H. R. (2000). *Texture and anisotropy: preferred orientations in polycrystals and their effect on materials properties*. Cambridge university press.
  15. Arsenlis, A., & Parks, D. M. (1999). Crystallographic aspects of geometrically-necessary and statistically-stored dislocation density. *Acta Materialia*, 47(5), 1597-1611.
  16. Polesak, F., Dreyer, C., Shultz, T., & Agnew, S. (2009). Blind study of the effect of processing history on the constitutive behaviour of alloy AZ31B. *Magnesium Technology 2009*, 491-496.
  17. ASTM E 2448 – 06, “Standard Test Method for Determining the Superplastic Properties of Metallic Sheet Materials” (ASTM International, West Conshohocken, PA, 2006).
  18. C.M. Sellars, W.J. Tegart, “Relationship between strength and structure in deformation at elevated temperature,” *Mem. Sci. Rev. Metall.*, 63 (1967) 731-745.
  19. Miller, V. M., Berman, T. D., Beyerlein, I. J., Jones, J. W., & Pollock, T. M. (2016). Prediction of the plastic anisotropy of magnesium alloys with synthetic textures and implications for the effect of texture on formability. *Materials Science and Engineering: A*, 675, 345-360.
  20. Luo, A. A., Powell, B. R., & Balogh, M. P. (2002). Creep and microstructure of magnesium-aluminum-calcium based alloys. *Metallurgical and Materials Transactions A*, 33(3), 567-574.
  21. Koike, J., Ohyama, R., Kobayashi, T., Suzuki, M., & Maruyama, K. (2003). Grain-boundary sliding in AZ31 magnesium alloys at room temperature to 523 K. *Materials Transactions*, 44(4), 445-451.
  22. Somekawa, H., Hirai, K., Watanabe, H., Takigawa, Y., & Higashi, K. (2005). Dislocation creep behavior in Mg–Al–Zn alloys. *Materials Science and Engineering: A*, 407(1), 53-61.
  23. Staroselsky, A., & Anand, L. (2003). A constitutive model for hcp materials deforming by slip and twinning: application to magnesium alloy AZ31B. *International Journal of Plasticity*, 19(10), 1843-1864.
  24. Sherby, O. D., & Weertman, J. (1979). Diffusion-controlled dislocation creep: a defense. *Acta Metallurgica*, 27(3), 387-400.
  25. Kassner, M. E. (2015). *Fundamentals of creep in metals and alloys*. Butterworth-Heinemann.
  26. Poirier, J.-P. (1985) Power-law creep and self-diffusion, in *Creep of crystals: High-temperature deformation processes in metals, ceramics, and minerals*, Cambridge University Press, pp. 111-114.
  27. Vagarali, S. S., & Langdon, T. G. (1981). Deformation mechanisms in hcp metals at elevated temperatures—I. Creep behavior of magnesium. *Acta Metallurgica*, 29(12), 1969-1982.
  28. Vagarali, S. S., & Langdon, T. G. (1982). Deformation mechanisms in hcp metals at elevated temperatures—II. Creep behavior of a Mg-0.8% Al solid solution alloy. *Acta Metallurgica*, 30(6), 1157-1170.
  29. Kombaiah, B., & Murty, K. L. (2015). Dislocation cross-slip controlled creep in Zircaloy-4 at high stresses. *Materials Science and Engineering: A*, 623, 114-123.
  30. Couret, A., & Caillard, D. (1985). An in situ study of prismatic glide in magnesium—I. The rate controlling mechanism. *Acta Metallurgica*, 33(8), 1447-1454.
  31. Edelin, G., & Poirier, J. P. (1973). Etude de la montée des dislocations au moyen d'expériences de fluage par diffusion dans le magnésium: II. Mesure de la vitesse de montée. *Philosophical Magazine*, 28(6), 1211-1223.

# Deviations from Theoretical Orientation Relationship Along Tensile Twin Boundaries in Magnesium

B. Leu, M. Arul Kumar, Y. Liu, and I. J. Beyerlein

## Abstract

Deformation twinning is a prevalent mode of plastic deformation in hexagonal close packed (HCP) magnesium. Twin domains are associated with significant lattice reorientation and localized shear. The theoretical misorientation angle for the most common  $\{10\bar{1}2\}$  tensile twin in magnesium is  $86.3^\circ$ . Through electron backscatter diffraction characterization of twinning microstructure, we show that the twin boundary misorientation at the twin tips is approximately  $85^\circ$ , and it is close to the theoretical value only along the central part of the twin. The variations in twin/matrix misorientation along the twin boundary control the twin thickening process by affecting the nucleation, glide of twinning partials, and migration of twinning facets. To understand this observation, we employ a 3D crystal plasticity model with explicit twinning. The model successfully captures the experimentally observed misorientation variation, and it reveals that the twin boundary misorientation variations are governed by the local plasticity that accommodates the characteristic twin shear.

## Keywords

Deformation twins • Misorientation • Crystal plasticity • Local stresses • Magnesium

## Introduction

Due to the scarcity of easy dislocation glide systems, deformation twins play a dominant role in the accommodation of plastic deformation of Mg and its alloys [1]. The formation and growth of twins create new sub-grain boundaries [2, 3], and characteristics of these boundaries control the local stresses and interactions with defects [4–7]. In this way, it significantly affects the mechanical properties of polycrystalline metals [8–11]. Thus, understanding the characteristics of twins and its boundaries is crucial for microstructure design and processing of advanced Mg alloys. In pure Mg,  $\{10\bar{1}2\}$  tensile twins are the most common twin to be activated when the c-axis of the crystal is subjected to elongation [2]. All twins are associated with a characteristic lattice misorientation and twinning shear. For  $\{10\bar{1}2\}$  tensile twins in Mg, the twin/matrix misorientation angle is  $86.3^\circ$  about  $\langle 11\bar{2}0 \rangle$  axis [12]. Very often, this theoretical relationship is used to identify twins within a deformed Mg microstructure.

Recently, the deviation in this twin/matrix orientation relationship was characterized by electron microscopy in several studies [13–18]. For example, Li and Zhang [15] showed that the misorientation angle of  $\{10\bar{1}2\}$  tensile twin can range from  $84^\circ$  to  $97^\circ$  in Mg alloys rather than the theoretical value of  $86.3^\circ$ . They argued that the local atomic shuffling is the responsible for this deviation. Zhang et al. [16] also observed an approximately  $4^\circ$  deviation in the twinning misorientation relationship, and they ascertain this deviation as a result of local dislocation–twin interactions. Similar observations have been reported for other twin types, like  $\{10\bar{1}1\}$  compression twins, and also in other material systems, like Ti and Co [17, 18]. Other proposals for this deviation in the twin/matrix misorientation in the existing literature include strain accommodation, twin–slip interactions, twin–twin interactions, and local atomic shuffling. These phenomena collectively are external factors that may

B. Leu (✉) · I. J. Beyerlein  
Materials Department, University of California at Santa Barbara,  
Santa Barbara, CA 93106, USA  
e-mail: [brandonleu@ucsb.edu](mailto:brandonleu@ucsb.edu)

M. Arul Kumar  
Materials Science and Technology Division, Los Alamos National  
Laboratory, Los Alamos, NM 8745, USA

Y. Liu  
Department of Materials Science and Engineering, Shanghai Jiao  
Tong University, Shanghai, 200240, China

I. J. Beyerlein  
Mechanical Engineering Department, University of California at  
Santa Barbara, Santa Barbara, CA 93106, USA

contribute to the development of variation in the twinning misorientation relationship. The question still remains on whether the underlying mechanism could instead be intrinsic. The origin of this deviation would be important as there is the potential that it could affect further twinning processes, such as twin boundary migration.

To address these questions, in this work, first we experimentally measure the twinning misorientation along  $\{10\bar{1}2\}$  tensile twins in HCP pure Mg. We observe similar deviations in the twin orientation relationship; that is the misorientation at the twin tip is approximately  $1.5^\circ$  lower than that of the middle. To interpret and quantify the effect on twin boundary migration, we employ a crystal plasticity fast Fourier transform (CP-FFT) model with the ability to model subgranular twin lamella explicitly [19, 20]. Using this model framework, we found that the accommodation of intrinsic twinning shear by dislocation plasticity can explain the observed variations in the twin/matrix misorientation. We also find that these deviations are associated with variations in the local stresses. Interestingly, these local stresses favor the formation of P/B facets and thus may help to migrate the twin boundaries, and eventually thicken the twins.

## Experimental Characterizations

Commercial purity polycrystalline Mg is used in this study. The material has a strong basal texture resulting from prior rolling. To activate  $\{10\bar{1}2\}$  tensile twins, Mg material is subjected to compression at  $10^{-3}/s$  strain-rate along an in-plane direction at room temperature. To activate a sufficient number of twins, sample was compressed to 1% strain. The deformed microstructure was imaged using electron backscatter diffraction (EBSD) technique with a step size of  $0.25 \mu\text{m}$ . An EBSD image of a representative region of the deformed Mg with the activation of several tensile twins is shown in Fig. 1a.

From these twins, we analyze further the twins that have terminated inside the grain, and not at the grain boundary. Those that terminate at grain boundaries could have their morphology affected by the properties of the neighboring grain. Figure 1b–d displays three different twins and the corresponding measured misorientation angle along the twin boundaries. For reference, the theoretical value is shown as a dashed line. For all three twins shown in Fig. 1, the measured misorientation angle in the middle of the twin away from the twin tip is close to the theoretical value. In contrast, at the twin tips, the misorientation angle is approximately  $1^\circ$ – $1.5^\circ$  lower than the theoretical value. Although similar misorientation variations have been reported in the literature,

here the spatial variation in the misorientation angle along the twin boundaries is reported for the first time.

## Numerical Calculations

To understand and interpret the measured misorientation angle variation shown in Fig. 1, a CP-FFT model is employed here [19, 20]. This model was originally developed to calculate and relate the effective and local responses associated with inter- and intra-granular stress states resulting from the heterogeneity in elastic and plastic properties between grains in polycrystalline materials [21, 22]. Recently, it was extended to model deformation twin lamellae explicitly [20]. The twinning portion of the model is briefly reviewed here. The constitutive behavior of an elasto-visco-plastic material under an infinitesimal strain approximation with twinning shear transformation can be written as

$$\boldsymbol{\sigma}(x) = \mathbf{C}(x) : \boldsymbol{\varepsilon}^{\text{el}}(x) = \mathbf{C}(x)(\boldsymbol{\varepsilon}(x) - \boldsymbol{\varepsilon}^{\text{pl}}(x) - \boldsymbol{\varepsilon}^{\text{tr}}(x)) \quad (1)$$

where  $\boldsymbol{\sigma}(x)$  is the Cauchy stress,  $\mathbf{C}(x)$  is the elastic stiffness tensor, and  $\boldsymbol{\varepsilon}^{\text{el}}(x)$  is the elastic strain at a material point  $x$ . In this work, we consider deformation twinning as the shear transformation process. The elastic strain can be written as the difference between the total strain  $\boldsymbol{\varepsilon}(x)$  and the plastic strain  $\boldsymbol{\varepsilon}^{\text{pl}}(x)$  due to dislocation slip and the transformation strain  $\boldsymbol{\varepsilon}^{\text{tr}}(x)$  associated with twinning. We solve the problem for the local stress field at material point  $x$  by using an implicit time discretization of the form:

$$\boldsymbol{\sigma}^{t+\Delta t}(x) = \mathbf{C}(x) : (\boldsymbol{\varepsilon}^{t+\Delta t}(x) - \boldsymbol{\varepsilon}^{\text{pl},t}(x) - \dot{\boldsymbol{\varepsilon}}^{\text{pl},t+\Delta t}(x, \boldsymbol{\sigma}^{t+\Delta t})\Delta t - \boldsymbol{\varepsilon}^{\text{tr},t}(x) - \Delta\boldsymbol{\varepsilon}^{\text{tr},t+\Delta t}(x)) \quad (2)$$

where

$$\dot{\boldsymbol{\varepsilon}}^{\text{pl}}(x) = \sum_{s=1}^N m^s(x) \dot{\gamma}^s(x) \text{ and } \Delta\boldsymbol{\varepsilon}^{\text{tr}}(x) = \mathbf{m}^{\text{tw}}(x) \Delta\gamma^{\text{tw}}(x). \quad (3)$$

The shear rate of slip system  $s$  is written as,

$$\dot{\gamma}^s(x) = \dot{\gamma}_0 \left( \frac{|\mathbf{m}^s(x) : \boldsymbol{\sigma}(x)|}{\tau_c^s} \right)^n \times \text{sgn}(\mathbf{m}^s(x) : \boldsymbol{\sigma}(x)) \quad (4)$$

where  $\mathbf{m}^s = \frac{1}{2}(\mathbf{b}^s \otimes \mathbf{n}^s + \mathbf{n}^s \otimes \mathbf{b}^s)$  is the symmetric part of the Schmid tensor, and  $\mathbf{b}^s$  and  $\mathbf{n}^s$  are the unit vectors along the slip direction and normal to the glide plane. The resistance  $\tau_c^s$  is the critical resolved shear stress associated with slip system  $s$ , and  $n$  is the stress exponent. Note that the  $\Delta\boldsymbol{\varepsilon}^{\text{tr}}(x)$  in Eq. 2 is zero outside of the twin domain.

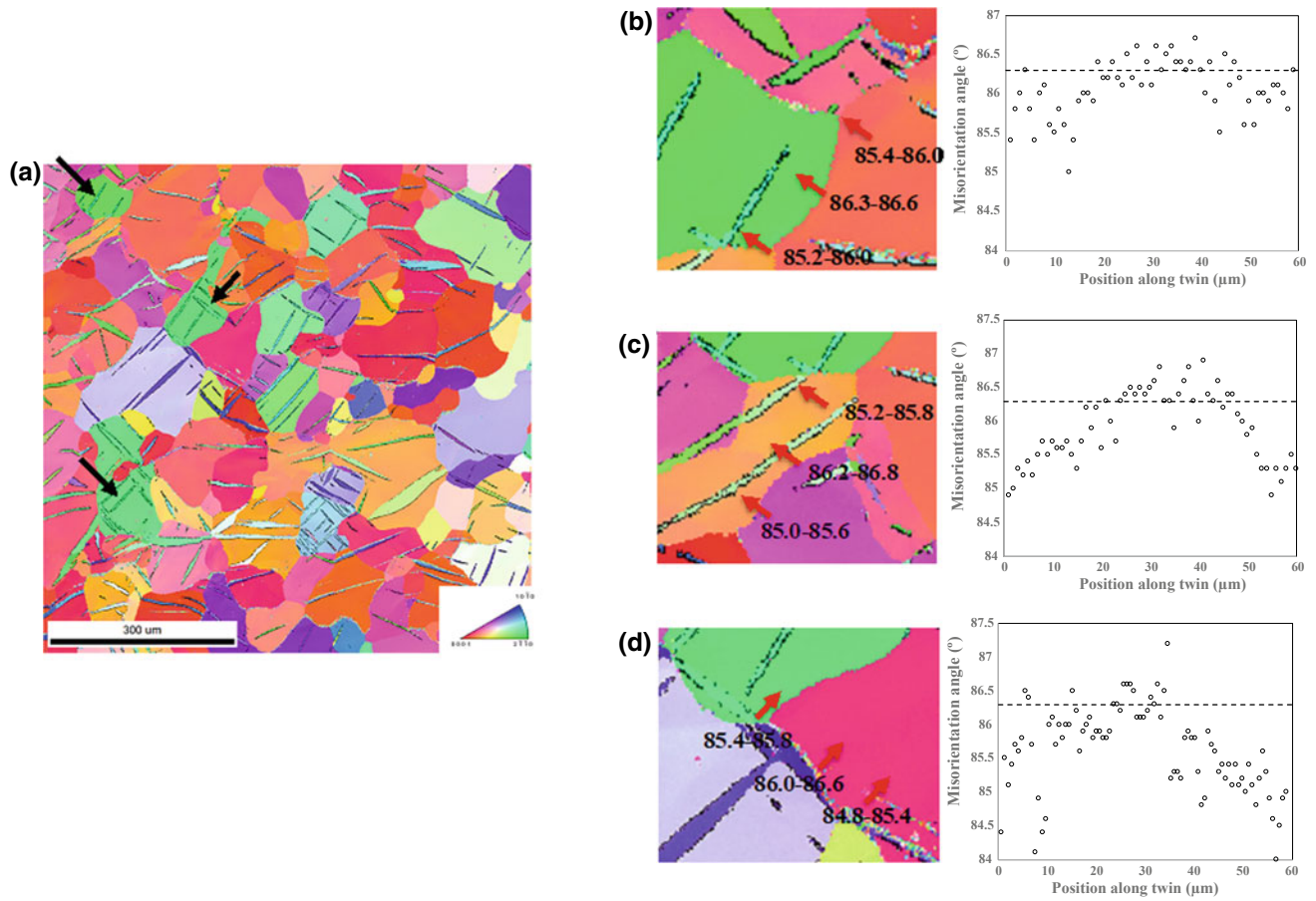


**Fig. 1** Experimentally observed variation in the twin misorientation relationship. **a** EBSD image of deformed microstructure shows the activation of  $\{10\bar{1}2\}$  tensile twins. **b–d** Three sample twins with the

The tensor  $\mathbf{m}^{\text{tw}} = \frac{1}{2}(\mathbf{b}^{\text{tw}} \otimes \mathbf{n}^{\text{tw}} + \mathbf{n}^{\text{tw}} \otimes \mathbf{b}^{\text{tw}})$  is the symmetric part of the Schmid tensor associated with the twinning system, where  $\mathbf{b}^{\text{tw}}$  and  $\mathbf{n}^{\text{tw}}$  are unit vectors along the twinning direction and the twin plane normal, respectively. The number of increments required to reach the characteristic twinning shear  $s^{\text{tw}}$  is

$$\Delta\gamma^{\text{tw}}(x) = \frac{s^{\text{tw}}}{N^{\text{twincr}}} \quad (5)$$

The time increment and the number of increments to achieve the twinning transformation  $N^{\text{twincr}}$  are set sufficiently low and high, respectively, to ensure convergence.

## Results and Discussion

In this work, we embed the tensile twin inside a grain to model twins that have terminated inside the grain and away from the neighbor. The simulation unit cell with a tensile twin is shown in Fig. 2a, which is discretized into

misorientation profile along the twin boundary. The deviation in twin misorientation relationship is significant at twin tips compared to twin middle

$3 \times 510 \times 510$  voxels. The c-axis of the central grain is oriented along the Z-direction, which corresponds to the Euler angles of  $(0^\circ, 0^\circ, 0^\circ)$  in Bunge convention. A buffer layer, representing a material with random orientation, five voxels thick, surrounds the grain. We first apply compression along the Y-direction, thus providing a sufficiently high resolved shear stress to activate the  $(01\bar{1}2)[0\bar{1}11]$  tensile twin. We then introduce this tensile twin in the pre-selected voxels by reorienting the crystal following twinning relationship and by imposing characteristic twinning shear. The volume fraction of the twin domains is taken as 1%. Deformation at all stages of the simulation is accommodated by a combination of anisotropic elasticity and visco-plasticity. The anisotropic elastic constants of Mg at room temperature in GPa are:  $C_{11} = 58.58$ ;  $C_{12} = 25.02$ ;  $C_{13} = 20.79$ ,  $C_{33} = 61.11$ , and  $C_{44} = 16.58$  [23]. The plasticity is accommodated by basal  $\langle a \rangle$ , prismatic  $\langle a \rangle$ , and pyramidal  $\langle c+a \rangle$  slip modes, and the corresponding critical resolved shear stress (in MPa) for its activation is 3.3, 35.2, and 86.2, respectively [24].

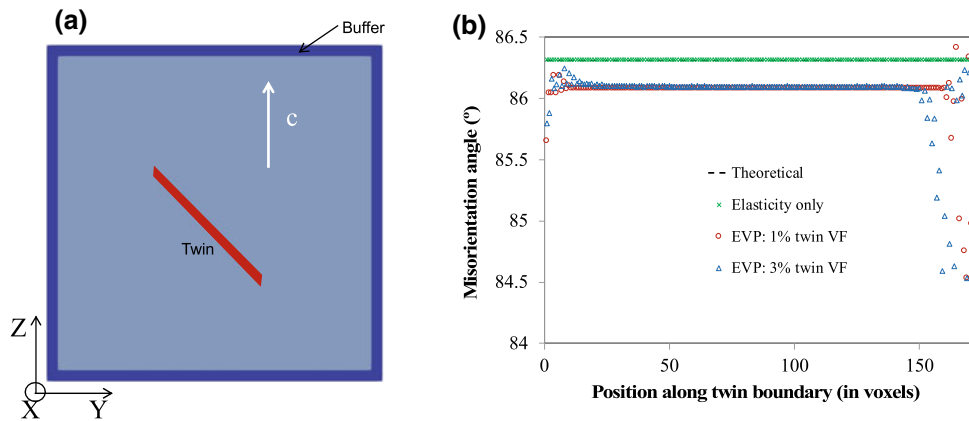


**Fig. 2** **a** EVP-FFT model setup for  $\{10\bar{1}2\}$  tensile twin simulations. The central grain orientation is  $(0^\circ, 0^\circ, 0^\circ)$  in Bunge convection, which aligns the grain *c*-axis with *Z*-direction. **b** Model predicted twin

misorientation angle profile along the twin boundary for only elasticity and for elasto-visco-plastic formulation. Theoretical relationship is shown in dashed line

### Origin of Twin Misorientation Variation

Figure 2b shows the variation of the misorientation angle along the tensile twin boundary calculated by the CP-FFT model. For reference, the theoretical misorientation value, which is  $86.3^\circ$ , is also shown in dashed line. To understand the independent effect of elasticity and dislocation plasticity on twin misorientation variation, the results of simulations that assume only elasticity are also plotted in Fig. 2b. The simulation with only elasticity does not alter the twinning misorientation angle from the theoretical one. The calculated result with elasto-visco-plasticity, however, predicts a variation in the twin/matrix misorientation angle. In particular, the misorientation angle is approximately  $1.5^\circ$  lower than the theoretical value at the twin tip, but not in the middle of the twin away from the tip. This variation is due to the accommodation of twinning shear by dislocation plasticity. This model prediction agrees well with the experimental observation as presented in Fig. 1. This analysis clearly demonstrates that the accommodation of twinning shear by plasticity gives rise to the variation in the twinning misorientation angle, and not anisotropic elasticity alone.

Further to understand the effect of twin volume fraction on this twinning misorientation variation, we have repeated the calculation with 3% twin volume fraction. We increase the volume fraction by increasing the twin thickness but without changing grain and twin dimensions. The calculated variation in the twin/matrix misorientation for both 1 and 3% volume fraction cases is shown in Fig. 2b. It suggests that the twin volume fraction does not alter the nature of variation in the twinning misorientation angle.

### Effect of Misorientation Variation on Boundary Migration

Twin growth in HCP metals is accomplished by the migration of twin boundaries in the parent crystal. Several mechanisms have been proposed for twin boundary migration [25–31]. The most commonly accepted mechanism is the migration of coherent twin boundary (CTB) by the formation and gliding of twin facets [28, 30–32]. Along CTBs, two types of facets are observed, such as the prismatic–basal (P/B) and basal–prismatic (B/P) [33–35]. In the P/B facet, the prismatic plane of the matrix grain is parallel to the basal plane of twin domain and vice versa for the B/P facet. The nature of stress required to the formation and gliding of these facets depend on the crystallographic configuration. The interplanar separation between basal and prismatic planes in pure Mg is  $5.21 \text{ \AA}$  and  $5.55 \text{ \AA}$ , respectively. Thus, in order to grow the twin by the migration of P/Bs or B/Ps, a normal compressive or tensile stress, respectively, needs to act on their planes.

The stress component normal to P/B and B/P facets along the twin boundary is plotted in Fig. 3a and b, respectively. Here, we show the normal stresses before and after the formation of the tensile twin. In the secondary vertical axis, the calculated twin/matrix misorientation angle is plotted for reference. Before twinning, the stress normal to P/B and B/P facets along the twin boundary is constant at approximately  $-40 \text{ MPa}$  (compressive) and  $2 \text{ MPa}$  (tensile), which favors the formation of tensile twin. After twinning, the normal stresses are varying along the twin boundary and particularly more heterogeneous at the twin tip. The normal stress at the



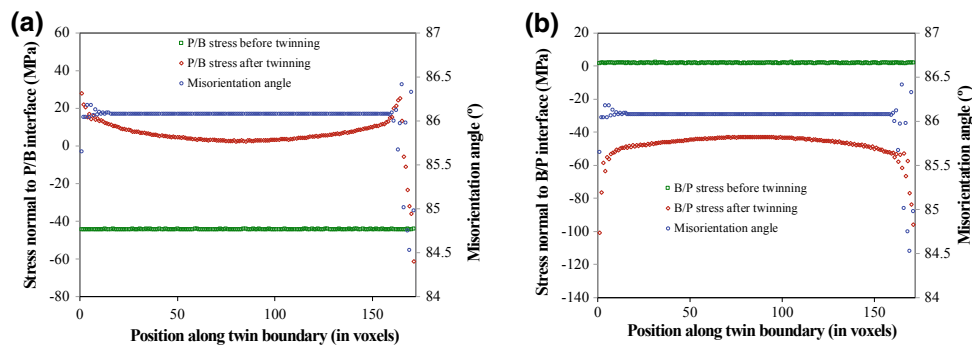


**Fig. 3** Variation in the driving stress for the formation of **a** P/B and **b** B/P facets along the twin boundary. The driving stresses are shown before and after twin formation. For comparison, the misorientation profile also shown in the second vertical axis

twin middle for both the P/B and B/P facet changed its nature and does not favor further twinning. The change in stress state (compression to tensile and vice versa) is associated with the stress-reversal due to twinning shear accommodation [19, 20, 36]. This is commonly referred to as the twin backstress. As a result, twin growth is only possible by imposing further favorable loading [19, 20, 37]. However, we see a compressive P/B normal stress at the twin tip, which can favor the formation and migration of P/B facets locally at the twin tip. A similar possibility for the formation and migration of B/P facet is, however, not observed. More interestingly, we see a favorable stress state for the migration of P/B facet in a material point where we have observed the deviation in the twinning misorientation angle. It suggests that the local dislocation plasticity-induced deviation in the twinning misorientation angle may favor the twin growth process by the formation and migration of twin facets.

## Summary

In this work, we have experimentally and numerically characterized the deviation in the twinning misorientation angle along  $\{10\bar{1}2\}$  tensile twin boundaries in pure Mg. From the EBSD measurements, we found that the twinning misorientation at the twin tip is approximately  $1.5^\circ$  lower than that of the twin middle. Using a full field CP-FFT based twinning model, we show that the accommodation of intrinsic twinning shear by dislocation plasticity, not by the anisotropic elasticity, generates the changes in the twinning misorientation observed in the experiment. Also, we found that the thickness of the twin does not change the nature of the variation in the twinning misorientation. Using the model predicted stresses, we show that local stresses, where we observed the deviation in twinning misorientation, favor the formation of P/B facets, thus, may help to migrate the twin boundaries, and eventually thicken the twin.

**Acknowledgements** This work is fully funded by the U.S. Department of Energy, Office of Basic Energy Sciences Project FWP 06SCPE401. I. J. B. acknowledges financial support from the National Science Foundation (NSF CMMI-1729887). B. L. acknowledges financial support from the National Defense Science and Engineering Graduate (NDSEG) Fellowship.

## References

1. M.H. Yoo, Slip, Twinning, and Fracture in Hexagonal Close-Packed Metals, *Metall Trans A* 12(3) (1981) 409-418.
2. I.J. Beyerlein, L. Capolungo, P.E. Marshall, R.J. McCabe, C.N. Tome, Statistical analyses of deformation twinning in magnesium (vol 90, pg 2161, 2010), *Philos Mag* 90(30) (2010) 4073-4074.
3. M.A. Kumar, M. Wroński, R.J. McCabe, L. Capolungo, K. Wierzbanski, C.N. Tome, Role of microstructure on twin nucleation and growth in HCP titanium: A statistical study, *Acta Mater* 148 (2018) 123-132.
4. A. Serra, D. Bacon, Computer simulation of screw dislocation interactions with twin boundaries in HCP metals, *Acta metallurgica et materialia* 43(12) (1995) 4465-4481.
5. A. Serra, D.J. Bacon, Interaction of a moving  $\{ \}$  twin boundary with perfect dislocations and loops in a hcp metal, *Philos Mag* 90 (7-8) (2010) 845-861.
6. A. Serra, D.J. Bacon, R.C. Pond, Twins as barriers to basal slip in hexagonal-close-packed metals, *Metallurgical and Materials Transactions A* 33(13) (2002) 809-812.
7. L. Jiang, M.A. Kumar, I.J. Beyerlein, X. Wang, D. Zhang, C. Wu, C. Cooper, T.J. Rupert, S. Mahajan, E.J. Lavernia, J.M. Schoenung, Twin formation from a twin boundary in Mg during in-situ nanomechanical testing, *Materials Science and Engineering: A* 759 (2019) 142-153.
8. G. Proust, C.N. Tome, A. Jain, S.R. Agnew, Modeling the effect of twinning and detwinning during strain-path changes of magnesium alloy AZ31, *Int J Plasticity* 25(5) (2009) 861-880.
9. A.A. Salem, S.R. Kalidindi, R.D. Doherty, S.L. Semiatin, Strain hardening due to deformation twinning in alpha-titanium: Mechanisms, *Metall Mater Trans A* 37a(1) (2006) 259-268.
10. Y.N. Wang, J.C. Huang, The role of twinning and untwinning in yielding behavior in hot-extruded Mg-Al-Zn alloy, *Acta Mater* 55 (3) (2007) 897-905.
11. M. Wronski, M. Arul Kumar, L. Capolungo, R. Madec, K. Wierzbanski, C.N. Tome, Deformation behavior of CP-titanium: Experiment and Crystal plasticity modeling, *Mat Sci Eng a-Struct* 724 (2018) 289-297.

12. M.H. Yoo, J.K. Lee, Deformation Twinning in Hcp Metals and Alloys, *Philos Mag A* 63(5) (1991) 987-1000.
13. X. Zhang, B. Li, X. Wu, Y. Zhu, Q. Ma, Q. Liu, P. Wang, M. Horstemeyer, Twin boundaries showing very large deviations from the twinning plane, *Scripta Mater* 67(10) (2012) 862-865.
14. M. Gharghoury, G. Weatherly, J. Embury, The interaction of twins and precipitates in a Mg-7.7 at.% Al alloy, *Philosophical Magazine A* 78(5) (1998) 1137-1149.
15. B. Li, E. Ma, Atomic shuffling dominated mechanism for deformation twinning in magnesium, *Phys Rev Lett* 103(3) (2009) 035503.
16. Y. Zhang, Z.S. Dong, J.T. Wang, J.Q. Liu, N. Gao, T.G. Langdon, An analytical approach and experimental confirmation of dislocation-twin boundary interactions in titanium, *J Mater Sci* 48(13) (2013) 4476-4483.
17. Q. Sun, X. Fang, Y. Wang, L. Tan, X. Zhang, Changes in misorientations of {1011} twin boundaries in deformed magnesium alloy, *J Mater Sci* 53(10) (2018) 7834-7844.
18. Y. Liu, X. Chen, K. Wei, L. Xiao, B. Chen, H. Long, Y. Yu, Z. Hu, H. Zhou, Effect of Micro-Steps on Twinning and Interfacial Segregation in Mg-Ag Alloy, *Materials* 12(8) (2019) 1307.
19. M.A. Kumar, I.J. Beyerlein, C.N. Tome, Effect of local stress fields on twin characteristics in HCP metals, *Acta Mater* 116 (2016) 143-154.
20. M.A. Kumar, A.K. Kanjarla, S.R. Niezgodna, R.A. Lebensohn, C. N. Tome, Numerical study of the stress state of a deformation twin in magnesium, *Acta Mater* 84 (2015) 349-358.
21. A.K. Kanjarla, R.A. Lebensohn, L. Balogh, C.N. Tome, Study of internal lattice strain distributions in stainless steel using a full-field elasto-viscoplastic formulation based on fast Fourier transforms, *Acta Mater* 60(6-7) (2012) 3094-3106.
22. R.A. Lebensohn, A.K. Kanjarla, P. Eisenlohr, An elasto-viscoplastic formulation based on fast Fourier transforms for the prediction of micromechanical fields in polycrystalline materials, *Int J Plasticity* 32-33 (2012) 59-69.
23. G. Simmons, H. Wang, Single crystal elastic constants and calculated aggregate properties: A Handbook, MIT press 1971.
24. I.J. Beyerlein, R.J. McCabe, C.N. Tome, Effect of microstructure on the nucleation of deformation twins in polycrystalline high-purity magnesium: A multi-scale modeling study, *J Mech Phys Solids* 59(5) (2011) 988-1003.
25. M. Ardeljan, I.J. Beyerlein, M. Knezevic, Effect of dislocation density-twin interactions on twin growth in AZ31 as revealed by explicit crystal plasticity finite element modeling, *Int J Plasticity* 99 (2017) 81-101.
26. M. Gong, V. Taupin, L. Capolungo, The kinetics of growth of twins: 3d perspectives, (in preparation) (2019).
27. J.T. Lloyd, A dislocation-based model for twin growth within and across grains, *P Roy Soc a-Math Phys* 474(2210) (2018).
28. A. Serra, D.J. Bacon, A new model for  $\{10\overline{1}\}$  twin growth in hcp metals, *Philos Mag A* 73(2) (1996) 333-343.
29. F. Wang, C.D. Barrett, R.J. McCabe, H. El Kadiri, L. Capolungo, S.R. Agnew, Dislocation induced twin growth and formation of basal stacking faults in  $\{10\overline{1}2\}$  twins in pure Mg, *Acta Mater* 165 (2019) 471-485.
30. B. Xu, L. Capolungo, D. Rodney, On the importance of prismatic/basal interfaces in the growth of (1012) twins in hexagonal close packed crystals, *Scripta Mater* 68(11) (2013) 901-904.
31. C.D. Barrett, H. El Kadiri, Impact of deformation faceting on  $\{10\overline{1}2\}$ ,  $\{10\overline{1}1\}$  and  $\{10\overline{1}3\}$  embryonic twin nucleation in hexagonal close-packed metals, *Acta Mater* 70 (2014) 137-161.
32. A. Ostapovets, A. Serra, Characterization of the matrix-twin interface of a  $\{10\overline{1}2\}$  twin during growth, *Philos Mag* 94 (25) (2014) 2827-2839.
33. Q. Sun, X. Zhang, Y. Ren, J. Tu, Q. Liu, Interfacial structure of  $\{10\overline{1}2\}$  twin tip in deformed magnesium alloy, *Scripta Mater* 90 (2014) 41-44.
34. Q. Sun, X.Y. Zhang, J. Tu, Y. Ren, H. Qin, Q. Liu, Characterization of basal-prismatic interface of  $\{10\overline{1}2\}$  twin in deformed titanium by high-resolution transmission electron microscopy, *Phil Mag Lett* 95(3) (2015) 145-151.
35. Y. Liu, N. Li, S. Shao, M. Gong, J. Wang, R.J. McCabe, Y. Jiang, C.N. Tome, Characterizing the boundary lateral to the shear direction of deformation twins in magnesium, *Nat Commun* 7 (2016) 11577.
36. M.A. Kumar, B. Clausen, L. Capolungo, R.J. McCabe, W. Liu, J. Z. Tischler, C.N. Tome, Deformation twinning and grain partitioning in a hexagonal close-packed magnesium alloy, *Nat Commun* 9 (2018).
37. M.A. Kumar, I.J. Beyerlein, R.A. Lebensohn, C.N. Tome, Modeling the effect of neighboring grains on twin growth in HCP polycrystals, *Model Simul Mater Sc* 25(6) (2017) Article 064007.

# The Role of Faceting in $\{10\bar{1}2\}$ Twin Nucleation

Christopher D. Barrett

## Abstract

$\{1012\}$  twinning is the most profuse twin mode in Mg and plays a major role in its plasticity and deformation. Identification of the mechanisms and locations of twinning nucleation is crucial to characterize the ensuing microstructural evolution and failure. Herein, we provide a new theory of hexagonal close-packed twin nucleation. In essence, the theory is that twins need a pre-existing interface upon which to grow. In the earliest stages of nucleation, this requirement implies that the twin must be able to facet onto the same plane as the local interface, whether it be a free surface, stacking fault, or grain boundary, and that the action of twinning must reduce the defect energy of the pre-existing structure in order to remain stable until it can grow large enough to emit disconnections. The theory is demonstrated on  $\{1012\}$  twin nucleation at grain boundaries and stacking faults in Mg via molecular dynamics.

## Keywords

Twinning • Nucleation • Magnesium • Molecular dynamics

## Introduction

$\{10\bar{1}2\}$  twinning is a dramatic plastic mechanism which is pervasive in hexagonal close-packed (hcp) materials. HCP materials play a critical role in many industries and hold potential for even greater market penetration if their properties can be further optimized. In particular, Ti and Mg alloys have better strength-to-weight ratios than Al or steel alloys, and thus are critical lightweight components. These materials often experience brittle failure due to twinning. This failure

might be avoidable if the twinning process was fully understood. The twinning process induces a  $90^\circ$  rotation of the crystal lattice, dramatically altering the microstructure and critical resolved shear stresses (CRSSs) of other modes within the twinned region. In Mg,  $\{10\bar{1}2\}$  twinning is so profuse that it often consumes the entire microstructure of heavily textured components. While the twinning process has been extensively studied over the last seventy years and many advances have been made, the nucleation process whereby these twins originate is still poorly understood.

Twin nucleation has been studied and discussed extensively since the 1950s. The simplest nucleation theory is that twins can spontaneously form in the crystal bulk by a uniform shape change in some region responding to applied load [1]. In contrast, others suggested that a pre-existing defect of some nature was necessary to catalyze the nucleation process [2, 3]. This was lent weight by observations of large scatter in the observed CRSSs for twinning and sensitivity to loading direction [3–6], indicating some non-Schmid behavior [7]. The theory of heterogenous twin nucleation was later extended into multiple forms involving prior slip or concomitant microslip [8–12], and dissociation of bulk dislocations into several twinning disconnections [13–21]. Recent advances have lent greater weight to these heterogenous theories than the homogenous nucleation idea [22–26], but the exact process is still not very well defined.

Wang has shown, [26–28], that  $\{10\bar{1}2\}$  twins have a minimum stable size, based on density functional theory (DFT) and atomistic results. When a twin is generated from a zonal mechanism based on dissociation of a lattice dislocation, at least eight twinned layers are necessary to prevent the embryo from collapsing. Additional work based on electron back-scatter diffraction (EBSD) has shown that twins nucleate more frequently at low-angle grain boundaries than at high-angle grain boundaries indicating that something about the structure of low-angle grain boundaries encourages twin nucleation.

Finally, recent results using both molecular dynamics and transmission electron microscopy have shown that small

C. D. Barrett (✉)  
Department of Mechanical Engineering, Mississippi State University, Starkville, MS 39762, USA  
e-mail: [barrett@me.msstate.edu](mailto:barrett@me.msstate.edu)

twin embryos do not have the lenticular morphology most often seen at the EBSD scale, but instead are heavily faceted [29, 30]. These facets have been shown to significantly enhance the glissile nature of the twin by a complex interaction process between disclinations at facet junctions and twinning disconnections [31, 32]. Additional interactions have been observed with other defects such as basal dislocations which again enhance the twin mobility [33, 34]. From the shear plane view, four facets are visible for the  $\{10\bar{1}2\}$  twin: the typical twin boundary  $\{10\bar{1}2\}$ , the conjugate twin boundary  $\{10\bar{1}2\}$ , the basal-prismatic boundary, and the prismatic-basal boundary. Additionally, several other facets are also active which are not visible from this projection [35].

This work uses molecular dynamics to spontaneously nucleate twins under stress in Mg. The nucleation process is carefully characterized to produce a new theory of twin nucleation which we expect to be applicable to all hcp materials. Both single crystal and bi-crystal simulations were used to identify common elements present in very different nucleation scenarios.

## Methodology

A single crystal with dimensions of 156 nm by 61 nm by 9.7 nm was generated with free surfaces in all dimensions. The z-direction was the shear plane normal. A semi-spherical region of atoms was removed in the center of one of the narrow faces to concentrate the initial plasticity away from the box corners. Equilibration was performed for at least 10 ps at 50 K and terminated with a pressure below 100 MPa using LAMMPS [36]. A constant strain rate of  $10^8 \text{s}^{-1}$  in uniaxial tension was applied in the  $\langle 0001 \rangle$  direction to favor  $\{10\bar{1}2\}$  twinning. An NVT ensemble was used with a EAM potential by [37].

The bi-crystal was generated with the  $\{0001\}$  plane of the upper grain appended to the  $\{10\bar{1}4\}$  plane of the lower grain, producing a misorientation of  $25.1^\circ$ . The  $[1\bar{2}10]$  direction was the tilt axis and periodic conditions were applied in that direction with free surfaces in the other two directions. The dimensions were 30.5 by 54 by 2.6 nm. The upper and lower crystals were equally sized. The simulation was equilibrated at 300 K similarly to the single crystal and then loaded with compression along the x-direction. This favored twinning in both grains, but more in the upper grain. Loading at  $10^8 \text{s}^{-1}$  was applied up to 1 GPa. The x-dimension was then held fixed, and the stress allowed to plastically dissipate. Time integration was done with a NVE ensemble.

For all simulations, OVITO [38] was used for visualization with potential energy and the basal plane vector [7] used for coloration.

Interfacial defect theory, developed by Pond and coworkers [39–43] and previously applied to hcp twinning by Serra [44–49], was used for characterization. This work was extended by Barrett and El Kadiri [32, 50] to characterize interactions between disclinations and disconnections on twin interfaces [30, 33, 51].

## Results

### Single Crystal Nucleation

Characterization of atomistic results is greatly improved by ready identification of the relevant planes and directions in raw atomistic data. To help the reader follow along with our analysis, we have produced the following key in Fig. 1 illustrating common planes and directions seen from a variety of view directions in hexagonal close-packed lattices.

Single crystal  $\{10\bar{1}2\}$  twin nucleation in Mg generally occurs in the same manner regardless of whether free surfaces or periodic boundaries are used and regardless of the presence of initial voids or dislocations in the simulation [7]. In Fig. 2, we illustrate a small embryo which has just formed. Loading of Mg single crystals in tension on the c-axis prevents easy slip, leaving only pyramidal  $\langle c+a \rangle$  slip and  $\{10\bar{1}2\}$  twinning as possible plastic mechanisms. In the MD timescale,  $\langle c+a \rangle$  slip nucleates more easily, at a tensile stress above 4GPa, which is a couple order of magnitude greater than the experimental yield for single crystals in this loading. It may be that there are alternate nucleation processes for  $\{10\bar{1}2\}$  twins which require a greater activation time and thus are not observed here. In the scenario observed,  $1/2 \langle c+a \rangle$  dislocations move across the lattice leaving a high-energy stacking fault. Then, a twin embryo forms on the fault which is faceted such that the directions  $[1\bar{2}10]^{\text{parent}}$  and  $[11\bar{2}3]^{\text{twin}}$  are aligned. Likewise, the directions  $[1\bar{2}10]^{\text{twin}}$  and  $[11\bar{2}3]^{\text{parent}}$  are aligned.

In Fig. 2, three facets are present with slightly different misorientations, and thus disclinations along their junctions. Two of them are  $\{10\bar{1}1\}$  twist facets as discussed by [35]. These have a strained coherent character with a strain field imposing that  $[2\bar{4}20]^{\text{parent}} = [11\bar{2}3]^{\text{twin}}$  and  $[2\bar{4}20]^{\text{twin}} = [11\bar{2}3]^{\text{parent}}$ . In our simulations, the facets were small and there were no misfit dislocations relieving this strain. The third facet is the BP facet which has been extensively



**Fig. 1** Common view directions along with directions and plane normals visible in HCP lattices

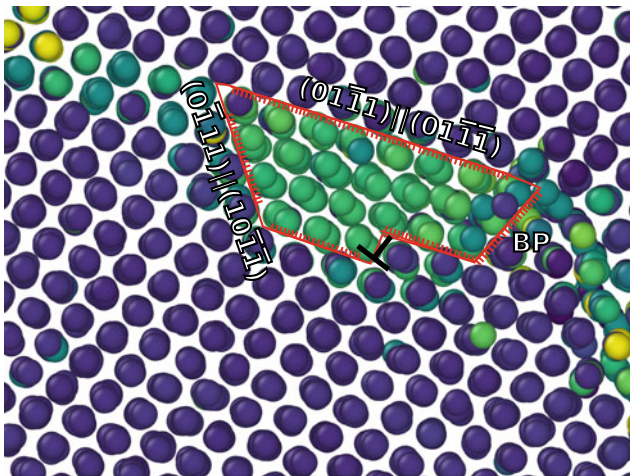
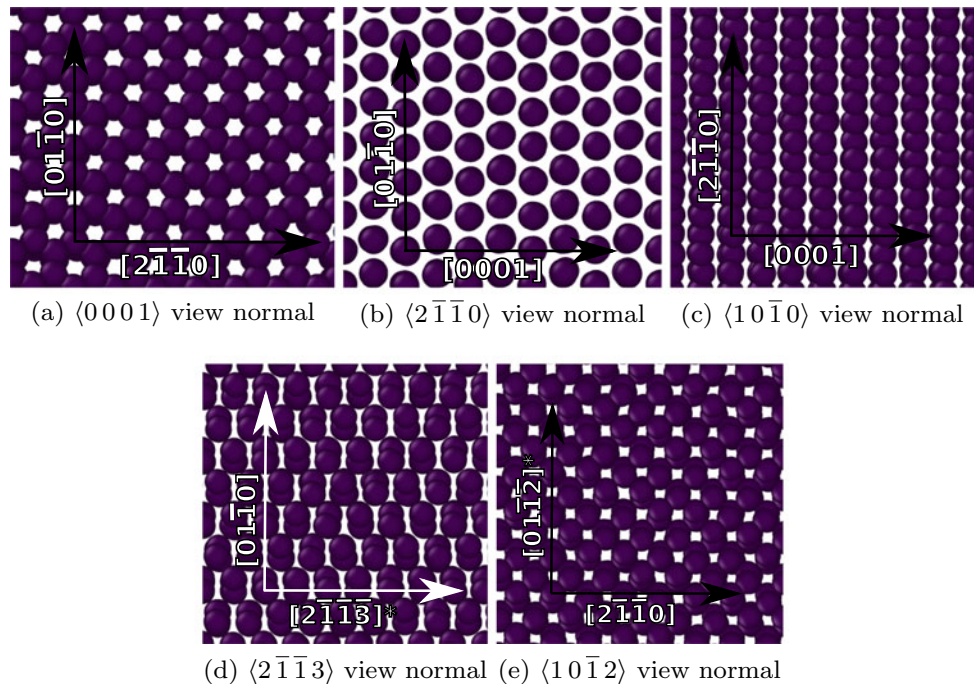


**Fig. 2**  $\{10\bar{1}2\}$  twin embryo viewed from the  $\langle 2\bar{1}\bar{1}0 \rangle$  plane growing off a  $\{10\bar{1}1\}$  stacking fault. Inside the twin, the view direction is  $\langle 2\bar{1}\bar{1}3 \rangle$

discussed elsewhere [32]. A disconnection is seen moving on one of the  $\{10\bar{1}1\}$  twist facets and growing the twin. Interfacial defect theory analysis suggests that this disconnection is glissile and can transform into a glissile disconnection on any of the other  $\{10\bar{1}2\}$  twin facets.

The embryo seen here shows close resemblance with those shown in [7, 32]. As these embryos continue to grow, they adopt an ellipsoidal, roughly egg-shaped form. A transition to the more needle-shaped morphology seen

experimentally is suggested in the largest simulations, but the simulation scale prevents a full transition to that shape.

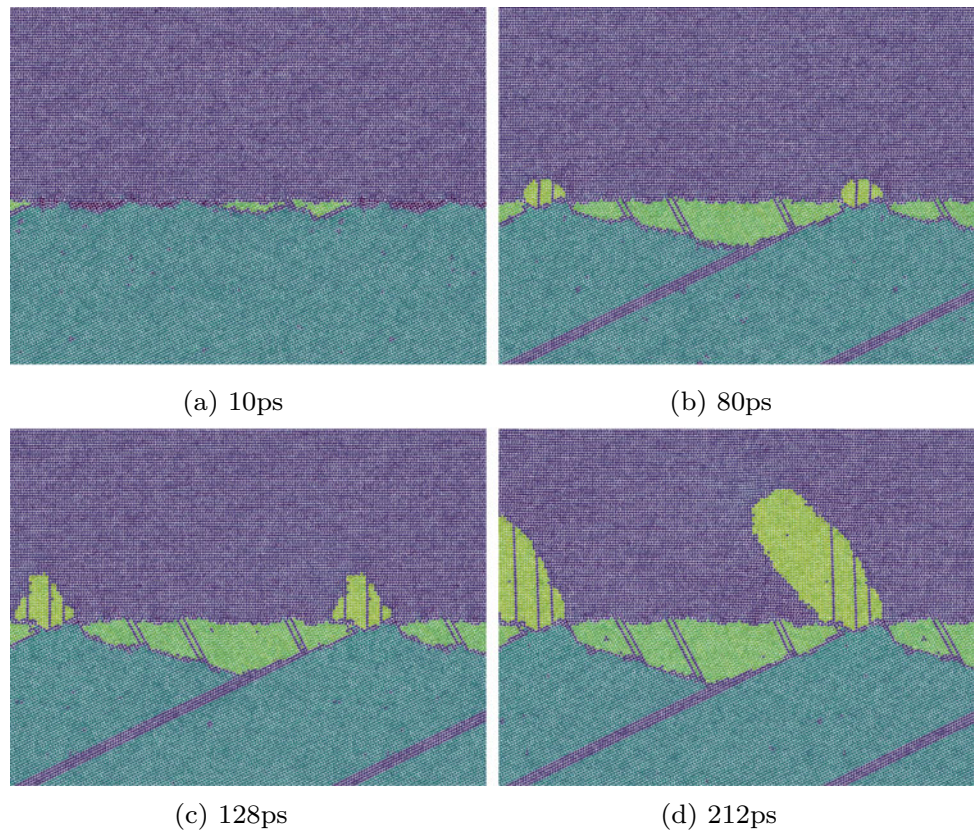
### Bi-crystal Nucleation

We also studied the case of grain boundary nucleation of  $\{10\bar{1}2\}$  twins. These simulations were able to nucleate at much lower stresses and probably hold more relevance to experimental results. We appended the  $\{1001\}$  and  $\{10\bar{1}4\}$  planes of the upper and lower crystals to create a high-energy asymmetric tilt boundary. This orientation was chosen because it has a very high energy, but the interface between a  $\{10\bar{1}2\}$  twin at the boundary with both the upper and lower grains should be low energy, thus enhancing the ease of nucleation. Figure 3 shows the nucleation process at several timesteps. These results are similar to earlier results by Wang et al. [52] for a symmetric tilt boundary with similar misorientation. Wang used a pileup of basal dislocations to encourage the nucleation process. In our work, no dislocations are present.

The initial very small embryos form during equilibration with no applied stress at all, illustrating the stability of the interfaces with the twin versus the low misorientation interface. Under applied load, the twins grow into both the upper and lower grains. These twin embryos show close to a needle-shaped morphology than the ones in single crystals. This is most likely because the misfit dislocations in the grain boundary discourage twin thickening.



**Fig. 3** A sequence of atomistic snapshots of the twin growing from the bi-crystal grain boundary. Twins inside the upper and lower grain are colored yellow–green and light green, respectively. Stripes through the twins are  $I_1$  faults



The applied loading of x-axis compression favors growth of the upper grain. However, the lower grain initially grows faster. Evidently, the asymmetric nature of the grain boundary affects the relative propensity for twinning within the two grains.

## Discussion

### $\{10\bar{1}2\}$ Twin Embryo Morphology

The  $\{10\bar{1}2\}$  twin nucleus makes extensive use of facets both within and outside of the shear plane. The role of these facets in the nucleation process is clearly critical. To help visualize the available facets in three dimensions, we have produced a schematic shown in Fig. 4. An embryo with all of these facets could appear to have an appearance like that of a cut gem. In a later publication, we will demonstrate that the formation and growth on all of these facets is interlinked and glissile movement of disconnections from one to another is permitted without any climb. The misorientations of most of the facets deviate from one another by  $4^\circ$  to  $8^\circ$ ; thus, the facet junctions are delineated by disclinations. In larger embryos, we have studied such as those published in [32], the embryo did make use of most or all of these facets but because of the disconnection lines spanning around the

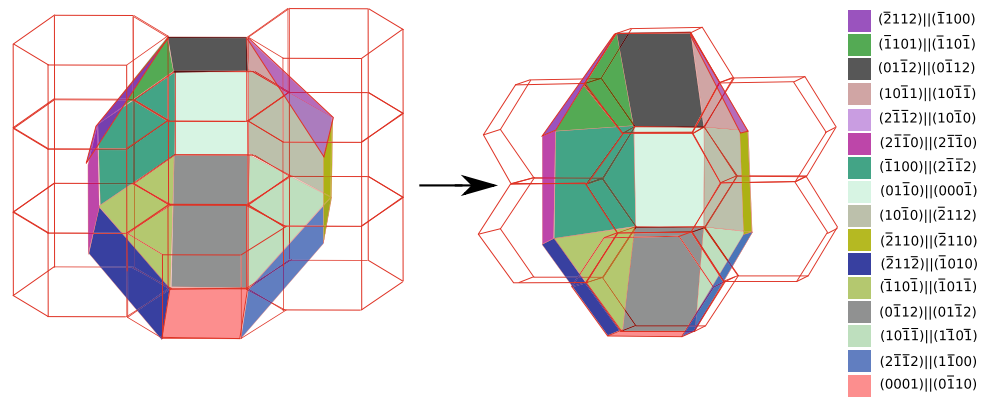
embryo, it had more of a rounded appearance rather than having sharp boundaries like the schematic in Fig. 4. The increasing disclination dipole and coherency strain energies as the embryo grows tend to force the twin to adopt a single preferred boundary—either  $(10\bar{1}2)$  or  $(10\bar{1}\bar{2})$ , which are the only two without any coherency strain. Thus, at larger scales,  $\{10\bar{1}2\}$  twins are generally seen with primarily these boundaries. Still, in highly deformed samples, even larger twins may have misorientations which deviate from that of the ideal twin boundary [53], by making more use of basal-prismatic and prismatic-basal boundaries, for example.

### Planar Nucleation of $\{10\bar{1}2\}$ Twins

By examining the details of the nucleation processes in both the single crystal and the bi-crystal cases, some common factors may be identified which we hypothesize play a critical role in  $\{10\bar{1}2\}$  twin nucleation. The most important of these is that in both cases the  $\{10\bar{1}2\}$  nucleated from a pre-existing planar defect. We propose that  $\{10\bar{1}2\}$  do not generate from dissociation of a single dislocation line because that is not planar. Rather, a stacking fault or a grain boundary is necessary for the initial nucleation.

Furthermore, we propose that the orientation of this planar fault must coincide with one of the many facet planes of

**Fig. 4** Complete set of known facets for  $\{10\bar{1}2\}$  twinning. The facets are capable of completely enclosing the embryo



the  $\{10\bar{1}2\}$  twin. This requirement was fulfilled in both simulations—the single crystal case generated first-order  $\langle c+a \rangle$  partial dislocations leaving a stacking fault on the  $\{10\bar{1}1\}$  plane. The  $\{2112\}$  plane is also a facet plane for  $\{10\bar{1}2\}$  twinning, so we theorize that second-order pyramidal  $\langle c+a \rangle$  slip could also produce a stacking fault from which a  $\{10\bar{1}2\}$  twin originated. In the bi-crystal asymmetric tilt boundary, the local structure was composed of a couple of structural units, primarily appending  $\{10\bar{1}2\}||\{10\bar{1}1\}$  planes and  $\{10\bar{1}4\}||\{0001\}$  planes. Some  $\{0001\}||\{10\bar{1}4\}$  local structures also appeared to be present. In any case, the twins nucleated from the basal planes move into both the upper and lower grains.

The final common factor in both simulations is that the nucleation of the twin provided significant energy relaxation compared to the pre-existing planar defect. In the bi-crystal case, this was so pronounced that the embryo formed with no applied load. It remained very small, only three layers thick, until loading was applied.

One of the primary difficulties in describing twin nucleation has been to explain a process which could reasonably produce the separation of the initial twinning disconnection dipole to form the first twinned region. In normal circumstance, there is a great attractive force driving the embryo to collapse. In our theory, the high-energy planar defect offsets this driving force by providing another driving force pushing the embryo to grow. Once the twin reaches the edge of the stacking fault, the trailing partial, or a misfit dislocation in the grain boundary, further energy relaxation by twin growth cannot be accomplished. Whether or not the nucleus grows into a full size twin then depends upon how large the embryo has grown and the applied stress state. In many scenarios, the embryo by this point will be larger than the critical size needed to shoot into the grain.

## Conclusions

We performed molecular dynamics simulations to investigate the nucleation of  $\{10\bar{1}2\}$  twins in Mg. Twins were nucleated in both single crystals and bi-crystals. Characterization of the twin embryos revealed that in both cases, twins nucleated on a pre-existing planar fault via faceting. The actual  $(10\bar{1}2)$  twin boundary was not present in the initial embryos, hindering easy identification. We propose that  $\{10\bar{1}2\}$  twins require a pre-existing high-energy planar defect to nucleate on one of the twin's faceting planes. In this scenario, the first 1–3 disconnection dipoles to form experience a driving force from the energy relaxation of the planar defect which overcomes their attractive nature and thus enables the embryo to stabilize. In scenarios where the applied loading is favorable and the embryo stabilizes above a critical size, shooting of  $\{10\bar{1}2\}$  disconnections into the lattice can occur.

## References

1. E. Orowan, AIME, New York p. 69 (1954)
2. P. Price, J. Appl. Phys. **32**(9), 1746 (1961)
3. J.W. Christian, *The Theory of Transformations in Metals and Alloys: Part I + II*. (Elsevier, 2002)
4. D. Oliver, Research **5**, 45 (1952)
5. N.P. Allen, B.E. Hopkins, J.E. McLennan, Proc. R. Soc. London, Ser. A **234**(1197), 221 (1956)
6. J.J. Cox, G. Horne, R. Mehl, T. Am. Soc. Metal **49**, 118 (1957)
7. C. Barrett, H. El Kadiri, M. Tschopp, J. Mech. Phys. Solids **60** (12), 2084 (2012). Cited By (since 1996) 0
8. R.L. Bell, R.W. Cahn, Proc. R. Soc. London, Ser. A **239**, 494 (1957)
9. R.W. Cahn, Il Nuovo Cimento (1943–1954) **10**, 350 (1953)

10. R.E. Reed-Hill, W.D. Robertson, *Trans. Met. Soc. AIME* **220**, 496 (1957)
11. A.M. Garde, E. Aigeltinger, R.E. Reed-Hill, *Metall. Trans. B* **4** (10), 2461 (1973)
12. R.E. Reed-Hill, in *The Inhomogeneity of Plastic Deformation*, ed. by R.E. Reed-Hill. American Society for Metals (American Society for Metals, Metals Park, OH, 1973), pp. 285–311
13. A.H. Cottrell, B.A. Bilby, *Philos. Mag. Series 7* **42**(329), 573 (1951)
14. N. Thompson, D. Millard, *Philos. Mag.* **43**, 422 (1952)
15. S. Mendelson, *J. Appl. Phys.* **40**(4), 1988 (1969)
16. S. Mendelson, *Mater. Sci. Eng.* **4**(4), 231 (1969)
17. S. Mendelson, *Nat. Bur. Stand. (US), Spec. Publ.* **317**, 495 (1970)
18. S. Mendelson, *J. Appl. Phys.* **41**(5), 1893 (1970)
19. S. Mendelson, *Scr. Metall.* **4**(1), 5 (1970)
20. K.P.D. Lagerlöf, J. Castaing, P. Pirouz, A.H. Heuer, *Philos. Mag. A* **82**(15), 2841 (2002)
21. L. Capolungo, D. Spearot, M. Cherkaoui, D. McDowell, J. Qu, K. Jacob, *Journal of the Mechanics and Physics of Solids* **55**(11), 2300 (2007)
22. L. Capolungo, I. Beyerlein, *Phys. Rev. B* **78**(2), 024117 (2008)
23. L. Capolungo, I.J. Beyerlein, G.C. Kaschner, C.N. Tomé, *Mater. Sci. Eng., A* **513–514**, 42 (2009)
24. I.J. Beyerlein, C.N. Tomé, *Proc. R. Soc. London, Ser. A* **466** (2121), 2517 (2010)
25. I. Beyerlein, L. Capolungo, P. Marshall, R. McCabe, C. Tomé, *Philosophical Magazine* **90**(16), 2161 (2010)
26. J. Wang, I.J. Beyerlein, C.N. Tomé, *Scr. Mater.* **63**(7), 741 (2010)
27. J. Wang, R.G. Hoagland, J.P. Hirth, L. Capolungo, I.J. Beyerlein, C.N. Tomé, *Scr. Mater.* **61**, 903 (2009)
28. J. Wang, J.P. Hirth, C.N. Tomé, *Acta Mater.* **57**, 5521 (2009)
29. J. Wang, L. Liu, C. Tomé, S. Mao, S. Gong, *Materials Research Letters* **1**(2), 81 (2013)
30. A. Ostapovets, A. Serra, *Journal of materials science* **52**(1), 533 (2017)
31. C.D. Barrett, H. El Kadiri, *Acta Materialia* **63**, 1 (2014)
32. C.D. Barrett, H. El Kadiri, *Acta Materialia* **70**, 137 (2014)
33. H. El Kadiri, C.D. Barrett, J. Wang, C.N. Tomé, *Acta Materialia* **85**, 354 (2015)
34. A. Serra, D.J. Bacon, *Philos. Mag. A* **73**(2), 333 (1996)
35. Y. Liu, N. Li, S. Shao, M. Gong, J. Wang, R. McCabe, Y. Jiang, C. Tomé, *Nature communications* **7**, 11577 (2016)
36. S. Plimpton, *J. Comput. Phys.* **117**(1), 1 (1995)
37. X. Liu, J. Adams, F. Ercolessi, J. Moriarty, *Modell. Simul. Mater. Sci. Eng.* **4**, 293 (1996)
38. A. Stukowski, *Modelling and Simulation in Materials Science and Engineering* **18** (2010)
39. R. Pond, *Philos. Mag. A* **47**(6), 49 (1983)
40. R. Pond, W. Bollmann, *Philosophical Transactions of the Royal Society of London. Series A, Mathematical and Physical Sciences* **292**(1395), 449 (1979)
41. R. Pond, *Dislocations and Properties of Real Materials* (Institute of Metals, 1985), chap. Interfaces and dislocations, pp. 71–93
42. R. Pond, A. Bastaweesy, *Le Journal de Physique Colloques* **46** (C4), 4 (1985)
43. R. Pond, M. Aindow, W. Clark, *Scr. Metall.* **21**(7), 971 (1987)
44. A. Serra, D.J. Bacon, *Philos. Mag. A* **63**(5), 1001 (1991)
45. A. Serra, D.J. Bacon, R.C. Pond, *Acta Metall.* **36**, 3183 (1988)
46. A. Serra, R.C. Pond, D.J. Bacon, *Acta Metall. Mater.* **39**(7), 1469 (1991)
47. A. Serra, D.J. Bacon, *Mater. Sci. Forum* **126**, 69 (1993)
48. A. Serra, D.J. Bacon, *Acta Metall. Mater.* **43**(12), 4465 (1995)
49. A. Serra, D.J. Bacon, R.C. Pond, *Metall. Mater. Trans. A* **33**(3), 809 (2002)
50. C.D. Barrett, H. El Kadiri, *Scripta Materialia* **84**, 15 (2014)
51. F. Wang, C.D. Barrett, R.J. McCabe, H. El Kadiri, L. Capolungo, S.R. Agnew, *Acta Materialia* **165**, 471 (2019)
52. J. Wang, S. Yadav, J. Hirth, C. Tomé, I. Beyerlein, *Materials Research Letters* **1**(3), 1 (2013)
53. J. Zhang, S.P. Joshi, *J. Mech. Phys. Solids* **60**(5), 945 (2012)

# In Situ TEM Investigation of $\langle c + a \rangle$ Dislocations in Magnesium

Bo-Yu Liu, Fei Liu, Bin Li, Jian-Feng Nie, and Zhi-Wei Shan

## Abstract

The ductility of magnesium is intimately related to  $\langle c + a \rangle$  dislocation. Understanding the behavior of  $\langle c + a \rangle$  dislocations is of critical importance for resolving the mechanical properties and for alloy design. By using in situ TEM mechanical testing of pillars of pure Mg single crystal, we found that  $\langle c + a \rangle$  dislocation can accommodate considerable plasticity. Our findings provide information on the mobility of  $\langle c + a \rangle$  dislocation and its relationship with plasticity of submicron-sized pure Mg. The experimental strategy can be extended to understanding the dislocation behaviors in other hexagonal metals.

## Keywords

Magnesium • In situ TEM •  $\langle c + a \rangle$  dislocation • Plasticity

## Introduction

Magnesium is the lightest structural metal, which is attracting worldwide interests because of its potential applications to higher energy efficiency and lower emissions by light weighting [1–4]. One bottleneck that hampers the widespread using of magnesium-based materials is their low ductility, which imposes severe constraints on cost-sensitive processing [5, 6]. The ductility of magnesium is closely related to pyramidal  $\langle c + a \rangle$  dislocations [7].  $\langle c + a \rangle$  dislocation slip can provide plastic strain along the  $c$ -axis, which is necessary for accommodating anisotropic plasticity of magnesium undergoing plastic forming, e.g. rolling and drawing. Over the past decades, understanding the fundamental behaviors of  $\langle c + a \rangle$  dislocations has been central to the research of ductility and formability of magnesium and its alloys [8–34]. Recent studies focus on whether  $\langle c + a \rangle$  dislocations can glide and therefore to accommodate plastic strain [35–50]. This issue is of critical importance in determining the strategy for the development of new wrought magnesium alloys. Our recent work demonstrated that at least for submicron-size pure magnesium, pyramidal  $\langle c + a \rangle$  dislocations of various characters (edge, screw, and mixed) can glide on both pyramidal I and II planes to generate large plasticity [50]. The current paper presents more experimental details and provides more experimental observations of mobile pyramidal  $\langle c + a \rangle$  dislocations in single crystal magnesium.

## Methods

In situ quantitative mechanical testing inside transmission electron microscope (TEM) can capture microstructure evolution in real time and obtain the corresponding mechanical data [50–55]. Figure 1 shows the sample preparation and experimental setup. The submicron-size pillars were fabricated by using focused ion beam (FIB). In situ TEM compression experiments were performed with a

B.-Y. Liu · F. Liu · Z.-W. Shan (✉)  
 State Key Laboratory for Mechanical Behavior of Materials,  
 Center for Advancing Materials Performance from the Nanoscale  
 (CAMP-Nano) and Hysitron Applied Research Center in China  
 (HARCC), Xi'an Jiaotong University, 710049 Xi'an, People's  
 Republic of China  
 e-mail: [zwshan@xjtu.edu.cn](mailto:zwshan@xjtu.edu.cn)

B. Li  
 Department of Chemical and Materials Engineering,  
 University of Nevada, Reno, USA

J.-F. Nie  
 Department of Materials Science and Engineering,  
 Monash University, Melbourne, VIC 3800, Australia

International Joint Laboratory for Light Alloys  
 (Ministry of Education), College of Materials Science and  
 Engineering, Chongqing University, 400044 Chongqing, China



**Fig. 1** Sample preparation and experimental setup. **a** The sample is pasted on a copper mount. The pillars are fabricated by FIB. **b** In situ TEM mechanical testing setup

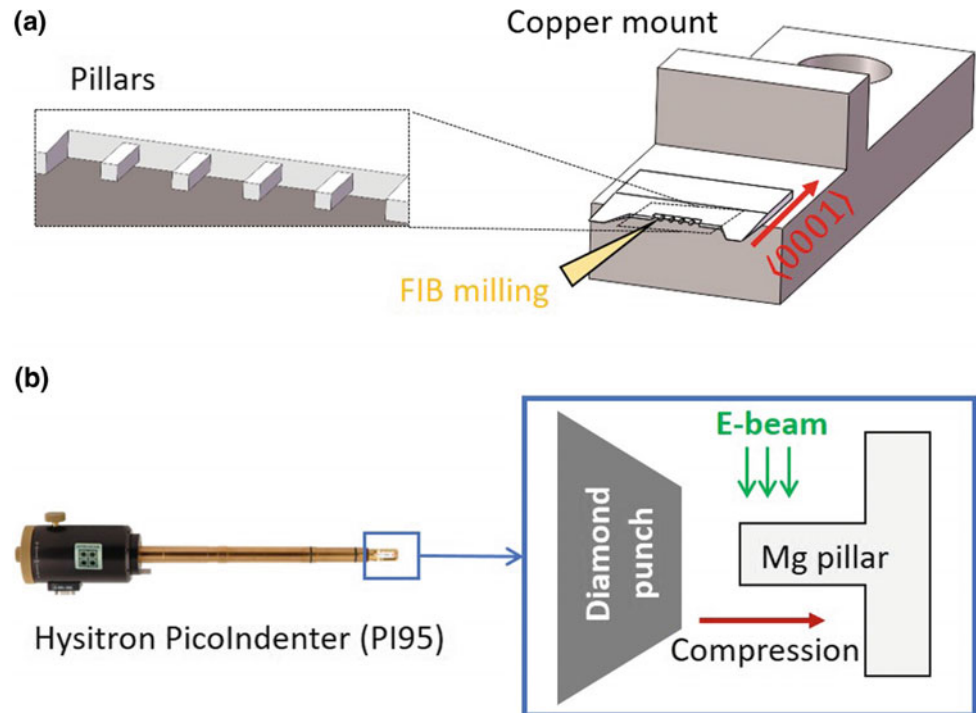
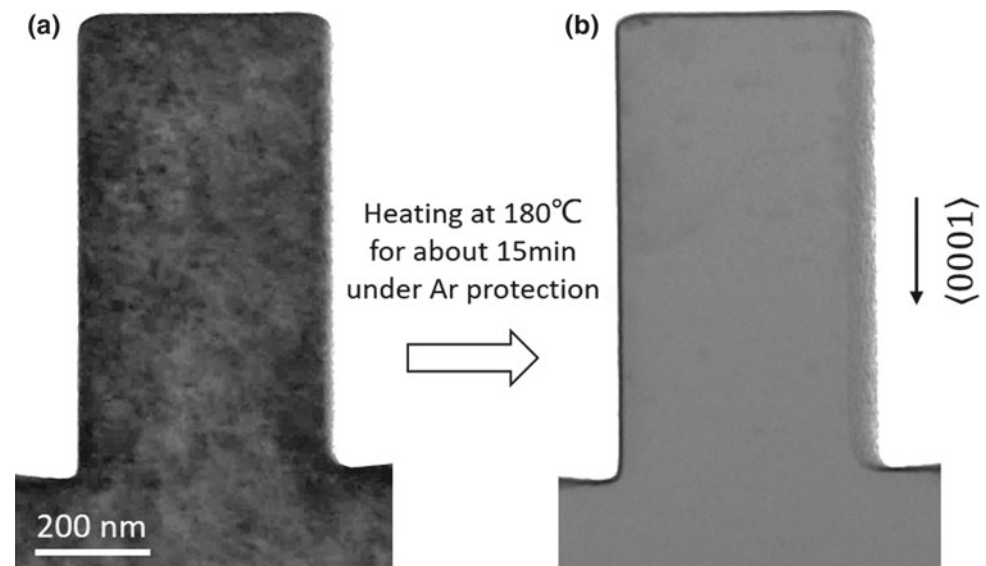


**Fig. 2** FIB-induced defects can be largely reduced by annealing. **a** As-FIBed pillar. **(b)** Annealed pillar. Zone axis  $\sim [2\bar{1}10]$



Hysitron PicoIndenter (PI95) inside a TEM (JEOL 2100F, 200 keV). In situ videos were recorded by Gatan 833 camera. The pillars were compressed by a diamond indenter with a flat punch. The compression tests were conducted under displacement control mode with the strain rate of  $10^{-3} \text{ s}^{-1}$ . The compressive loading direction is parallel to the axial direction of pillar that is close to  $\langle 0001 \rangle$ . The viewing direction (zone axis) is  $\sim \langle 2\bar{1}10 \rangle$ .

The FIB-induced defects on pillar surface will interfere with the contrast of dislocations. In order to reduce such interference, the samples were annealed at  $180^\circ\text{C}$  for about 15 min inside a tube furnace. Argon atmosphere was used to protect the magnesium sample from oxidation. Figure 2 shows a pillar before and after annealing. In the as-FIBed pillar, there were FIB-induced defects which were largely removed after annealing.



## Results

One typical example of pillar compression tests is shown in Fig. 3. The test was monitored under dark-field imaging condition with  $g = \{0002\}$ . In this imaging condition, only dislocations with Burgers vector containing  $\langle c \rangle$  component were visible. These dislocations activated under  $c$ -axis compression were proven to be  $\langle c+a \rangle$  dislocations by using  $g \cdot b$  contrast analysis [50]. The dislocations first appeared when the applied stress reached  $\sim 220$  MPa. They formed near the contact interface between the pillar top and the diamond punch. More dislocations formed and gradually propagated through the entire pillar during the loading. The test was terminated at 7.1% strain. No failure was observed

in this pillar. Note that higher plastic strains would be achievable if the tests continued. In the lower parts of this pillar, several  $\langle c+a \rangle$  dislocations can be clearly observed (marked by dashed frame, Fig. 3c).

The glide of three dislocations is displayed in Fig. 4. The initial position of these dislocations is marked by a series of colored dots: dislocation-1, red; dislocation-2, green; dislocation-3, orange (Fig. 4a). According to our previous TEM characterizations and geometrical analyses, the long and straight segments lying parallel to the intersection of pyramidal plane and basal plane are of edge types, while the rest of segments are of mixed or screw types [50]. Figure 4b shows the schematic drawing of the moving dislocations in the corresponding TEM images. The current and previous

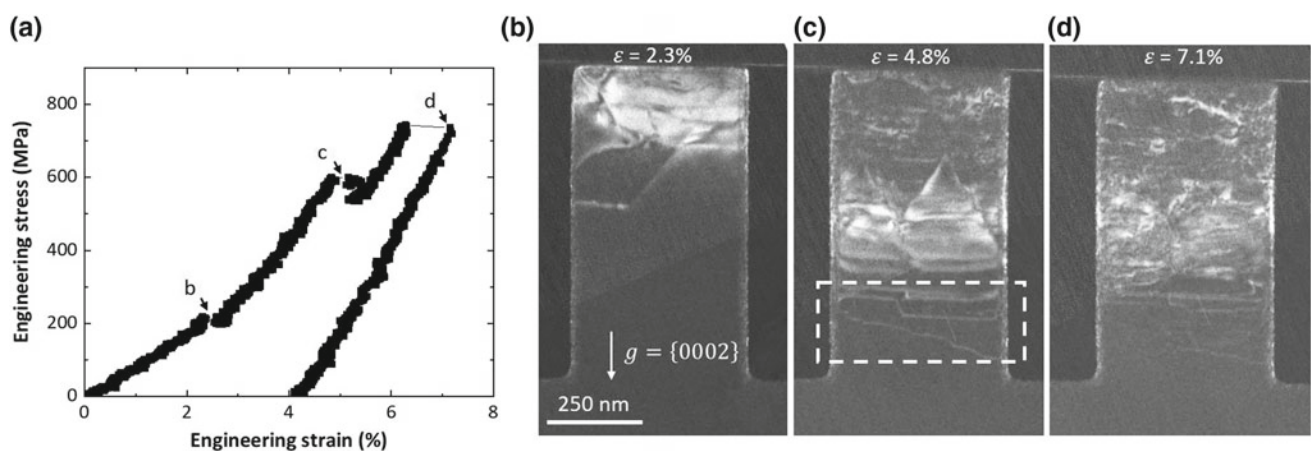


**Fig. 3** In situ TEM mechanical testing shows that  $\langle c+a \rangle$  dislocations are generated and glide during loading of a pillar. Loading direction,  $\sim [0001]$ . Zone axis,  $\sim [2\bar{1}\bar{1}0]$ . **a** Corresponding engineering stress–

strain curve. **b–d** Dark-field TEM images captured from in situ video show the formation and propagation of  $\langle c+a \rangle$  dislocations.  $\epsilon$ , engineering strain

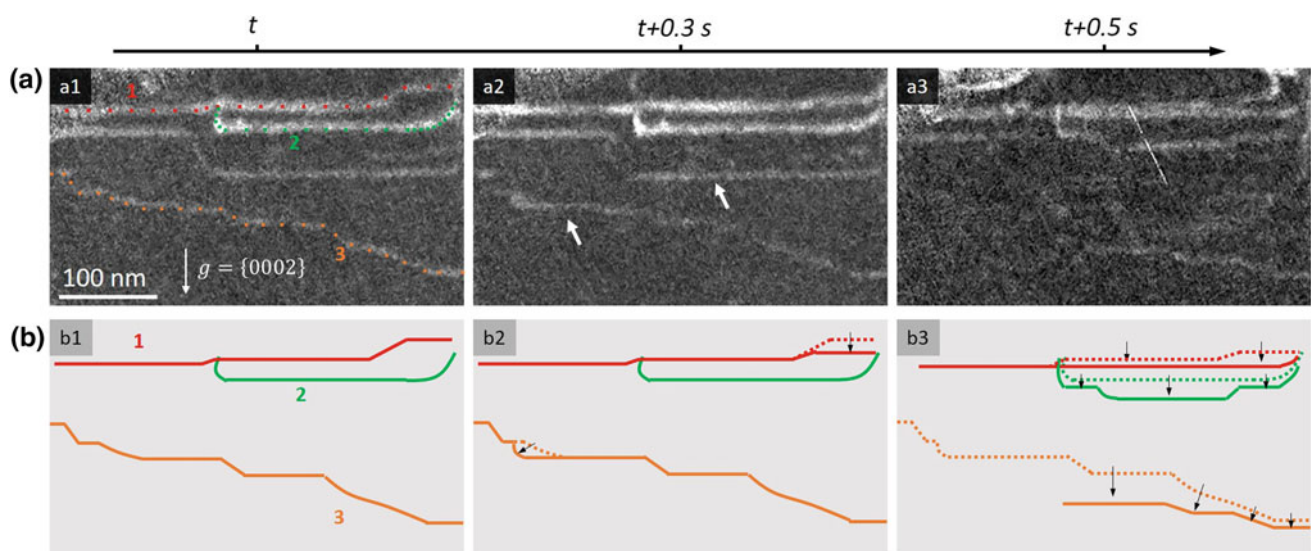


**Fig. 4** In situ TEM observation shows the movement of  $\langle c+a \rangle$  dislocations during loading. **a** A set of dark-field images captured from in situ movies with time sequence. Zone axis,  $\sim [2\bar{1}\bar{1}0]$ . **b** Schematic drawing of the moving dislocations in the corresponding TEM images

location of dislocations is represented by solid and dashed lines, respectively. The black arrows indicate the direction of dislocation movement. These dislocations exhibit zig-zag and half-loop configuration and therefore contain edge, screw, and mixed segments. The movement of these dislocations indicated that the  $\langle c+a \rangle$  edge, screw, and mixed dislocation are all glissile, contributing to plastic deformation. The pure edge segments are also observed to glide under applied stress, indicating that they are glissile. We also note that some parts of the dislocations disappeared during loading (marked by white arrows in Fig. 4a). These parts may have moved out to the pillar surface.

## Discussion

In submicron-sized crystals, the amount of preexisting dislocations should be less than that in bulk scale crystals. In the present work, the magnesium pillar was annealed, which further reduced the density of preexisting dislocations. Therefore, higher stress is needed to nucleate dislocations or activate dislocation sources in the submicron-sized magnesium pillars than that in larger pillars. For example, the yield stress for bulk and micron scale magnesium single crystal pillars under  $c$ -axis compression is in the range of 200–300 MPa [10, 21, 24]; when the sample size reduces to the submicron scale, the yield stress increases to 600–800 MPa [50]. Such high stresses can promote the formation and motion of  $\langle c+a \rangle$  dislocations to accommodate plasticity. Note that the failure strain for bulk magnesium single crystal under  $c$ -axis compression is usually less than 10% [10, 21], but for submicron-size magnesium the plastic strain can be as high as 30% [50]. Moreover, in our submicron-size magnesium pillars,  $\{10\bar{1}1\}$  contraction twin does not form. This deformation twinning mode often occurs in bulk scale magnesium under  $c$ -axis compression [56]. Contraction twins may introduce shear localization and stress concentration and serve as crack initiation sites. Therefore, the suppression of deformation twinning in small scale may also help prevent low-strain failure.

In magnesium and other hexagonal metals,  $\langle c+a \rangle$  slip can provide extra independent slip systems to meet the von Mises criterion and can provide  $c$ -axis strain. In contrast, type  $\langle a \rangle$  dislocations offer only four independent slip systems and cannot contribute to  $c$ -axis strain. Therefore,  $\langle c+a \rangle$  dislocation slip is important in promoting uniformity in plastic strain accommodation and overall ductility in magnesium. Our results find that  $\langle c+a \rangle$  dislocations are glissile and can contribute to considerable plasticity in submicron-size magnesium. This suggests that reducing grain size may be an effective way to improve the ductility of magnesium by promoting  $\langle c+a \rangle$  dislocation slip.

## Summary

By conducting in situ TEM mechanical testing, we have demonstrated that pyramidal  $\langle c+a \rangle$  edge, screw, and mixed dislocations are glissile. They can serve as predominant plasticity carrier when a submicron-sized magnesium crystal undergoes  $c$ -axis compression. Our results are expected to provide new insights into the mechanical behavior of magnesium at different length scales.

**Acknowledgements** This work was supported by the National Key Research and Development Program of China (No. 2017YFB0702001), National Natural Science Foundation of China (Nos. 51601141), China Postdoctoral Science Foundation (2016M600788), and funding from the Science and Technology Departments of Shaanxi, China (Nos. 2016KTZDGY-04-03, 2016KTZDGY-04-04). B. L. thanks the support from US National Science Foundation (CMMI-1635088). J. F. N. acknowledges the support from the Australian Research Council.

## References

1. L.-Y. Chen, et al., Nature (2015).
2. W. Xu, et al., Nat. Mater. (2015).
3. G. Wu, et al., Nature (2017).
4. T.M. Pollock, Science (2010).
5. B.-C. Suh, et al., Scr. Mater. (2014).
6. W.J. Joost, et al., Scr. Mater. (2017).
7. M.H. Yoo, Metall. Trans. A (1981).
8. H. Yoshinaga, et al., T. Jpn. I. Met. (1964).
9. J.F. Stohr, et al., Philos. Mag. (1972).
10. T. Obara, et al., Acta Metall. (1973).
11. S. Ando, et al., Non-Basal Slips in Magnesium and Magnesium-Lithium Alloy Single Crystals, Mater. Sci. Forum, 2000, pp. 1188-1191.
12. M.H. Yoo, et al., Mater. Sci. Eng., A (2001).
13. S.R. Agnew, et al., Metall. Mater. Trans. A (2002).
14. H. Tonda, et al., Metall. Mater. Trans. A (2002).
15. M.H. Yoo, et al., Metall. Mater. Trans. A (2002).
16. S.R. Agnew, et al., Scr. Mater. (2003).
17. J. Koike, et al., Acta Mater. (2003).
18. K. Mathis, et al., Acta Mater. (2004).
19. S.R. Agnew, et al., Int. J. Plast. (2005).
20. S. Agnew, et al., Acta Mater. (2006).
21. T. Kitahara, et al., Key Engineering Materials (2007).
22. O. Muránsky, et al., Mater. Sci. Eng. A (2008).
23. B. Li, et al., Philos. Mag. (2009).
24. C.M. Byer, et al., Scr. Mater. (2010).
25. B. Li, et al., Acta Mater. (2010).
26. E. Lilleodden, Scr. Mater. (2010).
27. B. Syed, et al., Scr. Mater. (2012).
28. Z. Yang, et al., Acta Mater. (2013).
29. J. Geng, et al., Philos. Mag. Lett. (2014).
30. H. Fan, et al., Mater. Sci. Eng. A (2015).
31. M. Itakura, et al., Phys. Rev. Lett. (2016).
32. K.Y. Xie, et al., Scr. Mater. (2016).
33. J. Jain, et al., Scr. Mater. (2017).
34. M.A. Shehadeh, et al., Comput. Mater. Sci. (2017).
35. S. Sandlöbes, et al., Acta Mater. (2011).
36. S.R. Agnew, Advances in Wrought Magnesium Alloys, Woodhead Publishing 2012, pp. 63-104.

37. S. Sandlöbes, et al., *Acta Mater.* (2012).
38. S. Sandlöbes, et al., *Mater. Sci. Eng. A* (2013).
39. Q. Yu, et al., *Proc. Natl. Acad. Sci.* (2013).
40. S. Sandlöbes, et al., *Acta Mater.* (2014).
41. Y. Tang, et al., *Acta Mater.* (2014).
42. S.R. Agnew, et al., *Acta Mater.* (2015).
43. Z. Wu, et al., *Nature* (2015).
44. Z. Wu, et al., *Scr. Mater.* (2016).
45. A. Kumar, et al., *Mater. Sci. Eng. A* (2017).
46. B. Li, et al., *Scr. Mater.* (2017).
47. S. Sandlobes, et al., *Sci. Rep.* (2017).
48. R. Ahmad, et al., *Scr. Mater.* (2018).
49. Z. Ding, et al., *Acta Mater.* (2018).
50. B.-Y. Liu, et al., *Science* (2019).
51. Z.W. Shan, *JOM* (2012).
52. B.Y. Liu, et al., *Nat. Commun.* (2014).
53. B.-Y. Liu, et al., *Scr. Mater.* (2015).
54. B.-Y. Liu, et al., *J. Mater. Sci. Technol.* (2018).
55. Y. Wang, et al., *Nat. Commun.* (2018).
56. M.R. Barnett, *Mater. Sci. Eng. A* (2007).

# Full-Field Crystal Plasticity Modeling of $\{10\bar{1}2\}$ Twin Nucleation

YubRaj Paudel, Christopher D. Barrett, and Haitham El Kadiri

## Abstract

Historically, the ability of crystal plasticity to incorporate the Schmid's law at each integration point has been a powerful tool to simulate and predict slip-induced localization at the single and polycrystal levels. Unfortunately, this remarkable capability has not been replicated for materials where twinning becomes a noticeable deformation mechanism. The challenge resides mainly in the biased regional lattice transformation associated with twin formation in defiance of its obedience to threshold stress. Inspired by results from micromechanics, digital image correlation, and molecular dynamics, we developed an explicit twinning nucleation criterion based on hydrostatic stress gradient and volume fraction of twin inside a grain. Characteristic twin spacing parameter is used as a function of twin height to determine site-specific nucleation points in the case of multiple twins. This approach offered a good reproduction of the microstructure evolution and autocatalysis phenomenon as affected by twinning in a tricrystal system.

## Keywords

Crystal plasticity • Hydrostatic stress • Twin spacing

## Introduction

Twinning is referred to as a “double edged sword” mechanism because of its ability to increase strength and ductility in a low-stacking fault energy cubic crystal system, however, it reduced ductility, anisotropy, and damage in orthorhombic and hexagonal close-packed (hcp) structures. In hcp metals, the lack of “easy” slip modes to accommodate  $\langle c \rangle$ -axis tension/compression [1] at low temperatures/high strain rates stokes a whole host of shear localization phenomena, including twinning and pyramidal  $\langle c + a \rangle$  slip. Twinning is a particular challenge as its polarity and lattice reorientation tend to cause strong asymmetry and anisotropy, respectively, which increases with texture strength. Furthermore, it has been shown that twinning interaction with microstructural defects contributes to strain incompatibilities and damage initiation [2].

In recent years, experimental studies through scanning electron microscope (SEM) and transmission electron microscope (TEM) along with atomistic simulations have shown several mechanisms associated with twinning such as twin–twin interaction [3–6], slip–twin interaction [7, 8], detwinning [9–11], twin–grain boundary interactions [12–14], and double twinning [15, 16]. At the microscale level, substantial efforts have been made to understand the mechanisms associated with twin nucleation, propagation, and growth, and upscale them to crystal plasticity models [17–22].

Crystal plasticity techniques have been a powerful tool to simulate and predict the slip behavior at the grain level and the subsequent heterogeneous stress/strain localization and texture evolution at the macroscopic level. In hexagonal close-packed (hcp) metals, crystal plasticity based on finite element methods (CPFEM) [11, 20, 23–26] and fast-Fourier transform (CPFFT) [21, 22, 27, 28] has been employed to capture the heterogeneous deformation behavior of twinning. However, most of the models lag physically motivated twin incorporation that reflects the early stages of embryonic

Y. Paudel · C. D. Barrett · H. El Kadiri (✉)  
Center for Advanced Vehicular Systems, Mississippi State University, Starkville, MS 39759, USA  
e-mail: [elkadiri@me.msstate.edu](mailto:elkadiri@me.msstate.edu)

C. D. Barrett · H. El Kadiri  
Department of Mechanical Engineering, Mississippi State University, Starkville, MS 39762, USA

H. El Kadiri  
Universite Internationale de Rabat, Rabat-Shore Rocade  
Rabat-Salé, Rabat, Morocco



twin nucleation and lengthwise burst. Most of the full-field crystal plasticity models employ phenomenological criteria to capture twinning, exemplified by pseudo-slip approach, absence of site-specific twin nucleation, and ensuing lack of reproducing the observed twin spacing including the case of multivariant twinning. Likewise, the evolution of deformation twins with strain, and ultimately calculations of constitutive response along with proper description of twin interfaces and twin boundaries are yet to be incorporated in crystal plasticity models. The Schmid factor based on far-field stress is inadequate to describe variant selection [29] and dynamics of twin expansion. The dependence of the twin nucleation stress on the grain size [30] has not yet been quantified in crystal plasticity models. In recent years, some of the full-field crystal plasticity approaches have been successful to introduce a site-specific twin nucleation [26, 31]; however, they do not ratify all the features of twinning and twin interfaces.

For any compound twin, a recent theory provides an analytical solution for the vector displacements for both shear and shuffle [32]. Shear, which is the most fundamental and unquestionable condition for dislocation and disconnection motion, is associated with the Schmid behavior. However, shuffles are related to the atomic movement due to diffusion. In general, the only component of stress that drives diffusion is the hydrostatic pressure or more precisely gradient of hydrostatic pressure. As shuffle is a pure diffusion phenomenon, it could be readily sensitive to the local state of hydrostatic pressure in the disconnection core as its glide along the twin interface. In an experimental study [33], an inherent difference in the stress state between contraction and compression showed profound implications on the ease of shuffle and the mobility of disconnections. A complex stress state acting on the  $\langle c \rangle$ -axis of the unit crystal lattice aided the shuffle associated with twin formation thereby reducing the required stress to induce shear through twinning or slip [33]. Inspired by these results stressing the effect of shuffles on twin nucleation and disconnection core width, we developed an explicit twinning nucleation criterion based on hydrostatic stress gradient and volume fraction of twin inside a grain.

## Twinning-Induced Microstructure

Proust et al. [34] showed that profuse twinning followed by rapid strain hardening led to a strain–path anisotropy in highly textured Mg alloy. Studies have shown that the high strain hardening is caused due to interactions between the twinning-induced microstructure and slip activities [3, 8, 17, 35, 36]. The dislocation transmutation reactions and slip–twin interactions are clearly evident through abundantly available residual slips in the vicinity of twin boundaries as

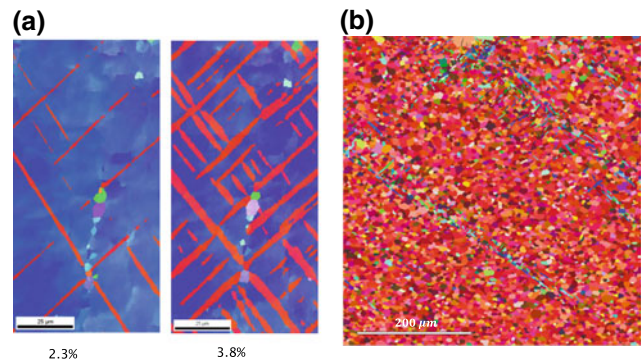


**Fig. 1** **a** Twinning-induced microstructure inside a single grain in Mg AM30 specimen [3] and **b** Twinning patterns in a polycrystal Mg AZ31 specimen during three-point bending [40]

observed from the TEM experiments [37]. A twinning-induced microstructure within a single grain of extruded Mg AM30 specimen under compression is also shown in Fig. 1a [3]. In a twinning-induced microstructure, a vivid characteristic twin spacing can be observed during twinning that should be quantified and upscaled to the crystal plasticity models. These characteristic twin spacings that depend on the height of twins [38] are observed in polycrystal with strongly basal texture [39, 40].

In Mg polycrystal, a characteristic twin spacing parameter was observed during three-point bending of strongly basal textured Mg AZ31 alloy [38]. As seen in Fig. 1b, a localized twinning pattern was observed with twins across multiple grains because of autocatalysis. Autocatalysis of a twin at low-angle misorientation boundary has previously been observed in many studies [40–42]. A micromechanical solution for an ellipsoidal twin in an infinite-half space domain showed that this characteristic twin spacing can be determined through the study of elastic response of a twin and it is directly proportional to the height of twin [38]. A digital image correlation (DIC) analysis performed on three-point bending of Mg AZ31 showed that the twinning-induced microstructure evolution follows the same characteristic twin spacing behavior predicted by a micromechanical-based analytical solution [40].

## New Crystal Plasticity Approach

As shuffles play an important role in atomic movement during disconnection glide, we justifiably added the contribution of hydrostatic stress gradient contribution to twin nucleation stresses as they pertain to diffusion which excludes contribution from deviatoric stresses. This initiative is well supported by various experimental findings and atomistic simulations emphasizing the role of defects in twin nucleation and mode selection. We naturally used a volume



fraction to determine twinning nucleation and used characteristic twin spacing that is a function of twin height to determine twinning-induced microstructure evolution.

In the current work, we will focus on crystal plasticity fast-Fourier transform (CPFFT) to incorporate the explicit twinning to accommodate deformation [43]. The elastic response for the twin is obtained using the technique used by Kumar et al. [21]. After each deformation step, strain and stress fields are determined based on the Green's function method solved using Lagrangian–Newton–Raphson method. The shear rate at each slip and twin systems is ensured by Eq. 1 at each integration point.

$$\dot{\gamma}^\alpha = \dot{\gamma}_0^\alpha \left| \frac{\tau^\alpha}{g^\alpha} \right|^{\frac{1}{m}} \quad (1)$$

The twinning criterion is based on the hydrostatic stress across the representative volume element (RVE) to determine whether twin forms or not within a grain. Twinning is the localized event and twin nucleation process is influenced by both shear and shuffle. In most of the twinning criteria, only the shear portion of twin is considered to determine whether the twin nucleated or not. However, shuffle is an important mechanism that ensures twinning through a diffusion process. Since diffusion is a function of hydrostatic pressure, the hydrostatic stress field in the material domain should be used as a twinning criterion. The hydrostatic stress ( $\sigma_h$ ) at any integration point can be determined by:

$$\sigma_h(x) = \frac{1}{3} \sum_i \sigma_{ii}(x) \quad (2)$$

The gradient of hydrostatic stress can then be calculated by

$$\nabla_i \sigma_h(x) = \frac{\sigma_h(x + x_i) - \sigma_h(x)}{\delta x_i} \quad (3)$$

Based on the accumulated twinning shear at each point, the twin volume fraction ( $f$ ) at each integration point in a RVE is determined using Schmid's law.

$$f(x) = \sum^t \dot{f}(x) \Delta t = \sum^t \frac{\dot{\gamma}(x)}{\gamma_{tw}} \Delta t \quad (4)$$

The volume fraction for twin systems in each grain is then calculated as the sum average of volume fraction at each point inside of the grain,  $i$ .

$$f_{\text{grain}^i}^\alpha = \frac{V(x)}{V(\text{grain}^i)} \sum_x^{\text{grain}^i} f^\alpha(x) \quad (5)$$

where  $V(x)$  is the volume of each integration point and  $V(\text{grain}^i)$  is the volume of each grain.

The twinning is nucleated with either of the two conditions:

1. if the gradient of hydrostatic pressure reaches a threshold value and/or
2. if the volume fraction of the grain reaches a threshold volume fraction.

The first condition allows for a twin to nucleate at the requirement of strain triaxiality. This addresses the issue of autocatalysis as the strain accommodated by a twin at a grain boundary creates stress triaxiality, when the gradient is enough, new twin nucleates. In the second case scenario, if the volume fraction within a grain is greater than the threshold volume fraction for that twin variant, then the twin nucleates. However, the number of twins nucleated depends upon the twin variant, grain morphology, and grain size. When nucleating a twin, a minimum thickness of twin is assumed. Based on the volume fraction of twin, the number of twin is determined by:

$$N_{\text{twins}}^\alpha(\text{grain}^i) = \frac{f^\alpha(\text{grain}^i)V(\text{grain}^i)}{t_{tw} * A_{tw}^\alpha(x_0)} \quad (6)$$

where  $f^\alpha(\text{grain}^i)$  is the volume fraction of twin system  $\alpha$ ,  $V(\text{grain}^i)$  is the volume of grain,  $t_{tw}$  is the minimum twin thickness, and  $A_{tw}^\alpha(x_0)$  is the area of the twinning plane inside a grain.  $x_0$  is the position of maximum gradient of hydrostatic pressure inside of the grain.

During nucleation of multiple twins at a time, a characteristic twin spacing parameter,  $k$ , is used to determine the separation distance between the twins. Twinning spacing, which is a function of twin height, is defined by:

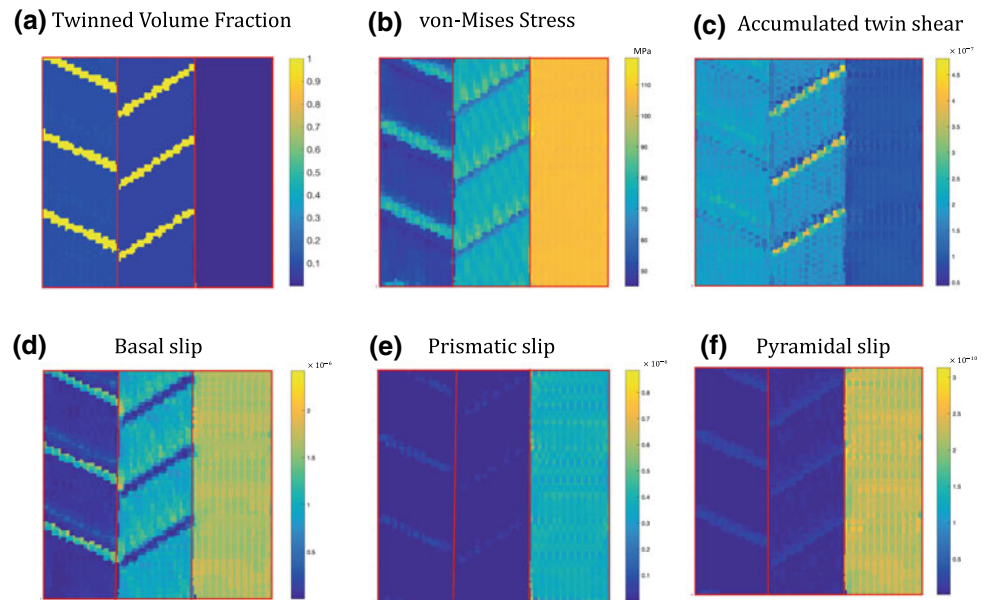
$$h_{tw} = k \times \sqrt{A_{tw}} \quad (7)$$

where  $A_{tw}$  is the area of the twinning plane in the grain used to calculate length of the twin.

The viscoplastic FFT formulation, modified to account for site-specific twin nucleation and characteristic twin spacing, is applied to predict the local behavior of tricrystal unit cells. The stress–strain response shows drops in von-Mises stress that corresponds with the formation of twins, which reflect the plateau in stress–strain curve during profuse twin nucleation. The site-specific twin is inserted for only predominant twin variant resulting single twin variant nucleated at every grain. However, this approach can be used to ensure multiple twin variants in a single twin.

Figure 2a shows the  $(1 \bar{1} 0 2)[\bar{1} 1 0 1]$  twin variant nucleation in grain 2 at strain 0.7%. The lower twin in grain 2 nucleates at the tip of the twin in grain 1, whereas other two twins in grain 2 follow characteristic twin spacing to nucleate. The von-Mises stress in Fig. 2b shows the stress field as a

**Fig. 2** At 0.7% strain, **a**  $(0\bar{1}12)$   $[01\bar{1}1]$  twin variant nucleates at grain 1 and  $(1\bar{1}02)[\bar{1}101]$  twin variant nucleates at grain 2, **b** von-Mises stress response on different grains, and deformation activities is shown for **c** twin, **d** basal, **e** prismatic and **f** pyramidal slip systems



At 0.7 % strain (Grain 2 twins)

result of twinning in grain 1 and grain 2. The stress relaxation due to twin formation in grain 1 and grain 2 is responsible for the stress drop that results in plateau region in stress–strain curve. Figure 2c shows the effects of accumulated shear in grain 3 due to twinning in grain 1 and grain 2. Likewise, the plastic strain carried by twin tip in the grain boundary of grain 3 is accommodated by basal, prismatic, and pyramidal  $\langle c+a \rangle$  slip systems as seen in Fig. 2d, e, and f respectively.

The twin variant in grain 2 is different from the twin variant nucleated in grain 1. The stress carried by twin in grain 1 resolved to both  $(0\bar{1}12)$   $[01\bar{1}1]$  and  $(1\bar{1}02)$   $[\bar{1}101]$  twin systems show that resolved shear stress for  $(1\bar{1}02)[\bar{1}101]$  twin variant is significantly higher than other twin variants including  $(0\bar{1}12)[01\bar{1}1]$  that twinned in grain 1. The nucleation of different twin variant as a result of twin accommodation at grain twin boundary has been previously observed in experiments [44].

With the implementation of characteristic twin spacing and site-specific twin nucleation criterion using hydrostatic pressure, we are able to reproduce the twin-lamellae induced microstructure that is observed in real experiments. Although the current model is not complete and has many limitations, this path for twinning criterion with multiple twins in crystal plasticity models is groundbreaking and should be evolved.

## Conclusions

This work incorporates the characteristic twin spacing mechanisms observed in twinning-induced microstructure with site-specific twin nucleation criterion based on

hydrostatic stress. Twinning process is a combination of twinning shear glide and shuffle mechanisms. This work makes an effort to include shuffle mechanism, which is a diffusion process that depends on hydrostatic stress, in a crystal plasticity framework to accurately incorporate the role of twinning in microstructure evolution, hardening, and damage initiation. The model can reproduce the multiple twins' nucleations with characteristic twin spacing, and butterfly-like twin structure at the grain boundary as a result of different twin variants nucleating on opposite sides of the grain boundary.

**Acknowledgements** Research was sponsored by the Army Research Laboratory and was accomplished under Cooperative Agreement Number W911NF-15-2-0025. The views and conclusions contained in this document are those of the authors and should not be interpreted as representing the official policies, either expressed or implied, of the Army Research Laboratory or the US Government. The US Government is authorized to reproduce and distribute reprints for Government purposes notwithstanding any copyright notation herein.

## References

1. A. Staroselsky, L. Anand, A constitutive model for hcp materials deforming by slip and twinning: application to magnesium alloy az31b, *International journal of Plasticity* 19 (2003) 1843–1864.
2. H. El Kadiri, A. Oppedal, A crystal plasticity theory for latent hardening by glide twinning through dislocation transmutation and twin accommodation effects, *Journal of the Mechanics and Physics of Solids* 58 (2010) 613–624.
3. H. El Kadiri, J. Kapil, A. Oppedal, L. Hector Jr, S. R. Agnew, M. Cherkaoui, S. Vogel, The effect of twin–twin interactions on the nucleation and propagation of  $\{101\bar{2}\}$  twinning in magnesium, *Acta Materialia* 61 (2013) 3549–3563 .

4. Q. Yu, J. Wang, Y. Jiang, R. J. McCabe, N. Li, C. N. Tomé, Twin-twin interactions in magnesium, *acta materialia* 77 (2014) 28–42.
5. L. Jiang, J. J. Jonas, A. A. Luo, A. K. Sachdev, S. Godet, Influence of  $\{1\ 0\ \bar{1}\ 2\}$  extension twinning on the flow behavior of az31 mg alloy, *Materials Science and Engineering: A* 445 (2007) 302–309 .
6. B. M. Morrow, R. J. McCabe, E. K. Cerreta, C. N. Tomé, Observations of the atomic structure of tensile and compressive twin boundaries and twin-twin interactions in zirconium, *Metallurgical and Materials Transactions A* 45 (2014) 5891–5897.
7. K. D. Molodov, T. Al-Samman, D. A. Molodov, Profuse slip transmission across twin boundaries in magnesium, *Acta Materialia* 124 (2017) 397–409.
8. F. Wang, C. D. Barrett, R. J. McCabe, H. El Kadiri, L. Capolungo, S. R. Agnew, Dislocation induced twin growth and formation of basal stacking faults in  $\{10\bar{1}2\}$  twins in pure mg, *Acta Materialia* 165 (2019) 471–485 .
9. D. W. Brown, A. Jain, S. R. Agnew, B. Clausen, Twinning and detwinning during cyclic deformation of mg alloy az31b, in: *Materials science forum*, volume 539, Trans Tech Publ, 2007, pp. 3407–3413.
10. B. M. Morrow, R. J. McCabe, E. K. Cerreta, C. N. Tomé, In-situ tem observation of twinning and detwinning during cyclic loading in mg, *metallurgical and materials Transactions a* 45 (2014) 36–40.
11. J. Wang, L. Liu, C. Tomé, S. Mao, S. Gong, Twinning and de-twinning via glide and climb of twinning dislocations along serrated coherent twin boundaries in hexagonal-close-packed metals, *Materials Research Letters* 1 (2013) 81–88.
12. J. Gilman, Mechanism of ortho kink-band formation in compressed zinc monocrystals, *JOM* 6 (1954) 621–629.
13. H. Rosenbaum, Non-basal slip and twin accommodation in zinc crystals, *Acta Metallurgica* 9 (1961) 742–748.
14. A. Fernández, A. Jérusalem, I. Gutiérrez-Urrutia, M. Pérez-Prado, Three-dimensional investigation of grain boundary-twin interactions in a mg az31 alloy by electron backscatter diffraction and continuum modeling, *Acta Materialia* 61 (2013) 7679–7692.
15. K. Hantzsche, J. Bohlen, J. Wendt, K. Kainer, S. Yi, D. Letzig, Effect of rare earth additions on microstructure and texture development of magnesium alloy sheets, *Scripta Materialia* 63 (2010) 725–730.
16. X. Huang, K. Suzuki, Y. Chino, Static recrystallization behavior of hot-rolled mg-zn-ce magnesium alloy sheet, *Journal of Alloys and Compounds* 724 (2017) 981–990.
17. H. El Kadiri, C. D. Barrett, J. Wang, C. N. Tomé, Why are  $\{1\ 0\ \bar{1}\ 2\}$  twins profuse in magnesium?, *Acta Materialia* 85 (2015) 354–361 .
18. L. Zhang, Y. Han, Twins formation and their role in nanostructuring of zirconium, *Materials Science and Engineering: A* 523 (2009) 130–133.
19. A. Oppedal, H. El Kadiri, C. Tomé, G. Kaschner, S. C. Vogel, J. Baird, M. Horstemeyer, Effect of dislocation transmutation on modeling hardening mechanisms by twinning in magnesium, *International Journal of Plasticity* 30 (2012) 41–61.
20. P. Wu, X. Guo, H. Qiao, D. Lloyd, A constitutive model of twin nucleation, propagation and growth in magnesium crystals, *Materials Science and Engineering: A* 625 (2015) 140–145.
21. M. A. Kumar, A. Kanjarla, S. Niezgodá, R. Lebensohn, C. Tomé, Numerical study of the stress state of a deformation twin in magnesium, *Acta Materialia* 84 (2015) 349–358.
22. M. A. Kumar, I. J. Beyerlein, C. N. Tomé, Effect of local stress fields on twin characteristics in hcp metals, *Acta Materialia* 116 (2016) 143–154.
23. H. Abdolvand, M. Majkut, J. Oddershede, J. P. Wright, M. R. Daymond, Study of 3-d stress development in parent and twin pairs of a hexagonal close-packed polycrystal: Part ii-crystal plasticity finite element modeling, *Acta Materialia* 93 (2015) 235–245.
24. J. Cheng, S. Ghosh, A crystal plasticity fe model for deformation with twin nucleation in magnesium alloys, *International Journal of Plasticity* 67 (2015) 148–170.
25. J. Cheng, S. Ghosh, Crystal plasticity finite element modeling of discrete twin evolution in polycrystalline magnesium, *Journal of the Mechanics and Physics of Solids* 99 (2017) 512–538.
26. J. Cheng, J. Shen, R. K. Mishra, S. Ghosh, Discrete twin evolution in mg alloys using a novel crystal plasticity finite element model, *Acta Materialia* 149 (2018) 142–153.
27. M. A. Kumar, I. J. Beyerlein, R. J. McCabe, C. N. Tome, Grain neighbour effects on twin transmission in hexagonal close-packed materials, *Nature communications* 7 (2016) 13826.
28. L. Jiang, M. A. Kumar, I. J. Beyerlein, X. Wang, D. Zhang, C. Wu, C. Cooper, T. J. Rupert, S. Mahajan, E. J. Lavernia, et al., Twin formation from a twin boundary in mg during in-situ nanomechanical testing, *Materials Science and Engineering: A* 759 (2019) 142–153.
29. L. Capolungo, P. Marshall, R. McCabe, I. Beyerlein, C. Tomé, Nucleation and growth of twins in Zr: a statistical study, *Acta Materialia* 57 (2009) 6047–6056.
30. E. El-Danaf, S. R. Kalidindi, R. D. Doherty, Influence of grain size and stacking-fault energy on deformation twinning in fcc metals, *Metallurgical and Materials Transactions A* 30 (1999) 1223–1233.
31. C. Liu, P. Shanthraj, M. Diehl, F. Roters, S. Dong, J. Dong, W. Ding, D. Raabe, An integrated crystal plasticity-phase field model for spatially resolved twin nucleation, propagation, and growth in hexagonal materials, *International Journal of Plasticity* 106 (2018) 203–227.
32. H. El Kadiri, C. D. Barrett, M. A. Tschopp, The candidacy of shuffle and shear during compound twinning in hexagonal close-packed structures, *Acta Materialia* 61 (2013) 7646–7659.
33. W. D. Russell, N. R. Bratton, R. D. Moser, Z. B. McClelland, C. D. Barrett, A. L. Oppedal, W. R. Whittington, H. Rhee, Y. Paudel, B. Paliwal, H. El Kadiri, In-situ characterization of the effect of twin-microstructure interactions on tensile- $\{1\ 0\ \bar{1}\ 2\}$  and contraction- $\{1\ 0\ \bar{1}\ 1\}$  nucleation, growth and damage in magnesium, (submitted) (2019).
34. G. Proust, C. N. Tomé, A. Jain, S. R. Agnew, Modeling the effect of twinning and detwinning during strain-path changes of magnesium alloy az31, *International Journal of Plasticity* 25 (2009) 861–880.
35. C. Barrett, F. Wang, S. Agnew, H. El Kadiri, Transmutation of basal dislocations by  $\{1\ 0\ \bar{1}\ 2\}$  twinning in magnesium, in: *Magnesium Technology 2017*, Springer, 2017, pp. 147–152.
36. F. Wang, K. Hazeli, K. Molodov, C. Barrett, T. Al-Samman, D. Molodov, A. Kontsos, K. Ramesh, H. El Kadiri, S. Agnew, Characteristic dislocation substructure in  $10\bar{1}2$  twins in hexagonal metals, *Scripta Materialia* 143 (2018) 81–85.
37. F. Wang, S. R. Agnew, Dislocation transmutation by tension twinning in magnesium alloy az31, *International Journal of Plasticity* 81 (2016) 63–86.
38. Y. Paudel, C. D. Barrett, M. A. Tschopp, K. Inal, H. El Kadiri, Beyond initial twin nucleation in hcp metals: micromechanical formulation for determining twin spacing during deformation, *Acta Materialia* 133 (2017) 134–146.
39. J. Baird, B. Li, S. Y. Parast, S. Horstemeyer, L. Hector Jr, P. Wang, M. Horstemeyer, Localized twin bands in sheet bending of a magnesium alloy, *Scripta Materialia* 67 (2012) 471–474.
40. Y. Paudel, J. Indeck, K. Hazeli, M. W. Priddy, K. Inal, H. Rhee, C. D. Barrett, W. R. Whittington, K. R. Limmer, H. El Kadiri, Characterization and modeling of  $\{1\ 0\ \bar{1}\ 2\}$  twin banding in magnesium, *Acta Materialia* (under review) (2019).

41. M. Mamivand, M. A. Zaeem, H. El Kadiri, Shape memory effect and pseudoelasticity behavior in tetragonal zirconia polycrystals: A phase field study, *International Journal of Plasticity* 60 (2014) 71–86.
42. F. Lin, M. Marteleur, J. Alkorta, P. J. Jacques, L. Delannay, Local stress field induced by twinning in a metastable  $\beta$  titanium alloy, in: *IOP Conference Series: Materials Science and Engineering*, volume 219, IOP Publishing, 2017, p. 012031 .
43. R. A. Lebensohn, A. K. Kanjarla, P. Eisenlohr, An elasto-viscoplastic formulation based on fast fourier transforms for the prediction of micromechanical fields in polycrystalline materials, *International Journal of Plasticity* 32 (2012) 59–69.
44. H. Qin, J. J. Jonas, Variant selection during secondary and tertiary twinning in pure titanium, *Acta Materialia* 75 (2014) 198–211.

# The Incorporation of Discrete Deformation Twins in a Crystal Plasticity Finite Element Framework

Matthew Kasemer and Paul Dawson

## Abstract

The most prevalent twinning models homogenize the local deformation response by considering twins as “pseudoslip” systems, obscuring the physical differences between slip and twinning—namely the discrete nature of twinning. Presented is a computational approach designed to consider discrete deformation twinning in a crystal plasticity finite element framework. A polycrystalline domain is pre-discretized at the sub-grain scale into lamellar regions dependent on the geometry of the twin systems, which facilitates a finite element mesh that is attendant to this geometry. A twin is activated in a lamellar region by applying essential velocities to its nodes and rapidly mapping their locations to their expected twinned positions. The rest of the body deforms by crystallographic slip to enforce mechanical equilibrium. Results indicate stress relaxation in the parent grain and regions of large stress concentrations in neighboring grains. These trends are discussed in light of global and local energetic observations.

## Keywords

Crystal plasticity • Finite element method • Twinning

## Extended Abstract

Hexagonal materials are used in demanding structural applications due to (broadly) their high strength, low density, resistance to corrosion, and other desirable properties. Metallic alloys tend to exhibit elastic and plastic single crystal

anisotropy. Magnesium, for example, tends to exhibit a fair degree of plastic anisotropy [1]. This tends to lead to complex deformation behavior, namely the development of heterogeneous plasticity both intra-grain and globally [2]. Mathematical models aid in the understanding of the relationship between the crystal response and the macroscopic response of a sample. The crystal plasticity finite element method (CPFEM) represents perhaps the most sophisticated tool in predicting the deformation response of polycrystals [3].

Typically, crystal plasticity finite element models consider crystallographic slip as their only mode of plastic deformation. Deformation twinning, however, may play a large role in the development of plasticity across a polycrystal composed of crystals exhibiting hexagonal symmetry. Various models have been developed to consider the deformation response due to twinning. The most popular choice—due to its simplicity, relative ease in implementation, and low marginal computational cost—is the so-called pseudo-slip model [4], in which the deformation response due to slip and twinning is homogenized locally, considering a variable “volume fraction” of material deforming by either slip or twinning. This model, while adept at predicting texture evolution and bulk response, ignores the discrete nature of twinning and obscures the relative rate disparities between slip and twinning, thus hampering the precise prediction of local stress fields.

Recent modeling efforts [5] have instead focused on attempting to model discrete deformation twins to better predict the complex local heterogeneity in the stress fields due to twinning. In this study, a discrete deformation twinning framework is proposed [6]. Broadly, this framework considers the deformation response of discrete regions, twinned at a relatively rapid rate—upholding the main physical differences between slip and twinning. The framework relies on the pre-discretization of a polycrystalline aggregate at the sub-grain scale into lamellar regions (a single crystal is illustrated for simplicity in Fig. 1). Lamellar regions are included by means of a novel multi-level tessellation algorithm, in which the polycrystal domain is first discretized into grains (via a Voronoi or Laguerre

M. Kasemer (✉)

Department of Mechanical Engineering, The University of Alabama, Tuscaloosa, USA  
e-mail: [mkasemer@eng.ua.edu](mailto:mkasemer@eng.ua.edu)

P. Dawson

Sibley School of Mechanical and Aerospace Engineering, Cornell University, Ithaca, USA



**Fig. 1** Single crystal discretized into lamellar regions, along with its mesh, and twin velocity field (reproduced from [6])

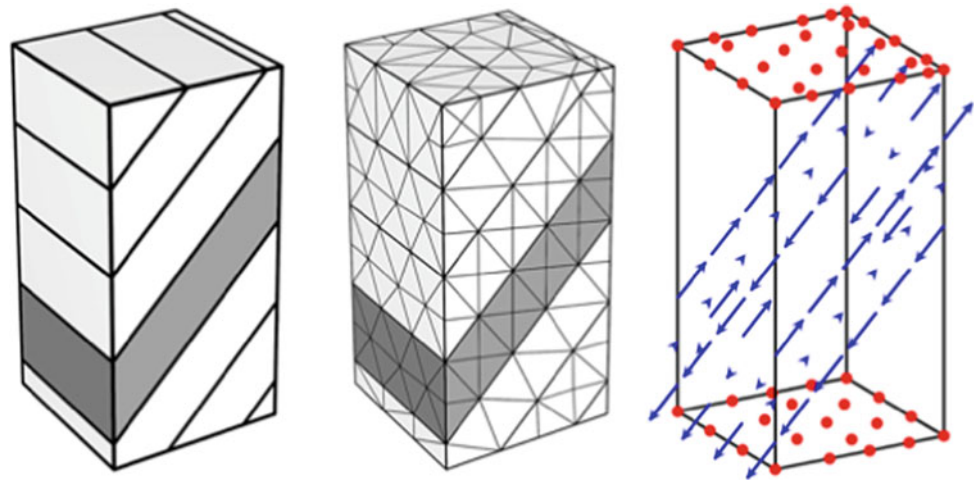


**Fig. 2** Von Mises stress field prior to and post-twin activation (reproduced from [6])



tessellation), and each grain is subsequently considered as a domain for further (lamellar) discretization. The spatial normals of these lamellar regions are calculated based on the crystallographic orientation of the grain and the twin system under consideration. Each lamellar region is assigned the same orientation as the parent crystal. Lamellar boundaries are not explicitly modeled as grain boundaries, and thus, a collection of lamella that forms a grain is considered a single crystal. These lamellar regions allow for the formation of a finite element mesh that conforms to these boundaries. Figure 1 further details the attendant finite element mesh (with an example lamellar region highlighted). Note how the lamellar regions facilitate in the formation of a mesh that adheres to these boundaries. At some point in deformation when a twin is considered for activation, the elements and nodes within a lamellar region are thus readily queried.

Upon twin activation, the elemental orientations are utilized to calculate an average deformation gradient due to twinning. This deformation gradient is used to be calculated the expected nodal positions due to twinning of each node within the lamellar region. Velocities are calculated and essential velocities placed on each node. A number of small time steps are taken until the point at which the twin is mapped to its final

location, and the essential velocities on the lamellar region are then relaxed. The elemental orientations are updated for each element in the lamellar region to their expected twinned orientations. The regions outside of the lamellar region accommodate this deformation via crystallographic slip, via the base CPFEM framework. At this point, the framework considers the twin region as a new grain, and deformation proceeds along the specified macroscopic deformation path.

This framework allows for the inspection of the complex stress fields that form due to twinning. Note in Fig. 2, for example, that the von Mises stress experiences a drop in the parent grain, especially in the vicinity of the twinned region, and sharp increases in neighboring grains at the twin tip. The consequences of a twinning event may be readily assessed via this framework. Most interesting is the assessment of local and global work metrics, calculated via the deformation rate/Cauchy stress conjugate, which allows for the comparison of the total, elastic, and plastic work over the course of twin activation. The framework additionally allows for the consideration of twin growth (thickening) via the successive activation of lamella neighboring the twinned region and is additionally poised to approach the problem of transformation induced plasticity, which exhibits similar modeling challenges.

Presented are results from simulations in which a single grain at the center of a polycrystalline aggregate is considered for twinning. Multiple simulations are performed in which a single lamellar region is activated at (1) various points in the deformation history, and (2) with various initial twin widths. Changes to the stress field as a function of twin width and the point of activation are discussed with respect to energetic metrics, and the comparisons are made to simulations performed considering only crystallographic slip.

---

## References

1. I.J. Beyerlein, L. Capolungo, P.E. Marshall, R.J. McCabe, C.N. Tomé, “Statistical analyses of deformation twinning in magnesium”, *Philos. Mag.*, 90(16) (2010), pp. 2161-2190, <https://doi.org/10.1080/14786431003630835>
2. M.P. Echlin, J.C. Stinville, V.M. Miller, W.C. Lenthe, T.M. Pollock, “Incipient slip and long range plastic strain localization in microtextured Ti-6Al-4 V titanium”, *Acta Mater.*, 114 (2016), pp. 164-175, <https://doi.org/10.1016/j.actamat.2016.04.057>
3. M. Kasemer, R. Quey, P. Dawson, “The influence of mechanical constraints introduced by  $\beta$  annealed microstructures on the yield strength and ductility of Ti-6Al-4 V”, *J. Mech. Phys. Solids*, 103 (2017), pp. 179-198, <https://doi.org/10.1016/j.jmps.2017.03.013>
4. S.R. Kalidindi, “Incorporation of deformation twinning in crystal plasticity models”, *J. Mech. Phys. Solids*, 46(2) (1998), pp. 267-271, 273-290, [https://doi.org/10.1016/S0022-5096\(97\)00051-3](https://doi.org/10.1016/S0022-5096(97)00051-3)
5. M. Ardeljan, R.J. McCabe, I.J. Beyerlein, M. Knezevic, “Explicit incorporation of deformation twins into crystal plasticity finite element models”, *Comput. Method Appl. M.*, 295 (2015), pp. 396-413, <https://doi.org/10.1016/j.cma.2015.07.003>
6. M. Kasemer, P. Dawson “A finite element methodology to incorporate kinematic activation of discrete deformation twins in a crystal plasticity framework”, *Comput. Method Appl. M.*, In Press (2019)

# On the Load Multiaxiality Effect on the Cyclic Behaviour of Magnesium Alloys

A. Gryguć, S. M. H. Karparvarfard, A. Roostaei, D. Toscano, S. Shaha, B. Behraves, and H. Jahed

## Abstract

While most fatigue-related studies on wrought magnesium alloys are under uniaxial push–pull loading condition, structural members are mostly under multiaxial stresses in real-life applications. This study addresses the effect of load multiaxiality on the cyclic behaviour of several wrought magnesium alloys: AZ31B, AM30, AZ80, and ZK60 under multiaxial tension/compression–torsion loading. In particular, the influence of the presence of shear on normal stress response and vice versa is studied. In addition, phase angle effects on the stress–strain response and fatigue life are discussed. Strain energy density (SED) is introduced as a suitable fatigue damage parameter to connect and compare uniaxial and multiaxial cases. It is shown that irrespective of loading direction and/or phase angle, SED closely correlates experimental results. Beyond strain of  $\sim 0.4$ – $0.5\%$ , the strain-controlled cyclic behaviour in uniaxial push–pull is dominated by twinning/de-twinning, while in pure shear deformation is dominated by basal slip. The effect of each of these load directions on the other in a multiaxial loading is considered in two cases: at low axial strain amplitudes the interaction is mutual, and at high axial strain amplitudes axial strain dominates. It is believed that the re-orientation of basal planes due to twinning/de-twinning caused by axial strain favours basal slip in twinned grains resulting in better accommodation of shear strain. Further, three load phase angles of 0, 45, and 90 were considered. It is observed that the phase angle has minimal effect on life at low axial strain values; however, at higher axial strain amplitudes out-of-phase angle causes more damage. The re-orientation of matrix due to twinning and rotation of the principal axis due to

phase angle shift increase the chance of different slip/twin systems to be activated resulting in lower lives.

## Keywords

Magnesium alloy • Multiaxial fatigue • Non-proportional loading • Deformation mechanism

## Introduction

There is a variety of different commercially available magnesium alloys which are suitable candidates for lightweighting applications; however, they generally fall within two categories, magnesium–aluminum alloy systems and alloys which are grain refined utilizing zirconium. Those alloys which fall under the magnesium–aluminum description can be further subdivided into the AZ family (aluminum–zinc), and AM family (aluminum–manganese); whereas, the most common Mg alloy system utilizing zirconium is ZK (or zinc–zirconium). In general, aluminum is the most common alloying element, acting to improve strength, hardness, and corrosion resistance, normally at the cost of reduced ductility [1]. For structural applications, an alloying content of  $\sim 5$ – $6\%$  aluminum results in the best compromise of strength and ductility, thus for this particular study two varieties of alloy from the AZ family were investigated AZ31 (3% Al) and AZ80 (8% Al) [1]. Furthermore, of the AM and ZK alloy families, the commercially available AM30 and ZK60 variants were those which were selected for this particular study.

Of the wrought varieties of magnesium alloys, texture development in the microstructure resulting from the thermomechanical processing is a well-documented phenomenon. The effect of this texture evolution upon the deformation behaviour and mechanical properties of AZ31 [2–6], AZ80 [7–12], AM30 [13, 14], and ZK60 [15–17] have been explored in detail by several researchers. From a metallurgical perspective, the role of texture has implications

A. Gryguć · S. M. H. Karparvarfard · A. Roostaei · D. Toscano · S. Shaha · B. Behraves · H. Jahed (✉)  
Fatigue and Stress Analysis Laboratory (FATSLab), University of Waterloo, Waterloo, ON N2L 3G1, Canada  
e-mail: [hamid.jahed@uwaterloo.ca](mailto:hamid.jahed@uwaterloo.ca)

on the microstructure at both the crystallographic and grain length scales [18]. In general, processing techniques such as rolling, forging, extrusion, or equal channel angular pressing (ECAP), result in appreciable textures, characterized by irregular “elongated” grain morphologies and bi-modal grain sizes [19]. More recently, it has been well documented that these types of processing methods introduce a strong basal texture where the alignment of the crystallographic axis (*or c-axis*) is coincident to the local compressive direction (i.e., perpendicular to the working plane) [2, 8–10, 20, 21].

The cyclic response of magnesium alloys is dominated by two different deformation mechanisms, slip and twinning [2]. The way in which the activation of each of these deformation mechanisms manifests itself in the cyclic response depends strongly on the orientation of the loading direction relative to the predominant crystallographic orientation resulting in an asymmetric hysteresis [22–25]. The asymmetry in the cyclic response of wrought magnesium alloys results from the twinning/de-twinning cyclic deformation mechanism induced by the 86.3° crystal re-orientation of the basal pole during tensile twinning [2, 26].

Under strain-controlled fatigue testing, many researchers have found that the response of wrought Mg alloys is influenced by a number of factors including the magnitude, mode, and direction of the loading; however, the multiaxial effects of the loading on the cyclic response have only recently been explored in a handful of studies. Sonsino [27] made very preliminary remarks indicating that aluminum and magnesium alloys exhibited similar tendencies to steel alloys linking ductility and sensitivity to non-proportionality in multiaxial loading [27]. This current work aims to further build upon this structure–properties relationship and explore the relationship between load multiaxiality and fatigue life/cyclic behaviour of several Mg alloys of various wrought forms.

## Materials and Experimental Methods

Four different wrought magnesium alloys are presented in this study, AZ31B extrusion forged at 250 °C, AM30 extrusion, AZ80 extrusion forged at 250 °C, and ZK60 extrusion forged at 250 °C. The alloys’ conditions are commercially available extrusion form and closed die precision forgings. In general, two different types of specimens were used in the experimental data presented here. Firstly, flat “dogbone” shaped specimens for the monotonic and pure axial strain-controlled tests according to the ASTM E8 and E606 standards, respectively. Secondly, hollow thin-walled tubular specimens were utilized for the pure shear and multiaxial tests according to ASTM E2207-08. All tests

were performed on an Instron biaxial tension–torsion load frame, and strain was controlled by axial or biaxial extensometer. Details regarding specimen geometries and test protocols are available within the cited literature for each alloy [3, 6, 14, 17, 28, 29].

All microstructure specimens were prepared by first hand-sanding with 600, 800, and 1200 grit SiC paper followed by polishing with 6, 3, 1, and 0.1 μ diamond paste with an oil based lubricant on imperial cloth. Finally, the samples were polished with 0.05 μ master prep colloidal silica followed by etching with acetic-picral as mentioned in [14]. Scanning electron microscope equipped with Quanta field emission gun was used to analyze microstructure.

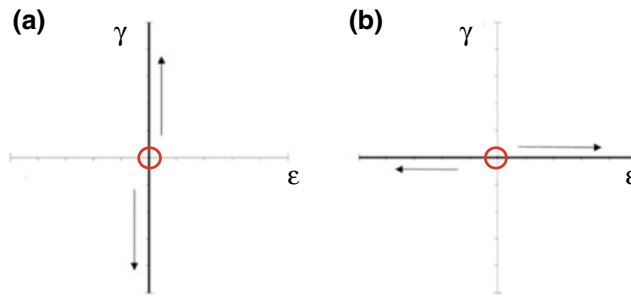
Texture analysis was performed on the polished and etched sample using a Bruker D8-Discover equipped with an advanced 2D area detector. The experiment was conducted by measuring incomplete pole figures of {0001}, {10-10}, {10-11}, and {1-102} planes for tilt angle  $\Psi$  between 0° and 75° and in axis rotation  $\Phi$  between 0° and 360° in the back reflection mode using CuK $\alpha$  radiation at 40 kV and 40 mA. Finally, the complete pole figures (PF) were calculated based on the measured incomplete pole figures using DIFFRAC. Suite texture software.

Table 1 contains monotonic properties and average grain size for all the chosen conditions for each alloy.

Figures 1 and 2 show the five loading paths for the fully reversed fatigue experiments. Path (a) is pure shear ( $\gamma$ ), (b) pure axial ( $\epsilon$ ), (c) biaxial proportional, (d) biaxial non-proportional (45° out of phase), and (e) biaxial non-proportional (90° out of phase). In general, all the experiments were strain control exclusively during cyclic loading in the low cycle fatigue LCF (<10,000 cycles) and changed to load control in the few tests where the response stabilized, and the life exceeded this threshold. Failure criterion was a 50% drop in the peak or valley loads/torques or catastrophic failure (through crack), whichever occurs first.

**Table 1** Summary of monotonic properties for various Mg alloys and processing conditions

	Condition	$\sigma_{YS}$ [MPa]	$\sigma_{UTS}$	$\epsilon_{FAIL}$ [%]	Grain size [ $\mu\text{m}$ ]
AZ31B	Forged (20 mm/s @ 250 °C) [6]	221	258	12.4	9.9
AM30	Extruded (-F) [28]	164	244	15.0	8.0–25.0
AZ80	Forged (20 mm/s @ 250 °C) [12]	286	385	15.3	10.0
ZK60	Forged (20 mm/s @ 250 °C)	281	336	15.5	5.8



**Fig. 1** Uniaxial loading paths used for fatigue experiments **a** pure shear and **b** pure axial

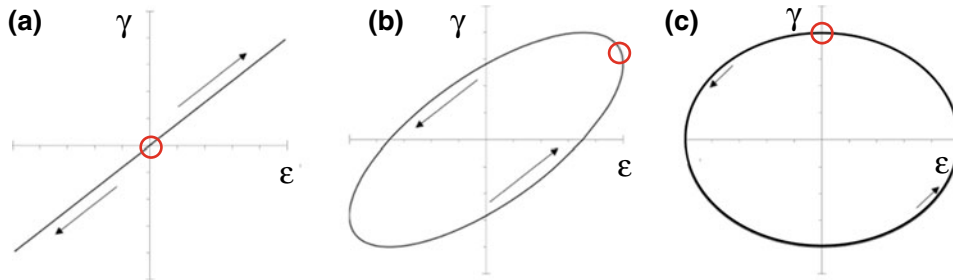


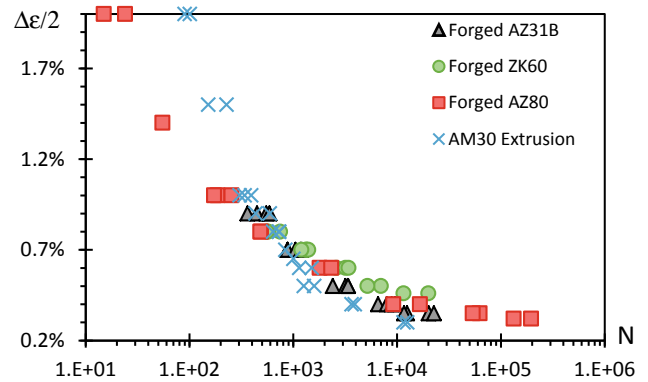
**Fig. 2** Multiaxial loading paths used for fatigue experiments **c** proportional (in-phase), **d** non-proportional 45° out of phase, **e** non-proportional 90° out of phase

## Results and Discussion

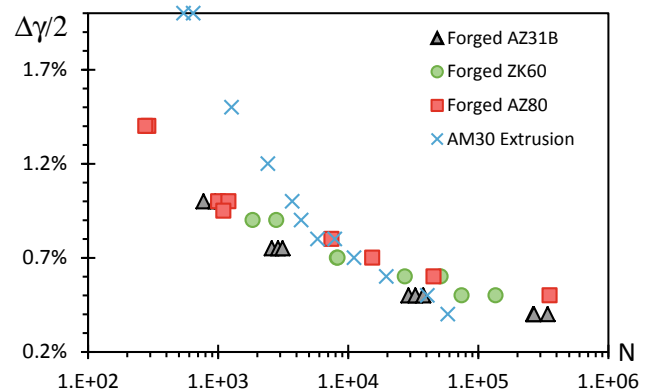
### Low Cycle Fatigue

Figure 3 illustrates the strain life response for load path (b) and Fig. 4 for load path (a) for all alloys/conditions.

It can be observed that the difference in life for pure axial loading (path b) is less than those in pure shear in the LCF regime. Several researchers [4, 29–33] have observed a “kink” in the axial strain life curve in various wrought Mg alloys in the regime of life between  $10^3$  and  $10^4$  cycles (0.4–0.5%) which varies depending on both the strain path and alloy/processing conditions. This can be observed in most of the alloys and conditions being presented in Fig. 3 for the pure axial load path (b). This results from a change in the cyclic deformation mechanism being twinning/de-twinning activity dominating the plastic deformation at strain amplitudes above the kink point and dislocation slip below the kink point. This transitional life between cyclic deformation mechanisms coincides with a meaningful mean stress development as the strain amplitude increases [4]. In contrast, the deformation mechanism in pure shear (load path a, for shear strains  $<1.5\%$ ) is not twinning/de-twinning dominated, and thus no distinguishable kink is observed for any of the materials as can be seen in Fig. 4. The two different deformation mechanisms in axial and shear cyclic loading are corroborated by fracture surface microstructure and the



**Fig. 3**  $\epsilon$ - $N$  curve for pure axial load path (b)



**Fig. 4**  $\gamma$ - $N$  curve for pure shear load path (a)



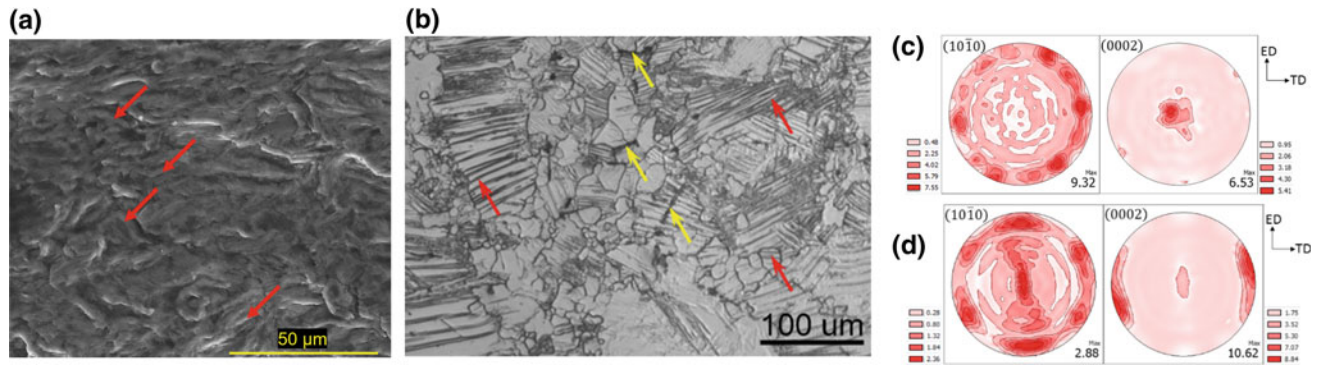


**Fig. 5** SEM images of **a** the fracture surface of an AZ31B sample tested at 0.4% axial strain amplitude showing evidence of extension twin lamellae (red arrows) near the crack initiation zone, **b** near the fracture surface of sample tested at 1% with red and yellow arrows showing the residual twins and cracks observed along twin boundaries,

respectively; **(c and d)** pole figures of the AM30 extrusion in as-received condition and after cyclic axial strain amplitude of 2%, respectively, showing the re-orientation of basal planes (0002) due to twinning

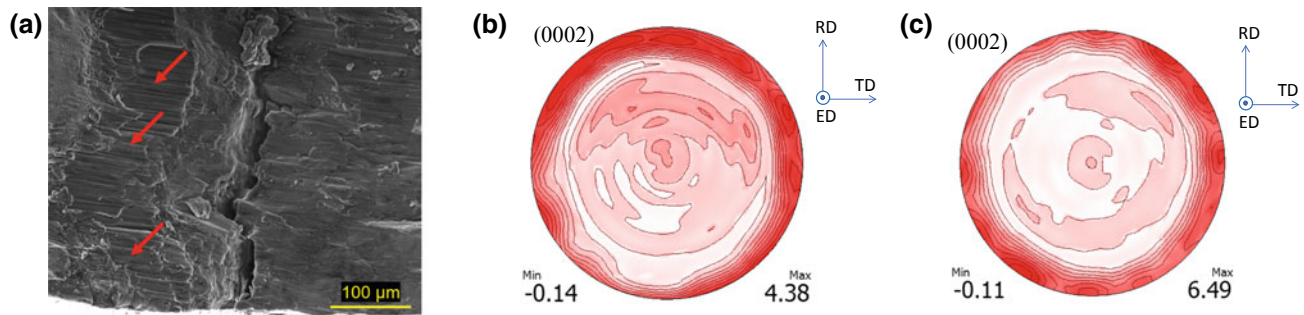


**Fig. 6** SEM images of **a** the fracture surface of the primary shear crack in AZ31B tested under cyclic shear strain of 0.4% showing extensive slip bands (red arrows) surrounding significant secondary cracks;

**(b and c)** pole figures of ZK60 before and after cyclic shear of 1.1%, respectively, confirming no change in the orientation of basal planes (0002)

texture evolution as shown in Figs. 5 and 6. Figure 5 shows twin formation in axial cyclic strain, and Fig. 6 shows slip deformation in cyclic shear strain.

### Energy as a Fatigue Damage Parameter

To establish a common background for comparing uniaxial and multiaxial cyclic tests, strain energy density (SED) as a measure of fatigue damage is adopted. Strain energy density has been suggested as a suitable fatigue damage parameter for variety of different materials [34–38], and particularly for wrought magnesium alloys [3, 10–12, 14, 39, 40]. Given the asymmetric and anisotropic behaviour of wrought magnesium alloys, SED has proven to be the most effective fatigue correlation parameter [14]. The total SED is implemented as a damage parameter and is constituted by its elastic and plastic components. The plastic component is defined as the area enveloped by the stabilized hysteresis loop. The elastic component which accounts for mean stress is defined as the following [41]:

$$\Delta E_e^+ = \frac{(\sigma_{\max} + \sigma_{\text{mean}})\sigma_a}{2E_{\text{cyc}}} (\text{Axial})$$

Similarly for shear, the following relationship is proposed.

$$\Delta E_e^+ = \frac{(\tau_{\max} + \tau_{\text{mean}})\tau_a}{2G_{\text{cyc}}} (\text{Shear})$$

where  $\sigma_{\max}$  is the maximum and  $\sigma_{\text{mean}}$  the mean axial stress for (path b), and  $\tau_{\max}$  &  $\tau_{\text{mean}}$  are the peak and mean shear stresses (path a) for the stabilized half-life response. Multiaxial cyclic tests path (c–e) was performed on AZ31B forged, AM30 extrusion, AZ80 forged, and ZK60 forged. The total SED for each test was taken as damage parameter to correlate with life. Figure 7 shows how well SED correlates fatigue data irrespective of loading path, for pure axial, pure shear, and multiaxial with any phase angle.

There are two separate effects which can be examined in biaxial responses of the various alloys and material conditions: primarily, the effect of the load multiaxiality, and secondly the effect of the level of non-proportionality or the

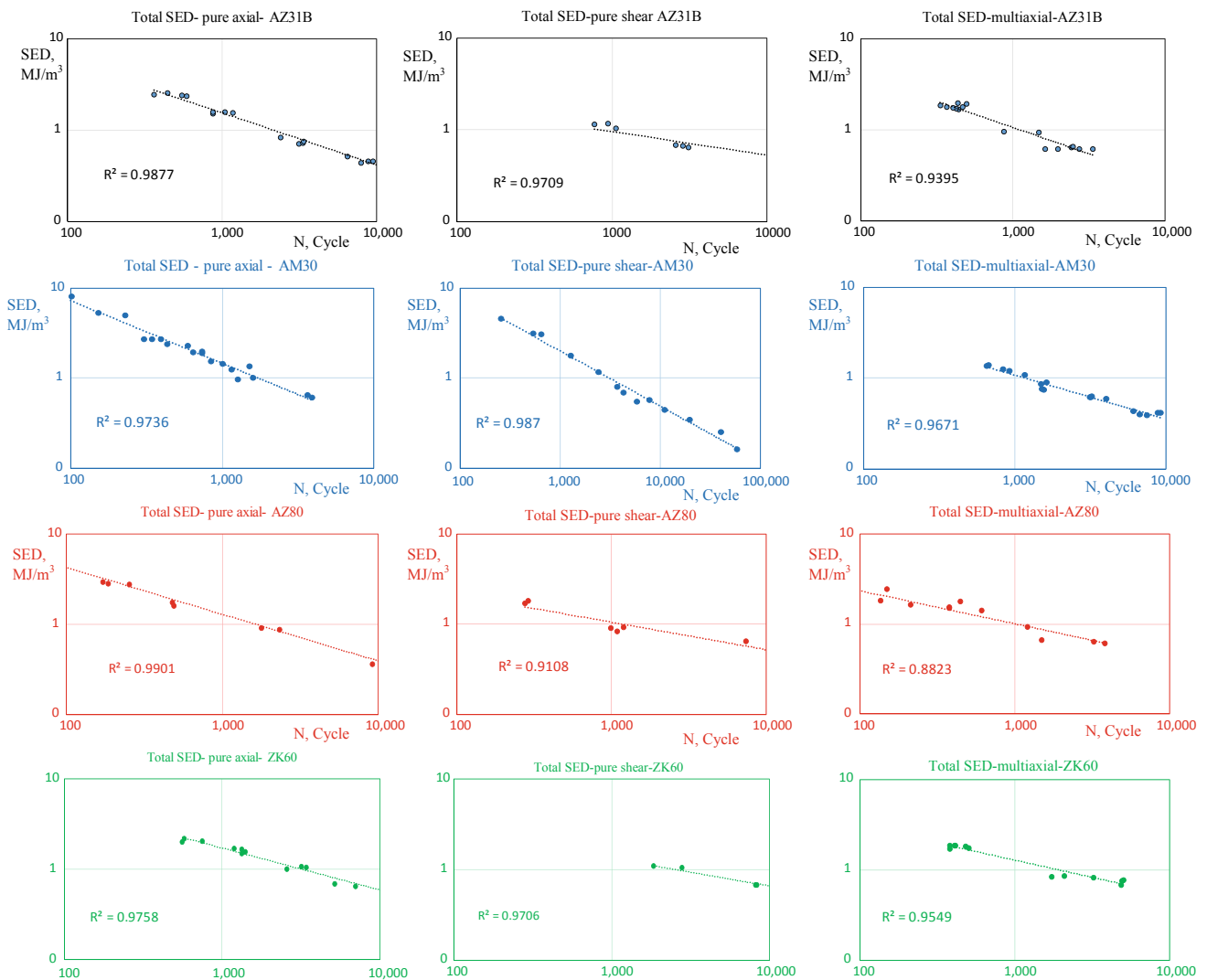
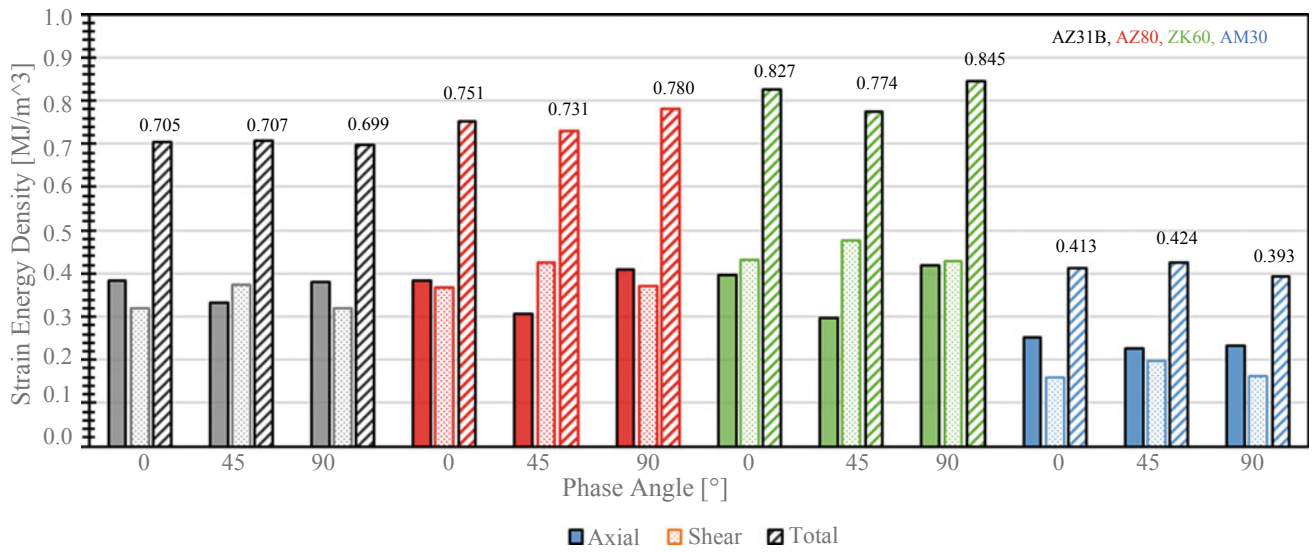


**Fig. 7** Total strain energy density correlation with life in pure axial, pure shear, and multiaxial strains for AZ31B, AM30, AZ80, and ZK60 at LCF

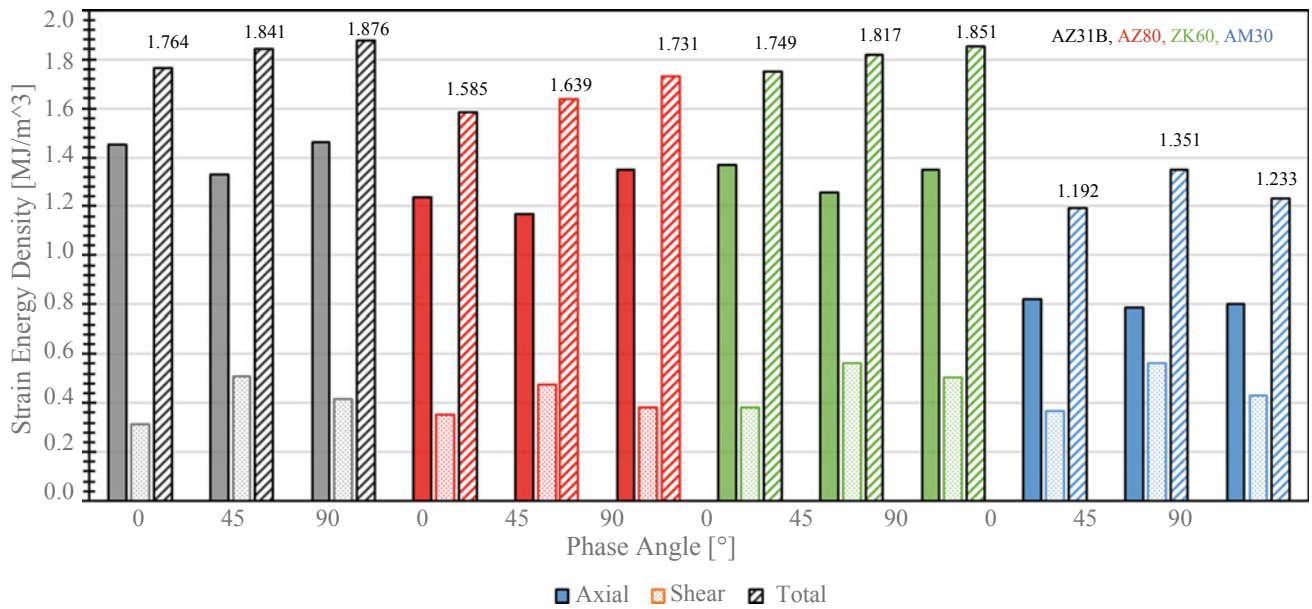
phase angle effect. Figures 8 and 9 illustrate the relationship between axial, shear, and total SED for the investigated alloys for a variety of phase angles with a low and high proportionality ratio, respectively.

Firstly, the load axes effect in biaxial loading is considered. There exists a threshold axial strain  $\epsilon$  amplitude where axial loading will begin to dominate the cyclic response and increase its proportion of total SED. This threshold corresponds with the “kink” observed in the uniaxial  $\epsilon$ - $N$  axial curve where the deformation mechanism shifts from predominantly elastic and small levels of slip-based plasticity behaviour at  $\epsilon < \epsilon_{\text{kink}}$  to twinning/de-twinning behaviour at strain amplitudes  $\epsilon > \epsilon_{\text{kink}}$ . Below this threshold ( $\epsilon < 0.4$ – $0.5\%$ ), and as depicted by Fig. 8, the share of axial SED and shear SED in total SED is the same and around  $\frac{1}{2}$  of the total SED. Within this regime, the damage is equally shared by

the two axes of loading. However, for biaxial loading with axial strain higher than the threshold ( $\epsilon > 0.5\%$ ), the axial SED becomes dominant, causing the majority of damage (e.g., close to 80% of the damage in AZ31B in Fig. 9). This is due to twinning/de-twinning caused by axial strain above the threshold. The re-orientation of basal planes due to twinning/de-twinning caused by axial strain favours basal slip in twinned grains resulting in better accommodation of shear strain. Hence, less energy is required for accommodating the shear strain as compared to the one required in the absence of axial strain. The dominance of axial strain in biaxial loading above the threshold is corroborated by the cracking mechanism. Figure 10 shows a typical macroscopic crack morphology for a failed sample under pure axial and pure shear strain path. It can be observed that the crack path morphology for pure shear loading (path a) is purely

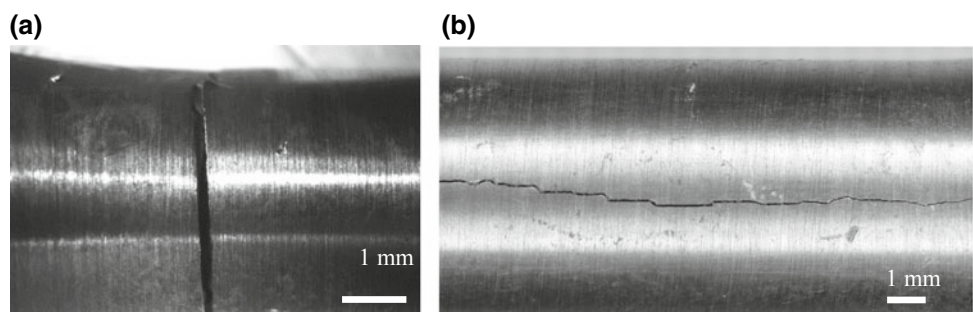


**Fig. 8** Relationship between axial, shear, and total SED for the investigated alloys for a variety of phase angles and a proportionality ratio of  $\epsilon/\gamma = 0.8$  and low axial strain amplitude (for B&W version note that from left to right, first three results are on AZ31B; second three results are on AZ80; third three results are on ZK60; and fourth three results are on AM30)



**Fig. 9** Relationship between axial, shear, and total SED for the investigated alloys for a variety of phase angles and a proportionality ratio of  $\epsilon/\gamma = 1.4$  with high axial strain amplitude (for B&W version note that from left to right, first three results are on AZ31B; second three results are on AZ80; third three results are on ZK60; and fourth three results are on AM30)

**Fig. 10** Macroscopic fracture morphology for an AZ80 failed sample under **a** pure axial **b** pure shear strain



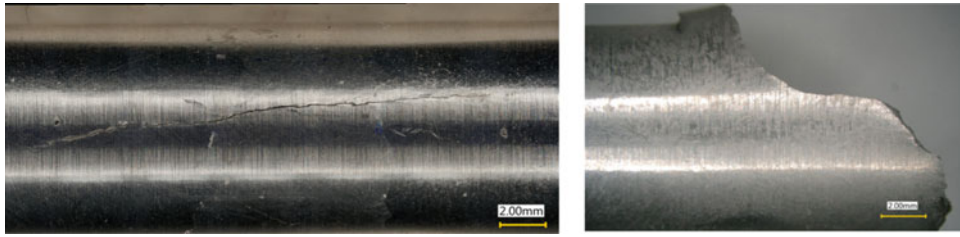


**Fig. 11** Macroscopic fracture morphology for a ZK60 failure **a** under 0.3% axial and 0.7% shear strain showing longitudinal crack, **b** under 0.6% axial and 0.7% shear strain showing transverse crack

longitudinal (aligned with the tubular specimen axis) while crack path for pure axial strain (path b) is transverse. In biaxial loading however, as depicted by Fig. 11, when the axial strain is above the threshold, the cracking is always transverse (Fig. 11b), irrespective of the level of shear strain amplitude. On the other hand, when the axial strain is below threshold (Fig. 11a) and shear strain is large, the cracking is longitudinal, confirming low influence of axial strain on final failure.

With regards to the sensitivity to the level of non-proportionality or phase angle effect, a few observations can be made. As depicted by Fig. 8, at low value of axial strain, there seems to be no effect of phase angle on total SED. This is clearly seen in the case of AZ31B for  $\varepsilon = 0.4\%$  and  $\gamma = 0.5\%$  where the total SED independent of the phase angle in all three cases is  $0.7 \text{ MJ/m}^3$ . For AZ80 and ZK60 at the same biaxial loading, the maximum difference of SED with respect to phase angles 0, 45, and 90 is 6% and 7%, respectively. This difference for AM30 biaxial loading with  $\varepsilon = 0.3\%$  and  $\gamma = 0.4\%$  is only 7%. However, at high axial strain values, as depicted by Fig. 9, the phase angle changes the total SED. For AZ31B, AZ80, and ZK60 biaxial loading with  $\varepsilon = 0.7\%$  and  $\gamma = 0.5\%$ , the SED increases (life decreases) as phase angle increases. For AM30 with lower biaxial loading of  $\varepsilon = 0.5\%$  and  $\gamma = 0.6\%$ , again the effect of load angle is visible. Xiong et al. [4] observed that in extruded AZ31B non-proportional loading results in a higher population of grains experiencing twinning/de-twinning as well as easier activation of various sets of twins AZ31B. These deformation induced twins can serve as sites for crack initiation which can potentially have a detrimental effect on fatigue life. Furthermore, the additional non-proportional hardening that can be induced by the rotation of the principal axis can also lead to higher cyclic energies and has the effect of further reducing the fatigue life [37]. The AM30 alloy behaved somewhat different, with longer life occurring at  $90^\circ$  than at  $45^\circ$ , due to the attenuation of the cyclic hardening in the axial direction under non-proportional loading, a phenomenon that as was observed by Roostaei and Jahed [29]. The variation in SED in all alloys at high biaxial strain amplitudes in Fig. 9 remains small and less than 12%. While

rotation of principal axes in out-of-phase loading accommodates more deformation mechanisms to occur, however, limited number of slip systems in magnesium alloys limits its detrimental effect [42].

## Conclusion

The effect of multiaxiality on the cyclic behaviour was studied for several Mg alloys of the extrusion and forge variety. Several different loading paths were presented, uniaxial and biaxial, with varying levels of non-proportionality. Based upon the results, the following conclusions can be drawn:

1. A distinct kink in the  $\varepsilon$ - $N$  response under pure axial loading for all the presented materials represents a fundamental shift in the cyclic deformation mechanism. This kink is associated with the onset of domination of twinning/de-twinning in materials response in uniaxial and biaxial loadings. No such kink is observed in the pure shear  $\varepsilon$ - $N$  response which is dominated by slip.
2. Strain energy density (SED) correlates all fatigue experimental results irrespective of the axes of loading.
3. Under multiaxial loading, at strain amplitudes above a certain “kink” threshold when sufficient plasticity is induced, the axial component tends to dominate the biaxial loading. Below this threshold, the sensitivity of the response to the relative intensity of each loading axis as well as the phase angle is quite low.
4. Under non-proportional loading, if the rotation of the principal axis causes the axial proportion of total SED to increase, it results in a lower fatigue life, and this was observed in AZ31, AZ80, and ZK60 alloys.
5. In the tubular specimens utilized, the crack path behaviour is characterized by transverse cracking (tensile type failure) for the majority of strain paths. The only exceptions to this are the pure shear load path which exhibited longitudinal cracking in the LCF regime and helical cracking ( $45^\circ$ ) in the HCF.
6. Under multiaxial loading, fatigue cracks normally initiate at the surface of the tubular sample regardless of the



relative magnitudes of each strain component. In general, this was true for all alloys and material conditions investigated.

7. The transverse cracking path was relatively insensitive to the level of non-proportionality of the loading.

**Acknowledgements** The authors would like to gratefully acknowledge the financial support of the Natural Sciences and Engineering Research Council of Canada (NSERC), Automotive Partnership Canada (APC) program under APCPJ 459269–13 grant with contributions from Multimatic Technical Centre, Ford Motor Company, and Centerline Windsor.

## References

1. B. R. Powell, P. E. Krajewski, and A. A. Luo, "Magnesium alloys for lightweight powertrains and automotive structures," *Mater. Des. Manuf. Light. Veh.*, pp. 114–173, 2010.
2. L. Wu *et al.*, "Twinning-detwinning behavior during the strain-controlled low-cycle fatigue testing of a wrought magnesium alloy, ZK60A," *Acta Mater.*, vol. 56, no. 4, pp. 688–695, 2008.
3. J. Albinmousa, H. Jahed, and S. Lambert, "Cyclic axial and cyclic torsional behaviour of extruded AZ31B magnesium alloy," *Int. J. Fatigue*, vol. 33, no. 11, pp. 1403–1416, 2011.
4. Y. Xiong, Q. Yu, and Y. Jiang, "Multiaxial fatigue of extruded AZ31B magnesium alloy," *Mater. Sci. Eng. A*, vol. 546, pp. 119–128, 2012.
5. D. Toscano, S. K. Shaha, B. Behraves, H. Jahed, and B. Williams, "Effect of forging on the low cycle fatigue behavior of cast AZ31B alloy," *Mater. Sci. Eng. A*, vol. 706, no. August, pp. 342–356, 2017.
6. D. Toscano, S. K. Shaha, B. Behraves, H. Jahed, and B. Williams, "Multiaxial Cyclic Response of Low Temperature Closed-Die Forged AZ31B Mg Alloy," *Miner. Met. Mater. Ser.*, pp. 289–296, 2019.
7. A. Gryguc, H. Jahed, B. Williams, and J. McKinley, "Magforge—Mechanical behaviour of forged AZ31B extruded magnesium in monotonic compression," *Mater. Sci. Forum*, vol. 828–829, pp. 291–297, 2015.
8. A. Gryguc, S. K. Shaha, H. Jahed, M. Wells, B. Williams, and J. McKinley, "Tensile and fatigue behaviour of as-forged AZ31B extrusion," *Frat. ed Integrita Strutt.*, vol. 10, no. 38, pp. 251–258, 2016.
9. A. Gryguc, S. K. Shaha, S. B. Behraves, H. Jahed, M. Wells, and B. Williams, "Compression Behaviour of Semi-Closed Die Forged AZ80 Extrusion," *Charact. Miner. Met. Mater. 2017*, pp. 361–369, 2017.
10. A. Gryguc *et al.*, "Monotonic and cyclic behaviour of cast and cast-forged AZ80 Mg," *Int. J. Fatigue*, vol. 104, pp. 136–149, 2017.
11. A. Gryguc *et al.*, "Low-cycle fatigue characterization and texture induced ratcheting behaviour of forged AZ80 Mg alloys," *Int. J. Fatigue*, vol. 116, pp. 429–438, 2018.
12. A. Gryguc *et al.*, "Multiaxial cyclic behaviour of extruded and forged AZ80 Mg alloy," *Int. J. Fatigue*, vol. 127, pp. 324–337, 2019.
13. A. A. Roostaei and H. Jahed, "A cyclic small-strain plasticity model for wrought Mg alloys under multiaxial loading: Numerical implementation and validation," *Int. J. Mech. Sci.*, vol. 145, no. July, pp. 318–329, 2018.
14. A. A. Roostaei and H. Jahed, "Role of loading direction on cyclic behaviour characteristics of AM30 extrusion and its fatigue damage modelling," *Mater. Sci. Eng. A*, vol. 670, pp. 26–40, 2016.
15. Y. Xiong and Y. Jiang, "Fatigue of ZK60 magnesium alloy under uniaxial loading," *Int. J. Fatigue*, vol. 64, pp. 74–83, 2014.
16. S. M. H. Karparvarfard, S. K. Shaha, S. B. Behraves, H. Jahed, and B. Williams, "12th International Fatigue Congress (FATIGUE 2018), MATEC Web of Conferences 165, 06009, 2018.
17. S. M. H. Karparvarfard, S. K. Shaha, S. B. Behraves, H. Jahed, and B. W. Williams, "Fatigue characteristics and modeling of cast and cast-forged ZK60 magnesium alloy," *Int. J. Fatigue*, vol. 118, no. November 2017, pp. 282–297, 2019.
18. J. Albinmousa, M. J. Adinoyi, and N. Merah, "Multiaxial fatigue of extruded ZK60 magnesium alloy," *Fatigue Fract. Eng. Mater. Struct.*, no. May, pp. 1–14, 2019.
19. F. Nový, M. Janeček, V. Škorik, J. Muller, and L. Wagner, "Very high cycle fatigue behaviour of as-extruded AZ31, AZ80, and ZK60 magnesium alloys," *Int. J. Mater. Res.*, vol. 100, no. 3, pp. 288–291, 2009.
20. S. Kleiner and P. J. Uggowitzer, "Mechanical anisotropy of extruded Mg-6% Al-1% Zn alloy," *Mater. Sci. Eng. A*, vol. 379, no. 1–2, pp. 258–263, 2004.
21. X. Y. Lou, M. Li, R. K. Boger, S. R. Agnew, and R. H. Wagoner, "Hardening evolution of AZ31B Mg sheet," *Int. J. Plast.*, vol. 23, no. 1, pp. 44–86, 2007.
22. L. Wu *et al.*, "Internal stress relaxation and load redistribution during the twinning-detwinning-dominated cyclic deformation of a wrought magnesium alloy, ZK60A," *Acta Mater.*, vol. 56, no. 14, pp. 3699–3707, 2008.
23. S. Dong *et al.*, "Characteristic cyclic plastic deformation in ZK60 magnesium alloy," *Int. J. Plast.*, vol. 91, pp. 25–47, 2017.
24. S. Dong, Y. Jiang, J. Dong, F. Wang, and W. Ding, "Cyclic deformation and fatigue of extruded ZK60 magnesium alloy with aging effects," *Mater. Sci. Eng. A*, vol. 615, pp. 262–272, 2014.
25. Q. Yu, J. Zhang, Y. Jiang, and Q. Li, "An experimental study on cyclic deformation and fatigue of extruded ZK60 magnesium alloy," *Int. J. Fatigue*, vol. 36, no. 1, pp. 47–58, 2012.
26. M. G. Jiang, H. Yan, and R. S. Chen, "Twinning, recrystallization and texture development during multi-directional impact forging in an AZ61 Mg alloy," *J. Alloys Compd.*, vol. 650, pp. 399–409, 2015.
27. C. M. Sonsino, "Material Influence on Multiaxial Fatigue Response," ICMFF9 proceedings, pp. 41–57.
28. J. Albinmousa *et al.*, "Monotonic and fatigue behavior of magnesium extrusion alloy AM30: An international benchmark test in the 'magnesium Front End Research and Development Project,'" *SAE Tech. Pap.*, vol. 9781118858, pp. 557–562, 2010.
29. A. A. Roostaei and H. Jahed, "Multiaxial cyclic behaviour and fatigue modelling of AM30 Mg alloy extrusion," *Int. J. Fatigue*, vol. 97, pp. 150–161, 2017.
30. Q. Yu, J. Zhang, Y. Jiang, and Q. Li, "Multiaxial fatigue of extruded AZ61A magnesium alloy," *Int. J. Fatigue*, vol. 33, no. 3, pp. 437–447, 2011.
31. F. Castro and Y. Jiang, "Fatigue life and early cracking predictions of extruded AZ31B magnesium alloy using critical plane approaches," *Int. J. Fatigue*, vol. 88, pp. 236–246, 2016.
32. Y. Xiong and Y. Jiang, "Cyclic deformation and fatigue of rolled AZ80 magnesium alloy along different material orientations," *Mater. Sci. Eng. A*, vol. 667, pp. 58–67, 2016.
33. Y. Xiong, Q. Yu, and Y. Jiang, "Cyclic deformation and fatigue of extruded AZ31B magnesium alloy under different strain ratios," *Mater. Sci. Eng. A*, vol. 649, pp. 93–103, 2016.



34. Golos K, Ellyin F. A total strain energy density theory for cumulative fatigue damage. *J Pressure Vessel Technol*;110:36–41,1988.
35. H. Jahed and A. Varvani-Farahani, “Upper and lower fatigue life limits model using energy-based fatigue properties,” *Int. J. Fatigue*, vol. 28, no. 5–6, pp. 467–473, 2006.
36. Jahed H, Varvani A, Noban M, Khalaji I, An energy-based fatigue life assessment model for various metallic materials under proportional and non-proportional loading conditions, *International Journal of Fatigue*, 2007, 29(4), 647–655.
37. Noban M, Jahed H, Ibrahim E, Ince A, Load path sensitivity and fatigue life estimation of 30CrNiMo8HH, *International Journal of Fatigue*, 2012, 37, 123–133.
38. Noban M, Jahed H, Winkler S, Ince A, Fatigue characterization and modeling of 30CrNiMo8HH under multiaxial loading, *Materials Science and Engineering A*, 2011, 528(6), 2484–2494.
39. S. H. Park, S. G. Hong, B. H. Lee, W. Bang and C. S. Lee, “Low-cycle fatigue characteristics of rolled Mg–3Al–1Zn alloy,” *International Journal of Fatigue*, vol. 32, pp. 1835–1842, 2010.
40. H. Jahed and J. Albinmousa, “Multiaxial behaviour of wrought magnesium alloys - A review and suitability of energy-based fatigue life model,” *Theor. Appl. Fract. Mech.*, vol. 73, pp. 97–108, 2014.
41. A. A. Roostaei, A. Pahlevanpour, S. B. Behraves, and H. Jahed, “On the definition of elastic strain energy density in fatigue modelling,” *Int. J. Fatigue*, vol. 121, no. December 2018, pp. 237–242, 2019.
42. D. Skibicki and Ł. Pejkowski, “The relationship between additional non-proportional hardening coefficient and fatigue life,” *Int. J. Fatigue*, vol. 123, no. February, pp. 66–78, 2019.

---

**Part V**

**Thermomechanical Processing**

# Deformation Driven Precipitation in Binary Magnesium Alloys

Suhas Eswarappa Prameela and Timothy P. Weihs

## Abstract

Unlike Aluminum (Al) alloys, precipitation strengthening of Magnesium (Mg) alloys has proven challenging. Precipitate density is typically too low, and precipitate size is often too large and elongated to enhance the resistance to plastic deformation significantly. Mimicking recent work in Al alloys, we are exploring how low-temperature plastic deformation can enhance the density, size, and morphology of common intermetallic particles and thereby lead to significant hardening in Mg alloys. The low temperatures tend to favor nucleation overgrowth, while the deformation provides vacancies and dislocations that can assist nucleation. Using equal channel angular extrusion, and moderate temperatures, we explore the processing and thermodynamic factors controlling nucleation and growth of precipitates in Mg–Al and Mg–Zn binary alloys.

## Keywords

Dynamic precipitation • Nucleation • Magnesium alloys • Nano precipitates • Strengthening

Magnesium alloys continue to receive significant interest from the broader scientific community, particularly from those interested in low-density structural materials [1, 2]. These lightweight alloys offer great potential for use in defense, transportation, electronics, and biomedical applications. There are now several research efforts focused on understanding the fundamental issues that control alloy processing and design. One of these efforts is driven to understand the role of initial microstructure and the controlling mechanisms during thermo-mechanical processing of Mg alloys, to create useful final microstructures. Possible attributes of such microstructures may include rich solute

clusters, fine precipitates, small grain sizes, and random textures that help to tailor strength and anisotropy [3–7]. However, despite these efforts, our abilities to design and fabricate magnesium alloys with all of these microstructural attributes are still limited.

One overarching idea for improving the microstructure of Mg alloys is to follow the approaches that have proven successful in developing Al alloys [8, 9]. For example, precipitate hardening in Al alloys has been very effective. Micro-alloying, conventional aging (T6 treatment), double stretch aging, and dynamic strain aging are a few examples of how one can create very useful microstructures with fine precipitates in Al alloys. Mimicking these techniques to precipitation harden Mg alloys has resulted in varying degrees of success. Some of the core challenges limiting success include our narrow understanding of the roles that vacancies, solute atoms, and dislocations play during thermo-mechanical processing in Mg alloys. Conventional wisdom suggests that when extensive deformation and the climb of the edge dislocations generate excess vacancies [10], the rate of atomic diffusion rises, leading to enhanced nucleation and growth. However, by limiting the duration of deformation and by relying on the annihilate of vacancies once deformation ceases, one can effectively use the mechanical generation of vacancies as a switch to enhance nucleation with a limited impact on coarsening through growth. One simply stops the deformation following nucleation to limit coarsening. Dislocations can also play a dominant role in precipitation through their local stress states. The hydrostatic stress fields around edge dislocations can reduce the nucleation barrier for the formation of intermetallics simply due to changes in density upon precipitate formation. Further still, these dislocations promote the formation of solute clusters that lower the barriers for nucleation even further and can thereby lead to a higher number of fine precipitates. Studies have focused on manipulating solute clusters, mobile dislocations, and forest dislocations to aid nucleation processes. The type of solute atoms present in the microstructure also plays a significant

S. Eswarappa Prameela · T. P. Weihs (✉)  
Department of Materials Science and Engineering, Hopkins  
Extreme Materials Institute, Johns Hopkins University, Baltimore,  
MD, USA  
e-mail: [weihs@jhu.edu](mailto:weihs@jhu.edu)

**Fig. 1** Mg-9Al (wt%) after ECAE 4Bc processing at 150°C  
**a** Continuous precipitates within the grain interior.  
**b** Discontinuous precipitates near the grain boundary

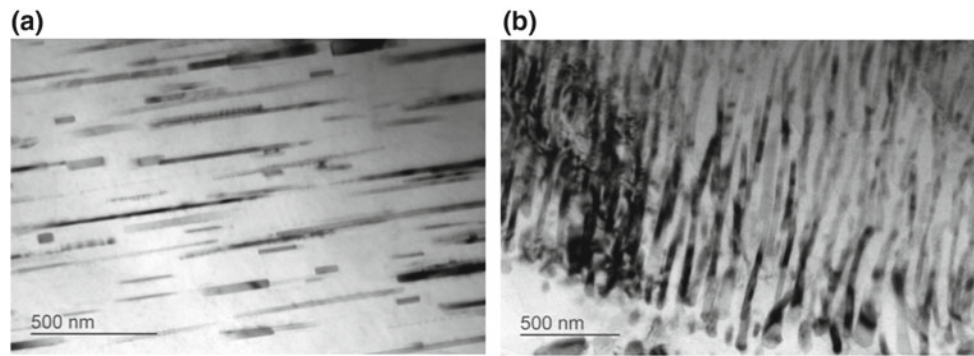
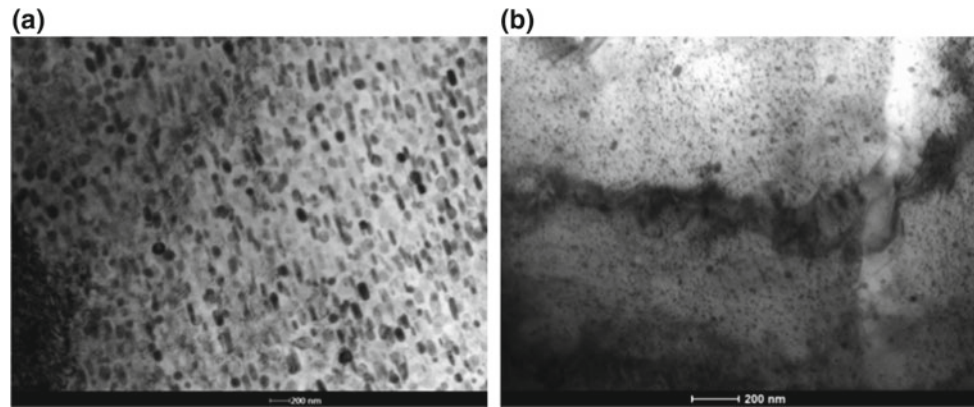


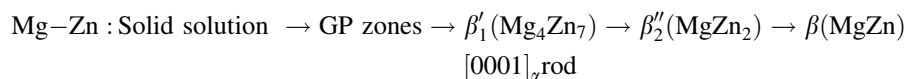
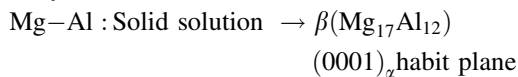
**Fig. 2** **a** Fine nano precipitates in Mg-9Al (wt%) alloy. **b** Fine nano precipitates in Mg-3Zn (wt%) alloy



role as it can directly influence the formation of GP (Guinier-Preston) zones and other metastable phases [11, 12].

In our studies, we consider two binary magnesium alloys (Mg-Zn and Mg-Al) without micro-alloying elements and attempt to manipulate the nucleation and growth of precipitates by controlling deformation. We do so at low temperatures to aid nucleation of fine precipitates while limiting intermetallic coarsening.

The phase transformation sequence in Mg-Al and Mg-Zn alloys is as follows [13]:



Conventional peaking aging of these alloys often results in large aspect ratio precipitates that are not favorable for strengthening [14]. For example, the T6 treatment of Mg-9Al (wt%) alloy creates continuous precipitates in the grain interiors and divorced eutectic type precipitates called

discontinuous precipitates [15] along the grain boundaries as shown in Fig. 1a and b, respectively.

In our work, binary magnesium alloys (Mg-9Al (wt%) and Mg-3Zn (wt%)) were dynamically aged by equal channel angular extrusion (ECAE). The extrusion was carried out at a rate of 0.15 mm/min at 150 °C and along the 4Bc route. Transmission electron micrographs show fine precipitates in Fig. 2a, b for both of these alloy systems after four passes.

We hypothesize that the severe plastic deformation (ECAE) injects a high density of dislocations during processing leading to an increased density of sites for nucleation

[16, 17]. The hydrostatic stress states around edge dislocations attract solute clusters and ease precipitation by dramatically lowering the barrier for nucleation of intermetallics. This leads to a very high number density of fine precipitates, as shown above in Fig. 2. The very tight

spacings and high number densities can result in significant Orowan strengthening and substantial increments in yield strengths [1, 18, 19]. Our work focuses on characterizing the impact of dislocations, as well as excess vacancies on this enhancement of precipitation in Mg alloys.

## References

1. X.L. Ma, S. Eswarappa Prameela, P. Yi, M. Fernandez, N.M. Krywopusk, L.J. Kecskes, T. Sano, M.L. Falk, T.P. Weihs, *Acta Mater.* 172 (2019) 185–199.
2. S.R. Agnew, J.F. Nie, *Scr. Mater.* 63 (2010) 671–673.
3. J. Robson, *Metall. Mater. Trans. A* 45 (2014) 5226–5235.
4. J.D. Robson, N. Stanford, M.R. Barnett, *Scr. Mater.* 63 (2010) 823–826.
5. N. Stanford, J. Geng, Y.B. Chun, C.H.J. Davies, J.F. Nie, M.R. Barnett, *Acta Mater.* 60 (2012) 218–228.
6. J.F. Nie, B.C. Muddle, H.I. Aaronson, S.P. Ringer, J.P. Hirth, *Metall. Mater. Trans. A* 33 (2002) 1649–1658.
7. S. Eswarappa Prameela, P. Yi, V. Liu, B. Medeiros, L.J. Kecskes, M.L. Falk, and T.P. Weihs, Effect of Second Phase Particle Size on the Recrystallized Microstructure of Mg–Al Alloys Following ECAE Processing, *Magnesium Technology 2020*. [https://doi.org/10.1007/978-3-030-36647-6\\_27](https://doi.org/10.1007/978-3-030-36647-6_27)
8. J.F. Nie, B.C. Muddle, *Mater. Sci. Eng. A* 319–321 (2001) 448–451.
9. W. Sun, Y. Zhu, R. Marceau, L. Wang, Q. Zhang, X. Gao, C. Hutchinson, *Science* 363 (2019) 972–975.
10. P. Yi, R.C. Cammarata, M.L. Falk, *Model. Simul. Mater. Sci. Eng.* 25 (2017) 085001.
11. J.F. Nie, B.C. Muddle, *Acta Mater.* 48 (2000) 1691–1703.
12. X. Gao, J.F. Nie, *Scr. Mater.* 58 (2008) 619–622.
13. J.-F. Nie, *Metall. Mater. Trans. A* 43 (2012) 3891–3939.
14. D. Mallick, S. Eswarappa-Prameela, V. Kannan, M. Zhao, J. Lloyd, T. Weihs, KT Ramesh, On the Role of Texture and Precipitate Orientation in Spall Failure of a Rolled Magnesium Alloy, in *Bulletin of the American Physical Society*, 2019, vol. Volume 64, Number 8. (<http://meetings.aps.org/Meeting/SHOCK19/Session/1C.2>)
15. J.B. Clark, *Acta Metall.* 16 (1968) 141–152.
16. Prameela, S. Eswarappa and Yi, Peng and Mediros, Beatriz and Liu, Vance and Keckes, Laszlo J. and Falk, Michael L. and Weihs, Timothy P., Deformation Assisted Nucleation of Continuous Nanoprecipitates in Mg–Al Alloys (11 11, 2019). Available at SSRN: <https://ssrn.com/abstract=3484667>
17. Ma, X., Eswarappa-Prameela, S., Krywopusk, N., Kecskes, L. J., Sano, T., & Weihs, T. P. (2018). Dynamic Precipitation in a Binary Mg–Al Alloy During Equal Channel Angular Extrusion (ECAE). *Microscopy and Microanalysis*, 24(S1), 2222–2223
18. J.F. Nie, *Acta Mater.* 56 (2008) 3169–3176.
19. J.F. Nie, *Scr. Mater.* 48 (2003) 1009–1015.



# Effect of Second Phase Particle Size on the Recrystallized Microstructure of Mg–Al Alloys Following ECAE Processing

Suhas Eswarappa Prameela, Peng Yi, Vance Liu, Beatriz Medeiros, Laszlo J. Kecskes, Michael L. Falk, and Timothy P. Weihs

## Abstract

Magnesium (Mg) alloys are excellent candidates for structural applications, given their high strength to weight ratios. Grain boundaries and precipitates can both contribute to strengthening in Mg alloys, but the design of high strength Mg alloys is challenging due to Mg's anisotropic crystal lattice and yield asymmetry. Herein, we focus on thermomechanical processing that involves grain refinement in the presence of precipitates. We seek an understanding of how small and large Mg<sub>17</sub>Al<sub>12</sub> intermetallic particles impact recrystallization and discontinuous precipitation in Mg–Al alloys. We do so by processing solution treated and peak aged Mg–9Al (wt%) alloys using equal channel angular extrusion (ECAE) along the Bc route at 150 °C. We find that the fine nanoprecipitates that nucleate within the solutionized grain interiors during ECAE processing lead to finer Mg grains in the recrystallized regions compared to those in the presence of the long lathlike precipitates produced during peak aging prior to ECAE processing.

## Keywords

Deformation processing • Nanoprecipitates • Nucleation and growth • Recrystallization • Magnesium alloys

S. Eswarappa Prameela (✉) · P. Yi · V. Liu · B. Medeiros · M. L. Falk · T. P. Weihs  
Department of Materials Science and Engineering, Johns Hopkins University, Baltimore, MD 21218, USA  
e-mail: [seswara3@jhu.edu](mailto:seswara3@jhu.edu)

S. Eswarappa Prameela · P. Yi · L. J. Kecskes · M. L. Falk · T. P. Weihs  
Hopkins Extreme Materials Institute, Johns Hopkins University, Baltimore, MD 21218, USA

M. L. Falk  
Department of Mechanical Engineering, Johns Hopkins University, Baltimore, MD 21218, USA

Department of Physics and Astronomy, Johns Hopkins University, Baltimore, MD 21218, USA

## Introduction

Robust and lightweight magnesium (Mg) alloys are desired in the automotive and defense industries, but the anisotropic behavior of Mg complicates our ability to control defect generation, texture development, and deformation behavior both during processing and in use. In particular, Mg's fundamental physical characteristics, including temperature-sensitive activation of different slip systems, strain rate sensitivities, and significant yield asymmetries, affect the selection of the most appropriate processing conditions [1–7]. Despite these limitations, we are gaining a better understanding of the underlying relationships related to the thermomechanical processing of Mg alloys, especially during severe plastic deformation (SPD). SPD techniques such as extrusion [8], rolling [9], or high-pressure torsion processing [10] have resulted in an extensive range of microstructures [4, 11]. A survey of these studies identifies specific challenges and opportunities in manipulating the microstructure of Mg and its alloys. One such instance is the possibility of creating fine grains with random texture, which improves strength and reduces the yield asymmetry. At the same time, continuous and discontinuous recrystallization processes have also been shown to enable grain refinement [12–14] and greater strengths. In certain alloy compositions, concurrent with recrystallization is the possible formation of fine precipitates [11, 13].

Precipitation is a phase transformation that involves nucleation and growth of second phase particles. There are three possible interactions between recrystallization and precipitation. First, both of these processes can occur simultaneously in different regions of a sample (e.g., precipitation in grain interior and recrystallization near grain boundary) during thermomechanical processing [13]. The second possibility is that recrystallization occurs alongside precipitation in the same region producing a combined reaction zone. The third instance is reprecipitation during recrystallization, wherein precipitates dissolve in the grains

undergoing recrystallization and reform within or next to the new grains [15]. In this effort, we seek to gain a deeper understanding of the mechanisms that control this third mode of interaction in a Mg–9Al (wt%) binary alloy. Specifically, we study how the size of the precipitates within the grain interior can influence the overall recrystallization fraction and the final grain size in a combined reaction zone that includes recrystallized Mg grains and reprecipitated  $Mg_{17}Al_{12}$  particles.

## Experimental Procedure

We procured ingots of Mg–9Al (wt%) alloy from Magnesium Elektron North America (MENA), Madison, IL. The ingots were solutionized by heating them at 385 °C for 6 h and at 420 °C for 16 h, followed by a cold-water quench. Chemical analysis of the ingot was carried out using optical emission spectroscopy (OES) as shown in Table 1.

Two routes were followed for thermomechanical processing, as shown in Fig. 1. For Route 1, solution treated samples were deformed along the 4Bc route by equal channel angular extrusion (ECAE) at a rate of 0.15 mm/min at 150 °C with a 0.45 MPa backpressure. For Route 2, solution treated samples were first peak aged in a furnace for 163 h at 150 °C followed by ECAE along the 4Bc route with a rate of 0.15 mm/min at 150 °C with a 0.45 MPa

backpressure. Samples were cut using a diamond wire saw after ECAE for light microscopy. We mechanically polished the sample using 800 and 1200 grit pads with water, followed by a cloth pad and OPS solution. Samples were then etched using a 2% Nital solution for characterization. Samples were also cut using a diamond wire saw for transmission electron microscopy (TEM). We then mechanically polished them to 50  $\mu\text{m}$  slices and punched 3 mm disks. A Gatan precision ion polishing system (PIPS) was used to perforate holes with a thin region near the periphery for TEM observation. We employed a TF30 microscope operating at 300 keV for microstructure observations.

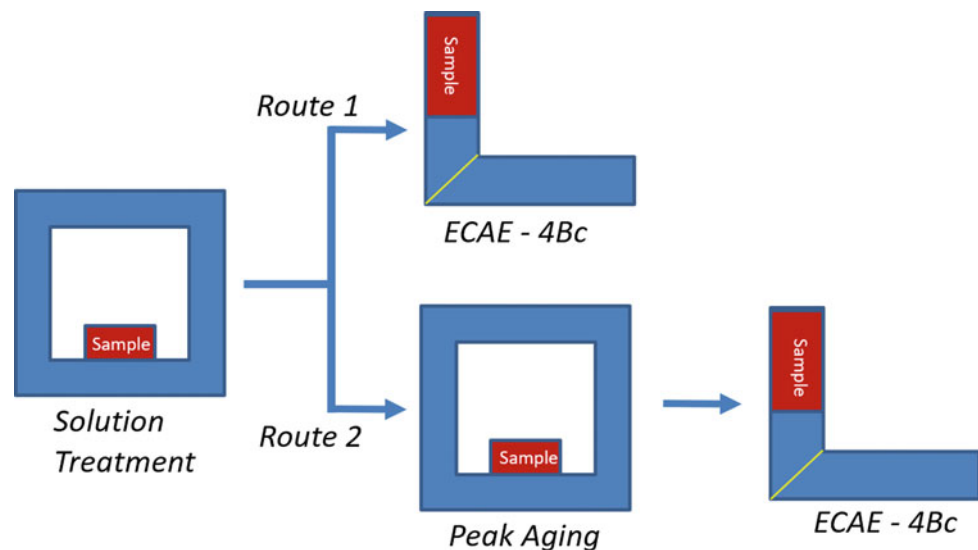
## Results and Discussion

Light microscopy studies on samples after solution treatment and after peak aging confirm that there is no recrystallization before the ECAE processing. The grain size increases slightly during peak aging treatment in Route 2, but is deemed negligible. Thus, before the ECAE processing, both sets of samples have similar grains and grain sizes. The extrusion of the peak aged samples in Route 2, though, proved more challenging. As Fig. 2 indicates, shear localization, fracture, and profuse twinning occurred near the edge of the peak aged samples during ECAE. We attribute this occurrence to the existence of the long precipitate laths within the microstructure and the

**Table 1** Primary constituents of the Mg–Al alloy as measured by optical emission spectroscopy

Chemical composition in weight percent (wt.%)										
Designation	Al	Cu	Mn	Zn	Ca	Ni	Be	Si	Fe	Mg
Mg–9Al (A9)	8.71	0.0002	0.005	<0.001	<0.001	0.0008	<0.0001	0.0020	0.0085	Balance

**Fig. 1** Schematic of the two thermomechanical processing routes. Route 1: a solution treated A9 sample is processed via ECAE (4Bc) at 150 °C; Route 2: a solution treated sample is peak aged and then processed via ECAE (4Bc) at 150 °C



use of relatively low backpressure. Route 1 samples had no such issues, and all four extrusion passes were successful. Following four passes at 150 °C, light micrographs of samples from both processing routes (1 and 2) reveal river-like features in light micrographs, indicating that recrystallization begins along boundaries and grows into the grain interiors during extrusion (Fig. 3).

In our previous study [13], we describe and show that the recrystallized regions in Fig. 3a grow in volume as a function of ECAE passes of the Mg–9Al solutionized samples at 150 °C. A MATLAB code was used to analyze the area fraction of these regions after four passes for both Route 1 and Route 2. The recrystallized fraction for the Route 1 (A9 4Bc) sample is 57.7%, and it is 80.6% for the Route 2 (A9 peak aged + 4Bc) sample. Our earlier [13] and current TEM analysis (Figs. 4 and 5) reveal that the recrystallized regions are combined reaction zones containing recrystallized Mg grains and relatively small  $Mg_{17}Al_{12}$  grains or precipitates sitting next to the Mg grains. The Mg grains contain near equilibrium concentrations of Al, as shown by HAADF-STEM and a random texture, as demonstrated by Kikuchi EBSD patterns [13].

The unrecrystallized portion of the microstructure also evolves during the ECAE processing in Route 1, and it is reported in detail in our earlier work [13]. At the end of the first pass, there are very few localized precipitates in the microstructure and some recrystallization near the grain boundary. After the second pass, the entire unrecrystallized region has a dense distribution of nanoprecipitates. The recrystallization region continues to grow as the number of passes increases, consuming the grain interior that contains finely spaced nanoprecipitates. At the start of the fourth pass, the microstructure still has a dense distribution of fine precipitates within the unrecrystallized grain interiors as shown in Fig. 4a, some of which will be recrystallized in the fourth and final pass. The nanoscale precipitates in the grain interiors of the Route 1 samples, with an almost spherical geometry and uniform distribution, stand in sharp contrast to the much larger, lathlike precipitates that result from peak-aging and are present in the grain interiors of the Route 2 samples prior to ECAE processing (Fig. 4c). (For completeness, we note that the precipitates are spaced more closely (discontinuous precipitates) near the grain boundary [16] in the Route 2 sample.)

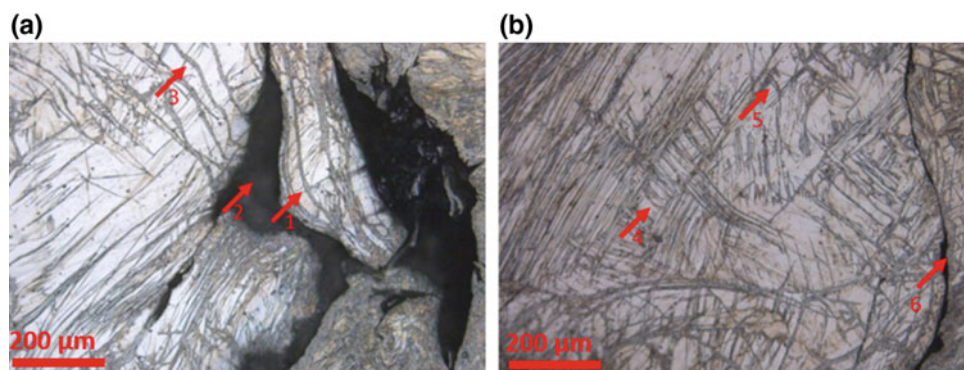


**Fig. 2** a, b Bright field light micrographs showing recrystallization bands (arrows 1 and 3), extensive twinning (arrows 4 and 5) and fracture (arrows 2 and 6) close to the edge of Route 2 A9 peak aged + 4Bc sample

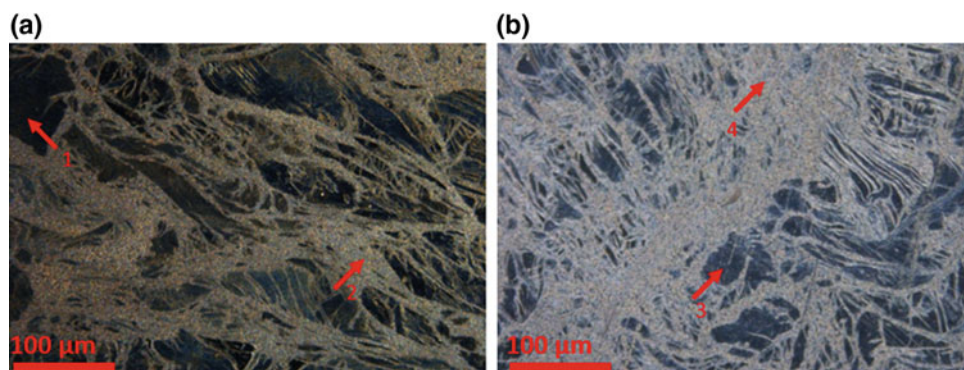


**Fig. 3** Darkfield light micrographs showing a unrecrystallized region (arrow 1) and recrystallized region (arrow 2) in the Route 1 A9 4Bc sample; b unrecrystallized region (arrow 3) and recrystallized region (arrow 4) in the Route 2 A9 peak aged + 4Bc sample



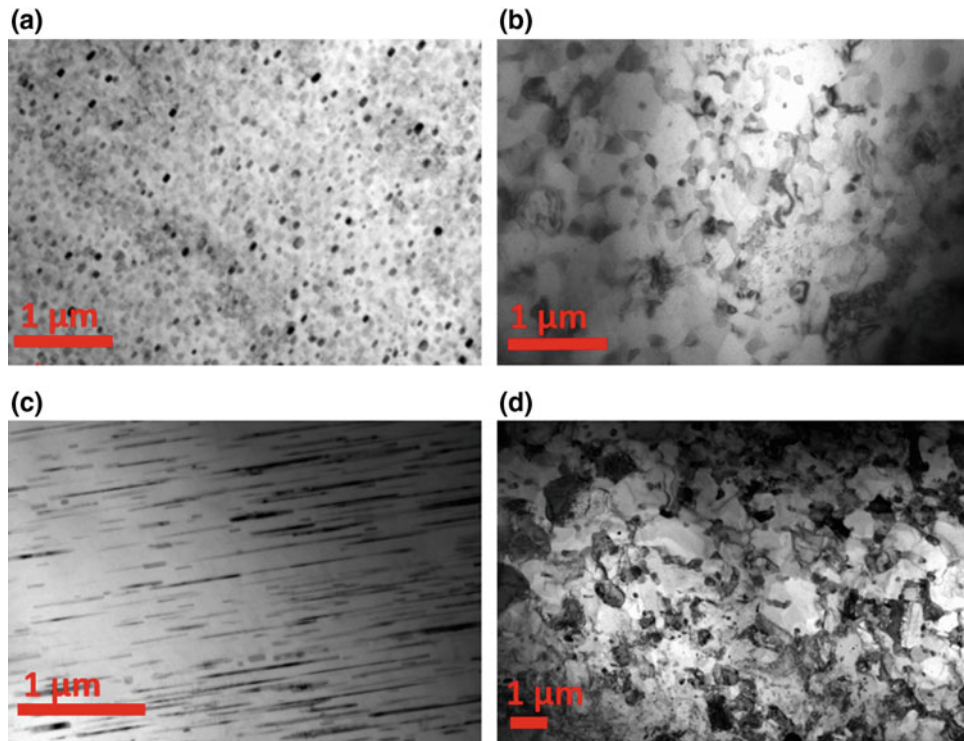


**Fig. 4** TEM micrographs showing **a** a dense distribution of  $Mg_{17}Al_{12}$  nanoprecipitates in the grain interior of the Route 1 A9 4Bc sample; **b** a combined reaction zone near a grain boundary in the Route 1 A9 4Bc sample; **c** a coarse distribution of Route 2  $Mg_{17}Al_{12}$  laths in the grain interior of the A9 peak aged + 4Bc sample; and **d** a combined reaction zone near a grain boundary in the Route 2 A9 peak aged + 4Bc sample (*Note that '4' here refers to the number of ECAE passes*)

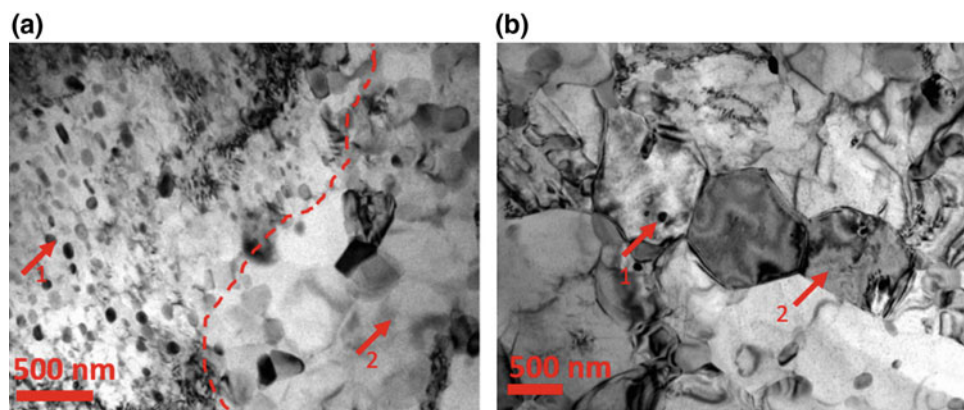


**Fig. 5** **a** Fine nanoprecipitates on the left (arrow 1) intersecting with the advancing combined reaction zone (arrow 2) in the A9 4Bc (Route 1) sample. The growth front of the combined reaction is shown by the dashed line; **b** fine  $Mg_{17}Al_{12}$  particle (arrow 1) within a large grain (similar to another Mg grain exemplified by arrow 2) in the combined reaction zone, as seen in the peak aged + A9 4Bc (Route 2) sample

In Fig. 4b, d, we show the recrystallized microstructures within the combined reaction zones for the Route 1 and 2 samples, respectively, that grow in volume with each ECAE pass. The TEM images reveal much finer Mg grain sizes in the Route 1 combined reaction zones compared to Route 2, and Fig. 6 shows a statistical analysis of these grain sizes.

Higher-resolution TEM images in Fig. 5 begin to reveal the interaction between recrystallization and precipitates. In Fig. 5a, a red dashed line marks the boundary between an original  $\sim 250 \mu m$  Mg grain and a recrystallized region for Route 1. We see fine precipitate particles within the original grain on the left side of the dashed red boundary. These precipitate particles form via continuous precipitation in the

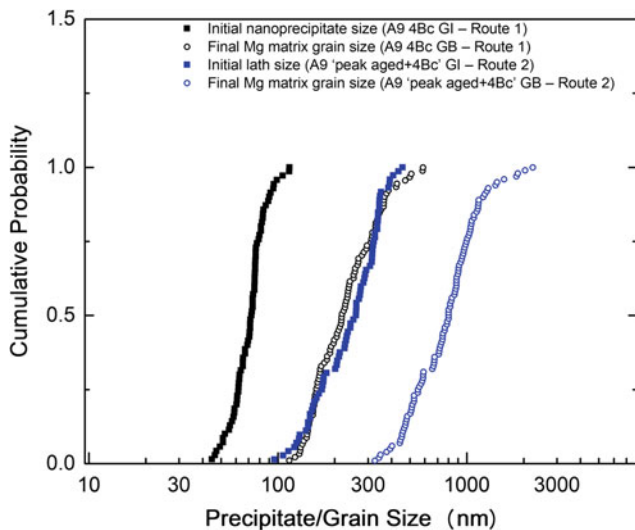


**Fig. 6** Cumulative density plots of the sizes of the initial  $\text{Mg}_{17}\text{Al}_{12}$  particle within grain interiors and the final recrystallized Mg matrix grains of the samples processed along Routes 1 and 2

original grain during the first two ECAE passes [13]. On the right side of the dashed red boundary, we see the combined reaction zone in the recrystallized region that contains small, precipitate-free Mg grains and larger  $\text{Mg}_{17}\text{Al}_{12}$  particles at the boundaries of the Mg grains. In the Route 2 sample, we did not capture a boundary between the unrecrystallized and recrystallized regions, in part due to the higher level of recrystallization in Route 2 samples. However, Fig. 5b reveals the microstructure in a recrystallized region after Route 2 processing. The  $\text{Mg}_{17}\text{Al}_{12}$  laths that initially resided in the grain interiors are absent, and as in Route 1, the resulting Mg grains are also much smaller than the larger ( $\sim 250 \mu\text{m}$ ), initial Mg grains. The recrystallization consumes the whole volume in Fig. 5b, and in contrast to the resulting Route 1 microstructure, the resulting Route 2 combined reaction zone shows that small  $\text{Mg}_{17}\text{Al}_{12}$  particles have reprecipitated both within and outside the new, small Mg grains.

To quantify differences in the microstructures for the two processing routes, we show a statistical analysis of the initial  $\text{Mg}_{17}\text{Al}_{12}$  precipitates in the grain interiors (Fig. 4a, c) and the final, recrystallized Mg grains (Fig. 4b, d) in the combined reaction zones for Routes 1 and 2 in Fig. 6. This figure reveals that the finer initial precipitates in Route 1 correlate with finer Mg grain sizes in the combined reaction zone while the larger initial precipitates (laths) in Route 2 correlate with larger Mg grains in the combined reaction zone.

Based on these results, we can state correlations that can be contrasted for Routes 1 and 2. The initial nanoscale  $\text{Mg}_{17}\text{Al}_{12}$  precipitates (72.31 nm average) that exist before and during recrystallization in Route 1 correlate with less recrystallization (57.7%), a finer average recrystallized Mg grain size (245.22 nm average), and a coarser reprecipitated

$\text{Mg}_{17}\text{Al}_{12}$  particle size (216.85 nm average, measured from Fig. 4b) compared to Route 2. In contrast, the much larger, lathlike  $\text{Mg}_{17}\text{Al}_{12}$  precipitates (252.7 nm average) that exist at the start of ECAE processing in Route 2 correlate with a higher area fraction of recrystallization (80.6%), a larger average recrystallized Mg grain size (838.69 nm average), and a finer reprecipitated  $\text{Mg}_{17}\text{Al}_{12}$  particle size (86.99 nm average, measured from Fig. 4d) compared to Route 1.

The difference in the recrystallized microstructures between the two routes is likely a result of the interaction between the precipitates and the recrystallization processes. The presence of precipitate particles before recrystallization could affect the nucleation and growth of the recrystallized grain [17]. Conversely, the kinetics of recrystallization could affect reprecipitation within the combined reaction zone.

We first consider the potential effect of the initial precipitates on the nucleation of new Mg grains, and the process called particle stimulated nucleation (PSN). When the precipitates are sufficiently large, they can stimulate the nucleation of new grains. The critical particle radius for PSN is given by  $r^* = 4\gamma/0.5\rho Gb^2$  where  $\gamma$  is the grain boundary free energy,  $\rho$  is the dislocation density,  $G$  is the shear modulus,  $b$  is the Burgers vector. Using  $0.5 \text{ J/m}^2$  for  $\gamma$ ,  $10^{14} \text{ m}^{-2}$  for  $\rho$ , 18 GPa for  $G$ , and  $3.2 \text{ \AA}$  for  $b$ , we obtain  $r^* \sim 20 \mu\text{m}$ . Robson et al. also reported a critical PSN radius greater than  $1 \mu\text{m}$  [18]. Given both the predicted and reported critical radii are larger than those measured for the initial particles in Route 1 and Route 2, we expect that PSN is inactive for both sets of samples. Instead of PSN, we anticipate that recrystallization is initiated from highly strained areas near grain boundaries, consistent with our observations and previous studies [13].

Based on Fig. 6, the average recrystallized Mg grain size for Route 2 (838.69 nm) is about 3.4 times the average recrystallized Mg grain size for Route 1 (245.22 nm). Given that the recrystallization area fraction for Route 2 (80.6%) is only 1.4 times larger than for Route 1 (57.7%), we estimate that the number of recrystallized grains for Route 2 must be 6 times lower than for Route 1. We explain this disparity by considering differences in the rates of nucleation of new Mg grains or differences in the growth of these Mg grains. In an earlier study [13], we considered the impact of solute content in unrecrystallized regions of Route 1 samples and its ability to promote nucleation of new Mg grains. Here, we focus on growth and assume that new Mg grains nucleate at a similar rate in both processing routes. Thus, the grains in Route 2 must be growing more rapidly than in Route 1. To seek an explanation for this hypothesis, we consider the pinning effects of the initial  $\text{Mg}_{17}\text{Al}_{12}$  particles.

It is well established that the Zener pinning effect of dense and small second phase particles prevents the growth of recrystallized grains. For example, Fig. 5a shows dense



and fine particles near the growth front of the recrystallized grain, and that could pin the growth front in the Route 1 sample. The critical grain size for continuing growth is  $d^* = 4\gamma / (0.5\rho Gb^2 - \frac{3F_v\gamma}{r})$ , where  $F_v$  is the volume fraction of the second phase (precipitate), and  $r$  is the second phase particle radius. This formula is derived for a spherical second phase particle, where  $F_v/r$  is also proportional to the inverse of the particle spacing, i.e.,  $L^{-1}$ . Given the average particle radius and spacing ( $L$ ) is much smaller for Route 1 [19],  $d^*$  is larger, and the recrystallized Mg grains are more likely to be pinned in Route 1 than in Route 2, once they nucleate. If the growth of recrystallized grains is hindered by the high density of fine precipitate particles in Route 1 processing, more grains must nucleate to consume the heavily deformed grains. In contrast, we argue that grain growth is less impeded and easier during Route 2 due to limited Zener pinning via the larger  $Mg_{17}Al_{12}$  particles. Once nucleated, the Mg grains can grow to a larger average size, and thus less nucleation of new Mg grains is required to recrystallize most of the sample volume.

As a final observation, we note that the boundaries of the recrystallized grains can serve as channels for solute transport within the combined reaction zone. Due to the finer recrystallized Mg grain size of the Route 1 samples, there are more grain boundaries. In turn, this enables a more rapid and efficient transport of Al, which allows more extensive coarsening of the  $Mg_{17}Al_{12}$  particles that have reprecipitated. This could explain why the average size of the reprecipitated particles following Route 1 processing is 216.85 nm, and it is only 86.99 nm following Route 2 processing. This difference in particle size also correlates with the much lower solute concentration in the recrystallized region in Route 1 compared to Route 2. The finer recrystallized Mg grain size of the Route 1 samples thus appears to be enabling a more rapid depletion of Al from the Mg matrix and a more extensive coarsening of the  $Mg_{17}Al_{12}$  particles.

## Conclusions

A binary Mg–Al alloy was used to study the effect of precipitate size and morphology on the evolution of the combined reaction zone and resulting grain sizes. Smaller  $Mg_{17}Al_{12}$  particles produced during the ECAE process appear to produce a strong pinning effect and are likely inhibiting the growth of recrystallized Mg grains. In contrast, large precipitate laths produced during peak aging before ECAE processing appear to promote recrystallization by enabling more extensive growth of the recrystallized Mg grains. In addition, the finer resulting Mg grain

size in Route 1 processing may promote the coarsening of the reprecipitated  $Mg_{17}Al_{12}$  particles via more extensive grain boundary diffusion compared to Route 2 samples. The step by step process by which fine particles or large laths dissolve and help in forming the combined reaction zone is still not clear. The competition between the dissolution rate of prior precipitates or laths and the nucleation rate of the new precipitates may play an essential role during this process, and an improved understanding of the interplay of precipitation, reprecipitation, growth, and recrystallization is needed.

**Acknowledgements** The authors would like to gratefully acknowledge the financial and technical support from the Center for Materials under Extreme Dynamic Environment (CMEDE). The research was sponsored by the Army Research Laboratory and was accomplished under Cooperative Agreement Number W911NF-12-2-0022. The views and conclusions contained in this document are those of the authors and should not be interpreted as representing the official policies, either expressed or implied, of the Army Research Laboratory or the US Government. The US Government is authorized to reproduce and distribute reprints for Government purposes notwithstanding any copyright notation herein.

## References

1. J. Robson, Anisotropy and Asymmetry of Yield in Magnesium Alloys at Room Temperature, *Metall. Mater. Trans. A*. 45 (2014) 5226–5235. <https://doi.org/10.1007/s11661-014-2453-4>.
2. J.D. Robson, N. Stanford, M.R. Barnett, Effect of particles in promoting twin nucleation in a Mg–5wt.% Zn alloy, *Scr. Mater.* 63 (2010) 823–826. <https://doi.org/10.1016/j.scriptamat.2010.06.026>.
3. S. Bagherzadeh, K. Abrinia, Y. Liu, Q. Han, The effect of combining high-intensity ultrasonic vibration with ECAP process on the process parameters and mechanical properties and microstructure of aluminum 1050, *Int. J. Adv. Manuf. Technol.* 88 (2016). <https://doi.org/10.1007/s00170-016-8779-x>.
4. Z. Wu, R. Ahmad, B. Yin, S. Sandlöbes, W.A. Curtin, Mechanistic origin and prediction of enhanced ductility in magnesium alloys, *Science*. 359 (2018) 447–452. <https://doi.org/10.1126/science.aap8716>.
5. D. Mallick, S. Eswarappa Prameela, V. Kannan, M. Zhao, J. Lyod, T.P. Weihs, K.T. Ramesh, On the Role of Texture and Precipitate Orientation in Spall Failure of a Rolled Magnesium Alloy, in *Bull. Am. Phys. Soc.* 64(8) (2019). <http://meetings.aps.org/Meeting/SHOCK19/Session/1C.2>.
6. X. Ma, S., Eswarappa-Prameela, N. Krywopusk, L.J. Kecskes, T. Sano, T. P. Weihs, Dynamic precipitation in a binary Mg–Al Alloy during Equal Channel Angular Extrusion (ECAE). *Microsc. Microanal.* 24(S1) (2018) 2222–2223.
7. S. Eswarappa Prameela, T.P. Weihs, Deformation Driven Precipitation in Binary Magnesium Alloys. *Magnes. Technol.* (2020). [https://doi.org/10.1007/978-3-030-36647-6\\_26](https://doi.org/10.1007/978-3-030-36647-6_26)
8. V.M. Segal, Engineering and commercialization of equal channel angular extrusion (ECAE), *Mater. Sci. Eng. A*. 386 (2004) 269–276. <https://doi.org/10.1016/j.msea.2004.07.023>.
9. T.-C. Chang, J.-Y. Wang, C.-M. O., S. Lee, Grain refining of magnesium alloy AZ31 by rolling, *J. Mater. Process. Technol.*

- 140 (2003) 588–591. [https://doi.org/10.1016/s0924-0136\(03\)00797-0](https://doi.org/10.1016/s0924-0136(03)00797-0).
10. A.S.J. Al-Zubaydi, A.P. Zhilyaev, S.C. Wang, P. Kucita, P.A.S. Reed, Evolution of microstructure in AZ91 alloy processed by high-pressure torsion, *J. Mater. Sci.* 51 (2016) 3380–3389. <https://doi.org/10.1007/s10853-015-9652-2>.
  11. J.-F. Nie, Precipitation and Hardening in Magnesium Alloys, *Metall. Mater. Trans. A.* 43 (2012) 3891–3939. <https://doi.org/10.1007/s11661-012-1217-2>.
  12. R. Cottam, J. Robson, G. Lorimer, B. Davis, Dynamic recrystallization of Mg and Mg–Y alloys: Crystallographic texture development, *Mater. Sci. Eng. A.* 485 (2008) 375–382. <https://doi.org/10.1016/j.msea.2007.08.016>.
  13. X.L. Ma, S. Eswarappa Prameela, P. Yi, M. Fernandez, N.M. Krywopusk, L.J. Kecskes, T. Sano, M.L. Falk, T.P. Weihs, Dynamic precipitation and recrystallization in Mg–9wt.%Al during equal-channel angular extrusion: A comparative study to conventional aging, *Acta Mater.* 172 (2019) 185–199. <https://doi.org/10.1016/j.actamat.2019.04.046>.
  14. Z.R. Zeng, Y.M. Zhu, S.W. Xu, M.Z. Bian, C.H.J. Davies, N. Birbilis, J.F. Nie, Texture evolution during static recrystallization of cold-rolled magnesium alloys, *Acta Mater.* 105 (2016) 479–494. <https://doi.org/10.1016/j.actamat.2015.12.045>.
  15. S.-H. Kim, J.U. Lee, Y.J. Kim, B.G. Moon, B.S. You, H.S. Kim, S.H. Park, Improvement in extrudability and mechanical properties of AZ91 alloy through extrusion with artificial cooling, *Mater. Sci. Eng. A.* 703 (2017) 1–8. <https://doi.org/10.1016/j.msea.2017.07.048>.
  16. J.B. Clark, Age hardening in a Mg–9 wt.% Al alloy, *Acta Metall.* 16 (1968) 141–152. [https://doi.org/10.1016/0001-6160\(68\)90109-0](https://doi.org/10.1016/0001-6160(68)90109-0).
  17. F.J. Humphreys, M. Hatherly, Chapter 9 - Recrystallization of Two-Phase Alloys, in: F.J. Humphreys, M. Hatherly (Eds.), *Recryst. Relat. Annealing Phenom.* Second Ed., Elsevier, Oxford, 2004: pp. 285–319. <https://doi.org/10.1016/b978-008044164-1/50013-x>.
  18. J.D. Robson, D.T. Henry, B. Davis, Particle effects on recrystallization in magnesium–manganese alloys: Particle-stimulated nucleation, *Acta Mater.* 57 (2009) 2739–2747. <https://doi.org/10.1016/j.actamat.2009.02.032>.
  19. S. Eswarappa Prameela, P. Yi, B. Medeiros, V. Liu, J.K. Laszlo, M.L. Falk, T.P. Weihs, Deformation assisted nucleation of continuous nanoprecipitates in Mg–Al Alloys (Nov 11 2019). Available at SSRN: <https://ssrn.com/abstract=3484667>.

# Relating Texture and Thermomechanical Processing Variables in Mg–Zn–Ca Alloys

Tracy D. Berman and John E. Allison

## Abstract

It is well known that the strong basal texture commonly produced in magnesium alloy sheets leads to poor formability at room temperature. A sizable body of work has explored how changing the alloy composition and rolling conditions can yield more desirable textures; however, important thermomechanical variables, such as the feed rate during rolling, are often not included in the literature, making it difficult to correlate how changes in processing affect the final crystallographic texture. This work explores the texture evolution and grain refinement in Mg–Zn–Ca alloys during plane strain compression (PSC) using a Gleeble thermomechanical simulator. This instrument allows for precise control and capture of the thermomechanical history of the sample. The texture and grain morphology of the compressed samples were characterized using electron backscatter diffraction (EBSD). The texture results will be used to identify which alloys and processing conditions should be scaled up for future rolling studies.

## Keywords

Texture • TMP • Grain refinement • Gleeble

## Introduction

The quest for magnesium alloy sheet with good low temperature formability has been ongoing. Mg alloys which include rare earth (RE) elements have demonstrated improved formability (often demonstrated with high Erichsen cup tests); this is generally attributed to the “rare earth” texture, which is marked by a spreading of the basal poles along the transverse direction in the sheet [1–5]. However,

the addition of RE elements can make the alloys costly, and supply is at the mercy of strategic planning.

Promising textures and sheet formability have also been observed in some non-RE-containing alloys, including in the Mg–Zn–Ca alloy system [1, 6–9]. It has been demonstrated that both Zn and Ca must be present in the alloy to achieve a low basal texture [9, 10]. Several studies have explored the mechanisms responsible for the texture reduction and include solute drag [11], an effect of particles in the alloy system modifying the recrystallization behavior [12], dynamic strain aging [13], and twinning effects [1, 7, 14].

Despite the amount of work done to develop formable magnesium alloy sheet, it is often difficult to draw firm conclusions. The thermomechanical processing (TMP) conditions also affect the texture evolution, and in the literature, it is common for several of the TMP variables used in the rolling process to be omitted, in particular the feedthrough rate of the sheet. It is also difficult to monitor the temperature of the sheets during rolling; though pre-rolling annealing and roll temperatures may be given, the temperature of the sheet will vary when passed between steps.

The Gleeble thermomechanical processing simulator allows for precise monitoring of the TMP conditions during deformation, and plane strain compression has frequently been used to simulate the rolling process [15, 16]. Thermocouples welded to the sample itself are used to control the processing conditions. An additional advantage of using the Gleeble is that less material is needed than would be required for rolling studies; several Gleeble plane strain compression specimens can be extracted from a small laboratory cast ingot.

This work explores the texture evolution and grain refinement that occurs during plane strain compression of a Mg–3Zn–0.1Ca alloy (designated as ZX30). This alloy was chosen to facilitate comparison with rolled sheet available in the literature [9, 10]. As the feedthrough rate (which relates to the strain rate) was not available in the literature, the effect of strain rate on the texture evolution was an important variable to explore.

T. D. Berman (✉) · J. E. Allison  
Materials Science and Engineering, University of Michigan, 2300  
Hayward St, Ann Arbor, MI 48109, USA  
e-mail: [tradiasa@umich.edu](mailto:tradiasa@umich.edu)

## Experimental

Cast ingots nominally 80 mm × 80 mm × 20 mm were received from the University of Florida. The ingots were solution treated at 350 °C at 24 h and then water quenched. Plane strain compression samples with dimensions of 20 mm × 15 mm × 10 mm were extracted from the centers of the ingots, with the 10 mm thickness direction of the samples being parallel to the 20 mm thickness direction of the ingot. The casting surfaces of the ingot, which exhibited columnar grains, were discarded.

Prior to insertion into the Gleeble system, surface oxides were removed using 1200 g SiC paper. Two k-type thermocouples were welded to each specimen. The center thermocouple is closest to the region undergoing deformation and most accurately represents the sheet temperature; however, it is vulnerable to breaking off during the deformation process as the region is compressed. Therefore, a second thermocouple, which is outside the deformation region, was used to regulate the temperature. The temperature difference between the two thermocouples was generally less than 10 °C, and usually 0 °C until the compressive strains were greater than 50%.

Several TMP processing variables were explored, including the number of passes (compression “hits” in the Gleeble), the strain rate, and the duration of the soak between passes. The TMP test matrix used is summarized in Table 1. All processing (pre-compression soak, compression, and annealing) was done at 350 °C. The heating rate to temperature was 5 °C/s. Once heated to 350 °C, the sample was held at this temperature 600 s (10 min). The sample was then subjected to multiple hits to a specific true strain at the given strain rate. The amount of time spent soaking the sample between hits was also varied (this is equivalent to the re-heating steps between rolling passes that allows for recovery and recrystallization to occur). All samples were subjected to a final post-deformation annealing treatment of 350 °C for 600 s (10 min) and then air quenched within the Gleeble chamber for 30 s.

Optical microscopy and electron backscatter diffraction (EBSD) were used to characterize the as-cast and deformed materials. The deformed samples were mounted such that the compression direction was normal to the grinding surface. The samples were ground to mid-thickness and then prepared using standard practices for magnesium alloys, using a diamond paste and an oil-based lubricant. The final preparation step before optical microscopy was etching in a solution of 10 mL water, 10 mL acetic acid, 4.3 g of picric acid (crystals), and 70 mL of ethanol for approximately three to five seconds. The final preparation step before EBSD was etching for approximately five seconds in a ~5 °C solution of 60 mL ethanol, 20 mL water, 15 mL glacial acetic acid, and 3 mL of nitric acid. Re-polishing for 10 min using 1 μm paste was sufficient to remove the prior etched surface when switching between preparation for the two characterization methods.

EBSD was conducted using a Tescan Mira3 electron microscope operated at 30 keV with a beam intensity setting of 20. EBSD pole figure orientation information is from an area at least 1 mm by 1 mm in dimensions, with a step size no larger than 5 μm. Multiple EBSD scans were taken on several of the samples, and the pole figures presented were generated by merging the orientation data from all relevant scans. Data analysis was done using both OIM Analysis and MTEX; in both cases, points with a confidence index of less than 0.1 were removed from the dataset. No cleaning was performed on the EBSD data presented in this work.

## Results

All of the thermomechanical processing conditions studied led to grain refinement in the compressed region. This was observed both optically (Fig. 1) and using EBSD (Fig. 2). The as-cast microstructure consisted of large dendritic grains on the order of 1 mm in diameter. In the reduced region, the average grain size was closer to 30 μm. In several of the

**Table 1** TMP conditions for Gleeble plane strain compression tests

Sample name	Number of passes	Strain per pass	Strain rate	Soak between passes (s)
ZX30_d06	5	0.2	0.1	600
ZX30_d10	5	0.2	0.5	600
ZX30_d11	10	0.2	0.1	600
ZX30_d13	5	0.2	0.1	300
ZX30_d14	5	0.2	0.1	120
ZX30_d15	10	0.2	0.1	600
ZX30_d16	10	0.2	0.25	600
ZX30_d17	10	0.2	0.5	600



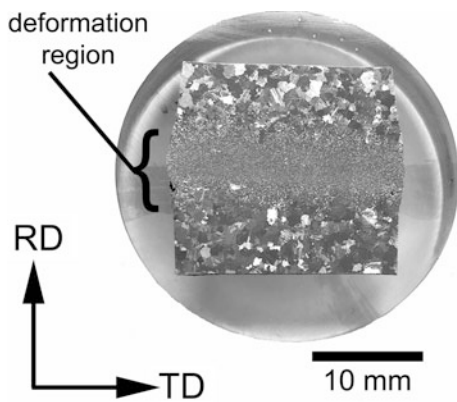


**Fig. 1** Photograph of sample ZX30\_d06. The top and bottom of the sample were unconstrained, and the middle of the specimen is the deformed region

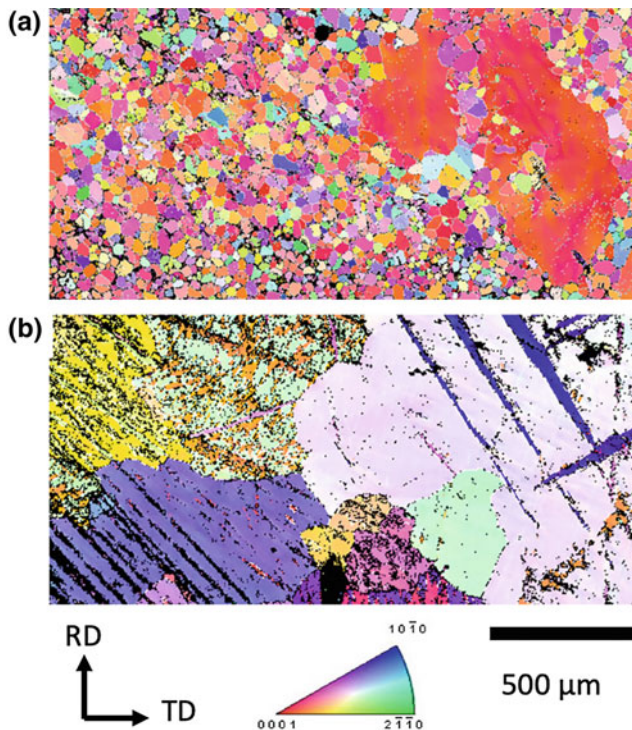


**Fig. 2** IPF maps of ZX30\_d06 in the **a** reduced and **b** non-compressed regions. Both maps are  $2000 \mu\text{m} \times 1000 \mu\text{m}$  in size

samples, a few large, dendritic structures remained in the reduced section, such as the one seen in the right-hand side of Fig. 2. These features were only observed in the samples subjected to five passes; increasing the number of passes (and therefore total strain) led to more uniform grain refinement.

One of the variables explored was the strain rate. Inverse pole figure (IPF) maps of samples having undergone ten passes are shown in Fig. 3, and their corresponding pole figures are shown in Fig. 4. The top two samples

(ZX30\_d11 and ZX30\_d15) are repeat tests of the same condition, with a strain rate of  $0.1 \text{ s}^{-1}$ . The strain rate was higher for the samples ZX30\_d16 and ZX30\_d17, at  $0.25 \text{ s}^{-1}$  and  $0.5 \text{ s}^{-1}$ , respectively. The resulting microstructure and texture do not show a strong dependence on the deformation strain rate within the range studied. None of the variables studied seemed to have a strong impact on the final grain size, which is shown in Fig. 5.

## Discussion

The impact of strain rate, number of deformation passes (total strain), and duration of intermediate annealing on the final microstructure of ZX30 samples subjected to plane strain compression was explored by studying the post-deformation microstructure, and texture using EBSD. Of all the variables studied, the most significant variable seemed to be the number of passes. Samples subjected to only five passes were prone to containing some larger, dendritic grains within the reduced section. It was observed that these larger grains tended to be basally oriented (such as the one shown in Fig. 2). If they were large grains from the original microstructure, the orientations should be random. This suggests preferential growth of the basally oriented grains, which has been reported in magnesium alloys [17]. It appears that increasing the total amount of strain can prevent the occurrence of these undesirable, large grains.

Variation of the length of the intermediate annealing step did not lead to any appreciable differences in grain size, as can be seen by comparing the grain size distributions of ZX30\_d06, ZX30\_d13, and ZX30\_d14 in Fig. 5; these samples had annealing treatment durations of 600 s, 300 s, and 120 s, respectively. The textures (not shown) were also quite similar. This suggests that all annealing durations studied led to similar amounts of recovery and that no significant grain growth (which would lead to a larger final grain size in the final microstructure) occurred. Future work will explore the microstructure and extent of recrystallization in the deformed microstructure and the static recrystallization kinetics.

Sample ZX30\_d16, deformed with a strain rate of  $0.25 \text{ s}^{-1}$ , curiously exhibits a larger grain size than the other conditions studied. We speculate that this is a stochastic variation in the grain size rather than anomalous behavior which will be the topic of future research. In addition, the basal pole figures of the two samples deformed with a strain rate of  $0.1 \text{ s}^{-1}$  for 10 passes are slightly different. Sample ZX30\_d15 (top right) shows a single peak, whereas sample ZX30\_d11 shows a double basal peak, with splitting along the RD direction. The difference may be due to an insufficient sampling area in the ZX30\_d15 sample. Only a  $1 \text{ mm}^2$  large region was examined for this sample, whereas the



**Fig. 3** IPF maps of samples having undergone 10 passes using different strain rates. All maps are shown on the same scale

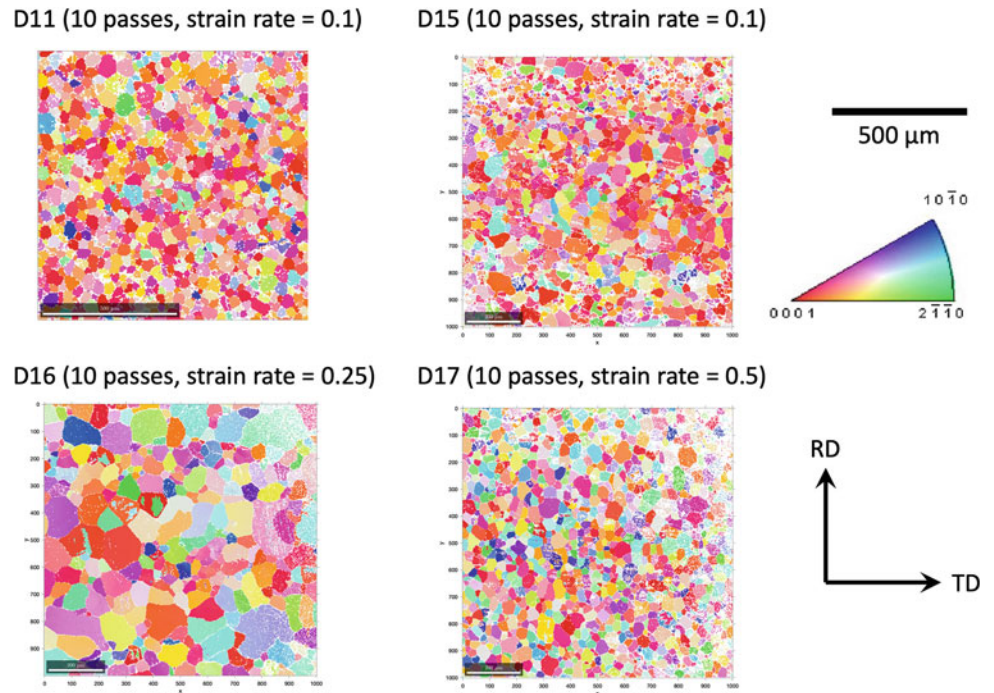
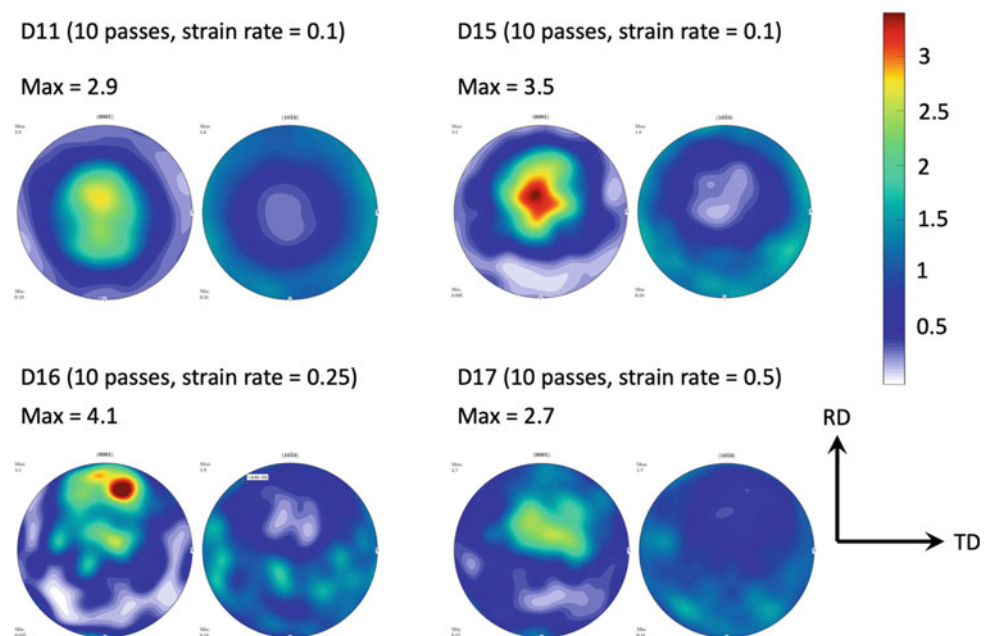


**Fig. 4** EBSD pole figures of ZX30 samples having undergone plane strain compression using different strain rates



EBSD scans used to generate the pole figure for ZX30\_d11 covered a 6 mm<sup>2</sup> area. It is recommended that EBSD scans measure the orientation of at least 1000 grains [18, 19]. The differences may also be due to variations within the initial microstructure.

Based on the EBSD data presented, it is difficult to conclude whether or not increasing the strain rate is more likely to lead to a more diffuse texture, or a texture with a more RE-like spread along the TD. The most promising texture was

that seen in samples ZX30\_d17. This is the only sample that showed a suggestion of TD spreading similar to that reported by Chino et al. [9], and it exhibits a low maximum basal texture intensity of 2.7 multiples of random density (MRD). Given that the complete TMP history of the sheet presented by Chino is unknown, it is unclear whether or not the differences between the textures reported here and in Ref. [9] are due to differences in processing conditions or whether plane strain compression does not adequately simulate the rolling

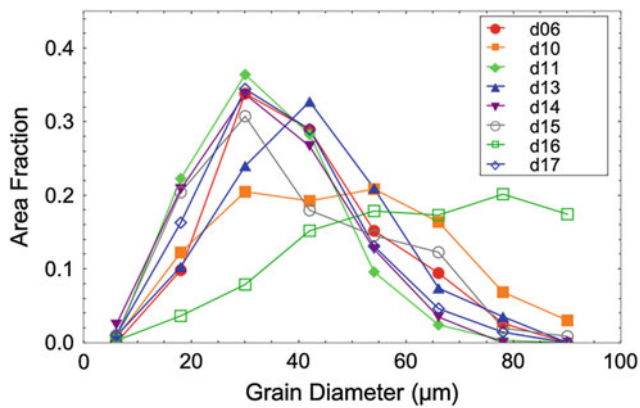


**Fig. 5** Grain size distributions of the ZX30 samples after plane strain compression

process in magnesium alloys (e.g., due to a lack of shearing). It has been demonstrated that texture is affected by altering the amount of shearing the sheet is subjected to during rolling [20]. Ongoing work is exploring comparing the texture of a rolled magnesium alloy sheet with a known TMP history to the texture produced using Gleeble plane strain compression tests with a comparable processing history.

While the higher strain rate may have improved the texture, it did not lead to improved grain refinement. Both strength and ductility can be improved through grain refinement in magnesium alloys [21, 22], and commercial sheet generally exhibits grain approximately 10  $\mu\text{m}$  in diameter [23]. Therefore, the most promising processing variation is likely increasing the strain per pass and or the total amount of strain. Recent work has demonstrated that a large number of passes ( $\sim 20$ ), with an increasing amount of strain per pass, can lead to desirable texture and formability in Mg alloy sheets [24]. Future work will explore replicating those processing histories using the Gleeble.

## Summary

The impact of strain rate, number of deformations passes (total strain), and duration of intermediate annealing on the final microstructure of ZX30 samples subjected to plane strain compression was explored. Of all the variables studied, the most significant variable seemed to be the number of deformation passes (the total final strain). A higher strain rate appears to also result in a more diffuse texture. In the present work, we were unable to reproduce the broad TD spreading seen in ZX30 rolled sheet textures as presented in the literature. It is unclear whether the difference in texture is due to being outside the TMP processing window the sheets experience during rolling or whether shearing is needed to replicate the texture evolution seen in magnesium alloy sheet.

## References

- Guan D, Liu X, Gao J, et al (2019) Exploring the mechanism of “Rare Earth” texture evolution in a lean Mg–Zn–Ca alloy. 9:1–11. <https://doi.org/10.1038/s41598-019-43415-z>
- Imandoust A, Barrett CD, Al-samman T, et al (2017) A review on the effect of rare-earth elements on texture evolution during processing of magnesium alloys. *J Mater Sci* 52:1–29. <https://doi.org/10.1007/s10853-016-0371-0>
- Hadorn JP, Hantzsche K, Yi SB, et al (2012) Role of Solute in the Texture Modification During Hot Deformation of Mg–Rare Earth Alloys. *Metall Mater Trans A* 43:1347–1362. <https://doi.org/10.1007/s11661-011-0923-5>
- Stanford N, Atwell D, Beer AG, et al (2008) Effect of microalloying with rare-earth elements on the texture of extruded magnesium-based alloys. *Scr Mater* 59:772–775. <https://doi.org/10.1016/j.scriptamat.2008.06.008>
- Griffiths D (2015) Explaining texture weakening and improved formability in magnesium rare earth alloys. *Mater Sci Technol* 31:10–24. <https://doi.org/10.1179/1743284714Y.0000000632>
- Lee JY, Yun YS, Suh BC, et al (2014) Comparison of static recrystallization behavior in hot rolled Mg–3Al–1Zn and Mg–3Zn–0.5Ca sheets. *J Alloys Compd* 589:240–246. <https://doi.org/10.1016/j.jallcom.2013.11.210>
- Kim DW, Suh BC, Shim MS, et al (2013) Texture evolution in Mg–Zn–Ca alloy sheets. *Metall Mater Trans A Phys Metall Mater Sci* 44:2950–2961. <https://doi.org/10.1007/s11661-013-1674-2>
- Suh BC, Kim JH, Bae JH, et al (2017) Effect of Sn addition on the microstructure and deformation behavior of Mg–3Al alloy. *Acta Mater* 124:268–279. <https://doi.org/10.1016/j.actamat.2016.11.020>
- Chino Y, Ueda T, Otomatsu Y, et al (2011) Effects of Ca on Tensile Properties and Stretch Formability at Room Temperature in Mg–Zn and Mg–Al Alloys. *Mater Trans* 52:1477–1482. <https://doi.org/10.2320/matertrans.M2011048>
- Lee JY, Yun YS, Kim WT, Kim DH (2014) Twinning and texture evolution in binary Mg–Ca and Mg–Zn alloys. *Met Mater Int* 20:885–891. <https://doi.org/10.1007/s12540-014-5012-z>
- Zeng ZR, Zhu YM, Xu SW, et al (2016) Texture evolution during static recrystallization of cold-rolled magnesium alloys. *Acta Mater* 105:479–494. <https://doi.org/10.1016/j.actamat.2015.12.045>
- Zhang B, Wang Y, Geng L, Lu C (2012) Effects of calcium on texture and mechanical properties of hot-extruded Mg–Zn–Ca alloys. *Mater Sci Eng A* 539:56–60. <https://doi.org/10.1016/j.msea.2012.01.030>
- Wang T, Jiang L, Mishra RK, Jonas JJ (2014) Effect of Ca addition on the intensity of the rare earth texture component in extruded magnesium alloys. *Metall Mater Trans A Phys Metall Mater Sci* 45:4698–4709. <https://doi.org/10.1007/s11661-014-2371-5>
- Zeng ZR, Bian MZ, Xu SW, et al (2016) Effects of dilute additions of Zn and Ca on ductility of magnesium alloy sheet. *Mater Sci Eng A* 674:459–471. <https://doi.org/10.1016/j.msea.2016.07.049>
- Nayan N, Gurao NP, Murty SVSN, et al (2015) Materials Characterization Microstructure and micro-texture evolution during large strain deformation of Inconel alloy IN718. *Mater Charact* 110:236–241. <https://doi.org/10.1016/j.matchar.2015.10.027>
- Kim J, Okayasu K, Fukutomi H (2012) Texture Evolution in AZ80 Magnesium Alloy by the Plane Strain Compression Deformation at High Temperature + 1. *Mater Trans* 53:1870–1875
- Bhattacharyya JJ, Agnew SR, Muralidharan G (2015) Texture enhancement during grain growth of magnesium alloy AZ31B. *Acta Mater* 86:80–94. <https://doi.org/10.1016/j.actamat.2014.12.009>
- Engler O (2009) Texture Analysis: Ceramic Transactions, Volume 201. In: Applications of Texture Analysis: Ceramic Transactions. pp 125–133

19. Wright SI, Nowell MM, Bingert JF (2007) A Comparison of Textures Measured Using X-Ray and Electron Backscatter Diffraction. *Metall Mater Trans A* 38:1845–1855. <https://doi.org/10.1007/s11661-007-9226-2>
20. Muralidharan G, Muth TR, Peter WH, et al (2013) Shear Rolling of Magnesium Sheet for Automotive, Defense, and Energy Applications, <https://info.oml.gov/sites/publications/files/Pub40045.pdf>. Accessed September 6, 2019.
21. Chapman JA, Wilson DV (1962) The Room-Temperature Ductility of Fine-Grain Magnesium. *J Inst Met* 91:39–40
22. Barnett MR, Atwell DL, Beer AG (2007) Grain Size in Mg Alloys : Recrystallization and Mechanical Consequences. *Mater Sci Forum* 558–559:433–440. <https://doi.org/10.4028/www.scientific.net/MSF.558-559.433>
23. Singh J, Kim MS, Lee JH, et al (2019) Microstructure evolution and deformation behaviors of E-form and AZ31Mg alloys during ex-situ mini-V-bending tests. *J Alloys Compd* 778:124–133. <https://doi.org/10.1016/j.jallcom.2018.11.138>
24. Shi R, Miao J, Luo AA (2019) A new magnesium sheet alloy and its multi-stage homogenization for simultaneously improved ductility and strength at room temperature. *Scr Mater* 171:92–97. <https://doi.org/10.1016/j.scriptamat.2019.06.027>

# Variation of Extrusion Process Parameter for the Magnesium Alloy ME21

G. Kurz, M. Nienaber, J. Bohlen, D. Letzig, and K. U. Kainer

## Abstract

Extrusion is an economic production process for the generation of semi-finished magnesium products that can be used for biomedical and automotive applications. This paper reports on the variation of process parameters (temperature and extrusion speed) in the aluminum-free magnesium alloy ME21 (Mg–2Mn–0, 6Ce–0,3) during extrusion in order to investigate their influence on strength and ductility of the produced profiles. The influence of the varied process parameters on the microstructure before and after heat treatment is shown. Furthermore, the mechanical properties of the extruded profiles are presented and discussed with respect to arising textures. The results of this work are used to discuss how to tailor the mechanical properties of the magnesium alloy ME21 during the extrusion process.

## Keywords

Magnesium • Extrusion • Aluminum-free • Magnesium sheet • Rare earth-containing alloys

## Introduction

In order to exploit the full potential of magnesium as a lightweight material, the use of thin-walled components, such as extruded flat profiles, is indispensable. The funding project for **F**unction-integrated **M**agnesium Lightweight Construction for Car Seat Structures (FUMAS), funded by the German Federal Ministry of Economics and Energy (BMWi), makes it possible for the first time to use magnesium in large quantities in highly stressed seat structures by the combination of extrusion and forming processes as well

as by the implementation of new design concepts. The project covers the development of a material adapted design and the production process. The production process includes the extrusion and the forming process, joining, and the coating for corrosion protection. Finally, it is planned to manufacture a prototype seat and test the seat in a crash test. One workpackage of the Magnesium Innovation Centre (MagIC) is the development of a robust and reproducible forming process. The work in this funding project is aimed at reducing the weight of a vehicle seat structure by using extruded magnesium parts in the seat back. Vehicle seats are among the most mechanically stressed components of the vehicle interior and therefore make a considerable contribution to the vehicle mass. Magnesium parts have so far been cast into small production volumes in the seat area. Weight saving potentials of 30–40% compared to a steel reference structure were shown. Compared to magnesium casting alloys, wrought magnesium alloys exhibit higher mechanical strength and elongation at fracture. The simple substitution of steel components by magnesium components, however, fails on the one hand due to the lower strength of magnesium and on the other hand due to suitable joining and corrosion protection solutions.

This paper shows the results of the trials for the optimization of the extrusion process. From the company TWI commercially available magnesium alloy ME21 (2 wt% manganese and up to 1 wt% of rare earth elements) was chosen to realize the seat back component, because of its good hot strength and hot workability compared to other magnesium alloys [1]. The alloying element manganese is contained in small quantities in many technical magnesium alloys to increase corrosion resistance. In magnesium alloys, manganese forms stable intermetallic phases in which impurities such as iron or silicon are bound. In addition, manganese increases tensile strength, improves casting behaviour, and leads to a grain refining effect [2]. Another reason for choosing this alloy is the absence of a low melting eutectic in contrast to aluminium-containing alloys. During extrusion, manganese provides a large process window and

G. Kurz (✉) · M. Nienaber · J. Bohlen · D. Letzig · K. U. Kainer  
Helmholtz-Zentrum Geesthacht – Magnesium Innovation Centre,  
Max-Planck-Straße 1, 21502 Geesthacht, Germany  
e-mail: [gerrit.kurz@hzg.de](mailto:gerrit.kurz@hzg.de)



allows relatively high extrusion speeds [1, 3], which makes this alloy economically interesting.

Typically, rare earth metals are used as cerium mischmetal (approx. 60% cerium, approx. 30% lanthanum, rest neodymium, praseodymium) as alloying additive. Rare earths increase the high-temperature strength and creep resistance [2]. In addition, studies show that the addition of rare earths has increased the activation of non-basal slip systems during the rolling process of binary magnesium alloys, which leads in combination with recrystallisation to a weakening of the basal texture component [4]. The effect of texture weakening of the basal component was also observed in extruded rare earth-containing magnesium alloys [1, 5]. Rolling tests with the alloy ME21 have shown that the mechanical properties do not change significantly depending on the RE content [6].

## Experimental Procedure

The aim of the investigations for the FUMAS project at the MagIC is to show a process window in which the seat back of a car seat after the manufacturing process has a fine-grained, globular, and homogeneous microstructure with corresponding precipitation behaviour. In order to investigate the influence of the extrusion parameters such as billet temperature  $300\text{ °C} \leq T_B \leq 450\text{ °C}$  and extrusion speed  $0.75\text{ mm/s} \leq v_p \leq 7.5\text{ mm/s}$  which was varied, see Table 1. The extrusion speed is in all described trials the ram velocity.

The company TWI, a commercial magnesium supplier, delivered cast feedstock material used for the extrusion trials. All delivered billets were heat-treated to homogenize the microstructure and to reduce the amount of precipitates. The samples for the microstructure and EDX analyses were taken from the two half slices of the billets top. For the extrusion trials, the billets were machined to four smaller billets with 49 mm in diameter and approx. 130 mm in length. The machined billets were pressed on a 2.5 MN extrusion press, built by the company Müller, with an extrusion ratio of 49 : 1 in a direct extrusion process to strips of 20 mm in width and 2 mm in thickness. Graphite was used as lubricant. After the extrusion tests, the influence of the grain size and the heat treatment condition of the starting material on the extrusion behavior, the microstructure, the texture, and the mechanical properties of the extruded flat profiles were

analyzed. In order to guarantee that sample was only taken from sections that experience homogeneous material flow, the first and last 1500 mm of the extrusion profile were not used. To compare the microstructure and texture development along the profile length, 20 mm sections were taken for each sample at the beginning (1500 mm), at the center (3000 mm), and at the end of the resulting strips (4500 mm). For microstructure analysis, standard metallographic sample preparation techniques were applied and an etchant based on picric acid was used to reveal grains and grain boundaries [7]. Texture measurements were done on the strip mid-planes using a Panalytical X-ray diffractometer setup. The pole figures were measured up to a tilt angle of 70° which allowed recalculation of full pole figures based on a MTEX software routine [8]. The (0001) and (10-10) pole figures of the sheets in as rolled and heat-treated condition are used in this work to present the texture of the strips at midplane. The mechanical parameters required 30 cm of the strip and the three dog bone-shaped tensile specimens with a measuring length of 18 mm were separated in the extrusion direction by wire erosion. The mechanical properties of the extruded strips were investigated by tensile tests with a constant initial strain rate of  $1.0 \times 10^{-3}\text{ s}^{-1}$ .

## Characterization of the Feedstock Material

The company TWI provided the ME21 material for the extrusion tests and six continuous cast sections. For chemical composition, see Table 2.

In contrast to typically RE-containing magnesium alloys, no cerium -based mischmetal was used as usual but only cerium and lanthanum. The delivered ME21 billets are characterized by a different macrostructure. Figure 1 shows the macrostructure and microstructure of three representative billets. This ranges from an extremely inhomogeneous coarse-grained structure with large elongated grains with an average grain size of  $10^{-2}\text{ mm}$  to a globular homogeneous fine-grained grain structure with an average grain size of around 2  $\mu\text{m}$ . Because the manufacturer could not provide any process parameters, it can only be assumed that the differences in microstructure are due to varying holding times of the melt (nucleation leads to a finer microstructure) or different cooling rates of the billets (grain growth can be inhibited). A chemical influence on the macrostructure

**Table 1** Process parameter of the extrusion trials

Extrusion temperature, $T_B$ (°C)	Extrusion speed, $v_p$ (mm/s)	Billet condition
450	0,75; 1,4; 2,8; 5,5; 7,5	Heat-treated at 500 °C for 8 h
400	0,75; 1,4; 2,8; 5,5; 7,5	Heat-treated at 500 °C for 8 h
350	0,75; 1,4; 2,8; 5,5; 7,5	Heat-treated at 500 °C for 8 h
300	1,4; 2,8; 5,5; 7,5	Heat-treated at 500 °C for 8 h



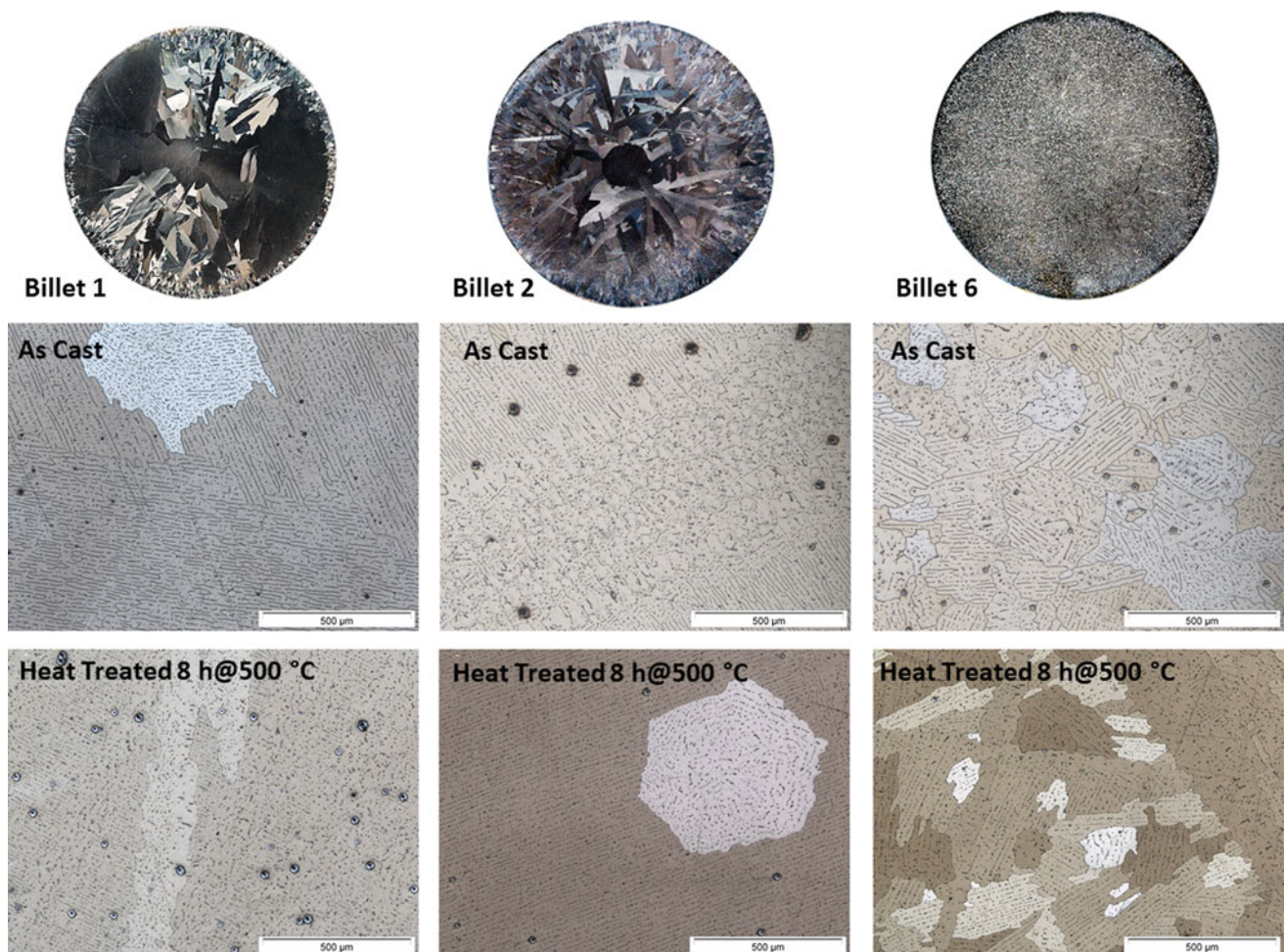
**Table 2** Chemical composition of the billets in wt%

Specimen	Mn	Ce	La	Fe	Cu	Ni
Section 1	1,78	0,549	0,345	0,00389	0,00202	0,00098
Section 2	2,18	0,555	0,360	0,00064	0,00231	0,00103
Section 3	2,07	0,546	0,353	0,00030	0,00229	0,00110
Section 4	1,98	0,587	0,382	0,00150	0,00222	0,00108
Section 5	1,97	0,591	0,384	0,00125	0,00217	0,00113
Section 6	1,81	0,507	0,362	0,00223	0,00208	0,00119

development can be excluded, because all billets have with small tolerance the same chemical composition.

All microstructures are characterized by an inhomogeneous dendritic microstructure because of the multiphase microstructure. Furthermore, all billets have a fine-grained edge zone as a result of the faster solidification at the mould wall. The microstructures also show a very high amount of precipitates, which is due to the low dissolubility of manganese, cerium, and lanthanum in the magnesium solid solution.

The subsequent heat treatment should reduce internal stresses and achieve homogenization or partial solution of the precipitation phases. Figure 1 compares selected areas of the microstructure of three selected billets in the cast and heat-treated condition. The 8-h heat treatment at 500 °C resulted in a partial solution but also a coarsening of the precipitates between the dendrite arms. The coarse Mn precipitates are not evidently dissolved in the microstructure by the heat treatment.

**Fig. 1** Macrostructure and microstructure of three representative billets in as-cast and heat-treated condition

## Influence of the Feedstock Properties

As shown in the previous paragraph, the billets of the starting material have a very different macrostructure. Therefore, it was first examined how the macrostructure affects the extrusion result. To do this, a billet with a diameter of 49 mm was selected from the initial billets 1, 2, and 6 in the cast and heat-treated condition. These billets were extruded at a temperature of 400 °C and a punch speed of 0.75 mm/s. Figure 2 shows the extrusion diagrams and punch pressure versus strip length. All curves show the typical shape for the direct extrusion process. As the profile length increases, the pressing pressure decreases as the friction force decreases as the billet length decreases. The billets in the cast condition show a very inhomogeneous plastic flow and require a higher maximum pressure than the billets in the heat-treated condition (Fig. 2). Because in the as-cast condition the precipitates  $Mg_{12}(Ce, La)$  are mainly located at the grain boundaries (Fig. 1), this could be the reason for the higher pressure. The heat-treated billet could be extruded with a more homogeneous plastic flow and lower punch pressure. It can be assumed that the heat treatment relieves internal stresses and allows the material to flow more easily and homogeneously. Due to the heat treatment, the precipitates are strongly agglomerated and were no longer so dominant located at the grain boundaries (Fig. 1). Figure 2 displays also the microstructures of the extruded strips. It can be clearly seen that the differences in

the microstructure of the three strips extruded out of the heat-treated billets are marginal. In the microstructure of all three strips, it can be observed that the material has a homogeneous microstructure. Globular bimodal grain structures are clearly visible here. In some cases, it also has grains that are longitudinally stretched along the extrusion direction. The average grain size of the three extruded profiles varies between 5.9 and 6.5  $\mu m$ . The precipitates also lie horizontally in the microstructure. Very large precipitates are visible, which are probably the (Mn) particles detected in the casting material. As a result, in the heat-treated condition, the macrostructure and the grain size have no significant influence on the extrusion result. So, it has been demonstrated that heat treatment can significantly improve extrusion performance.

## Influence of the Extrusion Temperature and Speed on Microstructure

In order to investigate the influence of process parameters speed and temperature extrusion trials with in Table 1 listed parameters have been performed. At 350 °C and a punch speed of 0.75 mm/s, a process limit has been reached, because the material flows inhomogeneous. Consequently, in the extrusion tests at 300 °C, the test with a punch speed of 0.75 mm/s was not carried out. An inhomogeneous material flow was also observed at 300 °C and 1.4 mm/s, but

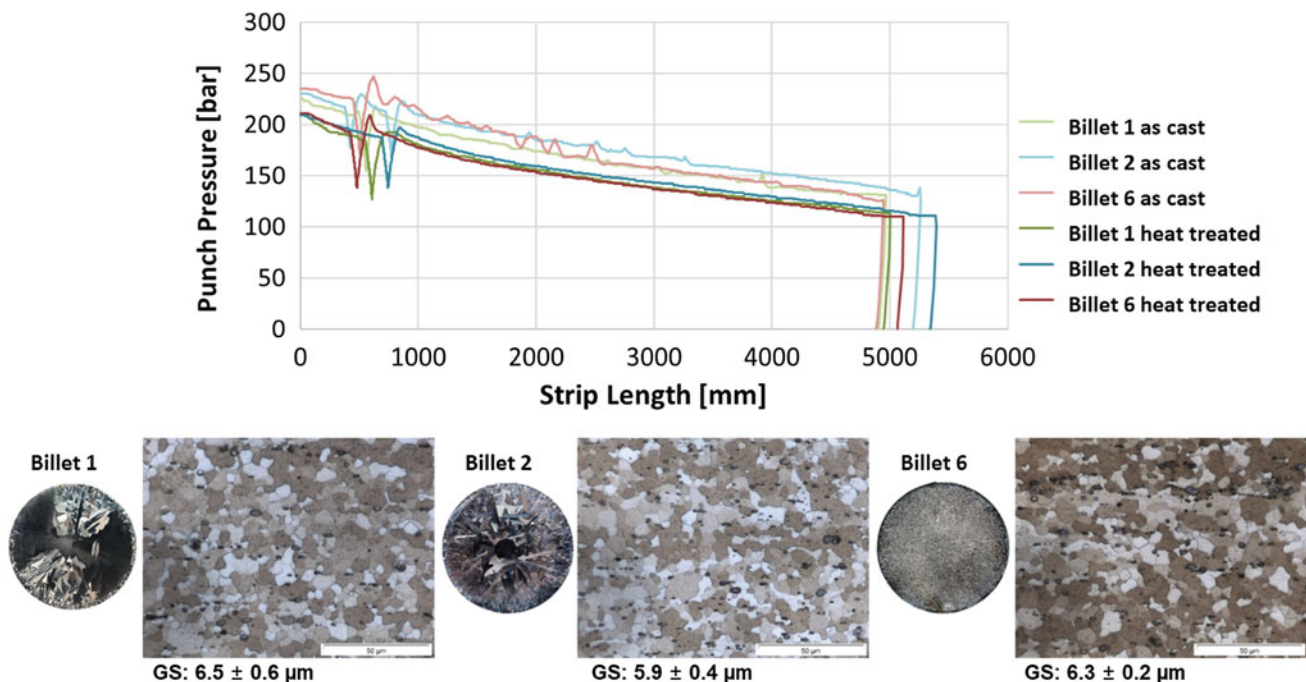


**Fig. 2** Extrusion diagrams of billet 1, 2, and 6 pressed at a temperature of 400 °C and a punch speed of 0.75 mm/s and the resulting microstructure of the extruded strips



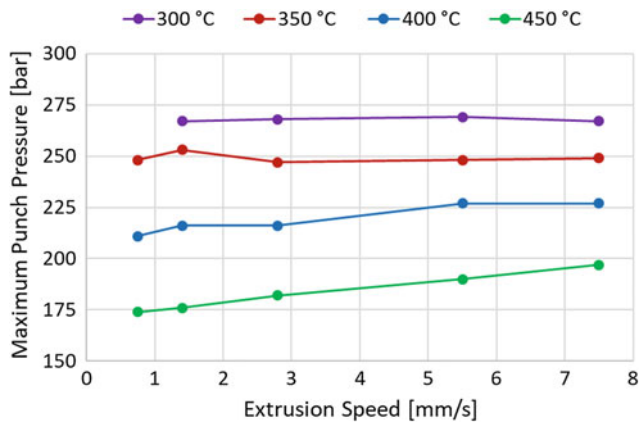


**Fig. 3** Maximum punch pressure versus extrusion speed of all extrusion trials of ME21

this inhomogeneous flow was not as pronounced as at 350 °C and 0.75 mm/s. For all trials, the punch pressure versus strip length was recorded. All extrusion diagrams show the typical curves mentioned above for direct extrusion. Figure 3 shows the maximum punch pressures as a function of the punch speed. The punch pressure drops with rising temperature, because the strength of the magnesium alloy ME21 decreases with higher temperature. The maximum punch pressure increases again with increasing punch speeds.

The microstructures shown in Fig. 4 were taken in the middle (300 cm) of the profiles, because the microstructures do not show any significant differences depending on the position where they were taken. The average grain size was determined by the line intersection method on three polarized images at 1000x magnification. To demonstrate the tendency of all results, only the results of the extruded profiles at 350 and 450 °C are presented in the following. Figure 4 shows the microstructures for the process temperatures of 350 and 450 °C as a function of the punch speed. After extrusion, all profiles extruded have a fine-grained completely recrystallized structure. The only exception is the microstructure of the strip extruded at 350 °C at the slowest speed of 0.75 mm/s; here is the microstructure only partly recrystallized. As a reason for this, it can be assumed that the temperature of 350 °C and the forming energy introduced at the extrusion speed of 0.75 mm/s do not allow dynamic recrystallization processes to take place completely. Depending on the extrusion speed, a clear influence of the billet temperature on the grain growth can be seen. In general, it can be observed that grain growth can be observed with increasing temperature. All microstructures exhibit a high density of precipitates, which are predominantly distributed horizontally in the direction of extrusion.

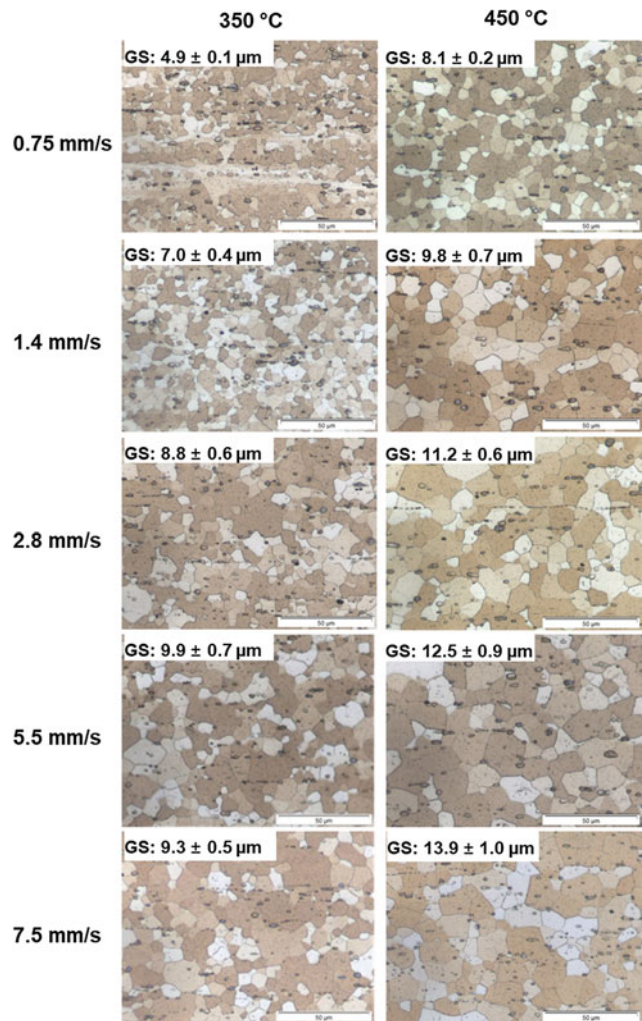


**Fig. 4** Microstructures of the ME21 strips extruded at 350 and 450 °C

The microstructure develops, depending on the extrusion parameters, temperature, and speed, from partially recrystallized to fine-grained to bimodal and finally to a coarse-grained microstructure. Despite the wide process window, the mean grain size varied only from 4 µm (300 °C and 1.4 mm/s) to 14 µm (450 °C and 7.5 mm/s). As already mentioned, the strongly suppressed grain growth can be attributed to the alloying of rare earths. Due to the rare earths, the grain boundary mobility is changed and restricted and consequently the grains can only grow to a limited extent [9]. The higher the applied deformation (low extrusion temperature and speed), the smaller the grain size. Because the energy is lowest at low temperature and speed, the dynamic recrystallization during the extrusion process and the static recrystallization during the cooling process can only take place to a limited extent. Due to the crystal structure, certain grain fractions can grow better, which leads to the formation of the bimodal microstructure.

## Influence of the Extrusion Temperature and Speed on Texture

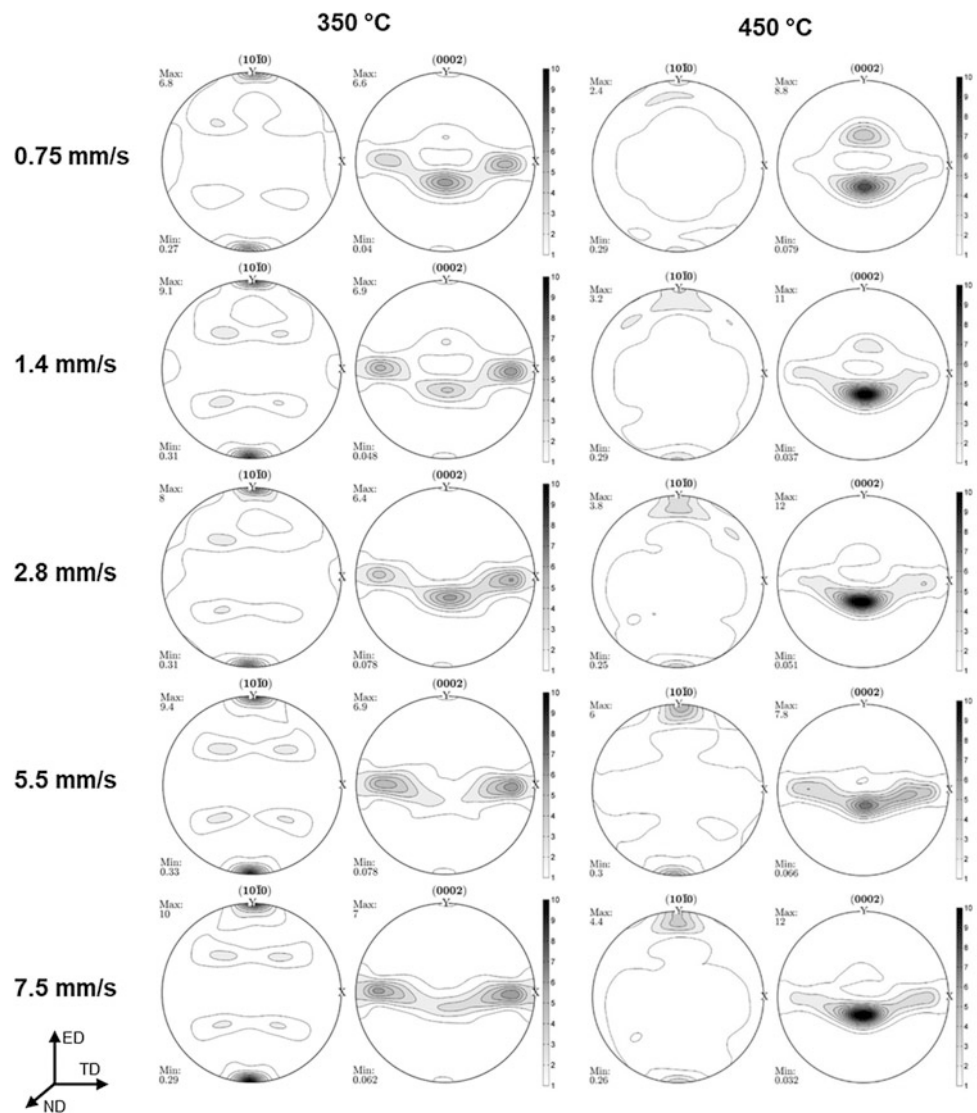
Figure 5 displays the (10-10) and (0002) pole figures of the profiles extruded at 450 and 350 °C. The extrusion tests carried out at 450 °C in Fig. 6 all show a very similar texture. Only the maximum pole figures' intensities vary. Basically, the pole figures show a strong basal (0002) component, which is tilted by approx. 25–30° from the normal plane into the opposite extrusion direction. As the extrusion speed increases, the maximum pole figure intensity increases from 8.8 to 12 m.r.d.

With increasing extrusion speed also a widening of the {11-20} <10-10> by 30° from transverse to normal direction tilted component is recognizable. This component correlates with the maximum intensity in the (10-10) pole figure. Here, the maximum intensity increases from 2.4 to

4.4 m.r.d. All textures show (10-10) fiber components in extrusion direction, which become more pronounced or rather more complete with increasing extrusion speed.

Figure 6 also shows the textures for the extrusion tests at 350 °C. In the maximum intensities of the (0002) pole figures, there is no significant influence of the punch speed. It fluctuates between 6.4 and 7.0 m.r.d. It is concise that from an extrusion speed of 5.5 mm/s no {0001} <10-10> component deflected by 25° in the transverse direction is visible. All textures show a <10-10> extrusion direction fiber; in addition, a component is tilted by 30° from transverse in normal direction with varying intensity {11-20} <10-10>. The maximum intensity of this component, i.e., the (10-10) pole figure, increases from 6.8 to 10.0 m.r.d. as the extrusion speed increases. In ME20 sheets [10] and extruded ME21 thin strips [11], which have a very similar alloy composition to the ME21 alloy used in this paper, textures were measured

**Fig. 5** Textures of the ME21 strips extruded at 350 and 450 °C



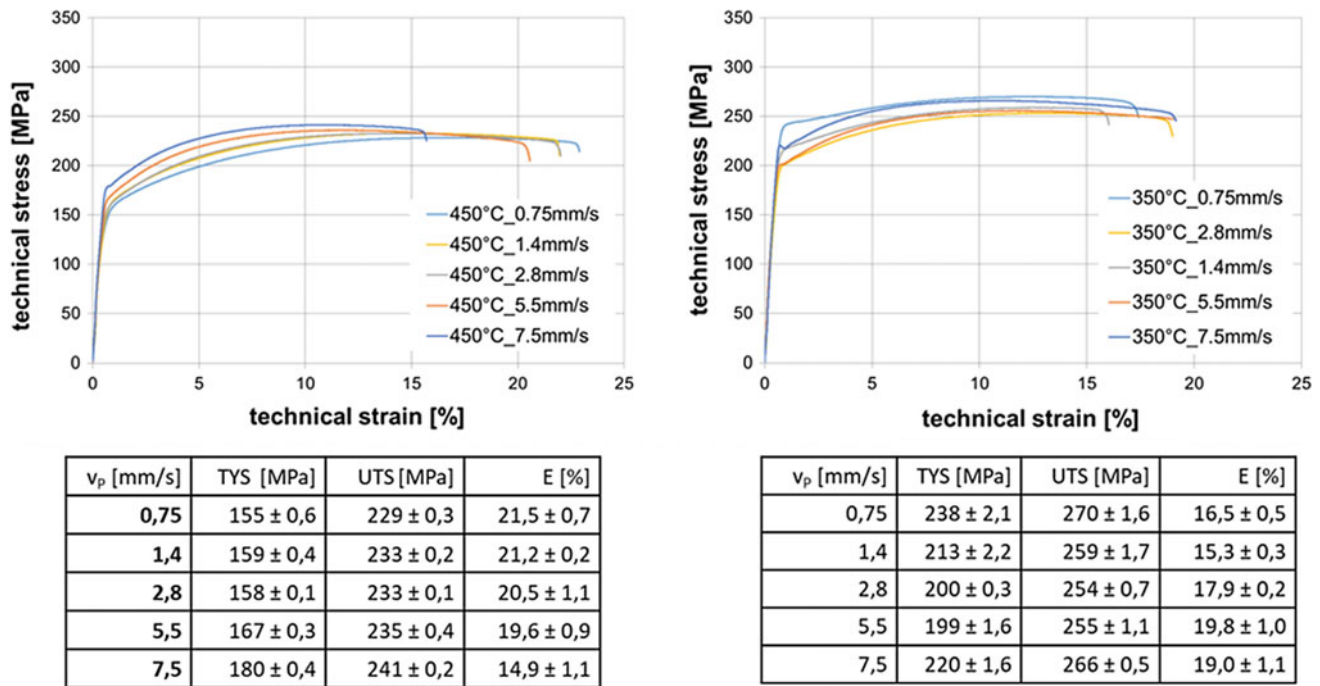


**Fig. 6** Stress–strain diagrams of the ME21 strips extruded at 450 and 350 °C and the values of tensile yield stress (TYS), the ultimate tensile stress (UTS), and fracture strain (E)

which also have a strongly pronounced  $\{0001\} \langle 10\text{-}10 \rangle$  component of similar shape tilted by  $25^\circ$  in rolling/extrusion direction. The three slip systems  $\langle a \rangle$  basal,  $\langle a \rangle$  prismatic, and  $\langle c+a \rangle$  pyramidal and the twin systems are necessary for the initiation of deformation in polycrystalline materials.

An additional reason for the formation of this texture component may be the different influence of dynamic recrystallization on grain growth in rare earth-containing magnesium alloys.

### Influence of the Extrusion Temperature and Speed on Mechanical Properties

The stress–strain diagrams obtained from the tensile tests performed at room temperature are exemplary shown for the strips extruded at 450 and 350 °C in Fig. 6. The averaged values of the measured variables and their standard deviation are shown in Fig. 6. Depending on the temperature, various tendencies can be observed as to how the mechanical properties change as the grain size increases. At 450 °C, an increase in the process speed, resulting in a coarsening of the grains, a decrease in elongation at break from 21.5 to 14.9%, an increase in yield strength by 25 MPa to 180 MPa, and an increase in strength by 13 MPa to 241 MPa are shown.

In contrast to the mechanical properties of the strips extruded at 450 °C, the mechanical properties resulting from

the at 350 °C extruded strips have no tendency in the measured values depending on the extrusion parameters. It is noteworthy that at a punch speed of 0.75 mm/s the curve has only a slightly pronounced convex slope. At the moderate punch speeds (1.4–5.5 mm/s), the maximum strength varies between 253 and 259 MPa and the tensile yield stress between 212 and 200 MPa. The elongation increases by 5% to almost 20%. A higher yield strength (220 MPa) and strength (265 MPa) are observed by the test at 7.5 mm/s.

Compared to mechanical properties of the at 450 °C extruded strips, the results of the strips extruded at 350 °C suggest that grain size is not always the dominant factor in plastic deformation. Also the texture, i.e., the inclination of the  $c$ -axis, correlates with the possibility of plastic deformation. At 450 °C the dominant texture component is the  $\{0001\} \langle 10\text{-}10 \rangle$  component tilted  $25^\circ$  in the extrusion direction. When applying a load in the extrusion direction, basal  $\langle a \rangle$  sliding systems can be activated very easily. The background is Schmid's shear stress law, which describes the critical shear stress required to move the dislocations on the most densely packed planes. In the optimum case, the planes are below  $45^\circ$  to the load direction. An explicit alignment of the preferred orientation along the load direction, i.e., a high maximum intensity of the  $\{0001\} \langle 10\text{-}10 \rangle$  by  $25^\circ$  in extrusion direction, increasingly favors the deformation process and results in low strength or high elongation at fracture along the alignment [12].



## Summary

The results of the extrusion trials for the FUMAS project reveal that the process parameters temperature and speed have not a very significant influence on the resulting ME21 strip properties. Heat treatment of the billets prior to extrusion greatly improves extrusion performance. Because of this reason, in the heat-treated condition, the macrostructure and the grain size have no significant influence on the extrusion result. There is a temperature and a partial speed influence on the flow behaviour and the maximum pressing pressures during extrusion. The variation of the process parameters in the investigated process window indicates a small influence on the grain size (5–14  $\mu\text{m}$ ) and no detectable influence on the morphology of the precipitates. Partial grain growth leads to a bimodal structure with increasing temperature and/or speed. With regard to the resulting texture, changes can be observed as a function of temperature. At higher temperatures, a strongly pronounced  $\{0001\} \langle 10\text{-}10 \rangle$  component appears, which is tilted by  $25^\circ$  in extrusion direction; at lower temperatures, the texture dominates a  $\{11\text{-}20\} \langle 10\text{-}10 \rangle$  component, which is tilted by  $30^\circ$  from transverse in normal direction. In general, the maximum intensity of the texture increases with increasing speed.

Looking at the mechanical properties of all strips, it can be seen that despite the large process window, the variation in properties is relatively small. It is also remarkable that the yield strength and tensile strength are lowest at  $450^\circ\text{C}$  and  $0.75\text{ mm/s}$  with  $\text{YTS} = 154\text{ MPa}$  and  $\text{UTS} = 228\text{ MPa}$  and highest at  $300^\circ\text{C}$  and  $1.4\text{ mm/s}$  with  $\text{YTS} = 221\text{ MPa}$  and  $\text{UTS} = 266\text{ MPa}$ . Consequently, the colder the extrusion temperature, the higher the strength of the profile and the lower the ductility. The results make clear the extrusion process of ME21 is very robust and parameter variation has only a small influence on the resulting material properties. This behavior is very beneficial for the production of the seat back, because the process control is variable.

**Acknowledgements** The German Federal Ministry of Economics and Energy (BMWi) fund the project “Function-integrated Magnesium Lightweight Construction for Car Seat Structures (FUMAS)”. We also want to thank the company TWI for supplying the feedstock material.

## References

- Huppmann M, Gall S, Müller S et al. (2010) Changes of the texture and the mechanical properties of the extruded Mg alloy ME21 as a function of the process parameters. *Materials Science and Engineering: A* 528:342–354
- Kammer C (2000) *Magnesium-Taschenbuch. Aluminium-Zentrale Düsseldorf*, Düsseldorf
- Illkova K, Dobroň P, Chmelík F et al. (2014) Effect of aluminium and calcium on the microstructure, texture, plastic deformation and related acoustic emission of extruded magnesium–manganese alloys. *Journal of Alloys and Compounds* 617:253–264
- Pekguleryuz MO (2012) Current developments in wrought magnesium alloys. 3–62
- Robson JD, Twier AM, Lorimer GW et al. (2011) Effect of extrusion conditions on microstructure, texture, and yield asymmetry in Mg–6Y–7Gd–0.5 wt%Zr alloy. *Materials Science and Engineering: A* 528:7247–7256
- Kurz G, Petersen T, Bohlen J et al. (2017) Variation of rare earth elements in the magnesium alloy ME21 for the sheet production. In: *Minerals, Metals and Materials Series*. p 353–363
- Kree V, Bohlen J, Letzig D et al. (2004) The metallographical examination of magnesium alloys. *Praktische Metallographie/ Practical Metallography* 41:233–246
- Bachmann F, Hielscher R, Schaeben H (2010) Texture Analysis with MTEX – Free and Open Source Software Toolbox. *Solid State Phenomena* 160:63–68
- Stanford N (2010) Micro-alloying Mg with Y, Ce, Gd and La for texture modification—A comparative study. *Materials Science and Engineering: A* 527:2669–2677
- Li X, Al-Samman T, Gottstein G (2011) Microstructure development and texture evolution of ME20 sheets processed by accumulative roll bonding. *Materials Letters* 65:1907–1910
- Bohlen J, Cano G, Drozdenko D et al. (2018) Processing Effects on the Formability of Magnesium Alloy Sheets. *Metals* 8:147
- Gehrmann R, Frommert MM, Gottstein G (2005) Texture effects on plastic deformation of magnesium. *Materials Science and Engineering: A* 395:338–349

# Asymmetric Rolling of TZ73 Magnesium Alloy to Improve Its Ductility

Krishna Kamlesh Verma, Satyam Suwas, and Subodh Kumar

## Abstract

Asymmetric rolling, i.e., upper and lower rolls having different circumferential speeds, is a novel technique to improve the ductility of Mg alloys. A newly developed TZ73 Mg alloy was squeeze cast, homogenized at 300 °C for 24 h, rolled at 350 °C by symmetric and asymmetric rolling, and annealed at 215 °C for 30 min. The microstructure was characterized by X-ray diffraction, scanning electron microscope equipped with energy-dispersive X-ray spectroscopy and electron backscattered diffraction. A weakening of basal texture with a concomitant increase in ductility was observed for asymmetrically rolled sheet while retaining the same strength as in symmetrically rolled sheet. Thus, tensile properties of 0.2% PS = 290 MPa, UTS = 332 MPa and El = 13% in hot rolled, and 0.2% PS = 182 MPa, UTS = 282 MPa and El = 21% in annealed condition were obtained for asymmetrically rolled sheet, which are extremely good for a rolled Mg alloy sheet.

## Keywords

Mg alloys • Asymmetric rolling • Microstructure • Crystallographic texture • Tensile properties

## Introduction

Mg-based alloys find wide applications in the automobile, aerospace, and electronics industries due to its low density, high specific strength, excellent machinability, and

K. K. Verma · S. Suwas · S. Kumar (✉)  
Department of Materials Engineering,  
Indian Institute of Science, Bangalore, 560012, India  
e-mail: [skumar@iisc.ac.in](mailto:skumar@iisc.ac.in)

K. K. Verma  
e-mail: [krishnakamlesh.iisc14@gmail.com](mailto:krishnakamlesh.iisc14@gmail.com)

S. Suwas  
e-mail: [satyamsuwas@iisc.ac.in](mailto:satyamsuwas@iisc.ac.in)

castability. The lightest structural Mg-based alloys reduce the greenhouse effect and enhance fuel efficiency [1–3]. However, Mg-based alloys in wrought processing conditions find limited applications due to its poor strength and limited formability at room temperature because of its hexagonal closed packed (HCP) crystal structure [4]. According to von Mises criterion, minimum five independent slip systems are required for the uniform plastic deformation of a polycrystalline material. For Mg, at room temperature deformation, basal (0001) <11 $\bar{2}$ 0> slip system dominates, which has minimum critical resolved shear stress (CRSS) value. The basal slip system has only two independent slip systems, which causes limited formability [5, 6].

For the development of high-strength and cost-effective Mg-based alloys, Mg–Sn alloy system has received attention as a promising candidate in the cast and wrought processing conditions. In Mg–Sn binary alloy system, the Mg<sub>2</sub>Sn intermetallic phase has a high melting temperature (770 °C), which is comparable to precipitates formed in Mg–RE-based alloys. The growth of dynamically recrystallized grains can be suppressed by effective grain boundary pinning by the fine Mg<sub>2</sub>Sn particles [7–9]. The presence of dynamically precipitated Mg<sub>2</sub>Sn particles at the grain boundary as well as within the grains leads to excellent tensile properties at room temperature. The strength of Mg–Sn-based alloys is enhanced with increasing Sn content but deteriorates its ductility due to the formation of a semi-continuous type of network at the grain boundary by the Mg<sub>2</sub>Sn phase. Liu et al. [8] reported that the optimum addition of the Sn in Mg–Sn-based alloys system is 5–7 wt.%. It is reported that Zn in solid solution improves strength and ductility for the Mg–Sn-based alloys [7, 9]. Therefore, for the present study, Zn was added as the third alloying element.

A strong basal texture is developed during the rolling process, which diminishes its ductility and formability [10, 11]. The weakening of basal texture leads to improvement in ductility and formability at room temperature. It has been reported that the introduction of shear stresses during deformation could lead to the modification of the

crystallographic texture in the rolled sheet [12, 13]. The asymmetric rolling (ASR) process is an effective method to improve ductility and formability of Mg-based alloys by introducing shear stresses and weakening the basal texture [14]. In the ASR process, the circumferential speeds of the upper and lower rollers are different, so the shear deformation is applied throughout the thickness of the sheet [15, 16]. In the present study, the homogenized TZ73 alloy is subjected to ASR and conventional symmetric rolling (SR) at 350 °C. For the ASR process, the circumferential speeds of the upper and lower rollers are selected as 0.03 m s<sup>-1</sup> and 0.15 m.s<sup>-1</sup> (speed ratio 1 : 5), respectively. For the SR process, the circumferential speed of both the rollers is 0.09 m s<sup>-1</sup> (speed ratio 1 : 1). The hot rolled sheets are annealed at 215 °C for 30 min. The rolled sheets are investigated in two conditions: (i) hot rolled (HR) and (ii) hot rolled and annealed (HRA). The microstructure, texture, and tensile behaviour are studied for ASR and SR processed sheets.

## Experimental Details

Commercially pure Mg (>99.80 wt.%), Sn (>99.97 wt.%), and Zn (>99.98 wt.%) ingots were charged into a graphite crucible and melted at 720 °C in a resistance pit furnace. The complete melting and casting were carried out under a protective argon gas atmosphere. Squeeze casting was adopted as the casting technique to refine the as-cast microstructure, in which the hot metal was poured into the preheated (200 °C) cylindrical die (Ø75 × 75 mm<sup>2</sup>) and a pressure of 100 MPa was applied till the completion of solidification. The obtained alloy composition was determined to be Mg–6.9Sn–2.6Zn and designated as TZ73 according to ASTM standard nomenclature. The plates of dimensions 10 × 30 × 50 mm<sup>3</sup> were machined from the cylindrical cast ingot for hot rolling. Prior to hot rolling, the as-cast plates were homogenized at 300 °C for 24 h (hereafter the homogenized samples will be designated as H300) and hot rolled at 350 °C to 1-mm-thick sheets. The thickness reduction of 80% was achieved in multiple passes. The hot rolled sheets were investigated in two conditions: (i) hot rolled (HR) and (ii) hot rolled and annealed (HRA). The flat tensile specimens of the dimension 10 × 2 × 1 mm<sup>3</sup> were machined via electron discharge machine (EDM) with the gauge length parallel to the rolling direction (RD), and tested on an INSTRON-5967 machine at room temperature and 1 × 10<sup>-3</sup> s<sup>-1</sup> strain rate. The standard metallographic techniques were adopted for microstructural analysis. The polished specimens were etched for 5 s using acetic-picric (1.5 g picric acid, 1.2 ml acetic acid, 2.5 ml distilled water, and 25 ml ethanol). The microstructure was examined under

a scanning electron microscope (FEI-ESEM Quanta 200) and electron probe micro-analyser (EPMA-JEOL-JXA-8530F) equipped with energy-dispersive X-ray spectroscopy (EDS) and wavelength dispersive X-ray spectroscopy (WDS). X'Pert Pro PANalytical diffractometer using CuK<sub>α</sub> radiation (λ = 0.154 nm) was used to identify the different phases present in the alloy. For the detailed microstructural and microtexture investigation, electron backscatter diffraction (EBSD) scan was recorded using advanced focused ion beam system (HELIOS G4 UX).

## Results and Discussion

### Phase Analysis and Microstructural Characterization

The XRD patterns for H300, SR, and ASR samples in HR condition are shown in Fig. 1. It reveals the presence of Mg and Mg<sub>2</sub>Sn phases in the TZ73 alloy. The highest peak intensity of Mg for the H300 sample was observed for pyramidal (10 $\bar{1}$ 1) planes, whereas, for SR and ASR samples, the highest peak intensity for Mg was observed for basal (0002) planes. Thus, the alloy gets textured after rolling; i.e., the basal plane normals are preferentially oriented perpendicular to rolling direction (RD).

Figure 2 represents the SEM micrographs for H300, SR, and ASR samples. Figure 2a shows that the H300 microstructure primarily consists of cells, with dendritic features at a few places, and Mg<sub>2</sub>Sn particles along the cell boundaries. Figure 2b shows that Mg<sub>2</sub>Sn particles get fragmented and aligned along RD for the SR sample. However, for the ASR sample, the shear stresses were introduced during deformation, which changes the material flow direction and alignment direction of Mg<sub>2</sub>Sn particles (Fig. 2c).

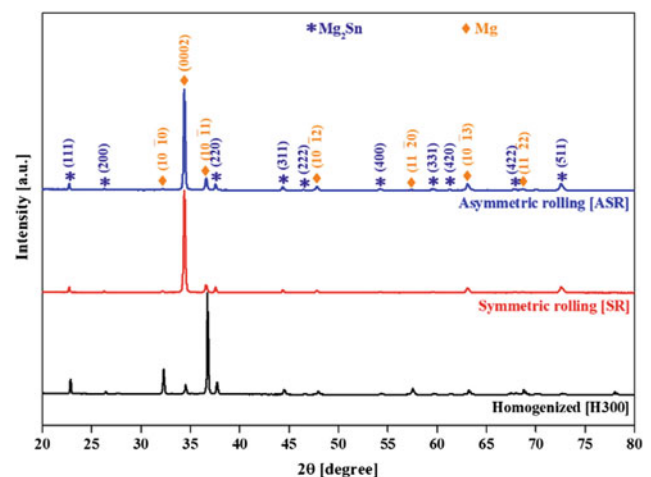
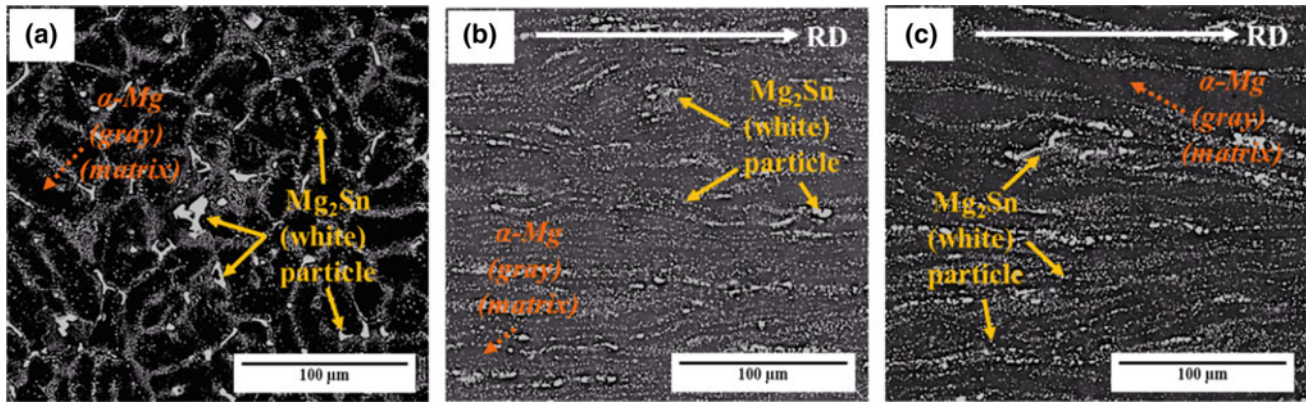


Fig. 1 X-ray diffraction pattern of TZ73 alloy



**Fig. 2** Backscattered scanning electron (SEM-BSE) micrographs **a** H300, **b** SR, and **c** ASR samples in HR condition

The distributed fine  $Mg_2Sn$  particles act as a nucleating site as well as a barrier to suppress the growth of the dynamically recrystallized (DRX) grains [17, 18]. The intense plastic strain was imposed on the entire sample during ASR deformation. An equation for the strain ( $\varepsilon$ ) imposed by ASR is proposed as follows [19]:

$$\varepsilon = \frac{2}{\sqrt{3}} \sqrt{\left[ 1 + \left\{ \frac{(1-r)^2}{r(2-r)} \tan(\theta) \right\}^2 \right]} \ln\left(\frac{1}{1-r}\right) \quad (1)$$

$$r = 1 - \left(\frac{T_f}{T_i}\right) \quad (2)$$

where  $T_i$  and  $T_f$  are the initial and final thicknesses of the sample before and after rolling and angle  $\theta$  is the apparent shear angle ( $\theta = 69^\circ$ ) caused by ASR. For the conventional SR, a true strain of 1.61 has been evaluated on the rolled sheet. However, for the ASR, in addition to the true strain, a shear strain of 1.86 is also imposed on the ASR sheet. The concomitant high shear stress significantly affects the texture and consequently tensile properties.

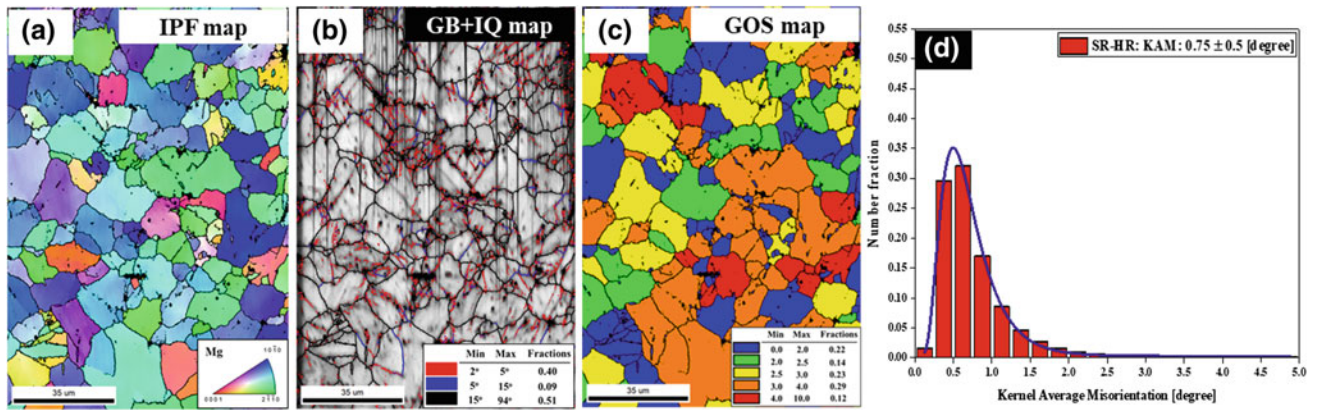
### Microstructural Characterization by EBSD

Figures 3 and 4 illustrate the EBSD maps for the SR and ASR processes in HR condition. The EBSD scan was carried out on the cross section (TD plane) of the rolled sheet. Figures 3a and 4a show the inverse pole figure (IPF) maps for SR and ASR processes. The IPF maps represent the orientation of the grains with respect to the sample frame of reference. Figures 3b and 4b represent grain boundary (GB) maps superimposed on the image quality (IQ) maps for SR and ASR processes. The low-angle grain boundaries (LAGBs) and high-angle grain boundaries (HAGBs) were calculated from the GB + IQ maps. Figures 3c and 4c show

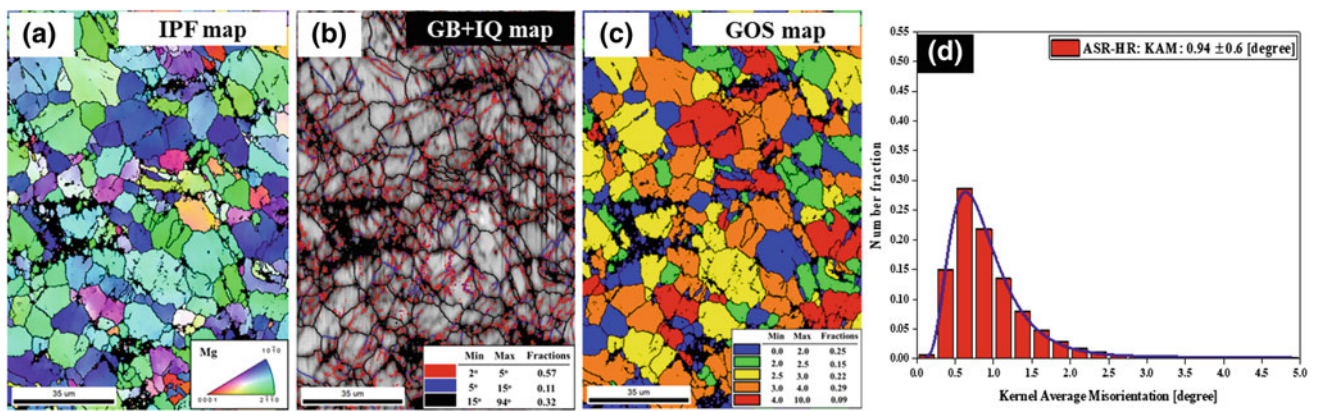
the grain orientation spread (GOS) maps for SR and ASR processes. The GOS maps represent the distribution of recrystallized and deformed grains. The fraction of dynamically recrystallized (DRX) and deformed grains were evaluated from the GOS maps. In order to ascertain the partitioning between recrystallized and deformed grains, three considerations were taken into account: (i) The DRX grains should be equiaxed with aspect ratio close to 1, while the deformed grains should be elongated with a high aspect ratio, (ii) the deformed grains should possess a high fraction of LAGBs and the recrystallized grains should have a low fraction of LAGBs, and (iii) in the texture criteria, the DRX grain in the hexagonal crystal is rotated by  $\sim 30^\circ$  around  $\langle 0001 \rangle$  with respect to the deformed grain [20, 21]. Therefore, the texture obtained from the partitioned DRX grains should show maximum  $\sim 30^\circ$  rotation and spread in pole figure (PF) and orientation distribution function (ODF), respectively. For the recrystallized grain and deformed grain fraction, the misorientation of  $\leq 2.5^\circ$  and  $> 2.5^\circ$  has been considered for recrystallized and deformed grains, respectively, and Figs. 3d and 4d represent the kernel average misorientation (KAM) plots for SR and ASR processes. The KAM value represents the local variation in misorientation. The average misorientation between a point in the scan and the average misorientation value is assigned as the KAM value. The number fraction is plotted as a function of the KAM values, and the overall KAM value is reported in Table 1. Figures 5 and 6 represent the IPF, GB + IQ, GOS, and KAM maps for the SR and ASR processes in HRA condition.

Table 1 shows all the values derived from EBSD scans for SR and ASR processes in HR and HRA conditions. It is observed that in the HR condition, the ASR process yields slightly finer grains, a higher fraction of LAGBs, almost the same fraction of DRX grains, and a higher KAM value, as compared to the SR process. After annealing treatment, the average grain size is reduced, fraction of HAGBs is





**Fig. 3** EBSD maps for SR in HR condition **a** IPF map, **b** IQ map, **c** GOS map, and **d** KAM plot



**Fig. 4** EBSD maps for ASR in HR condition **a** IPF map, **b** IQ map, **c** GOS map, and **d** KAM plot

**Table 1** Comparison between SR and ASR processes in HR and HRA conditions

Processing conditions	Processing conditions			
	SR-HR	ASR-HR	SR-HRA	ASR-HRA
Grain size ( $\mu\text{m}$ )	13.9	11.2	11.9	10.5
LAGBs (%)	49	68	26	20
HAGBs (%)	51	32	74	80
Recrystallized grain (%)	36	40	88	91
KAM	0.76°	0.94°	0.58°	0.57°

increased, fraction of recrystallized grains is increased, and KAM value is decreased, for both the SR and ASR processes. Thus, the difference in all the values between SR and ASR processes is reduced in HRA condition.

For the ASR process, in addition to the true strain, a shear strain of 1.86 is also imposed. Due to higher shear strain introduced during ASR, the higher strain gradient, hence higher KAM value is obtained as compared to SR process in HR condition. In addition to that, the fine  $\text{Mg}_2\text{Sn}$  particles near grain boundaries, which act as a nucleating site and a barrier to suppress the growth of DRX grains, promote the formation of fine recrystallized grains [22]. This leads to

finer grain size in ASR as compared to SR process in HR condition. It has been reported that the deformed grains should possess a high fraction of LAGBs and the recrystallized grains should have a low fraction of LAGBs [21]. Therefore, ASR exhibits higher fraction of LAGBs as compared to SR process in HR condition. After annealing at 215 °C, the strain gradient is reduced, which results in recrystallization of the deformed microstructure. The new fine recrystallized grains formed after annealing treatment lead to further refinement in grain size for both the SR and ASR processes. The KAM values for both the SR and ASR processes are reduced on annealing as strained regions are



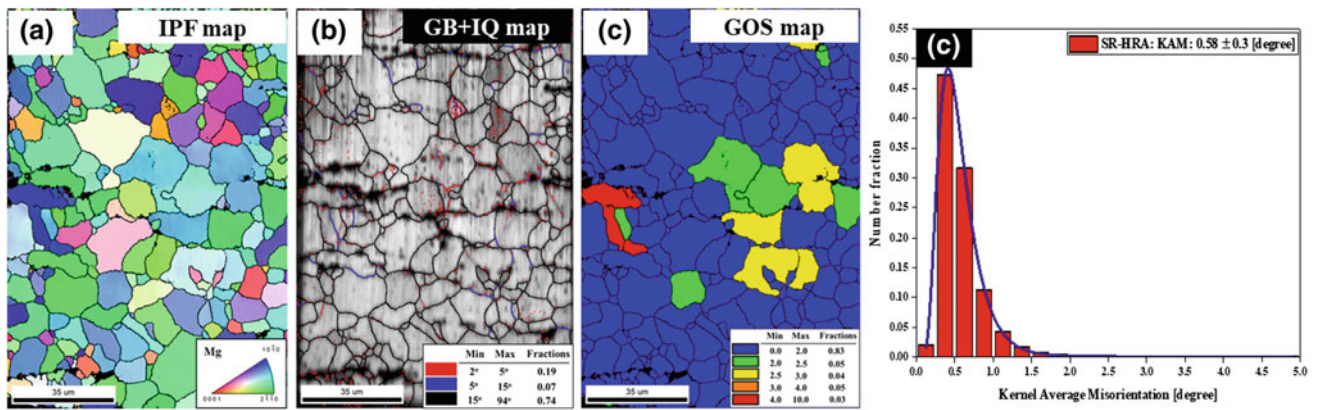


**Fig. 5** EBSD maps for SR in HRA condition **a** IPF map, **b** IQ map, **c** GOS map, and **d** KAM plot

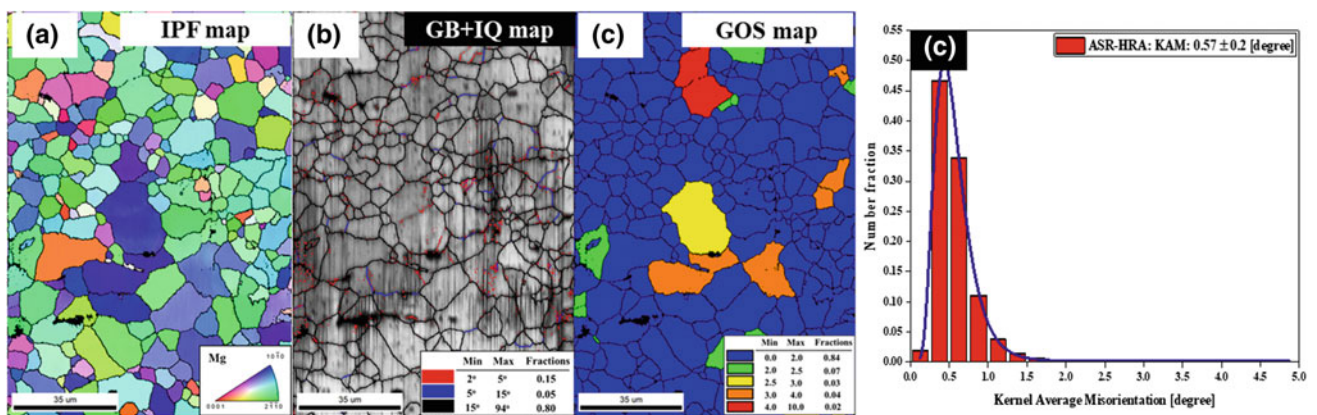


**Fig. 6** EBSD maps for ASR in HRA condition **a** IPF map, **b** IQ map, **c** GOS map, and **d** KAM plot

converted into recrystallized grains and LAGBs are converted into HAGBs.

### Crystallographic Texture Evolution

Figure 7a, e and b, f illustrate the basal (0002) and prismatic (10 $\bar{1}$ 0) pole figures (PFs) for SR and ASR processes, respectively, in HR condition. It is observed that both the processes result in basal texture after hot rolling. For the SR sample, the maximum basal pole intensity is calculated to be 18.8 (Fig. 7a). Along with {0001} <11 $\bar{2}$ 0> an additional {0001} <10 $\bar{1}$ 0> texture component is observed in (10 $\bar{1}$ 0) PF (Fig. 7b). However, for the ASR sample, the maximum basal texture intensity is reduced to 12.6 (Fig. 7e). The intensity of {0001} <11 $\bar{2}$ 0> and {0001} <10 $\bar{1}$ 0> texture components is also reduced in ASR (Fig. 7f) as compared to SR process. The basal pole intensity spread  $\sim 30^\circ$  is similar for both the SR and ASR processes, which exhibit a similar fraction of DRX grains in HR condition. Figure 7c, d and g, h show the  $\varphi_2 = 0^\circ$  and  $30^\circ$  sections of the ODFs for

SR and ASR processes, respectively, in HR condition. The presence of a continuous basal fiber is clearly visible in the ODF sections with maxima at the location of texture components {0001} <11 $\bar{2}$ 0> and {0001} <10 $\bar{1}$ 0> for the SR and ASR processes. However, the intensity is reduced for ASR as compared to the SR process. The spreading of basal fiber towards  $\phi$  angle  $\sim 30^\circ$  is similar for both the SR and ASR processes.

Figure 8a, e and b, f show the (0002) and (10 $\bar{1}$ 0) PFs for SR and ASR processes, respectively, in HRA condition. It is observed that the basal texture intensity is further reduced on annealing treatment. The maximum basal texture intensity is reduced to 16.5 for SR (Fig. 8a) and 9.2 for ASR process (Fig. 8e). Thus, the maximum basal texture intensity remains lower for ASR process in HRA condition as well. Additionally, {0001} <11 $\bar{2}$ 0> and {0001} <10 $\bar{1}$ 0> texture components are observed in (10 $\bar{1}$ 0) PFs with a lower intensity for ASR as compared to SR process in HRA condition (Fig. 8b, f). Figure 8c, d and g, h represent the  $\varphi_2 = 0^\circ$  and  $30^\circ$  ODFs sections for SR and ASR processes, respectively, in HRA condition. It is observed that the ASR

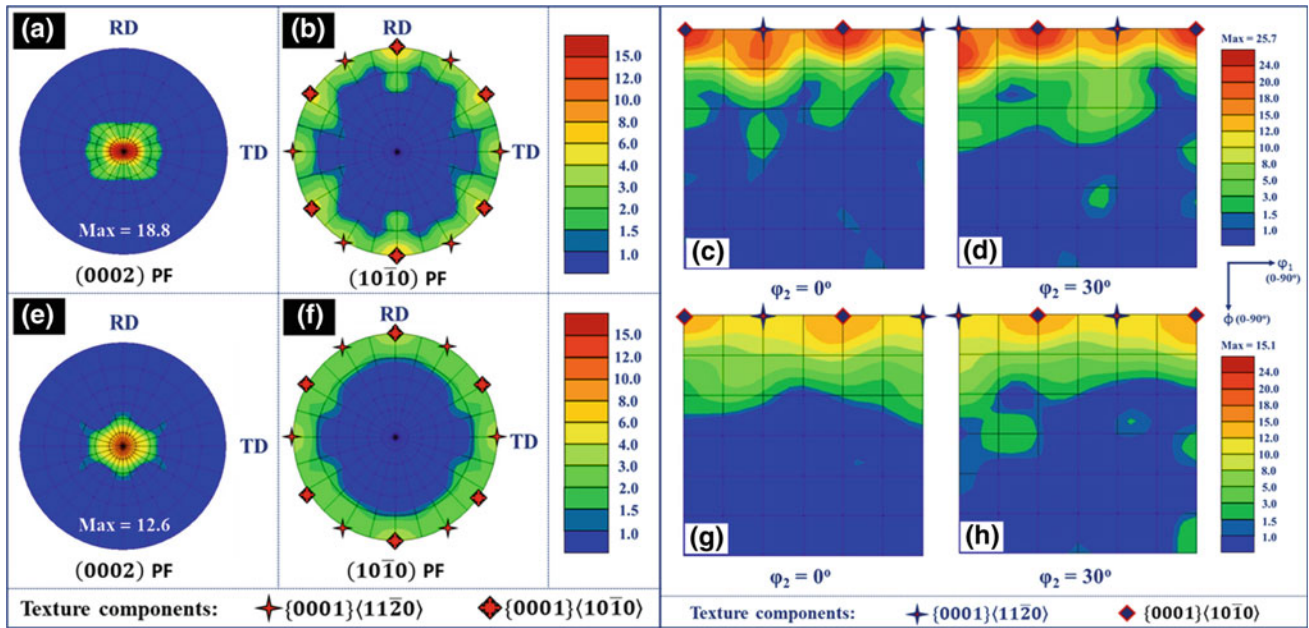


Fig. 7 PFs and ODFs for a–d SR and e–h ASR processes in HR condition

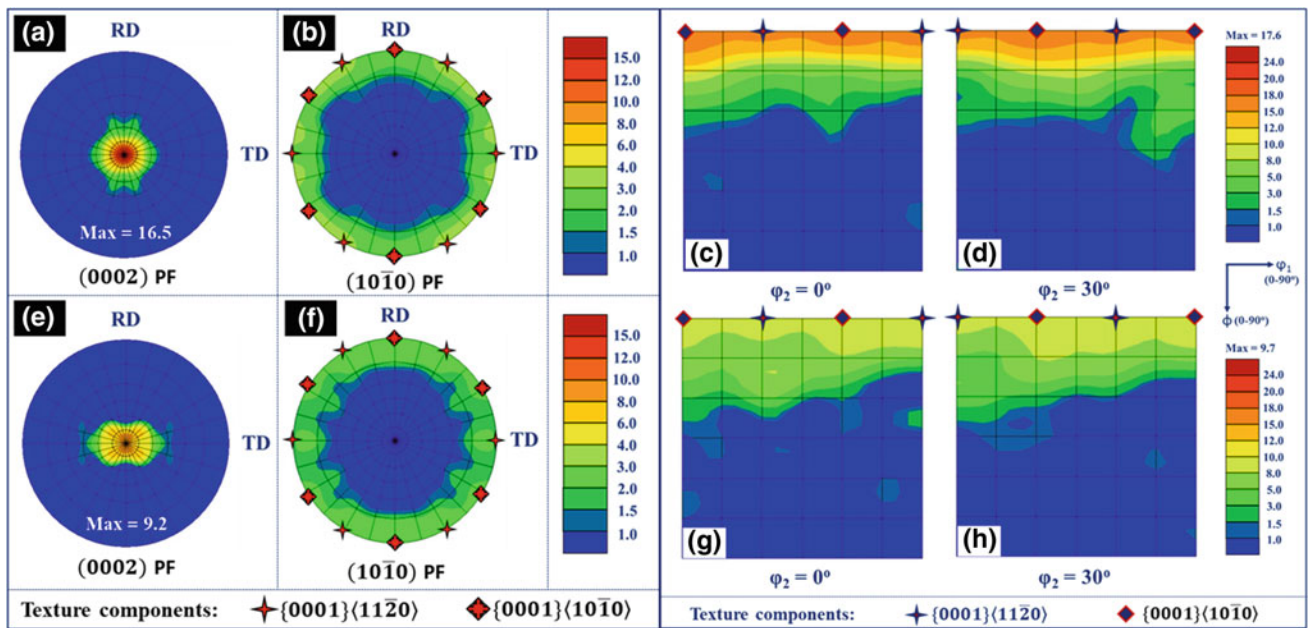


Fig. 8 PFs and ODFs for a–d SR and e–h ASR processes in HRA condition

process exhibits the presence of continuous basal fiber in the ODF sections with the weakened texture intensity. The intensity for the texture components  $\{0001\}\langle 11\bar{2}0 \rangle$  and  $\{0001\}\langle 10\bar{1}0 \rangle$  is observed to be lower for ASR as compared to the SR process. The spreading of basal fiber towards  $\phi$  angle  $\sim 30^\circ$  is more for ASR as compared to SR process. Thus, ASR results in a weaker basal texture than SR process in HR condition. The basal texture gets further

weakened on annealing, the basal texture still remaining weaker in ASR than SR process in HRA condition.

Crystallographic texture plays a significant role during the processing of Mg-based alloys. For Mg, the important slip systems are basal  $\{0001\}\langle 11\bar{2}0 \rangle$ ; prismatic  $\{1\bar{1}00\}\langle 11\bar{2}0 \rangle$ ; pyramidal-I  $\{10\bar{1}1\}\langle 11\bar{2}0 \rangle$  and  $\{10\bar{1}2\}\langle 11\bar{2}0 \rangle$ ; pyramidal-II  $\{11\bar{2}2\}\langle 11\bar{2}3 \rangle$  [20]. Each slip system gets activated when its critical resolved

shear stress (CRSS) is reached. Basal slip system is dominant at room temperature deformation because it has the lowest CRSS as compared to prismatic and pyramidal slip system. When the deformation temperature is higher than 250 °C, other non-basal slip systems also contribute significantly, which leads to higher formability for Mg alloys [23]. Several descriptions of deformation by ASR have been proposed [4, 24]. The shear stress is generated by the different circumferential velocities of the rollers during deformation [25]. The higher shear stress induced during ASR suppresses the basal texture. The weaker basal texture results in the activation of the non-basal slip, which leads to greater ductility and formability of Mg-based alloys [20, 23].

## Tensile Properties

Figure 9a shows the true stress–true strain curves and the corresponding tensile properties are reported in Fig. 9b for TZ73 alloy along RD for SR and ASR processes in HR and HRA conditions. In HR condition, the ASR sample exhibits almost the same strength but 3% higher elongation to failure (El) than the SR sample. It is observed that strength is reduced and elongation to failure is increased after annealing treatment. The ASR sample again exhibits almost the same strength but 2% higher elongation to failure in HRA condition.

The tensile properties of the TZ73 alloy are mainly attributed to fine grain size and solid solution strengthening by dissolved Zn and Sn atoms in  $\alpha$ -Mg matrix. During hot rolling highly thermally stable  $Mg_2Sn$  particles distributed along grain boundaries act as nucleation sites for DRX grains and preclude the DRX grain growth [17, 18]. The annealing treatment leads to further refinement of grains. The weaker

basal texture obtained in the ASR results in higher ductility than SR process in both HR and HRA conditions.

## Conclusions

The homogenized TZ73 alloy was hot rolled at 350 °C by SR and ASR processes followed by annealing at 215 °C for 30 min. The detailed investigations have been carried out to explore the microstructural, texture evolutions, and tensile properties. The analysis of the results led to the following main conclusions:

1. ASR is more effective process to introduce additional shear strain (1.86) along with true strain (1.61).
2. The ASR process yielded slightly finer grains, a higher fraction of LAGBs, almost the same fraction of DRX grains, and a higher KAM value as compared to the SR process in the HR condition.
3. After annealing treatment, the average grain size reduced, the fraction of HAGBs increased, fraction of recrystallized grains increased, and KAM value decreased, for both the SR and ASR processes.
4. The basal texture was weaker for ASR as compared to SR process in HR condition. The spreading of basal fiber towards  $\phi$  angle  $\sim 30^\circ$  was similar for both the SR and ASR processes in HR condition.
5. The basal texture was further weakened on annealing, the ASR still exhibiting weaker basal texture than the SR process in HRA condition. The spreading of basal fiber towards  $\phi$  angle  $\sim 30^\circ$  was more for ASR as compared to SR process in HRA condition.
6. In HR condition, the ASR sample exhibited almost the same strength but 3% higher elongation to failure

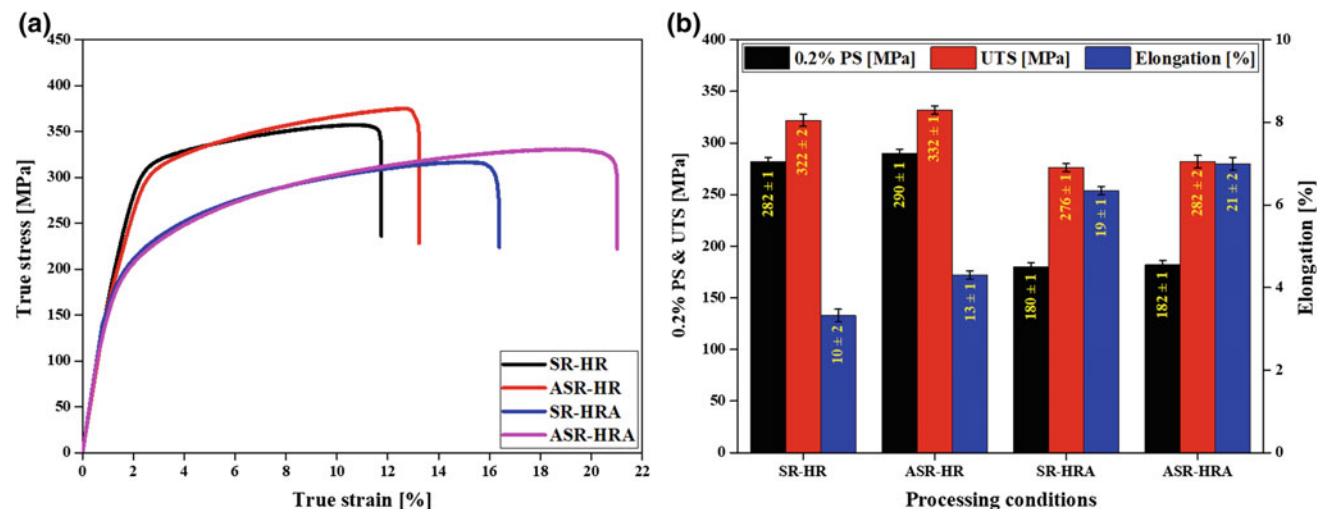


Fig. 9 a True stress–true strain curves and b tensile properties for TZ73 alloy



(El) than the SR sample. The strength was reduced and elongation to failure was increased after annealing treatment. The ASR sample again exhibited almost the same strength but 2% higher elongation to failure in HRA condition. The higher elongation in ASR process is attributed to the weaker basal texture.

- Thus, tensile properties of 0.2% PS = 290 MPa, UTS = 332 MPa and El = 13% in HR and 0.2% PS = 182 MPa, UTS = 282 MPa and El = 21% in HRA condition were obtained for the newly developed TZ73 alloy by using ASR process, which are extremely good for a rolled Mg alloy sheet.

**Acknowledgements** The authors gratefully acknowledge the financial support from the Science and Engineering Research Board (SERB) of the Department of Science and Technology (DST), Government of India. The authors are grateful to Prof. S. Seshan for his help and guidance in squeeze casting.

## References

- B.L. Mordike, T. Ebert, Magnesium Properties - applications - potential, *Mater. Sci. Eng. A* (2001). [https://doi.org/10.1016/S0921-5093\(00\)01351-4](https://doi.org/10.1016/S0921-5093(00)01351-4).
- E. Aghion, B. Bronfin, D. Eliezer, The role of the magnesium industry in protecting the environment, *J. Mater. Process. Technol.* 117 (2001) 381–385. [https://doi.org/10.1016/S0924-0136\(01\)00779-8](https://doi.org/10.1016/S0924-0136(01)00779-8).
- E. Aghion, B. Bronfin, Magnesium Alloys Development towards the 21st Century, *Mater. Sci. Forum.* 350–351 (2000) 19–30. <https://doi.org/10.4028/www.scientific.net/msf.350-351.19>.
- B. Beausir, S. Biswas, D.I. Kim, L.S. Tóth, S. Suwas, Analysis of microstructure and texture evolution in pure magnesium during symmetric and asymmetric rolling, *Acta Mater.* 57 (2009) 5061–5077. <https://doi.org/10.1016/j.actamat.2009.07.008>.
- R.K. Sabat, S.K. Sahoo, D. Panda, U.K. Mohanty, S. Suwas, Orientation dependent recrystallization mechanism during static annealing of pure magnesium, *Mater. Charact.* 132 (2017) 388–396. <https://doi.org/10.1016/j.matchar.2017.09.003>.
- S.V.S. Narayana Murty, N. Nayan, R. Madhavan, S.C. Sharma, K. M. George, S. Suwas, Analysis of Microstructure and Texture Evolution in Mg-3Al-1Zn Alloy Processed Through Groove Rolling, *J. Mater. Eng. Perform.* 24 (2015) 2091–2098. <https://doi.org/10.1007/s11665-015-1459-4>.
- T.T. Sasaki, K. Yamamoto, T. Honma, S. Kamado, K. Hono, A high-strength Mg–Sn–Zn–Al alloy extruded at low temperature, *Scr. Mater.* 59 (2008) 1111–1114. <https://doi.org/10.1016/j.scriptamat.2008.07.042>.
- H. Liu, Y. Chen, Y. Tang, S. Wei, G. Niu, The microstructure, tensile properties, and creep behavior of as-cast Mg-(1–10)%Sn alloys, *J. Alloys Compd.* 440 (2007) 122–126. <https://doi.org/10.1016/j.jallcom.2006.09.024>.
- Y.K. Kim, S.W. Sohn, D.H. Kim, W.T. Kim, D.H. Kim, Role of icosahedral phase in enhancing the strength of Mg–Sn–Zn–Al alloy, *J. Alloys Compd.* 549 (2013) 46–50. <https://doi.org/10.1016/j.jallcom.2012.09.050>.
- S. Biswas, D.-I. Kim, S. Suwas, Asymmetric and symmetric rolling of magnesium: Evolution of microstructure, texture and mechanical properties, *Mater. Sci. Eng. A* 550 (2012) 19–30. <https://doi.org/10.1016/j.msea.2012.03.099>.
- H. Watanabe, T. Mukai, K. Ishikawa, Effect of temperature of differential speed rolling on room temperature mechanical properties and texture in an AZ31 magnesium alloy, *J. Mater. Process. Technol.* (2007) 644–647. <https://doi.org/10.1016/j.jmatprotec.2006.08.010>.
- S.-H. Kim, B.-S. You, C. Dong Yim, Y.-M. Seo, Texture and microstructure changes in asymmetrically hot rolled AZ31 magnesium alloy sheets, *Mater. Lett.* 59 (2005) 3876–3880. <https://doi.org/10.1016/j.matlet.2005.07.024>.
- B. Radhakrishnan, S.B. Gorti, G.M. Stoica, G. Muralidharan, A.D. Stoica, X.-L. Wang, E.D. Specht, E. Kenik, T. Muth, Mesoscale Modeling and Validation of Texture Evolution during Asymmetric Rolling and Static Recrystallization of Magnesium Alloy AZ31B, *Metall. Mater. Trans. A* 43 (2012) 1509–1516. <https://doi.org/10.1007/s11661-011-0896-4>.
- W.J. Kim, J.B. Lee, W.Y. Kim, H.T. Jeong, H.G. Jeong, Microstructure and mechanical properties of Mg–Al–Zn alloy sheets severely deformed by asymmetrical rolling, *Scr. Mater.* 56 (2007) 309–312. <https://doi.org/10.1016/j.scriptamat.2006.09.034>.
- E. Toloie, R. Jamaati, Asymmetric cold rolling: A technique for achieving non-basal textures in AZ91 alloy, *Mater. Lett.* 249 (2019) 143–146. <https://doi.org/10.1016/j.matlet.2019.04.087>.
- S.-B. Kang, B.-K. Min, H.-W. Kim, D.S. Wilkinson, J. Kang, Effect of asymmetric rolling on the texture and mechanical properties of AA6111-aluminum sheet, *Metall. Mater. Trans. A* 36 (2005) 3141–3149. <https://doi.org/10.1007/s11661-005-0085-4>.
- N. El Mahallawy, A. Ahmed Diaa, M. Akdesir, H. Palkowski, Effect of Zn addition on the microstructure and mechanical properties of cast, rolled and extruded Mg–6Sn–xZn alloys, *Mater. Sci. Eng. A* 680 (2017) 47–53. <https://doi.org/10.1016/j.msea.2016.10.075>.
- W. Cheng, Q. Tian, H. Yu, B.S. You, H. Wang, Optimum parameters and kinetic analysis for hot working of a homogenized Mg–8Sn–1Al–1Zn alloy, *Mater. Des.* 85 (2015) 762–770. <https://doi.org/10.1016/j.matdes.2015.07.047>.
- Y.G. Ko, J. Suharto, J.S. Lee, B.H. Park, D.H. Shin, Effect of Roll Speed Ratio on Deformation Characteristics of IF Steel Subjected to Differential Speed Rolling, *Met. Mater. Int.* 19 (2013) 603–609. <https://doi.org/10.1007/s12540-013-3033-7>.
- Y. Wang, J. Huang, Texture analysis in hexagonal materials, *Mater. Chem. Phys.* 81 (2003) 11–26. [https://doi.org/10.1016/S0254-0584\(03\)00168-8](https://doi.org/10.1016/S0254-0584(03)00168-8).
- R.K. Nadella, I. Samajdar, G. Gottstein, Static Recrystallisation and Textural Changes, Magnesium: Proceedings of the 6th International Conference Magnesium Alloys and Their Applications (2005) 1052–1057. <https://doi.org/10.1002/3527603565.ch163>.
- J.F. Humphreys, Nucleation in Recrystallization, *Mater. Sci. Forum.* 467–470 (2004) 107–116. <https://doi.org/10.4028/www.scientific.net/msf.467-470.107>.
- R.K. Sabat, N. Bibhanshu, G.S. Avadhani, S. Kumar, S. Kandalam, S. Suwas, Superplasticity in high temperature magnesium alloy WE43, *Mater. Sci. Eng. A* 687 (2017) 85–92. <https://doi.org/10.1016/j.msea.2016.12.129>.
- A.N. Doğruoğlu, On constructing kinematically admissible velocity fields in cold sheet rolling, *J. Mater. Process. Technol.* 110 (2001) 287–299. [https://doi.org/10.1016/S0924-0136\(00\)00897-9](https://doi.org/10.1016/S0924-0136(00)00897-9).
- J. Sidor, A. Miroux, R. Petrov, L. Kestens, Microstructural and crystallographic aspects of conventional and asymmetric rolling processes, *Acta Mater.* 56 (2008) 2495–2507. <https://doi.org/10.1016/j.actamat.2008.01.042>.

# Friction Stir Processing of Magnesium Alloy with Spiral Tool Path Strategy

Abhishek Kumar, Aarush Sood, Nikhil Gotawala, Sushil Mishra, and Amber Shrivastava

## Abstract

Friction stir processing is a relatively new technique for microstructural modification to improve the mechanical properties of materials. Previous works have been primarily focused on the processing of the small regions. The objective of this work is to study the effect of tool design, tool rotation direction and tool overlap between passes on the processed region. A spiral tool path strategy is employed to process the complete blanks of a magnesium alloy. Three tool designs: tool with hexagonal, tapered and threaded pin, are used. Further, tool rotation direction and tool overlap between passes are varied across the experiments. The material flow and defects formed in the processed region are characterized. Preliminary results show that tool rotation direction and tool overlap significantly affect the defects formed in the processed region. The present work identifies the processing condition for defect-free processed region and refined microstructure of the Magnesium blank.

## Keywords

Friction stir processing • Magnesium • Defects

## Introduction

Magnesium is a strong candidate for lightweight applications in many sectors like automotive and aerospace. However, the hcp structure of magnesium limits its formability at room

temperature. Friction stir processing (FSP) is known to refine the grain size of the as-cast materials [1–4]. FSP has shown potential to improve the room-temperature ductility of Mg alloys, by achieving ultrafine grains [5, 6]. FSP is also shown to improve the superplasticity of AA7075 [7]. In the previous works, multi-pass tool path strategy is adopted to achieve the desired grain refinement during FSP [8]. The number of passes is more influential towards grain refinement than the traverse speed of the tool. Single-pass tool path may result in defect formation depending on the process parameters. Multi-pass tool path strategy tends to overcome this limitation, as defects can be eliminated over the successive passes. This is demonstrated with overlapping passes for friction stir welding (FSW) of aluminium alloys [9]. The multi-pass FSP can improve the machinability of aluminium alloys [10]. Nadammal et al. [11] reported dynamic recrystallization of aluminium upon multi-pass FSP. For multi-pass FSP, relatively smaller grains are observed between the passes as compared to the centre of nugget zone [12]. The multi-pass FSP also helps to achieve a stable microstructure up to 450 °C in aluminium alloy [12]. It is further reported that this phenomenon is alloy-independent. Chen et al. [13] observed an abnormal grain growth in stir zone from single-pass FSP with low tool rotation speed and showed that multi-pass FSP can control the abnormal grain growth. Further, multi-pass FSP improves the mechanical properties due to grain and second phase refinement in the stir zone [14]. The above-discussed studies are performed mostly on the aluminium alloys, and relatively small area of the workpiece is processed. Very limited work on the multi-pass FSP of Mg alloys is reported in the literature. In one study, the multi-pass FSP is used to fabricate a composite on the surface of as-cast Mg alloy [15].

In the present work, multi-pass FSP of as-cast Mg alloy is performed, using a spiral tool path strategy. The objectives of this study is to investigate the effect of tool shoulder overlap, tool rotation direction, and pin shape on the defect formation and microstructural evolution, upon multi-pass FSP of Mg alloy.

A. Kumar · A. Sood · N. Gotawala ·  
S. Mishra · A. Shrivastava (✉)  
Indian Institute of Technology Bombay, Mumbai, India  
e-mail: [ashrivastava.me@iitb.ac.in](mailto:ashrivastava.me@iitb.ac.in)



## Experimental Details

### Materials

The as-cast billet of Mg alloy with diameter of 120 mm is sliced into 3-mm-thick circular plates. The chemical analysis is performed using inductively coupled plasma atomic emission spectrometry (ICP-AES). Details of chemical composition analysis are given in Table 1.

Three different tool pin profiles are used in the present work, while the shoulder diameter is kept same for all tools. Tools are made of H13 tool steel with 55 HRC. Geometrical details of the tools are shown in Fig. 1.

### Tool Path Strategy

A spiral tool path strategy is adopted in the present work to process the blank. The blanks were clamped on the periphery with a circular clamping arrangement. The tool follows a spiral path with starting point at the centre of the blank as shown in Fig. 1. As the tool moves from inside to outside,

the tool shoulder overlaps with some of the processed region. The percentage overlap of the FSP tool is based on the tool shoulder diameter. In this work, experiments are performed with 60 and 80% tool shoulder overlap between consecutive passes. The spiral tool paths were created using PowerMill 2017 software. Figure 2 shows the schematic of the tool path. The tool rotation direction is varied across experiments. For clockwise tool rotation, advancing side (AS) is towards the workpiece centre and retreating side (RS) is away from the workpiece centre. For anticlockwise tool rotation, RS is towards the workpiece centre and AS is away from the workpiece centre.

### Microstructural Characterization

Microstructural observations are performed by optical microscopy and electron backscatter diffraction (EBSD) technique. Samples were cut using wire EDM and polished. The cross section of the processed area was observed with an optical microscope. Further, EBSD analysis was performed for processed samples without any defects. EBSD analysis

**Table 1** Element composition of material

Element	Al	Zn	Na	Mn	Fe	Ce	Mg
Weight (%)	3	0.018	0.022	0.446	0.058	0.2	Remaining

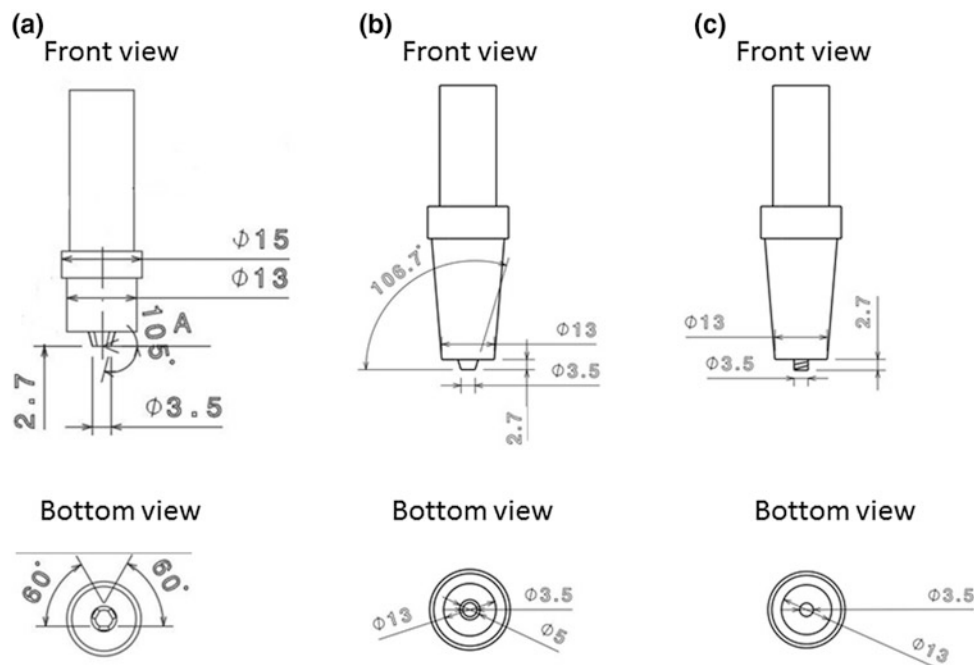
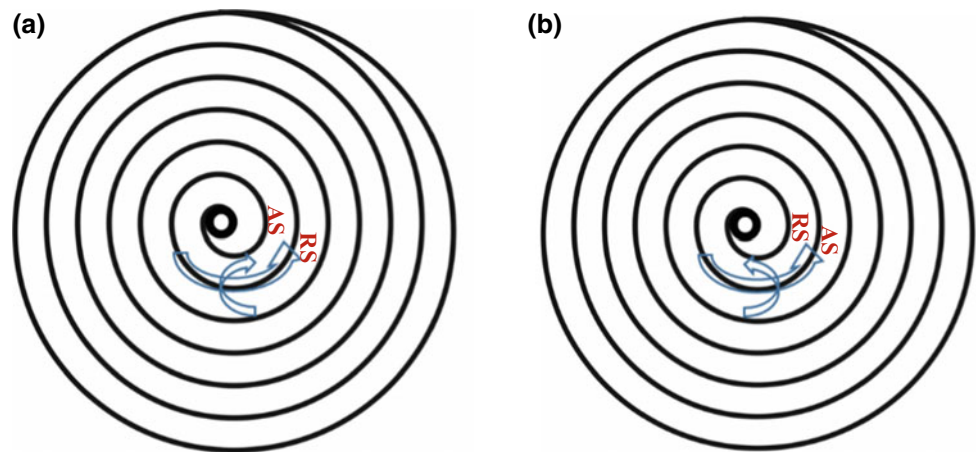


**Fig. 1** FSP Tool design with **a** hexagon tool pin, **b** tapered tool pin, and **c** threaded tool pin (linear dimensions in mm)

**Fig. 2** Schematic of spiral tool path with **a** clockwise tool rotation and **b** counterclockwise tool rotation



was done on Zeiss Gemini with an OXFORD fast CCD detector. The HKL software was used for the EBSD data analysis.

## Results

The processed specimens were cut using wire EDM, and the cross sections were polished and etched for microstructural observation. Figures 3 and 4 show the processed blanks for experiments 1 and 7, respectively. Figure 4 shows the location of the cross section removed for microstructural analysis. The hexagonal tool was used to improve the shearing of material during FSP. A threaded tool was used to improve the material movement along the

thickness direction. Initially, experiments 1, 5, and 8 were performed with hexagonal, threaded, and tapered tools, respectively, at 60% tool shoulder overlap with clockwise rotation. Tunnel defects were observed at the bottom of the cross sections for experiments 1, 5, and 8. Next, the tool shoulder overlap was increased to 80% and experiments 3 and 6 were performed with hexagonal and threaded tool with clockwise tool rotation. The tunnel defects were observed at the bottom of the cross sections for experiments 3 and 6 as well. Since tunnel defects were observed with the tools designed for improved material shearing and material movement, experiments with anticlockwise tool rotation direction were performed next. Results are categorized and presented according to the tool geometry, in the subsections below.



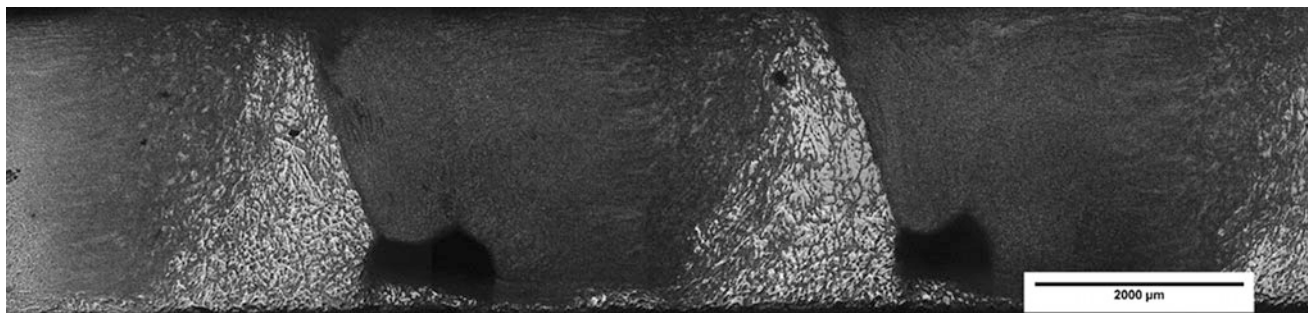
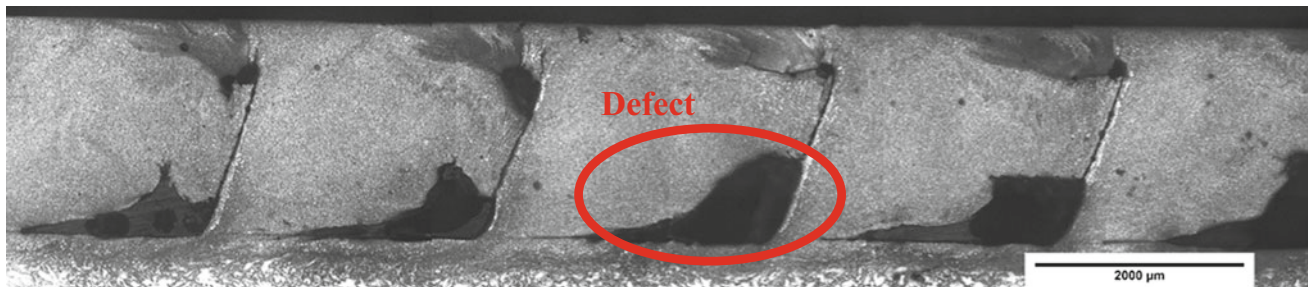
**Fig. 3** Processed blank for experiment 1



**Fig. 4** Processed blank for experiment 7

**Table 2** Experimental details for hexagonal tool

Experiment	Tool shoulder overlap (%)	Tool rotation (RPM)	Tool rotation direction	Tool velocity (mm/min)
1	60	1000	Clockwise	50
2	60	1000	Counterclockwise	50
3	80	1000	Clockwise	50
4	80	1000	Counterclockwise	50

**Fig. 5** Micrograph showing cross section for experiment 1**Fig. 6** Micrograph showing cross section for experiment 2**Fig. 7** Micrograph showing cross section for experiment 3

### FSP with Hexagon Tool Pin

Four experiments were performed using FSP tool with hexagon tool pin (Fig. 1a). The details of other process parameters during FSP are given in Table 2. The tool shoulder overlap and tool rotation direction are varied across

these experiments. Figures 5 and 6 show the micrographs of cross sections for experiments 1 and 2, respectively. For both the cases, tunnel defects are observed. The tool shoulder overlap was increased from 60 to 80% for experiments 3 and 4. The micrographs of experiments 3 and 4 are shown in Figs. 7 and 8, respectively. The FSP performed



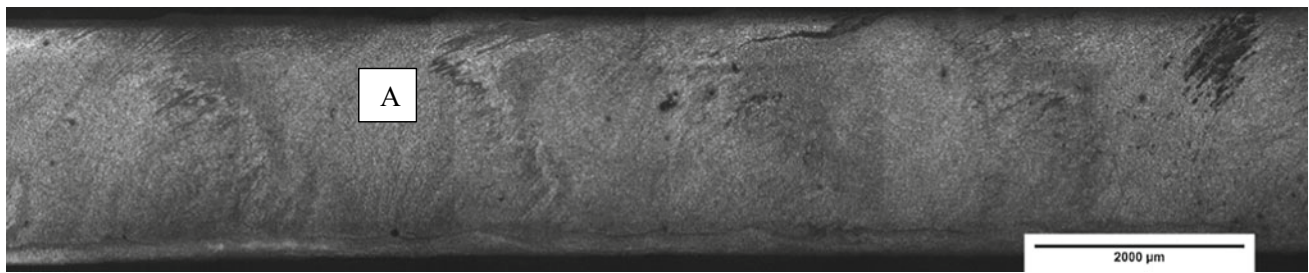


**Fig. 8** Micrograph showing cross section for experiment 4

**Table 3** Experimental details for threaded tools

Experiment	Tool shoulder overlap (%)	Tool rotation (RPM)	Tool rotation direction	Tool velocity (mm/min)
5	60	1000	Clockwise	50
6	80	1000	Clockwise	50
7	80	1000	Counterclockwise	50

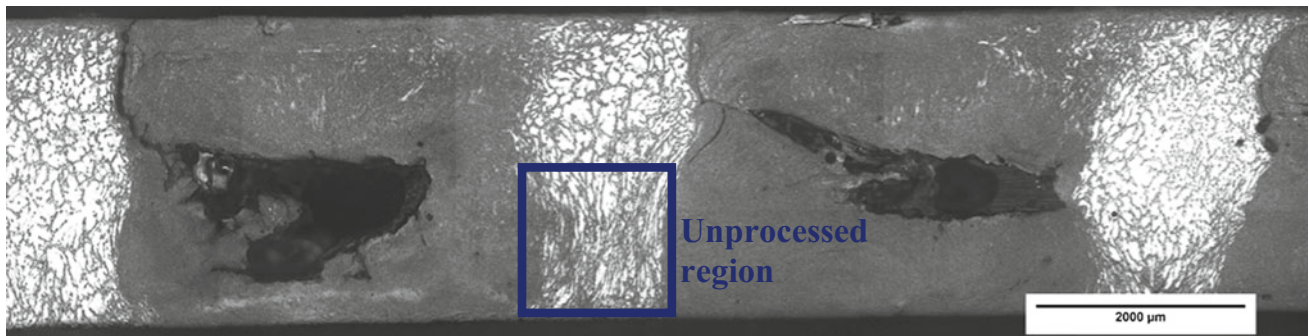


**Fig. 9** Micrograph showing cross section for experiment 5

with 80% overlap and counterclockwise tool rotation (Experiment 4, Table 2) resulted in defect-free processed region, as shown in Fig. 8.

### Experiments with Threaded Tool

Threaded tool pin is used in the previous works [16, 17], for friction stir welding and processing. The results show defect-free welding and elimination of cavities during friction stir processing. However, these works were performed on limited area of the workpiece. In this work, a tool with threaded pin (Fig. 1b) was used for the processing of complete blank using a spiral tool path. Table 3 lists the details of process parameters during FSP with threaded tool. Micrographs showing cross sections for experiments 5 and 6 are shown in Figs. 9 and 10, respectively. These

micrographs show tunnel defects are formed during clockwise rotation of tool, irrespective of the tool shoulder overlap (60% or 80%). The FSP performed with 80% tool shoulder overlap and counterclockwise tool rotation (Experiment 7, Table 3) resulted in defect-free processed region, as shown in Fig. 11.

### Experiments with Tapered Tool

To further observe the effect of tool shape, a tool with tapered pin is used as shown in Fig. 1c. The details of experiments performed with tapered tool are given in Table 4. The micrograph of cross section from experiment 8 is shown in Fig. 12; it shows tunnel defect at each spiral step. The tunnel defect is not observed for experiment 9 (80% tool shoulder overlap and counterclockwise tool



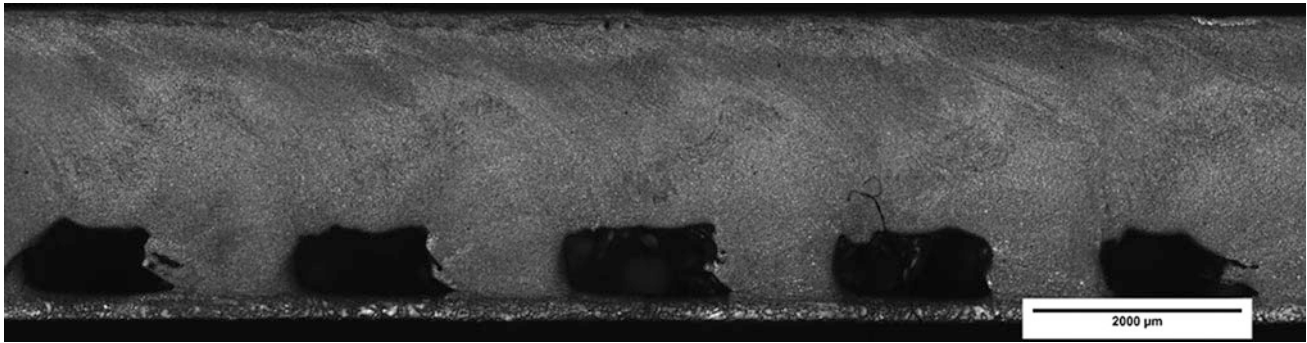


**Fig. 10** Micrograph showing cross section for experiment 6

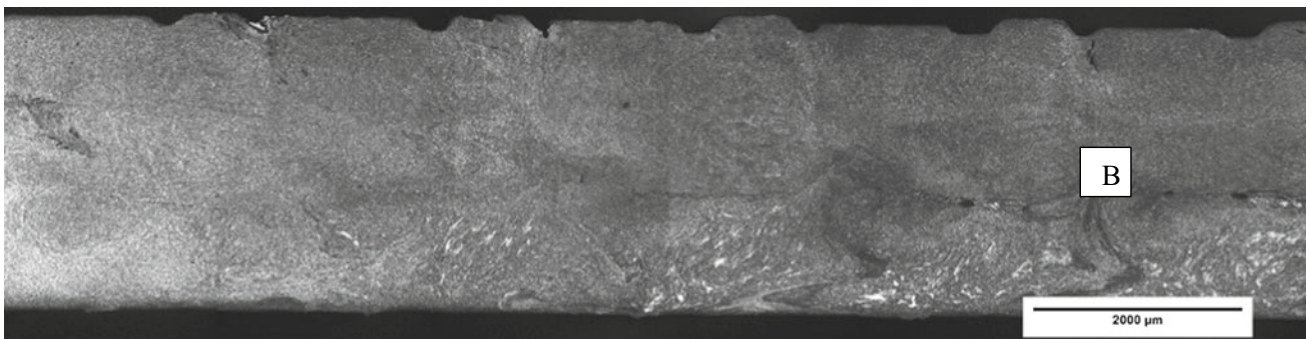


**Fig. 11** Micrograph showing cross section for experiment 7

**Table 4** Experimental details for tapered tool

Experiment	Tool shoulder overlap (%)	Tool rotation (RPM)	Tool rotation direction	Tool velocity (mm/min)
8	60	1000	Clockwise	50
9	80	1000	Counterclockwise	50

rotation), as shown in Fig. 13. This observation is consistent with experiments 4 and 7, performed with tool with hexagon pin and threaded pin, respectively.

## Discussion

### Effect of Tool Pin Design

Tunnel defects are observed for all the samples processed at 60% tool shoulder overlap, irrespective of the tool pin design and tool rotation direction. Further, tunnel defect is observed for the sample processed with hexagon tool and 80% tool shoulder overlap (Fig. 7). Threaded pin profile led to defects near the middle section of the blank thickness. For rest of the samples defects are observed at the bottom of the blank. This is due to relatively less material movement, owing to lower

temperatures at the bottom of the stir [16]. This leads to the formation of tunnel defects at the bottom. During processing with the threaded tool, threads encourage the vertical movement of material, which helps with the defects at the bottom. Relatively larger processed region is observed with hexagonal tool pin as compared to other pin profiles (Figs. 5, 9 and 12). In Fig. 12, the area encircled in blue colour shows the unprocessed region. Figure 9 indicates some material movement at the bottom of the plate, due to the threaded tool pin. For FSP tools with hexagonal and tapered pins, stir zones are wider at the top and narrow down near the bottom. For FSP tool with threaded tool pin, stir zone follows the pin geometry from top to bottom (Fig. 9). Larger unprocessed regions between passes are observed with threaded pin tool as compared to the other two tool pin geometries, for same processing parameters. The tunnel defects are observed for all the tools irrespective of tool pin profile. This suggests that

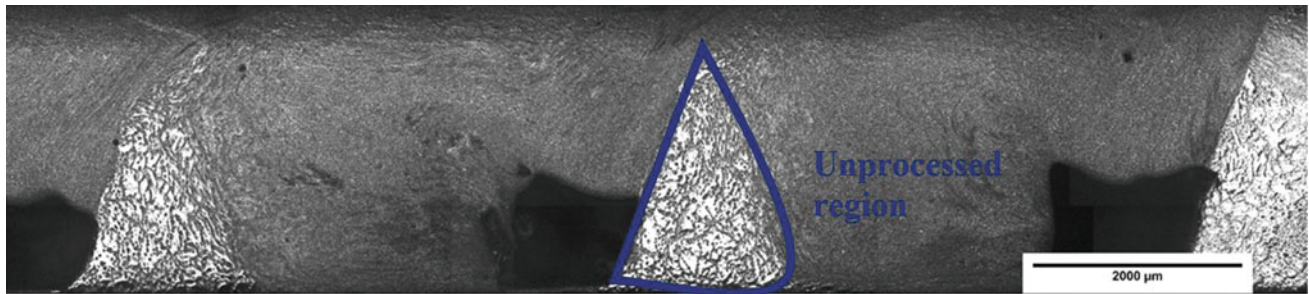


**Fig. 12** Micrograph showing cross section for experiment 8

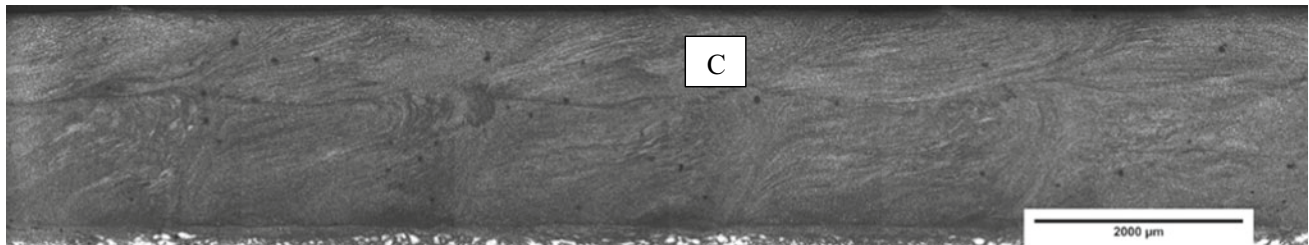


**Fig. 13** Micrograph showing cross section for experiment 9

defect formation is not effected by FSP tool design in a significant way, during multi-pass FSP.

### Effect of Tool Rotation Direction

In case of spiral tool path as shown in Fig. 1, tool rotation direction is an important parameter for defect-free processed region. Tool motion starts from the centre of the specimen and moves outward. The advancing side (AS) and retreating side (RS) depend on the tool rotation direction and traverse direction. During clockwise rotation, the AS is towards the centre of the specimen and it will be opposite for counterclockwise rotation, as shown in Fig. 1a, b. The tunnel defect formation takes place at the advancing side. Therefore, for clockwise tool rotation, the tunnel defect forms on the inner edge (towards the specimen centre) of the tool. As the tool moves radially outwards, the tunnel defect is left behind in the processed region. For counterclockwise tool rotation, the advancing side is at the outer edge of the tool and the tunnel defect also forms at the outer edge. As the tool moves radially outwards with certain tool shoulder overlap, the tool runs over the defect with its inner edge, which is retreating side. As the material moves around the tool from advancing side to retreating side, the defects formed during previous pass are filled and new defects may form at the advancing side. This leads to the outward propagation of the defects, and inner region becomes defect-free. Thus, the

counterclockwise tool rotation with sufficient tool shoulder overlap would keep shifting the tunnel defects towards the base material with successive passes and tunnel defect is observed only for the last pass.

### Effect of Tool Shoulder Overlap

At 60% overlap of tool shoulder, the defect formation takes place for both rotation directions. Also some unprocessed region is observed in Figs. 5 and 6. Based on these observations, the tool shoulder overlap was increased to 80% in the subsequent experiments. An increase in the tool shoulder overlap is accompanied by reduction in unprocessed region. By increasing the tool shoulder overlap, the number of successive passes required for a given area (to be processed) also increases. This would also increase the temperature during FSP. This increase in temperature favours the material movement and reduces the defect size. Therefore, increase in the tool shoulder overlap reduces the unprocessed region between successive passes and the size of the defects also decreases.

### Microstructural Evolution

The average grain size of as-cast Mg alloy was about 250 μm. Figure 14 shows the microstructure of the as-cast



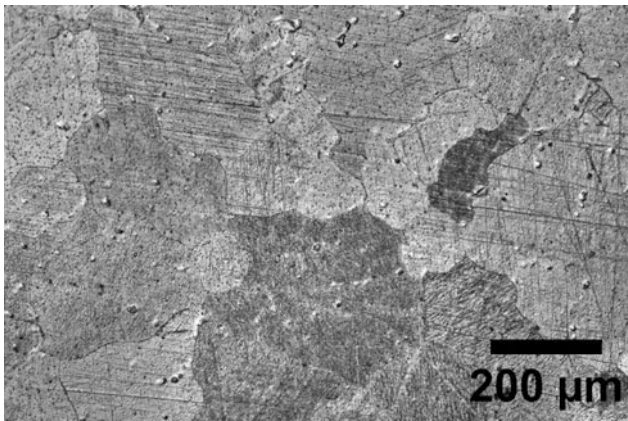
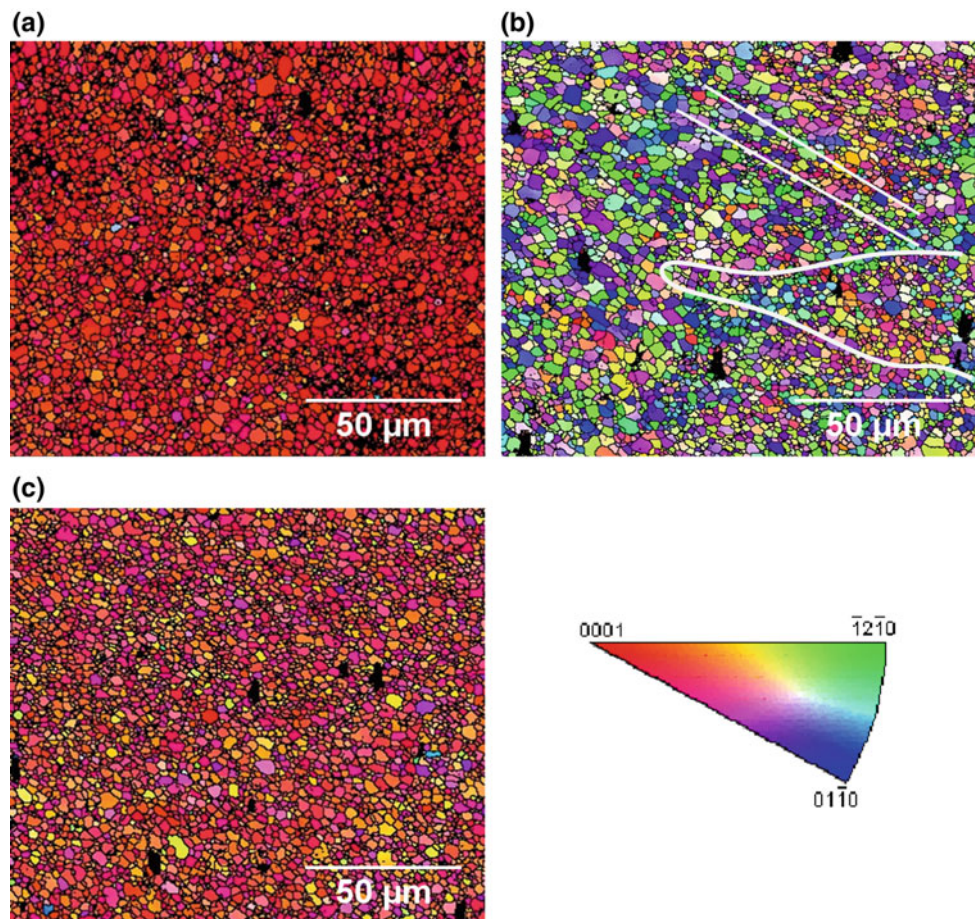


**Fig. 14** Microstructure of the as-cast Mg alloy

material. EBSD technique was used to observe the microstructural evolution upon FSP. Figure 15 shows the microstructure for the processed region for experiments 4, 7, and 9, respectively. During FSP, the material undergoes severe plastic deformation and significant temperature rise. This leads to dynamic recrystallization (DRX) and formation of fine grains. Figure 15b shows the EBSD result for the location B from Fig. 11. The area enclosed with white lines

**Fig. 15** EBSD inverse pole figure maps showing microstructure for **a** experiment 4, **b** experiment 7, and **c** experiment 9



shows a banded region with very fine grains. The microstructure for experiments 4 and 9 (Fig. 15a, c) shows similar reorientation of basal (0001) plane. However, the orientation of the grains varies through the thickness of the processed region. This observation is similar to Mironov et al. [18]. The EBSD results from present work suggest grain refinement through DRX and formation of bands of fine grains.

## Conclusions

In this work, a spiral tool path strategy was introduced to process a circular blank of Mg alloy. Different tool pin designs and tool shoulder overlaps were used for processing the specimens. The following conclusions are drawn:

- (1) Tunnel defects form for all tool pin designs during spiral motion of tool. Thus, the pin design has little effect on the defect formation during multi-pass FSP of Mg alloy.
- (2) For spiral tool path strategy, the tool rotation direction significantly effects the defect formation during FSP. The tunnel defect forms on the outer edge of the

tool for counterclockwise rotation, which leads to defect-free processed region.

- (3) For the tool designs presented, 80% tool shoulder overlap and counterclockwise tool rotation direction lead to fully consolidated processed region.
- (4) Banded regions with very fine grains are formed in the stir zone. Microstructural observations suggest grain refinement due to dynamic recrystallization.

## References

1. J.Q. Su, T. W. Nelson, and C. J. Sterling, "A new route to bulk nanocrystalline materials," *J. Mater. Res.*, vol. 18, no. 8, pp. 1757–1760, 2003.
2. C. I. Chang, X. H. Du, and J. C. Huang, "Achieving ultrafine grain size in Mg–Al–Zn alloy by friction stir processing," *Scr. Mater.*, vol. 57, no. 3, pp. 209–212, 2007.
3. C. I. Chang, C. J. Lee, and J. C. Huang, "Relationship between grain size and Zener-Holloman parameter during friction stir processing in AZ31Mg alloys," *Scr. Mater.*, vol. 51, no. 6, pp. 509–514, 2004.
4. B. M. Darras, M. K. Khraisheh, F. K. Abu-Farha, and M. A. Omar, "Friction stir processing of commercial AZ31 magnesium alloy," *J. Mater. Process. Technol.*, vol. 191, no. 1–3, pp. 77–81, 2007.
5. A.M. Jamili, A. Zarei-Hanzaki, H.R. Abedi, P. Minarik, and R. Soltani, "The microstructure, texture, and room temperature mechanical properties of friction stir processed Mg–Y–Nd alloy," *Mater. Sci. Eng. A*, pp. 244–253, 2017.
6. A. Raja, P. Biswas, and V. Pancholi, "Effect of layered microstructure on the superplasticity of friction stir processed AZ91 magnesium alloy," *Mater. Sci. Eng. A*, vol. 725, no. January, pp. 492–502, 2018.
7. R. S. Mishra, M. W. Mahoney, S. X. McFadden, N. A. Mara, and A. K. Mukherjee, "High strain rate superplasticity in a friction stir processed 7075 Al alloy," *Scr. Mater.*, vol. 42, no. 2, pp. 163–168, 1999.
8. M. M. El-Rayes and E. A. El-Danaf, "The influence of multi-pass friction stir processing on the microstructural and mechanical properties of Aluminum Alloy 6082," *J. Mater. Process. Technol.*, vol. 212, no. 5, pp. 1157–1168, 2012.
9. R. M. Leal and A. Loureiro, "Effect of overlapping friction stir welding passes in the quality of welds of aluminium alloys," *Mater. Des.*, vol. 29, no. 5, pp. 982–991, 2008.
10. S. K. Singh, R. J. Immanuel, S. Babu, S. K. Panigrahi, and G. D. Janaki Ram, "Influence of multi-pass friction stir processing on wear behaviour and machinability of an Al-Si hypoeutectic A356 alloy," *J. Mater. Process. Technol.*, vol. 236, pp. 252–262, 2016.
11. N. Nadammal, S. V. Kailas, J. Szpunar, and S. Suwas, "Microstructure and Texture Evolution during Single- and Multiple-Pass Friction Stir Processing of Heat-Treatable Aluminum Alloy 2024," *Metall. Mater. Trans. A*, vol. 48, no. 9, pp. 4247–4261, 2017.
12. N. Nadammal, S. V. Kailas, J. Szpunar, and S. Suwas, "Development of microstructure and texture during single and multiple pass friction stir processing of a strain hardenable aluminium alloy," *Mater. Charact.*, vol. 140, no. January, pp. 134–146, 2018.
13. Y. Chen, H. Ding, J. Li, Z. Cai, J. Zhao and W. Yang, "Influence of multi-pass friction stir processing on the microstructure and mechanical properties of Al-5083 alloy," *Mater. Sci. Eng. A*, vol. 650, pp. 281–289, 2016.
14. Y. Chen, H. Ding, S. Malopheyev, R. Kaibyshev, Z. H. Cai, and W. Yang, "Influence of multi-pass friction stir processing on microstructure and mechanical properties of 7B04–O Al alloy," *Trans. Nonferrous Met. Soc. China (English Ed.)*, vol. 27, no. 4, pp. 789–796, 2017.
15. M. Sharifitabar, M. Kashefi, and S. Khorshahian, "Effect of friction stir processing pass sequence on properties of Mg–ZrSiO<sub>4</sub>–Al<sub>2</sub>O<sub>3</sub> surface hybrid micro/nano-composites," *Mater. Des.*, vol. 108, pp. 1–7, 2016.
16. G. Padmanaban and V. Balasubramanian, "Selection of FSW tool pin profile, shoulder diameter and material for joining AZ31B magnesium alloy - An experimental approach," *Mater. Des.*, vol. 30, no. 7, pp. 2647–2656, 2009.
17. M. Azizieh, R. Bahadori, M. Abbasi, E. Y. Yoon, and H. S. Kim, "Effect of friction stir processing on the microstructure of pure magnesium castings," *Int. J. Cast Met. Res.*, vol. 28, no. 6, pp. 345–351, 2015.
18. S. Mironov, T. Onuma, Y. S. Sato, and H. Kokawa, "Microstructure evolution during friction-stir welding of AZ31 magnesium alloy," *Acta Mater.*, vol. 100, pp. 301–312, 2015.



# Joining Dissimilar Materials via Rotational Hammer Riveting Technique

Tianhao Wang, Scott Whalen, Piyush Upadhyay,  
and Keerti Kappagantula

## Abstract

A robust, economically viable joining method for Mg/Al and Mg/CFRP could enable multi-material assemblies that decrease vehicle weight while offering more flexibility for designers. However, certain challenges exist for joining Mg/Al and Mg/CFRP. Mechanical joining, such as conventional riveting, clinching and bolting do not form a metallurgical bond between the fastener and metal sheet being fastened. Large differences in physical and mechanical properties of metals and polymers make joining Al or Mg to CFRP challenging via various welding techniques. For Mg/Al pair, solid-phase and fusion-based welding results in rapid formation of brittle intermetallic compounds at the interface leading to premature interfacial fracture under mechanical loading. In this study, a Rotational Hammer Rivet (RHR) technique was developed to fabricate Mg/CFRP and Mg/Al joints. With RHR technique, direct joining between Mg/Al and Mg/CFRP were replaced by joining Mg rivet head and top Mg sheet. Through heat generated by plastic deformation of an Mg rivet, RHR creates a metallurgical bond between rivet head and Mg sheet which seals corrosive electrolyte from penetrating around the rivet head.

## Keywords

Riveting • Magnesium alloys • CFRP •  
Dissimilar joining • Light-weighting

## Introduction

As one of the oldest joining methods, riveting still plays a very important role in manufacturing industry. Especially, the increased use of multi-material and hybrid structures has boosted the requirement for joining dissimilar materials, and riveting is suitable for joining dissimilar materials [1]. In recent decades, requirements to improve fuel efficiency in the transport industries necessitate a higher usage of light-weight structural materials such as magnesium (Mg) and its alloys since their densities are around 65% of that of aluminum (Al) but with comparable strength [2]. As such, using Mg rivets in place of traditionally used steel or aluminum ones would augment vehicle light-weighting. However, while this has been explored in the past, literature shows that conventional cold driven riveting is not possible for Mg alloys due to its low formability [3]. Since Mg alloys are readily formable at elevated temperatures [4], hot driven riveting has been investigated for magnesium rivets [5]. But the prohibitively slow heating process and cycle time have been a barrier to industry adaptation. Therefore, in this study, a rotational hammer riveting (RHR) technique was developed and applied on magnesium studs to obtain rivet heads that are metallurgically joined to the underlying magnesium sheet. In contrast to hot and cold driven riveting where the only deformation is due to linear hammering, RHR takes advantage of heat generated by plastic shear deformation of Mg while a specially designed rotating tool plunges on an Mg stud.

Because of the desire to increase the use of lightweight structural materials such as aluminum alloys, magnesium alloys and carbon fiber reinforced polymers (CFRP) in industries, a mechanically robust joining method for combinations of these materials, namely Mg/Al and Mg/CFRP can enable decreased vehicle weight while offering more flexibility for vehicle designers [6, 7]. However, certain challenges exist for joining Mg/Al and Mg/CFRP. For example, mechanical joining methods such as conventional

T. Wang · S. Whalen · P. Upadhyay · K. Kappagantula (✉)  
Applied Materials & Manufacturing Group, Energy Processes  
& Materials Division, Energy & Environment Directorate, Pacific  
Northwest National Laboratory, 908 Battelle Blvd., MS K2-03,  
Richland, WA 99354, USA  
e-mail: [ksk@pnnl.gov](mailto:ksk@pnnl.gov)

rivets, threaded fasteners and bolted joints cannot seal the interfaces between the rivet head and Mg sheet against penetration of corrosive electrolyte. With various welding techniques including solid-state and fusion welding methods, brittle intermetallic compounds  $Al_xMg_y$  formed rapidly at the Mg/Al interface, which facilitated a weak dissimilar joint [8]. Additionally, large differences of physical, chemical, and mechanical properties of metals and polymers make joining Al or Mg/CFRP challenging by applying conventional welding methods. The RHR technique addresses these challenges since metallurgical bonding formed between the rivet head and top Mg sheet. Tool design and process parameters including rotation rate and plunge speed were optimized based on microstructural characterization and mechanical performance of the dissimilar Mg/Al and Mg/CFRP joints.

## Experiments and Methods

### Base Materials

In this study, Mg (AZ31), CFRP and Al (AA7055) sheets with thickness of 2.4, 3.1 and 2.5 mm, respectively, were used. The CFRP, commercially available as Ultramid Advanced N XA-3454, is a 40% short carbon fiber reinforced grade of PA9T obtained from BASF Corporation. Mechanical properties of AZ31, CFRP, and AA7055 are listed in Table 1.

### Tool Design

Two H13 tools utilized in this study are shown in Fig. 1. Both the tools were 12.7 mm in diameter with concavity of  $10^\circ$  (tool#1) and  $20^\circ$  (tool #2). The detailed schematic of tool geometry including dimensions used to calculate cap volume (volume within tool concavity) and AZ31 insert volume is shown in Fig. 2a, b shown. According to the diameter ( $D_{\text{tool}}$ ) and concave degree ( $\theta$ ) of the RHR tools, cap volume ( $V_{\text{cap}}$ ) and cap-height ( $H_{\text{cap}}$ ) were calculated via Eqs. (1) and (2). On the other hand, the height ( $H_{\text{insert}}$ ) and volume ( $V_{\text{insert}}$ ) of AZ31 insert were related by Eq. (3). For tool #1 ( $\theta = 10^\circ$ ),  $H_{\text{cap}}$  of 0.5 mm and  $V_{\text{cap}}$  of  $29.4 \text{ mm}^3$  were obtained. For tool #2 ( $\theta = 20^\circ$ ),  $H_{\text{cap}}$  of 1.1 mm and



Fig. 1 Pictures of RHR tools #1 and #2

$V_{\text{cap}}$  of  $60.8 \text{ mm}^3$  were obtained. In addition, a coefficient of  $\alpha$  ( $\geq 1$ ) is used to balance  $V_{\text{ex}}$  and  $V_{\text{cap}}$  as shown in Eq. (4). This is because insert height can guarantee enough material for fully forming a rivet head. In this study, it was found that  $\alpha$  should be greater than 2.

$$V_{\text{cap}} = \frac{\pi D_{\text{tool}}^3 \cdot (2 + \cos \theta)(1 - \cos \theta)^2}{24(\sin \theta)^3} \quad (1)$$

$$H_{\text{cap}} = \frac{D_{\text{tool}} \cdot (1 - \cos \theta)}{2 \sin \theta} \quad (2)$$

$$V_{\text{insert}} = \frac{\pi}{4} D_{\text{insert}}^2 \cdot H_{\text{insert}} \quad (3)$$

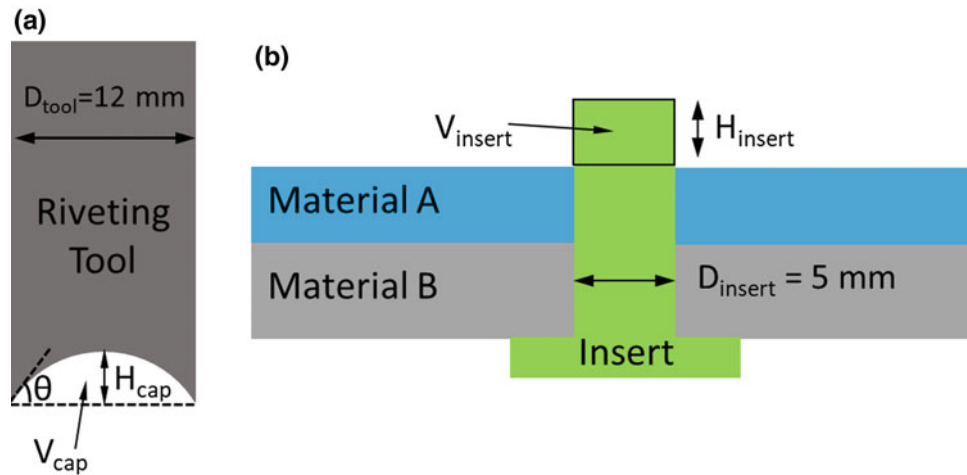
$$\alpha \cdot V_{\text{insert}} = V_{\text{cap}} \quad (4)$$

### Experimental Setup and Process Parameters

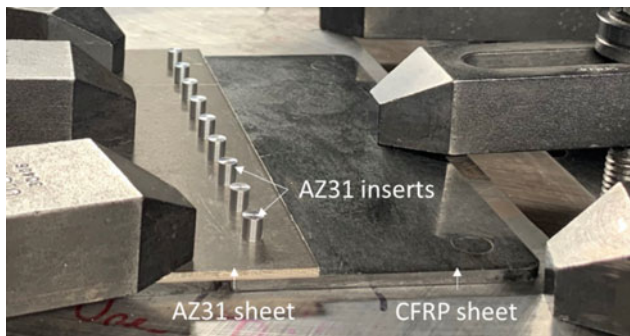
$\varnothing 5 \text{ mm}$  holes were predrilled on the AZ31, CFRP and AA7055 sheets and center to center spacing of 15 mm. AZ31 inserts were penetrated through bottom sheet, and the height of AZ31 inserts was designed such that they contained sufficient volume to form a rivet head during the joining process as discussed in Fig. 2. Setup for riveting AZ31/CFRP sheets with AZ31 inserts is shown in Fig. 3. As for riveting AZ31/AA7055 sheets with AZ31 inserts, the bottom CFRP sheet was replaced with AA7055 sheet. For riveted AZ31/CFRP and AZ31/AA7055 sheets obtained with tool #1, the rotation rate was 1000 RPM with varying plunge speed.

Table 1 Mechanical properties of base materials

Materials	Tensile strength (MPa)	Elongation (%)
AZ31	260	15
CFRP	274	1
AA7055	640	10



**Fig. 2** Schematic of volume calculation of the **a** tool dimensions and **b** insert dimensions



**Fig. 3** Setup of RHR process

### Sample Preparation and Characterization

Riveted AZ31/CFRP and AZ31/AA7055 joints were cut along the centerline of AZ31 inserts. Specimens for microstructural analysis were mounted in epoxy and polished to a final surface finish of  $0.05 \mu\text{m}$  using colloidal silica. Optical microscopy was performed on cross-sections of the samples. In order to perform lap shear tensile testing, riveted AZ31/CFRP joints and AZ31/AA7055 joints were prepared such that the width of the specimens was about 15 mm with the AZ31 insert located at the center. Lap shear tensile tests were performed at room temperature using an MTS test frame at an extension rate of 1.27 mm/min. The lap shear tensile test configuration of AZ31/CFRP with AZ31 insert is shown in Fig. 4.

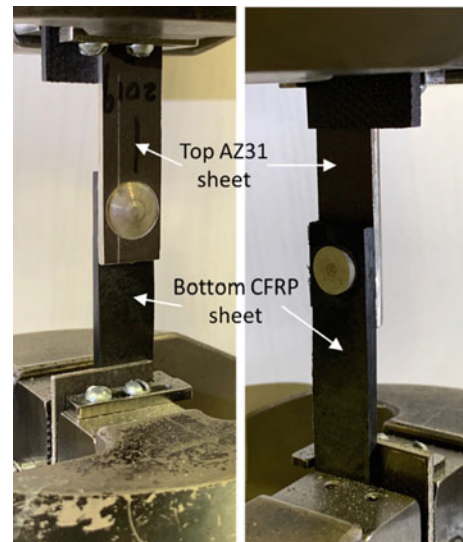


**Fig. 4** Picture of lap shear tensile test configuration of AZ31/CFRP with AZ31 insert

## Results and Discussion

### Mechanism of RHR

Schematic of RHR process is shown in Fig. 5. Friction between the rotating tool and AZ31 insert produces heat, which softens Mg insert. Under the combined effect of heat

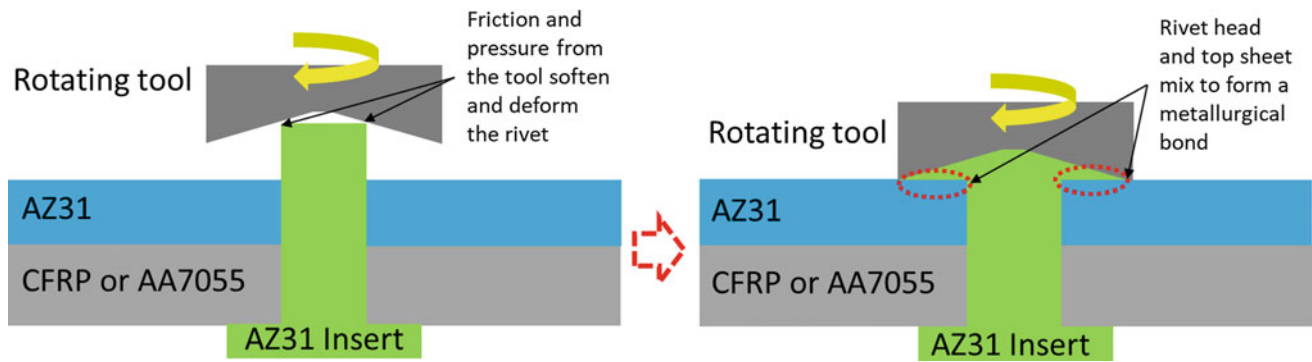


**Fig. 5** Mechanism and schematic of rotational hammer riveting technique

and pressure from the tool, AZ31 insert head is plastically deformed and mixed with the top AZ31 sheet to form a metallurgical bond while simultaneously creating a traditional rivet head. With various bottom sheets used in this study, AZ31/CFRP and AZ31/AA7055 joints were both obtained with RHR of AZ31 inserts, as shown in Fig. 5.

### Rivet Appearance and Microstructure

For riveted AZ31/CFRP sheets obtained with tool #1, the rivet surface is smooth and completely formed (Fig. 6a). The cross-section of riveted AZ31/CFRP shows that the rivet

head is mixed optimally with the top AZ31 sheet while some deflection of CFRP sheet is observed (Fig. 6b). Comparably, for riveted AZ31/AA7055 sheets obtained with tool #1, the rivet surface is shiny and completely formed (Fig. 6c). The cross-section of riveted AZ31/AA7055 shows that the rivet head is mixed sufficiently with the top AZ31 sheet (Fig. 6d).

Riveting AZ31/CFRP sheets with tool #2 were also investigated. It is, however, difficult to find stable riveting parameters due to the higher concavity. Figure 7a shows the rivet appearance with constant rotation rate of 1000 RPM and plunge speed of 60 mm/min. It shows that rivet head has a propensity to stick on the tool after riveting. Figure 7b shows the cross-section of the rivet that displayed a good surface appearance. The head is

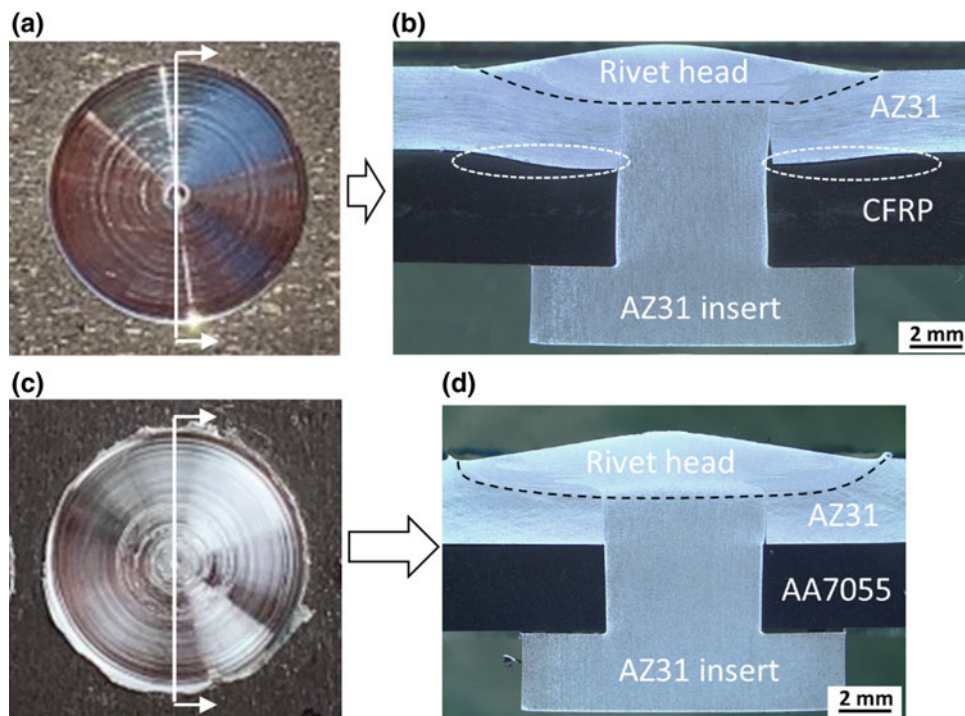


**Fig. 6** a Rivet head top view and b cross-section of riveted AZ31/CFRP sheets with AZ31 insert (Tool #1), and c rivet head surface and d cross-section of riveted AZ31/AA7055 sheets with AZ31 insert (Tool #1). Black dotted lines are approximate representations of

metallurgical bonding between the formed rivet head and stop AZ31 sheet. (b) and (d), and deflection of CFRP in labelled with white dotted ellipses in (b)



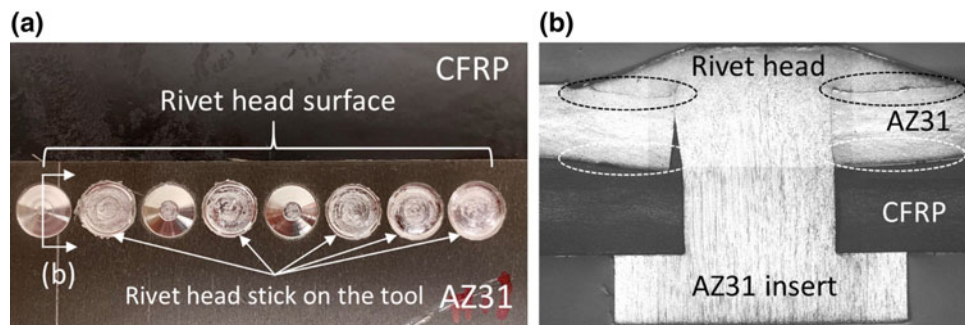


**Fig. 7** **a** Rivet head appearance and **b** cross-section of riveted AZ31/CFRP sheets with AZ31 insert via tool #2. Note that the unmixed region between rivet head and top AZ31 sheet is labelled with

black dotted ellipses in **(b)**, and deflection of CFRP is labelled with white dotted ellipses in **(b)**

not completely mixed with top AZ31 sheet and deflection of CFRP is more severe than the joints obtained with tool #1 (Fig. 6a–b). The higher concavity tool face appears to have impeded mixing at the head/sheet interface.

joints break through the AZ31 insert shank. Lap shear tensile tests show that peak load of riveted AZ31/CFRP was  $\sim 1.2$  kN and peak load of riveted AZ31/AA7055 is  $\sim 2.5$  kN.

## Mechanical Characterization

Lap shear tensile tests were conducted on riveted AZ31/CFRP joints and riveted AZ31/AA7055 joined by tool #1. Fracture modes varied for riveted AZ31/CFRP and riveted AZ31/AA7055 joints. As shown in Fig. 8a<sub>1–2</sub>, riveted AZ31/CFRP joints break through the CFRP from the edges of the pre-drilled holes. As shown in Fig. 8b<sub>1–2</sub>, riveted AZ31/AA7055

## Conclusion

A novel riveting method—RHR—was developed and applied to join AZ31/CFRP and AZ31/AA7055 assemblies with AZ31 rivets. The mechanism of RHR process was also provided which addresses challenges inherent to cold and hot riveting with Mg alloys. With RHR, the deforming rivet head forms a metallurgical bond with the top sheet being fastened. Different tool designs were investigated for their rivet head surface appearance and cross-section morphology. Tool #1 with 10° concavity demonstrated and better mixing between rivet cap and top AZ31 sheet compared to tool #2 with 20° concavity. Mechanical response of riveted AZ31/CFRP and AZ31/AA7055 was studied via lap shear tensile testing. Riveted AZ31/CFRP displayed a peak load of  $\sim 1.2$  kN with fracture at the CFRP predrilled hole, while riveted AZ31/AA7055 displayed a peak load of  $\sim 2.5$  kN with fracture through AZ31 insert shank. RHR process has demonstrated promise in utilizing low formability materials like magnesium that can enable multi-material design. The process robustness, cycle time and performance of joints in different loading conditions will be investigated in future work.

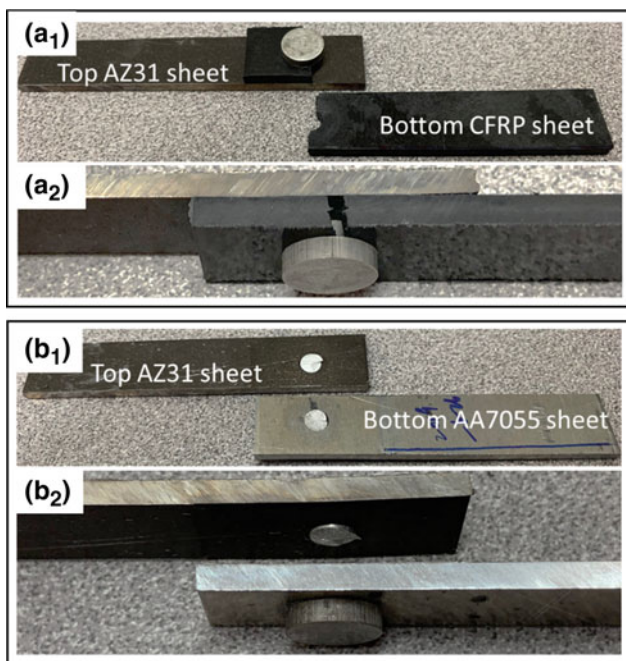


**Fig. 8** Pictures of **a**<sub>1–2</sub> fractured joint of AZ31/CFRP and **b**<sub>1–2</sub> fractured joint of AZ31/AA7055

**Acknowledgements** The authors acknowledge the U.S. Department of Energy Vehicles Technologies Office (DOE/VTO) for financial support of this work under the Joining Core program. The Pacific Northwest National Laboratory is operated by the Battelle Memorial Institute for the U.S. Department of Energy under contract DE-AC06-76LO1830. The publisher, by accepting the article for publication, acknowledges that the U.S. Government retains a non-exclusive, paid-up, irrevocable, worldwide license to publish or reproduce the published form of this manuscript, or allow others to do so, for U.S. Government purposes. The authors would like to thank Timothy Roosendaal, Timothy McAllister, and Anthony Guzman for their assistance in material characterization and testing.

## References

1. Martinsen, K., Hu, S.J. and Carlson, B.E., 2015. Joining of dissimilar materials. *CIRP Annals*, 64(2), pp. 679–699. <https://www.sciencedirect.com/science/article/pii/S0007850615001456?via%3Dihub>
2. Luo, A.A., 2002. Magnesium: current and potential automotive applications. *jom*, 54(2), pp. 42–48. <https://link.springer.com/article/10.1007/BF02701073>
3. Kaiser, F., Letzig, D., Bohlen, J., Styczynski, A., Hartig, C. and Kainer, K.U., 2003. Anisotropic properties of magnesium sheet AZ31. In *Materials Science Forum* (Vol. 419, pp. 315–320). Trans Tech Publications Ltd., Zurich-Uetikon, Switzerland. <https://www.cheric.org/research/tech/periodicals/view.php?seq=1254083>
4. Trang, T.T.T., Zhang, J.H., Kim, J.H., Zargarani, A., Hwang, J.H., Suh, B.C. and Kim, N.J., 2018. Designing a magnesium alloy with high strength and high formability. *Nature communications*, 9(1), p. 2522. <https://www.ncbi.nlm.nih.gov/pmc/articles/PMC6023917/#CR3>
5. Gann, J.A., 1931. Magnesium Industry's Lightest Structural Metal (No. 310044). SAE Technical Paper. <https://www.sae.org/publications/technical-papers/content/310044/>
6. Cole, G.S. and Sherman, A.M., 1995. Light-weight materials for automotive applications. *Materials characterization*, 35(1), pp. 3–9. <https://www.sciencedirect.com/science/article/pii/S044580395000631>
7. JC, H. and Chen, M., 2003. Fabrication of high performance magnesium/carbon-fiber/PEEK laminated composites. *Materials Transactions*, 44(8), pp. 1613–1619. [https://www.jstage.jst.go.jp/article/matertrans/44/8/44\\_8\\_1613/\\_article/-char/ja/](https://www.jstage.jst.go.jp/article/matertrans/44/8/44_8_1613/_article/-char/ja/)
8. Liu, L., Ren, D. and Liu, F., 2014. A review of dissimilar welding techniques for magnesium alloys to aluminum alloys. *Materials*, 7(5), pp. 3735–3757. <https://www.mdpi.com/1996-1944/7/5/3735/htm>

---

**Part VI**  
**Corrosion**

# Anomalous Hydrogen Evolution on Magnesium

Aline D. Gabbardo and G. S. Frankel

## Abstract

When Mg undergoes anodic polarization in a corrosive environment, the rate of hydrogen evolution (HE) increases with increasing applied anodic potential or current, which is opposite of the expected behavior based on standard electrochemical kinetics. This anomalous HE has been the recent focus of researchers worldwide. In this work, the behavior of sputtered Mg thin films and scratched Mg electrodes is presented. HE vanished when the potential of a pit in Mg thin films was increased into the region where a salt film formed. The peak anodic current on scratched samples was not anomalous, as it decreased slightly with increased potential. These observations indicate that the HE rate on Mg depends on the nature of the surface and that anomalous HE results from the surface being more catalytic to the HE reaction with increasing dissolution rate.

## Keywords

Magnesium • Corrosion • Anomalous hydrogen evolution

## Extended Abstract

A thorough understanding of Mg corrosion properties is necessary for further developments in its application for engineering structural components. However, the Mg dissolution mechanism cannot be easily explained with classical electrochemical theories and further experimental clarification is still needed. The typical kinetics for electrochemical reactions follow activated state theory as described by the Butler–Volmer equation and, for sufficiently large difference in potential from the reversible potential, the Tafel equation

describes the relation of current density ( $i$ ) and overpotential [1]. Based on the Tafel equation, the anodic current density increases exponentially and the cathodic current density decreases exponentially with increasing potential. A potentiostat only measures the net current, or net current density if the electrode area is known, ( $i_{\text{net}} = i_{\text{anodic}} - |i_{\text{cathodic}}|$ ). At high anodic potentials,  $i_{\text{cathodic}}$  is expected to be very low, and  $i_{\text{net}}$  is approximately equal to  $i_{\text{anodic}}$ . However, the behavior of Mg during anodic dissolution is different than that predicted by the theories described above [2]. The phenomenon is usually called the negative difference effect (NDE) and more recently the anomalous hydrogen evolution (anomalous HE) [2]. The cathodic reaction rate, described by the hydrogen evolution current density ( $i_{\text{H}_2}$ ), is expected to decrease as the applied potential increases above the OCP, but many authors have shown that for Mg the hydrogen evolution current density increases as the anodic applied potential increases [2–5]. This situation complicates the evaluation of Mg corrosion properties through standard electrochemical tests such as polarization curves because the measured  $i_{\text{net}}$  does not equal  $i_{\text{anodic}}$  at high anodic overpotentials [3]. Understanding the mechanism of the anomalous HE phenomenon could facilitate the development of new Mg alloys and more efficient corrosion protection systems for Mg.

Some of the recent theories to explain anomalous HE assumes that the behavior is a localized phenomenon that happens on sites close to the Mg dissolving areas, whereas in others the anomalous HE phenomenon is associated with the actual active dissolving sites on the Mg surface [6–8]. The effects of impurities, corrosion product film and the role of the active surfaces have all been reviewed in detail elsewhere [4, 5].

In this work, the 2D pit growth method and the scratched electrode technique were used as new approaches to further understand the anomalous HE phenomenon [9–11]. The 2D pit growth method has been used to study pitting corrosion in Al and stainless steel [12, 13], but can also be used to evaluate the anomalous HE phenomenon on Mg [9, 10]. The pit growth in metallic thin films is two-dimensional, allowing

A. D. Gabbardo · G. S. Frankel (✉)  
Fontana Corrosion Center, The Ohio State University, Columbus,  
OH 43210, USA  
e-mail: [frankel.10@osu.edu](mailto:frankel.10@osu.edu)



$i_{\text{anodic}}$  and  $i_{\text{net}}$  to be measured by recording the surface of a single growing pit. The pit cathodic current density ( $i_{\text{cathodic}}$ ) can be indirectly obtained by  $i_{\text{net}} = i_{\text{anodic}} - |i_{\text{cathodic}}|$ , which accounts for the hydrogen evolution rate ( $i_{\text{H}_2}$ ) in the case of Mg. One advantage of this method in comparison with volumetric or gravimetric hydrogen measurements [14] is that the active corroding area, or the 2D pit wall, is tracked in space by the recorded video. It was therefore confirmed that the location of the anomalous HE phenomenon is the active Mg surface [9] and the mechanism is more related to the state of the corroding surface than to the accumulation of impurities or corrosion products. 2D pits have small active areas and thus low ohmic resistance, allowing for the application of higher potentials. When high enough potential is applied, a salt film covers the active surface and the anomalous HE vanishes [10]. The hypothesis is that direct contact of water with the active Mg surface is blocked in this case and HE decreases. The anomalous HE is then a consequence of the increased catalytic activity for the HER of the active sites created during dissolution and it will increase with increasing dissolution rate but will decrease or vanish if these sites are blocked. The scratched electrode technique was used to evaluate the corrosion kinetics of freshly generated Mg surfaces mechanically created in situ by a diamond scribe [11]. Active sites are thought to be fresh, film-free, surfaces. In fact, it was observed that the catalytic activity for the HER increased on the scratched surface when compared to a filmed surface and this increased catalytic activity persisted until repassivation (or reformation of a monolayer of Mg hydroxide). Interestingly, the peak hydrogen evolution current density on the scratched samples was not anomalous, as it decreased slightly with increased potential. The HE rate only depends on the transient state of the Mg surface created by the diamond scribe and is directly related to the catalytic activity of this surface for the HER, in line with the previous results.

## References

1. Frankel GS, Landolt D (2003), "Kinetics," Ch. 1.3, Encyclopedia of Electrochemistry, Volume 4, Stratmann M, Frankel GS, eds., Wiley-VCH, Weinheim, Germany

2. Esmaily M, Svensson JE, Fajardo S, et al. (2017) Fundamentals and advances in magnesium alloy corrosion. *Progress in Materials Science* 89: 92–193. <https://doi.org/10.1016/j.pmatsci.2017.04.011>
3. Frankel GS, Samaniego A, Birbilis N (2013) Evolution of hydrogen at dissolving magnesium surfaces. *Corrosion Science* 70: 104–111. <https://doi.org/10.1016/j.corsci.2013.01.017>
4. Frankel GS, Fajardo S, Lynch BM (2015) Introductory lecture on corrosion chemistry: a focus on anodic hydrogen evolution on Al and Mg. *Faraday Discussions* 180: 11–33. doi:180: 11–33. <https://doi.org/10.1039/c5fd00066a>
5. Thomas S, Medhekar NV, Frankel GS, Birbilis N (2015) Corrosion mechanism and hydrogen evolution on Mg. *Current Opinion in Solid State & Materials Science* 19(2): 85–94. <https://doi.org/10.1016/j.cossms.2014.09.005>
6. Fajardo S, Glover CF, Williams G, Frankel GS (2016) The Source of Anodic Hydrogen Evolution on Ultra High Purity Magnesium. *Electrochimica Acta* 212: 510–521. <https://doi.org/10.1016/j.electacta.2016.07.018>
7. Michailidou E, McMurray HN, Williams G (2018) Quantifying the Role of Transition Metal Electrodeposition in the Cathodic Activation of Corroding Magnesium. *Journal of the Electrochemical Society* 165(5): C195–C205. <https://doi.org/10.1149/2.0251805jes>
8. Yang Y, Scenini F, Curioni M (2016) A study on magnesium corrosion by real-time imaging and electrochemical methods: relationship between local processes and hydrogen evolution. *Electrochimica Acta* 198: 174–184. <https://doi.org/10.1016/j.electacta.2016.03.043>
9. Gabbardo AD, Frankel GS (2019) Application of 2D Pit Growth Method to Mg Thin Films: Part I. Initiation, Growth and Repassivation. *Journal of The Electrochemical Society* 166(11): C3254–C3265. <https://doi.org/10.1149/2.0331911jes>
10. Gabbardo AD, Viswanathan G, Frankel GS (2019) Application of 2D Pit Growth Method to Mg Thin Films: Part II. Salt Film and Hydrogen Evolution. *Journal of The Electrochemical Society* 166(11): C3266–C3274. <https://doi.org/10.1149/2.0351911jes>
11. Gabbardo AD, Frankel GS (2019) Hydrogen evolution on bare Mg surfaces using the scratched electrode technique. *Corrosion Science*. <https://doi.org/10.1016/j.corsci.2019.108321>
12. Frankel GS (1990) The Growth of 2-D Pits in Thin-Film Aluminum. *Corrosion Science* 30(12): 1203–1218. [https://doi.org/10.1016/0010-938x\(90\)90199-f](https://doi.org/10.1016/0010-938x(90)90199-f)
13. Ryan MP, Laycock NJ, Isaacs HS, Newman RC (1999) Corrosion pits in thin films of stainless steel. *Journal of the Electrochemical Society* 146(1): 91–97. <https://doi.org/10.1149/1.1391569>
14. Fajardo S, Frankel GS (2015) Gravimetric Method for Hydrogen Evolution Measurements on Dissolving Magnesium. *Journal of the Electrochemical Society* 162(14): C693–C701. <https://doi.org/10.1149/2.0241514jes>

# Numerical Investigation of Micro-Galvanic Corrosion in Mg Alloys: Role of the Cathodic Intermetallic Phase Size and Spatial Distributions

V. K. Beura, P. Garg, V. V. Joshi, and K. N. Solanki

## Abstract

Magnesium alloys are of increasing interest in structural applications due to their low-density, moderate specific strength and stiffness, recyclability, and high damping among other properties. However, the wide-scale applicability of magnesium alloys in structural applications has been limited due to many factors including its poor corrosion resistance. In this work, a numerical investigation to simulate the micro-galvanic corrosion behavior was performed to examine the influence of the size and distribution of cathodic intermetallic phase ( $\beta$ -Mg<sub>17</sub>Al<sub>12</sub>) in a Mg matrix. The ratio of cathodic to anodic surface area was kept constant in each simulation condition to understand the effect of size and spacing distributions. In general, fragmentation of a larger intermetallic particle into smaller ones was determined to enhance the localized current density. However, the uniform distribution rather than clustered or non-uniform distribution of this small intermetallic phase throughout the matrix was found to reduce the overall dissolution current density and hence, pitting corrosion severity.

## Keywords

Cathodic particles • Numerical simulation • Localized corrosion • Fragmentation

## Introduction

A combination of high strength to weight ratio, excellent biocompatibility, and superior damping capacity makes magnesium (Mg) based alloys a prime material for

V. K. Beura · P. Garg · K. N. Solanki (✉)  
School for Engineering of Matter, Transport and Energy,  
Arizona State University, Tempe, AZ 85287, USA  
e-mail: [kiran.solanki@asu.edu](mailto:kiran.solanki@asu.edu)

V. V. Joshi  
Pacific Northwest National Laboratory, Energy and Environment  
Directorate, 902 Battelle Boulevard, Richland, WA 99354, USA

automotive, biomedical and structural applications [1–5]. However, poor corrosion resistance of these alloys limits their widespread applicability. For instance, with Mg being the most electrochemically active element in the periodic table, Mg-based alloys undergo severe galvanic corrosion while forming joints with other structural materials [6]. In addition, Mg alloys undergo localized corrosion due to the presence of cathodic second phase particles and inclusion within the matrix [7–9]. The severity of localized corrosion is strongly dependent on the size and spacing distributions of the second phase within the Mg matrix. Besides cathodic particles, grain size [10, 11], crystal texture [12, 13] and prior processing conditions [14, 15] also alters the general corrosion behavior of Mg alloys. Therefore, suitable optimization of mentioned parameters (e.g., particle size and spacing distribution, heat treatment, etc.) can be done to tailor and improve the corrosion resistance of Mg alloys.

In most Mg alloys, Al<sub>8</sub>Mn<sub>5</sub> and  $\beta$ -Mg<sub>17</sub>Al<sub>12</sub> are the main cathodic intermetallic particles [7, 16] and their size/spacing distribution depends on different thermo-mechanical heat treatment processes. Many studies have focused on understanding the influence of change in the cathodic particle distribution on the corrosion behavior as well as mechanical properties of Mg alloys [17–21]. Fragmentation and rearrangement of  $\beta$  phase along with generation of different defects like vacancies, dislocation, and twins have been observed to degrade the corrosion resistance of hot-extruded AZ91 alloy with respect to its cast counterpart [15]. Similarly, the corrosion susceptibility of equal channel angular extrusion (ECAE) processed Mg alloys was found higher in comparison to as-cast pure Mg and AZ31 alloys due to its high dislocation density and smaller deformed grains [22, 23]. In contrast, Zhang et al. showed that extruded Mg alloys have enhanced corrosion resistance in comparison to as-cast Mg alloy due to grain refinement and rearrangement of second phase particles although there is an increase in dislocation and defect density with deformation [24]. This ambiguity arises from the presence and inter-dependance of a number of factors like grain size, texture, defect density

due to deformation, second phase particle size and distribution in the matrix. Therefore, it is highly important to understand the individual effect of each parameter as well as their interdependence to design future generations of Mg-based alloys.

It is difficult to deconvolute the effect of above-mentioned parameters through experimental technique performed by different thermo-mechanical processes due to their interdependence and complexity of real-time corrosion process. However, a combined approach of experiments along with simulations can be a viable approach to tackle this problem. Many studies have been performed to simulate the galvanic corrosion [25–28] and localized corrosion behavior in aluminum [29, 30] and magnesium alloys [31] and validated with the required experimental work [32]. However, a limited number of works have been performed to apply the simulation methodology to study the influence of above-described parameters on the corrosion behavior of Mg-based alloys. Taleb et al. [33] studied the effect of grain size on corrosion behavior through a simulation study using cellular automata model. Similarly, Deshpande [31] investigated the effect of  $\beta$  phase morphology and phase fraction on micro galvanic corrosion behavior of Mg alloys using a finite element based model. However, generally during thermo-mechanical processing in combination to phase morphology its distribution varies keeping average surface fraction constant and this variation in distribution affects the corrosion properties as observed experimentally in ECAE, extrusion, and shear assisted processing and extrusion (ShAPE) [34–36] of Mg-based alloys. Therefore, in this study, a finite element based numerical framework was used to study the effect of size and distribution of cathodic intermetallic phase ( $\beta$ -Mg<sub>17</sub>Al<sub>12</sub>) on localized corrosion behavior of Mg alloy. A single cathodic intermetallic phase was disintegrated into several smaller particles keeping the overall cathodic surface area hence cathode to anode ratio constant, to observe the effect of fragmentation on current density of the system. Additionally, spatial distribution of fragmented particles was varied by changing the radial separation distance between them to observe the effect of distribution on the localized corrosion behavior of Mg alloy.

## Model Development

The micro-galvanic/localized corrosion behavior between the matrix phase ( $\alpha$ ) and the cathodic intermetallic phase ( $\beta$ ) in Mg alloys was simulated using Comsol simulation software. The governing Nernst plank equation was solved in the electrolyte domain over the anode and cathode electrode surface in the stationary mode. Mass transfer of ionic species in the aqueous electrolyte can be described by the

contribution from diffusion, migration, and convection which can be expressed by the Nernst Plank Equation as [27]:

$$\frac{\partial c_i}{\partial t} = -D_i \nabla^2 c_i - z_i F u_i \nabla \cdot (c_i \nabla \varphi) + \nabla \cdot (c_i V) \quad (1)$$

where  $D_i$  is the diffusion coefficient,  $c_i$  is the concentration,  $z_i$  is the charge number,  $u_i$  is the mobility of different species involved in the electrochemical processes.  $F$ , and  $\varphi$ , are Faraday constant, and electric potential measured with respect to standard calomel electrode and electrolyte velocity ( $V$ ), respectively. Nernst plank equation (Eq. 1) can be further simplified for steady-state conditions with the following assumptions (i) negligible concentration gradient due to the well-mixed electrolyte solution; (ii) the solvent is incompressible; and (iii) the electrolyte solution is electroneutral, i.e.,  $\sum z_i c_i = 0$  to Eq. 2.

$$\nabla^2 \varphi = 0 \quad (2)$$

Equation 2 represents the Laplace of electric potential with the upper bound of corrosion rate after neglecting the transport term due to diffusion and convection. Equation 2 was solved numerically in the electrolyte domain with appropriate boundary conditions like in the anodic and cathodic surface gradient of electrolyte potential field is directly proportional to current density, and can be written as:

$$j = -\sigma \nabla_n \varphi \quad (3)$$

where  $\sigma$  is the conductivity of electrolyte (2.5 S/m).

Two computational domains were used in this study to simulate the localized corrosion behavior of Mg alloy (Fig. 1). Figure 1a shows a square domain of size 50  $\mu\text{m}$   $\times$  50  $\mu\text{m}$  that represents the electrolyte over cathode ( $\beta$ ) and anode ( $\alpha$ ) 1D electrode surface and it was used to study the effect of second phase particle size and separation on localized corrosion behavior in Sects. 3.1 and 3.2 respectively. The cylindrical domain, shown in Fig. 1b was used to study the effect of second phase particle fragmentation and distribution on localized corrosion behavior in Sect. 3.3. The cylindrical domain has base diameter of 50  $\mu\text{m}$  and height of 50  $\mu\text{m}$  that represents the electrolyte over cathode ( $\beta$ ) and anode ( $\alpha$ ) 2D electrode surface. Volume and conductivity of the electrolytes in both the domains were kept constant throughout the study. However, the size of electrode surfaces was varied keeping combined electrode surface length (50  $\mu\text{m}$ ) and electrode surface area (1962.5  $\mu\text{m}^2$ ) constant in both 1D and 2D computational domains, respectively. Insulating boundary conditions were used at all boundaries of the computational domain except for the electrode surfaces where electrolyte potential was solved using Eq. 3.

Furthermore, current density evolution at cathode and anode electrode surfaces was solved using anodic and cathodic Tafel extrapolation parameters as input variables. Experimental polarization curves for alpha ( $\alpha$ ) and beta ( $\beta$ ) were used [31] to extract the required electrochemical parameters using EC-lab software. Table 1 shows the list of electrochemical parameters used to simulate micro-galvanic corrosion behavior in Mg alloy.

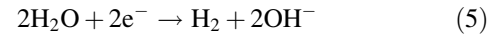
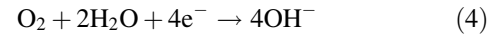
## Result and Discussion

### Effect of Second Phase Particle Size

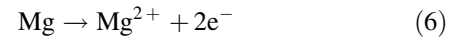
The variation in size of second phase particles in Mg alloys ranging from micrometers to nanometers is significantly dependent on the prior heat treatment and thermo-mechanical processing of the alloy [37]. Localized corrosion in Mg alloys also depends on the size of the cathodic phases beside their composition. Therefore, to understand the size effect of  $\beta$  phase on corrosion behavior particles of different radius ( $R_{\text{particles}}$ ) were used to study the variation of cathodic and anodic current density in the electrochemical system. Figure 2 shows the variation of current density as a function of cathodic particle size from 2 to 10  $\mu\text{m}$ . The cathodic current density increased on the  $\beta$  phase surface with increase in surface area of the second phase particle. Thus, the larger surface area provides more sites for cathodic reactions like hydrogen evolution and oxygen reduction (Eqs. 4 and 5) and drives the anodic reactions on the Mg matrix adjacent to the particle. The cathodic current density increased from  $-23.5$  to  $-17.5$   $\text{A}/\text{m}^2$ , around 30%, with increase of  $R_{\text{particle}}$  from 2 to 10  $\mu\text{m}$ . This increase in cathodic current density enhanced anodic dissolution

reaction on Mg matrix (Eq. 6) which shows an eight-fold increase in anodic current density as  $R_{\text{particle}}$  increased from 2 to 10  $\mu\text{m}$  (Fig. 2b). Thus, the region with bigger cathodic particle enhances localized matrix dissolution which makes the usage of alloy more detrimental for longer term as compared to the alloy with smaller cathodic particles.

Cathodic reaction:



Anodic reaction:



### Effect of Second Phase Particle Separation

Along with second phase particle size and composition, the separation between the particles also plays a crucial role to determine the intensity of localized corrosion. This separation distance depends on several factors like mechanical deformation, heat treatment, and other thermo-mechanical processing. The separation distance controls the interaction between two cathodic particles as well as the transport of reacting species within the local electrolyte. To observe the effect of separation distance ( $S$ ) two identical particles of different sizes ( $R_{\text{particle}}$ ) were used to study the corrosion behavior of the common matrix present in between them. Figure 3a shows the variation in anodic current density of the common matrix as a function of the separation distance. The anodic current density of the matrix increased with

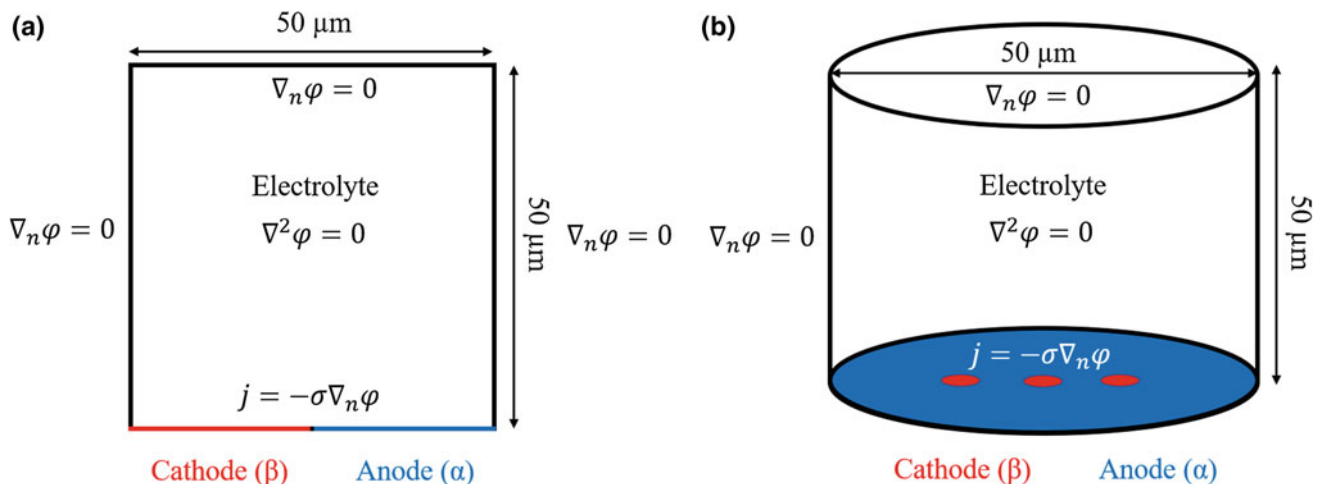


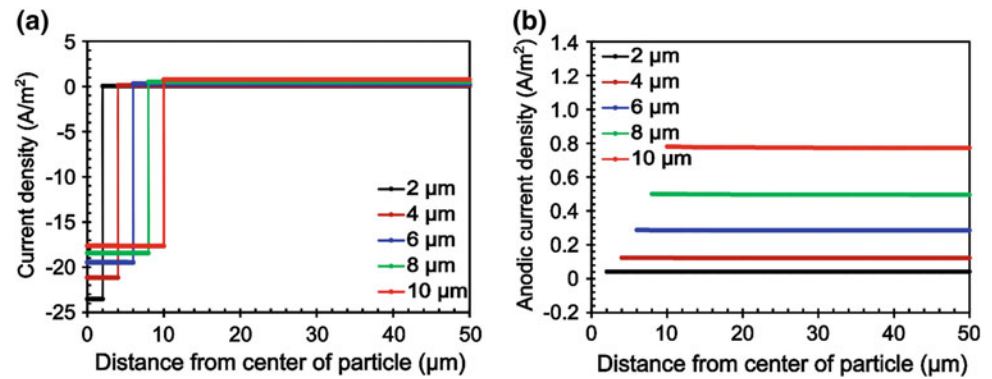
**Fig. 1** Computational domain of electrochemical system with necessary equations and boundary conditions for reacting and insulating surfaces. Red and blue lines/circles, respectively represent the cathode and anode electrode a 1D and b 2D surfaces



**Table 1** Electrochemical parameters used in this study to simulate the corrosion behavior of Mg alloy

Electrochemical parameters	Alpha ( $\alpha$ )	Beta ( $\beta$ )
Corrosion potential (V, SCE)	-1.424	-1.151
Exchange current density ( $A/m^2$ )	0.081	0.017
Tafel slope (V/decade)	0.008	-0.0835
Electrolyte conductivity (S/m)	2.5	

**Fig. 2** Effect of cathodic  $\beta$  phase size on the corrosion behavior a Variation in cathodic and anodic current density with  $\beta$  phase size ( $R_{\text{particle}}$ ). b Variation in anodic current density of adjacent matrix with  $\beta$  phase size ( $R_{\text{particle}}$ )



decreasing the separation distance between the particles which directly corresponds to the higher dissolution reaction at the matrix. As the separation distance increased further, a parabolic variation of matrix anodic current density was observed which was highest at the interface of cathodic particle and the matrix and it gradually decreased as we move away from interface showing a decrease in the inter-particle interaction. This variation of current density can be correlated with anodic and cathodic reactions on both the surfaces and their transport within the electrolyte. Due to shorter distance between particles like  $0.4 \mu\text{m}$ , availability of reducible species like  $\text{O}_2$  is easier due to smaller transport distances between the anode and cathode surfaces. This enhancement in anodic current density due to separation distance varies with size of the cathodic particle shown in Fig. 3b. A fivefold increase in current density can be observed with increase in  $R_{\text{particle}}$  from 2 to  $10 \mu\text{m}$ .

### Effect of Second Phase Particle Fragmentation and Separation

Generally, during processing and real-time applications both cast and processed Mg alloys undergo extreme conditions of high strain-rate deformation and/or high-temperature applications that lead to variation in cathodic particles distribution keeping the average area fraction constant. This process can also lead to the disintegration of larger cathodic particles into clusters of small-sized particles. Therefore, to understand the effect of such a complex process along with other microstructural changes can be a difficult task in terms of experimental characterization. Hence, a simulation study has

been implemented to understand effect of this phenomenon on corrosion behavior of Mg alloys. A cathodic  $\beta$  phase particle with  $10 \mu\text{m}$  radius was fragmented into smaller particles keeping the overall cathodic surface area and the ratio of anode to cathode surface area constant. Hence, the radius ( $R$ ) of fragmented particles decreased gradually with increasing number of fragmentations ( $N$ ). Furthermore, the separation distance ( $S$ ) between the fragmented particles was varied from  $0.2$  to  $20 \mu\text{m}$  to observe the effect of separation between the particles on corrosion behavior. Figure 4 shows variation in magnitude of electrolyte current density with change in the number of fragmentations ( $N$ ) and separation distance ( $S$ ) between the cathodic particles.

The electrolyte current density was observed to vary from  $0$  to  $23.7 A/m^2$  throughout the surface with a maximum in the region near to the cathodic particle (Fig. 4a). Furthermore, maximum current density around the cathodic particles found to increase as the number of fragmentation increased from  $N = 1$  to  $7$  (Fig. 4a). The system with maximum number of fragmentations ( $N = 7$ ) and the smallest separation distance ( $S = 0.2 \mu\text{m}$ ) had the highest electrolyte current density at the cathodic particles (Fig. 4b). Whereas, the electrolyte current density was minimum at the cathodic particles in the same system with highest separation distance ( $S = 20 \mu\text{m}$ ). To further understand these effects average electrolyte current density was calculated for each particle radius and corresponding all of the separation distances (Fig. 5).

Average electrolyte current density of single cathodic particle ( $R = 10 \mu\text{m}$ ) serves as a reference point for other measurements (black horizontal line at  $2.175 A/m^2$  in Fig. 5). The average electrolyte current density was found

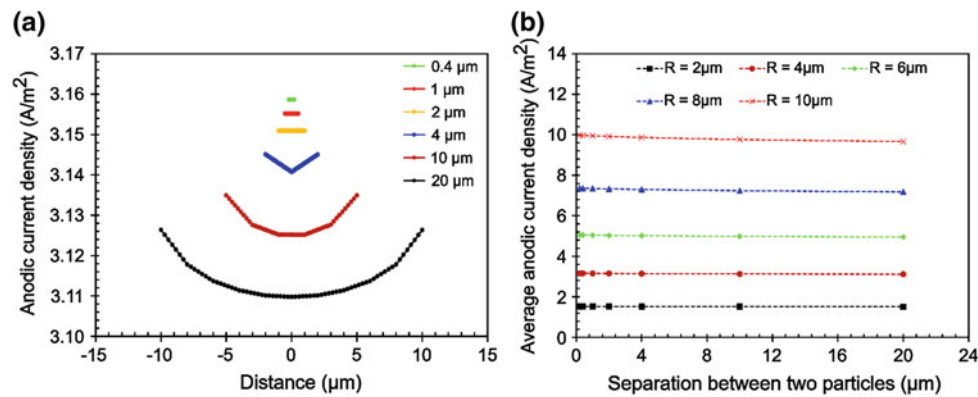


**Fig. 3** Effect of cathodic β phase separation on corrosion behavior. Separation distance of zero represents the center point between two particles and +ve/-ve distances represent displacement along left/right directions, respectively. a Variation in anodic current density of matrix

between two 4 μm β phase as a function of their separation. b The average anodic current density of the matrix between two β phases as a function of phase size and separation distance

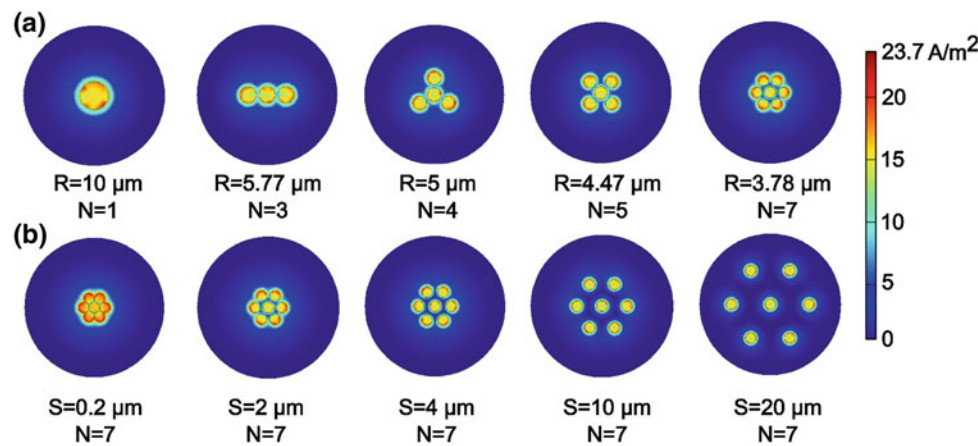


**Fig. 4** Effect of cathodic particle distribution on the magnitude of electrolyte current density. a Fragmentation of single cathodic β phase into different number of particles (N) with different size (R) keeping

overall anode to cathode ratio constant. b Change in anodic current density with increasing separation distance (S) between multiple fragmentations (N = 7) of cathodic particles of same radius

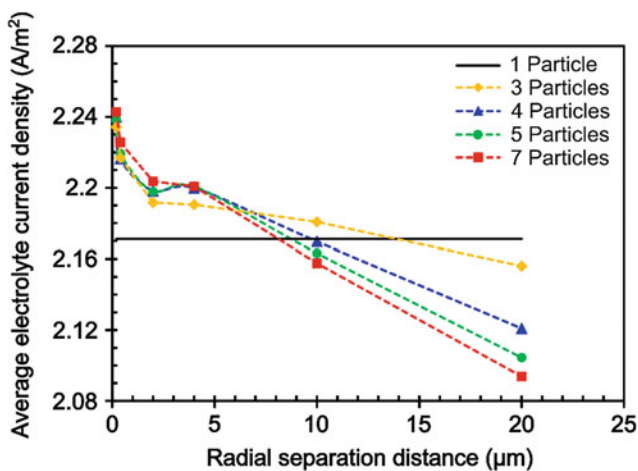


**Fig. 5** Variation of average electrolyte current density with cathodic β phase fragmentations (i.e., number of particles) from a larger particle and their radial separation from the center particle

to decrease with increasing the separation distance between the particles which suggests towards a decrease in corrosion susceptibility of the alloy. These results display a similar trend observed in Fig. 3, where the anodic current density of Mg matrix decreased with the increasing separation distance between two identical cathodic particles. However, if the average electrolyte current densities for different numbers of particles were compared it shows interesting behavior. The electrochemical system with 7 particles has the highest value of average electrolyte current density than other systems (1, 3, 4, 5 particles) in the range of radial separation distance 0.2 and 4 μm. On the other hand, 7 particle system showed the lowest value of average electrolyte current density at a radial separation distance of 10 and 20 μm as compared to the other systems. Furthermore, the systems with 1, 3, 4, 5 particles showed similar behavior as the average electrolyte current density of the

system with larger number of particle systems is lower as compared to the system with lower number of particles at the radial separation distance of 10 and 20  $\mu\text{m}$ . This behavior is due to decrease in the interparticle interaction and more homogenous distribution of cathodic particles with a higher number of fragmentation and radial separation. Therefore, to process a corrosion-resistant Mg alloy using various thermo-mechanical processing methods like ECAP, extrusion or ShAPE an effort should be made to have a possible smallest average particle size and the highest separation distance between the particles.

## Conclusions

A comprehensive finite element based simulation study was carried out to understand the effect of size and distribution of second phase cathodic particles on localized corrosion behavior of Mg alloys. The key observations of this work are:

1. Larger cathodic particles ( $R_{\text{particle}} = 10 \mu\text{m}$ ) enhanced anodic dissolution of the localized matrix due to enhanced cathodic reaction on their surface in comparison to the smaller size cathodic particles.
2. Interparticle interaction between two cathodic particles decreased with an increase in separation distance which reduced the anodic dissolution rate of common Mg matrix between them.
3. Corrosion behavior of Mg alloys depends on fragmentation and distribution of large cathodic particles into a cluster of smaller particles. In particular, increase in number of fragmentation enhances corrosion susceptibility of the localized system till the radial separation between the particles was less than a critical value (10  $\mu\text{m}$ ). However, once the separation is more than the critical value larger number of fragmentation shows the least susceptibility for corrosion.

**Acknowledgements** The authors would like to thank Pacific Northwest National Laboratory and the Office of Naval Research (N000141110793) for their financial assistance.

## References

1. M. Esmaily, J.E. Svensson, S. Fajardo, N. Birbilis, G.S. Frankel, S. Virtanen, R. Arrabal, S. Thomas, L.G. Johansson, Fundamentals and advances in magnesium alloy corrosion, *Progress in Materials Science*. 89 (2017) 92–193. <https://doi.org/10.1016/j.pmatsci.2017.04.011>.
2. G. Song, Recent Progress in Corrosion and Protection of Magnesium Alloys, *Advanced Engineering Materials*. 7 (2005) 563–586. <https://doi.org/10.1002/adem.200500013>.
3. N.T. Kirkland, J. Lespagnol, N. Birbilis, M.P. Staiger, A survey of bio-corrosion rates of magnesium alloys, *Corrosion Science*. 52 (2010) 287–291. <https://doi.org/10.1016/j.corsci.2009.09.033>.
4. P. Garg, I. Adlakha, K.N. Solanki, Effect of solutes on ideal shear resistance and electronic properties of magnesium: A first-principles study, *Acta Materialia*. 153 (2018) 327–335. <https://doi.org/10.1016/j.actamat.2018.05.014>.
5. C. Kale, M. Rajagopalan, S. Turnage, B. Hornbuckle, K. Darling, S.N. Mathaudhu, K.N. Solanki, On the roles of stress-triaxiality and strain-rate on the deformation behavior of AZ31 magnesium alloys, *Materials Research Letters*. 6 (2018) 152–158. <https://doi.org/10.1080/21663831.2017.1417923>.
6. G. Song, B. Johannesson, S. Hapugoda, D. StJohn, Galvanic corrosion of magnesium alloy AZ91D in contact with an aluminium alloy, steel and zinc, *Corrosion Science*. 46 (2004) 955–977. [https://doi.org/10.1016/s0010-938x\(03\)00190-2](https://doi.org/10.1016/s0010-938x(03)00190-2).
7. O. Lunder, J.E. Lein, T.K. Aune, K. Nisancioglu, The Role of Mg<sub>17</sub>Al<sub>12</sub> Phase in the Corrosion of Mg Alloy AZ91, *CORROSION*. 45 (1989) 741–748. <https://doi.org/10.5006/1.3585029>.
8. S. Mathieu, C. Rapin, J. Steinmetz, P. Steinmetz, A corrosion study of the main constituent phases of AZ91 magnesium alloys, *Corrosion Science*. 45 (2003) 2741–2755. [https://doi.org/10.1016/s0010-938x\(03\)00109-4](https://doi.org/10.1016/s0010-938x(03)00109-4).
9. R. Ambat, N.N. Aung, W. Zhou, Evaluation of microstructural effects on corrosion behaviour of AZ91D magnesium alloy, *Corrosion Science*. (2000) 23.
10. N.N. Aung, W. Zhou, Effect of grain size and twins on corrosion behaviour of AZ31B magnesium alloy, *Corrosion Science*. 52 (2010) 589–594. <https://doi.org/10.1016/j.corsci.2009.10.018>.
11. K.D. Ralston, N. Birbilis, Effect of Grain Size on Corrosion: A Review, *CORROSION*. 66 (2010) 075005-075005-13. <https://doi.org/10.5006/1.3462912>.
12. G.-L. Song, R. Mishra, Z. Xu, Crystallographic orientation and electrochemical activity of AZ31 Mg alloy, *Electrochemistry Communications*. 12 (2010) 1009–1012. <https://doi.org/10.1016/j.elecom.2010.05.011>.
13. Z. Pu, G.-L. Song, S. Yang, J.C. Outeiro, O.W. Dillon, D.A. Puleo, I.S. Jawahir, Grain refined and basal textured surface produced by burnishing for improved corrosion performance of AZ31B Mg alloy, *Corrosion Science*. 57 (2012) 192–201. <https://doi.org/10.1016/j.corsci.2011.12.018>.
14. H. Wang, Y. Estrin, H. Fu, G. Song, Z. Zúberová, The Effect of Pre-Processing and Grain Structure on the Bio-Corrosion and Fatigue Resistance of Magnesium Alloy AZ31, *Advanced Engineering Materials*. 9 (2007) 967–972. <https://doi.org/10.1002/adem.200700200>.
15. T. Zhang, Y. Shao, G. Meng, Z. Cui, F. Wang, Corrosion of hot extrusion AZ91 magnesium alloy: I-relation between the microstructure and corrosion behavior, *Corrosion Science*. 53 (2011) 1960–1968. <https://doi.org/10.1016/j.corsci.2011.02.015>.
16. A. Pardo, M.C. Merino, A.E. Coy, F. Viejo, R. Arrabal, S. Feliú, Influence of microstructure and composition on the corrosion behaviour of Mg/Al alloys in chloride media, *Electrochimica Acta*. 53 (2008) 7890–7902. <https://doi.org/10.1016/j.electacta.2008.06.001>.
17. S. Lee, S.H. Lee, D.H. Kim, Effect of Y, Sr, and Nd additions on the microstructure and microfracture mechanism of squeeze-cast AZ91-X magnesium alloys, *Metallurgical and Materials Transactions A*. 29 (1998) 1221–1235. <https://doi.org/10.1007/s11661-998-0249-0>.
18. D.K. Xu, W.N. Tang, L. Liu, Y.B. Xu, E.H. Han, Effect of Y concentration on the microstructure and mechanical properties of as-cast Mg–Zn–Y–Zr alloys, *Journal of Alloys and Compounds*. 432 (2007) 129–134. <https://doi.org/10.1016/j.jallcom.2006.05.123>.

19. M. Horstemeyer, High cycle fatigue of a die cast AZ91E-T4 magnesium alloy, *Acta Materialia*. 52 (2004) 1327–1336. <https://doi.org/10.1016/j.actamat.2003.11.018>.
20. H. Feng, S. Liu, Y. Du, T. Lei, R. Zeng, T. Yuan, Effect of the second phases on corrosion behavior of the Mg-Al-Zn alloys, *Journal of Alloys and Compounds*. 695 (2017) 2330–2338. <https://doi.org/10.1016/j.jallcom.2016.11.100>.
21. X. Chen, F. Pan, J. Mao, J. Wang, D. Zhang, A. Tang, J. Peng, Effect of heat treatment on strain hardening of ZK60 Mg alloy, *Materials & Design*. 32 (2011) 1526–1530. <https://doi.org/10.1016/j.matdes.2010.10.008>.
22. G.B. Hamu, D. Eliezer, L. Wagner, The relation between severe plastic deformation microstructure and corrosion behavior of AZ31 magnesium alloy, *Journal of Alloys and Compounds*. 468 (2009) 222–229. <https://doi.org/10.1016/j.jallcom.2008.01.084>.
23. D. Song, A. Ma, J. Jiang, P. Lin, D. Yang, J. Fan, Corrosion behavior of equal-channel-angular-pressed pure magnesium in NaCl aqueous solution, *Corrosion Science*. 52 (2010) 481–490. <https://doi.org/10.1016/j.corsci.2009.10.004>.
24. Z. Zhang, H. Xu, qiang Wang, Corrosion and mechanical properties of hot-extruded AZ31 magnesium alloys, *Transactions of Nonferrous Metals Society of China*. 18 (2008) s140–s144. [https://doi.org/10.1016/s1003-6326\(10\)60190-2](https://doi.org/10.1016/s1003-6326(10)60190-2).
25. I. Adlakha, B.G. Bazehhour, N.C. Muthgowda, K.N. Solanki, Effect of mechanical loading on the galvanic corrosion behavior of a magnesium-steel structural joint, *Corrosion Science*. 133 (2018) 300–309. <https://doi.org/10.1016/j.corsci.2018.01.038>.
26. K.B. Deshpande, Validated numerical modelling of galvanic corrosion for couples: Magnesium alloy (AE44)–mild steel and AE44–aluminium alloy (AA6063) in brine solution, *Corrosion Science*. 52 (2010) 3514–3522. <https://doi.org/10.1016/j.corsci.2010.06.031>.
27. B. Gholami Bazehhour, I. Adlakha, K.N. Solanki, Role of Static and Cyclic Deformation on the Corrosion Behavior of a Magnesium-Steel Structural Joint, *JOM*. 69 (2017) 2328–2334. <https://doi.org/10.1007/s11837-017-2433-4>.
28. K.A. Spies, V.V. Viswanathan, A. Soulami, Y. Hovanski, V.V. Joshi, Galvanically Graded Interface: A Computational Model for Mitigating Galvanic Corrosion Between Magnesium and Mild Steel, in: V.V. Joshi, J.B. Jordon, D. Orlov, N.R. Neelameggham (Eds.), *Magnesium Technology 2019*, Springer International Publishing, Cham, 2019: pp. 135–144. [https://doi.org/10.1007/978-3-030-05789-3\\_21](https://doi.org/10.1007/978-3-030-05789-3_21).
29. L. Yin, Y. Jin, C. Leygraf, N. Birbilis, J. Pan, Numerical Simulation of Micro-Galvanic Corrosion in Al Alloys: Effect of Geometric Factors, *Journal of The Electrochemical Society*. 164 (2017) C75–C84. <https://doi.org/10.1149/2.1221702jes>.
30. J. Xiao, S. Chaudhuri, Predictive modeling of localized corrosion: An application to aluminum alloys, *Electrochimica Acta*. 56 (2011) 5630–5641. <https://doi.org/10.1016/j.electacta.2011.04.019>.
31. K.B. Deshpande, Numerical modeling of micro-galvanic corrosion, *Electrochimica Acta*. 56 (2011) 1737–1745. <https://doi.org/10.1016/j.electacta.2010.09.044>.
32. N. Murer, R. Oltra, B. Vuillemin, O. Néel, Numerical modelling of the galvanic coupling in aluminium alloys: A discussion on the application of local probe techniques, *Corrosion Science*. 52 (2010) 130–139. <https://doi.org/10.1016/j.corsci.2009.08.051>.
33. A. Taleb, J. Stafiej, Numerical simulation of the effect of grain size on corrosion processes: Surface roughness oscillation and cluster detachment, *Corrosion Science*. 53 (2011) 2508–2513. <https://doi.org/10.1016/j.corsci.2011.04.008>.
34. J.T. Darsell, N.R. Overman, V.V. Joshi, S.A. Whalen, S.N. Mathaudhu, Shear Assisted Processing and Extrusion (ShAPE™) of AZ91E Flake: A Study of Tooling Features and Processing Effects, *Journal of Materials Engineering and Performance*. 27 (2018) 4150–4161. <https://doi.org/10.1007/s11665-018-3509-1>.
35. N.R. Overman, S.A. Whalen, M.E. Bowden, M.J. Olszta, K. Kruska, T. Clark, E.L. Stevens, J.T. Darsell, V.V. Joshi, X. Jiang, K.F. Mattlin, S.N. Mathaudhu, Homogenization and texture development in rapidly solidified AZ91E consolidated by Shear Assisted Processing and Extrusion (ShAPE), *Materials Science and Engineering: A*. 701 (2017) 56–68. <https://doi.org/10.1016/j.msea.2017.06.062>.
36. S. Whalen, N. Overman, V. Joshi, T. Varga, D. Graff, C. Lavender, Magnesium alloy ZK60 tubing made by Shear Assisted Processing and Extrusion (ShAPE), *Materials Science and Engineering: A*. 755 (2019) 278–288. <https://doi.org/10.1016/j.msea.2019.04.013>.
37. W. Fu, R. Wang, K. Wu, J. Kuang, J. Zhang, G. Liu, J. Sun, The influences of multiscale second-phase particles on strength and ductility of cast Mg alloys, *Journal of Materials Science*. 54 (2019) 2628–2647. <https://doi.org/10.1007/s10853-018-2980-2>.



# The Corrosion Behavior of High Purity Mg According to Process History

Sang Kyu Woo, Byeong-Chan Suh, Nam Ryong Kim, Ha Sik Kim, and Chang Dong Yim

## Abstract

This study paid attention to the big difference between the corrosion rates of permanent mold cast and hot-extruded pure Mg. Fe existed as different state according to process history, which affected the corrosion behavior of pure Mg largely. The corrosion rate of high purity Mg was measured extremely low when Fe was dissolved into the matrix as a solid solution while it increased dramatically when Fe was precipitated as a second phase. The precipitation behavior of the second phase containing Fe was affected by other impurities as much as thermal history, which affected the corrosion behavior of high purity Mg. It is suggested from this study that the tolerance limit of Fe is strongly dependent on the content of Fe, the sort and content of other impurities and process history, which should be considered to design the composition and processing route of high corrosion-resistant Mg alloy.

## Keywords

High-purity magnesium • Impurity • Micro-galvanic corrosion • Processing history

## Introduction

Mg alloys have many advantages such as high specific strength and damping capacity but they also have some disadvantages such as poor corrosion resistance and

formability. These weaknesses must be overcome for the widespread application of Mg alloys. The corrosion behavior of Mg is affected by various factors and it is well known that the effects of impurities including Fe are very dominant [1–7]. In other words, the corrosion rate of Mg is strongly dependent on the purity of the Mg. In casting of pure Mg, very fast corrosion rates from several mm/y to several hundred mm/y have been reported for the commercially pure Mg [1–4] while high pure Mg with well-controlled level of impurities showed much slower corrosion rate of below 1 mm/y [1–6]. The pure Mg with ultra-high purity showed an extremely slow corrosion rate of 0.25 mm/y [7]. However, there was large difference between the corrosion rates of pure Mg reported from previous studies in spite of similar content of Fe [3, 5, 8, 9]. Liu et al. [3] and Zhao et al. [5] reported the slow corrosion rate of 1 mm/y for pure Mg containing 45 ppm Fe while Prado et al. [8] reported much faster corrosion rate of over 600 mm/y for pure Mg containing 40 ppm Fe. Yang et al. [9] showed the corrosion rate of 4 mm/y for pure Mg containing 13 ppm Fe which was much lower than 40 ppm. It is interesting that the content of Fe in the pure Mg studied previously [3, 5, 8, 9] was similar but the processing route was different. The pure Mg treated by thermo-mechanical process (TMP) showed faster corrosion rate than as-cast pure Mg. Liu et al. [3], Song et al. [10] and Sudholz et al. [11] reported that the corrosion rate of pure Mg cast increased significantly by additional process such as heat treatment.

Although there are many studies on the corrosion behavior of pure Mg, the reason for the different corrosion behavior according to the processing route in spite of similar Fe content was not clearly examined yet. In this study, the corrosion rate of pure Mg with high purity prepared by different processes including permanent mold casting, homogenization heat treatment after casting, hot extrusion and annealing after hot extrusion was systematically evaluated and analyzed on the basis of microstructure in order to clarify the corrosion mechanism of pure Mg.

S. K. Woo · N. R. Kim · C. D. Yim (✉)  
Advanced Materials Engineering, University of Science and Technology, 217 Gajungro, Yuseong-gu, Daejeon, 34113, Republic of Korea  
e-mail: [cdyim03@kims.re.kr](mailto:cdyim03@kims.re.kr)

B.-C. Suh · H. S. Kim · C. D. Yim  
Advanced Metals Division, Korea Institute of Materials Science, 797 Changwondaero, Seongsan-gu, Changwon, 51508, Republic of Korea

## Experimental Procedure

Pure Mg ingot with purity of 99.99% (4N) was used as raw material for preparation of test specimens. The ingot was put into a graphite crucible and heated to 700 °C under a protective atmosphere of CO<sub>2</sub> and SF<sub>6</sub> gases using electrical resistance furnace. The stirring and bubbling were carried out for refining of the molten Mg with Ar gas at a flow rate of 0.5 L/min. at 700 °C for 10 min and the dross on the surface was removed after holding for 30 min. The molten Mg at 700 °C was poured into a metal mold preheated to 200 °C through a filter. A billet for hot extrusion was prepared by the same procedure as mentioned above. Before extrusion, a homogenization heat treatment was carried out for 24 h at 400 °C. After heat treatment, the billet was machined into the billet of 78 mm in diameter and 110 mm in length for extrusion. The machined billet was preheated to 350 °C and then directly extruded through a rectangular die. The die and container were also preheated to 350 °C. The extrusion ratio and ram speeds were 25:1 and 1 mm/sec., respectively. Table 1 shows the composition of pure Mg measured by spark optical emission spectroscopy (OES).

The specimen for microstructural observation was cut from the cast and extruded plate and mounted by epoxy resin. The mounted specimen was mechanically ground using SiC papers up to #2400 grit and then polished using 3 μm diamond paste and water-free oxide polishing suspension (OPS). The polished specimen was etched using a mixed solution of 1 mL of nitric acid, 20 mL of distilled water, 20 mL of acetic acid, and 70 mL of ethylene glycol. The microstructures of specimens were observed by an optical microscope (OM, Nikon Optiphot 200), scanning electron microscope (SEM, IT-300 and JSM-7001F, JEOL) equipped with an energy-dispersive X-ray spectroscopy (EDS) and a backscattered secondary electron (BSE). The composition and diffraction pattern analysis were performed using a transmission electron microscope (TEM, JEM 2100F, JEOL). The focused ion beam (FIB, Helios UMS II, FEI) was used to confirm and to prepare the particles.

The corrosion rate of pure Mg prepared by different processing routes was evaluated by the immersion test. The specimen of 40 mm in width, 40 mm in length, and 3 mm in thickness was machined from the cast and extruded plates and then ground mechanically using SiC papers up to #2400 grit. The specimens were immersed in 3.5 wt% NaCl

for 72 h and temperature was maintained at 25 °C in temperature control chamber. After immersion test during given period, the specimens were cleaned through immersion in a mixed solution of 170 g/L CrO<sub>3</sub> + 10 g/L AgNO<sub>3</sub> to remove the corrosion products, and then the weight loss of the specimen was measured. The corrosion rate was determined as the average value of at least three test results, and the standard deviation was expressed with an error bar. KPFM (kelvin probe force microscopy) analysis was carried out using AFM (atomic force microscopy, Nanoscope V Multimode 8, Bruker) to analyze the effect of the particles on the corrosion behavior. The Volta potential difference (VPD) was measured and the variation of corrosion behavior was investigated. All measurements were carried out using a Pt-coated probe at a temperature of about 22 °C and relative humidity of about 20%.

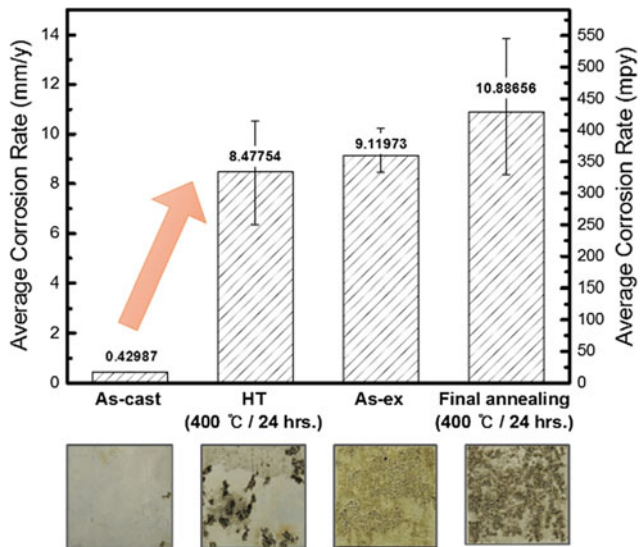
## Results and Discussion

Figure 1 shows the average corrosion rates and external surfaces after immersion test of pure Mg specimens prepared through different processing routes. The corrosion rate was calculated from weight loss before and after immersion test and the average value was determined from the results of three specimens. The corrosion rate of as-cast pure Mg dramatically increased after homogenization heat treatment from  $0.430 \pm 0.012$  to  $8.478 \pm 2.095$  mm/y. The corrosion rate increased more after hot extrusion and annealing after hot extrusion. As shown in Fig. 1, only a few small pits were observed around edge in as-cast pure Mg and corrosion occurred rarely in other areas after 72 h immersion in 3.5 wt % NaCl solution. On the other hand, very deep pits were observed in the pure Mg homogenized after casting. In the case of as-extruded specimen, the pits were more widely formed over whole surface and the size and distribution uniformity of the pits increased by annealing. As shown in Fig. 1, the corrosion behavior of pure Mg changed largely according to the processing route in spite of same composition.

Figure 2a shows the BSE image of the particle observed in the as-extruded pure Mg and Fig. 2b shows the composition of the particle analyzed by the EDS. These particles were identified as particles containing Fe and Si and hardly observed in the as-cast pure Mg. The specimens for TEM

**Table 1** Chemical composition of HP pure Mg measured by spark OES

Alloy	Mg	Al	Mn	Fe	Si	Ca	Cu	Ni
		wt.ppm						
HP pure Mg	Bal.	<1	22	19	19	25	4	<5



**Fig. 1** Average corrosion rates and corroded surfaces of pure Mg specimens with high purity prepared by different processing routes after immersion/n in 3.5 wt% NaCl solution during 72 h

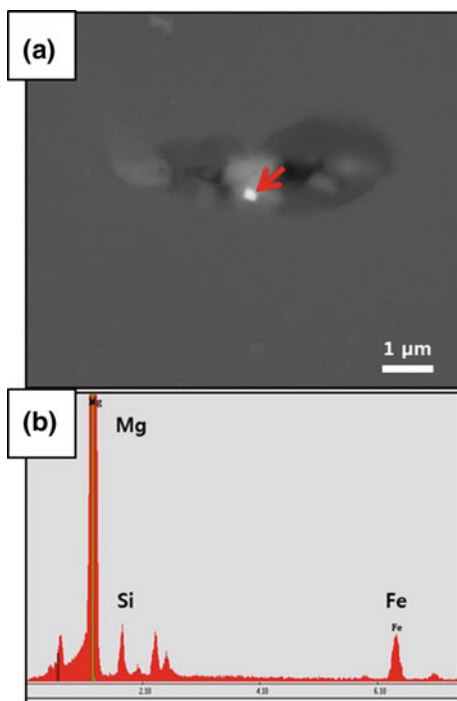


**Fig. 2** Backscattered secondary electron images and composition analysis of particle in as-extruded HP pure Mg; **a** BSE images of particle, **b** composition of particle analyzed by EDS

analysis were taken from the area containing the particles in Fig. 2a using FIB, and systematic analysis on the particle was carried out.

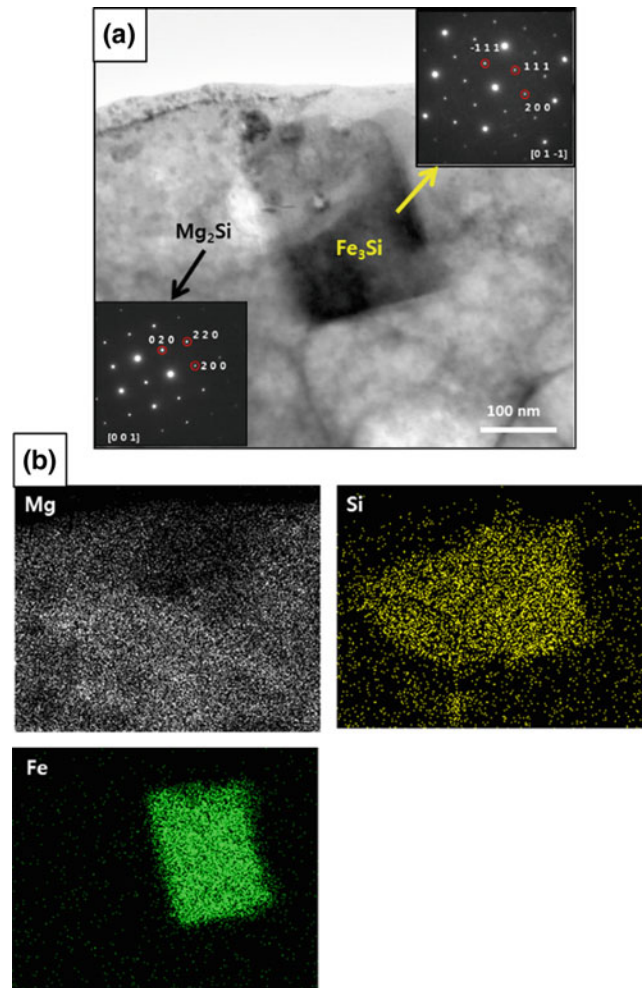


**Fig. 3** TEM analysis of Fe-containing particle and Si-rich particle; **a** STEM image and diffraction patterns of  $\text{Fe}_3\text{Si}$  and  $\text{Mg}_2\text{Si}$  phases, **b** elemental maps of Mg, Si, and Fe

Figure 3a shows the STEM image and diffraction pattern of particles observed in the as-extruded pure Mg and Fig. 3b shows the elemental mapping results of Mg, Fe, and Si. As shown in Fig. 3, Fe was detected with Si and the molar ratio of Fe to Si was about 3:1. The particle-containing Fe and Si was identified as the  $\text{Fe}_3\text{Si}$  particle having a DO3 structure on the basis of results of EDS and diffraction pattern analysis. The Si-rich particle was detected together with  $\text{Fe}_3\text{Si}$  particle and it was identified as the  $\text{Mg}_2\text{Si}$  particle having a cF12 structure.

It is well known that there is potential difference between the matrix and the secondary phase particle in Mg-based material and this difference is one of the major reasons for poor corrosion resistance of Mg-based material. Therefore, the potential difference between the secondary phase particles and the matrix of the pure Mg was measured by KPFM



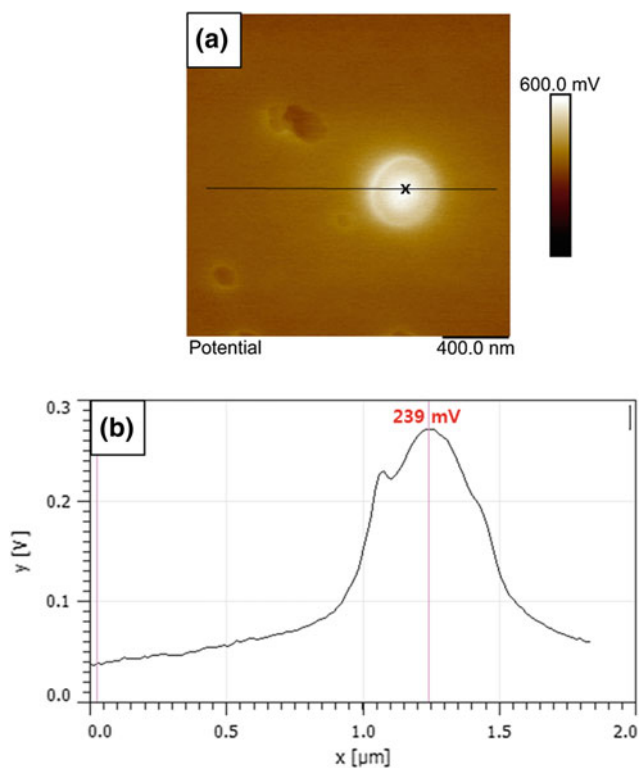


**Fig. 4** KPFM results of as-extruded pure Mg; **a** Volta potential difference (VPD) map, **b** Line profile of potential for Fe<sub>3</sub>Si particle and Mg matrix on VPD map

in order to investigate the effect of secondary phase particles on the corrosion behavior of pure Mg.

Figure 4a is a Volta potential difference map (VPD map) based on KPFM measurement for the area containing Fe<sub>3</sub>Si particle and a line profile of the potential values for each phase is shown in Fig. 4b. As shown in Fig. 4, Fe<sub>3</sub>Si particle has a relatively higher potential compared to the Mg matrix. This makes it clear that the Fe<sub>3</sub>Si particle would serve as the main cathodic source and the micro-galvanic corrosion between the Fe<sub>3</sub>Si particle and the matrix was main corrosion mechanism of as-extruded pure Mg. As shown in Fig. 5a, corrosion occurred preferentially around Fe<sub>3</sub>Si particle and Fe<sub>3</sub>Si particle was covered with oxide as shown in Fig. 5b.

On the basis of the results shown above, it seemed that the Fe-containing particle played an important role in corrosion behavior of pure Mg prepared by different processing routes. Therefore, it is necessary to investigate the reason why Fe-containing particle was not observed in the as-cast pure Mg although the content of impurities was same. Liu et al. [3] reported that 180 ppm, which is the point of BCC phase formation, is in good agreement with experimental tolerance limit of Fe (150–170 ppm) based on the equilibrium phase diagram of Mg–Fe [2, 3, 12]. It indicates that the presence of this BCC phase is closely related to the tolerance

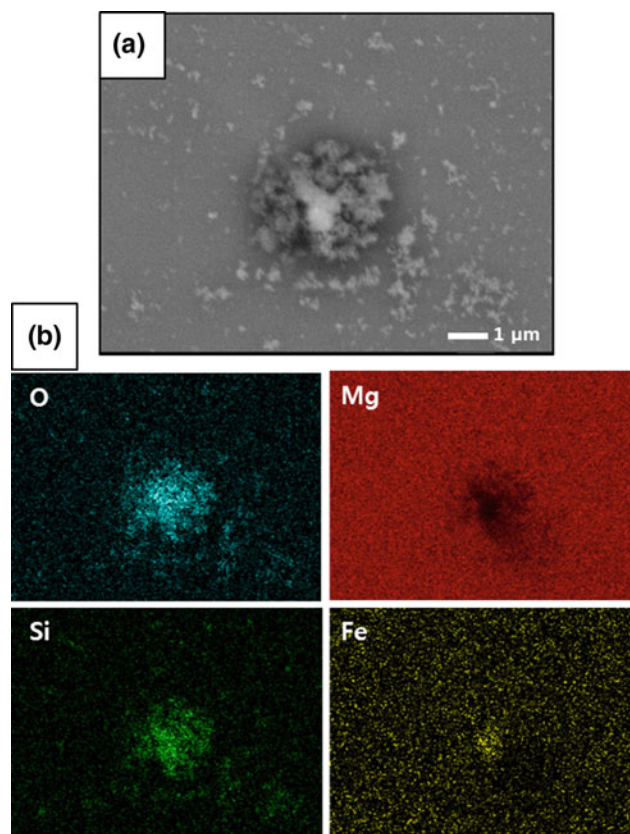


**Fig. 5** The corroded morphology of Fe-containing particle in as-extruded pure Mg after immersion in 3.5% NaCl solution; **a** BSE images of particle, **b** Elemental maps of Mg, O, Si and Fe

limit of Fe. Liu et al. [3] suggested that in pure Mg having less than 180 ppm of Fe, the two-phase region of  $\alpha$ -Mg and liquid Mg was very narrow and then Fe might be dissolved in the Mg lattice as a supersaturated solid solution during non-equilibrium solidification. In this case, as in the case of pure Mg having Fe of 10 ppm or less, the BCC phase does not exist and micro-galvanic corrosion does not occur, which results in low corrosion rate. They also insisted that the precipitation of BCC phase by heat treatment might cause an increase in the corrosion rate [3]. These suggestions are reasonable, but it is necessary to investigate the Mg–Fe–Si phase diagram instead of the Mg–Fe phase diagram in consideration of the fact that Si was always detected with Fe as in this study.

Figure 6 shows the Mg–Fe–Si equilibrium phase diagram calculated using the Factsage software. As shown in Fig. 6, Fe does not always exist alone and forms various Fe–Si phases depending on temperature and composition. Therefore, the influence of Si on the microstructure and corrosion behavior of pure Mg should be considered simultaneously. Yang et al. [13] carried out the study on the corrosion behavior of pure Mg having similar content of Fe and reported that high content of Si caused precipitation of



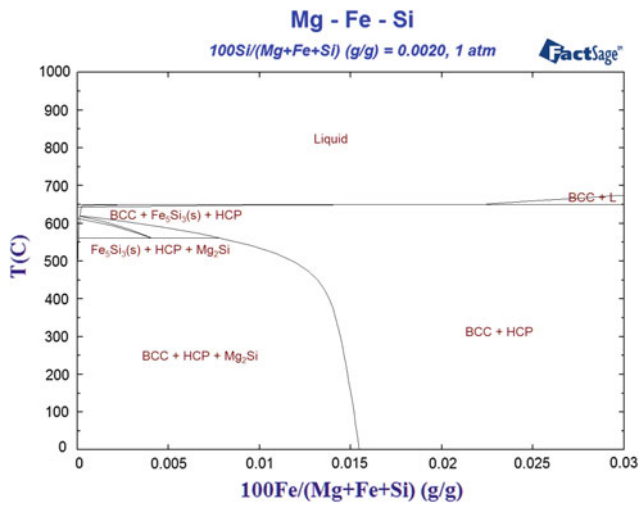


**Fig. 6** Mg–Fe–20 ppm Si phase diagram calculated with the Factsage software

Fe-rich phase during casting, which resulted in significant increase of the corrosion rate even though Fe content was low. It indicates that the presence of Si can lead to differences in corrosion rates in spite of similar Fe content.

In as-cast pure Mg containing low contents of Fe and Si, Fe would not precipitate during casting and exist as a supersaturated solid solution due to non-equilibrium solidification. Therefore, micro-galvanic corrosion would rarely occur in the as-cast pure Mg specimen, which resulted in slow corrosion rate. According to the phase diagram as shown in Fig. 6, Fe would be precipitated as BCC phase particle-containing Fe and Si during homogenization heat treatment. According to the Volta potential difference as shown in Fig. 4, micro-galvanic corrosion between the Mg matrix and BCC phase particle would occur actively, which resulted in fast corrosion rate. The corrosion rates of as-extruded pure Mg and annealed pure Mg after extrusion were a little faster than that of homogenized pure Mg after casting. It seemed that volume fraction and/or size of BCC phase particle would increase during preheating before extrusion and annealing, which resulted in slightly faster corrosion rate.

In order to demonstrate that precipitation of the particle-containing Fe and Si during homogenization heat treatment was the main factor of faster corrosion rate, the corrosion rate of as-extruded pure Mg prepared without homogenization heat treatment was compared with the corrosion rates of as-cast and as-extruded pure Mg with homogenization heat treatment as shown in Fig. 7. As shown in Fig. 7, the corrosion rate of as-extruded pure Mg

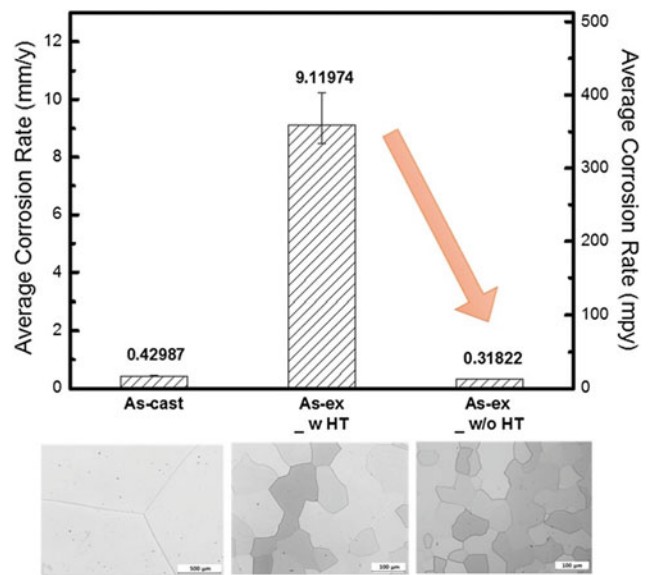


**Fig. 7** Average corrosion rates of pure Mg specimens prepared by different processing routes and microstructures of each specimen observed by OM

prepared without homogenization heat treatment was similar to the as-cast pure Mg. Therefore, it is reasonable that the tolerance limit of Fe cannot be determined simply from solubility of Fe based on Mg–Fe binary phase diagram and the microstructural change according to the processing route and the interaction between Fe and other elements should be considered to design alloy with high corrosion resistance.

Even so, it is worth considering the possibility that other factors have affected the difference in corrosion behavior such as grain size. The grain size and the grain boundary distribution can vary largely depending on the process history and can affect the corrosion resistance [14–16]. However, there is still debated about the effect of grain size and grain boundaries on corrosion behavior. Ralston et al. [16] states that it is difficult to control grain size and it is difficult to completely exclude other variables (secondary phase, impurities, etc.). In this study, as shown in Fig. 7, there is a big difference in corrosion rate between two extruded materials with similar microstructure. For that reason, even if grain size effect on corrosion rate, it would be reasonable to assume that it would not have been a major factor in controlling the overall corrosion rate.

Additionally, similar studies on commercially available high purity Mg alloys need to be conducted in addition, but so far, there have been no reported researches on these findings. Therefore, in the future, the studies of corrosion resistance of commercial purity pure Mg and various purities

Mg alloys will be carried out in terms of impurity control according to the processing history, for the broad applicability of the present results.

## Conclusions

In this study, the corrosion rates of pure Mg specimens prepared by various processing routes were measured by immersion test and compared. The as-cast specimen showed a much slower corrosion rate than those of specimens prepared by other processing routes. The difference in corrosion rate according to the processing route resulted from the microstructural change. Fe existed as supersaturated solid solution in as-cast specimen while Fe was precipitated with Si as Fe–Si phase particle during homogenization heat treatment and then remained as second phase particle in as-extruded specimen and annealed specimen after extrusion. The micro-galvanic corrosion occurred due to the potential difference between the Mg matrix and the Fe–Si phase particle, which resulted in fast corrosion rate. In order to evaluate the effect of impurities on the corrosion behavior of Mg-based material, the processing route and the interaction with other elements should be considered.

## References

- Atrens A, Song GL, Liu M, Shi Z, Cao F, Dargusch MS (2015) Review of Recent Developments in the Field of Magnesium Corrosion. *Adv. Eng. Mater.* 17:400–453.
- Song G, Atrens A (2003) Understanding magnesium corrosion - A framework for improved alloy performance. *Adv. Eng. Mater.* 5:837–858.
- Liu M, Uggowitzer PJ, Nagasekhar AV, Schmutz P, Easton M, Song GL, Atrens A (2009) Calculated phase diagrams and the corrosion of die-cast Mg–Al alloys. *Corros. Sci.* 51:602–619.
- Qiao Z, Shi Z, Hort N, Abidin NIZ, Atrens A (2012) Corrosion behaviour of a nominally high purity Mg ingot produced by permanent mould direct chill casting. *Corros. Sci.* 61:185–207.
- Zhao MC, Liu M, Song GL, Atrens A (2008) Influence of microstructure on corrosion of as-cast ZE41. *Adv. Eng. Mater.* 10:104–111.
- Shi Z, Atrens A (2011) An innovative specimen configuration for the study of Mg corrosion. *Corros. Sci.* 53:226–246.
- F. Cao, Shi Z, Hofstetter J, Uggowitzer PJ, Song GL, Liu M, Atrens A (2013) Corrosion of ultra-high-purity Mg in 3.5% NaCl solution saturated with Mg(OH)<sub>2</sub>. *Corros. Sci.* 75:78–99.
- Pardo A, Merino MC, Coy AE, Arrabal R, Viejo F, Matykina E (2008) Corrosion behaviour of magnesium/aluminium alloys in 3.5 wt.% NaCl. *Corros. Sci.* 50:823–834.
- Yang J, Yim CD, You BS (2016) Characteristics of Surface Films Formed on Mg–Sn Alloys in NaCl Solution. *J. Electrochem. Soc.* 163(8):C395–C401.
- Song D, Ma A, Jiang J, Lin P, Yang D, Fan J (2010) Corrosion behavior of equalchannel-angular-pressed pure magnesium in NaCl aqueous solution. *Corros. Sci.* 52:481–490.
- Sudholz AD, Gusieva K, Chen XB, Muddle BC, Gibson MA, Birbilis N (2011) Electrochemical behaviour and corrosion of Mg–Y alloys. *Corros. Sci.* 53:2277–2282.
- Hanawalt JD, Nelson CE, Peloubet JA (1942) Corrosion studies of magnesium and its alloys. *Trans. Metal. Soc. AIME* 147:273–298.
- Yang L, Zhou X, Liang SM, Schmid-Fetzer R, Fan Z, Scamans G, Robson J, Thompson G (2015) Effect of traces of silicon on the formation of Fe-rich particles in pure magnesium and the corrosion susceptibility of magnesium. *J. Alloys Compd.* 619:396–400.
- Rohrer GS (2011) Grain boundary energy anisotropy: a review. *J. Mater. Sci.* 46:5881–5895.
- Ha HY, Kang JY, Kim SG, Kim BC, Park SS, Yim CD, You BS (2014) Influences of metallurgical factors on the corrosion behaviour of extruded binary Mg–Sn alloys. *Corros. Sci.* 82:369–379.
- Ralston KD, Birbilis N, Davies CHJ (2010) Revealing the relationship between grain size and corrosion rate of metals. *Scr. Mater.* 63:1201–1204.

# Design of the Magnesium Composite with High Corrosion Resistance and High Deformability

Yue-Cun Wang, Bo-Yu Liu, and Zhi-Wei Shan

## Abstract

Magnesium is one of the most promising lightweight materials. However, its competitiveness has been severely reduced by the poor corrosion resistance, low strength, poor deformability, and formability. Here, we propose to design a novel magnesium-based composite prepared by the powder metallurgy using the magnesium nanoparticles with a  $\text{MgCO}_3$  protective layer, which can be obtained via the transformation from the native or corroded surface at room temperature and may effectively improve the anti-corrosion as well as deformability of submicron-scale magnesium.

## Keywords

Magnesium carbonate • Anti-corrosion • Plasticity

## Introduction

Magnesium has been widely recognized as one of the most potential lightweighting materials and is desirable in applications ranging from automotive, 3C products, air/space industry etc. [1–3]. However, the lightest structural metal suffers from some intrinsic issues, such as the poor corrosion resistance, low strength, poor room temperature deformability and formability. One primary reason for the inadequate corrosion resistance of magnesium is that the native surface film formed in the air mainly consists of  $\text{Mg}(\text{OH})_2$  and  $\text{MgO}$ , which is porous and unprotective, especially in the humid environment [4, 5]. Therefore, one of the widely applied strategies in industry to protect magnesium based materials

from corrosion is to create a surface coating, as a barrier to isolate Mg metal from the external environmental attack [6, 7]. Nevertheless, most of the coatings have little to do with improving the ductility and strength of magnesium, or even deteriorate the mechanical property of magnesium surface [8]. Recently, the nanoscale magnesium carbonate ( $\text{MgCO}_3$ ) layer on magnesium surface has been found that it can effectively improve the anti-corrosion performance of magnesium alloys, and meanwhile this protective layer can elevate the yield stress, suppress plastic instability and prolong compressive strains without cracking or peeling off from the surface of the small-sized magnesium [9]. Inspired by this finding, we propose to design a novel magnesium composite composed of the magnesium nanoparticles with the thin  $\text{MgCO}_3$  layer on individual nanoparticles. The composite is expected to have good corrosion resistance, improved deformability and strength.

## Experimental

Observation of the reaction process of Mg oxide or hydroxide with  $\text{CO}_2$  at room temperature was conducted by the environmental transmission electron microscope (E-TEM, Hitachi H9500). The carbonation was done after the 20 min exposure to the 300 keV, 0.1 A/cm<sup>2</sup> electron beam irradiation in 4 Pa  $\text{CO}_2$  atmosphere. The Mg alloy micropillar was firstly fabricated via the focused ion beam milling and then immersed in deionized water for about 1 min, after which the fluffy corroded surface mainly composed of Mg hydroxide can be obtained.

## Results and Discussion

In principle,  $\text{MgCO}_3$  can be obtained via the chemical reaction,  $\text{MgO} + \text{CO}_2 \rightarrow \text{MgCO}_3$ , which usually occurs at high temperatures of 400 °C or above [10]. We have found a way to transform the magnesium oxide/hydroxide or the

Y.-C. Wang · B.-Y. Liu · Z.-W. Shan (✉)

Center for Advancing Materials Performance from the Nanoscale (CAMP-Nano) & Hysitron Applied Research Center in China (HARCC), State Key Laboratory for Mechanical Behavior of Materials, Xi'an Jiaotong University, Xi'an, 710049, People's Republic of China  
e-mail: [zwshan@xjtu.edu.cn](mailto:zwshan@xjtu.edu.cn)

corroded surface into  $\text{MgCO}_3$  barrier layer, without extra heating [9, 11]. Figure 1 shows the room temperature transformation from aggregated flakes of nanoscale  $\text{MgO}$  lamella into a piece of dense amorphous product, and the Scanning TEM (STEM) energy dispersive spectroscopy (EDS) maps demonstrate that the product is the  $\text{Mg}$  carbonate.

Not only the magnesium oxide but also the magnesium hydroxide can react with the  $\text{CO}_2$  excited by the high-energy electron beam. Figure 2a demonstrates the TEM image of magnesium, which was pre-corroded in the deionized water for 1 min and has the fluffy hydroxide corrosion product on

its surface. After the  $\text{CO}_2$  gas was flown into the environmental TEM chamber, the fluffy  $\text{Mg}(\text{OH})_2$  gradually shrank around the pillar due to reaction with  $\text{CO}_2$ . The reaction product— $\text{MgCO}_3$  wrapped around the metal, resulting in a smooth surface (Fig. 2b–c). Our preliminary work has testified the protective effect of the  $\text{MgCO}_3$  layer as the anti-corrosion barrier in aqueous environments [9]. However, being a ceramic material, bulk  $\text{MgCO}_3$  is intrinsically brittle, and how about the deformation behavior of its nanoscale counterpart?

The amorphous  $\text{MgCO}_3$  transformed from the carbonation of magnesium oxide was bridge tangled between two broken parts of the supporting holey carbon film deposited on the copper TEM grid. Under electron beam irradiation, a pulling force was generated when the carbon film is being

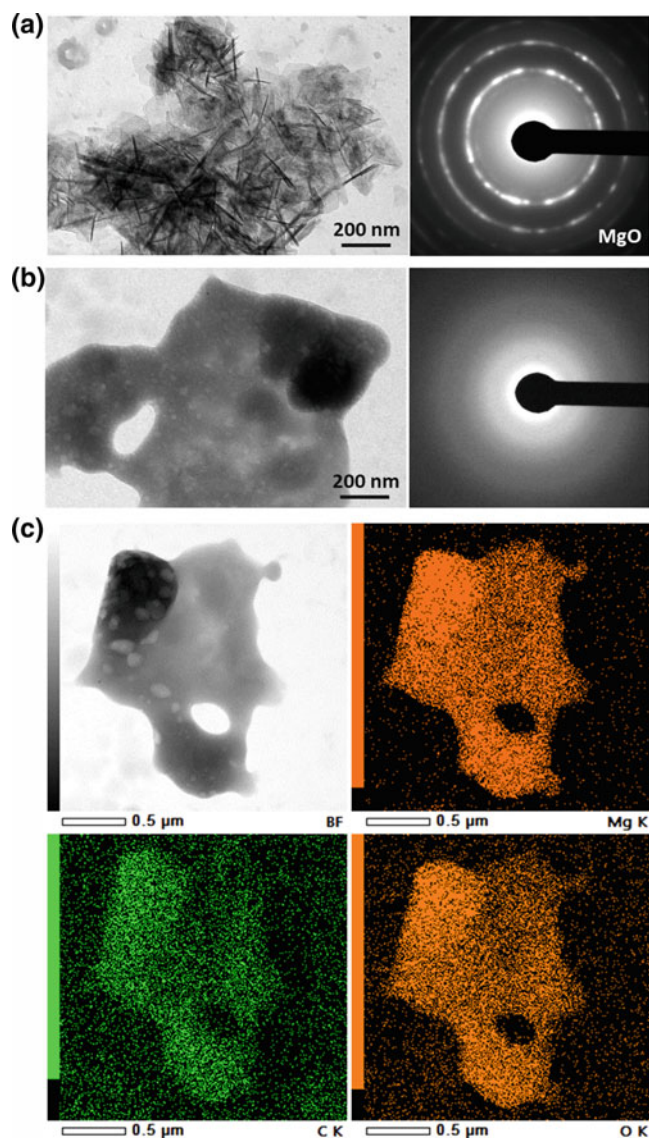


**Fig. 1** a TEM image and diffraction pattern of  $\text{MgO}$  crystal flakes. b After the 20 min exposure to the electron beam irradiation in 4 Pa  $\text{CO}_2$  atmosphere, the  $\text{MgO}$  flakes were transformed into a piece of amorphous product with many bubbles. c STEM EDS maps showing the elements distribution of  $\text{Mg}$ ,  $\text{C}$  and  $\text{O}$  in the product

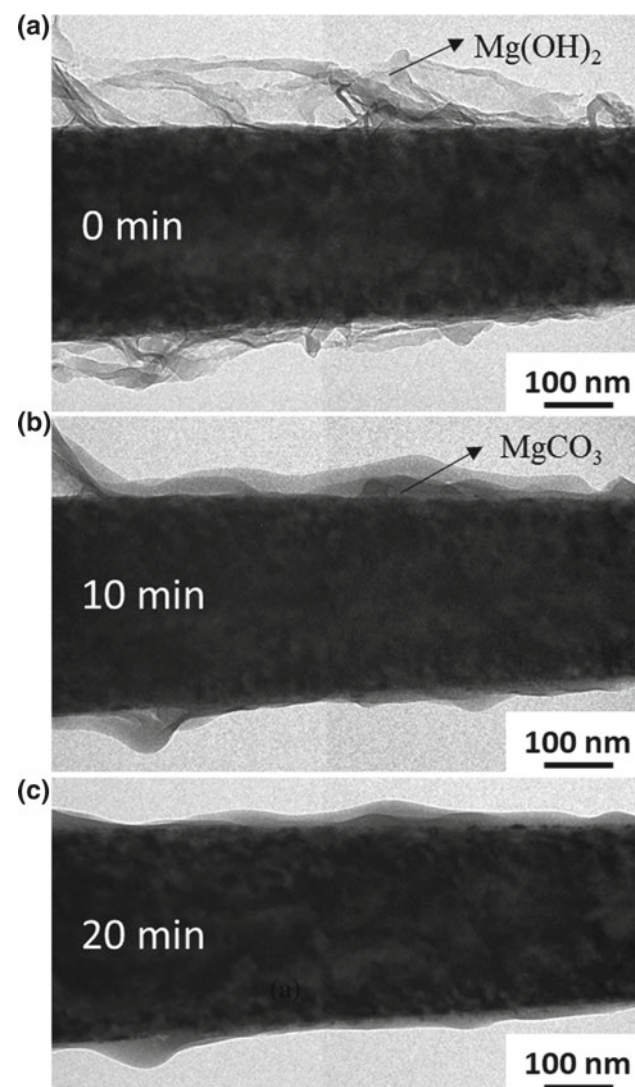


**Fig. 2** In situ transformation from the fluffy hydroxide corroded surface of a ZK60 Mg pillar into a compact  $\text{MgCO}_3$  barrier layer in 4 Pa  $\text{CO}_2$  with the electron beam irradiation



illuminated and the in situ tensile deformation was captured. Figure 3a–d show the superplastic flow experienced by  $\text{MgCO}_3$  during the tensile deformation. Noted that the nano-bubbles in  $\text{MgCO}_3$  are the unescaped  $\text{CO}_2$  gas during reaction. The superplastic  $\text{MgCO}_3$  layer on magnesium surface has been found to be able to elevate the yield stress, suppress plastic instability and prolong compressive strains without peeling off from the submicron-scale magnesium metal substrate [9].

Besides the expensive high-energy electron beam,  $\text{CO}_2$  gas can also be excited by the dielectric discharge or glow discharge as well, existing in the non-thermal plasma state, and react with magnesium oxide or hydroxide without extra heating [9, 11, 12]. This inspires us to scale up our findings inside TEM for designing a bulk magnesium based material with good comprehensive performances, such as the high corrosion resistance, high strength, and deformability. Figure 4 shows the design idea schematically. First, the magnesium nanoparticles with the air-formed oxide/hydroxide film are treated in the non-thermal  $\text{CO}_2$  plasma

(carbonation process), after which the nanoparticles are magnesium carbonate coated. The magnesium nanoparticles can be synthesized by cryomilling [13], and the average size of magnesium nanoparticles should be 100 nm or below, since it was reported that the small dimensions lead to high strengths and more uniform deformation of magnesium by promoting the latent hardening and dislocation storage, resulting in high ductility [14]. Secondly, consolidating magnesium nanoparticles with  $\text{MgCO}_3$  coating. Spark plasma sintering (SPS), which has been proved to be able to effectively sinter nanoparticles into a dense bulk at low temperatures very quickly with the preservation of the nanocrystalline microstructure [15], can be used for the consolidation. The core of this technique is considerable electric currents and the uniaxial pressure loading at the same time [16].

Turing the brittle native magnesium oxide into the ductile amorphous  $\text{MgCO}_3$  on magnesium surface is expected to inhibit the embrittlement of the powder metallurgy magnesium caused by the inevitable oxide introduction [17].

**Fig. 3** Uniaxial tension of the amorphous magnesium carbonate transformed from the hydroxide corrosion product inside TEM

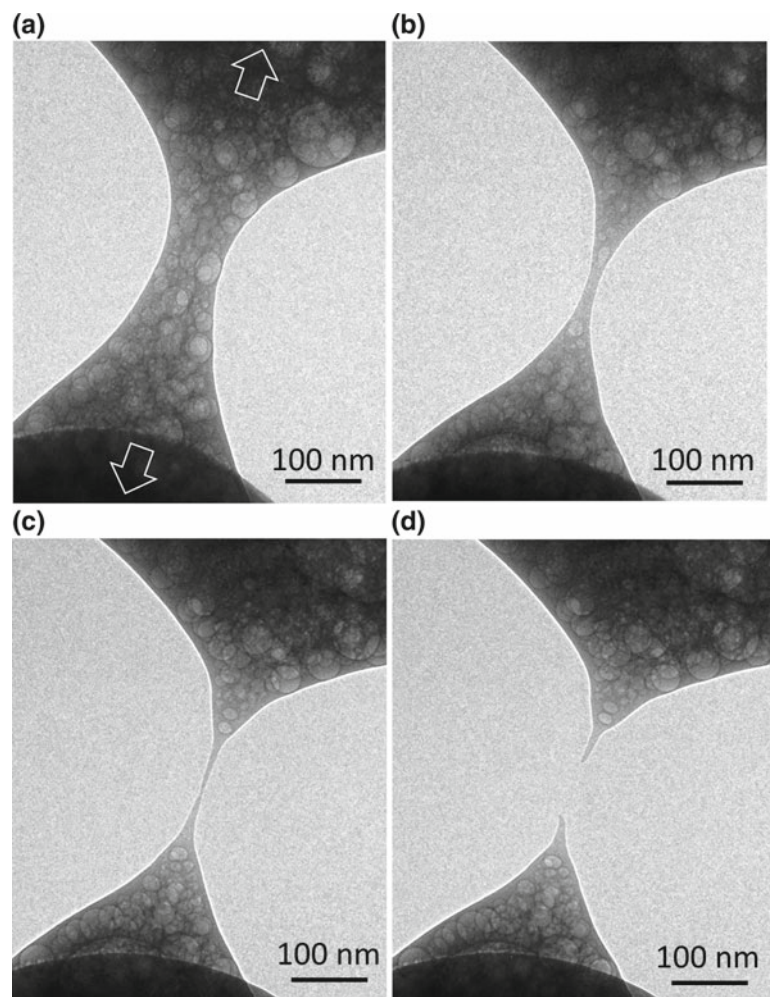
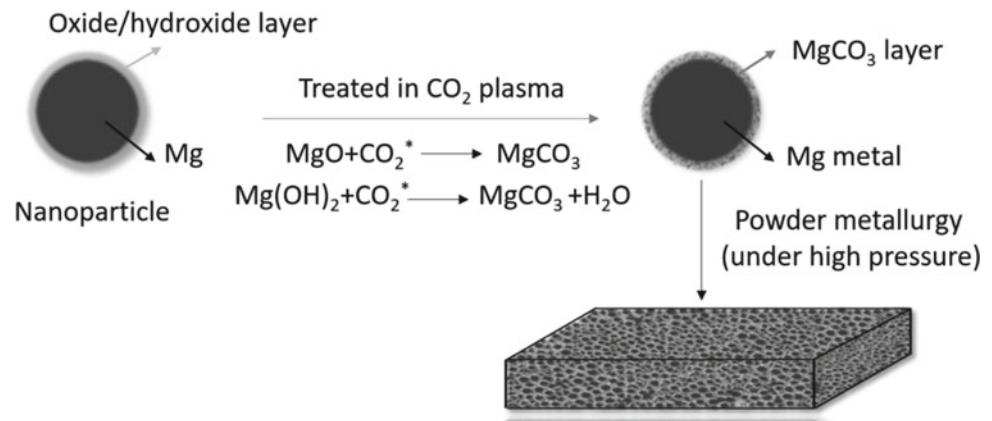


**Fig. 4** Schematic illustration showing the design of the magnesium based composite



## Summary

Via carbonation of the air-formed porous oxide/hydroxide film or hydrate corrosion products on magnesium at room temperature, a compact amorphous MgCO<sub>3</sub> layer, which demonstrates the incredible plastic deformability and can well protect the magnesium substrate free from the aqueous corrosion, has been obtained. Inspired by this, we propose to design a powder metallurgy magnesium composite by consolidating the magnesium nanoparticles with the nanoscale MgCO<sub>3</sub> coating. The novel magnesium based composite is expected to be corrosion resistant and meanwhile have improved strength and good deformability.

**Acknowledgements** The authors acknowledge the support provided by grants from NSFC (51902249, 51621063). The authors also thank the supports from the National Key Research and Development Program of China (No. 2017YFB0702001) and Technology Department of Shaanxi Province (2016KTZDGY-04-03 and 2016KTZDGY-04-04). We also appreciate the support from the 111 project (B06025).

## References

1. Knochel P. A flash of magnesium. *Nature Chemistry* (2009) 740–740.
2. Esmaily M, Svensson JE, Fajardo S, Birbilis N, Frankel GS, Virtanen S, Arrabal R, Thomas S, Johansson LG. Fundamentals and advances in magnesium alloy corrosion. *Progress in Materials Science* 89 (2017) 92–193.
3. Pollock TM. Weight loss with magnesium alloys. *Science* 328 (2010) 986–987.
4. Nordlien J, Ono S, Masuko N, Nisancioglu K. A TEM investigation of naturally formed oxide films on pure magnesium. *Corrosion science* 39 (1997) 1397–1414.
5. Nordlien JH, Nisancioglu K, Ono S, Masuko N. Morphology and Structure of Water-Formed Oxides on Ternary MgAl Alloys. *Journal of the Electrochemical Society* 144 (1997) 461–466.
6. Gray J, Luan B. Protective coatings on magnesium and its alloys—a critical review. *Journal of alloys and compounds* 336 (2002) 88–113.
7. Hu R-G, Zhang S, Bu J-F, Lin C-J, Song G-L. Recent progress in corrosion protection of magnesium alloys by organic coatings. *Progress in Organic Coatings* 73 (2012) 129–141.
8. Gray JE, Luan B. Protective coatings on magnesium and its alloys—a critical review. *Journal of Alloys & Compounds* 336 (2002) 0–113.
9. Wang Y, Liu B, Zhao Xa, Zhang X, Miao Y, Yang N, Yang B, Zhang L, Kuang W, Li J. Turning a native or corroded Mg alloy surface into an anti-corrosion coating in excited CO<sub>2</sub>. *Nature communications* 9 (2018) 4058.
10. Feng B, An H, Tan E. Screening of CO<sub>2</sub> adsorbing materials for zero emission power generation systems. *Energy & Fuels* 21 (2007) 426–434.
11. Zhang L, Tang Y, Peng Q, Yang T, Liu Q, Wang Y, Li Y, Du C, Sun Y, Cui L. Ceramic nanowelding. *Nature communications* 9 (2018) 96.
12. Gupta P, Tenhundfeld G, Daigle EO. Electrolytic plasma technology: Science and engineering - an overview. *Surface & Coatings Technology* 201 (2007) 8746–8760.
13. Park YS, Chung KH, Kim NJ, Lavernia EJ. Microstructural investigation of nanocrystalline bulk Al–Mg alloy fabricated by cryomilling and extrusion. *Materials Science & Engineering A* 374 (2004) 211–216.
14. Qian Y, Liang Q, Mishra RK, Ju L, Minor AM. Reducing deformation anisotropy to achieve ultrahigh strength and ductility in Mg at the nanoscale. *Pnas* 110 (2013) 13289–13293.
15. Ye J, Ajdelsztajn L, Schoenung JM. Bulk nanocrystalline aluminum 5083 alloy fabricated by a novel technique: Cryomilling and spark plasma sintering. *Metallurgical & Materials Transactions A* 37 (2006) 2569–2579.
16. Munir ZA, Anselmi-Tamburini U, Ohyanagi M. The effect of electric field and pressure on the synthesis and consolidation of materials: A review of the spark plasma sintering method. *Journal of Materials Science* 41 (2006) 763–777.
17. Kondoh K, Fukuda H, Umeda J, Imai H, Fugetsu B, Endo M. Microstructural and mechanical analysis of carbon nanotube reinforced magnesium alloy powder composites. *Materials Science & Engineering A* 527 (2010) 4103–4108.

# Advanced Immersion Testing of Model Mg-Alloys for Biomedical Applications

Dmytro Orlov, Bastien Reinwalt, Ilyes Tayeb-Bey, Lars Wadsö, Jelena Horky, Andrea Ojdanic, Erhard Schafler, and Michael Zehetbauer

## Abstract

The acceleration of developing magnesium alloys for biomedicine requires the advancement of experimental methods evaluating their performance. We have been developing an advanced immersion testing method for the assessment of biomedical Mg alloy degradation in aqueous environments. It is based on the combination of isothermal calorimetry with pressure measurement in the reaction cell. Such a combination allows in situ quantitative analysis of chemical reactions based on both the enthalpy (heat) of the process itself and hydrogen gas generated as one of the reaction products. Here, we

analyze the evolution of the degradation rate of a ternary Mg–5.0Zn–0.3Ca intended for biomedical applications and two model binary Mg–5.0Zn and Mg–0.3Ca alloys (in as-cast and solutionized states) in 0.9% NaCl water solution and a simulated body fluid (SBF). The results obtained using the novel method are critically compared to more traditional immersion testing with hydrogen collection.

## Keywords

Magnesium alloys • Degradation • Immersion testing • Isothermal calorimetry • Pressure measurements

D. Orlov (✉)  
Division of Materials Engineering, LTH, Lund University,  
P.O. Box 118 Lund, 22100, Sweden  
e-mail: [dmytro.orlov@material.lth.se](mailto:dmytro.orlov@material.lth.se)

B. Reinwalt  
École Nationale Supérieure de Physique, Électronique, Matériaux,  
Institut Polytechnique de Grenoble, 3, Parvis Louis Néel,  
CS 50257 38016 Grenoble Cedex 01, France  
e-mail: [bastien.reinwalt@grenoble-inp.org](mailto:bastien.reinwalt@grenoble-inp.org)

I. Tayeb-Bey  
Institut National des Sciences Appliquées de Lyon, 20 Avenue  
Albert Einstein, 69621 Villeurbanne Cedex, France  
e-mail: [ilyes.tayeb-bey@insa-lyon.fr](mailto:ilyes.tayeb-bey@insa-lyon.fr)

L. Wadsö  
Division of Building Materials, LTH, Lund University,  
John Ericssons Väg 1, 223 63 Lund, Sweden  
e-mail: [lars.wadso@byggtek.lth.se](mailto:lars.wadso@byggtek.lth.se)

J. Horky  
Center for Health & Bioresources, Biomedical Systems, AIT  
Austrian Institute of Technology, 2700 Wr. Neustadt, Austria  
e-mail: [Jelena.Horky@ait.ac.at](mailto:Jelena.Horky@ait.ac.at)

A. Ojdanic · E. Schafler · M. Zehetbauer  
Physics of Nanostructured Materials, Faculty of Physics,  
University of Vienna, 1090 Vienna, Austria  
e-mail: [andrea.ojdanic@univie.ac.at](mailto:andrea.ojdanic@univie.ac.at)

E. Schafler  
e-mail: [erhard.schafler@univie.ac.at](mailto:erhard.schafler@univie.ac.at)

M. Zehetbauer  
e-mail: [michael.zehetbauer@univie.ac.at](mailto:michael.zehetbauer@univie.ac.at)

## Introduction

Although applications of magnesium (Mg) and its alloys continue growing in interest as the lightest structural metal, their practical utilisation is still restricted largely due to high corrosion rate [1, 2]. The later has been the subject of many studies on both the fundamental understanding of mechanisms and the applied aspects of protection. Nevertheless, the process is still not well understood, nor is the problem mitigated, because of its complexity as well as dynamic nature and heavy dependence on local fluctuations of thermal and electrochemical variables [2]. This situation is even more complex in biomedical applications when Mg alloy implants work in dynamically changing environment, while having to degrade homogeneously at a well predictable rate [3, 4].

The recent literature surveys on progress in Mg alloy corrosion [1, 2] suggest the development of new experimental techniques for multimodal correlative assessment of Mg corrosion in order to understand the process, and hence to find the best ways to control it. Our further literature survey also revealed that authors typically have a perfect notion of the thermodynamics in Mg corrosion process and start their analysis from respective descriptions. However,

afterwards the focus shifts to the electrochemical aspects of the process that fulfil the thermodynamics, but the later becomes omitted in the direct discussion of results. This most likely takes place because of difficulties in the direct measurements of respective thermodynamic characteristics. Instead, the discussions are usually focused on the electrochemistry of the process, characteristics of which can be directly measured by well-established experimental methods. However, electrochemistry-based techniques have their own deficiencies that limit full understanding of corrosion process.

Over the past several years, we have been developing in Lund University a new instrumentation based on isothermal calorimetry [5, 6], which allows the analysis of thermodynamics in Mg corrosion process based on the direct measurements of heat production rate (thermal power). The calorimetric measurements are combined with pressure measurements to detect the evolution of hydrogen in the course of chemical reactions. The measured thermal power  $P$  (W) is then used to calculate the process enthalpy  $\Delta H$  (J/mol) from the rate of a process  $dn/dt$  (mol/s) according to the equation  $\Delta H = P/(dn/dt)$  where  $n$  (mol) is the amount of material degraded over time  $t$ . In deriving this equation, we assumed the activity of a single process, while it can also be used for evaluating the combined effect of several activities in more complex processes in practice.

In this work, we present our recent results on the application of the newly developed instrumentation to the analysis of degradation rate in a ternary Mg–5.0Zn–0.3Ca alloy intended for biomedical applications and two model binary Mg–5.0Zn and Mg–0.3Ca alloys (in as-cast and solutionized states) in 0.9% NaCl water solution and a simulated body fluid (SBF). In parallel, we carried out similar tests on the same materials using more traditional ‘standard’ immersion testing technique with corrosion rates calculated from hydrogen collection. The results obtained using the novel method are critically compared to the standard immersion testing with hydrogen collection.

## Materials and Methods

A ternary alloy Mg–5.0Zn–0.3Ca (hereafter referred to as ZX50) intended for bio-medical applications, and two model binary Mg–5.0Zn and Mg–0.3Ca alloys (hereafter referred to as Z5 and X0, respectively) were used in this study. All the compositions are given in weight percent (wt%). The materials were die-cast at the LKR Leichtmetallkompetenzzentrum Ranshofen, a subsidiary of Austrian Institute of Technology, Austria. One set of samples for testing was kept

in the as-cast condition, while another one was solution treated for 12 h at 350 °C (Z5) or for 24 h at 450 °C (X0 and XZ50) and quenched in ice water to room temperature to achieve super-saturated solid solution (SSSS) states. Specimens for testing were cut using a diamond-wire saw and ground on SiC paper in several steps down to grit 2000 in water-free environment. For standard immersion testing, disk-shaped specimens with diameter 10 mm  $\times$  1 mm thickness were used, while square specimens 9 mm  $\times$  9 mm  $\times$  1 mm of approximately the same total surface area (3.5–4.2 cm<sup>2</sup>) were used for isothermal calorimetry testing. The last step of grinding and washing specimens in ethanol were carried out immediately before the immersion testing.

The majority of tests was carried out in a simulated body fluid according to a compositions for m-SBF and SBF27 suggested in [7] and [8], respectively, buffered with HEPES (or TRIS), and NaOH (or HCl) was used to control pH = 7.35 (at 37 °C). As a reference, a mild electrolyte made of 0.9wt% NaCl solution in de-ionized H<sub>2</sub>O was also used in the present study for the immersion testing by isothermal calorimetry. This is a physiological serum typically used in biomedicine, even though its Cl<sup>−</sup> concentration (154 mmol/L) does not exactly match that in human blood plasma (103 mmol/L) [7].

In the standard immersion testing, see Fig. 1, at least four specimens were examined for each alloy. At least two tests were performed in parallel for each material and condition, and two specimens were tested (immersed) together in 250 ml of SBF to improve the accuracy of experiments. The tests were running for up to 21 days at 37 °C, and SBF solution was changed every 7 days. The amount of hydrogen gas evolving from the corrosion process was determined regularly, at least every 4 h. To calculate the corrosion rate, the volume of hydrogen gas was normalized by the initial sample surface area and a numerical derivation was applied. Then the curves were smoothened by a moving average algorithm and an average of at least two independent measurements was calculated.

The calorimetric measurements were also carried out for at least four specimens in parallel at 37 °C in a modified TAM Air calorimeter (Thermometric, now TA Instruments) by using custom-designed calorimetric vials that provide capability for pressure measurements, as can be seen in Fig. 2. The details of this setup were presented elsewhere [5, 6]. For the present work the setup was tailored slightly by removing a syringe and having oversized buffer vial (100 ml) for collecting the generated H<sub>2</sub> gas. This minimized the risk of leaks and made it possible to achieve accurate data readings by keeping the pressure close to atmospheric over the entire experiment time of at least 24 h. In the present measurements, we used 17 ml of the electrolyte placed



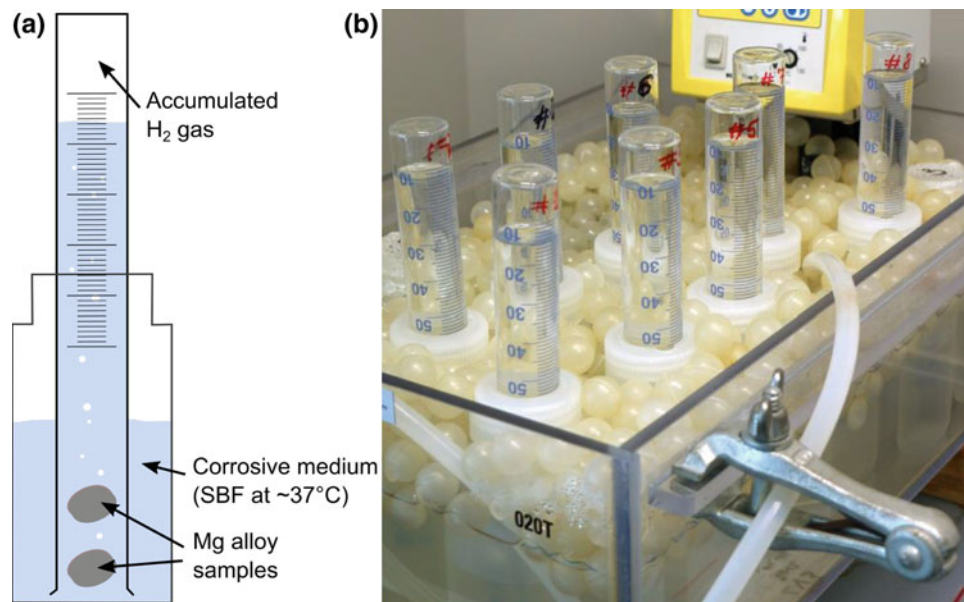


**Fig. 1** A schematic of one cell for immersion testing with the collection of hydrogen gas (a), and a photograph of eight cells assembled in an experimental instrument with thermostating (b). SBF in (a) states for simulated body fluid, see text for further details (Colours online)

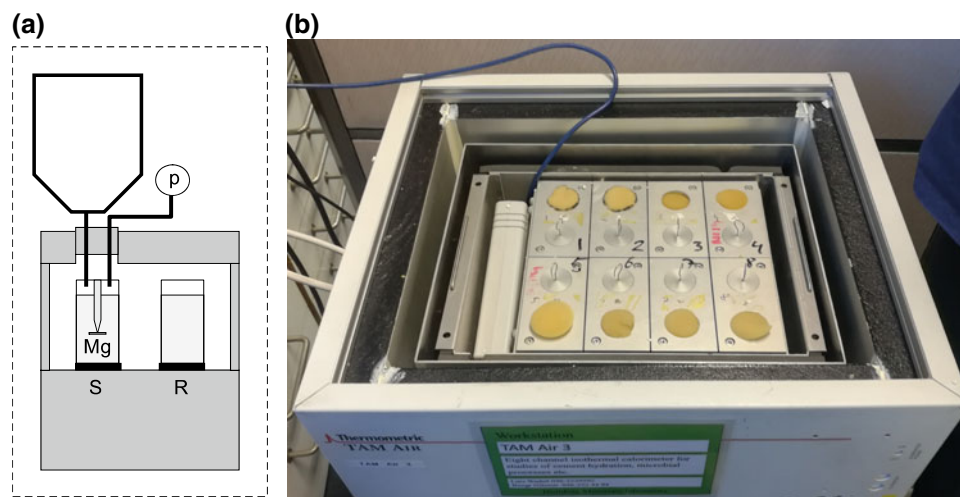


**Fig. 2** A schematic of one isothermal heat conduction calorimeter cell (a) and a photograph of eight cells assembled in an experimental instrument (b). The dashed line in (a) is the extent of the temperature-controlled environment: S and R are the sample and the reference parts of the cell; the thick black and the dark gray parts are

the Peltier heat sensor and the calorimeter heat sink, respectively; the black lines are stainless steel tubes connected to the oversized gas collection buffer and the pressure sensor P; Mg is the magnesium alloy specimen submerged on an inert polymer pin holder in a test fluid inside a glass vial (Colours online)

in 20 ml glass vials. During testing, the specimens were placed in the center of the electrolyte volume, on the tip of a plastic rod, fastened by a small amount of photopolymer adhesive, as is shown in Fig. 2a.

Immediately after testing, the specimens were extracted from the vials, quickly washed in deionized water and ethanol, and finally dried gently in the stream of cold air. After that, examination of corroded surfaces was carried out using an optical microscope.

## Results and Discussion

The results of immersion testing for the initial 24 h of measurements are presented in Fig. 3. The data from isothermal calorimetry measurements are presented as dotted lines while those from the standard immersion testing are shown as oversized dots.

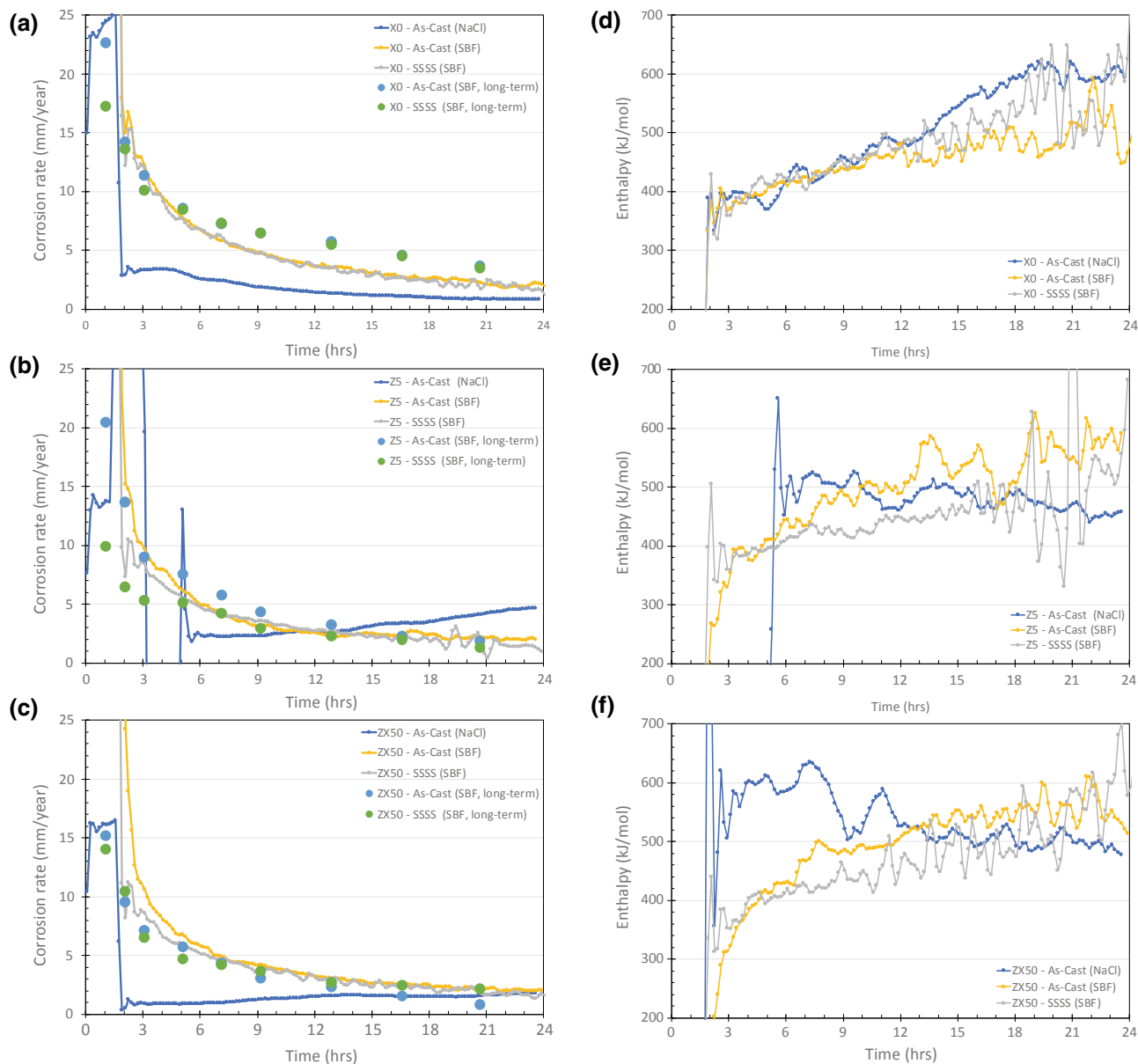


**Fig. 3** Evolution of corrosion rates (a–c) and enthalpies (d–f) in the alloys of interest during immersion testing. Dotted lines show the results from 1-day measurements in isothermal calorimeter while oversized-dot data in (a–c) show the results from standard immersion

First of all, a very good consistency in the results between the two different methods can be seen in Fig. 3a–c for both qualitative trends and quantitative values for all the three Mg alloys, especially at the later stages of 24-h measurements. The small variation between the data are within the experimental error. The significant scattering of data within the initial 2 h (up to 6 h in the case of Z5) in the calorimeter-based measurements can be attributed to the stabilization of heat flow and initial reactions on the Mg surfaces slightly affected by ambient-air corrosion. Such a scattering is not visible in the standard immersion setup due

to lower data acquisition rate leading to higher averaging, or smoothing, of the results. It can also be seen in Fig. 3a–c that the corrosion rate of all the alloys tested in SBF quickly reduces from approximately 25 mm/y down to less than 2 mm/y within the first 24 h following an exponential trend.

In the X0 alloy, Fig. 3a, the exponential trend does not depend on the precipitate state, i.e. curves for the material in the as-cast and the SSSS conditions overlap almost perfectly with corrosion rates decreasing from approximately 15 mm/y after 2 h down to 2.3 mm/y and 1.7 mm/y, respectively, after 24 h. Such dependencies hold for both the

21-day testing. Note that the enthalpies are all shown positive, even if they are negative according to the thermochemical sign convention (Colours online)

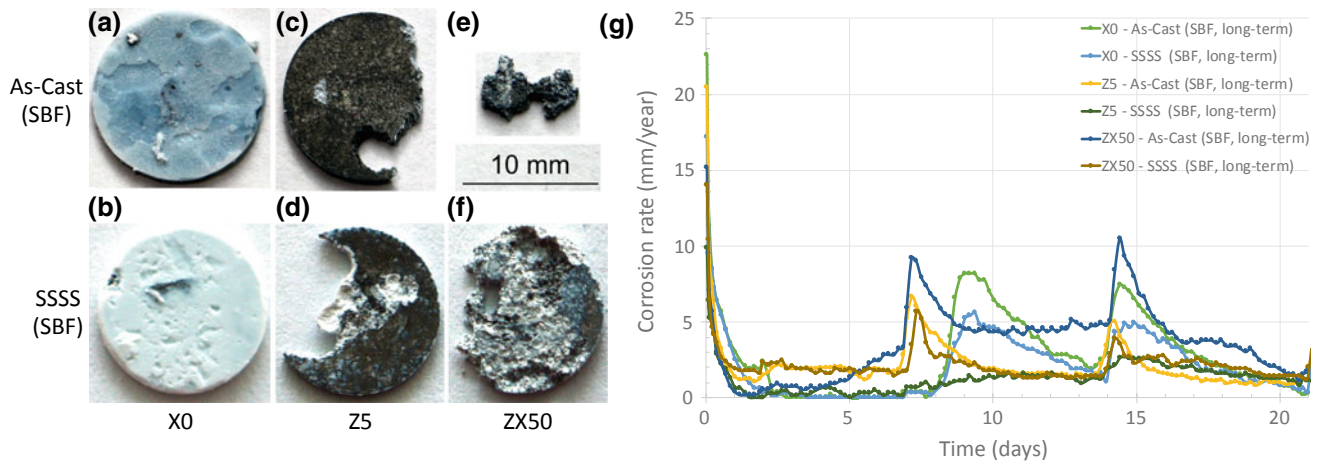


**Fig. 4** Optical micrographs of corroded specimen surfaces after 21-day exposure in SBF (a–f), and corrosion rates re-calculated from hydrogen gas collection (g), in the alloys of interest during standard

21-day immersion testing. Please keep in mind that the SBF was renewed every 7 days leading to a rapid increase in corrosion rates (Colours online)

isothermal calorimetry and the standard immersion testing while the latter shows slightly higher rates including 3.0 mm/y for the as-cast and 2.5 mm/y for the SSSS conditions after 24 h. The as-cast alloy tested in NaCl solution shows a similar trend but lower rates from 3 mm/y after 2 h slowly decreasing down to 1.3 mm/y until approximately 20 h, and then staying at that level until the end of experiment.

In the Z5 alloy, Fig. 3b, the trends of testing in SBF are similar while the as-cast condition reveals slightly higher rates compared to SSSS that decrease from 15 mm/y to 10 mm/y after 2 h down to 2.9 mm/y and 1.4 mm/y after 24 h, respectively. The standard long-term tests demonstrate similar dependencies with the corrosion rates after 24 h being 1.4 mm/y with very large deviation for the as-cast and 0.6 mm/y for the SSSS conditions. It is interesting to note that the as-cast Z5 alloy tested in NaCl solution shows a completely different trend. From relatively low values of 2.2 mm/y at the measurements stabilization after 6 h, the corrosion rate increases to approximately 4.7 mm/y after 24 h.

The ZX50 alloy, Fig. 3c, demonstrates trends very similar to the alloy Z5 at slightly lower absolute values. The differences in corrosion rates between the as-cast and the SSSS condition are less, while after 24 h testing in SBF they are 2.1 mm/y and 1.4 mm/y for the as-cast and the SSSS conditions, respectively, in the isothermal calorimetry measurements, and 0.4 mm/y and 1.9 mm/y in the standard immersion tests. The corrosion rate of the as-cast ZX50 alloy tested in the NaCl solution increases from 0.5 mm/y after 2 h up to 1.9 mm/y after 24 h.

The evolution of corrosion rates beyond 24 h is presented in Fig. 4g along with the photographs showing the appearances of degraded specimens at the end of 21-day exposure

during the standard immersion testing, Fig. 4a–f. It can be seen that the trends set within the initial 24 h in general hold until the end of 21-day testing. The two sharp rises of corrosion rates in almost all the samples at day 7 and day 14 followed by gradual decays are associated with the change (refreshment) of electrolyte on these days.

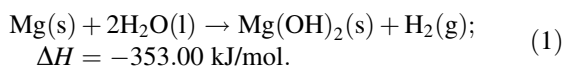
In the case of alloy X0, corrosion rates in both the as-cast and the SSSS microstructure conditions appear at the same very low level within the first 7 days of exposure. However, the change of solution leads to a significantly higher increase of corrosion rate in the as-cast sample. This holds in both the changes at day 7 and day 14, and therefore can be associated with the more stable/protective film from degradation products forming on the SSSS sample surface. This speculation is supported by the photographs in Fig. 4 revealing a somewhat transparent corrosion film on significantly distorted as-cast X0 sample surface (Fig. 4a), and a dense white non-transparent film on well preserved SSSS X0 sample (Fig. 4b). The rates of corrosion at the end of testing of the as-cast and the SSSS X0 samples were 0.95 mm/y and 0.80 mm/y, respectively.

Alloy Z5 demonstrates significantly higher corrosion rates over the entire testing period as well as different trends. The as-cast sample seems to be sensitive to the changes of SBF, while the SSSS is not. After having similar corrosion rates towards the end of day 1, the values diverge afterwards. In the as-cast sample they increase to approximately 2 mm/y and stay at this level, except for spikes and decays at around days 7–10 and 14–17 associated with the change of SBF. By contrast, the corrosion rate of the SSSS sample after day 1 decreases further to the level of alloy X0 and remains such until day 7. Afterwards, it starts increasing gradually and after day 10 it levels out at the same values as the as-cast sample. After day 14, the corrosion rate increases slightly

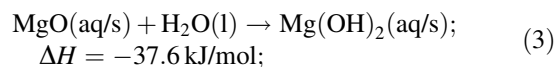
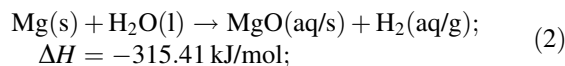
again until day 15, and then slowly decreases until the end of the test still staying at the level somewhat higher than the as-cast sample. The last decrease of corrosion rate in the SSSS and the as-cast samples can be associated with the reduction of total surface areas due to the consumption of significant material volumes during the degradation. The evidence of this can be found in the photographs of Fig. 4c and d revealing the irregular shapes of semi-degraded samples. The rates of corrosion at the end of testing of the as-cast and the SSSS Z5 samples were 1.0 mm/y and 1.3 mm/y, respectively, with large standard deviations. The latter as well as the higher absolute value in the SSSS sample can be associated with the irregular shapes of specimens and large remaining SSSS sample volume (higher total surface area) at that stage.

In comparison with the already described cases, the evolution of corrosion rates in the ZX50 samples demonstrates a kind of mixed trends and absolute values. Both the as-cast and the SSSS samples have rather high sensitivity to the changes of SBF. Corrosion rates in both the material conditions converge to approximately 2.6 mm/y in the middle of day 1 and continue decreasing at different rates. The latter sample then saturates at approximately 1.75 mm/y, and stays at this level, except the spikes and decays at around days 7–10 and 14–17 caused by the changes of SBF, and a decrease in rate after day 18 because of the reduction of total sample area. In the case of the as-cast sample, the corrosion rate reaches its minimum of 0.2 mm/y after day 2, increases to 0.76 mm/y within the following day, and stays at this level until day 5. Afterwards, it increases rapidly and stabilizes at 4.5 mm/y level at day 10, remains stable until the second change of SBF, decreases again to a stable level of 3.8 mm/y between days 17–18, and continues decreasing rapidly afterwards. The rates of corrosion at the end of testing of the as-cast and the SSSS ZX50 samples were 1.9 mm/y and 1.4 mm/y, respectively, also with large values of standard deviations. The latter can be explained by the irregular shapes of specimens at that stage. As can be seen in Fig. 4e, f, the as-cast specimen degrades almost entirely while the SSSS one is severely degraded and still has a thin-layer coverage by the degradation products.

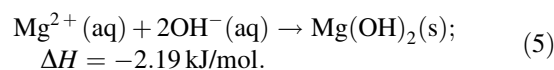
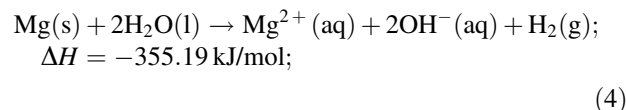
For the understanding of enthalpy evolutions in Fig. 3d, f, let us first review the most important chemical reactions expected in this case along with their enthalpies of formation  $\Delta H$ . According to a review by Song [2], the most stable product of Mg degradation in aqueous media is magnesium hydroxide  $\text{Mg}(\text{OH})_2$ , which can be formed in a single-step reaction:



Magnesium hydroxide may also form in a two-step reaction with intermediate magnesium oxide formation:



or another two-step reaction involving solutioning and precipitation of  $\text{Mg}^{2+}$  and  $\text{OH}^-$  ions:



In addition to these, other oxides and hydroxides may form in Mg alloys, i.e. those of Ca and Zn in our case. Furthermore, a spectrum of other compounds may form including carbonates, phosphates, hydrates, etc. when testing in more complex media such as simulated body fluids, for instance. The complete list will not be presented here (this can be found elsewhere, e.g. [3, 7]), neither their enthalpies calculated. We can just note that their reactions of formation will affect the heat generated or consumed and thus detected in our experiments.

Let us start the analysis of our data from the experiments in NaCl solution since they are easier to understand. The stages of enthalpy evolutions on the time scale correlate rather well with the pressure measurements. In the case of alloy X0, Fig. 3d, the reliable readings begin after 2 h at the level 350–400 kJ/mol. The enthalpy remains at this level for approximately another 3 h, then grows steadily until hour 19, and then saturates at this level until the end of experiment. The initial measured enthalpy level correlates well with the enthalpy of Mg dissolution and water reduction, i.e. the formation of  $\text{Mg}^{2+}$  and  $\text{OH}^-$  ions dissolving in the surrounding fluid. The following increase in measured enthalpy levels might be associated with the saturation of working media with the ions, the beginning of their precipitation into  $\text{Mg}(\text{OH})_2$ , and the increasing rate of other compound formation, e.g. MgO. The levelling of enthalpy growth at 600 kJ/mol level after 19 h of exposure may correspond to a steadily propagating corrosion reaction. Both samples tested in SBF demonstrate a very short ‘initiation’ stage and steady enthalpy growth up to approximately 12 h. Afterwards, the enthalpy of as-cast sample levels out at slightly below 500 kJ/mol level, while the SSSS sample continues the growth at a lower rate than the sample in NaCl solution.



Such behavior can be attributed to the fact that SBF is already nearly saturated with various ions and needs little time to complete the saturation process. The following lower levels of enthalpy also indicate the progress of lower-enthalpy reactions not available in the NaCl solution.

In the case of alloy Z5, Fig. 3e, the reliable readings of enthalpy in NaCl solution testing start after 6 h at 500 kJ/mol level, which appears already saturated. Afterwards, the enthalpy shows significant variations along with a slight decrease of mean value to approximately 425 kJ/mol level. The immersion in SBF produces lower enthalpy values in both sample conditions while increasing to a level of 400 kJ/mol after six hours. After that, the enthalpy values show a significant decrease of the growth rate while the amplitude of value variation is increased. In the SSSS sample the latter is more stable until hour 18. Afterwards, however, it varies significantly, which can be associated with the fracture of degradation products and interplay of various chemical reactions.

In the alloy ZX50 tested in NaCl solution, Fig. 3f, the enthalpy level of 600 kJ/mol is very high from the beginning. Between hours 6–12, it decreases in absolute value down to 500 kJ/mol and oscillates slightly around this level until the end of the test. The enthalpies of testing in SBF start at the same level as alloy X0 and proceed by trends similar to those in the Z5 sample with lower amplitudes of variation.

Summarizing the above, it can be said that the elaborated new instrumentation allows degradation rate measurements very consistent with more traditional immersion testing. At the same time, the combination of isothermal calorimetry measurements giving direct information on corrosion process thermodynamics, with pressure measurements giving direct quantification of corrosion rate from hydrogen evolution, can provide further insights into the degradation of Mg alloys. The enthalpies calculated need to be investigated further to assess, e.g., if the high values measured (600 kJ/mol) are true, and to what exactly reactions they can be attributed.

Out of the three materials investigated in this study, the alloy X0 (Mg–0.3Ca) demonstrates the best corrosion resistance (lowest degradation rates) in relatively aggressive NaCl solution, and even more so in SBF. The corrosion process takes place at rather low enthalpy intensity and H<sub>2</sub> gas generation rate. The evolutions of these parameters in time are rather stable, and are further improved through the electrochemical homogenization of the material by solid solution treatment, as can be seen from the formation of thick oxide film on the sample surfaces. The Mg–5.0%Zn alloy Z5 demonstrates the lowest corrosion resistance, which can be attributed to the electrochemically heterogeneous

microstructure due to the high concentration of alloying element. Solid-solution treatment improves the corrosion resistance, but it still remains at a level significantly higher than that of the alloy X0. The alloy ZX50 (Mg–5.0%Zn–0.3Ca) demonstrates somewhat similar values in the solution-treated condition. The measured enthalpies of materials' degradation in SBF suggest parallel running of several reactions that will be investigated in further studies.

---

## Conclusions

In this work, the dependences of degradation rate on chemical composition, microstructure state and corrosion media were studied in a ternary Mg–5.0Zn–0.3Ca and two binary Mg–5.0Zn and Mg–0.3Ca alloys. The latter alloy in super-saturated solid solution state tested in SBF demonstrates the highest corrosion resistance owing to the formation of a stable degradation film on its surface. The in-house developed instrumentation based on the combination of isothermal calorimetry and pressure measurements reveals very good consistency with more traditional immersion testing methods while giving further insights in the process from the thermodynamics perspective.

**Acknowledgements** JH, AO, ES and MZ gratefully acknowledge the use of equipment within the Faculty Center for Nanostructure Research, the Machine Shop and Technical Services at the Faculty of Physics, University Vienna, Austria, as well as the AIT Austrian Institute of Technology, Austria for the casting of the Mg bars. We also appreciate financial support from the Austrian Science Funds (FWF) within project I2815-N36 and the Slovenian Research Agency (ARRS) through Research Project J2-7157.

---

## References

1. M. Esmaily, J.E. Svensson, S. Fajardo, N. Birbilis, G.S. Frankel, S. Virtanen, R. Arrabal, S. Thomas, L.G. Johansson, Fundamentals and advances in magnesium alloy corrosion, *Progress in Materials Science* 89 (2017) 92–193.
2. G.L. Song, 1 - Corrosion electrochemistry of magnesium (Mg) and its alloys, in: G.-l. Song (Ed.), *Corrosion of Magnesium Alloys*, Woodhead Publishing 2011, pp. 3–65.
3. N.A. Agha, F. Feyerabend, B. Mihailova, S. Heidrich, U. Bismayer, R. Willumeit-Römer, Magnesium degradation influenced by buffering salts in concentrations typical of in vitro and in vivo models, *Materials Science and Engineering: C* 58 (2016) 817–825.
4. F. Witte, Reprint of: The history of biodegradable magnesium implants: A review, *Acta Biomaterialia* 23, Supplement (2015) S28–S40.
5. L. Wadsö, D. Orlov, Adding dimensions to the immersion testing of magnesium corrosion, in: O. D, J. V, S. K, N. N (Eds.) *TMS Annual Meeting & Exhibition. TMS 2018: Magnesium Technology* Phoenix AZ, USA, 2018, pp. 31–36.

6. L. Wadsö, N. Hort, D. Orlov, Effect of Alloying with Rare-Earth Metals on the Degradation of Magnesium Alloys Studied Using a Combination of Isothermal Calorimetry and Pressure Measurements, *Magnesium Technology 2019*, Springer International Publishing, Cham, 2019, pp. 121–126.
7. A. Oyane, H.-M. Kim, T. Furuya, T. Kokubo, T. Miyazaki, T. Nakamura, Preparation and assessment of revised simulated body fluids, *Journal of Biomedical Materials Research Part A* 65A(2) (2003) 188–195.
8. L. Müller, F.A. Müller, Preparation of SBF with different  $\text{HCO}_3^-$  content and its influence on the composition of biomimetic apatites, *Acta Biomaterialia* 2(2) (2006) 181–189.

# Effect of 2 wt% Ag Addition on Corrosion Properties of ZK40 for Biodegradable Applications

M. AbdelGawad, B. Mansoor, M. W. Vaughan, and I. Karaman

## Abstract

The antibacterial effects of silver make it an attractive alloying element for biodegradable Mg alloys to treat possible inflammation and infections caused by the degrading orthopedic implants. In this study, as-extruded Mg–4%Zn–0.5%Zr (ZK40) alloy was alloyed with Ag, specifically 2 wt%, and subjected to a heat treatment at 350 °C for 7 days. The mechanical and corrosion responses were studied in two orthogonal planes (transverse and extrusion) before and after silver addition to explore its potential for biodegradable orthopedic applications. Corrosion characteristics were assessed at 37 °C in Hank's solution for 24 h via electrochemical impedance spectroscopy (EIS), potentiodynamic polarization (PD) and open circuit potential (OCP). As-extruded and heat-treated ZK40 alloy displayed an inhomogeneous microstructure containing large, coarse grains, Zn–Zr rich secondary phase and some fine grain regions. While in ZK40–Ag, both planes showed a relatively more homogeneous microstructure but with some agglomeration of Zn–Ag rich secondary phases. Here, we present our initial results on the different corrosion behaviors observed in the two materials.

## Keywords

Mg alloys • Biodegradation • EIS • Microstructure • Silver

## Introduction

Temporary orthopedic implants are designed to restore the functionality of fractured load-bearing joints and bones by providing temporary support during the healing process. Biodegradable implants have attracted attention for decades now due to their superiority over permanent implants where they are able to sustain the joint/bone for the required duration and then progressively degrade afterwards. This eliminates the need for a second removal surgery which is inevitable when using permanent implants. Furthermore, permanent implants are associated with several lifelong problems such as prolonged physical irritation, chronic inflammation and endothelial dysfunction [1, 2]. Magnesium (Mg) alloys have proven to be promising candidates exhibiting excellent biocompatibility due to the presence of Mg which is an essential element in bone and soft tissue [3]. In addition, Mg and its alloys have elastic moduli (37.5–65 GPa) similar to that of the human bone (3–20 GPa) preventing the possibility of mechanical failure of the implant due to stress shielding or implant loosening [4]. Research has shown successful in vivo testing, in addition to clinical trials, where Mg-based implants helped stimulate the formation of new bone around the implantation site [3, 5, 6].

Biodegradable implants are designed to maintain their mechanical integrity while fulfilling their intended function. A major drawback that still prevents the commercialization of Mg-based orthopedic implants is their rapid degradation specifically at the early implantation stages where degradation is usually the fastest [6]. Uncontrollable degradation can lead to failure of the implant before the bone is completely healed as well as the excessive release of metallic ions beyond their toxicity limits [1]. Consequently, numerous design strategies have been proposed to develop biocompatible Mg alloys with sufficient strength and controllable corrosion characteristics [1, 4, 7, 8].

Most of the Mg alloys reported are based on commercial Mg alloys that were primarily developed for the

M. AbdelGawad · B. Mansoor (✉)  
Mechanical Engineering Program, Texas A&M University at  
Qatar, Doha, Qatar  
e-mail: [bilal.mansoor@qatar.tamu.edu](mailto:bilal.mansoor@qatar.tamu.edu)

M. AbdelGawad · B. Mansoor · I. Karaman  
Mechanical Engineering Department, Texas A&M University at  
Qatar, College Station, TX, USA

B. Mansoor · M. W. Vaughan · I. Karaman  
Materials Science and Engineering Program, Texas A&M  
University at Qatar, College Station, TX, USA

transportation and aerospace industry since they usually satisfy the required mechanical strength. Solution strengthening, grain size control and, precipitation hardening are all methods used on these commercially available alloys to tailor their corrosion behavior. In addition, efforts have been made to improve their mechanical and corrosion behavior through micro-alloying, heat treatments and/or severe plastic deformation [9–14]. Mg–Zn alloys have been studied extensively for biomedical applications since the two main constituents are Mg and Zinc (Zn) which are both essential nutrients for the human body and therefore biocompatible [15–20]. Chen et al. conducted in vitro and in vivo tests on Mg–Zn alloy using mouse pre-osteoblastic MC3T3-E1 cells and compared it with polymer poly-L-lactic acid (PLLA) implant and concluded that Mg–Zn alloy allowed for better cell attachment and mineralization as well as new bone formation [21]. In addition, previous work has been done by the authors using commercial Mg–Zn alloy with rare earth addition (ZE41 and EZ33) where their biodegradation characteristics were studied in Hank's solution and NaCl [22, 23]. In an attempt to investigate different alloying systems, Mg–Zn–Zr alloys (ZK series) were considered for this study since they are also potential candidates as biomaterials considering that Zirconium (Zr) is also a biocompatible element that is non-toxic to the human body in small amounts [24]. Furthermore, Zr is known to be an excellent grain refiner in Mg alloys and has been shown to improve its corrosion resistance when alloyed in small amounts <0.5 wt % [25].

On the other hand, Ag is known to have superior antibacterial effects and can be effective on some antibiotic-resistant microbes such as Methicillin-resistant *Staphylococcus aureus* (MRSA) [26]. Tie et al. developed three binary Mg–X Ag alloys (where X = 2, 4 and 6 wt%) and studied their mechanical and corrosion characteristics, as well in vitro cytocompatibility [26]. It was concluded that Ag improved the mechanical strength of Mg and that although the corrosion rate of the Mg increased with increasing addition of Ag, the susceptibility of Mg to pitting corrosion decreased. Localized corrosion has been reported to be more critical than uniform corrosion to the mechanical integrity of biodegradable materials owing to the accelerated loss of mechanical strength within a short period of time [27]. Furthermore, Ben-Hamu et al. studied the corrosion behavior and microstructural evolution of Mg–Zn–Ag alloys by varying the concentration of Ag between 0, 1, 2 and 3 wt

%Ag [28]. It was reported that the increasing addition of Ag resulted in an increased refinement of the grains and an increase in the hardness. However, an improvement in corrosion resistance was only witnessed when the Ag addition was up to 2 wt%Ag.

In this preliminary work, as-extruded ZK40 (Mg 95.0 wt %, Zn 4.5 wt%, Zr 0.5 wt%) was selected as a base material to investigate the effect of 2 wt% Ag addition (ZK40–Ag) on its mechanical properties and in vitro corrosion characteristics using Hank's solution at 37 °C. Microstructural analysis was performed on the as-extruded alloys before and after suitable heat-treatments. Mechanical testing was carried out by way of compression tests and Vicker's microhardness while corrosion response was accessed by employing electrochemical techniques such as Open Circuit Potential (OCP), Electrochemical Impedance Spectroscopy (EIS) and Potentiodynamic Polarization (PD).

## Experimental Methods

### Materials

ZK40 and ZK40–Ag ingots were produced by gravity die casting under argon atmosphere. Table 1 shows the wt% nominal chemical composition of both alloys. First, commercially obtained ZK40 and Ag were melted at 750 °C in a steel crucible and held for 30 min with continuous stirring and later cast into billets. The cast ingots were hot extruded with an extrusion ratio of 15.6 using a die heated at 350 °C to produce 27.5 mm × 27.5 mm square cross-section billets. In an attempt to solutionize the as-extruded billets and homogenize the grain structure, a long duration heat treatment of 350 °C for 7 days in Argon atmosphere was performed.

### Microstructure

Microstructures of the as-extruded and solution-treated billets were observed using optical microscopy. EDM machined, disc-shaped samples with ~1.7 cm<sup>2</sup> cross-sectional area were mounted in cold-curing epoxy resin and grinded using silicon carbide paper up to 1200 grit. Polishing of the samples was done using 3 µm and 1 µm diamond suspensions. The polished surfaces were washed with ethanol and dried with air.

**Table 1** The nominal wt% chemical compositions of ZK40 and ZK40–Ag

Alloy	Composition (wt%)					
	Zinc	Zirconium	Silver	Manganese	Calcium	Magnesium
ZK40	4.7	0.35	<0.01	0.01	N/A	Remainder
ZK40–Ag	4.89	0.18	2.56	0.01	0.01	Remainder



Specimens were etched using acetic-picric solution (4.2 g picric acid, 70 ml ethanol, 10 ml acetic acid and 10 ml distilled water).

## Mechanical Properties

Cylindrical samples of 3 mm diameter and 6 mm in length were used for compression testing. Tests were performed at ambient temperature and conducted at an initial strain rate of  $10^{-3}$ /s using electromechanical MTS Insight 30 kN machine. The load cell used was 5 kN and testing was done in triplicates. Vickers micro-hardness tests were conducted as well with a load of 100 gf and a dwell time of 15 s.

## Electrochemical Tests

Electrochemical tests were conducted using a Gamry Multiport™ three-electrode cell: the sample acted as the working electrode, a graphite rod was used as a counter-electrode and Ag/AgCl as a reference electrode. Similar samples to those used for microstructural analysis were used for EIS, however the samples were grinded up to 800 SiC grit on all sides before mounting. This is to prevent crevice corrosion occurring between the sample and the epoxy. Prior to mounting as well, an insulated wire was attached to the back of the specimen to provide the electrical connection to perform the electrochemical testing. One surface of the sample was exposed by grinding up to 1200 SiC and then immersed

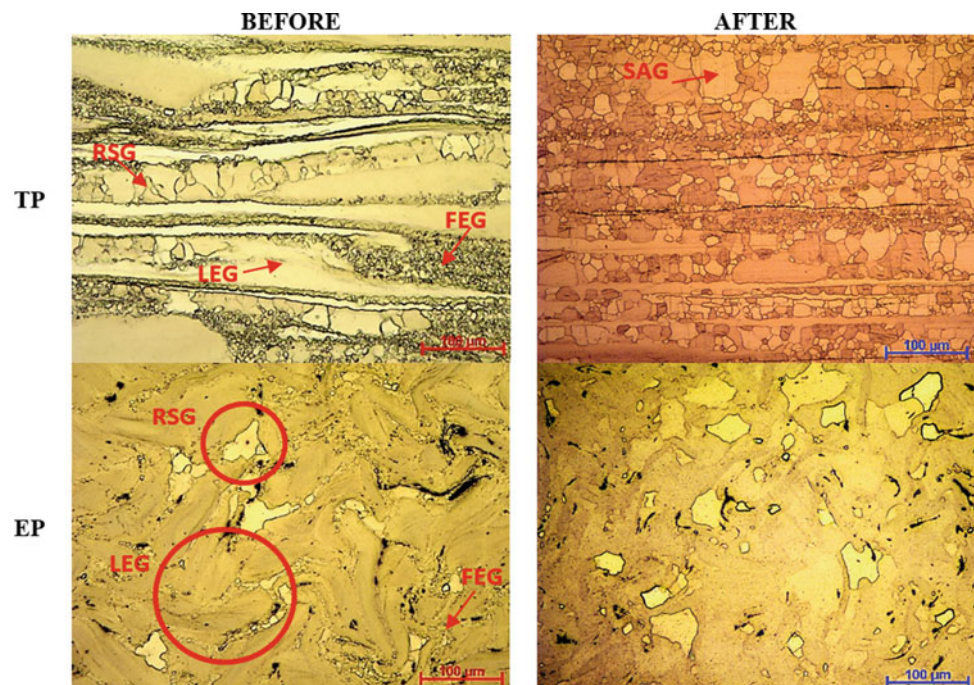
into 1000 ml of Hank's solution at 37 °C. The pH of the solution was maintained at 7.4 using 0.1 M HEPES [4-(2-hydroxyethyl)-1-piperazineethanesulfonic acid] buffering solution. The experiments were conducted for a total of 24 h using Electrochemical Impedance Spectroscopy (EIS) by sweeping the frequency between  $10^5$  and  $10^{-2}$  Hz at 10 mV AC amplitude. Open circuit potential (OCP) was measured in parallel with EIS at different time points to observe the change in corrosion behavior with respect to time. Potentiodynamic polarization (PD) was also carried out at the end of the testing period at a scanning rate of 1 mV/s from  $-2.5$  to  $+0.5$  V.

## Results and Discussion

### Microstructure Analysis

Figure 1 shows optical micrographs of ZK40 before and after heat treatment at 350 °C for 7 days along two orthogonal planes i.e. transverse plane (TP) and extrusion plane (EP). In the as-extruded ZK40, the microstructure along transverse plane is similar to what has been observed in other extruded Mg alloys [29–31]. The as-extruded microstructure contains long, elongated grains (LEG) oriented along the extrusion direction, in addition to two other types of grains: fine equiaxed grains (FEG) and row stacked grains (RSG) that can also be observed. Azeem et al. and others have reported that among these three types of grains, LEGs are reminiscent of the as-cast microstructure and FEGs are

**Fig. 1** Microstructure of the two orthogonal planes for ZK40 before and after heat treatment (TP—Transverse Plane and EP—Extrusion Plane)



dynamically recrystallized grains (DRX), while RSGs are misaligned grains that have undergone DRX but at a lower rate due to their misalignment [32]. Aligned grains are those that have their basal plane aligned with the extrusion direction, which is one of the most common slip systems for deformation in Mg [33]. The plastic energy stored in misaligned grains is lower than that of the aligned grains, therefore they recrystallize at a lower rate resulting in bands of large recrystallized grains stacked in a row-like structure [32].

Apart from the Mg matrix, the presence of other Zn–Zr rich phases in the microstructure seen as dark streaks along the extrusion direction was confirmed by a preliminary Energy Dispersive X-ray Spectroscopy (EDX) analysis (Fig. 2). After heat treatment, the LEGs recrystallize but thinner LEGs are still observed throughout the microstructure. Also, some reduction in the distribution of Zn–Zr rich phases is seen, however, the long-duration heat treat regime did not fully solutionize them. Furthermore, an overall homogenization of the grain structure is observed as well as an increase in the grain size of FEGs.

In case of the extrusion plane of ZK40 (Fig. 1), the grain morphologies that were observed in the transverse plane are not easily distinguishable. Some LEGs are visible as large grains and swirling outlines of Zn–Zr-rich phases are observed along the LEG grain boundaries as well as dark particles within the grains. FEGs are seen as small, fine equiaxed grains while RSGs are shown as coarser grains, both smaller in grain size than LEGs. Post-heat treatment, the decrease in volume fraction of Zn–Zr rich phases are apparent and grain sizes seem to have homogenized and increased due to static recrystallization (RX), as seen in the transverse plane.

Optical micrographs of ZK40–Ag before and after heat treatment are shown in Fig. 3. Prior to the heat treatment, the

addition of 2 wt% Ag resulted in an increase in the volume fraction of secondary phases as presented by the darker and thicker streaks in the transverse plane which is reflected by large, sized dark patches in the extrusion plane. Furthermore, the composition of the secondary phases is altered, as shown by EDX analysis in Fig. 4, and the grain structure is more homogenous now with smaller, equiaxed grains which can be observed in both planes. Ben-Hamu et al. reported similar findings when 1, 2, and 3 wt% Ag was added to Mg–6Zn alloy [28]. The smaller grain size in ZK40–Ag, compared to ZK40, could be explained by the constricting of grain growth and DRX that normally occur during extrusion as a result of the increased volume fraction of the secondary phases [34].

Similar to ZK40, heat treatment of the ZK40–Ag alloy resulted in an agglomerated morphology of secondary phases and an increase in grain size but the effect was significantly more pronounced. The secondary phase agglomeration is apparent in the transverse plane micrograph by the thicker, more disperse dark streaks oriented along the extrusion direction as opposed to the extrusion plane. From the microstructures, in Figs. 1 and 3, it was concluded that the main effect of Ag on microstructure was the aggregation of secondary phases in addition to an increase in their volume fraction. Furthermore, the grain size distribution was more homogenous with Ag addition compared to the as-extruded ZK40 condition.

## Mechanical Properties

The mechanical properties of as-extruded and heat-treated ZK40 and ZK40–Ag alloys were investigated through microhardness measurements and compression tests (Figs. 5 and 6). It was observed that in ZK40, extrusion plane

**Fig. 2** BSE micrograph of the transverse plane and EDX spectrum of as-extruded ZK40

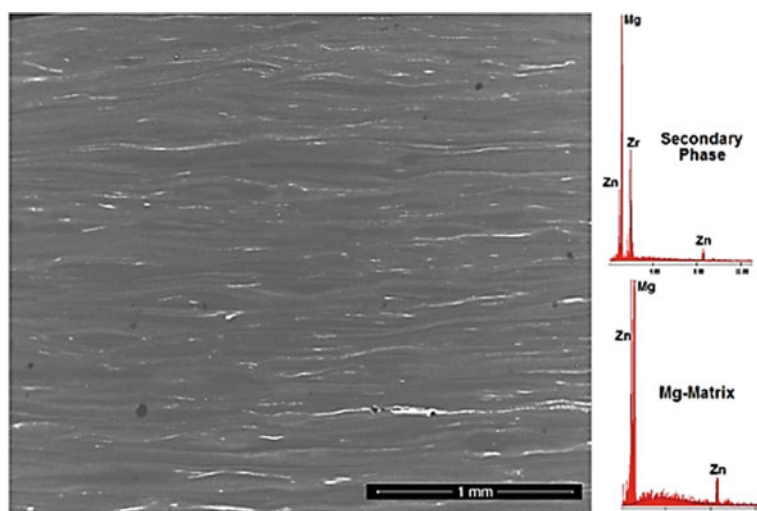




**Fig. 3** Microstructure of the two orthogonal planes for ZK40–Ag before and after heat treatment

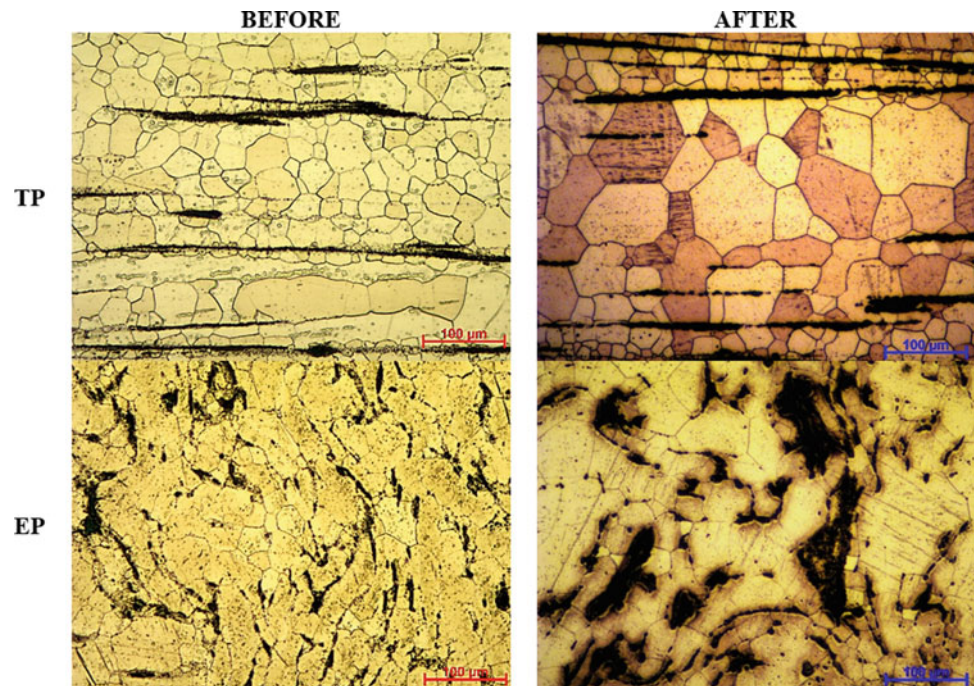
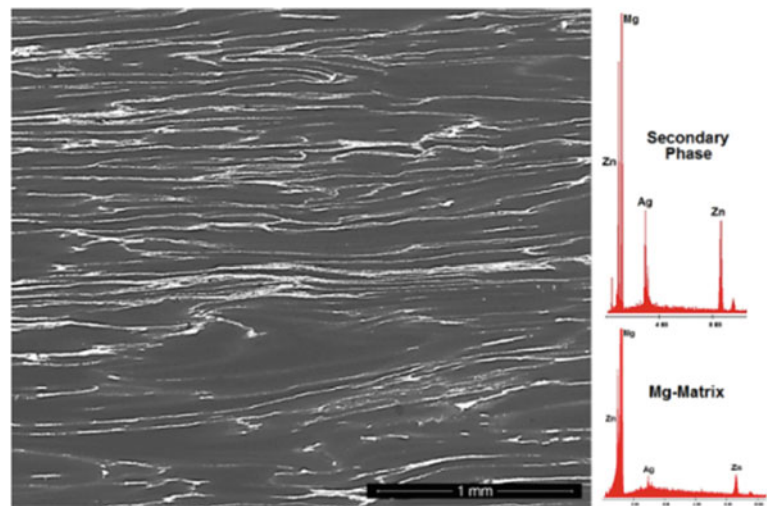


**Fig. 4** BSE micrograph of the transverse plane and EDX spectrum of as-extruded ZK40–Ag



exhibited higher hardness than transverse plane while in ZK40–Ag transverse plane exhibited higher hardness than extrusion plane. Among the two alloys, ZK40–Ag displayed higher microhardness than ZK40 in the transverse plane while it displayed less hardness in the extrusion plane. Mandal et al. reported that adding 0.1 at.% of Ag to Mg–2.4Zn alloy resulted in an increase in hardness of about 20 HV for the as-cast homogenized condition, due to secondary phase precipitation [35]. This is in agreement with the trend observed in the transverse plane between ZK40 and ZK40–Ag. However, the increase in HV was not as significant as that reported by Mandal et al. which could be due to the larger grain size observed in ZK40–Ag after solutionizing as

larger grain sizes tend to counteract the hardening benefits of precipitates [28].

In contrast, the extrusion plane of ZK40–Ag displayed less hardness than ZK40. It is worthwhile to note that microhardness measurements were taken within the matrix while excluding the precipitates. In an effort to investigate the decrease in microhardness of ZK40–Ag, measurements of the precipitates were taken and their average was found to be 130 HV, which is more than double the hardness values of the Mg matrix. Furthermore, since Ag resulted in the aggregation of the secondary phases, particularly in the extrusion plane, the volume fraction of secondary phases within the matrix would be less. Therefore, a decrease in the

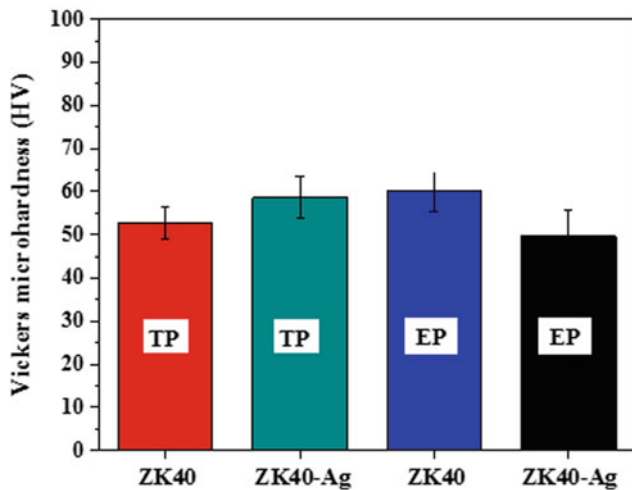


**Fig. 5** Effect of Ag addition on Vicker's microhardness of ZK40 in the two orthogonal planes

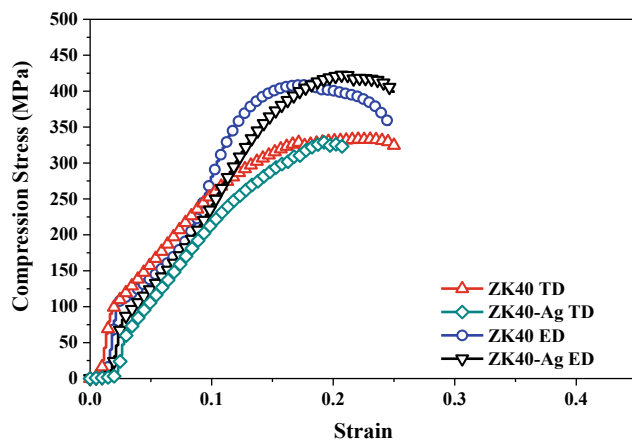


**Fig. 6** Stress–strain curves of ZK40 and ZK40–Ag at room temperature under compressive loading applied along with the two orthogonal directions (TD—Transverse Direction and ED—Extrusion Direction)

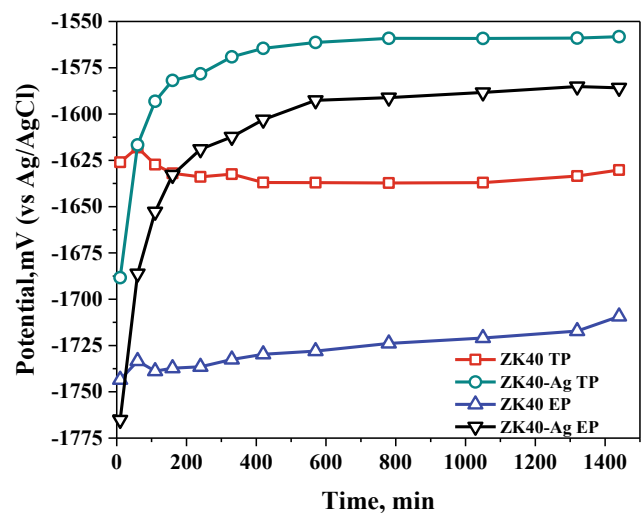
hardness of the matrix is perhaps expected. There may be other factors that lead to this microhardness trend reversal in ZK40–Ag compared to ZK40 such as Zn depletion of the Mg matrix due to Ag-rich precipitates which is observed while comparing the EDX spectrum of the matrices of both alloys in Figs. 2 and 4.

Figure 6 shows the compression stress-strain curves of ZK40 compared to ZK40–Ag along with the two orthogonal directions, i.e., transverse and extrusion directions. In ZK40, the ultimate compressive strength in the extrusion direction was higher compared to the transverse direction with similar ductility observed in both planes. Looking back at the microstructures, the comparatively homogenized grain structure and absence of LEGs in the extrusion plane led to an increased compressive strength which was similar to the microhardness results in Fig. 5. A similar trend was also

observed in the ZK40–Ag with the extrusion direction showing higher values of compressive strength than the transverse direction. Of all the directions tested, the highest compressive strength was observed for ZK40–Ag in the extrusion direction which is opposite to the trend observed in the microhardness measurements (Fig. 5). The agglomeration of the secondary phases as well as the depletion of Zn into the matrix could explain why the overall hardness of the ZK40–Ag was less in the extrusion plane but still had a positive impact on the compressive strength of the alloy. Further investigation is needed to fully understand the role of secondary phases and grain structure on the mechanical properties of both alloys.

### Open Circuit Potential

The reactivity of a metal surface can be determined based upon the open circuit potential (OCP) of the alloy throughout the immersion time. The OCP of both alloys in the transverse and extrusion planes is presented in Fig. 7. Both orthogonal planes of ZK40 experienced a decrease in their potential after their first few hours of immersion, while an increase was observed towards the end of the 24 h. The OCP for the extrusion plane specifically continued to increase steadily after the small drop during the initial hours, which implies that the surface film of the extrusion plane is able to maintain its integrity throughout the testing period, although it is at a lower potential than the transverse plane. ZK40–Ag OCP curve shows a plateau which is at a more positive potential than ZK40. This is expected since the addition of Ag causes an increase in secondary phases and as reported



**Fig. 7** Open circuit potential (OCP) of ZK40 and ZK40–Ag at 37 °C throughout 24 h of immersion in Hank's solution for both transverse (TP) and extrusion (EP) planes



by Gusieva et al., Ag is more noble than Mg [36]. During the initial few minutes of immersion, the OCP of ZK40–Ag in transverse plane experienced the sharpest increase which indicates the increased stability of the surface film being formed. ZK40 transverse plane also reached the same OCP value of around 1615 mV which also shows that the film-forming on the surface of ZK40 transverse is stable as well. After 24 h of immersion, both OCPs of ZK40–Ag have reached a plateau and therefore signifying the continuous breaking down of the developed surface film. The alloy, however, is still presenting higher potential than ZK40 and

that is a result of the higher volume fraction of secondary phases present that are cathodic to the matrix. Consequently, microgalvanic cells were formed between the matrix and the secondary phases, thereby causing corrosion of the matrix. Since most of the Ag was found in the secondary phases and Ag is nobler than Mg, the presence of Ag continued to be enhanced as the matrix was continuously being compromised. This explains why the plateau occurred at a more positive potential for both planes of ZK40–Ag compared to the planes of ZK40. As immersion time increased, the slopes for all OCP started to decrease indicating that the developed films were losing their integrity and breaking down.

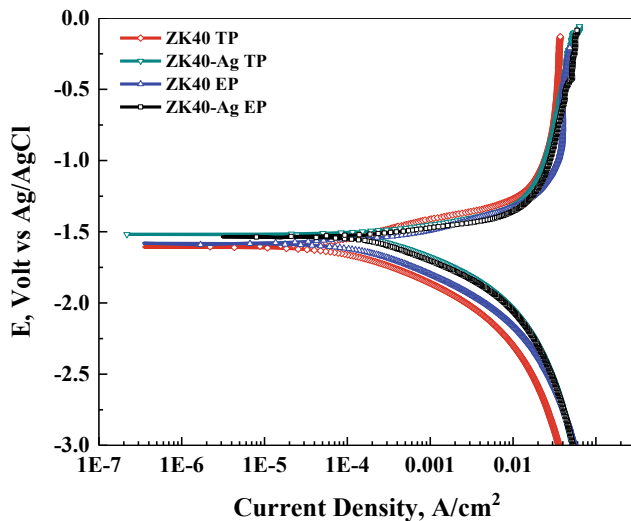


**Fig. 8** Potentiodynamic curves of ZK40 and ZK40–Ag at 37 °C after 24 h of immersion in Hank's solution for both transverse (TP) and extrusion (EP) planes

### Potentiodynamic Polarization Curves

The potentiodynamic (PD) curves of ZK40 and ZK40–Ag in the transverse and extrusion planes are shown in Fig. 8. In both planes, ZK40–Ag displayed a more positive potential than ZK40 which is in agreement with the OCP results. This was also consistent with the ennobling effect of Ag as reported by Mandal et al. where the addition of Ag resulted in a shift in the corrosion potential towards a more positive value [35]. Furthermore, the intersection between the anodic and cathodic branch, which is an indication of the corrosion rate occurs at a higher corrosion current,  $i_{\text{corr}}$ , when Ag is added compared to no Ag addition. Gusieva et al. presented similar results where the increased addition of Ag resulted in an increase in cathodically controlled kinetics and a more positive  $E_{\text{corr}}$  value, which increased the value of  $i_{\text{corr}}$  [37]. The increase in corrosion current led to an increase in corrosion rate which is in agreement with EIS results presented in Fig. 9.

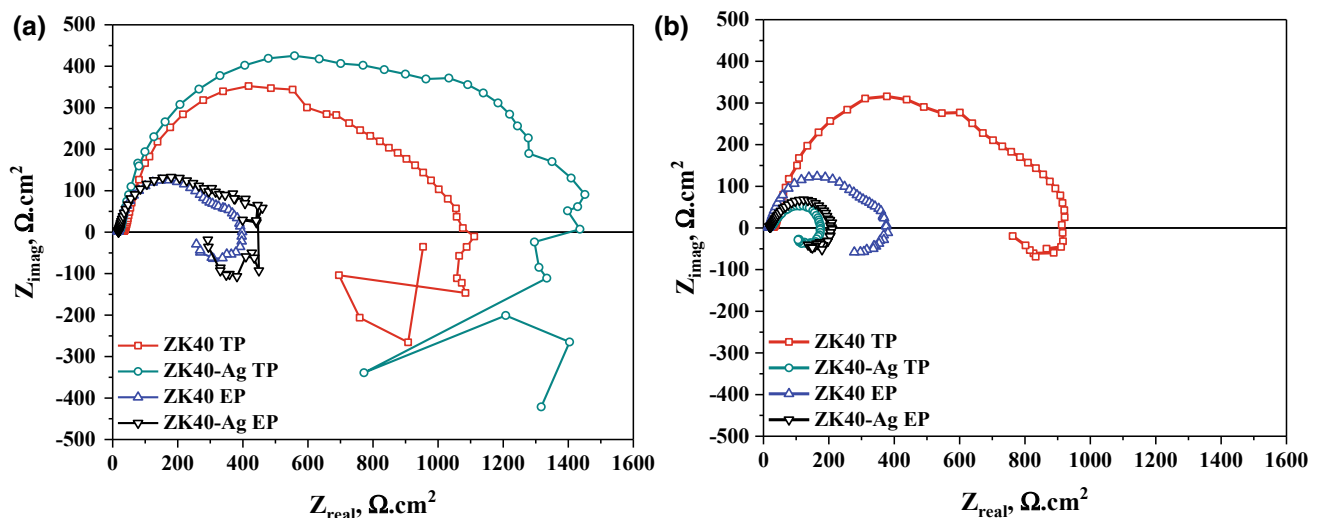


**Fig. 9** Nyquist plots of ZK40 and ZK40–Ag at 37 °C after **a** 1 h of immersion and **b** 24 h of immersion in Hank's solution for both transverse (TP) and extrusion (EP) planes

## Electrochemical Corrosion Measurements

Electrochemical Impedance Spectroscopy (EIS) is a technique that investigates the processes occurring at the metal surface using AC polarization [38]. The EIS Nyquist plots for ZK40 and ZK40–Ag immersed in Hank's solution at 37 °C for 1 and 24 h for both planes are presented in Fig. 9. All plots are distinguished by two capacitive loops at high and medium frequencies and an inductance loop at low frequencies. The trends seen in both plots are in accordance with the results observed in OCP plots. After the first hour of immersion, the transverse planes for ZK40 and ZK40–Ag both exhibited a significant increase in corrosion resistance which is evident with the large diameter of the capacitive loop. However, by the end of the experimental period, both planes of ZK40 had a higher corrosion resistance than both planes of ZK40–Ag. The drastic decrease in the corrosion resistance of the alloy with Ag addition is due to the enhanced microgalvanic corrosion caused by the larger volume fraction of secondary phases as observed in Figs. 1 and 3. Furthermore, as was observed in Fig. 7, the corrosion resistance of ZK40 in the extrusion plane experienced minimal, if no change at all, throughout the 24 h of immersion. Further analysis using circuit fittings could give some insight on the reasons behind this behavior.

Another interesting observation that was also noticed is that overall the transverse plane experienced much better corrosion resistance than the extrusion plane. Considering the microstructure of both alloys that are shown in Figs. 1 and 3, the extrusion plane has a more homogenous, fine-grained structure and smaller grains especially in ZK40. A homogenous grain structure has been reported to present improved protection against corrosion because of its ability to form a more stable corrosion layer [39, 40]. However, in this case the structure of the matrix is not the only factor influencing the corrosion behavior of the alloy. The volume fraction and distribution of the secondary phases also play an important role in determining how the alloy would behave in corrosive environments. The microstructures of the transverse planes for ZK40 and ZK40–Ag (Figs. 1 and 3, respectively) show that the distribution of the secondary phases are sparse and are interconnected to form dark streaks. Zhang et al. reported that discontinuous secondary phases have a detrimental effect on the corrosion resistance of Mg–Nd–Zn–Zr as they studied the influence of increasing Ag addition (0, 0.2, 0.4 and 0.8 wt%) [39]. The distribution of secondary phases in extrusion plane for both alloys, on the other hand, is disconnected and is dispersed throughout the matrix. Post-immersion microstructures are necessary to be able to confirm these observations.

## Conclusions

The following are the conclusions of this work:

1. Microstructure analysis revealed that the addition of silver followed by a heat treatment of 350 °C for 7 days resulted in a homogenized microstructure with larger grain size. Furthermore, the composition and distribution of secondary phases were altered and their volume fraction increased. Both the transverse and extrusion planes showed the same trends.
2. Addition of silver led to an increase in hardness between the transverse planes of ZK40 and ZK40–Ag but a decrease in hardness measurements in the extrusion plane. A contradictory result was observed during compression where an increase in compressive strength in the extrusion plane was noted while the transverse plane barely witnessed any change in strength. This is could be due to the shape and distribution of secondary phases as well as their composition. Further analysis will aid in explaining these results.
3. ZK40–Ag presented a more positive OCP than ZK40 independent of the plane being tested. This was attributed to the increased volume fraction of secondary phases that have a more positive potential than the  $\alpha$ -Mg matrix due to the presence of Ag. During the initial hours of immersion, the transverse planes for both alloys showed a more stable surface film. However, as immersion time increased, the developed films in both planes for ZK40–Ag seemed unable to maintain their integrity in comparison with ZK40.
4. PD results show that the addition of Ag resulted in an increase in cathodically controlled kinetics and a more positive  $E_{\text{corr}}$  value, therefore causing an increase in  $i_{\text{corr}}$  values and corrosion rates.
5. EIS results were in agreement with PD and OCP results. After the first hours of immersion, the transverse planes for ZK40 and ZK40–Ag both exhibited a significant increase in corrosion resistance, however, by the end of the testing period, ZK40 presented improved corrosion resistance than ZK40–Ag. This is in agreement with the literature stating that Ag has a negative effect on the corrosion characteristics of Mg alloys.
6. This work lays the foundation to understanding the role of microstructural features, as a result of Ag addition, on the mechanical and corrosion characteristics of Mg alloys. The authors plan to apply severe plastic deformation to a suitable system in the future to further improve the properties presented herein.

**Acknowledgements** This research was performed with support from the Qatar Foundation under the National Priorities Research Program grant# NPRP 8-856-2-364. The authors acknowledge this financial support with gratitude.

## References

- Chen Y, Xu Z, Smith C, Sankar J (2014) Recent advances on the development of magnesium alloys for biodegradable implants. *Acta Biomater* 10:4561–4573. <https://doi.org/10.1016/j.actbio.2014.07.005>
- Wang J, Smith CE, Sankar J, et al (2015) Absorbable magnesium-based stent: physiological factors to consider for in vitro degradation assessments. *Regen Biomater* 2:59–69. <https://doi.org/10.1093/rb/rbu015>
- Staiger MP, Pietak AM, Huadmai J, Dias G (2006) Magnesium and its alloys as orthopedic biomaterials: A review. *Biomaterials* 27:1728–1734. <https://doi.org/10.1016/j.biomaterials.2005.10.003>
- Li X, Liu X, Wu S, et al (2016) Design of magnesium alloys with controllable degradation for biomedical implants: From bulk to surface. *Acta Biomater* 45:2–30. <https://doi.org/10.1016/j.actbio.2016.09.005>
- Witte F, Kaese V, Haferkamp H, et al (2005) In vivo corrosion of four magnesium alloys and the associated bone response. *Biomaterials* 26:3557–3563. <https://doi.org/10.1016/j.biomaterials.2004.09.049>
- Zhao D, Witte F, Lu F, et al (2017) Current status on clinical applications of magnesium-based orthopaedic implants: A review from clinical translational perspective. *Biomaterials* 112:287–302. <https://doi.org/10.1016/j.biomaterials.2016.10.017>
- Ding Y, Wen C, Hodgson P, Li Y (2014) Effects of alloying elements on the corrosion behavior and biocompatibility of biodegradable magnesium alloys: a review. *J Mater Chem B* 2:1912–1933. <https://doi.org/10.1039/C3TB21746A>
- Gawlik MM, Wiese B, Desharnais V, et al (2018) The effect of surface treatments on the degradation of biomedical Mg alloys—a review paper. *Materials (Basel)* 11:1–29. <https://doi.org/10.3390/ma11122561>
- Ratna Sunil B, Sampath Kumar TS, Chakkingal U, et al (2016) In vitro and in vivo studies of biodegradable fine grained AZ31 magnesium alloy produced by equal channel angular pressing. *Mater Sci Eng C* 59:356–367. <https://doi.org/10.1016/j.msec.2015.10.028>
- Minárik P, Král R, Čížek J, Chmelík F (2016) Effect of different c/a ratio on the microstructure and mechanical properties in magnesium alloys processed by ECAP. *Acta Mater* 107:83–95. <https://doi.org/10.1016/j.actamat.2015.12.050>
- Saha P, Roy M, Datta MK, et al (2015) Effects of grain refinement on the biocorrosion and in vitro bioactivity of magnesium. *Mater Sci Eng C* 57:294–303. <https://doi.org/10.1016/j.msec.2015.07.033>
- Buzolin RH, Mohedano M, Mendis CL, et al (2017) As cast microstructures on the mechanical and corrosion behaviour of ZK40 modified with Gd and Nd additions. *Mater Sci Eng A* 682:238–247. <https://doi.org/10.1016/j.msea.2016.11.022>
- Yuan Y, Ma A, Jiang J, et al (2013) Optimizing the strength and ductility of AZ91 Mg alloy by ECAP and subsequent aging. *Mater Sci Eng A* 588:329–334. <https://doi.org/10.1016/j.msea.2013.09.052>
- Mokhtarishirazabad M, Azadi M, Hossein Farrahi G, et al (2013) Improvement of high temperature fatigue lifetime in AZ91 magnesium alloy by heat treatment. *Mater Sci Eng A* 588:357–365. <https://doi.org/10.1016/j.msea.2013.09.067>
- Lu Y, Bradshaw AR, Chiu YL, Jones IP (2015) Effects of secondary phase and grain size on the corrosion of biodegradable Mg–Zn–Ca alloys. *Mater Sci Eng C* 48:480–486. <https://doi.org/10.1016/j.msec.2014.12.049>
- Zhang S, Zhang X, Zhao C, et al (2010) Research on an Mg–Zn alloy as a degradable biomaterial. *Acta Biomater* 6:626–640. <https://doi.org/10.1016/j.actbio.2009.06.028>
- Mostaed E, Vedani M, Hashempour M, Bestetti M (2014) Influence of ECAP process on mechanical and corrosion properties of pure Mg and ZK60 magnesium alloy for biodegradable stent applications. *Biomater* 4:e28283. <https://doi.org/10.4161/biom.28283>
- Song X, Chang L, Wang J, et al (2018) Investigation on the in vitro cytocompatibility of Mg–Zn–Y–Nd–Zr alloys as degradable orthopaedic implant materials. *J Mater Sci Mater Med* 29. <https://doi.org/10.1007/s10856-018-6050-8>
- Guan RG, Cipriano AF, Zhao ZY, et al (2013) Development and evaluation of a magnesium–zinc–strontium alloy for biomedical applications - Alloy processing, microstructure, mechanical properties, and biodegradation. *Mater Sci Eng C* 33:3661–3669. <https://doi.org/10.1016/j.msec.2013.04.054>
- Vinogradov A, Vasilev E, Kopylov V, et al (2019) High Performance Fine-Grained Biodegradable Mg–Zn–Ca Alloys Processed by Severe Plastic Deformation. *Metals (Basel)* 9:186. <https://doi.org/10.3390/met9020186>
- Chen D, He Y, Tao H, et al (2011) Biocompatibility of magnesium–zinc alloy in biodegradable orthopedic implants. *Int J Mol Med* 28:343–348. <https://doi.org/10.3892/ijmm.2011.707>
- AbdelGawad M, Mansoor B, Chaudhry AU (2018) Corrosion Characteristics of Two Rare Earth Containing Magnesium Alloys BT - Magnesium Technology 2018. In: Orlov D, Joshi V, Solanki KN, Neelameggham NR (eds). Springer International Publishing, Cham, pp 43–53
- AbdelGawad M, Chaudhry AU, Mansoor B (2019) The Influence of Temperature and Medium on Corrosion Response of ZE41 and EZ33. In: Joshi VV, Jordon JB, Orlov D, Neelameggham NR (eds) Magnesium Technology 2019. Springer International Publishing, Cham, pp 159–167
- Hong D, Saha P, Chou DT, et al (2013) In vitro degradation and cytotoxicity response of Mg–4% Zn–0.5% Zr (ZK40) alloy as a potential biodegradable material. *Acta Biomater* 9:8534–8547. <https://doi.org/10.1016/j.actbio.2013.07.001>
- Song G (2005) Recent progress in corrosion and protection of magnesium alloys. *Adv Eng Mater* 7:563–586. <https://doi.org/10.1002/adem.200500013>
- Tie D, Feyerabend F, Hort N, et al (2014) In vitro mechanical and corrosion properties of biodegradable Mg–Ag alloys. *Mater Corros* 65:569–576. <https://doi.org/10.1002/maco.201206903>
- Kannan MB, Raman RKS (2008) In vitro degradation and mechanical integrity of calcium-containing magnesium alloys in modified-simulated body fluid. *Biomaterials* 29:2306–2314. <https://doi.org/10.1016/j.biomaterials.2008.02.003>
- Ben-Hamu G, Eliezer D, Kaya A, et al (2006) Microstructure and corrosion behavior of Mg–Zn–Ag alloys. *Mater Sci Eng A* 435–436:579–587. <https://doi.org/10.1016/j.msea.2006.07.109>
- Zhang X, Yuan G, Niu J, et al (2012) Microstructure, mechanical properties, biocorrosion behavior, and cytotoxicity of as-extruded Mg–Nd–Zn–Zr alloy with different extrusion ratios. *J Mech Behav Biomed Mater* 9:153–162. <https://doi.org/10.1016/j.jmbbm.2012.02.002>
- Minárik P, Král R, Pešička J, et al (2016) Microstructure characterization of LAE442 magnesium alloy processed by extrusion and ECAP. *Mater Charact* 112:1–10. <https://doi.org/10.1016/j.matchar.2015.12.002>

31. Mostaed E, Hashempour M, Fabrizi A, et al (2014) Microstructure, texture evolution, mechanical properties and corrosion behavior of ECAP processed ZK60 magnesium alloy for biodegradable applications. *J Mech Behav Biomed Mater* 37:307–322. <https://doi.org/10.1016/j.jmbbm.2014.05.024>
32. Azeem MA, Tewari A, Mishra S, et al (2010) Development of novel grain morphology during hot extrusion of magnesium AZ21 alloy. *Acta Mater* 58:1495–1502. <https://doi.org/10.1016/j.actamat.2009.10.056>
33. Song GL (2012) The effect of texture on the corrosion behavior of AZ31 Mg alloy. *Jom* 64:671–679. <https://doi.org/10.1007/s11837-012-0341-1>
34. Ben-Hamu G, Eliezer D, Shin KS (2006) Influence of Si, Ca and Ag addition on corrosion behaviour of new wrought Mg-Zn alloys. *Mater Sci Technol* 22:1213–1218. <https://doi.org/10.1179/174328406X109203>
35. Mandal M, Moon AP, Deo G, et al (2014) Corrosion behavior of Mg-2.4Zn alloy micro-alloyed with Ag and Ca. *Corros Sci* 78:172–182. <https://doi.org/10.1016/j.corsci.2013.09.012>
36. Gusieva K, Davies CHJ, Scully JR, Birbilis N (2015) Corrosion of magnesium alloys: the role of alloying. *Int Mater Rev* 60:169–194. <https://doi.org/10.1179/1743280414Y.0000000046>
37. Gusieva K, Sato T, Sha G, et al (2013) Influence of low level Ag additions on Mg-alloy AZ91. *Adv Eng Mater* 15:485–490. <https://doi.org/10.1002/adem.201200321>
38. Kirkland NT, Birbilis N, Staiger MP (2012) Assessing the corrosion of biodegradable magnesium implants: A critical review of current methodologies and their limitations. *Acta Biomater* 8:925–936. <https://doi.org/10.1016/j.actbio.2011.11.014>
39. Zhang X, Ba Z, Wang Z, et al (2013) Influence of silver addition on microstructure and corrosion behavior of Mg-Nd-Zn-Zr alloys for biomedical application. *Mater Lett* 100:188–191. <https://doi.org/10.1016/j.matlet.2013.03.061>
40. Lin DJ, Hung FY, Liu HJ, Yeh ML (2017) Dynamic Corrosion and Material Characteristics of Mg-Zn-Zr Mini-Tubes: The Influence of Microstructures and Extrusion Parameters. *Adv Eng Mater* 19:1–11. <https://doi.org/10.1002/adem.201700159>



# Study of In Vitro Biodegradation Behavior of Mg–2.5Zn–xES Composite

Srinivasan Murugan, Paul C. Okonkwo, Ahmed Bahgat, Gururaj Parande, Aboubakr M. Abdullah, and Manoj Gupta

## Abstract

In this study, zinc (Zn) and eggshell (ES) reinforced biodegradable magnesium alloy (Mg–2.5Zn) and environment concise (eco) composite (Mg–2.5Zn–xES) was fabricated using disintegrated melt deposition (DMD) technique. In vitro experiments were conducted to study the biodegradation behavior of Mg–2.5Zn and Mg–2.5Zn–xES ( $x = 3$  and  $7$  wt%) using simulated body fluid (SBF) under standard human body temperature of  $37$  °C. Using electrochemical Impedance Spectroscopy (EIS), electrochemical analysis was performed to study in vitro degradation behavior of alloy and composite. EIS revealed increased in vitro degradation of the biodegradable magnesium alloy and ecofriendly composite as percentage of ES reinforcement was increased. X-ray diffraction (XRD) was performed to observe the chemical composition of elements and reaction products present in the degraded samples after corrosion process. Scanning electron microscopy (SEM) analysis showed variations in surface morphology of the alloy and composite before and after degradation. SEM result revealed presence of defects in the tested samples after degradation process.

## Keywords

Magnesium • Eggshell • DMD • Biodegradation • SBF • EIS

## Introduction

Increasing demand to reduce greenhouse gas emissions has made the researchers to explore and develop lightweight materials at economical price, since the beginning of twenty-first century [1]. For the past two decades, magnesium (Mg) has emerged as a potential candidate in decreasing use of steel and aluminium. Mg has found its application in aerospace, automotive, sporting, and biomedical equipment due to less density and higher specific strength [1–4]. Stainless steel (SS) and titanium (Ti) are used as permanent/temporary human body implant for more than a century in biomedical application [4]. SS/Ti with higher elastic modulus used as orthopedic implants has major drawback of high stress shielding. Bioresorbable Mg has relatively closer elastic modulus compared to that of the natural bone which reduces the stress shielding effect as well as reduces healing time [5, 6]. Bioresorbable characteristics of Mg cause it to dissolve in human body which eliminates the cost of revision surgery and patients risk from surgical procedures. Mg is an essential mineral for metabolism in human body and the excess drained out in the form of urine [7].

Degradation/corrosion rate of pure Mg limits its use as orthopedic implant to maintain structural strength in physiological environment. Alloying elements for biomedical application are determined based on availability and ease of disposal, toxicity, and biocompatibility. Proper choice of alloying elements like Calcium (Ca), Zinc (Zn), Tin (Sn), Zirconium (Zr), etc., can control the rate of corrosion over stipulated period [8]. Zn is abundant in nature with high nutritional value, able to improve the corrosion resistant and highly biodegradable in physiological environment [9]. While Ca stimulates human bone growth, addition of Ca to Mg improves the mechanical properties and corrosion resistance of the material implanted in the human body [9]. Researches were performed to add eggshell that contains 95% of calcium carbonate and the hydroxyapatite derived

S. Murugan (✉) · P. C. Okonkwo  
Department of Mechanical and Mechatronics Engineering,  
Dhofar University, Salalah, Oman  
e-mail: [smurugan@du.edu.om](mailto:smurugan@du.edu.om)

A. Bahgat · A. M. Abdullah  
Centre for Advanced Materials, Qatar University, Doha, Qatar

G. Parande · M. Gupta  
Department of Mechanical Engineering, National University of  
Singapore, Singapore, Singapore

from eggshell synthesis used as bone graft material [10–12]. Ca is a natural source in eggshell waste which used as a reinforcement in Mg matrix to form eco (environmental concise) composite [13]. The results showed a considerable increase in mechanical properties and damping behavior at room temperature [14]. Damping is considered to be an important parameter which aids in mitigating the vibrations prolonged into human body caused by movements of the recipient and the stresses induced in the bone-implant interface.

This study focused on understanding the in vitro corrosion behavior of pure Mg alloyed with Zn and reinforced with xES ( $x = 0, 3, 7\%$ ) in a SBF at 37 °C. The prepared biodegradable composite was subjected to EIS analysis for two weeks. The materials were initially prepared using disintegrated melt deposition (DMD) [15–17] and hot extruded to 8 mm diameter. Then, the samples were further polarized to study the biodegradation behavior using EIS. SEM and XRD were employed to characterize the surface morphology and chemical composition of the Mg–2.5Zn–xES composite.

## Materials and Methods

The biodegradable magnesium alloys were prepared by melting pure Mg under argon gas jacket along with 2.5 wt% Zn and varying amount of eggshell ( $x = 3 \text{ wt\%}$  and  $7 \text{ wt\%}$  designated as 3ES and 7ES, respectively) to form three different material composition. Pure Mg turnings, powders of Zn and eggshell stacked like sandwich in a graphite crucible, was then superheated to a temperature of 750 °C and stirred with zirtex 25 [18] coated steel stirrer. The stirring was carried to form a vortex for 5 min at 450 rev/min. The melt was tapped at the bottom of the crucible through a graphite nozzle at 25 Lpm. The disintegrated melt was deposited into a graphite coated steel substrate to form cast billets of 50 mm in diameter. Furthermore, hot extrusion was carried to homogenize the cast billet using 150 T hydraulic press. The hot extrusion was carried at 350 °C to obtain the

billets of 8 mm in diameter with an extrusion ratio of 20.25:1. Colloidal graphite was used as lubricant.

A three-electrode double-jacketed 250 ml in vitro corrosion cell was used, in which a graphite rod, Mg coupon (only 50 mm<sup>2</sup> is exposed to the SBF), and saturated calomel electrode were the counter, working and reference electrodes, respectively [19]. The cell was maintained at 37 °C  $\pm$  0.5 °C using a thermostat water circulator. A thermometer was used to monitor the temperature of the electrolyte before and during the experiments. A Reference GAMRY 3000 potentiostat (Warminster, PA, USA) was used to perform the electrochemical measurements. Electrochemical impedance spectroscopy (EIS) measurements of Mg alloys were investigated for 2 weeks immersion in SBF solution in a frequency range of 10<sup>-2</sup> to 10<sup>5</sup> Hz with an AC amplitude of 5 mV. Tafel experiment was carried out at a constant scan rate of 0.3 mV/s within scan range of  $\pm$ 250 mV versus the open-circuit potential (OCP). The SBF composition was prepared as described in Table 1 [20].

Characterizing the degraded surfaces is vital to analyze the in vitro corrosion behavior of the samples after EIS electrochemical analysis. XRD (X'Pert-Pro MPD, PANalytical Co., Netherlands) was utilized to study different phases on the in vitro corroded samples. The morphology of the corroded surface was examined by Field emission scanning electron microscopy (FEI NOVA NANOSEM 450, Hillsboro, OR, USA) with an accelerating voltage of 20 kV.

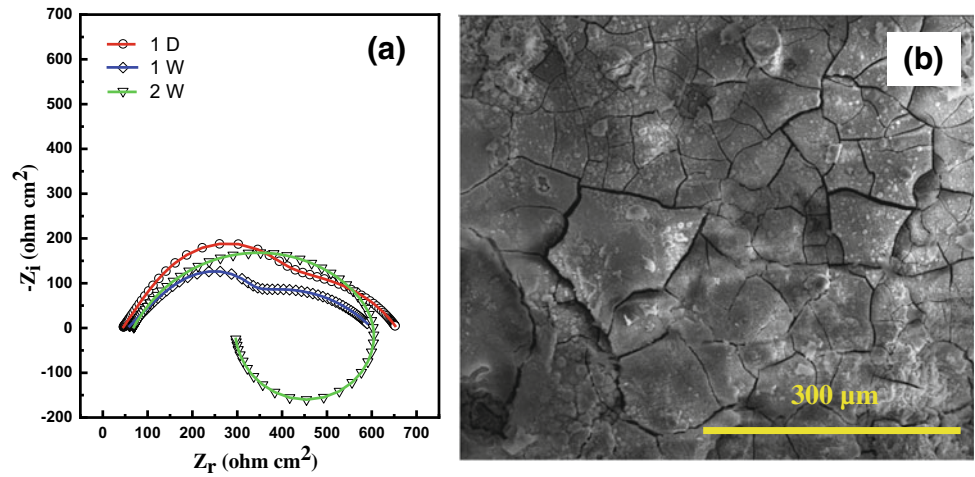
## Results and Discussion

The in vitro degradation of Mg–2.5Zn alloy and eco-composites using electrochemical impedance spectroscopy (EIS) was carried in simulated physiological environment. As shown in Figs. 1a, 2a and 3a, Nyquist plots revealed the in vitro degradation behaviors of the bioresorbable Mg samples. Nyquist plots showed the data obtained for 2 W (336 h) of immersion. The trend in the loops shows the corrosion rate evolution of the tested samples at different immersion duration.

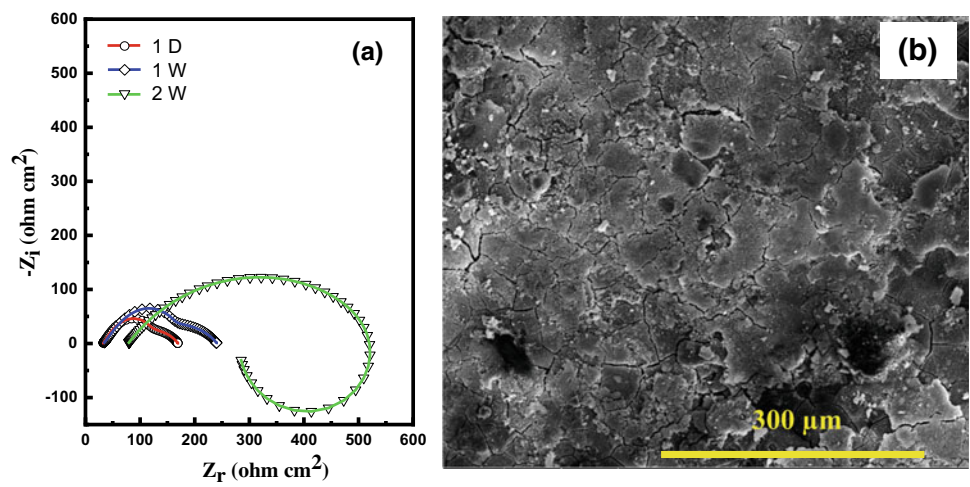
**Table 1** Regents for preparing SBF (pH7.40, 1 L) [20]

Order	Reagent	Amount
1	NaCl	8.035 g
2	NaHCO <sub>3</sub>	0.355 g
3	KCl	0.225 g
4	K <sub>2</sub> HPO <sub>4</sub> · 3H <sub>2</sub> O	0.231 g
5	MgCl <sub>2</sub> · 6H <sub>2</sub> O	0.311 g
6	1 M HCl	39 mL
7	CaCl <sub>2</sub>	0.292 g
8	Na <sub>2</sub> SO <sub>4</sub>	0.072 g
9	(CH <sub>2</sub> OH) <sub>3</sub> CNH <sub>2</sub>	6.118 g
10	1.0 M HCl	0–5 mL

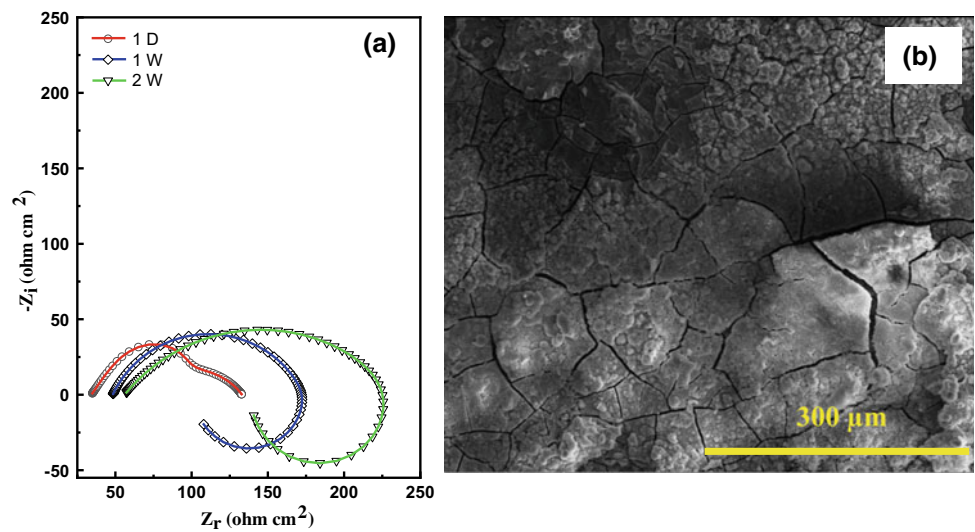
**Fig. 1** Mg-2.5Zn **a** Nyquist plot, **b** SEM image of degraded surface after 336 h (2 W)

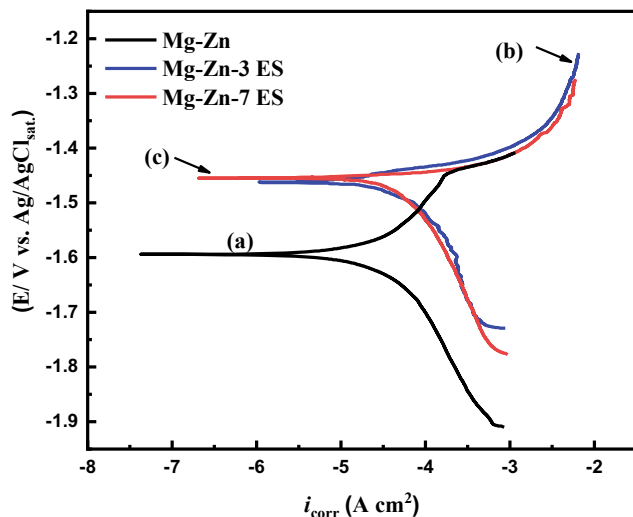


**Fig. 2** Mg-2.5Zn-3ES **a** Nyquist plot, **b** SEM image of degraded surface after 336 h (2 W)



**Fig. 3** Mg-2.5Zn-7ES **a** Nyquist plot, **b** SEM image of degraded surface after 336 h (2 W)

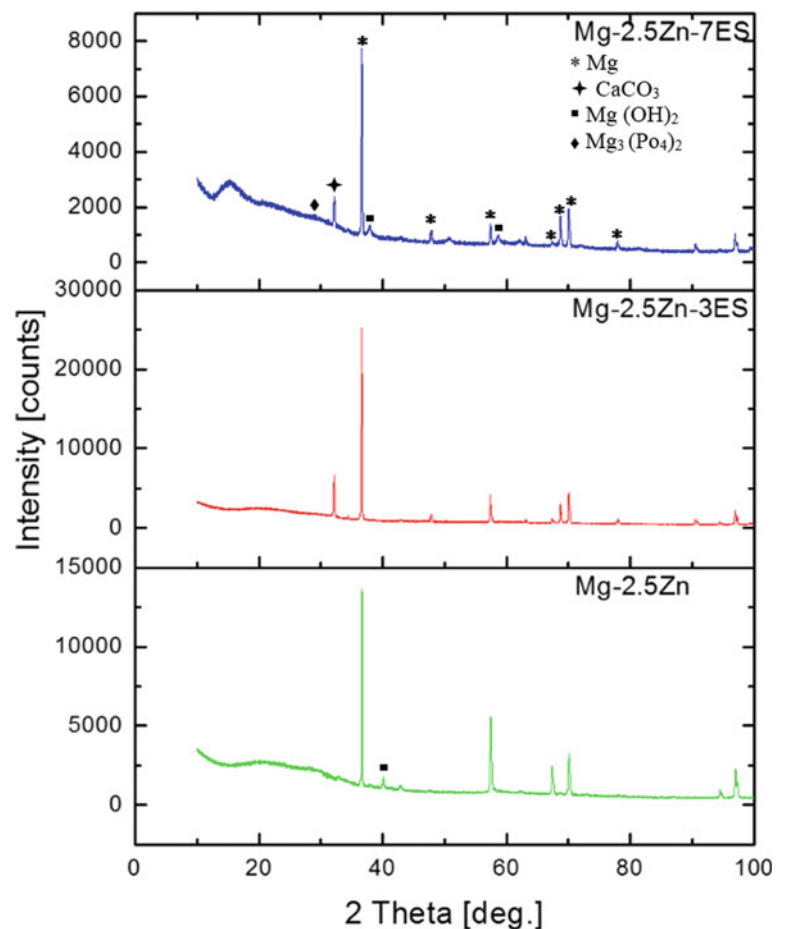




**Fig. 4** Tafel curves of a Mg-Zn, Mg-Zn-3ES and Mg-Zn-7ES alloys specimens in SBF solution

From the plots, it is evident that the curves are categorized by a semicircle in the high and middle region and a capacitive semicircle in the low-frequency region. The corrosion resistance is distinguished by the larger dimension of the capacitive loop.

**Fig. 5** XRD correspond to the EIS reaction products after 2 W immersion



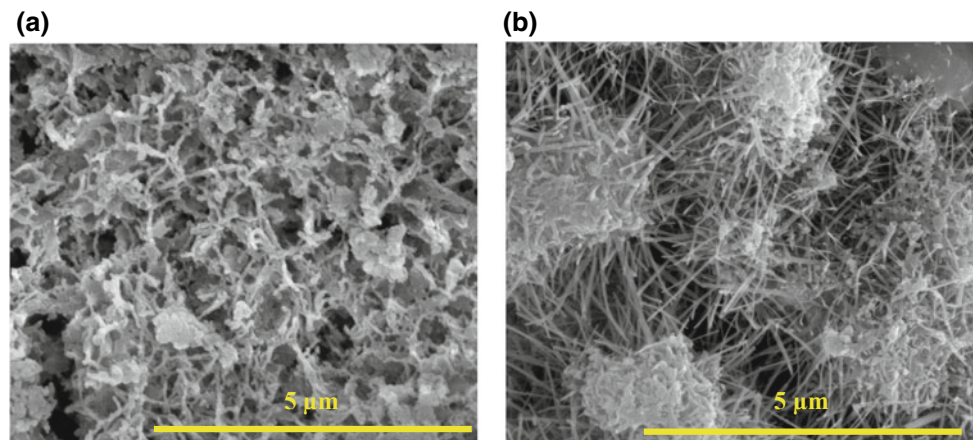
It can be seen from Figs. 1a, 2a, and 3a, that the composition with 7ES has the lowest polarization resistance of  $225 \Omega \text{ cm}^2$  after 2 weeks immersion. Mg-2.5Zn alloy has the maximum polarization resistance of  $590 \Omega \text{ cm}^2$  for the same duration. These changes were attributed to mass transportation, charge transfer reaction, and pitting corrosion during the in vitro degradation process.

Figure 4 illustrates the Tafel curves of the Mg alloys in SBF solution. It can be noticed that Mg-Zn alloy has the lowest corrosion current density of  $29 \mu\text{A cm}^{-2}$  in comparison with  $33$  and  $37 \mu\text{A cm}^{-2}$  of Mg-2.5Zn-3ES and Mg-2.5Zn-7ES alloys, respectively. These results are matching with the EIS measurements for the 1st-day immersion of Mg-2.5Zn alloys.

To understand the morphology of the corroded sample surfaces, SEM analyses were employed. As depicted in Figs. 1b, 2b, and 3b clear morphological changes were observed due to the immersion in SBF for 2 W. The reaction products were loose and distributed on the surface of the corroded samples. There were various cracks developed on the degraded sample surfaces and can be attributed to the sample shrinkage during drying. The XRD patterns in Fig. 5 elucidate the reaction products after immersion of 336 h, which is in good agreement with earlier findings [10, 21].



**Fig. 6** Growth of needle like apatite due to addition of ES particles **a** 3ES, **b** 7ES



Growth of apatite [22] is observed in Fig. 6a, b due to the interaction of ES particle with SBF during the two weeks of immersion.

## Conclusion

The work demonstrated the in vitro degradation behaviour of Mg–2.5Zn alloy and Mg–2.5Zn–xES composite. The in vitro degradation was carried in simulated body fluid using electrochemical impedance spectroscopy. The EIS and Tafel plots indicated Mg–2.5Zn alloy has good corrosion resistance. 3ES eco-composite is relatively lower in the corrosion resistance than that of Mg–2.5Zn alloy after 2 weeks of immersion. The pitting corrosion is the dominant corrosion mechanism in all the tested samples. Apatite growth is observed on the eco-composite specimens after two weeks of immersion electrochemical analysis.

## References

- Abbassi F, Srinivasan M, Loganathan C, Narayanasamy R, Gupta M (2016) Experimental and numerical analyses of magnesium alloy hot workability. *J Mag All* 4(4), 295–301
- Niinomi M, Nakai M, Hieda J (2012) Development of new metallic alloys for biomedical applications. *Acta Bio* 8(11), 3888–3903
- Gupta M (2018) A snapshot of remarkable potential of mg-based materials as implants. *Mat Sci Eng Int J* 2(1), 30–33
- Jafari S, Raman RS (2017) In-vitro biodegradation and corrosion-assisted cracking of a coated magnesium alloy in modified-simulated body fluid. *Mater Sci Eng C* 78, 278–287
- Johnston S, Shi Z, Venezuela J, Wen C, Dargusch MS, Atrons A (2019) Investigating Mg biocorrosion in vitro: lessons learned and recommendations. *JOM*, 71(4), 1406–1413
- Parande G, Manakari V, Meenashisundaram GK, Gupta M (2016) Enhancing the hardness/compression/damping response of magnesium by reinforcing with biocompatible silica nanoparticulates. *Int J Mater Res* 107(12), 1091–1099
- Jingyuan Y, Jianzhong W, Qiang L, Jian S, Jianming C, Xudong S (2016) Effect of Zn on Microstructures and Properties of Mg-Zn Alloys Prepared by Powder Metallurgy Method. *Rar Met Mater Engi* 45(11), 2757–2762
- Li H, Zhen Y, Qin L (2014) Progress of biodegradable metals. *Prog Natur Sci Mat Int* 24(5), 414–422
- O'Neill E, Awale G, Daneshmandi L, Umerah O, Lo KWH (2018) The roles of ions on bone regeneration. *Dru disc tod* 23(4), 879–890
- Kattimani V, Lingamaneni KP, Yalamanchili S, Mupparapu M (2019) Use of eggshell-derived nano-hydroxyapatite as novel bone graft substitute—A randomized controlled clinical study. *J biomat appl* 34(4), 597–614
- Lee SW, Kim SG, Balázs C, Chae WS, Lee HO (2012) Comparative study of hydroxyapatite from eggshells and synthetic hydroxyapatite for bone regeneration. *Or sur or med or path or rad* 113(3), 348–355
- Kumar GS, Girija EK (2013) Flower-like hydroxyapatite nanostructure obtained from eggshell: A candidate for biomedical applications. *Cer Int* 39(7), 8293–8299
- Parande G, Manakari V, Koppaarthi SDS, Gupta M (2018) Utilizing Low-Cost Eggshell Particles to Enhance the Mechanical Response of Mg–2.5 Zn Magnesium Alloy Matrix. *Adv Eng Mat*, 20(5), 1700919
- Lu H, Wang X, Zhang T, Cheng Z, Fang Q (2009) Design, fabrication, and properties of high damping metal matrix composites—a review. *Mater* 2(3), 958–977
- Chen Y, Shim VPW, Gupta M (2014) Dynamic Tensile Response of Magnesium Nanocomposites. *Appl Mech Mat* 566, 56–60
- Srinivasan M, Loganathan C, Narayanasamy R, Senthilkumar V, Nguyen QB, Gupta M (2013) Study on hot deformation behavior and microstructure evolution of cast-extruded AZ31B magnesium alloy and nanocomposite using processing map. *Mat Des* 47, 449–455
- Meenashisundaram G, Nai M, Gupta M (2015). Effects of primary processing techniques and significance of hall-petch strengthening on the mechanical response of magnesium matrix composites containing TiO<sub>2</sub> nanoparticulates. *Nanomat* 5(3), 1256–1283
- Nguyen QB, Gupta M (2010) Enhancing compressive response of AZ31B using nano-Al<sub>2</sub>O<sub>3</sub> and copper additions. *J All Comp* 490 (1–2), 382–387
- El-Haddad MA, Radwan AB, Sliem MH, Hassan WM, Abdullah AM (2019) Highly efficient eco-friendly corrosion inhibitor for mild steel in 5 M HCl at elevated temperatures: experimental & molecular dynamics study. *Sci rep* 9(1), 3695

20. Kokubo T, Takadama H (2006) How useful is SBF in predicting in vivo bone bioactivity? *Biomater* 27(15), 2907–2915
21. Sunil BR, Kumar AA, Kumar TS, Chakkingal U (2013) Role of biomineralization on the degradation of fine grained AZ31 magnesium alloy processed by groove pressing. *Mat Science Eng C* 33(3), 1607–1615
22. Harandi SE, Mirshahi M, Koleini S, Idris MH, Jafari H, Kadir MR (2013) Effect of calcium content on the microstructure, hardness and in-vitro corrosion behavior of biodegradable Mg-Ca binary alloy. *Mat Res* 16(1), 11–18

# Corrosion Behavior of Squeeze Cast Mg Alloy AM60-Based Hybrid Nanocomposite

Xinyu Geng, Luyang Ren, Zixi Sun, Henry Hu, and Xueyuan Nie

## Abstract

Micron-sized alumina ( $\text{Al}_2\text{O}_3$ ) short fibre and/or nano-sized alumina ( $\text{Al}_2\text{O}_3$ ) particles were squeezed cast into Mg AM60 alloy. Two types of 7 vol.% Fibre/AM60, and (7 vol. % Fibre + 3 vol.% nano-particle)/AM60 composites, as well as the unreinforced matrix alloy were prepared. The corrosion behaviors of the composites as well as the unreinforced matrix alloy were investigated by using the potential dynamic polarization test. Compared with the matrix alloy, the introduction of micron-sized alumina fibres decreased the corrosion resistance of Mg alloy AM60 considerably due to the presence of excessive interfaces between the fibre and matrix. The high density of grain boundaries and the absence of noble precipitates such as  $\beta\text{-Mg}_{17}\text{Al}_{12}$  phases and Al–Mn intermetallics at the grain boundaries in the composites should be for the reduction in their corrosion resistance. The addition of the nano-sized particles led to almost no further reduction in the corrosion resistance of the composite.

## Keywords

Magnesium-based hybrid nanocomposite (MHNC) • Corrosion resistance • Mg alloy • Micron-sized alumina ( $\text{Al}_2\text{O}_3$ ) short fibre • Nano-sized alumina ( $\text{Al}_2\text{O}_3$ ) particles

## Introduction

Magnesium (Mg) based materials have become one of the most significant candidates for structural engineering applications due to their lightweight, high thermal conductivity, and good ductility. In automotive industry, magnesium alloys are widely used for building vehicle components such as instrumental panels, cylinder head covers, intake manifolds, transfer cases and so on. Further expansion of new magnesium-based engineering applications is still on-going owing to the stringent government regulations on auto emissions and weight reduction. Hence, magnesium-based metal matrix composites (MMCs) including fiber-reinforced composites, particle reinforced composites and fiber-particle hybrid reinforced composites are emerging and being investigated for the improvement of mechanical properties of monolithic matrix alloys, including high yield strength, tensile strength, creep resistance, thermal shock resistance and wear resistance [1–6].

In the past few years, magnesium alloy-based hybrid composites are emerging since the combined advantages of different sizes of short fibres, and particles provide a high degree of design freedom, which enable fibres to increase strengths and particles to improve wear resistance [6]. Mondal et al. [7] studied the corrosion behavior of creep resistant AE42 magnesium alloy hybrid composites containing micron-sized  $\text{Al}_2\text{O}_3$  short fibres and SiC particles. The corrosion rates of different reinforcements combination was evaluated by potential dynamic polarization tests in 5 wt % NaCl solution. Their results showed that the tested composites exhibited much higher corrosion rates as compared to that of the unreinforced alloy. The addition of micron-sized SiC particles increased the corrosion rates of the hybrid composites by over 30%. Zhang et al. [6] pointed out that the introduction of micron-size reinforcements into the hybrid composite adversely affected the plasticity of Mg matrix alloys due to particle or fibre cracking and void formation at reinforcement-matrix interface leading to

X. Geng · L. Ren · Z. Sun · H. Hu (✉) · X. Nie  
Department of Mechanical, Automotive and Materials  
Engineering, University of Windsor, 401 Sunset Ave, Windsor,  
ON N9B 3P4, Canada  
e-mail: [huh@uwindsor.ca](mailto:huh@uwindsor.ca)

X. Geng  
e-mail: [gengx@uwindsor.ca](mailto:gengx@uwindsor.ca)

L. Ren  
e-mail: [ren11h@uwindsor.ca](mailto:ren11h@uwindsor.ca)

Z. Sun  
e-mail: [sun13h@uwindsor.ca](mailto:sun13h@uwindsor.ca)

X. Nie  
e-mail: [xnie@uwindsor.ca](mailto:xnie@uwindsor.ca)

accelerated failure. Recently, the study by Zhou et al. [8] demonstrated that the replacement of the micron-sized particles with the nanoparticles in the Mg-based hybrid composite effectively recovered the ductility of the composite by almost 120%. However, the introduction of foreign particles and/or fibre could deteriorate the corrosion resistance of magnesium alloys. Research on the corrosion behavior of the MHNC in the open literature is scarce.

In the present work, the microstructures of the monolithic matrix alloy AM60, its micron fibre-only composite and the MHNC were analyzed by the optical (OM) and scanning electron microscopes (SEM) and X-ray energy dispersive spectroscopy (EDS). The corrosion behavior of the monolithic matrix alloy AM60, its micron fibre-only composite and the MHNC were assessed by potentiodynamic polarization tests. The changes of the surface morphologies of the tested matrix alloy and composites were analyzed by electron scanning microscopy, and corrosion products were identified by the (EDS) analyses.

---

## Experimental Procedure

### Composites Preparation

Magnesium alloy AM60 with a chemical composition (wt%) of 6.0Al–0.22Zn–0.4Mn–0.1Si–0.01Cu–0.004Fe–0.002Ni–Mg was chosen as matrix alloy. Nano-sized Al<sub>2</sub>O<sub>3</sub> ceramic particles with an average particulate size of 100 nm and Al<sub>2</sub>O<sub>3</sub> short fibres with an average diameter of 4 μm and length of 50 μm were employed as raw materials for the preparation of hybrid reinforcements since they are relatively inexpensive and possess adequate properties.

During composite fabrication, a hybrid preform was first preheated to 700 °C. Then, molten matrix alloy AM60 at 750 °C infiltrated into the preheated preform under an applied pressure of 90 MPa. The pressure was maintained at the desired level for 30 s.

For fabrication of composites, a preform and squeeze casting process were employed. Two different types of 7 vol.% micron fibre/AM60, and (7 vol.% Fibre + 3 vol.% nano-particle)/AM60 composites were prepared, which were named the fibre-only composite (7FC), and the MHNC-7F3NP, respectively. In the hybrid composite, the short fibres constituted the primary reinforcement phase, and the particles served as the secondary reinforcement phase. For the purpose of comparison, the base alloy AM60 was also squeeze cast. The details of the process for fabricating the composites are given in references 6 and 8.

## Electrochemical Experimentation

Electrochemical studies were carried out by using EC-LAB SP-150 electrochemical apparatus with corrosion analysis EC-lab software. A three-electrode cell was set up through assigning the samples as working electrode, Ag/AgCl/sat'd KCl electrode as a reference electrode and a Pt metal electrode as counter-electrode. At the beginning of experiments, samples were held in a salt solution allowing the open circuit potential to settle to a constant value. Potentiodynamic polarization scans were conducted at a rate of 10 mV/s from –0.5 V versus open circuit potential in a more noble direction up to 0.5 V versus the reference electrode. Machined samples were ground with silicon carbide papers with various grades from 280 to 2500 grit and then cleaned in acetone, rinsed with deionized water and dried prior to potentiodynamic polarization. The values of corrosion potential ( $E_{\text{corr}}$ ) and current density ( $i_{\text{corr}}$ ) were determined at the intersection between the anodic and cathodic Tafel slopes, which were extrapolated by the linear parts of the polarization curves.

### Analyses of Corrosion Surface

The detailed features of the corroded surfaces were characterized at high magnifications using a FEI Quanta 200 FEG (Tokyo, Japan) scanning electron microscope (SEM) with a maximum resolution of 100 nm in a backscattered (BSE) mode/1 μm in X-ray diffraction mapping mode, and maximum useful magnification of 30,000. The corroded surfaces of the unreinforced alloy AM60, and the 7FC and MHNC-7F3NP composites were analyzed by the SEM in secondary electron (SE) mode to ascertain their corrosion mechanisms. Energy dispersive X-ray (EDS) analyses were used to define the elements distribution.

---

## Results and Discussion

### Electrochemical Tests

Figure 1 shows the polarization curves of the as-cast unreinforced alloy AM60, and 7FC and MHNC composites. Potentiodynamic polarization curves, measured in 3.5 wt% NaCl solution, were similar for the three tested materials. A summary of the results of potentiodynamic corrosion tests was given in Table 1. The corrosion potentials were in the range from –1.417 to –1.441 V (SCE), typical of



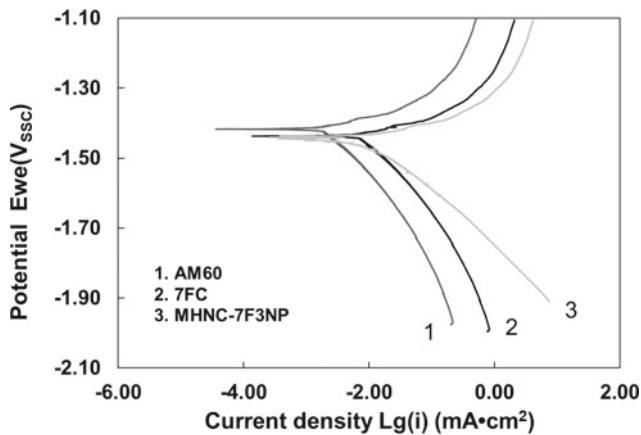


**Fig. 1** Polarization curves of the as-cast AM60, 7FC and MHNC-7F3NP composites

magnesium alloys. The curves indicated film breakdown at potentials immediately above the corrosion potential with characteristically low apparent Tafel slopes of about 52.9–29.1 mV/decade. At high current densities, the curves were affected by a potential drop due to the solution resistance, and on the cathodic side by the additional resistance due to the formation of hydrogen bubbles. At the end of the tests, the electrodes were covered by a black layer of corrosion products. The color of the products was changed to white after they dried.

Figure 2 displays the corrosion current densities and potentials of the as-cast AM60, and the 7FC and MHNC-7F3NP composites based on the data extracted from Fig. 1. Among the three tested materials, the unreinforced alloy AM60 (Curve 1) had a negative corrosion potential (−1.417 V), which was the highest, while the value of its corrosion current density ( $4.71 \mu\text{A}/\text{cm}^2$ ) was the lowest. Compared to that of the AM60, the polarization curve of the 7FC composite (Curve 2) was shifted to the right and downward. The value of the corrosion potential of the 7FC composite was more negative than that of the AM60 alloy, although the 7FC composite had a corrosion current density higher than that of the AM60 alloy. The polarization curve of the MHNC-7F3NP composite (Curve 3) exhibited a shift to the left and downward in comparison with that of the FC. The MHNC-7F3NP composite possessed a slightly lower corrosion potential and higher density than that of the 7FC.

The corrosion potentials, corrosion current density, and anodic/cathodic Tafel slopes (anodic:  $\beta_a$  and cathodic:  $\beta_c$ ) were derived from the test data. Based on the approximate linear polarization at the corrosion potential ( $E_{\text{corr}}$ ), polarization resistance ( $R_p$ ) values were determined by the relationship [9]:

$$R_p = \frac{\beta_a * \beta_c}{2.3 * i_{\text{corr}} * (\beta_a + \beta_c)} \quad (1)$$

where  $i_{\text{corr}}$  is the corrosion current density. The data in Table 1 denoted that the corrosion resistance of the AM60 alloy ( $4.07 \text{ k}\Omega \text{ cm}^2$ ) was decreased by the introduction of micron-sized fibres and nano-sized particles. The 7FC composite possessed a high corrosion current density, which was 20% higher than that of the matrix AM60 alloy. The corrosion resistance of the 7FC composite ( $2.08 \text{ k}\Omega \text{ cm}^2$ ) was only a half of that of the matrix alloy. The addition of the micron-sized fibres as reinforcement significantly reduced the corrosion resistance of the matrix alloy AM60 by almost 50%. The corrosion resistance of the MHNC-7F3NP was  $1.88 \text{ k}\Omega \text{ cm}^2$ . The presence of the nano-sized particles resulted in a reduction of the corrosion resistance of the 7FC composite from  $2.08$  to  $1.88 \text{ k}\Omega \text{ cm}^2$  by  $0.20 \text{ k}\Omega \text{ cm}^2$ . This observation indicated that the introduction of the nano-sized particles up to 3 vol.% had almost no effect on the corrosion resistance of the FC composite.

In the Tafel extrapolation method for measuring corrosion rates of Mg-based materials, the corrosion current density,  $i_{\text{corr}}$  ( $\mu\text{A}/\text{cm}^2$ ) is estimated by Tafel extrapolation of the cathodic branch of the polarisation curve, and the obtained  $i_{\text{corr}}$  can be linearly related to the average corrosion rate,  $P_i$  (mm/year) by the following equation [7, 10, 11]

$$P_i = 0.02285 \times i_{\text{corr}} \quad (2)$$

The calculated  $P_i$  values are listed in Table 1. Corrosion rates determined based on Tafel extrapolations demonstrate quantitatively the corrosion nature of various materials, although they are somewhat different from those obtained from weight loss or hydrogen evolution measurement [11]. Figure 3 shows the corrosion rates of the as-cast unreinforced alloy AM60, and 7FC and MHNC composites, which were 0.108, 0.130 and 0.136 mm/year, respectively. The introduction of the micron  $\text{Al}_2\text{O}_3$  fibres increased the

**Table 1** Electrochemical parameters of the unreinforced alloy AM60, and the 7FC and MHNC-7F3NP composites

Materials	$\beta_a$ (mV/dec)	$\beta_c$ (mV/dec)	$i_{\text{corr}}$ ( $\mu\text{A}/\text{cm}^2$ )	$R_p$ ( $\text{k}\Omega \text{ cm}^2$ )	$E_{\text{corr}}$ (V)	$P_i$ (mm/year)
AM60	52.9	262.5	4.71	4.07	−1.417	0.108
7FC	31.8	188.7	5.68	2.08	−1.437	0.130
MHNC-7F3NP	29.1	128	5.95	1.88	−1.441	0.136

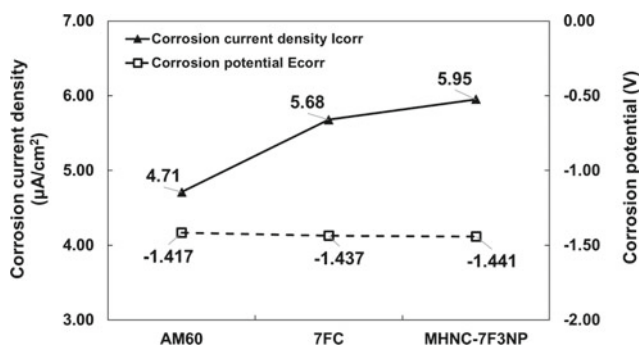


**Fig. 2** Corrosion current densities and potentials of the as-cast AM60, and the 7FC and MHNC-7F3NP composites

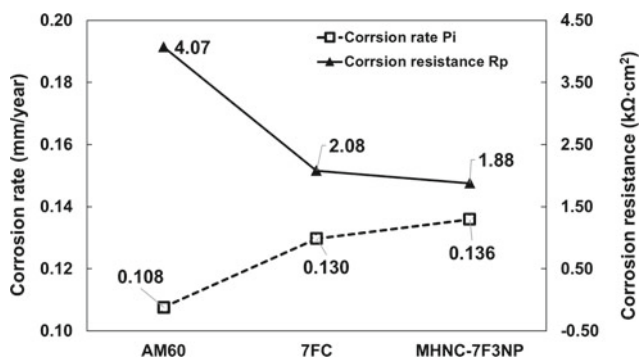


**Fig. 3** Corrosion resistances and rates of the as-cast AM60, and the 7FC and MHNC-7F3NP composites

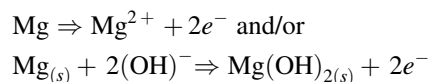
corrosion rate of the matrix alloy by 20%. But, the corrosion rate of the composite rose by only 4% with the further addition of the nano  $\text{Al}_2\text{O}_3$  particles.

### Corroded Surfaces and Corrosion Mechanisms

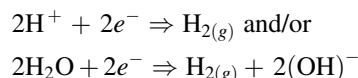
The surface morphologies of the corroded unreinforced alloy AM60, and 7FC and MHNC-7F3NP composites are shown in Fig. 4, after they were immersed in 3.5 wt% NaCl aqueous solution for one hour. The SEM micrograph given in Fig. 4a showed a layer of discontinuous film with corroded products. Figure 5 presents the EDS spectra showing the presence of oxygen and chlorine in the corroded surface of the unreinforced alloy AM60, and 7FC and MHNC-7F3NP composites, which suggested there were  $\text{Mg}(\text{OH})_2$  and  $\text{MgCl}$  in the corroded products. The corrosion behavior of AM60 alloy was significantly influenced by the alloy elements, such as aluminum and manganese. The formation of the surface morphology on the corroded unreinforced alloy AM60 resulted from a combined effect of galvanic

corrosion, and pitting corrosion. The presence of different phases in the microstructure of the unreinforced alloy AM60 should be responsible for these types of corrosion mechanisms. The eutectic  $\beta\text{-Mg}_{17}\text{Al}_{12}$  and Al-Mn intermetallic phases in the Mg-Al alloy could serve as cathodic sites, and the primary  $\alpha\text{-Mg}$  matrix would be anodic.

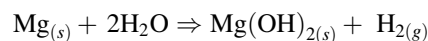
Anodic reaction:



Cathodic reaction:



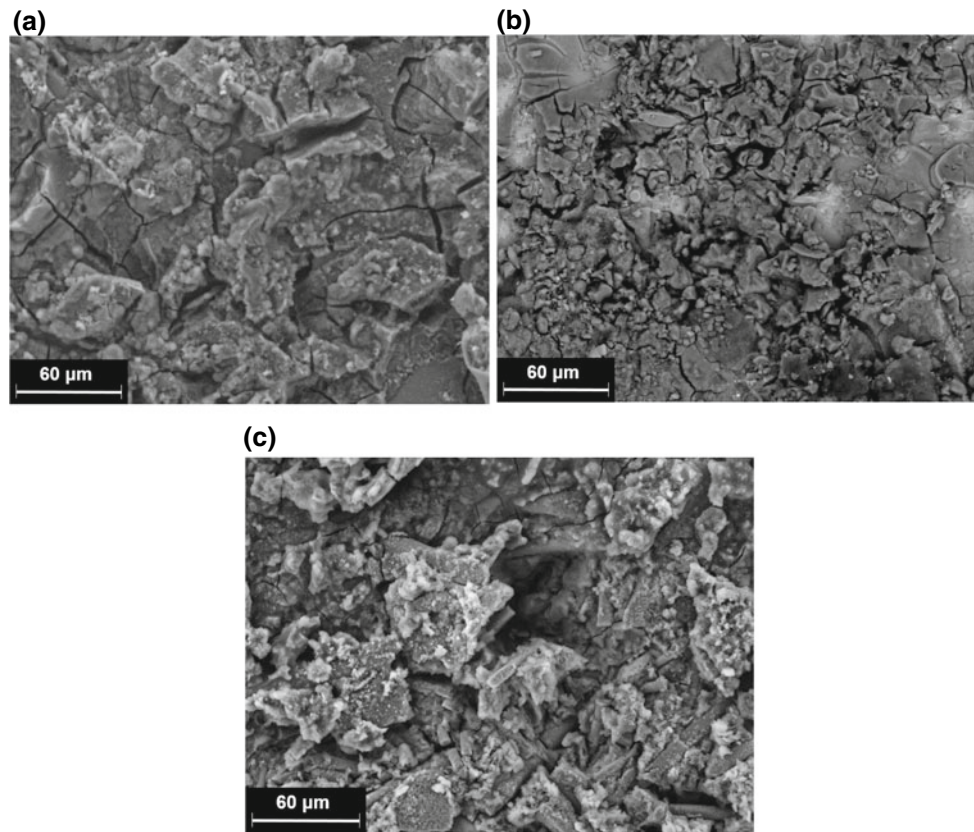
The overall reaction is:



As pointed out by Bakkar and Neubert [12, 13] for magnesium alloy AS41, owing to the high pH region around cathodic area, the passivation surface which contained  $\text{MgO}/\text{Mg}(\text{OH})_2$  was formed. The generation of hydrogen and the continuous formation of hydroxide ions kept increasing the pH value and the protective film grew thicker consequently. At the anodic region, the protective film was hardly to be formed due the pH was too low and  $\text{Mg}^{2+}$  was produced at a high rate from the alloy surface and the pit developed. As a result of maintaining electroneutrality, chloride ions were attracted into the pit. As the corrosion proceeded, the pit grew bigger and deeper and led to the formation of the discontinuous film. Song et al. [14] found that, in magnesium alloy AZ91, the  $\beta\text{-Mg}_{17}\text{Al}_{12}$  phase mainly served as a galvanic cathode and accelerated the corrosion process of the primary  $\beta\text{-Mg}$  matrix if the volume fraction of  $\beta\text{-Mg}_{17}\text{Al}_{12}$  phase was small, although the  $\beta\text{-Mg}_{17}\text{Al}_{12}$  phase was very stable in NaCl solutions and was inert to corrosion. Besides the  $\beta\text{-Mg}_{17}\text{Al}_{12}$  phase, the most potent cathodes in an Mg-Al alloy are the iron-rich precipitate phases. Heavy metal contamination promoted a general pitting attack.

Figures 4b, c present a SEM micrograph showing the surface morphology of the 7FC and MHNC-7F3NP composites after corrosion testing, which exhibited thick but irregular and loose films. The large and deep corrosion attack can be clearly observed on two composites samples which could be attributed to the crevice attacks of reinforcements.

**Fig. 4** SEM micrographs in SE mode showing corroded surfaces of **a** the unreinforced alloy AM60, and the **b** 7FC and **c** MHNC-7F3NP composites



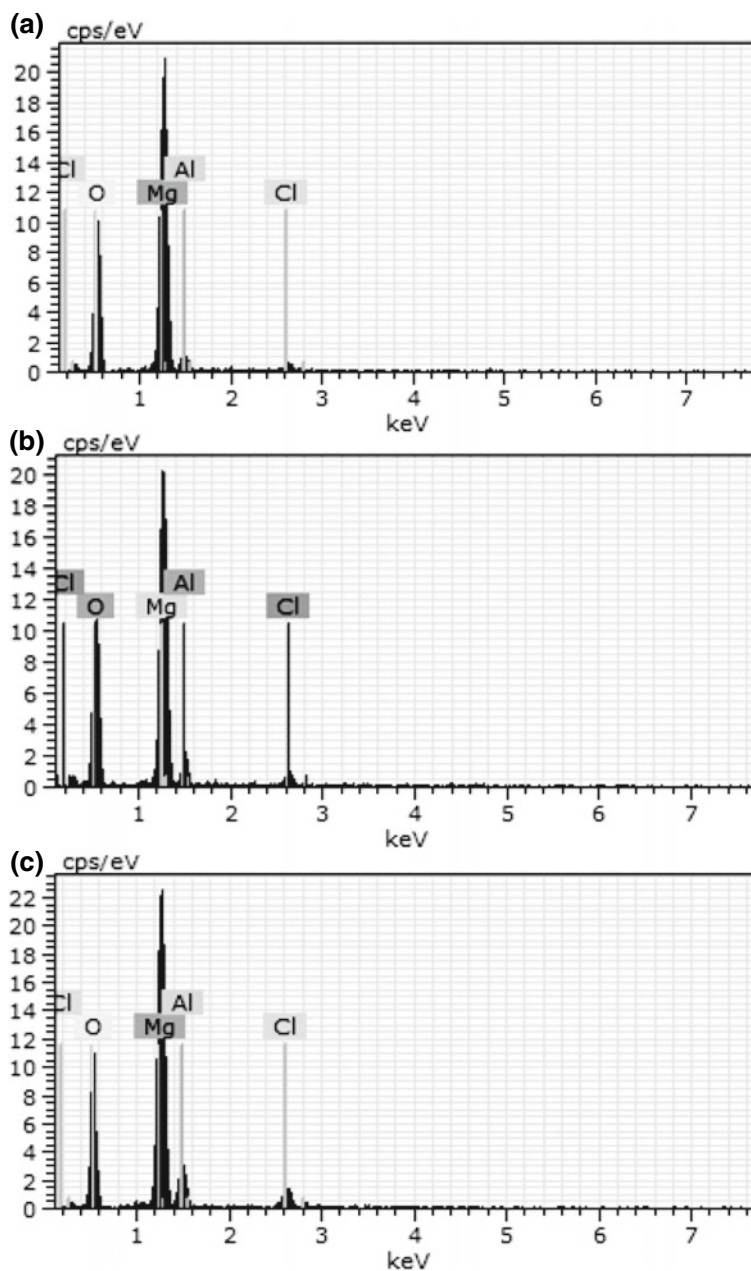
It is known that galvanic corrosion is the primary prospect when active magnesium is coupled with a relatively noble material [12]. But, no galvanic interaction between the alloy matrix and reinforcing fibers and particles could take place since the  $\text{Al}_2\text{O}_3$  fibers and particles are an insulator. Hypothetically, it implies that the addition of  $\text{Al}_2\text{O}_3$  fiber to the AM60 alloy should increase the corrosion resistance of the composite.

The previous corrosion study on pure magnesium was carried out in the same 3.5% NaCl solution [15]. It has found that the grain refinement decreased the corrosion resistance of magnesium, which was attributed to the higher density of grain boundaries and other defects from the grain refinement. However, in the case of fiber-reinforced composite, the high density of grain boundaries might not be the main mechanism of decreasing corrosion resistance. The changes in the grain boundary precipitation might appear to be another reason for the reduction in corrosion resistance for the composites. The existence of noble precipitates such as  $\text{Mg}_{17}\text{Al}_{12}$  phases at the grain boundaries makes the grain boundaries more corrosion resistant than the matrix and

increases the overall corrosion resistance of the material [7]. In the 7FC and MHNC-7F3NP composites, the lack of such relatively more noble precipitates at the grain boundaries could result in a low corrosion resistance.

The introduction of the fibers and particles in the 7FC and MHNC-7F3NP composites generated new interfaces between the matrix alloy and reinforcements. As both the fibers and particles existed, a large number of new interfaces generated in the composite. As a result, the presence of the new interfaces broke the continuity of the matrix and formed preferential spots for corrosion attack. The poor corrosion resistance of the composites should be attributed to the irregular and less adherent film. No evidence of any localized corrosion or galvanic enhanced corrosion around either the fibres or particles was found. The entire matrix alloy in the composites was uniformly corroded as the remaining fibres and particles stood out of the surface. This type of corrosion was observed in  $\text{SiC}_p/\text{ZC71}$  composites by Nunez-lopez et al. [16]. For their practical applications in corrosive environment, the developed composites need to be treated for surface protection, of which investigation proceeds.

**Fig. 5** EDS spectra identifying oxygen and chlorine for the **a** unreinforced alloy AM60, and **b** 7FC and **c** MHNC-7F3NP composites, respectively, which corresponds the SEM graphs in Fig. 4



## Conclusions

1. The results of the electrochemical tests indicate that the unreinforced as-cast base magnesium alloy AM60 exhibited corrosion resistance higher than its composites, and the reinforcement of the micron-sized  $\text{Al}_2\text{O}_3$  fibers and/or nano-sized  $\text{Al}_2\text{O}_3$  particles deteriorated the corrosion resistance of the 7FC and MHNC-7F3NP composites. The addition of the micron-sized fibres at 7 vol.% as reinforcement significantly reduced the corrosion resistance of the matrix alloy AM60 from 4.07 to 2.08  $\text{k}\Omega \text{cm}^2$  by almost 50%. The presence of the nano-sized particles resulted in a reduction of the corrosion resistance of the 7FC composite from 2.08 to 1.88  $\text{k}\Omega \text{cm}^2$  by 0.20  $\text{k}\Omega \text{cm}^2$ . This observation indicated that the introduction of the nano-sized particles up to 3 vol.% had almost no effect on the corrosion resistance of the FC composite.
2. The formation of the surface morphology on the corroded unreinforced alloy AM60 resulted from a combined effect of galvanic corrosion, and pitting corrosion. The presence of different phases in the microstructure of the unreinforced alloy AM60 should be responsible for these types of corrosion mechanisms.



3. No galvanic interaction between the alloy matrix and reinforcing fibers and particles could take place since the  $\text{Al}_2\text{O}_3$  fibers and particles are an insulator. In the composites, the lack of such relatively more noble precipitates such as  $\beta\text{-Mg}_{17}\text{Al}_{12}$  phases and Al–Mn intermetallics at the grain boundaries could result in a low corrosion resistance, although the high density of grain boundaries might not be the main mechanism of decreasing in corrosion resistance.
4. The introduction of the fibers and particles in the 7FC and MHNC-7F3NP composites generated new interfaces between the matrix alloy and reinforcements, which broke the continuity of the matrix and formed preferential spots for corrosion attack. The poor corrosion resistance of the composites should be attributed to the irregular and less adherent film on their surface.

**Acknowledgements** The authors would like to thank the Natural Sciences and Engineering Research Council of Canada, and University of Windsor for supporting this work.

## References

1. Zhang Q, Hu H, Lo J (2011) Solidification of discontinuous  $\text{Al}_2\text{O}_3$  fiber reinforced magnesium (AM60) matrix composite. *Defect and Diffusion Forum.* 312–315: 277–282
2. Banerji A, Hu H, Alpas AT (2012) Ultra-mild wear of  $\text{Al}_2\text{O}_3$  fibre and particle reinforced magnesium matrix composites. *Adv. Mat. Res.* 445: 503–508
3. Banerji A, Hu H, Alpas AT (2013) Sliding wear mechanisms of magnesium composites AM60 reinforced with  $\text{Al}_2\text{O}_3$  fibers under ultra-mild wear conditions. *Wear.* 301: 626–635
4. Zhang X, Fang L, Zhang Q, Hu H, Nie X (2014) Fabrication and tensile properties of  $\text{Al}_2\text{O}_3$  particle and fibre hybrid magnesium-based composites. *J. Chin. Ceramic Soc.* 1(2): 122–128
5. Zhang X, Fang L, Xiong B, Hu H (2015) Microstructure and tensile properties of Mg(AM60)/ $\text{Al}_2\text{O}_3$  metal matrix composites with varying volume fractions of fiber reinforcement. *J. Mater. Eng. Perform.* 24(12): 4601–4611
6. Zhang X, Zhang Q, Hu H (2014) Tensile behavior and microstructure of magnesium AM60-based hybrid composite containing  $\text{Al}_2\text{O}_3$  fibres and particles. *Mat. Sci. Eng. A.* 607: 269–276
7. Mondal AK, Blawert C, Kumar S (2015) Corrosion behaviour of creep-resistant AE42 magnesium alloy-based hybrid composites developed for powertrain applications. *Materials and Corrosion.* 66 (10), 1150–1158
8. Zhou J, Ren L, Geng X, Fang L, Hu H (2017) As-cast magnesium AM60-based hybrid nanocomposite containing alumina fibres and nanoparticles: Microstructure and tensile behavior. *Materials Science & Engineering A.* <https://doi.org/10.1016/j.msea.2017.10.070>.
9. Revie RW (ed) (2000) *Uhlig's Corrosion Handbook*. 2nd ed, John Wiley & Sons, New York
10. Shi Z, Atrens A (2011) An innovative specimen configuration for the study of Mg Corrosion. *Corrosion Science.* 53:226–246.
11. Shi Z, Liu M, Atrens A (2010) Measurement of the corrosion rate of magnesium alloys using Tafel extrapolation. *Corrosion Science.* 52:579–588
12. Bakkar A, Neubert V (2007) Corrosion characterisation of alumina–magnesium metal matrix composites. *Corrosion science.* 49(3):1110–1130
13. Bakkar A, Neubert V (2009) Corrosion behaviour of carbon fibres/magnesium metal matrix composite and electrochemical response of its constituents. *Electrochimica Acta,* 54(5):1597–1606
14. Song GL, Atrens A (1999) Corrosion mechanisms of magnesium alloys. *Adv. Eng. Mater.* 1(1):11–33
15. Ghali E (ed) (2010) *Corrosion resistance of aluminum and magnesium alloy: Understanding, Performance, and Testing.* Wiley, New York
16. Nunez-lopez CA, Skeldon P, Thomson GE, Lyon P, Karimzadeh H, Wilks TE (1995) The corrosion behaviour of Mg alloy ZC71/SiCp metal matrix composites. *Corrosion Science.* 37 (5):689–708

---

**Part VII**

**Solidification and Production of Magnesium**

# Thermodynamic Descriptions of the Quaternary Mg–Al–Zn–Sn System and Their Experimental Validation

Ting Cheng and Lijun Zhang

## Abstract

A brief review on the thermodynamic descriptions of all the sub-binary and ternary systems in the Mg–Al–Zn–Sn system available in the literature was first performed, from which the most reliable ones were chosen. After that, thermodynamic description of the quaternary Mg–Al–Zn–Sn system was established via the direct extrapolation of the chosen thermodynamic descriptions of the sub-binary and ternary systems in the framework of CALculation of PHase Diagrams (CALPHAD) approach. The reliability of the established thermodynamic database was finally validated through a comprehensive comparison of the model-predicted solidified microstructure characteristics and phase fractions in different quaternary alloys with the experimental ones.

## Keywords

Mg–Al–Zn–Sn • CALPHAD • Thermodynamic assessment • Scheil simulation

## Introduction

The low density of magnesium alloys makes them an attractive material for lightweight components in industry, automobiles, and aerospace fields [1, 2]. For the past years, numerous researches have been carried out on different magnesium alloys [3, 4], among which the Mg–RE (rare earth)-based alloys show excellent mechanical properties and good corrosion resistance. However, the prices and reserves of RE elements limit the application of Mg–RE-based alloys in commercial domain. Therefore, the development of RE-free magnesium alloys is very crucial. However, the previous studies indicate the mechanical

properties of the current RE-free magnesium alloys are still not exceedingly good enough, compared with Mg–RE-based alloys. Thus, the development of novel RE-free magnesium alloys is in urgent need. Nowadays, the computational thermodynamics based on the CALculation of PHase Diagrams (CALPHAD) approach [5] become an efficient tool that supplies valuable information to guide the design of alloys and/or the optimization of preparation processing. The development cycle and costs of novel alloys can be then significantly reduced with the aid of the computational thermodynamics. The key point for the alloy design driven by the computational thermodynamics lies in the accurate thermodynamic database of the target alloy system. With the accurate thermodynamic database, the multicomponent phase equilibria at any composition/temperature/pressure can be easily obtained. Moreover, the solidification process of cast alloys of industrial relevance can also be predicted according to, i.e., the Scheil–Gulliver simulations.

In the field of RE-free magnesium alloys, the AZ (Mg–Al–Zn) and AT (Mg–Al–Sn) series magnesium alloys have recently attracted more and more research attention of researchers [6, 7] due to their low cost. Aluminum is a common alloy element in magnesium alloys. Al addition can improve the casting properties and mechanical properties of magnesium alloys. As a major additive in magnesium alloys, Zn can play a role in solution strengthening and second phase strengthening, thus improving the creep resistance of magnesium alloys. As a special alloy element, Sn additional in magnesium alloys can induce the Mg<sub>2</sub>Sn phase with high melting point that may suppress the slip of grain boundary and improve the mechanical properties of alloys. Therefore, if the optimal amounts of additional Al, Zn, and Sn in Mg alloys can be designed, the optimal mechanical properties of RE-free Mg–Al–Zn–Sn alloys can be achieved. However, most of the current researches on AZ and AT series magnesium alloys depends on trial-and-error experimental investigation [8], which is very difficult to fully exploit the potential of AZ and AT series alloys. In order to perform the computational thermodynamics-driven alloy design of the

T. Cheng · L. Zhang (✉)  
State Key Laboratory of Powder Metallurgy, Central South University, Changsha, 410083, China  
e-mail: [lijun.zhang@csu.edu.cn](mailto:lijun.zhang@csu.edu.cn)

Mg–Al–Zn–Sn system, the accurate thermodynamic descriptions of quaternary Mg–Al–Zn–Sn system are the prerequisite, but still missing in the literature.

Consequently, the major research targets of the present paper are (i) to perform a comprehensive review on the thermodynamic descriptions of all sub-binary and ternary systems in the Mg–Al–Zn–Sn quaternary system, (ii) to construct a self-consistent set of thermodynamic descriptions of the Mg–Al–Zn–Sn quaternary system based on all sub-binary and ternary systems, and (iii) to validate the present thermodynamic database of the Mg–Al–Zn–Sn quaternary system by comparing the Scheil–Gulliver solidification simulation of two casting alloys with the experimental ones available in the literature.

## Review on Thermodynamic Descriptions for Binary Systems

### Mg–Al

The Mg–Al binary system is of particular importance to the magnesium and aluminum industry. The Mg–Al system consists of three solution phases (liquid,  $(\text{Mg})_{\text{hcp}}$ , and  $(\text{Al})_{\text{fcc}}$ ) and three intermetallic compounds  $\beta$  ( $\text{Al}_3\text{Mg}_2$ ),  $\gamma$  ( $\text{Al}_{12}\text{Mg}_{17}$ ) and  $\varepsilon$  ( $\text{Al}_{30}\text{Mg}_{23}$ ) phases. In 1977, the calculated phase diagram of Mg–Al system was firstly presented by Saboungi and Hsu [9]. In their work, the authors treated the  $\gamma$  phase as a stoichiometric compound, which is unreasonable in fact. The calculated eutectic temperature and compositions of  $(\text{Al})_{\text{fcc}}$  and  $\beta$  phases are inconsistent with the experimental ones. From the literature [10], some major issues were found in the work of Ludecke and Hack. The calculated results by Ludecke and Hack show that  $\text{Al}_3\text{Mg}_2$  phase disappears at low temperatures. In addition, the calculated phase equilibria in Mg-rich side are not accurate. Murray [11] re-assessed the Mg–Al system in 1982. The author treated  $\gamma$  phase as two sub-lattice model, i.e., that one sub-lattice is occupied by Al and Mg and the other is occupied by Al and vacancies. It should be noted the  $\gamma$  phase owns an  $\alpha$ -Mn structure with four sub-lattices without the vacancy occupation. Hence, such treatment for  $\gamma$  phase is inappropriate. Afterwards, the thermodynamic descriptions of Mg–Al system were reported by Saunders [10] and Zuo and Chang [12], respectively. In their work, the phase  $\zeta$  not  $\varepsilon$  phase was considered in the Mg–Al system. However, the results of [13] indicated the  $\varepsilon$  phase is stable. Based on the experimental results of [13], Chartrand and Pelton [14] reviewed the Mg–Al system again. Later, Liang et al. [15] re-optimized this system based on the new experimental data [16]. The calculated results from [15] can well reproduce most of the reported experimental ones. Therefore, the thermodynamic parameters from Liang et al. [15] are

adopted in the present work for construction of the Mg–Al–Zn–Sn quaternary system.

### Mg–Zn

As an important binary system, the Mg–Zn system has been experimentally and thermodynamically investigated by many groups. In this binary system, liquid,  $(\text{Mg})_{\text{hcp}}$ ,  $(\text{Zn})_{\text{hcp}}$ , and five intermetallic compounds (i.e.,  $\text{MgZn}_2$ ,  $\text{Mg}_2\text{Zn}_3$ ,  $\text{Mg}_7\text{Zn}_3$ ,  $\text{Mg}_{12}\text{Zn}_{13}$ , and  $\text{Mg}_2\text{Zn}_{11}$ ) exist. In 1988, a comprehensive thermodynamic assessment of Mg–Zn system was carried out by Clark et al. [17] based on the reported experimental data by Chadwick [18], Hume-Rothery and Rounsefell [19], and Park and Wyman [20]. Nevertheless, Higashi et al. [21] pointed that  $\text{Mg}_7\text{Zn}_3$  phase was placed at the hypereutectic part in the Mg-rich side according to Clark et al. [17]. Afterwards, the thermodynamic descriptions of Mg–Zn system were performed by Agarwal et al. [22], Liang et al. [15], and Wasiur-Rahman and Medraj [23], respectively. Agarwal et al. [22] treated all the intermetallic compounds as stoichiometric compounds. However, Park and Wyman [20] and Massalski [24] reported that  $\text{MgZn}_2$  phase owns a certain homogeneity range that has been considered in the assessment of Liang et al. [15] and Wasiur-Rahman and Medraj [23]. Besides, the liquid phase was described using the Bragg–Williams model by Agarwal et al. [22] and Liang et al. [15], while in the assessment by Wasiur-Rahman and Medraj [23], the modified quasi-chemical model (MQM) was employed to describe the liquid phase. Later, Ghosh et al. [25] re-assessed the Mg–Zn system based on the recently reported enthalpy of formation, entropy, and  $C_p$  information of intermediate phases [26–29]. The thermodynamic descriptions by [15] have been used to establish the thermodynamic descriptions of Mg–Sn–Zn [30], Cu–Mg–Zn [31], Mg–Zn–Gd [32]. In consideration of the consistence of thermodynamic database, the thermodynamic parameters from [15] are selected in the present work.

### Mg–Sn

As a simple binary eutectic system, the Mg–Sn system includes two eutectic reactions and a congruently melting compound,  $\text{Mg}_2\text{Sn}$ . The phase equilibrium information of binary Mg–Sn system was crucially assessed by Nayeb-Hashemi and Clark [33]. In 1984, Fries and Lukas [34] re-optimized the Mg–Sn system based on the published experimental information. Afterwards, the thermodynamic descriptions of this binary system were performed by Jung et al. [35, 36] and Kang and Pelton [37], respectively. In the work of [35–37], the high temperature  $C_p$  values of  $\text{Mg}_2\text{Sn}$  were evaluated according to the assumption of



$C_p(\text{Mg}_2\text{Sn}) = 2C_p(\text{Mg}) + C_p(\text{Sn})$ . Recently, the thermodynamic descriptions of Mg–Sn binary system were updated by Meng et al. [30], who took into account the newly reported heat capacities and heat contents of  $\text{Mg}_2\text{Sn}$  at low temperatures [38]. Later, Ghosh et al. [25] re-optimized the Mg–Sn system. The liquid phase was described with the MQM. It should be noted a better agreement between the experimental data and thermodynamic calculations from [30] is achieved, compared with previous ones [25, 33–37]. Therefore, the thermodynamic parameters of [30] are directly adopted in the present work.

## Al–Zn, Al–Sn, and Zn–Sn

Al and Zn are crucial alloy elements in the magnesium alloys. Hence, the investigation on the Al–Zn binary system is also necessary. There are two solid solution phases, i.e.,  $(\text{Al})_{\text{fcc}}$  and  $(\text{Zn})_{\text{hcp}}$ , and three invariant reactions. As early as 1973, Hultgren et al. [39] reviewed the thermodynamic properties and phase equilibria of the Al–Zn system. Later, the thermodynamic assessment of this binary system was carried out by Murray [40]. However, the calculated results by [40] are not in good agreement with the experimental data in the literature. Subsequently, Mey and Effenberg [41] thermodynamically updated this system. However, their calculated phase boundaries between  $(\text{Al})_{\text{fcc}2}$  and  $(\text{Al})_{\text{fcc}2} + (\text{Zn})_{\text{hcp}}$ , as well as those for the miscibility gap of the  $(\text{Al})_{\text{fcc}}$  phase are obviously different from the reported experimental ones. Afterwards, thermodynamic assessment of the Al–Zn binary system was performed by Mey [42], Chen and Chang [43], and Mathon et al. [44], respectively. The thermodynamic descriptions by [42–44] give very similar results. Among the three assessments, the thermodynamic descriptions of Al–Zn system reported by Mey [42] have been applied to construct the thermodynamic databases for the Al–Mg–Zn [15], Al–Zn–Ti [45], and Al–Cu–Zn [46] systems. In consideration of the compatibility of thermodynamic database in multicomponent systems, the thermodynamic parameters of Al–Zn system by [42] were directly employed in the present work.

As a simple eutectic binary system, the Al–Sn system consists of three solution phases, i.e., liquid,  $(\text{Al})_{\text{fcc}}$ , and  $(\text{Mg})_{\text{hcp}}$ . The Al–Sn system was first reviewed by Hayes [47]. Subsequently, the thermodynamic parameters from [47] were included in COST 507 database [48]. Afterwards, Kang and Pelton [37] thermodynamically reviewed the Al–Sn binary system by modeling the liquid phase with MQM. However, the groups of authors [37, 47] did not take into account the solubility of Sn in  $(\text{Al})_{\text{fcc}}$  during their thermodynamic assessments. It should be noted the calculated solubility of Sn in  $(\text{Al})_{\text{fcc}}$  by Hayes [47] is much larger than the reported experimental data. In addition, Flandorfer et al.

[49] presented the new experimental data on the enthalpies of mixing in the liquid phase of this system. In the recent, the present authors [50] re-optimized the Al–Sn binary system by taking into account the new experimental information [49]. The calculated phase equilibria and thermodynamic properties from [50] show better agreements with comprehensive experimental data and have a significant improvement compared with previous assessments [37, 47]. Thus, the thermodynamic parameters by Cheng et al. [50] were directly employed in this work.

Similarly, the Sn–Zn is also a simple eutectic system, consisting of three solution phases, i.e., liquid,  $(\text{Sn})_{\text{bcc}}$ , and  $(\text{Zn})_{\text{hcp}}$ . The Sn–Zn binary system was thermodynamically assessed by several groups [51–53]. Among them, Lee [51] comprehensively reviewed the Sn–Zn binary system based on the experimental data. The calculated results from Lee [51] can better reproduce the reported experimental data. Hence, the thermodynamic descriptions from [51] were employed in the present work.

All the calculated phase diagrams of the Mg–Al, Mg–Zn, Mg–Sn, Al–Zn, Al–Sn, and Sn–Zn binary systems according to the adopted thermodynamic descriptions from Refs. [15, 30, 42, 50, 51] are shown in Fig. 1, respectively.

---

## Review on Thermodynamic Descriptions for Ternary Systems

### Mg–Al–Zn

Because Al and Zn are basic alloy elements for a series of high-strength magnesium/aluminum alloys. Thus, the thermodynamic descriptions of Mg–Al–Zn are of importance and can serve as the basis for the quaternary and higher-order systems. For Mg–Al–Zn ternary system, there are two ternary phases, which named as  $\phi$  with the nominal composition  $(\text{Al}, \text{Zn})_5\text{Mg}_6$  and T with the nominal composition  $(\text{Al}, \text{Zn})_{49}\text{Mg}_{32}$  (note that it was denoted  $\tau$  in [15]), respectively. In addition, a ternary quasi-crystal phase named as Q was reported. The ternary Mg–Al–Zn system was initially assessed by Chen [54] using the technology from Chen and co-workers based on the PMLFKT program [55] for computing the phase equilibria. It should be noted that the models for  $\text{MgZn}_2$  and T phases are different from those for their isotopic phases in the Al–Mg–Cu system [56]. Afterwards, Liang et al. [57] assessed the Mg–Al–Zn system based on the thermodynamic descriptions of the Mg–Al [12], Mg–Zn [22] and Al–Zn [43] binary systems. In their work, three different models (disordered solution phases, stoichiometric compounds, and semi-stoichiometric phases) are used to different phases in this system.

Subsequently, Liang et al. [15] experimentally and thermodynamically investigated the Mg–Al–Zn ternary system.

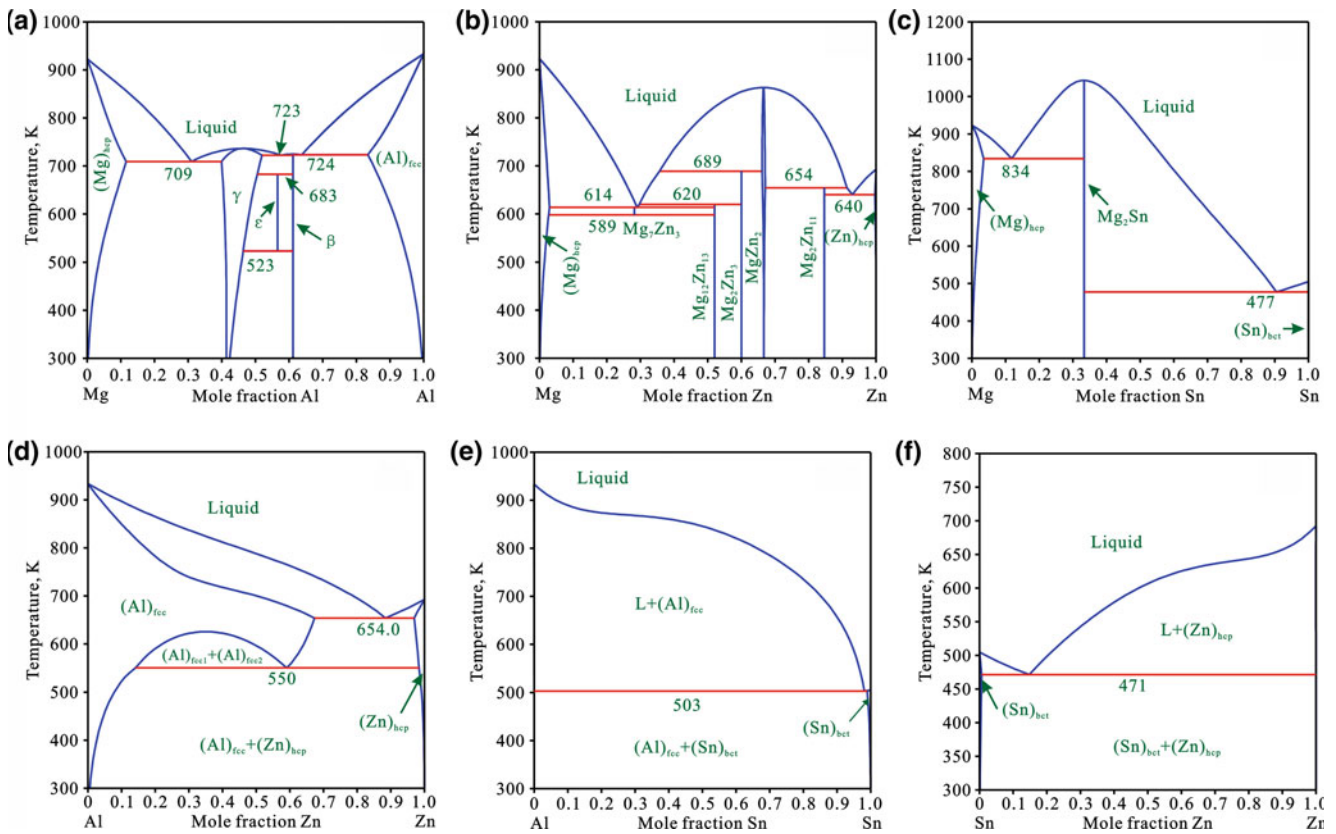


**Fig. 1** Calculated phase diagrams of **a** Mg–Al, **b** Mg–Zn, **c** Mg–Sn, **d** Al–Zn, **e** Al–Sn, and **f** Zn–Sn binary systems by Liang et al. [15], Meng et al. [30], Mey [42], Cheng et al. [50], and Lee [51], respectively

In their work, 34 ternary samples were annealed at 335 °C for 19 days. The phase equilibria were determined by X-ray diffraction (XRD), differential scanning calorimetry (DSC), and differential thermal analysis (DTA). In addition, the compositions of these phases were investigated by electron probe microanalysis (EPMA) and listed in the literature. The experiments were performed to provide the experimental information of the ternary solubilities of the Mg–Al and Mg–Zn phases, as well as to improve the cognitions of extensions of the homogeneity ranges of  $\phi$  and T phases. These experimental data together with the constitutional, thermochemical, and crystallographic data from the literature were considered in their optimization. Moreover, the thermodynamic descriptions of Mg–Al–Zn system were established based on the thermodynamic descriptions of the Mg–Al [15], Mg–Zn [15], and Al–Zn systems [42], which have been discussed in detail in Sect. 3. The calculated results from [15] can well reproduce most of the experimental data. The calculated vertical and isothermal sections in ternary Mg–Al–Zn system from [15] are shown in Figs. 2 and 3, respectively.

### Mg–Al–Sn

In the Mg–Al–Sn ternary system, no ternary phase was reported, and no ternary solubilities of the binary intermetallic compounds were observed. In 2006, Doernberg et al. [58] experimentally and thermodynamically investigated the Mg–Al–Sn system. There are 9 samples placed in a Ta capsule which were melted in argon atmosphere. Seven samples are with high magnesium contents, with Mg content varying between 61.7 and 75 at.%. The other two contained 26 and 33.3 at.% Mg, respectively. The isothermal equilibration at 400 °C was performed for 3 weeks. The liquidus of different vertical sections was determined by DTA and DSC. The microstructure of those alloys was investigated by XRD and scanning electron microscope (SEM). The calculated phase diagrams from [58] are in good agreement with their own experimental results and reported experimental data from other literature. Afterwards, the thermodynamic descriptions of the Mg–Al–Sn ternary system were carried out by Kang and Pelton [37]. In their work, the short-range ordering was taken into account for the liquid phase. A series

**Fig. 2** Calculated vertical sections in Mg–Al–Zn system along **a** 36 at.% Mg, and **b** 20 at.% Zn by Liang et al. [15]

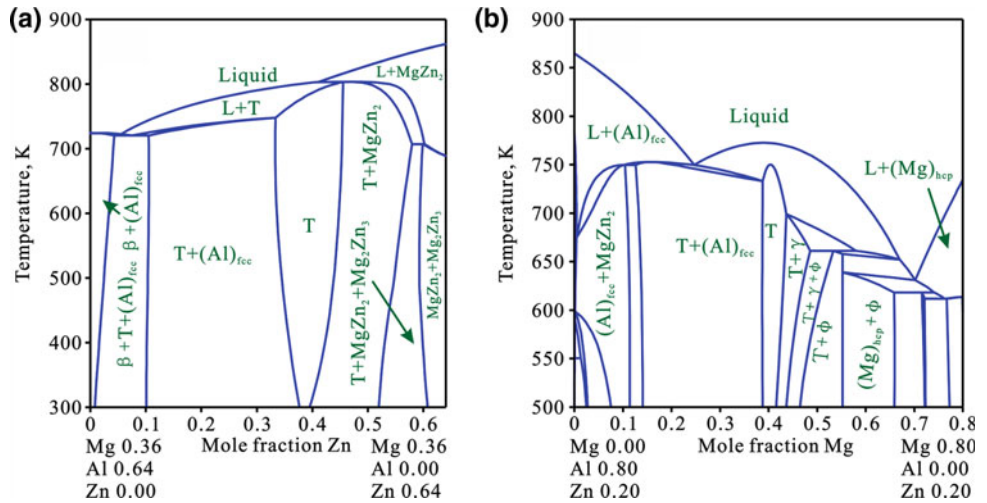
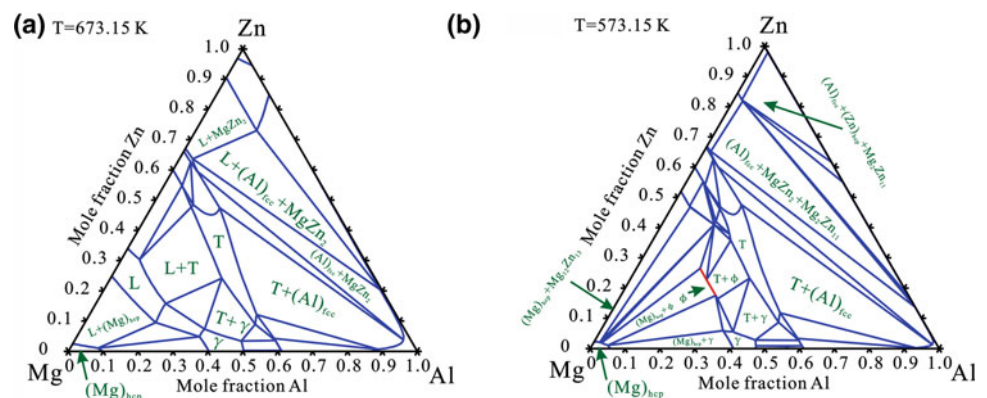


**Fig. 3** Calculated isothermal sections of the ternary Mg–Al–Zn system at 673.15 K and 573.15 K from Liang et al. [15]



of calculated vertical sections of Mg–Al–Sn were shown in their literature. The calculated results can well reproduce the experimental data. Recently, Cheng et al. [50] re-optimized the Mg–Al–Sn system and established a self-consistent thermodynamic database for this ternary system. In their work, the ternary liquid was described with associated solution model. A comprehensive comparison between the calculated phase equilibria/thermodynamic properties and the experimental data from the literature showed that their calculate results are in good agreement with these experimental information. Besides, the results of Scheil simulations furthermore validated the reliability of these thermodynamic descriptions. The vertical and isothermal sections due to [50] are shown in Figs. 4 and 5, respectively.

### Mg–Zn–Sn

For Mg–Zn–Sn ternary system, no ternary phase was reported in the previous investigations. In 2006, Bamberger [59] presented the calculated phase diagrams of Mg–Al–Sn system based on the commercial Mg database. However,

only the isothermal section at 450 °C was shown. Jun et al. [60] assessed the Mg–Zn–Sn system. In their work, the authors did not report the thermodynamic parameters and only showed the liquidus projection. Moreover, the experimental validation for the calculated results did not take into account in their work.

The thermodynamic descriptions of Mg–Zn–Sn ternary system were performed by Meng et al. [30] using CALPHAD approach. In their work, the Mg–Sn system was updated and the thermodynamic parameters of Mg–Zn [15] and Sn–Zn [51] systems were directly adopted in their work. The associated solution model was applied for the Mg–Zn–Sn ternary liquid phase consisting of Mg, Zn, Sn, and Mg<sub>2</sub>Sn. Meng et al. [30] showed that the calculated liquidus projection and vertical sections are in a reasonable agreement with most of reported experimental data. Afterwards, Ghosh et al. [25] re-optimized the ternary Mg–Zn–Sn system based on Mg–Sn, Mg–Zn, and Sn–Zn systems from their own work. Their calculated results are also consistent with the equilibrium invariant points. The typical vertical and isothermal sections due to [30] are shown in Figs. 6 and 7, respectively.

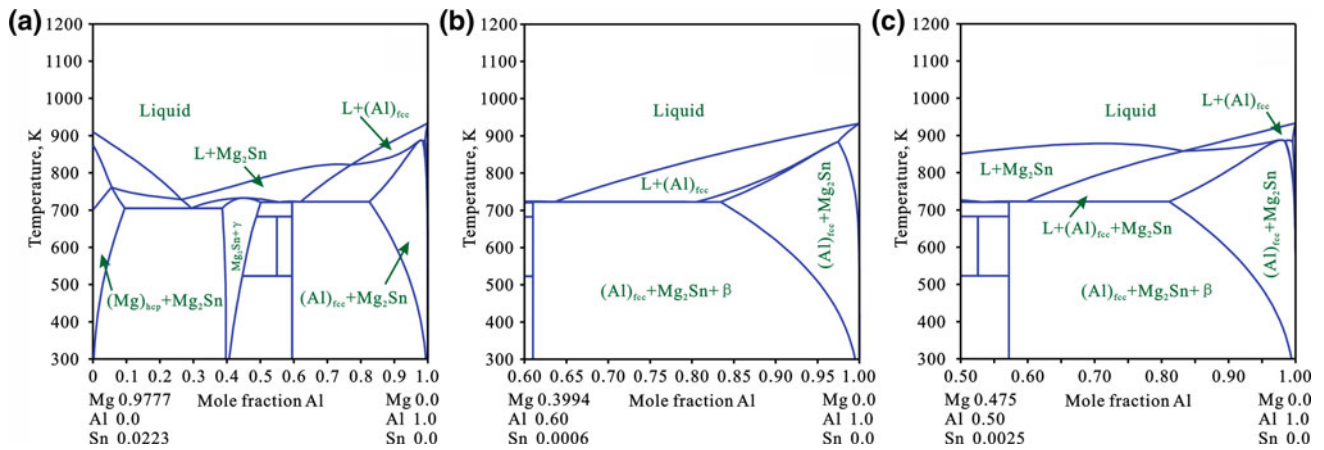


**Fig. 4** Calculated vertical sections close to the Mg–Al side of ternary Mg–Al–Sn system: **a** Mg<sub>0.9777</sub>Sn<sub>0.0223</sub>—Al, **b** Mg<sub>0.9985</sub>Sn<sub>0.0015</sub>—Al, and **c** Mg<sub>0.95</sub>Sn<sub>0.05</sub>—Al according to Cheng et al. [50]

**Fig. 5** Calculated isothermal sections of the ternary Mg–Al–Sn system at 623.15 K and 573.15 K according to Cheng et al. [50]

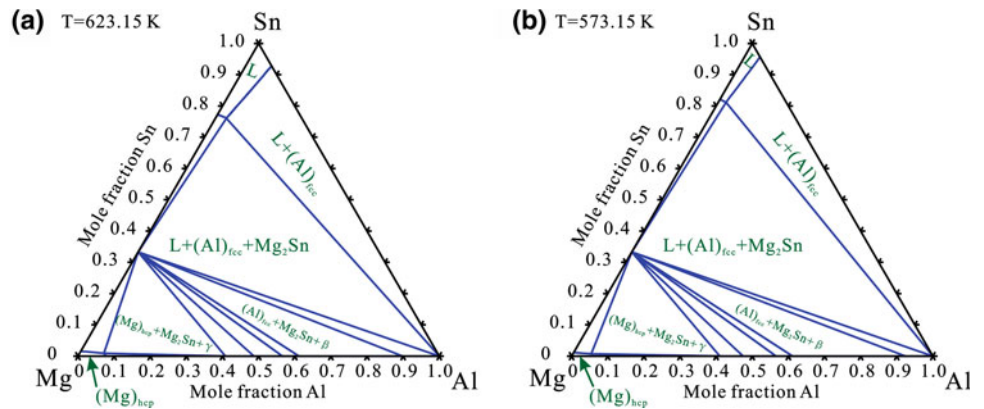
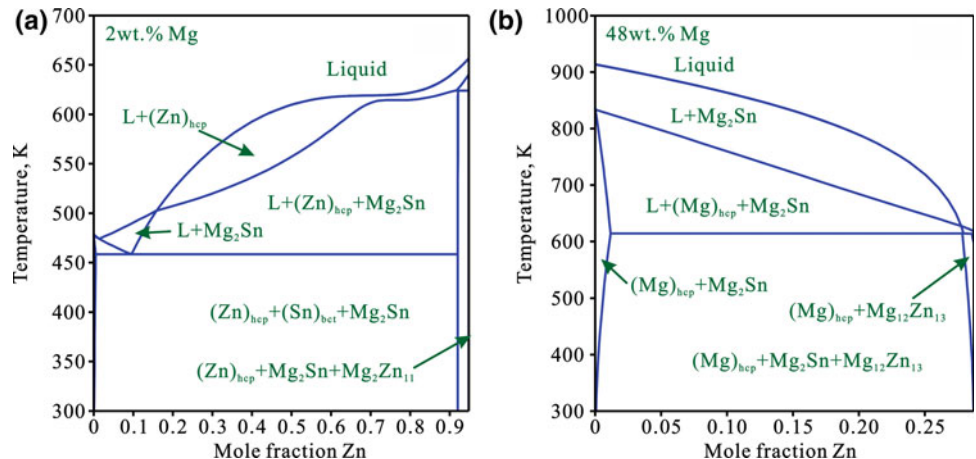


**Fig. 6** Calculated vertical sections in Mg–Zn–Sn system along **a** 2 wt% Mg, and **b** 48 wt% Mg by Meng et al. [30]



## Al–Zn–Sn

For the Al–Zn–Sn ternary system, no ternary compound was observed. The thermodynamic assessment of Al–Zn–Sn system was initially performed by Hayes [47] by means of CALPHAD method. Later, many groups [61–66]

investigated the experimental enthalpies of mixing of the liquid phase, activities of Al in the liquid and phase equilibria information. In consideration of these new experimental data, Cheng and Zhang [67] thermodynamically re-assessed the Al–Zn–Sn system based on the thermodynamic descriptions of Al–Sn [50], Al–Zn [42], and



**Fig. 7** Calculated isothermal sections of the ternary Mg–Zn–Sn system at 623.15 K and 573.15 K from Meng et al. [30]

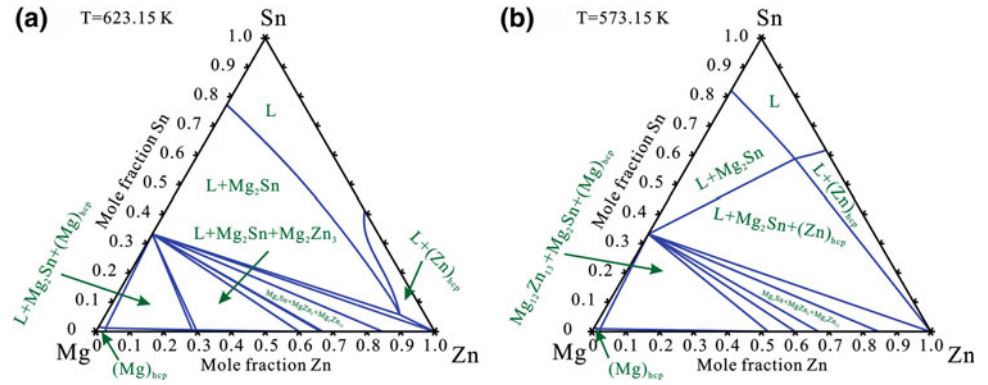
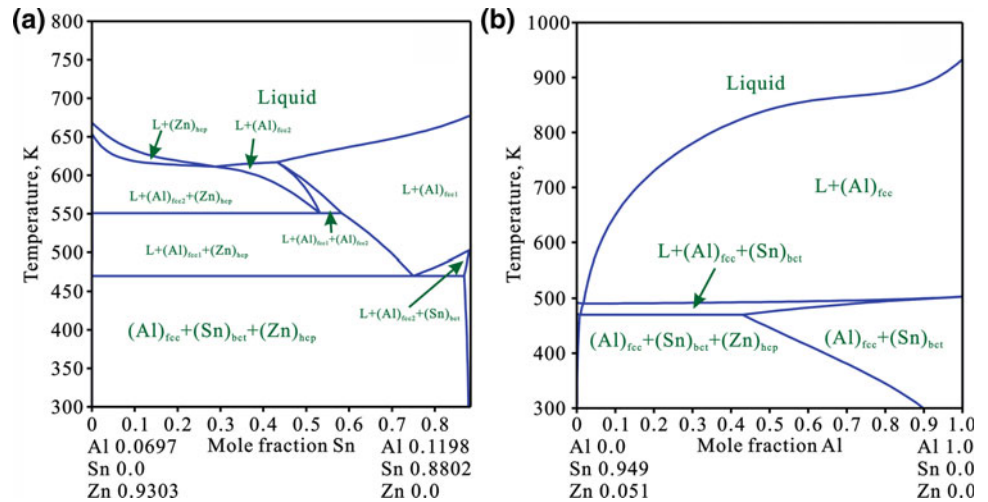


**Fig. 8** Calculated vertical sections in Al–Zn–Sn system along **a**  $\text{Al}_{0.0697}\text{Zn}_{0.9303}$ — $\text{Al}_{0.1198}\text{Sn}_{0.8802}$  and **b**  $\text{Sn}_{0.949}\text{Zn}_{0.051}$ —Al by Cheng and Zhang [67]



Sn–Zn [51] binary systems. The thermodynamic descriptions from [67] are very consistent with most of the experimental data. The calculated vertical sections and isothermal sections from [67] are shown in Figs. 8 and 9, respectively.

## Thermodynamic Models

The thermodynamic parameters of the pure elements Mg, Al, Zn and Sn were directly taken from SGTE compilation of Dinsdale [68].

In Mg–Sn binary system, the short-range ordering was taken into account for the liquid phase that was described using the associated model [69]. Hence, the associated model, which is possible to be integrated with the substitutional solution model, was also adopted for the liquid phase in the Mg–Al–Zn–Sn quaternary system. The liquid phase was treated as five species (i.e., Mg, Al, Zn,  $\text{Mg}_2\text{Sn}$ , and Sn) and four elements (i.e., Mg, Al, Zn, and Sn), among which  $\text{Mg}_2\text{Sn}$  is the associated cluster. The  $(\text{Mg})_{\text{hcp}}$ ,  $(\text{Al})_{\text{fcc}}$ ,  $(\text{Zn})_{\text{hcp}}$ , and  $(\text{Sn})_{\text{bct}}$  were described as completely disordered solutions. For Mg–Al–Zn–Sn quaternary system, the molar Gibbs energy of the solution phase (i.e., liquid,  $(\text{Mg})_{\text{hcp}}$ ,

$(\text{Al})_{\text{fcc}}$ ,  $(\text{Zn})_{\text{hcp}}$ , and  $(\text{Sn})_{\text{bct}}$ ) can be expressed as follows [70]:

$$G_m^\phi = \sum_i x_i^0 G_i^\phi + RT \sum_i x_i \ln x_i + {}^E G_m^\phi \quad (1)$$

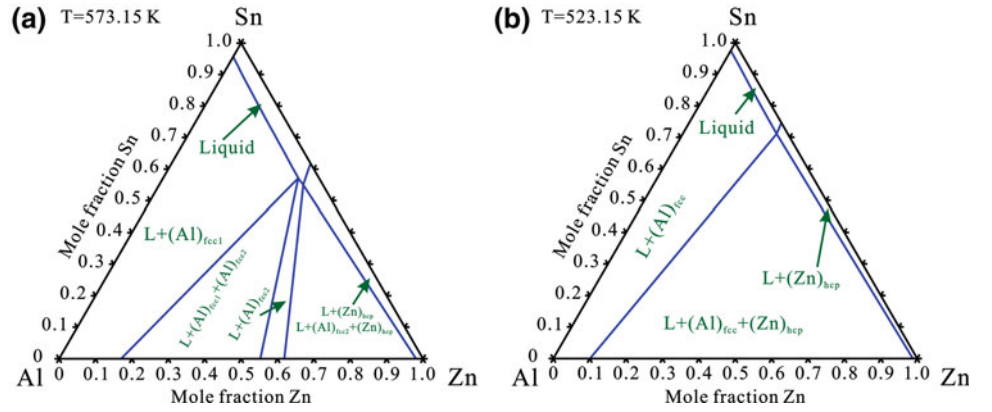
where  $R$  is the gas constant,  $\phi$  represents the solution phase,  $x_i$  and  ${}^0 G_i^\phi$  denote the mole fraction and the molar Gibbs energy of the elements  $i$  ( $i = \text{Mg}, \text{Al}, \text{Zn}, \text{Mg}_2\text{Sn}$ , or Sn for the liquid phase while  $i = \text{Mg}, \text{Al}, \text{Zn}$ , or Sn for the solid solution phases), and  ${}^E G_m^\phi$  represents the excess Gibbs energy, which can be expressed by the Redlich–Kister polynomial:

$${}^E G_m^\phi = \sum_{i \neq j} x_i x_j L_{i,j}^\phi + \sum_{i \neq j \neq k} x_i x_j x_k L_{i,j,k}^\phi + \sum_i \sum_{j > i} \sum_{k > j} \sum_{l > k} x_i x_j x_k x_l L_{i,j,k,l}^\phi \quad (2)$$

with

$$L_{i,j}^\phi = \sum_{j > i, v=0}^n {}^v L_{i,j}^\phi (x_i - x_j)^v \quad (3)$$

**Fig. 9** Calculated isothermal sections of the ternary Al–Sn–Zn system at 573.15 K and 523.15 K from Cheng and Zhang [67]



$$L_{i,j,k}^{\phi} = {}^iL_{i,j,k}^{\phi}(x_i + \eta_{i,j,k}) + {}^jL_{i,j,k}^{\phi}(x_j + \eta_{i,j,k}) + {}^kL_{i,j,k}^{\phi}(x_k + \eta_{i,j,k}) \quad (4)$$

$$\eta_{i,j,k} = (1 - x_i - x_j - x_k)/3 \quad (5)$$

${}^vL_{i,j}^{\phi}$  ( $i, j = \text{Mg, Al, Zn, Mg}_2\text{Sn, or Sn}$  for the liquid phase, while  $i, j = \text{Mg, Al, Zn, or Sn}$  for the solid solution phases, and  $i \neq j$ ) and  ${}^{i/j/k}L_{i,j,k}^{\phi}$  ( $i, j, k = \text{Mg, Al, Zn, Mg}_2\text{Sn, or Sn}$  for the liquid phase, while  $i, j, k = \text{Mg, Al, Zn, or Sn}$  for the solid solution phases, and  $i \neq j \neq k$ ) are the binary and ternary interaction parameters, respectively. These parameters are usually expressed as  $a + bT$ . The  $a$  and  $b$  represent the interaction coefficients.

### Thermodynamic Descriptions for Mg–Al–Zn–Sn Quaternary System

Up to now, no accurate thermodynamic descriptions for Mg–Al–Zn–Sn quaternary system have been reported. In the present work, all the sub-binary and ternary systems were comprehensively reviewed in the above sections. Based on the above assessment, the thermodynamic parameters of Mg–Al–Zn, Mg–Al–Sn, Mg–Zn–Sn, and Al–Zn–Sn systems due to [15, 30, 50, 67] were directly employed in this work. Through the CALPHAD approach, a thermodynamic description of Mg–Al–Zn–Sn quaternary system is then established based on the Muggianu extrapolation [71].

Figure 10a shows the calculated isothermal section of Mg–Al–Zn–Sn quaternary system at 573.15 K and 10 at.% Sn. Compared with Fig. 3b, the existence of  $\text{Mg}_2\text{Sn}$  was conformed in this isothermal section. Due to the addition of Sn, the number and types of phases in the corresponding regions change. The existence of  $\text{Mg}_2\text{Sn}$  could improve the strength of Mg alloys. Figure 10b shows the calculated vertical section of this quaternary system along  $\text{Mg}_{0.90}\text{Al}_{0.06}\text{Zn}_{0.02}\text{Sn}_{0.02}$ – $\text{Mg}_{0.98}\text{Zn}_{0.02}$ . Taking point A as

an example, it can be found that the  $(\text{Mg})_{\text{hcp}}$ ,  $\text{Mg}_{12}\text{Zn}_{13}$ , and  $\text{Mg}_2\text{Sn}$  are finally solidified structure. It is very obvious that the  $\text{Mg}_{12}\text{Zn}_{13}$  will not appear in the Mg–Al–Sn system. Thus, it can be seen that the addition of 2 at.% Zn has a great influence on phase diagrams of Mg–Al–Sn ternary system. According to Fig. 10, it should be noted the addition of Sn/Zn has a great influence on the Mg–Al–Zn/Mg–Al–Sn ternary system. Hence, the establishment of self-consistent thermodynamic database of the Mg–Al–Zn–Sn quaternary system is of importance.

### Experimental Validation

Kim et al. [72] investigated the microstructures of 5 as-cast Mg–Al–Zn–Sn alloys by means of optical microscope (OM), SEM, and XRD. The corresponding optical micrographs and SEM images were also provided in the original publication [72]. In their work, ingot was fabricated by a squeeze cast. The quaternary alloys were induction melted at 750 °C in a mild steel crucible under protective atmosphere and cast into a permanent mould.

In the present work, the solidified phase fractions of two as-cast samples (Mg–5Al–1Zn–1Sn (wt%) and Mg–5Al–1Zn–5Sn (wt%)) from [72] were counted by using the Image-Pro software based on the SEM images. To validate the reliability of established thermodynamic database of this quaternary system, the Scheil solidification simulations were performed to obtain the solidified phase fractions for the two as-cast alloys. The simulation results were then compared with the experimental data. The Scheil solidification mode, which is based on the assumption of the fast diffusion in the liquid phase but no diffusion in the solid, is much closer to the actual casting conditions, compared with the equilibrium solidification. Based on the current simulation results, the solidification sequences for Mg–5Al–1Zn–1Sn are  $L \rightarrow (\text{Mg})_{\text{hcp}}$ ,  $L \rightarrow \gamma + (\text{Mg})_{\text{hcp}}$ , and  $L \rightarrow (\text{Mg})_{\text{hcp}} + \gamma + \text{Mg}_2\text{Sn}$ ,

**Fig. 10** **a** Calculated isothermal section of the quaternary Mg–Al–Zn–Sn system at 573.15 K and 10 at.% Sn, **b** Calculated vertical section of the quaternary Mg–Al–Zn–Sn system along  $\text{Mg}_{0.90}\text{Al}_{0.06}\text{Zn}_{0.02}\text{Sn}_{0.02}$ – $\text{Mg}_{0.98}\text{Zn}_{0.02}$ , in the present work

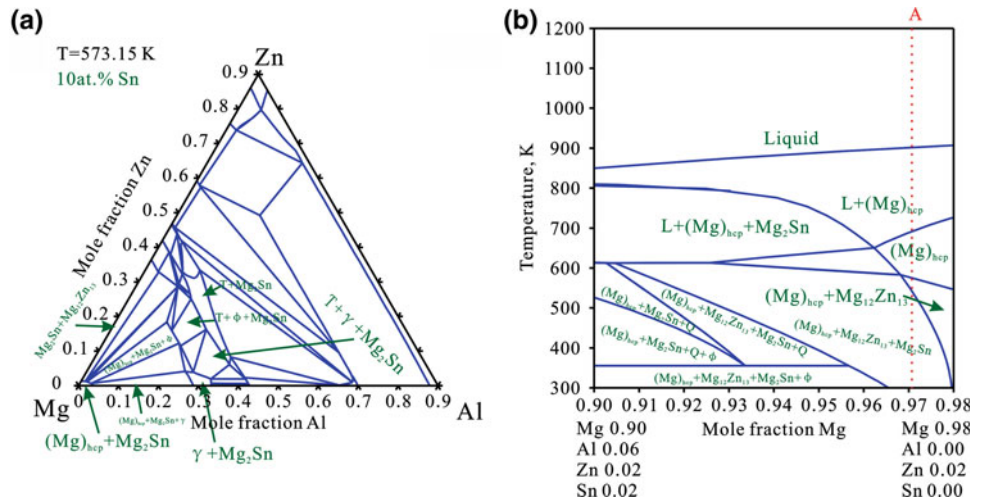
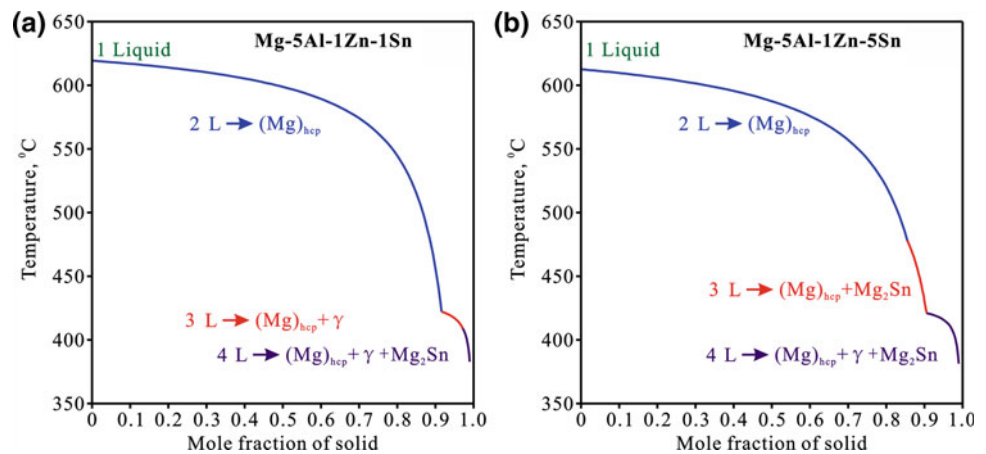


**Fig. 11** Simulated solidification paths of **a** Mg–5Al–1Zn–1Sn (wt %) and **b** Mg–5Al–1Zn–5Sn (wt %) under the Scheil–Gulliver conditions, respectively



while the solidification sequences for Mg–5Al–1Zn–5Sn are  $L \rightarrow (\text{Mg})_{\text{hcp}}$ ,  $L \rightarrow \text{Mg}_2\text{Sn} + (\text{Mg})_{\text{hcp}}$ , and  $L \rightarrow (\text{Mg})_{\text{hcp}} + \gamma + \text{Mg}_2\text{Sn}$ . The predicted final microstructures of the two alloys contain  $\text{Mg}_2\text{Sn}$ ,  $(\text{Mg})_{\text{hcp}}$ , and  $\gamma$  phases, which are the consistent as the actual as-cast samples. The simulated solidification paths of the two quaternary alloys are shown in Fig. 11. Moreover, Table 1 shows the contrast results of solidification phase fractions between the calculated results and experimental ones. It should be noted that the experimental values were the average ones determined directly by using the Image-Pro software based on the corresponding SEM images from the original publication [72]. According to

Table 1, it should be noted that predicted values for solidified phases are in good agreement with the experimental ones.

## Conclusions

- All thermodynamic descriptions of Mg–Al, Mg–Zn, Mg–Sn, Al–Zn, Al–Sn, and Zn–Sn binary systems were crucially evaluated.
- All thermodynamic descriptions of Mg–Al–Zn, Mg–Al–Sn, Mg–Zn–Sn, and Al–Zn–Sn ternary systems were crucially reviewed.

**Table 1** Solidified phase fractions obtained by Scheil simulation and experimental statistics

Alloy No. (wt%)	Phase	Calculated results (vol.%)	Experimental statistics (vol.%)
Mg–5Al–1Zn–1Sn	$(\text{Mg})_{\text{hcp}}$	95.3	$96.7 \pm 0.2$
	$\text{Al}_{12}\text{Mg}_{17}(\gamma) + \text{Mg}_2\text{Sn}$	4.7	$3.3 \pm 0.2$
Mg–5Al–1Zn–5Sn	$(\text{Mg})_{\text{hcp}}$	92.6	$93.6 \pm 0.3$
	$\text{Al}_{12}\text{Mg}_{17}(\gamma) + \text{Mg}_2\text{Sn}$	7.4	$6.4 \pm 0.3$

- A self-consistent Mg–Al–Zn–Sn quaternary system was established. Moreover, a comparison between the Scheil simulation results and the experimental data showed a very good agreement, indicating that this quaternary thermodynamic database is reliable.

**Acknowledgements** The financial support from the National Key Research and Development Program of China (Grant No. 2016YFB0301101), the National Natural Science Foundation of China (Grant No. 51602351), and the Hunan Provincial Science and Technology Program of China (Grant No. 2017RS3002)-Huxiang Youth Talent Plan is acknowledged.

## References

- Kang YB, Aliravci C, Spencer PJ (2009) Thermodynamic and volumetric databases and software for magnesium alloys. *JOM* 61 (5):75–82.
- Imandoust A, Barrett CD, Al-Samman (2017) A review on the effect of rare-earth elements on texture evolution during processing of magnesium alloys. *J. Mater. Sci.* 52(1):1–29.
- Lyu S, Li G, Hu T (2018) A new cast Mg–Y–Sm–Zn–Zr alloy with high hardness. *Mater. Lett.* 217:79–82.
- Zhang Y, Yang L, Dai J (2014) Effect of Ca and Sr on the compressive creep behavior of Mg–4Al–RE based magnesium alloys. *Mater. Design* 63:439–445.
- Shi R, Luo AA (2018) Applications of CALPHAD modeling and databases in advanced lightweight metallic materials. *Calphad* 62:1–17.
- Pan H, Ren Y, Fu H (2016) Recent developments in rare-earth free wrought magnesium alloys having high strength: A review. *J. Alloys Compd.* 663:321–331.
- Park SH, Jung JG, Kim YM (2015) A new high-strength extruded Mg–8Al–4Sn–2Zn alloy. *Mater. Lett.* 139:35–38.
- Liu C, Chen H, He C (2016) Effects of Zn additions on the microstructure and hardness of Mg–9Al–6Sn alloy. *Mater. Charact.* 113:214–221.
- Saboungi ML, Hsu CC (1977) Computation of isothermal sections of the Al–H–Mg system. *Calphad* 1(3):237–251.
- Saunders N (1990) A review and thermodynamic assessment of the Al–Mg and Mg–Li systems. *Calphad* 14(1):61–70.
- Murray JL (1982) The Al–Mg (aluminum–magnesium) system. *J. Phase Equilib.* 3(1):60.
- Zuo Y, Chang YA (1993) Thermodynamic calculation of the Al–Mg phase diagram. *Calphad* 17(2):161–174.
- Goel NC, Cahoon JR, Mikkelsen B (1989) An experimental technique for the rapid determination of binary phase diagrams: the Al–Mg system. *Metall. Trans. A* 20(2):197–203.
- Chartrand P, Pelton AD (1994) Critical evaluation and optimization of the thermodynamic properties and phase diagrams of the Al–Mg, Al–Sr, Mg–Sr, and Al–Mg–Sr systems. *J. Phase Equilib.* 15 (6):591–605.
- Liang P, Tarfa T, Robinson JA (1998) Experimental investigation and thermodynamic calculation of the Al–Mg–Zn system. *Thermochim. Acta* 314(1–2):87–110.
- Su HL, Harmelin M, Donnadiu P (1997) Experimental investigation of the Mg–Al phase diagram from 47 to 63 at.% Al. *J. Alloys Compd.* 247(1–2):57–65.
- Clark JB, Zabdyr L, Moser Z (1988) Phase diagrams of binary magnesium alloys. ASM International, Materials Park, OH, 353–364.
- Chadwick RJ (1928) The constitution of the alloys of magnesium and zinc. *J. I. Met.* 449:285–299.
- Hume-Rothery W, Rounsefell ED (1929) The system magnesium–zinc. *J. I. Met.* 41:119–138.
- Park JJ, Wyman LL (1957) Phase relationship in Mg alloys. WADC Technical Report 57–504: Astia Document No. AD142110.
- Higashi I, Shiotani N, Uda M (1981) The crystal structure of Mg<sub>51</sub>Zn<sub>20</sub>. *J. Solid State Chem.* 36(2):225–233.
- Agarwal R, Fries SG, Lukas HL (1992) Assessment of the Mg–Zn System. *Z. Metallkd.* 83(4):216–223.
- Wasiur-Rahman S, Medraj M (2009) Critical assessment and thermodynamic modeling of the binary Mg–Zn, Ca–Zn and ternary Mg–Ca–Zn systems. *Intermetallics* 17(10):847–864.
- Massalski E, Ohio TB (1990) Metals A. S. M. Binary Alloy Phase Diagrams Park.
- Ghosh P, Mezbahul-Islam MD, Medraj M (2012) Critical assessment and thermodynamic modeling of Mg–Zn, Mg–Sn, Sn–Zn and Mg–Sn–Zn systems. *Calphad* 36:28–43.
- Morishita M, Koyama K, Shikada S (2004) Standard gibbs energy of formation of Mg<sub>48</sub>Zn<sub>52</sub> determined by solution calorimetry and measurement of heat capacity from near absolute zero kelvin. *Metall. Mater. Trans. B* 35(5):891–895.
- Morishita M, Yamamoto H, Shikada S (2006) Thermodynamics of the formation of magnesium–zinc intermetallic compounds in the temperature range from absolute zero to high temperature. *Acta Mater.* 54(11):3151–3159.
- Morishita M, Koyama K, Shikada S (2005) Calorimetric study of Mg<sub>2</sub>Zn<sub>3</sub>. *Z. Metallkd.* 96(1):32–37.
- Morishita M, Koyama K (2003) Calorimetric study of MgZn<sub>2</sub> and Mg<sub>2</sub>Zn<sub>11</sub>. *Z. Metallkd.* 94(9):967–971.
- Meng FG, Wang J, Liu LB (2010) Thermodynamic modeling of the Mg–Sn–Zn ternary system. *J. Alloy. Compd.* 508(2):570–581.
- Liang P, Seifert HJ, Lukas HL (1998) Thermodynamic modelling of the Cu–Mg–Zn ternary system. *Calphad* 22(4):527–544.
- Qi HY, Huang GX, Bo H (2012) Experimental investigation and thermodynamic assessment of the Mg–Zn–Gd system focused on Mg-rich corner. *J. Mater. Sci.* 47(3):1319–1330.
- Nayeb-Hashemi AA, Clark JB (1984) The Mg–Sn (Magnesium–Tin) system. *Bull. Alloy Phase Diagrams* 5(5):466–476.
- Fries SG, Lukas HL (1993) Optimisation of the Mg–Sn system. *J. Chim. Phys.* 90:181–187.
- Jung IH, Kang DH, Park WJ (2007) Thermodynamic modeling of the Mg–Si–Sn system. *Calphad* 31(2):192–200.
- Jung IH, Kim J (2010) Thermodynamic modeling of the Mg–Ge–Si, Mg–Ge–Sn, Mg–Pb–Si and Mg–Pb–Sn systems. *J. Alloys Compd.* 494(1–2):137–147.
- Kang YB, Pelton AD (2010) Modeling short-range ordering in liquids: the Mg–Al–Sn system. *Calphad* 34(2):180–188.
- Morishita M, Koyama K (2005) Standard entropy of formation of SnMg<sub>2</sub> at 298 K. *J. Alloys Compd.* 398(1–2):12–15.
- Hultgren R, Desai PD, Hawkins DT (1973) Selected Values of the Thermodynamic Properties of Binary Alloys, American Society for Metals, Metals Park, Ohio.
- Murray JL (1983) The Al–Zn (aluminum–zinc) system. *Bull. Alloy Phase Diagrams* 4(1):55–73.
- Mey SA, Effenberg G (1986) A thermodynamic evaluation of the aluminum–zinc system. *Z. Metallkd.* 77(7):449–453.
- Mey SA (1993) Re-evaluation of the aluminum–zinc system. *Z. Metallkd.* 84(7):451–455.



43. Chen SL, Chang YA (1993) A thermodynamic analysis of the Al-Zn system and phase diagram calculation. *Calphad* 17(2):113–124.
44. Mathon M, Jardet K, Aragon E (2000) Al-Ga-Zn system: reassessments of the three binary systems and discussion on possible estimations and on optimisation of the ternary system. *Calphad* 24(3):253–284.
45. Luo Q, Li Q, Zhang JY (2013) Experimental investigation and thermodynamic optimization of the Al-Zn-Ti system in the Al-rich corner. *Intermetallics* 33:73–80.
46. Liang SM, Schmid-Fetzer R (2016) Thermodynamic assessment of the Al-Cu-Zn system, Part III: Al-Cu-Zn ternary system. *Calphad* 52:21–37.
47. Hayes FH (1991) User aspects of phase diagrams: proceedings of the International Conference, held at the Joint Research Centre, Petten, The Netherlands, 25–27th June, 1990. Woodhead Pub Ltd.
48. Ansara I, Dinsdale AT, Rand MH (1998) COST 507, thermochemical database for light metal alloys, in: European Communities, vol. 2, Belgium.
49. Flandorfer H, Rechchach M, Elmahfoudi A (2011) Enthalpies of mixing of liquid systems for lead free soldering: Al-Cu-Sn system. *J. Chem. Thermodyn.* 43(11):1612–1622.
50. Cheng T, Tang Y, Zhang L (2019) Update of thermodynamic descriptions of the binary Al-Sn and ternary Mg-Al-Sn systems. *Calphad* 64:354–363.
51. Lee BJ (1996) Thermodynamic assessments of the Sn-Zn and In-Zn binary systems. *Calphad* 20(4):471–480.
52. Ohtani H, Miyashita M, Ishida K (1999) Thermodynamic study of the Sn-Ag-Zn system. *J. Jpn. I. Met.* 63:685–694.
53. Yang C, Chen F, Gierlotka W (2008) Thermodynamic properties and phase equilibria of Sn-Bi-Zn ternary alloys. *Mater. Chem. Phys.* 112(1):94–103.
54. Chen SL (1994): Ph.D. Thesis, University of Wisconsin–Madison, Madison, WI.
55. Kattner UR, Boettinger WJ (1992) Thermodynamic calculation of the ternary Ti-Al-Nb system. *Mat. Sci. Eng. A-Struct.* 152(1–2):9–17.
56. Chen SL, Zuo Y, Liang H (1997) A thermodynamic description for the ternary Al-Mg-Cu system. *Metall. Mater. Trans. A* 28(2):435–446.
57. Liang H, Chen SL, Chang YA (1997) A thermodynamic description of the Al-Mg-Zn system. *Metall. Mater. Trans. A* 28(9):1725–1734.
58. Doernberg E, Kozlov A, Schmid-Fetzer R (2007) Experimental investigation and thermodynamic calculation of Mg-Al-Sn phase equilibria and solidification microstructures. *J. Phase Equilib. Diff.* 28(6):523–535.
59. Bamberger M (2006) Phase formation in Mg-Sn-Zn alloys—thermodynamic calculations versus experimental verification. *J. Mater. Sci.* 41(10):2821–2829.
60. Jung IH, Park WJ, Ahn S (2006) Thermodynamic modeling of the Mg-Sn-Zn-Al system and its application to mg alloy design. *Magnesium Technology 2006*:457–461.
61. Lin KL, Wen LH, Liu TP (1998) The microstructures of the Sn-Zn-Al solder alloys. *J. Electron. Mater.* 27(3):97–105.
62. Sidorov V, Drápala J, Uporov S (2011) Some physical properties of Al-Sn-Zn melts. *EPJ Web of Conferences. EDP Sciences* 15:01022.
63. Smetana B, Zlá S, Kroupa A (2012) Phase transition temperatures of Sn-Zn-Al system and their comparison with calculated phase diagrams. *J. Therm. Anal. Calorim.* 110(1):369–378.
64. Drápala J, Kostiučková G, Smetana B (2015) Thermodynamic and experimental study of tin-zinc-aluminum ternary system. *Adv. Sci., Eng. Med.* 7(4):291–295.
65. Knott S, Mikula A (2002) Thermodynamic properties of liquid Al-Sn-Zn alloys: A possible new lead-free solder material. *Mater. Trans.* 43(8):1868–1872.
66. Knott S, Flandorfer H, Mikula A (2005) Calorimetric investigations of the two ternary systems Al-Sn-Zn and Ag-Sn-Zn. *Z. Metallkd.* 96(1):38–44.
67. Cheng T, Zhang LJ (2019) Thermodynamic re-assessment of the Al-Sn-Zn ternary system. *J. Min. Metall. Sect. B-Metall.* 55(3):439–449.
68. Dinsdale AT (1991) SGTE data for pure elements. *Calphad* 15(4):317–425.
69. Ansara I, Burton B, Chen Q (2000) Models for composition dependence. *Calphad* 24(1):19–40.
70. Hao D, Hu B, Zhang K (2014) The quaternary Al-Fe-Ni-Si phase equilibria in Al-rich corner: experimental measurement and thermodynamic modeling. *J. Mater. Sci.* 49(3):1157–1169.
71. Muggianu YM, Gambino M, Bros JP (1975) Enthalpies of formation of liquid alloys. *J. Chim. Phys.* 72(1):83–88.
72. Kim BH, Jeon JJ, Park KC (2008) Microstructural characterisation and mechanical properties of Mg-xSn-5Al-1Zn alloys. *Int. J. Cast Metals Res.* 21(1–4):186–192.

# Investigation and Modelling of the Influence of Cooling Rates on the Microstructure of AZ91 Alloys

S. Gavras, M. U. Bilal, D. Tolnai, and N. Hort

## Abstract

An increasingly important tool in modern experimental investigations is the ability to accurately produce a digital model or “digital twin” of samples and their properties. This goes hand-in-hand with the primary tenant of Industry 4.0 which is to provide advanced manufacturing solutions through the use of cyber-physical systems. A comparison of various quenching media, namely liquid nitrogen, water at 5 °C, water at 20 °C and in the air on the microstructure of permanent mould cast AZ91 alloys was investigated. Particular emphasis was centred on the changes in microstructural features such as grain size and dendrite arm spacing. Phase-field method was used to produce a digital twin and qualitative analysis of the investigated cooling rates on AZ91. The combination of practical microstructural investigations and the simulated microstructures will advance the knowledge of cooling rate influences on AZ91 and their ability to be accurately simulated to assist with property and microstructural predictions.

## Keywords

AZ91 • Quenching • Microstructure • Model • Digital twin

## Introduction

There is increasing importance to be able to simulate and/or predict the properties of materials in order to expedite production and also to decrease costs. If one were to know, in advance, the microstructure or material properties via some form of model, then production processes could be streamlined. Thus, a decrease in overall production costs can be

achieved. As such, a “digital twin” or computer model is an invaluable tool for modern alloy development. As one of the most commonly used magnesium alloys, AZ91 is an ideal selection to produce a model. A common practice which can help to modify the microstructures of cast materials such as Mg alloys is quenching. Changing the cooling rates of a material via quenching has been used to affect a number of microstructural features such as grain size, interdendritic arm spacing, concentration of solute in solid solution, etc. [1, 2]. By selecting four different quenching media with different cooling rates such as air, 20 °C water, 5 °C water and liquid nitrogen (LN<sub>2</sub>) differences in the microstructure of AZ91 are expected. The AZ91 alloys are quenched immediately following casting. To generate a digital twin of the microstructure, the phase-field method has been employed. In computational materials science, this method is notably a versatile technique for simulating microstructure or interfacial evolution at the microscale. Steinbach et al. [3] pioneered such work and proposed the multi phase-field approach to capture the complete physics behind solidification and related phenomena for an arbitrary number of phases. The idea revolves around tracking the interface in space  $x$  and time  $t$ , and is represented quantitatively by the phase-field variable  $\phi(x, t)$ . This variable refers to the local phase fraction of a phase in  $N$  phase system and is defined in the range of  $0 \leq \phi \leq 1$ , where 0 and 1 point to either existence or non-existence of any representative phase while values between 0 and 1 correspond to the diffused nature of the interface between phases. The phase-field variables are constrained in such a way that the sum is unity, i.e.,

$$\sum_{\alpha=1}^N \phi_{\alpha} = 1 \quad (1)$$

This allows easy identification of all interfacial and bulk contributions. In general, the multi phase-field model introduces the total free energy density  $F$  given as:

S. Gavras (✉) · M. U. Bilal · D. Tolnai · N. Hort  
 Institute of Materials Science, Helmholtz-Zentrum Geesthacht,  
 Max-Planck Str. 1, Geesthacht, 21502, Germany  
 e-mail: [sarkis.gavras@hzg.de](mailto:sarkis.gavras@hzg.de)

$$F = \int_{\Omega} (f^{\text{chem}} + f^{\text{int}} + f^{\text{mech}} + \dots) d\Omega \quad (2)$$

$F$  can be obtained as an integral sum of chemical free energy density  $f^{\text{chem}}$ , interfacial free energy density  $f^{\text{int}}$  and mechanical free energy density  $f^{\text{mech}}$  over the domain  $\Omega$ . The first two hold vital importance for simulating solidification or growth process and other free energies like mechanical, magnetic, electrical, etc. can be added for more detailed studies. The  $f^{\text{chem}}$  and  $f^{\text{int}}$  are given as

$$f^{\text{chem}} = \sum_{\alpha=1}^N \phi_{\alpha} f_{\alpha}(c_{\alpha}) + \sum_{i=1}^{n_i} \mu^i \left[ c^i - \sum_{\alpha=1}^N (\phi_{\alpha} c_{\alpha}^i) \right] \quad (3)$$

$$f^{\text{int}} = \sum_{\alpha=1, \beta \neq \alpha}^N \frac{4\sigma_{\alpha\beta}}{\eta} \left\{ -\frac{\eta^2}{\pi^2} \nabla \phi_{\alpha} \cdot \nabla \phi_{\beta} + \phi_{\alpha} \phi_{\beta} \right\} \quad (4)$$

where  $\phi_{\alpha}$  (or  $\phi_{\beta}$ ) is the phase-field variable of phase  $\alpha$  (or  $\beta$ ),  $f_{\alpha}(c_{\alpha})$  is the chemical-free energy of phase  $\alpha$ ,  $\mu^i$  is the chemical potential,  $c^i$  is the total concentration of component  $i$ ,  $c_{\alpha}^i$  is the concentration of component  $i$  in phase  $\alpha$  and  $n_i$  is the number of components in the system. In  $f^{\text{int}}$ ,  $\sigma_{\alpha\beta}$  is the interfacial energy between phases  $\alpha$  and  $\beta$ , and  $\eta$  is the interface width. Each contribution depends on various state variables passed initially as an input parameter. Substituting Eqs. 3 and 4 in Eq. 2, the kinetics of phase evolution can be written as

$$\dot{\phi}_{\alpha} = \sum_{\alpha \neq \beta}^N M_{\alpha\beta} \left[ \frac{\delta F}{\delta \phi_{\beta}} - \frac{\delta F}{\delta \phi_{\alpha}} \right] \quad (5)$$

where  $M_{\alpha\beta}$  is the phase-field mobility. The kinetics of diffusion of each component  $i$  is given as

$$\dot{c}^i = \nabla \cdot (D^i \nabla c^i) \quad (6)$$

here  $D^i$  is the diffusion coefficient of component  $i$ . The evolution of phase-field and concentration tracks the microstructural changes for a given set of parameters.

## Experimental Methods

The alloys were cast by permanent mould indirect chill casting, described in greater detail in [4]. The composition was measured via Spark-Optical Emission Spectroscopy using an Ametek-Spectro Spectrolab M9. AZ91 ingots were quenched in air, 20 °C water, 5 °C water or liquid nitrogen from an initial temperature of approximately 700 °C. The AZ91 alloys were ground and polished using standard metallography sample preparation techniques for microstructural

investigations. In order to record polarised optical micrographs of the different samples, each sample was etched in an acetic acid, picric acid, and ethanol solution for approximately 2 s. Optical micrographs are recorded for each of the quenched samples using a Leica DMLM optical microscope using polarised light. Grain size measurements were obtained using the linear intercept method. Grain size measurements were measured from three regions from each sample and averaged to obtain grain size statistics. A TESCAN Vega3 Scanning Electron Microscope (SEM) in backscattered electron (BSE) mode was used to investigate changes to the microstructure and for qualitative compositional analysis via energy-dispersive X-ray spectroscopy (EDXS). Intermetallic area fraction measurements were obtained from five regions per quenched sample. SEM micrographs of those regions were converted to binary contrast images and ImageJ software was used to determine the area fraction of intermetallic. To produce a digital twin, simulations were performed for Mg–9Al–1Zn (wt%) in 2D (500  $\mu\text{m} \times 1 \mu\text{m} \times 500 \mu\text{m}$ ) in a coupled environment of two commercial tools Thermo-Calc (TQ interface) and MICRESS. As given in Eq. 1, only chemical and interfacial contributions were taken into consideration. The chemical part is responsible for the thermodynamics which is provided by Thermo-Calc on the basis of Gibbs energy data using the CALPHAD methodology [5]. On the other hand, the interfacial part takes care of how interfaces of similar and different phases behave and also controls the morphology of grains. A number of processing, material and numerical parameters needed to be initialized for setting up the model. The type of coupling in MICRESS was set to “concentration” in which the phase-field is coupled with the concentration field, and diffusion and solute partitioning are evaluated. An automatic time stepping criteria was chosen with grid spacing of 1  $\mu\text{m}$  and interface width of 4  $\mu\text{m}$ . In the present simulations, heterogeneous nucleation was achieved using the seed density model, i.e., allowing seeds of various radii to nucleate if the critical undercooling permits, to have an equiaxed microstructure. The model required a predefined density-radius distribution of grains and was only applied to  $\alpha$ -Mg, while Mg<sub>17</sub>Al<sub>12</sub> was set to precipitate in the interfacial regions. The temperature model with heat extraction rate as an input parameter was selected for equiaxed growth. The different cooling conditions in simulations were implemented by varying the heat extraction rate  $\dot{h}$ , i.e., high value of  $\dot{h}$  refers to high cooling rate. The extraction rates implemented in this study were  $\dot{h} = 5, 15, 25$  and  $35 \text{ J/cm}^3 \text{ s}$ . The model assumes homogenous temperature, with no temperature gradients, which is approximated from the mean values of heat extraction rate and specific heat over the whole domain. The thermodynamic data, i.e., nucleation undercooling, driving force, solute partitioning,

diffusion coefficient/matrix, etc., are communicated by the TQ interface which is then used by the phase-field and diffusion solvers of MICRESS. The pairwise interfacial energies of phases and anisotropy parameters to exhibit hexagonal anisotropy of liquid/ $\alpha$ -Mg interface were adopted from the existing literature [6]. Other simulation specific numerical parameters were calibrated according to instructions mentioned in the software's manual [7]. In general, the TQ interface and four MICRESS models namely: nucleation, multi phase-field, diffusion and temperature work side by side to yield the microstructure. The simulation starts with a pure liquid phase followed by the nucleation  $\alpha$ -Mg and afterwards with  $Mg_{17}Al_{12}$  in the interdendritic regions. The simulation ends as soon as the solid fraction reaches 100%.

## Results and Discussion

The composition of each AZ91 casting quenched in air, 20 °C water, 5 °C water or  $LN_2$  is given in Table 1. In general, each casting of AZ91 has a comparable composition with the exception of the casting used to quench in 5 °C water. This casting has approximately 1 wt% more Al in comparison to the other 3 alloys cast as a result of it being the final ingot cast. This may explain, in combination with a possible higher amount of oxide (owing to it being the final casting) the greater amount of voids and inclusions present as shown in Fig. 1g. However, the compositional range of the castings given in Table 1 all still falls within the accepted margins for AZ91 alloys. Additionally, there is still sufficient surface area from AZ91 quenched in 5 °C water to perform unimpeded microstructural analysis.

In Fig. 1, the influence of different cooling rates on the microstructure, in terms of grain size and interdendritic arm spacing is apparent. It is interesting to note, however, that the grain size does not decrease proportionally with respect to the temperature of the quenching media.

The AZ91 castings left to cool in air have the largest grains and the greater interdendritic arm spacing Fig. 1a–b. It would be understandable if one would then expect the 20 °C water quenched AZ91 sample to have the next largest grain size since this is the next “warmest” quenching media. Table 2 shows quite the opposite. The AZ91 sample quenched in  $LN_2$  (the coldest quenching medium selected,

–196 °C) has the next largest average grain size. This is due to the Leidenfrost effect [8] which occurs when an object that is significantly hotter (in this case approximately 700 °C) than the boiling point of the liquid (in this case –196 °C) come in contact. An insulating vapour is produced around the AZ91 casting, which prevents the  $LN_2$  from rapidly quenching the material. Thus, the expected rapid cooling properties of the  $LN_2$  are significantly reduced. Furthermore, from Table 2, both water at 20 °C and water at 5 °C are shown to be more effective quenching media with regards to average grain size reduction. The average grain size of AZ91 quenched in 5 °C water is approximately 25% of the size of grains in AZ91 quenched in air (Table 2).

The different cooling rates also have an influence on the intermetallic morphology and area fraction. Figure 2 shows micrographs of the AZ91 alloys following their respective quenching. The air quenched alloy (Fig. 2a) is composed of  $\alpha$ -Mg, a continuous  $\beta$  phase,  $Mg_{17}Al_{12}$  and an Al–Mn rich phase [9] (which appears brighter in the SEM micrographs).

The morphology of the intermetallic changes in the  $LN_2$  quenched alloy from continuous to a eutectic morphology composed of  $\beta$  phase and  $\alpha$ -eutectic, Fig. 2b. This structure is maintained in the 20 and 5 °C water quenched AZ91 alloys but with a lower area fraction of intermetallic. This is due to the greater amounts of solute remaining in solid solution as a result of the more rapid cooling rates [10]. Table 4 shows the decrease in intermetallic area fraction from the air quenched alloy ( $7.3 \pm 1.8\%$  intermetallic) to the  $LN_2$  and water quenched alloys (<5% intermetallic).

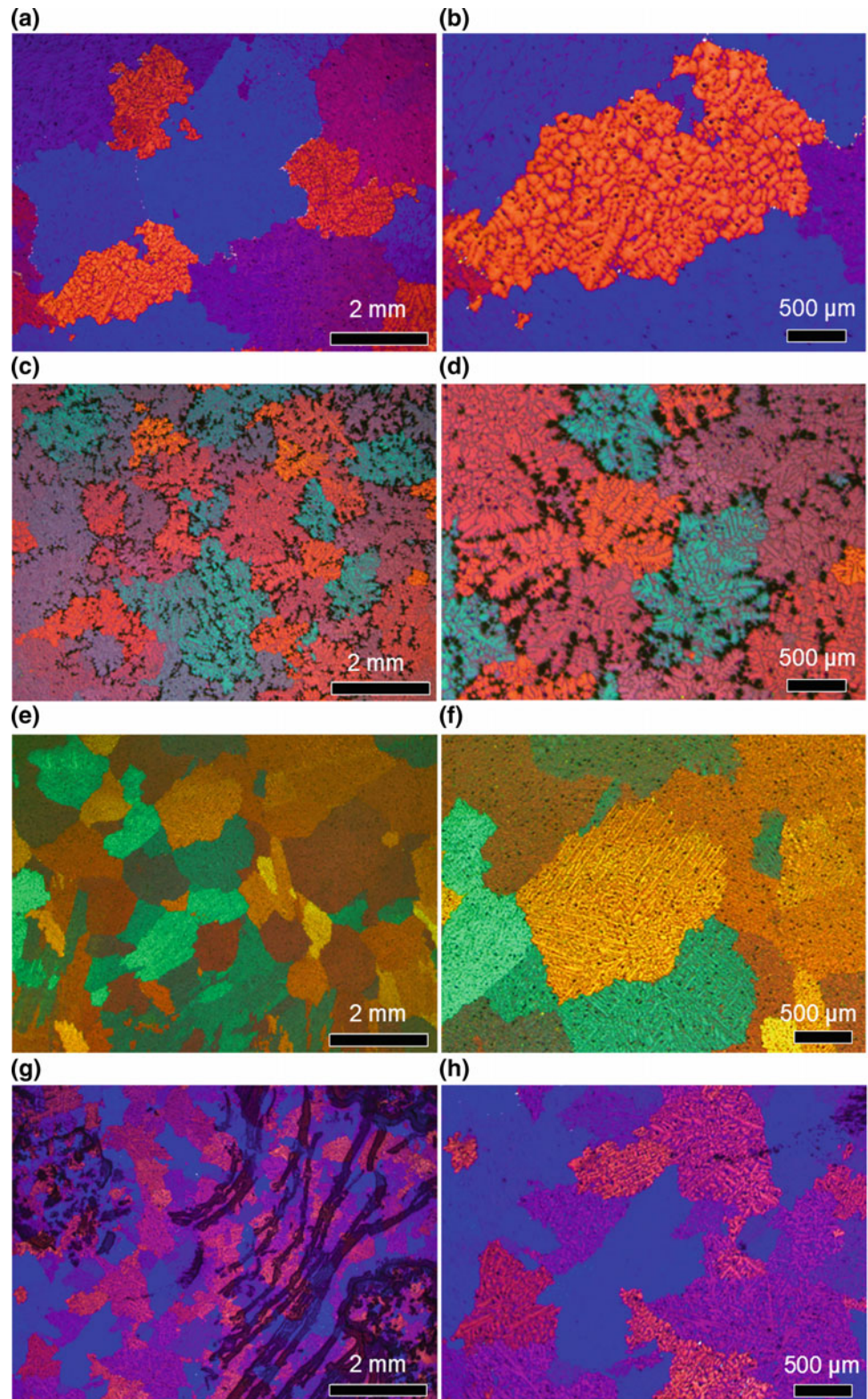
Digital twins generated by the phase-field model are used to comprehend the underlying physics behind solidification phenomena. Figure 3 depicts the four simulated microstructures with  $\dot{h} = 5, 15, 25$  and  $35 \text{ J/cm}^3 \text{ s}$ . It is evident that the increasing cooling rate leads to small (or fine) grains. The grain size from the experiments appears to be exceptionally large as compared to simulations. The grain size of these twins is sensitive to parameters such as the inoculant's initial size, density, critical undercooling, shielding distance, etc. Absence of these physical parameters for nucleation makes it challenging to achieve such large grain sizes. In this regard, the simulated microstructures, in which final grain size is sensitive to the density and size of initially precipitated grains, can only be seen in terms of qualitative comparison with the experiments.

**Table 1** Compositional measurements via Spark-Optical Emission Spectroscopy for each casting of AZ91 ingot

Quenching media	AZ91 Composition in wt%								
	Al	Mn	Zn	Be	Ca	Cu	Fe	Ni	Si
Air	8.99	0.23	0.67	0.00082	0.0003	0.0028	0.0007	0.0011	0.014
20 °C water	8.8	0.26	0.65	0.00092	0.0004	0.0026	0.0012	0.0011	0.015
5 °C water	9.8	0.29	0.73	0.0042	0.0005	0.0031	0.0005	<0.0002	0.0079
Liquid nitrogen	8.99	0.22	0.68	0.00078	0.0004	0.0028	0.0009	0.0011	0.015

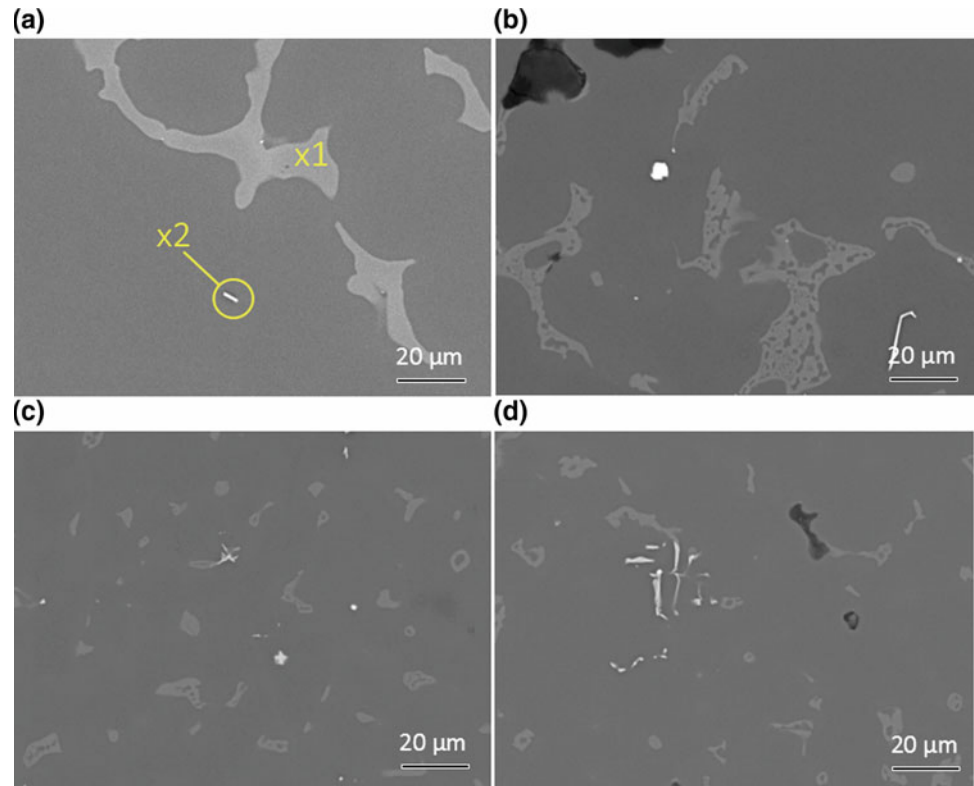


**Fig. 1** Polarised light optical micrographs of AZ91 quenched in **a–b** air, **c–d** liquid nitrogen, **e–f** 20 °C water and **g–h** 5 °C water



**Table 2** Average grain sizes of AZ91 quenched in different media following casting

Quenching media	Average grain size $\pm$ SD (mm)
Air	2.26 ( $\pm$ 0.16)
Liquid nitrogen	1.35 ( $\pm$ 0.13)
20 °C water	0.80 ( $\pm$ 0.08)
5 °C water	0.61 ( $\pm$ 0.05)

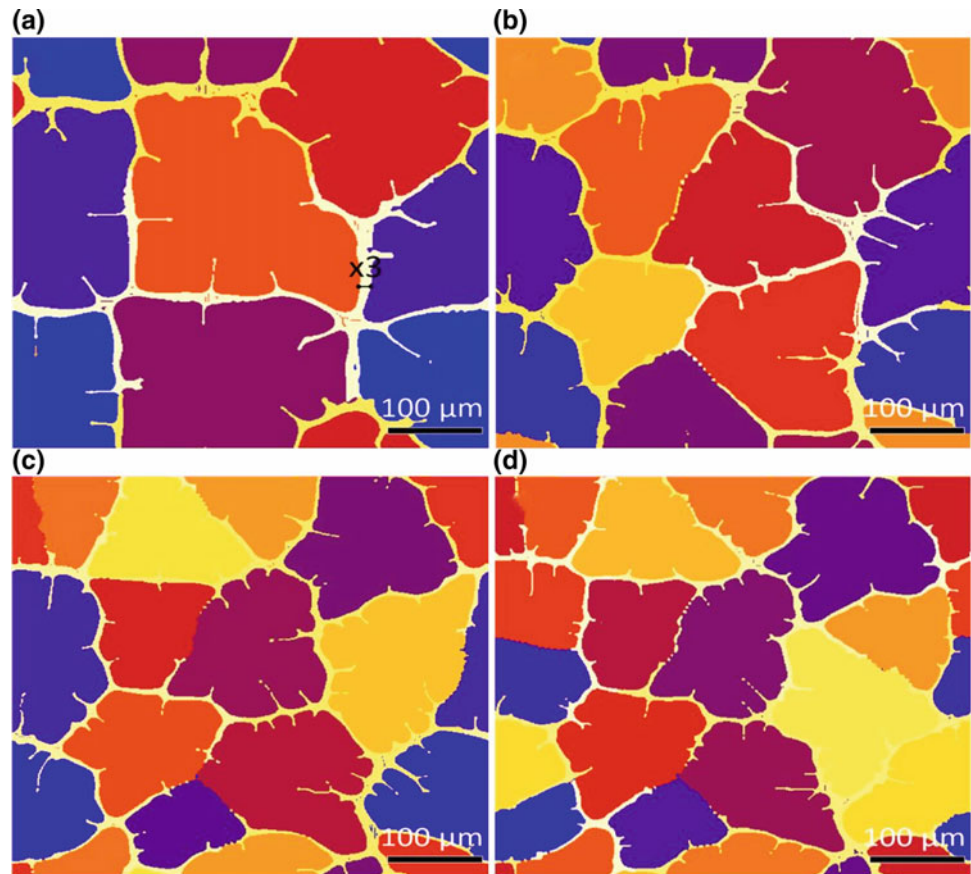
**Fig. 2** Backscattered electron SEM micrographs of AZ91 quenched in **a** air, **b** liquid nitrogen, **c** 20 °C water and **d** 5 °C water. Note in **a** x1 and x2 are EDXS point measurements given in Table 3**Table 3** EDXS point scan measurements of x1 and x2 of AZ91 air quenched intermetallics shown in Fig. 2a

Element	wt%	
	x1	x2
Mg	58.3	1.6
Al	38.0	44.0
Si	0.2	0.36
Mn	0.0	54.1
Zn	3.5	0.0

**Table 4** Average area fraction of intermetallic particles of AZ91 quenched in different media

Quenching media	Average area fraction $\pm$ SD (%)
Air	7.3 ( $\pm$ 1.8)
Liquid nitrogen	4.6 ( $\pm$ 0.5)
20 °C water	4.5 ( $\pm$ 0.7)
5 °C water	3.0 ( $\pm$ 0.6)

**Fig. 3** Simulated microstructures with varying cooling conditions; **a**  $\dot{h} = 5 \text{ J/cm}^3 \text{ s}$ , **b**  $\dot{h} = 15 \text{ J/cm}^3 \text{ s}$ , **c**  $\dot{h} = 25 \text{ J/cm}^3 \text{ s}$  and **d**  $\dot{h} = 35 \text{ J/cm}^3 \text{ s}$ . Note in **a** x3 is virtual EDXS line measurement given in Fig. 4



One can also notice that the increasing heat extraction rate affects the morphology. The grains prefer to exhibit dendritic morphology rather than globular for higher values of  $\dot{h}$ . Furthermore, the grain refining effect is more pronounced as  $\dot{h}$  changes from 5 to 25  $\text{J/cm}^3 \text{ s}$ . The twins are more sensitive to changes with lower values of  $\dot{h}$  than higher values, as no effective change in grain size can be observed for 25 to 35  $\text{J/cm}^3 \text{ s}$ . Similar observations of grain size have been reported elsewhere in the benchmark studies of technical magnesium alloys [6].

Figure 4 represents the virtual EDXS of line x3 for microstructure  $\dot{h} = 5 \text{ J/cm}^3 \text{ s}$ . The concentrations of Al and Zn in the interdendritic region are similar to the one observed in experiments. The phase-field method has predicted the correct concentrations of alloying elements. It benefits in capturing the concentration kinetics/maps and can lead to insight knowledge of phenomena like solute pile-up or segregation in cases where slow diffusing elements, e.g., Mn, are involved [11]. Since simulations are performed for a ternary system, i.e., Mg, Al, and Zn, a slight difference between the experimental and modelled concentrations is possibly caused by the absence of elements which are present in the casting.

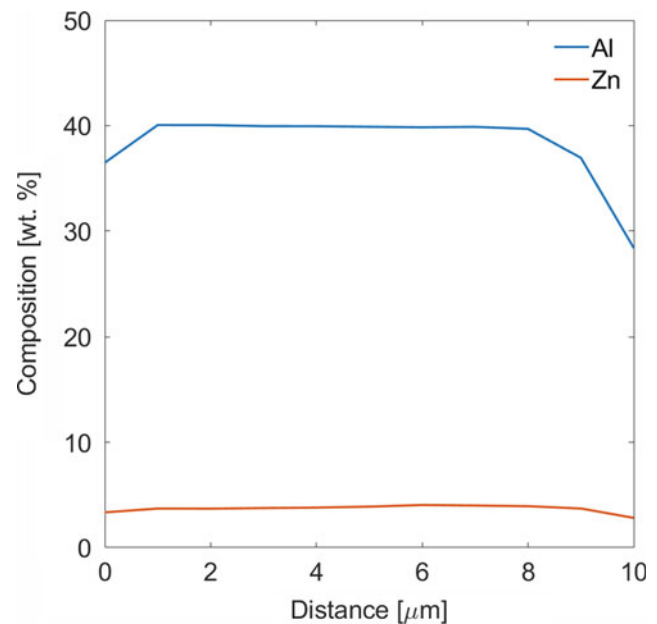


**Fig. 4** Virtual EDXS line scan of the region marked as x3 in Fig. 3a



## Conclusions

AZ91 cast alloys were quenched in air, 20 °C water, 5 °C water or liquid nitrogen immediately following casting. The alloy microstructures were investigated via optical and scanning electron microscopy. The AZ91 alloy left to cool in air (air quenched) had the largest average grain size. As a result of the Leidenfrost effect, the AZ91 quenched in liquid nitrogen had the next largest grain size then followed by the 20 and 5 °C water quenched alloys.

On the other hand, the phase-field simulation results are in accordance with the experiments to an extent that the varying cooling conditions yield different grain sizes. The modelled concentrations in the interdendritic region also comply with the EDXS measurement. Simulated digital twins have smaller grains as compared to the experiments due to lack of nucleation parameters. However, these twins as a preliminary attempt potentially fulfil the purpose of a qualitative comparison with the experiments and reveal a better understanding of physics behind solidification.

## References

1. A.K. Dahle, Y.C. Lee, M.D. Nave, P.L. Schaffer, and D.H. StJohn: *Journal of Light Metals*, Vol. 1, (2001), p. 61.
2. M. Paliwal and I.-H. Jung: *Acta Materialia*, Vol. 61, (2013), p. 4848.
3. I. Steinbach, F. Pezzolla, B. Nestler, M. Seeßelberg, R. Prieler, G. J. Schmitz, and J.L.L. Rezende: *Physica D: Nonlinear Phenomena*, Vol. 94, (1996), p. 135.
4. F.R. Elsayed, N. Hort, M.A. Salgado Ordorica, and K.U. Kainer: *Materials Science Forum. Trans Tech Publ*, (2011), p. 65.
5. <http://www.calphad.org/>, Z.-K. Liu, Editor.
6. J. Eiken: *Int. J. Mat. Res.*, Vol. 101, (2010), p. 503.
7. [www.micress.com](http://www.micress.com).
8. J.G. Leidenfrost, *De aquae communis nonnullis qualitatibus tractatus*. (Ovenius, 1756).
9. I. Polmear, *Light Alloys. Materials & Mechanical Science*. (Butterworth-Heinemann, 2005).
10. F. Yavari and S.G. Shabestari: *Journal of Thermal Analysis and Calorimetry*, Vol. 129, (2017), p. 655.
11. K. Grätz, J. Eiken, and R. Schmid-Fetzer: *Int. J. Mat. Res.*, Vol. 105, (2014), p. 130.



# The Independent Effects of Cooling Rate and Na Addition on Hydrogen Storage Properties in Hypo-eutectic Mg Alloys

Manjin Kim, Yahia Ali, Stuart D. McDonald, Trevor B. Abbott, and Kazuhiro Nogita

## Abstract

The addition of trace concentrations of elements such as Na and Sr along with rapid cooling is well-established method for modification of the faceted eutectic Si in Al–Si. There have been some efforts to extend this strategy to Mg-based alloys. For example, it has been reported that trace Na addition to Mg–Ni alloys can also refine the eutectic Mg<sub>2</sub>Ni phase and facilitate functional property improvements such as hydrogen absorption kinetics. In this work, we have extended this strategy to a variety of other Mg-based alloys such as Mg–Ni and Mg–La alloys through the addition of trace elements and use of different cooling rates. The modification of the eutectic morphology in these alloys is discussed with regard to the Jackson parameters which were calculated using data from Thermo-Calc. The relationship between eutectic modification and hydrogen absorption kinetics in these alloys is investigated. The work has demonstrated, contrary to prior expectations, that microstructural refinement and hydrogen absorption kinetics are not necessarily correlated.

## Keywords

Magnesium • Eutectic modification • Hydrogen storage properties • Microstructure

## Introduction

Metal hydrides which can store hydrogen in solid state have been widely studied due to their favourable safety profile and high energy density. Among many metal elements, magnesium-based alloys have received attention due to advantages such as high gravimetric hydrogen capacity (7.6 wt% H/Mg), abundant reserves, low density, and economics. However, there are still barriers for the commercialisation of Mg hydrides for hydrogen storage systems such as a high formation enthalpy of MgH<sub>2</sub> (–75.2 kJ/mol) and sluggish sorption kinetics and activation processes [1]. Thus further studies are required to improve hydrogen sorption properties for practical applications including investigating how catalytic elements and microstructural modification can influence the thermodynamics and kinetics of the hydriding/dehydriding processes.

One approach to improve the hydrogen storage properties of Mg-based alloys is refinement of the microstructure of Mg-based materials. High-energy ball milling (HEBM) is one of the popular methods to enhance the hydrogen storage performance of metals and alloys by producing nanosized powder and increasing the defect density [2–5]. However, nanosized Mg synthesised by HEBM is very reactive and prone to oxidation; thus, extreme care must be taken during handling. In addition, this technique is less efficient for mass production since significant energy consumption is required.

Another strategy to improve hydrogen sorption properties of Mg-based alloys is the addition of catalytic components. The use of a catalyst facilitates faster hydrogen dissociation as well as re-combination steps during hydriding/dehydriding reactions. A multitude of materials such as transition metals [6, 7], rare-earth metals [8, 9], metal oxides [10, 11], and carbon-based materials [12, 13] have been studied for this purpose. We have previously found that trace sodium additions before casting can accelerate the hydrogen absorption process of Mg–Ni alloys and refine the eutectic increasing the density of twinning in the Mg<sub>2</sub>Ni intermetallic

M. Kim (✉) · Y. Ali · S. D. McDonald · T. B. Abbott · K. Nogita  
School of Mechanical and Mining Engineering, The University of Queensland, Brisbane, QLD 4072, Australia  
e-mail: [manjin.kim@uq.edu.au](mailto:manjin.kim@uq.edu.au)

T. B. Abbott  
School of Engineering, RMIT University, Carlton, VIC 3053, Australia

Magontec Ltd., Sydney, NSW 2000, Australia

phase [14, 15]. It is well known that eutectic modifiers such as Na, Sr, Ca, and Eu can refine the faceted/non-faceted eutectic in Al–Si (in some cases) and Al–Ge systems creating impurity-induced twinning via a re-entrant edge mechanism [16–18]. In addition, recently Wu et al. reported faceted/non-faceted eutectic of hypo-eutectic Al–Mg<sub>2</sub>Si cast alloys can be modified by Bi additions and Sc additions [19, 20]. It is also reported that Na has a modification effect on the eutectic Mg<sub>2</sub>Si phase in the Al–Mg<sub>2</sub>Si alloy system [21]. Microstructure modification via addition of chemical elements during casting is a preferred method compared to other modification techniques such as rapid solidification, hot extrusion, and heat treatment since it is a simple and economic process [22, 23].

Nogita et al. invented a method of “producing a hydrogen storage material including the steps of: forming a Mg–Ni melt having up to 50 wt% Ni; adding up to 2 wt% of a refining element to the melt under a non-oxidising atmosphere, the refining element having atomic radius within the range of 1–1.65 times the atomic radius of magnesium, such as at least one element selected from the group consisting of Zr, Na, K, Ba, Ca, Sr, La, Y, Yb, Rb, and Cs; and solidifying the melt to produce the hydrogen storage material”, and this IP has been registered worldwide [24]. They have suggested that the improved hydrogen absorption kinetics are attributed to refinement of eutectic Mg–Mg<sub>2</sub>Ni and a high density of twinning that resides in the faceted Mg<sub>2</sub>Ni phase that grows via a re-entrant edge mechanism [14].

However, the microstructure of the eutectic can also be significantly affected and modified by cooling rate during

solidification. In this study, we have extended this eutectic modification strategy via minor addition of Na to a variety of other Mg-based alloys, adding Na to the alloys and solidifying at two different cooling rates. Since Mg acts as the main hydrogen storage reservoir and additions of alloying elements reduce the total hydrogen storage capacity of Mg-based alloys, the alloys at hypo-eutectic composition were cast. The effect of Na addition and cooling rate during solidification on microstructure and the morphology of intermetallic phases in these alloys is discussed in association with the Jackson parameter. Mg–La and Mg–Ni alloys are chosen as examples of the Mg-based alloys cast in this study for hydrogen absorption test, and their hydrogen absorption kinetics are discussed.

## Experimental Details

A variety of Mg-based binary (8 wt% Ni, 5 wt% La, 23 wt% Y, 12 wt% Cu, and 1 wt% Si) alloys of commercial purity (99.9%) and hypo-eutectic composition were prepared with permanent mould casting process. Figure 1 shows the phase diagrams of these systems with the composition of the experimental alloys indicated.

Mg metal was placed in a steel crucible using an electric resistance furnace at a temperature of 800 °C under a protective gas composed of 1% SF<sub>6</sub> in CO<sub>2</sub>. When Mg was fully melted, the alloying elements were added to the Mg melt. After complete melting and dissolution, an addition of 0.2 wt% Na was introduced just prior to casting. To ensure that the

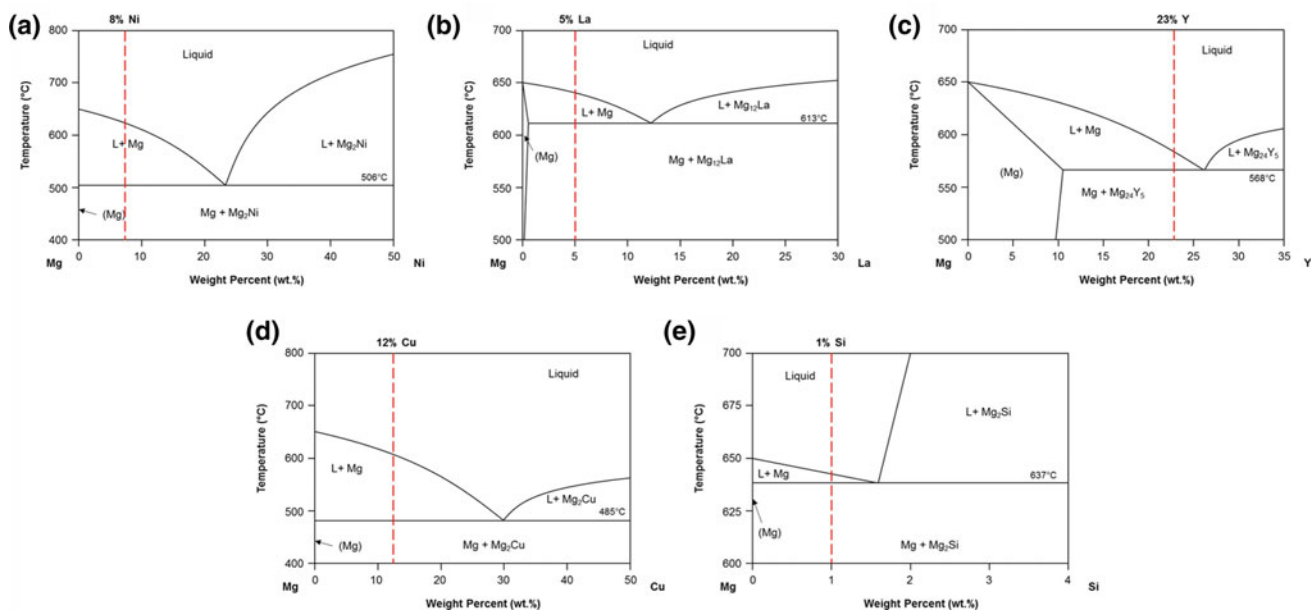


**Fig. 1** Composition of Mg-based alloys cast in this study is indicated (vertical dashed lines) in schematic phase diagrams based on the available literature; **a** Mg–Ni [25], **b** Mg–La [26], **c** Mg–Y [27], **d** Mg–Cu [28], and **e** Mg–Si [29]

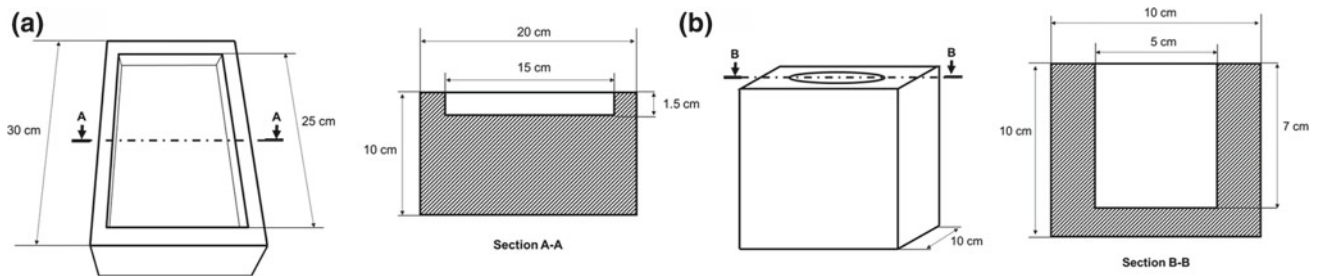


**Fig. 2** A schematic image of the experimental moulds; **a** an aluminium block preheated to 150 °C for casting at fast cooling rate and **b** a steel mould preheated to 600 °C for casting at moderate cooling rate

**Table 1** Volume percent of eutectic and theoretical maximum H<sub>2</sub> storage capacity of each Mg-based alloys cast in this study

Alloys	Volume percent of eutectic (vol %)	Theoretical maximum H <sub>2</sub> storage capacity (wt %)
Mg-8%Ni [30]	26.6	7.03
Mg-5%La	40.0	7.40
Mg-23%Y	84.6	6.65
Mg-12%Cu	29.5	6.60
Mg-1%Si	77.0	7.53

melts solidified at different cooling rates, two different types of mould and preheating temperatures were applied. For casting with a fast cooling rate, an aluminium block with a shallow cavity (25 cm × 15 cm × 1.5 cm) preheated to 150 °C was used, while a steel mould with cylindrical cavity of diameter 5 cm preheated to 600 °C was used for casting with a moderate cooling rate. A schematic image of the experimental moulds used for casting is shown in Fig. 2.

Hereafter, the samples are labelled with the composition of the alloys and the cooling rates applied during solidification. For example, Mg-8 wt%Ni-0.2 wt%Na alloys solidified at fast cooling rate and moderate cooling rate are labelled to Mg-8Ni-0.2Na\_FC and Mg-8Ni-0.2Na\_MC, respectively. The as-cast alloys were mechanically ground and sieved through an aperture size of 125 μm to produce a fine powder sample for hydrogen absorption testing. For hydrogen absorption measurements, a Sieverts-type apparatus (Suzuki Shokan, Japan) was used with 0.2 g of powdered sample loaded in a chamber which was evacuated before heating to 350 °C for 2 h. An initial condition of 2 MPa H<sub>2</sub> and 350 °C was applied for the measurement period. The microstructure of the alloys was investigated using scanning electron microscope (Hitachi-TM3030 and JEOL-6610, Japan) and an optical microscopy. The Jackson parameters for each of the intermetallic phases in the hypo-eutectic Mg-based alloys were calculated using Thermo-Calc with the MG 4.0 database. Table 1 shows the volume percent of eutectic calculated using lever rule and theoretical maximum H<sub>2</sub> storage capacity (based on the hydrogen absorption

reactions and atomic weight of each element) of each Mg-based alloys cast in this study.

## Results and Discussion

### Calculation of the Jackson Parameter of the Intermetallic Phases in Hypo-eutectic Mg-Based Alloys

In solidification, the Jackson parameter,  $\alpha$ , is defined as

$$\alpha = \frac{\Delta S_f}{R} = \frac{\Delta H_f}{RT_m}$$

where  $\Delta S_f$  is the entropy of fusion,  $\Delta H_f$  is the enthalpy of fusion,  $R$  is the gas constant, and  $T_m$  is the melting temperature and is a useful indication of a growth morphology of a phase. If the  $\alpha$  value is smaller than 2, there is a tendency that the crystal grows with a non-faceted solid-liquid interface, while larger  $\alpha$  value indicates that the crystal is likely to grow with a faceted solid-liquid interface [31]. However, during eutectic reaction, the intermetallic phases start to solidify at the eutectic temperature. Therefore, we have calculated two different values of each Jackson parameter, namely  $\alpha_m$  which is a Jackson parameter calculated using the melting temperature ( $T_m$ ) and enthalpy of fusion ( $\Delta H_m$ ) at the composition where intermetallic is located in the phase diagram. The other one is  $\alpha_e$  calculated

**Table 2** Jackson's parameters of the intermetallic phases in each binary hypo-eutectic Mg-based alloys calculated using Thermo-Calc with MG 4.0 database

Alloys (wt%)	Intermetallic phase	$H_m$ [J/mol]	$T_m$ [K]	$H_e$ [J/mol]	$T_e$ [K]	$\alpha_m$	$\alpha_e$
Mg–8Ni [30]	Mg <sub>2</sub> Ni	13,347.53	1037.18	12,020.36	779.15	1.55	1.86
Mg–5La	Mg <sub>12</sub> La	9639.97	927.88	8346.32	886.15	1.25	1.13
Mg–23Y	Mg <sub>24</sub> Y <sub>5</sub>	8423.47	892.21	8610.39	841.15	1.14	1.23
Mg–12Cu	Mg <sub>2</sub> Cu	11,820.65	840.81	9678.49	758.15	1.69	1.54
Mg–1Si	Mg <sub>2</sub> Si	28,681.78	1354.72	22,318.30	910.15	2.55	2.95

using the melt temperature ( $T_e$ ) and enthalpy of fusion ( $\Delta H_e$ ) at eutectic point. The calculated Jackson parameters of the intermetallic phases in each binary hypo-eutectic Mg-based alloy are listed in Table 2. There are minor differences between the calculated values of  $\alpha_m$  and  $\alpha_e$  although none were significant enough to change the classification of a given growth mode. The calculated values indicate that Mg<sub>2</sub>Ni, Mg<sub>12</sub>La, Mg<sub>24</sub>Y<sub>5</sub>, and Mg<sub>2</sub>Cu have a Jackson parameter less than 2, while Mg<sub>2</sub>Si has a Jackson parameter larger than 2.

## Microstructures

The microstructures of Mg-based alloys with/without trace Na addition solidified at moderate cooling rate are shown in Fig. 1. An SEM in backscattered electron mode was used for microstructure observation of Mg–8Ni [30], Mg–5La, Mg–23Y, and Mg–12Cu alloys, while an optical microscope was used for Mg–1Si alloys as this provided the best contrast between the Mg and Mg<sub>2</sub>Si intermetallic. In the case of Mg–8Ni alloys, Mg–Mg<sub>2</sub>Ni eutectic was refined after the trace Na addition which corresponds well with our previous studies in this system [14, 32]. The  $\alpha_e$  value of 1.86 is very close to the threshold value ( $\alpha = 2$ ). Thus, the morphology of Mg<sub>2</sub>Ni is susceptible to morphology changes with Na additions. However, the non-faceted intermetallic phases of other alloys having Jackson parameters that are further below theoretical transition value of 2 including Mg<sub>12</sub>La, Mg<sub>24</sub>Y<sub>5</sub>, and Mg<sub>2</sub>Cu did not show any recognisable change in morphology or even became coarser as shown in Fig. 3c–j. Interestingly, the faceted Mg<sub>2</sub>Si phase which has a Jackson parameter larger than 2 became coarser after Na was added to the alloy. This result conflicts with that of the eutectic modification in Al–Si and Al–Ge alloys using chemical modifiers based on impurity-induced twinning [16–18]. It is acknowledged, however, that the effect of trace additions in determining the nucleation pattern, which was not determined in this research, also plays a significant role in determining the eutectic growth velocity and morphology [33].

Figure 4 shows the microstructures of hypo-eutectic Mg-based alloys solidified at fast cooling rates with/without

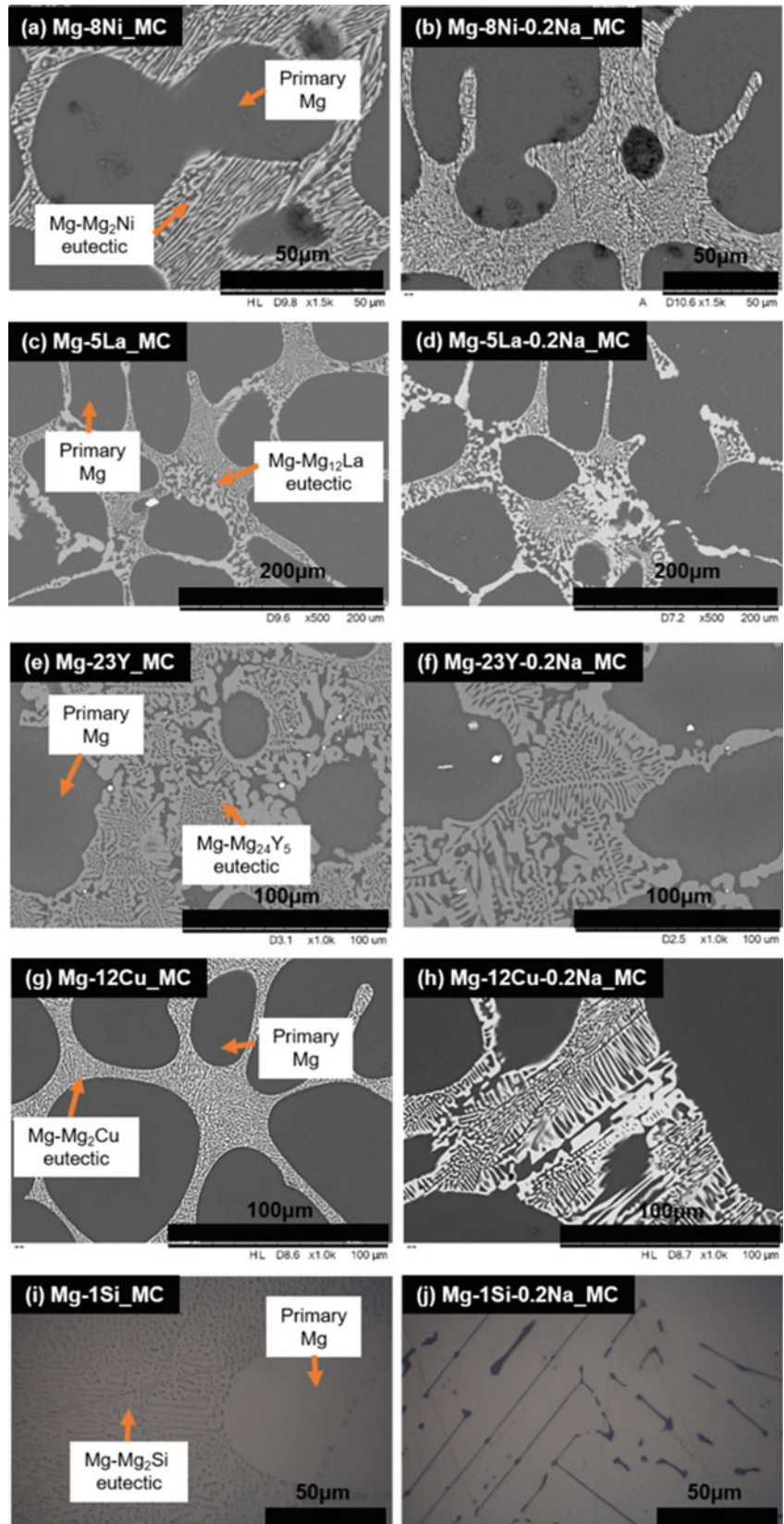
Na addition. The smaller size of the Mg primary phase and more compact or well-refined eutectic of these alloys is consistent with the faster cooling rate. As shown in Fig. 4, none of alloys showed any coarse faceted intermetallic phases regardless of the presence of Na. In the case of the Mg–1Si alloy, the well-refined and fibrous morphology of the Mg<sub>2</sub>Si phase conflicts with the predictions made based on the Jackson parameter ( $\alpha > 2$ ). Also, no further refinement effect on the eutectic in these Mg-based alloys solidified at fast cooling rates was observed with the addition of Na. In the case of Mg–1Si alloy beyond the Na addition seems to be associated with a slightly coarser Mg<sub>2</sub>Si phase in the eutectic as shown in Fig. 4j in this study. However, it is difficult to conclude that Na does not have any potential for modification of the Mg<sub>2</sub>Si phase, and further studies in terms of the dependency of Na addition level and cooling rate on eutectic Mg<sub>2</sub>Si phase are required. For example, Emamy et al. [21] have added Na up to 0.15 wt% to an Al–Mg<sub>2</sub>Si alloy and observed eutectic refinement of the Mg<sub>2</sub>Si phase and Bi and Sc have shown a modification effect on the Mg<sub>2</sub>Si in Al–M<sub>2</sub>Si alloys [19, 20]. Interestingly, there are some reports that excess amounts of chemical refiner additions increase the size of the Mg<sub>2</sub>Si phase. Wu et al. reported that eutectic Mg<sub>2</sub>Si can be refined when Sc is added up to 0.25 wt% but the higher content of Sc addition increases the size of the eutectic Mg<sub>2</sub>Si phase [20]. Guo et al. also reported that primary Mg<sub>2</sub>Si phase became coarser when the Bi content exceeded 0.8 wt% [22]. Therefore, there is still a possibility that eutectic Mg<sub>2</sub>Si may be refined by adding a lower quantity of Na than 0.2 wt% or different chemical refiners such as Bi or Sc. In addition, eutectic refinement can also be achieved by increasing the cooling rate. The difference of segregation of Na ahead of the eutectic Mg phase may also differ that ahead of the Al phase when considering Al–Mg<sub>2</sub>Si eutectic, and this may also influence the concentration of Na required for modification.

## Hydrogen Absorption Kinetics

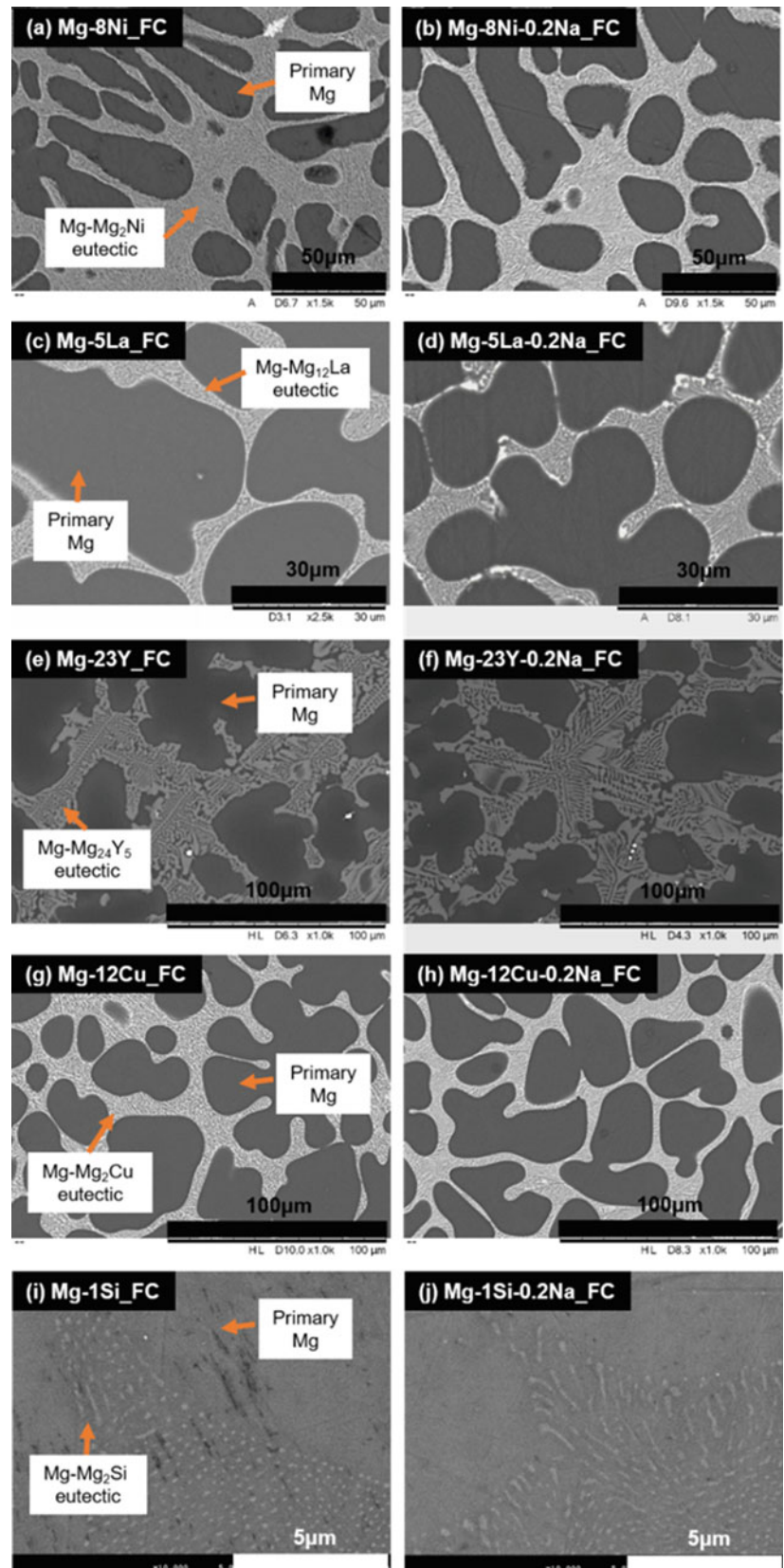
A long activation process is one of the disadvantages of Mg-based alloys for hydrogen storage systems. In particular, the first hydrogen absorption processes take a disproportionately long time and at least 4–5 absorption/desorption



**Fig. 3** Typical micrographs of Mg-based alloys with/without Na addition solidified at moderate cooling rate: **a, b** Mg–Ni [30], **c, d** Mg–La, **e, f** Mg–Y, **g, h** Mg–Cu, and **i, j** Mg–Si



**Fig. 4** Typical micrographs of Mg-based alloys with/without Na addition solidified at fast cooling rate: **a, b** Mg–Ni [30], **c, d** Mg–La, **e, f** Mg–Y, **g, h** Mg–Cu, and **i, j** Mg–Si



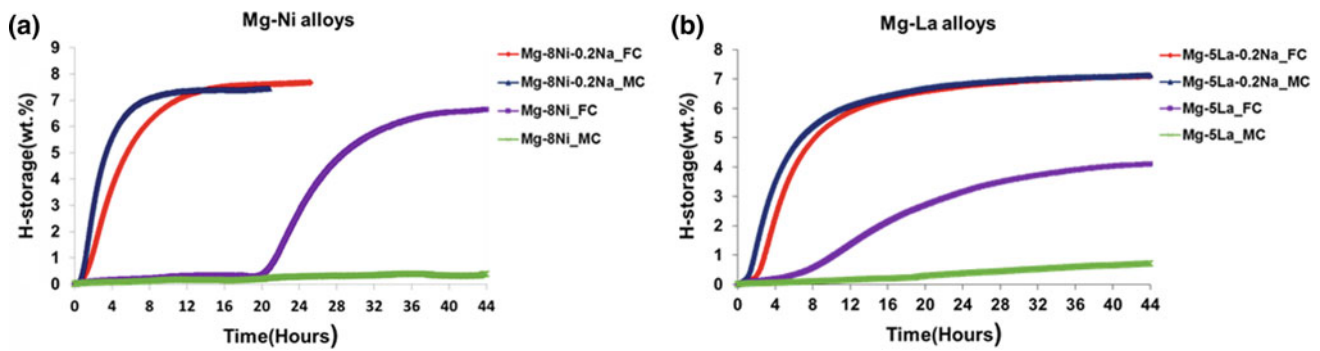


**Fig. 5** First hydrogen absorption curves of **a** Mg–8Ni alloys [30] and **b** Mg–5La alloys with fast and moderate cooling, with and without an addition of 0.2 wt% Na

cycles are required to fully activate the Mg-based alloys [34, 35]. The effects of trace Na additions on eutectic morphology and hydrogen storage properties are studied on Mg–5La alloys. For comparison, results of Mg–8Ni alloys are also included [30]. Moreover, since the cost of La has economic advantages compared to Ni, the performance of this alloy is of interest for impact in the hydrogen storage and transport industries. These tests represent the first hydrogen absorption with no activation procedure. Figure 5a shows the first hydrogen absorption curves of the Mg–8Ni alloys. From the microstructure observations, the eutectic was refined when Na was added to the Mg–8Ni alloy as shown in Fig. 3b and faster hydrogen absorption kinetics were observed from the Mg–8Ni–0.2Na\_MC sample compared to the Mg–8Ni\_MC sample. This result agrees well with our previous studies into the hydrogen absorption kinetics of Mg–Ni alloys showing there is an improvement in alloys which contained refined eutectic after Na is added [14]. However, it is also clear from Fig. 5 that at the higher cooling rate conditions (Mg–8Ni\_FC) the addition of Na improves the hydrogen absorption kinetics despite little difference in the eutectic morphology with and without Na. Therefore, while refinement itself seems to be associated with an improvement in kinetics, Na additions improve the kinetics somewhat independently of the morphology.

The independent effects of Na additions compared to eutectic morphology changes are also clear from the Mg–La alloys. The hydrogen absorption curves of four different Mg–5La alloys are represented in Fig. 5b. Interestingly, once Na was added to the alloys, a significant improvement of hydrogen absorption kinetics was achieved compared to the Na-free samples despite no eutectic refinement occurring as a result of the Na additions. As shown in Figs. 3 and 4, there is no significant change in the microstructure of the Mg–5La alloys due to Na additions. In our previous research in the Mg–Ni system, we observed refined eutectic with Na additions and it hypothesised that refinement of the eutectic facilitated the hydrogen absorption process [14, 32].

However, the result of this study shows there is an independent effect of Na additions in improving the hydrogen absorption kinetics of Mg-based alloys and that this effect is more significant than microstructure refinement and is not confined to the Mg–Ni system. Nevertheless, the effect of microstructure refinement on hydrogen absorption reactions is still present. Among unmodified alloys, Mg–8Ni\_FC and Mg–5La\_FC alloys solidified at fast cooling rates show better hydrogen absorption kinetics than those solidified at moderate cooling rates (Mg–8Ni\_MC and Mg–5La\_MC alloys). The fine eutectic achieved by a faster cooling rate during solidification may promote preferential diffusion along the interphase boundaries [36, 37]. Thus, the fine eutectic can increase the density of interphase boundaries between the Mg and Mg<sub>12</sub>La intermetallics providing more hydrogen diffusion pathways. Moreover, crystallographic defects such as twinning, dislocations, and stacking faults can also enhance hydrogen sorption kinetics allowing better hydrogen diffusivity [38–40]. Therefore, further investigations using other characterisation approaches such as transmission electron microscopy and synchrotron X-ray powder diffraction are required for a better understanding of the mechanisms of hydrogen absorption associated with additions of Na to Mg-based alloys.

## Conclusions

Eutectic modification strategies based on a re-entrant edge mechanism in Al–Si and Al–Ge alloys have been tested in a variety of hypo-eutectic Mg-based alloys. Trace amounts of Na were added to the alloys solidified at different cooling rates. The Jackson parameters of the intermetallic phase were calculated using Thermo-Calc with MG4.0 database and discussed in regard to eutectic modification of these alloys. No significant changes of the eutectic structure of the Mg-based alloys were observed fast cooling rates; however, some alloys solidified at moderate cooling rates did show

modification of the eutectic structure with Na additions. The first hydrogen absorption curves of Mg–8Ni and Mg–5La alloys with and without Na were measured. It was shown that Na additions were associated with a significant improvement in hydrogen absorption kinetics and that this effect is independent of morphological changes in the microstructure. An increased cooling rate was independently associated with an improvement in hydrogen storage kinetics; however, this effect was small when compared to the addition of Na. This work has demonstrated, contrary to prior expectations, that microstructural refinement and hydrogen absorption kinetics are not necessarily correlated.

**Acknowledgements** This work supported by funding from the Australian Research Council Linkage Project LP160100690 and Australian Government Research Training Program (RTP) Scholarship that have contributed to this research. The authors acknowledge Dr. Christopher Gourlay (Faculty of Engineering, Department of Materials, Imperial College London) for calculation of Jackson Parameter and the facilities, and the scientific and technical assistance, of the Australian Microscopy & Microanalysis Research Facility at the Centre for Microscopy and Microanalysis.

## References

- Sakintuna, B., F. Lamari-Darkrim and M. Hirscher (2007). "Metal hydride materials for solid hydrogen storage: A review." *International Journal of Hydrogen Energy* **32**(9): 1121–1140.
- Huot, J., E. Akiba and T. Takada (1995). "Mechanical alloying of MgNi compounds under hydrogen and inert atmosphere." *Journal of Alloys and Compounds* **231**(1): 815–819.
- Huot, J., G. Liang, S. Boily, A. Van Neste and R. Schulz (1999). "Structural study and hydrogen sorption kinetics of ball-milled magnesium hydride." *Journal of Alloys and Compounds* **293–295**: 495–500.
- Doppiu, S., L. Schultz and O. Gutfleisch (2007). "In situ pressure and temperature monitoring during the conversion of Mg into MgH<sub>2</sub> by high-pressure reactive ball milling." *Journal of Alloys and Compounds* **427**(1): 204–208.
- Crivello, J. C., R. V. Denys, M. Dornheim, M. Felderhoff, D. M. Grant, J. Huot, T. R. Jensen, P. de Jongh, M. Latroche, G. S. Walker, C. J. Webb and V. A. Yartys (2016). "Mg-based compounds for hydrogen and energy storage." *Applied Physics A* **122**(2).
- Liang, G., J. Huot, S. Boily, A. Van Neste and R. Schulz (1999). "Catalytic effect of transition metals on hydrogen sorption in nanocrystalline ball milled MgH<sub>2</sub>–Tm (Tm = Ti, V, Mn, Fe and Ni) systems." *Journal of Alloys and Compounds* **292**(1): 247–252.
- Denis, A., E. Sellier, C. Aymonier and J. L. Bobet (2009). "Hydrogen sorption properties of magnesium particles decorated with metallic nanoparticles as catalyst." *Journal of Alloys and Compounds* **476**(1): 152–159.
- Li, Z., X. Liu, L. Jiang and S. Wang (2007). "Characterization of Mg–20 wt% Ni–Y hydrogen storage composite prepared by reactive mechanical alloying." *International Journal of Hydrogen Energy* **32**(12): 1869–1874.
- Kalinichenka, S., L. Röntzsch, T. Riedl, T. Weißgärber and B. Kieback (2011). "Hydrogen storage properties and microstructure of melt-spun Mg<sub>90</sub>Ni<sub>8</sub>RE<sub>2</sub> (RE = Y, Nd, Gd)." *International Journal of Hydrogen Energy* **36**(17): 10808–10815.
- Barkhordarian, G., T. Klassen and R. Bormann (2003). "Fast hydrogen sorption kinetics of nanocrystalline Mg using Nb<sub>2</sub>O<sub>5</sub> as catalyst." *Scripta Materialia* **49**(3): 213–217.
- Polanski, M. and J. Bystrzycki (2009). "Comparative studies of the influence of different nano-sized metal oxides on the hydrogen sorption properties of magnesium hydride." *Journal of Alloys and Compounds* **486**(1): 697–701.
- Janot, R., L. Aymard, A. Rougier, G. A. Nazri and J. M. Tarascon (2003). "Enhanced hydrogen sorption capacities and kinetics of Mg<sub>2</sub>Ni alloys by ball-milling with carbon and Pd coating." *Journal of Materials Research* **18**(8): 1749–1752.
- Takasaki, A., Y. Furuya and M. Katayama (2007). "Mechanical alloying of graphite and magnesium powders, and their hydrogenation." *Journal of Alloys and Compounds* **446–447**: 110–113.
- Nogita, K., S. Ockert, J. Pierce, M. C. Greaves, C. M. Gourlay and A. K. Dahle (2009). "Engineering the Mg–Mg<sub>2</sub>Ni eutectic transformation to produce improved hydrogen storage alloys." *International Journal of Hydrogen Energy* **34**(18): 7686–7691.
- Tran, X. Q., S. D. McDonald, Q. Gu, S. Matsumura and K. Nogita (2016). "Effect of trace Na additions on the hydrogen absorption kinetics of Mg<sub>2</sub>Ni." *Journal of Materials Research* **31**(09): 1316–1327.
- Lu, S.-Z. and A. Hellawell (1987). "The mechanism of silicon modification in aluminum-silicon alloys: Impurity induced twinning." *Metallurgical Transactions A* **18**(10): 1721–1733.
- Makhlouf, M. M. and H. V. Guthy (2001). "The aluminum–silicon eutectic reaction: mechanisms and crystallography." *Journal of Light Metals* **1**(4): 199–218.
- Li, J. H., N. Wanderka, Z. Balogh, P. Stender, H. Kropf, M. Albu, Y. Tsunekawa, F. Hofer, G. Schmitz and P. Schumacher (2016). "Effects of trace elements (Y and Ca) on the eutectic Ge in Al–Ge based alloys." *Acta Materialia* **111**: 85–95.
- Wu, X.-F., Y. Wang, K.-Y. Wang, R.-D. Zhao and F.-F. Wu (2018). "Enhanced mechanical properties of hypoeutectic Al–10Mg<sub>2</sub>Si cast alloys by Bi addition." *Journal of Alloys and Compounds* **767**: 163–172.
- Wu, X.-F., K.-Y. Wang, F.-F. Wu, R.-D. Zhao, M.-H. Chen, J. Xiang, S.-N. Ma and Y. Zhang (2019). "Simultaneous grain refinement and eutectic Mg<sub>2</sub>Si modification in hypoeutectic Al–11Mg<sub>2</sub>Si alloys by Sc addition." *Journal of Alloys and Compounds* **791**: 402–410.
- Emamy, M., R. Khorshidi and A. H. Raouf (2011). "The influence of pure Na on the microstructure and tensile properties of Al–Mg<sub>2</sub>Si metal matrix composite." *Materials Science and Engineering: A* **528**(13): 4337–4342.
- Guo, E. J., B. X. Ma and L. P. Wang (2008). "Modification of Mg<sub>2</sub>Si morphology in Mg–Si alloys with Bi." *Journal of Materials Processing Technology* **206**(1): 161–166.
- Ye, L., J. Hu, C. Tang, X. Zhang, Y. Deng, Z. Liu and Z. Zhou (2013). "Modification of Mg<sub>2</sub>Si in Mg–Si alloys with gadolinium." *Materials Characterization* **79**: 1–6.
- Nogita, K. and A. K. Dahle (2006). Magnesium alloys for hydrogen storage. International patent. WO/2006/060851. 15 June 2006.
- Nayeb-Hashemi, A. A. and J. B. Clark (1985). "The Mg–Ni (Magnesium–Nickel) system." *Bulletin of Alloy Phase Diagrams* **6**(3): 238–244.
- Nayeb-Hashemi, A. A. and J. B. Clark (1988). "The La–Mg (Lanthanum–Magnesium) system." *Journal of Phase Equilibria* **9**(2): 172–178.
- Guo, C., Z. Du and C. Li (2007). "A thermodynamic description of the Gd–Mg–Y system." *Calphad* **31**(1): 75–88.
- Nayeb-Hashemi, A. A. and J. B. Clark (1984). "The Cu–Mg (Copper–Magnesium) system." *Bulletin of Alloy Phase Diagrams* **5**(1): 36–43.



29. Okamoto, H. (2007). "Mg-Si (Magnesium-Silicon)." *Journal of Phase Equilibria and Diffusion* **28**(2): 229.
30. Kim, M., Y. Ali, S. D. McDonald, T. B. Abbott and K. Nogita (2019). Effect of Na addition and cooling rate on activation of Mg-Ni alloys for hydrogen storage *2019 International Conference on Nanospace Materials*. Australia, (To be submitted).
31. Kurz, W. and D. J. Fisher (1992). *Fundamentals of Solidification*, Trans Tech Publications Ltd.
32. Tran, X. Q., S. D. McDonald, Q. Gu, X. F. Tan and K. Nogita (2017). "Effect of trace Na additions on the hydriding kinetics of hypo-eutectic Mg-Ni alloys." *International Journal of Hydrogen Energy* **42**(10): 6851–6861.
33. McDonald, S. D., K. Nogita and A. K. Dahle (2004). "Eutectic nucleation in Al-Si alloys." *Acta Materialia* **52**(14): 4273–4280.
34. Yang, T., Z. Yuan, W. Bu, Z. Jia, Y. Qi and Y. Zhang (2016). "Evolution of the phase structure and hydrogen storage thermodynamics and kinetics of Mg88Y12 binary alloy." *International Journal of Hydrogen Energy* **41**(4): 2689–2699.
35. Yang, T., Z. Yuan, W. Bu, Z. Jia, Y. Qi and Y. Zhang (2016). "Effect of elemental substitution on the structure and hydrogen storage properties of LaMgNi4 alloy." *Materials & Design* **93**: 46–52.
36. Čermák, J. and L. Král (2008). "Hydrogen diffusion in Mg-H and Mg-Ni-H alloys." *Acta Materialia* **56**(12): 2677–2686.
37. Kim, J. and C. C. Tasan (2019). "Microstructural and micro-mechanical characterization during hydrogen charging: An in situ scanning electron microscopy study." *International Journal of Hydrogen Energy* **44**(12): 6333–6343.
38. Danaie, M., S. X. Tao, P. Kalisvaart and D. Mitlin (2010). "Analysis of deformation twins and the partially dehydrogenated microstructure in nanocrystalline magnesium hydride (MgH<sub>2</sub>) powder." *Acta Materialia* **58**(8): 3162–3172.
39. Deutges, M., H. P. Barth, Y. Chen, C. Borchers and R. Kirchheim (2015). "Hydrogen diffusivities as a measure of relative dislocation densities in palladium and increase of the density by plastic deformation in the presence of dissolved hydrogen." *Acta Materialia* **82**: 266–274.
40. Hongo, T., K. Edalati, M. Arita, J. Matsuda, E. Akiba and Z. Horita (2015). "Significance of grain boundaries and stacking faults on hydrogen storage properties of Mg<sub>2</sub>Ni intermetallics processed by high-pressure torsion." *Acta Materialia* **92**: 46–54.

# Producing High Purity Magnesium (99.99%) Directly by Pidgeon Process

Bo Yang, Fei Liu, Bo-Yu Liu, Zhi-Min Chang, Lu-Yao Mao, Jiao Li, and Zhi-Wei Shan

## Abstract

Pure magnesium is the foundation of the entire magnesium industry. Over 90% of the pure magnesium on the market is produced in China using Pidgeon process. Even though the quality of pure magnesium has been improved significantly in the past decades, the majority of them is still suffering the following problems: The purity is only ~99.9%; there are still too many kinds of harmful impurity elements with their content fluctuating greatly in an uncontrollable manner. The impurities can be passed to magnesium alloys and degrade their properties significantly, especially their corrosion resistance ability. This leaves people an impression that Pidgeon process cannot produce high purity magnesium directly. As a consequence, it has long been accepted that producing high purity magnesium requires additional processes, which is usually costly and time-consuming. After analyzing the impurities' source of the Pidgeon process, we developed a new technique that can produce high purity magnesium (99.99%) directly by Pidgeon process without significantly increasing the costs. The application of this new technique is expected to benefit the entire magnesium industry.

## Keywords

High purity • Filtration • Pidgeon process • Low cost

## Introduction

Over 80% of the world's pure magnesium yielded in China in 2018 [1] and more than 95% of them was produced through Pidgeon process. However, by in-depth research in the primary magnesium enterprises, we found that the quality of pure magnesium was worrying in terms of purity. Taking a top primary magnesium enterprise located in Yulin, Shaan Xi, China, for example, near 98% of its products in 2018 could only reach the 99.90% level, which was the second-lowest purity standard in the *Pure Magnesium Standard of China, GB/T 3499-2011*. There are too many kinds of harmful impurity elements with their content fluctuating greatly in an uncontrollable manner and these impurities in raw material can be passed to magnesium alloys, degrading their qualities and having a negative impact on their reputation. High purity magnesium (>99.99%) is not only critical in manufacturing high purity sponge titanium and high-performance magnesium alloys, but also has a trendy application in the fields of Mg-based biomedical implants [2], Mg-based anodes in batteries [3].

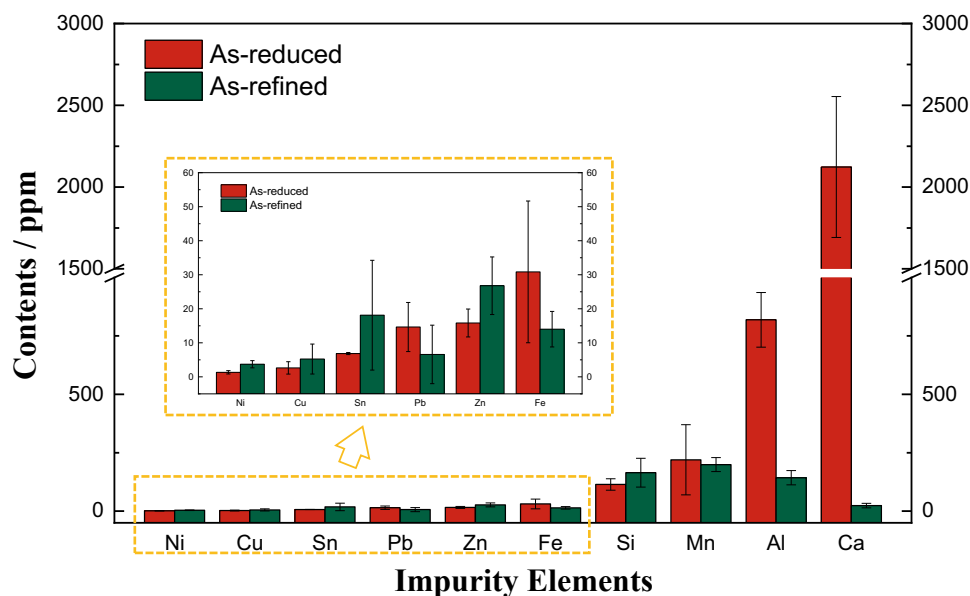
It has long been accepted that Pidgeon process, with only traditional flux refining method, cannot produce high purity magnesium. Additional processes are necessary for further purification such as vacuum distillation method, which is usually costly and time-consuming. Here we developed a new technique that can produce high purity magnesium (>99.99%) directly through the Pidgeon process without obviously increasing the cost.

The main impurities in primary magnesium are Si, Mn, Al, Ca, Fe, etc. We first investigated the source of these impurities. Traditional Pidgeon process has two main steps, reduction and refinement, which are two possible source of impurities. As-reduced magnesium, also called crude magnesium, is the magnesium extracted from the reactant pellets in the reduction retort. As-refined magnesium is the commercial pure magnesium that refined by flux refining. Comparison of impurity elements content between the

B. Yang · F. Liu · B.-Y. Liu · Z.-M. Chang · L.-Y. Mao · J. Li · Z.-W. Shan (✉)

Engineering Research Center for Magnesium-Based New Materials, Center for Advancing Materials Performance from the Nanoscale (CAMP-Nano) & Hysitron Applied Research Center in China (HARCC), State Key Laboratory for Mechanical Behavior Materials, Xi'an Jiaotong University, Xi'an, 710049, People's Republic of China  
e-mail: [zwshan@xjtu.edu.cn](mailto:zwshan@xjtu.edu.cn)

**Fig. 1** Comparison of impurity elements content between the as-reduced and as-refined magnesium ingots. Almost all the impurities come from the reduction step, and the flux refining cannot remove all impurities and can even bring in some kinds of impurities



as-reduced and as-refined magnesium ingots is shown in Fig. 1. The flux refining significantly decreased the content of Ca, from over 2000 ppm to about 50 ppm, and then Al, from over 800 ppm to about 200 ppm. However, the refining effect on other impurities, like Mn, Fe and Pb, is not significant because the flux does not interact with elements that are less chemical active than Mg [4]. Surprisingly, the content of some other impurities even increased after refining, such as Ni, Cu, Sn and Si. The above analyses suggest that almost all the impurities come from the reduction step, and the flux refining cannot remove all impurities and can even bring some impurities. Therefore, if the impurities can be removed from the magnesium vapor during the reduction step, a much better refining effect can be expected.

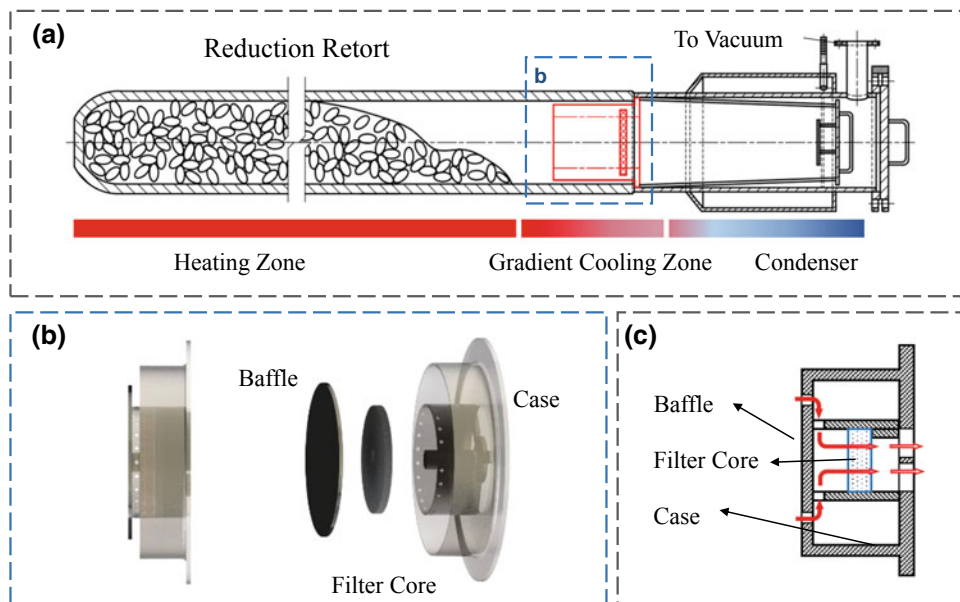
## Experimental Setup

We then investigated how to purify magnesium vapor in the reduction process. Figure 2a is a schematic diagram of the reduction retort. It is divided into three parts according to the temperature difference: heating zone, gradient cooling zone and condenser. Most part of the reduction retort belongs to the heating zone, where the reduction reaction happens under an average temperature of around 1250 °C and a vacuum of 13 Pa. The part covered by the recycled coolant jacket is the condenser, where magnesium condensation takes place. Gradient cooling zone is the region between these two parts. The temperature gradually decreases along the gradient cooling zone. The magnesium vapor and

impurities generate from the heating zone, migrate along the gradient cooling zone and finally all stop in condenser. These impurities generally have two states, condensed state and gas state. The impurities in condensed state, like small particles of reactant, are carried into the condenser by the airflow when pumping starts or by the metal vapor stream during reaction. For these impurities, the best place to set filter is the gradient cooling zone. For impurities in gas state, we use commercial thermodynamics software, Factsage, to predict their condense behaviors. Based on the calculate results, we find that some impurities should condense or deposit at a high temperature, while others will condense or deposit at a relative lower temperature. The first kind of gaseous impurity might be effectively blocked by the filter. For the second kind gaseous impurity, specially designed filter core is needed.

A specially designed filter was placed in the gradient cooling zone (marked by blue-dashed frame, Fig. 2a). The filter consists of three parts, a case, a filter core and a baffle (Fig. 2b). A special structure of the case was designed to make sure that the filter could be fixed onto the proper position in the gradient cooling zone. Two kinds of filter core were selected to capture the impurities. The baffle can protect the filter core from direct thermal shock from magnesium vapor stream in high temperature. Figure 2c shows the cross-section structure of the filter. Vapor flow could be disturbed by this twisted inner structure and mixed intensively so that the temperature field could be more uniform. All the experiments were carried out in the magnesium plants of Fugu JingFu Coal Chemical Co. LTD.

**Fig. 2** Details of our filter design. **a** Schematic diagram of a reduction retort. It can be divided into three parts by temperature, heating zone, gradient cooling zone and condenser. **b** The filter consists of three parts, a case, a filter core and a baffle. **c** The cross-section structure of the filter



## Results

After a reduction period of about 11 h, condensed magnesium ingots with shining appearance were obtained. The mass of them is in the range of 25–31 kg, which were comparable to that of the control group without filter. Note that this indicated that impurities did not clog the holes in the filter, otherwise we should see obvious decrease in yield.

In order to minimize the system error, the crude Mg produced next day, using the same reduction retort in the same furnace, was specially selected as the control experiment group. Samples were cut from the same position from both magnesium ingots with or without filter. The purity was measured by optical emission spectrometry (OES, Thermo Scientific ARL3460). Most of the impurities dramatically decreased after the filter was inserted. Figure 3 shows examples of Mn, Si and Al, which are the key impurities in primary magnesium. The content of these elements reached the standard of Mg9999 (*Pure Magnesium Standard of China, GB/T 3499-2011*).

Note that the content of Ca was still more than 1000 ppm, only reduced less than half, but it can be largely removed by the following flux refining process (see in Fig. 1). Moreover, the content of iron was 14 ppm, Sn was 17 ppm and other impurities' content, like Ni, Cu, Pb, etc., was all in very low level, which are not mentioned here.

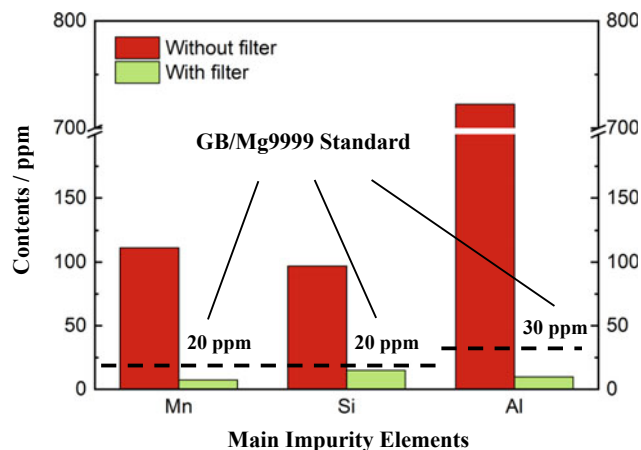


**Fig. 3** The contents of key impurity elements can be dramatically decreased by using the filter. The contents of key impurities including Mn, Si and Al, in the magnesium ingot made in our experiment meet the standard of Mg9999

So far it is really difficult to control the content of calcium in the as-reduced magnesium. That is because it is very difficult to obtain the ideal and accurate temperature distribution in the plant with only limited reform, especially when every retort is on its full capacity. It is worth to mention, however, that we achieved the high purity Mg (>99.99%, Ca < 10 ppm, Si < 10 ppm, Fe < 10 ppm, Mn ~5 ppm, Al undetectable, using OES GNR S5) directly by Pidgeon



**Table 1** Chemical component of industrial as-reduced magnesium produced with or without filter and laboratory as-reduced magnesium using filter

	Purity (wt%)	Impurity element content (ppm)									
	Mg	Ca	Al	Mn	Si	Fe	Zn	Pb	Sn	Cu	Ni
Industrial, without filter	99.62	2833	722	111	97	12	11	11	31	<5	<10
Industrial, with filter	99.80	1926	10	7	15	14	6	6	17	<5	<10
Laboratory, with filter	>99.99	<10	<10	5	<10	<10	9	9	10	<5	<10

reduction without any refinement in our lab study, 50 grams per cycle, by accurately controlling the cooling path and using appropriate filters. Analysis results for all elements of the magnesium mentioned above are listed in Table 1.

(Nos. 2016KTZDGY-04-03, 2016KTZDGY-04-04 and 201805064ZD15CG48). We acknowledge Wei-Yin Zhang (Fugu JingFu Coal Chemical Co. LTD) for providing the raw materials. The authors declare no competing financial interests.

## Summary

Pidgeon process can be a very “clean” method and 99.99% high purity magnesium can be produced directly through the reduction process without costly and time-consuming additional processes.

**Acknowledgements** This work was supported by the National Key Research and Development Program of China (No. 2017YFB0702001), National Natural Science Foundation of China (Nos. 51601141), China Postdoctoral Science Foundation (2016M600788), and funding from the Science and Technology Departments of Shaanxi and Xi’an, China

## References

1. E.L. Bray, Magnesium metal U.S. Geological Survey, 2019 Minerals Yearbook, 2019.
2. Y. Liu, Y. Zheng, X.H. Chen, J.A. Yang, H. Pan, D. Chen, L. Wang, J. Zhang, D. Zhu, S. Wu, K.W.K. Yeung, R.C. Zeng, Y. Han, S. Guan, Fundamental Theory of Biodegradable Metals—Definition, Criteria, and Design, *Advanced Functional Materials* 29 (18) (2019) 1805402.
3. S. Mohamed, S. Friedrich, B. Friedrich, Refining Principles and Technical Methodologies to Produce Ultra-Pure Magnesium for High-Tech Applications, *Metals* 9(1) (2019) 85.
4. R.-Y. Xu, *Silicothermic Reduction Process of Magnesium*, Central South University Press, 2003.

# Research on Properties of Prefabricated Pellets of Silicothermic Process After Calcination in Flowing Argon Atmosphere

Junhua Guo, Ting'an Zhang, Daxue Fu, Jibiao Han, Zonghui Ji, and Zhi'he Dou

## Abstract

In the Pidgeon process, the separation of calcination and reduction process leads to a long production cycle and high energy consumption. Based on the novel preparation method of pellets of silicothermic process, the low-grade magnesite with abundant resources in Liaoning Province was used as raw material, calcium source, reducing agent, and fluorite were added to pelletizer directly and then calcined and reduced in flowing argon atmosphere. The properties and micromorphology of prefabricated pellets after calcination were investigated in the work. The experimental results showed that the hydration activity and compressive strength of prefabricated pellets after calcination reached 23.0% and 998 N, respectively. The recovery ratio of magnesium metal was more than 80% in the reduction process. The research on calcination of prefabricated pellets in flowing gas provided a theoretical basis for continuous extraction of magnesium.

## Keywords

Flowing argon • Prefabricated pellets • Calcination • Silicothermic process

## Introduction

Magnesium metal has a wide range of industrial applications, such as the preparation of titanium, zirconium, beryllium and other metal reductants [1], hot metal desulfurizer [2], also used as high-performance hydrogen storage

materials [3, 4]. Magnesium alloys are also widely used in aviation, transportation, and 3C industries because of their excellent specific strength and stiffness [5–7]. The extraction methods of magnesium include magnesium chloride melting electrolysis and silicothermic reduction under high temperature and high vacuum. Silicothermic process is widely used in magnesium industry because of its simple process and easy operation. However, due to the long production cycle, high energy consumption, and high cost of reducing agent, the price of raw magnesium remains high [8, 9]. Therefore, the development of new technology and equipment to reduce energy consumption and shorten cycle time has become the focus of the attention of researcher.

Due to these problems of silicothermic process, aluminothermic process and carbothermic process have been widely studied. The aluminothermic process has the advantages of low reaction temperature, fast reaction speed, and short reaction period, but the high price of aluminium powder limits its industrial application [10–12]. Coke is a reductant in carbothermal process, which has a wide range of sources and low price. However, magnesium vapor will be oxidized by CO gas generated simultaneously during reduction, which seriously reduces the recovery of magnesium metal [13–15]. Although CSIRO Minerals Research Institute put forward the idea of rapid condensation with Laval nozzle and dissolving magnesium vapor with alloy to solve the problem of separation of magnesium vapor and CO in the process of extraction of magnesium by carbothermal process [16], which makes the industrialization of carbothermal process possible, it is still in the research stage. Mintek Company of South Africa has put forward MTMP process [17]. Although it can be produced continuously, the operation temperature of the process is high (1700–1750 °C), which requires strictly material properties and service life of the reaction furnace. Some researchers have also proposed new technologies such as extraction of magnesium by microwave and thermal reduction of magnesium from seawater [18, 19], which are in the exploratory stage.

J. Guo · T. Zhang (✉) · D. Fu · J. Han · Z. Ji · Z. Dou  
Key Laboratory of Ecological Metallurgy of Multi-Metal  
Intergrown Ores of Education Ministry, School of Metallurgy of  
Northeastern University, Special Metallurgy and Process  
Engineering Institute, Shenyang, Liaoning 110819, China  
e-mail: zta2000@163.net

One of the reasons for long production period, high energy consumption, and discontinuous production of silicothermic process is that the calcination and reduction process of dolomite are separated. The calcined dolomite needs to be cooled at a certain temperature before mixing and pelletizing. In order to solve this problem, Zhang et al. [20, 21] proposed a novel preparation method of pellets for silicothermic process, which is that dolomite, ferrosilicon, and fluorite are mixed to produce pellets and then calcined. Fu et al. [22] only studied the compressive strength of prefabricated pellets after calcination. Based on the novel preparation method of pellets of silicothermic process, the low-grade magnesite with abundant resources in Liaoning Province was used as raw material, calcium source, reducing agent, and fluorite were added to pelletizer directly without binder and then calcined in flowing argon atmosphere. The properties of calcined pellets were studied in the paper comprehensively, which provided a theoretical basis for rapid continuous extraction of magnesium.

## Experiments

### Raw Materials

The experimental raw materials are low-grade magnesite and ferrosilicon as well as analytical-grade drugs, including calcium carbonate and calcium fluoride. Among them, ferrosilicon comes from Henan, China, with 74.13% silicon content. Magnesite comes from Liaoning, China. The chemical compositions are shown in Table 1.

The XRD pattern of magnesite is shown in Fig. 1. The main phase is  $\text{MgCO}_3$  with a small amount of  $\text{CaCO}_3$ . Table 1 shows a small amount of  $\text{SiO}_2$ ,  $\text{Fe}_2\text{O}_3$ , and  $\text{Al}_2\text{O}_3$ .

### Experimental Equipment

Pellets were pressed by briquetting equipment. The briquetting equipment is shown in Fig. 2. The calcination process was carried out in a vertical tube furnace. The equipment schematic diagram is shown in Fig. 3.

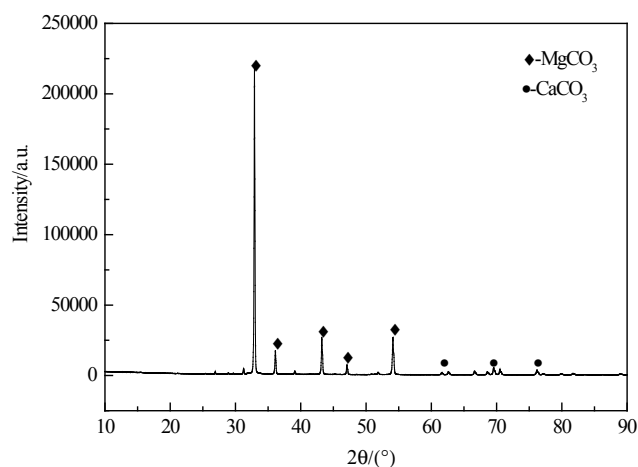


Fig. 1 XRD pattern of magnesite

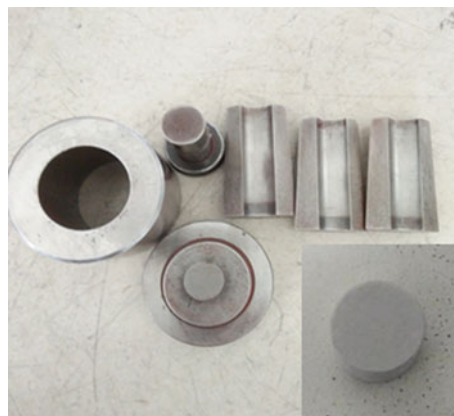


Fig. 2 Briquetting equipment and pellet

### Experimental Procedures

First magnesite and ferrosilicon were crushed and grinded to a certain size, then fine magnesite, reductant, calcium carbonate, and fluorite were mixed evenly in a certain proportion, and then pressed into cylindrical pellets with a diameter of 15 mm by briquetting equipment. Then the pressed pellets were put into corundum crucible with porous. Then the crucible was put into a vertical tube furnace with flowing

Table 1 Chemical composition of magnesite

Ore	Ignition loss	$\text{SiO}_2$	$\text{Al}_2\text{O}_3$	$\text{Fe}_2\text{O}_3$	CaO	MgO
Magnesite	51.92	0.75	0.19	0.74	0.90	45.50

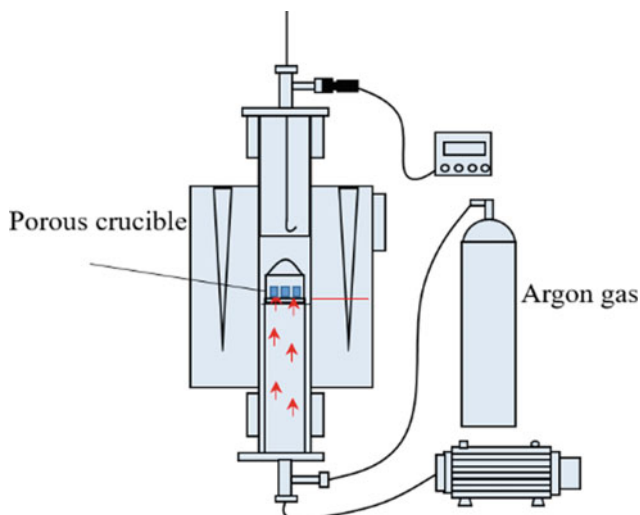


**Fig. 3** Schematic diagram of vertical tube furnace

argon gas and calcined at a certain temperature. After calcination for a period of time, the properties of calcined pellets were tested.

## Results and Discussion

### Effect of Briquetting Pressure on Pellet Properties

The new pellets used for extraction of magnesium may be broken up during transportation and calcination, which affects the recovery ratio of magnesium in reduction process. Therefore, the effect of briquetting pressure on the properties of calcined pellets was investigated. Because the diameters of briquetting equipment and pellet are not different, the equipment display pressure and actual pellet pressure are also different. When the equipment pressure indication is 5 MPa, 10 MPa, 15 MPa, 20 MPa, and 25 MPa, the corresponding actual pellet pressure is 69.69 MPa, 139.38 MPa, 209.07 MPa, 278.76 MPa, and 348.45 MPa, respectively. In the following content, the briquetting pressure is expressed by the pressure readings of the equipment. Figures 4 and 5 show mass loss rate, hydration activity, and compressive strength of pellets calcined at 1000 °C for 1 h, respectively. These results indicate that the mass loss rate and hydration activity of the pellets are higher when the briquetting pressure was 15 MPa, 40.08%, and 23.0%, respectively. The compressive strength of pellets increases with the increase of briquetting pressure before and after calcination. The maximum compressive strength is 3827 N and 916 N at 25 MPa, respectively. Comparing with the pellets before and after calcination, the load on the pellets after calcination is obviously reduced. The analysis shows that the calcined pellets produce CO<sub>2</sub>, which causes many pores in the pellets and reduces the density of the pellets, so it is easier to crush.

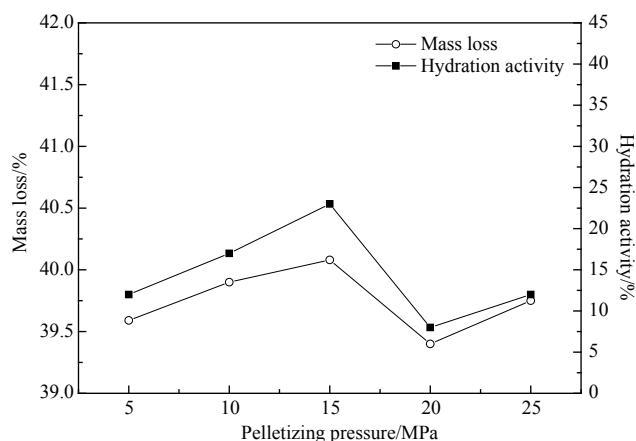


**Fig. 4** Mass loss and hydration activity after calcination under different briquetting pressures

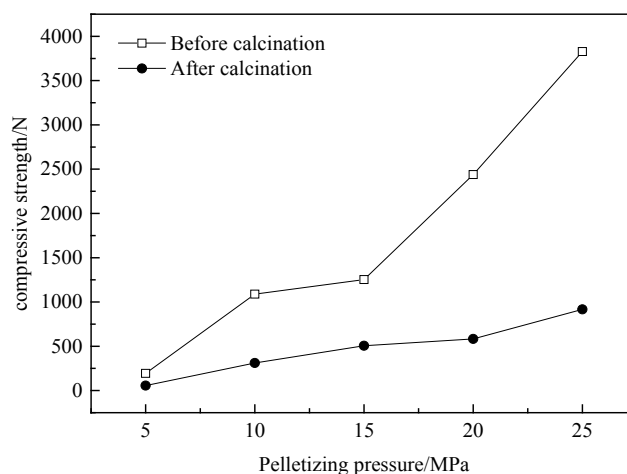


**Fig. 5** Compressive strength before and after calcination under different briquetting pressures

### Effect of Magnesite Grain Size on Pellet Properties

As a raw material for extraction of magnesium, the particle size of magnesite is closely related to the density and specific surface area of prefabricated pellets, which may affect the activity of pellets. Figure 6 shows the mass loss, hydration activity of prefabricated pellets with different magnesite grain size after calcination at 1000 °C for 1 h. It can be seen that the effect of magnesite grain size on pellet activity is not significant in calcination stage. The weight loss rate of pellets with different particle size fluctuates around 39.40%, and the hydration activity fluctuates around 13%. From Fig. 7, it can be seen that the compressive strength of pellets before calcination is high, which can reach 3198 N at 160 mesh, while the maximum compressive strength of pellets after calcination is 950 N, and the compressive strength decreases with the decrease of magnesite grain size.



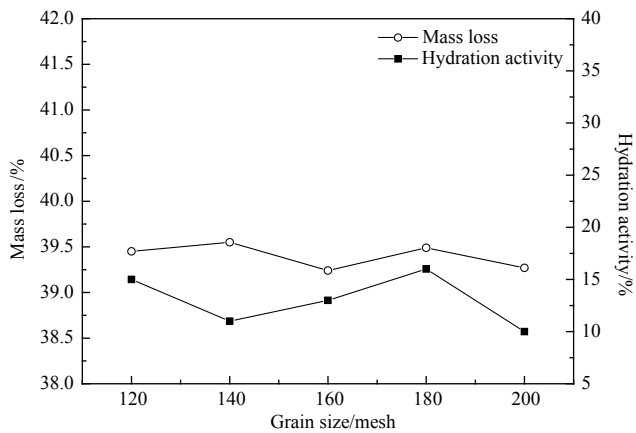


**Fig. 6** Effect of magnesite grain size on mass loss and hydration activity of calcined pellets

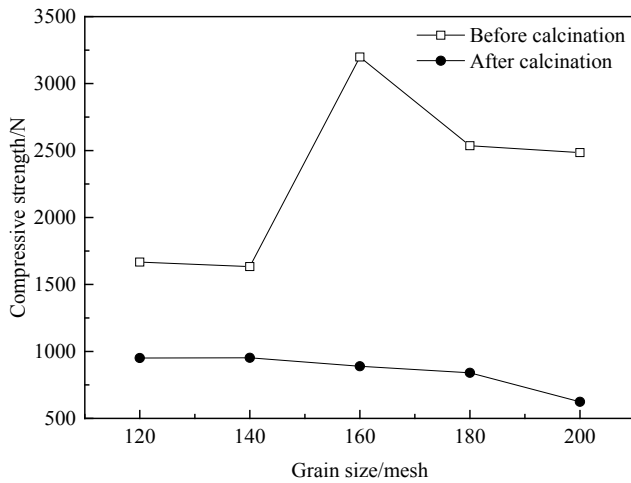


**Fig. 7** Effect of magnesite grain size on the compressive strength of pellets before and after calcination

### Effect of Temperature and Time on Pellet Properties

The calcination temperature and time are directly related to the kinetics of the calcination process. In order to determine the appropriate calcination temperature and time, the effects of different calcination temperatures (900 °C, 950 °C, 1000 °C, 1050 °C) and calcination time (0.5 h, 1 h, 1.5 h, 2 h) on the properties of pellets were investigated experimentally. Figure 8 shows that the mass loss rate remains about 40.50% after 0.5 h at different temperatures. With the extension of time, the weight loss rate basically does not change. It can be determined that the complete decomposition of carbonate takes only 0.5 h. Figure 9 shows the XRD diffraction pattern of the calcined product after calcining at 900 °C for 0.5 h. It can be proved that the carbonate is completely decomposed and the phase CaO and MgO are produced.

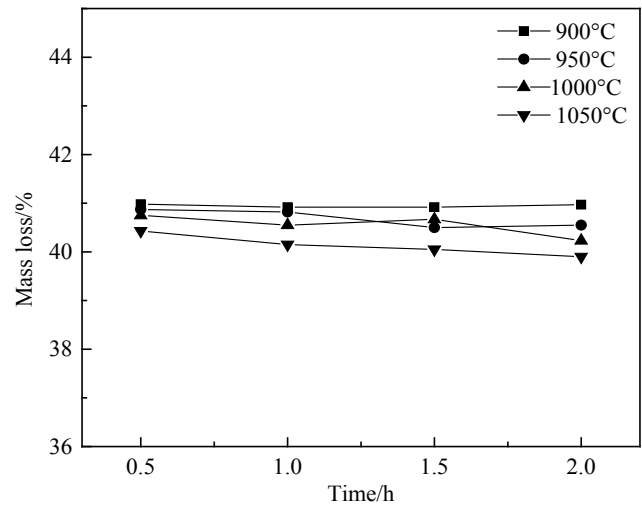


**Fig. 8** Effect of temperature and time on mass loss

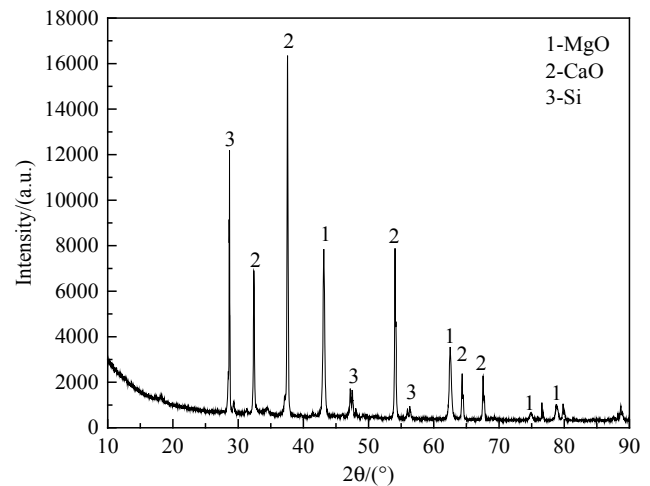


**Fig. 9** XRD pattern of products calcined at 900 °C for 0.5 h

Figure 10 shows that the calcination temperature has a significant effect on the activity of pellets. The higher the temperature, the lower the activity of pellets. The hydration activity of pellets at 900 °C is the highest, which is 20%. With the extension of calcination time, the change of pellet activity below 1000 °C is not obvious. With the extension of calcination time at 1050 °C, the activity decreases gradually. The intensity of diffraction peaks of calcined products at different temperatures is shown in Fig. 11. It can be seen that with the increase of temperature, the intensity of diffraction peaks of MgO and CaO decreases. The analysis shows that the crystal structure of the products is destroyed at high temperatures, thus affecting the activity of the products. Therefore, calcination at high temperatures will reduce the hydration activity of pellets. It can be seen from Fig. 12 that the compressive strength of pellets decreases with the

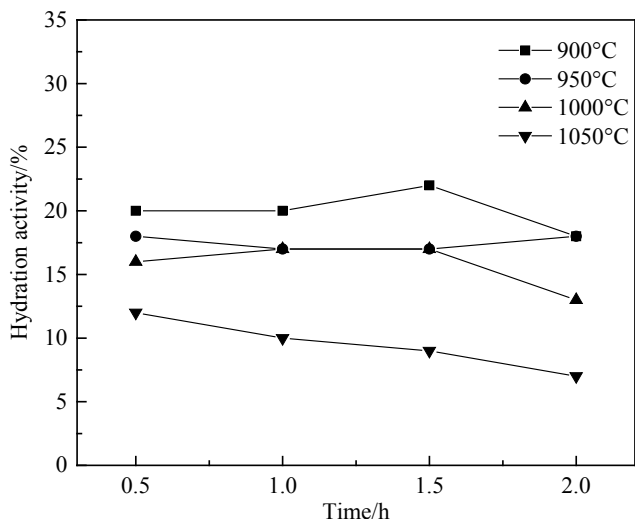


Fig. 10 Effect of temperature and time on hydration activity

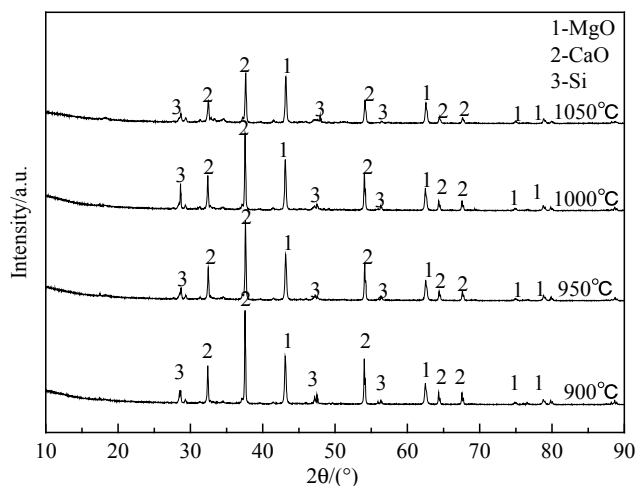


Fig. 11 XRD pattern of calcined products at different temperatures

increase of calcination temperature. The maximum compressive strength of pellets is 998 N at 900 °C. With the extension of calcination time, the compressive strength of pellets decreases slightly, and at the same temperature, the compressive strength of pellets calcined for 0.5 h is better.

The micromorphology of calcined products is analyzed as shown in Fig. 13. It can be seen from the figure that magnesite particles have been completely decomposed into MgO. The grain size of MgO is uniform and the boundary is clear. From 900 to 1050 °C, with the increase of calcination temperature, the MgO grains change from spherical to irregular shape, and then the grains gradually agglomerate together, resulting in cracks in the pellets. According to

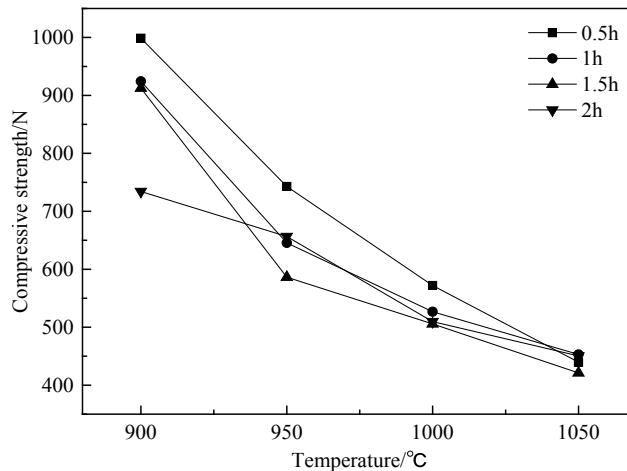


Fig. 12 Effects of temperature and time on the compressive strength of pellets

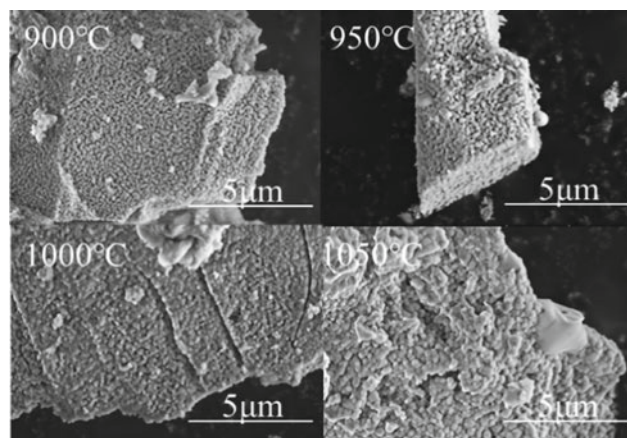


Fig. 13 SEM images of calcined products at different temperatures

relevant reports [23, 24], pseudocrystalline structure of magnesite is produced after calcination, which still maintains the original crystal structure of magnesite. With the increase of calcination temperature, the further agglomeration and growth of grains lead to the destruction of pseudocrystalline structure and the shrinkage of particle volume [25, 26]. In addition, with the time prolonging, the grains further agglomerate and grow, the pseudocrystalline structure is gradually broken, the volume of particles continues to shrink, resulting in the loosening of the whole pellet, and thus, the compressive strength of the pellets reduces.

Considering the above factors, when pellets with 15 MPa briquetting pressure were calcined at 900 °C for 0.5 h and then reduced at 1300 °C for 2 h in a reactor with flowing argon, the recovery of magnesium was over 80%.

## Conclusions

1. The mass loss rate and hydration activity of pellets were the highest at 15 MPa, 40.08%, and 23.0%, respectively. The compressive strength of pellets increased with the increase of briquetting pressure. The grain size of magnesite had no significant effect on the properties of pellets.
2. The hydration activity and compressive strength of pellets were affected by temperature. The hydration activity and compressive strength of pellets decreased with the increase of temperature. The hydration activity and compressive strength were the highest at 900 °C, which were 23% and 998 N, respectively.
3. When the briquetting pressure was 15 MPa, the calcination temperature was 900 °C and the calcination time was 0.5 h, and thus, the pellet performance was better.

**Acknowledgements** This work was supported by National Natural Science Foundation of China under Grants (51504058; U1508217; 51404054; 51374064), the Fundamental Research Funds for the Central Universities of China (N162504003, N140204013), the Fund of Liaoning S&T Project (201601003, LZ2014021).

## References

1. Kyunsuk Choi, Hanshin Choi, and Il. Sohn. Understanding the Magnesiothermic Reduction Mechanism of TiO<sub>2</sub> to Produce Ti. *Metallurgical and Materials Transactions B*, 2017. 48(2): 922–932.
2. Anil Kumar, Zacharah Elanjickal Chacko, Madurai Malathi, et al. Desulfurization of Hot Metal Through In Situ Generation of Magnesium in 30-kg Molten Iron Bath-Influence of Inert Gas Flow Rate. *Steel Research International*, 2014. 85(5): 927–934.
3. Partha Saha, Moni Kanchan Datta, Oleg I. Velikokhatnyi, et al. Rechargeable magnesium battery: Current status and key challenges for the future. *Progress in Materials Science*, 2014. 66: 1–86.
4. V.A. Yartys, M.V. Lototsky, E. Akiba, et al. Magnesium based materials for hydrogen based energy storage: Past, present and future. *International Journal of Hydrogen Energy*, 2019. 44(15): 7809–7859.
5. William J. Joost, Paul E. Krajewski. Towards magnesium alloys for high-volume automotive applications. *Scripta Materialia*, 2017. 128: 107–112.
6. Anil Kumar, Santosh Kumar, and N.K. Mukhopadhyay. Introduction to magnesium alloy processing technology and development of low-cost stir casting process for magnesium alloy and its composites. *Journal of Magnesium and Alloys*, 2018. 6(3): 245–254.
7. Mustafa Kemal Kulekci. Magnesium and its alloys applications in automotive industry. *The International Journal of Advanced Manufacturing Technology*, 2007. 39(9–10): 851–865.
8. Feng Gao, Zuo-ren Nie, Zhihong Wang, et al. Assessing environmental impact of magnesium production using Pidgeon process in China. *Transactions of Nonferrous Metals Society of China*, 2008. 18(3): 749–754.
9. Jindan Du, Weijian Han, Yinghong Peng. Life cycle greenhouse gases, energy and cost assessment of automobiles using magnesium from Chinese Pidgeon process. *Journal of Cleaner Production*, 2010. 18(2): 112–119.
10. Daxue Fu, Nai-xiang Feng, Yao-wu Wang, et al. Kinetics of extracting magnesium from mixture of calcined magnesite and calcined dolomite by vacuum aluminothermic reduction. *Transactions of Nonferrous Metals Society of China*, 2014. 24(3): 839–847.
11. Lan Hong, Keiji Okumura, Masamichi Sano. Nonisothermal gravimetric investigation on kinetics of reduction of magnesia by aluminum. *Metallurgical and Materials Transactions B*, 1998. 30B: 1999–2003.
12. Yaowu Wang, Naixiang Feng, Jing You, et al. Study on extracting aluminum hydroxide from reduction slag of magnesium smelting by vacuum aluminothermic reduction. *Light Metals 2011*, 2011: 205–209.
13. Boris A. Chubukov, Scott C. Rowe, Aaron W. Palumbo, et al. Investigation of continuous carbothermal reduction of magnesia by magnesium vapor condensation onto a moving bed of solid particles. *Powder Technology*, 2019: 2–11.
14. Geoffrey Brooks, Simon Trang, Peter Witt, M.N.H. Khan, Michael Nagle. *The Carbothermic Route to Magnesium*. JOM, 2006: 51–55.
15. Li Rongti, Pan Wei, Masamichi Sano. Kinetics and mechanism of carbothermic reduction of magnesia. *Metallurgical and Materials Transactions B-Process Metallurgy and Materials Processing Science*, 2003. 34(4): 433–437.
16. Leon H. Prentice, Nawshad Haque. Magsonic™ carbothermal technology compared with the electrolytic and Pidgeon Processes. *Magnesium Technology*, 2012: 37–41.
17. M. Abdellatif. Review of the development work on the Mintek thermal magnesium process(MTMP). *South Afr Inst Min Metall*, 2011. 111: 393–399.
18. Yaron Aviezer, Liat Birnhack, Avi Leon, et al. A new thermal-reduction-based approach for producing Mg from seawater. *Hydrometallurgy*, 2017. 169: 520–533.
19. Yuji Wada, Satoshi Fujii, Eiichi Suzuki, et al. Smelting Magnesium Metal using a Microwave Pidgeon Method. *Sci Rep*, 2017. 7: 1–7.
20. Daxue Fu, Ting'an Zhang, Zhihe Dou, et al. A new energy-efficient and environmentally friendly process to produce magnesium. *Canadian Metallurgical Quarterly*, 2017. 56(4): 418–425.
21. Ming Wen, Ting-an Zhang, Zhi-he Dou, et al. Research on new type materials preparation for magnesium production by Silicothermic process. *Magnesium Technology 2013*: 75–79.
22. Daxue Fu, Lukui Guan, Ming Wen, et al. Study on compressive strength of pellets for the novel silicothermic process. *Magnesium Technology*, 2015: 49–53.
23. Birchal V S S, Rocha S D F, Ciminelli V S T. The effect of magnesite calcination conditions on magnesia hydration. *Minerals Engineering*, 2000, 13(14): 1629–1633.
24. Turániová L, Paholič. G, Mateová. K. Stimulating the thermal decomposition of magnesite. *Thermochimica Acta*, 1996, 277: 75–84.
25. Kan-Sen Chou, Gee-Yang Tien, Wen-Long Wu. Particle Size Distributions in Calcined Powders. *Journal of the American Ceramic Society*, 1985, 68(5): 118–120.
26. Daxue Fu, Yaowu Wang, Jianping Peng, et al. Improvements of Mg-Extraction from Magnesite and Dolomite by Aluminothermic Reduction in Vacuum. *Journal of Vacuum Science and Technology*, 2014, 34(1): 60–67.

# Producing Pure Magnesium Through Silicothermic Under the Atmospheric Pressure

Fei Liu, Bo Yang, Bo-Yu Liu, Jiao Li, Zhi-Min Chang, and Zhi-Wei Shan

## Abstract

The majority of pure magnesium produced worldwide is made by using silicothermic method (Pidgeon process). However, the Pidgeon process suffers poor efficiency, low industrial concentration, and intermittent production. The main reason is that Pidgeon process requires to keep the reaction chamber in a vacuum state during the entire reduction process. By analyzing the thermodynamic reaction principle, we reveal that it is the low magnesium partial pressure instead of vacuum that is necessary for the silicothermic process. Based on this understanding, we develop a new technique that can produce pure magnesium under the atmospheric pressure by using silicothermic method. Flowing argon is used to carry away the magnesium vapor around the reactants, which reduces the local magnesium partial pressure. The magnesium production efficiency reaches 82.36% that is comparable to the widely used Pidgeon method, and high purity of magnesium with 99.97 wt% after melting is produced directly. The industrialized application of this exciting technique is expected to help the silicothermic to realize high efficiency, automated, and continuous production while at the same time completely change the poor production conditions, and reduce energy consumption and pollution.

## Keywords

Smelting • Silicothermic • Atmospheric pressure • Flowing argon

## Introduction

As the lightest structural metal, magnesium has promising applications in energy intensive sectors such as automobile and aerospace industry. China produces most of primary magnesium. In 2018, the amounts of primary magnesium produced by China were about 800,000 tons, which accounts for about 80% of the world's total production [1]. As the dominant process of primary magnesium production in China, Pidgeon process suffers several technical drawbacks, such as high labor intensity, low production efficiency, high energy consumption, and serious environmental pollution [2]. One of the most important origins of these problems is the fact that Pidgeon process requires vacuum, which makes the continuous and automated production very difficult. Once the terminal application markets of magnesium-based materials fully open, which will require a large amount of primary magnesium, such backward process will hamper the development of entire magnesium industry. Therefore, a new magnesium production process that can achieve continuous, automated and low pollution is pressingly needed. Recently, some efforts have been made to modify the reduction tank [3–5] and reducing agent [6–11] to improve the thermal reduction process. However, problems such as low efficiency, low automation, and high pollution are not fully solved because these modified processes still require vacuum. The method for the preparation of magnesium under inert gas proposed by J.R. Wynnycyk et al. is of great value in achieving efficient, automated, and continuous production [12–16]. However, this method has not been able to develop into an industrial production process for magnesium. Moreover, only limited number of studies attempted to investigate the kinetics of the reaction of individual pellet [17–19]. The current work mainly targets on the development of this new magnesium production process under atmospheric pressure.

F. Liu · B. Yang · B.-Y. Liu · J. Li · Z.-M. Chang · Z.-W. Shan (✉)

Engineering Research Center for Magnesium-Based New Materials, Center for Advancing Materials Performance from the Nanoscale (CAMP-Nano) & Hysitron Applied Research Center in China (HARCC), State Key Laboratory for Mechanical Behavior of Materials, Xi'an Jiaotong University, Xi'an, 710049, People's Republic of China  
e-mail: [zwshan@xjtu.edu.cn](mailto:zwshan@xjtu.edu.cn)



## Analyses of Reaction Principle Under Atmospheric Pressure

To reduce magnesium from magnesium oxide by silicon under atmospheric pressure, the temperature needs to exceed 2373 °C [20]. Such high temperature will dramatically increase the cost of heating devices and the materials of reduction tank. By introducing calcium oxide into the slag, the reaction temperature decreases to 1750 °C. Some efforts have to be made to produce primary magnesium under the atmospheric pressure at such applicable temperature [21–27]. However, such a method still suffers ultra-high energy consumption and cost. Most of these efforts stopped after China built large number of primary magnesium plants using the low cost Pidgeon process.

As for the formation of magnesium oxide with magnesium vapor, the standard Gibbs free energy change ( $\Delta G^\theta$ ) of the reaction between magnesium and oxygen is related to the pressure of vapor [20],

$$\Delta G_{\text{Real}}^\theta = \Delta G^\theta - RT \ln \frac{P_{\text{Mg}}}{P^\theta} \quad (1)$$

where  $\Delta G_{\text{Real}}^\theta$  is the real standard Gibbs free energy change ( $\Delta G^\theta$ ), and  $R$  is the gas constant equal to 8.314 J/(mol · K).  $T$  is the absolute temperature.

$\Delta G_{\text{Real}}^\theta$  is larger than  $\Delta G^\theta$  when magnesium partial pressure ( $P_{\text{Mg}}$ ) is lower than standard atmosphere ( $P^\theta$ ). That is to say, by reducing the magnesium partial pressure, the temperature of reaction can decrease effectively. That is why in vacuum the Pidgeon process can be proceeded even the temperature is 1200 °C, which is much lower than the 2373 °C mentioned above [28, 29]. Figure 1 shows the schematic diagram of magnesium partial pressure ( $P_{\text{Mg}}$ ) around the surface of reactants reduced by vacuum and flowing argon.  $P_{\text{Mg}}$  is reduced in vacuum mainly through the pressure gradient between reactants zone and condensation zone (the condensation zone is the place where magnesium crown forms, and this place is close to the vacuum pump).

Under flowing argon, magnesium atoms generated from pellets collide with argon atoms and move to condensation zone together with the flowing argon atoms. In the latter case, the  $P_{\text{Mg}}$  around reactants can also be significantly decreased.

## Methods

The raw materials used in our experiments, including calcined dolomite, ferrosilicon, and calcium fluoride, are provided by Fugu JingFu Coal Chemical Co. LTD (Yulin, Shaanxi Province, China). The chemical component in weight is 49.85% CaO, 30.67% MgO, 12.63% Si, 4.19% Fe, and 2.5% CaF<sub>2</sub>. The experiment of reduction is conducted in a vertical tube furnace with 700 mm heating zone and 500 mm uniform temperature zone, which can achieve temperature up to 1500 °C. The experimental setup is shown in Fig. 2a. A series of sealable graphite tubes with different length are placed inside the corundum tube. The flowing rates of argon are controlled by the flowmeter and reducing valve. Argon is heated to 1200 °C in the preheating zone and blew through the surface of reactants. High purity argon (99.99%) is used in all experiments. The air in the tube is pumped before experiment, and the pumping is stopped when heating started. The purity of collected pure magnesium is analyzed by arc spark optical emission spectroscopy (OES, GNR, S5).

One typical result is shown in Fig. 2b. Most of the produced magnesium vapor condensed on the condenser. The condensed products grow mainly in the form of dendrites, which shows fresh and reflective surface without obvious impurities and oxidation. A magnesium ingot was melt using these dendritic magnesium in an induction furnace with a high purity graphite crucible (>99.99%) under argon atmosphere. The surface of the magnesium ingot was polished by the lathe. The final product is shown in Fig. 2c.

Surprisingly, the magnesium produced by this method is very pure. Table 1 compares the purity and main impurities of industrial crude magnesium produced under vacuum and

**Fig. 1** Schematic diagram of how to reduce the magnesium partial pressure ( $P_{\text{Mg}}$ ) around the reactants. **a** Vacuum. **b** Flowing argon

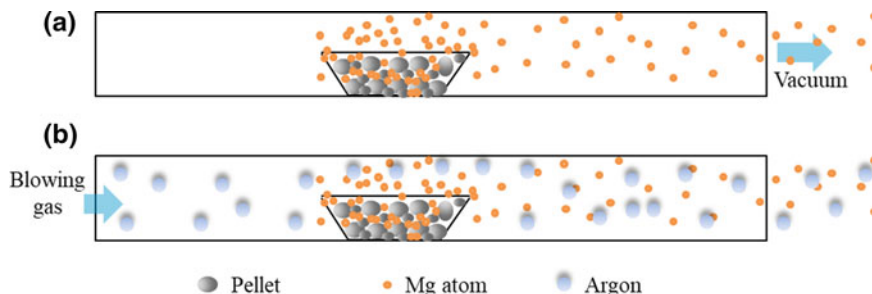


**Fig. 2** Experimental setup of magnesium reduction under atmospheric pressure with flowing argon and the collected pure magnesium. **a** Experimental setup. **b** Condensed magnesium dendrites on the condenser. **c** Magnesium ingot made by melting the magnesium dendrites

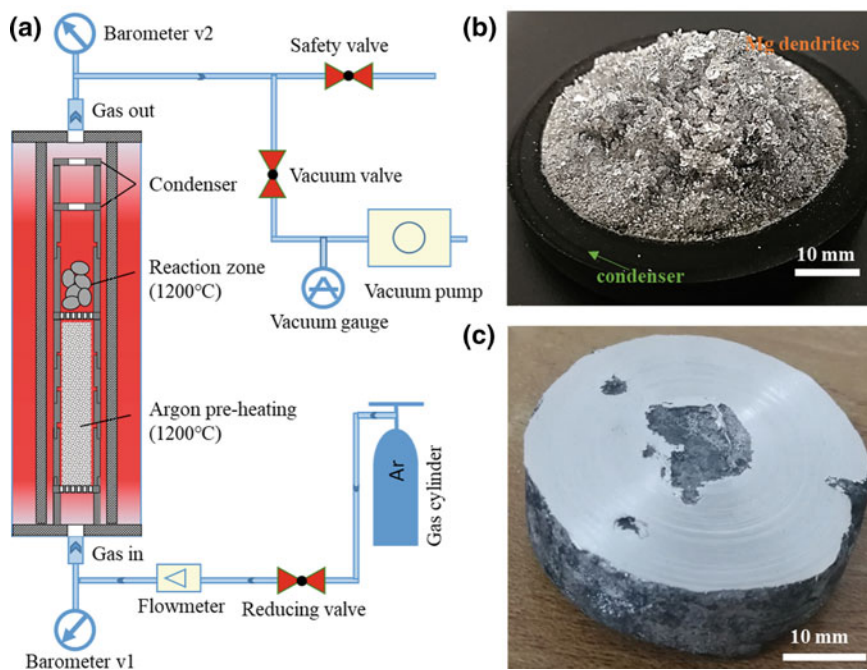


**Table 1** Chemical component of industrial crude magnesium and magnesium ingot made in this work

Purity (wt%)	Impurity element content (ppm)									
	Mg	Ca	Si	Mn	Al	Sn	Zn	Fe	Ni	Cu
Industrial	99.67	2122.54	114.12	219.67	819.07	6.84	15.83	30.84	<10	<5
Our study	99.97	85	87.75	22.75	40.75	9.25	15.5	<10	<10	<5

the ingot produced in this work. It can be seen that magnesium with higher purity of 99.97 wt% can be directly produced under atmospheric pressure. The contents of main impurities in our study like Ca, Mn, Si, Al, and Fe are much lower than that in industrial crude magnesium. Therefore, the production method developed in this work is expected to produce high purity magnesium.

We effectively achieved the heating of large flow rate of argon. By reacting at 1200 °C for 2 h, we achieved the reduction efficiency of 82.36%, which is comparable to the reduction efficiency in industry that uses Pidgeon method under vacuum. We also found that increasing argon flow rate could effectively enhance the reduction efficiency.

This new method for the production of pure magnesium using carrier gas is expected to solve the problems in conventional vacuum-based approach. Although such process will incur some additional costs due to the use of argon, it is

estimated that the industrialization of such process will reduce the overall cost by about 15–20% because this process can achieve large-scale and continuous production, and the argon can be recycled.

## Summary

Magnesium partial pressure is the key factor in silicothermic process and can be effectively decreased by vacuum or flowing argon. By conducting the silicothermic reduction under flowing argon at atmospheric pressure, we achieved the production efficiency of 82.36%, which is comparable to industrial efficiency under vacuum condition. And high purity of magnesium with 99.97 wt% was produced by the method developed in this work.

**Acknowledgements** This work was supported by the National Key Research and Development Program of China (No. 2017YFB0702001), National Natural Science Foundation of China (Nos. 51601141), China Postdoctoral Science Foundation (2016M600788), and funding from the Science and Technology Departments of Shaanxi and Xi'an, China (Nos. 2016KTZDGY-04-03, 2016KTZDGY-04-04 and 201805064ZD15CG48). We acknowledge Wei-Yin Zhang (Fugu JingFu Coal Chemical Co. LTD) for providing the raw materials. The authors declare no competing financial interests.

## References

1. E.L. Bray, Magnesium metal U.S. Geological Survey, 2019 Minerals Yearbook, 2019.
2. M. Halmann, A. Frei, A. Steinfeld, Magnesium Production by the Pidgeon Process Involving Dolomite Calcination and MgO Silicothermic Reduction: Thermodynamic and Environmental Analyses, *Industrial & Engineering Chemistry Research* 47(7) (2008) 2146–2154.
3. C. Zhang, C. Wang, S. Zhang, L. Guo, Experimental and Numerical Studies on a One-Step Method for the Production of Mg in the Silicothermic Reduction Process, *Industrial & Engineering Chemistry Research* 54(36) (2015) 8883–8892.
4. J. Deng, X. Wang, Experimental Research on the Inner Thermal Magnesium Reduction Process, *Materials Reports* 28(24) (2014) 81–179.
5. Z. Fan, X. Wang, Development of new shaft semi-continuous magnesium smelting furnace with internal electro-thermal process, *China Nonferrous Metallurgy* 4 (2012) 3.
6. R. Winand, M.v. Gysel, A. Fontana, L. Segers, Production of magnesium by vacuum carbothermic reduction of calcined dolomite, (1990).
7. L.H. Prentice, M.W. Nagle, T.R.D. Barton, S. Tassios, B.T. Kuan, P.J. Witt, K.K. Constanti-Carey, Carbothermal Production Of Magnesium: Csiro's Magsonic™ Process, *Magnesium Technology 2012* (2012).
8. D. Xia, Y. Shang, A new style magnesium reduction process deoxidizing by liquid calcium, *Light Metal* 2 (2008) 3.
9. J. Long, Y. Wang, N. Feng, Magnesium Production by Aluminothermic Reduction in Vacuum, *Journal of Vacuum Science and Technology* 32(4) (2013) 6.
10. W. HU, N. Feng, Y. Di, J. Peng, Study on vacuum thermal reduction of calcined dolomite with Al-Si-Fe alloy as reductant, *Vacuum* 47(5) (2010) 3.
11. H. Pei, B. Xu, Y. Li, B. Yang, Q. Yu, Study on the thermal decomposition behavior of magnesite in carbothermic reduction extraction process for magnesium in vacuum, *Light Metals* (1) (2010) 5.
12. J.R. Wynnycyk, E. Tackie, G. Chen, The Problem of Limited Recoveries in the Pidgeon Process for Magnesium Production, *Canadian Metallurgical Quarterly* 30(3) (1991) 139–143.
13. J.R. Wynnycyk, Production of magnesium metal, Canada, 1985.
14. S.K. Barua, J.R. Wynnycyk, Kinetics of the Silicothermic Reduction of Calcined Dolomite in Flowing Hydrogen, *Canadian Metallurgical Quarterly* 20(3) (1981) 295–306.
15. S.K. Barua, Silicothermic Reduction of Calcined Dolomite in Flowing Gases: Study of Physical Parameters of briquettes and Reaction Kinetics, 1979.
16. J.R. Wynnycyk, E.N. Tackie, Bench-scale investigation of magnesium winning, *Light Metals (Cham) (Light Metals (Warrendale, Pa.)), Springer International Publ., Minerals, Metals & Materials Society, 1988, pp. 807–815.*
17. W. Wulandari, G.A. Brooks, M.A. Rhamdhani, B.J. Monaghan, Kinetic analysis of silicothermic process under flowing argon atmosphere, *Canadian Metallurgical Quarterly* 53(1) (2013) 17–25.
18. W. Wulandari, G. Brooks, A. Rhamdhani, B.J. Monaghan, Kinetics of silicothermic reduction of calcined dolomite in flowing argon atmosphere, *Faculty of Engineering - Papers*, 2010.
19. K.A.E. Barawy, I.M. Morsi, M.B. Morsi and S.R. Abdel-Gawad, Silicothermic Reduction of Dolomite Ore under Inert Atmosphere, *Canadian Metallurgical Quarterly* 41, No. 1 (2002) 15–28.
20. O. Kubaschewski, E.L. Evans, C.B. Alcock, *Metallurgical thermochemistry*, Pergamon Press 1967.
21. C. Faure, J. Marchal, Magnesium by the Magnetherm Process, 1964.
22. M. Abdellatif, Pilot Plant Demonstration Of The Mintek Thermal Magnesium Process, (2006).
23. M. Abdellatif, Mintek Thermal Magnesium Process (MTMP): Theoretical and Operational Aspects, 2006.
24. M. Abdellatif, Refining Testwork on Crude Magnesium Produced in the Mintek Thermal Magnesium Process, 2006.
25. R.T. Jones, T.R. Curr, *Pyrometallurgy at Mintek, Southern African Pyrometallurgy* (2006).
26. A. Schoukens, M. Abdellatif, M. Freeman, Technological Breakthrough of the Mintek Thermal Magnesium Process, 2006.
27. M. Abdellatif, Mintek Thermal Magnesium Process: Status and Prospective, 2008.
28. L.M. Pidgeon, J. M. Toguri, High-temperature studies of metallurgical processes Part I. The Thermal reduction of Magnesium Oxide with Silicon, *Canadian Journal of Chemistry* 39 (1961).
29. L.M. Pidgeon, J. M. Toguri, High-Temperature Studies of Metallurgical Processes Part II. The Thermal Reduction of Calcined Dolomite With Silicon, *Canadian Journal of Chemistry* 40 (1962).

# Effect of Temperature on Magnesium Vapor Condensation in Inert Carrier Gas

Jibiao Han, Ting'an Zhang, Daxue Fu, Junhua Guo, Zonghui Ji, and Zhihe Dou

## Abstract

The process of magnesium extraction by silicothermic process is in vacuum, which leads to discontinuous production. The condensation of magnesium vapor in inert gas is an important step to realize continuous magnesium production. In this paper, the condensation behavior of magnesium vapor in inert carrier gas is studied. The effects of temperatures on the condensation phenomenon, temperature in condensation zone, direct recovery rate of condensation, and microstructure of magnesium vapor were investigated. The results show that three different condensation appearance can be obtained by magnesium condensation in argon gas conditions, and the size has significant difference, and large particles of condensed magnesium are more than 500  $\mu\text{m}$ , small particles of magnesium from 50 to 100  $\mu\text{m}$  and powdered magnesium less than 10  $\mu\text{m}$ . With the increase of temperature, the initial condensation temperature of magnesium vapor increases from 680.2 to 745.1  $^{\circ}\text{C}$ , small particles of magnesium increases, while the powdered magnesium keeps constant; the direct recovery rate of large particles of magnesium decreases from 27.1 to 15.4%, and the direct recovery rate of condensed magnesium of small particles increases; higher purity of magnesium can be obtained at different temperatures, which can provide theoretical support for continuous magnesium production process.

## Keywords

Magnesium vapor • Inert gas • Initial condensation temperature • Condensation microstructure

## Introduction

As the lightest structural material in industrial applications [1, 2], magnesium is widely used in metallurgy, mechanical manufacturing, aerospace, and other fields [3]. The energy consumption and pollution have been reduced with the continuous development of magnesium production by silicothermic process [4], but it still belongs to high energy consumption metallurgical process [5]; the continuous process cannot be achieved because of the existence of vacuum.

Therefore, the new technologies and processes was put forward for the existing problems in magnesium production by experts and scholars. The kinetics of magnesium reduction by silicothermic process was studied by Fu [6–9] et al.; a new process by prefabricated pellet silicothermic process was put forward, which shortened the period of magnesium production. Tian [10–13] collected magnesium powder by carbothermal reduction at 1280  $^{\circ}\text{C}$  and found that magnesium reacted inversely with CO to form magnesium oxide. The nucleation and growth process of magnesium vapor under vacuum conditions was described by Yang [14, 15], and the effects of condensation temperature, temperature gradient, and saturated vapor pressure on the morphology of magnesium crystals were explained. Xiong [16, 17] continued to study the condensation behavior and obtained the volatilization and condensation rules of pure magnesium under vacuum conditions. The Australian CSIRO Research Institute [18] uses supersonic gas injection to rapidly cool magnesium vapor to obtain condensed magnesium powder which is not easy to explode. Other experts and scholars have studied the collection of magnesium vapor condensation [19], which provides ideas for the continuous production of magnesium extracting.

All the above studies are based on vacuum conditions. In order to achieve continuous production, magnesium vapor condensation needs to be carried out in non-vacuum conditions. So the condensation behavior of magnesium vapor in argon carrier was studied using metal magnesium as raw material in this paper. The effects of temperature in constant

J. Han · T. Zhang (✉) · D. Fu · J. Guo · Z. Ji · Z. Dou  
Key Laboratory of Ecological Metallurgy of Multi-Metal  
Intergrown Ores of Ministry of Education, Special Metallurgy and  
Process Engineering Institute, Northeastern University, Shenyang,  
110819, Liaoning, China  
e-mail: zta2000@163.net



temperature zone of magnesium vapor on initial condensation temperature, direct recovery rate, and condensation microstructure were studied experimentally in order to understand the condensation law of magnesium vapor and provide a condensation method for continuous production of magnesium.

## Experiment

### Experimental Materials

Condensation experiments of pure magnesium (99.9%) were carried out to obtain the condensation law of magnesium vapor.

### Experimental Method

Measure the furnace temperature before placing the sample. The 15 g ( $\pm 0.5$  g) magnesium ingot was put into the tube furnace (in a corundum crucible) and volatilized for 2 h at 1000–1200 °C. The experimental device is shown in Fig. 1.

Pure argon (99.99%) was continuously flowed into the tube at a flow rate of 0.2 m<sup>3</sup>/h, and the magnesium vapor was fully mixed with argon and then moved to a

low-temperature zone for condensation. Graphite paper (0.2 mm thick) is lined inside the tube to collect magnesium vapor condensation products, and the condensation diagram is shown in Fig. 2.

The center position of the tube furnace is 0 cm, which is the raw material placement position (that is the central position of the furnace which is the initial temperature position of the furnace temperature measurement). Magnesium vapor condenses at different positions after volatilization in argon gas flow. Large particles condense at  $T_1$ – $T_2$ , small particles condense at  $T_2$ – $T_3$ , and powder condense after  $T_3$  (the condensation temperature changes with different conditions). After collection, the condensate was weighed and characterized by XRD and SEM.

The formula for calculating the percentage of condensation mass is as follows:

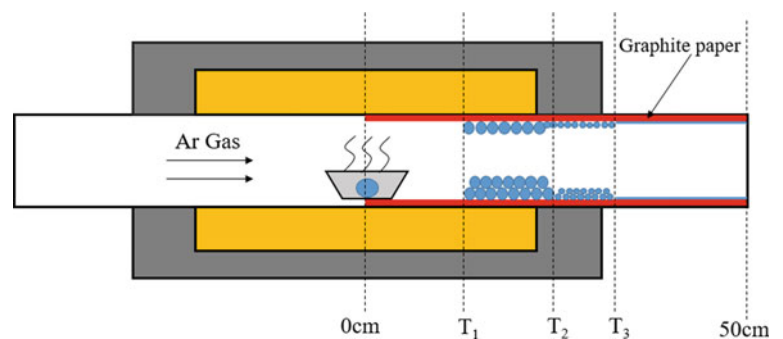
$$w_i = \frac{m_i}{m_t} \quad (1)$$

- $w_i$  represents the mass fraction of magnesium vapor condensation in different regions,
- $m_i$  represents the mass of magnesium vapor condensation products in different regions, and
- $m_t$  represents the total mass of magnesium.

**Fig. 1** Tube furnace experimental device



**Fig. 2** Schematic diagram of magnesium vapor condensation



## Results and Discussion

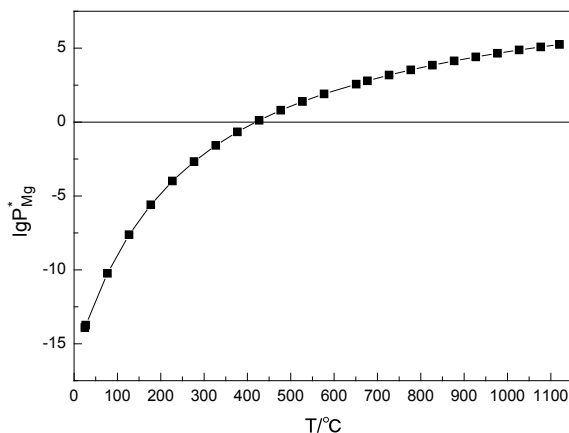
### Description of Experimental Principle and Phenomena

According to Eqs. 2 and 3 [20], the relationship between saturated vapor pressure and temperature can be obtained in Fig. 3 which shows that when the temperature decreases, the saturated vapor pressure of magnesium vapor decreases gradually. When the actual partial pressure of magnesium vapor is greater than the saturated vapor pressure, the magnesium vapor begins to condense.

$$\lg P(\text{Pa}) = 14.92 - \frac{7550}{T} - 1.41 \lg T(298-924 \text{ K}) \quad (2)$$

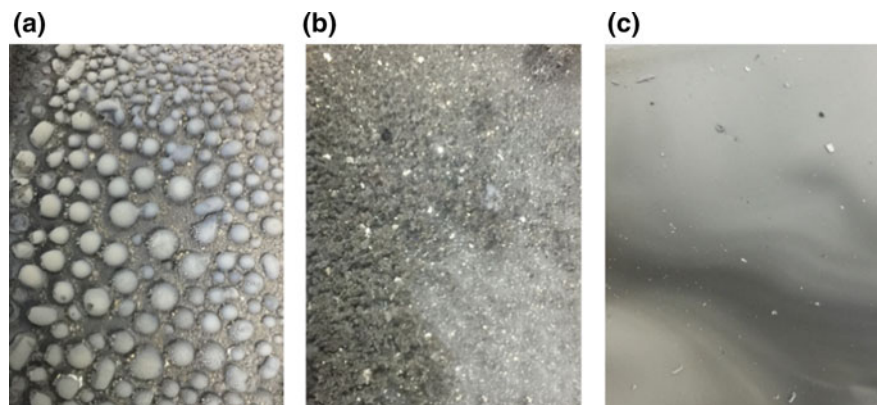
$$\lg P(\text{Pa}) = 13.54 - \frac{7780}{T} - 0.86 \lg T(924-1393 \text{ K}) \quad (3)$$

Different forms of condensation products appear during the evaporation condensation process of magnesium vapor



**Fig. 3** Relationship between saturated vapor pressure and temperature

**Fig. 4** Condensation of magnesium vapor in different regions



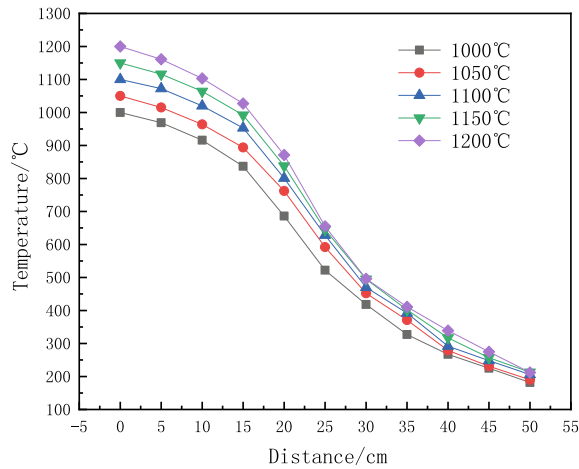
in argon at 1000–1200 °C. The phenomenon of condensation products at 1100 °C is shown in Fig. 4.

Figure 4a is Mg vapor condensation in  $T_1-T_2$  region, which is droplet condensation with large particles; 4 (b) is small particle condensation in  $T_2-T_3$ ; and 4 (c) is powder condensation after  $T_3$ . As can be seen from the figure, with the decrease of temperature in the condensation zone, the particle size of magnesium vapor decreases, from large droplets to small particles, and finally to powder. The reason is that the magnesium vapor moves far from the furnace center, the temperature decreases, and the magnesium vapor condenses. As the magnesium vapor continues to move, the condensation process reduces the partial pressure of magnesium vapor, the lower partial pressure leads to the direct conversion of magnesium vapor into powdered magnesium without liquefaction, so the magnesium particles size decrease gradually, which shown in Fig. 4.

### Effect of Temperature in Constant Temperature Zone on Condensation Temperature of Condensation Products at Different Positions

Temperature is the main factor affecting the condensation of magnesium vapor, so the effect of temperature in constant temperature zone (1000–1200 °C) on the condensation behavior of magnesium vapor was studied experimentally. 0 cm is the central position of the furnace, and the corresponding data are the central temperature of the furnace. The temperature distribution of the tube furnace was measured which is shown in Fig. 5. The purpose of temperature measurement is to obtain the condensation temperature of magnesium vapor in different regions after obtaining the condensation products of magnesium vapor. As the distance increases, the temperature decreases.

The initial temperature of magnesium vapor condensation varies with the temperature distribution of furnace and the temperature in constant temperature zone. Figure 6 shows



**Fig. 5** Relationship between furnace temperature distribution and distance

the variation of Mg initial temperature at different condensation zones. With the increase of temperature in constant temperature zone, the initial condensation temperature of large and small particles of condensed magnesium increases, from 680.2 °C to 745.1 °C and 599.7 °C to 659.5 °C, respectively; the initial condensation temperature of powdered condensed magnesium is maintained between 495 and 508 °C; although there is an increasing trend, it remains basically unchanged. This is because the volatilization rate of magnesium vapor increases with the increase of temperature in constant temperature zone, and the partial pressure of magnesium vapor increases at the constant flow rate of argon; after the two stages of condensation, the vapor pressure is very low, so  $T_3$  basically remains unchanged. When the temperature change in the constant temperature zone is from 1000 to 1200 °C, the initial condensation

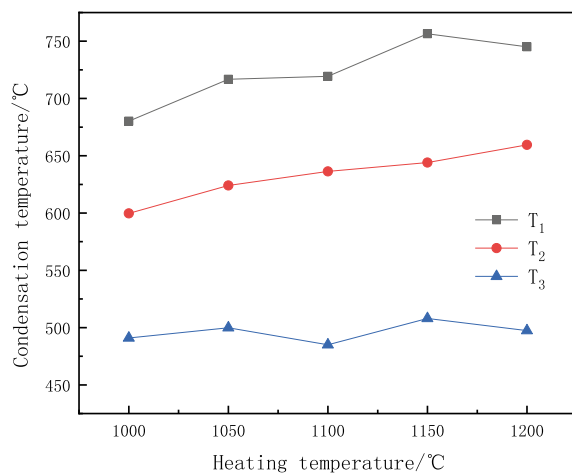


**Fig. 6** Relationship between initial temperature of magnesium vapor condensation in different regions and temperature in constant temperature zone

temperature of large and small particles of condensed magnesium rises 64.9 and 59.8 °C, respectively. From the relationship between saturated vapor pressure and temperature and three-phase diagram [21] of metal magnesium, it can be seen that the condensation temperature increases with the increase of saturated vapor pressure. When the vapor pressure is higher than the saturated vapor pressure, the magnesium vapor condenses. Therefore, the vapor pressure of magnesium vapor is the key factor affecting the condensation temperature, and the temperature in the constant temperature zone plays an important role in changing the vapor pressure of magnesium vapor.

### Effect of Temperature in Constant Temperature Zone on the Direct Recovery Rate of Different Forms of Condensation Products

The change of temperature in the constant temperature zone not only affects the initial condensation temperature of magnesium vapor, but also affects the condensation direct recovery rate of magnesium vapor. The relationship between temperature and condensation direct recovery rate of magnesium vapor in different regions is shown in Fig. 7.

Some of the magnesium vapor is taken out of the furnace because of the condensation is in the carrier gas flow process; therefore, with the increase of temperature, the total recovery rate of magnesium is 60–67%. Magnesium vapor pressure increases at high temperature, which makes it easier to condense. With the increase of temperature, the direct recovery rate of large particles of condensed magnesium decreases from 27.1 to 15.4%, when the temperature is 1000 °C and does not reach the boiling point of magnesium, the direct recovery rate is low, the volatilization is slow, and

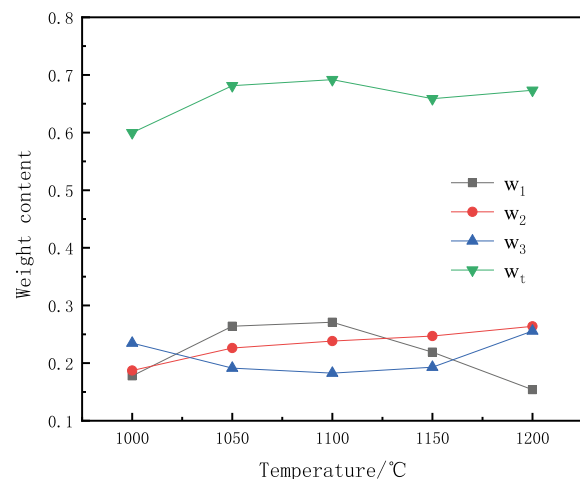


**Fig. 7** Relationship between temperature and condensation direct recovery rate of magnesium vapor in different regions

the vapor pressure is low, so it is difficult to condensate at a constant temperature. However, the direct recovery rate of large particles of condensed magnesium decreases with the increase of temperature due to the re-evaporation of magnesium after condensation. The direct recovery rate of condensed magnesium from small particles increased from 18.7 to 26.4%.

### Microstructure and Composition of Condensation Products

Figure 8 shows the microstructure and composition of magnesium vapor condensation in different regions in the flow rate of 0.2 m<sup>3</sup>/h argon at 1100 °C.

Figure 8a shows large particles of condensed magnesium with a particle size of more than 500 μm; most of them are spherical or hemispherical. Figure 8b shows a small particles of condensed magnesium with a particle size ranging from 50 to 100 μm; most of the particles are massive structure. In Fig. 8c, the particle size of powdered condensed magnesium is less than 10 μm. This figure proves that magnesium vapor with different temperatures in condensation temperature zone can collect different microstructure of magnesium. From EDS images, the purity of magnesium is higher and not oxidized. The reason for the existence of carbon element is that the magnesium metal is collected by condensation on graphite paper.

As shown in Fig. 9, X-ray diffraction analysis of three regions of large particles of condensed Mg (1), small particles of condensed Mg (2) and powder of Mg (3) at 1100 °C,

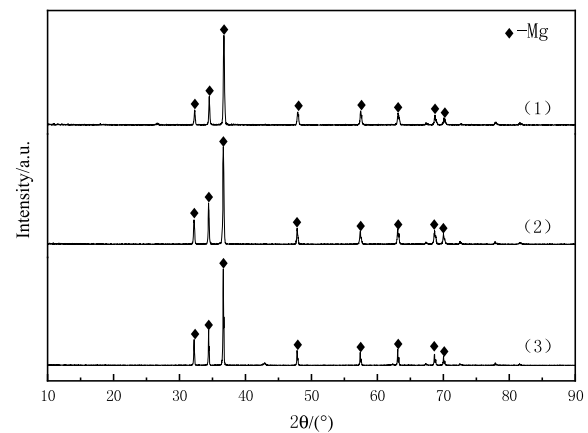


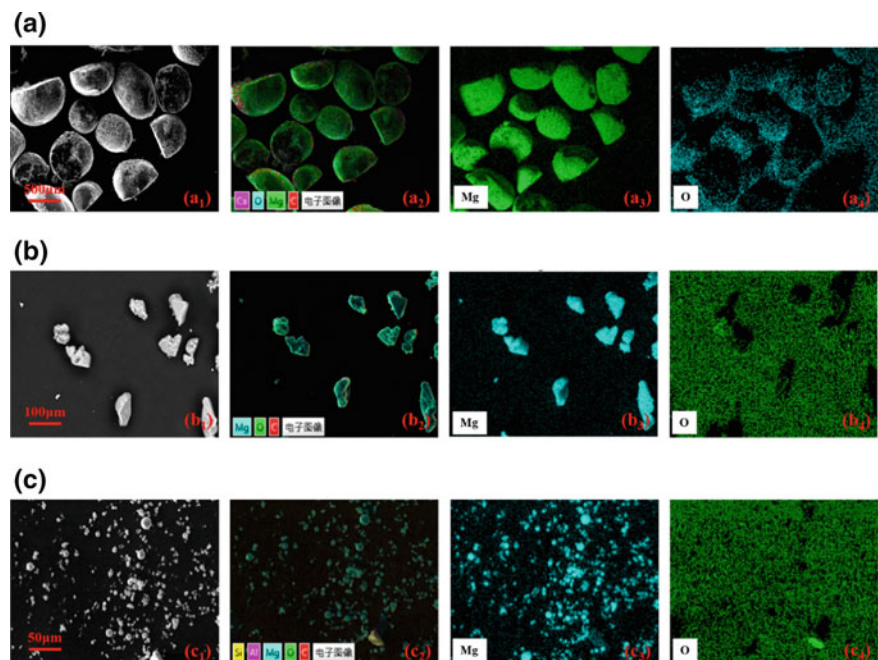
Fig. 9 XRD analysis of condensation products in different condensation regions

the XRD diffraction peak corresponds to the characteristic peak of magnesium, which indicates that the product is pure magnesium and has good crystallization. Therefore, magnesium collected by condensation has high purity and is not oxidized in inert gas.

### Conclusions

The condensation behavior of magnesium vapor was studied in inert gas at 1000–1200 °C. The effect of temperature in different constant temperature zone on condensation temperature and condensation direct recovery rate was analyzed, and the microstructure and composition of condensation products were obtained. The conclusions are as follows:

Fig. 8 Microstructure and composition of magnesium vapor condensation in different condensation regions





- (1) With the increase of the temperature in the constant temperature zone, the initial condensation temperature of large particles of magnesium increases from 680.2 to 745.1 °C and that of small particles of magnesium from 599.7 to 659.5 °C, while the powdered magnesium is kept between 485 and 508 °C, with little change.
- (2) With the increase of temperature, the direct recovery rate of magnesium and small particles of magnesium increases, while the direct recovery rate of large particles of magnesium decreases, and the powdered magnesium changes accordingly.
- (3) Three different microstructures of magnesium were obtained after magnesium condensation in argon gas flow; the results show that large particles of condensed magnesium are more than 500 μm, small particles of magnesium from 50 to 100 μm, and powdered magnesium less than 10 μm.
- (4) The microstructure and composition analysis showed that the condensed magnesium obtained by this method was not oxidized and has high purity, which can provide support for continuous magnesium production process.

**Acknowledgements** This work was supported by National Natural Science Foundation of China under Grants (51504058; U1508217; 51404054; 51374064), the Fundamental Research Funds for the Central Universities of China (N162504003, N140204013), and the Fund of Liaoning S&T Project (201601003, LZ2014021).

## References

1. Hanco G, Antrekowitsch H, Ebner P (2002) Recycling automotive magnesium scrap. *JOM* 54(2): 51–54.
2. Li R, Pan W, Sano M, et al. (2002) Kinetics of reduction of magnesia with carbon. *Thermochimica Acta* 390(1):145–151.
3. Zhu Z, Zhang L. W, Sen-Dong G. U (2012) Stress relaxation test of Hastelloy C-276 alloy and its creep constitutive equation. *Chinese Journal of Nonferrous Metals* 22(4):1063–1067.
4. Chao W, Chao Z, Shao J. Z, et al. (2015) The Effect of CaF<sub>2</sub> on the Magnesium Production with Silicothermal Process. *International Journal of Mineral Processing* 142.
5. Wada Y, Fujii S, Suzuki E, et al. (2017) Smelting Magnesium Metal using a Microwave Pidgeon Method. *Scientific Reports* 7:46512.
6. Fu D. X, Feng N. X, Wang Y. W (2012) Study on the Kinetics and Mechanism of Grain Growth during the Thermal Decomposition of Magnesite. *Bulletin of the Korean Chemical Society* 33 (8):2483–2488.
7. Fu D. X, Wang Y. W, Peng J. P, et al. (2014) Mechanism of extracting magnesium from mixture of calcined magnesite and calcined dolomite by vacuum aluminothermic reduction. *Transactions of Nonferrous Metals Society of China* 24(8):2677–2686.
8. Fu D. X, Zhang T. A, Guan L. K, et al. (2016) Magnesium Production by Silicothermal Reduction of Dolime in Pre-prepared Dolomite Pellets. *JOM* 68(12):3208–3213.
9. Fu D. X, Feng N. X, Wang Y. W, et al. (2014) Kinetics of extracting magnesium from mixture of calcined magnesite and calcined dolomite by vacuum aluminothermic reduction. *Transactions of Nonferrous Metals Society of China* 24(3):839–847.
10. Tian Y, Xu B. Q, Yang C. B, et al. (2014) Analysis of Magnesia Carbothermic Reduction Process in Vacuum. *Metallurgical & Materials Transactions B* 45(5):1936–1941.
11. Tian Y, Tao Q, Yang B, et al. (2012) Behavior Analysis of CaF<sub>2</sub> in Magnesia Carbothermic Reduction Process in Vacuum. *Metallurgical & Materials Transactions B* 43(3):657–661.
12. Liu H, Tian Y, Yang B, et al. (2015) Condensation of Mg-vapor in vacuum carbothermic reduction of magnesia. *Journal of Vacuum Science and Technology* 35(7):867–871.
13. Tian Y, Xu B. Q, Yang C. B, et al. (2016) Study on mechanism of magnesia production by reversion reaction process in vacuum, Paper presented at the 145th TMS Annual Meeting, Nashville, TN, 14–18 February 14 2016.
14. Yang C. B, Yang T, Tao Q. U, et al. (2014) Magnesium vapor nucleation in phase transitions and condensation under vacuum conditions. *Transactions of Nonferrous Metals Society of China* 24 (2):561–569.
15. Yang C. B, Tian Y, Qu T, et al. (2014) Analysis of the behavior of magnesium and CO vapor in the carbothermic reduction of magnesia in a vacuum. *Journal of Magnesium and Alloys* 2 (1):50–58.
16. Xiong N, Tian Y, Yang B, et al. (2018) Volatilization and condensation behaviours of Mg under vacuum. *Vacuum* 156:463–468.
17. Xiong N, Tian Y, Yang B, et al. (2019) Results of recent investigations of magnesia carbothermal reduction in vacuum. *Vacuum* 160:213–225.
18. Brooks G, Trang S, Witt P, et al. (2006) The carbothermic route to magnesium. *JOM* 58(5):51–55.
19. Bin G. Y, Wang Y, Wang S. Y, et al. (2015) Effect of Argon Flow Rate on the Condensation of Magnesium Vapor from Carbothermic Reduction of Magnesia. *Magnesium Technology*:61–65.
20. Dai Y. N, Yang B (2000) *The vacuum metallurgy of nonferrous metals*. Metallurgical Industry Press, Beijing.
21. Minevich E, Moayed A, Wacksman J, et al. (1956) *Principles of physical metallurgy*. D.VAN nostrand company, New York.

---

**Part VIII**

**Fundamentals, Mechanical Behavior, Twinning,  
Plasticity, and Texture II**

# Mapping Anisotropy and Triaxiality Effects in Magnesium Alloys

Padmeya P. Indurkar, Shahmeer Baweja, Robert Perez, Amol Vuppuluri, and Shailendra P. Joshi

## Abstract

Microstructure, material properties, and macroscopic stress state closely interact in determining the strength and fracture resistance of ductile metals. While a fair understanding of the microstructure-stress interaction on strength, deformation stability, and damage has been achieved for common engineering alloys, the same is not true for magnesium (Mg) alloys. A fundamental understanding of how the net plastic anisotropy influences the macroscopic load-deformation characteristics and deformation stability will potentially aid the development of high-performance Mg alloys. A concerted multi-scale computational effort is essential in providing a deeper understanding of the deformation micromechanics of Mg alloys. In this paper, we investigate the microstructure-property linkages under tensile and compressive loading states through high-fidelity crystal plasticity modeling and simulation. Extended investigations along this path should enable the development of guidelines for damage-tolerant design of Mg alloys.

## Keywords

HCP materials • Texture • Statistical response • Crystal plasticity • Plastic anisotropy

## Introduction

Magnesium (Mg) alloys are promising candidates as light-weight structural metals owing to their high power-to-weight ratio. However, its low symmetry hexagonal close packed (HCP) crystal induces complex plastic behavior, which may have implications on the macroscopic properties such as ductility and formability. Although the HCP crystal structure hosts a large number of slip systems, it often suffers from the deficiency in the number of slip modes for general plastic straining by slip from the viewpoint of the von Mises criterion. This paucity of slip deformation is negotiated by the occurrence of deformation twinning. Moreover, the slip and twin modes vary significantly, both in their critical strengths and hardening behaviors, and exhibit complex interactions with each other resulting in intrinsic plastic anisotropy and tension-compression asymmetry at the single crystal scale. Notably, the anisotropic and asymmetric behaviors are pervasive even in polycrystals, particularly in highly textured microstructures.

Understanding the interaction between intrinsic and induced plastic anisotropy, texture, damage, and stress state are important to enable designing strong, fracture-resistant Mg alloys [1–8]. Recent work has focused on textural effects in the response of notched single crystal and polycrystalline specimens under tensile loading [3, 5]. Similar studies under compressive loading states are lacking.

In this work, we interrogate the role of plastic anisotropy—intrinsic and textural on the material response of Mg alloys. In particular, we simulate polycrystalline aggregate representative volume elements (RVEs) with synthetic textures that mimic experimental rolling textures and investigate their behaviors under tensile and compressive states. In doing so, the RVE explicitly resolves individual grains, and the plasticity within each grain is modeled using a three-dimensional crystal plasticity framework [9]. Our primary interest here is to understand the structure-property linkages of *damage-free* Mg alloys. To that end, we extract

P. P. Indurkar  
Department of Mechanical Engineering, National University of Singapore, Singapore, 117575, Singapore

P. P. Indurkar · S. Baweja · R. Perez · A. Vuppuluri · S. P. Joshi (✉)  
Department of Mechanical Engineering, University of Houston, Houston, TX 77204-4006, USA  
e-mail: [shailendra@uh.edu](mailto:shailendra@uh.edu)

the statistical aspects of yield and hardening behaviors, macroscopic deformation anisotropy, and textural evolution. The stochastic macroscopic behaviors are related to the relevant microscale deformation mechanisms. We analyze these behaviors for two levels of intrinsic (defined at the level of a single crystal) plastic anisotropy—one with a high anisotropy (representing pure Mg) and the other with a relatively lower intrinsic anisotropy (e.g. AZ31).

## Model Formulation

### Polycrystalline Aggregate FEM Model

Three-dimensional Voronoi tessellations of a cubic domain are generated using the Tessellation module ( $-T$ ) in NEPER [10]. The cubic domain of dimension  $L_0$  comprises  $N_g$  grains. Figure 1 shows the polycrystal representative volume element (RVE) with  $N_g = 300$ . The tessellation is kept fixed to mitigate any second-order effects arising from topological deviations. The RVE is meshed using meshing module ( $-M$ ) in NEPER with nearly 84,000 fully integrated tetrahedral finite elements with each grain comprising about 279 finite elements. Such a fine finite element discretization is deemed sufficient based on our recent study [5]. The discretized RVE is exported to ABAQUS/STANDARD<sup>®</sup>, which embeds textural information described in the following paragraph.

Individual grains within the RVE are characterized by distinct crystallographic labels, which are essentially the sets of Euler angles (Fig. 1)  $[E] = [\bar{\varphi}_1 \pm \varphi_1^s, \bar{\Phi} \pm \Phi^s, \bar{\varphi}_2 \pm \varphi_2^s]$ . Each Euler angle is assumed to follow a normal distribution with mean values  $[\bar{\varphi}_1, \bar{\Phi}, \bar{\varphi}_2]$  and standard deviations  $\varphi_1^s, \Phi^s, \varphi_2^s$ . Focusing on rolled sheet materials [1], the texture is assigned as follows: First, each grain  $g$  within the RVE is initialized as a single crystal with its principal crystal axes,  $[1\bar{2}10], [10\bar{1}0]$  and  $[0001]$ , respectively, aligned with the sheet axes—rolling (L), transverse (T), and the short-transverse (S) directions. Next, setting  $\bar{\varphi}_1 = \bar{\Phi} = \bar{\varphi}_2 = 0$ , we randomly<sup>1</sup> pick three Euler angles  $[E^g = \varphi_1^g, \Phi^g, \varphi_2^g]$  from their respective normal distributions that are bounded by  $\pm 3\varphi_1^s, \pm 3\Phi^s, \pm 3\varphi_2^s$  (Table 1). Next, a rotation matrix resulting from  $[E^g]$  is applied to the initial aligned crystal axes to align it with respect to the sheet axes (L-T-S). A second rotation matrix is used to map the L-T-S triad with the global  $x$ - $y$ - $z$  triad (loading frame) such that the L-direction is aligned with the  $y$ -axis, which is the global loading direction. All the Euler angle sets  $[E^g]$  are accounted for with this additional rotation to achieve the textured crystal geometry aligned along loading direction.

A nominal strain rate ( $\dot{\epsilon}^{\text{app}} = 1 \times 10^{-3} \text{s}^{-1}$ ) is applied along  $y$ -direction. To ensure a uniaxial stress state,  $\dot{\epsilon}^{\text{app}}$  is applied at the mid-node of the RVE top-face, while the bottom-face is restricted from translating along the  $y$ -direction thereby also arresting RVE rigid rotations about the  $x$ - and  $z$ -directions. Similarly, the left-face is restricted from translating along  $x$ -direction thereby also arresting rigid rotations about  $y$ -axis. Intersection node of front, left, and bottom faces is pinned to avoid translation along  $z$ . Hence, the RVE deforms longitudinally through top-face (along  $y$ -axis) and laterally through right and back faces (along the  $x$ - and  $z$ -directions, respectively). The macroscopic stress state generated in the RVE is  $\Sigma = \Sigma_{yy}(\mathbf{e}_y \otimes \mathbf{e}_y)$ , where  $\mathbf{e}_y$  is the unit vector in the  $y$ -direction. The macroscopic logarithmic state of strain generated by this stress state is  $\mathbf{E} = E_{xx}(\mathbf{e}_x \otimes \mathbf{e}_x) + E_{yy}(\mathbf{e}_y \otimes \mathbf{e}_y) + E_{zz}(\mathbf{e}_z \otimes \mathbf{e}_z)$  where  $E_{xx} = \ln(L_x/L_0)$ ,  $E_{yy} = \ln(L_y/L_0)$ , and  $E_{zz} = \ln(L_z/L_0)$ . The Lankford ratio is calculated as  $R_L = E_{TT}/E_{SS} = E_{xx}/E_{zz}$ . Finally, the von Mises equivalent stress is  $\Sigma_{\text{eq}} = \sqrt{(3/2)\Sigma':\Sigma'} = |\Sigma_{yy}|$ , and the corresponding effective strain is  $E_{\text{eq}} = \sqrt{(2/3)\mathbf{E}':\mathbf{E}'}$  where  $\Sigma'$  are the deviatoric stresses and  $\mathbf{E}'$  are the corresponding deviatoric strains.

### HCP Crystal Plasticity

The constitutive material considered here comprises 18 slip systems and 12 twin systems (Table 2), and a finite strain rate-dependent viscoplastic flow rule is employed for each of these plasticity modes using rate-tangent method, followed with twinning/spin-induced lattice reorientation. A detailed algorithmic description of this scheme and its FE implementation can be found in [9]. Two sets of material parameters are considered. In Table 3, one set of parameters is representative of 99.97% pure Mg; the corresponding set of parameters in the parentheses is representative of an Mg alloy (AZ31B) [3, 5].

## Results and Discussion

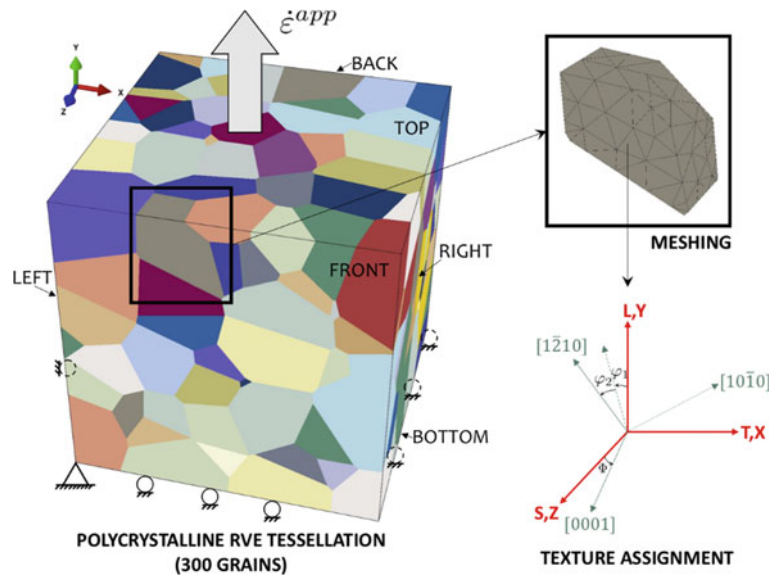
### Tensile Response

Figure 2a shows the stochastic responses of pure Mg and an Mg alloy (AZ31) under uniaxial tensile loading along the rolling direction (L). The solid lines with symbols denote the average response of the five textures (Table 1), and the shaded regions indicate one standard deviation resulting from textural deviations. Figure 2a indicates that, when loaded in tension along the L-direction, a reasonably large textural variation (case E is  $\sim 30\%$  weaker than case A) does

<sup>1</sup>We use the *randn* utility in MATLAB<sup>®</sup>.



**Fig. 1** Definition of crystal orientations in a polycrystal aggregate of HCP single crystals. The sheet directions L, T, and S are, respectively, aligned with the global y, x, and z axes. Typical FE mesh details of a grain are shown



**Table 1** Texture cases considered in this work

Angles ↓ / cases →	A (°)	B (°)	C (°)	D (°)	E (°)
$\varphi_1^\sigma$	20	20	30	30	30
$\Phi^\sigma$	10	20	10	20	20
$\varphi_2^\sigma$	0	0	0	0	10

**Table 2** Slip and twin systems observed in Mg single crystals

Mechanisms	Slip/twin plane	Slip/twin direction	No. of systems
Basal $\langle a \rangle$ slip	(0001)	$\langle 11\bar{2}0 \rangle$	3
Prismatic $\langle a \rangle$ slip	$\{10\bar{1}0\}$	$\langle 11\bar{2}0 \rangle$	3
Pyramidal $\langle a \rangle$ slip	$\{10\bar{1}1\}$	$\langle 11\bar{2}0 \rangle$	6
Pyramidal $\langle c + a \rangle$ slip	$\{11\bar{2}2\}$	$\langle 11\bar{2}3 \rangle$	6
Extension twinning	$\{10\bar{1}2\}$	$\langle 10\bar{1}1 \rangle$	6
Contraction twinning	$\{10\bar{1}1\}$	$\langle 10\bar{1}2 \rangle$	6

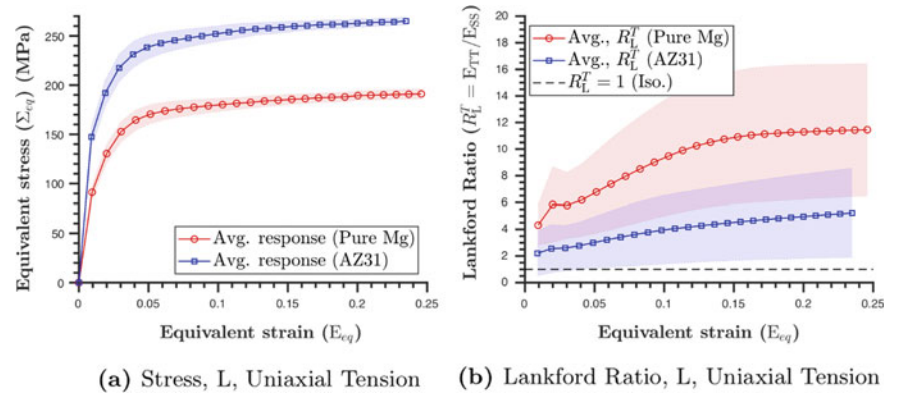
**Table 3** Material properties for pure Mg and (in brackets) Mg alloy (AZ31B)

Mechanisms	$\tau_0$ (MPa)	$h_0$ (MPa)	$\tau_s$ (MPa)		$\tau_0^i / \tau_0^{\text{pris.asl.}}$
Basal $\langle a \rangle$ slip	0.5 (10)	20 (50)	–		0.02 (0.18)
Prismatic $\langle a \rangle$ slip	25 (55)	1500	85 (110)		1
Pyramidal $\langle a \rangle$ slip	25 (55)	1500	85 (110)		1
Pyramidal $\langle c + a \rangle$ slip	40 (60)	3000	150 (170)		1.6 (1.09)
Extension twinning	$\tau_0$ (MPa)	$h_{\text{et}}$ (MPa)	$\tau_{s\_et}$ (MPa)	$h_{\text{et\_sl}}$ (MPa)	0.14 (0.27)
	3.5 (15)	100 (120)	20 (30)	100	
Contraction twinning	$\tau_0$ (MPa)	$H_{\text{ct}}$ (MPa)	$H_{\text{ct\_sl}}$ (MPa)	$b$	2.2(1.55)
	55 (85)	6000	15	0.05	

not result in a significant variation in the overall stress–strain response. Further, the standard deviation about the mean tends to decrease with increasing strain. Only over a narrow intermediate strain regime ( $0.03 \leq E_{\text{eq}} \leq 0.06$ ) does the

deviation appear to be of some significance. The upper bound of the standard deviation coincides with case A, while the lower bound coincides with case E. Moreover, these observations hold in both cases, which suggest that the

**Fig. 2** Stress–strain ( $\Sigma_{eq} - E_{eq}$ ) responses and Lankford ratio ( $R_L^T$ ) evolution under uniaxial tension along the rolling (L) direction



intrinsic crystallographic anisotropy plays a negligible role, if any, in the stochastic response of these materials.

In terms of the correlation between the yield strength and texture,  $A > C > B > D > E$ ; the average response (solid lines with symbols) lies between cases *C* and *B* (for both pure Mg and Mg alloy), which indicates the stronger effect of variation of  $\Phi$  than  $\varphi_1$ . It follows from the notion that deviations of  $[1\bar{2}10]$  due to  $\varphi_1$  variation do not cause a significant variability in yield strength as Mg is expected to exhibit transverse isotropy in the L-T plane. The higher strength and somewhat higher hardening in the Mg alloy relative to pure Mg are a consequence of the higher  $\tau_0$  and  $\tau_s$  for the prismatic  $\langle a \rangle$  mode—a favorable mechanism in both materials (cf. Fig. 3b).

In comparison, the lateral deformation anisotropy defined by the Lankford ratio  $R_L^T = E_{TT}/E_{SS}$  is more sensitive to textural deviations (Fig. 2b). For a given material, it deviates significantly from isotropy ( $R_L^T = 1$ ). Pure Mg exhibits an overall higher lateral anisotropy compared to the Mg alloy. The average value of  $R_L^T$  for pure Mg is  $\sim 8$  while that for the Mg alloy is  $\sim 3$ . These values are consistent with recent studies on smooth and notched rounded bars [1, 5]. The effect of texture and material anisotropy on  $R_L^T$  for smooth cylindrical tensile specimens was discussed in [3, 5] which concluded in lateral anisotropy causing elliptical cross sectioned specimens with the S- and T-directions as the major and minor axes, respectively. Textured pure Mg specimens at areal notch strain of 0.2 had  $R_L^T \sim 45$  for a textural variation defined by  $[E^\sigma] = [30^\circ, 0, 0]$ . For a similar texture, the polycrystalline Mg alloy gave  $R_L^T \sim 35$  while  $R_L^T \sim 2.5$  for  $[E^\sigma] = [0^\circ, 10^\circ, 0]$ . The tempering of the lateral anisotropy in the Mg alloy seems to be related to the lower difference in the initial and saturation strengths of pyramidal  $\langle a \rangle$  and pyramidal  $c+a$  modes compared to pure Mg. In other words, the harder the pyramidal  $\langle c+a \rangle$  the more difficult is the contraction of the  $c$  axis, which is on average oriented along S. Further, the evolution of Lankford ratio for pure Mg is more sensitive to the texture compared to Mg alloy.

Among the different textures, case *C* (case *A* is a close second) is most laterally anisotropic for both pure Mg and AZ31. On the other hand, in both materials, case *D* has the lowest  $R_L^T$  (and not case *E* as one would expect). That is, for a given  $\varphi_1$ , the lateral deformation anisotropy decreases with increasing  $\Phi$ ; on the other hand, if both  $\varphi_1$  and  $\Phi$  are held constant in the initial texture, a variation of  $\varphi_2$  does not seem to push  $R_L^T \rightarrow 1$ . Instead, the deformation tends to become more anisotropic. Hence, case *D* consistently has a lower  $R_L^T$  (closer to 1) than case *E* for both materials.

## Compressive Response

Figure 4a shows the average macroscopic response of the RVEs when loaded in compression along the rolling (L) direction. As in the tensile loading case, the shaded regions indicate one standard deviation resulting from textural variations (cf. Table 1). From the nature of the stress–strain responses, it is evident that extension twinning is a preferred and dominant deformation mode in the initial stages, which results in the characteristic sigmoidal response. Surprisingly, the effect of textural variation is even weaker than in the tensile loading case. Note that the anisotropy ratio of the CRSS values between extension twinning and pyramidal  $\langle c+a \rangle$  is  $\sim 4$  for the Mg alloy, while it is much larger ( $\sim 11$ ) for pure Mg. In other words, even with nearly 30% textural weakening (relative to the strong texture, case *A*) and  $\sim 60\%$  enhancement of the CRSS for extension twinning, deformation twinning remains a dominant deformation mode, thereby producing an overall softer response under uniaxial compression along the L-direction.

In both material systems, the upper bound of the shaded regions corresponds to case *C* (case *A* is a close second), while lower bound corresponds to case *B* (case *D* is close). From the viewpoint of textures, deviations in  $\Phi$  tend to weaken the post-twinning hardening. The intermediate hardening (between the two plateau-like regions) also depends on the textural strength, albeit weakly.

**Fig. 3** Average relative activities of different mechanisms ( $\bar{\zeta}^i$ ) and twinning volume fraction ( $\bar{f}^i$ ) evolution responses for the polycrystalline textures considered under uniaxial tension along the rolling (L) direction

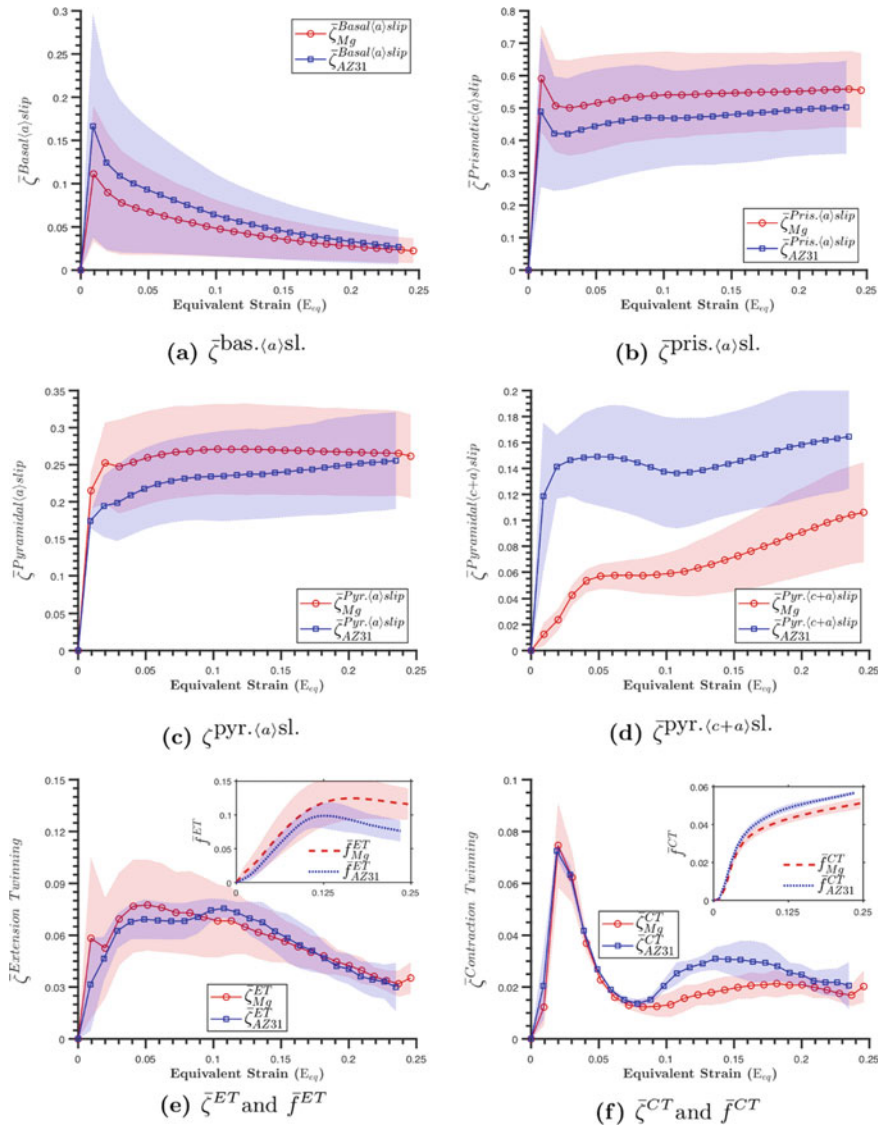
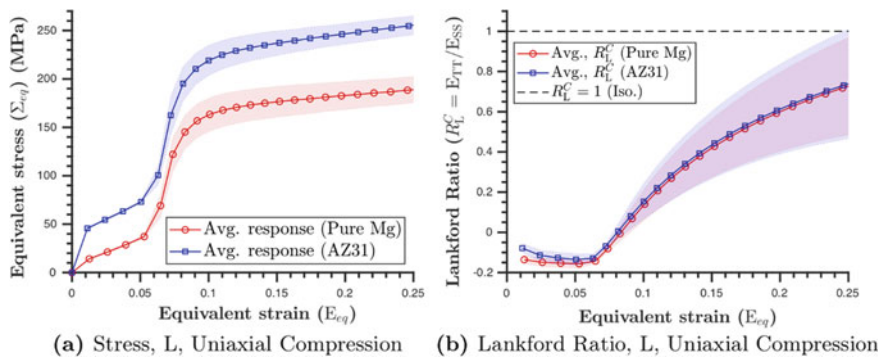


**Fig. 4** Average equivalent stress ( $\Sigma_{eq}$ ) and Lankford ratio ( $R_L^C$ ) evolution responses for the group of polycrystalline textures considered under uniaxial compression along rolling (L) direction



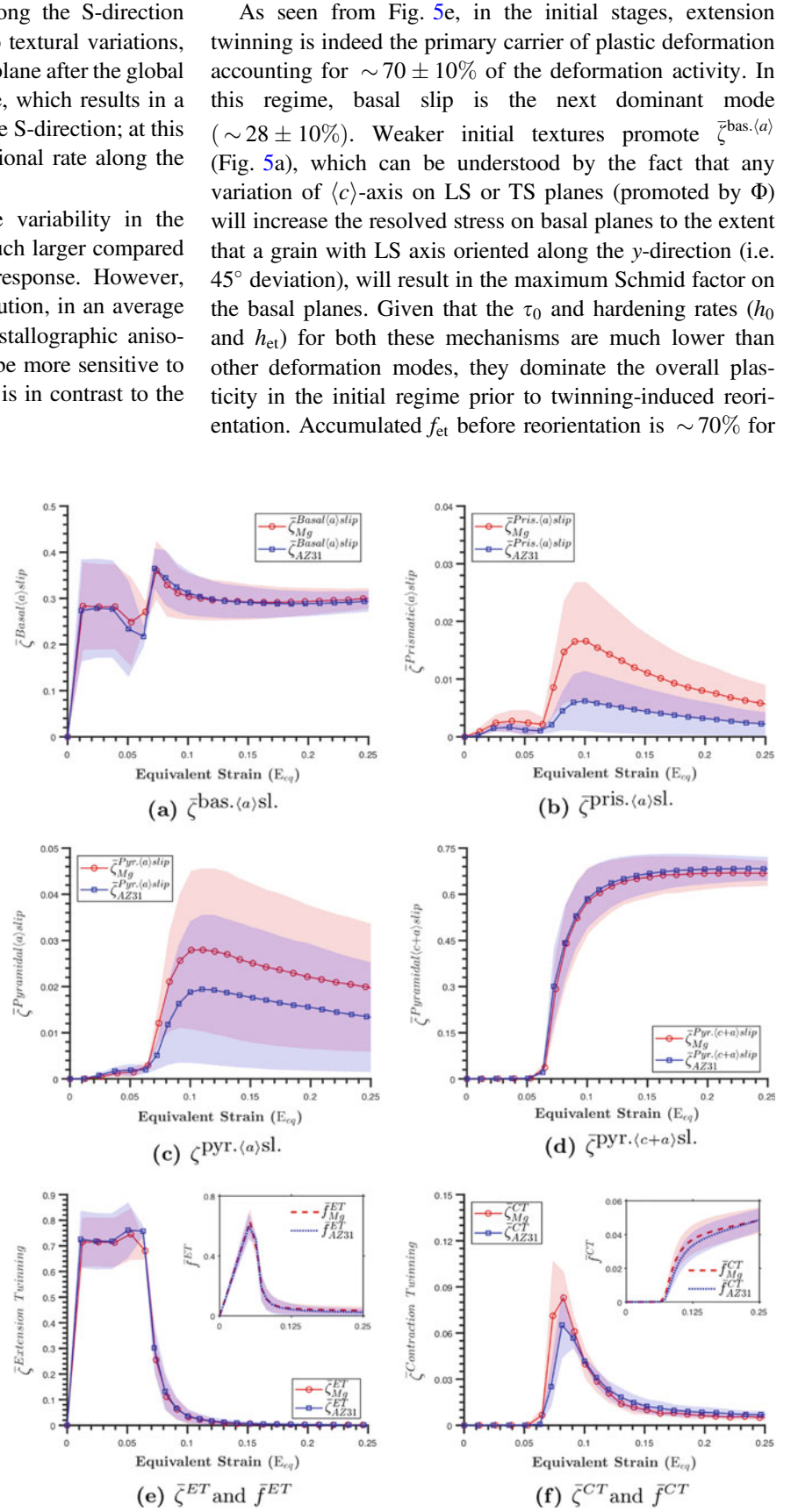
Interestingly, the evolution of Lankford ratios for both materials stands in stark contrast to its counterpart under the tensile loading on several counts (cf. Figure 4b). First, the qualitative nature of the evolution is different: it transitions from  $R_L^C < 0$  to  $R_L^C > 0$ , unlike the tensile case where  $R_L^C \gg 1$  throughout the deformation. The transition coincides with the

equivalent strain at which the twinning-induced rapid hardening kicks in. Second, the ratio tends toward 1, indicating a decrease in the lateral strain anisotropy with progressive deformation. Physically, under uniaxial compression along the L-direction, the lateral extension along the S-direction is easier compared to that along the T-direction; in fact, extension along

the T-direction stagnates while that along the S-direction evolves rapidly during twinning. Due to textural variations, the  $\langle c \rangle$  tends to be distributed in the L-T plane after the global reorientation process is largely complete, which results in a decrease in the rate of extension along the S-direction; at this stage, there is an increase in the extensional rate along the T-direction, which leads to  $R_L^C \rightarrow 1$ .

As in the tensile loading case, the variability in the Lankford ratios (in both materials) is much larger compared to the variability in the stress–strain response. However, unlike the tensile counterpart, their evolution, in an average sense, is insensitive to the intrinsic crystallographic anisotropy. Further, the Mg alloy appears to be more sensitive to textural variations than pure Mg, which is in contrast to the tensile loading scenario.

**Fig. 5** Average relative activities of different mechanisms ( $\bar{\zeta}^i$ ) and twinning volume fraction ( $f^i$ ) evolution responses for the polycrystalline textures considered under uniaxial compression along the rolling (L) direction



As seen from Fig. 5e, in the initial stages, extension twinning is indeed the primary carrier of plastic deformation accounting for  $\sim 70 \pm 10\%$  of the deformation activity. In this regime, basal slip is the next dominant mode ( $\sim 28 \pm 10\%$ ). Weaker initial textures promote  $\bar{\zeta}^{\text{bas.}(a)}$  (Fig. 5a), which can be understood by the fact that any variation of  $\langle c \rangle$ -axis on LS or TS planes (promoted by  $\Phi$ ) will increase the resolved stress on basal planes to the extent that a grain with LS axis oriented along the y-direction (i.e.  $45^\circ$  deviation), will result in the maximum Schmid factor on the basal planes. Given that the  $\tau_0$  and hardening rates ( $h_0$  and  $h_{\text{et}}$ ) for both these mechanisms are much lower than other deformation modes, they dominate the overall plasticity in the initial regime prior to twinning-induced reorientation. Accumulated  $f_{\text{et}}$  before reorientation is  $\sim 70\%$  for



both materials reinforcing the pervasive nature of twinning even in weaker textures. After reorientation, pyramidal  $\langle c+a \rangle$  dominates the response for both materials accounting for  $\sim 70 \pm 5\%$  of the total deformation activity; the remainder contributions come from prismatic  $\langle a \rangle$  and pyramidal  $\langle a \rangle$  modes. Interestingly, unlike in the tensile loading case where pure Mg showed much higher pyramidal  $\langle c+a \rangle$  activity compared to that in the Mg alloy, in the compressive loading case, it is largely insensitive to the intrinsic crystallographic anisotropy. Clearly, the large variability in the relative activities translates into the corresponding variability in the Lankford ratios (cf. Fig. 4b) that does not result in very high standard deviation in strength response as these mechanisms have similar CRSS and hardening responses.

## Texture Evolution

Figure 6 is a collage of textural evolution under both loading states for the sharpest (case A), weakest (case E), and

intermediate (case D) initial textures. The texture plots are created using MTEX [11]. Due to the variability of  $\varphi_1$ , the  $[1\bar{2}10]$  directions of individual grains deviate from the tensile loading direction (L). At the grain scale, with increasing  $\varphi_1$ , one of the two active prismatic  $\langle a \rangle$  variants becomes a preferred system (based on a Schmid factor); as a result, lattice spin occurs causing crystal rotation that effects textural sharpening by pushing  $(10\bar{1}0)$  away from the initial pole along T towards L (cf. Fig. 6a, d). A further effect is that the intensity of  $(10\bar{1}0)$  poles along T is reduced. The relative reduction in the  $[0001]$  pole intensity is much smaller due to the dearth of the activity of mechanisms that can cause spin of  $\langle c \rangle$  axis, namely pyramidal  $\langle c+a \rangle$ , ET, and CT (all  $<10\%$ ). Moreover, similar plastic strain accrual on the conjugate variants of these mechanisms will reduce the net spin.

Under compression, twinning causes an instantaneous change in texture. Apart from the significant shifting in the poles, the textural deviation is also marked by reduction in intensity of the newly aligned poles. Schmid analysis indicates that compression along the L-direction can activate

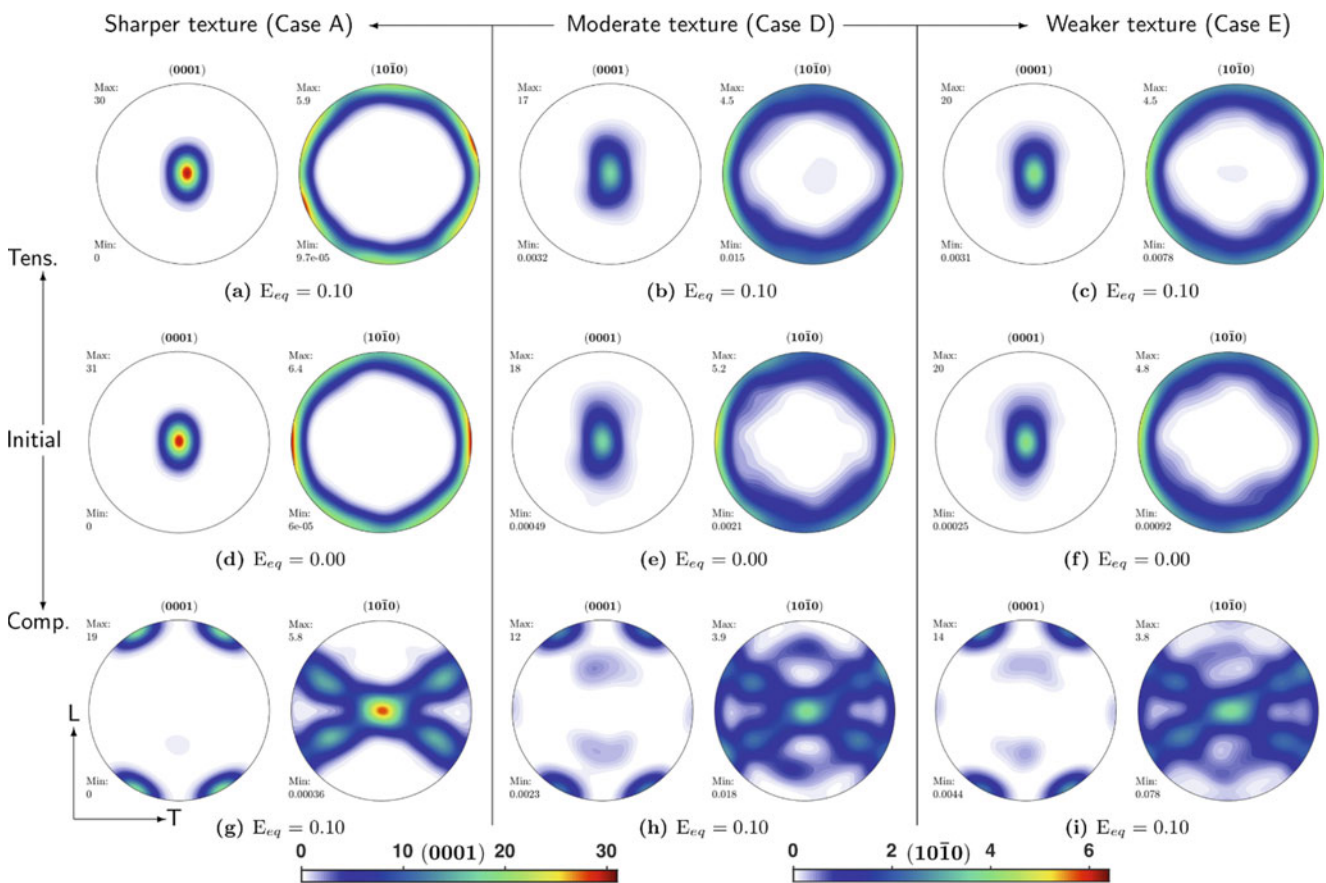


**Fig. 6** Evolution of  $[0001]$  and  $[10\bar{1}0]$  pole figures on the LT plane for textures A, D, and E under uniaxial tension and compression along the rolling (L) direction. The central row shows initial textures, with central column being for moderate initial texture (case D), left for sharper initial texture (case A), and right for weaker initial texture (case E). Top

row shows deformed texture under tension, while the bottom row shows deformed texture under compression (both at  $E_{eq} = 0.10$ ). The color bars show intensities plotted in pole figures for  $[0001]$  (left) and  $[10\bar{1}0]$  (right) poles, respectively

four twin variants:  $(0\bar{1}12)[01\bar{1}1]$ ,  $(01\bar{1}2)[0\bar{1}11]$ ,  $(1\bar{1}02)[\bar{1}101]$  and  $(\bar{1}102)[1\bar{1}01]$ ; as such, an individual grain in the ensemble has equal probability of reorienting its  $\langle c \rangle$  axis along one of these directions in the LT plane, effectively splitting the intensity of  $[0001]$  poles into these four regions. This transition is more evident for a sharper texture, cf. Figure 6d, g. The change in  $[0001]$  poles is correspondingly marked by the emergence of  $[10\bar{1}0]$  poles out of the LT plane as shown in Fig. 6g.

An initial sharper texture undergoes relatively larger weakening with deformation (see maximum pole intensity values). For progressively weaker initial textures, the evolution remains qualitatively similar to the sharper texture, although with some additional aspects. In particular, note the emergence of two  $[0001]$  poles closer to the initial  $[10\bar{1}0]$  poles on the LT plane. These poles are formed because, with increasing spread in texture, there is a decreasing resolved stress on the four twin variants most active in case A but marked by an increase in resolved shear stress on the remaining two variants ( $(10\bar{1}2)[\bar{1}011]$  and  $(\bar{1}012)[10\bar{1}1]$ ) whose twin directions ( $[\bar{1}011]$  and  $[10\bar{1}1]$ , respectively) result in reoriented  $\langle c \rangle$  axis along  $\langle 10\bar{1}0 \rangle$ . This also results in these reoriented grains having their  $[10\bar{1}0]$  poles emerging on LT plane.

**Summary:** In this work, we investigate the stochastic behavior of Mg polycrystals by considering several synthetic textures that mimic experimental rolled textures. Focus is laid on quantifying the behavior under monotonic tensile and compressive loading along the rolling direction. The salient outcomes are as follows:

1. In tensile loading, the Lankford ratio increases with deformation, exhibiting a strong sensitivity to plastic anisotropy both, crystallographic and textural. This sensitivity is consistent with the sensitivity of the deformation mechanisms to textural variability. Yet, the variability of the deformation mechanisms (and by extension, of the lateral strains) does not reflect in the variability of the stress–strain responses. Interestingly, this observation holds even in the case of a high crystallographic anisotropy, e.g. pure Mg.
2. In compressive loading, even for relatively weak textures, the extension twinning mode governs the initial response. The stress–strain response is relatively insensitive to the initial texture during the stage, while extension twinning is active. However, the sensitivity of the stress–strain response to textural variability is exacerbated once twinning-induced material hardening occurs. In contrast to the tensile case, the Lankford ratio evolution is non-monotonic; the lateral strains approach

isotropic state at high strains. Moreover, the deformation anisotropy is insensitive to the intrinsic crystallographic anisotropy, unlike the tensile case.

**Acknowledgements** Partial support for PPI, SPJ, and SB was provided by the Army Research Laboratory and was accomplished under Cooperative Agreement Number W911NF-12-2-0022. SPJ and AV acknowledge partial support from University of Houston start-up funds. RP acknowledges support under the Undergraduate Research Apprenticeship Program (URAP) from the Army Education Outreach Program (AEOP). The views and conclusions contained in this document are those of the authors and should not be interpreted as representing the official policies, either expressed or implied, of the Army Research Laboratory or the U.S. Government. The U.S. Government is authorized to reproduce and distribute reprints for Government purposes notwithstanding any copyright notation herein. PPI acknowledges partial support from NUS Research Scholarship.

## References

1. B. Kondori and A. A. Benzerga, “Effect of Stress Triaxiality on the Flow and Fracture of Mg Alloy AZ31,” *Metallurgical and Materials Transactions A*, vol. 45, no. 8, pp. 3292–3307, 2014.
2. B. Kondori and A. A. Benzerga, “On the notch ductility of a magnesium-rare earth alloy,” *Materials Science and Engineering: A*, vol. 647, pp. 74–83, 2015.
3. B. Selvarajou, B. Kondori, A. A. Benzerga and S. P. Joshi, “On plastic flow in notched hexagonal close packed single crystals,” *Journal of the Mechanics and Physics of Solids*, vol. 94, pp. 273–297, 2016.
4. M. J. Nemcko and D. S. Wilkinson, “Impact of microstructure on void growth and linkage in pure magnesium,” *International Journal of Fracture*, vol. 200, no. 1–2, pp. 31–47, 2016.
5. B. Selvarajou and S. P. Joshi, “Three dimensional simulations of texture and triaxiality effects on the plasticity of magnesium alloys,” *Acta Materialia*, vol. 127, pp. 54–72, 2017.
6. N. S. Prasad, R. Narasimhan and S. Suwas, “Effect of notch acuity on the fracture behavior of AZ31 Mg alloy,” *Engineering Fracture Mechanics*, vol. 187, pp. 241–261, 2018.
7. B. Selvarajou and S. P. Joshi, “Void growth and coalescence in hexagonal close packed crystals,” *Journal of the Mechanics and Physics of Solids*, vol. 125, pp. 198–224, 2019.
8. P. P. Indurkar and S. P. Joshi, “Void Growth and Coalescence in Porous Plastic Solids With Sigmoidal Hardening,” *Journal of Applied Mechanics*, vol. 86, no. 9, 2019.
9. J. Zhang and S. P. Joshi, “Phenomenological crystal plasticity modeling and detailed micromechanical investigations of pure magnesium,” *Journal of the Mechanics and Physics of Solids*, vol. 60, no. 5, pp. 945–972, 2012.
10. R. Quey, P. R. Dawson and F. Barbe, “Large-scale 3D random polycrystals for the finite element method: Generation, meshing and remeshing,” *Computer Methods in Applied Mechanics and Engineering*, vol. 200, no. 17, pp. 1729–1745, 2011.
11. F. Bachmann, R. Hielscher and H. Schaeben, “Texture analysis with MTEX - free and open source software toolbox,” in *Solid State Phenomena*, Trans Tech Publ, 2010, pp. 63–68.

# Cold Formability of Extruded Magnesium Bands

Maria Nienaber, Jan Bohlen, Jose Victoria-Hernández, Sangbong Yi, Karl Ulrich Kainer, and Dietmar Letzig

## Abstract

Three magnesium alloys with texture and microstructure modifying elements, binary M2, and the alloyed counterparts with Ca (MX21) and rare earth element (ME21) were extruded to flat bands under similar conditions. The microstructure and texture in extrusion significantly differ from those developed in rolled magnesium sheets. The influence on the mechanical properties and the forming behaviour, in terms of Erichsen values, with relation to microstructure, texture, and strain rate sensitivity was examined. A clear difference in texture development and strain rate sensitivity is shown in dependence on the alloying composition. In addition, not only the texture, but also the microstructure has a great influence on formability.

## Keywords

Magnesium • Extrusion • Magnesium sheet • Formability • Erichsen value

## Introduction

The full potential of magnesium as a lightweight material can only be exploited if it is clear which deformation mechanisms are active in Mg flat products at room temperature. Plastic deformation is basically controlled by dislocation slip, twinning, and grain boundary sliding. In general, the hexagonal structure of Mg is responsible for the fact that the formability at room temperature is limited due to the low number of active slip systems. Therefore, the control of grain size and texture during thermomechanical processing (rolling or extrusion) is the enabler to improve the

properties and broaden the range of applications of Mg wrought alloys. Usually commercial wrought alloys have a strong basal texture during the manufacturing process, which causes a limited formability at room temperature.

Many studies have shown that the addition of rare earth elements (RE) or Ca weakens the texture and, consequently, improves formability [1–4]. The grain size also seems to influence the deformation behaviour considerably. It has been shown that, depending on grain size and strain rate, a flat band with a strong basal texture can be deformed very well [5, 6].

Somekawa et al. [7] has already investigated the stretchability of binary Mn alloys very precisely and shows that high Erichsen values can be achieved with slow deformation speed, although it reveals a typical basal texture, i.e. a distinct alignment of basal planes parallel to the sample surface. Grain boundary sliding (GBS) is assumed to be the main deformation mechanism. Nevertheless, the binary alloy showed low strength, which is not optimal for an industrial application [8].

In this work, the binary master alloy with 2 wt% Mn (M2) and the alloyed counterparts with Ca (MX21) and RE (ME21) are produced by direct extrusion with a similar fine-grained microstructure. It is assumed that the addition of Ca and RE will result in an increase of strength. The mechanical properties and the forming behavior (Erichsen test) with respect to microstructure, texture, and strain rate sensitivity are presented and discussed.

## Experimental Procedures

Table 1 shows the chemical compositions of the alloys used in this study analyzed by spark emission spectroscopy (SPECTRO, SPECTROLAB M). Ca was added in the form of flakes, Ce as Ce mixed metal (Ce 50%, La 30%, Nd 16%, Pr 4%), and M2 as a master alloy. The MX21 and ME21 alloys were produced using a modified gravity casting process including directional solidification in a crucible [9]. For

M. Nienaber · J. Bohlen · J. Victoria-Hernández · S. Yi · K. U. Kainer · D. Letzig (✉)  
Helmholtz-Zentrum Geesthacht—Magnesium Innovation Centre,  
Max-Planck-Straße 1, 21502 Geesthacht, Germany  
e-mail: [Dietmar.Letzig@hzg.de](mailto:Dietmar.Letzig@hzg.de)

the extrusion process, billets with a diameter of 49 mm and a length of 150 mm were machined using cast material (ME21, MX21) and master alloy (M2). The homogenization of these billets was carried out for 16 h at 500 °C (for M2 and ME21) and 400 °C (for MX21) in a circulating air furnace.

The extrusion experiments were performed using a 2.5 MN automatic extrusion press of Müller Engineering. The manufacturing of the Mg bands with a width of 40 mm and a thickness of 2 mm, corresponding to an extrusion ratio  $R = 1:24.5$ , was carried out by direct extrusion with an extrusion speed of 0.6 mm/s (profile exit speed of 0.9 m/min).

As the alloys have different strengths and consequently different flow behaviours, the extrusion temperature varies in order to obtain a similar microstructure. The extrusion temperature of 150, 300, and 350 °C was applied for M2, MX21, and ME21, respectively. The billets were preheated for one hour at process temperature. In order to achieve a partially recrystallized microstructure, all tests were extruded at the lower process window.

Microstructural analysis was performed using light microscopy and scanning electron microscope (SEM). The samples for the microstructural analysis were taken from the extruded bands so that the micrographs show the plane stretched by the extrusion direction and the normal direction of the strip. The specimens were embedded with cold embedding compound Demotec 30. The samples were first ground with fine SiC paper (#800, #1200 and #2500) and then polished with 1 µm diamond suspension and OPS (oxide polishing suspension). An etchant was mixed with picric acid according to Kree et al. [10]. Because Mn-containing alloys are very difficult to etch, 0.5 ml nitric acid was added to the etchant to make the grain boundaries better visible. The specimens were etched for 5–10 s. For a better analysis of the homogeneity of the microstructure, images with polarized light were also taken. Sample preparation for the SEM investigations was carried out without etching.

The quantitative texture measurements were performed on samples, which had been ground down to the center and then polished, with an X-ray diffractometer (PANalytical Type X'Pert PRO MRD) using Cu-K $\alpha$  radiation with a beam size of  $2 \times 1 \text{ mm}^2$ . Six pole figures, (0 0 0 2), {1 0 -1 0}, {1 1 -2 1}, {1 0 -1 1}, {1 0 -1 2}, and {1 1 -2 3} were measured up to a tilt angle of 70°. The orientation distribution function was calculated using an open-source code

MTEX [11]. In this study, the textures are represented in the form of the recalculated (0 0 0 2)- and {1 0 -1 0} pole figures.

For the tensile tests in extrusion direction (ED) and transverse direction (TD), bone-shaped samples according to Din 50125 H (modified) with a measuring length of 18 mm and a width of 5 mm were tested. The tests were performed at room temperature with a quasi-static strain rate of  $10^{-3} \text{ s}^{-1}$  and  $10^{-4} \text{ s}^{-1}$  using a universal testing machine (ZwickTM Z050).

The stretch forming behavior (Erichsen value (IE)) was investigated on complete sections of the extruded bands with a lubricant (OKS 352) at room temperature. The tests were carried out with a blank holding force of 10 kN, a punch diameter of 20 mm, and a forming rate (punch displacement) of 5 and 0.5 mm/min.

## Results and Discussion

The microstructures of the extrusion bands show a duplex microstructure consisting of recrystallized fine grains and non-recrystallized coarse grains elongated along the ED in all three alloys, in Fig. 1. It is not possible to determine the grain size in any alloy due to the fact that all microstructures are only partially recrystallized. It seems that the addition of the alloying elements Ca and RE makes the recrystallized area coarser than in the binary Mn alloy.

M2 was extruded at 150 °C and shows (Fig. 1a) strongly deformed areas and deformation bands due to the very low extrusion temperature. With polarized light, Fig. 1d, it can be clearly seen that there are areas consisting of newly formed recrystallized grains in addition to the strongly deformed elongated grains. In addition, a grain size difference can also be observed in the recrystallized areas. The SEM image in SE mode of M2 (Fig. 1g) reveals finely distributed Mn particles in the matrix in addition to the coarse Mn chunks. These can also be detected in MX21 (Fig. 1e) and ME21 (Fig. 1f).

The ternary alloys also contain particle stringers. These are precipitates from the original cast structure, which have also been deformed and are linearly oriented in the direction of extrusion. Consequently, these are not newly formed precipitates resulting from the process.

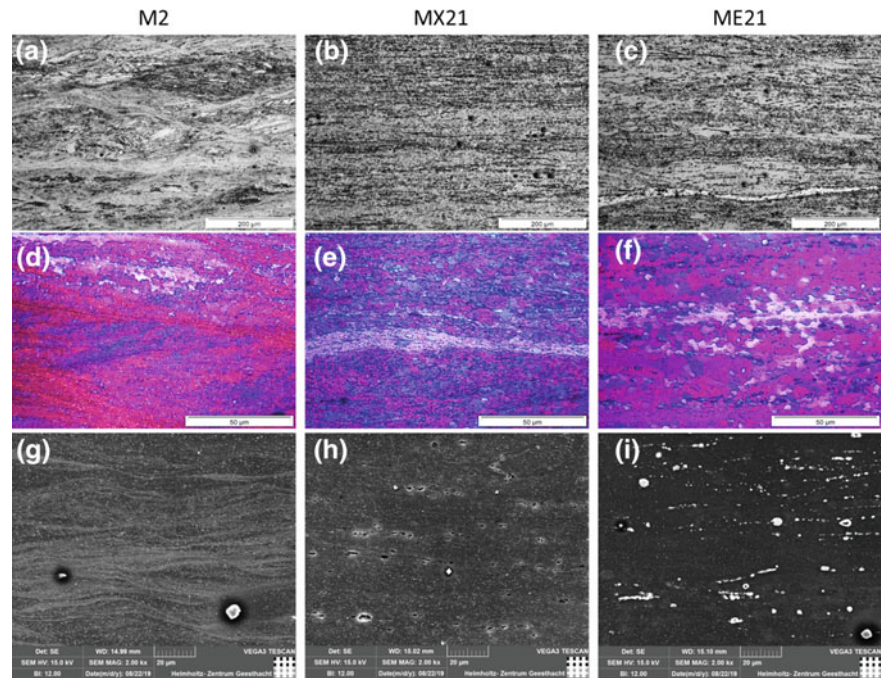
Thermodynamic calculations with PANDAT<sup>TM</sup> software revealed that Mn does not form any stable compounds with

**Table 1** Alloys in this study and their chemical composition; in wt %; Mg balance

Alloy	Mn	Ca	Ce	La	Nd	Pr
M2	2.0	–	–	–		
MX21	2.26	1.04				
ME21	2.0		0.50	0.31	0.13	0.038



**Fig. 1** Micrographs from longitudinal sections (ED horizontal) of the extruded flat bands in 200 $\times$ , 1000 $\times$  (polarized) and SE contrast in 2000 $\times$  magnification. M2 (a, d), MX21 (b, e), ME21 (c, f)



Mg, Ca, or RE, in the ternary alloys. Hence, possible intermetallic phase for the stringers in MX21 is  $Mg_2Ca$  and at ME21  $Mg_{12}RE$ . Despite the higher extrusion temperature comparing to M2, ME21 and MX21 exhibit a similar inhomogeneous fine-grained microstructure. In addition, the resulting high press forces indicate that all alloys were extruded at the lower limit of the process window. One reason for this could be that the addition of Ca or RE to M2 results in solid solution hardening. Hence, higher temperatures are required to get the material to flow. It is also known that the addition of Ca and RE delays recrystallization [4, 12]. Thus, a larger fraction of non-recrystallized microstructure could strengthen the material, resulting in more stress or temperature being needed for extrusion.

The influence of the alloying elements on the texture development can be clearly seen (Fig. 2). It is to note that the addition of RE or Ca effectively weakens the intensity of the basal texture. M2 (Fig. 2a) shows a strong pronounced  $\langle 0001 \rangle$  fiber parallel to the normal direction (ND) and a broader angular tilt of basal planes to the extrusion direction rather than to the transverse direction. With a maximum intensity of 14 m.r.d., the M2 alloy has the highest intensity in the basal pole figure. Prismatic planes are randomly distributed parallel to the ND and weakly pronounced with 2.8 m.r.d. This texture occurs not only in binary Mn alloys but is also typical for rolled or extruded AZ31 [13–15].

The texture of MX21 differs significantly from that of M2. The basal pole figure shows the well-known separation of the center pole into two poles that tilt from ND towards ED. Rare earths or calcium as an alloying element can lead to this texture formation [13, 16, 17]. The prismatic planes

show a weak preferred alignments in ED and TD with the max pole density of 2.4 m.r.d.

With the maximum intensity of 6.5 m.r.d. ME21 clearly has the weakest basal pole intensities (Fig. 2c). A weak texture with split peaks of the basal planes in TD and ED can be seen. The split in ED is similar to the texture of MX21. The double peak in TD corresponds to a pronounced prismatic component in the  $\{10\text{-}10\}$  pole figure that is perpendicular to the prism plane. This prismatic component is often associated with non-recrystallized structures and can develop through deformation mechanisms [2, 18].

The stress–strain diagrams obtained from the tensile tests performed at room temperature are shown for exemplary specimens in ED and TD in Fig. 3. In order to show the influence of the alloy addition on the strain rate sensitivity, the trials were carried out at a strain rate of  $10^{-3}$  and  $10^{-4}$  1/s. The averaged values of the measured variables (3 tests) and their standard deviation are listed in Table 2.

M2 (Fig. 3a) shows a relatively low uniform elongation and a significant decrease in stress values until fracture. This behaviour is often associated with grain boundary sliding as an active deformation mechanism [5, 14]. This behavior is independent on the strain rate. Influence by the strain rate is not the shape of the curves but the values.

The stress level (yield stress (TYS) and ultimate tensile stress (UTS)) decreases with the lower strain rate, whereas the fracture strain increases regardless of the testing direction. The uniform strain shows no direct relation to the strain rate. In general, the stress level and fracture strain are higher in TD than in ED. Only the uniform elongation is higher in ED than in TD.

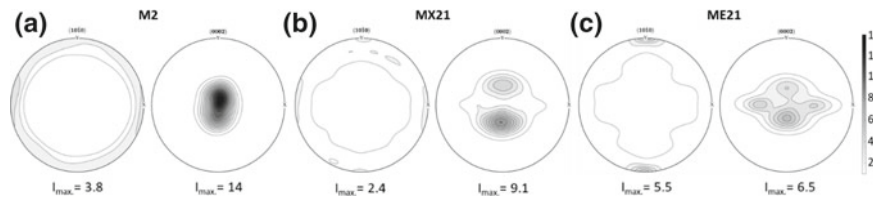


**Fig. 2** Recalculated pole figures of the as-extruded bands of **a** M2, **b** MX21, **c** ME21

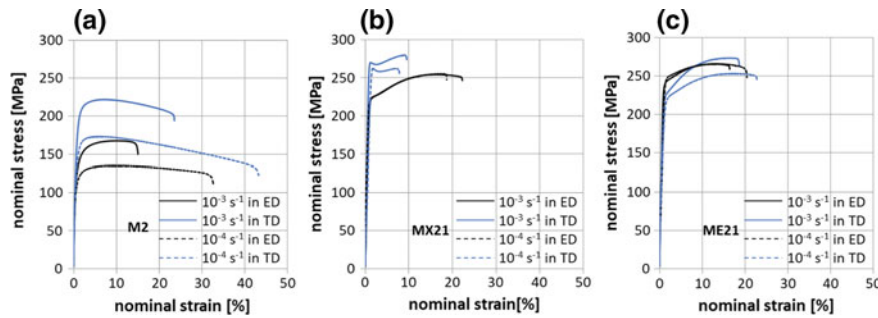


**Fig. 3** Engineering stress–strain diagrams from tensile tests in ED and TD at room temperature and a varied strain rate of  $10^{-3}\text{ s}^{-1}$  and  $10^{-4}\text{ s}^{-1}$  for the extruded band for alloy M2 (a), MX21 (b), ME21 (c)

**Table 2** Mechanical properties from tensile test in extrusion direction (ED) and transverse direction (TD) at room temperature of the extruded bands (TYS: tensile yield stress, UTS: ultimate tensile stress)

Alloy	Strain rate [1/s]	Direction	TYS [MPa]	UTS [MPa]	Uniform strain [%]	Fracture strain [%]
M2	$10^{-3}$	ED	120 ( $\pm 4$ )	164 ( $\pm 5$ )	9.8 ( $\pm 0.8$ )	14.6 ( $\pm 2.0$ )
		TD	176 ( $\pm 3$ )	221 ( $\pm 3$ )	6.3 ( $\pm 0.3$ )	21.4 ( $\pm 1.6$ )
	$10^{-4}$	ED	103 ( $\pm 4$ )	134 ( $\pm 3$ )	8.7 ( $\pm 0.2$ )	35.0 ( $\pm 4.0$ )
		TD	140 ( $\pm 0$ )	174 ( $\pm 1$ )	5.1 ( $\pm 0.5$ )	43.3 ( $\pm 3.0$ )
MX21	$10^{-3}$	ED	199 ( $\pm 8$ )	254 ( $\pm 1$ )	15.9 ( $\pm 0.7$ )	22.4 ( $\pm 2.3$ )
		TD	268 ( $\pm 3$ )	281 ( $\pm 3$ )	8.1 ( $\pm 0.5$ )	8.8 ( $\pm 0.5$ )
	$10^{-4}$	ED	208 ( $\pm 11$ )	248 ( $\pm 7$ )	14.7 ( $\pm 3.5$ )	16.1 ( $\pm 4.2$ )
		TD	256 ( $\pm 4$ )	262 ( $\pm 1$ )	6.4 ( $\pm 0.2$ )	6.9 ( $\pm 0.4$ )
ME21	$10^{-3}$	ED	226 ( $\pm 15$ )	264 ( $\pm 6$ )	11.8 ( $\pm 0.3$ )	14.7 ( $\pm 1.1$ )
		TD	211 ( $\pm 7$ )	269 ( $\pm 7$ )	15.3 ( $\pm 0.1$ )	17.9 ( $\pm 0.6$ )
	$10^{-4}$	ED	226 ( $\pm 14$ )	252 ( $\pm 12$ )	12.9 ( $\pm 0.6$ )	19.5 ( $\pm 2.4$ )
		TD	204 ( $\pm 8$ )	248 ( $\pm 5$ )	15.9 ( $\pm 0.2$ )	21.8 ( $\pm 0.9$ )

The reason for the higher strength in the TD is the pronounced basal-type texture with a slight spread basal pole into the ED. The tendency that the tensile direction (texture) influences the yield stress has been confirmed in wrought Mg alloys with a strong basal texture [19, 20].

Similar to M2, MX21 (Fig. 3b) presents a pronounced anisotropy as a function of the tensile direction. For M2, the shape of the curves was still similar despite the anisotropy, but not for MX21. MX21 shows no significant strain rate sensitivity apart from the pronounced anisotropy (also different shapes of curves). The UTS is by far the highest and the elongations the lowest. It is remarkable that only the

stress–strain curve of the specimen in TD shows yield instability at the yield point independent of the strain rate, while the specimen in ED shows a typical strain hardening behaviour. It can be assumed that the pronounced yield stress is achieved by interaction of particles or solute and dislocations (hypothetically also twin formation). This suggests that, in addition to the Mn particles, finely dispersed Ca particles are also distributed in the matrix. One reason for this anisotropy is the texture. Due to the split peak in the basal pole figure and almost no orientation in the transverse direction, flow in the extrusion direction is mainly possible, which enables a relatively high fracture strain of almost

16%. Owing to the low number of active slip planes in the transverse direction, the shape of the curve shows high strength values and rapid hardening [21–23].

The lowest anisotropy is found in ME21 (Fig. 3c). There is nearly no difference in stress and strain in TD and ED. In general, the mechanical properties and the curve shape, which is a classical continuous transition from elastic to plastic deformation and a continuous decrease of the slope during strain hardening, are comparable to MX21 in ED. A slight strain rate sensitivity can be seen in the elongation. A higher fracture strain in TD and ED tends to be achieved at a lower strain rate. In the case of uniform strain in TD and ED and strength in ED, no influence of the strain rate is visible. The lower anisotropy of the ME21 alloy seems to be closely related to the quadruple basal poles [24].

In general, the Ca- and RE-added alloys have higher TYS and UTS. The strengthening behaviour of the alloys can probably be attributed to the presence of dispersed phases. Solid solution hardening can also be a reason for the higher strengths.

Figure 4 shows the force–displacement curves during the Erichsen test at room temperature with different forming speeds of 5 mm/min (fast) and 0.5 mm/min (slow).

M2 shows a clear difference of the force–displacement curve as a function of the forming speed. The force increases more slowly with a lower forming speed. A longer deformation path is achieved and a higher force at fracture. MX21 and ME21 do not show this behaviour depending on the forming speed. This has already been observed in the tensile tests. Looking at the hardening behavior, MX21 and ME21

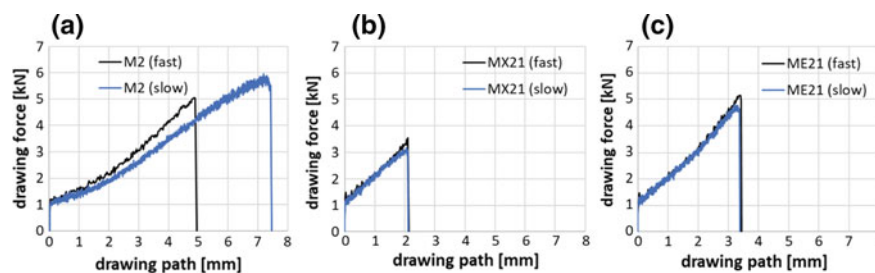
have a maximum force of approximately 2 kN after 1 mm drawing path, whereas M2 is only slightly above 1 kN.

Figure 5 summarises the values in the form of the Erichsen value (IE). In addition, a representative test result is shown. This IE corresponds to the drawing length until the fracture of the sample, i.e. the depth of the cup formed by biaxial stretching.

MX21 has the lowest IE with 2.2 (fast) and 2.1 (slow). This result can be understood as a result of the pronounced mechanical anisotropy which is attributed from the texture.

ME21 has slightly higher values with 3.2 and 3.4. Actually, this sample provides the weak texture with basal pole split in ED and TD that is acknowledged for a good formability. Also the mechanical properties, weak anisotropy, and high elongation (almost 20%) let expect better IE. The reason for the low IE value could be the high amount of secondary phases (stringer) or a work hardened condition.

M2 alloy has the strongest deformation speed dependence of IE values, i.e. 4.8 mm for fast forming and 7.3 mm for slow forming speed. In fact, with a strong alignment of the basal planes ((0001) fiber parallel to ND) like in M2, the ability to activate the basal slip is lower in the tensile test as well as in the Erichsen test. Hence, a high stress and a low elongation are expected under such condition. M2 shows exactly the opposite behaviour. The tensile tests show very high elongation and low stress level. The IE is also by far the highest (independent of the strain rate). Accordingly, it can be presumed that in the case of M2, basal slip is not the dominant deformation mechanism. It can be assumed that grain boundary sliding is the main deformation mechanism,



**Fig. 4** Force versus path curves in Erichsen tests at room temperature with different forming rate 5 mm/min (fast) and 0.5 mm/min (slow) for M2 (a), MX21 (b), ME21 (c)

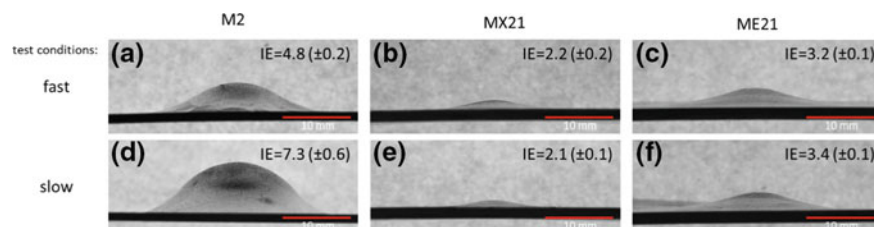


**Fig. 5** Specimens after the Erichsen test at room temperature with a forming rate of 5 mm/min (fast) (M2 (a), MX21 (b), ME21 (c)) and 0.5 mm/min (slow) (M2 (d), MX21 (e), ME21 (f))

since a strong strain rate sensitivity has also been observed. It has already been shown that binary Mn alloys exhibit a  $m$ -value above 0.3 at low strain rate. This suggests that grain boundary sliding is activated [25].

## Summary

The influence of Ca and RE addition on the forming behaviour of 2 wt% Mn alloy was investigated in terms of axial and biaxial deformation with strain rate variation. The alloys were directly extruded at the lower limit of the process window. This resulted in a partially recrystallized microstructure in all three alloys. The extrusion of the Ca or RE added alloys require a significantly high temperature, in comparison with the binary alloy.

In addition, the strong (0001) fiber texture parallel to ND in the M2 alloy altered to a weak texture with basal pole split in the ED in MX21 alloy, while a quadrupole basal texture is formed in the ME21 alloy. The M2 alloy shows a clear influence of the strain rate on the mechanical behaviour, which indicates grain boundary sliding as a controlled mechanism. This behaviour is not observed in the Ca- and RE-added alloys, but a significant increase in strength.

## References

- Chino Y, Sassa K, Mabuchi M (2009) Texture and stretch formability of a rolled Mg–Zn alloy containing dilute content of Y. *Materials Science and Engineering: A* 513–514:394–400
- Bohlen J, Yi S, Letzig D et al. (2010) Effect of rare earth elements on the microstructure and texture development in magnesium–manganese alloys during extrusion. *Materials Science and Engineering: A* 527:7092–7098
- Stanford N (2010) The effect of calcium on the texture, microstructure and mechanical properties of extruded Mg–Mn–Ca alloys. *Materials Science and Engineering: A* 528:314–322
- Stanford N, Barnett MR (2008) The origin of “rare earth” texture development in extruded Mg-based alloys and its effect on tensile ductility. *Materials Science and Engineering: A* 496:399–408
- Zeng Z, Nie JF, Xu SW et al. (2017) Super-formable pure magnesium at room temperature. *Nat Commun* 8:972
- Figueiredo RB, Poggiali FSJ, Silva CLP et al. (2015) The influence of grain size and strain rate on the mechanical behavior of pure magnesium. *Journal of Materials Science* 51:3013–3024
- Somekawa H, Kinoshita A, Washio K et al. (2016) Enhancement of room temperature stretch formability via grain boundary sliding in magnesium alloy. *Materials Science and Engineering: A* 676:427–433
- Klaumünzer D, Hernandez JV, Yi S et al. (2019) Magnesium Process and Alloy Development for Applications in the Automotive Industry. In: Joshi VV, Jordon JB, Orlov D, Neelameggham NR (eds) *Magnesium Technology* 2019. Springer International Publishing, Cham, p 15–20
- Elsayed FR, Hort N, Salgado Ordorica MA et al. (2011) Magnesium Permanent Mold Castings Optimization. *Materials Science Forum* 690:65–68
- Kree V, Bohlen J, Letzig D et al. (2004) The Metallographical Examination of Magnesium Alloys. *Practical Metallography* 41:233–246
- Bachmann F, Hielscher R, Schaeben H (2010) Texture Analysis with MTEX – Free and Open Source Software Toolbox. *Solid State Phenomena* 160:63–68
- Zeng X, Minárik P, Dobroň P et al. (2019) Role of deformation mechanisms and grain growth in microstructure evolution during recrystallization of Mg–Nd based alloys. *Scripta Materialia* 166:53–57
- Brokmeier H-G (2018) Hot Rectangular Extrusion Textures of Six Mg-Alloys Via Neutron Diffraction. *Advanced Engineering Materials* 20:1700234
- Somekawa H, Singh A (2018) Superior room temperature ductility of magnesium dilute binary alloy via grain boundary sliding. *Scripta Materialia* 150:26–30
- Styczynski A, Hartig C, Bohlen J et al. (2004) Cold rolling textures in AZ31 wrought magnesium alloy. *Scripta Materialia* 50:943–947
- Al-Samman T, Li X (2011) Sheet texture modification in magnesium-based alloys by selective rare earth alloying. *Materials Science and Engineering: A* 528:3809–3822
- Stanford N (2013) The effect of rare earth elements on the behaviour of magnesium-based alloys: Part 2 – recrystallisation and texture development. *Materials Science and Engineering: A* 565:469–475
- Yi S, Brokmeier HG, Letzig D (2010) Microstructural evolution during the annealing of an extruded AZ31 magnesium alloy. *Journal of Alloys and Compounds* 506:364–371
- Somekawa H, Kinoshita A, Kato A (2017) Great room temperature stretch formability of fine-grained Mg–Mn alloy. *Materials Science and Engineering: A* 697:217–223
- Agnew SR, Duygulu Ö (2005) Plastic anisotropy and the role of non-basal slip in magnesium alloy AZ31B. *International Journal of Plasticity* 21:1161–1193
- Bohlen J, Cano G, Drozdenko D et al. (2018) Processing Effects on the Formability of Magnesium Alloy Sheets. *Metals* 8:147
- Gall S, Coelho RS, Müller S et al. (2013) Mechanical properties and forming behavior of extruded AZ31 and ME21 magnesium alloy sheets. *Materials Science and Engineering: A* 579:180–187
- Bohlen J, Nürnberg MR, Senn JW et al. (2007) The texture and anisotropy of magnesium–zinc–rare earth alloy sheets. *Acta Materialia* 55:2101–2112
- He J, Jiang B, Xu J et al. (2017) Effect of texture symmetry on mechanical performance and corrosion resistance of magnesium alloy sheet. *Journal of Alloys and Compounds* 723:213–224
- Somekawa H, Basha DA, Singh A (2018) Room temperature grain boundary sliding behavior of fine-grained Mg–Mn alloys. *Materials Science and Engineering: A* 730:355–362



# The Effect of Plastic Deformation on the Precipitation Hardening Behavior of Biodegradable Mg–Sr–Ca–Zn Based Alloys

Matteo Nicolosi, Baoqi Guo, Mihriban Pekguleryuz, and Mert Celikin

## Abstract

In this study, the precipitation hardening behaviour of Mg–Sr–Ca–Zn based alloy system with trace additions was investigated. The as-cast microstructure was found to be composed of Mg<sub>2</sub>(Ca, Sr) interdendritic phases surrounding the  $\alpha$ -Mg matrix. The effect of temperature as well as initial plastic deformation on the precipitation hardening behaviour was analyzed via ageing treatments. More effective age-hardening response was achieved via ageing at 150 °C both in as-cast and deformed samples. Prior plastic deformation resulted in changes in precipitation kinetics.

## Keywords

Magnesium alloy • Age hardening • Dynamic precipitation • Microstructural characterization

## Introduction

To date, bone healing after severe fractures is mainly facilitated by implanting permanent fixation devices such as pins, screws, and plates. These are typically made of permanent materials (e.g. stainless steel, cobalt-chromium, and titanium) that may cause long-term erosion, infection, or lack of growth in orthopaedic applications [1–4]. Therefore, after healing, a second operation is required to remove them. Mg based biodegradable alloys have shown promising results due to their good biocompatibility. However, high initial

bio-corrosion rates of current state of the art Mg-alloys lead to the loss of mechanical integrity prior to the completion of healing [1]. Biodegradable implants should provide high corrosion resistance and strength while needed, and subsequently dissolve.

Most common Mg-alloys, which contain aluminium (Al) and Rare-earths (RE), exhibit good mechanical properties as well as corrosion resistance. However, they are reported to be harmful for the human health [5]. As a consequence, recent studies have been focusing more on alloying additions naturally present in the human body such as Ca, Zn, Mn, Li, Si, and Sr, which reduce risks associated with toxicity. Prior studies have confirmed that additions of Ca, Sr, and Ca + Sr at specific levels improve the bio-degradation resistance of Mg-alloys but lack mechanical strength [5, 6]. Recently, Zn and Mn additions have been found to be beneficial in increasing bio-corrosion resistance, as well as mechanical performance, in Mg–Ca based systems [7, 8]. Previous works have also highlighted that, in Mg–Ca alloys the corrosion resistance decreases with increasing secondary phases (Mg<sub>2</sub>Ca) [9]. On the other hand, the formation of more dispersed secondary phases through the performing of heat-treatments has been proven to be responsible for reducing the micro-galvanic effect and increasing mechanical properties [7].

Calcium (Ca) is a fundamental element present in human bones and the release of Ca ions is beneficial to the bone healing process [10]. Zinc (Zn), on the other hand, influences both mechanical properties and corrosion resistance of the alloy. The effect of Zn content is studied for Mg–Zn–Mn alloys and it was found that for compositions between 0 and 3 wt% the grain size decreases and the mechanical properties consequently increase remarkably [10]. Oh et al. characterised the precipitation process and nanoscale precipitates occurring during age hardening for the ternary system Mg–Ca–Zn [11]. They identified the composition Mg-0.3Ca-0.3Zn to be the composition capable of leading to the maximum hardness upon age hardening, with any further addition in Zn leading to a lower final hardness.

M. Nicolosi · M. Celikin (✉)  
School of Mechanical and Materials Engineering, University  
College Dublin, Belfield, Dublin 4, Ireland  
e-mail: [mert.celikin@ucd.ie](mailto:mert.celikin@ucd.ie)

B. Guo · M. Pekguleryuz  
McGill University, Mining and Materials Engineering, 3610  
University St., Wong Bldg., Rm 2140, Montreal, QC H3A 2B2,  
Canada  
e-mail: [mihriban.pekguleryuz@mcgill.ca](mailto:mihriban.pekguleryuz@mcgill.ca)

They attributed this to the fact that Zn is effective in enhancing the results of age hardening only as an additive to the Mg-0.3Ca alloy, rather than as a constituent alloying element. Strontium has also been investigated as potential alloying element for Mg-alloys in biodegradable implant applications. Being a Group II element, it behaves in a similar manner to Ca and can be found in hydroxyapatite and other biomedical compounds as its substitute [12, 13]. Secondly, Strontium Ranelate (SR) is responsible for bone mineral intensity improvement as well as bone strengthening [14]. Moreover, from a mechanical point of view, Sr acts as grain refiner due to the formation of compounds at the grain boundaries [15]. A recent study by Brar et al. [16] investigated the effect of Zn concentration in Mg-Zn-Sr alloys to the age-hardening behaviour. Upon ageing at 180 °C, increase in Zn content increased age-hardening response.

The aim of this study is to understand the age-hardening behaviour of Mg-Sr-Ca-Zn based alloy system with trace additions. The effects of temperature and plastic deformation on the age-hardening behaviour are investigated.

## Experimental Procedure

Mg-Ca-Sr-Zn alloys prepared using commercial purity Mg, Mg-Ca (30%wt) master alloy, pure Zn and Sr. The alloy composition is given in weight % unless otherwise stated. Pure Mg was melted using an induction furnace under a protective atmosphere of CO<sub>2</sub> + 0.5%SF<sub>6</sub>. Mg-Ca master alloy was added at around 700 °C. Upon holding for 10–15 min, Sr and Zn added. The melt was cast from a temperature of 720 °C into a boron nitride coated steel mould (pre-heated to 400 °C) to produce plate castings of 130 mm × 100 mm × 7 mm. The chemical composition of the alloy is given in Table 1.

Specimens were prepared by cutting thin (approximately 3 mm thick) slices of material from the cast billets using a low speed diamond cutting saw. SEM analysis was conducted at 15 kV via FEI Quanta 3D FEG Dual Beam scanning electron microscope (SEM) and with a Hitachi TM4000Plus table-top SEM. Prior to imaging, the samples were ground using grinding paper with increasing grit size, up to a final size of 2500. To avoid oxidation of the surface,

the specimens were cleaned using iso-propyl alcohol. After grinding, the samples were polished up to 1 μm diamond suspension and iso-propyl alcohol as lubricant. Compositional results obtained by EDS analysis from five different measurements performed on five different areas of the samples. Age-hardening treatments were carried out using a WhipMix Pro 200 Series Furnace at 423 and 473 K. After the isothermal hold, the specimens were immediately quenched in chilled tap water. As-cast and heat-treated samples were tested for hardness after each step of the isothermal treatment using a Mitutoyo AVK-C2 Vickers hardness tester applying a load of 2 kg. Seven different measurements were performed for each sample at every ageing step. After hardness tests were completed, samples were ground up to 2500 grit in order to remove all indentations before the next step of the isothermal treatment.

## Results and Discussion

The SEM micrographs of the as-cast Mg-0.3Ca-0.3Sr-0.1Zn alloy revealed a typical microstructure with interdendritic phases surrounding the α-Mg matrix. EDS point analyses (Table 2) conducted on both interdendritic regions and the matrix. Dendritic regions were found to be rich in Ca and Sr.

The elemental analysis of the as-cast interdendritic phase (Table 2), revealed Ca to Sr ratio is approximately ~1/6 for the Mg-0.3Ca-0.3Sr-0.1Zn alloy. By comparison with previous studies (Table 3), it was therefore possible to identify the potential phase as Mg<sub>2</sub>(Ca, Sr). Authors previous works showed that Mg<sub>2</sub>(Ca, Sr) phase has hcp structure with lattice parameters  $a = 6.36 \text{ \AA}$  and  $c = 10.01 \text{ \AA}$  [17].

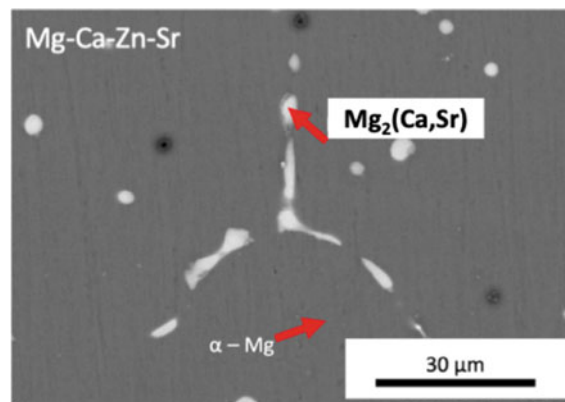
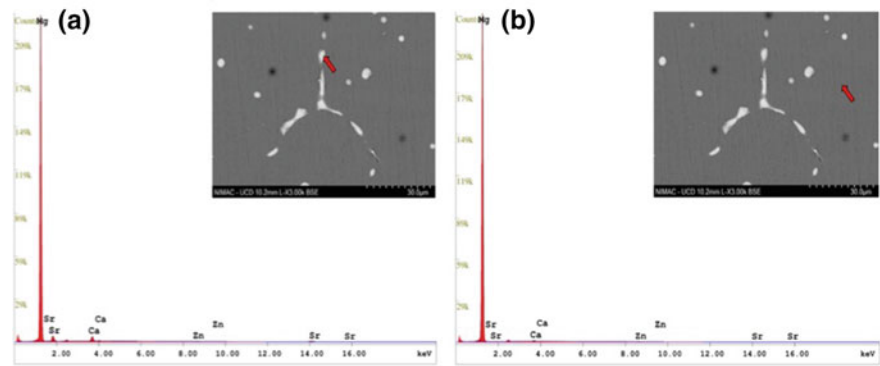


**Fig. 1** SEM image of as-cast Mg-0.3Ca-0.3Sr-0.1Zn alloy

**Table 1** Elemental composition obtained via ICP

Element	Ca	Sr	Zn	Mg
	0.33	0.33	0.13	Bal.

**Fig. 2** EDS spectra acquired from. **a** Interdendritic regions and **b** matrix



## Age-Hardening Treatment

Figure 3 shows the precipitation hardening response of the Mg-0.3Ca-0.3Sr-0.1Zn alloy upon isothermally aged at 150 and 200 °C for different durations. Vickers hardness in the as-cast form was 37.7  $H_V$ ; when heat-treated at 150 °C, after 240 min the hardness peaked at 44.50  $H_V$ ; whereas, when heat-treated at 200 °C, after 120 min the hardness reached the maximum value of 42.60  $H_V$ . Higher peak hardness values were obtained for ageing temperature of 150 °C compared to 200 °C. Moreover, consistent with increased

precipitation kinetics, higher ageing temperature shortened the duration to achieve maximum hardness.

Figure 4 shows the precipitation hardening response of the plastically deformed Mg-0.3Ca-0.3Sr-0.1Zn alloy when isothermally treated at 150 and 200 °C for different durations. Due to the increased dislocation density, as-cast hardness, prior to the performing of any isothermal treatments, was higher than that reported for the as-cast samples. Similar to as-cast condition, ageing at 150 °C leads to more effective hardening compared to 200 °C. Moreover, slightly higher peak hardness value found in age-hardened samples with prior deformation (49.4) in comparison to as-cast alloy

**Table 2** EDS analysis from interdendritic phase and matrix

Alloy system	Mg (wt%)	Ca (wt%)	Zn (wt%)	Sr (wt%)
Mg-0.3Ca-0.3Sr-0.1Zn (interdendritic phase)	92.06 (SD 1.05)	2.22 (SD 0.83)	0.46 (SD 0.09)	5.73 (SD 1.29)
Mg-0.3Ca-0.3Sr-0.1Zn (matrix)	98.90 (SD 0.14)	0.69 (SD 0.06)	0.16 (SD 0.02)	0.25 (SD 0.14)

**Table 3** Crystal structure of Ca and Sr containing intermetallic compounds

Phase	Prototype	Space group	Pearson symbol	Comments	References
Ca–Sr	Cu	cF4	Fm $\bar{3}$ m	$Ca_{(1-x)}Sr$ , $x = 0-1$ at 298 K	[18]
Ca–Sr	Mg	hP2	$P6_3/mmc$	$Ca_{(1-x)}Sr$ , $x = 0-1$ at 698 K	[18]
Ca–Sr	W	cI2	Im $\bar{3}$ m	$Ca_{(1-x)}Sr$ , $x = 0-1$ at 903 K	[18]
Interdendritic $Mg_2(Ca, Sr)$	$MgZn_2$	hP12	$P6_3/mmc$	$a = 6.212$ , $c = 10.050$	[19]
Interdendritic $Mg_2(Ca, Sr)$	(C14-leaves)			$a = 6.36$ , $c = 10.01$ Ca/Sr = 1/6	[17]
Globular Ca–Sr (Mg)	–	–		hcp ( $a = 6.42$ , $c = 9.44$ ) Ca/Sr = 3/2	[17]

**Fig. 3** Age-hardening response of Mg-0.3Ca-0.3Sr-0.1Zn alloy at 150 and 200 °C

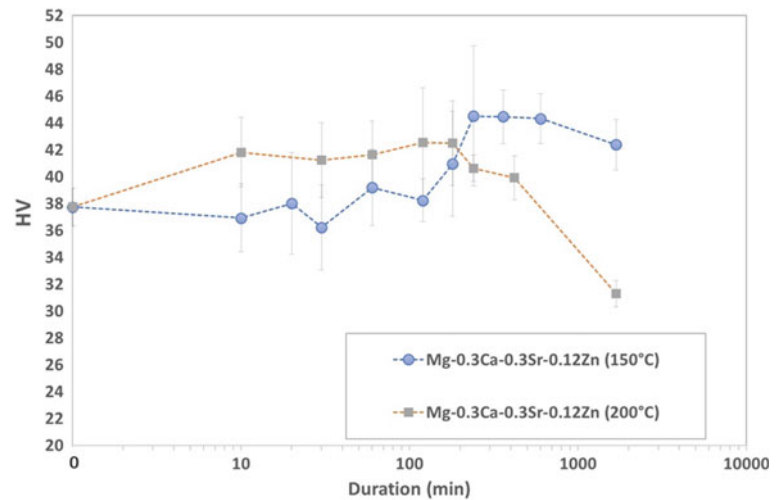
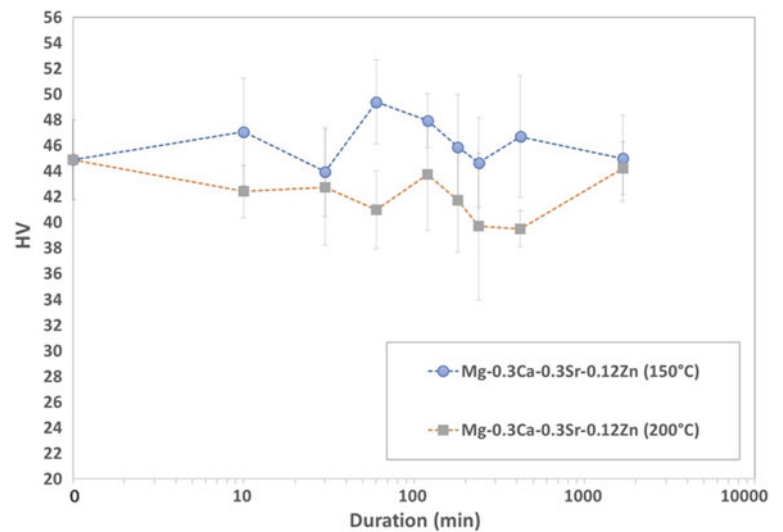


**Fig. 4** Age-hardening response of pre-deformed Mg-0.3Ca-0.3Sr-0.1Zn alloy at 150 and 200 °C



(44.5). Precipitation kinetics have changed due to the increased density of dislocations in deformed sample. Duration to achieve peak hardness is shortened, hence it can be stated that dislocations enhanced the nucleation/growth rate of precipitates.

## Conclusions

Age-hardening behaviour of Mg-0.3Ca-0.3Sr-0.1Zn alloy was investigated both in as-cast and deformed conditions. Mg<sub>2</sub>(Ca, Sr) intermetallic phase was found to be covering dendritic regions around  $\alpha$ -Mg matrix. It was determined that in both as-cast and deformed conditions, isothermal hardening at 150 °C was more effective for precipitation hardening in comparison to 200 °C. Prior plastic deformation increased the rate of nucleation and growth kinetics of precipitates.

## References

1. M. P. Staiger, A. M. Pietak, J. Huadmai, and G. Dias, "Magnesium and its alloys as orthopedic biomaterials: A review," vol. 27, pp. 1728–1734, 2006.
2. A. Pietak, P. Mahoney, G. J. Dias, and M. P. Staiger, "Bone-like matrix formation on magnesium and magnesium alloys," pp. 407–415, 2008.
3. D. A. Puleo and W. W. Huh, "Acute Toxicity of Metal Ions in Cultures of Osteogenic Cells Derived from Bone Marrow Stromal Cells," pp. 109–116, 1995.
4. B. Y. J. Jacobs, M. D. J. L. Gilbert, D. Ph, and R. M. Urbant, "Current Concepts Review Corrosion of Metal Orthopaedic Implants," pp. 268–282, 1998.
5. W. Jiang *et al.*, "In vitro evaluation of MgSr and MgCaSr alloys via direct culture with bone marrow derived mesenchymal stem cells," *Acta Biomater.*, vol. 72, pp. 407–423, 2018.
6. H. B. Henderson, V. Ramaswamy, A. E. Wilson-heid, M. S. Kesler, J. B. Allen, and M. V Manuel, "Mechanical and degradation property improvement in a biocompatible Mg- Ca-Sr alloy by thermomechanical processing," *J. Mech. Behav. Biomed. Mater.*, vol. 80, no. July 2017, pp. 285–292, 2018.



7. Y. Zhang, J. Li, and J. Li, "Effects of microstructure transformation on mechanical properties, corrosion behaviors of Mg-Zn-Mn-Ca alloys in simulated body fluid," *J. Mech. Behav. Biomed. Mater.*, vol. 80, no. July 2017, pp. 246–257, 2018.
8. D. Hyun, B. Woo, J. Young, K. Mox, and I. Min, "Effect of Mn addition on corrosion properties of biodegradable Mg-4Zn-0.5Ca-xMn alloys," *J. Alloys Compd.*, vol. 695, pp. 1166–1174, 2017.
9. Z. Li, X. Gu, S. Lou, and Y. Zheng, "The development of binary Mg-Ca alloys for use as biodegradable materials within bone," *Biomaterials*, vol. 29, no. 10, pp. 1329–1344, 2008.
10. N. Li and Y. Zheng, "Novel Magnesium Alloys Developed for Biomedical Application: A Review," *J. Mater. Sci. Technol.*, vol. 29, no. 6, pp. 489–502, 2013.
11. J. C. Oh, T. Ohkubo, T. Mukai, and K. Hono, "TEM and 3DAP characterization of an age-hardened Mg – Ca – Zn alloy," vol. 53, pp. 675–679, 2005.
12. R. V. Suganthi, K. Elayaraja, M. I. A. Joshy, V. S. Chandra, E. K. Girija, and S. N. Kalkura, "Fibrous growth of strontium substituted hydroxyapatite and its drug release," *Mater. Sci. Eng. C*, vol. 31, no. 3, pp. 593–599, 2011.
13. W. Zhang *et al.*, "Effects of strontium in modified biomaterials," *Acta Biomater.*, vol. 7, no. 2, pp. 800–808, 2011.
14. S. G. Dahl *et al.*, "Incorporation and distribution of strontium in bone," *Bone*, vol. 28, no. 4, pp. 446–453, 2001.
15. X. Zeng, Y. Wang, W. Ding, A. A. Luo, and A. K. Sachdev, "Effect of strontium on the microstructure, mechanical properties, and fracture behavior of AZ31 magnesium alloy," *Metall. Mater. Trans. A Phys. Metall. Mater. Sci.*, vol. 37, no. 4, pp. 1333–1341, 2006.
16. H. Brar, J. Wang, and M. V Manuel, "Investigation of the mechanical and degradation properties of Mg–Sr and Mg–Zn–Sr alloys for use as potential biodegradable implant materials," *J. Mech. Behav. Biomed. Mater.*, pp. 87–95, 2012.
17. M. Bornapour, M. Celikin, M. Cerruti, and M. Pekguleryuz, "Magnesium implant alloy with low levels of strontium and calcium: The third element effect and phase selection improve bio-corrosion resistance and mechanical performance," *Mater. Sci. Eng. C*, vol. 35, no. 1, pp. 267–282, 2014.
18. P. Villars, *Pearson's Handbook, Desk Edition: Crystallographic Data for Intermetallic Phases*, vol. 1. ASM international Materials Park, OH, 1997.
19. Y. Zhong, "Investigation in Mg-Al-Ca-Sr-Zn System by Computational Thermodynamics Approach Coupled with First-Principles Energetics and Experiments," no. December, 2005.

# Experimental Investigation of Raster Tool Path Strategy for Friction Stir Processing of Magnesium Alloy

Abhishek Kumar, Nikhil Gotawala, Aarush Sood,  
Sushil Mishra, and Amber Shrivastava

## Abstract

Friction stir processing is an emerging method for refining the grain structure of the metals. Single pass friction stir processing of magnesium alloys has been reported in the literature, and very few works address the multi-pass friction stir processing. However, most of the studies are limited to a very small region and do not show the properties of complete processed blank. In the present work, a raster tool path strategy is adopted to modify the microstructure of the as-cast magnesium alloy. The tool rotation direction and tool shoulder overlap are varied to process the magnesium samples. The microstructural evolution of the processed samples is investigated. Experimental observations show that raster scan parameters significantly affect the microstructural variation within each sample and across the samples. Based on the findings, a raster tool path strategy is proposed for grain refinement without any defect in the processed region.

## Keywords

Friction stir processing • Magnesium • Defects

## Introduction

Friction stir processing (FSP) is an advanced technique used for refining grains in metals and alloys. In general, grain refinement in metals leads to improvement in ductility, formability, and superplasticity [1–4]. Magnesium is lighter than aluminum and steel. This makes Mg useful towards weight reduction of structural components. However, due to limited

workability of Mg, most of the Mg alloy components are cast structures. FSP is a promising technology for improving the mechanical properties of Mg alloys. Darras et al. [5] showed the effect of various process parameters on the microstructural characteristics of a Mg alloy. Authors reported finer grains and homogenized microstructure in the stir zone. A significant yield strength reduction in stir zone was observed by Woo et al. [6], for FSP of a Mg alloy. Chang et al. [7] successfully achieved ultrafine grains of 100–300 nm in size, by controlling the cooling rate during FSP of Mg alloys. Further, a relationship between Zener–Holloman parameters and grain size for AZ31 is developed by Chang et al. [8]. Raja et al. [9] performed multi-pass FSP of AZ91 and analyzed the effect of layered microstructure on superplasticity. Many other works have reported the enhancement of mechanical properties of Mg alloys upon FSP [10–15]. However, most of these efforts are based on single pass FSP. For the case of multi-pass FSP, most of the reported work is performed with aluminum alloys [16–20]. A very few attempts are made to study the effect of multi-pass strategy on Mg alloys. Sharifitabar et al. [12] investigated multi-pass strategy for FSP of Mg alloy. However, the tool overlap between passes was 100%, *i.e.*, FSP tool processed the same region over successive passes. The multi-pass strategy of FSP introduces tool overlap between successive passes as an additional process parameter, compared to single pass FSP. Further depending on the tool rotation direction, the advancing side (AS) and retreating side (RS) would switch between the base material (not yet processed) and the already processed material (in the previous pass owing to tool overlap). This can significantly influence the defect formation/propagation during FSP. The raster scanning pattern for multi-pass strategy is deployed in this work. The present work focuses on two different raster scanning patterns: unidirectional raster and bidirectional raster for FSP of a complete workpiece blank. The objective of this work is to investigate the effect of tool rotation direction and tool overlap on the defect formation/propagation and microstructural development, during multi-pass FSP with raster scanning patterns of Mg alloy. Based on the findings, a

A. Kumar

Department of Metallurgical Engineering and Materials Science,  
Indian Institute of Technology Bombay, Mumbai, India

N. Gotawala · A. Sood · S. Mishra · A. Shrivastava (✉)

Department of Mechanical Engineering, Indian Institute of  
Technology Bombay, Mumbai, India

e-mail: [ashrivastava.me@iitb.ac.in](mailto:ashrivastava.me@iitb.ac.in)

raster tool path strategy is proposed for grain refinement without any defect in the processed region.

## Experimental Methods

### Materials

The as-cast Mg alloy was received in the form of a billet with 120 mm diameter. This billet was sliced into 3 mm thick blanks. The chemical composition of the as-received material is given in Table 1.

A hexagonal FSP tool made of H13 tool steel is used in this study. The tool geometry is shown in Fig. 1.

### Tool Path Strategy

In this work, a raster type tool path strategy is adopted. The schematic representations of different raster scanning patterns: unidirectional and bidirectional raster are shown in Fig. 2. For both the raster scanning patterns, the FSP tool started at the outer periphery of the Mg blank, as shown in Fig. 2. For bidirectional raster scanning pattern, the FSP tool travels in a straight line and performs a u-turn as it approaches the end of the blank along the straight line. Upon completing the u-turn, the FSP tool travels in the opposite direction as compared to the previous pass (Fig. 2a). For unidirectional raster scanning pattern, the FSP tool travels in a straight line and leaves the blank at the end of the straight line. Then, FSP tool travels in air and takes position next to the starting point of the previous pass (dashed lines in Fig. 1b), for plunging and next pass. The FSP tool overlap determines the distance between the consecutive passes. In this tool path strategy, the FSP tool travels in the same direction during all the passes.

### Friction Stir Processing

Mg blanks were friction stir processed with four different combinations of tool path strategies and tool shoulder overlap. First Mg blank was processed with bidirectional raster tool path strategy. One half of this Mg blank was processed with 60% tool shoulder overlap and other half with and 80%. Second Mg blank was processed with unidirectional raster tool path strategy. One half of this Mg blank was processed with 80% tool shoulder overlap and

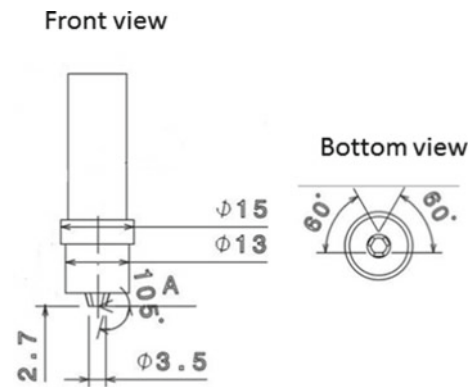


Fig. 1 FSP tool geometry (linear dimensions in mm)

other half with 90% tool shoulder overlap. For all these experiments, the FSP tool travel speed was 50 mm/min, and tool rotation speed was 1000 rpm in clockwise direction.

### Microstructural Characterization

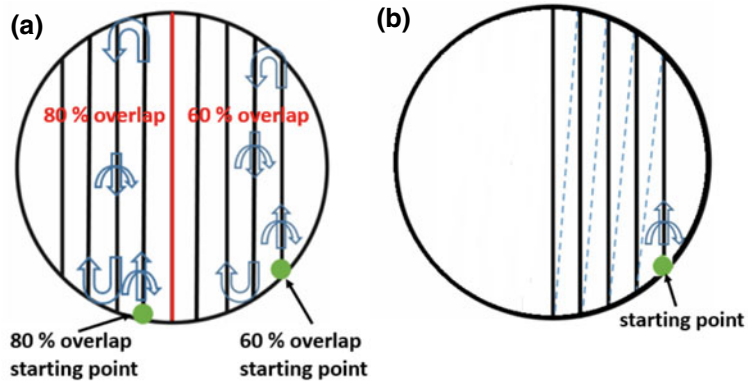
To observe the microstructural changes, samples were prepared from each processed blank, by polishing and etching the cross-sections. Zeiss optical microscope was used at low magnification, to create the montage images for observing the complete cross-sections and overlapping stir zones. Based on the optical images, regions were identified for electron back scattered diffraction (EBSD) analysis. For EBSD analysis, samples were polished with SiC paper and further electro-polished. Zeiss Gemini scanning electron microscope (SEM) equipped with OXFORD fast CCD detector was used for EBSD.

## Results and Discussion

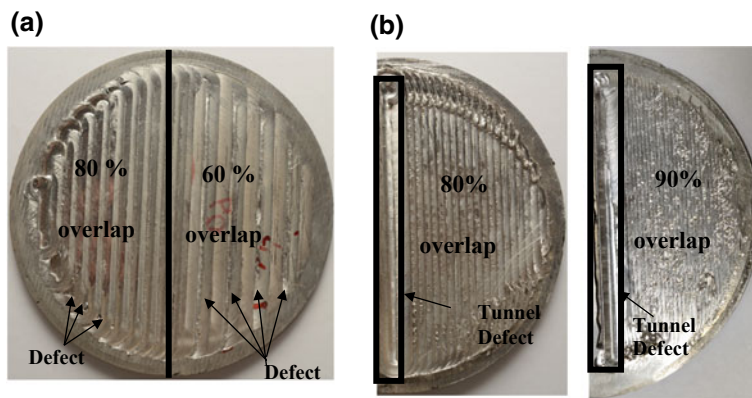
Figure 3 shows the processed Mg blanks. The Mg blank in Fig. 3a was processed with bidirectional tool path strategy, such that the tool shoulder overlap was 60% for one half and 80% for second half of the blank. Defects were observed over each pass for both 60 and 80% tool shoulder overlap with bidirectional tool path strategy. So, the tool shoulder overlap was increased to 80 and 90% for Mg blank processed with unidirectional tool path strategy (Fig. 3b). Figure 4 shows the microstructure of the as-received Mg. Large grains with an average grain size of about 250  $\mu\text{m}$  are observed, due to as-cast nature of the material.

Table 1 Element composition of material

Element	Al	Zn	Na	Mn	Fe	Ce	Mg
Weight %	3	0.018	0.022	0.446	0.058	0.2	Remaining



**Fig. 2** a Bidirectional raster pattern, b unidirectional raster pattern



**Fig. 3** Processed blank with. a Bidirectional and b unidirectional raster tool path strategy

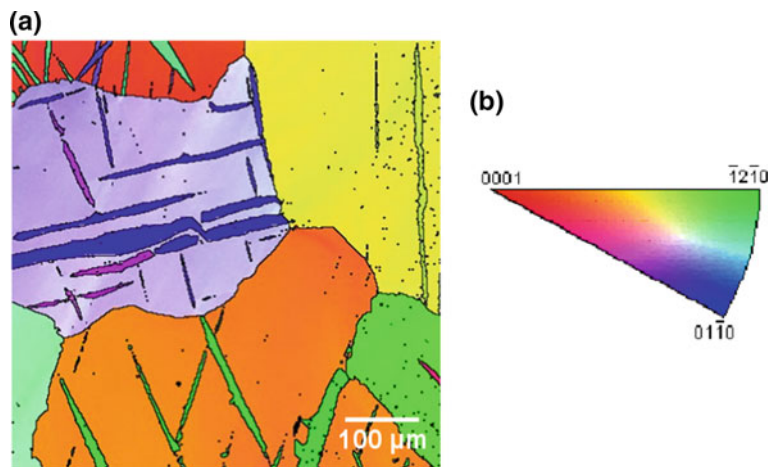


**Fig. 4** IPF map of as-cast magnesium

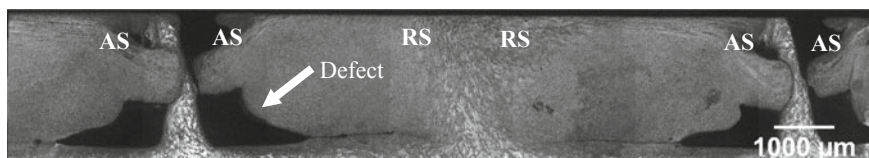


**Fig. 5** Blank processed at 60% tool shoulder overlap and bidirectional raster tool path



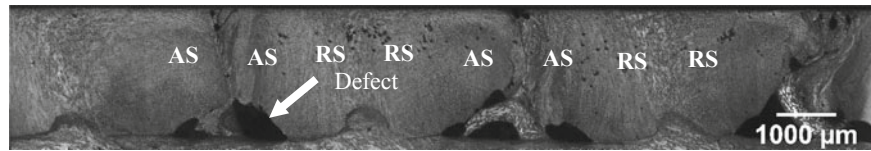


**Fig. 6** Blank processed at 80% tool shoulder overlap and bidirectional raster tool path

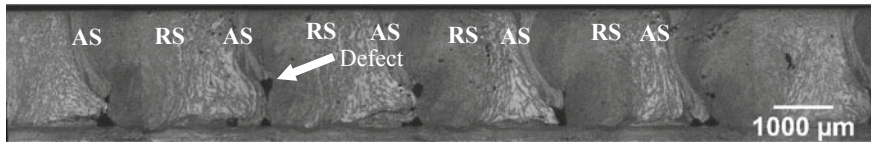


**Fig. 7** Blank processed at 80% tool shoulder overlap and unidirectional raster tool path

Figure 5 shows the cross-section of the blank section processed at 60% tool shoulder overlap with bidirectional raster tool path strategy. It can be noticed that defects are formed at the advancing side. There is also some unprocessed region with 60% tool shoulder overlap. Figure 6 shows the cross-section of the blank section processed at 80% tool shoulder overlap with bidirectional raster tool path strategy. With 80% tool shoulder overlap, defect size is smaller in comparison with 60% tool shoulder overlap, and unprocessed region is also reduced. Figures 7 and 8 show the cross-section of the blank sections processed at 80 and 90% tool shoulder overlap with unidirectional raster tool path strategy. It can be noticed that defects and unprocessed regions are observed at 80% tool shoulder overlap. However, defect size is very small in comparison with the blank section processed at the same tool shoulder overlap with bidirectional raster tool path strategy. No defects are observed in the bulk of the Mg blank, at 90% tool shoulder overlap with unidirectional raster tool path strategy. However, a tunnel defect is observed over the last pass for the samples processed at both the tool shoulder overlaps (80 and 90%) with unidirectional raster tool path strategy.

It is observed that the size of unprocessed region reduces with increase in tool shoulder overlap, for both raster scan patterns. The stir zone is the widest at the top and narrows down towards the bottom of the FSP tool pin. This geometry of stir zone would lead to unprocessed regions in between passes. With increase in tool shoulder overlap, the size of the unprocessed region would reduce. At very high tool shoulder overlaps, the stir regions from consecutive passes would come together or may overlap, leading to no unprocessed region. Larger tool shoulder overlaps would also lead to higher temperatures during FSP, which improves the material movement and results in wider stir zones. This further suppress the unprocessed regions. At larger tool shoulder overlaps, relatively higher temperatures and improved

material movement also limit the size of the defect formed during FSP. This is very well captured by the experimental observations, as the size of tunnel defect reduces with increase in tool shoulder overlap, for both raster scan patterns.

Depending on the tool rotation direction, the advancing side and retreating side would switch between the base material (not yet processed) and the already processed material (in the previous pass owing to tool overlap). The tunnel defects form at the advancing side during FSP. Therefore, it would be advantageous to set the tool rotation direction such that the advancing side is towards the base material (not yet processed). For bidirectional raster tool path strategy, the advancing sides from two consecutive passes come together (Figs. 5 and 6). This would lead to the accumulation of defects (in the processed blank) formed at the advancing sides over the consecutive passes. For unidirectional raster tool path strategy, the advancing side of the previous pass overlaps with the retreating side of the current pass (Figs. 7 and 8). This offers the opportunity to fill the defects formed in the previous pass. This is very well captured by the experimental results, as the defect size formed during FSP with bidirectional tool path is very small in comparison with the unidirectional tool path, for same tool shoulder overlap of 80%. Given sufficient tool shoulder overlap between passes, all the defects from the previous pass would be filled during the current pass, and fresh defects may form at the advancing side of the current pass. That is, the defects would keep shifting towards the base material with each pass, and a tunnel defect would be present only for the last pass. This is very well captured by the experiments as no defects are observed in the blank's bulk (Fig. 8), and a tunnel defect is observed for the last pass (Fig. 3b).

Banded regions are observed in the processed Mg blank without defects (Fig. 8). These are formed due to localised

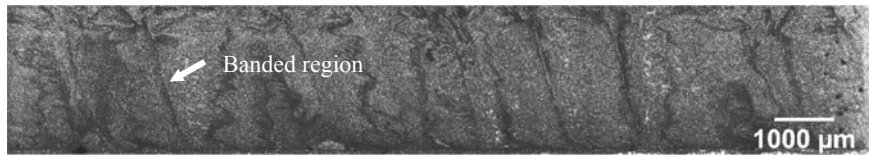


**Fig. 8** Blank processed at 90% tool shoulder overlap and unidirectional raster tool path

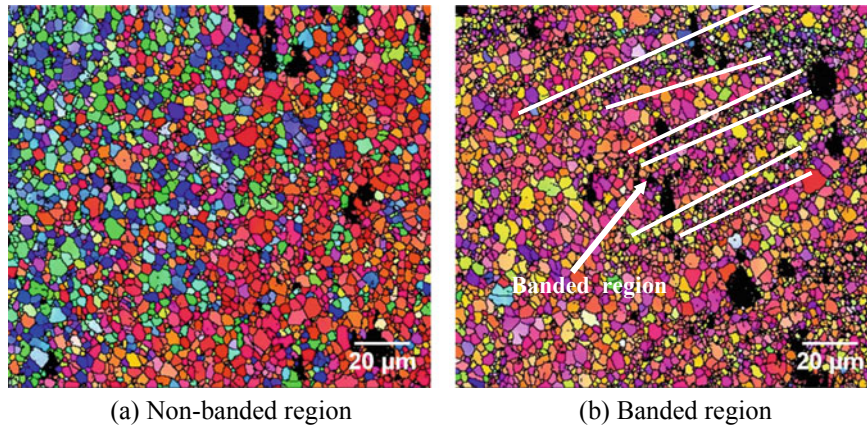


**Fig. 9** EBSD of blank processed at 90% tool shoulder overlap and unidirectional raster tool path

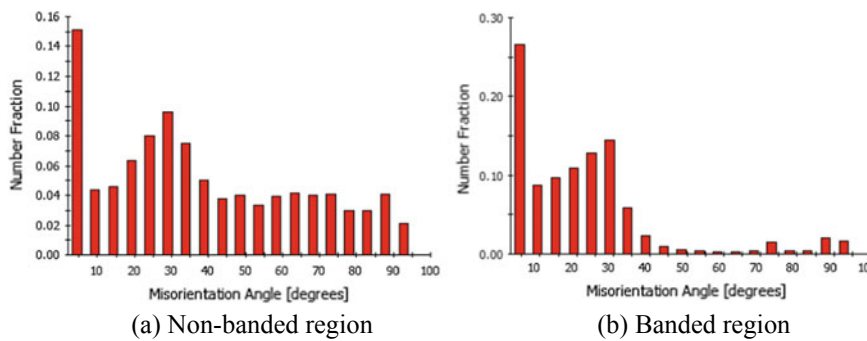


**Fig. 10** Misorientation angle

deformation of material [21]. Figure 9a, b show the EBSD images of non-banded and banded regions observed in the Mg blank processed at 90% tools shoulder overlap with unidirectional tool path strategy. These figures indicate highly textured structure in the stir zone. The grain size is much smaller as compared to the as-received (as-cast) material. Figure 9b reveals very small grains in the banded region. This is due to the high strain rate deformation. Figure 10a, b shows the misorientation angle of non-banded and banded regions, respectively. A large fraction of grains have misorientation angle less than 30°. Average misorientation angles of non-banded and banded regions are 38.29° and 21.66°. These results show that upon dynamic recrystallization, lower angle grain boundaries were formed.

## Conclusions and Future Work

In the present work, two raster tool path strategies: unidirectional and bidirectional, are used to friction stir process the Mg blanks. Based on the microstructural characterization, the following conclusions are drawn:

1. The size of unprocessed region and defects reduces with increase in the tool shoulder overlap, for both tool path strategies.
2. During bidirectional raster tool path strategy, the advancing and retreating sides switch between the base material and processed material, with each pass. This restricts the outward propagation (towards base material)

of the defects on the advancing side, leading to the accumulation of the defects in the processed blank.

3. During unidirectional raster tool path strategy, advancing side from the previous pass coincides with the retreating side of the current pass. This leads to the filling of the defects formed during the previous pass.
4. At sufficiently large tool shoulder overlap with unidirectional raster tool path strategy, defects formed during the previous pass are completely filled by the current pass, leading to a defect free processed blank bulk.
5. A banded region per pass with fine grains is observed for processed Mg blank without defects, indicating severe plastic deformation near FSP tool pin due to high strain rate.

The workpiece blanks can also be friction stir processed with a spiral tool path strategy. The microstructural evolution upon FSP with raster tool path strategy is expected to be more anisotropic as compared to the spiral tool path strategy. This is owing to the alignment of the consecutive FSP passes in same direction during FSP with raster tool path strategy. Further microstructural and mechanical tests are required to study the extent of anisotropy observed in the specimens friction stir processed with raster tool path strategy.

## References

1. S. Mironov, T. Onuma, Y. S. Sato, and H. Kokawa, "Microstructure evolution during friction-stir welding of AZ31 magnesium alloy," *Acta Mater.*, vol. 100, pp. 301–312, 2015.
2. N. Kumar, D. Choudhuri, R. Banerjee, and R. S. Mishra, "Strength and ductility optimization of Mg-Y-Nd-Zr alloy by microstructural design," *Int. J. Plast.*, vol. 68, pp. 77–97, 2015.
3. J. Q. Su, T. W. Nelson, and C. J. Sterling, "Grain refinement of aluminum alloys by friction stir processing," *Philos. Mag.*, vol. 86, no. 1, pp. 1–24, 2006.
4. M. Azizieh, R. Bahadori, M. Abbasi, E. Y. Yoon, and H. S. Kim, "Effect of friction stir processing on the microstructure of pure magnesium castings," *Int. J. Cast Met. Res.*, vol. 28, no. 6, pp. 345–351, 2015.
5. B. M. Darras, M. K. Khraisheh, F. K. Abu-Farha, and M. A. Omar, "Friction stir processing of commercial AZ31 magnesium alloy," *J. Mater. Process. Technol.*, vol. 191, no. 1–3, pp. 77–81, 2007.
6. W. Woo, H. Choo, M. B. Prime, Z. Feng, and B. Clausen, "Microstructure, texture and residual stress in a friction-stir-processed AZ31B magnesium alloy," *Acta Mater.*, vol. 56, no. 8, pp. 1701–1711, 2008.
7. C. I. Chang, X. H. Du, and J. C. Huang, "Achieving ultrafine grain size in Mg-Al-Zn alloy by friction stir processing," *Scr. Mater.*, vol. 57, no. 3, pp. 209–212, 2007.
8. C. I. Chang, C. J. Lee, and J. C. Huang, "Relationship between grain size and Zener-Holloman parameter during friction stir processing in AZ31 Mg alloys," *Scr. Mater.*, vol. 51, no. 6, pp. 509–514, 2004.
9. A. Raja, P. Biswas, and V. Pancholi, "Effect of layered microstructure on the superplasticity of friction stir processed AZ91 magnesium alloy," *Mater. Sci. Eng. A*, vol. 725, no. January, pp. 492–502, 2018.
10. L. Huang, K. Wang, W. Wang, J. Yuan, K. Qiao, T. Yang, P. Peng, and T. Li, "Effects of grain size and texture on stress corrosion cracking of friction stir processed AZ80 magnesium alloy," *Eng. Fail. Anal.*, vol. 92, no. June, pp. 392–404, 2018.
11. A.M. Jamili, A. Zarei-Hanzaki, H.R. Abedi, P. Minarik and R. Soltani, "The microstructure, texture, and room temperature mechanical properties of friction stir processed Mg-Y-Nd alloy," *Mater. Sci. Eng. A*, pp. 244–253, 2017.
12. M. Sharifitabar, M. Kashefi, and S. Khorshahian, "Effect of friction stir processing pass sequence on properties of Mg-ZrSiO<sub>4</sub>-Al<sub>2</sub>O<sub>3</sub> surface hybrid micro/nano-composites," *Mater. Des.*, vol. 108, pp. 1–7, 2016.
13. F. Khan and S. K. Panigrahi, "Achieving excellent thermal stability and very high activation energy in an ultra fine-grained magnesium silver rare earth alloy prepared by friction stir processing," *Mater. Sci. Eng. A*, vol. 675, pp. 338–344, 2016.
14. N. Kumar, R. S. Mishra, N. B. Dahotre, R. E. Brennan, K. J. Doherty, and K. C. Cho, "Effect of friction stir processing on microstructure and mechanical properties of laser-processed Mg 4Y 3Nd alloy," *Mater. Des.*, vol. 110, pp. 663–675, 2016.
15. S. Arokiasamy and B. Anand Ronald, "Experimental investigations on the enhancement of mechanical properties of magnesium-based hybrid metal matrix composites through friction stir processing," *Int. J. Adv. Manuf. Technol.*, vol. 93, no. 1–4, pp. 493–503, 2017.
16. Y. Chen, H. Ding, S. Malopheyev, R. Kaibyshev, Z. Cai, and W. Yang, "Influence of multi-pass friction stir processing on microstructure and mechanical properties of 7B04-O Al alloy," *Trans. Nonferrous Met. Soc. China (English Ed.)*, vol. 27, no. 4, pp. 789–796, 2017.
17. Y. Chen, H. Ding, J. Li, Z. Cai, J. Zhao and W. Yang, "Influence of multi-pass friction stir processing on the microstructure and mechanical properties of Al-5083 alloy," *Mater. Sci. Eng. A*, vol. 650, pp. 281–289, 2016.
18. S. K. Singh, R. J. Immanuel, S. Babu, S. K. Panigrahi, and G. D. Janaki Ram, "Influence of multi-pass friction stir processing on wear behaviour and machinability of an Al-Si hypoeutectic A356 alloy," *J. Mater. Process. Technol.*, vol. 236, pp. 252–262, 2016.
19. N. Nadammal, S. V. Kailas, J. Szpunar, and S. Suwas, "Microstructure and Texture Evolution during Single- and Multiple-Pass Friction Stir Processing of Heat-Treatable Aluminum Alloy 2024," *Metall. Mater. Trans. A Phys. Metall. Mater. Sci.*, vol. 48, no. 9, pp. 4247–4261, 2017.
20. M. M. El-Rayes and E. A. El-Danaf, "The influence of multi-pass friction stir processing on the microstructural and mechanical properties of Aluminum Alloy 6082," *J. Mater. Process. Technol.*, vol. 212, no. 5, pp. 1157–1168, 2012.
21. K. N. Krishnan, "On the formation of onion rings in friction stir welds," *Mater. Sci. Eng. A*, vol. 327, pp. 246–251, 2002.

# Quantitative Relationship Analysis of Mechanical Properties with Microstructure and Texture Evolution in AZ Series Alloys

Joung Sik Suh, Byeong-Chan Suh, Jun Ho Bae, Sang Eun Lee, Byoung-Gi Moon, and Young Min Kim

## Abstract

The present study investigated the correlation between microstructure, texture, and mechanical properties of AZ31 sheets. In magnesium alloys, microstructural and texture factors have a decisive influence on mechanical properties due to their specific  $c/a$  ratios for hexagonal close-packed structure. It is well known that the yield strengths of Mg alloys are followed by the Hall–Petch relation. Nevertheless, AZ-based sheets with relatively large grain size exhibit higher yield strength than those with finer microstructure. This is mainly due to the texture strengthening. For this reason, there is an increasing need to quantify the contribution of texture and microstructure to mechanical properties in Mg alloys. A multiple regression analysis is conducted to explore the quantitative correlation of the mechanical properties with the microstructure and texture factors, such as grain size, phase fraction of secondary particles, maximum intensity of basal poles, and Schmid factor for basal  $\langle a \rangle$  slip. This study focuses on evaluating quantitatively the relative weights of microstructure and texture evolution such as grain refinement and texture weakening, when determining yield strength depending on loading direction at room temperature.

## Keywords

Magnesium • Microstructure • Texture • Mechanical properties • Regression analysis

## Introduction

Magnesium (Mg) and its alloys in hexagonal close-packed structure have the limited number of active slip systems at room temperature [1]. Typical wrought Mg alloys such as AZ series develop strong basal texture during rolling [2]. This texture with a preferred orientation, where the basal planes are parallel to the sheet plane, causes mechanical anisotropy and poor formability at room temperature [3]. The limited formability of Mg alloy sheets is one of the main reasons hindering industrial applications. Grain refinement and texture modification can improve the forming characteristics of Mg alloys [4].

Grain boundary strengthening is an important strengthening mechanism in Mg alloys [5]. It is well known that grain refinement significantly improves mechanical properties, especially yield strength (YS). Empirical Hall–Petch-type relationships [6, 7] have been successfully developed for Mg alloys. Nonetheless, these relationships are highly sensitive to the material history, especially with respect to texture [5]. For this reason, a simple Hall–Petch relation cannot adequately capture the grain size dependence of strength [5]. Furthermore, texture also plays a considerable role in determining YS, because of their insufficient deformation mechanisms in Mg alloys. Strengthening or weakening of basal texture can result in an increase or decrease in YS, respectively. In particular, the preferred orientation and formation of basal texture are directly related to the activity of basal slip regarding the loading direction. Basal slip is the softest mechanism for plastic deformation available in Mg alloys. It is responsible for accommodating a significant fraction of the total plastic strain at room temperature [5]. Basal slip in Mg and its alloys clearly abides by the Schmid’s law: When the stress on the slip plane and along the slip direction reaches a critical value, slip ensues [8]. Thus, Schmid factor is a useful indicator for analyzing the activation of a certain slip system with respect to the

J. S. Suh (✉) · B.-C. Suh · J. H. Bae · S. E. Lee · B.-G. Moon · Y. M. Kim  
Advanced Metals Division, Korea Institute of Materials Science, Changwon, 51508, Republic of Korea  
e-mail: [jssuh@kims.re.kr](mailto:jssuh@kims.re.kr)



loading direction. Maximum pole intensity can also characterize the degree of the preferred orientation of basal texture. Moreover, the fraction and distribution of secondary particles lead to impeding dislocation motion, resulting in precipitation strengthening. Therefore, there is an increasing need to quantify the contributions and interactions of texture and microstructure development for YS of Mg alloys.

Regression is a popular statistical method, because it is used as a prediction tool to investigate the relationship between dependent and independent parameters [9]. Multiple regression analysis is one of the most efficient and powerful hypothesis testing techniques among all statistical methods [10]. This approach offers the advantage of investigating the relative importance of some predictor variables with respect to a response variable [10]. For this reason, regression methods have a variety of applications such as engineering, physics, chemical science, and medicine [9]. Especially, in the field of metallurgical engineering, the applications of data modeling are rapidly increasing to predict material properties [11] and optimize alloy compositions [12] and process conditions [12].

The present study investigates the correlation between microstructure, texture, and YS of AZ31 sheets. In Mg alloys, microstructural and texture factors play a decisive role in determining mechanical properties due to their specific  $c/a$  ratios for hexagonal close-packed structure. Multiple linear regression and multiple polynomial regression are performed to explore the quantitative correlation of the specific microstructure and texture factors with YS depending on loading direction: average grain size, phase fraction of secondary particles, maximum intensity of basal poles, and Schmid factor for basal  $\langle a \rangle$  slip regarding the tensile direction. Average grain size fraction of the second phases is associated with grain boundary strengthening and precipitation hardening, respectively. Maximum intensity of (0001) pole figure and its Schmid factor represent the strength of basal texture and activation of basal slip with respect to the tensile direction. This study aims to quantitatively evaluate the relative importance of microstructure and texture development such as grain refinement and texture weakening, when determining loading direction-dependent YS at room temperature.

## Materials and Methods

### Datasets and Descriptive Statistics

Multiregression analysis requires data that correctly represents the system. Experimental data on AZ31 sheets processed by various thermo-mechanical treatments were used in this study. The referred literatures investigate the microstructure and texture-dependent mechanical properties regarding the effect of equal channel angular pressing [13], differential speed extrusion [14], asymmetric porthole die extrusion [15], and extrusion combined with preforming [16]. They provide data on average grain size, maximum intensity of basal texture ( $I_{\max}$ ), Schmid factor for basal  $\langle a \rangle$  slip ( $m_{\text{basal}}$ ), and loading direction-dependent YS. On the other hand, there is a lack of quantitative data for the phase fraction of secondary particles (denoted as second phase). For this reason, the sum of phase fraction of total secondary particles is numerically calculated with FactSage v7.3 (CRCT–Thermalfact Inc. & GTT-Technologies) regarding the process conditions of the above-mentioned literatures. A total of 35 datasets are available, consisting of the input variables (average grain size, phase fraction of secondary particles, maximum intensity of basal texture, and Schmid factor for basal slip with respect to tensile direction) and the output variable (YS depending on tensile direction). For model development and validation, the 27 and 8 datasets are divided into training and testing data, respectively. The statistics of the training and testing data are tabulated in Tables 1 and 2, respectively. All the input and output variables were normalized between 0.1 and 0.9 as follows:

$$x_{\text{norm}} = 0.8(x - x_{\min}) / (x_{\max} - x_{\min}) + 0.1 \quad (1)$$

where  $x_{\text{norm}}$  is the normalized value of variable  $x$ .  $x_{\min}$  and  $x_{\max}$  are the minimum and maximum values of  $x$ , respectively.

### Multiple Regression Analysis

Multiple linear and polynomial regression calculates the best-fit line for one or more XY datasets. In addition, multiple regression is used to analyze the relationship between

**Table 1** Statistics of training dataset for predicting YS of AZ31 sheets

Variable		Minimum	Maximum	Mean	Standard deviation
Input	Grain size ( $\mu\text{m}$ )	4.80	17.20	9.77	6.24
	Second phase (%)	0.32	0.59	0.41	0.14
	$I_{\max}$ (m.r.d.)	5.60	16.60	10.96	5.50
	$m_{\text{basal}}$ (–)	0.16	0.35	0.23	0.10
Output	YS (MPa)	127.0	253.8	185.5	63.46

**Table 2** Statistics of testing dataset for predicting YS of AZ31 sheets

Variable		Minimum	Maximum	Mean	Standard deviation
Input	Grain size ( $\mu\text{m}$ )	4.80	17.20	9.79	6.24
	Second phase (%)	0.32	0.59	0.39	0.14
	$I_{\text{max}}$ (m.r.d.)	5.60	16.59	10.66	5.50
	$m_{\text{basal}}$ (-)	0.11	0.32	0.24	0.11
Output	YS (MPa)	142.1	244.4	184.0	51.43

multiple predictors and a response variable. For a given database, multiple linear regression (MLR) is the simplest way to predict the output, assuming that the output variable can be represented by a linear combination of input variables. The model for MLR is as follows:

$$y_i = \beta_0 + \beta_1 x_{i,1} + \beta_2 x_{i,2} + \dots + \beta_k x_{i,k} + \varepsilon_i \quad (2)$$

where  $y_i$  is the dependent variable for the  $i_{\text{th}}$  case,  $b_0$  is intercept,  $x_{i,k}$  is the  $k_{\text{th}}$  independent (predictor) variable,  $\beta_k$  is the regression coefficient, and  $\varepsilon_i$  is the random error component.

Multiple polynomial regression (MPR) analyzes the relationship between one dependent variable and two or more independent variables and by fitting a polynomial equation into the measured data. In this study, a quadratic polynomial regression model (e.g., for two variables) is selected to develop a statistical model for multiple independent variables:

$$y_i = \beta_0 + \beta_1 x_{i,1} + \beta_2 x_{i,2} + \beta_3 x_{i,1} x_{i,2} + \beta_4 x_{i,1}^2 + \beta_5 x_{i,2}^2 + \varepsilon_i \quad (3)$$

In the present study, the analyses with MLR and MPR are performed with Origin 2017 (OriginLab Corporation) using stepwise backward elimination with four independent variables.

## Performance Criteria

Three common metrics are used to evaluate the performance of regression model by calculating the differences between the measured and predicted YS: adjusted coefficient of determination ( $\text{Adj } R^2$ ), root mean square error (RMSE), and mean absolute error (MAE). The statistical parameters are defined as:

$$R^2 = 1 - \frac{\sum_{i=1}^n (y_i - \hat{y}_i)^2}{\sum_{i=1}^n (y_i - \bar{y}_i)^2} \quad (4)$$

$$\text{Adj } R^2 = R^2 - \frac{(1 - R^2)k}{n - (k + 1)} \quad (5)$$

$$\text{RSME} = \sqrt{\frac{1}{n} \sum_{i=1}^n (y_i - \hat{y}_i)^2} \quad (6)$$

$$\text{MAE} = \frac{100}{n} \sum_{i=1}^n |y_i - \hat{y}_i| \quad (7)$$

where  $\hat{y}_i$  presents the predicted value of the dependent variable by regression model,  $y_i$  is the measured one,  $\bar{y}_i$  is the mean of the dependent variable, and  $n$  is the number of datasets. The value of  $R^2$  is always between zero and one,  $0 \leq R^2 \leq 1$ . An  $R^2$  value of 0.9 or above is very good, a value above 0.8 is good, and a value of 0.6 or above may be satisfactory in some applications [17, 18]. If the calculated value of the MAE is less than 10%, it can be interpreted as a good and accurate prediction and a good prediction of 10–20%, an acceptable prediction of 20–50%, and a false prediction of 50% or more [19].

## Results and Discussion

Figure 1 shows the scatter matrix displaying linear fit between each input variable and tensile direction-dependent YS. For AZ31 sheets, it can be generally expected that grain size and texture strength among the individual variables have a dominant influence on YS considering the hardening mechanism of Mg alloys. According to the Hall–Petch relationship [6, 7], grain refinement leads to an increase in strength. Furthermore, strengthening or weakening of basal texture is associated with an increase or decrease in strength. Based on the thermodynamic calculations, the phase fraction of the secondary particles is very low, and thus, it is difficult to expect a hardening by dynamic precipitation of  $\text{Mg}_{17}\text{Al}_{12}$  phases. In this regard, the linear regression analysis indicates that grain size and second phase are not significantly related to the changes in YS as shown in Fig. 1. On the other hand,  $I_{\text{max}}$  and  $m_{\text{basal}}$  have a strong relationship with YS. Since the experimental data of the cited literatures deal with the tensile properties in the extrusion direction,  $45^\circ$ , and the transverse direction, it can be seen that basal texture plays a major role in determining YS. Based on this, multiple regression

**Fig. 1** Scatter matrix displaying linear fit between each input variable and YS in training datasets

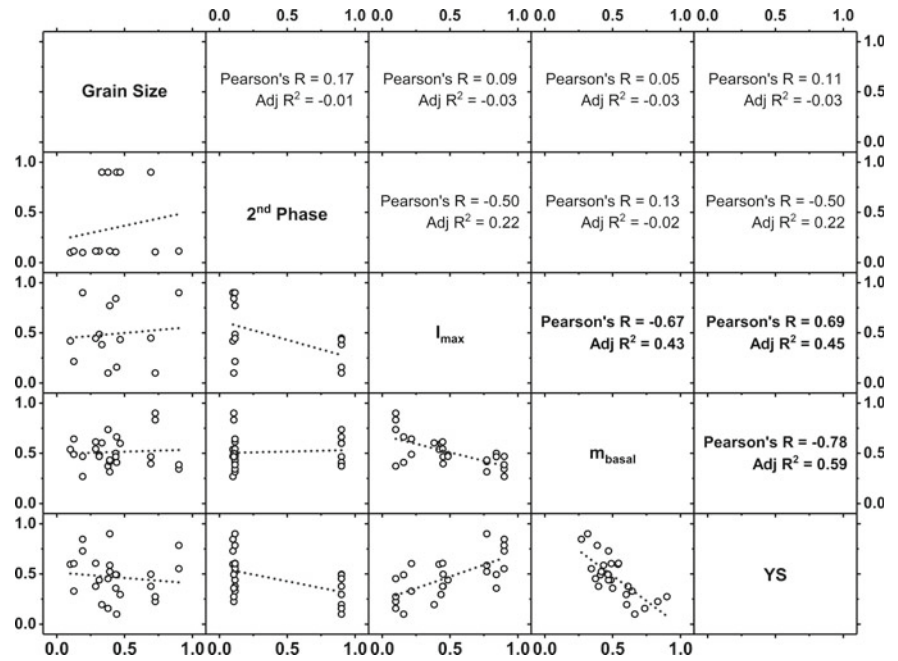


**Table 3** Results of ANOVA for different regression models

Model	Mean squares regression	Mean squares residual	F-value	p-value
MLR	0.39237	0.01156	33.94	1.01e-7
MPR	1.35231	0.01129	119.82	1.34e-14

analysis is performed using stepwise backward elimination with four independent variables.

Table 3 presents the results of analysis of variance (ANOVA) for different regression models. ANOVA provides information about the level of variation in the regression model and forms the basis for the significance test.  $F$ -value indicates that as the value deviates more from 1, the fitted model is more significantly different from the model  $y = \text{constant}$ . If the  $p$ -value for  $F$ -test is less than a certain level  $\alpha$  (usually be 5%), it can be concluded that the fitted

model differs significantly from the mean of the dependent variable. This can be inferred that the fitted model is a nonlinear curve or a linear curve with slope that is significantly different from zero. Based on this, each  $p$ -value is completely close to zero, so that each model fitted by MLR and MPR is acceptable.

Tables 4, 5, and 6 describe the results of MLR and MPR analysis. As a result of the backward elimination method, MLR and MPR achieve the best results with different combinations of the input variables. In case of MLR, the

**Table 4** Results of MLR analysis

Best parameter	Coefficient	Standard error	$t$ -value	$p$ -value
Intercept	1.04382	0.07657	13.63294	8.53e-13
Second phase	-0.2371	0.05758	-4.11735	3.92e-04
$m_{\text{basal}}$	-0.96044	0.14144	-6.79039	5.05e-07

**Table 5** Results of MPR analysis

Best parameter	Coefficient	Standard error	$t$ -value	$p$ -value
Intercept	1.85129	0.224	8.26454	3.43e-08
Grain size	-2.6258	0.58788	-4.46652	1.93e-04
$m_{\text{basal}}$	-2.08813	0.37932	-5.50488	1.57e-05
Grain size * $m_{\text{basal}}$	2.07418	0.64319	3.22482	3.90e-03
(Grain size) <sup>2</sup>	1.5295	0.40451	3.78111	1.03e-03

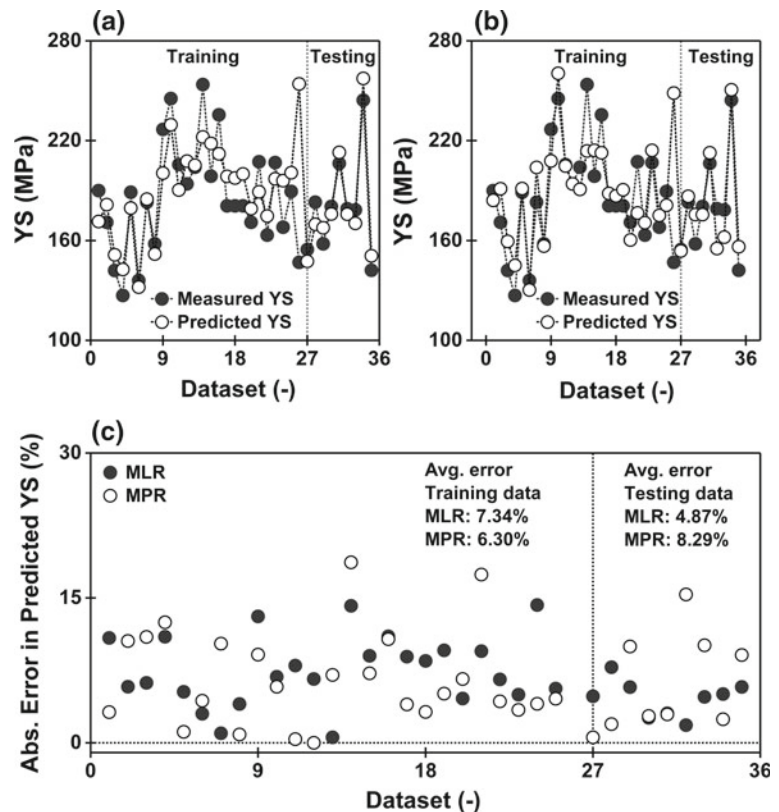
**Table 6** Adjusted  $R^2$  and error in training and testing datasets of MLR and MPR model

Model	Training data			Testing data		
	Adj $R^2$	RMSE	MAE	Adj $R^2$	RMSE	MAE
MLR	0.717	0.108	8.713	0.842	0.057	4.124
MPR	0.724	0.106	7.462	0.414	0.085	7.538

main predictors are second phase and  $m_{\text{basal}}$  with the  $p$ -value less than 0.05. Since  $I_{\text{max}}$  and  $m_{\text{basal}}$  correlate with each other, a regression model including both factors is not appropriate.  $I_{\text{max}}$  represents the overall intensity of texture, but not the distribution or orientation of the basal plane. For this reason,  $m_{\text{basal}}$ , which reflects the distribution of the basal plane and quantifies the degree of activation of the basal plane along the loading direction, is more suitable for predicting YS. Table 4 shows that only  $m_{\text{basal}}$  obtains a  $p$ -value less than 0.05 instead of  $I_{\text{max}}$ . On the other hand, the fraction of second phase is not correlated alone with YS, and hence, it is not expected to be included in multiple regression analysis. In addition, the correlation between the second phase and  $m_{\text{basal}}$  is very weak. This may reduce the reliability of MLR analysis. However, the coefficient of  $m_{\text{basal}}$  is 0.96, which is four times higher than that of the secondary phase fraction. That is, this supports that  $m_{\text{basal}}$  plays a major role in determining YS. Above all, the strongest merit of MLR analysis is to grasp the relative weight of each predictor intuitively.

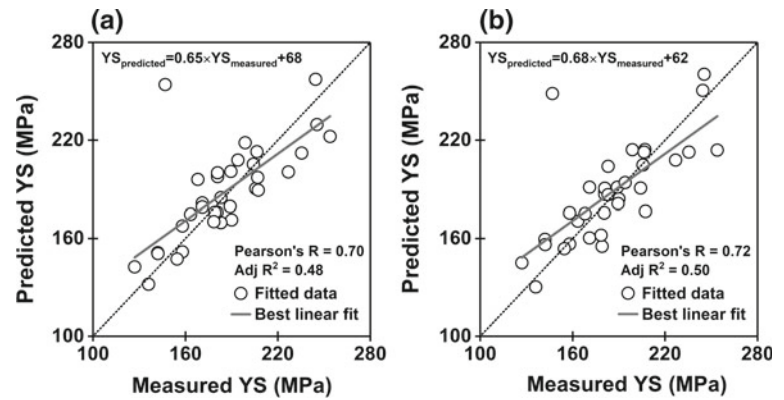
MPR has a best fit with a combination of grain size and  $m_{\text{basal}}$  through the backward elimination of four predictors. In Table 5, the coefficient of grain size,  $m_{\text{basal}}$  (grain size \*  $m_{\text{basal}}$ ) and (grain size)<sup>2</sup> have low  $p$ -value less than 0.05. Hence, these parameters can be considered to exert a significant effect on YS. Furthermore, the coefficient of determination implies how well the regression model predicts the response value. As listed in Table 6, Adj  $R^2$  of MLR and MPR with the training datasets is 0.717 and 0.724, respectively. So these two are almost identical. Moreover, MPR exhibits a relatively lower RMSE and MAE than those of MLR. On the other hand, MLR shows much better predictive performance than MPR within the testing datasets.

Nevertheless, it is difficult to assess which method is better given the comprehensive consideration of Figs. 2 and 3. According to the above-mentioned performance criteria, Fig. 2 presents that both models are satisfied with MAE value less than 10%. However, Fig. 3 shows that the efficiencies of both models with Adj  $R^2$  of  $\sim 0.5$  are not reliable for the entire datasets. Both models tend to overestimate YS

**Fig. 2** Comparison of the predicted YS with the measured value: **a** MLR, **b** MPR, and **c** MAE in predicted YS



**Fig. 3** Relationship between the measured and predicted YS:  
a MLR, b MPR



compared to the measurements. If the input variable changes, the output variable may increase and then decrease again. This characteristic is difficult to predict in both models in this study. For this reason, more flexible and general data modeling techniques are necessary to improve the accuracy and efficiency of regression models. In this respect, artificial neural network provides a powerful alternative to data modeling. As the next step, new research is underway on data modeling to predict the mechanical properties of Mg alloys based on microstructure and texture development using artificial neural network. Furthermore, it is essential to secure the data on the material properties that take into account process and deformation history to improve the reliability of predictive modeling.

## Conclusions

The present study investigates the correlation between microstructure, texture, and mechanical properties of AZ31 sheets. For this, a multiple regression analysis is performed to explore the quantitative correlation of the yield strength (YS) with the microstructure and texture factors: grain size, phase fraction of secondary particles, maximum intensity of basal poles, and Schmid factor for basal  $\langle a \rangle$  slip. The results of MLR and MPR models show that  $m_{\text{basal}}$  plays a dominant role in determining YS of AZ31 sheets in the collected datasets. However, both models have a tendency to overestimate YS compared to the measured values. Moreover, the efficiencies of two models with Adj  $R^2$  of  $\sim 0.5$  are not reliable in the total datasets. For this reason, more flexible and general data modeling techniques are necessary to improve the accuracy and efficiency of regression models. In this respect, artificial neural network provides a strong alternative to data modeling. Furthermore, it is vital to secure material property data with process and deformation history for improvement in the reliability of predictive modeling.

**Acknowledgements** This research was supported by the Fundamental Research Program (PNK6620) of the Korea Institute of Materials Science (KIMS).

## References

1. Nguyen NT, Seo OS, Lee CA, Lee MG, Kim JH, Kim HY (2014) Mechanical behavior of AZ31B Mg alloy sheets under monotonic and cyclic loadings at room and moderately elevated temperatures. *Mater* 7:1271–1295. <https://doi.org/10.3390/ma7021271>
2. Roberts CS (1960) Magnesium and its alloys. Wiley, New York
3. Styczynski A, Hartig CH, Bohlen J, Letzig D (2004) Cold rolling textures in AZ31 wrought magnesium alloy. *Scr Mater* 50:943–947. <https://doi.org/10.1016/j.scriptamat.2004.01.010>
4. Yi S, Bohlen J, Heinemann F, Letzig D (2010) Mechanical anisotropy and deep drawing behaviour of AZ31 and ZE10 magnesium alloy sheets. 58:592–605. <https://doi.org/10.1016/j.actamat.2009.09.038>
5. Agnew SR (2012) Deformation mechanisms of magnesium alloys. In: Bettles C, Barnett M (ed) *Advances in wrought magnesium alloys*; Woodhead Publishing Limited, Cambridge, pp 63–104
6. Hall EO (1951) The deformation and ageing of mild steel: III discussion of results. *Proc Phys Soc Sect B* 64:747–753.
7. Petch NJ (1953) The cleavage strength of polycrystals. *J Iron Steel Inst* 174:25–28
8. Schmid E, Boas W (1935) *Kristallplastizität*. Julius Springer, Berlin
9. Akhlaghi YG, Ma X, Zhao X, Shittu S, Li J (2019) A statistical model for dew point air cooler based on the multiple polynomial regression approach. *Energy* 181:868–881. <https://doi.org/10.1016/j.energy.2019.05.213>
10. Badgujara TY, Wani VP (2018) Stamping process parameter optimization with multiple regression analysis approach. *Mater Today-Proc* 5:4498–4507
11. Li CL, Narayana PL, Reddy NS, Choi SW, Yeom JT, Hong JK, Park CH (2019) Modeling hot deformation behavior of low-cost Ti–2Al–9.2Mo–2Fe beta titanium alloy using a deep neural network. *J Mater Sci Technol* 35:907–916 <https://doi.org/10.1016/j.jmst.2018.11.018>
12. Wu X, Zhang H, Cui H, Ma Z, Song W, Yang W, Jia L, Zhang H (2019) Quantitative relationship analysis of mechanical properties with Mg content and heat treatment parameters in Al–7Si alloys using artificial neural network. *Mater* <https://doi.org/10.3390/ma12050718>

13. Suh J, Victoria-Hernández J, Letzig D, Golle R, Volk W (2016) Effect of processing route on texture and cold formability of AZ31 Mg alloy sheets processed by ECAP. *Mater Sci Eng A* 669:159–170. <https://doi.org/10.1016/j.msea.2016.05.027>
14. Wang Q, Jiang B, Tang A, Ma S, Jiang Z, Chai Y, Liu B, Pana F (2017) Ameliorating the mechanical properties of magnesium alloy: role of texture. *Mater Sci Eng A* 689:395–403. <https://doi.org/10.1016/j.msea.2017.02.067>
15. Wang Q, Song J, Jiang B, Tang A, Chai Y, Yang T, Huang G, Pan F (2018) An investigation on microstructure, texture and formability of AZ31 sheet processed by asymmetric porthole die extrusion. *Mater Sci Eng A* 720:85–97. <https://doi.org/10.1016/j.msea.2018.02.055>
16. He J, Mao Y, Fu Y, Jiang B, Xiong K, Zhang S, Pan S (2019) Improving the room-temperature formability of Mg–3Al–1Zn alloy sheet by introducing an orthogonal four-peak texture. *J Alloys Compd* 797:443–445. <https://doi.org/10.1016/j.jallcom.2019.05.087>
17. Aczel AD (1989) *Complete business statistics*. McGraw-Hill Higher Education, Irwin
18. Ostertagová E (2011) *Applied statistic (in Slovak)*. Elfa Košice, Slovakia
19. Lewis CD (1982) *Industrial and business forecasting methods*. Butterworths, London

# On the Influence of Twinning and Detwinning on the Deformation of Mg at the Micron Scale

Mohammadhadi Maghsoudi, Gyuseok Kim, Markus Ziehmer, and Erica T. Lilleodden

## Abstract

The influence of twinning and detwinning on the constitutive mechanical response of Mg was investigated via microcompression tests of single-crystalline pillars of nominal [0001] and [10-10] orientations, and bicrystalline pillars containing a single  $\{10\bar{1}2\}$  twin boundary. The [0001] pillars exhibit the highest initial yield strength while the [10-10] and bicrystalline pillars initially yield at significantly lower stress, at which twin nucleation and growth or migration commence. Depending on the extent of straining, the [10-10] and bicrystalline pillars exhibit a secondary yield point associated with the deformation of the newly formed [0001] oriented pillar. The mechanical results point to an anisotropy in the mechanical consequence of twin motion, as characterized through the comparison of the three micropillar orientations; a twin-mediated hardening is indicated by the relative stress-strain behavior.

## Keywords

Micromechanics • Magnesium • Twinning • Work hardening

## Introduction

Deformation twinning plays an important role in Mg in order to satisfy the Taylor criterion during an arbitrary shape change [1, 2]. In particular, twinning modes can accommodate strain along with the [0001] direction; however, while tension along the [0001] axis leads to twinning, compression along the [0001] axis does not; pyramidal slip accommodates the strain along the [0001] axis during compression. That is to say, twinning is not symmetric. The effect of twinning, or more specifically twin migration, on the mechanical behavior of Mg has been studied [3–6], but a unified response is not yet well established. A pronounced increase of the hardening rate as a result of detwinning has been reported and discussed in terms of strong dislocation-twin boundary interactions [3, 4]. On the contrary, Cáceres et al. [5, 6], has argued that profuse twinning has little or no effect on the overall strain hardening behavior of Mg polycrystals, due to the weak role that twin boundaries play as a barrier to dislocations. Common to all of these experiments is that the reported strain hardening associated with detwinning (or twinning) may be strongly influenced by the polycrystallinity of the samples; neighboring grains lead to variations in the stress field and deformation constraints. A true assessment of mechanical behavior associated with twinning and detwinning, and any associated anisotropy, is best carried out on isolated single twin boundaries. In the present study, microcompression testing was used to explore twinning and detwinning in pure Mg and, more specifically, the influence of twinning and detwinning on the [0001] compression behavior.

## Experimental

A high purity Mg single crystal (99.99 wt% Mg) and a polycrystalline Mg (99.85 wt% Mg) sample with a very coarse grain size of  $\sim 700$ – $800 \mu\text{m}$  were mechanically

M. Maghsoudi (✉) · G. Kim · M. Ziehmer · E. T. Lilleodden  
Helmholtz-Zentrum Geesthacht, Institute of Materials Research,  
Materials Mechanics, 21502 Geesthacht, Germany  
e-mail: [Mohammadhadi.maghsoudi@hzg.de](mailto:Mohammadhadi.maghsoudi@hzg.de)

G. Kim  
Quattrone Nanofabrication Facility, University of Pennsylvania,  
3205 Walnut Street, Philadelphia, 19104, PA, USA

E. T. Lilleodden  
Hamburg University of Technology, Institute of Advanced  
Ceramics, 21073 Hamburg, Germany

ground and polished using standard metallographic procedures. The single-crystal sample was prepared with a surface normal of [10-10]. The polycrystalline sample was characterized using electron backscatter diffraction (EBSD) in order to identify orientations of interest for pillar preparation. Specifically, a region with surface normal orientated close to the [0001] containing a twinned region with a rotation of the  $c$ -axis of about  $86^\circ$  around the  $[2\bar{1}10]$  axis was identified. The twinned region has a surface normal close to the [10-10].

Micropillars were fabricated in the selected regions using focused ion beam (FIB) milling with an FEI Nanolab 200 Dualbeam scanning electron and FIB microscope with a Ga ion source. An annular milling protocol with an accelerating voltage of 30 kV and varying currents was used. Final milling was carried out using a single pass, annular milling step using a beam current of 0.5 nA. Specifically, micropillars with approximate diameters of 4  $\mu\text{m}$  and height to diameter ratio of about 3 were fabricated in the single crystalline regions, and at the twinned region in order to create bicrystalline micropillars. A nominally fixed diameter was chosen in order to circumvent well-known size effects. The micropillar orientations are shown schematically in Fig. 1a, showing the inclination of the twin boundary. In order to ensure an accurate assessment of the micropillar geometry, a FIB-milled cross-section through the center of a sacrificial column is carried out, as introduced by Lilleodden [7]. The pillar is first covered with a thin Pt layer in order to protect the surface and allow clear identification of the edges of the pillar. Then a cross-section is made using live secondary electron imaging during the milling process so that the milling is terminated as soon as the mid-point of the pillar is reached. The resultant 2D image of the pillar cross-section provides the highest accuracy for measuring the height and diameter of the pillar. This is shown in Fig. 1b.

The microcompression tests were conducted with a Nanoindenter XP (Agilent) equipped with a flat-ended conical indenter with a 10  $\mu\text{m}$  diameter circular punch

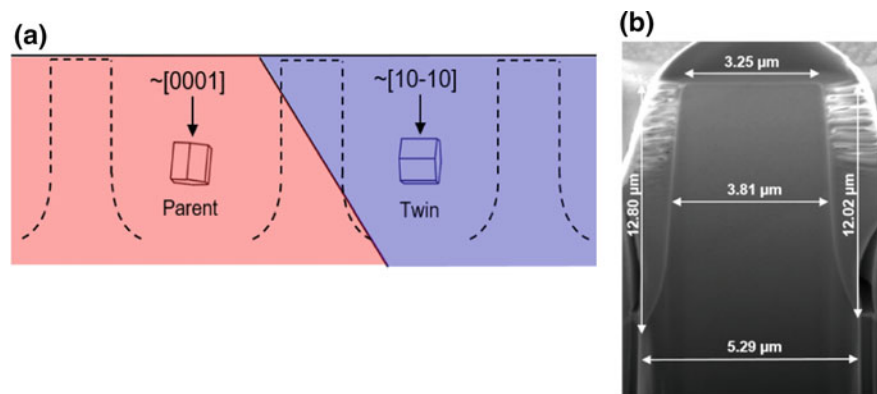
using a constant displacement rate of 0.01  $\mu\text{m/s}$  to different targeted engineering strains. The height of the pillar and mid-height diameter, as shown in Fig. 1, were used to calculate the engineering stress and strain, as described elsewhere [8]. In order to identify and compare the yield strengths of the pillars, the approach of Kupka et al. [8] was adopted. Here, a critical reduction to 45% of the peak value of the slope of the load-displacement curve was used as a criterion to define the point of yield and the corresponding stress is taken as the yield strength. *Post mortem* microstructural characterization was performed on cross-sections of the deformed microcolumns using a FIB lift-out technique. EBSD measurements were performed at 15 kV acceleration voltage and 2.2 nA beam current using an EDAX/TSL detector operating in a FEI Nanolab 200 Dualbeam microscope at a working distance of 10 mm. The EDAX OIM Analysis<sup>TM</sup> 7 software was used to process the EBSD data.

## Results and Discussion

Representative engineering stress-strain curves associated with the microcompression of single crystalline [0001], [10-10] and the bicrystalline micropillars to an approximate strain of 10% are presented in Fig. 2.

All three orientations show fairly smooth and overlapping initial loading curves. The [0001] micropillar reaches the highest initial stress, at around 210 MPa at which point a small strain burst occurs followed by a jerky-like hardening regime and then a massive strain burst at a stress level of around 365 MPa. In the case of [0001] compression, twinning does not occur, but rather the activation of up to six equivalent pyramidal  $\pi_2$  slip systems having  $\langle c+a \rangle$  Burgers vector is suggested in the literature to account for the axial strain and strain [7]. This is supported by direct observation of the active slip systems achieved through transmission electron microscopy [9, 10]. The reorientation due to plastic deformation combined with the increasing

**Fig. 1** **a** Schematic illustration of fabricated micropillars inside the parent grain, twin grain and at the twin boundary, **b** FIB cross-section of a sacrificed micropillar showing the geometry of a typical sample prior to deformation





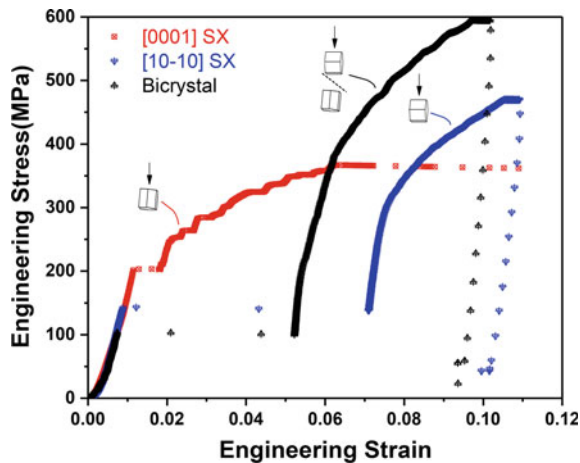


**Fig. 2** Engineering stress-strain curves for [0001] single crystal, [10-10] single crystal and bicrystalline micropillars compressed to 10% strain. SX points to single crystal

applied stress due to hardening finally leads to a massive strain burst associated with basal slip, as already described by Lilleodden [7].

The mechanical response of the single-crystalline [10-10] pillars also show smooth, largely elastic loading up to a stress of nearly 150 MPa. At this critical stress a large strain extension to a strain of around 6% occurs. Upon continued loading, the stress is shown to linearly increase followed by secondary yield and strain hardening. A similar response is found for the bicrystalline pillars. The stress increases linearly up to a stress plateau of around 100 MPa, at which the strain extends to 4%, and then the stress shows a steep increase up to a secondary yield point and strain hardening. Compared to the bicrystalline and [10-10] single-crystalline pillars after secondary yield, the [0001] single-crystalline pillar shows larger, more distinct strain bursts. This

difference in the stress-strain behavior after yielding is consistent with the size and number of slip steps formed on the outer surface of the deformed pillars. The [0001] single crystal shows large distinct slip steps at the unloaded state, whereas many fine slip steps are found in the case of the [10-10] oriented and bicrystalline pillars.

The plateau stress observed for the [10-10] and bicrystalline pillars are associated with twinning and detwinning, respectively. This is revealed in Fig. 3, where EBSD measurements of cross-sections of the pillars deformed to approximately 5% strain—a strain still within the plateau stress—indicate the re-orientation of the pillars to a nominal [0001] compression axis. In the case of the [0001] pillar (Fig. 3a), the initial orientation is maintained; no twinning occurs, as expected, and only a single yield point is found. In the case of the bicrystalline pillar the twin boundary has migrated out of the pillar (Fig. 3b), while a single twin has nucleated near the top of the pillar and migrated through nearly the entire pillar in the case of the [10-10] pillar (Fig. 3c); a resultant twin boundary near the base of the pillar is shown.

As stated earlier, the convention proposed by Kupka et al. [8] was used to quantify yield stress, using a critical reduction to 45% of the peak value of the slope of the load-displacement curve as the yield criterion. While this is nearly trivial for the initial [0001] pillars due to the sharp strain burst at 210 MPa, the approach was critical to identifying the secondary yield points in the twinned and detwinned pillars. The results show that the twinned and detwinned micropillars undergo secondary yield at a stress of 280 and 370 MPa, respectively.

We now consider the influence of detwinning and twinning on the compression response along the [0001] axis via a comparison of the yield and strain-hardening characteristics

**Fig. 3** EBSD maps of micropillars cross-sections after 5% deformation. **a** [0001] single crystal pillar, **b** bicrystalline pillar, and **c** [10-10] single crystal pillar

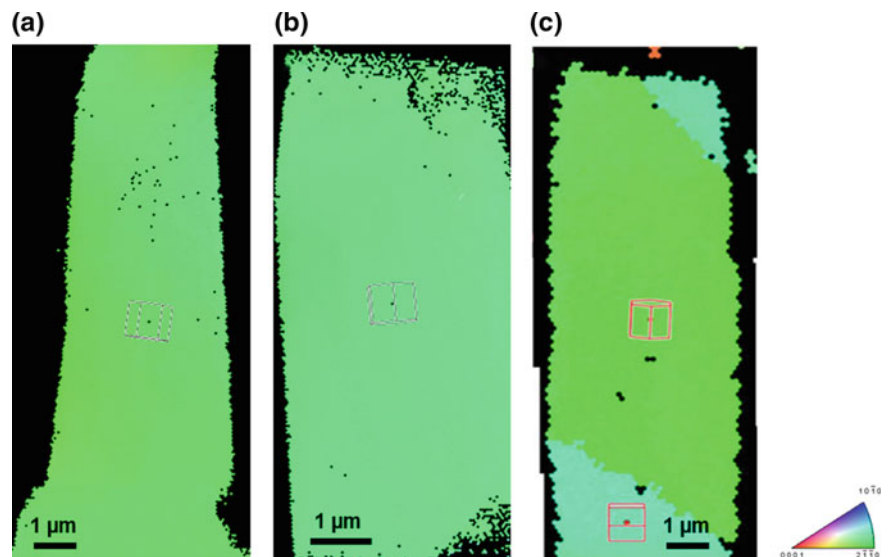
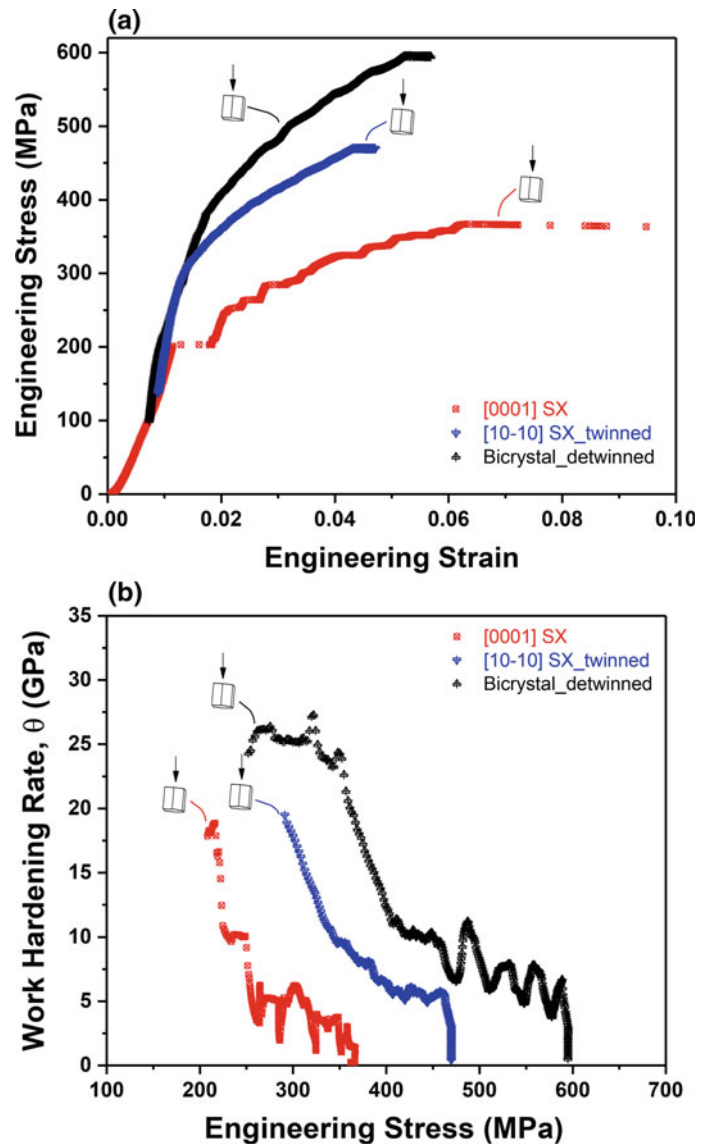


**Fig. 4** **a** Micromechanical response of the bicrystalline as well as the [10-10] single crystal pillar translated to the initial loading curve of the [0001] single crystal pillar, and **b** work hardening rate as a function of true stress for the three micropillars. SX points to single crystal



of the three pillars in their [0001] compression orientation, as is shown in Fig. 4. Here, the loading curves beyond the saturation of twinning or detwinning are shifted to the initial loading curves of the initially [0001] pillars (Fig. 4a). Interestingly, the twin migration stress, i.e., the plateau stress for the twinned [10-10] pillars, is significantly higher than for the detwinned bicrystalline pillars, whereas the secondary yield stress shows the opposite dependence; secondary yielding occurs more readily in the twinned pillars than in the detwinned pillars.

In any case, the secondary yield stress is significantly higher, as is the hardening rate (Fig. 4b), for both the initially bicrystalline and [10-10] pillars relative to the [0001] single crystalline pillars. This indicates that twin boundary migration itself affects both yield and hardening. While

plastic deformation can readily lead to an increase in yield stress, this typically leads to a decrease in the strain hardening rate. Thus, the observations of a simultaneous increase in yield strength and hardening rate cannot be simply explained by the development of dislocation density during the plateau regime. While twinning is not often considered to contribute significantly to dislocation density [6], the results here point to the formation of some defect structure in the wake of the twin, which serves as a strengthening mechanism. This may also explain why the [0001] single crystalline pillars show larger, more distinct strain bursts and slip steps compared to the twinned or detwinned volumes after secondary flow; the residual dislocation debris formed during twinning or detwinning would limit the mean free path of the mobile dislocations, limited the extent of massive slip

on well-spaced slip planes. Such twin mediated plastic flow must be further investigated to identify the relevant dislocation structures resultant from twin migration.

---

## Concluding Remarks

Microcompression experiments were conducted on single and bicrystalline pillars in order to investigate the influence of twinning and detwinning on the [0001] compression response of Mg. The microcompression results that the migration of a twin boundary leads to strengthening and an increase in work hardening rate in the subsequent [0001] compression. This was observed for the case of detwinning in bicrystalline micropillars as well as from twinning of initially [10-10] oriented micropillars, when compared to initially single-crystalline [0001] micropillars. It is argued that the simultaneous increase in yield strength and hardening rate of the twinned and detwinned micropillars must originate from the formation of dislocation debris formed in the wake of twin boundary motion. The results presented here point to the importance of further studies in order to develop more advanced constitutive formulations of twinning, especially in the context of crystal plasticity models.

## References

1. Christian, J.W. and S. Mahajan, *Deformation twinning*. Progress in materials science, 1995. **39**(1-2): p. 1–157.
2. Kocks, U. and D. Westlake, *The importance of twinning for the ductility of CPH polycrystals*. AIME MET SOC TRANS, 1967. **239**(7): p. 1107–1109.
3. Wang, Y. and J. Huang, *The role of twinning and untwinning in yielding behavior in hot-extruded Mg–Al–Zn alloy*. Acta materialia, 2007. **55**(3): p. 897–905.
4. Sarker, D. and D. Chen, *Detwinning and strain hardening of an extruded magnesium alloy during compression*. Scripta materialia, 2012. **67**(2): p. 165–168.
5. Cáceres, C. and A. Blake, *On the strain hardening behaviour of magnesium at room temperature*. Materials Science and Engineering: A, 2007. **462**(1–2): p. 193–196.
6. Cáceres, C., P. Lukáč, and A. Blake, *Strain hardening due to {10 1 2} twinning in pure magnesium*. Philosophical Magazine, 2008. **88**(7): p. 991–1003.
7. Lilleodden, E., *Microcompression study of Mg (0 0 0 1) single crystal*. Scripta Materialia, 2010. **62**(8): p. 532–535.
8. Kupka, D., N. Huber, and E. Lilleodden, *A combined experimental-numerical approach for elasto-plastic fracture of individual grain boundaries*. Journal of the Mechanics and Physics of Solids, 2014. **64**: p. 455–467.
9. Byer, C.M. and K. Ramesh, *Effects of the initial dislocation density on size effects in single-crystal magnesium*. Acta Materialia, 2013. **61**(10): p. 3808–3818.
10. Kim, G.S., *Small volume investigation of slip and twinning in magnesium single crystals*. 2011, Grenoble.

# An Investigation on the Microstructure and Mechanical Properties of the Hot-Dip-Aluminized-Q235/AZ91D Bimetallic Material Produced by Solid–Liquid Compound Casting

Jun Cheng, Jian-hua Zhao, Yao Tang, and Jing-jing Shang-guan

## Abstract

The hot-dip-aluminized-Q235/AZ91D bimetallic material was acquired by casting the melted magnesium alloy into the mould where the hot-dip-aluminized-Q235 had been inserted to achieve the lightweight with optimal mechanical properties. The microstructure and mechanical properties of the hot-dip-aluminized-Q235/AZ91D was investigated in this study. The results revealed that the metallurgical reaction in the interface zone which could be divided into two different layers was formed between Q235 and AZ91D. The layer close to AZ91D was composed of  $MgAl_2O_4$  and  $Al_{12}Mg_{17}$ , and the layer adjacent to Q235 was comprised of  $FeAl_3$ . What's more, the average microhardness of the interface zone was higher than AZ91D substrate and Q235. Moreover, the average microhardness of the layer close to Q235 (469.6HV) was much higher than the layer adjacent to AZ91D (136HV) due to the generation of  $FeAl_3$  and  $MgAl_2O_4$ . In addition, the shear strength of Q235/AZ91D was about 8.22 MPa.

## Keywords

Intermediate compound • Solid–liquid compound casting • Hot-dip aluminum coating

## Introduction

Under the context that all countries tried to promote the energy conservation, magnesium and magnesium alloy were more and more employed in the auto mobile due to its

lightest weight and recyclability [1, 2]. While, it's bad corrosion resistance and poor room temperature plasticity limited its further application [3, 4]. By contrast, steel will continue to occupy a dominant position in the application of industrial production with the successful development of mechanical properties [5]. Hence, the combination of steel and magnesium alloy will realize the light weight with the suitable mechanical properties. Actually, the huge differences between Mg and Fe lead to the huge challenges to the joint of Mg and Fe. According to Fe–Mg diagram [6], the solid solution of Mg in Fe and Fe in Mg were both close to zero. In addition, no intermetallic compound was formed between Mg and Fe, and there was a huge difference in melting temperature of Mg and Fe. Currently, the joint of Mg and Fe has been acquired by many methods such as ERW (electric resistance welding) [7], FSW (friction stir welding) [8], LW (laser welding) [9, 10], diffusion welding [11], and ultrasonic spot welding [12]. There is a common point that the interlayers such as zinc, aluminum, copper and tin are beneficial to realize the joint of magnesium and steel. For example, the friction stir welding was applied by Chen and Nakata [8] to realize the joining of AZ31 Mg alloy and steel (zinc coated steel and brushed finish steel). The metallurgical reaction layers which was composed of Mg–Zn eutectic structure and Fe–Al binary phase was generated between magnesium alloy and steel. In another paper, Elthalabawy and Khan [11] reported the joining of the 316L stainless steel and AZ31magnesium via diffusion welding, and in the interface zone the interfacial compound such as  $MgNi_2$  and Fe–Ni binary phases were generated, which was beneficial to the improvement of shear strength.

Solid–liquid compound casting is a forming process via pouring liquid metal into solid metal to get the connected bimetallic material, which has been applied to fabricate different bimetallic materials such as Fe/Mg [13, 14], Fe/Al [15], Al/Mg [16, 17], Al/Cu [18] and Al/Al [19] by many researchers. For instance, compound casting technology was used by Zhao et al. [13, 14] to realize the combination of AZ91D and steel (hot-dip galvanized-45 steel and

J. Zhao (✉)

State Key Laboratory of Mechanical Transmission, Chongqing University, Chongqing, 400044, China  
e-mail: zjhwzf@sina.com

J. Cheng · J. Zhao · Y. Tang · J. Shang-guan  
College of Materials Science and Engineering, Chongqing University, Chongqing, 400045, China



aluminized-0Cr19Ni9). They observed that the intermediate compound was formed in the interface zone of AZ91D and steel and results indicated intermediate compound was beneficial to the shear strength of steel/AZ91D bimetallic material.

In this study, the hot-dip aluminized-Q235/AZ91D bimetallic material was acquired via casting the melted AZ91D magnesium alloy into the mould where the hot-dip aluminized-Q235 has been inserted. This method was the combination of solid-liquid compound casting and hot-dip aluminum technology, which not only realize the joint of AZ91D and Q235, but also improve the corrosion resistance. The microstructure and phase composition of the interface zone between aluminized-Q235 and AZ91D were investigated. In addition, both the microhardness and the shear test were applied to estimate the mechanical properties of the joint of Mg/Fe.

## Material and Experience

### Material

The materials used in this study were the AZ91D magnesium alloy, hot-dip aluminized-Q235 and RJ-2 flux. Among them, the AZ91D magnesium alloy and hot-dip aluminized-Q235 were employed as the substrate and inserts, respectively. Besides, the RJ-2 flux was applied to prevent from the oxidation of AZ91D magnesium alloy. The chemical compositions of these materials were listed in Table 1.

### Preparation of Aluminized-Q235/AZ91D

First of all, the hot-dip aluminized-Q235 was grounded with silicon carbide papers up to 3000 grit to coarse the surface, and then cleaned in ethyl alcohol to remove any dirty mark. Next, the aluminized-Q235 was inserted into the mould and then they are both preheated in the box-type furnace at 200 °C for one hour. At the same time, the AZ91D was placed into the graphite crucible under the protection of RJ2 covering flux. Finally, the molten AZ91D magnesium alloy was casted into the mould with hot-dip aluminized-Q235 at 720 °C.

**Table 1** Chemical composition (wt%) of materials used in this study

Materials	Al	Zn	Mn	Si	Fe	Ni	Cu	Mg	C	S	P
AZ91D	8.5–9.0	0.45–0.5	0.17–0.4	≤0.05	≤0.004	≤0.01	≤0.02	Bal.	–	–	–
Q235	–	–	0.3–0.65	≤0.30	Bal.	–	–	–	0.14–0.22	≤0.05	≤0.045

## The Simulation of Casting Process

In order to achieve insert's surface temperature over time, the process simulation of mould filling, thermal conduction, and solidification during the casting procedure was applied via using an Any-Casting (version 6.0) casting simulation software. In order to enhance the accuracy of result, the hot-dip aluminized-coating on the surface of the insert and other section were set as pure aluminum and Q235 steel, respectively. In addition, the steel mould, hot-dip-aluminized-Q235 and cast block were divided into 4993104 meshes in total. After that, the related basic parameters were set and the 6 sensors were placed in positions above the surfaces of hot-dip aluminum coating as displayed in Fig. 1.

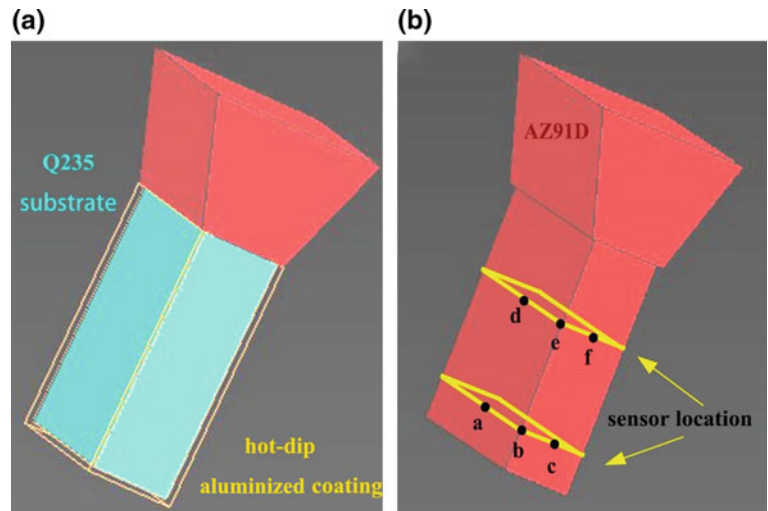
### Microstructural Characterizations

In order to figure out the interface zone between aluminized-Q235 and AZ91D, the specimens with the dimension of 10mm × 10mm × 10mm were cut from the cross-section of the cast by electrical discharge wire cutting machine, and then grounded with silicon carbide papers up to 3000 grit. After that, the specimens were etched with 3 vol.% HNO<sub>3</sub> in the alcohol solution. Next, the TESCANVEGAIII scanning electron microscope (SEM) with the energy dispersive X-ray spectrometer (EDS) detector were applied to analyses the microstructure and phase composition of the interface zone between aluminized-Q235 and AZ91D. In addition, the XRD technology was employed to obtain the phase composition in the interface zone at the speed of 4° per minute from 10° to 90°.

### Mechanical Properties

The shear test and microhardness test were applied to estimate the mechanical properties of aluminized-Q235/AZ91D bimetallic material. The Everone MH-3L microhardness tester was employed to receive the microhardness distribution from AZ91D to A356 along vertical direction of the interface in different positions with a holding time of 15 s and a testing load of 100 g. Furthermore, the shear strength of aluminized-Q235/AZ91D

**Fig. 1** Schematic diagram of sensor positions in hot-dip aluminized-Q235/AZ91D bimetal model for casting simulation



bimetallic material was conducted by the shear equipment as shown in Fig. 2. What’s more, the related calculation equation [16] was shown in the below:

$$\delta_{\tau} = \frac{F_{\max}}{2hk}$$

where  $F_{\max}$  is the maximum load,  $h$  is the thickness of the specimens, and  $k$  is the length of the specimen.

## Results and Discussion

### Microstructures and Compositions

The cross-sectioned galvanized-Q235/AZ91D and its corresponding EDS line scan were displayed in Fig. 3. It could be deduced that there were two different layers in the interface zone: the layer close to AZ91D (layer I) and the layer adjacent to Q235 (layer II). In addition, EDS line scan illustrated the content variation of magnesium, aluminum and iron elements from Q235 to the AZ91D. Apparently, the content of iron element from Q235 to AZ91D decreased gradually, while the content of magnesium increased inch by inch. Besides, it was worth noting that the content of

aluminum element in the layer close to Q235 was the highest than other position.

The EDS map scanning spectra (Fig. 4) displayed the distribution of magnesium, iron, aluminum and oxygen elements in Fig. 3. The columnar phase in the layer II was composed of aluminum and iron elements, and the content of aluminum element in this phase was higher than other elements. What’s more, the white phase in the layer I comprised of aluminum, oxygen and magnesium elements, while the block phase in this layer consisted of magnesium and aluminum elements.

The SEM micrographs at the interface of the hot-dip-aluminized-Q235/AZ91D were showed in Fig. 5a, and the SEM micrographs of the areas as marked ‘A’ to ‘C’ in Fig. 5a at enlarged drawing was displayed in Fig. 5b, c, and d, respectively. As showed in Fig. 5b, c, and d, the

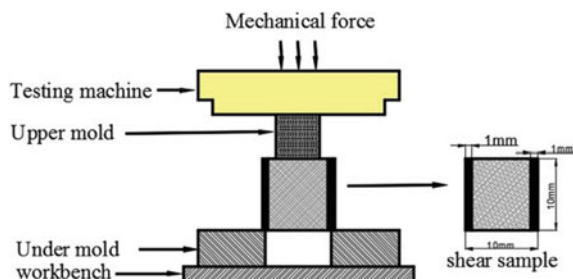


**Fig. 2** Schematic illustrations of the shear test

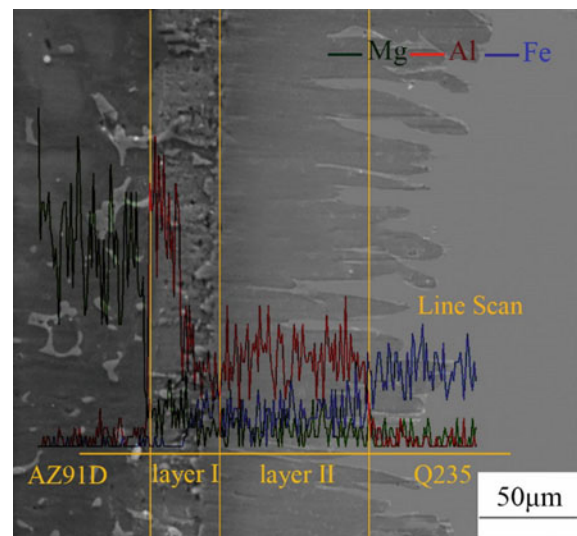
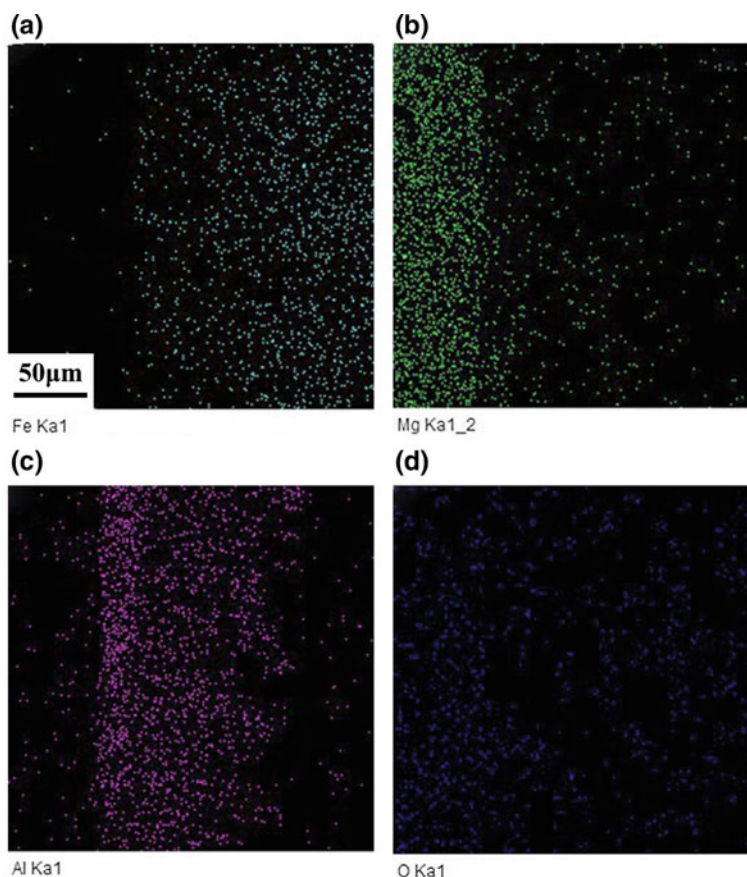


**Fig. 3** SEM micrograph and EDS line scan of interfacial microstructure of hot-dip aluminized-Q235/AZ91D interface

**Fig. 4** EDS map scanning spectra at the interface of the hot-dip aluminized-Q235/AZ91D as showed in Fig. 3



constituents of the two layers differed from each other. Based on the formation of the phases with different morphology and composition between Q235 and AZ91D, it could be inferred that the interdiffusion was the dominant factor in this process.

In order to figure out the phase composition in the interface zone between aluminized-Q235 and AZ91D, the EDS point scan was conducted on different phases. The result of magnesium, aluminum, iron and oxygen contents by EDS point scan at several points was conducted in Table 2.

The XRD point scan technology was employed to prove the accuracy of EDS line and point scan, and the related result was displayed in Fig. 6, which could confirm the existence of phases including  $\text{FeAl}_3$ ,  $\alpha\text{-Mg}$ ,  $\text{MgAl}_2\text{O}_4$ , and  $\text{Al}_{12}\text{Mg}_{17}$  in the testing section. However, the testing section was a little more than that of the interface zone. According to the report [10, 17], the phases of AZ91D and Q235 substrate were mainly composed of eutectic structure ( $\alpha\text{-Mg} + \text{Al}_{12}\text{Mg}_{17}$ ),  $\alpha\text{-Mg}$  and ferrite, respectively. Therefore, it could be deduced that there were  $\text{FeAl}_3$ ,  $\alpha\text{-Mg}$ ,  $\text{MgAl}_2\text{O}_4$ , and  $\text{Al}_{12}\text{Mg}_{17}$  in the interface zone.

Based on the result and analysis in the above, the interfacial compound in the interface zone between Q235 and AZ91D was acquired accurately. The layer close to AZ91D was composed of  $\text{Al}_{12}\text{Mg}_{17}$  and  $\text{MgAl}_2\text{O}_4$ . Among them, the

$\text{MgAl}_2\text{O}_4$  was generated on the basis of the equation [14]  $\text{Mg(l)} + \text{Al}_2\text{O}_3\text{(s)} \rightarrow \text{MgO(s)} + \text{Al(l)}$  and  $\text{MgO} + \text{Al}_2\text{O}_3 \rightarrow \text{MgAl}_2\text{O}_4$ . What's more,  $\text{Al}_{12}\text{Mg}_{17}$  was formed based on the equation  $\text{L} \rightarrow \text{Al}_{12}\text{Mg}_{17} + \alpha\text{-Mg}$ . The layer close to Q235 comprised of  $\text{FeAl}_3$ , which was generated due to the metallurgical reaction and diffusion.

### Formation Mechanism of the Interface Zone

The formation of the interface zone of hot-dip aluminized-Q235/AZ91D bimetallic material via solid–liquid compound casting was investigated in the below. The casting simulation result showed the surface temperature and time curve of hot-dip aluminized-coating at the positions which have been illustrated in Fig. 7, as AZ91D liquid magnesium alloy filled into the cavity, the surface temperature was quickly reached at 588 °C, and then slowly decreased to room temperature. So, it could be deduced that the hot-dip aluminized-coating was hardly melted. To sum up, the process of the formation of the interface zone of hot-dip aluminized-Q235/AZ91 bimetallic material via solid–liquid compound casting could be divided into four different stages: (1) filling the cavity; (2) partially solidification and diffusion; (3) Metallurgical reaction; (4) solidification.

**Fig. 5** SEM micrographs at the interface of the hot-dip aluminized-Q235/AZ91D: **a** general view, **b**, **c**, and **d** areas A, B, and C in **(a)**, respectively

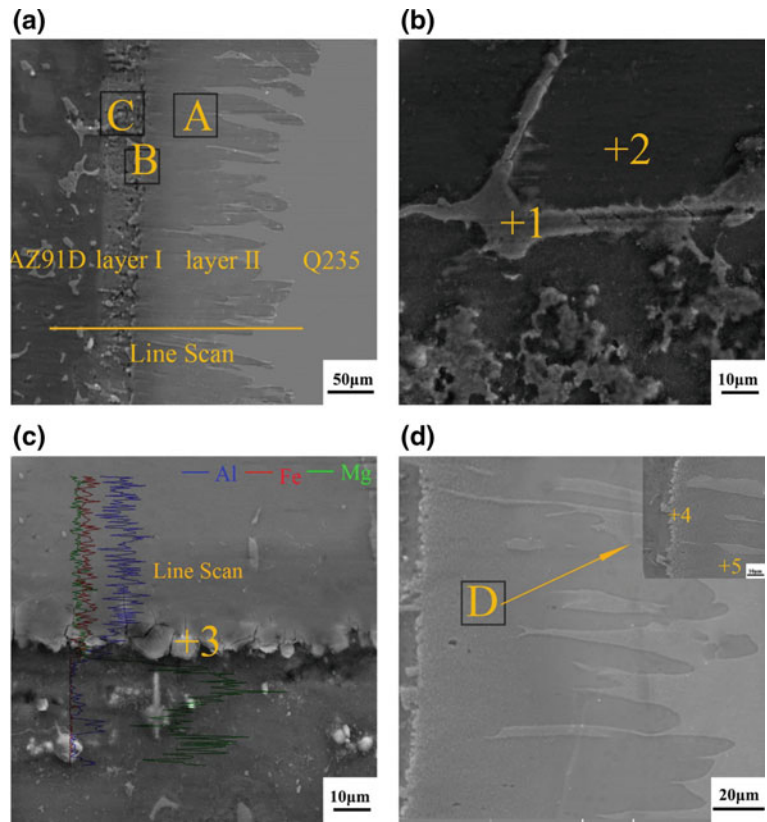


**Table 2** Composition of atomic percent of 1 through 5 points in Fig. 5 by EDS

Point	X(Mg)/%	X(Al)/%	X(Fe)/%	X(O)/%
1	65.33	34.67		
2	92.32	7.53	0.15	
3	24.55	16.59	5.73	53.13
4	26.17	13.13	3.35	57.36
5	28.13	71.87		

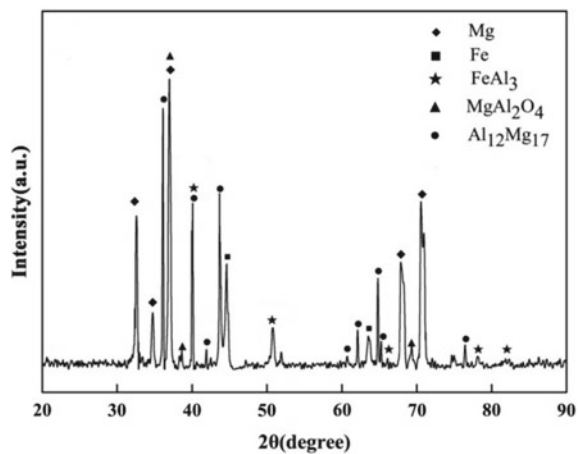


**Fig. 6** XRD diffraction pattern of the hot-dip aluminized-Q235/AZ91D compound interface

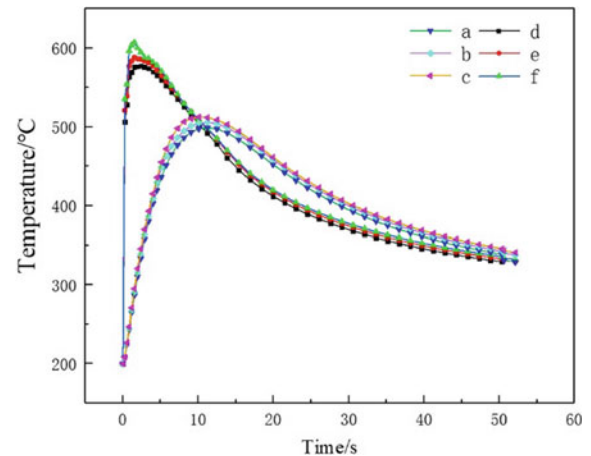
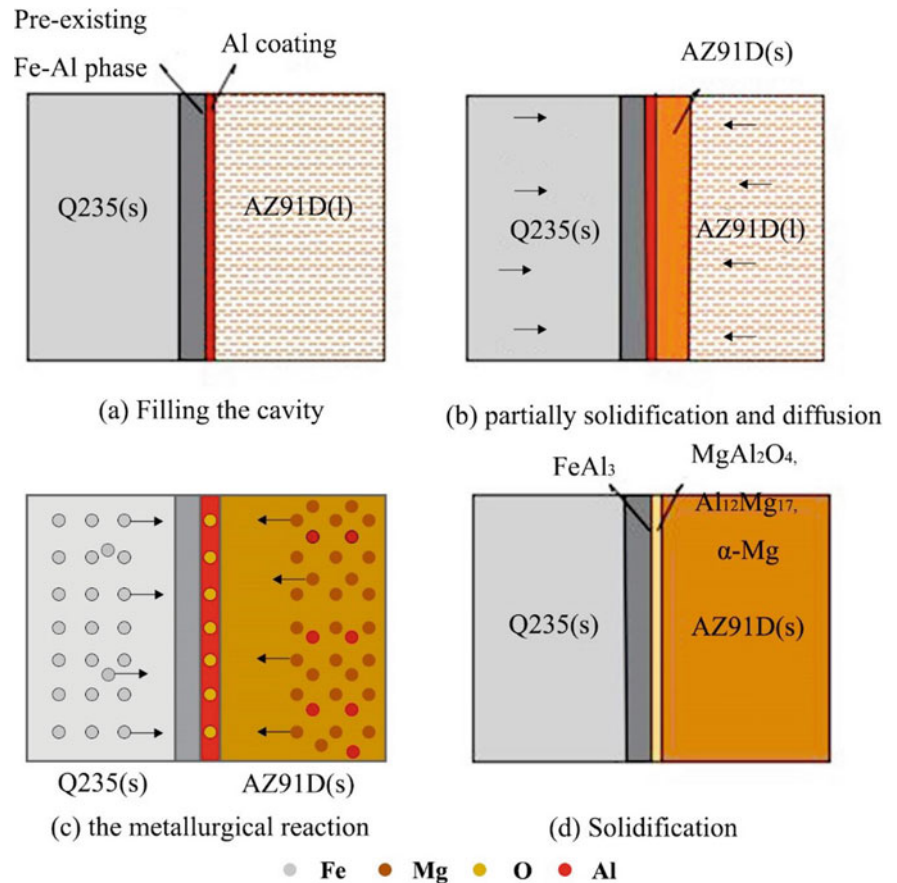


**Fig. 7** The time-temperature curve of different positions from 'a' to 'h' as shown in Fig. 1

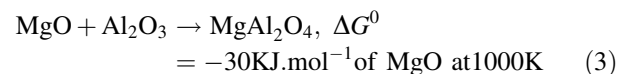
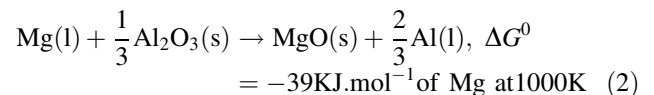


**Fig. 8** Schematic illustration of the formation of the interface of the hot-dip aluminized-Q235/AZ91D bimetal via the liquid–solid compound process



At the first stage, the liquid magnesium alloy was quickly filling the cavity. And then, at the second stage, the liquid magnesium alloy solidified layer by layer from near the bottom of the die. Under the heat of liquid magnesium, the solidified magnesium layer close to hot-dip aluminized Q235 and hot-dip aluminum Q235 reacted with each other. At the same time, under concentration gradient, iron element in the Q235 substrate and magnesium element in the AZ91D diffused into the hot-dip aluminum coating. Next, at the third stage, the metallurgical reaction occurred. At the side of AZ91D, the liquid magnesium reacted with  $\text{Al}_2\text{O}_3$  to produce the  $\text{MgAl}_2\text{O}_4$  on the basis of the equation  $\text{Mg}(\text{l}) + \text{Al}_2\text{O}_3(\text{s}) \rightarrow \text{MgO}(\text{s}) + \text{Al}(\text{l})$  and  $\text{MgO} + \text{Al}_2\text{O}_3 \rightarrow \text{MgAl}_2\text{O}_4$ . In addition, the content of magnesium element was high, while the content of aluminum element was so low. Therefore, the  $\text{Al}_{12}\text{Mg}_{17}$  was formed due to the equation  $\text{L} \rightarrow \text{Al}_{12}\text{Mg}_{17} + \alpha\text{-Mg}$ . At side of the Q235, the iron element firstly reacted with aluminum element to generate  $\text{FeAl}_3$ , because the binding energy of iron and aluminum was lower than aluminum and magnesium. Finally, the metallurgical interface zone which consisted of  $\text{FeAl}_3$ ,  $\text{MgAl}_2\text{O}_4$ , and  $\text{Al}_{12}\text{Mg}_{17}$  was formed between aluminized-Q235 and AZ91D after solidification, obtaining hot-dip aluminized-Q235/AZ91D bimetallic material. Actually, the

formation of the interface zone may be contributed to many factors, and it should be researched in the future (Fig. 8).



### Microhardness of the Interface Zone

The microhardness distribution of the hot-dip aluminized-Q235/AZ91D along the direction perpendicular to the interface from aluminized-Q235 to AZ91D was displayed in Fig. 9. It could be clearly seen that the microhardness from AZ91D to aluminized-Q235 was firstly increased from 56HV to 136HV and then went up to 469.63HV, and at last decreased to 172.2HV. The average microhardness of the layer close to Q235 (469.63HV) was much higher than the layer adjacent to AZ91D (136HV) due to the formation of  $\text{FeAl}_3$ , and the average microhardness of the layer adjacent to AZ91D was

**Fig. 9** **a** SEM micrograph of the interface in hot-dip aluminized-Q235/AZ91D bimetallic material; **b** the average values of Vickers microhardness profiles across the interface as marked by yellow dashed lines in (a)

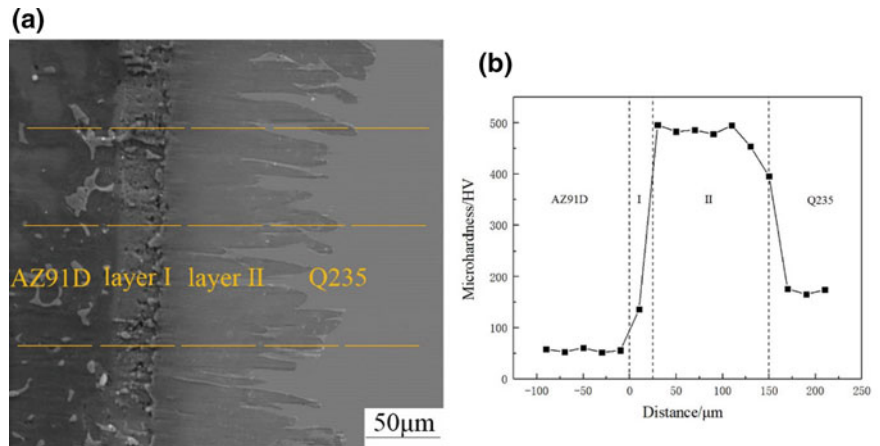


**Table 3** The shear strength of hot-dip aluminized-Q235/AZ91D bimetallic material

Sample	Shear strength (MPa)	Average shear strength (MPa)
aluminized-Q235/AZ91D	7.53 9.14 7.99	8.22

much higher than AZ91D substrate (56HV) was attributed to the existence of  $MgAl_2O_4$ .

## Shear Strength

The shear test was one of the best methods to estimate the bond strength between aluminized-Q235 and AZ91D, and the related result was displayed in Table 3. It could be clearly seen that the average bond strength of galvanized-Q235/AZ91D bimetallic material was 8.22 MPa which was higher than bare-Q235/AZ91D bimetallic material due to the existence of metallurgical bonding. Actually, the bond strength of bare-Q235/AZ91D bimetallic material was close to zero [13] because the bare-Q235/AZ91D was broken during the wire cut electrical discharge machining.

## Conclusion

The microstructure and mechanical properties of hot-dip aluminized-Q235/AZ91D bimetallic material have been discussed systematically, and the major conclusion was displayed in the below:

(1) The metallurgical reaction layer was formed between hot-dip aluminized-Q235 and AZ91D magnesium alloy via casting the melted magnesium alloy into the mould where the hot-dip aluminized-Q235 has been inserted and it can be divided into two different layers. The layer close to AZ91D comprised of  $MgAl_2O_4$  and  $Al_{12}Mg_{17}$ , and the layer adjacent to Q235 was composed of  $FeAl_3$ .

- (2) The average microhardness from Q235 to the AZ91D was gradually increasing from 172.2HV to 56HV, and the average microhardness of the layer close to AZ91D (136HV) was much bigger than the layer adjacent to Q235 (469.6HV) due to the existence of  $FeAl_3$  and  $MgAl_2O_4$ .
- (3) The shear strength of hot-dip aluminized-Q235/AZ91D bimetallic material was about 8.22 MPa due to the existence of metallurgical bonding.

**Acknowledgements** This work was supported by the National Natural Science Foundation of China (Nos. 51875062). This work was partly supported by the National Engineering Research Centre for Magnesium Alloys of China (cstc2015yykfC0001).

## References

1. T.E. B.L. Mordike (2001) Magnesium—properties—applications—potential. *MAT SCI ENG A-STRUCT.* 302:37-45.
2. M.K. Kulekci (2007) Magnesium and its alloys applications in automotive industry. *INT J ADV MANUF TECH* 39(9-10): 851-865.
3. A. Atrens, G.-L. Song, F. Cao, Z. Shi, P.K. Bowen (2013) Advances in Mg corrosion and research suggestions. *J. Magnes. Alloy* 1(3): 177-200.
4. G. Song (2005) Recent Progress in Corrosion and Protection of Magnesium Alloys. *ADV ENG MATER* 7(7): 563-586.
5. A.Z.-H. Pooriya Dastranjy Nezhadfar, Seok Su Sohn, Hamid Reza Abedi (2016) The microstructure evolution and room temperature deformation behavior of ferrite-based lightweight steel. *MAT SCI ENG A-STRUCT.* 665: 10-16.
6. ASM International (1992) Alloy Phase Diagrams of ASM Handbook, 8th edn.

7. L. Liu, L. Xiao, D.L. Chen, J.C. Feng, S. Kim, Y. Zhou (2013) Microstructure and fatigue properties of Mg-to-steel dissimilar resistance spot welds. *MATER DESIGN*. 45: 336-342.
8. K.N. Y. C. Chen (2010) Effect of surface states of steel on microstructure and mechanical properties of lap joints of magnesium alloy and steel by friction stir welding. *SCI TECHNOL WELD JOI* 15(4): 293-298.
9. G. Song, J. Yu, T. Li, J. Wang, L. Liu (2018) Effect of laser-GTAW hybrid welding heat input on the performance of Mg/Steel butt joint. *J MANUF PROCESS*. 31: 131-138.
10. G. Song, C. Shan (2013) Microstructures of laser-tungsten inert gas hybrid welding of dissimilar AZ31 Mg alloy and Q235 steel with Ni as interlayer, *MATER RES INNOV* 15(2): 145-149.
11. W.M. Elthalabawy, T.I. Khan (2010) Microstructural development of diffusion-brazed austenitic stainless steel to magnesium alloy using a nickel interlayer, *MATER CHARACTER* 61(7): 703-712.
12. M. Shakil, N.H. Tariq, M. Ahmad, M.A. Choudhary, J.I. Akhter, S.S. Babu (2014) Effect of ultrasonic welding parameters on microstructure and mechanical properties of dissimilar joints. *MATER DESIGN*. 55: 263-273.
13. J.C. Cheng, Jun); Zhao, JH (Zhao, Jian-hua); Zhang, JY (Zhang, Jin-yong); Guo, Y (Guo, Yu); He, K (He, Ke); Shang-guan, JJ (Shang-guan, Jing-Jing); Wen, FL (Wen, Fu-lin) (2019) Microstructure and Mechanical Properties of Galvanized-45 Steel/AZ91D Bimetallic Material by Liquid-Solid Compound Casting. *MATERIALS* 12(10): 1-14.
14. J.-h. Zhao, W.-q. Zhao, S. Qu, Y.-q. Zhang (2019) Microstructures and mechanical properties of AZ91D/0Cr19Ni9 bimetal composite prepared by liquid-solid compound casting. *T NONFERR METAL SOC* 29(1): 51-58.
15. W. Jiang, Z. Fan, C. Li (2015) Improved steel/aluminum bonding in bimetallic castings by a compound casting process. *J MATER PROCESS TECH*. 226: 25-31.
16. K. He, J. Zhao, P. Li, J. He, Q. Tang (2016) Investigation on microstructures and properties of arc-sprayed-Al/AZ91D bimetallic material by solid-liquid compound casting. *MATER DESIGN*. 112: 553-564.
17. G. Li, W. Jiang, W. Yang, Z. Jiang, F. Guan, H. Jiang, Z. Fan (2018) New Insights into the Characterization and Formation of the Interface of A356/AZ91D Bimetallic Composites Fabricated by Compound Casting. *METALL MATER TRANS A* 50(2): 1076-1090.
18. Y. Hu, Y.-q. Chen, L. Li, H.-d. Hu, Z.-a. Zhu (2016) Microstructure and properties of Al/Cu bimetal in liquid-solid compound casting process. *T NONFERR METAL SOC* 26(6): 1555-1563.
19. W. Jiang, Z. Jiang, G. Li, Y. Wu, Z. Fan (2017) Microstructure of Al/Al bimetallic composites by lost foam casting with Zn interlayer. *MATER SCI TECH-LOND* 34(4): 487-492.

---

**Part IX**  
**Poster Session**



# Effect of Zinc on Solidification and Aging Behaviour of Magnesium Alloys Containing Rare Earths

A. Javaid and F. Czerwinski

## Abstract

Magnesium sheet continuously creates a great interest with potentials in a wide range of technically advanced applications. The interest was initially driven by a reduction in fuel consumption within transportation sectors and was later expanded to consumer electronic housings, components in electrification of vehicles, and aerospace applications. In a search for alloys with suitable formability, a particular attention is paid to Mg–Zn–RE (rare earth) grades. It is known that the presence of Zn in binary Mg–Zn alloys leads to enhanced strength and ductility. However, the effect of Zn on alloy formability in the presence of rare earths is less pronounced. In this report, the solidification and aging behavior of Mg–xZn–1Nd ( $x = 1, 2, 4$  wt%) alloys are described. To analyze the phase nucleation and growth during melting and solidification, the Universal Metallurgical Simulator and Analyzer (UMSA) was used. Hardness values of Mg–Zn–Nd alloys increased with increasing Zn contents both in as-cast and after heat treatments with changes being accompanied by the alloy structure refinement. The results are discussed in terms of the role Zn plays in properties of magnesium alloys containing rare earths. Increasing Zn content in the Mg–xZn–1Nd alloy sheets led to a moderate increase in ultimate tensile strength and yield stress but substantial reduction in ductility.

## Keywords

Magnesium sheet • Twin-roll casting • Rolling • Heat treatment • Wrought Mg–Zn–Nd alloys

## Introduction

At present, most magnesium use in the auto industry is limited to die-cast parts, although wrought alloys hold great promise for use in structural applications related to aerospace and automotive sectors. In particular, the advanced magnesium sheet technology offers tremendous opportunities for automobile designers to significantly reduce the vehicle weight. However, the use of magnesium sheet is severely limited in light-weighting initiatives because of its high manufacturing cost, low formability at room temperature, and relatively high tendency to corrosion [1]. The high cost and poor formability of magnesium sheet can partly be overcome by the use of twin-roll casting (TRC) technology and development of wrought magnesium alloys, formable at room temperature. Recently, magnesium-rare earth alloys are increasingly being investigated due to their promising results in terms of weakening the basal texture and improving the formability of rolled sheet [2] [3]. Rare earth elements have very low solubility in magnesium and usually form with intermetallic compounds. In addition to weakening the basal texture and improving ductility, rare earths increase strength, creep—corrosion—and flammability resistance of magnesium [4, 5]. The presence of rare earth elements in magnesium alloys also improves castability, grain refining, and age hardening. Among rare earths used in Mg alloys, neodymium is one of the most promising choices. According to Ref. [6], light rare earth (LRE) elements have higher tendency to segregate to magnesium grain boundary than heavy rare earths (HRE). This would suggest that Nd, as an LRE, should be more effective in terms of the solute drag.

An effectiveness of zinc is comparable to aluminum in terms of improving castability and strengthening of magnesium. By adding up to 3 wt% zinc, the solidification shrinkage can be compensated along with increasing tensile strength [7]. Moreover, zinc helps to overcome the harmful corrosive effect of iron and nickel impurities that might be present in

A. Javaid (✉) · F. Czerwinski  
 CanmetMATERIALS, Natural Resources Canada, 183 Longwood  
 Rd. South, Hamilton, ON L8P 0A5, Canada  
 e-mail: [Amjad.Javaid@Canada.ca](mailto:Amjad.Javaid@Canada.ca)

F. Czerwinski  
 e-mail: [Frank.Czerwinski@Canada.ca](mailto:Frank.Czerwinski@Canada.ca)

magnesium alloys [8]. Additions of Zn to Mg–RE alloys have been shown to significantly improve mechanical properties such as elevated temperature creep resistance [9]. Additions of 0.2 and 0.5 wt% Zn to the extruded Mg–3Nd (wt%) alloy led to improvement in room temperature tensile properties [10]. In magnesium alloys, zinc is used as a major alloying element in a combination with Zr and/or rare earth elements. It has very low solid solubility in magnesium and forms many intermetallic compounds so alloys can be strengthened through precipitation hardening [11]. The use of Zn at low levels of the order of 1.5 wt% affects the aging response with high levels changing the form of zinc-containing precipitates, causing hardness reduction. In the presence of Nd and Gd, increasing Zn in the range of 0–1.3 wt% delayed the onset of over aging, but a content of 1.3 wt% lowered the peak hardness and tensile properties [12]. In this paper, we present an influence of zinc on some properties of Nd-containing magnesium alloys.

## Experimental Procedure

### Alloy Casting

The subjects of this investigation are three Mg–xZn–1Nd experimental alloys with 1, 2, and 4 wt% of Zn. The chemical composition of alloys is listed in Table 1.

Alloy melts with a weight of 40 kg, and each was prepared using a mild steel crucible in a resistance furnace under a protective atmosphere of CO<sub>2</sub> + 0.5% SF<sub>6</sub> mixture. The charge make-up is comprised of elemental Mg, Zn, and Nd, each with a purity of 99.99%. Alloying elements were added to molten magnesium melt at 730 °C. No grain refiner was used. After verifying the chemical composition and removal of dross/oxide from the melt surface, the final sample was tested by optical emission spectroscopy and the melt was poured at 730 °C. To generate microstructures influenced by different solidification rates, a water-cooled wedge-shaped copper mold was used for casting. The shape and dimensions of wedge castings are shown in Ref. [13]. The cooling rate during solidification was measured using 4 K-type thermocouples, positioned along the centerline and corresponding to 10, 15, 20, and 30 mm of the wedge thickness. As revealed by measurements, the cooling rate

varied from 30 °C/s at the base to 110 °C/s at the tip of the wedge [14].

### Thermal Analysis

To investigate the phase nucleation and growth during melting and solidification, the Universal Metallurgical Simulator and Analyzer (UMSA) was used. Measurements were conducted using cylindrical samples with a diameter of 31 mm and a length of 35 mm with pre-drilled hole and an insert of the stainless steel tube for a thermocouple. The test samples were processed in thin stainless steel foil, having negligible effect on heat transfer, coated with boron nitride, and protected against oxidation in the UMSA chamber by an inert argon atmosphere. Controlled heating to 735 °C at a rate of 0.4 °C/s was followed by isothermal holding at 735 °C for 5 min and natural cooling to 50 °C at a rate of 0.2 °C/s. For each sample, the heating/cooling cycles were repeated three times to establish repeatability of measurements.

### Heat Treatment

As-cast samples sectioned from wedge castings were homogenized (T4) for 24 h at 400 °C, following by water quenching. Initially, the samples were placed in the furnace and heated slowly to 400 °C with a heating rate of 3 °C/min. Then, samples were subjected to aging at 200 °C for 8 and 16 h (T6).

### Sheet Rolling

Hot rolling of Mg–Zn–Nd alloy ingots to the 1.50 mm thick sheet was conducted using a pilot-scale rolling mill. The roller diameter was 156.3 mm for top roll and 156.9 mm for bottom roll, and roller length was 203.2 mm. The aim was to optimize the hot rolling schedule in order to produce a quality sheet with a fine and homogeneous microstructure. The 25-mm-thick-ingot slices were heated to 400 °C under argon and kept at that temperature for 10 h to homogenize before rolling. Three different rolling temperatures of 350, 400, and 450 °C were used at one rolling speed of 30 rpm

**Table 1** Chemical composition of magnesium alloys investigated in this study

Alloys	Chemical composition (weight %)					
	Nd	Zn	Fe	Ni	Cu	Si
Mg–1Zn–1Nd	0.92	1.00	<0.005	<0.005	<0.005	<0.005
Mg–2Zn–1Nd	0.98	2.03	<0.005	<0.005	<0.005	<0.005
Mg–4Zn–1Nd	0.96	3.94	<0.005	<0.005	<0.005	<0.005

with rolls preheated to 100 °C. Before rolling, the sliced plates were soaked for 1 h at the hot rolling temperature to ensure the proper through heating. The entry temperature was kept constant, by reheating the plate between passes. Typically, a thickness reduction of 10–15% per pass was obtained.

## Property and Microstructure Characterization

The sub-sized tensile test samples were extracted from the as-rolled and annealed state. Each value of strength and elongation is the average of six specimens tested in rolling directions (RD) and transverse (TD) directions. Tensile tests were performed at room temperature and a strain rate of  $5 \times 10^{-3} \text{ s}^{-1}$ . Flat tensile sample was manufactured according to standard ASTM E8M with gage of 25 mm and cross section of  $6 \times$  sheet thickness of 1.5–1.7 mm. Hardness was measured using a superficial rockwell hardness tester with a steel ball indenter of 2.5 mm in diameter under the load of 150 N. Hardness values were determined by taking an average of five readings. Metallographic samples, selected from locations with distinct solidification rates, were prepared using the conventional surface preparation process starting from grinding to polishing and then chemically etched using 10% HF and/or acetic glycol to reveal the dendritic structure. The optical microscope was used for microstructural characterizations of magnesium alloys tested.

## Results and Discussion

### Melting and Solidification Characteristics

The thermal analysis output data, collected during melting and solidification, were used to determine changes of temperature versus time and first derivative of temperature versus time. The melting/solidification characteristics determined for alloys tested are listed in Table 2.

The thermal analysis of Mg–1Zn–1Nd, Mg–2Zn–1Nd, and Mg–4Zn–1Nd alloys in the form of heating/cooling curves of temperature versus time, recorded during heating and cooling cycles, is shown in Fig. 1a, and first derivative

of the heating/cooling curves as a function of temperature is shown in Fig. 1b.

In Fig. 1, two major metallurgical reactions are revealed through two temperature arrests, marked as “c” and “d” on heating and cooling curves, respectively. During cooling, the first solid formed is the  $\alpha$ -Mg dendritic phase that nucleated from the melt at the liquidus temperature. During solidification of the  $\alpha$ -Mg phase, the melt temperature increased as the latent heat evolved, and this point was clearly visible as a sudden change in the first derivative curve (point “d” in Fig. 1b). Further cooling beyond point “d” resulted in a growth of  $\alpha$ -Mg dendrites. The next change in the first derivative curve corresponded to the nucleation of the  $\beta$ - (Mg–Zn–Nd) eutectic phase. This point is marked as “e”.

Analysis of alloys Mg–1Zn–1Nd, Mg–2Zn–1Nd, and Mg–4Zn–1Nd provides the evidence on the role of Zn for 1 wt% Nd. As shown in Fig. 1a, there are obvious shifts in location of characteristic points on first derivative curves. An increased content of Zn from 1 to 2 wt% and then to 4 wt% caused reduction of the liquidus temperature from 646 to 640 °C and to 635 °C. These changes are larger for the solidus temperature, which decreased from 485 °C for 1 wt% Zn to 482 °C for 2 wt% Zn and to 460 °C for 4 wt% Zn.

### Effect of Solidification Rate and Zn Content on Alloy Microstructure

#### As-Cast Microstructure

The general microstructure of alloys tested after casting is shown in Fig. 2. For the same solidification rate of 30 °C/s, increasing in Zn content leads to slight structural refinement. The structural refinement was described by secondary dendrite arms spacing (SDAS) in Fig. 2. In addition to more visible sub-grain structure, a content of intermetallic compounds is increased. The difference is more pronounced when increasing Zn content from 2 to 4 wt%.

The phase composition for alloys tested here was calculated with FactSage, assuming equilibrium and non-equilibrium solidification, in our previous paper [15]. For equilibrium conditions, the Mg–1Zn–1Nd alloy the phases present involved 96.90%  $\alpha$ -Mg, 2.19% FCC–MgNd, 0.91% Mg<sub>12</sub>Zn<sub>13</sub>. Increasing Zn content to 2% for the same 1 wt% Nd (Mg–2Zn–

**Table 2** Melting/solidification characteristics of investigated alloys, determined based on UMSA analysis. Measurements were conducted at heating rate of 0.4 °C/s and cooling rate of 0.2 °C/s

Alloys	Liquidus, °C	Solidus, °C	Melting/solidification range, °C	Eutectics $\beta$ , °C
Mg–1Zn–1Nd	646	485	161	507
Mg–2Zn–1Nd	640	482	158	491
Mg–4Zn–1Nd	635	460	175	463

**Fig. 1** Temperature versus time (a) and first derivatives of heating/cooling curves (b) of Mg-xZn-1Nd alloys tested by UMMA showing the effect of Zn. In heating/cooling plots, critical points are marked as: liquidus-c, d, solidus-a, f, and eutectics-b, e

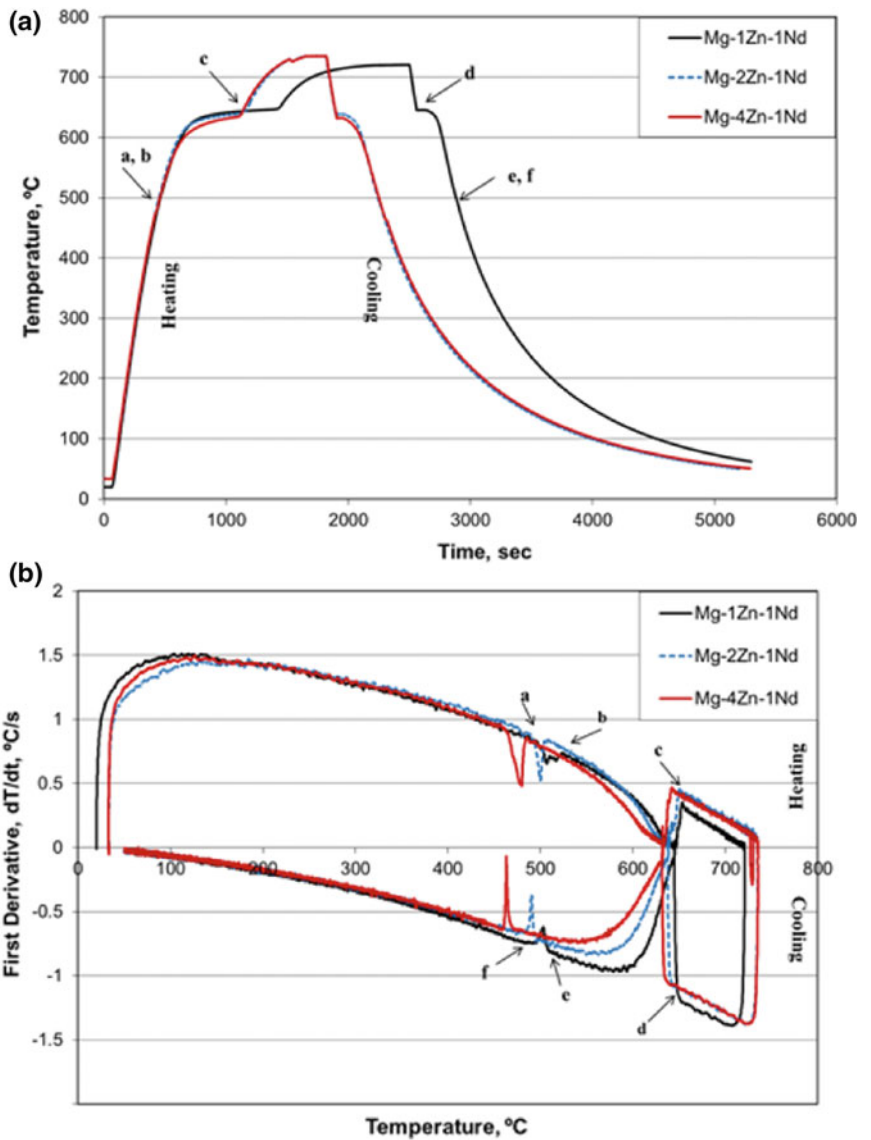
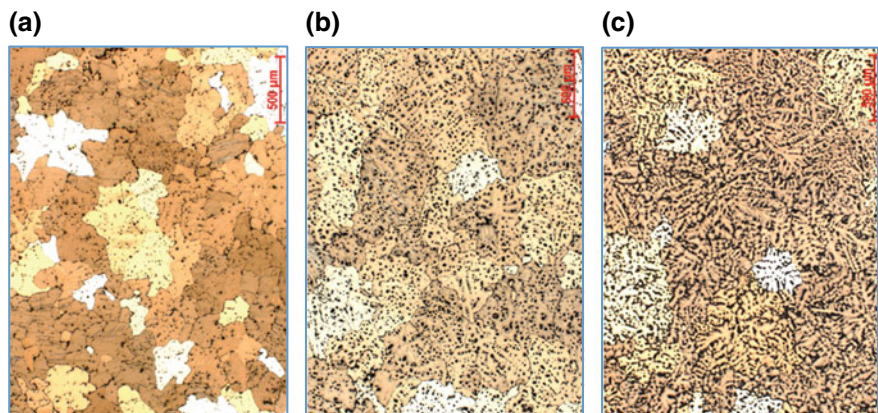


**Fig. 2** Microstructure of as-cast Mg-xZn-1Nd alloys containing a 1 wt% Zn b 2 wt% Zn, and c 4 wt% Zn





1Nd alloy) increased a content of  $Mg_{12}Zn_{13}$  phase from 0.91 to 2.29 wt%, at the expense of MgNd.

For the Mg–4Zn–1Nd alloy with the highest content of Zn among all the alloys tested, the contribution of  $Mg_{12}Zn_{13}$  increased to almost 5%. In case of non-equilibrium solidification for the Mg–1Zn–1Nd alloy, the predicted composition reached 96.53%  $\alpha$ -Mg, 2.11% BCC–MgNdZn, 0.06%  $Mg_{12}Zn_{13}$ , 1.30%  $Mg_{51}Zn_{20}$ . However, a comparison between FactSage computer predictions and experimental verification indicated some discrepancies as specified in Ref. [15]. For high magnification of optical images, the readers are referred to our journal paper [15] that shows precipitates only.

### Secondary Dendrite Arm Spacing (SDAS)

SDAS is most commonly measured by the linear intercept method, and this technique was used in the present study. An assessment of the role of both the solidification rate and alloying additions is shown quantitatively through measurement of the SDAS values. It is clear that the cooling rate during solidification affected the refinement of microstructure within all alloys tested (Fig. 3). An increase of cooling rate from 30 °C/s at the wedge thickness of 30 mm to 110 °C/s at the wedge thickness of 10 mm resulted in a reduction of SDAS from roughly 45  $\mu$ m to almost 15  $\mu$ m. The SDAS reduction depends on Zn content: for 1 and 2 wt% Zn effect is comparable with SDAS decreased from 37–45  $\mu$ m to about 20  $\mu$ m. For 4 wt% Zn, SDAS was generally smaller and reduced from 30 to 15  $\mu$ m. The role of Zn additions is emphasized in Fig. 3b, showing that an increase of Zn content from 1 to 4 wt% reduced almost twice the average SDAS from 30 to 15  $\mu$ m.

### Effect of Heat Treatment on Alloy Microstructure and Hardness

#### Microstructure After Homogenizing and Aging

The purpose of heat treatment was to assess the alloy response to homogenizing and aging, and evaluate the role of Zn content. The microstructure after solution treatment at 400 °C for 24 h is shown in Fig. 4. It was expected that water quench after solutionizing will prevent a precipitation of intermetallic compounds. When this was generally true for 1 and 2 wt% Zn (Fig. 4a, b), for 4 wt% Zn, the image contrast indicates the presence of precipitates. However, their alignment in inter-dendritic spaces suggests that they could remain undissolved from casting state rather than precipitate after solutionizing heat treatment.

As portrayed in Fig. 5, aging at 200 °C for 8 h led to precipitation of intermetallic compounds. When for 1 wt% Zn, amount of precipitates visible under magnification of optical microscope was still small, and for 2 wt% Zn,

precipitates are clearly seen. For 4 wt% Zn, amount of precipitates substantially increased as compared to those remaining after casting. Increasing aging time from 8 to 16 h increased the volume of precipitates for all Zn contents tested (Fig. 6). It is of interest that the difference in precipitate density between 2 and 4 wt% Zn seen after 8 h of aging disappeared. As shown in Fig. 6b and c, an intensive precipitation occurred for 2 wt% Zn, so the precipitate density reached the level observed for Zn content of 4 wt%.

### Influence of Heat Treatment on Alloy Hardness

A summary of hardness measurements after casting and heat treatment is shown in Fig. 7. The first observation is that for all alloy compositions the hardness after aging did not reach the level the alloys had directly after casting. Only for 1 wt% Zn and 16 h of aging, alloy practically regained the as-cast state hardness. Moreover, hardness increased with Zn content both in as-cast state and after heat treatments. A relatively small increase in hardness as compared to the solutionized state would suggest that not all compounds present after casting dissolved during heating at 400 °C for 24 h. This finding is supported by earlier microscopic observations revealing the presence of precipitates after solutionizing treatment.

### Effect of Zn on Alloy Strength After Hot Rolling

For development of magnesium sheet, the ultimate goal is to control its properties. An example of tensile properties of Mg-xZn-1Nd sheet hot-rolled at temperatures from 350 to 450 °C is shown in Fig. 8. The rolling temperature is not distinguished in Fig. 8. The graph shows that for increase in Zn content from 1 to 4 wt% there is moderate and similar increase in ultimate tensile strength and yield stress of the order of 10%. At the same time, there is much higher reduction in sheet ductility associated with the same increase in Zn content. It seems that precipitates formed in alloys with higher Zn content contribute to ductility reduction. Detailed microstructural investigation is required to explain that substantial ductility reduction.

### Role of Alloying Elements of Nd and Zn in Mg Sheet Development

Neodymium is a beneficial alloying addition in magnesium alloys as it reduces intensity of the basal texture while increasing strength and ductility [16]. Furthermore, the highly stable eutectic phases formed after the addition of rare earth elements act as effective strengthener in magnesium alloys. Among the rare earth elements, neodymium has the highest solid solubility in magnesium and for this reason

**Fig. 3** Measurements of SDAS in Mg- $x$ Zn-1Nd alloys: **a** effect of wedge thickness (cooling rate) on average SDAS, cooling rate varies from 30 °C/s at wedge thickness of 30 mm to 110 °C/s at the wedge thickness of 10 mm; **b** effect of Zn content on SDAS

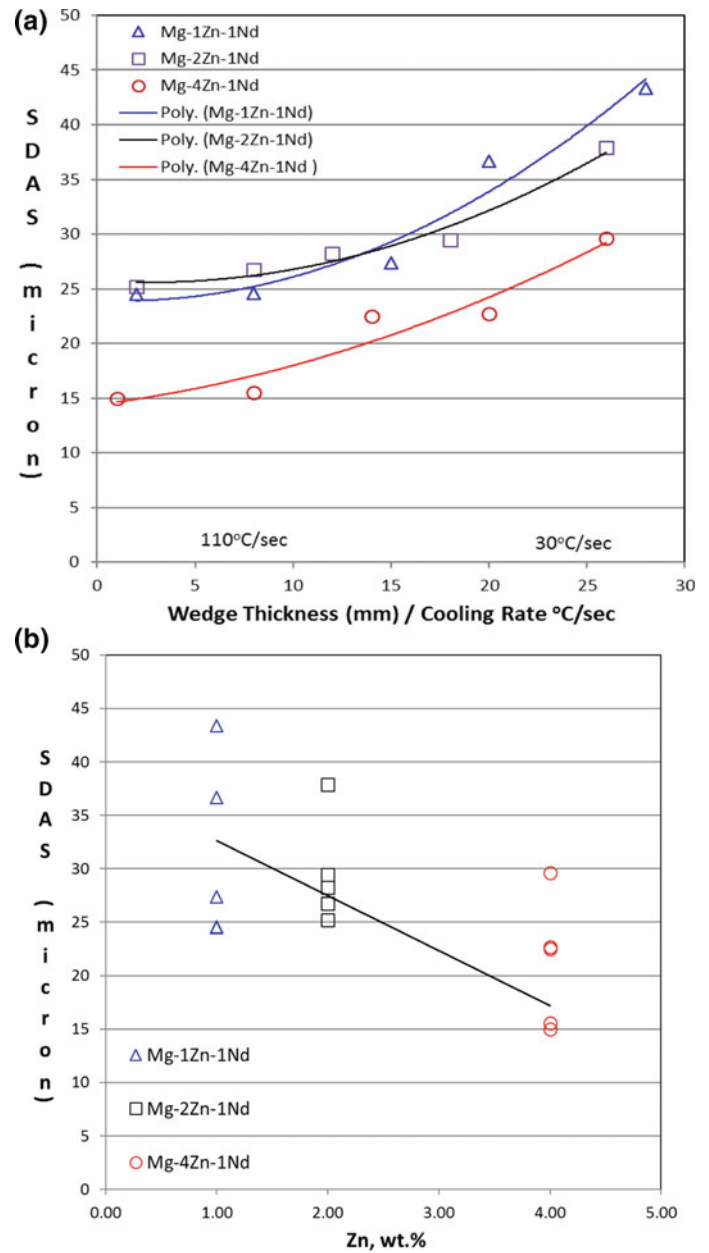


**Fig. 4** Effect of solutionizing at 400 °C for 24 h with water quench on microstructure of Mg- $x$ Zn-1Nd alloys containing **a** 1 wt% Zn, **b** 2 wt% Zn, and **c** 4 wt% Zn

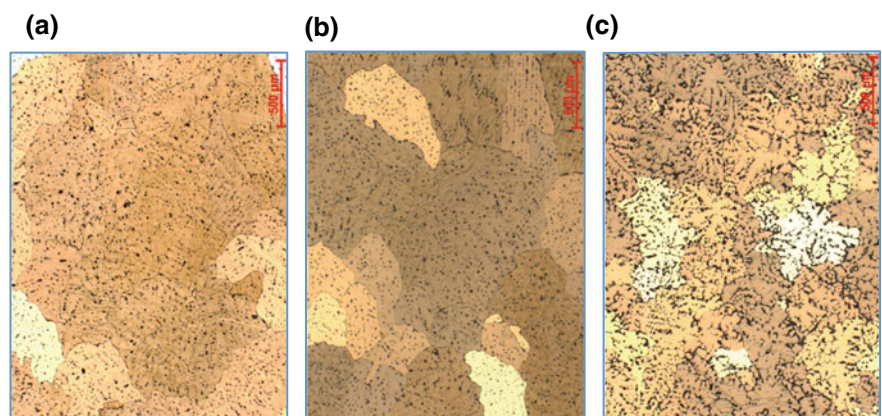


**Fig. 5** Microstructure of Mg–Zn–Nd alloys after aging at 200 °C for 8 h: **a** 1 wt% Zn, **b** 2 wt% Zn, and **c** 4 wt% Zn

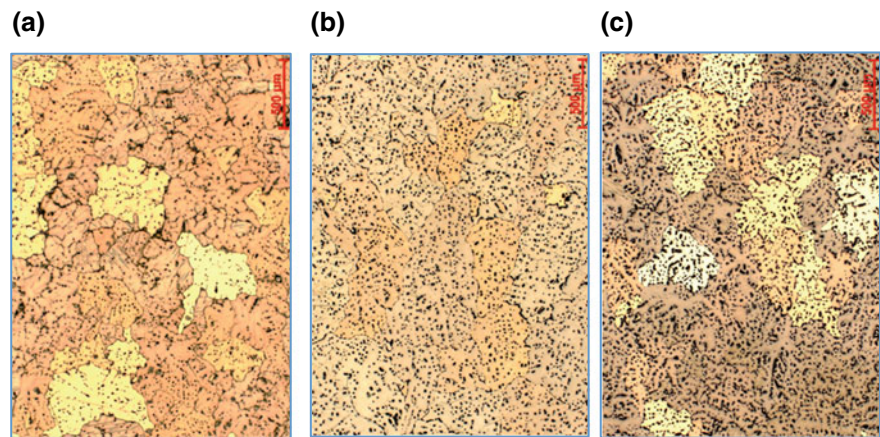


**Fig. 6** Microstructure of Mg–Zn–Nd alloys after aging at 200 °C for 16 h: **a** 1 wt% Zn, **b** 2 wt% Zn, and **c** 4 wt% Zn

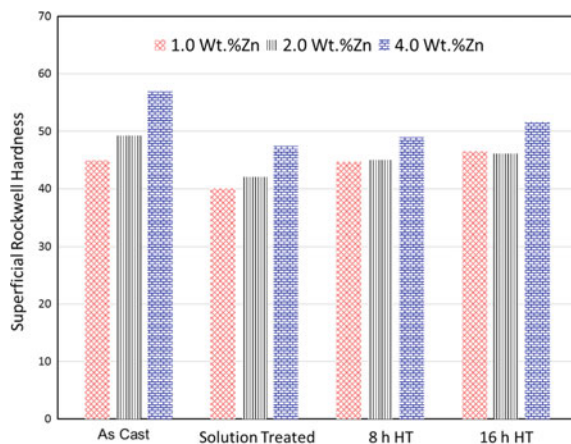
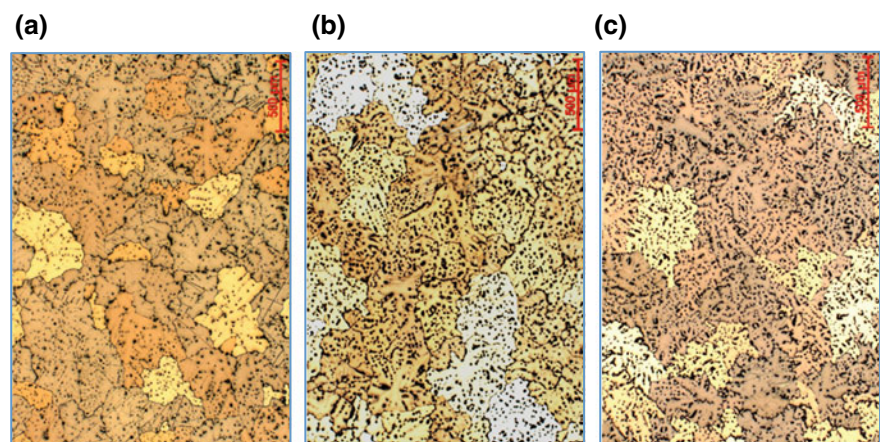


**Fig. 7** Hardness of Mg–xZn–1Nd ( $x = 1, 2, 4$  wt%) alloys after casting and heat treatment

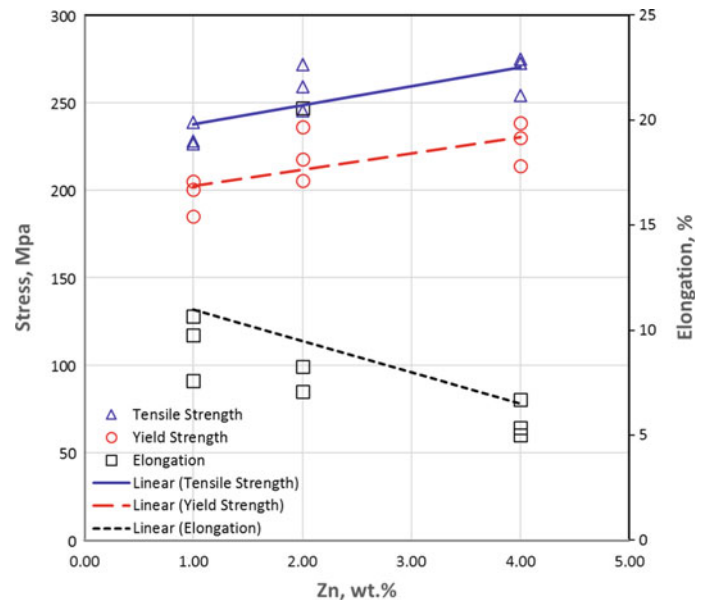
shows best response to age hardening. According to Ref. [17], the presence of  $Mg_3Nd$  hard phase contributed to better strength of Nd-containing magnesium alloys as compared to alloys containing Ce or La. On the other hand, it was reported that the microstructure of Mg–Nd alloys consists of

dendritic  $\alpha$ -Mg and divorced eutectic phase  $Mg_{12}Nd$ . The improvement in strength with increase in Nd content was attributed to both solid solution hardening and precipitation hardening [18].

Additions of Zn to Mg–rare earth (Mg–RE) alloys have been shown to significantly improve mechanical properties such as elevated temperature creep resistance [19, 20]. In particular, 0.2 wt% Zn and 0.5 wt% Zn added to extruded Mg–3Nd% alloys contributed to higher tensile properties at room temperatures [7]. An additional objective of Zn additions is their influence on precipitation hardening during heat treatment. For example, additions of Zn of the order of 1.5 wt% enhance the aging response but higher contents may change the form of Zn-containing precipitates, causing hardness reduction. In the presence of Nd and Gd, increasing Zn in the range of 0–1.3% delayed the onset of over aging but at a content of 1.3% lowered the peak hardness and tensile properties [21]. An additional advantage of Zn in rare earth-containing Mg alloys is that it may lower concentrations of RE additions required to achieve similar mechanical properties compared to Mg–RE alloys that do not have Zn additions. Since rare earths are rather expensive, this



**Fig. 8** Effect of Zn content on tensile properties of 1.50 mm thick sheet manufactured by hot rolling at temperatures from 350 to 450 °C. The individual rolling temperature is not distinguished



possibility may contribute to cost reduction, promoting the use of rare earths in industrial applications.

## Conclusions

For the Mg- $x$ Zn-1Nd ( $x = 1, 2, 4$  wt%) alloys, two major reactions were identified during solidification; formation of  $\alpha$ -Mg dendrites followed by the eutectic transformation. For 1 wt% Nd, increasing Zn content from 1 to 2 and 4 wt% caused a reduction in liquidus temperature from 646 to 640 °C and to 635 °C. For solidus, a reduction was even larger with temperature reaching 485 °C for 1 wt% Zn to 482 °C for 2 wt% Zn and to 460 °C for 4 wt% Zn. Accordingly, the eutectic temperature reduced from 507 °C for 1 wt% Zn to 491 °C for 2 wt% Zn and to 463 °C for 4 wt% Zn.

Increasing Zn content in the Mg- $x$ Zn-1Nd alloy led to general refinement of its solidification of microstructure for cooling range tested from 30 to 110 °C/s. When increasing Zn content from 1 to 4 wt%, an average value of the secondary dendrite arm spacing is reduced from over 30 to 15  $\mu$ m.

Although increasing Zn content led to higher density of precipitates after T6 treatment, hardness of all Mg- $x$ Zn-1Nd alloys tested was below the level measured in as-cast state. For aging temperature of 200 °C, slightly higher hardness increases were achieved after 16 h than that after 8 h of exposure. It appears that solutionizing treatment at 400 °C for 24 h was not sufficient to dissolve all intermetallic compounds in the alloy matrix.

For sheets rolled at temperatures from 350 to 450 °C, increasing Zn content in the Mg- $x$ Zn-1Nd alloy led to an increase in ultimate tensile strength and yield stress but

reduction in ductility. When an increase in tensile strength and yield stress was moderate of the order of 10%, the reduction in ductility of approximately 30% was rather substantial.

**Acknowledgements** The authors would like to thank the Innovative Casting team at CanmetMATERIALS for casting experiments, Marta Aniolek for assistance with thermal analysis, and Renata Zavadil with microscopy.

## References

1. F. Czerwinski, "Magnesium Alloys - Design, Processing and Applications," *InTech*, pp. 299, January 14, 2011.
2. A. Luo, R. K. Mishra and R. K. Sachdev, "High-Ductility Magnesium-Zinc-Cerium Extrusion Alloys," *Scripta Materialia*, vol. 64, pp. 410-413., 2011.
3. R. K. Mishra, "Influence of Cerium on Texture and Ductility of Magnesium Extrusions," *Scripta Materialia*, vol. 59, pp. 562-565., 2008.
4. C. Bettles and M. Gibson, "Current wrought magnesium alloys: strengths and weaknesses," *JOM*, pp. 26-49, May 2005.
5. F. Czerwinski, "The reactive element effect on high temperature oxidation of magnesium," *Int. Mater. Rev.*, vol. 50, no. 5, p. 264-296., 2015.
6. J. Robson, "Effect of rare earth additions on the texture of wrought magnesium alloys: the role of grain boundary segregation," *Metallurgical and Materials Transaction A*, vol. 48, no. 8, pp. 3205-3212, 2014.
7. K. U. Kainer, "The current state of technology and potential for further development of magnesium applications," *Magnesium Alloys and Technologies*, pp. 1-22, 2003.
8. "Magnesium and Magnesium Alloys," in *ASM Speciality Handbook*, 1999, pp. 12-25.
9. M. A. Gibson, M. Easton, V. Tyag, M. Murray and G. Dunlop, "Magnesium Technology 2008," in *TMS*, 2008.



10. A. Luo, R. K. Mishra, B. R. Powell and A. K. Sachdev, "Materials Science Form. Trans. Tech Publi 5, 69 (2012)," vol. 69, 2012.
11. Magnesium and Magnesium Alloys, ASM Speciality Handbook, September 1999.
12. L. Gill, G. Lorimer and P. Lyon, "Microstructure and property relationship of Mg-RE-Zn," Germany, International Conference on Magnesium Alloys and their Applications.
13. A. Javaid, F. Czerwinski, R. Zavadil and M. Aniolek, "Solidification characteristics of magnesium alloys with addition of rare earth elements, In: TMS Magnesium," *TMS magnesium Technology 2014*, 2014.
14. Y. He, A. Javaid and E. Essadiqi, "Numerical simulation and experimental study of the solidification of a wedge-shaped AZ31 Mg alloy casting," *Can. Metall. Quartly*, vol. 48, p. pp. 145–156, (2009).
15. A. Javaid, A. Hadadzadeh and F. Czerwinski, "Solidification behaviour of diluted Mg-Zn-Nd alloys," *Journal of Alloys and Compounds*, vol. 782, pp. 132-148, 2019.
16. J. Yan, Y. Sun, F. Xue, S. Xue and W. Tao, "Yan, J.; SunMicrostructure and mechanical properties in cast magnesium-neodymium binary alloys," *Mater. Sci. Eng. A*, vol. 476, p. 366–371, 2008.
17. T. Chia, M. Easton and M. G. N. J. N. S. Zhu, "The effect of alloy composition on the microstructure and tensile properties of binary Mg-RE alloys," *Intermetallics*, vol. 17, pp. 481-490, 2009.
18. A. Javaid, M. Kozdras and F. Czerwinski, "Overcoming barriers to magnesium rolling," *Adv. Mater. Process*, vol. 176, no. 4, p. 16–21, 2018.
19. C. Bettles, M. Gibson and S. Zhu, *Mater. Sci. Eng. A*, vol. 505, p. 6, 2009.
20. D. Choudhuri, D. Jaeger, M. Gibbson and R. Banerjee, *Sripta Mater.*, vol. 86, p. 32, 2014.
21. L. Gill, G. Lorimer and P. Lyon, "Microstructure and property relationships of Mg-RE-Zn-Zr," in *DGM International Conference on Magnesium Alloys and their Applications*, Germany, 2003.

# Influence of Manganese on Deformation Behavior of Magnesium Under Dynamic Loading

Ryutaro Goeda, Masatake Yamaguchi, Tatsuya Nakatsuji, Naoko Ikeo, and Toshiji Mukai

## Abstract

Magnesium alloys are promising lightweight structural materials. However, their practical utilization requires improvement of strength and ductility. Adding manganese as a solute improves the room-temperature ductility of magnesium alloys by facilitating grain boundary sliding, but its effects on deformation behavior under dynamic loading remain unclear. Accordingly, we investigated the strain rate dependence of both the flow stress and the deformation mechanism of Mg–Mn alloys via tensile tests over a wide range of strain rates. Grain boundary sliding induced relatively larger elongation under quasi-static conditions. On the contrary, the Mg–Mn alloy exhibited limited necking in the high strain rate regime dominated by intergranular fracture.

## Keywords

Mg–Mn binary alloy • split-Hopkinson pressure bar (SHPB) • Deformation behavior • Tensile elongation • Strain rate dependence

## Introduction

In recent years, there has been an increasing demand for realizing a low-carbon society. Thus, reducing exhaust gas emissions from transportation equipment such as trains and automobiles is required. One common approach for reducing exhaust gas emissions is decreasing the weight of the transportation equipment. At present, the main structural

materials used for transportation equipment are stainless steel and aluminum alloys. However, magnesium alloys have been shown to improve the fuel efficiency and performance of transportation equipment [1–3]. Magnesium is the lightest of the practical metals and has the eighth largest Clarke number (indicating its abundance in the Earth's crust as a naturally occurring metal) after iron and aluminum. Thus, magnesium is considered as a promising structural material. However, magnesium has higher plastic anisotropy than stainless steel and aluminum alloys owing to its hexagonal close-packed crystal structure [4]. Moreover, magnesium has lower strength and ductility at room temperature than conventional structural materials. One effective strategy for overcoming these limitations is solid solution strengthening. In this study, we focused on manganese as a solute element for magnesium alloys. Somekawa et al. previously reported that manganese segregates along the grain boundaries of magnesium and greatly facilitates grain boundary sliding, thereby dramatically improving room-temperature ductility [5].

In the evaluation of structural materials for transportation equipment, it is important to acquire material data under a wide range of strain rate conditions from the low to high strain rate regimes. Many magnesium alloys have strain rate-dependence in their mechanical properties [6–8], and it is important to determine the strain rate sensitivity of the deformation behavior of materials used in transportation equipment. However, the mechanical properties of Mg–Mn alloys have been evaluated at only low strain rates [5], and the effects of manganese addition on deformation behavior under dynamic conditions are not yet entirely understood. Therefore, in this study, we performed high-rate tensile tests using the split Hopkinson pressure bar (SHPB) method to evaluate the deformation behavior occurring during the collision of transportation equipment. In addition, we conducted quasi-static tensile tests using an Instron universal testing machine. By conducting tensile tests at both low and high strain rates, we investigated the strain rate dependence

R. Goeda · T. Nakatsuji · N. Ikeo · T. Mukai (✉)  
Graduate School of Engineering Faculty of Engineering, Kobe University, 1-1 Rokkodai-Cho, Nada, Kobe, Hyogo 657-8501, Japan  
e-mail: [mukai@mech.kobe-u.ac.jp](mailto:mukai@mech.kobe-u.ac.jp)

M. Yamaguchi  
Japan Atomic Energy Agency, 765-1 Funaishikawa, Tokai-Mura, Naka-Gun, Ibaraki, 319-1184, Japan

of both the flow stress and the deformation mechanism of Mg–Mn alloys.

## Experimental Methods

### Testing Apparatus

In this study, high rate-tensile tests were conducted using the SHPB method. An SHPB testing machine is composed of three elastic bars: a striker tube, an incident bar, and a transmission bar. The striker tube is accelerated by compressed air, whereupon it collides with the flange part of the incident bar to generate a tensile stress wave that propagates through the incident bar. Then, a dynamic load can be applied to a specimen positioned between the incident bar and the transmission bar. The apparatus configuration and analytical methods are described in detail below.

Figure 1 is a schematic of the high-rate tensile testing machine used in this study. There is currently no standard design for SHPB devices, and testing machines are typically constructed from common components [9]. The main component is a symmetrical incident bar and a transmission bar, between which the test specimen is positioned. The pressure bars must retain elasticity even during the deformation of the specimen, such that a one-dimensional elastic wave propagates through the pressure bars [9]. In other words, the pressure bars in an SHPB testing machine must be fabricated from high-strength structural materials. There are also standards regarding the lengths and diameters of the pressure bars [9]. The incident bar and the transmission bar must have one degree of freedom in the axial direction and be arranged in a uniaxial manner. Strain gauges measure the change in strain over time and are attached to the incident bar and the transmission bar in a symmetrical manner parallel to the axis.

The signal from a strain gauge is obtained as a small change in resistance. In this study, the change in resistance was converted into a voltage difference from equilibrium by using a bridge box. This voltage difference was then amplified by using an amplifier and then displayed and recorded by using an oscilloscope. A bridge circuit was used for the conversion of the strain gauge output. A Wheatstone bridge was constructed by combining variable resistors and

two fixed resistors, whose resistance was comparable to that of the two strain gauges, and the change in resistance of the strain gauge was then output as a voltage. In this study, the same strain gauge as the one used for load detection was applied as a fixed resistor in the bridge circuit, such that the change in resistance due to external temperature variation could be neglected.

### Calculation of Stress–Strain Relation

In this section, the measurement of stress waves in the SHPB and calculation method of stress–strain relation are explained. First, the striker tube collides with the flange part of the incident bar, generating a tensile stress wave in the incident bar. This tensile stress wave propagates through the incident bar, and when it reaches the boundary between the incident bar and the specimen, it is partially reflected at the free end and becomes a compression stress wave. The residual tensile stress wave is transmitted through the specimen and propagates into the transmission bar. These three stress waves, namely, the incident wave, the reflected wave, and the transmitted wave were measured using the strain gauges attached to the incident bar and the transmission bar. Because the stress wave is a one-dimensional elastic wave, the absolute value of the measured incident wave is equal to the sum of the absolute values of the reflected wave and the transmitted wave.

Because the stress wave is a one-dimensional elastic wave as described in the previous subsection, the stress and the displacement can be calculated by performing measurements at a single arbitrary point in the pressure bars. Let the incident strain be  $\varepsilon_i$ , the transmitted strain be  $\varepsilon_t$  and the reflected strain be  $\varepsilon_r$ . Figure 2 depicts the relationship between each parameter and the pressure bars and the specimen.

According to the theory of one-dimensional elastic wave propagation, the strain rate can be expressed by Eq. (1) using the strain in the pressure bars [9]:

$$\dot{\varepsilon} = \frac{C_b}{l_0} (-\varepsilon_i + \varepsilon_r + \varepsilon_t) \quad (1)$$

where  $C_b$  and  $l_0$  represent the wave velocity in the longitudinal direction in the pressure bars and the gauge length of

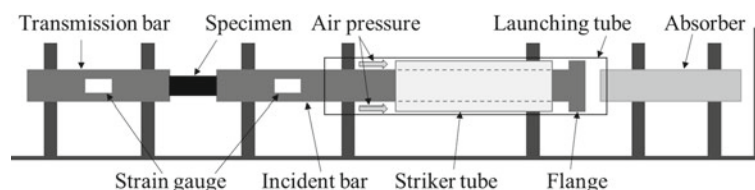
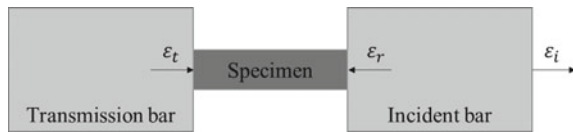


Fig. 1 Schematic illustration of SHPB testing machine



**Fig. 2** Equilibrium of elastic strains between the incident bar and the transmission bar

the specimen. When the specimen is in the state of stress balance, because the forces applied to both ends of the specimen are balanced, Eq. (2) can be obtained:

$$\varepsilon_t = \varepsilon_i + \varepsilon_r \quad (2)$$

Substituting Eq. (2) into Eq. (1) gives Eq. (3):

$$\dot{\varepsilon} = \frac{2C_b \varepsilon_r}{l_0} \quad (3)$$

In addition, strain can be obtained by the integrated value of the strain rate as the following Eq. (4):

$$\varepsilon(t) = \int_0^t \dot{\varepsilon}(t) dt \quad (4)$$

In general, the nominal stress can be obtained by dividing the load by the initial cross-sectional area of the gauge portion of the specimen. The nominal stress can be obtained by dividing the load transmitted through the specimen, as measured using the strain gauges, by the initial cross-sectional area of the gauge portion of the specimen  $A_0$ :

$$\sigma(t) = \frac{AE\varepsilon_r}{A_0} \quad (5)$$

where  $A$  and  $E$  are the cross-sectional area and Young's modulus of the pressure bars, respectively. In this analytical method, the reflected wave is used to measure the strain in the specimen, whereas the transmitted wave is used to measure the stress. This analytical theory is referred to as one-wave analysis [9], and this theory was used in the present study.

### Configuration of the Testing Machine

Table 1 summarizes the dimensions and materials of the incident bar, the transmission bar, and the striker tube used in the high-rate tensile testing machine. To prevent stress

wave interference during the tensile tests, the strain gauges were attached 1000 mm from the incident bar/specimen interface and 400 mm from the transmission bar/specimen interface.

### Testing Material and Conditions

The material examined in this study was extruded Mg–0.18 at.% Mn alloy with an average grain size of approximately 1.2  $\mu\text{m}$ . The specimens for the tensile tests were prepared from the extruded material via a machining process and were 5 mm in length and 2.5 mm in diameter.

The tensile tests were conducted using an Instron universal testing machine and the SHPB tensile testing machine. The conditions were  $1.0 \times 10^{-4} \text{ s}^{-1}$  in the low strain rate regime and  $1.2 \times 10^3 \text{ s}^{-1}$  in the high strain rate regime.

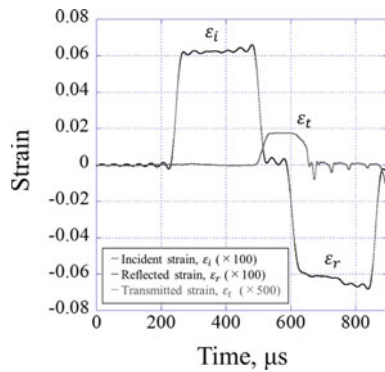
### Results and Discussion

Figure 3 presents the waveforms obtained from the strain gauges during the high-rate tensile tests of the Mg–Mn alloy. Because there was no stress wave interference, the stress–strain relation of the sample was calculated using the analytical theory described in section “[Calculation of stress–strain relation](#)”. Variations in the calculated strain rate and nominal stress as a function of nominal strain are shown in Fig. 4. Figure 5 shows the true stress–strain relation in the high-rate tensile tests obtained via one-wave analysis and the true stress–strain curve obtained from the quasi-static tensile tests. From the true stress–strain curves presented in Fig. 5, the strain rate dependence of the flow stress was confirmed. With increasing strain rate, the flow stress increased significantly, whereas the fracture elongation decreased drastically. Figure 6 is a photograph showing the appearance of specimens before and after the tensile test at  $1.0 \times 10^{-4} \text{ s}^{-1}$ . Under the low strain rate condition of  $1.0 \times 10^{-4} \text{ s}^{-1}$ , the flow stress exhibited an almost constant value after yielding and no work hardening was observed. In the low strain rate regime, grain boundary sliding was the dominant deformation mechanism, and as a result, the specimen underwent uniform deformation with large elongation as shown in Fig. 6. These observations are in accordance with previously

**Table 1** Specifications of the pressure bars used in the high-rate tensile testing machine

Pressure bar	Diameter [mm]	Length [mm]	Material
Incident bar	16	2000	SKD11
Transmission bar	16	1400	SKD11
Striker tube	–	570	SUS304





**Fig. 3** Stress waves detected by the strain gauges on the incident bar and transmission bar during the high-rate tensile tests

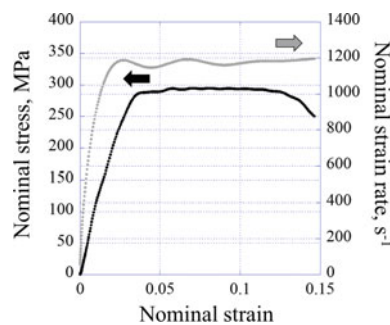


**Fig. 4** Variations in the calculated strain rate and nominal stress as a function of nominal strain

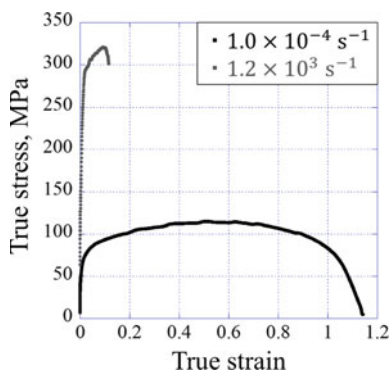


**Fig. 5** True stress–strain curves of the Mg–Mn alloy under tension

reported results of tensile tests of Mg–Mn alloys [7, 10]. In contrast, under the high strain rate condition of  $1.2 \times 10^3 \text{ s}^{-1}$ , the material exhibited work hardening after yielding, and the deformation mechanism was considered distinct from that observed in the low strain rate regime. Figure 7 shows the deformation behavior during a high-rate

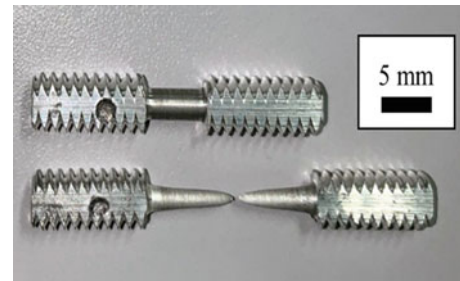


**Fig. 6** Appearance of specimens before (top) and after (bottom) the quasi-static tensile test

tensile test, as observed with an ultrahigh-speed camera. Figure 7a and b show the gauge portion of the specimen before the tensile test and just before fracture, respectively. Compared with the specimen after the quasi-static tensile test shown in Fig. 6, these observations confirm that deformation was limited in the high strain rate regime and the specimen fractured with extremely small elongation. From the images shown in Fig. 7, the reduction in the cross-sectional area of the gauge portion of the specimen prior to fracture was calculated to be only 16.9%, indicating that the Mg–Mn alloy exhibited brittle fracture without localized necking under dynamic conditions. From these results, it is clear that the deformability of the Mg–Mn alloy was remarkably decreased when grain boundary sliding was limited, and from the perspective of dislocation slip, it is suggested that the addition of manganese to magnesium has little effect on improving the plastic anisotropy.

## Summary

In this study, tensile tests of an Mg–Mn alloy were conducted under high and low strain rate conditions. The results confirmed that the Mg–Mn alloy exhibited strain rate dependence of both the flow stress and the deformation mechanism. Upon increasing the strain rate, the flow stress increased greatly while the elongation reduced significantly. As reported previously, the large elongation in the low strain rate regime is attributed to grain boundary sliding [7, 10]. In the high strain rate regime, the Mg–Mn alloy exhibited work hardening after yielding, suggesting the occurrence of deformation mechanisms other than grain boundary sliding, such as dislocation slip. Mg–Mn alloy exhibited small elongation without necking under conditions where grain boundary sliding was limited. Therefore, it appears that manganese addition has little effect on improving the plastic anisotropy of magnesium.

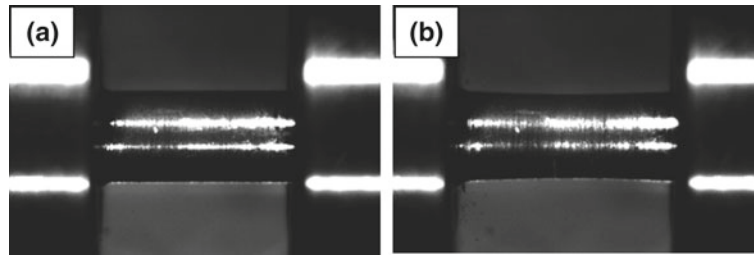


**Fig. 7** Observed deformation behavior during a high-rate tensile test: **a** before the test and **b** just before fracture

**Acknowledgements** This work was financially supported by JSPS KAKENHI (Grant Number 17H01327).

## References

1. Yasufumi SUZUKI, Weight reduction of railway vehicles by applying aluminum alloy and its future problems, *Journal of Japan Institute of Light Metals*, Vol. 60, No. 11 (2010), pp. 565–570.
2. Hisashi Mori, Kenji Fujino, Ken Kurita, Yasumasa Chino, Naobumi Saito, Masafumi Noda, Hiroshi Komai, Hisashi Obara, Application of the Flame-Retardant Magnesium Alloy to High Speed Rail Vehicles, *Materia Japan*, Vol. 52, No. 10 (2013), pp. 484–490.
3. Yasufumi Suzuki, *New Materials for high Speed Railway Vehicle*, *Tetsu-to-Hagane*, Vol. 79, No. 8 (1993), pp. 568–575.
4. R. Ohyama, J. Koike, M. Suzuki, K. Maruyama, Texture Dependence of Elongation Anisotropy in an AZ61 Magnesium Alloy Sheet, *J. Japan Inst. Metals*, Vol. 68, No. 1 (2004), pp. 27–33.
5. Hidetoshi Somekawa, Dudekula Althaf Basha, Alok Singh, Room temperature grain boundary sliding behavior of fine-grained Mg-Mn alloys, *Materials Science and Engineering A* 730 (2018) 355–362.
6. Na Zhou, Zhenyan Zhang, Li Jin, Jie Dong, Bin Chen, and Wenjiang Ding, Ductility improvement by twinning and twin-slip interaction in a Mg-Y alloy, *Materials & Design*, Vol. 56 (2014), pp. 996–974.
7. Hidetoshi Somekawa, Yoshiaki Osawa, Alok Singh, Kota Washio, Akira Kato and Toshiji Mukai, Effect of Micro-Alloying Elements on Deformation Behavior in Mg-Y Binary Alloys, *Materials Transactions*, Vol. 55, No. 1 (2014), pp. 182–187.
8. I. Ulacia, N.V. Dudamell, F. Gölvez, S. Yi, M. T. Pérez-Prado, and I. Hurtado, Mechanical behavior and microstructural evolution of a Mg AZ31 sheet at dynamic strain rates, *Acta Materialia*, Vol. 58, No. 8 (2010), pp. 2988–2998.
9. George T. (Rusty) Gray, *Classic Split-Hopkinson Pressure Bar Testing*, *ASM Handbook Volume, 09* (2004), pp 462–465.
10. Hidetoshi Somekawa, Alok Singh, Superior room temperature ductility of magnesium dilute binary alloy via grain boundary sliding, *Scripta Materialia*, Vol. 150 (2018), pp. 26–30.

# Microstructure and Hardness of Porous Magnesium Processed by Powder Metallurgy Using Polystyrene as the Space Holder

Ning Zou and Qizhen Li

## Abstract

Porous magnesium (Mg) with different overall porosities ( $4.1 \pm 0.5$ ,  $6.1 \pm 1.3$ ,  $12.9 \pm 3.3$ , and  $19.0 \pm 6.2\%$ ) were manufactured by powder metallurgy using polystyrene (PS) as the space holder. The samples were either hot pressed or cold pressed. Two types of PS were used to study the effect of molecular weight (Mw) of polymer space holder on properties of porous Mg. Porous Mg contained small amount of MgO. The utilization of lower Mw PS as the space holder introduced less amount of MgO into porous Mg. Average pore size increased from  $2.0 \pm 0.03$  to  $7.9 \pm 3.3$   $\mu\text{m}$  with overall porosity increasing from  $4.1 \pm 0.5$  to  $19.0 \pm 6.2\%$ . Hardness of porous Mg decreased with overall porosity increasing. Using PS as the space holder, porous Mg by hot pressing route exhibited higher hardness than that by cold pressing route.

## Keywords

Porous magnesium • Polystyrene • Powder metallurgy

## Introduction

Porous Mg has great potential to be used for biodegradable implants due to its suitable mechanical properties, biodegradability, and biocompatibility [1, 2]. The introduction of pores into Mg also allows bone or tissue ingrowth and accelerates the osseointegration and healing process [3]. Powder metallurgy is a popular way to manufacture porous Mg with the addition of space holders [4–15], such as carbamide [4–9], ammonium bicarbonate [10], Poly(methyl

methacrylate) (PMMA) [11],  $\text{Cs}_2\text{CO}_3$ ,  $\text{ZrH}_2$ ,  $\text{CaH}_2$  [16], naphthalene [17], and camphene [18].

Polymers are widely used as a space holder/template for the synthesis of porous materials [19–22]. For example, polystyrene (PS) was used to fabricate nanoporous gold and nickel [20–22]. Only PMMA particles, one type of polymer, were reported as space holder for porous Mg [11]. PMMA particles used by Bi et al. [11] were almost spherical shapes with diameter of 50–100  $\mu\text{m}$ . The pores were closed-cell with two different sizes, about 100  $\mu\text{m}$  and 5–10  $\mu\text{m}$ , respectively. One advantage of using PS rather than PMMA is that PS can be dissolved in tetrahydrofuran (THF) without certain size, which contributes to processing smaller pores and can manufacture possible interconnected pores. PS can be mixed with Mg powders by dissolving PS in THF solution through solution blending. Solution blending is to mix materials in liquid state, then evaporate the solvent, and press the mixture into bulk sample [23]. PS can be decomposed and removed at high temperatures ( $>460$  °C) in Argon atmosphere [24, 25], and thus we can use PS as the space holder to create pores inside Mg. To our best knowledge, PS was not used for processing porous Mg in the published literature.

The compaction processing (compaction pressure and temperature) affected the properties of materials. Compaction pressure was reported to affect the hardness of Mg–PS composites [26] and strength of porous Mg [13]. However, the effect of compaction temperature was not reported. It is meaningful to find out how the compaction temperature, e.g. lower than  $T_g$  and higher than  $T_g$ , affects the processing and properties of fabricated porous samples. The glass transition temperature ( $T_g$ ) of PS is 107 °C [27]. Meanwhile, there are different commercial PS with different molecular weight (Mw) available, the question of choosing which Mw of PS needs to be addressed.

This work used PS as the space holder to process porous Mg. The effects of different Mw and compaction temperature on properties of porous Mg were also investigated.

N. Zou · Q. Li (✉)

School of Mechanical and Materials Engineering, Washington State University, Pullman, WA 99164, USA  
e-mail: qizhen.li@wsu.edu

## Experimental

Mg powders (density 1.738 g/cm<sup>3</sup>, ~99.8%, ~325mesh, Alfa-Aesar), two kinds of PS with different Mw (Sigma-Aldrich, PS (Mw 45,000), and PSI (Mw 192,000)), and THF (J. T. Baker) are raw materials. Mg powders are same as our previous research [18], with an average size of 45.3 μm.

Porous Mg was processed by powder metallurgy with three steps: mixing, compacting, and sintering. Firstly, Mg particles were mixed with PS in THF solution, and they were kept mixing and stirring for about 4 h until THF evaporated out. Secondly, compression molding technique [28] was applied to compress PS–Mg mixtures by 30 MPa into a dimension of 5 × 10 × 10 mm at 20 ~ 25 °C and 190 ~ 200 °C respectively. Mixtures compacted at 20 ~ 25 °C is named cold pressing, while mixtures compacted at 190 ~ 200 °C is named hot pressing. Thirdly, PS–Mg mixtures were sintered by two steps in Argon atmosphere. PS was decomposed and removed by sintering at 500 °C for 3 h at first, followed by sintering at 630 °C for 3 h. For metallography, the fabricated samples were cold mounted first, then they were grinded by sandpaper, and finally they were polished using 1 μm alumina powder in ethanol. Porous Mg with different overall porosities, 19.0 ± 6.2%, 12.9 ± 3.3%, and 6.1 ± 1.3%, respectively, were fabricated by changing weight percentage of PS. Overall porosities were represented by average porosity afterwards. Pure Mg powders were compressed and sintered under the same pressing condition with the overall porosity of 4.1 ± 0.5%.

Microstructure of processed porous Mg was characterized by optical microscopy (OM). 40 hardness test readings of samples were taken by Vickers hardness tester (loading 500 g, time 10 s). 19.0% porous Mg with PS mixture before sintering, 19.0% porous Mg with PSI mixture before sintering, 19.0% porous Mg using PS as the space holder, and 12.9% porous Mg using PSI as the space holder were analyzed by X-ray Diffraction (XRD, Rigaku Miniflex 600). Average pore size and overall porosities were measured and calculated based on microstructure by linear intercept, similar to the method to calculate the grain size. Multiple lines (total length  $L$ ) are drawn first. The total length of pores intercepted with lines is measured as  $L_p$  and the total number of pores is counted as  $N$ . The porosity is calculated by  $L_p/L$  and the pore size is calculated by  $L_p/N$ . 5 figures were repeated for each type of porous Mg.

## Results and Discussion

### Microstructure

PS–Mg and PSI–Mg mixtures for 19.0% porous Mg before the sintering step have the same XRD pattern as pure Mg, as shown in Fig. 1. PS and PSI were not detected in the XRD pattern as there was low weight fraction of PS in mixtures. 19.0% porous Mg using PS as the space holder contains a little MgO remained as the impurity phase, showed by the (200) peak at 42.8° in Fig. 1, while 12.9% porous Mg using PSI as the space holder has higher (200) peak at 42.8° and (220) peak at 62.2°. This indicates that using higher Mw PS as the space holder introduces more amount of MgO into porous Mg. PS was decomposed into low Mw gaseous products during sintering, including toluene, benzene, and oligomers of styrene [23]. MgO is formed as Mg reacts with these compounds containing oxygen. For high Mw PSI, compounds contain higher molecular weight gaseous products with higher amount of oxygen, which leads to higher MgO contents. MgO impurity was also reported in other porous Mg processed by powder metallurgy [5, 6, 11, 15].

Microstructure of 19.0, 12.9, and 6.1% porous Mg using PS and PSI as the space holder by hot pressing route are shown in Figs. 2 and 3 respectively. Figure 2 also shows the microstructure of 4.1% porous Mg. Microstructure of 19.0, 12.9, and 6.1% porous Mg using PS as the space holder by cold pressing route are shown in Fig. 4. The dark parts are pores while the bright/yellow parts are Mg in Figs. 2, 3 and 4. The microstructure shows that pores have different pore

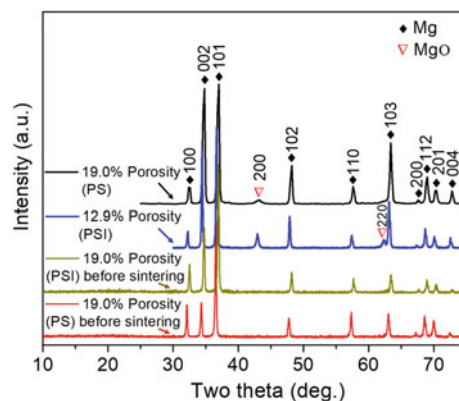


**Fig. 1** Indexed XRD for PS–Mg and PSI–Mg composites before sintering, and porous Mg



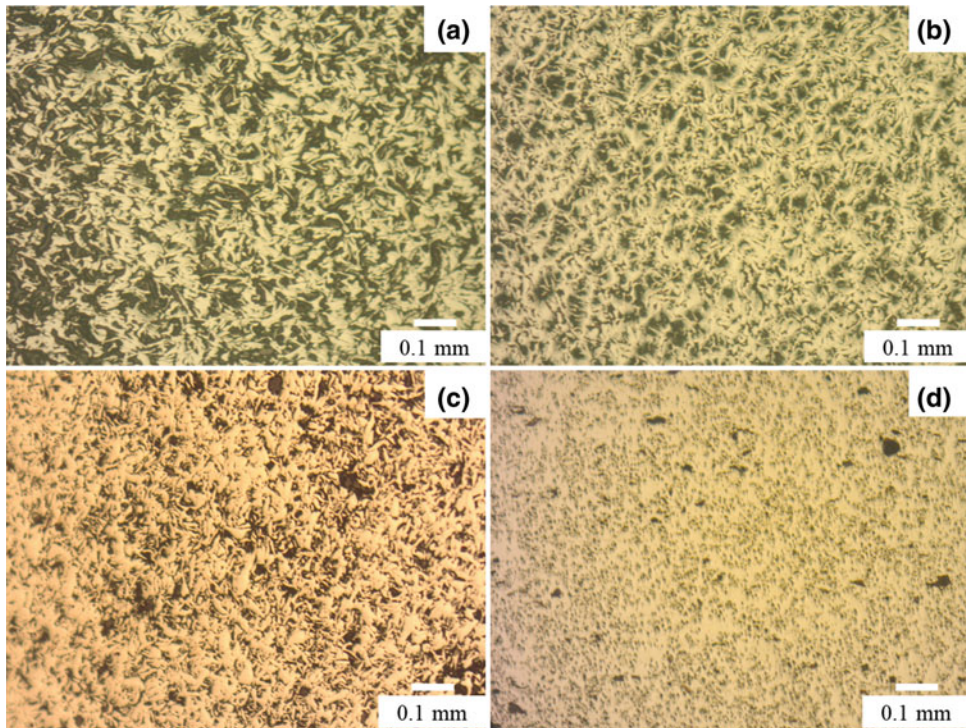


**Fig. 2** Microstructure of porous Mg using PS by hot pressing route with different porosities, **a** 19.0%, **b** 12.9%, **c** 6.1%, and **d** 4.1%

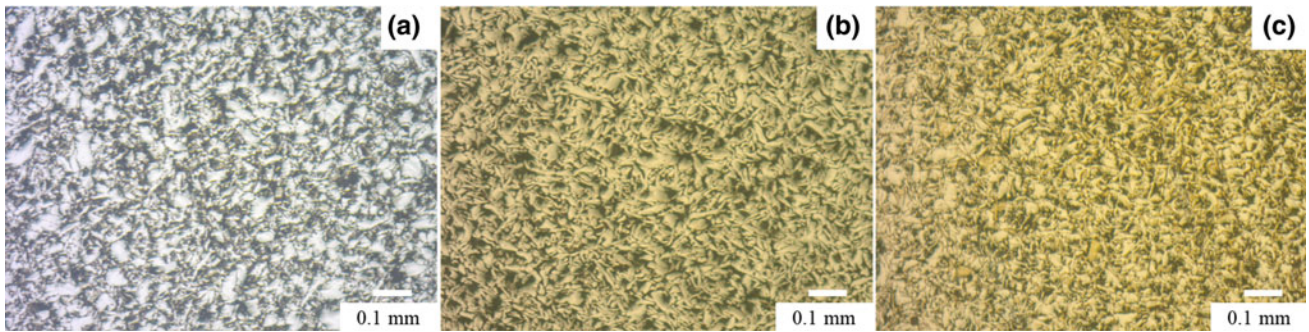


**Fig. 3** Microstructure of porous Mg using PSI by hot pressing route with different porosities: **a** 19.0%, **b** 12.9%, and **c** 6.1%

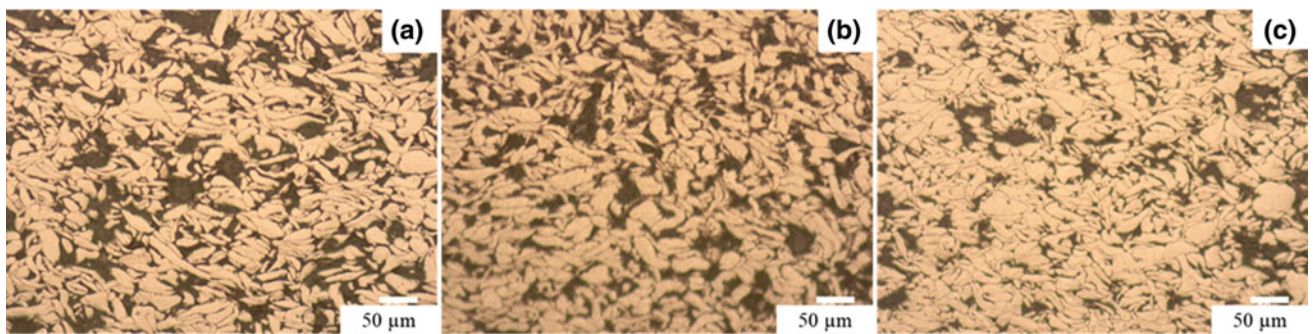


**Fig. 4** Microstructure of porous Mg using PS by cold pressing route with different porosities, **a** 19.0%, **b** 12.9%, and **c** 6.1%

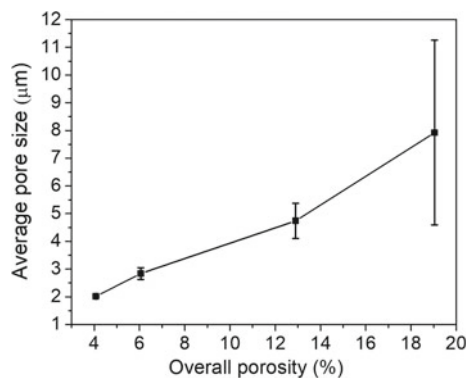


**Fig. 5** Average pore size of porous Mg using PS by hot pressing route changes with different porosities

sizes and irregular pore shape. Porous Mg using PS by hot pressing route also shows smaller pore size than porous Mg using PS by cold pressing route, as shown in Figs. 2 and 4. Meanwhile, porous Mg by hot pressing route has more uniform pores than that by cold pressing, which could be explained by the low mobility of PS at low temperature and part of PS is aggregated [26]. We can clearly find several big pores in Fig. 4. Average pore size of porous Mg using PS by hot pressing route increases from  $2.0 \pm 0.03$  to  $7.9 \pm 3.3 \mu\text{m}$  with the increase of overall porosity from 4.1 to 19.0%, as shown in Fig. 5. This relationship between overall porosity and pore size was also reported by our previous research [5]. The pores are found in 4.1% porous Mg without using space holders in Fig. 2d, as there are possible gas and pores between powder before the sintering and these pores are kept inside.

## Mechanical Behavior

Hardness is the resistance of the material against permanent damage on the surface under the compressive force. Hardness can correlate with strength and higher hardness correlates with higher strength. Hardness of porous Mg using PS as the space holder by hot pressing route decreases from  $21.5 \pm 2.9$  to  $12.9 \pm 3.2$  HV, while hardness of porous Mg using PS as the space holder by cold pressing route decreases from  $15.6 \pm 3.6$  to  $12.7 \pm 0.7$  HV, with the increase of porosity from 6.1 to 19.0%, as shown in Fig. 6. Hardness of 4.1% porous Mg without using space holder is  $23.0 \pm 5.6$  HV. Hardness of porous Mg using PSI as the space holder by hot pressing route decreases from  $21.2 \pm 3.7$  to  $15.7 \pm 4.5$  HV with the increase of porosity from 6.1 to 19.0%, as shown in Fig. 6. Porous Mg by hot pressing route has higher hardness than that by cold pressing route. The possible reason is that PS has higher mobility by hot pressing route compared with cold pressing route [26],

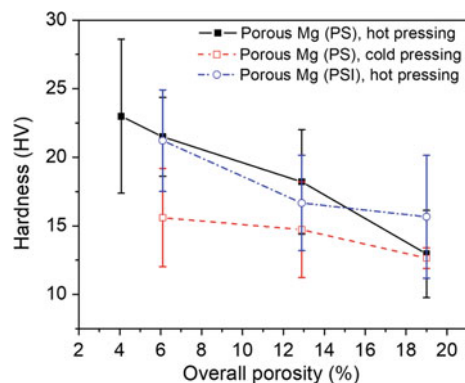


**Fig. 6** Hardness of fabricated porous Mg by different temperature pressing routes and different PS (PS and PSI)

which contributes to combining the mixture well together before sintering. The big pores produced in cold pressing routes could lead to lower hardness of porous Mg as shown in Fig. 4. The two different Mw PS shows little effect on hardness of porous Mg in Fig. 6, but low Mw PS can fabricate high purity porous Mg as shown in Fig. 1. Different compaction temperature (hot pressing route and cold pressing route) shows big effect on hardness of porous Mg in Fig. 6 and hot pressing route is preferred to fabricate porous Mg with high strength. The range for strength of natural bone is 0.2–80 MPa [29]. Strength is about 1/3 times of hardness (HV) [30] and 1 HV is about 9.8 MPa. The estimated strength of porous Mg is about 70 to 42.1 MPa when hardness is from 21.5 to 12.9 HV. The estimated strength of porous Mg matches with strength of natural bone, which reveals that porous Mg has suitable strength bone implant.

## Conclusion

Porous Mg with several overall porosities (6.1, 12.9 and 19.0%) was manufactured by powder metallurgy using PS as the space holder. PS was removed through the sintering process at Argon atmosphere. Porous Mg contains small amount of MgO. Low Mw PS introduces more amount of MgO into porous Mg than high Mw PS. Low Mw PS is a better space holder candidate than high Mw PSI. Average pore size increases from  $2.0 \pm 0.03$  to  $7.9 \pm 3.3 \mu\text{m}$  with overall porosity increasing from 4.1 to 19.0%. Hardness of porous Mg decreased with overall porosity increasing. Hardness of porous Mg using PS as the space holder by hot pressing route, which decreases from  $21.5 \pm 2.9$  to  $12.9 \pm 3.2$  HV with the increase of porosity from 6.1 to 19.0%, is higher than that by cold pressing route. The estimated strength of porous Mg shows suitable strength for bone implants.



**Acknowledgements** Financial support from the National Science Foundation under Award No. 1449607 is greatly appreciated. The authors thank Mr. Chin-Shih Hsu for collecting XRD data.

## References

1. M. Yazdimamaghani, M. Razavi, D. Vashae, K. Moharamzadeh, A.R. Boccaccini, L. Tayebi (2017) Porous magnesium-based scaffolds for tissue engineering. *Mater. Sci. Eng., C* 71:1253–1266.
2. A. Kucharczyk, K. Naplocha, J.W. Kaczmar, H. Dieringa, K.U. Kainer (2017) Current Status and Recent Developments in Porous Magnesium Fabrication. *Adv. Eng. Mater.* 20(1):1700562.
3. M.Q. Cheng, T. Wahafu, G.F. Jiang, W. Liu, Y.Q. Qiao, X.C. Peng, T. Cheng, X.L. Zhang, G. He, X.Y. Liu (2016) A novel open-porous magnesium scaffold with controllable microstructures and properties for bone regeneration. *Sci. Rep.* 6:24134.
4. C.E. Wen, Y. Yamada, K. Shimojima, Y. Chino, H. Hosokawa, M. Mabuchi (2004) Compressibility of porous magnesium foam: dependency on porosity and pore size. *Mater. Lett.* 58(3–4):357–360.
5. N. Zou, Q. Li (2016) Compressive mechanical property of porous magnesium composites reinforced by carbon nanotubes. *J. Mater. Sci.* 51(11):5232–5239.
6. H. Cay, H. Xu, Q. Li (2013) Mechanical behavior of porous magnesium/alumina composites with high strength and low density. *Mater. Sci. Eng., A* 574:137–142.
7. Q. Li (2016) Effect of porosity and carbon composition on pore microstructure of magnesium/carbon nanotube composite foams. *Mater. Des.* 89:978–987.
8. Q. Li (2014) Carbon nanotube reinforced porous magnesium composite: 3D nondestructive microstructure characterization using x-ray micro-computed tomography. *Mater. Lett.* 133:83–86.
9. H. Xu, Q. Li (2017) Effect of carbon nanofiber concentration on mechanical properties of porous magnesium composites: experimental and theoretical analysis. *Mater. Sci. Eng. A* 706:249–255.
10. J. Capek, D. Vojtech (2014) Effect of sintering conditions on the microstructural and mechanical characteristics of porous magnesium materials prepared by powder metallurgy. *Mater. Sci. Eng., C* 35:21–8.
11. Y. Bi, Y. Zheng, Y. Li (2015) Microstructure and mechanical properties of sintered porous magnesium using polymethyl methacrylate as the space holder. *Mater. Lett.* 161:583–586.
12. C. Wen, M. Mabuchi, Y. Yamada, K. Shimojima, Y. Chino, T. Asahina (2001) Processing of biocompatible porous Ti and Mg. *Scr. Mater.* 45(10):1147–1153.
13. G.L. Hao, F.S. Han, W.D. Li (2009) Processing and mechanical properties of magnesium foams. *J. Porous Mater.* 16(3):251–256.
14. J. Shen, Y. Feng, S.-l. Wang, Y. Xu, X.-b. Zhang (2006) Processing of Biocompatible Porous Magnesium and Study on its Mechanical Property. *[J] Met. Funct. Mater.* 3:003.
15. H. Zhuang, Y. Han, A. Feng (2008) Preparation, mechanical properties and in vitro biodegradation of porous magnesium scaffolds. *Mater. Sci. Eng., C* 28(8):1462–1466.
16. J.O. Gil Posada, P.J. Hall (2014) SANS characterization of porous magnesium for hydrogen storage. *Int. J. Hydrogen Energy* 39(16):8321–8330.
17. S. Dutta, K.B. Devi, M. Roy (2017) Processing and degradation behavior of porous magnesium scaffold for biomedical applications. *Adv. Powder Technol.* 28(12):3204–3212.
18. N. Zou, Q. Li (2018) Mechanical Properties of Lightweight Porous Magnesium Processed Through Powder Metallurgy. *JOM* 70(5):650–655.
19. D. Wu, F. Xu, B. Sun, R. Fu, H. He, K. Matyjaszewski (2012) Design and preparation of porous polymers. *Chem. Rev.* 112(7):3959–4015.
20. H.Y. Hsueh, Y.C. Huang, R.M. Ho, C.H. Lai, T. Makida, H. Hasegawa (2011) Nanoporous gyroid nickel from block copolymer templates via electroless plating. *Adv. Mater.* 23(27):3041–3046.
21. H. Kim, Y. Kim (2009) Preparation of nanoporous gold using PS bead, Ludox and nanoporous alumina as physical templates. *Curr. Appl. Phys.* 9(1):S88–S90.
22. P. Bartlett, J. Baumberg, P.R. Birkin, M. Ghanem, M. Netti (2002) Highly ordered macroporous gold and platinum films formed by electrochemical deposition through templates assembled from submicron diameter monodisperse polystyrene spheres. *Chem. Mater.* 14(5):2199–2208.
23. H. Zou, S. Wu, J. Shen (2008) Polymer/silica nanocomposites: preparation, characterization, properties, and applications. *Chem. Rev.* 108(9):3893–3957.
24. A.T. Rodriguez, M. Chen, Z. Chen, C.J. Brinker, H. Fan (2006) Nanoporous carbon nanotubes synthesized through confined hydrogen-bonding self-assembly. *J. Am. Chem. Soc.* 128(29):9276–9277.
25. S. Shivkumar, X. Yao, M. Makhlof (1995) Polymer-melt interactions during casting formation in the lost foam process. *Scr. Metall. Mater.* 33(1).
26. N. Zou, Q. Li (2018) Effect of Compaction Pressure and Magnesium Weight Fraction on Hardness of Recycled-Polystyrene Matrix Composite. *JOM* 70(8):1454–1458.
27. J. Rieger (1996) The glass transition temperature of polystyrene: results of a round robin test. *J. Therm. Anal. Calorim.* 46(3–4):965–972.
28. A. Singha, R.K. Rana (2013) Fabrication of polystyrene/agave particle biocomposites using compression molding technique: evaluation of flammability, biodegradability, mechanical and thermal behaviour. *Bull. Mater. Sci.* 36(7):1207–1216.
29. L.J. Gibson (1985) The mechanical behaviour of cancellous bone. *Journal of biomechanics* 18(5):317–328.
30. P. Zhang, S.X. Li, Z.F. Zhang (2011) General relationship between strength and hardness. *Mater. Sci. Eng., A* 529:62–73.



---

## Correction to: Effects of Zn Additions on the Room Temperature Formability and Strength in Mg–1.2Al–0.5Ca–0.4Mn Alloy Sheets

Z. H. Li, T. T. Sasaki, M. Z. Bian, T. Nakata, Y. Yoshida, N. Kawabe, S. Kamado, and K. Hono

---

### Correction to:

Chapter “Effects of Zn Additions on the Room Temperature Formability and Strength in Mg–1.2Al–0.5Ca–0.4Mn Alloy Sheets” in: J. B. Jordon et al. (eds.), *Magnesium Technology 2020, The Minerals, Metals & Materials Series*, [https://doi.org/10.1007/978-3-030-36647-6\\_18](https://doi.org/10.1007/978-3-030-36647-6_18)

The original version of this chapter was inadvertently published with incorrect Figure.

Author provided figure corrections has been updated: Figure 4 has been removed and remaining figures are renumbered.

The Chapter and book have been updated with the changes.

---

The updated version of this chapter can be found at [https://doi.org/10.1007/978-3-030-36647-6\\_18](https://doi.org/10.1007/978-3-030-36647-6_18)

© The Minerals, Metals & Materials Society 2020  
J. B. Jordon et al. (eds.), *Magnesium Technology 2020*, The Minerals, Metals & Materials Series, [https://doi.org/10.1007/978-3-030-36647-6\\_58](https://doi.org/10.1007/978-3-030-36647-6_58)



---

## Author Index

### A

Abbott, Trevor B., 289  
AbdelGawad, M., 243  
Abdullah, Aboubakr M., 253  
Agnew, Sean R., 115  
Ahmad, Rasool, 19  
Ali, Yahia, 289  
Allison, John, 25  
Allison, John E., 175  
Arul Kumar, M., 123  
Asle Zaeem, Mohsen, 51

### B

Bae, Jun Ho, 347  
Bahgat, Ahmed, 253  
Barrett, Christopher D., 129, 141  
Barriobero-Vila, P., 37  
Baweja, Shahmeer, 321  
Behraves, B., 151  
Berman, Tracy D., 175  
Beura, V.K., 217  
Beyerlein, I.J., 123  
Bhattacharyya, Jishnu J., 115  
Bian, M.Z., 105  
Bilal, M.U., 281  
Bohlen, Jan, 87, 181, 329

### C

Cain, T.W., 43  
Capolungo, Laurent, 3  
Caris, Josh, 61  
Celikin, Mert, 335  
Chang, Zhi-Min, 299, 309  
Cheng, Jun, 361  
Cheng, Ting, 269  
Chen, Houwen, 71  
Chen, Tao, 55  
Chou, Kuo-Chih, 101  
Curtin, W.A., 19  
Czerwinski, F., 371

### D

Dang, Khanh, 3  
Dawson, Paul, 147  
Dong, Xixi, 31

Dou, Zhi'he, 303, 313

### E

El Kadiri, Haitham, 141  
Eswarappa Prameela, Suhas, 163, 167

### F

Falk, Michael L., 167  
Frankel, G.S., 215  
Fu, Daxue, 303, 313

### G

Gabbardo, Aline D., 215  
Garg, P., 217  
Gavras, S., 37, 281  
Geng, Xinyu, 259  
Goeda, Ryutaro, 381  
Gotawala, Nikhil, 197, 341  
Graham, John, 3  
Gryguć, A., 151  
Guo, Baoqi, 335  
Guo, Junhua, 303, 313  
Gupta, Manoj, 253

### H

Han, Jibiao, 303, 313  
Hono, K., 105  
Horkey, Jelena, 235  
Horstemeyer, Mark F., 13  
Hort, Norbert, 79, 281  
Huang, Guangsheng, 15  
Hu, Henry, 259

### I

Ikeo, Naoko, 381  
Indurkar, Padmeya P., 321

### J

Jahed, H., 151  
Javaid, A., 371  
Jiang, Bin, 15  
Jiang, Xianquan, 79

Ji, Shouxun, 31  
 Ji, Zonghui, 303, 313  
 Joshi, Shailendra P., 321  
 Joshi, V.V., 217

**K**

Kainer, Karl Ulrich, 181, 329  
 Kamado, S., 105  
 Kappagantula, Keerti, 207  
 Karaman, I., 243  
 Karparvarfard, S.M.H., 151  
 Kasemer, Matthew, 147  
 Kawabe, N., 105  
 Kecskes, Laszlo J., 167  
 Kim, Gyuseok, 355  
 Kim, Ha Sik, 225  
 Kim, Manjin, 289  
 Kim, Nam Ryong, 225  
 Kim, Young Min, 347  
 Korgiopoulos, Konstantinos, 95  
 Kumar, Abhishek, 197, 341  
 Kumar, Mariyappan Arul, 3  
 Kumar, Subodh, 189  
 Kurz, G., 181

**L**

Labukas, J. P., 43  
 Lebensohn, Ricardo A., 115  
 Lee, Sang Eun, 347  
 Letzig, Dietmar, 87, 181, 329  
 Leu, B., 123  
 Li, Bin, 135  
 Li, Dajian, 55  
 Li, Jiao, 299, 309  
 Lilleodden, Erica T., 355  
 Li, Qian, 101  
 Li, Qizhen, 387  
 Liu, Bo-Yu, 135, 231, 299, 309  
 Liu, Fei, 135, 299, 309  
 Liu, Jiawei, 55  
 Liu, Vance, 167  
 Liu, Weili, 79  
 Liu, Yue, 3, 123  
 Li, Z.H., 105  
 Luo, Alan A., 61  
 Luo, Qun, 101

**M**

Maghsoudi, Mohammadhadi, 355  
 Mahata, Avik, 51  
 Mansoor, B., 243  
 Mao, Lu-Yao, 299  
 McCabe, Rodney J., 3  
 McDonald, Stuart D., 289  
 Medeiros, Beatriz, 167  
 Meier, Janet, 61  
 Mishra, Rajiv S., 7  
 Mishra, Sushil, 197, 341  
 Moon, Byoung-Gi, 347  
 Mukai, Toshiji, 381  
 Murugan, Srinivasan, 253

**N**

Nakata, T., 105  
 Nakatsuji, Tatsuya, 381  
 Nicolosi, Matteo, 335  
 Nie, Jian-Feng, 71, 135  
 Nienaber, Maria, 181, 329  
 Nie, Xueyuan, 259  
 Nogita, Kazuhiro, 289  
 Nyberg, Eric A., 31

**O**

Ojdanic, Andrea, 235  
 Okonkwo, Paul C., 253  
 Orlov, Dmytro, 235

**P**

Pan, Fusheng, 15, 55  
 Parande, Gururaj, 253  
 Paudel, YubRaj, 141  
 Pegkuleryuz, Mihriban, 95, 335  
 Perez, Robert, 321

**R**

Rätzke, Klaus, 87  
 Reinwalt, Bastien, 235  
 Ren, Luyang, 259  
 Ritzo, Michael A., 115  
 Roostaei, A., 151

**S**

Sasaki, T.T., 105  
 Schafler, Erhard, 235  
 Schell, N., 37  
 Schmid-Fetzer, Rainer, 71  
 Shaha, S., 151  
 Shang-guan, Jing-jing, 361  
 Shan, Zhi-Wei, 135, 231, 299, 309  
 Shi, Hui, 101  
 Shi, Qianying, 25  
 Shrivastava, Amber, 197, 341  
 Solanki, K.N., 217  
 Song, Jiangfeng, 15  
 Sood, Aarush, 197, 341  
 Stark, A., 37  
 Suh, Byeong-Chan, 225, 347  
 Suh, Joung Sik, 347  
 Sun, Jingli, 79  
 Sun, Zixi, 259  
 Suwas, Satyam, 189

**T**

Tang, Aitao, 55  
 Tang, Pengzhang, 3  
 Tang, Yao, 361  
 Tayeb-Bey, Ilyes, 235  
 Tolnai, D., 37, 281  
 Tomé, Carlos N., 3  
 Toscano, D., 151  
 Trinh, Huu Chanh, 87

**U**

Upadhyay, Piyush, [207](#)

**V**

Vaughan, M.W., [243](#)  
Verma, Krishna Kamlesh, [189](#)  
Victoria-Hernández, Jose, [329](#)  
Vuppuluri, Amol, [321](#)

**W**

Wadsö, Lars, [235](#)  
Wang, Shujuan, [3](#)  
Wang, Tianhao, [207](#)  
Wang, Yue-Cun, [231](#)  
Weihs, Timothy P., [163](#), [167](#)  
Whalen, Scott, [207](#)  
Williams, Bruce, [25](#)  
Woo, Sang Kyu, [225](#)  
Wu, Jiajia, [55](#)  
Wu, Zhaoxuan, [19](#)

**X**

Xiao, Lu, [79](#)

Xu, Yuling, [79](#)

**Y**

Yamaguchi, Masatake, [381](#)  
Yang, Bo, [299](#), [309](#)  
Yang, Li, [55](#)  
Yang, Lixiang, [79](#)  
Yim, Chang Dong, [225](#)  
Yin, Binglun, [19](#)  
Yi, Peng, [167](#)  
Yi, Sangbong, [87](#), [329](#)  
Yoshida, Y., [105](#)  
Yuan, Yuan, [55](#)

**Z**

Zehetbauer, Michael, [235](#)  
Zhang, Dingfei, [15](#)  
Zhang, Jieyu, [101](#)  
Zhang, Lijun, [269](#)  
Zhang, Ting'an, [303](#), [313](#)  
Zhao, Jian-hua, [361](#)  
Zhao, Xiaojun, [71](#)  
Ziehmer, Markus, [355](#)  
Zou, Ning, [387](#)

# Subject Index

- A**  
Age-hardening, 37, 47, 71, 335, 336, 371, 377  
Age-hardening treatment, 337  
Aging response and precipitation, 28  
Alloy, 7–9, 13, 15, 25–32, 35, 37, 38, 40–47, 55–58, 61–63, 66, 68, 71–73, 76, 77, 79–81, 83, 87–90, 92, 93, 95–99, 101, 103–111, 120, 135, 142, 151–153, 157, 167, 168, 172, 175, 181, 182, 186, 189, 190, 195–197, 217, 219, 221, 226, 229, 236, 238–241, 243, 244, 246–250, 253, 254, 256, 257, 259–265, 269, 271, 277, 281, 283, 287, 290, 292, 295, 303, 329–333, 335–338, 348, 371–373, 375, 378, 381, 383, 384  
Alloy casting, 372  
Al–Zn–Sn, 274–277  
Analyses of corrosion surface, 260  
Analyses of reaction principle under atmospheric pressure, 310  
Anisotropy, 15, 89, 90, 116, 118, 141, 142, 147, 283, 321, 322, 324–328, 332, 333, 347, 355  
Anti-corrosion, 55, 231, 232  
Application of a two-stage settling treatment in synthesis and purification of AZ91 alloy, The, 58  
As-cast microstructure, 26, 27, 29, 38, 72, 176, 190, 245, 335, 373  
Asymmetric rolling, 189, 190  
Atmospheric pressure, 309–311  
AZ91, 13, 31, 55–58, 95, 96, 217, 262, 281–285, 287, 364
- B**  
Bake-hardening, 105, 106  
Base materials, 208  
Biodegradation, 244, 253, 254
- C**  
Calcination, 303–308  
Calcium, 87, 93, 244, 253, 301, 303, 304, 310, 331, 335  
CALculation of PHase Diagrams (CALPHAD), 25–27, 29, 61, 62, 66–68, 101, 269, 273, 274, 276, 282  
Calculation of settling velocity of precipitates with density and temperature dependence, 56  
Calculation of stress-strain relation, 382  
Calculation of the Jackson parameter of the intermetallic phases in hypo-eutectic Mg-based alloys, 291  
Carbon Fiber Reinforced Polymer (CFRP), 207–211  
Cathodic particles, 217, 219–222  
Characterization of the feedstock material, 182  
Climb, 115–118, 120, 121, 132  
Composites preparation, 260  
Compressive response, 324  
Condensation microstructure, 314  
Configuration of the testing machine, 383  
Corroded surfaces and corrosion mechanisms, 262  
Corrosion, 9, 13, 14, 37, 43–47, 55, 64, 147, 181, 215–222, 225–236, 238–241, 243–245, 249, 250, 253, 254, 256, 257, 259–265, 335, 371  
Corrosion resistance, 7, 31, 32, 37, 43, 47, 55, 151, 181, 217, 225, 227, 229, 231, 233, 241, 244, 250, 253, 256, 257, 259–261, 263–265, 269, 299, 335, 361, 362  
Crystallographic texture, 118, 175, 190, 194  
Crystallographic texture evolution, 193  
Crystal plasticity, 116, 120, 123, 124, 141–144, 147, 321, 359  
Crystal structure, 8, 15, 43–45, 98, 185, 189, 306, 307, 321, 337, 381
- D**  
Data sets and descriptive statistics, 348  
Defects, 51, 53, 79, 123, 129–133, 136, 141, 142, 197–204, 217, 253, 263, 295, 341, 342, 344–346  
Deformation, 9, 15, 37, 40–43, 51, 87, 88, 91–93, 110, 115–118, 120, 123–125, 129, 138, 141–144, 147–149, 151–154, 157, 167, 175–177, 185, 187, 189–191, 195, 204, 207, 217–220, 233, 244, 246, 250, 321, 322, 324–331, 333, 335–338, 347, 352, 355–358, 382–384  
Deformation behavior, 37, 141, 147, 167, 232, 381, 384, 385  
Deformation mechanism, 5, 8, 42, 87, 110, 115, 118, 141, 152, 153, 155, 157, 329, 331, 333, 381–384  
Deformation twins, 107, 123, 142, 147  
Degradation, 235, 236, 239–241, 243, 253, 254, 256, 257, 335  
Determination of iron solubility in the AZ91 melt, 56  
Die cast-ability, 32, 33  
Die-cast magnesium piston, 34  
Diffraction, 26, 37, 38, 40–42, 44, 61, 62, 71–73, 80, 88, 101, 106, 117, 123, 124, 129, 175, 176, 189, 190, 198, 226, 227, 232, 253, 260, 272, 295, 306, 317, 356, 365, 388  
Digital twin, 281, 282  
Disintegrated Melt Deposition (DMD), 253, 254  
Dislocation, 9, 25, 40, 61, 83, 111, 115, 116, 118, 120, 121, 123, 124, 126, 127, 129–133, 135, 137, 138, 142, 153, 171, 217, 233, 329, 337, 348, 355, 358, 359, 384  
Ductility, 19–23  
Ductility enhancement via accelerated cross-slip, 20  
Dynamic precipitation, 349
- E**  
Effect of briquetting pressure on pellet properties, 305  
Effect of heat treatment on alloy microstructure and hardness, 375



- Effect of magnesite grain size on pellet properties, 305  
 Effect of misorientation variation on boundary migration, 126  
 Effect of second phase particle fragmentation and separation, 220  
 Effect of second phase particle separation, 219  
 Effect of second phase particle size, 167, 218, 219  
 Effect of solidification rate and Zn content on alloy microstructure, 373  
 Effect of temperature and time on pellet properties, 306  
 Effect of tool pin design, 202  
 Effect of tool rotation direction, 203  
 Effect of tool shoulder overlap, 197, 203  
 Effect of Zn on alloy strength after hot rolling, 375  
 Electrochemical corrosion measurement, 250  
 Electrochemical experimentation, 260  
 Electrochemical Impedance Spectroscopy (EIS), 243–245, 249, 250, 253, 254, 256, 257  
 Electrochemical testing, 44, 245  
 Electrochemical tests, 215, 245, 260, 264  
 Energy as a fatigue damage parameter, 154  
 Equilibrium phase formation in heat treatment simulation, 73  
 Erichsen value, 105, 330, 333  
 Eutectic modification, 289, 290, 292, 295  
 Experimental setup and process parameters, 208  
 Experimental techniques, 80, 235  
 Experiments with tapered tool, 201  
 Experiments with threaded tool, 201  
 Extrusion, 9, 15, 29, 152, 154, 157, 167–169, 181, 182, 184–187, 217, 218, 222, 225, 226, 229, 230, 243–250, 254, 290, 329–332, 348, 349
- F**  
 Flowing argon, 303–305, 307, 309–311  
 Formability, 7, 25, 37, 43, 87, 88, 91–93, 105, 106, 110, 120, 135, 175, 179, 189, 190, 195, 197, 207, 211, 225, 231, 321, 329, 333, 347, 371  
 Formation mechanism of the interface zone, 364  
 Fragmentation, 217, 218, 220–222  
 Friction Stir Processing (FSP), 7, 9, 197, 201, 341, 342, 344, 346  
 Friction stir processing as a microstructural engineering tool, 9
- G**  
 Germanium, 44  
 Gleeble, 175, 176, 179  
 Glide, 116–118, 120, 121, 123, 124, 135, 137, 138, 142, 144  
 Grain refinement, 15, 167, 175–177, 179, 197, 204, 205, 217, 263, 347–349
- H**  
 HCP crystal plasticity, 322  
 HCP materials, 129, 130  
 Heat treatment, 26–29, 62, 75, 77, 80, 181–184, 217, 219, 225, 226, 228–230, 243–247, 250, 290, 372, 375, 377  
 High pressure die casting, 31–35  
 High purity, 55, 58, 102, 225, 227, 229, 299, 301, 309–311, 317, 318, 355, 390  
 Hot-dip aluminum coating, 362, 366  
 Hydrogen absorption kinetics, 289, 290, 292, 295, 296  
 Hydrogen storage properties, 289, 295
- I**  
 ICME, 71  
 Immersion testing, 235–239, 241  
 Impurity, 47, 55, 230, 290, 292, 299–301, 388
- Inert gas, 309, 313, 317  
 Influence of heat treatment on alloy hardness, 375  
 Influence of the extrusion temperature and speed on mechanical properties, 187  
 Influence of the extrusion temperature and speed on microstructure, 184  
 Influence of the extrusion temperature and speed on texture, 186  
 Influence of the feedstock properties, 184  
 Initial condensation temperature, 313, 314, 316, 318  
 In-situ TEM, 120, 135–138  
 Intermediate compound, 362  
 Iron, 55–59, 181, 262, 301, 363, 364, 366, 371, 381  
 Isothermal calorimetry, 235–237, 239, 241
- L**  
 Light-weighting, 197, 207, 371  
 Lithium, 43, 44  
 Localized corrosion, 44, 46, 217–219, 222, 244, 263  
 Local stresses, 123, 124, 127  
 Long Period Stacking Order (LPSO), 61–63, 65–68  
 Low cost, 79, 269, 310  
 Low cycle fatigue, 152, 153
- M**  
 Magnesium, 7, 9, 13–15, 31–35, 43, 44, 79, 87, 88, 93, 95, 96, 105, 117, 123, 135, 136, 138, 147, 151, 167, 168, 181–183, 197, 207, 211, 215, 217, 231–235, 240, 243, 244, 253, 259, 263, 270–272, 289, 290, 299–305, 307, 309–311, 313–318, 321, 329, 341, 343, 347, 361, 363, 364, 366, 371, 372, 375, 381, 384  
 Magnesium alloy (Mg alloy), 5, 7–9, 13–15, 20, 23, 25, 28, 31–35, 37, 43–47, 55, 56, 58, 61, 71, 73, 77, 79, 80, 83, 87, 89, 93, 95, 101, 105, 115–120, 123, 135, 151–154, 157, 167, 175–177, 179, 181, 182, 185, 187, 189, 195–198, 203, 204, 207, 211, 215, 217–220, 222, 225, 229–231, 235, 237, 238, 240, 241, 243–245, 250, 253, 254, 256, 259–262, 264, 269, 271, 276, 281, 286, 289, 299, 303, 321–324, 326, 327, 329, 335, 347–349, 352, 361, 362, 364, 366, 367, 371–373, 375, 377, 381  
 Magnesium-Based Hybrid Nanocomposite (MHNC), 260–265  
 Magnesium carbonate, 231, 233  
 Magnesium sheet, 207, 371, 375  
 Magnesium vapor, 300, 303, 309, 310, 313–317  
 Material preparation, 32  
 Materials, 7, 30, 38, 42, 43, 55, 56, 58, 79, 83, 95, 101, 105, 124, 129, 130, 135, 141, 143, 147, 152–154, 157, 176, 187, 197, 198, 207, 208, 211, 217, 229, 231, 236, 241, 243, 244, 253, 254, 259–261, 281, 289, 296, 303, 309, 310, 314, 322, 324–327, 335, 348, 361, 362, 381–383, 387  
 Materials processing and microstructural characterization, 44  
 Mechanical behavior, 37, 138, 355, 390  
 Mechanical characterization, 211  
 Mechanical properties, 7, 9, 15, 31, 34, 61, 79, 83, 89, 90, 96, 97, 105, 106, 110, 123, 135, 151, 181, 182, 187, 197, 207, 208, 217, 244–246, 248, 253, 254, 259, 269, 329, 332, 333, 335, 347, 348, 352, 361, 362, 367, 372, 377, 381, 387  
 Mechanism of RHR, 209, 211  
 Melting and solidification characteristics, 373  
 Methods, 13, 37, 38, 44, 56, 62, 95, 116, 117, 135, 141, 143, 152, 176, 207, 208, 222, 235, 236, 238, 241, 244, 254, 282, 289, 303, 310, 348, 361, 367, 382  
 Mg–Al, 25, 31, 32, 51, 95–99, 120, 167, 168, 172, 262, 270–272, 274, 277  
 Mg alloys, 129, 142  
 Mg–Al–Sn, 269, 272–274, 276, 277  
 Mg–Al–Zn, 87, 95, 105, 269, 271–273, 276, 277  
 Mg–Al–Zn–Sn, 269, 270, 275–278

- Mg–La–Zn alloys, 101–104  
Mg–RE alloy, 25, 28  
Mg–Sn, 189, 270–273, 275, 277  
Mg–Zn, 175, 244, 256, 270–273, 277, 335, 336, 371–373, 377  
Mg–Zn–Sn, 273–277  
Micro-galvanic corrosion, 217, 219, 228–230  
Microhardness of the interface zone, 361, 366  
Micromechanics, 141, 321  
Micron-sized alumina (Al<sub>2</sub>O<sub>3</sub>) short fibre, 259  
Microstructural analysis, 62, 64, 67, 190, 199, 209, 244, 245, 283, 330  
Microstructural characterization, 26, 198, 208, 342, 356, 362, 373  
Microstructural characterization by EBSD, 191  
Microstructural efficiency and alloying efficiency, 8, 9  
Microstructural evolution, 25, 26, 129, 197, 203, 204, 244  
Microstructure, 8, 9, 13, 15, 25–29, 37, 38, 41, 44, 45, 61, 64, 71, 79, 80, 87–89, 91–93, 95, 96, 98, 101, 102, 105–107, 110, 117, 123–125, 129, 135, 141–144, 151–153, 167–169, 171, 177, 178, 181–185, 189, 190, 192, 197, 203, 204, 225, 228, 229, 233, 239, 241, 243–247, 250, 262, 264, 269, 272, 281–283, 286, 289–292, 295, 296, 313, 317, 318, 321, 329–331, 336, 347, 348, 352, 361–363, 367, 372, 373, 375–378, 387–389  
Microstructures and compositions, 363  
Microstructures of as-cast Mg–La–Zn alloys, 103  
Misorientation, 4, 41, 42, 123–127, 130–132, 142, 191  
Model, 13, 15, 27, 51, 61–63, 67, 116, 117, 120, 121, 123–127, 141, 142, 144, 147, 218, 235, 236, 269, 270, 273, 275, 281–283, 349–352, 363  
Model development, 218, 348  
Model formulation, 322  
Modeling and experimental methods, 62  
Modeling background, 116  
Multiple regression analysis, 347, 348, 350–352
- N**  
Nano-sized alumina (Al<sub>2</sub>O<sub>3</sub>) particles, 259  
Non-proportional loading, 157  
Nucleation and growth, 92, 167, 171, 313, 338, 355, 371, 372  
Numerical calculations, 124
- O**  
Open circuit potential, 43, 44, 243–245, 248, 260  
Origin of twin misorientation variation, 126
- P**  
Passivity, 44, 47  
Performance criteria, 349, 351  
Phase analysis and microstructural characterization, 190  
Phase field and 3D molecular dynamic simulations, 3, 4  
Pidgeon process, 299, 303, 309, 310  
Plastic anisotropy, 115, 147, 321, 322, 328, 381, 384  
Plasticity, 115–118, 120, 123–127, 129, 130, 135, 138, 147, 148, 155, 157, 259, 321, 322, 326, 361  
Polycrystalline aggregate FEM model, 322  
Polystyrene, 387  
Porous magnesium, 387  
Potentiodynamic polarization curves, 45, 249, 260  
Powder metallurgy, 231, 233, 234, 387, 388, 390  
Precipitation, 8, 9, 25, 28, 29, 47, 63, 95, 102, 167, 170, 172, 182, 183, 225, 228, 229, 240, 244, 247, 263, 335, 337, 338, 348, 372, 375, 377  
Prefabricated pellets, 303–305  
Pressure measurements, 236, 240, 241  
Processing history, 179, 230  
Property and microstructure characterization, 373  
Purification, 44, 55, 57, 58, 299
- Q**  
Quenching, 26, 106, 281, 283, 285, 372
- R**  
Rare earth, 25, 31, 35, 37, 47, 61, 71, 79, 87, 89, 96, 175, 181, 182, 187, 244, 269, 289, 329, 371, 372, 375, 377  
Raw materials, 62, 96, 101, 260, 304, 310, 312, 388  
Recrystallization, 37, 42, 87, 88, 91–93, 105, 107, 108, 110, 167–172, 175–177, 185, 187, 192, 197, 204, 205, 331  
Regression analysis, 348, 349  
Representative results, 22  
Rivet appearance and microstructure, 210  
Riveting, 207, 208, 210, 211  
Role of alloying elements of Nd and Zn in Mg sheet development, 375  
Rolling, 44, 87, 88, 105, 106, 110, 117, 124, 135, 152, 167, 175, 176, 178, 179, 182, 187, 189–191, 193, 195, 321, 322, 324–329, 347, 372, 373, 375, 378
- S**  
Sample preparation and characterization, 209  
Scheil simulation, 277, 278  
Scheil solidification simulation of as-cast state, 76, 77  
Secondary Dendrite Arm Spacing (SDAS), 373, 375, 376  
Secondary phases, 38, 39, 61, 65, 77, 243, 246–250, 333, 335  
Shear strength, 361, 362, 367  
Sheet rolling, 372  
Silicothermic, 309  
Silicothermic process, 303, 304, 309, 313  
Silver, 243, 244, 250  
Simulated Body Fluid (SBF), 235–241, 253, 254, 256, 257  
Simulation of casting process, The, 362  
Solid–liquid compound casting, 361, 362, 364  
Solution heat treated microstructure, 27, 28  
Split-Hopkinson Pressure Bar (SHPB), 381–383  
Statistical EBSD analysis of twin sections, 3, 4  
Strain rate dependence, 381, 383  
Synchrotron radiation, 37, 38, 40, 41
- T**  
Tensile elongation, 83, 95  
Tensile properties, 32–34, 96, 98, 107, 189, 191, 195, 196, 349, 372, 375, 377, 378  
Tensile properties at elevated temperatures, 33  
Tensile response, 322  
Tensile tests at room and elevated temperatures, 32  
Testing apparatus, 382  
Testing material and conditions, 383  
Texture, 8, 9, 15, 25, 28, 29, 37, 43, 87–89, 92, 93, 105–111, 115–118, 121, 124, 141, 142, 151, 152, 167, 169, 175, 177–179, 182, 186, 187, 189–191, 193–196, 217, 321–324, 327–333, 347–349, 351, 352, 371, 375  
Texture evolution, 9, 37, 106, 107, 115–118, 120, 141, 147, 151, 154, 175, 327, 347  
Texture weakening, 28, 87, 182, 347, 348  
Theory, 19–23  
Thermal analysis, 272, 372, 373  
Thermal conductivity, 31, 32, 101–104, 259  
Thermodynamical Processing (TMP), 175, 176, 178, 179, 225  
Thermodynamic assessment, 72, 73, 270, 271, 274

Thermodynamic calculations, [26](#), [29](#), [95](#), [96](#), [98](#), [101](#), [271](#), [349](#)  
Thermodynamic modeling, [71](#), [72](#)  
Thermodynamic models, [275](#)  
Thermodynamics, [235](#), [236](#), [241](#), [269](#), [282](#), [289](#), [300](#)  
Thermodynamic simulation of QEZ alloys in the Mg–Ag–Nd–Zn system, [73](#)  
Tool design, [197](#), [198](#), [203](#), [208](#)  
Tool path strategy, [197](#), [198](#), [204](#)  
Twinning, [5](#), [8](#), [37](#), [40–42](#), [87](#), [116](#), [120](#), [123–127](#), [129](#), [130](#), [132](#), [133](#), [138](#), [141–144](#), [147–149](#), [151–155](#), [157](#), [168](#), [169](#), [175](#), [289](#), [290](#), [292](#), [295](#), [321–329](#), [355–359](#)

Twin-roll casting, [105](#)  
Two-stage isothermal treat of AZ91 alloy, [56](#)  
Two-stage settling treatment in synthesis and purification of AZ91 alloy, [56](#)

## W

Work hardening, [7](#), [9](#), [358](#), [359](#), [383](#), [384](#)